



This book is provided in digital form with the permission of the rightsholder as part of a Google project to make the world's books discoverable online.

The rightsholder has graciously given you the freedom to download all pages of this book. No additional commercial or other uses have been granted.

Please note that all copyrights remain reserved.

#### **About Google Books**

Google's mission is to organize the world's information and to make it universally accessible and useful. Google Books helps readers discover the world's books while helping authors and publishers reach new audiences. You can search through the full text of this book on the web at <http://books.google.com/>

# ME RD'19

## PROCEEDINGS OF MECHANICAL ENGINEERING RESEARCH DAY 2019

[www3.utm.edu.my/care/proceedings](http://www3.utm.edu.my/care/proceedings)

**31 July 2019 | Kampus Teknologi UTeM**

Edited by:  
**Mohd Fadzli Bin Abdollah**

**First published 2019**

Copyright © 2019 by Centre for Advanced Research on Energy (CARe)

All rights reserved. No part of this publication may be reproduced, stored in a retrieval system, or transmitted, electronic, mechanical photocopying, recording or otherwise, without the prior permission of the Publisher.

**ISBN: 978-967-2145-65-3 (online)**

**Published and Printed in Malaysia by:**

Centre for Advanced Research on Energy,

Faculty of Mechanical Engineering, Universiti Teknikal Malaysia Melaka,

Hang Tuah Jaya, 76100 Durian Tunggal, Melaka, MALAYSIA.

Tel: +606 270 4335 | E-mail: care@utem.edu.my

[www.utem.edu.my/care](http://www.utem.edu.my/care)

# Preface

This open access e-proceedings contains a compilation of 161 selected papers from the 6<sup>th</sup> Mechanical Engineering Research Day (MERD'19) that was held at Kampus Teknologi UTeM, Melaka, Malaysia, on 31 July 2019. The event was jointly organized by the Faculty of Mechanical Engineering and Centre for Advanced Research on Energy, Universiti Teknikal Malaysia Melaka. This year, MERD is also be co-organized by Sekolah Tinggi Teknologi Bandung (STTB), and Performance of Rolling Bearings Laboratory, Shanghai University (ShU).

It was gratifying to all of us when the response for MERD'19 is overwhelming as the technical committees received almost 200 submissions from various areas of mechanical engineering and related fields to facilitate the mutual understanding of fundamentals, theory and applications including Automotive and Aeronautics, Additive Manufacturing, Advanced Materials and Processes, Computer Modeling and Simulation, Condition Based Maintenance and Monitoring, Energy Engineering and Management, Engineering Education, Mechanical Design and Optimization, Mechanical Vibration and Control, Structural and Mechanical Testing, Surface Engineering and Tribology, Thermal and Fluids. All submitted papers are then peer-reviewed, revised according to the reviewers' comments and ultimately 161 papers were accepted for publication in this proceeding. This open access e-proceedings can be viewed or downloaded via [www3.utem.edu.my/care/proceedings](http://www3.utem.edu.my/care/proceedings). We hope that this proceeding will serve as a valuable reference for researchers.

With the large number of submissions, the event has achieved its main objective which is to bring together educators, researchers and practitioners to share their findings and perhaps sustaining the research culture in the university and industry.

As the editor-in-chief, I would like to express our gratitude to the fellow review members for their tireless effort in reviewing the submitted papers for this proceeding. I also would like to say special thanks to all the authors for promptly revising their papers according to the proceeding requirements. Special thanks are extended to the organizer of the MERD'19.

Thank you

*Mohd Fadzli Bin Abdollah*

Editor-in-Chief

# **Editorial Board**

## **Editor-in-Chief**

Mohd Fadzli Bin Abdollah - Universiti Teknikal Malaysia Melaka, Malaysia

## **Editorial Board Members**

Hilmi Amiruddin - Universiti Teknikal Malaysia Melaka, Malaysia

Rainah Ismail - Universiti Teknikal Malaysia Melaka, Malaysia

Ahmad Rivai - Sekolah Tinggi Teknik Bandung, Indonesia

Xiaoyang Chen - Shanghai University, China

# Reviewers

Abd Rahman Dullah - UTeM, Malaysia  
Abdelrafe M. Elzamly - Alaqsa University, Palastine  
Abdul Mutualib Leman - UTHM, Malaysia  
Abdul Rafeq Saleman - UTeM, Malaysia  
Abdul Talib Din - UTeM, Malaysia  
Abu Bakar Sulong - UKM, Malaysia  
Abu Ubaidah Shamsudin - UTHM, Malaysia  
Afiqah Omar - MIROS, Malaysia  
Ahmad Rivai - Sekolah Tinggi Teknologi Bandung, Indonesia  
Ahmad Anas Yusof - UTeM, Malaysia  
Ahmad Fuad Ab Ghani - UTeM, Malaysia  
Ahmad Qushairi Mohamad - UTM, Malaysia  
Ahmad Yusuf Ismail - Institut Teknologi Adhi Tama Surabaya, Indonesia  
Aidah Jumahat - UiTM, Malaysia  
Akiyuki Takahashi - Tokyo University of Science, Japan  
Amiril Sahab Abdul Sani - UMP, Malaysia  
Amrik Singh Phuman Singh - UTeM, Malaysia  
Anita Akmar Kamarolzaman - UTeM, Malaysia  
Asmalina Mohamed Saat - UniKL, Malaysia  
Athif Faudzi - UTM, Malaysia  
Azlin Fazlina Osman - UniMAP, Malaysia  
Azma Putra - UTeM, Malaysia  
Azmi Ahmad - Kementerian Belia dan Sukan, Malaysia  
Aznifa Mahyam Zaharudin - UiTM, Malaysia  
Baljit Singh - UKM, Malaysia  
Boon Tuan Tee - UTeM, Malaysia  
Chan Choon Kit - INTI International University, Malaysia  
Che Ku Eddy Nizwan Che Ku Husin - UMP, Malaysia  
Cheng See Yuan - UTeM, Malaysia  
Chow Khoon Keat - UTeM, Malaysia  
De Pretto Laura - Leeds Trinity University, United Kingdom  
Erween Abd. Rahim - UTHM, Malaysia  
Fadhlina Che Ros - UPNM, Malaysia  
Fahmi Arif - Institut Teknologi Nasional Bandung, Indonesia  
Faiz Redza Ramli - UTeM, Malaysia  
Fatimah Al-Zahrah Mohd Sa'At - UTeM, Malaysia  
Fauziyah Salehuddin - UTeM, Malaysia  
Fitrian Imaduddin - Universitas Sebelas Maret, Indonesia  
Fudhail Abdul Munir - UTeM, Malaysia  
Hamid Yusoff - UiTM, Malaysia  
Hasan Zuhudi Abdullah - UTHM, Malaysia  
Hermansaputro Hermansaputro - Universitas Sebelas Maret, Indonesia  
Hiew Mun Poon - UTAR, Malaysia  
Hilmi Amiruddin - UTeM, Malaysia  
Intan Sharhida Othman - UTeM, Malaysia  
Jaharah A. Ghani - UKM, Malaysia  
Jong-Ning Aoh - National Chung Cheng University, Taiwan

Juffrizal Karjanto - UTeM, Malaysia  
Juri Saedon - UiTM, Malaysia  
Juwaiddah Sharifuddin - UPM, Malaysia  
Juyana A. Wahab - UniMAP, Malaysia  
Kamarul Arifin Zakaria - UTeM, Malaysia  
Khairil Anas Md Rezali - UPM, Malaysia  
Khairur Rijal Jamaludin - UTM, Malaysia  
Liew Pay Jun - UTeM, Malaysia  
M.M. Noor - UMP, Malaysia  
Mahamad Hisyam Mahamad Basri - UiTM, Malaysia  
Mahanum Zamperi - UTeM, Malaysia  
Maizlinda Izwana Idris - UTHM, Malaysia  
Mariyam Jameelah Ghazali - UKM, Malaysia  
Martin Choirul Fatah - Sekolah Tinggi Teknik, Indonesia  
Masjuri Musa - UTeM, Malaysia  
Mastura Mohammad Taha - UTeM, Malaysia  
Mazian Mohammad - UniSEL, Malaysia  
Mimi Azlina Abu Bakar - UiTM, Malaysia  
Mohamad Ali Ahmad - UiTM, Malaysia  
Mohamad Bashree Abu Bakar - UMK, Malaysia  
Mohamad Firdaus Sukri - UTeM, Malaysia  
Mohamed Nasrul Mohamed Hatta - UTHM, Malaysia  
Mohd Afzanizam Mohd Rosli - UTeM, Malaysia  
Mohd Ahadlin Mohd Daud - UTeM, Malaysia  
Mohd Azman Abdullah - UTeM, Malaysia  
Mohd Fadzli Bin Abdollah - UTeM, Malaysia  
Mohd Faizal Tokeran - Jabatan Tenaga Manusia Malaysia, Malaysia  
Mohd Farid Said - UTM, Malaysia  
Mohd Faridz Mohd Yunoh - MR Technology Sdn. Bhd., Malaysia  
Mohd Fauzi Mamat - UTeM, Malaysia  
Mohd Hafidzal Mohd Hanafi - UTeM, Malaysia  
Mohd Hafis Sulaiman - UniMAP, Malaysia  
Mohd Haizal Mohd Husin - UTeM, Malaysia  
Mohd Helmy Abd Wahab - UTHM, Malaysia  
Mohd Hilmi Othman - UTHM, Malaysia  
Mohd Juzaila Abd. Latif - UTeM, Malaysia  
Mohd Kamaruddin Abd Hamid - UTM, Malaysia  
Mohd Khairi Mohamed Nor - UTeM, Malaysia  
Mohd Rizal Alkahari - UTeM, Malaysia  
Mohd Shahir Kasim - UTeM, Malaysia  
Mohd Shahril Mohd Hassan@Abdul Ghani - Politeknik Muadzam Shah, Malaysia  
Mohd Shawal Jadin - UMP, Malaysia  
Mohd Zaid Akop - UTeM, Malaysia  
Mohd Zaifulrizal Zainol - UniKL, Malaysia  
Mohd Zakaria Mohammad Nasir - UTeM, Malaysia  
Mohd Zuhri Mohamed Yusoff - UPM, Malaysia  
Mohd Zulkefli Selamat - UTeM, Malaysia  
Mohd Zulkifly Abdullah - USM, Malaysia  
Mohdridzwan Ishak - UPM, Malaysia  
Muhammad Khafidh - Universitas Islam Indonesia, Indonesia

Muhammad Hussain Ismail - UiTM, Malaysia  
Muhammad Syafiq Syed Mohamed - UTeM, Malaysia  
Nabilah Ibrahim - UTeM, Malaysia  
Nadlene Razali - UTeM, Malaysia  
Nicholas Kuan Hoo Tien - UNIMAS, Malaysia  
Nidzamuddin Md. Yusof - UTeM, Malaysia  
Noorazizi Mohd Samsuddin - UTM, Malaysia  
Nor Atiqah Zolpakar - UMP, Malaysia  
Nor Azmmi Masripan - UTeM, Malaysia  
Nor Faizah Haminudin - UTeM, Malaysia  
Nor Hisham Jalani - Jabatan Tenaga Manusia, Malaysia  
Noraiham Mohamad - UTeM, Malaysia  
Noreffendy Tamaldin - UTeM, Malaysia  
Norihan Abdul Hamid - UTeM, Malaysia  
Norshahida Sarifuddin - IIUM, Malaysia  
Nortazi Sanusi - UKM, Malaysia  
Nur Azmah Nordin - UTM, Malaysia  
Nur Izan Syahriah Hussein - UTeM, Malaysia  
Nurhidayah Bahar - UM, Malaysia  
Nurin Wahidah Mohd Zulkifli - UM, Malaysia  
Nurul Ain Abdul Latiff - UM, Malaysia  
Priyadarshi Biplab Kumar - National Institute of Technology, India  
Rainah Ismail - UTeM, Malaysia  
Ramdziah Md.Nasir - USM, Malaysia  
Ramli Junid - UMP, Malaysia  
Ratchatin Chancharoen - Chulalongkorn University, Thailand  
Rita Mohd Said - UniMAP, Malaysia  
Safarudin Gazali Herawan - Universitas Bina Nusantara, Indonesia  
Saiful Bahri Mohamed - UNISZA, Malaysia  
Saiful Izwan Abd Razak - UTM, Malaysia  
Saurabh Yadav - Indian Institute of Technology Indore, India  
Shafiz Affendi Mohd Yusof - University of Wollongong in Dubai, UAE  
Shafizal Mat - UTeM, Malaysia  
Shahira Liza Kamis - UTM, Malaysia  
Shajahan Maidin - UTeM, Malaysia  
Shamsuddin Sulaiman - UPM, Malaysia  
Shamsul Anuar Shamsudin - UTeM, Malaysia  
Sharena Mohamad Isa - UNIKL, Malaysia  
Shazarel Shamsudin - UTHM, Malaysia  
Siti Hajar Sheikh Md. Fadzullah - UTeM, Malaysia  
Siti Nor Habibah Hassan - UTeM, Malaysia  
Siti Nurhaida Khalil - UTeM, Malaysia  
Siti Shafiqah Ahmad Shaharuddin - IIUM, Malaysia  
Sivakumar Dhar Malingam - UTeM, Malaysia  
Su Hoe Yeak - UTM, Malaysia  
Susthitha Menon - UKM, Malaysia  
Syaril Azrad Md Ali - UPM, Malaysia  
Toshio Hattori - Gifu University, Japan  
Umar Al-Amani Haji Azlan - UTeM, Malaysia  
Umar Zakir Abdul Hamid - UTM, Malaysia

V. Anandakrishnan - NIT Tiruchirappalli, India  
Vasudev Madav - NIT Surathkal, India  
Vinod Kumar Sharma - Vellore Institute of Technology Vellore, India  
Wenzhong Wang - Beijing Institute of Technology, China  
Yan Chiew Wong - UTeM, Malaysia  
Yasser Suhaimi Mohd - MARDI, Malaysia  
Yuhani Yusof - UMP, Malaysia  
Zaini Yunos - UTHM, Malaysia  
Zakri Ghazalli - UMP, Malaysia  
Zulfan Adi Putra - UTP, Malaysia  
Zulkeflee Abdullah - UTeM, Malaysia  
Zun Liang Chuan - UMP, Malaysia  
Zuraini Othman - UTeM, Malaysia  
Zurriati Mohd Ali - UiTM, Malaysia

# Table of Contents

Preface .....	i
Editorial Board .....	ii
Reviewers .....	iii
Table of Contents .....	vii

No.	Title	Authors	Page
<b>Theme 1: Additive Manufacturing</b>			
001	Application of AFCM method on lap joint using low energy arc welding technologies	<i>Saiful Din Sabdin, Nur Izan Syahriah Hussein, Mohammad Kamil Sued, Rashdan Awang</i>	1
002	Thermal degradation study of acrylonitrile butadiene styrene (ABS) composites for FFF	<i>Syaza Najwa Mohd Farhan Han, Mastura Mohammad Taha, Muhd Ridzuan Mansor, Muhammad Mufqi Aminallah</i>	3
003	Pinless friction stir welding for weld thin plate cold rolled steel sheet	<i>Muhammad Aizat Mohd Abd Wahab, Mohammad Khairul Azmi Mohd Kassim, Mohammad Kamil Sued, Shikh Ismail Fairus Shikh Zakaria, Siti Noor Najihah Mohd Nasir</i>	5
004	Influence of process parameters on dimensional accuracy in GMAW based additive manufacturing	<i>Nor Ana Rosli, Mohd Rizal Alkahari, Faiz Redza Ramli, Shafizal Mat, Ahmad Anas Yusof</i>	7
005	Total volatile organic compound (TVOC) exposure from recycle polyamide nylon powder during selective laser sintering process	<i>Amir Abdullah Muhamad Damanhuri, A. Shamsul Rahimi A. Subki, Azian Hariri, Muhammad Hafidz Fazli Md Fauadi, Mohammad Rafi Omar, Abdul Munir Hidayat Shah Lubis</i>	10
006	Factors for increasing additive manufacturing (3D printing)	<i>Ai Nurhayati, Ahmad Rivai, Rina Indrayani</i>	12
007	Effects of current and wire feed direction in WAAM-TIG	<i>Johnnie Liew Zhong Li, Mohd Rizal Alkahari, Nor Ana Rosli, Faiz Redza Ramli, Rafidah Hasan</i>	14
008	Electromyography sensing on tibialis and peroneus muscle against improvised flat feet orthotic insole	<i>Umi Hayati Ahmad, Nuratifah Abdul Kudus, Mohd Hidayat Ab Rahman, Nurul Syifaa' Jamaluddin</i>	16
009	Topological optimized engine bracket for additive manufacturing	<i>Faiz Redza Ramli, Zaitul Akma Said, Mohd Rizal Alkahari, Shafizal Mat, Mohd Nizam Sudin</i>	19
010	Modeling and fabrication of protective mask with high complexity pattern using low-cost additive manufacturing design tool and systems	<i>Syahibudil Ikhwan Abdul Kudus, Ahmad Afiq Baharuddin, Mastura Mohammad Taha, Mohammad Rafi Omar, Mohd Idain Fahmy Rosley, Shafizal Mat</i>	21

011	Solution for pes planus discomfort using corrective personalized orthotic insole via additive manufacturing	<i>Zulkeflee Abdullah, Mariam Md Ghazaly, Azlinda Muhamad, Mawaddah Haslyanti, Mohd Amran Md Ali, Mohd Shahir Kasim, Mohammad Kamil Sued</i>	23
-----	---	--	----

**Theme 2: Advanced Materials and Processes**

012	Internal oxidation and oxide scales formation of Fe-33Ni-19Cr alloy	<i>Noraziana Parimin, Esah Hamzah</i>	26
013	Effect of semi-solid forming temperature and heat treatment on mechanical properties of Mg-Al-Zn Alloy (AZ91D) for automotive application	<i>M.R.M. Kamal, N.F. Bazilah, A. Luhat, M.H. Idris, M.S. Salleh, W.F.F.W. Ali</i>	28
014	Fabricate flow channel of bipolar plate through milling machining process	<i>Mohd Zulkefli Selamat, HamzaitulAkmarizal Hamdan, Mohd Basri Ali, Sivakumar Dhar Malingam</i>	30
015	Development of biodegradable plastic with natural sources as packaging material	<i>Mohammad Khalid Wahid, Mohd Nazri Ahmad, Nurul Ain Maidin, Mohd Hairizal Osman, Mohd Hidayat Ab Rahman</i>	33
016	Preliminary study of mechanical properties for different curing period of kenaf mix with glutinous rice through tensile and impact test	<i>Mohd Afzhal Shamsudin, Muhammad Hanif Mansor, Muhammad Ilman Hakimi Chua Abdullah, Mohd Noor Asril Saadun</i>	35
017	The effects of filler fibre sizes on the mechanical and fracture morphology of dried banana leaves filled recycled polypropylene	<i>Thinakaran Narayanan, Jeefferie Abd Razak, Intan Sharhida Othman</i>	37
018	Flexural properties of thermoplastics corn starch reinforced short pineapple leaf fibre composites laminates at various ply	<i>Nazri Huzaimi Zakaria, Mohd Zulkifli Selamat, Mohd Zamani Ngali, Abd Fuad Ab Ghani, Nur Rohaiza Izamuddin</i>	40
019	Effect of carbon nanotube-silane addition on mechanical properties of chloroprene rubber-filled carbon black	<i>Kok-Tee Lau, Jeefferie Abd Razak, Hairul Effendy Ab Maulod, Noraiham Muhamad, Mohamad Hanif Hashim, Solament Arumugam, Hoi Ern Kok, See Ern Chung, Nurzallia Mohd Saad</i>	42
020	Study of the oil palm empty fruit bunch as fiber reinforcement on composite material	<i>Mohd Fariduddin Mukhtar, Mohamed Saiful Firdaus Hussin, Amir Abdullah Muhammad Damanhuri, Khairul Amri Tofrowaih, Khairul Azri Azlan, Noor Saffreena Hamdan, Adam Samsudin</i>	45
021	Reduction of corrosion rate of aluminum alloy 6061 through anodization	<i>Md Fahmi Abd Samad, Raihana Ramle</i>	47
022	Effect of thin metal adhesion layer and thermal annealing process on microheater coil structure quality	<i>Norihan Abdul Hamid, Syafeeza Ahmad Radzi, Mazree Ibrahim</i>	50
023	Characteristics of the superficial oxide layer on the aluminium (99.4% purity) granules during in-situ melting	<i>Aslinda Saleh, Mohd Hasbullah Idris, Norfazillah Talib, Haslina Abdullah, Lee Woon Kiow</i>	52
024	Thrust force and tool wear investigation of micro drilling for carbon fiber reinforced polymer (CFRP) material	<i>N. Syuhada Nasir, N. Ab Wahab, R. Izamshah, H. Sasahara, S.A. Sundi</i>	54

025	Thermal properties and structure morphology of SLSG/SBE: Effect of filler content	<i>Zurina Shamsudin, Masturah Mesri, Rafidah Hasan, Jariah Mohamad Juoi, Zaleha Mustafa</i>	57
026	Design optimization of a new material for portable magnetic clamping plate for conventional milling process	<i>N. Ab Wahab, Syafiq Abdul Latiff, Tuan Nur Anis Anisha Tuan Nunek, Hambali Boejang, N. Syuhada Nasir</i>	59
027	Design improvement of fixable clamping jig for milling machine based on surface roughness	<i>N. Ab Wahab, Azizi Arif Bin Onn, M. Nabil Nordin, Abd Khahar Nordin, N. Syuhada Nasir</i>	61
028	Investigations on macro-drilling by indigenously developed ECM apparatus	<i>Sunil Pathak, Siti Nadiah Mohd Saffe, Irshad Ahamad Khilji</i>	64
029	Morphological changes of porous NiTi dental screw implant by metal injection moulding (MIM)	<i>Mashitah Maso'od, Muhammad Hussain Ismail, Muhammad Asif Ahmad Khushaini, Mohd Zul Iman Mohd Yusuf, Rohana Ahmad</i>	66
030	The optimization of welding parameter for AISI 1020 using robot welding	<i>Mohd Hairizal Osman, Mohammad Khalid Wahid, Mohd Nazri Ahmad, Nurul Ain Maidin, Mohd Hidayat Ab Rahman</i>	68
031	Effect of Nb element on the oxide formation of Fe-40Ni-24Cr alloy	<i>Noraziana Parimin, Esah Hamzah</i>	70
032	Tensile properties of graphene nanoplatelets/carbon black filled chloroprene rubber composites for engine mounting	<i>Noraiham Mohamad, Cheng Lin Yi, Khairu Ilwani Karim, Mazliah Mazlan, Hairul Effendy Ab Maulod, Mohd Shahrizan Othman, Nurzallia Mohd Saad, Siow Ming Onn, Jeefferie Abd Razak</i>	72
033	Fabrication of Al-Zn based metal matrix composites with bamboo leaf ash	<i>Maibam Bindya Devi, Anil Kumar Birru</i>	74
034	Hygrothermal effect on kenaf fiber/epoxy reinforced aluminium laminates (KeRALL) fabricated via compression moulding	<i>Edynoor Osman, Mohd Warikh Abd. Rashid, Mohd Edeerozey Abd Manaf, Toshihiro Moriga</i>	76
035	Synthesis and characterization of aluminium metal matrix composite with addition of bamboo leaf ash	<i>B. Praveen Kumar, Anil Kumar Birru, Chandan Mondal</i>	78
036	Microstructural properties of yttria stabilized zirconia (YSZ) prepared by ceramic injection moulding (CIM)	<i>Mahfuzah Zainudin, Muhammad Hussain Ismail, Nor Shamimi Shaari, Muhammad Faris Abd Manap, Rosniza Rabilah, Muhammad Faris Syafiq Khalid</i>	80
037	Effect of sintering parameters on Cu/CNTs using quartz tube furnace under argon atmosphere	<i>Nor Shamimi Shaari, Muhammad Hussain Ismail, Mahfuzah Zainudin, Ros Atikah Abd Kadir, Mazyan Yahaya, Rosniza Rabilah</i>	82
038	Functional properties of hybrid MWCNT-Ag filled epoxy electrically conductive adhesive	<i>Sow Jin Huat, S.H.S.M. Fadzullah, M.M. Nasaruddin, N.A.B. Masripan, M.R. Mansor, M.A. Salim</i>	84
039	Agglomerated TiO <sub>2</sub> powder synthesized by different methods for cold spray coating	<i>A.R. Toibah, M. Yamada, M. Fukumoto</i>	86
040	Analysis on noise absorption coefficient for polyurethane filled by waste tire dust (PU-WTD) composite foam using response surface method	<i>Jeefferie Abd Razak, Nor Amalina Rasmi, Marina Mohamad, Noraiham Mohamad, Saw Chun Lin, Lau Kok Tee</i>	88

041	The effect of water content on biomechanical behavior of articular cartilage: An experimental study	<i>Mohd Juzaila Abd Latif, Yew Sin Ru, Mohamad Shukri Zakaria</i>	91
042	The effect of water content of articular cartilage on low-field magnetic resonance imaging	<i>Mohd Juzaila Abd Latif, Tan Kae Chin, Nur Hazwani Mokhtar</i>	93
043	Transesterification of waste cooking oil into green polyols based on FTIR spectral analysis	<i>Jeefferie Abd Razak, Marina Mohamad, Mazlin Aida Mahamood, Noraiham Mohamad, Rose Farahiyan Munawar, Syahriza Ismail, Lau Kok Tee, Abdul Munir Hidayat Syah Lubis</i>	95

**Theme 3: Automotive and Aeronautics**

044	Effect of motorcycle brake operating parameters on braking performance on inertia roller brake dynamometer	<i>R.J. Talib, N.I. Ismail, M. Hisyam Basri, M.A.H. Fahmi, A.M. Zaharudin, R.Z. Tajudin</i>	97
045	Effect welding speed on thin plate lap joint using low energy arc welding technologies	<i>Saiful Din Sabdin, Nur Izan Syahriah Hussein, Mohammad Kamil Sued</i>	99
046	Motion sickness mitigation in autonomous vehicles by calming effect through vibration	<i>Nidzamuddin Md. Yusof, Juffrizal Karjanto, Nakul Shetty, Jacques Terken, Matthias Rautenberg</i>	101
047	Fatigue life-based reliability assessment of a leaf spring under random strain loads	<i>Lennie Abdullah, Salvinder Singh Karam Singh, Abdul Hadi Azman, Shahrum Abdullah, Ahmad Kamal Ariffin</i>	104
048	Case study of the Lion Air JT-610 falling at Karawang, Indonesia: The critical time of the plane lost contact	<i>Tiara Nurhuda, Ahmad Rivai, Ai Nurhayati</i>	107
049	Experimental investigation of engine performance of algae fuel addition in diesel fuel engine	<i>Hazim Sharudin, Nik Rosli Abdullah, Nur Athirah Rahim, M. Ridzuan Arifin, M.N.A.M. Yusoff, N.W.M. Zulkifli</i>	109
050	The performance of POME-algae-diesel as a fuel in diesel engines	<i>Hazim Sharudin, F.N.A.R. Shah, Nik Rosli Abdullah, M. Hisyam Basri, N.I. Ismail, Arif Pahmi, Y. Huzaifah</i>	111
051	Study of EMI reduction techniques in the automotive DC-DC converter	<i>Sivanyanam Rajamanickam, Siva Kumar Subramaniam, Zamre Abd Ghani</i>	113
052	Analysis of efficiency on different types of fuel for perodua Myvi car	<i>Muhamad Aimran Azhari, Ezzatul Farhain Azmi, Adam Samsudin</i>	116
053	Development of Brady-Tachy heart automotive monitoring (BT-Heartomotive) device to prevent motor-vehicle accident	<i>Mohd Azrul Hisham Mohd Adib, Muhamad Hazim Khalili, Nur Hazreen Mohd Hasni</i>	118
054	Stability improvement of motor control unit for automatic steering system	<i>Mohd Zakaria Mohammad Nasir, Mohd Hanif Harun, Fauzi Ahmad</i>	120
055	Vehicle analysis design of vehicle occupant packaging analysis	<i>A. Hazim N. Azman, Nur Hazwani Mokhtar</i>	122
056	Aerodynamic efficiency of paper planes	<i>N.I. Ismail, R.J. Talib, Hazim Sharudin, M.M. Mahadzir, M. Hisyam Basri, R. Rabilah</i>	124

057	Heterogeneous catalyst from white clams for biodiesel production	<i>Mahanum Mohd Zamberi, Farid Nasir Ani, Mohd Fadzli Bin Abdollah, Nur Hazwani Mokhtar</i>	126
058	Comparison of mathematical models for vertical tire load estimation	<i>Amrik Singh Phuman Singh, Intan Zaurah Mat Darus</i>	128
059	Analysis of intake geometry on multi-cylinder of internal combustion engine performance	<i>Arif Pahmi, M.E. Mustaffa, Hazim Sharudin, M. Hisyam Basri, N.I. Ismail, Mohd Fauzi Ismail, R.J. Talib</i>	130

**Theme 4: Computer Modeling and Simulation**

060	Kinetic modeling for palm oil epoxidation using genetics algorithm	<i>Mohd Jumain Jalil, Alif Farhan Mohd Yamin, Khairul Azhar Kamal, Hamzah Hafizuddin, Muhammad Salman Samin</i>	132
061	Comparative study of modeling method of synthetic-jet-assisted mixing	<i>Hong Mun Hoh, Cheng See Yuan, Lim Kim Chuan</i>	134
062	MyPhysio – A proposed telephysiotherapy system to reduce patient hospital waiting time and improve patient monitoring	<i>Lee Pik Yun, Raja Rina Raja Ikram</i>	136
063	Multifractal analysis for durability predictive criterion of suspension coil spring signal	<i>C.H. Chin, S. Abdullah, S.S.K. Singh, A.K. Ariffin, D. Schramm</i>	139
064	Modified Anand model parameters for 95.5Sn-4.0Ag-0.5Cu lead-free solder material	<i>A.F.M. Yamin, N.N. Azmi, N.A. Norrdin, H. Yusoff</i>	142
065	Feature identification from product reviews for product evaluation modeling	<i>Syaza Athirah Ramli, Soon Chong Johnson Lim, Ming Foong Lee</i>	145
066	Mathematical modeling of a simple quarter road vehicle suspension systems on sinusoidal road profile	<i>Adam Samsudin, Ezzatul Farhain Azmi, Amar Faiz Zainal Abidin, Mohd Fariduddin Mukhtar, Abdul Munir Hidayat Syah Lubis, Muhammad Ilman Hakimi Chua Abdullah</i>	147
067	Impact of optimization on high-k material gate spacer in DG-FinFET device	<i>Ameer F. Roslan, F. Salehuddin, A.S.M. Zain, K.E. Kaharudin</i>	150
068	The vortex shedding for an inclined flat plate of thrombosis using CFD simulation	<i>Nursyaira Mohd Salleh, Mohamad Shukri Zakaria, Mohd Juzaila Abd Latif</i>	152
069	Development of an integrated vaccine system (IVS) for vaccination healthcare database	<i>Mohd Azrul Hisham Mohd Adib, Muhammad Shahminan Lukman, Nur Hazreen Mohd Hasni</i>	155
070	Enhanced electron mobility in strained Si/SiGe 19nm n-channel MOSFET device	<i>Ahmad F.N.C. Razak, F. Salehuddin, Ameer F. Roslan, A.S.M. Zain, K.E. Kaharudin</i>	157
071	The omni-directional of autonomous underwater vehicle (AUV)	<i>Mohd Shahriel Mohd Aras, Keek Joe Siang, Grace Wong Mee Sing, Mohd Bazli Bahar, Mohamad Haniff Harun, Ho Gui Yan</i>	159
072	Quality of Service (QoS) in campus network: Significant survey	<i>Khaled J K Hommouda, Zulkiflee Muslim</i>	162

073	Taguchi GRA for multi-response optimization of 16nm WS <sub>2</sub> /TiO <sub>2</sub> NMOS device	<i>Nor F. Shamsudin, F. Salehuddin, Ameer F. Roslan, A.S.M. Zain, K.E. Kaharudin, A.H. Afifah Maheran, I. Ahmad</i>	165
074	Intruder system with raspberry pi in rural areas of Malaysia	<i>Kasthuri Subaramaniam, Abdul Samad Shibghatullah, Harry Lean Fu Liang, Zaheera Zainal Abidin</i>	167
075	Enhancing performance of wireless local area network using channel assignment	<i>Noor Atiqah Fatahurahman, Zaheera Zainal Abidin, Abdul Samad Shibghatullah, Effendi Mohamad</i>	169
076	Finite element analysis on critical relative slippage of bolted joint under transverse loading	<i>Hairul Bakri, Mohd Adnin Hamidi, Mohd Shukri Yob</i>	172
077	Analysis of SOI PD-MOSFET device using different gate spacer materials	<i>S. Husna S. Hameed, F. Salehuddin, Ameer F. Roslan, Aida Maziah Manin, Noreazira Mohd Daud, A.H. Afifah Maheran, A.S.M. Zain, K.E. Kaharudin</i>	174

**Theme 5: Condition Based Maintenance and Monitoring**

078	Characteristic of metal magnetic memory signals under uniaxial fatigue loading for SAE1045 steel	<i>Siti Norbaya Sahadan, Shahrum Abdullah, Azli Ariffin, Salvinder Singh Karam Singh</i>	176
079	Counterproductive work behavior, organizational support, personality traits and emotional intelligence among industrial workplace	<i>Norida Abdullah, Ali Hafizar Mohd Rawi, Mohd Firdaus Abdullah</i>	178
080	Improvement of work system through designing pedal control facilities for nenggala tactical vehicles in the workshop of the national Indonesian army equipment center	<i>Rimba Krishna Sukma Dewi, Angling Sugiatna, Bedy Ubaedillah</i>	180
081	Determination of correlation between age and working period: a study of NIHL between case and control group	<i>Rosniza Rabilah, N.I. Ismail, Mahfuzah Zainudin, Nor Shamimi Shaari, Nor Azirah Mohd Fohimi</i>	184
082	Development of smart infant-wrap ( <i>InfaWrap</i> ) device for neonates	<i>Mohd Azrul Hisham Mohd Adib, Mohammad Asyurul Abd Rashid, Nur Hazreen Mohd Hasni</i>	186
083	Development of bilirubin jaundice ( <i>BiliDice</i> ) device for neonates	<i>Mohd Azrul Hisham Mohd Adib, Mohd Hanafi Abdul Rahim, Nur Hazreen Mohd Hasni</i>	188
084	Acoustic emission technology for monitoring die condition in sheet metal forming process	<i>Ng Chuan Huat, Wong Hui Ing, Lai Chee Fung, Shamy Nazrein Md Yahaya, Rahizar Ramli, Sim Hoi Yin</i>	190

**Theme 6: Energy Engineering and Management**

085	Finite element analysis of the thermal response test for road thermoelectric energy harvesting system (RTEHs)	<i>K.N. Khamil, M.F.M. Sabri, A.M. Yusop, M.S. Sharuddin</i>	193
-----	---	--	-----

086	Determination of solar panel maximum output power using predictor variables method	<i>Aziah Khamis, Nurdiana Nordin, Lim Li Yao</i>	196
087	An experimental study of the cooking stove waste heat energy conversion using thermoelectric generator for night market application	<i>Mohd Arizam Abdul Wahap, A. Shamsul Rahimi Subki, Shahrizal Saat, Mohammad Haidir Maslan, Mohd Sharimienizam Harun</i>	199
088	Current Consumption and welding force measurement of bobbin friction stir welding on 6 mm thick AA1100	<i>Siti Noor Najihah Mohd Nasir, Mohammad Kamil Sued, Muhammad Zaimi Zainal Abidin</i>	201
089	Barriers and motivation of the solid waste management among manufacturing companies in Malaysia	<i>Nor Ratna Masrom, Najiah Atira Abd Rahman, Mohammed Hariri Bakri, Raja Zuraidah Raja Mohd Rasi, Badru At Tamam Daut, Irwan Ibrahim</i>	203
090	Methodological hardware design and development of health monitoring	<i>Muhammad Faiz Aqil Ahmad Fairuz, Ranjit Singh Sarban Singh, Muhamad Izzat Nurdin</i>	205
091	Measurement and analysis of energy consumption in a university building	<i>Abdalraouf Alhammali, Shamsul Shamsudin</i>	207
092	An integrated approach of monitoring indoor environment inside building	<i>Afiqah Ngah Nasaruddin, Tee Boon Tuan, Musthafah Mohd Tahir</i>	209
093	Investigation on air conditioning oversizing impact using computational approach	<i>Abdul Qayyum Abdul Halim, Tee Boon Tuan, Wan Shah WaliAllah Wan Mat Zain, Afiq Mohamad Johari</i>	211
094	Performance analysis of DC-DC converters for road pavement thermoelectric system	<i>Muhammad Syadza Sharuddin, Azdiana Md. Yusop, Ahmad Sadhiqin Mohd Isir, Khairun Nisa Khamil</i>	214

**Theme 7: Engineering Education**

095	Classroom design attributes: An investigation of staffs' and students' preferences	<i>Hii Ching Lik, Ong Sze Pheng, Chiang Choon Lai, Laura De Pretto, Cheng Heng Pang, Darlene Elizabeth Tan</i>	216
096	Enhancing classroom engagement through web-based interactive tools	<i>Chiang Choon Lai, Hii Ching Lik, Ong Sze Pheng, Lim Siew Shee, Tiong Timm Joyce, Nurzulaikha Rosli</i>	218
097	MyMUET – An interactive crowdsourced Malaysia University English Test online learning application	<i>Yarshini Thamilarasan , Raja Rina Raja Ikram, Muliati Sidek</i>	221
098	The suitability of the case teaching method and problem-solving strategies to improve problem solving skills of undergraduate: A literature review on mechanical engineering	<i>Tiara Nurhuda, Agus Rahmat Hermawanto, Abdul Fatah</i>	223
099	The impact of EQ, SQ and IQ towards AQ using path analysis and Rasch logit for modelling purpose among mechanical engineering students	<i>Mohd Effendi @ Ewan Bin Mohd Matore</i>	225
100	Line balancing of two-sided assembly cell in lean manufacturing	<i>Kamarudin Abu Bakar, Anis Masyitah Musa</i>	227

101	Structural Equation Model (SEM) in assimilating EQ, SQ and AQ for mechanical students' context	<i>Mohd Effendi @ Ewan Bin Mhd Matore</i>	230
102	Variability in the group's academic background is weakly associated to the outcome of a Problem-Based Learning project attainment for engineering undergraduates	<i>Nurdiana Nordin, Fariz Ali @ Ibrahim, Muhammad Herman Jamaluddin</i>	232

**Theme 8: Mechanical Design and Optimization**

103	Parameter effects on thrust force for one-shot drilling of carbon fibre reinforced plastics (CFRP)	<i>Mohd Fairuz Jaafar, Mohd Shukor Salleh, Raja Izamshah Raja Abdullah, Muhamad Hafiz Hassan, Mohammad Shah All-Hafiz Mohd Shahrim, Syahrul Azwan Sundi @ Suandi, Mohd Shahir Kasim</i>	235
104	Conceptualizing new product development by inserting value via blue ocean strategy	<i>M.F.M. Sam, H. Hafizuddin, B.C. Chew, Sivaraos, Y.F. Yusof</i>	237
105	Essential values for the airless tyres to be developed as a new product	<i>M.F.M. Sam, H. Hafizuddin, B.C. Chew, Sivaraos, Y.F. Yusof</i>	241
106	Process redesign to increase throughput and improved product flow for bake-wares-producing company	<i>Dzullijah Ibrahim, Hamid Yusoff, Yusli Yaakob, Norasikin Hussin</i>	243
107	Effects of driving signal waveforms on the force characteristics of a tubular linear switched reluctance actuator (T-LSRA)	<i>Fawwaz Nadzmy, Mariam Md Ghazaly, Chin Kiat Yeo, Siau Ping Tee, Shin Horng Chong</i>	245
108	Assessment on manual handling lifting precast concrete panel process via NIOSH equation	<i>Sinatu Sadiah Shapie, Hussein Md Zan, Seri Rahayu Kamat</i>	248
109	Fuzzy-analytical hierarchy process (Fuzzy-AHP) approach for choosing the best design concept of material transport system	<i>Khairun Najmi Kamaludin, Lokman Abdullah, Nur Adila Shaffini Suhaimi</i>	250
110	The innovative tungku for new mother recovers during postnatal period	<i>Mohammad Kamil Sued, T. Joseph Sahaya Anand, Laavanya Sothi, Sim Yiew Yiew, Abdul Aziz Ajid, Gogulan Manickavelu</i>	253
111	Design and development of origami corner chair for children with Cerebral Palsy	<i>Mohd Azlan Mohamed, Umi Hayati Ahmad, Nur Hanis Harun, Mohd Kamal Musa, Mohd Qadafie Ibrahim, Nurul Amira Jallil, Muhammad Noor Ikmal Abdul Jalil</i>	255
112	Indoor cabinet fertigation: A new concept design for urban agriculture	<i>Mohd Arizam Abdul Wahap, Umi Hayati Ahmad, Mohd Kamal Musa, Mohd Qadafie Ibrahim, Ng Shek Yi</i>	257
113	The mechanical transmission system glutinous rice shredder	<i>Rosad Ma'ali El Hadi, Rina Indrayani, Agus Rahmat Hermawanto</i>	260
114	Energy absorption of circular honeycomb out-of-plane dynamic impact under oblique loading	<i>Sze Pei Tan, Siti Nadiah Mohd Saffe, Siti Aishah Rusdan</i>	264
115	Optimization of process parameters for synthesis of graphene on copper by oil palm fiber source	<i>Noor Ayuma Mat Tahir, Mohd Rody Bin Mohamad Zin, Mohd Fadzli Bin Abdollah, Noreffendy Tamaldin, Hilmi Amiruddin</i>	266

116	Reverse engineering process of car side mirror using convectional and 3D scanning methods	<i>Shafizal Mat, Ng Shu Tyng, Faiz Redza Ramli, Mohd Rizal Alkahari, Mohamad Ridzuan Jamli, Syahibudil Ikhwan Abdul Kudus</i>	269
-----	---	---	-----

**Theme 9: Mechanical Vibration and Control**

117	Effect of damage on vibration characteristic of FDM printed lattice structure material	<i>Muhamad Syafwan Azmi, Rainah Ismail, Rafidah Hasan, Azma Putra, Muhammad Nasruddin Nurdin</i>	271
118	Wireless control of two wheels self-balancing robot using arduino microcontroller	<i>Nurul Muthmainnah Mohd Noor, Ahmad Nurussalam Yusof</i>	273
119	The assessment of vibration level among female passengers in Malaysia KTM commuter	<i>Fatimah Abdullah, Wan Hasrulnizzam Wan Mahmood, Seri Rahayu Kamat</i>	275
120	Parametric study on absorption coefficient of inhomogeneous double-layer MPP	<i>Ali I. Mosa, A. Putra, R. Ramlan, Al-Ameri Esraa</i>	277
121	Study of sound absorption of micro perforated panel with visco-thermal effects	<i>Al-Ameri Esraa, A. Putra, Ali I. Mosa, R.M. Dan</i>	280
122	Development of 3D-printed vibration dynamic absorber	<i>Mohamad Syafiq Hamdan, Azma Putra, Mohd Rizal Alkahari</i>	282
123	Vibration analysis for angular misalignment on spur and helical gear	<i>K. Amri Tofrowaih, Abdul Munir Hidayat Syah Lubis, Mohd Anas Amir</i>	284
124	3D-printed lattice structure as sound absorber	<i>Muhammad Fakrul Syahid Che Hamid, A. Putra, D.H. Kassim, M.R. Alkahari</i>	287
125	Experimental determination of sound absorption coefficient of green materials polymer from different compositions	<i>Farah Liana, Mohamad Ali Ahmad</i>	289
126	Mobile robotic arm with embedded PID system	<i>Khairuddin Osman, Muhammad Irshad Shaffar Saman, Nur Syahirah Eshah Budin Shah, Norzahirah Zainuddin</i>	291
127	Motion characteristics of a tubular linear switched reluctance actuator (T-LSRA) using phase-to-phase switching algorithm	<i>Chin Kiat Yeo, Mariam Md Ghazaly, Siau Ping Tee, Fawwaz Nadzmy, Shin Horng Chong, Zulkeflee Abdullah</i>	294
128	Positioning control performance of a rotary switched reluctance actuator (SRA) using modified PID control scheme	<i>Siau Ping Tee, Mariam Md Ghazaly, Chin Kiat Yeo, Fawwaz Nadzmy, Shin Horng Chong, Zulkeflee Abdullah</i>	297

**Theme 10: Structural and Mechanical Testing**

129	Dynamic compression properties of E-glass/basalt and E-glass/flax using SHPB	<i>Muhamad Shahirul Mat Jusoh, Mohd Yazid Yahya, Haris Ahmad Israr Ahmad</i>	299
130	Multiple linear regression application for generating entropy characteristics of magnesium alloy	<i>M.A. Fauthan, S. Abdullah, M.F. Abdullah, I.F. Mohamed</i>	301
131	Microhardness and sound velocity characterization of heat treated AISI 1050 carbon steel	<i>Zakiah Abd Halim, Nur Farah Hani Nor Alzahari</i>	304

132	Investigation on the effects of electrospinning distance and applied voltage on morphology of poly(vinyl alcohol) electrospun nanofibres	<i>Abdul Hamid Nurfaizey, Fatin Hanani Abdullah, Siti Hajar Sheikh Md Fadzullah, Zaleha Mustafa, Mohd Azli Salim, Mohd Zaid Akop</i>	306
133	A study on tensile properties of poly(vinyl alcohol) electrospun nanofibers	<i>Abdul Hamid Nurfaizey, Nor Amalina Azmi, Nor Azmmi Masripan, Zaleha Mustafa2, Adzni Md. Saad, Faizil Wasbari</i>	308
134	An investigation on degree of crystallinity of poly(vinyl alcohol) electrospun nanofibers	<i>Abdul Hamid Nurfaizey, Nur Hidayah Hashim, Zaleha Mustafa, Mohd Afzanizam Rosli, Muhd Ridzuan Mansor, Nadlene Razali</i>	310
135	Study on modulus of ABS single strut and reclaimed carbon fibre	<i>Rafidah Hasan, Zurina Shamsudin, Muhammad Fakhrur Iqbal Muslim, Azira Mat Yusof</i>	312
136	Design of bamboo bending tools on bird cage making based on anthropometric analysis	<i>Teguh Aprianto, Herman Ruswan Suwarman, Mochamad Saidiman</i>	314
137	Prediction of crack propagation direction in fretting fatigue	<i>M.H. Maslan, O. Ifayefunmi, M.A.A. Wahap</i>	316

**Theme 11: Surface Engineering and Tribology**

138	Effect of edge trimming parameters on surface quality of carbon fiber reinforced polymer composites (CFRP): Taguchi Method	<i>S.A. Sundi, R. Izamshah, M.S. Kasim, M.F. Jaafar, N. Syuhada Nasir, M.H. Hassan</i>	318
139	Optimization of treated SN 0W20 grade engine oil enhance with hBN nanoparticles	<i>Muhammad Ilman Hakimi Chua Abdullah, Mohd Redzuan Jamil, Mohd Fadzli Bin Abdollah</i>	320
140	Characterization of aluminium oxide composites	<i>Sunil Pathak, Balmukund Dhakar</i>	322
141	Friction and wear mechanisms of palm kernel activated carbon polymer composite by Raman spectroscopy study	<i>Dayang Nor Fatin Mahmud, Hilmi Amiruddin, Mohd Fadzli Bin Abdollah, Nor Azmmi Bin Masripan, Mohd Rody Bin Mohamad Zin, Noreffendy Tamaldin</i>	325
142	An Investigation of chip formation on different penetration angle for orthopaedic surgical bone drilling	<i>M.S. Noorazizi, K.R. Jamaludin, S. Sarip, R. Izamshah, R. Zamri, L. Abdullah, M.N. Maslan</i>	328
143	Effect of single zincating duration on the properties of copper activated aluminium Alloy 7075 substrate	<i>Intan Sharhida Othman, Marco Starink, Shun Chai Wang</i>	330
144	Surface characterization of oxide films formed on aluminium alloy with the incorporation of graphite	<i>Syazwani Mohamad, Shahira Liza Kamis, Jun Ishimatsu</i>	333
145	Optimization of waste cooking oil enhanced with hBN nanoparticles	<i>Muhammad Ilman Hakimi Chua Abdullah, Aliatul Syafiqah Nabilah Mohamad, Abdul Munir Hidayat Syah Lubis, Adam Samsudin, Mohd Afdhal Shamsudin, Mohd Fadzli Bin Abdollah</i>	335

146	Tribological influence of hBN and MoS <sub>2</sub> nanoparticles as additive in modified jatropha based oil nanofluids	<i>Norfazillah Talib, Shahirah Azua A Khalid, Lee Woon Kiow, Haslina Abdullah, Nor Athirah Jamaluddin, Aslinda Saleh</i>	338
147	Tribological properties characterization of green polyol	<i>Abdul Munir Hidayat Syah Lubis, Adam Samsudin, Jeefferie Abd Razak, Muhammad Ilman Hakimi Chua Abdullah, Amir Abdullah Muhamad Damanhuri, Khairul Amri Tofrowaih, Mohd Fariduddin Mukhtar</i>	340
148	Superhydrophilicity of laser surface textured TiO <sub>2</sub> coating for self-cleaning surfaces	<i>Yusliza Yusuf, Mariyam Jameelah Ghazali, Mohd Fadzli Bin Abdollah, Yuichi Otsuka, Susumu Nakamura</i>	342
149	Various quarry dust content influences the tribological properties of Ni-P composite coating	<i>Muhamad Ammar Farhan Maula Mohd Azam, Intan Sharhida Othman, Mohd Shahir Kasim, Jariah Muhamad Juoi, Mohd Rody Bin Mohamad Zin</i>	344
150	Surface topography study of CNC milled zirconia dental restoration	<i>Rahimah Abdul Hamid, Wan Nur Amirah Wan Muhamad, Raja Izamshah Raja Abdullah, Mohd. Shahir Kasim</i>	347
151	The effect of coconut fibre as friction modifier on mechanical and tribological characteristics of friction materials	<i>Hazim Sharudin, R.J. Talib, M. Hisyam Basri, N.I. Ismail, Arif Pahmi, M.F.S. Khalid</i>	349
152	Adhesion modelling for load-dependence, double-Hertz based elliptical contacts	<i>Nurul Hilwa Mohd Zini, Matthijn de Rooij, Mohammad Bazrafshan, Aydar Akchurin, Dik Schipper, Nurhidayah Ismail</i>	351

**Theme 12: Thermal and Fluids**

153	A simulation study of tubercles effect of aerodynamics performance on delta wing	<i>Hamid Yusoff, Dzullijah Ibrahim, Aliff Farhan Mohd Yamin, Mohamad Rafiuddin Abdul Razak, Salina Budin, Shafiq Suhaimi</i>	353
154	Experimental test of a standing-wave thermocoustic rig	<i>Fatimah Al Zahrah Mohd Saat, Dahlia Johari, Ernie Mat Tokit</i>	355
155	Simulation study of drying chamber for marine product	<i>Nur Izzati Mohd Azhar, Mohd Afzanizam Mohd Rosli, Ahmad Syakir Ghazali, Hiew Sit Jing</i>	358
156	Investigation of heat effects on electronic sensors in a lightning detection system	<i>Tuan Nurul Husna Tuan Zakaria, Maslan Zainon, Maaspaliza Azri, Zikri Abadi Baharudin, Ahmad Aizan Zulkefle, Ahmad Idil Abdul Rahman, Mohd Ariff Mat Hanafiah, Shahrudin Zakaria</i>	360
157	Mathematical modeling of two-phase flow under Dusty Williamson fluid model	<i>N.S. Arifin, S.M. Zokri, A.R.M. Kasim, M.Z. Salleh</i>	362
158	Turbulence measurements in the centerline region of a turbulent round jet using a software-driven laser doppler system	<i>Mohd Rusdy Yaacob, Preben Buchhave, Clara Marika Velte</i>	365
159	The application of spectral methods in two-dimension fluid flow	<i>Farida Nurmala Sihotang, Diyah Wijayati, Robi Dany Riupassa</i>	367
160	DeltaEC prediction of pressure along a quarterwave thermoacoustic test rig	<i>Dahlia Johari, Ernie Mattokit, Fatimah Al Zahrah Mohd Saat, Normah Mohd Ghazali</i>	370

161	Continuous water quality monitoring for water hydraulics applications in food processor	<i>Ahmad Anas Yusof, Suhaimi Misha, Syarizal Bakri</i>	373
-----	---	--	-----

# Application of ACFM method on lap joint using low energy arc welding technologies

Saiful Din Sabdin<sup>1,\*</sup>, Nur Izan Syahriah Hussein<sup>1</sup>, Mohammad Kamil Sued<sup>1</sup>, Rashdan Awang<sup>2</sup>

<sup>1)</sup> Fakulti Kejuruteraan Pembuatan, Universiti Teknikal Malaysia Melaka,  
Hang Tuah Jaya, 76100 Durian Tunggal, Melaka, Malaysia

<sup>2)</sup> TWI Technology (S.E. Asia) Sdn Bhd, No.1 Jalan Utarid U5/13 Section U5,  
40150 Shah Alam , Selangor Darul Ehsan, Malaysia

\*Corresponding e-mail: saifulkdh@yahoo.com

**Keywords:** Thin plate; arc welding; steel; heat input

**ABSTRACT** – Low energy arc welding is one of the modern technologies joining of GMAW process. Commonly inspections technique is used in manufacturing and industrial which the processes involved meet those requirements especially in welding technology field. The main objective from this experiment is to identify the defect from thin plate sheet joining lap joint in relation to heat input on high strength steel plate joint. The study of this paper covers only the inspection effects using ACFM (Application of Alternating Current Field Measurement) method on the weldment low arc technology after cooling down to room temperature.

## 1. INTRODUCTION

Nowadays the ACFM technique mostly used at manufacturing industries such as automotive, maritime, oil & gas, aerospace and other applications. Significantly, the ACFM is from conventional eddy currents and locally used unidirectional and constant electric field in the sample. This method provides a number of benefits including the ability to mathematically model the perturbations produced by a simple defect. The technique therefore allows crack and depth sizing is needed to be carried out by comparing measured field disturbances to predict disturbances around pre-defined defects. The technique was originally developed for the detection and sizing of fatigue cracks, which tend to be single planar defects compatible with the model [1-2].

Low energy arc technology was a short circuit which sends a signal that retracts the welding filler material, giving the weld time to cool before each drop is placed. This leaves a smooth weld that is stronger than that of a hotter weld. This works well on thin metal that is prone to warping and the weld burning through the material. This type of welding is more efficient than other GMAW methods when the metal is thinner than 10mm, anything greater than the expense begins to overcome traditional welding.

## 2. METHODOLOGY

The Alternating Current Field Measurement (ACFM) technique is an electromagnetic technique that is capable of both detecting and sizing (length and depth) surface breaking cracks in metals. Figure 1 shows the signal basis of the technique which is constantly alternating current tangential solenoid that remote from the test surface. Inducing current electric in the sample

surface is to be done to create unidirectional and uniform strength over a localized area under the solenoid. When there are no defects present in this area, this current electric will be undisturbed. Here, if a crack is present, the uniform current is disturbed, and it will flow around the ends and down the faces of the crack.

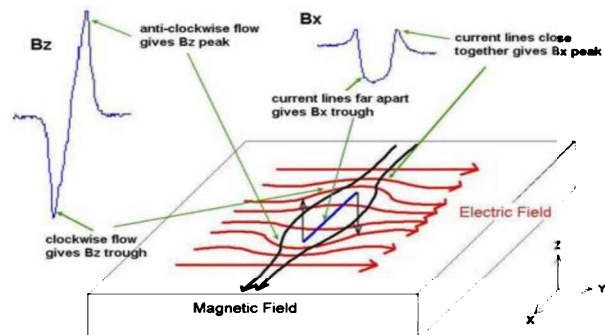


Figure 1 ACFM currents flowing around a defect and signals from scan along the defect

The experiments were conducted according to the information welding parameter in table 1. The robot welding used in this study was KUKA type KRC4 and the system is equipped by EWM ColdArc power source [3]. Specimens dimension with dissimilar thickness of 250 mm × 50 mm x 1.0 mm and 250 mm x 50 mm x 0.8 mm were fabricated. The material plate is high strength steel on lap joint [4]. The chosen parameters for the pprocess is bead-on-plate and the experiments are performed and corresponding heat input values are detailed in Table 1.

Table 1 Welding Parameter

Heat input (kJ/mm)	Ampere (A)	Voltage (v)	Welding speed (mm/min)
0.026	40	6	550

## 3. RESULTS AND DISCUSSION

An overview of Figure 2 showed the defect signal response on welding plate. Four defects were identified on plate measurement on Figures 2(a) and 2(b) representing depth and length of defect on the highlight circle. Figure 2(c) In the presence of a defect, the butterfly loop is drawn in the screen and for manual operation the operator looks for this distinctive shape to

decide whether a crack is present or not. The biggest defect was on zone 3 the center of welding joint plate.

Figure 3 shows the measurement length and depth on signal in weld zone. The most defect on area zone 3 is the length of 148 mm and the depth of 29 mm. The lowest defect on area zone 1 is the length of 60 mm and the depth of 7 mm. The results indicate that the heat input is affected from the weldment size. Interestingly, there were also differences correlated with the results obtained by previous researchers [5].

Table 2 shows the visual defect by zone. Visual examination showed that unequal cladding of the welding joints occurred. According to ISO 5817 which is the standard quality for the welding, welded joints can be classified according to uniform and regular joint EN ISO 5817. The results obtained was actual throat is more than design throat of fillet weld lap joint.

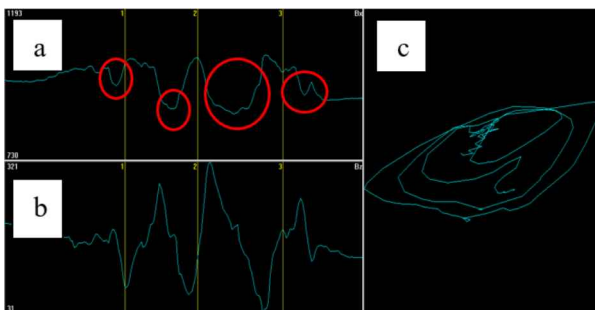


Figure 2 Signal response to defect

a) B<sub>x</sub> signal of depth plate 200 mm, b) B<sub>z</sub> signal of length plate 200 mm and c) signal butterfly plot.

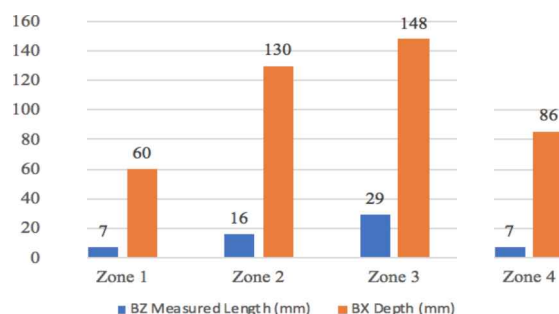


Figure 3 Graph measurement zone area.

From the experiment results there are four defects on the join using ACFM equipment more easily and accurately. The defect on weldment join is incomplete fusion and the underfill was noted. The ACFM method process proves to be suitable for inspection welding thin sheet metal. It is essential to determine the right parameter to minimize defect in the product.

#### 4. CONCLUSION

The most significant findings from this study is that The ACFM method is relevant to experiment and investigate thin plate defect. After completing this work, several conclusions are made from the results shown above.

(a) ACFM has been shown to be effective for inspection of simulated surface breaking geometrical defects and electromagnetic

discontinuities in high strength steel plates.

- (b) The technique has also obtained good results in thin skin application with higher accuracy.
- (c) The technique has also inspected through coatings, making it a useful and adaptable inspection technique for the new millennium.

Table 2 Visual defect zone area.

Defect area	Zone
	1
	2
	3
	4

#### ACKNOWLEDGEMENT

The authors would like to thank the Faculty of Manufacturing Engineering, Universiti Teknikal Malaysia Melaka (UTeM) and TWI Technology (S.E. Asia) Sdn Bhd for educational and technical support throughout this research.

#### REFERENCES

- [1] Ge, J., Li, W., Chen, G., Yin, X., Wu, Y., Yuan, X., & Zhao, M. (2016). New parameters for the ACFM inspection of different materials. *Insight-Non-Destructive Testing and Condition Monitoring*, 58(6), 313-317.
- [2] Farrell, S. P., Lugg, M., & Avery, K. (2015, March). Application of Alternating Current Field Measurement for Determination of Surface Cracks and Welds in Steel Structures at Lift-off. In *ASNT 24th Research Symposium 2015* (pp. 24-28).
- [3] Sabdin, S. D., Hussein, N. I. S., Sued, M. K., & Ayof, M. N. (2018). Joining of Thin Plates Using Various Arc Welding Heat Sources—A Review. *Journal of Advanced Manufacturing Technology (JAMT)*, 12(1 (1)), 357-370.
- [4] Sabdin, S. D., Hussein, N. I. S., Sued, M. K., Ayof, M. N., Ayob, M. S., & Rahim, M. A. S. A. (2018). Weld bead reinforcement on cold rolled carbon steel sheet joint using ColdArc technology. *Proceedings of Mechanical Engineering Research Day 2018*, 197-198.
- [5] Ge, J., Li, W., Chen, G., Yin, X., Wu, Y., Yuan, X., & Zhao, M. (2016). New parameters for the ACFM inspection of different materials. *Insight-Non-Destructive Testing and Condition Monitoring*, 58(6), 313-317.

# Thermal degradation study of acrylonitrile butadiene styrene (ABS) composites for FFF

Syaza Najwa Mohd Farhan Han<sup>1</sup>, Mastura Mohammad Taha<sup>2,3,\*</sup>, Muhd Ridzuan Mansor<sup>1,3</sup>, Muhammad Mufqi Aminallah<sup>2</sup>

<sup>1)</sup> Fakulti Kejuruteraan Mekanikal, Universiti Teknikal Malaysia Melaka,  
Hang Tuah Jaya, 76100 Durian Tunggal, Melaka, Malaysia

<sup>2)</sup> Fakulti Teknologi Kejuruteraan Mekanikal dan Pembuatan, Universiti Teknikal Malaysia Melaka,  
Hang Tuah Jaya, 76100 Durian Tunggal, Melaka, Malaysia

<sup>3)</sup> Centre for Advanced Research on Energy, Universiti Teknikal Malaysia Melaka,  
Hang Tuah Jaya, 76100 Durian Tunggal, Melaka, Malaysia

\*Corresponding e-mail: mastura.taha@utem.edu.my

**Keywords:** ABS composites; thermal degradation; fused filament fabrication

**ABSTRACT** – Thermal stability of material is the main concern in producing filament for FFF. Hence, this paper investigates thermal stability of commercialized ABS filament, neat ABS, kenaf fiber, 2.5% and 5% of kenaf fiber reinforced ABS composites. TGA test was performed to measure the degradation temperature. Results indicate that the degradation temperature for commercialized ABS filament, neat ABS and kenaf fiber are 345.16°C 326.83°C and 240.53°C respectively. Meanwhile, addition of kenaf fiber into ABS polymer decreased the thermal stability of composites. Therefore, kenaf fiber reinforced ABS composites is suitable for FFF since extrude temperature used at FFF is less than 250°C.

## 1. INTRODUCTION

Fused Filament Fabrication (FFF) is the most significant technique for Additive Manufacturing (AM) and has been used widely based on the capability of FFF to print three-dimensional objects. Besides, FFF can fabricate geometrically complex shape [1] and cost-effectiveness [2] in producing 3D objects with good resolution output.

Thermoplastic is the mainly used material for FFF such as Acrylonitrile Butadiene Styrene (ABS) and Polylactic Acid (PLA). Currently, wide range of material have been introduced from neat bio(polymer) to (bio)composites [3]. However, the suitability of composites material is one of the disadvantages as the compatibility between the matrix and reinforcement requires intensive research based on the temperature of materials which the melting point is not too high or not to low since the heating element of commercially available FFF can operate around 300°Celsius [4].

Natural fiber reinforced polymer composites (NFRC) has been used nowadays in many applications such as automotive, aerospace and medical due to its lightweight and environmentally friendly material [5]. The disadvantage of natural fiber such as low thermal stability limits the usage of NFRC for FFF. Torrado et al. [6] investigate effect of jute fiber reinforced ABS composites on FFF and found that the high temperature of extrusion process can cause decomposition of jute fiber. Montalvo et al. [7] study on wood plastic composites (WPC) and found that the decomposition of

WPC is between 300°C and 500°C. So, it is vital to study the thermal stability of NFRC before the NFRC filament is produced and extruded on FFF.

Thus, the aim of this study is to investigate the thermal degradation of commercialized ABS filament, kenaf fiber, neat ABS and different loadings of NFRC by using thermogravimetric analysis (TGA) to identify the decomposition temperature (°C).

## 2. METHODOLOGY

There are five types of test samples which are commercialized ABS filament, kenaf fiber, neat ABS, 2.5% kenaf fiber reinforced ABS composites and 5% kenaf fiber reinforced ABS composites.

Commercialized ABS filament was cut into 3mm length and the weight is between 5-15mg. Neat ABS and kenaf fiber is weighed to obtain 5-15mg since the material is already in a pellets and powder form respectively. Then, an internal mixture model HAAKE Rheomix OS was used to mix 2.5 wt.% kenaf powder reinforced ABS composites and 5 wt.% kenaf powder reinforced ABS composites. The mixture was mixed at 180°C with the speed 50 rpm for 12 minutes for each mixing. After the mixing of two specimens is completed. The material was crushed by a crusher machine to obtain specimens in form of granules. Then, the granules for 2.5 wt.% and 5 wt.% percent of kenaf fiber reinforced ABS composites was weighed between 5-15mg.

The model used for TGA is TGA 1 (Thermogravimetric Analyzer) of Mettler Toledo. The temperature used for all samples is 25°C to 550°C with heating rate 10°C min⁻¹ and the atmosphere used is nitrogen gas. TGA is conducted to measure the change in mass of the sample as a function of increasing temperature and the final residue yield on set of degradation temperature were recorded.

## 3. RESULTS AND DISCUSSION

Figure 1 shows the results of TGA curves for commercialized ABS filament, kenaf fiber, neat ABS, 2.5 wt.% kenaf fiber reinforced ABS composites and 5 wt.% kenaf fiber reinforced polymer composites.

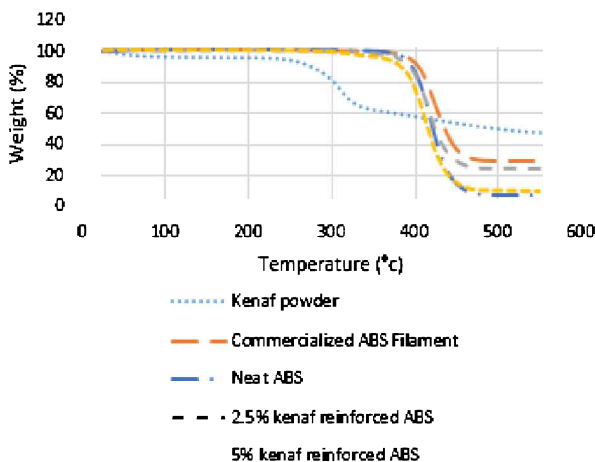


Figure 1 TGA curves for all specimen.

Table 1 Decomposition temperature and final weigh after decomposition of all specimen.

Materials	Decomposition temperature (°C)	Final weight after decomposition (%)
Kenaf powder	240.53	8.36
Commercialized ABS filament	345.16	4.6
Neat ABS	326.83	2.65
2.5% kenaf fiber	320.94	3.34
5% kenaf fiber	312.39	3.46

The data from curves were extracted and presented in Table 1. The commercialized ABS filament decomposition temperature and remaining weight is slightly higher compare to neat ABS with 5.6% and 38% respectively. Then, neat ABS have the higher decomposition temperature compare to 2.5% and 5% of kenaf fiber reinforced ABS composites.

Meanwhile, it is found that the thermal stability of kenaf fiber is the lowest with 240.53°C respectively for decomposition temperature. The overall weight loss of kenaf fiber could be divided into three different steps. For the first step, weight loss occurs at below 100°C about 6% from initial weight. Then, the second weight loss occurred around 260°C with 12.5% where this is the initial stage of thermal degradation. The last step is referred to the major thermal degradation occur with maximum weight loss at 325°C. The weight loss occurs due to the vaporization from fiber and decomposition of cellulose [8].

As the content of kenaf fiber is increased, the decomposition temperature of composites is decreased since kenaf fiber has low thermal stability compare to ABS polymer. This result is supported by Azwa and Yousif [9] where the addition of natural fiber in composites cause the thermal stability to reduce due to the less stable fibers. The increasing percentage of fiber lower the thermal stability due to weaken hydrogen bonding and the decreases of mobility cellulose chains in cellulose [10].

#### 4. CONCLUSION

In conclusion, the degradation temperature of commercialized ABS filament is higher than neat ABS. Besides, the thermal stability of kenaf fiber was significantly lower than commercialized ABS filament and neat ABS, so the increasing content of kenaf fiber in reinforced ABS composites can reduced the thermal stability of the composites. Therefore, 2.5% and 5% of kenaf fiber reinforced ABS composites can be used as filament in FFF since the extrude temperature use at 3D printer is less than 250°C.

#### ACKNOWLEDGEMENT

The authors would like to acknowledge Faculty of Mechanical Engineering, Faculty of Mechanical and Manufacturing Engineering Technology of Universiti Teknikal Malaysia Melaka and the financial supports provided through grant no (PJP/2018/FTK(4A)/S01594).

#### REFERENCES

- [1] MacDonald, E., & Wicker, R. (2016). Multiprocess 3D printing for increasing component functionality. *Science*, 353(6307).
- [2] Noorani, R. (2006). *Rapid prototyping: principles and applications*. John Wiley & Sons Incorporated.
- [3] Le Duigou, A., Castro, M., Bevan R., & Martin, N. (2016). 3D printing of wood fibre biocomposites: From mechanical to actuation functionality. *Materials & Design*, 96, 106-114.
- [4] Salem Bala, A., & bin Wahab, S. (2016). Elements and materials improve the FDM products: A review. In *Advaced Engineering Forum*, 16, 33-51.
- [5] Ramamoorthy, S. K., Skrifvars, M., & Persson, A. (2015). A review of natural fibers used in biocomposites: plant, animal and regenerated cellulose fibers. *Polymer reviews*, 55(1), 107-162.
- [6] Torrado, A. R., Shemelya, C. M., English, J. D., Lin, Y., Wicker, R. B., & Roberson, D. A. (2015). Characterizing the effect of additives to ABS on the mechanical property anisotropy of specimens fabricated by material extrusion 3D printing. *Additive Manufacturing*, 6, 16-29.
- [7] Montalvo, J. I., & Hidalgo, M. A. 3D printing with natural reinforced filaments. In *Solid Freeform Fabrication (SFF) Symposium*, 922-934.
- [8] Fauzi, F. A., Ghazalli, Z., Siregar, J. P., & Tezara, C. (2016). Investigation of thermal behaviour for natural fibers reinforced epoxy using thermogravimetric and differential scanning calorimetric analysis. In *MATEC Web of Conferences*, 78.
- [9] Azwa, Z. N., & Yousif, B. F. (2013). Thermal degradation study of kenaf fiber/epoxy composites using thermo gravimetric analysis. In *Proceeding of the 3<sup>rd</sup> Malaysian Postgraduate Conference (MPC 2013)*, 256-264.
- [10] Aji, I. S., Zainudin, E. S., Khalina, A., Sapuan, S. M., & Khairul, M. D. (2011). Thermal property determination of hybridized kenaf/PALF reinforced HDPE composite by thermogravimetric analysis. *Journal of thermal analysis and calorimetry*, 109(2), 893-900.

# Pinless friction stir welding for weld thin plate cold rolled steel sheet

Muhammad Aizat Mohd Abd Wahab<sup>1</sup>, Mohammad Khairul Azmi Mohd Kassim<sup>2</sup>, Mohammad Kamil Sued<sup>2,3,\*</sup>, Shikh Ismail Fairus Shikh Zakaria<sup>1</sup>, Siti Noor Najihah Mohd Nasir<sup>2</sup>

<sup>1)</sup> Fakulti Teknologi Kejuruteraan Mekanikal Pembuatan, Universiti Teknikal Malaysia Melaka,  
Hang Tuah Jaya, 76100 Durian Tunggal, Melaka, Malaysia

<sup>2)</sup> Fakulti Kejuruteraan Pembuatan, Universiti Teknikal Malaysia Melaka,  
Hang Tuah Jaya, 76100 Durian Tunggal, Melaka, Malaysia

<sup>3)</sup> Advance Manufacturing Centre, Universiti Teknikal Malaysia Melaka,  
Hang Tuah Jaya, 76100 Durian Tunggal, Melaka, Malaysia

\*Corresponding e-mail: kamil@utem.edu.my

**Keywords:** Pinless friction stir welding; process Parameter; SPCC

**ABSTRACT** – Pinless Friction Stir Welding provides various advantages in designing tool compared to the traditional Friction Stir Welding such as simple fixtures and simpler tool. The relationship of parameters is investigated by conducting a mechanical testing at the welded workpieces. Temperature distribution and current consumption during welding are recorded. Two set of parameters used which are 900rpm and 1050rpm for rotational speed; 45mm/min and 75mm/min for welding speed. It shows that lower rotational speed with higher welding speed is producing a higher strength weld which 132.34 MPa for tensile and around 150 HV for microhardness. This technique are highly recommended for aerospace application since having higher strength.

## 1. INTRODUCTION

Welding is a permanent process that joining two or more parts by application of heat and pressure [1]. New solid-state welding has been derived from Conventional Friction Stir Welding (CFSW) which are Pinless Friction Stir Welding (PFSW) [2]. In PFSW, tool design was an important characteristic since it produces a uniformity of welding joint. Furthermore, PFSW let the tool design to be in various type of design since different type of tool design produced a different heat during welding [3]. If the metal flow is inconsistent or inadequate heat during process, it leaded to the defects produce in welding structure [4]. Basically, the application of pin in FSW are resulting undesirable keyhole at welded area. The existed of keyhole are inviting the corrosion at the welded part [5]. Once the corrosion occurred at the welded area, it reduced the weld strength.

## 2. METHODOLOGY

Type of material used in this study was Cold Rolled Carbon Steel Sheet (SPCC) with 1mm thickness. The SPCC sheet are 174mm in length with 140mm for width. While for pinless tool, it was fabricate using tool steel, H13. The dimension of the tool just consists of shoulder and tool holder which are 10mm for shoulder diameter and 20mm for tool holder diameter. To make sure all the experiments are run smoothly, 3-axis Haas CNC Milling machine has been applied as the FSW machine. During this study, various of parameter are applied. However, there is certain parameter from preliminary test that give an acceptable weld product. Table 1 shows the parameter

that selected for this study.

Table 1 Parameter setup based on preliminary test.

Experiment	Rotational speed (rpm)	Welding speed (mm/min)
Run 1	900	45
		75
Run 2	1050	45
		75

During PFSW process, data of temperature and current are recorded. For the mechanical testing, tensile and microhardness test were conducted. Testing are running following ASTM E8 for tensile and ASTM E384 for microhardness. Maximum loaded used was 2kg with 10s of dwell time.

## 3. RESULTS AND DISCUSSION

Figure 1 and 2 shows the surface appearance after running PFSW process. It shows the excessive of flash at weld area. This happened due to the outflow of the plasticized material that are underneath of the shoulder. Furthermore, an insufficient heat during welding making the process occur below the required temperature. By looking at the welded area, there is a dark colour due to the heat during welding process. However, the dark colour is ununiform since thin plate are use in this study. Therefore, the contact between pinless tool and workpiece are not uniform. Moreover, by applying thin material for this study, it was hard to get a smooth weld result since thin material are easily to distort once having higher temperature.

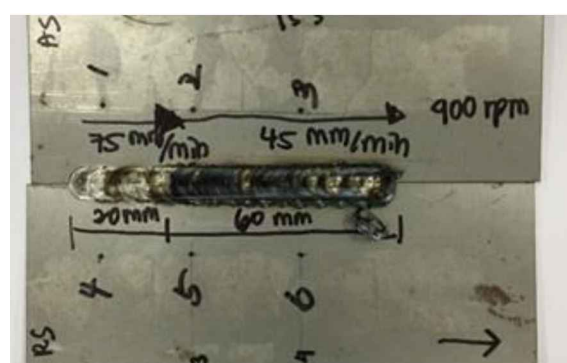


Figure 1 Visual inspection of this study; 900rpm with 75mm/min and 45mm/min.

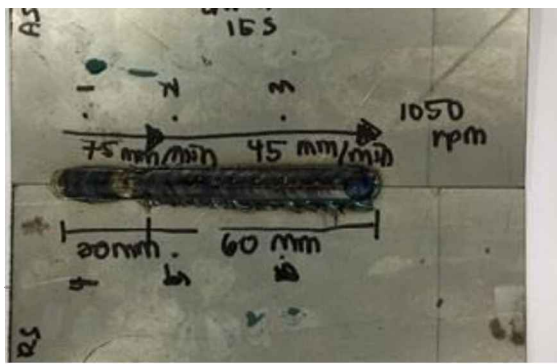


Figure 2 Visual inspection of this study; 1050rpm with 75mm/min and 45mm/min.

Table 2 represent the result of tensile test for this study. Based on the result recorded, it shows that parameter applied give a huge influence for this study. Moreover, higher welding speed are resulting to the higher tensile strength. It was stated that the tensile strength is improve by increasing of welding speed. However, the result recorded are still below from the base material resulted. It believed that stirring effect affected the arrangement of particle inside the material. It was stated that the stirring of particle that including heat are changes the arrangement of the particle inside the material.

Table 2 Results of tensile strength.

Experiment	Rotational speed (rpm)	Welding speed (mm/min)	Tensile strength (MPa)
Base Material	-	-	194.04
Run 1	900	45	93.85
		75	132.34
Run 2	1050	45	34.04
		75	118.24

Figure 3 and 4 showing a similar pattern which are the welded area having higher hardness value. The hardness value decreased when the data recorded far from welded area. This are because of the heat that produced during process that make the welded area more solid. Once the heat and force are focus on one spot, it will improve the hardness.

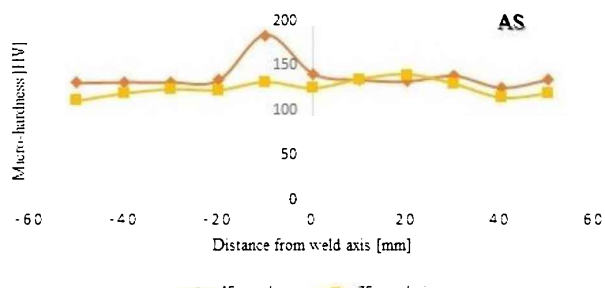


Figure 3 Micro-hardness result; 900 rpm with 45mm/min and 75mm/min.

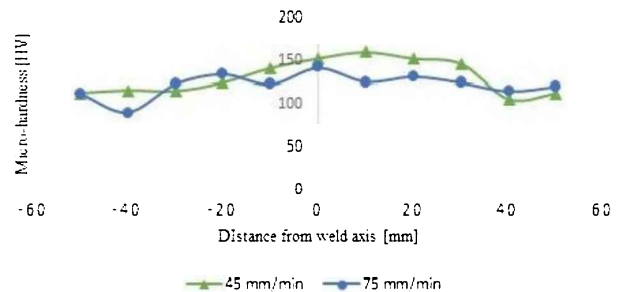


Figure 4 Micro-hardness result; 1050rpm with 45mm/min and 75mm/min.

However, there is flash at the welded part. This are because of the outflow of material underneath the shoulder due to the high plunging tool depth. Next, the surface groove produced because of the abnormal stirring since there is only flat surface at the shoulder.

#### 4. CONCLUSION

Based on the result achieved, it shows that lower rotational speed with a higher welding speed are giving higher welding strength based on the tensile and micro-hardness test. There is still some defects showing in the welded product such as flash surface groove. Next, a good heat generated during process will produced a good quality of welding product.

#### ACKNOWLEDGEMENT

The author would like to thank the Universiti Teknikal Malaysia Melaka (UTeM) and both faculty which are Fakulti Teknologi Kejuruteraan Mekanikal Pembuatan and Fakulti Kejuruteraan Pembuatan for accepting this study.

#### REFERENCES

- [1] Leitao, C., Emílio, B., Chaparro, B. M., & Rodrigues, D. M. (2009). Formability of similar and dissimilar friction stir welded AA 5182-H111 and AA 6016-T4 tailored blanks. *Materials & Design*, 30(8), 3235-3242.
- [2] Liu, Z., Cui, H., Ji, S., Xu, M., & Meng, X. (2016). Improving joint features and mechanical properties of pinless friction stir welding of alcald 2A12-T4 aluminum alloy. *Journal of Materials Science & Technology*, 32(12), 1372-1377.
- [3] Godiganur, V. S., & Biradar, S. (2014). Comparison of friction stir welding technique with conventional welding methods. *International Journal of Research in Engineering and Technology*, 3, 572-6.
- [4] Tan, C. W., Jiang, Z. G., Li, L. Q., Chen, Y. B., & Chen, X. Y. (2013). Microstructural evolution and mechanical properties of dissimilar Al–Cu joints produced by friction stir welding. *Materials & Design*, 51, 466-473.
- [5] Kuang, B., Shen, Y., Chen, W., Yao, X., Xu, H., Gao, J., & Zhang, J. (2015). The dissimilar friction stir lap welding of 1A99 Al to pure Cu using Zn as filler metal with “pinless” tool configuration. *Materials & Design*, 68, 54-62.

# Influence of process parameters on dimensional accuracy in GMAW based additive manufacturing

Nor Ana Rosli<sup>1</sup>, Mohd Rizal Alkahari<sup>1,2,\*</sup>, Faiz Redza Ramli<sup>1,3</sup>, Shafizal Mat<sup>1,3</sup>, Ahmad Anas Yusof<sup>1,3</sup>

<sup>1)</sup> Fakulti Kejuruteraan Mekanikal, Universiti Teknikal Malaysia Melaka,

Hang Tuah Jaya, 76100 Durian Tunggal, Melaka, Malaysia

<sup>2)</sup> Advanced Manufacturing Centre, Universiti Teknikal Malaysia Melaka,

Hang Tuah Jaya, 76100 Durian Tunggal, Melaka, Malaysia

<sup>3)</sup> Centre for Advanced Research on Energy, Universiti Teknikal Malaysia Melaka,

Hang Tuah Jaya, 76100 Durian Tunggal, Melaka, Malaysia

\*Corresponding e-mail: rizalalkahari@utem.edu.my

**Keywords:** 3D printing; additive manufacturing; wire arc additive manufacturing (WAAM)

**ABSTRACT** – Additive manufacturing (AM) or 3D printing began to emerge as important manufacturing technology. Wire and arc additive manufacturing (WAAM) is one of the most promising among AM technologies for metallic components. Their applicability to produce fully dense metal parts and large near net shape has attracted more attention from industries. However, the most important barrier is the quality of the printed parts which prevent its wider adoption. Currently, only a few studies dedicated to the optimization of the process parameters. Thus, the presented paper studies the effect of welding voltage, travel speed and heat input on percentage difference of height.

## 1. INTRODUCTION

The growth of 3D printing technology is tremendously are in the extreme level. The technology offers a promising way to produce any parts with complex geometries directly from computer aided digital designs. Clearly the advantage of AM it allows the creation of internal feature that impossible to be produced using conventional processing. WAAM systems require and energy source, automatic wire feed system, computer numerical controlled gantries or robotic system [1]. The energy source used to melt the metal wire and deposition of the metal.

However, WAAM process received less attention than others AM technique. This due to unacceptable surface finish of fabricated parts and resultant poor geometrical accuracy always keep WAAM from an industrial application such as aerospace and structural industry [2]. Usually, in order to remove unwanted geometry post-processing processes such as machining are required for any components that are built by depositing a series of overlapping beads using arc welding. Upon selecting of geometrical parts, arc welding and wire feed material contributes significantly on process parameters. Therefore, wider commercial uptake with WAAM is limited by the inability to work with acceptable surface finish and geometry. Besides that, determine the parameter setting is important for the improvement of welding quality and reduction of cost. Thus, this present study explores the effect of WAAM process parameters on the geometrical characteristics of metal deposited beads. The models in view of rectangular metal deposited with size 50 mm x 10 mm x 40 mm.

## 2. EXPERIMENTAL SETUP

The test was performed using in house developed 3D printing system [3] which is integrated with Gas Metal Arc Welding (GMAW) as shown in Figure 1. The experiment has been carried out on a substrate of a mild steel plate of 6 mm thickness, 300 mm long and 300 mm wide. An ER 70S-6 server as a filler wire with 0.8 mm diameter coaxial along GMAW. This work used the zig-zag tool path pattern.

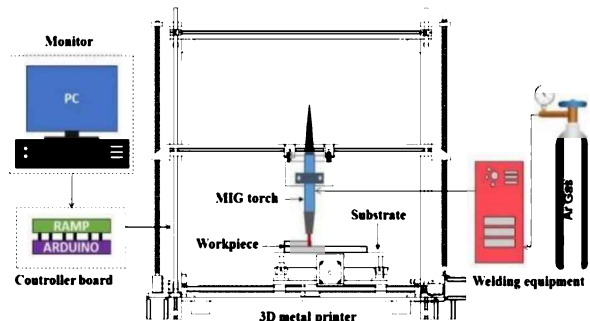


Figure 1 Experimental setup.

The process parameters involved as shown in Table 1. In order to ensure the depositing process steady, the 3D printing speed was kept in the range from 20 to 80 mm/s. The wire feed speed was set at 2800 mm/min. Welding voltage was varied from 18.5 to 22.5 V. Meanwhile, constant nozzle to plate distance, layer height and welding current were used for deposition sample, which was 5 mm, 2 mm and 100 A respectively. It should be noted that the range of parameters is designed just seldom used in practical application. A total of 9 samples were printed using varying process parameters. The first five samples with the varying voltage between 18.5 to 22.5 V were printed. Next four samples were printed by varying speed between 20 to 80 mm/s.

Table 1 Process parameters.

Parameter	Range
Travel speed, v (mm/s)	20 – 80
Wire feed speed (mm/min)	2800
Nozzle to plate distance (mm)	5
Layer height (mm)	2
Welding current, I (A)	100
Welding voltage, V (volt)	18.5 - 22.5

### 3. RESULTS AND DISCUSSION

The result presented the effect of heat input on the dimensional accuracy of height weld bead deposition. The combination of welding voltage and travel speed produce significance impact on accuracy due to inappropriate heat input distribution. Figure 2 shows a graphical way of illustration the percentage of dimensional change in height due to heat input distribution at a different voltage.

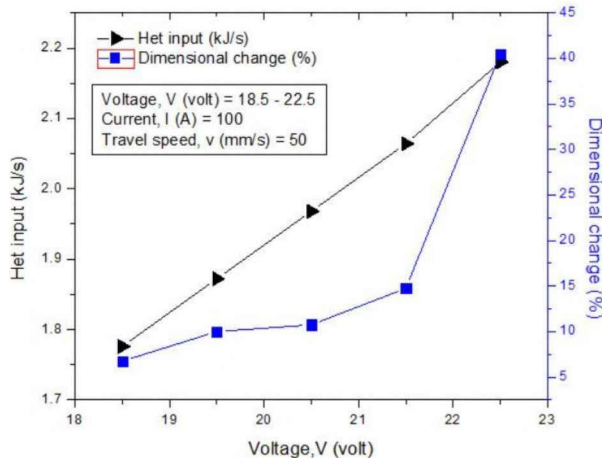


Figure 2 Relationship between the voltage, heat input and percentage of dimensional change.

It can be observed form these graphs a clear direct relation between heat input and voltage was identified. The most striking result emerges from the less heat input which produces the less dimensional change in height. The minimum percentage difference was 6.75% at 18.5V and heat input 1.776 kJ/s. These findings seem consistent with other researcher perspectives with the influence of heat input in acquired the acceptable geometrical accuracy. Suryakumar concludes the great importance for better geometric resolution is less heat input and better heat distribution [4]. Due to continued deposition with excessive heat input in the local area result in poor dimensional tolerance and surface finish. The relationship of speed, heat input, and dimensional change is indicated in Figure 3. The graph shows gradually decreasing of heat input while the travel speed is increasing.

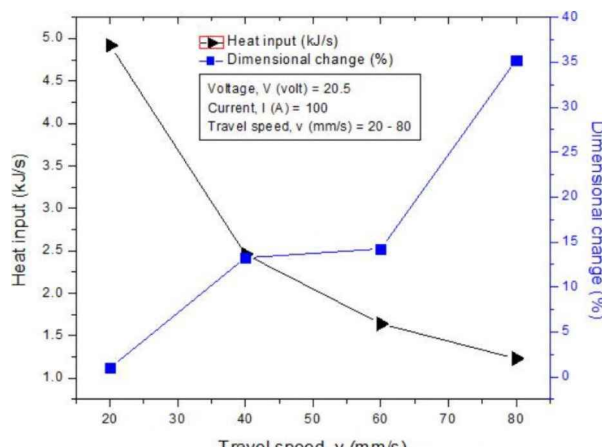


Figure 3 Relationship between the speed, heat input and percentage of dimensional change.

The minimum percentage of dimensional change is 1% and slightly decrease than former experiments. The greatest percentage difference of height about 21% at travel speed 60 mm/s to 80 mm/s. It is noticeable that, low heat input can be achieved by using higher speed. However, unacceptable geometries were found if less heat input and fast moving speed. It can be seen the height of the deposited layers decrease with an increase in travel speed. Higher speed is preferred to achieve high productivity, but it should be appropriate with the combination of others parameters. The minimum percentage difference was 1% at travel speed 20 mm/s and heat input 4.920 kJ/s as shown in Figure 4. This shows the importance of travel speed in deposition the weld bead. As the rate of travel speed reduces, the exposure time of weld beads is increasing and resulting higher heat input. Moreover, the increase of heat input found to be more prominent at high current setting. Xiongrong Li points out that high heat input is needed to achieve full penetration but fairly acceptable speed to prevent high distortion.

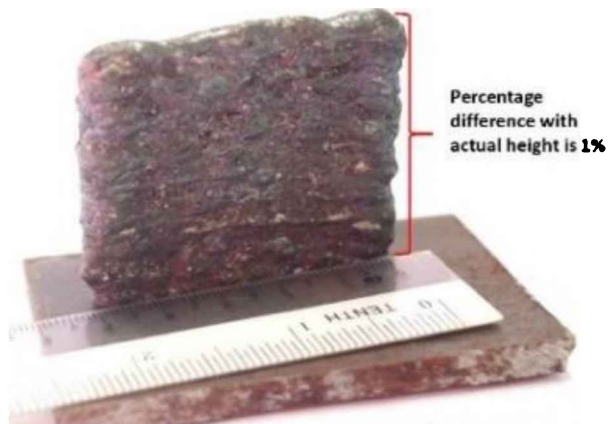


Figure 4 Sample with minimum dimensional change.

### 4. CONCLUSION

This study has presented an analysis of the effect of welding voltage, travel speed, heat input on percentage difference of height. Taking into account the effect of heat input, the result reveals the increasing of heat input forms excessive weld bead and produce large percentage difference than actual. Hence, it is important to optimize the parameter so that a relatively good dimensional accuracy printed part can be achieved.

### ACKNOWLEDGEMENT

The authors would like to thank Universiti Teknikal Malaysia Melaka (UTeM) for PJP/2017/FKM/H1I5/S01548 and Ministry of Energy, Science, Technology, Environment & Climate Change (MESTECC) for research grant 03-01-14-SF0145.

### REFERENCES

- [1] Wu, B., Pan, Z., Ding, D., Cuiuri, D., Li, H., Xu, J. & Norrish, J. (2018). A review of the wire arc additive manufacturing of metals: Properties, defects and quality improvement. *Journal of Manufacturing Process*, 35, 127–139.
- [2] Paskual, A., Alvarez, P. & Suárez, A. (2018). Study on arc welding process for high deposition rate

- additive manufacturing. *Procedia CIRP*, 68, 358-362.
- [3] Rosli, N.A., Alkahari, M.R., Ramli, F.R., Maidin, S., Sudin, M.N., Subramoniam, S. & Furumoto, T. (2018). Design and Development of a low cost 3D metal printer. *Journal of Mechanical Engineering Research & Development*, 41(3), 47-54.
- [4] Suryakumar, S., Karunakaran, K.P., Bernard, A., Chandrasekhar, U., Raghavender, N. & Sharma, D. (2011). Weld bead modeling and process optimization in hybrid layered manufacturing. *Computer-Aided Design*, 43(4), 331-344.

# Total volatile organic compound (TVOC) exposure from recycle polyamide nylon powder during selective laser sintering process

Amir Abdullah Muhamad Damanhuri<sup>1,\*</sup>, A.Shamsul Rahimi A.Subki<sup>2</sup>, Azian Hariri<sup>3</sup>, Muhammad Hafidz Fazli Md Fauadi<sup>4</sup>, Mohammad Rafi Omar<sup>1</sup>, Abdul Munir Hidayat Shah Lubis<sup>1</sup>

<sup>1)</sup> Fakulti Teknologi Kejuruteraan Mekanikal dan Pembuatan, Universiti Teknikal Malaysia Melaka, Hang Tuah Jaya, 76100 Durian Tunggal, Melaka, Malaysia

<sup>2)</sup> Fakulti Teknologi Kejuruteraan Elektrik dan Elektronik, Universiti Teknikal Malaysia Melaka, Hang Tuah Jaya, 76100 Durian Tunggal, Melaka, Malaysia

<sup>3)</sup> Fakulti Kejuruteraan Mekanikal dan Pembuatan, Universiti Tun Hussein Onn Malaysia, 86400, Parit Raja, Bt Pahat, Johor, Malaysia

<sup>4)</sup> Fakulti Kejuruteraan Pembuatan, Universiti Teknikal Malaysia Melaka, Hang Tuah Jaya, 76100 Durian Tunggal, Melaka, Malaysia

\*Corresponding e-mail: amir.abdullah@utem.edu.my

**Keywords:** Total volatile organic compound; selective laser sintering; exposure

**ABSTRACT** – Polyamide nylon (PA12) is semi crystalline polymers that are common materials used in selective laser sintering (SLS) process. Usually, unsintered powder will be recycled to used back for SLS printing. Therefore, this study investigates the exposure of total volatile organic compound (TVOC) from recycle polyamide nylon during SLS printing process. Prior to the investigation, the recycle powder was sent for thermogravimetric analysis (TGA). Calibration block was set to be print SLS machine, filled with 30kg of powder. Real time sampling was accordingly to Industry Code of Practice by DOSH Malaysia for 8 hours indoor sampling. TGA revealed that no composition loss during normal sintered temperature. The highest TVOC emission present at post printing process (powder cake breakout) of 1.7ppm. Mitigation strategies are suggested to reduced occupational exposure of TVOC emission to the SLS operators.

## 1. INTRODUCTION

Nowadays, 3D printer is now a common machine to general public due to its rapid prototyping. Military, medical devices, aerospace and automotive are fields that use additive manufacturing (AM) of 3D printer to print their prototype and products. There are several type of AM categories such as photo polymerization, material extrusion, powder bed fusion, direct energy deposition, sheet lamination, material jetting, and binder jetting. Selective laser sintering meanwhile includes in the category of powder bed fusion [1]. Polymers powder especially polyamide nylon are common material used in SLS. During SLS printing process, only powder which heated by the scanning action will crystallize to become the final product, and others remain and turn to recycled powder. However, the use of these powder in nontraditional manufacturing environments may pose health risks to group of people that are handling SLS printing process. AM machine can release volatile organic compounds chemical and particles into air while printing processes [2]. They are not built with air cleaning system; the situation could be worst if use in an enclosed space without proper air flow or ventilation. Studies show that VOC have negative impacts on human

and environmental health [3]. Therefore, this study aims to investigates the exposure of total volatile organic compound (TVOC) during 3D printing of SLS process from recycle powder of polyamide nylon (PA12).

## 2. METHODOLOGY

The recycle polyamide nylon powder were collected from SLS Laboratory Fakulti Teknologi Kejuruteraan Mekanikal dan Pembuatan, FTKMP of Universiti Teknikal Malaysia Melaka ( $2^{\circ}16'40.4"N$   $102^{\circ}16'32.4"E$ ). The powder has been heated 172 °C laser temperature during 3D printing previously. Prior to the exposure analysis, the recycle powder were sent for Thermogravimetric Analysis (TGA) using Thermal Gravimetric Analyzer Linseis Model. Thermal analysis was conducted at room temperature until 600 °C with heating rate of 10 °C/min. The SLS 3D printer use for this project is Farsoon SS402P that operated with scanner of dynamic focusing, high accuracy galvo scanning system. The machine has external dimension size of 2660mm x 1540mm x 2150mm with weight of 3000 kg. The maximum printing prototype are 350 mm x 350 mm x 350 mm with capacity of 60kg powder. The type of laser is carbon dioxide (CO<sub>2</sub>) with 100W power, and laser wave length is 0.3 mm with scanning speed of 12.7 m/s. The thickness of powder layer for every rotating roller pass through was set to be 0.2mm. The sintered temperature of powder chamber was set to 190°C. Calibration block with dimension of 56 mm X 56 mm and 9 mm thickness was set to be print with 30kg of recycle powder [4]. The TVOC emission monitoring from SLS printing process divided into four phases [5], where: a) pre-printing, b) powder preparation (mixing powder), c) printing, and d) post printing.

Indoor sampling was perform in SLS Laboratory of FTKMP accordingly to DOSH Malaysia Indoor Air Quality Code of Practice (ICOP DOSH 2010) [6]. The laboratory was divided into two rooms as depicted at Figure 1. To measure the TVOCs, a ppbRAE monitor (ppbRAE 3000, USA, RAE System Inc) was used for real time sampling of 8 hours printing process. The instrument set to be 1 meter from floor, at 5 minutes

interval sampling.

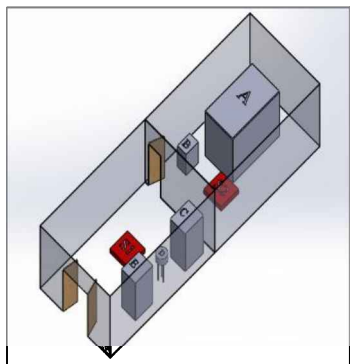


Figure 1 SLS Laboratory and sampling locations.

### 3. RESULT AND DISCUSSION

Thermogravimetry analysis (TGA) and Difference Thermo Gravimetry (DTG) are plotted in Figure 2. TGA present several step of mass loss from recycle polyamide nylon namely (i) at temperature around 300°C, a low level of water absorption which is about 10% was observed, (ii) at around 300°C to 400°C with another 10% loss, (iii) at around 400°C to 480°C, corresponds to the most important mass loss during thermal decomposition and (iv) final mass loss at 550°C [7].

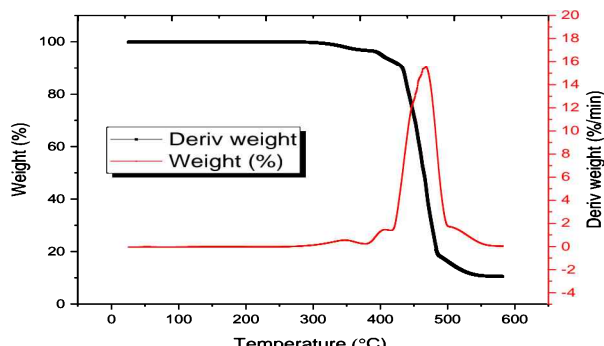


Figure 2 TGA and DTG analysis.

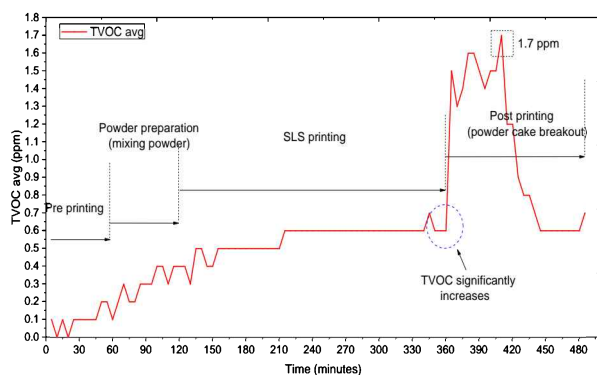


Figure 3 TVOC exposure during SLS printing process.

The emission of TVOC from SLS printing process were depicted at Figure 3. The TVOC slowly increase during preparation powder phase and maintain at a constant amount during SLS printing prototype. However, the emission gradually increases and at 360 minutes, where powder cake was taken out from SLS chamber for powder cake breakout phase and same

agreement with Preez S.D. et al.,[5]. The TVOC shows highest value of emission at 410 minutes (1.7ppm). The influence of powder cake temperature significantly increase the emission of TVOC [3].

### 4. CONCLUSION

In this study, the TVOC emission from recycle polyamide nylon (PA12) was present. The TGA analysis shows there was no significant amount of thermal composition lost at normal sintered temperature (200 °C). Meanwhile, the TVOC emission hit the highest value during post printing process. The emission increases slowly at the beginning of process, and stable during SLS printing phase. The present of TVOC emission during SLS printing process shows potential health hazard to the operators. Mitigation strategies such ventilation and suitable personal protective equipment are necessary to make sure operators works in safe environment.

### ACKNOWLEDGEMENT

The author would like to gratitude and acknowledge Universiti Teknikal Malaysia Melaka for the funding under short term grant, UTeM/PJP/2018/FTK (11A)/S01612.

### REFERENCE

- [1] Prakash, K. S., Nancharaih, T., & Rao, V. S. (2018). Additive Manufacturing Techniques in Manufacturing-An Overview. *Materials Today: Proceedings*, 5(2), 3873-3882.
- [2] Azimi, P., Zhao, D., Pouzet, C., Crain, N. E., & Stephens, B. (2016). Emissions of ultrafine particles and volatile organic compounds from commercially available desktop three-dimensional printers with multiple filaments. *Environmental Science & Technology*, 50(3), 1260-1268.
- [3] Damanhuri, A. A. M., Leman, A. M., Abdullah, A. H., & Hariri, A. (2015). Effect of toner coverage percentage and speed of laser printer on total volatile organic compound (TVOC). *Chemical Engineering Transactions*, 45, 1381-1386.
- [4] Afshar-Mohajer, N., Wu, C. Y., Ladun, T., Rajon, D. A., & Huang, Y. (2015). Characterization of particulate matters and total VOC emissions from a binder jetting 3D printer. *Building and Environment*, 93, 293-301.
- [5] Du Preez, S., Johnson, A., LeBouf, R. F., Linde, S. J., Stefański, A. B., & Du Plessis, J. (2018). Exposures during industrial 3-D printing and post-processing tasks. *Rapid Prototyping Journal*, 24(5), 865-871.
- [6] DOSH Malaysia. (2010). Industry code of practice on indoor air quality 2010, JKPP DP (S) 127/379/4.39. 1-50.
- [7] Chen, P., Wu, H., Zhu, W., Yang, L., Li, Z., Yan, C., ... & Shi, Y. (2018). Investigation into the processability, recyclability and crystalline structure of selective laser sintered Polyamide 6 in comparison with Polyamide 12. *Polymer Testing*, 69, 366-374.

# Factors for increasing additive manufacturing (3D printing)

Ai Nurhayati\*, Ahmad Rivai, Rina Indrayani

Faculty of Industrial Engineering, Sekolah Tinggi Teknologi Bandung, Soekarno-Hatta, 378 Bandung, Indonesia

\*Corresponding e-mail: ain38375@gmail.com

**Keywords:** 3D printing; analysis factors; SPSS

**ABSTRACT** – 3D printing is needed in the industrial world, especially for prototyping. The problem found is that the product results are not as expected by consumers. The purpose of this research is to find out what factors can improve 3D printing products to meet user expectations. This research uses factor analysis method with SPSS version 25 software to find out factors that can improve 3D printing products. The results of the analysis show that the output material factor of 3D printing is the main factor for the improvement of 3D printing products.

## 1. INTRODUCTION

Additive manufacturing is often referred to as 3D printing. There are several general steps in the 3D printing process. The generic Additive Manufacturing (AM) process is [1]:

- (a) Step 1: CAD
- (b) Step 2: Conversion to STL
- (c) Step 3: Transfer to AM machine and STL File Manipulation
- (d) Step 4: Machine Setup
- (e) Step 5: Build
- (f) Step 6: Removal
- (g) Step 7: Post-processing
- (h) Step 8: Application

The consumption growth rate of 3D printing is increasing year by year as shown in Figure 1. The level of 3D printing needs is predicted to continue to rise to reach \$ 21 billion by 2020 in the international world. This is a good opportunity for Indonesia to be able to increase 3D printing manufacturers in the country of Indonesia.

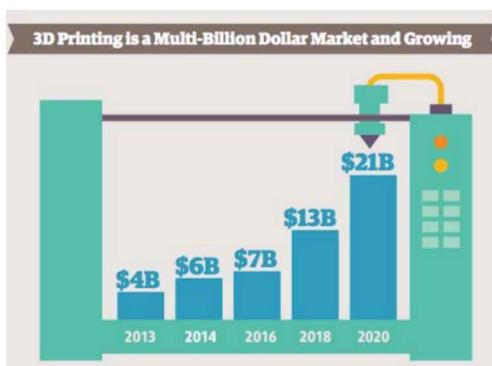


Figure 1 The growth rate of 3D printing [2].

The majority of the use of 3D printing in the world is to make prototypes by 55% as shown in Figure 2. The department that most often uses 3D printing is the research and development department as shown in Figure 3.

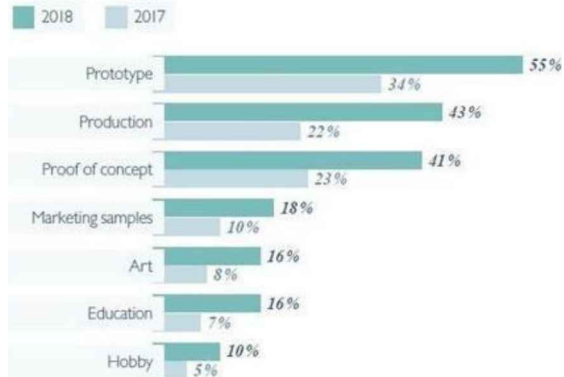


Figure 2 3D printing applications [3].

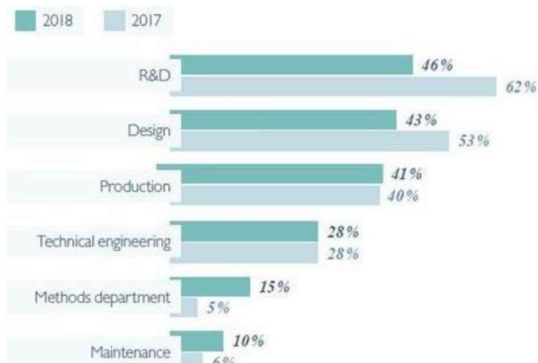


Figure 3 3D printing users by the department [3].

3D printing is very attractive to the Indonesian people, especially for the purpose of making prototypes. The problem found is that the product results are not as expected. The problem is to find out what factors can improve 3D printing products in order to meet the expectations of the Indonesian people. 3D printing manufacturers need to know what factors need to be improved in developing 3D printing products to be useful in accordance with customer expectations. The purpose of this research is to find out what factors can improve 3D printing products to meet user expectations. Several factors were considered in focus group discussions that could affect the performance improvement of 3D printing products. There are 8 factors as follows: time, cost, quality, material, effect, simple, easy to use, and color. In this study using the factor analysis method through the SPSS version 25 software program.

## 2. METHODOLOGY

Factor analysis is a statistical method used to describe variability among observed, correlated variables in terms of a potentially lower number of unobserved variables called factors. Factor analysis is a multivariate

analysis method used to group large numbers of variables into a small group of variables. The aim of all factor analytic techniques is to explain patterns of covariation among observed variables using unobserved constructs [4]. Factor analysis is one method that is useful for establishing evidence for validity [5]. Factor analysis method allows us to describe many variables using a few factors. This method helps us to select a small group of variables of representative variables from a larger set. In factor analysis we represent the variables  $y_1, y_2, \dots, y_p$  as linear combinations of a few random variables  $f_1, f_2, \dots, f_m$  ( $m < p$ ) called factors [6]. Factor analysis decision process [7]:

- (a) The objective of factor analysis
- (b) Designing a factor analysis
- (c) Assumptions in factor analysis
- (d) Deriving factors and assessing the overall fit
- (e) Interpreting the factors
- (f) Validation of factor analysis
- (g) Additional uses of factor analysis results.

The use of factor analysis is widespread; examples can be found in highly ranked journals in many disciplines, including industrial engineering, economics, and manufacture [8]. The method used in this study is factor analysis using SPSS version 25 software.

### 3. RESULTS AND DISCUSSION

Based on the results of interviews and field surveys that are discussed and considered in focus group discussions, there were 8 variables that influenced the improvement of 3D printing tools. These variables are time, cost, quality, material, effect, simple, easy to use, and color. From the eight variables then processed by factor analysis method use SPSS version 25 software.

The output of the factor analysis method is presented in Table 1. The KMO value is above 0.5 and the significant number is below 0.05 which indicates that the research data can be processed further.

Table 1 KMO and Bartlett's test.

Kaiser-Meyer-Olkin measure of sampling adequacy	0,673
Bartlett's test of Sphericity	Approx. Chi-Square
	Df
	Sig.

The results obtained that there are four variables that influence the improvement of 3D printing products as shown in Table 2.

In Table 3, it can be seen that the components or factors are sorted from the lowest value to the highest value. The highest factor influencing the performance improvement of 3D printing tools is material factors.

Table 2 Anti-image matrices.

	Time	Quality	Output	Material
Anti-image	.803	-.210	,021	-,177
Covariance	Quality -.210	,786	-,102	-,120
	Output ,021	-,102	,688	-,312
	Material -,177	-,120	-,312	,614
Anti-image	Time ,702 <sup>a</sup>	-,264	,028	-,252
Correlation	Quality -,264	,756 <sup>a</sup>	-,138	-,173
	Output ,028	-,138	,637 <sup>a</sup>	-,479
	Material -,252	-,173	-,479	,640 <sup>a</sup>

<sup>a</sup> Measures of Sampling Adequacy (MSA).

Table 3 Component matrix.

	Component
Time	0,646
Quality	0,697
Output	0,726
Material	0,817

Extraction method: Principal component analysis.

### 4. CONCLUSION

Based on the results of the research show that material factors are the main factors that can improve the performance of 3D printing to obtain product output that is in accordance with customer expectations.

### REFERENCES

- [1] Gibson, I., Rosen, D. W., & Stucker, B. (2014). *Additive manufacturing technologies* (Vol. 17). New York: Springer.
- [2] Computer world: Electronic References. 3D printing industry to triple in four years to \$21B. Retrieved April 30, 2019, from <https://www.computerworld.com>.
- [3] Forbes: Electronic References. The state of 3D printing, 2018. Retrieved April 30, 2019, from <https://www.forbes.com>.
- [4] Wright, A. G. (2017). The current state and future of factor analysis in personality disorder research. *Personality Disorders: Theory, Research, and Treatment*, 8(1), 14.
- [5] Wetzel, A. P. (2012). Factor analysis methods and validity evidence: a review of instrument development across the medical education continuum. *Academic Medicine*, 87(8), 1060-1069.
- [6] Rencher, A. C., & Christensen, W. F. (2002). *Méthods of multivariate analysis*. a john wiley & sons. INC.: Toronto, ON, Canada.
- [7] Hair, J. F., Black, W. C., Babin, B. J., & Anderson, R. E. (2010). *Multivariate data analysis*: Global edition.
- [8] Van der Eijk, C., & Rose, J. (2015). Risky business: factor analysis of survey data—assessing the probability of incorrect dimensionalisation. *PLoS one*, 10(3), e0118900.

## Effects of current and wire feed direction in WAAM-TIG

Johnnie Liew Zhong Li<sup>1</sup>, Mohd Rizal Alkahari<sup>1,2,\*</sup>, Nor Ana Rosli<sup>1</sup>, Faiz Redza Ramli<sup>1,3</sup>, Rafidah Hasan<sup>1,3</sup>

<sup>1)</sup>Fakulti Kejuruteraan Mekanikal, Universiti Teknikal Malaysia Melaka,  
Hang Tuah Jaya, 76100 Durian Tunggal, Melaka, Malaysia

<sup>2)</sup>Advanced Manufacturing Centre, Universiti Teknikal Malaysia Melaka,  
Hang Tuah Jaya, 76100 Durian Tunggal, Melaka, Malaysia

<sup>3)</sup>Centre for Advanced Research on Energy, Universiti Teknikal Malaysia Melaka,  
Hang Tuah Jaya, 76100 Durian Tunggal, Melaka, Malaysia

\*Corresponding e-mail: rizalalkahari@utem.edu.my

**Keywords:** 3D printing; additive manufacturing; wire arc additive manufacturing (WAAM)

**ABSTRACT** – WAAM-TIG has many parameters affecting the fabricated structure. This paper reports the effect of current and wire feed direction on the weld bead of TIG. Detail design and experimental set up are provided. Different current values and wire speed direction are tested. The structure of specimens is tabulated, compared and analyzed. The current and wire feed direction can significantly affect the fabricated metal part. The optimal current range for this open sources TIG 3D metal printer is 75A to 85A. Front wire feedstock direction is recommended in WAAM-TIG.

### 1. INTRODUCTION

Wire arc additive manufacturing (WAAM) is increasingly being used worldwide due to its capabilities of reducing the cost and time. Generally, AM technology was invented to remove the limitation of traditional subtractive manufacturing (SM) [1]. There are three types commonly used heat sources used in WAAM which are metal inert gas welding (MIG), tungsten inert gas welding (TIG) and plasma arc welding (PAW) [2]. WAAM-MIG process is easier and more convenient compared to WAAM-TIG and WAAM-PAW due to its continuous wire spool with the welding torch which does not have wire feed direction problem. MIG uses a direct feeding spool system which is the MIG wire feed is coaxially with the welding torch and does not encounter the problem of wire feed angle and orientation. Unlike MIG, tungsten inert gas welding (TIG) and plasma arc welding (PAW) need an external wire feed machine to supply the additive materials. Angles and positions of the external wire feed can affect the quality and appearance of the weld bead.

TIG deposition rate is around 1kg/h [3]. TIG welding process is normally used to consolidate thin and middle-sized metal by melting it with an arc that created between non-consumable electrode and the workpiece with the existence of inert gas such as argon and helium gas. Shielding gases play a role to shelter the weld pool from being oxidized and contaminated. In this research, the effect of current and wire feed direction in TIG are studied.

### 2. METHODOLOGY

A 20mm×20mm of a square single line is drawn by using CATIA. The experiment was carried out on an aluminum plate. An open source 3D printing is used with

CEA MATRIX 400 AC/DC TIG welder is used as the heat source. ER5356 aluminum rod is used as the feedstock. The schematic diagram of the machine setup is shown in Figure 1.

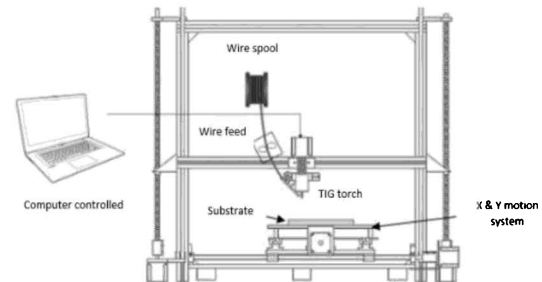


Figure 1 Schematic diagram of machine setup.

Table 1 Parameters setting.

Parameter	Unit	Values
Current	A	65 - 85
Wire feed angle	degree	45
Wire feed rate	mm/min	1200
Travel speed	mm/s	1.5
Stand-off distance	mm	5
Voltage	V	65

The machine and welding parameter are shown in Table 1. 20mm×20mm square line was printed with different current. The wire feed stock was placed on three different directions as shown in Figure 2. The sample is print from the starting point to point 1 in -ve x-direction which the wire feed is placed in front of the torch. Direction B is print from point 1 to point 2 in -ve y-direction which the wire feed is in the side position whereas direction C prints from point 2 to point 3 in +ve x-direction as the wire feed position is behind the torch. Direction D is print from point 3 to ending point which is the wire feed position is same as direction B.

### 3. RESULTS AND DISCUSSION

All samples were successfully fabricated. Figure 3 shows the comparison of weld bead width with different current values and directions. The molten pool size is getting larger as the current value increases and affecting weld bead width. The sample 65A and 70A produce a little droplets deposition and discontinuous deposition respectively. It was shown that the range 65A to 70A

could not melt the aluminum rod as shown in Figure 3(a) and 3(b). The continuous deposition was achieved when the current set to 75A. Unfortunately, the weld bead is overlapped in direction C in which the wire feedstock is placed behind the torch. For sample 80A, the single layer was fabricated better than sample 75A as the deposition is smooth and no defects or overlap occur in all directions. Deposition of sample 80A and sample 85A are alike but the weld bead width of the sample 85A is wider. It is because of the heat affected zone (HAZ) for sample 85A is higher than 80A. The range of HAZ is depending on the rate of heat input and the heat input increases as the current increases [4]. Thus, the width of sample 85A is wider than sample 80A. Wire feeding direction can affect the waveform and width of the single weld bead layer. The width of direction A, B, C and D for sample 80A are 6.60mm, 6.15mm, 7.61mm, and 7.98mm respectively. Direction A and B's weld bead is more constant than direction C and D. The conditions of the welding process can be indicated through the weld bead appearance. The welding process and deposition looks stable at current 80A. However, things changed in different wire feed directions. It was obviously shown that the direction A which is the wire feed placed in front of the torch has the best weld bead appearance compares to other wire feed directions [5]. The overlap commonly occurred in the direction C which the wire feed is placed behind the torch as shown in Figure 3(c), (d) and (e).

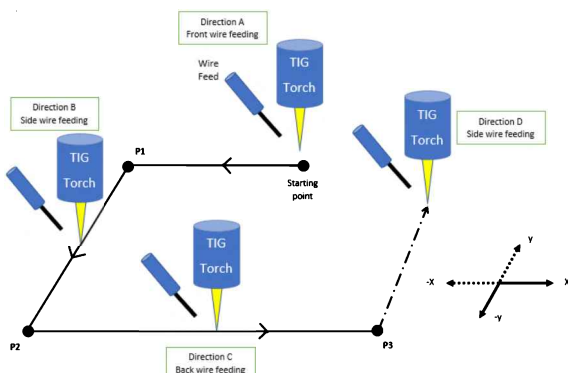


Figure 2 Wire feed direction.

Based on the results, 80A has the most satisfied weld bead appearance in direction A where the wire feed is placed in front of the torch. Thus, five layers specimen was fabricated using 80A in direction A as shown in Figure. The specimen was fabricated layer upon layer and form into a rectangular wall. The height 11mm which is 2mm taller than the CAD dimension. Inclusion and depression were found in the fabricated rectangular wall. This phenomenon occurs are generally due to the imperfection in wire especially the wire rod is twisted.

#### 4. CONCLUSION

The current and wire feed direction can significantly affect the fabricated metal part. The optimal current range for this open sources TIG 3D metal printer is 75A to 85A. Front wire feedstock direction is recommended in WAAM-TIG. Multiple layers are possible to be fabricated with suitable parameter and it can be explored detailedly in future. However, the application of TIG in WAAM requires modification on

the wire feeding system as the WAAM-TIG very much dependent on the wire position which affects its dimension accuracy.

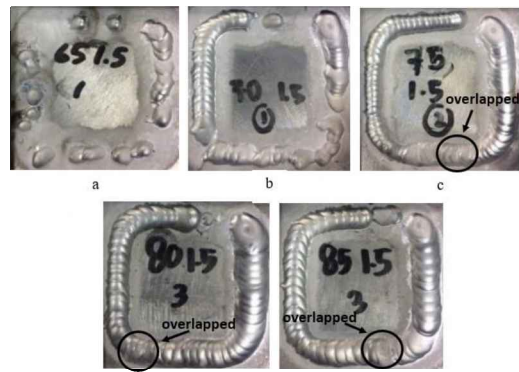


Figure 3 Deposition of sample at (a) 65A, (b) 70A, (c) 75A, (d) 80A & (e) 85A.



Figure 4 Inclusion and depression occurred on five layers specimen using WAAM-TIG at 80A and Direction A (front wire feed).

#### ACKNOWLEDGEMENT

The authors would like to thank Universiti Teknikal Malaysia Melaka (UTeM) and Ministry of Energy, Science, Technology, Environment & Climate change (MESTECC) for research grant 03-01-14-SF0145.

#### REFERENCES

- [1] Rosli, N. A., Alkahari, M. R., Ramli, F. R., Maidin, S., Sudin, M. N., Subramoniam, S., & Furumoto, T. (2018). Design and development of a low-cost 3D metal printer. *Journal of Mechanical Engineering Research and Developments*, 41(3), 47-54.
- [2] Xiong, J., Lei, Y. Y., Chen, H., & Zhang, G. J. (2017). Fabrication of inclined thin-walled parts in multi-layer-single-pass GMAW-based additive manufacturing with a flat position deposition. *Journal of Materials Processing Technology*, 240, 397-410.
- [3] Almeida, P. S., & Williams, S. (2010). Innovatie process model of Ti-6Al-4V additive layer manufacturing using cold metal transfer (CMT). *Proceeding of the 21<sup>st</sup> Annual International Solid Freeform, Unvinersity of Texas Austin*.
- [4] Mamat, S., & Jamlan, S. (2015). Effect of welding heat input on microstructure and mechanical properties at coarse grain heat affected zone ABS grade a steel. *ARPJ Journal of Engineering and Applied Sciences*. 10(20), 9487-9495.
- [5] Ding, D. H., Pan, Z. X., Cuiuri, D., & Li, H. J. (2015). Wire-feed additive manufacturing of metal components: technologies, developments and future interests. *International Journal of Advanced Manufacturing Technology*. 81(1-4), 465-481.

# Electromyography sensing on tibialis and peroneus muscle against improvised flat feet orthotic insole

Umi Hayati Ahmad\*, Nuratifah Abdul Kudus, Mohd Hidayat Ab Rahman, Nurul Syifaa' Jamaluddin

Fakulti Teknologi Kejuruteraan Mekanikal dan Pembuatan, Universiti Teknikal Malaysia Melaka,  
Hang Tuah Jaya, 76100 Durian Tunggal, Melaka, Malaysia

\*Corresponding e-mail: umihayati@utem.edu.my

**Keywords:** Orthotic; flatfeet; tibialis peroneus

**ABSTRACT** – The objectives of this paper are to investigate the muscle activity against improvised flat feet orthotics insole using electromyography. Length, width and thickness of orthotics insole are based on average size of flat feet respondents. Flexifoam X were filled up in the fabricated wood mould. The comparison between fabricated and existing orthotics insole shows different result during evaluation using electromyography on tibialis anterior and peroneus longus generated by muscle strength responsible for lower limb movement. The different material for each insole contributes to vary result on average median frequency and root mean square that produce by the muscle from each respondent.

## 1. INTRODUCTION

Walking is when only one foot at a time leaves contact with the ground. According to research, the average human walks a day is about three thousand steps. Running is when both feet are off the ground with each step. Running is a method of terrestrial locomotion allowing humans to move rapidly on foot that is related to the movement of the lower limb. Brown, C. [1] stated that in 1865, Everett H. Dunbar makes a breakthrough by inventing an arch support orthotic Arch orthotics is a shoe insole that is design like the shape of an arch and it is a function to provide support or cushion to feet and help to curb pain on feet. Everett H. Dunbar inserts a layer of leather between the insole and outsole of the shoe that is shaped like an arch which resembles the shape of feet. While in 1905, Whitman Brace invents the first full foot orthotic that is made of heavy metal.

According to Bateni, H. [2] the orthotics insole can provide postural stability and reduce foot pain for the sports usage. Mercer and Horsch [3] stated that orthotic insoles can support the feet controlling abnormal for motion in order to prevent it from moving inward or outward. This study aims to improve the efficiency of the orthotic insole for flat feet focus on sports usage and measure the muscle fatigue using electromyography on tibialis and peroneus muscles.

## 2. METHODOLOGY

Questionnaire has been distributed among students in UTeM in order to know the population of flat feet in UTeM (N=40), the flat feet respondents amongst them are only (N=8). Morphological chart as shown in Figure 1 and concept screening were used in this study to generate suitable design for flat feet correspondent based on their requirement during survey.

Criteria	Criteria 1	Criteria 2	Criteria 3	Criteria 4
Arch Support				
Heel support				
Heel Pad				
Metatarsal support				
Heel type				
Lightweight Aesthetic	Light material Slim form	Minimal Part No Assembly	Thin Curved Surface	Simplicity

Figure 1 Morphological chart of orthotic insole characteristic.

There are main characteristics of orthotics insole that help a person with flat feet to reduce the pain during sports activities, they are deep heel cup, heel pad, metatarsal pad, and sufficient arch support. This improvised orthotic insole is designed with standard dimensions from both male and female.

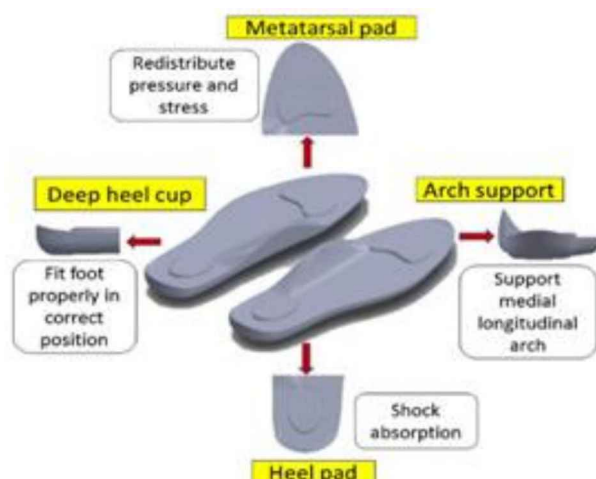


Figure 2 Characteristic of fabricated orthotic insole.



Figure 3 Fabrication of orthotic insole.

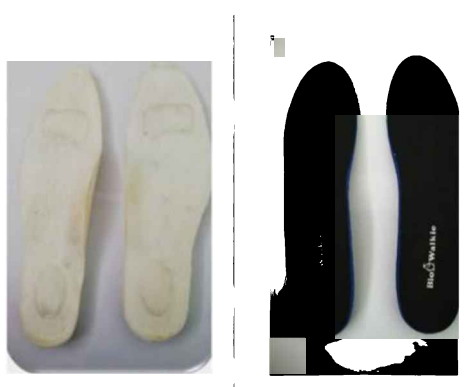


Figure 4 Fabricated insole with existing insole.

### 3. RESULTS AND DISCUSSION

Wireless sensors are set on lower limb muscles of tibialis anterior and peroneus longus muscles. EMG signal is recorded and collected via the wireless connections between the Trigno EMG sensors from Delsys and Trigno Wireless Foundation System. The Trigno EMG sensors are transmitted and gathered signals in the Trigno Wireless Foundation System. The collected data are filtered and been analysis by using time domain analysis which is the root mean square (RMS).

The RMS amplitude obtain for tibialis anterior muscle and peroneus muscle for fabricating and existing insole, each respondent portrays different value of muscle fatigue for left and right side of tibialis anterior and peroneus longus muscles. Many factors influence the muscle fatigue of the people. According to Mehta and Shortz [4], obesity may influence the alteration of muscle fiber type composition.

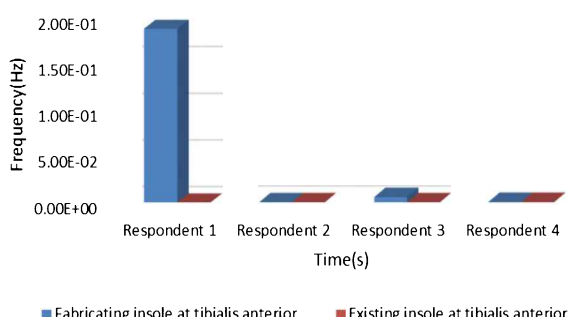


Figure 5 Average RMS amplitude on tibialis anterior muscle.

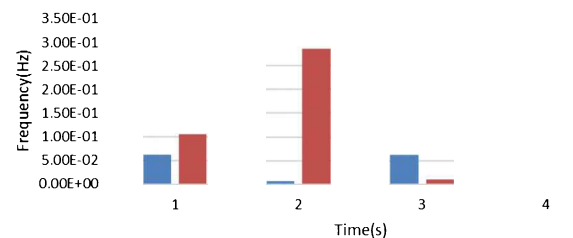


Figure 5 Average RMS amplitude on peroneus longus muscle.

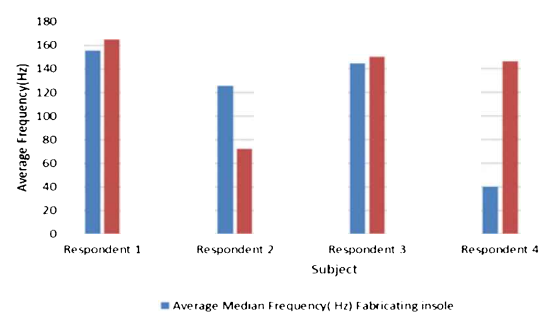


Figure 6 Average median frequency on tibialis anterior muscle.

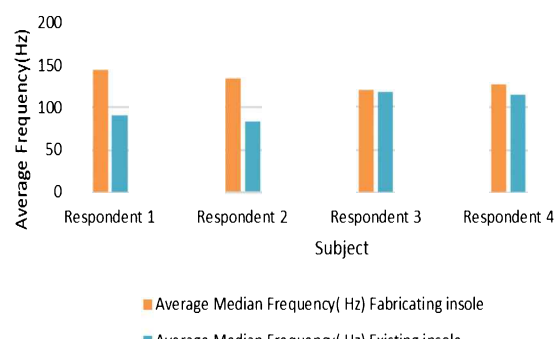


Figure 7 Average median frequency on peroneus longus muscle.

### 4. CONCLUSION

The comparison of the measured data of electromyography (EMG) on time domain analysis with RMS amplitude and median frequency (MDF) for the fabricating insole and the existing insole showed that the fabricating insole is suitable and give slightly better performance compared to the existing insole, thus the objective of the study is achieved.

### ACKNOWLEDGEMENT

The authors gratefully acknowledge the support of Universiti Teknikal Malaysia Melaka through Short Term Grant PJP/2018/FTK (14D)/S01640.

### REFERENCES

- [1] Brown, C. (2013). Clinical Advantage: Making Your Own Temporary Foot Orthosis. Orthopaedic Practice, (26;3:14), 204-205. Retrieved from [https://www.orthopt.org/uploads/content\\_files/files/FASIG26.3.pdf](https://www.orthopt.org/uploads/content_files/files/FASIG26.3.pdf)
- [2] Bateni, H. (2013). Changes of postural steadiness following use of prefabricated orthotic

- insoles. *Journal of Applied Biomechanics*, 29(2), 174-179.
- [3] Mercer, J. A., & Horsch, S. (2015). Heel-toe running: A new look at the influence of foot strike pattern on impact force. *Journal of Exercise Science & Fitness*, 13(1), 29-34.
- [4] Mehta, R. K., & Shortz, A. E. (2014). Obesity-related differences in neural correlates of force control. *European Journal of Applied Physiology*, 114(1), 197-204.

# Topological optimized engine bracket for additive manufacturing

Faiz Redza Ramli<sup>1,2,\*</sup>, Zaitul Akma Said<sup>1</sup>, Mohd Rizal Alkahari<sup>1,3</sup>, Shafizal Mat<sup>1,2</sup>, Mohd Nizam Sudin<sup>1,2</sup>

<sup>1)</sup> Fakulti Kejuruteraan Mekanikal, Universiti Teknikal Malaysia Melaka,  
Hang Tuah Jaya, 76100 Durian Tunggal, Melaka, Malaysia

<sup>2)</sup> Centre for Advanced Research on Energy, Universiti Teknikal Malaysia Melaka,  
Hang Tuah Jaya, 76100 Durian Tunggal, Melaka, Malaysia

<sup>3)</sup> Advance Manufacturing Centre, Universiti Teknikal Malaysia Melaka,  
Hang Tuah Jaya, 76100 Durian Tunggal, Melaka, Malaysia

\*Corresponding e-mail: faiz@utem.edu.my

**Keywords:** Topology optimization; 3D Printing; additive manufacturing

**ABSTRACT** – Engine bracket plays a crucial role in the design of an aircraft where the bracket mass directly influences the performance of aircraft. The objective of this paper is to obtain a fully optimized lightweight of engine bracket design with capability to withstand the load of the engine by using topology optimization technique and to identify the target specification baseline in terms of raw material mass, support material mass and printing time of additive manufacturing. Two topology optimization engine designs were studied by using *SolidThinking Inspire*. Afterwards the optimize design was compared with 300 existing topology optimized. The mass of engine bracket has been successfully reduced by 49% from original design without sacrificing the performance. Based on the baseline, the design is acceptable with range of 75% from all the 300 existing topological design.

## 1. INTRODUCTION

An engine bracket is commonly fabricated by conventional manufacturing process which in general is not fully optimized either for the performance or for the mass reduction. The role of this bracket is to hold and support the weight of the aircraft engine during handling on the engine throughout the operation time. The bracket offered an opportunity for weight reduction which is directly may reduce the cost of material.

Topology optimization (TO) is a method where material is removed by response to a given sets of loads, boundary condition and constraint. Design space is important in TO where removal of material will take place. Krishna et al. [1] found that when two beams are analyzed by using TO with different design region setting, a designer can achieve both requirements of high mass reduction while maintaining the stiffness of the part. The reduction of mass by TO might affected the performance of the product as in [2], where the stiffness of the topology optimized part reduced without sacrificing its performance requirement.

TO often produced complex geometry which is not feasible to be manufactured by conventional manufacturing but maybe produced by Additive Manufacturing (AM). However, AM suffered in printing overhanging parts and AM need support material to print the design [3]. In AM, when there is an overhang part, support structure is generated when the angle between the boundary normal and the build direction

exceeds a certain threshold. Furthermore, Leary et al.[4] have studied on optimal topology for AM which is a method for enabling AM of support-free optimal structures for FDM and found that part manufacture with support-free design and no support design have lesser printing time compare to part with support. Thus, it is important to obtain a fully optimized lightweight of engine bracket design by TO technique and to propose a design based on these AM limitations.

## 2. METHODOLOGY

### 2.1 Topology Optimization

The TO process began with the GE engine bracket design and was optimized by using Solid Thinking Inspire software. The load conditions by a design space are shown in Figure 1. The original mass of the bracket is 2.1912 kg. The design spaces were divided into two which are Topology Optimization I (TO I) and Topology Optimization II (TO II). TO I design space is located at clevis arm while TO II is located at the hole.

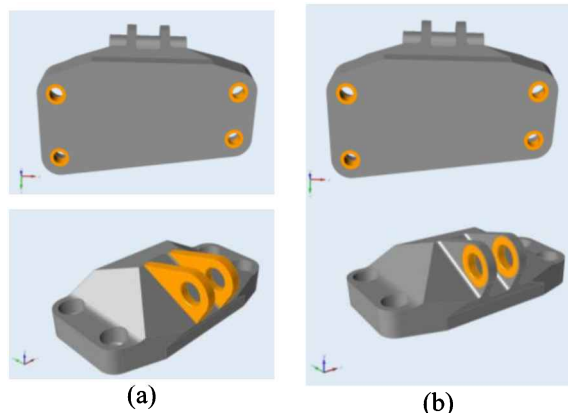


Figure 1 Design space for TO process in grey colour (a) TO I and (b) TO II.

There are four different load conditions which are for load condition 1 which is the 35,586 N maximum static linear of vertical load, load condition 2 which is 37,810 N maximum static linear of horizontal load, load condition 3 for maximum static linear of 42,258 N of 42 degrees from vertical and torsional load of 564 Nm at the intersection of centreline of pin and midpoint between clevis arms. In addition, supports at the bolt location are added as the rotation is allowed. The

element size and thickness constraints are auto generated which are 0.0026162 m and 0.00762 m respectively. Analysis on the stiffness was conducted on the topology optimized design in order to ensure that the von Mises stress do not violate the 903 MPa of material yield strength used which is Ti-6Al-4V by using the same load conditions.

## 2.2 Analysis on Target Specification Baseline

300 existing topology optimized designs of engine bracket were analyzed by using FDM software in term of raw material mass, support material mass and printing time needed to be manufactured by AM.

## 3. RESULTS AND DISCUSSION

### 3.1 Topology Optimization Results

Figure 2 shows the result of TO process on engine bracket for both design spaces applied. It is shown that a lot material has been removed from the original design.

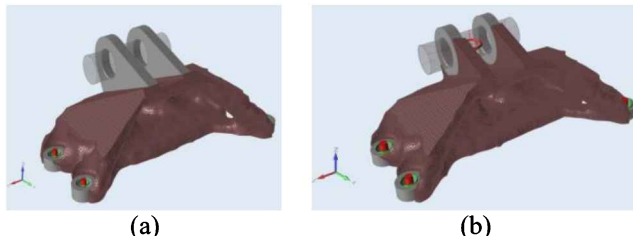


Figure 2 Topology optimized design of engine bracket  
(a) TO I and (b) TO II.

Table 1 shows the comparison for von Mises stress and mass for original design, topology optimized design from TO I and topology optimized design from TO II of engine bracket. As a result, TO I was accepted since the von Mises stresses for all load conditions did not exceed 903 MPa of material yield strength.

Table 1 Comparison for von Mises stress and mass for original design, TO I and TO II.

Design of engine bracket	Von Mises Stress (MPa)				Mass (kg)	
	Load condition					
	1	2	3	4		
Original	677.6	477.3	530.4	771.0	2.191	
TO I	819.3	510.3	579.4	886.6	1.041	
TO II	824.6	537.7	589.2	916.0	1.015	

### 3.2 Analysis on Target Specification Baseline

Topology optimized design from TO I was analyzed by FDM software for the AM output and plotted on the graph for baseline target specification. From the graph of support material mass against raw material mass as shown in Figure 3 and Figure 4, TO I showed 49% reduction of raw material mass needed to be manufactured by AM from the original design. However, there was support material mass needed for TO I. A modification was performed in order to achieve both constraints for TO and AM.

## 4. CONCLUSION

Topology optimization on engine bracket has reduced the mass by 49% from original design without sacrificing the performance. Based on the baseline, TO I

is acceptable with range of 75%.

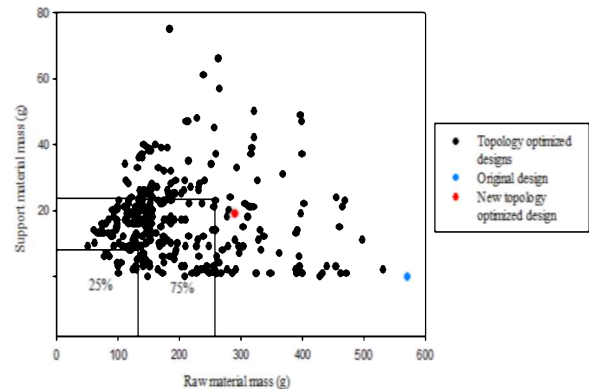


Figure 3 Support material vs raw material mass.

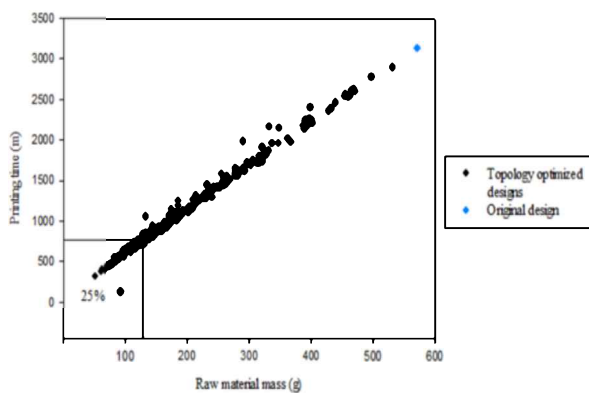


Figure 4 Printing time vs raw material mass.

## ACKNOWLEDGMENT

The authors gratefully acknowledge use of the services and facilities of the Fakulti Kejuruteraan Mekanikal, Universiti Teknikal Malaysia Melaka (UTeM). This research has been supported by the grant from Universiti Teknikal Malaysia Melaka (Grant no.: PJP/2019/FKM(6A)).

## REFERENCES

- [1] Krishna, L. S. R., Mahesh, N., & Sateesh, N. (2017). Topology optimization using solid isotropic material with penalization technique for additive manufacturing. *Materials today: proceedings*, 4(2), 1414-1422.
- [2] Sudin, M. N., Tahir, M. M., Ramli, F. R., & Shamsuddin, S. A. (2014). Topology optimization in automotive brake pedal redesign. *International Journal of Engineering and Technology (IJET)*, 6(1), 398-402.
- [3] Nazan, M. A., Ramli, F. R., Alkahari, M. R., Sudin, M. N., & Abdullah, M. A. (2017). Process parameter optimization of 3D printer using response surface method. *ARPN Journal of Engineering and Applied Sciences*, 12(7), 2291-2296.
- [4] Leary, M., Merli, L., Torti, F., Mazur, M., & Brandt, M. (2014). Optimal topology for additive manufacture: A method for enabling additive manufacture of support-free optimal structures. *Materials & Design*, 63, 678-690.

# Modeling and fabrication of protective mask with high complexity pattern using low-cost additive manufacturing design tool and systems

Syahibudil Ikhwan Abdul Kudus<sup>1,3,\*</sup>, Ahmad Afiq Baharuddin<sup>1</sup>, Mastura Mohammad Taha<sup>1,3</sup>, Mohammad Rafi Omar<sup>1,3</sup>, Mohd Idain Fahmy Rosley<sup>1,3</sup>, Shafizal Mat<sup>2,3</sup>

<sup>1)</sup> Fakulti Teknologi Kejuruteraan Mekanikal & Pembuatan, Universiti Teknikal Malaysia Melaka,  
Hang Tuah Jaya, 76100 Durian Tunggal, Melaka, Malaysia

<sup>2)</sup> Fakulti Kejuruteraan Mekanikal, Universiti Teknikal Malaysia Melaka,  
Hang Tuah Jaya, 76100 Durian Tunggal, Melaka, Malaysia

<sup>3)</sup> Centre for Advanced Research on Energy, Universiti Teknikal Malaysia Melaka,  
Hang Tuah Jaya, 76100 Durian Tunggal, Melaka, Malaysia

\*Corresponding e-mail: syahibudil@utem.edu.my

**Keywords:** Additive manufacturing; CAD modeling; high complexity pattern

**ABSTRACT** – This study explores the capability to produce a complex 3-dimensional (3D) modeling using Computer Aided Design (CAD) software in combination with Additive Manufacturing (AM) systems to design and manufacture a protective mask. This study aims to produce a high complexity design pattern on the customised protective mask. The 3D modeling of the protective mask was made using AM-enabled CAD software. The protective mask was manufactured using three types of AM printers, and the 3D printed products were compared. The comparative study indicated that the presented approach offers a feasible alternative to the current practices.

## 1. INTRODUCTION

The application of Additive Manufacturing (AM) in wearables and assistive device has been widely recognised. AM has been used to manufacture custom-fitting medical devices such as facial prosthetics and implants directly from 3D CAD data. AM is a process of joining materials layer-by-layer to make parts from 3D CAD data [1]. The main benefit of AM in product designs is that it allows geometrical freedom, thus, create possibilities for customisation, increased product functionality, and greater complexity in manufacturing objects.

A protective mask is an item designed to protect portions of the wearer's face, including nose and eyes area from contact with objects. It must comply specific requirements that are comfort, light, and easy to use. Most protective mask were manufactured using solid polymeric materials, such as polycarbonate. There are several problems arise from the existing design of the protective mask. The solid design of existing mask lacks ventilation causing users to feel uncomfortable, thus contributes to perspiration and odour issues [4,5]. Moreover, the weight of the protective mask also have implication on the user as it provide loads on the users' face.

The unique capabilities of AM and the existence of AM-enabled CAD software (e.g., Autodesk Meshmixer) provide opportunities to improve product performance and lowering overall manufacturing cost. By adapting high complexity pattern in the product such as Voronoi, the protective mask would not only look attractive, but

also improve skin ventilation and reduce weight [3].

## 2. METHODOLOGY

Two tasks have been carried out to develop the protective mask: (i) modeling of the protective mask – aimed to obtain the 3D data of the protective mask, and (ii) fabrication process – experimented use of AM printing system.

For the first task, the 3D modelling data of the protective mask design was obtained from the standard mannequin face and has been manipulated using Autodesk Meshmixer CAD software. For the second task, three types of 3D printing machine were used to fabricate the design. They are Up! Plus, Flashforge Creator Pro, and Projet 1000.

Up! Plus and Flashforge Creator Pro are Fused Deposition Modeling (FDM) types of machines that used material extrusion technology to fabricate the part. Acrylonitrile butadiene styrene (ABS) and polylactic acid (PLA) thermoplastic filament were used for those machines respectively. On the other hand, Projet 1000 is a Digital Light Processing (DLP) type of machine that used vat-photopolymerisation technology. Photopolymer resin was used to build the part. The process workflow of the protective mask is shown in Figure 1 below.

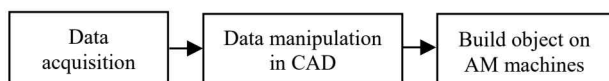


Figure 1 The process workflow [3].

During data acquisition, the measurement of the mannequin head is not precise, but rather general in length, width and height. Therefore, it needs to be dimensioned according to the real measurement of the human head. The face model wireframe was re-meshed so that the mesh triangle become smaller and denser. This step was taken in order to enable the selection process of face area that subjected to make the protective mask easier. The face is then being selected, and the size and shape of the protective mask design were determined. This step was crucial in order to establish the base of the protective mask 3D modeling. The selected mesh triangle is shown in Figure 2.



Figure 2 Selected mesh triangle on the face model.

The selected area of the protective mask then were offsets so that it provides a gap between the inner surface of the protective mask and the face. This provides airflow and space between the protective mask and the face. The selected area then was extruded to produce solid part. The thickness of the part is essential since it affects the overall condition of part weight, time taken to fabricate, and the minimum thickness requirement of the AM machines. The extruded part of the selected area also produces slight sharp edges. Therefore, smoothing those edges was performed (see Figure 3),

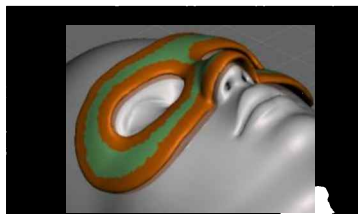


Figure 3 Smoothened mask area

The final step was applying a pattern on the protective mask design. The Voronoi pattern has been chosen to be applied to the design (see Figure 4). Nevertheless, the durability of the mask needs to be considered during this process. The 3D model data then were exported to \*.STL file and printed using 3D printing machines stated above.

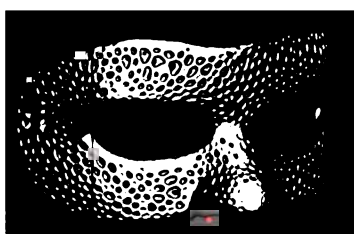


Figure 4 The protective mask with Voronoi pattern

### 3. RESULTS AND DISCUSSION

Table 1 shows the finished protective mask with Voronoi pattern on it and was compared based on printing time, weight, dimension and part cost. As in Table 1, it can be seen that all types of machines used in the study are capable of producing a part with high complexity pattern. All machines fabricate exact size according to original dimensions as produced in Meshmixer.

Part fabricated using Flashforge Creator Pro takes the longest time of 31 hours to produce. This was due to slow printing time, but it provides superior in detail and finishing. It produces the lightest weight and the cheapest cost amongst all. On the other hand, part fabricated using Projet 1000 has the greatest weight of 89 grams. The result also clearly shows that part produced by Projet

1000 has the highest part cost of RM176.95. Projet 1000 also is the best machine to fabricate the protective mask in terms of finishings, but the user need to adapt with the heavier part. Part printed from Up! Plus, has almost equal printing time with Projet 1000, but observation shows that it has the worst surface finish. It also heavier and costlier compared to Flashforge Creator Pro.

Table 1 Printed protective mask.

Printer type	Part	Material	Printing time	Weight (g)	Dimension (mm)	Cost (RM)
Up! Plus		ABS	10 hours			
Flashforge Creator Pro		PLA	31 hours	73	159.8 x 90.7 x 90.9	
Projet 1000		Resin	9 hours	89	159.8 x 90.7 x 90.9	176.95

### 4. CONCLUSION

In conclusion, designing and fabricating the protective mask from AM-enabled tool and system is fairly a straightforward process. The concept of using AM to fabricate such product is not new, but the ability to utilise the tool and systems is crucially important. Various techniques on handling CAD software has been learned in order to produce the CAD model that meets the requirements. The use of Meshmixer as a design tool to create high complexity pattern have made a significant contribution to the design and fabrication process. The selection of printing machine is also crucial because different machine produces different characteristics (e.g., visual), process capabilities (e.g., accuracy) and product costs.

### REFERENCES

- [1] ISO/ASTM International (2016). ISO/ASTM 52900: Standard Terminology for Additive Manufacturing Technologies. Retrieved from <https://www.sis.se/api/document/preview/919975/>
- [2] Baronio, G., Volonghi, P., & Signoroni, A. (2017). Concept and Design of a 3D Printed Support to Assist Hand Scanning for the Realization of Customized Orthosis. *Applied Bionics and Biomechanics*, 2017, 8 pages.
- [3] Paterson, A. M., Donnison, E., Bibb, R. J., & Campbell, R. I. (2014). Computer-aided design to support fabrication of wrist splints using 3D printing: A feasibility study. *Hand Therapy*, 19(4), 102–113.

# Solution for pes planus discomfort using corrective personalized orthotic insole via additive manufacturing

Zulkeflee Abdullah<sup>1,2,\*</sup>, Mariam Md Ghazaly<sup>3</sup>, Azlinda Muhamad<sup>4</sup>, Mawaddah Haslyanti<sup>1</sup>, Mohd Amran Md Ali<sup>1</sup>, Mohd Shahir Kasim<sup>1</sup>, Mohammad Kamil Sued<sup>1</sup>

<sup>1)</sup> Fakulti Kejuruteraan Pembuatan, Universiti Teknikal Malaysia Melaka,  
Hang Tuah Jaya, 76100 Durian Tunggal, Melaka, Malaysia

<sup>2)</sup> Advanced Manufacturing Centre, Universiti Teknikal Malaysia Melaka,  
Hang Tuah Jaya, 76100 Durian Tunggal, Melaka, Malaysia

<sup>3)</sup> Fakulti Kejuruteraan Elektrik, Universiti Teknikal Malaysia Melaka,  
Hang Tuah Jaya, 76100 Durian Tunggal, Melaka, Malaysia

<sup>4)</sup> Politeknik Muadzam Shah, 26700 Muadzam Shah, Pahang, Malaysia

\*Corresponding e-mail: zulkeflee@utem.edu.my

**Keywords:** Additive manufacturing; pes planus; orthotics insole

**ABSTRACT** – This paper discussed the solution for pes planus discomfort using corrective personalized orthotic insole via additive manufacturing. The process starts from Pes Planus Screening, 3D reconstruction and foot modification. The optimization of the 3D printing process was evaluated by determining the suitable method, tools and material used when using Thermoplastic Polyurethane (TPU), a type of flexible material. TPU is difficult to print, therefore the optimized process of the FDM machine need to be determined in order to produce the customize insole. The finding shows that this new method of printing customize insole using TPU is faster, and more cost effective.

## 1. INTRODUCTION

Pes planus affects 20-25% of adult population word wide which causes bone structure changes and joint disorders. Pes planus also creates strained muscles and discomfort to patients. Foot orthotic devices are designed to support, correct the deformities and improve the movement of joints or limbs. Normally, foot orthotic device such as corrective insole gets the demand from patients with foot problems. Pes Planus also known as Flat Foot is the condition in which the arch of the foot collapses, with the entire foot in contact with the ground [1]. Figure 1 shows the difference between normal foot and flat foot.

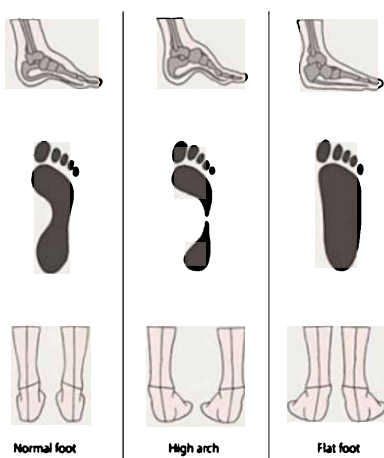


Figure 1 Normal, high arch, flat foot.

According to Jin et al. [2], there are two types of foot orthotic which are custom and off-the-shelf. Custom orthoses can fit the patient's body and perform better than off-the-shelf orthoses. Due to the large range of dimensions' characteristic for each individual, a mass production is not suitable for the custom insole productions. For this reason, it is necessary to consider another approach, such as rapid prototyping technology. According to Comoros and Baritz [3], 8.8% of the rapid prototyping technologies and additive manufacturing are used for medical industry. The rapid prototyping technologies and additive manufacturing could provide benefits in terms of production time and patient satisfaction. This report will cover the development of flat foot insole, possibility and benefit of using additive manufacturing, focusing in fused deposition modelling in producing flat foot insole.

## 2. METHODOLOGY

This project is designing a Customised Pes Planus (Flat Foot) Orthotic Insole Using Additive Manufacturing. This device is used to correct Pes Planus problem among human. The method and procedure for the processes starts from Pes Planus Screening by expert, Photogrammetry, 3D reconstruction and foot modification using software. Then insole 3D modelling is generated and integrated into CAD software, then printed using FDM machine. Lastly Corrective Ability Evaluation by Expert. TPU, among potential flexible material will be used (Figure 2).

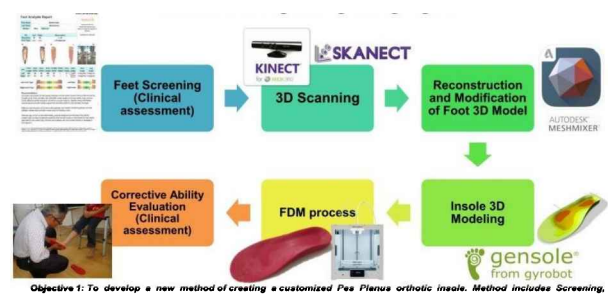


Figure 2 Steps of customized orthotic insole development process.

## 2.1 Feet screening

Pes Planus problem on feet and then screening by orthotics expert. Expert confirmation on the patient's feet condition of Pes Planus. Foot sensor insole was used here. Then the process of Insole sensor validation was done.

## 2.2 3D scanning – customized insole design

Low-cost 3D scanning solution: Microsoft® Kinect™ for XBOX 360 (gaming sensor) and our Faro Arm high end scanner at the Rapid Prototyping Lab was used to get the images. Occipital Skanect software was used to process the images.

## 2.3 3D reconstruction & foot modification – customized insole design

Autodesk Meshmixer software was used here. Firstly, 3D models imported from Skanect mesh, (.stl) & remove the unwanted geometry. Secondly, the details were smoothed out. Lastly, the foot alignment corrected to normal conditions. In here all problematic foot will be corrected to be a normal healthy foot according to the parameters recommended by orthotics expert.

## 2.4 Insole 3D Modeling – customized insole design

Gensole browser-based tool was used here. Gensole will generate insoles for 3D Printing from Gyrobot. The 3D model in .AMF files then exported into slicer for 3D printer toolpath creation.

## 2.5 FDM process (TPU)

FDM process parameters will be used in the study. Determination of parameters to be used in the FDM process is based on the optimum value obtained from the literature reviews.

## 2.5 Corrective ability evaluation

Expert confirmation on the patient's feet condition of Pes Planus. Patient has been asked to position their foot so that the plantar surface takes the normal disposition. The corrective ability of the orthotic insole has been assessed by experts to ensure the reliability of the results obtained. Experts are positive on the resulted insole provide optimal foot correction effects.

## 3. RESULTS AND DISCUSSION

The solution for pes planus (flat-foot) discomfort using corrective personalized orthotic insole using additive manufacturing process was verified in the previous section and has given good results. For validation of the customize insole, each patient has been certified to have a pes planus problem by an orthopaedist practitioner. At the 3D scanning stage, the 3D scanning was performed using Kinect™ for XBOX 360 (Microsoft®) paired with Skanect software as a low-cost solution. The results show comparable images with the Faro Arm Scanner but with less images quality. At the 3D Reconstruction & Foot Modification stage, there are two phases of works conducted by using Autodesk Meshmixer ver. 3.5. First phase is reconstruction of foot model. The second phase is modification of Pes Planus foot model. The foot alignment was then corrected to normal foot conditions. Then at the Pes Planus Orthotic Insole 3D

modeling using Gensole stage, the aim is correct the Pes Planus condition in Figure 3(a) to a perfect feet condition shown in Figure 3(b). Figure 4 shows the successful customize insole 3D printed using TPU flexible material.

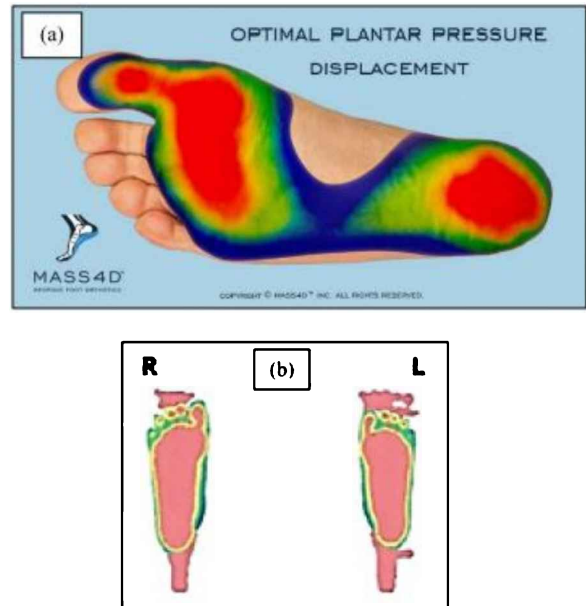


Figure 3 Pes planus vs optimal feet. (a) Feet with pes planus problem and (b) optimal foot.



Figure 4 successful customize insole 3D printed using TPU flexible material tested on patient by the orthotics expert (Dr Ahmad Tajuddin Abdullah, an Orthopedic & Traumatology Surgeon from Mahkota Orthotics and Prosthetic). Without and with personalize insole.

## 4. CONCLUSIONS

In conclusion, the customized pes planus (flat foot) orthotic insole using additive manufacturing was successfully verified. This study was devoted to developing customized Pes Planus orthotic insole using FDM and has the potentially contribution to the orthotic industry. The optimization was evaluated by determining the suitable method, tools and material used when using TPU flexible material. The process parameters of the FDM machine also need to be determined in order to produce the customize insole. The study showed the feasibility using low-cost 3D scan solution without compromising the quality, simplicity of using user-friendly CAD software. This study has shown that the additive manufacturing technology has the potential to be

applied in the medical industry, particularly in orthotic and prosthetic manufacturing. Future works includes clinical assessment to ensure that corrective processes are effective.

#### **ACKNOWLEDGEMENT**

This research is supported by Universiti Teknikal Malaysia Melaka grant no. JURNAL/2018/FKE/Q00006.

#### **REFERENCES**

- [1] Moorthy, T. N. & Sulaiman S. F. (2015). Individualizing characteristics of footprints in Malaysian Malays for person identification from a forensic perspective. *Egyptian Journal of Forensic Sciences*, 7, 13–22.
- [2] Jin, Y. A., Plott, J., Chen, R., Wensman, J., & Shih, A. (2015). Additive manufacturing of custom orthoses and prostheses—A review. *Procedia CIRP*, 36, 199–204.
- [3] Cotoros, D. & Baritz, M. (2012). Implementing rapid prototyping technologies for corrective insoles. *International Journal of Modern Manufacturing Technologies*, IV(1), 41–46.

# Internal oxidation and oxide scales formation of Fe-33Ni-19Cr alloy

Noraziana Parimin<sup>1,\*</sup>, Esah Hamzah<sup>2</sup>

<sup>1)</sup> School of Materials Engineering, Universiti Malaysia Perlis, 02600 Arau, Perlis, Malaysia

<sup>2)</sup> Faculty of Mechanical Engineering, Universiti Teknologi Malaysia, 81310 Skudai, Johor, Malaysia

\*Corresponding e-mail: noraziana@unimap.edu.my

**Keywords:** Internal oxidation; oxide scale growth; Fe-33Ni-19Cr alloy

**ABSTRACT** – The internal oxidation and oxide scales formation of solution-treated Fe-33Ni-19Cr alloy was investigated. The internal oxidation and oxide scales was initiated by exposure of Fe-33Ni-19Cr alloy to 900°C for 500 hours in laboratory air. The oxide scales formation and cross-sectional analysis during discontinuous isothermal oxidation was examined using XRD and SEM-EDX techniques. Coarse-grained of solution-treated Fe-33Ni-19Cr alloy exhibited the thicker internal oxidation along grain boundary area compared to fine-grained sample, which are 56.0µm and 24.5µm, respectively. The formation of oxide scales was complex, composed of Cr<sub>2</sub>O<sub>3</sub>, Cr<sub>1.3</sub>Fe<sub>0.7</sub>O<sub>3</sub>, (Cr<sub>0.88</sub>Ti<sub>0.12</sub>)<sub>2</sub>O<sub>3</sub>, Fe<sub>2</sub>O<sub>3</sub>, Fe<sub>3</sub>O<sub>4</sub>, MnCr<sub>2</sub>O<sub>4</sub>, MnFe<sub>2</sub>O<sub>4</sub>, FeCr<sub>2</sub>O<sub>4</sub>, NiCr<sub>2</sub>O<sub>4</sub>, NiFe<sub>2</sub>O<sub>4</sub>, TiO<sub>2</sub> and (Ti<sub>0.97</sub>Cr<sub>0.03</sub>)O<sub>2</sub>.

## 1. INTRODUCTION

Fe-33Ni-19Cr alloy is heat-resistant alloy which developed a protective oxide scales at high temperature applications. Alloying elements that can form strengthening phases are commonly added to enhanced excellent mechanical, physical properties and oxidation resistance [1-2]. Internal oxidation is a common phenomenon observed in metal alloys at high temperatures, usually greater than 600°C [1,3]. The formation of internal oxidation tends to penetrate along the grain boundary area underneath the oxide-metal interface. Selected alloying element such as Al and Si enhanced the formation of the Al<sub>2</sub>O<sub>3</sub> and SiO<sub>2</sub> oxide beneath the oxide layer, penetrating based metal as internal oxide precipitates, which both oxides contributed to the protective consequence at experienced temperature condition [4-5]. During high temperature exposure of Fe-33Ni-19Cr alloy, the alloy is closely dependable to their oxide scales formation which contributed to further protective conditions at high temperature. Therefore, special attention was paid in this study to the stability of internal oxidation and oxide scales formation to enhanced excellent protective barrier of this oxidation resistant material.

## 2. METHODOLOGY

Fe-33Ni-19Cr alloy was used in this study with the measured chemical compositions (in wt%): 32.5 Ni, 18.9 Cr, 0.08 C, 0.053 Al, 0.49 Ti, 0.32 Si, 0.56 Mn, 0.01 P, 0.08 Cu and balance Fe. A test samples of 3mm thickness with nominal dimensions of 10mm x 10mm x 3mm were cut from as-received alloy, then undergo a solution treatment process for 3 hours at three different temperatures, namely 950°C, 1050°C and 1150°C followed by water quench. These samples are denoted as

solution-treated 950°C (ST950), solution-treated 1050°C (ST1050) and solution-treated 1150°C (ST1150). The results showed that the average grain size increased with increase in solution treatment temperature, which are 54.55µm, 60.96µm and 70.37µm for ST950, ST1050 and ST1150, respectively. The isothermal oxidation tests were investigated by means of discontinuous testing at 900°C up to 500 hours in laboratory air. The phase analysis and cross-sectional examination of oxidized samples was characterized by X-ray Diffraction (XRD), Scanning Electron Microscopy (SEM) and Energy Dispersive X-Ray Spectroscopy (EDX).

## 3. RESULTS AND DISCUSSION

### 3.1 Phase analysis of oxide scale formation

Phase identification using XRD technique of Fe-33Ni-19Cr alloy after isothermal oxidation at 900°C for 500 hours were composed of four major phases, with corresponding to their crystal structure, namely, austenite, corundum, spinel and fluorite. The formation of most intense austenite peaks corresponding to the based alloy. The corundum type oxides composed of Cr<sub>2</sub>O<sub>3</sub>, Cr<sub>1.3</sub>Fe<sub>0.7</sub>O<sub>3</sub>, (Cr<sub>0.88</sub>Ti<sub>0.12</sub>)<sub>2</sub>O<sub>3</sub> and Fe<sub>2</sub>O<sub>3</sub> were observed. The spinel oxides also detected composed of MnCr<sub>2</sub>O<sub>4</sub>, MnFe<sub>2</sub>O<sub>4</sub>, FeCr<sub>2</sub>O<sub>4</sub>, NiCr<sub>2</sub>O<sub>4</sub>, NiFe<sub>2</sub>O<sub>4</sub>, and Fe<sub>3</sub>O<sub>4</sub>. In addition, the Ti-rich oxides phases also detected composed of TiO<sub>2</sub> and (Ti<sub>0.97</sub>Cr<sub>0.03</sub>)O<sub>2</sub> oxide with fluorite crystal structure. The formation of Cr-Ti rich oxide was aforementioned to mitigate the Cr evaporation effect due to the lower Cr vapor pressure of (Cr,Ti)<sub>2</sub>O<sub>3</sub> compared to Cr<sub>2</sub>O<sub>3</sub>. Furthermore, the addition of Mn alloying element to the Fe-Ni-Cr system will give beneficial effect to the oxide scale formation due to the formation of outer Cr/Mn-spinel layer, which is known to reduce the development of volatile Cr-species [5]. Moreover, the formation of Cr/Mn-spinel layer consists of MnCr<sub>2</sub>O<sub>4</sub> reflect the rapid diffusion of Mn in Cr<sub>2</sub>O<sub>3</sub> oxide phase.

### 3.2 Cross-sectional analysis of internal oxidation

An elemental line scan SEM-EDX analysis for cross-sectional ST950 sample is shown in Figure 1. It was found that the oxide scale formed was approximately 10 µm. This sample formed a several oxide layers which are labeled as area 1, 2, 3 and 4. The cross-sectional image for ST950 sample in Figure 1 shows a formation of Cr-Mn oxide at the outer oxide layer at area 1, estimated composed of MnCr<sub>2</sub>O<sub>4</sub> and/or Cr<sub>2</sub>O<sub>3</sub> oxide phases. It was also found that thick oxides formed to cover the entire alloy surface indicate excellent protective oxide layer. This is due to the formation of Mn-Cr spinel oxides which will increase the efficiency of

protective oxide behavior because the higher solubility of Mn and Cr that will reduce the Cr volatile effect at high temperature. The Cr and Mn were depleted at area 2, indicating the enrichment of elements Fe, Ni and O. Whereas, at area 3 which is at the scale-metal interface, the enrichment of element Cr and O were recorded, indicating the formation of  $\text{Cr}_2\text{O}_3$  oxide. In addition, at point 4, indicated the enrichment of elements Al and O representing the formation of Al oxide precipitate. Similar argument made by [4-5] which stated that Al alloying addition tend to developed the Al oxide layer underneath the oxide scale, penetrating based metal as internal oxide precipitates.

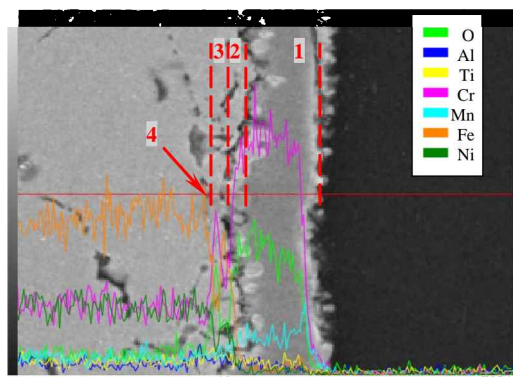


Figure 1 Cross-sectional SEM line scan image of ST950 (Magnification 2500 $\times$ ).

Figure 2 shows SEM image of Fe-33Ni-19Cr alloy oxidized at 900°C for 500 hours. It shows that oxidation not only occurred on the surface but internally as well. The depth of internal oxidation increases as the grain size of the alloy increases. This is due to the large grain size with relatively few grain boundaries did not form protective oxide layer but more porous structure. Thus it allows the diffusion of  $\text{O}^{2-}$  ion into the metal to form internal mixed oxides. Sample ST950 with fine grain for example has internal oxidation up to 24.5 $\mu\text{m}$ . Whereas for coarse grain ST1150 sample, the internal oxidation occurred up to 56.0 $\mu\text{m}$  in depth.

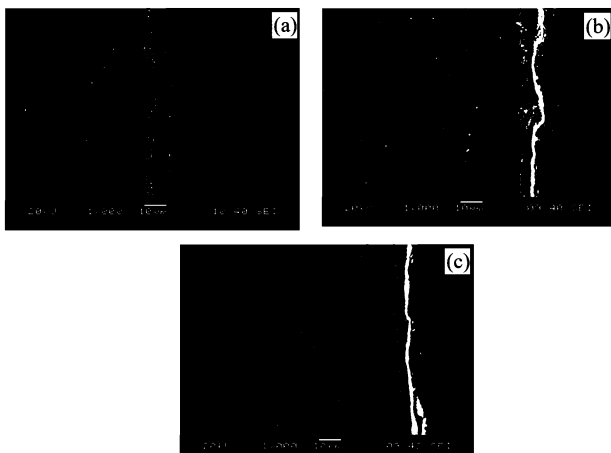


Figure 2 Cross-sectional SEM images of; (a) ST950, (b) ST1050 and (c) ST1150.

The mechanism of internal oxidation is discussed as followed. The formation of voids in the oxide scale may generated by fast metal ion diffusion along grain

boundary. Besides, oxide scale distortion and cracking due to the development of growth stress in the scale bring to the void formation. The scale above the voids generally contains a grain boundary oxide. The grain boundary area begins to open up around the void, if fast outward diffusion of metal ion along the grain boundary than through the lattice. The continuous diffusion process will open the grain boundary area as a channel of a void linkage. When open, the channel permits the oxygen ion to transmit down the channel to the metal and formed the inner oxide scale and filled the grain boundary area. The formation of internal oxide scale was restricted by the hindrance from adjacent grain which acts as a break path for further oxide penetration. The internal oxide will go deeper to the grain boundary area for the coarse grain due to the faraway location of adjacent grain to stop the penetration path. While for fine grain, the depth of the internal oxide penetration was diminishing by nearby adjacent grain, results in less internal oxide penetration. The channel will close when the void along grain boundary area filled with oxide.

#### 4. SUMMARY

The isothermal oxidation of solution-treated Fe-33Ni-19Cr alloy has been investigated at 900°C. Several oxide scales were formed on the alloy surface which increase the efficiency of protective oxide behavior. It also found that the internal oxidation was formed along the grain boundary area, which also contributed to further protection when the channel and void along grain boundary area was closed and filled with oxide scales.

#### ACKNOWLEDGEMENT

The authors would like to thank the Ministry of Education Malaysia for the research fund under the Fundamental Research Grant Scheme (FRGS) (Project Code. FRGS/1/2016/TK05/UNIMAP/02/4).

#### REFERENCES

- [1] Pan, T. J., Li, Y. S., Yang, Q., Feng, R. F., & Hirose, A. (2011). Internal oxidation and phase transformations of multi-phase Fe-Ni-Al and Fe-Ni-Al-Cr alloys induced by KCl corrosion. *Corrosion Science*, 53, 2115-2121.
- [2] Xu, Y. X., Lu, J. T., Yang, X. W., Yan, J. B., & Li, W. Y. (2017). Effect and role of alloyed Nb on the air oxidation behavior of Ni-Cr-Fe alloys at 1000°C. *Corrosion Science*, 127, 10-20.
- [3] Langelier, B., Persaud, S. Y., Newman, R. C., & Botton, G. A. (2016). An atom probe tomography study of internal oxidation processes in Alloy 600. *Acta Materialia*, 109, 55-68.
- [4] Cao, G., Firouzdor, V., Sridharan, K., Anderson, M. & Allen, T. R. (2012). Corrosion of austenitic alloys in high temperature supercritical carbon dioxide. *Corrosion Science*, 60, 246–255.
- [5] Zurek, J., Young, D. J., Essuman, E., Hansel, M., Penkalla, H. J., Niewolak, L., & Quadakkers, W. J. (2008). Growth and adherence of chromia based surface scales on Ni-Base alloys in high- and low- $\text{pO}_2$  gases. *Materials Science and Engineering A*, 477, 259-270.

# Effect of semi-solid forming temperature and heat treatment on mechanical properties of Mg-Al-Zn Alloy (AZ91D) for automotive application

M.R.M. Kamal<sup>1,2\*</sup>, N.F. Bazilah<sup>1</sup>, A. Luhat<sup>1</sup>, M.H. Idris<sup>2</sup>, M.S. Salleh<sup>3</sup>, W.F.F.W. Ali<sup>2</sup>

<sup>1)</sup> Fakulti Teknologi Kejuruteraan Mekanikal dan Pembuatan, Universiti Teknikal Malaysia Melaka,  
Hang Tuah Jaya, 76100 Durian Tunggal, Melaka, Malaysia

<sup>2)</sup> School of Mechanical Engineering, Faculty of Engineering, Universiti Teknologi Malaysia,  
81310 Skudai, Johor, Malaysia

<sup>3)</sup> Fakulti Kejuruteraan Pembuatan, Universiti Teknikal Malaysia Melaka,  
Hang Tuah Jaya, 76100 Durian Tunggal, Melaka, Malaysia

\*Email: mohamadridzuan@utem.edu.my

**Keywords:** Ultimate tensile test; hardness; heat treatment

**ABSTRACT** – Magnesium alloy usage in manufacturing engineering components resulting in weight reduction and as a consequence, reduction in fuel and energy consumption. Magnesium has a relatively low density and roughly 30% lower than aluminum. However, magnesium is considered to be difficult to deform because of the HCP structure. In this present work, the effect of semi-solid forming temperature and heat treatment on mechanical properties of Mg-Al-Zn were investigated. Mg-Al-Zn ingot was machined into a billet and formed with three different temperatures and underwent T4 heat treatment process. To determine the mechanical properties of the magnesium alloy, tensile and hardness test were performed and the result indicates that the highest average maximum tensile stress was achieved at 209 MPa at 530°C after forming with T4 heat treatment and highest hardness value was at 21.44 HRB at 560°C. The heat treatment of T4 had proved its capability to alter the microstructure and gave out the higher hardening quality.

## 1. INTRODUCTION

Mg is one of the most widely distributed elements in nature, ranks eighth, accounting for about 2.25% of the mass of the earth's crust. Mg, however, has poor workability at room temperature owing to its crystal structure [1]. In the past few years, the usage of Mg in the automobile industry is significantly increased. Although the automobile industry will keep on to be the foremost driving force for the future growth in magnesium applications, other areas, such as aerospace, electronics, and health care, will take a sizeable share of the magnesium market in the near future. Further growth in magnesium applications will basically depend on the successful development of new processing technologies that capable of fabricating high quality and low-cost components with higher operating temperatures.

## 2. METHODOLOGY

An ingot AZ91D magnesium alloy was used as experimental material in this work. AZ91D contains 9% of aluminum and 1% zinc and the balance is magnesium, which is a commercial use for the die casting process. Ingot was cut and machined into a billet dimension Ø20

x 100mm as in Figure 1(a). T4 heat treatment involves 20 hours of process time at 415°C. The sample label A1 and A2 is a reference billet and T4 heat treated respectively. Sample B1, B2, and B3 has undergone a forming temperature of 510°C, 530°C and 560°C by induction heating as in figure 1b) and figure 1c) show the as-form billet. K type thermocouple was used to determine the forming temperature. The summary of the experimental parameter as in Table 1.

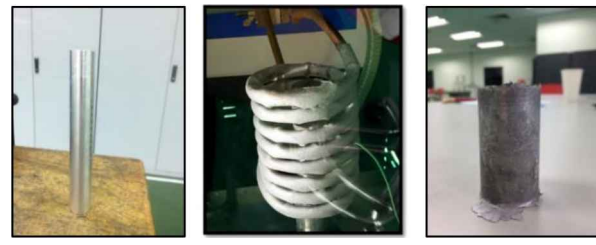


Figure 1 (a) Billet, (b) induction heating and (c) as-form billet.

Table 1 Experimental process parameter.

Samples	Process parameter	Forming temperature
A1	Reference Billet	-
A2	T4 HT	-
B1	Induction heating + Forming	510°C
B2	Induction heating + Forming	530°C
B3	Induction heating + Forming	560°C
C1	Induction heating + Forming + T4 HT	510°C
C2	Induction heating + Forming + T4 HT	530°C
C3	Induction heating + Forming + T4 HT	560°C

After all the samples were formed and undergo the heat treatment processes, samples were cut into a tensile test dimension by wire electrical discharge machining according to ASTM 557M-10 with a thickness of 6mm. For the Rockwell hardness test, the 100kgf load with indenter of 1/16 inch steel ball was used.

### 3. RESULTS AND DISCUSSION

Figure 2 shows a comparison of Ultimate Tensile Strength (UTS) of all samples. The UTS for as-cast (A1) is 219 MPa, as-cast + T4 heat treatment (A2) is 255 MPa. Forming at 510°C (B1) is 157 MPa, forming at 530°C (B2) is 161 MPa, forming at 510°C (B3) is 150, forming at 510°C + T4 heat treatment (C1) is 182 MPa, forming at 530°C + T4 heat treatment (C2) is 209 MPa, and lastly forming at 560°C + T4 heat treatment (C3) is 174 MPa, The graph from figure 2 showed forming at 560°C (B3) obtained the lowest UTS when compared to the all average of the samples and highly differences from expected. Although the highest UTS receive from the sample as-cast + T4 heat treatment (A2), the samples are not yet formed compare with the sample forming at 530°C + T4 heat treatment (C2). In the term of finish goods, samples that are already formed is more reliable compared to as-cast. The UTS trend from sample B1, B2, B3, C1, C2, and C3 was slightly increased at the forming temperature of 530°C and decrease at the temperature 560°C. It shows that the sensitivity to temperature gives a significant effect on the strength of the forming material. Meanwhile, at the as-cast stage, the strength of AZ91D is high compared to the at the forming stage. The forming sample in this study showed an inconsistent result where it's value does not exceed the as-cast UTS result. In the previous study on the effect of forming on A390 aluminum's mechanical properties, the UTS can reach as high as 293MPa, this kind of result was to expected when tested on AZ91D forming sample.

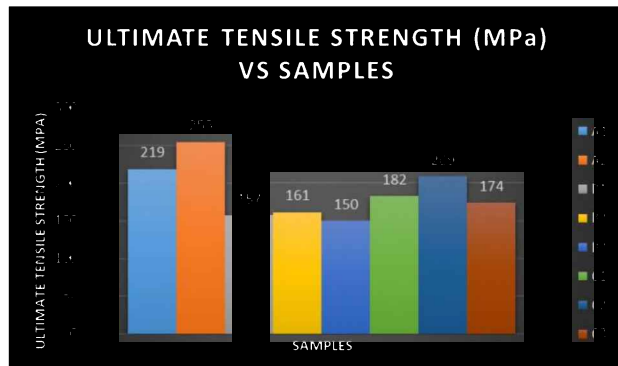


Figure 2 Ultimate tensile strength vs. samples.

Figure 3 shows a comparison of the hardness test (HRB) of all samples. The hardness test for as-cast (A1) is 13.41 HRB, as-cast + T4 heat treatment (A2) is 13.26HRB. Forming at 510°C (B1) is 17.63HRB, forming at 530°C (B2) is 17.52HRB, forming at 510°C (B3) is 21.44HRB, forming at 510°C + T4 heat treatment (C1) is 16.77HRB, forming at 530°C + T4 heat treatment (C2) is 17.52HRB, and lastly forming at 560°C + T4 heat treatment (C3) is 21.07HRB. The graph from figure 3 showed as-cast +T4 (A2) obtained the lowest hardness value when compared to all average of the samples. The

highest hardness value is forming at 560°C and forming at 560°C+T4 heat treatment where 21.44 HRB and 21.07HRB respectively. It shows that forming temperature at 560 °C gives a significant effect on the hardness of AZ91D material but gives among the lowest ultimate tensile strength value.

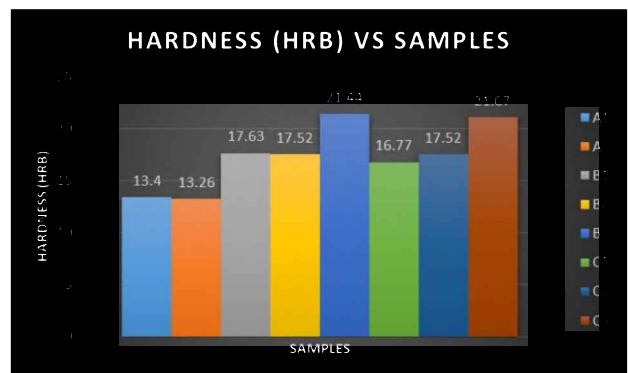


Figure 3 Hardness vs. samples.

### 4. CONCLUSION

The mechanical properties covered in this study was tested using a tensile test where the ultimate tensile strength (UTS) was observed. The result of the tensile test showed that the T4 gave out the highest UTS for the as-cast sample. Meanwhile, it varies when it comes to semisolid forming sample. In the result of the hardness value in the Rockwell test showed that forming with 560°C gave out the highest value. Meanwhile, the hardness value of the forming at 560°C + T4 sample gives the second highest. T4 heat treatment and without heat treatment were both comparable, with T4 showed a slightly lower value. This could be the result of lack in precipitate by T4 treatment or probably due to the indent might partially land on the  $\alpha$ -mg region or eutectic mixture causing a variety of the result.

### ACKNOWLEDGMENT

The authors gratefully acknowledged the financial support from Universiti Teknikal Malaysia Melaka and The Ministry of Education, Malaysia under Research Grant number. PJP/2018/FTK(2C)/S01586.

### REFERENCES

- [1] Yan, J., Xie, J., Yuan, J. S., Zhang, J. Y., & Guo, T. (2014). The influence of alloy elements on Mg-Al alloy and its development Prospect. *Applied Mechanics and Materials*, 687, 4283-4286.
- [2] Furui, M., Sakashita, S., Suzuki, S., Aida, T., Ishisaka, Y., Yamamoto, M., & Ohta, M. (2017). Aging property of AZ91D magnesium alloy screw thread-rolled at room temperature using extrusion-torsion simultaneous processing. *Materials Science Forum*, 879, 2450-2455.

# Fabricate flow channel of bipolar plate through milling machining process

Mohd Zulkefli.Selamat<sup>1,2,\*</sup>, HamzaitulAkmarizal Hamdan<sup>1,2</sup>, Mohd Basri Ali<sup>1,2</sup>, Sivakumar Dhar Malingam<sup>1,2</sup>

<sup>1)</sup> Fakulti Kejuruteraan Mekanikal, Universiti Teknikal Malaysia Melaka,

Hang Tuah Jaya, 76100 Durian Tunggal, Melaka, Malaysia

<sup>2)</sup> Centre for Advanced Research on Energy, Universiti Teknikal Malaysia Melaka,

Hang Tuah Jaya, 76100 Durian Tunggal, Melaka, Malaysia

\*Corresponding e-mail: zulkeflis@utem.edu.my

**Keywords:** PEMFC bipolar plate; serpentine; interdigitated

**ABSTRACT** – This research objective is investigating the accuracy of producing flow channel on a bipolar plate by the machining process. The bipolar plates used are G/CB/Fe/PP composites, V shape of the serpentine and U shape of the interdigitated flow channel has been selected. The flow channel fabricated by machining used flat End Mill with a diameter of 1.5 mm as cutting tool to fabricate the flow channel. The specimen dimensions of width, channel width 1, channel width 2 and channel depth have been measured and compare to actual drawing. Serpentine (V shape) and interdigitated (U shape) specimens with 2 mm width delivers better dimension accuracy with less of the 4.13% margin of error. Except the channel depth with the maximum margin of error is 30.2 % for U shape, but for serpentine (V shape) the channel depth with the maximum margin of error is 18 % which is better than U shape.

## 1. INTRODUCTION

Polymer Electrolyte Membrane Fuel Cell or Proton Exchange Membrane Fuel Cell (PEMFC) has been identified as a power source for many applications and the development of this sector rapidly expanding from year to year. It is because of PEMFC promising many advantages compared to other fuel cells, such as low temperature operation, quick startup time and dynamic operation capabilities [1]. PEMFC has huge potential to be commercialized because of high energy conversion efficiency and low pollutant emission [2].

In commercialize of PEMFC high cost and durability of PEMFC become a barrier to widespread the commercialization [3]. Bipolar plate were categories by it flow channel design. The most popular flow channel designs are serpentine and interdigitated flow channel as shown in Figure 1. The serpentine flow channel was popular as their pressure drop requirements and water removal rate correlates each other [4]. Interdigitated flow channel consists of multiple dead-ended flow channels and it forced gas flow through the adjacent diffusion layer.

Graphite has become major bipolar plate materials due to adequate electrical conductivity, light weight and good corrosion resistance but producing precise flow field channels is difficult and expensive due to brittleness issue [5]. Conducting Polymer Composite (CPC) offers better mechanical properties to withstand the stress force during the machining process. This research aim is to investigate the fabrication of flow

channel through the machining process of specimen dimensions (width, channel width 1, channel width 2 and channel depth) of flow channel will be measured and compare with actual drawing.

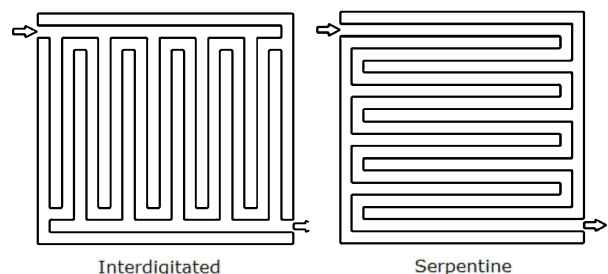


Figure 1 Interdigitated and serpentine flow channel.

## 2. METHODOLOGY

### 2.1 Fabrication of Polymer Composites

All fillers were mixed by using ball mill machine for 1½ hours. After that, G/CB/Fe/PP were further mixed using Haake Poly lab Rheodrive Internal Mixer machine at the temperature of 200°C, rotor speed of 50 RPM and duration time of 15 minutes. After that the mixture was collected and has been pulverized to further refine using Retsch ZM200 Pulverizer. Compression molding method has been chosen to shape the sample and Gotech (GT 7014 – A) hot press machine was used. The temperature has been set at 185°C, preheating times is about 10 minutes and pressure was set at 50 tons and the duration of pressing time is about 10 minutes. After that the mold has been cooled down about 15 minutes before specimen released from mould.

### 2.2 Flow Channel Drawing Process

Flow channel was drawn by a CAD program. Main parameters have been selected as show in Table 1.

Table 1 Parameters of flow field design.

Parameters of flow channel	Plate
Dimension	50 mm x 50 mm
Type of flow channel	U Interdigitated & V Serpentine
Width of flow channel	1 mm & 2 mm
Depth of flow channel	0.5 mm
Taper angle of flow channel	45°

They are three different designs were drawn,

serpentine V with 1 mm and 2 mm depth and interdigitated U shape with 2 mm depth. Figure 2 shows a CAD drawing for both flow channel design.

### 2.3 Fabrication of Flow Channel by Machining

The machining process of flow channel for U and V shapes on the surface of plate was used Bridgeport Model GX 710 with spindle speed of 4000 RPM, feed

rate of 400 mm/min and cutting tool is flat End Mills with a diameter of 1.5 mm.

### 2.4 Measurement Test

The specimens were measured to determine the dimension parameters. Smartscope CNC500 was used to measure specimen dimensions (width, channel width 1, channel width 2 and channel depth).

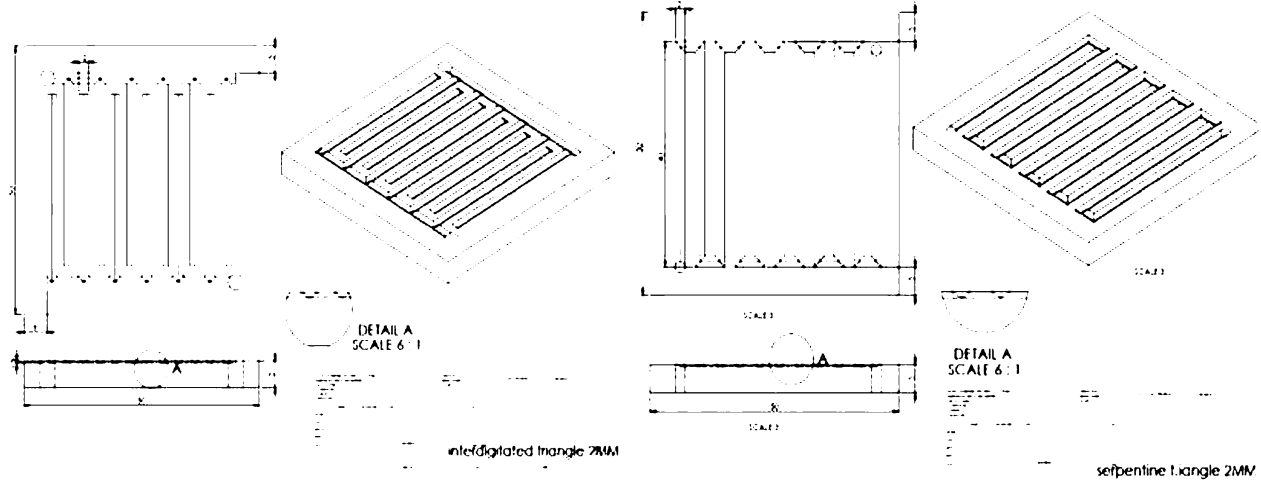


Figure 2 CAD drawing for serpentine and interdigititated.



Figure 3 Smartscope CNC500.

## 3. RESULTS AND DISCUSSION

### 3.1 Serpentine V Shape

Figure 4 shown serpentine flow channel type specimens. Both specimens are serpentine V shape with 45° draft angles with 2 mm and 1 mm channel width.

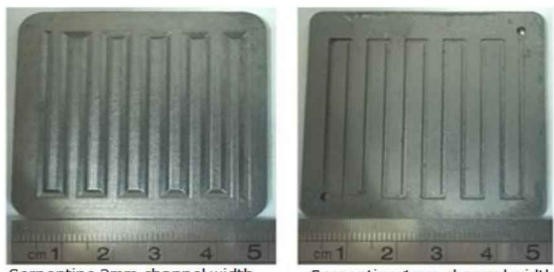


Figure 4 Serpentine V shape flow channel specimens.

### 3.2 Interdigititated U Shape

Figure 5 shown the interdigititated flow channel with 2 mm channel width.



Figure 5 Interdigititated U shape flow channel.

### 3.3 Measurement Test Result

There are 4 dimensional points which are 1 up to 4 were measured and recorded using Smartscope. While

Table 2 shows measured value of dimension versus drawing.

Table 2 Specimen measurement vs drawing.

No	Point of Dimensions	Drawings (mm)	Serpentine (V shape)						Interdigitated (U shape)		
			1 mm channel		2 mm channel						
			Spec.	Different	Spec.	Different	Spec.	mm	%		
1	Width	50	49.97	0.03	0.06	50.096	-0.096	0.192	49.91	0.081	0.162
2	Channel Width 1	1 or 2	1.7	-0.7	70.0	1.946	0.054	2.7	2.034	-0.034	1.7
3	Channel Width 2	1 or 2	1.374	-0.374	37.4	1.919	0.081	4.05	2.022	-0.022	1.1
4	Channel Depth	0.5	0.556	-0.056	11.2	0.591	0.091	18.2	0.651	-0.151	30.2

Table 2 shows that V shape serpentine and U shape interdigitated specimens with 2 mm channel produce by machining process have a better dimension accuracy than serpentine with 1 mm channel width. Meanwhile, Serpentine and interdigitated specimens with 2 mm width delivers better dimension accuracy with less of the 4.13% margin of error. Except the channel depth with the maximum margin of error is 30.2 % for U shape, but for serpentine (V shape) the channel depth with the maximum margin of error is 18 %.

## 4. CONCLUSION

As a conclusion, the flow channel of bipolar plate is suitable to be machined due to its good mechanical properties to withstand the stress force during the machining process. Serpentine and interdigitated specimen with 2 mm width delivers better dimension accuracy with less of the 4.13% margin of error except the channel depth.

## ACKNOWLEDGEMENT

The authors would like to thank the Malaysia Ministry of Higher Education, Malaysia and Ministry of Science, Technology and Innovation for sponsoring this work under Grant FRGS (RACE) /2013/FKM/TK2/2 F00203 and Universiti Teknikal Malaysia Melaka (UTeM) for financially sponsoring during this research.

## REFERENCES

- [1] Baker, R., Zhang, J. (2011). Proton exchange membrane or polymer electrolyte membrane (pem) fuel cells. *Electrochemistry Encyclopedia*.
- [2] Kumar, A., & Reddy, R. G. (2003). Effect of channel dimensions and shape in the flow-field distributor on the performance of polymer electrolyte membrane fuel cells. *Journal of power sources*, 113(1), 11-18.
- [3] Selamat, M. Z., Sahari, J., Muhamad, N., & Muchtar, A. (2011). Simultaneous Optimization for multiple responses on the compression moulding parameters of composite graphite-polypropylene using Taguchi method. *Key Engineering Materials*, 471, 361-366.
- [4] Yusuf, M. Y. M., Selamat, M. Z., Sahari, J., Daud, M. A. M., Tahir, M. M., & Hamdan, H. A. (2017). Fabrication of a flow channel for production of polymer composite bipolar plate through hot compression molding. *Journal of Mechanical Engineering and Sciences*, 11(1), 2428-2442.
- [5] Selamat, M. Z., Masron, F., Yusuf, M., Yusri, M., Kamarolzaman, A. A., Mohd Tahir, M., & Herawan, S. G. (2015). Effect of stannum on properties of graphite/stannum composite for bipolar plate. *Applied Mechanics and Materials*, 699, 157-162.

# Development of biodegradable plastic with natural sources as packaging material

Mohammad Khalid Wahid\*, Mohd Nazri Ahmad, Nurul Ain Maidin, Mohd Hairizal Osman, Mohd Hidayat Ab Rahman

Fakulti Teknologi Kejuruteraan Mekanikal dan Pembuatan, Universiti Teknikal Malaysia Melaka,  
Hang Tuah Jaya, 76100 Durian Tunggal, Melaka, Malaysia

\*Corresponding e-mail: mohammadkhalid@utem.edu.my

**Keywords:** Biodegradable; plastic; fiber

**ABSTRACT** – This paper presents the comparison of mechanical properties of three different biodegradable plastics made from tapioca starch that mixture with natural fiber such as oil palm fiber and sugar cane fiber. The application of this research is to produce biodegradable plastic packaging for the food industry purpose. Tapioca starch was used as the main ingredient with sugar cane fiber and oil palm fiber mixture in three different variations. Then these biodegradable plastics were evaluated with the tensile test and biodegradable test. The tensile test had shown that sugar cane fiber sample has 0.29 MPa, oil palm fiber has 1.12 MPa and mixture fiber has 0.33 MPa.

## 1. INTRODUCTION

Starch is a biodegradable, inexpensive and abundantly available polysaccharide molecule. It is widely distributed in the form of tiny granules as the reserve carbohydrate in stems, roots, grains and fruits of all forms of green leafed plants [1]. Tapioca flour was the thermoplastic material through the disruption of the molecular chains under specific conditions of temperature and presence of plasticizer. The process of compression molding was selected as the manufacturing process in which recharges containing chopped fibers were compressed in a mold. The structural fibers need to produce were volume fraction homogeneous and isotropic fiber orientation structure. This changes the fiber caused by the flow characteristics that are produced during the charging process. The mechanical properties of the final product are determined predominantly by fiber [2]. Tensile properties of composites are improved by adding fibers to the polymer matrix of the fiber strength and stiffness values were higher than the matrix [3]. Environmental properties evaluation of the natural fiber biopolymer composite were depended on the ingredient composite, filler content, fibers orientation, interfacial bonding, and the processing applied in the fabricated process. Biodegradation test was performed to evaluate performance degradation rates and environmental impacts caused by the sample. In the research, works were included biodegradation testing in weathering test and soil test. The objectives of this research are to produce biodegradable plastics with a complete investigation of the tensile strength and evaluated the biodegradation level of each sample.

## 2. METHODOLOGY

The raw material that involved in this study were are tapioca starch as a matrix material and the reinforcement which are sugar cane fiber and oil palm fiber. The glycerol was selected as the plasticizers in this composite. The liquid form of glycerol from vegetables was used in this study. Tapioca starch was selected as a matrix in the composite fabrication. Tapioca was abstract into the powder form. Tapioca starch is available in the market as a commodity tapioca starch. In this study, nature fiber was obtained from sugar cane and oil palm fiber. The cleaning process should be emphasized to ensure that the fiber is not contaminated with foreign bodies. The nature fiber was crushed into the blender to get the specific length and size. The drying process should be repeated to ensure that the fiber density is constant and make sure no moisture entrapped between the sugar cane and oil palm fiber. The formulation was divided into three main compositions of the weight ratio of the fiber loading. Then all the raw materials that used were weighed according to the analytical balance. In this research, the glycerol content is fixed in 5% addition as an additive in the mixture. Table 1 shows the composition of raw materials

Table 1 Sample composition.

Sample	Fiber	Tapioca	Glycerol
Sugar Cane Fiber	60 %	35%	5%
Oil Palm Fiber	60%	35%	5%
Mixture Fiber	30%+ 30%	35%	5%

After the fabrication of these composites was made by compression molding process, the samples were prepared for tensile test (ASTM D638-10) and biodegradable test or soil test (ASTM-6400-99). Each sample was labeled for each container. The time and date were recorded on the sample material placed in the ground. This biodegradable test was regularly checked to monitor the status of degradation since has been planted. Eventually, final inspection in two weeks after planted the specimens.

### 3. RESULTS AND DISCUSSION

The results had established and observed in Figure 1, Figure 2 and Figure 3. From the product point of view, the product from oil palm fiber was darker as compared to the product of sugarcane which was brighter in terms of color display. This was due to the original color of the base material which did not change during the process. Meanwhile, the product of a mixture of oil palm and sugar cane fiber look was in intermediate color brightness. These color difference of the composite significantly important because showed physical appearance for the finished product.



Figure 1 Biodegradable plastic of oil palm fiber.



Figure 2 Biodegradable plastic of sugar cane fiber.



Figure 3 Biodegradable plastic of mixture fiber.

The average tensile test results and modulus young were shown in Table 2. These were averaging of five samples tested. The average ultimate tensile stress of palm fiber samples had shown highest value of 1.12 MPa as compared to sugar cane fibers that shown the lowest result of 0.29 MPa. Meanwhile average ultimate tensile stress of the mixture of oil palm fiber and sugar cane yield point was 0.33 MPa

Table 2 Tensile test results.

Sample	Ultimate Tensile Strength (MPa)	Modulus Young (MPa)
Sugar Cane Fiber	0.29	154.68
Oil Palm Fiber	1.12	217.67
Mixture Fiber	0.33	132.40

There are many factors that can affect the performance of natural fiber reinforced composites [4]. The difference was due to the strength of the features that were present in palm fiber were tough and compact as compared to the fiber from sugar cane. Modulus young's also known as the elastic modulus was a measurement of the material stiffness. In order to adjust the stiffness of

the material it was to normalize the load with the cross-sectional area. For biodegradable test result for each samples had shown in Figure 4, Figure 5 and Figure 6 after two week run the test.

### 4. CONCLUSION

As the conclusion of this research, the product of biodegradable plastics using starch and nature fiber were successfully prepared by mixing process, heating process, molding process, and drying process. Two standard tests were carried out to characterize the tensile strength test and the biodegradable test had shown significant result that these biodegradable plastics can performed as a packaging product and eco-friendly.



Figure 4 Sugar cane biodegradable test result.



Figure 5 Oil palm biodegradable test result.

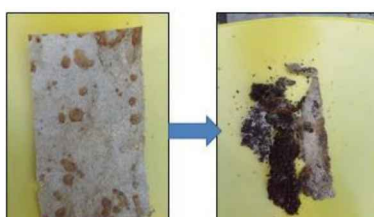


Figure 6 Mixture fiber biodegradable test result.

### REFERENCES

- [1] Neelam, K., Vijay, S., & Lalit, S. (2012). Various techniques for the modification of starch and the applications of its derivatives. *International research Journal of pharmacy*, 3(5), 25-31.
- [2] Kim, M. S., Lee, W. I., Han, W. S., & Vautrin, A. (2011). Optimisation of location and dimension of SMC precharge in compression moulding process. *Computers & Structures*, 89(15-16), 1523-1534.
- [3] Ku, H., Wang, H., Pattarachaiyakoop, N., & Trada, M. (2011). A review on the tensile properties of natural fiber reinforced polymer composites. *Composites Part B: Engineering*, 42(4), 856-873.
- [4] Ku, H., Wang, H., Pattarachaiyakoop, N., & Trada, M. (2011). A review on the tensile properties of natural fiber reinforced polymer composites. *Composites Part B: Engineering*, 42(4), 856-873.

# Preliminary study of mechanical properties for different curing period of kenaf mix with glutinous rice through tensile and impact test

Mohd Afdhal Shamsudin<sup>1,3,\*</sup>, Muhammad Hanif Mansor<sup>1</sup>, Muhammad Ilman Hakimi Chua Abdullah<sup>1,3</sup>, Mohd Noor Asril Saadun<sup>2,3</sup>

<sup>1)</sup> Fakulti Teknologi Kejuruteraan Mekanikal Dan Pembuatan, Universiti Teknikal Malaysia Melaka,  
Hang Tuah Jaya, 76100 Durian Tunggal, Melaka, Malaysia

<sup>2)</sup> Fakulti Kejuruteraan Mekanikal, Universiti Teknikal Malaysia Melaka,  
Hang Tuah Jaya, 76100 Durian Tunggal, Melaka, Malaysia

<sup>3)</sup> Centre for Advanced Research on Energy, Universiti Teknikal Malaysia Melaka,  
Hang Tuah Jaya, 76100 Durian Tunggal, Melaka, Malaysia

\*Corresponding e-mail: afdhal@utem.edu.my

**Keywords:** Kenaf fibre; glutinous rice; fibre

**ABSTRACT** – The purpose of this research is to analyse new composition of naturally made resin reinforced kenaf fibre on the mechanical properties of kenaf mix with natural binder. The naturally made resin used is glutinous rice that acts as a reinforcing substance for kenaf fibre. Total 24 samples were prepared by mixing the glutinous rice layer by layer with variations of kenaf in the middle. The samples were tested through tensile test and charpy impact test to identify its mechanical properties. The best composition for tensile and charpy impact test are 40% and 45% of kenaf fibre respectively.

## 1. INTRODUCTION

Kenaf or Hibiscus cannabinus is one of the herbaceous, annual, and short-photoperiod fiber which obtained from the stems of the plants in the Malvaceae family [1]. Kenaf is a type of fiber which has very light weight and porous where the bulk density of kenaf is at 0.10 until 0.20 g/cm<sup>2</sup> [2]. Furthermore, it is biodegradable and does not have side effect to the environment and human's health. Nowadays, many kenaf fiber-reinforced composite has been used in many engineering applications or industrial sectors such as construction, automotive, marine and other mass production industries.

There is increasing in the awareness toward the environment since now the temperature of the world has increasing and the environment pollution becomes worst. Synthetic fibre causes a problem to environment and human's health. This is because the source to make is from petrochemical sources which are made up using high temperature industrial processes such as hot extrusion which produce a high amount of carbon dioxide. Temperature of the world has increased and causes the sea level increase.

Waste management system in Malaysia is very poor because the cost of dispose of the waste is increasing where the waste produced by Malaysia is 30000 every day and only 5% of it can be recycle. More than 50% of plastic product is made up from fossil fuels [3]. After human used it, they discard to the environment by burning it since it is very hard to dispose. The burning process cause a major problem since it can produce toxic gas and it is harmful toward environment and human.

## 2. METHODOLOGY

The gel time for glutinous rice was prepared with 5 samples and dried under room temperature. The room temperatures were estimated to be 32°C. All 5 samples were calculated to obtain the average time required for the glutinous rice to cure from moist-solid state to hard and durable surface. The test procedure and mould was prepared according to ASTM D3039 for tensile testing and ASTM D6110 for impact testing. The kenaf was 100% filled inside the mould and total weight is measured as shown in Figure 1.



Figure 1 (a) Kenaf in impact mould and (b) kenaf in tensile mould.

Sample calculation in obtaining the percentage of kenaf during sample preparation as indicated below:

$$\text{Mass of impact mould} = 50.047\text{g}$$

$$\text{Mass of tensile mould} = 114.360\text{g}$$

$$\text{Mass of impact mould + kenaf} = 52.622\text{g}$$

$$\text{Mass of tensile mould + kenaf} = 118.949\text{g}$$

$$\text{Mass of kenaf in impact mould} = 2.575\text{g}$$

$$\text{Mass of kenaf in tensile mould} = 4.589\text{g}$$

Table 1 Composition for both impact & tensile.

Composition for impact specimen	Composition for tensile specimen
$\frac{30}{100} \times 2.575\text{g} = 0.7725\text{g}$	$\frac{30}{100} \times 4.589\text{g} = 1.3767\text{g}$
$\frac{35}{100} \times 2.575\text{g} = 0.9013\text{g}$	$\frac{35}{100} \times 4.589\text{g} = 1.6062\text{g}$
$\frac{40}{100} \times 2.575\text{g} = 1.0300\text{g}$	$\frac{40}{100} \times 4.589\text{g} = 1.8356\text{g}$
$\frac{45}{100} \times 2.575\text{g} = 1.1588\text{g}$	$\frac{45}{100} \times 4.589\text{g} = 2.0651\text{g}$
$\frac{50}{100} \times 2.575\text{g} = 1.2875\text{g}$	$\frac{50}{100} \times 4.589\text{g} = 2.2945\text{g}$
$\frac{55}{100} \times 2.575\text{g} = 1.4163\text{g}$	$\frac{55}{100} \times 4.589\text{g} = 2.5240\text{g}$

Table 1 show the total weight of kenaf in one sample starting for 30wt.% up to 55wt.% for both impact and tensile specimens [4]. The glutinous rice was mix with water for about 1:1 ratio and allowed to be heated in the next process. After 15-20 minutes later, the water was filtered and reheat by using a glutinous rice cooker. Next stage is mixing slaked lime with water and added to the filtered glutinous rice Last but not least, the complete specimen was inserted into impact and tensile mould.

The first layer of the specimen is glutinous rice, followed by kenaf and another layer of glutinous rice again to fully wrap the kenaf. There are 6 compositions related which is 30%, 35%, 40%, 45%, 50%, 55%. The mechanical properties of kenaf mix with a natural binder were conducted using tensile test and impact test based on ASTM D3039 and ASTM D6110 standard respectively.

### 3. RESULTS AND DISCUSSION

Based on Figure 2 and Figure 3, the specimen of kenaf composition 40% to 45% is the most suitable choice standard to replicate or design products made from composition of glutinous rice and kenaf due to highest value of modulus of elasticity and has the highest resistance for plastic deformation before fracture. Moreover, it can support more load compare to the rest of composition.

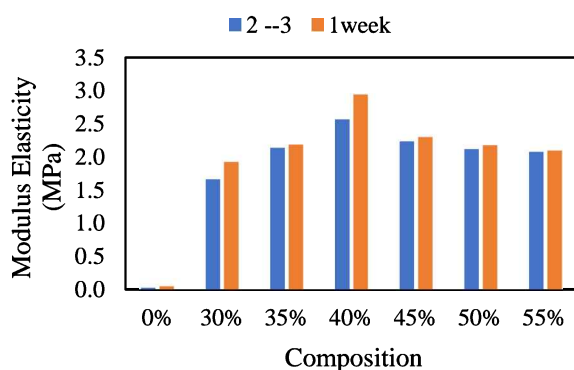


Figure 2 Modulus of elasticity for 1 week and 2-3 days curing time for each composition.

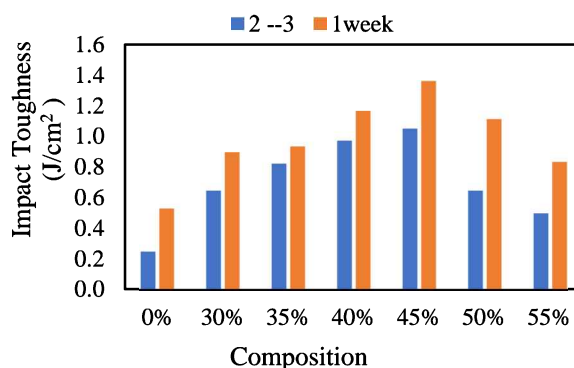


Figure 3 Impact toughness for 1 week and 2-3 days curing time for each composition.

Furthermore, it was clearly showing that 1-week cure has higher interfacial bonding compare to 2-3 days'

cure [5]. The comparison of curing time indicates that the longer the curing time, the higher the value of tensile strength, Young's Modulus and fracture strain on the specimen. Therefore, it can be concluded that the mechanical properties of kenaf fibre highly depend on the curing time where the longer the curing time, the better the interfacial bonding.

Higher degree of curing would result in higher cross-linking density which in return increases E-Modulus. Besides that, it would also decrease the strain of fracture occurred on the specimen cause Young's modulus is relatively independent of the specimen's range of composition. It is observed that the Young's modulus and automatic modulus are relatively sensitive to the change of composition [6].

### 4. CONCLUSION

As conclusion, the new composition of naturally made resin reinforced kenaf fiber was successfully made by using glutinous rice reinforced with kenaf fiber. From result, 40% and 45% composition indicate the highest value of Young's Modulus and impact toughness which is 2.945MPa and 1.36 J/cm<sup>2</sup> respectively for 1 week curing time. Further work needed to evaluate information about the surface topography and composition of the kenaf fibre.

### ACKNOWLEDGEMENT

This work was supported by Faculty of Mechanical and Manufacturing Engineering Technology, Universiti Teknikal Malaysia Melaka.

### REFERENCES

- [1] Basri, M. H. A., Abdu, A., Junejo, N., Hamid, H. A., & Ahmed, K. (2014). Journey of kenaf in Malaysia: A Review. *Scientific Research and Essays*, 9(11), 458-470.
- [2] Yahya, M. N., & Chin, D. D. V. S. (2017, August). A review on the potential of natural fibre for sound absorption application. *IOP Conference Series: Materials Science and Engineering*, 226(1), 012014.
- [3] Elsawy, M. A., Kim, K. H., Park, J. W., & Deep, A. (2017). Hydrolytic degradation of polylactic acid (PLA) and its composites. *Renewable and Sustainable Energy Reviews*, 79, 1346-1352.
- [4] Kaewpirom, S., & Worrarat, C. (2014). Preparation and properties of pineapple leaf fiber reinforced poly (lactic acid) green composites. *Fibers and Polymers*, 15(7), 1469-1477.
- [5] Samsudin, N. S., Shamsudin, M. A., & Abdullah, M. I. H. C. (2017). Effect of different composition of kenaf fiber and polyester as composite fiber substitution on elasticity profile properties. *Proceedings of Mechanical Engineering Research Day 2017*, 2017, 333-334.
- [6] Naik, D. L., & Kiran, R. (2018). On anisotropy, strain rate and size effects in vat photopolymerization based specimens. *Additive Manufacturing*, 23, 181-196.

# The effects of filler fibre sizes on the mechanical and fracture morphology of dried banana leaves filled recycled polypropylene

Thinakaran Narayanan<sup>1,2,\*</sup>, Jiefferie Abd Razak<sup>1</sup>, Intan Sharhida Othman<sup>1</sup>

<sup>1)</sup> Fakulti Kejuruteraan Pembuatan, Universiti Teknikal Malaysia Melaka,  
Hang Tuah Jaya, 76100, Durian Tunggal, Melaka, Malaysia

<sup>2)</sup> Department of Mechanical Polymer, National Youth High Skill Institute (IKTBN) Sepang,  
Bandar Baru Salak Tinggi, 43900, Sepang, Selangor, Malaysia

\*Corresponding e-mail: thinakaran@utem.edu.my / thinakaran@kbs.gov.my

**Keywords:** DBLF; filler size; mechanical

**ABSTRACT** – Natural fibre play an important role in the mechanical properties. The composite between dried banana leaves fibre (DBLF) and waste polypropylene (rPP). DBLF has been grounded into 10 $\mu\text{m}$  and 30 $\mu\text{m}$  of fibre sizes and the rPP crushed into finer particles. Composites are prepared through melting device and an injection moulding process for both fibre sizes and loading (0, 10, 20, 30 and 40) wt. %. It resulted more strength in tensile of 10 $\mu\text{m}$  rPP/DBLF composite meanwhile, adding in fibre loading and bigger fibre size content causes lesser in tensile properties and poor surface interaction between rPP/DBLF composites.

## 1. INTRODUCTION

Nowadays the application of natural fibres in polymer industries looks increasing tremendously [1]. The function of natural fibres as a secondary phase seems enhance the new dimension in structure stability, superior resistance in impact properties, magnificent strength in mechanical properties, superior abrasion resistance as well as thermal stability. In this study, the waste from an injection moulding scrap namely polypropylene (rPP) was loaded with dried banana leaves fibre (DBLF), for rPP/DBLF composites fabrication [1-4]. This green composition between plastic lump and natural fibres have greater and terrific mechanical properties as well as physical properties. Green composition become an outstanding product since it is eco friendly and safe to human application. In this study, dried banana leaves fibre (DBLF) has been applied as functional filler for recycled polypropylene (rPP) matrix which was emitted lump from an injection moulding process. For this intention, the waste polypropylene collected from an injection moulding process, and grounded into fine particles by using an industrial crusher. It follows by, some compounding step and hot compression technique were operated for rPP/DBLF composites production. In principle, natural fibre is commonly used as an extender to reduce the percentage of plastic usage, and increase the mechanical properties. For this reason, to understand the role of DBLF as latest green functional filler for polymer matrix composites, with the specific objectives were to determine the effects of fibre size and fibre loading in rPP composites production

## 2. METHODOLOGY

### 2.1 Raw Materials

The matured banana leaves from *musa acuminate* sp. species taken from reserved area located in IKTBN Sepang and chipped into smaller size at about 40-50mm length and 1-2mm in width. The chipped leaves dried for conditioning purpose for 24 hours at 80°C. The leaves were grounded to two sieve sizes 10 $\mu\text{m}$  and 30 $\mu\text{m}$ . the analysis of fibre size was carried out by using Malvern Instruments Mastersizer 2000 version 5.54. The range of measurement area in this system was between 0.020- $\mu\text{m}$  to 2000- $\mu\text{m}$ . The grounded fibre air conditioned at 80°C and humidity 65% for 3 days before executing fibre size analysis. Recycled Polypropylene (rPP) are collected from the waste produced by injection moulding process. The collected rPP lump was first cleansed and isolated for any contamination or impurities elimination. Lastly the compounding process of rPP/DBLF composites was performed via double steps of melt-blending process at various fibre loadings (0, 10, 20, 30 and 40) wt. %.

### 2.2 Tensile Testing of rPP/DBLF Composites

The tensile test for rPP/DBLF composites were performed in accordance to ASTM D638 – Type 1. The test was carried out at controlled atmosphere of 22±1°C, at relative humidity of 60%. Testing was performed at 10 mm/mins of cross-head speed by using a Universal Testing Machine (GoTech). For each loading, about five samples were tested for data averaging purpose.

### 2.3 Fracture Surface Morphological Observation of rPP/DBLF Composites

The fracture surfaces of the selected samples of rPP/DBLF composite was observed under the Scanning Electron Microscope (SEM) observation. At first, the fractured surface was mounted onto the stub with carbon tape before being coated with gold-palladium (Au-Pd) thin conductive coating, using a sputter coater model Polaron E-1500, to eliminate the charging effects during observation. The fracture surface images were captured by using Zeiss Evo VPSEM at 7.00kV accelerating voltage for 100x of magnification power at secondary electron detection.

### 3. RESULTS AND DISCUSSION

The following Figure 1 presented both fibre size analysis result of grounded dried banana leaves that has been sieved at two different sizes 10 $\mu\text{m}$  and 30 $\mu\text{m}$ . Based on Figure 1, multi wide distribution of fibres sizes was recorded, varying from almost 0 to 35 $\mu\text{m}$ . The analysis of 10 $\mu\text{m}$  size group showed that 18 % of volume recorded

(red line) while the fibre size of 30 $\mu\text{m}$  (green line) has peaked at 11% of volume itself. The percentile analysis shows that for both fibre size almost 50 % - 60 % of the screened DBL fibre samples are having sizes in between 10 $\mu\text{m}$  - 30 $\mu\text{m}$  and the rest of them are out of the range required.

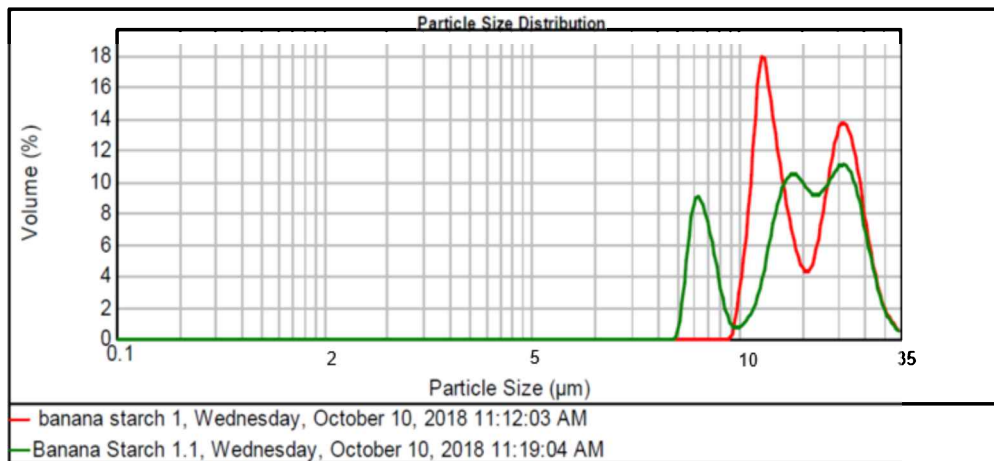


Figure 1 Particle size analysis (PSA) of 10 $\mu\text{m}$  grounded DBL fibre (red line) and 30 $\mu\text{m}$  DBLF fibre (green line).

Figure 2 shows a scanning electron microscope (SEM) micrograph observation for grounded DBL fibre at 100X of magnification. There a few samples randomly taken, and a mean value was then calculated to yield a final averaged result of 10 $\mu\text{m}$  -30 $\mu\text{m}$ . Thus, the prepared DBL fibre was verified having the averaged length for both sample sieve sizes about 10.4 $\mu\text{m}$  and 32.4 $\mu\text{m}$ , these surface and shape feature are important in influencing the matrix-filler interaction, between the rPP and grounded DBL fibre.

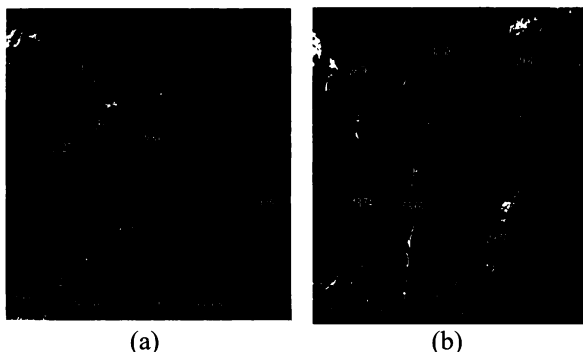


Figure 2 SEM micrograph of raw grounded (a) 10 $\mu\text{m}$  and (b) 30 $\mu\text{m}$  DBL fibre.

The following Figure 3 has presented the resulted tensile strength (TS) for rPP based composites filled with two different fibre sizes 10 $\mu\text{m}$  and 30 $\mu\text{m}$  at various loadings (wt.%). It was clearly found that, by DBLF with smaller fibre size into rPP matrix, the TS was significantly increased up to +22.30% of positive improvement (refer to green bar), in comparison to the 30 $\mu\text{m}$  DBL fibre size (refer to blue bar). However, adding up of DBLF filler more than 30wt% has reducing the composites performance, which responsible lowering the TS values for both fibre size. Overall results proven that

the size of fibre will play a major role which was produced superior outcome, that make a big impact to the composite properties.

### 4. CONCLUSION

In conclusion, from this study, the effects of DBL fibre loadings as well as the effect of fibre size towards the investigated tensile and fracture morphological properties of rPP/DBLF composites were fully explored and understood. Based on the experimental results, it was found that, about 30wt% of 10 $\mu\text{m}$  size DBL fibre addition has enough to enhance the TS for positive improvements compared to 30 $\mu\text{m}$  fibre size. This positive finding provides another alternative of degradable plastic-based composite to be selected and utilized for various promising applications.

### REFERENCES

- [1] Ramesh, M., Atreya, T. S. A., Aswin, U. S., Eashwar, H., & Deepa, C. (2014). Processing and mechanical property evaluation of banana fiber reinforced polymer composites. *Procedia Engineering*, 97, 563-572.
- [2] Yin, S., Tuladhar, R., Combe, M., Collister, T., Jacob, M., & Shanks, R. (2013). Mechanical properties of recycled plastic fibres for reinforcing concrete. *Fibre Concrete*, 1-10.
- [3] Bolka, S., Slapnik, J., Rudolf, R., Bobovnik, R., & Mešl, M. (2018). Thermal and mechanical properties of biocomposites based on green PE-HD and hemp fibers. *Contemporary Materials*, 1(8), 80-90.
- [4] Bátori, V., Jabbari, M., Åkesson, D., Lennartsson, P. R., Taherzadeh, M. J., & Zamani, A. (2017). Production of pectin-cellulose biofilms: A new approach for citrus waste recycling. *International Journal of Polymer Science*, 2017, 1-9.

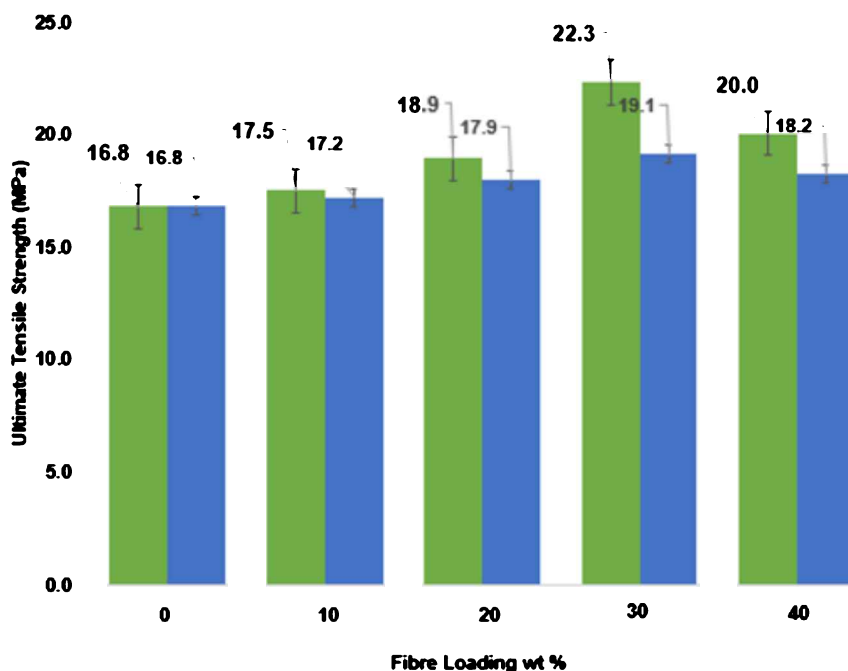


Figure 3 TS plots for fibre size 10 $\mu\text{m}$  (green bar) and 30 $\mu\text{m}$  (blue bar) DBLF at different wt% of loadings in *rPP* based composites.

# Flexural properties of thermoplastics corn starch reinforced short pineapple leaf fibre composites laminates at various ply

Nazri Huzaimi Zakaria<sup>1,3,\*</sup>, Mohd Zulkifli Selamat<sup>2,3</sup>, Mohd Zamani Ngali<sup>4</sup>, Abd Fuad Ab Ghani<sup>1,3</sup>, Nur Rohaiza Izamuddin<sup>1</sup>

<sup>1)</sup> Fakulti Teknologi Kejuruteraan Mekanikal dan Pembuatan, Universiti Teknikal Malaysia Melaka, Hang Tuah Jaya, 76100 Durian Tunggal, Melaka, Malaysia

<sup>2)</sup> Fakulti Kejuruteraan Mekanikal, Universiti Teknikal Malaysia Melaka, Hang Tuah Jaya, 76100 Durian Tunggal, Melaka, Malaysia

<sup>3)</sup> Centre for Advanced Research on Energy, Universiti Teknikal Malaysia Melaka, Hang Tuah Jaya, 76100 Durian Tunggal, Melaka, Malaysia

<sup>4)</sup> Fakulti Kejuruteraan Mekanikal dan Pembuatan, Universiti Tun Hussein Onn Malaysia, 86400, Parit Raja, Batu Pahat, Johor, Malaysia

\*Corresponding e-mail: nazrihuzaimi@utem.edu.my

**Keywords:** cornstarch; PALF; biopolymer

**ABSTRACT** – This study intends to investigate the characteristic of thermoplastic corn starch (TPCS) composite reinforced short pineapple leaf fibre (PALF) was prepared using laminates (sandwich) methods based on five various plies. The composite was fabricated by using 2mm of fibre length and evaluated the properties of different fibre loading (20 wt%, 30 wt%, 40 wt%, 50 wt% and 60 wt%). The flexural strength and flexural modulus of short PALF/TPCS composite were studied and compared. The PALF content at 50 wt% showed the highest mechanical properties value compared to other fibre content.

## 1. INTRODUCTION

Environmental consciousness, new rules, and legislation are forcing industries to look for new materials that are environmentally friendly [1]. The research community has expressed rising interest in using PALF as to reinforce thermoplastic and thermoset polymer composites due to their excellent mechanical properties compared to other natural fibres [2]. For the development of natural fibre composites, the material construction can easily be manipulated in many ways, such as varying the fibre loadings, fibre ratio, fibre type (short, long), fibre orientation (random, unidirectional, woven), number of ply, and ply stacking sequence [3].

Previous literature review revealed that there are several studies which reported on the effect of ply to the mechanical properties of hybrid natural fibre composite laminates such as for kenaf/Kevlar reinforced epoxy composites [4] and oil palm empty fruit bunch (OPEFB)/jute reinforced epoxy composites [5]. In addition, Mansor et al. [6] also emphasized that the final hybrid composites product quality was also influenced by the ply stacking sequence due to the interaction between the combined fibres and matrix.

In this paper, the biopolymer composite based on natural fibre (PALF) reinforced TPCS composites was prepared by using laminates (sandwich) methods at five various plies. The main objective of this study was to explore the effect of varying fibre loading on the various ply to the PALF reinforced TPCS composite on the flexural properties. Five different ply formations were

developed by using a compression moulding (Hot Press Machine) process. All samples were subjected to flexural tests based on ASTM D790 standard to determine the optimum flexural strength and flexural modulus of the laminates PALF/TPCS composites.

## 2. METHODOLOGY

### 2.1 Raw Materials

Corn starch (CS) used in this study was taken from the manufacturing type and in powder form. CS powder and glycerol were procured from Polyscientific Enterprise Sdn. Bhd. The type of glycerol was Qrec G4018-1-2500. The PALF from Josapine cultivars were purchased from cultivated areas in Kampung Parit Puteri Menangis, Pontian, Johor, Malaysia.

### 2.2 Sample Preparation

Thermoplastics corn starch was prepared from blended 70 wt% of native corn starch and 30 wt% of glycerol via hand-mixed and high speed mixer.

Five various fibre stacking sequences were applied to prepare the laminates PALF/TPCS composites as shown in Table 1 where the total weight of the PALF/TPCS composites was 40g. All short PALF were randomly orientated within the ply.

All laminates were subjected to compression moulding (Hot Press Machine) at 750 kg/cm<sup>2</sup> and at 165 °C temperature for 15 minutes followed by cure for 30 minutes. The laminates were fabricated based on a mild steel mould with fixed length x width x height of 140 mm x 60 mm x 3 mm.

Table 1 Compositions of PALF/TPCS composite laminates (sandwich) at various plies.

Loading	PALF (wt%)	TPCS (wt%)		
20/80	10	10	27	26
30/70	15	15	23	24
40/60	20	20	20	20
50/50	25	25	17	16
60/40	30	30	13	14
				13

### 2.3 Flexural Testing

Flexural tests were conducted according to ASTM

D-790 at the room temperature. The samples were prepared with dimensions of 140 mm (L) x 13 mm (W) x 3mm (T) by using a circular saw. The tests were carried out on five replications using a Universal Testing Machine (INSTRON 5556) with a 5 kN load cell; the crosshead speed was maintained at 2 mm/min.

### 3. RESULTS AND DISCUSSION

Figure 1 shows the overall results on flexural strength and modulus of PALF/TPCS composite which prepared via laminates method.

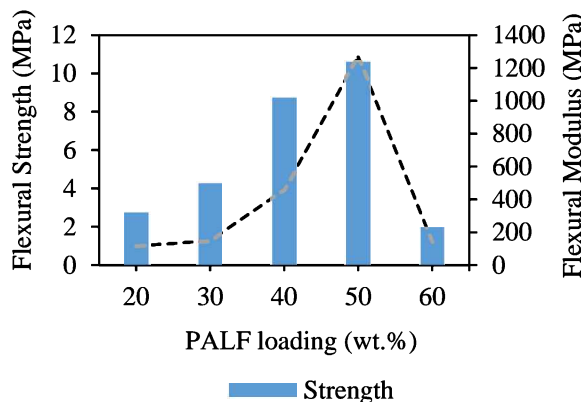


Figure 1 The flexural strength and modulus against PALF loading (wt%).

In general, the flexural test results show increasing trend until the optimum result at 50 wt% and drastically drop at 60 wt% of fibre loading. This trend is similar to the flexural modulus. The highest flexural strength was achieved at 10.58 MPa and flexural modulus was 1266 MPa. Both flexural strength and modulus of PALF/TPCS composites increased with increasing PALF content in the composites. However, the lowest flexural strength was observed at 60 wt% of fibre loading about 1.99 MPa and flexural modulus around 1.42 MPa.

A higher flexural strength of the PALF/TPCS composites might be attributed to a similar hydrophilic character of PLAF and TPCS, which led to great compatibility between them. The combination of compatible materials is often associated with improvement in mechanical properties of the resulting materials [7].

### 4. CONCLUSION

Biopolymer composite from TPCS reinforced short PALF was successfully prepared via laminates method in five various ply by using hot press machine in this study. The results show that TPCS and short PALF are compatible. The addition of PALF (up to 50 wt%) able to improve the flexural strength and modulus of composites. PALF reinforced with 50 wt% TPCS shows the highest value of flexural strength and modulus as compared to other composites. Meanwhile, TPCS reinforced with 60 wt% PALF shows the lowest result on flexural properties. Based on this indicator, TPCS blended with 50 wt% PALF has huge potential to be a good biopolymer composites.

### ACKNOWLEDGEMENT

The authors would like to thank Faculty of Mechanical and Manufacturing Engineering, Universiti Tun Hussein Onn Malaysia and Advance Materials Research Group (A-Mat), Faculty of Mechanical and Manufacturing Engineering Technology, Faculty of Mechanical Engineering, Universiti Teknikal Malaysia Melaka for financial sustenance and the utilisation of their facilities and besides the Ministry of Higher Education Malaysia for providing the scholarship award to complete this study.

### REFERENCES

- [1] Juraidi, J. M., Shuhairul, N., Azuan, S. S., & Anuar, N. I. S. (2013). A comparison of tensile properties of polyester composites reinforced with pineapple leaf fiber and pineapple peduncle fiber. In *IOP Conference Series: Materials Science and Engineering* (Vol. 50, No. 1, p. 012071). IOP Publishing.
- [2] Siregar, J. P., Cionita, T., Bachtiar, D., & Rejab, M. R. M. (2015). Tensile properties of pineapple leaf fibre reinforced unsaturated polyester composites. In *Applied Mechanics and Materials* (Vol. 695, pp. 159-162). Trans Tech Publications.
- [3] Hamid, N. A., Abdullah, N. H. N., Mansor, M. R., Rosli, M. A. M., & Akop, M. Z. (2010). An Experimental Study of the Influence of Fiber Architecture on the Strength of Polymer Composite Material. *Journal of Mechanical Engineering and Technology (JMET)*, 2(2).
- [4] Yahaya, R., Sapuan, S. M., Jawaid, M., Leman, Z., & Zainudin, E. S. (2015). Effect of layering sequence and chemical treatment on the mechanical properties of woven kenaf–aramid hybrid laminated composites. *Materials & Design*, 67, 173-179.
- [5] Jawaid, M., & Khalil, H. A. (2011). Effect of layering pattern on the dynamic mechanical properties and thermal degradation of oil palm-jute fibers reinforced epoxy hybrid composite. *BioResources*, 6(3), 2309-2322.
- [6] Mansor, M. R., Hadi, M. A. A., Taufiq, M. J., Salim, M. A., & Saad, A. M. (2018). Fabrication of hybrid oil palm empty fruit bunch and kenaf reinforced epoxy composite panels at varying fiber layering sequence. *1st Colloquium Paper: Advanced Materials and Mechanical Engineering Research*, 1.
- [7] The, D. P., Debeaufort, F., Voilley, A., & Luu, D. (2009). Biopolymer interactions affect the functional properties of edible films based on agar, cassava starch and arabinoxylan blends. *Journal of Food Engineering*, 90(4), 548-558.

# Effect of carbon nanotube-silane addition on mechanical properties of chloroprene rubber-filled carbon black

Kok-Tee Lau<sup>1,2,\*</sup>, Jeefferie Abd Razak<sup>2,3</sup>, Hairul Effendy Ab Maulod<sup>1,2</sup>, Noraiham Muhamad<sup>2,3</sup>, Mohamad Hanif Hashim<sup>1</sup>, Solament Arumugam<sup>1</sup>, Hoi Ern Kok<sup>1</sup>, See Ern Chung<sup>1</sup>, Nurzallia Mohd Saad<sup>4</sup>

<sup>1)</sup> Fakulti Teknologi Kejuruteraan Mekanikal dan Pembuatan, Universiti Teknikal Malaysia Melaka, 76100 Durian Tunggal, Melaka, Malaysia

<sup>2)</sup> Carbon Research Technology Research Group, Advanced Manufacturing Centre, Universiti Teknikal Malaysia Melaka, 76100 Durian Tunggal, Melaka, Malaysia

<sup>3)</sup> Fakulti Kejuruteraan Pembuatan, Universiti Teknikal Malaysia Melaka, 76100 Durian Tunggal, Melaka, Malaysia

<sup>4)</sup> Sunrich Integrated Sdn. Bhd., 53 & 54, Industrial Estate, 70450 Seremban, Negeri Sembilan, Malaysia

Corresponding e-mail: \*ktlau@utem.edu.my

**Keywords:** Electromagnetic interference (EMI); synthetic rubber; silane coupling agent

**ABSTRACT** – This study is to investigate the effect of carbon nanotube (CNT)-silane addition on tensile strength and elastic modulus of chloroprene rubber (CR)-filled carbon black (CB). The CR-filled CB was prepared by internal mixing, followed by roll-mill process in which CNT-silane dispersion was added. For comparison, CR-filled CB without CNTs and added with as-received CNTs were prepared. CR composite added with CNT-silane dispersion displayed 4% higher tensile strength and elastic modulus than CR-filled CB added with dry CNTs. FESEM micrograph shows CNT-silane dispersion addition produced better CNTs dispersion in the compound, thus verified the mechanical data.

## 1. INTRODUCTION

Recent flexible and stretchable electronics applications create high demands for flexible and durable materials [1]. Chloroprene-filled CNT rubber has been investigated for the electromagnetic shielding application [2]. Nevertheless, there are continuous studies to outcome CNTs agglomeration, for example by Krainoi et al. where CNTs was mixed with rubber in latex form [3]. Although promising results were reported, some of the methods are not feasible and incurs high manufacturing cost. Furthermore, CNT powder becomes airborne quite easily when pouring during compounding process, contributes to materials loss and air contamination. Thus, it is desirable to maintain CNTs in liquid dispersion through improvement in conventional manufacturing processing set up. In this study, we report the effect of CNT-silane dispersion addition on CR-filled CNT on the tensile strength and elastic modulus. Materials and manufacturing process of the compound is also presented.

## 2. METHODOLOGY

CR master batch with formulation as stated in Table 1 was prepared using internal mixer (Yi Tzung) operating at 60 °C, rotor speed of 900 rpm and mixing time of 8 mins. Subsequently, the CR match batch was divided into three smaller portions and then were calendered separately with different formulations (refer Table 2) using two-roll mill (model: MT2-2, Yi Tzung) at rotor speed of 19.3 rpm (front) and 22.5 rpm (back) and mixing

time of 5 min. All chemicals used in the formulations are from industrial grade.

Table 2 shows CNTs was added as second filler for CNT and CNT-Silane samples. During roll-mill, as-received CNTs was added in dry form for CNT samples, whereas, CNTs was added in dispersion form for CNT-Silane samples. CNT-Silane dispersion was prepared with the ultrasonication of 1.25 g Si-69 silane coupling agent in the 100 mL ethanol solution (95%). Then, as-received CNTs was mixed into the Si-69 solution. Additional 100 mL ethanol solution was then added, followed by further agitation by ultrasonication for 60 min. As control, CR compound samples without CNTs (which is an established formulation) were also prepared.

Table1 Formulations of master batch

Chemicals	Loading (phr)
Chloroprene (CR)	100
Zinc oxide (ZnO)	5
Stearic Acid (ST Acid)	0.5
Nocrac AD-F	2
Coumarone Resin (G90)	8
Carbon Black (N550)	40

Sheet samples (sample size = 4) for tensile test were prepared by hot press process in the respective sheet-shaped cavity steel molds, at 160°C and pressure of 110 kg-force for 10 min. Tensile tests were performed according to JIS K 6251 standard using Tensometer (model: UR-2060, U-CAN DYNATEX) to obtain tensile strength and elastic modulus data. Surface of tensile fracture samples were observed using Field-emission Scanning Electron Microscope (FESEM, 3 kV accelerating voltage, secondary electron emission mode, Merlin compact-60-25, Carl Zeis).

## 3. RESULTS AND DISCUSSION

### 3.1 Tensile Test

Tensile strength (TS) with standard error bar plots in Figure 1 show that CNT-Silane addition able to negate the deteriorating effect of CNT addition. TS of samples filled with CNT-Silane is comparable to the controlled samples and was 3% higher than the CNT samples. The low TS of

the CNT samples may be caused by formation of CNTs agglomerations in the CR compound, resulted in an earlier failure. This agglomeration problem was resolved with the usage of CNTs treated with Si-69 coupling agent. Nevertheless, CNT-Silane did not perform well as reinforcement agent, thus the TS did not improve significantly in comparison with controlled samples. It appears that presence of silane provided lubrication effect to the compound which permitted macromolecular chain slippage.

Table 2 Second formulations added during roll mill.

Chemicals	Loading (phr) for		
	CNT	CNT-Silane <sup>#</sup>	Control
Carbon Nanotubes (CNTs)	1	1 <sup>#</sup>	0
Magnesium Oxide (MGO)	4	4	0
Ethylene Thiourea (ETU-80)	0.7	0.7	0.7
N-Cyclohexyl-2-Benzothiazole Sulphenamide (CBS)	0.75	0.75	0.75

#Amount of added CNT (in dispersion form) was controlled at 1 phr dry weight of CNTs. Silane and ethanol solution were not included in phr calculation.

However, addition of CNT-silane helped to improve the stiffness characteristic by enhancing the tensile modulus at 300% of elongation (refer Figure 2). This condition might contribute by the ability of silane to assist CNT dispersion during compounding with CR. Better dispersion of CNT-silane provide good network between them within the CR matrix to resist the deformation. This can be the reason of the enhanced stiffness value.

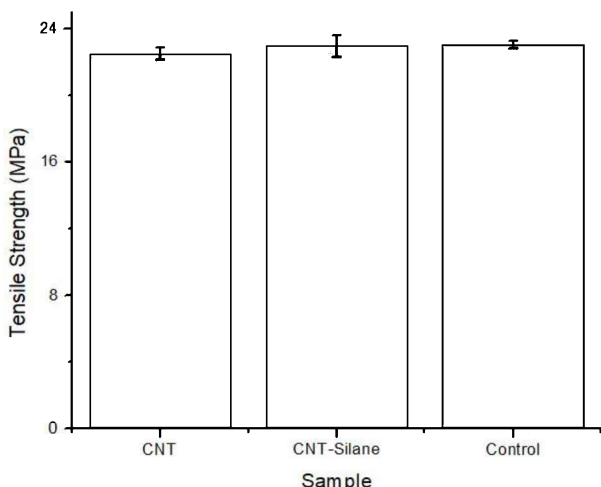


Figure 1 Tensile strength of CR compound samples.

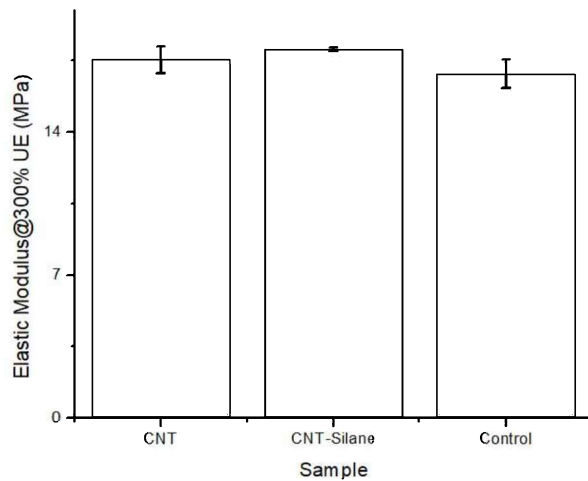


Figure 2 Elastic modulus (at 300% elongation) of CR compound samples.

FESEM micrograph in Figure 3 shows CNTs dispersed better after addition of silane. Thus, verified the mechanical data.

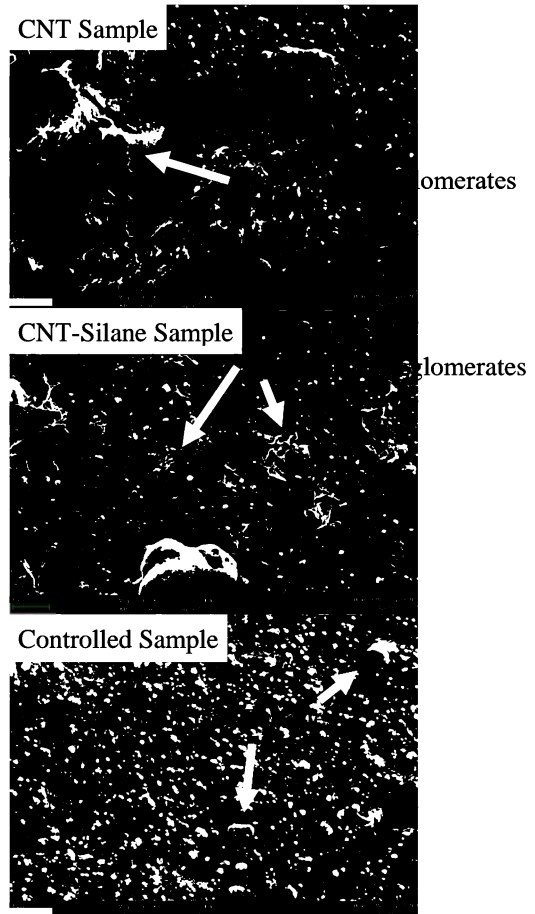


Figure 3 FESEM micrograph of surface of tensile fracture samples.

#### 4. CONCLUSION

CNT-silane addition into CR-filled CB showed higher tensile strength and elastic modulus than CR-filled CB added using as-received CNTs. FESEM showed a better CNTs dispersion in the CR matrix for the former.

Future work needs to investigate the effect of direct mixing of as-received CNTs and silane coupling agent into the CR compound, on the mechanical properties of CR compound. The study could decrease the processing steps of CR compound processing using silane addition.

#### ACKNOWLEDGMENT

The authors wish to thank Sunrich Integrated Sdn. Bhd. for providing sample preparation and mechanical properties characterization facilities.

#### REFERENCES

- [1] Dahiya, R. (2019). E-Skin: From Humanoids to Humans. *Proceedings of the IEEE*, 107(2), 247-252.
- [2] Kapgate, B. P., & Das, C. (2016). Electronic Applications of Chloroprene Rubber and Its Composites. In *Flexible and Stretchable Electronic Composites* (pp. 279-304). Springer, Cham.
- [3] Krainoi, A., Nakaramontri, Y., Wisunthorn, S., Pichaiyut, S., Nakason, C., Kummerlöwe, C., ... & Kiatkamjornwong, S. (2019). Influence of carbon nanotube and ionic liquid on properties of natural rubber nanocomposites. *Express Polymer Letters*, 13(4), 327-348.

# Study of the oil palm empty fruit bunch as fiber reinforcement on composite material

Mohd Fariduddin Mukhtar<sup>1,3,\*</sup>, Mohamed Saiful Firdaus Hussin<sup>1</sup>, Amir Abdullah Muhammad Damanhuri<sup>1</sup>, Khairul Amri Tofrowaih<sup>1</sup>, Khairul Azri Azlan<sup>1</sup>, Noor Saffreena Hamdan<sup>1</sup>, Adam Samsudin<sup>2</sup>

<sup>1)</sup> Fakulti Teknologi Kejuruteraan Mekanikal dan Pembuatan, Universiti Teknikal Malaysia Melaka, Hang Tuah Jaya, 76100 Durian Tunggal, Melaka, Malaysia

<sup>2)</sup> Fakulti Teknologi Kejuruteraan Elektrik dan Elektronik, Universiti Teknikal Malaysia Melaka, Hang Tuah Jaya, 76100 Durian Tunggal, Melaka, Malaysia

<sup>3)</sup> Advanced Manufacturing Centre, Universiti Teknikal Malaysia Melaka, Hang Tuah Jaya, 76100 Durian Tunggal, Melaka, Malaysia

\*Corresponding e-mail: fariduddin@utem.edu.my

**Keywords:** Oil palm; fruit bunch; material

**ABSTRACT** – The aim for this research is to study the characteristics of oil palm empty fruit bunch (OPEFB) as a fiber reinforcement on natural composite. Two group samples used OPEFB with different type of resin which is epoxy and polyester regarding to different fiber volume fraction. Hardness test, impact test and water absorption test were used. Results shows that sample with 50% fiber content displayed the highest hardness and impact value while in water absorption, it also shows the lowest value for both resins. OPEFB behaved as a significant adhesion between the matrix and composite. As a conclusion, to make a better composite, OPEFB and resin matrix should be mixed equally for better characteristics.

## 1. INTRODUCTION

Discovery of new advance material always give ideas for new advance material innovation. Overcome any limitation of the source of material for the traditional composite material such as glass fiber, natural fiber is renewable reinforcement to replace traditional composite material. Natural fiber appears to have low cost and easy to gain as the material is highly renewable and it helps for global sustaining the environment [1].

Nowadays, the replacement of natural fiber in composite polymer is interesting topics as it proves to be good performance from previous study, natural fiber can be an alternative approach because it has many properties and able to increase the strength ratio of the composite [2]. In aim of this research is to study the compatibility of natural fiber with two different resin matrices by using impact test, hardness test and water absorption test.

## 2. METHODOLOGY

OPEFB were used as fiber reinforcement and chopped into smaller size, divided into three part with different fiber volume fraction (25%, 50% and 75%) as in Figure 1 and the fraction were given as in Table 1. The mould prepared size is 20cm x 30cm and waxed with mirror glaze as release agent. The material then fabricated using epoxy and polyester, so there will be two different type of composite panel. Wet hand lay-up is implemented into this fabrication process for both type of resin, as the epoxy resin is for ambient cure. The samples then cut into smaller pieces by following dimension for testing. Total sample prepared for test is six.



Figure 1 Sample of 25% and 50% V<sub>f</sub>.

Table 1 Sample's fiber volume fraction (V<sub>f</sub>).

Sample	Fiber volume fraction (%)	
	OPEFB fiber	Resin
1	25	75
2	50	50
3	75	25

Samples were then undergone three different test which is hardness test, impact test and water absorption test. For water absorption test, OPEFB composite panel specimens were immersed into distilled water at room temperature for different time duration. Distilled water is used to prevent any additional substance such as chlorine involve in this test to avoid any miss reading result caused by unwanted existence during process. All the specimens are soaked onto different container and for different time duration. The differences between the absorption percentage were calculated using Equation (1).

$$\frac{W_f - W_i}{W_i} \times 100\% \quad (1)$$

Where  $W_f$  = final weight and  $W_i$  = initial weight.

## 3. RESULTS AND DISCUSSION

Figure 2 shows the result of both type of sample with different fiber volume fraction (V<sub>f</sub>) of Hardness test. The graph shows that sample of OPEFB-polyester is harder than epoxy with the highest percentage 79.2 type D. By referring 75% V<sub>f</sub> while the softest is epoxy with 50% V<sub>f</sub>, 66.6 type D. Roughly, polyester resin is the harder sample based on the graph below.

In Figure 3, for impact test result, the result of the Epoxy-OPEFB shows the highest result for impact test

is E50 with 50% V<sub>f</sub>, impact amount receive averagely 3.66J compare to other two samples, E75(75% V<sub>f</sub>), is the lowest with average impact result is 2.20 while E25 (25% V<sub>f</sub>) is 2.33. The difference value between E75 and E25 is not big.

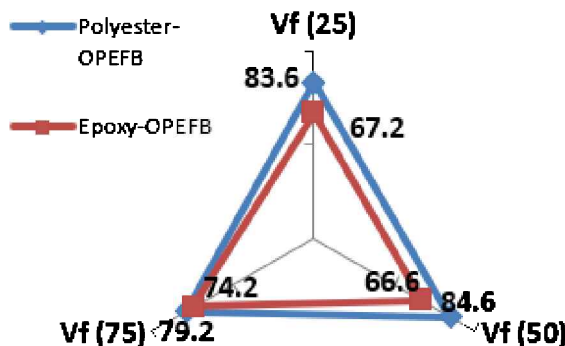


Figure 2 Hardness test.

This result concludes that, the 50% V<sub>f</sub> work well with the matrix resin and performs good impact properties. The highest value from all three polyester-OPEFB impact test is sample P50 with fiber volume fraction is 50%. The lowest value is from sample P25, with average value is only 0.90 Joule, while the average impact value for P75 is 1.16J. From the graph it is indicate the 50% V<sub>f</sub> is holds the highest value of impact.

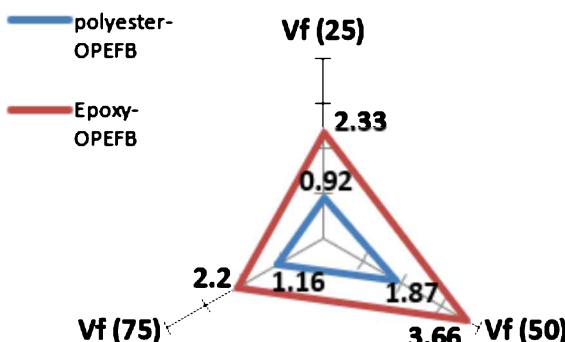


Figure 3 Impact test.

However, the variance of the water absorption for the first 2 days shows all the specimens absorb 1% of water mass then increasingly absorb about 0.845% averagely in next 4 days. The 0.2% different show the absorb activities has slowed down. This is cause by the effect from defects occurs on the specimens. Compare all the three sample, E75 (V<sub>f</sub> is 75%) shows the high absorbed water, while E50 (V<sub>f</sub> is 50%) is the lowest absorbed water then E25 (V<sub>f</sub> is 25%).

Less V<sub>f</sub> should have low absorption rate, this is indicating the fiber is hydrophilic nature that tend to absorb water. At final stage the absorption rate is decrease gradually and the samples having saturated state where there is no area or void to fill in. Each sample's absorption rate ends on 3.2%, 2.4%, 2.931% for E75, E50 and E25 respectively.

While for polyester, With increasingly from 0% of V<sub>f</sub>(the Wi : initial weight) to 0.6864% absorption for the first two days. The samples (P75) rate increase 0.766% making it total absorption percentage is 1.450%. this rapid rate decreases when final immersion duration ends

on day 10, with total final immersion of P75 is 1.862%. Different with P25 and P50, both of sample absorption result is close different. With the first 48 hours, only 0.475% and 0.526% absorption rate for P25 and P50 respectively.

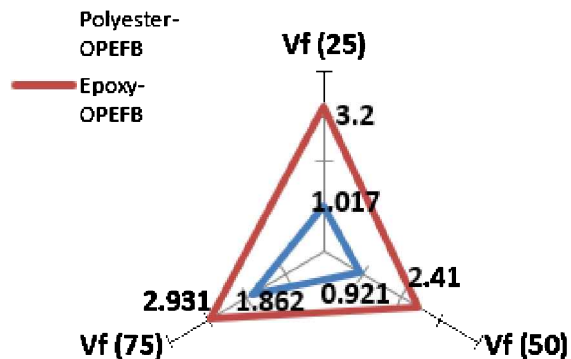


Figure 4 Water absorption comparison.

#### 4. CONCLUSIONS

From the project, all the test has done, and the discussion is explained, so the main objective is successfully achieved. The ability of both type of resin to be compatible with the natural fiber OPEFB have been prove by tests. From the hardness test, it is shows that Polyester-resin is the hardest material compare to Epoxy-OPEFB in this project. This is speculating that the Epoxy resin which using ambient cure maybe have disadvantage.

But, in impact test every specimen work well. The highest impact value is from Epoxy-OPEFB sample, which is indicated, the resin and fiber can work well together with natural fiber performing good impact test result. Other testing is water absorption test. This test is used to calculate the amount rate of water absorption of the sample. The natural fiber is known as hydrophilic material is chosen to study, if the ability to absorb liquid can implement by using two different resins. The result proves that, the higher fiber volume fraction causing the sample to absorb more water, while 50% of V<sub>f</sub> perform better result. From all three tests, the OPEFB can be one of the choices for being reinforced fiber in polymer composite. But, the application of this material is limited to low strength product usage. OPEFB is doubtful to perform well in high strength application.

#### ACKNOWLEDGMENT

The author would like to thank Universiti Teknikal Malaysia Melaka for funding this project through short term grant PJP/2019/FTKEE(3A)/S01655.

#### REFERENCES

- [1] Saheb, D. N., & Jog, J. P. (1999). Natural fiber polymer composites: a review. *Advances in Polymer Technology: Journal of the Polymer Processing Institute*, 18(4), 351-363.
- [2] Al-Oqla, F. M., & Sapuan, S. M. (2014). Natural fiber reinforced polymer composites in industrial applications: feasibility of date palm fibers for sustainable automotive industry. *Journal of Cleaner Production*, 66, 347-354.

# Reduction of corrosion rate of aluminum alloy 6061 through anodization

Md Fahmi Abd Samad\*, Raihana Ramle

Fakulti Kejuruteraan Mekanikal, Universiti Teknikal Malaysia Melaka,  
Hang Tuah Jaya, 76100 Durian Tunggal, Melaka, Malaysia

\*Corresponding e-mail: mdfahmi@utem.edu.my

**Keywords:** Corrosion; aluminum alloy; anodizing

**ABSTRACT** – This paper focuses on reducing the corrosion rate of aluminum alloy 6061 through anodizing. The study involves characterizing corrosion phenomenon in relation to parameters involved in an anodizing process, in particular the current density of anodizing, and its corrosion environment, specifically, the pH value and concentration of sodium chloride (NaCl) solution where the alloy is placed. The cleaning process is in accordance to ASTM G 1-90(1999). It concludes that corrosion rate may be reduced through an increase of current density during anodizing and such improvement was also observed even with high concentration and low pH of corrosion accelerator solution.

## 1. INTRODUCTION

Aluminum alloy has emerged as the best material applied in automotive industries for structural application. It is also known as the second-best material, second only to steel, in metal industry. The preference has been based on characteristics such as light weight, non-rusting properties, reasonably good strength, easy fabrication and favorable economics, coupled with modern metallurgical control of structure and properties.

However, like any other metal material, aluminium alloy suffers from some disadvantages. These include its tendency to serrated yielding during stretching and drawing, loss of strength during annealing of paint bake cycle, and corrosion [1,2].

This paper provides an extension to the study of corrosion protection of aluminium alloy, by relating directly an observed corrosion phenomenon to the parameters of anodizing.

## 2. METHODOLOGY

The raw materials were Aluminum Alloy 6061-T4 sheet. For the anodizing process, the complete list of equipment was as follows:

- a) Beakers
- b) Power supply 0-100 volt
- c) Crocodile clips
- d) Sulfuric Acid ( $H_2SO_4$ )
- e) Test samples (Al-6061)

The material was cut into 30 mm long and 1.695 mm thickness test samples. The samples to be set as the cathode in the anodization was cut as 10 mm width whereas the anode was cut as 30 mm width. Next, each of the samples was placed in designated beaker containing  $H_2SO_4$  and connected to electrical current source where different current density is applied.

After 20 – 30 minutes of anodizing, the samples

were immersed into different concentration of sodium chloride (NaCl) for corrosion acceleration. In accordance to ASTM G 1-90(1999), the cleaning process involves the use of sand paper grade 250 followed by sand paper grade 1250 (as a polishing guide), a solution of 50ml phosphoric acid and 20 g chromium trioxide, and also nitric acid [3].

In the calculation of corrosion rate, the following equation was applied

$$\text{Corrosion rate} = \frac{K \times W}{A \times T \times D}$$

Where:

$K$  – a constant depending on the corrosion unit expression

$T$  – time of exposure in hours

$A$  – area in  $cm^2$

$W$  – mass loss in g

$D$  – density in  $g/cm^3$

The procedure to examine pitting corrosion in this project is referred from ASTM G 46-94 (Reapproved 1999) standard.

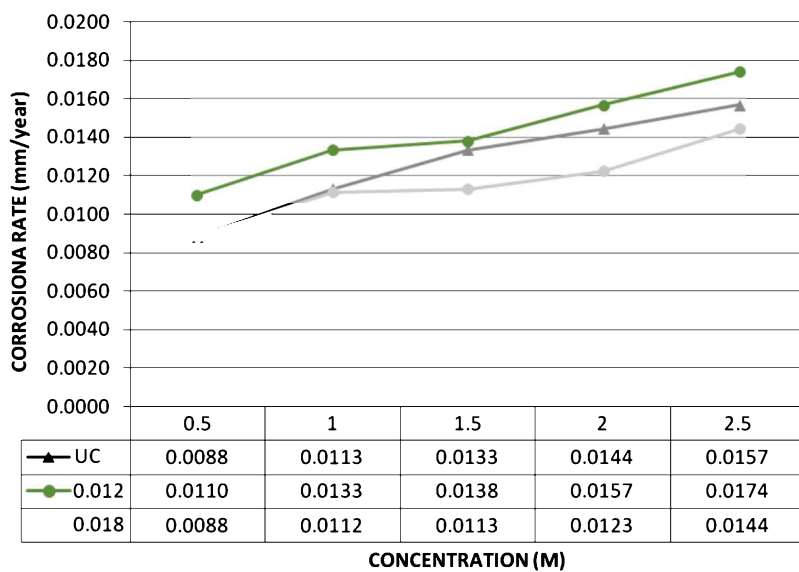
## 3. RESULTS AND DISCUSSION

The rate of corrosion was determined and presented as in Figure 1. It shows that the rate of corrosion increases as the concentration of NaCl increases. From this study, it is also seen that the level of current density also has an effect on the rate of corrosion of the sample. It is obtained that with higher current density, the corrosion rate decreases.

This may be due to high growth rate of oxide when using high current density, as confirmed by Chung et al. [5]. The solution concentration and also the anodizing process characterizes the electrochemical nature of the corrosion process. These factors are of considerable importance when evaluating corrosion resistance.

The plot of the corrosion rate versus pH value of the solution concentration shows that there is a nonlinear descending relationship between the corrosion rate and pH value of the solution (Figure 2). Based on the Pourbaix diagram, within the pH limits of its passive range (generally between 4 to 8.5), aluminum corrodes in aqueous solution because their oxides are soluble in many acids and bases, yielding  $Al^3$  ions in the former and  $AlO_2^-$  ions in the latter [6].

Figure 3 shows two images captured using scanning electron microscope that shows the visual characteristics of the corrosion. It very much resembles pitting corrosion.



Legend: UC: uncoated; 0.012: 0.012 A/mm<sup>2</sup>; 0.018: 0.018 A/mm<sup>2</sup>  
Figure 1 Corrosion rate versus concentration of corrosion solution.

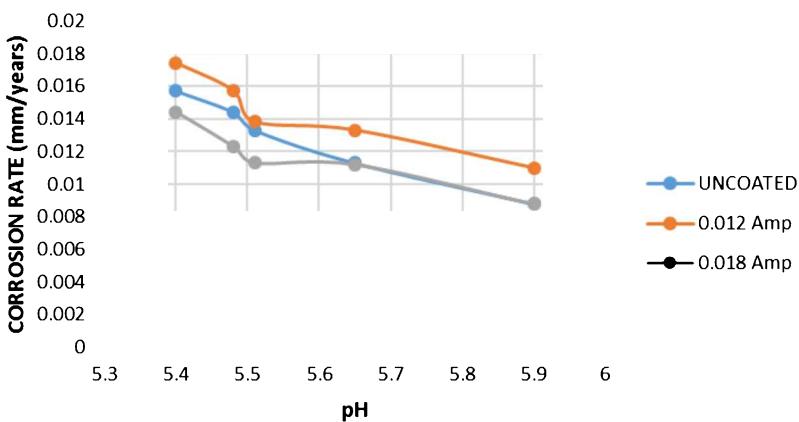


Figure 2 Corrosion Rate versus pH.

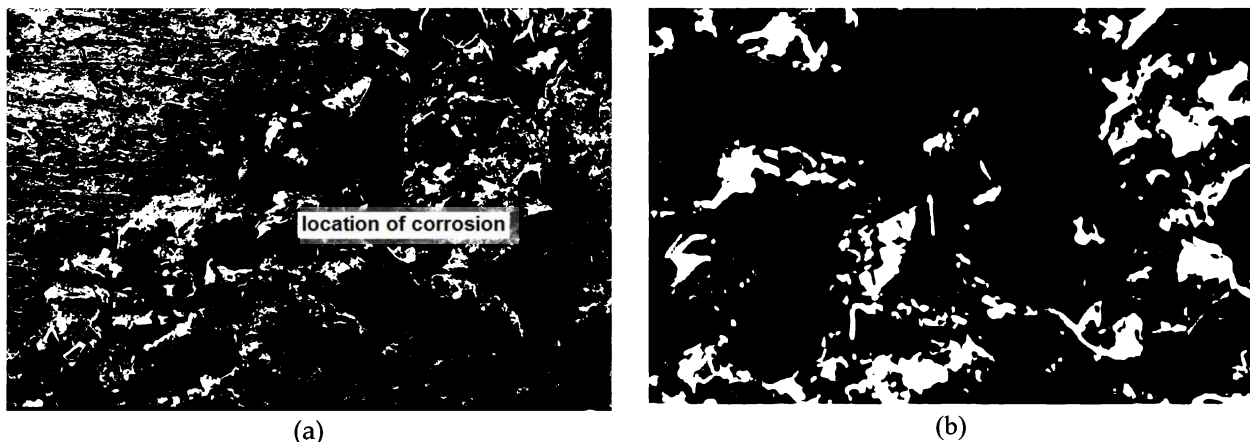


Figure 3 SEM image for uncoated sample in (a) 1.0 M NaCl solution; (b) 1.5 M NaCl solution.

#### 4. CONCLUSION

The test shows that when in contact with the surface of aluminum alloy 6061, the increase in current density during anodizing decreases the mass loss, hence corrosion rate. Aside from this, this project identified that rate of corrosion in aluminum alloy 6061 has an increasing trend towards the increment of NaCl solution concentration. Furthermore, by the decrement of solution pH value, the rate of corrosion increases. The corrosion

rate may be further reduced with the increase of current density during anodizing.

Other factors that may contribute to rate of corrosion is the electrode potential of material. By referring to the electrode potential, studies have shown that aluminum alloy 6061 is more active than sodium hydroxide (NaOH) and more susceptible to oxidation. A more realistic and practical ranking however may be provided by the galvanic series.

## REFERENCES

- [1] Ghali, E. (2010). *Corrosion resistance of aluminum and magnesium alloys: understanding, performance, and testing* (Vol. 12). John Wiley & Sons.
- [2] Sivasankaran, S. (Ed.). (2017). *Aluminium Alloys: Recent Trends in Processing, Characterization, Mechanical behavior and Applications*. BoD—Books on Demand.
- [3] ASTM Committee G-1 on Corrosion of Metals. (2017). *Standard practice for preparing, cleaning, and evaluating corrosion test specimens*. ASTM international.
- [4] ASTM G46-94. (2005). *Standard guide for examination and evaluation of pitting corrosion*. ASTM international.
- [5] Chung, I. C., Chung, C. K., & Su, Y. K. (2017). Effect of current density and concentration on microstructure and corrosion behavior of 6061 Al alloy in sulfuric acid. *Surface and Coatings Technology*, 313, 299-306.
- [6] Ashby, M. F., & Jones, D. R. H. (2012). *Engineering materials 1: an introduction to properties, applications and design* (Vol. 1). Elsevier.

# Effect of thin metal adhesion layer and thermal annealing process on microheater coil structure quality

Norihan Abdul Hamid<sup>1,3,\*</sup>, Syafeeza Ahmad Radzi<sup>2,3</sup>, Mazree Ibrahim<sup>4</sup>

<sup>1)</sup> Centre for Telecommunication Research Innovation, Universiti Teknikal Malaysia Melaka,  
Hang Tuah Jaya, 76100 Durian Tunggal, Melaka, Malaysia

<sup>2)</sup> Centre for Robotics and Industrial Automation, Universiti Teknikal Malaysia Melaka,  
Hang Tuah Jaya, 76100 Durian Tunggal, Melaka, Malaysia

<sup>3)</sup> Fakulti Kejuruteraan Elektronik dan Kejuruteraan Komputer, Universiti Teknikal Malaysia Melaka,  
Hang Tuah Jaya, 76100 Durian Tunggal, Melaka, Malaysia

<sup>4)</sup> Fakulti Teknologi Kejuruteraan Elektrik dan Elektronik, Universiti Teknikal Malaysia Melaka,  
Hang Tuah Jaya, 76100 Durian Tunggal, Melaka, Malaysia

\*Corresponding e-mail: norihan.hamid@utem.edu.my

**Keywords:** Micro heater; annealing process; adhesion layer, metal deposition

**ABSTRACT** – Aims of this paper is to investigate and study the effect of metal adhesion layer and thermal annealing process to improve the metal layer quality and bonding of the micro-heating elements so that thermal power generation can be improved. A thin metal adhesion layer is deposited on the borosilicate glass substrate using a metal sputtering process, then the sample was carried out in nitrogen atmosphere by thermal annealing treatment at an optimum of 450°C in 30 minutes. The results show that the quality and the crystal properties of metal has improved besides structural defect and resistance of the conductor was reduced to obtain higher thermal generation.

## 1. INTRODUCTION

The existence of a metallic layer as a heater coil structure for the micro heater on the surface of the borosilicate glass substrate with low resistance value is necessary [1] to enable higher thermal power generation performance. However, a conventional microelectromechanical system (MEMS) fabrication technique has been known to have a high impact on heater elements thus increasing the metal resistance that may lead to the degradation of thermal generation performance.

In general, the adhesion layer may improve the metal adhesion on substrate, reduce resistance and obtain smooth surface [2], while the annealing treatment process may improve crystallinity and energy impurity. No doubt, metal element with lower resistance value will improve the quality of metal conductive layer which has good ohmic contact and reduces the resistance [1, 3].

Therefore, in this study, the effect of the adhesion layer and thermal annealing process on a microheater coil structure were investigated. The influence of annealing treatment on physical metal surface and structure was observed using an optical microscope while SEM is used to analyze the structural properties. Then the performance of heat generation was measured and compared to the previous micro heater coil structure without the adhesion layer and annealing treatment process.

## 2. MICRO HEATER STRUCTURE

The microheater structure consists of microheater built with metal resistive material that has higher thermal conductivity for a heater element structure and deposited on a thin substrate structure made of borosilicate glass material as illustrated in figure 1. For a simple geometry design, ease of fabrication process and produce a higher rate in small volume production, a square meander geometry design of heater element was chosen.

Normally the heater element, induced with the small voltage on the heater pad hence allow current flows through the heater element form one side to another. This conduction process will allow the heater to produce high thermal distribution for various kind of application in microdevice components such as micro pump [4], gas detector [5, 6] and etc. The total dimension of the microheater is approximately 10 mm x 15 mm x 2.4 mm with the thickness material from 1 to 10 um for heater element and substrate respectively. The length of the heater element is approximately 32 mm.

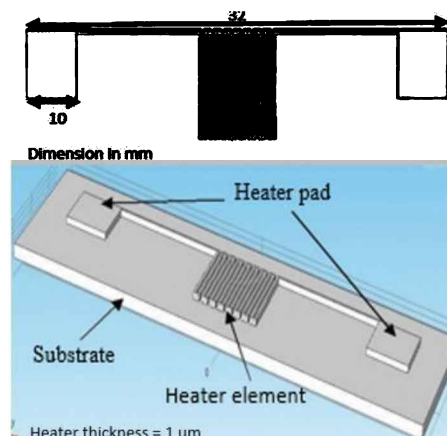


Figure 1 Top and side view of heater structure.

## 3. EXPERIMENTAL PREPARATION

A thin borosilicate glass substrate was cleaned with a common glass substrate cleaning process with acetone, isopropanol and deionized (DI) water. Next, the heater geometry structure was developed using a mask lithography process and immersed into the developer until the pattern appeared on the surface of the glass

substrate. Then, the glass substrate was deposited with or without adhesion layer. In this experiment, 50 nm Chromium (Cr) was chosen as the adhesion layer [2,3,4] due to high binding material strength with oxygen and able to passivate with various many material surfaces [1,3]. Then a higher resistive element of 500 nm Platinum (Pt) was deposited on the top of Cr act as a heater structure element. Both of metal deposition on the glass substrate was done by a metal sputtering process in the sputter chamber with argon ambient at  $2.0 \times 10^{-3}$  Torr, 30 mm working distance and operating current of 30 mA. After that, both metal layers were lifted and immersed in the ultrasonic bath at approximately 2 minutes to reveal the deposited metal heater element structure. The sample then was placed in the furnace for thermal annealing treatment about 30 minutes at a temperature of 450°C to enhance their structural property. The annealing temperature was chosen by considering the effect of the temperature on metal quality previously [1,4, 5]

#### 4. RESULTS AND DISCUSSION

The differences of chromium deposition compared to without any adhesion can be seen clearly at the end of the process using an optical microscope seen in figure 2. The glass substrate with a chromium layer in figure 2 (a) was observed to provide a better adhesive layer, accurate element size, provide a uniform surface and less fracture. While the image in figure 2 (b) shows its bad attachment layer, the element size is smaller than the actual size, uneven surfaces besides there are small fractures and holes on the surface element. In addition, the resistance measurement results also show that elements with a chromium adhesive agent have lower resistance than non-coated metal chromium elements [5].

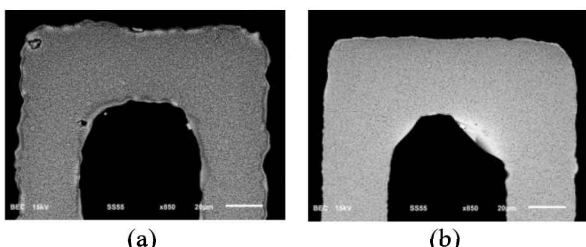


Figure 2 The image of a metal structure with (a) and without (b) Cr as the adhesion layer using an optical microscope.

Figure 3 depicted surface morphology of thin metal structure layer before and after the annealing process using scanning electron microscopy (SEM) machine. Figure 3(a) shows that the metal structure is slightly uniform with the substrate cover with some void and cracks. From the surface topology, it can be seen that there is a different size of cluster composed on the metal microparticle, while Figure 3(b) shows an improvement in crystallinity after the annealing process. Hence the surface enhanced with smaller voids, pinholes or cracks on the substrate. At the same time, the annealing treatment also gives an improvement in mean grain size. This may be due to the tendency of a particle to shake and made coalesce arrangement from smaller clusters into larger clusters during the annealing process [3].

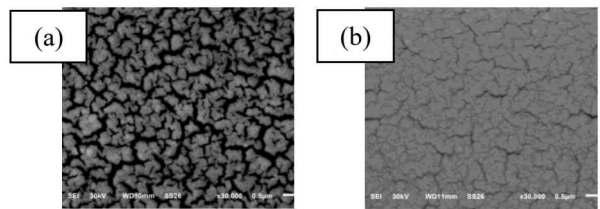


Figure 3 SEM image of platinum (a) before (b) after annealing.

#### 5. CONCLUSION

Effect of thin metal adhesion and thermal annealing process on micro heater coil structure quality have been investigated and studies. No doubt by depositing an adhesion layer on the borosilicate glass surface its can give better attachment of metal structure hence, provide an actual size and uniform surface of the heater element structure. At the same time, better adhesion can also reduce the conductor element. While thermal annealing treatment on metal conductor structure can reduce the structural defect and conductor resistance thus improve the crystallinity. By reducing the resistance, lower power consumption will be achievable to obtain higher thermal generation.

#### ACKNOWLEDGMENT

Authors are thanks to Centre for Telecommunication Research Innovation (CeTRI), Fakulti Kejuruteraan Elektronik and Kejuruteraan Komputer, Universiti Teknikal Malaysia Melaka for the moral, operational and financial support they provided

#### REFERENCES

- [1] Yunas, J., Said, M. M., Pawinanto, R. E., & Majlis, B. Y. (2016). Enhancement of metal coil quality on selective p-silicon based planar electromagnetic coil by thermal annealing process. *Microsystem Technologies*, 22(10), 2493-2497.
- [2] Chang, W. Y., & Hsieh, Y. S. (2016). Multilayer microheater based on glass substrate using MEMS technology. *Microelectronic Engineering*, 149, 25-30.
- [3] Abdul Hamid, N., Yunas, J., Yeop Majlis, B., Hamzah, A. A., & Bais, B. (2015). Microfabrication of Si3N4-polyimide membrane for thermo-pneumatic actuator. *Microelectronics International*, 32(1), 18-24.
- [4] Butt, M. A., & Fomchenkov, S. A. (2017). Thermal effect on the optical and morphological properties of TiO<sub>2</sub> thin films obtained by annealing a Ti metal layer. *Journal of the Korean Physical Society*, 70(2), 169-172.
- [5] Hamid, N. A., Majlis, B. Y., Yunas, J., & Dehzangi, A. (2013, September). Annealing effects on structural and electrical properties of micro heater conductor element. In *RSM 2013 IEEE Regional Symposium on Micro and Nanoelectronics* (pp. 77-80).
- [6] Bedoui, S., Gomri, S., Samet, H., & Kachouri, A. (2016, March). Design and electro-thermal analysis of a platinum micro heater for gas sensors. In *2016 13th International Multi-Conference on Systems, Signals & Devices (SSD)* (pp. 558-561).

# Characteristics of the superficial oxide layer on the aluminium (99.4% purity) granules during in-situ melting

Aslinda Saleh<sup>1,\*</sup>, Mohd Hasbullah Idris<sup>2</sup>, Norfazillah Talib<sup>3</sup>, Haslina Abdullah<sup>3</sup>, Lee Woon Kiow<sup>3</sup>

<sup>1)</sup> Faculty of Engineering Technology, Universiti Tun Hussien Onn Malaysia,  
Pagoh Higher Education Hub, 84600 Pagoh, Muar, Johor, Malaysia

<sup>2)</sup> School of Mechanical Engineering, Faculty of Engineering, Universiti Teknologi Malaysia,  
81310 UTM Skudai, Johor, Malaysia

<sup>3)</sup> Faculty of Mechanical and Manufacturing Engineering, Universiti Tun Hussein Onn Malaysia,  
86400 Parit Raja, Batu Pahat, Johor, Malaysia

\*Corresponding e-mail: aslinda@uthm.edu.my

**Keywords:** In-situ melting; aluminum; oxidation

**ABSTRACT** – This study was conducted to develop alternative approach for a pouring free casting process that would reduce the turbulence due to pouring action in the conventional casting process resulted with porosity in the cast product. The in-situ melting was employed for investment casting of 99.4% purity aluminium (Al) granules by heating the granules at the temperature 700, 750, 800 and 850°C for 30 and 60 min. However, the Al granules oxidised forming superficial ( $\text{Al}_2\text{O}_3$ ) layer that increased in thickness as the temperature and duration were increased hinders the complete melting of the granules.

## 1. INTRODUCTION

Casting is a versatile manufacturing process which can cast any metal into products such as household products and even engineering parts. However producing sound aluminium (Al) casting is challenging due to the nature of the liquid aluminium that absorbed hydrogen from the environment which resulted with gas porosity in the solidified casting. In fact, the reaction of liquid aluminium alloy with moisture and/or oxygen develops very thin oxide layer on the surface of the molten metal when pouring into mould the entrained and folded surface oxide ( $\text{Al}_2\text{O}_3$ ) film known as the bifilm developed due to turbulence. The bifilm remains in the solidified casting act as nucleation sites for the pore/porosity formation that decrease the mechanical properties of the casting [1].

Several attempts have been employed to reduce the porosity such as by melt treatment, and adopt turbulence free filling system. The melt treatment requires molten metal degassing with inert gas [2], degassing with ultrasonic vibration [3,4], fluxing with chloride and fluoride salt [5].

Alternatively, turbulence free filling system including tilt casting [6], bottom filling [7], low pressure bottom filling [8], in-situ melting [9] and in-situ microwave casting [10] were developed to overcome the issue. It was found that the in-situ melting and in-situ casting approaches has potential to become a pouring free casting process however the former design of experiment and equipment used in in-situ casting was complex and costly. The in-situ melting approach is more simple and economic however melting granular metal or alloy is a challenge to the metal caster as they oxidised during

heating at high temperature which hindered the complete melting of the granules. This study investigates the characteristics of the superficial oxide layer formed on the pure aluminium granules that effects the incomplete melting of those granules.

## 2. METHODOLOGY

50g of the 99.4 % pure aluminium (Al) granules with cylindrical shape sized 4mm diameter and 5-6mm height were charged into a pre-prepared cylinder ceramic investment casting mould made of six layers of ceramic with measured mould thickness between 6 to 7mm. The filled mould were shaken gently by hand to allow the granules occupy the entire mould geometry. The mould was placed in a high temperature muffle furnace (KSL-1800X for heating at four different temperatures of 700, 750, 800 and 850°C for the duration of 30 and 60 min. The furnace accuracy and the heating rate was  $\pm 1^\circ\text{C}$  and  $10^\circ\text{C}/\text{min}$  respectively. The heated samples were left to cool slowly in the furnace.

Metallography samples were prepared and characterised using the field emission scanning electron microscopy (FESEM) equipped with energy dispersive x-ray spectroscopy (EDS).

## 3. RESULTS AND DISCUSSION

It was visually observed that the pure Al granules unable to completely melted and produced a casting even after being heated at the temperature 850°C which is beyond its melting temperature (660°C). However the heated Al granules were agglomerated took the shape of the ceramic investment casting mould which indicated the granules might partially melted or fully melted however being encapsulated by superficial oxide layer as previously described by the author [11].

### 3.1 Morphology of the superficial oxide layer

SEM observation revealed the morphology of the Al granules after heated at the temperature of 850°C for 30min containing oxides particles as shown in Figure 1. The oxide particles presence as individual oxide nodules at the certain area while some oxides were agglomerated. The oxides formed on the surface of Al granules heated at 700 and 750°C individually dispersed while for 800°C the individual oxides grew line by line and agglomerated on the surface. The growth of the oxide nodules was due

to the migration of ions simultaneously occurred either by diffusion of Al to the oxide-gas interface or the oxygen ion transported to the oxide-metal interface through the cracks on the oxide layer [12].

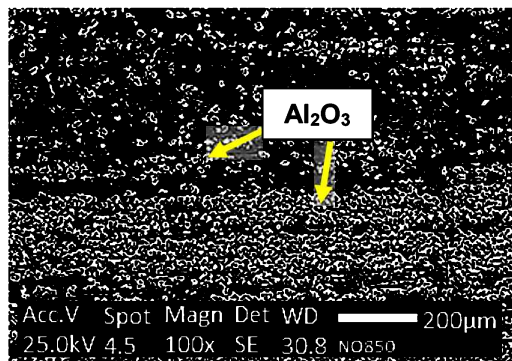


Figure 1 Oxide particles on the Al granule after heated the temperature of 850°C for 30min.

### 3.2 Oxide element and thickness

Figure 2 shows the EDS peaks indicated the presence of 68.79 wt % Al and 31.21 wt % O in the sample which proved that the Al granules oxidized during in-situ melting forming a superficial oxide layer which is the aluminium oxide ( $\text{Al}_2\text{O}_3$ ).

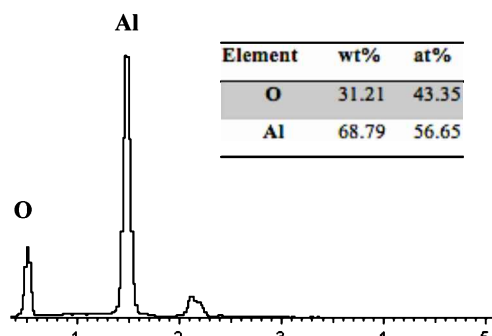


Figure 2 EDS analysis result of the Al granules after heated the temperature of 850°C for 30min.

While, Table 1 listed the thickness of the superficial oxide layer (measured from the cross section cut sample) were increased when the Al granules were heated at the temperature of 700, 750, 800 and 850°C for both heating duration of 30 and 60 min. In average, prolonged heating duration from 30 to 60 min increased the thickness of the oxide layer. It was due to the cracking of the oxide layer at elevated temperature (850°C) facilitating the Al ion diffusion to the oxide surface and oxidised as it in contact with air resulted with the increased oxide size [13].

Table 1 Thickness of the superficial oxide layer.

Temp. (°C)	Duration (min)	
	30	60
	Thickness (μm)	
700	0.949	0.704
750	0.286	0.588
800	1.109	1.988
850	8.515	10.610

### 4. CONCLUSION

It can be concluded that the superficial oxide layer on the surface of the heated Al granules is aluminium oxide ( $\text{Al}_2\text{O}_3$ ) that randomly presence as individual nodules on the granules' surface (700 and 750°C), line up (800°C) and uniformly agglomerated (850°C). Prolong heating duration and elevated temperature (850°C) had greater influence on the increment of the superficial oxide layer thickness. The increased of oxide layer thickness as the temperature was increased hindered the possibility of the in-situ melting of the Al granules even though was heated beyond the melting temperature due to the tiny melted Al was encapsulate by the oxide.

### REFERENCES

- [1] Dispinar, D., & Campbell, J. (2011). Porosity, hydrogen and bifilm content in Al alloy castings. *Materials Science and Engineering: A*, 528(10–11), 3860–3865
- [2] Dispinar, D., Akhtar, S., Nordmark, A., Di Sabatino, M., & Arnberg, L. (2010). Degassing, hydrogen and porosity phenomena in A356. *Materials Science and Engineering: A*, 527(16–17), 3719–3725
- [3] Barbosa, J., & Puga, H. (2017). Ultrasonic melt processing in the low pressure investment casting of Al alloys. *Journal of Materials Processing Technology*, 244, 150–156
- [4] Haghayeghi, R., Bahai, H., & Kapranos, P. (2012). Effect of ultrasonic argon degassing on dissolved hydrogen in aluminium alloy. *Materials Letters*, 82, 230–232
- [5] Puga, H., Barbosa, J., Azevedo, T., Ribeiro, S., & Alves, J. L. (2016). Low pressure sand casting of ultrasonically degassed Al7SiMg alloy: Modelling and experimental validation of mould filling. *Materials & Design*, 94, 384–391.
- [6] Harding, R. A., Wickins, M., Wang, H., Djambazov, G., & Pericleous, K. A. (2011). Development of a turbulence-free casting technique for titanium aluminides. *Intermetallics*, 19(6), 805–813.
- [7] Wang, T., Yao, S., & Shen, W. (2015). A submerged-gate casting method. *Journal of Materials Processing Technology*, 222, 21–26.
- [8] Jafari, H., Idris, M. H., Ourdjini, A., & Kadir, M. R. A. (2013). Influence of flux on melting characteristics and surface quality of in-situ melting AZ91D. *Materials and Manufacturing Processes*, 28(2), 148–153.
- [9] Saleh, A., & Idris, M. H., (2015). Oxidation of pure aluminium granules during in-situ melting. *Advance Materials Research*, 1125, 28–32
- [10] Anžel, I. (2000). High temperature oxidation of metals and alloys. *Metalurgija-Journal of Metallurgy*, 325–336.
- [11] Coker, E. N. (2013). The oxidation of aluminum at high temperature studied by Thermogravimetric Analysis and Differential Scanning Calorimetry. *Sandia National Laboratories*, 7–9.

# Thrust force and tool wear investigation of micro drilling for carbon fiber reinforced polymer (CFRP) material

N. Syuhada Nasir<sup>1,\*</sup>, N. Ab Wahab<sup>1</sup>, R. Izamshah<sup>2</sup>, H. Sasahara<sup>3</sup>, S.A. Sundi<sup>1</sup>

<sup>1)</sup> Fakulti Teknologi Kejuruteraan Mekanikal dan Pembuatan, Universiti Teknikal Malaysia Melaka,  
Hang Tuah Jaya, 76100 Durian Tunggal, Melaka, Malaysia

<sup>2)</sup> Advanced Manufacturing Center, Universiti Teknikal Malaysia Melaka,  
Hang Tuah Jaya, 76100 Durian Tunggal, Melaka, Malaysia

<sup>3)</sup> Department of Mechanical Systems Engineering, Tokyo University of Agriculture and Technology, Japan

\*Corresponding e-mail: nsyuhada\_mn@yahoo.com

**Keywords:** CFRP; thrust force; tool wear

**ABSTRACT** – Micro drilling of Carbon fiber reinforced polymer (CFRP) poses numerous challenges due to its anisotropic structure and non-uniform material properties. High cutting force and rapid tool wear are few of the common problems in dealing with this material which correlate with the drilling parameters. Therefore, understanding on the relationship between the parameters and the materials response is crucial for the success of the drilling process. Experimental micro drilling process with variable spindle speed and constant feed was carried out to investigate the effects of machining parameter on thrust force and tool wear. It was observed that, thrust force and tool wear have small effect towards the parameter range studies. Hence, it can be concluded that the investigation work need to be extends by taking into accounts on the influence of feed rate and range of parameter study.

## 1. INTRODUCTION

CFRP is widely use especially for aircraft and automotive component. It provides high strength to weight ratio and excellence material properties [1]. In general, CFRP components are produced near to net shape which required additional machining process especially for the assembly process [2]. Drilling CFRP poses numerous challenges due to its anisotropic structure and inhomogeneity of material properties between the plies [3]. Therefore, selection of optimum parameter plays important role to achieve good hole quality at low cost and shorter cycle time [4].

Challenge in drilling the CFRP can be divided into two different categories which are on the tool and the material itself [5]. Defects on the CFRP like delamination and fiber pullout are commonly occur during drilling process [6]. This paper will emphasize on the tool wear and thrust force. Few studies revealed that the delamination rate are related to thrust force and it can be noted that minimum damage can be obtained by controlling the thrust force below the critical value which significantly related with the cutting parameters namely spindle speed and feed rate [7-10].

## 2. METHODOLOGY

### 2.1 Experimental Setup

The experiments were based on micro drilling CFRP composites panel at different spindle speed and constant feed rate. The micro drilling process was carried

out using router machine Haas Gantry Router with the maximum spindle speed of 10,000 rpm. The cutting parameters were used in this experiment is tabulated in Table 1.

The holding fixture which ensured the safety gap between panel and dynamometer was fabricated and used throughout the experiments. The fixture was mounted on a 3-axis Kistler 5233A1 dynamometer for measuring drilling thrust force. Experiment setup is shown in Figure 1.

Table 1 Cutting parameters.

Parameter/Levels	1	2	3
Spindle speed (rpm)	10,000	9,000	8,000
Feed rate (mm/min)	200	200	200
No. of drilled hole	400	400	400

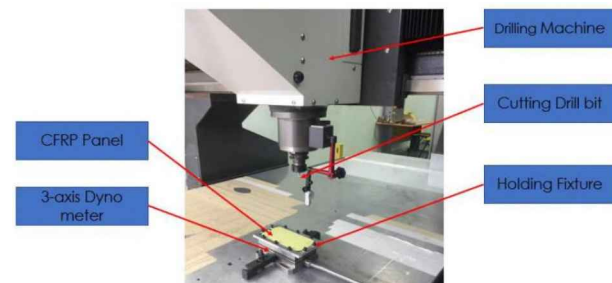


Figure 1 Experimental setup.

### 2.2 Workpiece and Cutting Tools

CFRP composites panels with dimension of 184 mm x 86 mm and maximum thickness of 3.8 mm were used as the workpieces. The panels were manufactured by Hexcel® based on AS4 Carbon Fiber and epoxy matrix with 57.42% nominal fiber volume [11].

Two (2) flutes TiAlN coated solid carbide drill bit with diameter of 0.9 mm and tolerance of +0.004 mm was used. The drill bit has point angle of 130°. Recommended from supplier, minimum spindle speed is 8000 rpm and maximum cutting depth is 9.2 mm [12]. A new fresh drill bit was employed for all the experimental runs.

### 2.3 Experiment's Responses

During the experiments, the thrust force values was measured using 3-axis Kistler 5233A1 dynamometer and

the output from dynamometer was processed by DynoWare software. After the experiments, each tool was observed and captured by using Scanning Electron Microscope (SEM) with 80 times magnification.

### 3. RESULTS AND DISCUSSION

#### 3.1 Experimental Result of Thrust Force

Table 2 shows the result of thrust force for all the experiments. From the table, the average thrust force for all trial were almost similar which were in the range 3.6 N. There are two possible reasons for this reason, firstly is due to the range of applied spindle were too small that result in small thrust magnitudes and secondly due to the thickness of the material that are too thin which produced less impact [13].

Table 2 Thrust force.

Exp.	Fx	Fy	Fz	Average Thrust Force (N)
1	1.740	1.800	3.662	<b>3.662</b>
2	1.755	1.862	3.623	<b>3.632</b>
3	1.785	1.846	3.662	<b>3.662</b>

However, since the values were almost similar for all the experiments, the setting of the dynamometer have re-confirmed. We found that the range of force was set on the control unit was not match with the setting in DynoWare software. Both setting should have similar range as per Figure 2 for Fx, Fy and Fz. This error might cause the values of average force that we obtained become inaccurate.

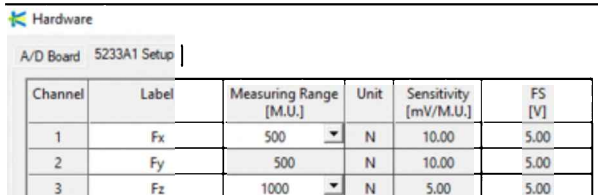


Figure 2 DynoWare interface for range of force.

#### 3.1 Experimental Result of Tool Wear

Image of tool wear was observed under SEM after the experiment. Figure 3 shows the comparison of drill bit before and after each of the experiment. From Figure 3, it can be observed the degradation of the cutting edge material after 400 of holes. In addition, the cutting-edge roundness (CER) diameter increase progressively with the number of drilled compare for all of the experimental runs. It indicated that the cutting edge progressively affected by adhesion wear due to the abrasiveness of the chips produced from the CFRP material [14].

However, accurate estimation of tool life can't be predicted since the tool orientation placed under the SEM need to be properly marked on the same location before and after the drilling process. As for future investigation, special purpose jig needs to be fabricated prior to experiment to ensure the tool orientation and angle are standardizing for accurate measurement.

### 5. CONCLUSION

In conclusions, it was found that the spindle speed has less significant impact on the thrust force. However, for future experimental work the spindle speed range can be further increase. Also, feed rate variation and its interaction with the spindle speed towards thrust force and tool wear are subject that worth to be studied.

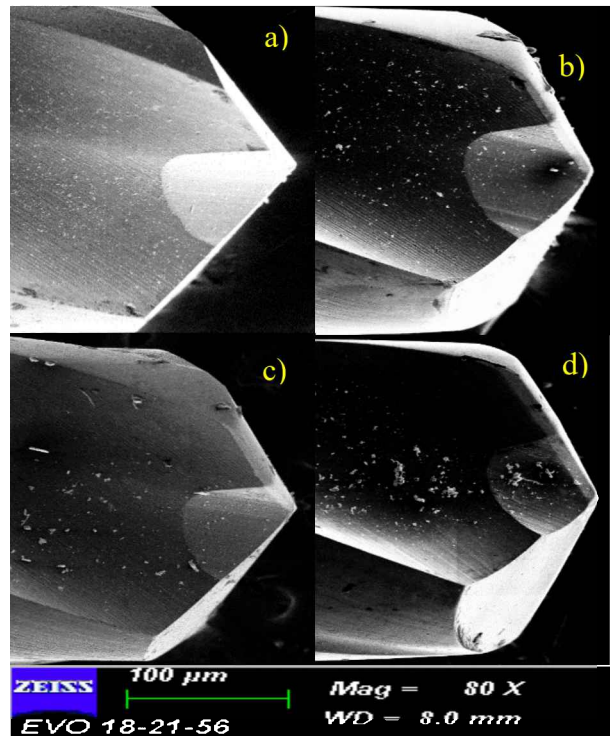


Figure 3 SEM tool image under (a) new tool, (b) Exp. 1, (c) Exp. 2 and (d) Exp. 3.

### ACKNOWLEDGEMENT

This work is partially supported by Universiti Teknikal Malaysia Melaka (UTeM) and the Malaysia Ministry of Higher Education for the financial funding under Grant No. FRGS/2018/FTKMP-AMC/F00387.

### REFERENCES

- [1] Jaafar, M. F., Salleh, M. S., Izamshah, R. Hassan, M. H., Sundi, S. A., Hafiz, M. S. A., & Kasim, M. S. (2019). Influence on thrust force and delamination for one shot drilling of carbon fibre reinforced plastic. *International Journal of Mechanical & Mechatronics Engineering*, 19(1), 43–56, 2019.
- [2] Voss, R., Henerichs, M., & Kuster, F. (2016). Comparison of conventional drilling and orbital drilling in machining carbon fibre reinforced plastics (CFRP). *CIRP Annals*, 65(1), 137-140.
- [3] Sauer, K., Dix, M., & Putz, M. (2018). Process Forces Analysis and a New Feed Control Strategy for Drilling of Unidirectional Carbon Fiber Reinforced Plastics (UD-CFRP). *Journal of Manufacturing and Materials Processing*, 2(3), 46.
- [4] Shunmugesh, K., & Panneerselvam, K. (2016). Optimization of Process Parameters in Micro-drilling of Carbon Fiber Reinforced Polymer (CFRP) Using Taguchi and Grey Relational

- Analysis. *Polymers and Polymer Composites*, 24(7), 499-506.
- [5] Faraz, A., Biermann, D., & Weinert, K. (2009). Cutting edge rounding: An innovative tool wear criterion in drilling CFRP composite laminates. *International Journal of Machine Tools and Manufacture*, 49(15), 1185-1196.
- [6] Su, F., Zheng, L., Sun, F., Wang, Z., Deng, Z., & Qiu, X. (2018). Novel drill bit based on the step-control scheme for reducing the CFRP delamination. *Journal of Materials Processing Technology*, 262, 157-167.
- [7] Tsao, C. C., & Chiu, Y. C. (2011). Evaluation of drilling parameters on thrust force in drilling carbon fiber reinforced plastic (CFRP) composite laminates using compound core-special drills. *International Journal of Machine Tools and Manufacture*, 51(9), 740-744.
- [8] Tsao, C. C., & Hocheng, H. (2003). The effect of chisel length and associated pilot hole on delamination when drilling composite materials. *International Journal of Machine Tools and Manufacture*, 43(11), 1087-1092.
- [9] Ho-Cheng, H., & Dharan, C. K. H. (1990). Delamination during drilling in composite laminates. *Journal of Engineering for Industry*, 112(3), 236-239.
- [10] Alhadeff, L. L., Marshall, M. B., Curtis, D. T., & Slatter, T. (2019). Protocol for tool wear measurement in micro-milling. *Wear*, 420, 54-67.
- [11] Hexcel Composites, S. A. (2010). HexPly® M21 product data sheet, publication FTA002e.
- [12] Hoffmann Group. (2018). Data Sheet for Solid carbide HPC micro-drill +0.004 0,9 mm.
- [13] Joshi, S., Rawat, K., & Balan, A. S. S. (2018). A novel approach to predict the delamination factor for dry and cryogenic drilling of CFRP. *Journal of Materials Processing Technology*, 262, 521-531.
- [14] Hassan, M. H., Abdullah J., Mahmud, A. S., & Supran, A. (2018). Effect of drill geometry and drilling parameters on the formation of adhesion layer in drilling compositemetal stack-up material. *Journal of Mechanical Engineering, SI* 5(2), 90-98.

# Thermal properties and structure morphology of SLSG/SBE: Effect of filler content

Zurina Shamsudin<sup>1,\*</sup>, Masturah Mesri<sup>1</sup>, Rafidah Hasan<sup>2</sup>, Jariah Mohamad Juoi<sup>1</sup>, Zaleha Mustafa<sup>1</sup>

<sup>1)</sup> Fakulti Kejuruteraan Pembuatan Universiti Teknikal Malaysia Melaka,

Hang Tuah Jaya, 76100 Durian Tunggal, Melaka, Malaysia

<sup>2)</sup> Fakulti Kejuruteraan Mekanikal, Universiti Teknikal Malaysia Melaka,

Hang Tuah Jaya, 76100 Durian Tunggal, Melaka, Malaysia

\*Corresponding e-mail: zurina.shamsudin@utem.edu.my

**Keywords:** Soda lime silicate glass; spent bleach earth; eggshell

**ABSTRACT** – The influence of different filler content on the properties of recycle glass composite was investigated. Samples prepared involved direct sintering process. This study is focused on thermal properties using thermogravimetric analysis (TGA) and microstructural analysis by using scanning electron microscopy (SEM). The results showed that high loading of filler content reduced percentage of weight loss of the samples. Microstructure analysis indicated that the present of pores in recycle glass composites was contributed by less amount of filler content.

## 1. INTRODUCTION

Waste materials from soda lime silicate glass (SLSG) and spent bleach earth (SBE) in the environment have high potential to become a critical factor to human, animals and vegetation when concentration of waste in excess [1]. Recycling is the best way to reduce waste disposal and convert into beneficial product [2]. Generally, waste glass has turned into glass-ceramic composite via conventional method which is heat treatment that involve two stages which are nucleation and crystallization [3]. Salleh et al (2018) worked on SLSG reinforced with SBE reported that crystallization without nucleation stage has shown improvement on densification which enhanced properties glass-ceramic composite [3]. However, the densification has a limit which depends on the percentage of base composition and the thermal properties. These properties played a role in controlling the final properties of the glass composite. In this study, natural waste from eggshell (ES) is introduced as filler in SLSG/SBE composite which similar with cockle shell that contains about 94wt% calcium carbonate ( $\text{CaCO}_3$ ) in its composition and has applied as filler in waste glass [4,5]. The use of ES in waste glass has not much been reported in literature. Thus, with estimated thermal properties and microstructure data, it is expected to identify some factors that lead to the development of SLSG/SBE/ ES composite. Structural morphology will be examined in order to relate the properties of composite with the effect of ES inclusion.

## 2. METHODOLOGY

Glass waste from soda lime silicate glass (SLSG) was collected from the household waste. The preparation of the glass waste undergoes crushing, planetary ball mill and sieving at 100 $\mu\text{m}$  and 40 $\mu\text{m}$ . ES were collected from

household kitchen and then crushed using planetary ball mill and sieve to fine powders (<40  $\mu\text{m}$ ). The raw SBE has undergone a cleaning process to extract oil using sonication process followed by filtration and dry in drying oven until the SBE was in powdery form. Particle size of SLSG, SBE and ES was determined using particle size analyzer, Mastersizer 2000 (Malvern Instrument Ltd model). The compositions shown in Table 1. All samples were produced using conventional ball milling and uniaxial pressing before sintering. The green bodies were proceeded to sintering treatments using laboratory electric furnace Carbolite 1300 model at 800°C at constant heating rate of 2°C /min and 1 hour holding time. Thermal properties were conducted using thermogravimetric analysis (TGA) (TA instrument Q50). Three types of raw materials weighed at 15mg and placed on aluminum pan then heated to 1000°C at 10°C /min. The microstructure of the glass waste composites observed using SEM EVO 50 at accelerated 15kV. Surfaces of the specimen were coated with a conductive platinum layer using Mini Sputter Coater (UK).

Table 1 Ratio of filler content in recycle glass composite

Sample code	SLSG (wt %)	SBE (wt %)	ES (wt %)
A	65	32	3
B	60	34	6
C	55	36	10

## 3. RESULTS AND DISCUSSION

TGA curve for SLSG, SBE and ES is presented in Figure 1. Upon heating the SLSG, SBE and ES powders to 1000°C at 10°C /min, the sample showed endothermic and exothermic peaks which represented as transition glass,  $T_g$ .  $T_g$  is the center of temperature range in which a noncrystalline solid changes from glass brittle to viscous. The value of glass transition was determined by referring derivatives weight curve.

The intersection between two points that showed endothermic slope represented  $T_g$ . The  $T_g$  of SLSG was determined approximately 514.27°C [3] while SBE is 680°C and ES is 432.48°C. Percentage of weight loss at  $T_g$  for SLSG is as much 0.0008613 mg (0.006485%), for SBE is 0.5184 mg (3.934%) and ES is 2.819 mg (20%). The weight loss indicates quantity in mass of the material burned at degradation temperature. The loss in weight is due to pyrolysis of the material upon the nature of the in

situ degradation reaction of the samples Figure 1 shows SBE contributed high percentage of weight loss compared to SLSG and ES. TGA curve shows that the residue is where the powders fully heated from 0°C until 1000°C has detected. Weight of SLSG that fully heated is 13.25 mg (99.73%), SBE is 9.125mg (69.25%) and ES is 10.39 mg (73.69%).

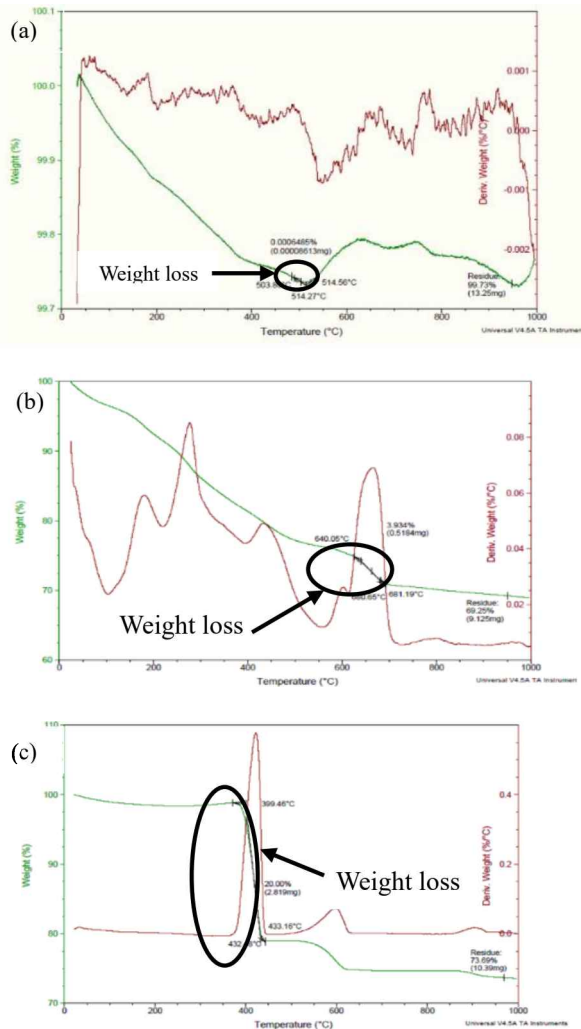


Figure 1 TGA curve for (a) SLSG, (b) SBE, (c) ES.

The TGA results with the microstructure observed in Figure 2. Generally, the increased in weight percent ratio of ES will reduce pores denoted in circular since ES is dominant and less degrade within the composite. As shown in Figure 2 (c), ES with 10wt% produces less pore as filler content increase and presumed to strengthen the microstructure by becoming dense and adhere to SLSG. Compared to 3wt% of ES sample, more closed pores were observed which may be attributed to imperfections in composite.

#### 4. CONCLUSION

Results in this study illustrate the amount of filler content effect to the thermal properties and microstructure of the materials. Recycle glass ceramic

has been sintered at 800°C at rate of 2°C/min and 1 hour holding time. The increased of filler content decreased the percentage of weight loss. SEM analysis showed the variation of microstructure because of the changes in filler content. Therefore, less filler content produced pores appeared to be closer and denser which reveal the filler content influence the composite.

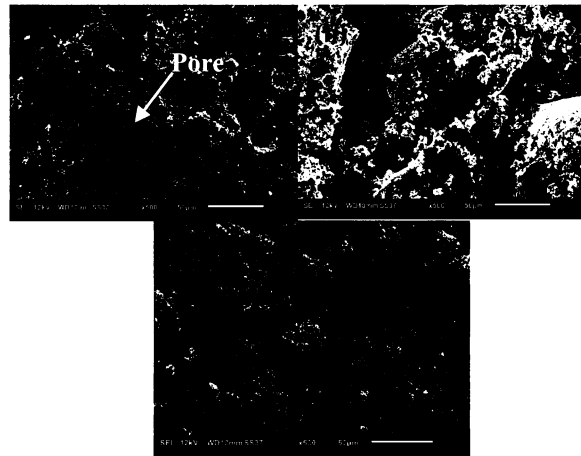


Figure 2 SEM analyses for (a) 3wt%, (b) 6wt%, (c) 10wt%.

#### ACKNOWLEDGEMENT

The authors would like to thank the financial support from Universiti Teknikal Malaysia Melaka through Grant FRGS/2018/FKP-AMC/F00380.

#### REFERENCES

- [1] Mohamed, M., Yusup, S., & Maitra, S. (2012). Decomposition study of calcium carbonate in cockle shell. *Journal of Engineering Science and Technology*, 7(1), 1-10.
- [2] Jia, S., Chen, K., & Chen, Z. (2018, February). Research on the Properties of the Waste Glass Concrete Composite Foundation. In *IOP Conference Series: Earth and Environmental Science* (Vol. 113, No. 1, p. 012098). IOP Publishing.
- [3] Salleh, N., Shamsudin, Z., & Mustafa, J. J. Z. (2017). Effects of heating rates and SBE loading on sintered properties of spent bleach earth/recycled glass composite. *Journal of Mechanical Engineering and Sciences*, 11(4), 3104-3115.
- [4] Souza, M. T., Maia, B. G., Teixeira, L. B., de Oliveira, K. G., Teixeira, A. H., & de Oliveira, A. P. N. (2017). Glass foams produced from glass bottles and eggshell wastes. *Process Safety and Environmental Protection*, 111, 60-64.
- [5] Shamsudin, Z., Razali, A. H., Suzaim, F. H., Mustafa, Z., Rahim, T. A., & Hodzic, A. (2018). Preliminary investigation on the physical properties and morphological of sintered cockle shell/recycled soda lime silicate composite. *Journal of Advanced Manufacturing Technology*, 12(1 (3)), 125-138.

# Design optimization of a new material for portable magnetic clamping plate for conventional milling process

N. Ab Wahab\*, Syafiq Abdul Latiff, Tuan Nur Anis Anisha Tuan Nunek, Hambali Boejang, N. Syuhada Nasir

Fakulti Teknologi Kejuruteraan Mekanikal dan Pembuatan, Universiti Teknikal Malaysia Melaka,  
Hang Tuah Jaya, 76100 Durian Tunggal, Melaka, Malaysia

\*Corresponding e-mail: norfariza@utem.edu.my

**Keywords:** Stainless steel 304; milling process; spindle speed

**ABSTRACT** – This research was carried out to study Design Optimization of a New Material for Portable Magnetic Clamping Plate for Conventional Milling Process. The purpose of this project to replace the type of plate material used on the MagCLAMP product from PVC to stainless steel 304. The three parameters are spindle speed, feed rate and time setting. Taguchi method is used in the experiment. This experiment failed because the MagCLAMP product was unable to function properly. However, analytics data for the time setting parameter has been recorded. This project has its own limit to hold some thin and small magnetic materials.

## 1. INTRODUCTION

The milling machine is the flexible conventional machine tools with extensive metal cutting capabilities. Milling includes various types of operations and machines, based on the scale from small individual parts to large and heavy grinding operations. Moreover, the importance of studying the clamping system in milling operations is evident when the time distribution in milling is studied: According to Sandvik Cormorant, up to 20% of the time is devoted to loading or unloading and setting of the pieces on the clamping system, an identical percentage that occupies the actual machining time [1].

In addition, today's machines have the capability to machine up to five axes, but most conventional clamping do not give access to all five faces of a part. These magnetic clamps usually use electromagnets or permanent magnets to hold materials or workpieces during machining [2].



Figure 1 Portable magnetic clamping (MagCLAMP).

## 2. METHODOLOGY

The method is used to achieve the objective of the project that will accomplish a perfect result. Design optimization of portable magnetic clamping includes problem statement, material selection, improvement design for portable magnetic plate, comparisons between existing plate and optimization plate, and quotation of optimization plate.

The selection of plate material was carried out after doing some research. The type of material used as a plate for the MagCLAMP product is stainless steel 304. Stainless steel 304 is an austenitic steel type having at least 18% chromium and 8% nickel is combined with a carbon maximum of 0.08% [3].

Table 1 Physical properties of stainless steel 304.

Type of material	Percentage
Chromium	18%
Nickel	8%
carbon	0.08% Max

Table 2 The comparison between existing and optimization of the MagCLAMP plate.

Contains	Existing	Optimization
Material	PVC plate	Stainless steel 304
Cost	Cheaper	Less cheap
Durability	Required to change	Long lasting
Mass	Minimize the mass	Maximize the mass to product
Machining process	Water jet	Laser cut

Table 3 Bill of material of plate (BOM).

No .	Part Name	Expectation size (mm)	Types of material	Price	Data
1	MagCLAMP plate	(200 x 200 x 2) mm	Stainless steel 304	60.00	1

In laser cutting, the raw material stainless steel 304 must be cut in the diameter 154 mm. Flatness test had been carried out to inspect the change or variation on the part's surface. Soft material has a better rigidity of the flexible clamping compared to hard material such as aluminium [4]. Before laser cutting, machining process is run, the programming about the drawing of plate needs to be complete in the main computer system. The thickness of the stainless steel 304 is 2 mm Figure 2 shows the dimension of PVC plate produce from the

machining of water jet.

The machining parameters used are Depth of cut (DC), Spindle speed (N), and Feed rate (f). The effect of machining parameters on surface roughness is evaluated and the optimum cutting condition for minimizing the surface roughness is determined. The predicted values are confirmed by using validation experiments. A L9 orthogonal array, Taguchi method and analysis of variance (ANOVA) are used to formulate the experimental layout, to predict the optimal choice for Portable Mag Clamp by analyzing the effect of each parameter for milling machining characteristics.

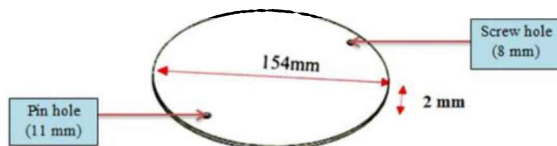


Figure 2 The dimension of PVC plate.

### 3. RESULTS AND DISCUSSION

Through machining parameter testing, all information can be discussed whether the expected results will meet the stated objectives or there are any problems that cause the study cannot be continued as expected. As a result, the facing process as shown in figure 3 to be carried out on the specimen cannot be continued as the specimen moves when it is subjected to a cutting tool milling machine.



Figure 3 Facing process on the mild steel specimen.

Different ways have been done to restore magnetic force, but the all things did not give a good result, until the idea of converting the original plate type had been done. However, the conversion to the PVC plate does not imply that the magnetic force is strong again. Specimens are still moving when applied cutting tools with lower spindle speed 410 rpm. Further experiments to obtain sample specimen machining cannot be carried out. In other words, the objective of the project to obtain data analysis using the Taguchi method is failed.

On averages the value of conventional vice milling shown in Figure 12 is 55.0 Sec, while the value for portable magnetic clamping is 7.9 Sec. The difference the

installation of portable magnetic clamping on the milling machine was more efficient and faster than the existing clamping. Apart from fast installation, the ability to use it to handle machining work can be done quickly

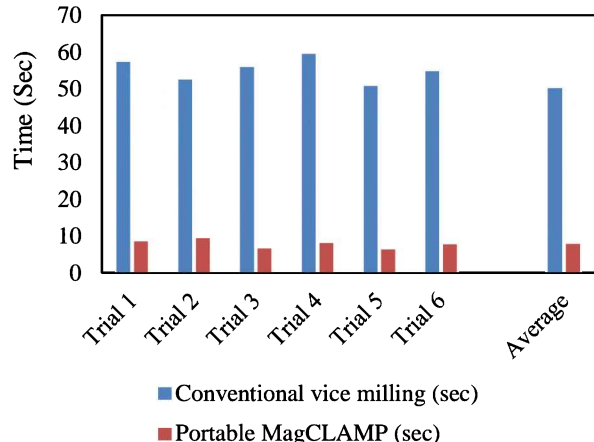


Figure 4 Comparison chart between two types of clamps.

### 4. CONCLUSION

In conclusion, this plate change was successfully implemented and achieved the first objective of the thesis. However, the study to obtain the analysis data through the Taguchi method was unsuccessful. This is due to the problem with the portable magnetic clamping product itself. The portable MagCLAMP product is unable to function properly due to its weak magnetic attraction. The specimens used in the study move from their original state when machining process was carried out. Other than that, the study to compare the speed of installation of two clamping, conventional vice milling, and portable magnetic clamping was successfully performed. The result of time setting parameter was tabulated in the table.

### REFERENCES

- [1] Cantano, J., Alonso, J. M., Peláez, G., Gago, I., Ulloa, A. F., & Ares, J. E. (2015). Magnetic chuck failure prediction: towards the use of non-conventional clamping in milling operations. *Procedia engineering*, 132, 419-426.
- [2] Felix, A., & Melkote, S. N. (1999). Effect of workpiece flatness and surface finish on the holding force of a magnetic chuck. *Journal of manufacturing science and engineering*, 121(4), 811-814.
- [3] Michler, T. (2016). Austenitic Stainless Steels. Reference Module in Materials Science and Materials Engineering. doi:10.1016/b978-0-12-803581-8.02509-1
- [4] Ab Wahab, N., Rani, M. H. B. A., bin Nordin, A. K., bin Nordin, N. F., bin Ibrahim, M. A., Basar, M. F., & Boejang, H. B. (2018). Design and Development of Fixable Clamping for Milling Machine Based on Machining Performance. *International Journal of Applied Engineering Research*, 13(1), 576-581.

# Design improvement of fixable clamping jig for milling machine based on surface roughness

N. Ab Wahab\*, Azizi Arif Bin Onn, M. Nabil Nordin, Abd Khahar Nordin, N. Syuhada Nasir

Fakulti Teknologi Kejuruteraan Mekanikal dan Pembuatan, Universiti Teknikal Malaysia Melaka,  
Hang Tuah Jaya, 76100 Durian Tunggal, Melaka, Malaysia

\*Corresponding e-mail: norfariza@utem.edu.my

**Keywords:** Fixable clamping; jig; surface roughness

**ABSTRACT** – Jigs provide a means of manufacturing interchangeable parts since they establish a relation with predetermined tolerances between the work and the cutting tool. Objective of this project is to optimize and analyze of the fixable clamping jig for milling machine. The method is modified clamp mechanism from previous jig, optimize the design, and analyze the result in term of surface roughness. From the result, the average of Ra value using current vise is 3.468 and fixable clamping is 1.657. Delrin is used as a workpiece. While for aluminum, the average of Ra value using current vise is 3.069, and fixable clamping is 5.908.

## 1. INTRODUCTION

Mass production of workpiece is based on the concept of interchangeability according to which every part produced within an established tolerance. Once the jig is properly set up, any number of duplicate parts may be readily produced without additional set up. This reduces operation time and increase productivity.

The fixture designing and developed is well-thought-out as complex process that demands the understanding of dissimilar areas, such as geometry, tolerances, dimensions, procedures and manufacturing processes. All outcomes and conclusions gained from the literature review and the interaction with fixture designers are used as guide to design the current research work [1]. While, the operations that often used by a manufacturer in a milling machine is face milling, end milling, slotting, thread milling, plain milling and side milling, etc. [2]. Most of the industry are use the milling machine to produce the die, aerospace, automotive and machinery design.

The problem that have at previous jig show that the angle of the clamping has some error which is lifted up 4-degree error of clamp. Degree error is one of the most critical part in machining operation. The clamped product will be vibrating during machining process because the clamping does not clamp a product well. This problem can affect the result for the of the clamped product and quality of the product will be reduce. The quality of a product can be measure from a surface roughness testing. The lower the Ra value will increase the quality of product. Second problem from the previous jig is the thickness of the base jig. The base of the jig is too thick which is 50 mm. When the thickness is high the weight of the jig will be increase, so to reduce the weight, the thickness will be reduce to 35 mm. Next, a sketch of the improvement product is drawn to solve the problem statement. The sketch is redrawing by using Solidwork software.

The clamping of this machine also has its own

weakness which is only limited surface of the workpiece can be cut in one clamp. This can increase the time setup of the clamping during machining process. Hence, this flexible clamping was developed and the objectives are:

- To modified clamp mechanism of the previous jig.
- To optimize the design of the fixable clamping jig for milling machine.
- To analyze the result of fixable clamping jig in term of force.

## 2. RESEARCH METHODOLOGY

### 2.1 Optimization of Design

In this stage, the problem that have at previous jig show that the angle of the clamping has some error which is lifted up 4-degree error of clamp for this problem, the clamp mechanism will be change from the previous jig. Next, a sketch of the product is drawn to solve the problem statement. Then, the sketch is redrawing by using Solidwork software. Figure 1 shows the final expected product to be process.

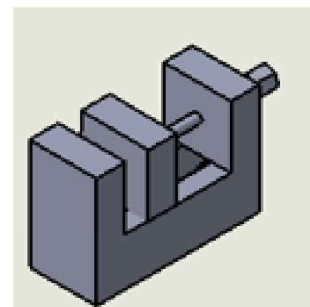


Figure 1 New design clamping vice using Solidwork.

Second problem from the previous jig is the thickness of the base jig. The base of the jig is too thick which is 50 mm. When the thickness is high the weight of the jig will be increase, so to reduce the weight, the thickness will be reduce to 35 mm. Next, a sketch of the improvement product is drawn to solve the problem statement. The sketch is redrawing by using Solidwork software.

### 2.2 Optimization of the Result

The result will be evaluated base on the surface roughness of the material that use the jig. The dry cutting condition is used for this project because it is a milling process where as the liquid is not used during the machining process. The cutting parameters that will be set is cutting speed, depth of cut and feed rate.

### 2.3 Analyze of the Result

To analyze the result, the experiment will be done by using Portable Surface Roughness Tester, SJ-401. There are two types of material used in this testing which is aluminium and Delrin. The result for surface roughness will analyze using statistical method which is take arithmetic mean surface roughness.

## 3. RESULTS AND DISCUSSION

### 3.1 Optimization Product and Process

In base part, the changes are in its shape and use one material to make this base as shown in Figure 2 below. It is because the base part in the previous clamping is use two part. So, the usage of the material is higher and the cost also increase. Process for making the previous base is too many and time to make it is long and increase cost. However, the size of this this base is has been rescale from 170mm high and 198mm wide to 170mm high and 150mm wide.

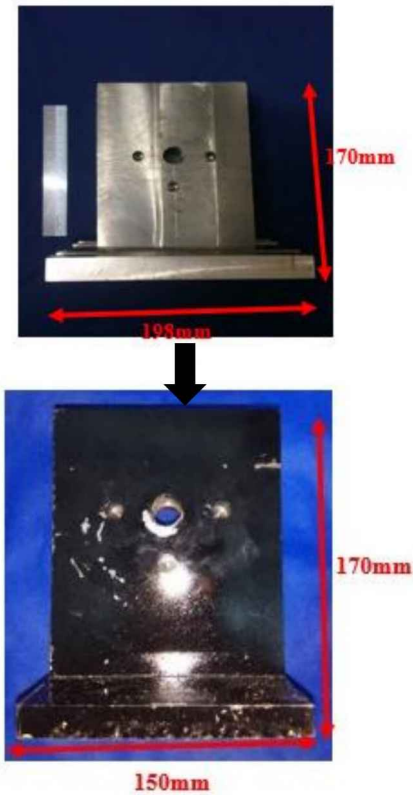


Figure 2 Improvement of base part.

All the part in clamping vise are using conventional milling machine. The process that have been use are squaring, slotting and pocketing. The part in the clamping vise that have been changing and making improvement are clamp jaw and beam of the vise.

For the beam of the vise have improve from previous beam by go through slotting process to make the clamping vise can attach with the beam of the vise.

After the clamping part was assembled, clamping part and base had assembled each other by inserting the pin and nut at the clamping part into the base part. Next, the rod at the base part was move into the clamping part until both assembled parts was tightened.

During the process making the product, that have some problem occur and the change of the design and the

diameter of the part. The part that have go through improvement from the planning before is clamp vise and add nut at the rod. The nut was put at the rod for lock the rotation on any degree. This solution occurs for the problem for miscalculate for the drill D10 to D11at 3 point. When nut not be added at the rod, the vice will be vibrated and effect the surface finish of the work piece because the gap between lock pin and pin hole. Lock add with the rod to lock the rotation can be refer in Figure 16.

The other problem that have been face in the product after do the machining by doing tapping process is the thread of the screw not reaching area in the end of the hole. This finding was unexpected and the problem cause for human error and parallax error because during tapping process the hand not perpendicular to the surface of the base. So, the clamping vice not parallel to the base and cause surface machining have different depth but this problem can be overcome by doing squaring by using this jig.

For initial planning, that the two-analysis process for analyze the product which are product force by using dynamometer and surface roughness. But the analysis process that have been done is surface roughness only. This problem occurs because of the limited time for produce the product.

### 3.2 Surface Roughness Testing

Table 1 shown that the average of Ra value using current vise as a clamping method is higher than using fixable clamping as a clamping method which are 3.468 when using current vise and 1.657 when using fixable clamping. This proves that fixable clamping can be used as a clamping method due to its surface finish is better than using current vise.

Table 1 Comparison of Ra value for Delrin as a workpiece.

Reading	Ra value using current vise	Ra value using fixable clamping
1	3.134	2.174
2	3.728	1.793
3	3.093	1.530
4	3.434	1.592
5	3.544	1.745
6	3.912	1.656
7	3.428	1.112
Average	<b>3.468</b>	<b>1.657</b>

Table 2 Comparison of Ra value for Aluminum as a work piece.

Reading	Ra value using current vise	Ra value using fixable clamping
1	3.227	6.317
2	1.655	4.216
3	3.319	5.703
4	2.875	5.961
5	2.866	7.374
6	4.815	5.959
7	2.724	5.829
Average	<b>3.069</b>	<b>5.908</b>

Table 2 shown that the average of Ra value using current vise as a clamping method is lower than using fixable clamping as a clamping method using current vise is 3.069 compared to using flexible clamping is 5.908. This proves that the surface finish when using current vise is better than using fixable clamping as a clamping method.

#### 4. CONCLUSION

For a conclusion, this project was developed to optimize and overcome the problem occur for the previous fixable clamping and using current vise at milling machine. From the result above, it proves that the fixable clamping can solve a degree error and increase a quality of a product clamped. It is because a fixable clamping clamps a workpiece much better compare to the current vise. This fixable clamping is able to rotate 90 degree for both sides. So, all surfaces of the work piece can be cut in one single clamp. As all the three of the objectives was accomplished, the outcomes demonstrated that Ra value by using fixable clamping is lower than current vice clamp when the work piece is Delrin. While, when the work piece is aluminium, the Ra value for current vice clamp is lower than fixable clamping. This demonstrates the unbending nature of fixable isn't useful for hard material contrasted with delicate material, for example, Delrin.

#### ACKNOWLEDGEMENT

This work was partially supported by Universiti Teknikal Malaysia Melaka (UTeM) and the Malaysia Ministry of Higher Education for the financial funding under Grant No. FRGS/2018/FTKMP-AMC/F00387.

#### REFERENCES

- [1] Rezanja, V. H. R. N. S., Kvaliteto, I., & Prevleke, R. O. B. (2014). The effect of the cutting speed on the cutting forces and surface finish when milling chromium 210 Cr12 steel hardfacings with uncoated cutting tools. *Materiali in tehnologije*, 48(3), 373-378.
- [2] Vukelic, D., Tadic, B., Miljanic, D., Budak, I., Todorovic, P. M., Randjelovic, S., & Jeremic, B. M. (2012). Novel workpiece clamping method for increased machining performance. *Tehnički vjesnik*, 19(4), 837-846.
- [3] Ab Wahab, N. B., Rani, M. A., Nordin, A. K., Tamin, N. F., & Onn, A. A. (2017). Development of fixable rotation clamping method for milling machine. *Proceedings of Mechanical Engineering Research Day 2017*, 2017, 109-110.
- [4] Ab Wahab, N., Rani, M. H. B. A., bin Nordin, A. K., bin Nordin, N. F., bin Ibrahim, M. A., Basar, M. F., & Boejang, H. B. (2018). Design and Development of Fixable Clamping for Milling Machine Based on Machining Performance. *International Journal of Applied Engineering Research*, 13(1), 576-581.

# Investigations on macro-drilling by indigenously developed ECM apparatus

Sunil Pathak, Siti Nadiah Mohd Saffe\*, Irshad Ahamad Khilji

Fakulti Teknologi Kejuruteraan, Universiti Malaysia Pahang, Lebuhraya Tun Razak, 25000 Pahang, Malaysia

\*Corresponding e-mail: sitinadiah@ump.edu.my

**Keywords:** Macro-drilling; ECM; non-conventional machining

**ABSTRACT** - New materials such as hastalloy, nitrallloy, nimonicies, carbides etc., are difficult to be machined and find applications in aircrafts, nuclear reactors, turbines, Special cutting tools etc. Although most of the new machining processes have been developed specifically for newer materials that are difficult to be machined, some of these processes were used in the production of complex shapes and cavities. The present work is focused on development of Electrochemical Machining (ECM) and its testing for macro-drilling application. The apparatus has been indigenously developed and study of few of the most important parameters of ECM has been done on material removal rate.

## 1. INTRODUCTION

Electrochemical machining (ECM) works on the Faraday's laws governed electrolysis phenomenon in a container called as electrochemical cell which consists of two electrodes (i.e., anode connected to positive terminal of direct current (DC) supply and cathode connected to negative terminal of DC supply) separated by each other by an appropriate inter electrode gap (IEG) and submerged in a suitable electrolyte solution enabling the electrochemical reactions to occur. Some cells have a diaphragm or membrane between the anode and cathode which separates reaction products at anode and cathode [1-2].

Being a non-contact process ECM has a unique feature of machining of difficult to machine materials. Both of the tool and work piece must be electrically conductive materials for electrochemical machining process to work. During an electrolysis process, ECM is also based on a controlled anodic electrochemical dissolution process of the work piece with the tool in an electrolytic cell. The materials get removed (dissolved) from the work piece based on the Faraday's law of electrolysis [3-8].

In the present work an indigenous apparatus of ECM has been developed for macro drilling operation. Total seven experiments using five most important parameters of ECM namely inter electrode gap (IEG), applied voltage, electrolyte concentration, electrolyte temperature and flow rate has been done to test the developed apparatus for the considered response i.e. material removal rate.

## 2. METHODOLOGY

Figure 1(a) shows a photograph of the developed machining chamber arrangements and Figure 1(b) depicts the full photograph of the developed ECM apparatus. Copper has been selected as workpiece and

toll materials due to their higher electrical conductivity and easily availability. Copper sulphate ( $\text{CuSO}_4$ ) has been chosen as electrolyte due to its stability over wide range of PH value and compatibility with the selected workpiece material.

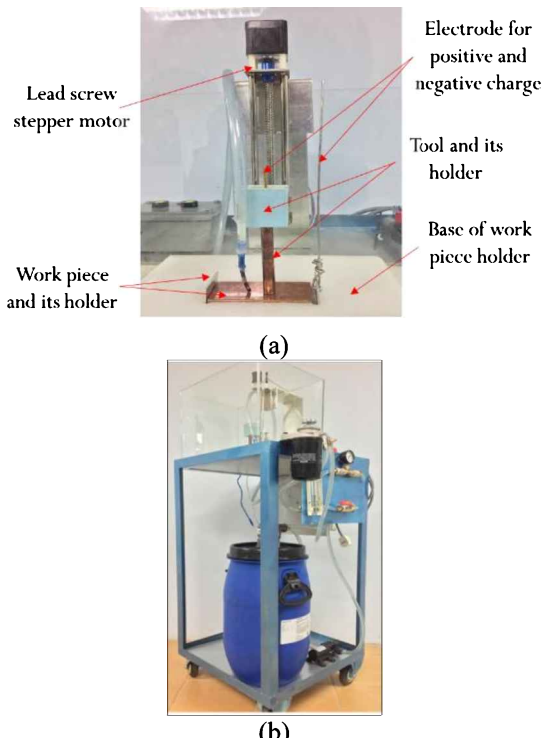


Figure 1 Photograph of (a) machining chamber; (b) ECM apparatus.

## 3. RESULTS AND DISCUSSION

Experimental runs are taken on ECM setup by varying machining parameters and by keeping IEG constant as shown in Table 1. To measure the result of the experiments, the device is used for material removal rate (MRR) measurement. Measurement of MRR is started by comparing the weight of work piece before and after the machining. Based on the results, all experiment did not produce a hole and not a hole-through on the work piece. The results after machining on copper plate are shown in Figure 2. Moreover, the experiment no.7 has the highest MRR amongst seven experiments, followed by experiment no. 5, no.6, no.3, no.2, no.1 and no.4. It is clear that among these seven experiments, only experiment no.7 that has better result of not a hole-through the material as in Figure 5(g). The result of MRR is shown in Table 2. A comparison between the numbers of experiment in a graphical form is shown in Figure 3.

From that achievement, it needs longer machining time to produce a hole through the work piece. As the machining time is only 2400 seconds, so that it needs around 4800 seconds to produce a hole through 6 mm thickness of copper with the diameter of tool is 12 mm. As mention that the diameter of the tool is 12 mm, the machining process will make the machining time longer than usually and required a high voltage.

Table 1 Experimental combination of machining parameters.

Exp	IEG (mm)	Concentration (%)	Flow rate (lpm)	Voltage (V)	Temperature (°C)
1	0.5	50	2.5	3	24
2	0.5	100	2.5	20	24
3	0.5	100	3.0	30	30
4	0.5	100	3.0	2	30
5	0.5	100	3.0	20	24
6	0.5	100	3.5	30	30
7	0.5	100	3.5	40	40

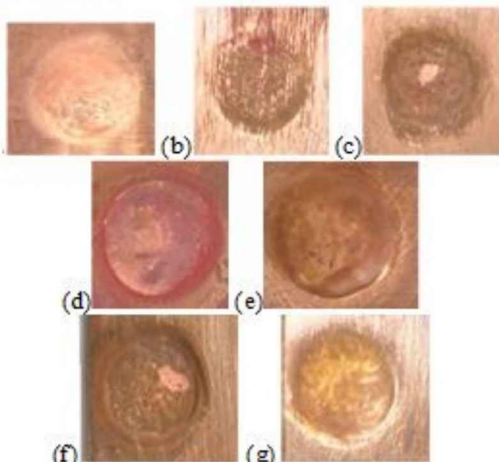


Figure 2 Result on work pieces for each experiment.

Table 2 Experimental results.

Exp.	Machining time (s)	Weight (g)			MRR ( $\times 10^{-4}$ g/s)
		$m_i$	$m_f$	$\Delta m$	
1	3000	231.102	231.084	0.018	0.06
2	900	232.430	232.062	0.368	4.09
3	3600	232.062	230.101	1.961	5.45
4	3720	230.101	230.090	0.011	0.03
5	2700	231.091	229.297	1.794	6.64
6	3600	229.297	226.998	2.299	6.39
7	2400	230.085	227.311	2.774	11.56

#### 4. CONCLUSION

As the conclusion, a fully operational electrochemical machining machine was designed and developed. Several experimental studies are successfully conducted on the developed ECM setup. The experiments are completed on 6 mm thickness of copper plate. The maximum MRR produced is  $11.56 \times 10^{-4}$  g/s when the parameters set as voltage 40 V, IEG 0.5 mm and electrolyte pressure 3.5 LPM. The MRR is increased as the voltage increases. The minimum MRR ( $0.03 \times 10^{-4}$  g/s) is produced when the parameters set as voltage 2 V, IEG 0.5 mm and electrolyte flow rate 3.0 LPM.

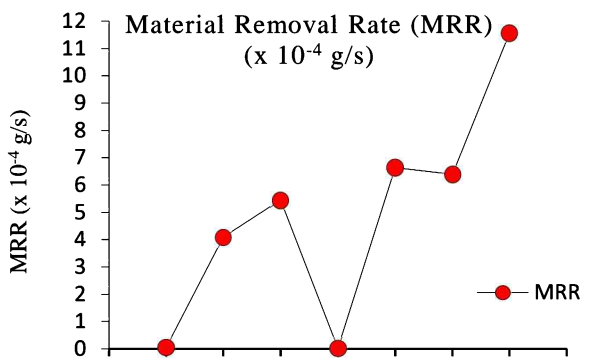


Figure 3 Comparison of MRR.

#### ACKNOWLEDGEMENT

Authors acknowledge the financial support provided by Research & Innovation Department under, Universiti Malaysia Pahang under Grant No. RDU180303.

#### REFERENCES

- [1] Pathak, S., Jain, N. K., & Palani, I. A. (2016). Investigations on surface quality, surface integrity and specific energy consumption in finishing of straight bevel gears by PECH process. *The International Journal of Advanced Manufacturing Technology*, 85(9-12), 2207-2222.
- [2] Pathak, S., Jain, N. K., & Palani, I. A. (2016). Effect of honing gear hardness on microgeometry and surface quality improvement of straight bevel gears in PECH process. *The International Journal of Advanced Manufacturing Technology*, 85(9-12), 2197-2205.
- [3] Pathak, S., & Jain, N. K. (2017). Critical review of electrochemical honing (ECH): sustainable and alternative gear finishing process. Part 1: conventional processes and introduction to ECH. *Transactions of the IMF*, 95(3), 147-157.
- [4] Pathak, S., & Jain, N. K. (2018). Performance of pulsed-electrochemical honing and pulsed-electrochemical finishing in improving quality of bevel gears. *Manufacturing Review*, 5(14), 1-9.
- [5] Jain, N. K., Pathak, S., & Alam, M. (2018). Synthesis of Copper Nanoparticles by Pulsed Electrochemical Dissolution Process. *Industrial & Engineering Chemistry Research*, 58(2), 602-608.
- [6] Rajurkar, K. P., Zhu, D., McGeough, J. A., Kozak, J., & De Silva, A. (1999). New developments in electro-chemical machining. *CIRP Annals*, 48(2), 567-579.
- [7] Kurita, T., Chikamori, K., Kubota, S., & Hattori, M. (2006). A study of three-dimensional shape machining with an ECμM system. *International Journal of Machine Tools and Manufacture*, 46(12-13), 1311-1318.
- [8] Stofesky, D. B. (2006, January). Manufacturing with microECM. In *ASME 2006 International Manufacturing Science and Engineering Conference* (pp. 1025-1031).

# Morphological changes of porous NiTi dental screw implant by metal injection moulding (MIM)

Mashitah Maso'od<sup>1,2</sup>, Muhammad Hussain Ismail<sup>1,2,\*</sup>, Muhammad Asif Ahmad Khushaini<sup>3</sup>, Mohd Zul Iman Mohd Yusuf<sup>3</sup>, Rohana Ahmad<sup>4</sup>

<sup>1)</sup> Faculty of Mechanical Engineering, Universiti Teknologi MARA, 40450, Shah Alam, Selangor, Malaysia

<sup>2)</sup> Industrial Metallurgy Research Group (IMReG), Universiti Teknologi MARA, 40450, Shah Alam, Selangor, Malaysia

<sup>3)</sup> Nitium Technology Sdn Bhd, B-1-16, Vista Alam, Jalan Ikhtisas 14/1,

Seksyen 14, 40000, Shah Alam, Selangor, Malaysia

<sup>4)</sup> Faculty of Dentistry, Universiti Teknologi MARA, 47000, Sungai Buloh, Selangor, Malaysia

\*Corresponding e-mail: hussain305@salam.uitm.edu.my

**Keywords:** Porous NiTi; metal injection moulding; scanning electron microscopy

**ABSTRACT** – In the present work, porous NiTi dental screw was successfully fabricated by Metal Injection moulding (MIM), starting with elemental Ni and Ti powders. Morphological changes at every processing stage were investigated and evaluated in order to understand the formation of porous structure. The porous structure developed helps in reducing the problem of ‘stress shielding affects’ between natural bones and dense metallic implant. NiTi is expected to improve the osseointegration process between living tissues and implant accompanied by its great biocompatibility as well as excellent mechanical properties.

## 1. INTRODUCTION

One of the main issues of existing dense biomedical implant is the mismatch between implant and human bone. In order to reduce the mismatch, extensive research have been done widely in creating porous structure in metals, thus reducing the stiffness values. Daudt et al. [1] stated that titanium (Ti) is preferable as bone implant due to its great integration between chemical resistance, mechanical behaviours and biocompatibility. NiTi SMA is one of the promising Ti alloy used in biomedical owing to its two unique properties of pseudoelasticity (PE) and shape memory effect (SME). Li et al. [2] stated that porous NiTi was successfully implemented in medical field as implant for orthopaedics, traumatology and others plus as cryogenous applicator in Russia. Furthermore, it is also excellent in biocompatibility and resistance to corrosion. Many studies related to biological completion using porous NiTi showed that the material displayed biocompatibility behaviour in terms of in vitro and in vivo as discussed in the previous study [3].

In almost all methods carried out on porous metals, powder metallurgy (PM) is the most promising in creating porous structure owing to the nature of the process which starting with metal powders. According to German [4], there are three main reasons in utilizing metal powders including; 1) economical production of complex shape, 2) fabricating unique alloy & microstructure and lastly, 3) ability to process special materials. The current study is referring to continuation work by Ismail et al. [5], mainly focusing on producing the intricate final product of screw-shaped implant.

## 2. METHODOLOGY

In this research, spherical-shaped elemental powders of Nickel and Titanium with particle sizes of 20 $\mu$ m and 22 $\mu$ m, respectively were used. Metal Injection Moulding (MIM) composed of four main process; mixing, injection, debinding and sintering. Prior to preparation of feedstock, both elemental powders were mixed manually in glovebox followed by speed mixer. The binder system consisted of water soluble system, mainly consist of PEG was used as previously researched [6]. The as-mixed powders and binders were blended/mixed using Dual-Assymmetric Centrifuge (DAC) speed mixer at different speeds ranging from 800 rpm to 1400 rpm. Then, the powder-binder composition was injected into screw implant mold shaped as schematically shown in Figure 1.

Prior to sintering, the samples underwent water leaching process in warm water followed by drying in an oven to remove excess water. Using high vacuum furnace, the as-leached samples were sintered at temperatures of 1150°C. Using Scanning Electron Microscopy (SEM), each morphology of NiTi feedstock, as-leached and as-sintered samples were recorded to analyse the changes after each process and observe the formation of porous structure of NiTi.

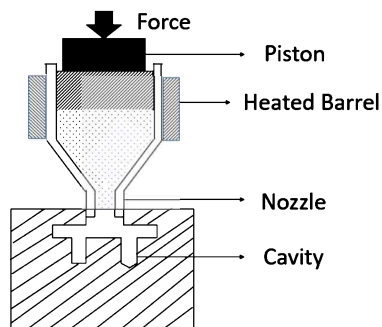


Figure 1 Schematic illustration of injection moulding.

## 3. RESULTS AND DISCUSSION

The morphological changes of each sample at different processing stages can be referred in the SEM images as shown. Figure 2 (a) clearly shows the NiTi feedstock where elemental powders of Ni and Ti is mixed with the water-soluble binder. The formation of pores

started to establish during the PEG removal during water leaching/debinding process as shown in Figure 2 (b). The binders were completely extracted throughout sintering phase forming smaller sizes of pores with interconnected struts. Binder system act as the space holder phase as it filled the gap areas between the as-mixed NiTi powders arrangement. Through water leaching and sintering process, the elimination of PEG and PMMA had created open porosity approximately with the loss of binder composition as previous discussed [5]. Ismail et. al. [6] stated that the transient liquid phase followed by Kirkendall diffusion helps created high level of porosity during sintering process.

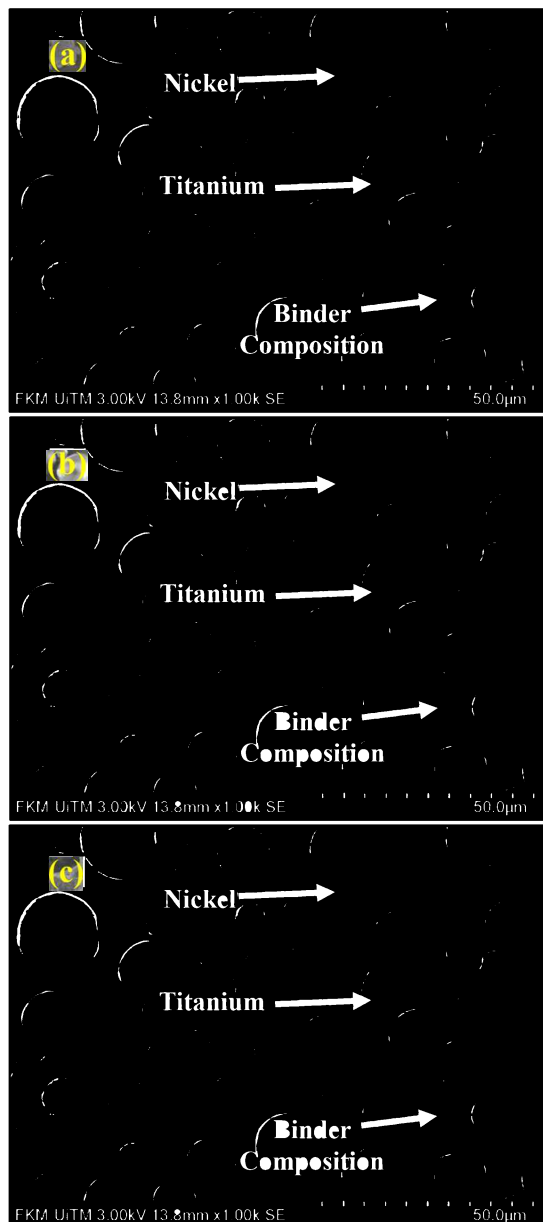


Figure 2 (a) NiTi feedstock; (b) as-leached NiTi and (c) as-sintered NiTi.

### 3. CONCLUSION

The fabrication of porous NiTi dental screw implant was successfully fabricated using Metal Injection Moulding (MIM). The formation of porous structure is co-related to each processing phase mainly through the removal of water-soluble binder system that act as the space holder connecting the spaces between the Ni and Ti powders. During sintering, pore structure was formed originated from transient liquid phase and Kirkendall effect.

### ACKNOWLEDGEMENT

We thank our collaboration partners, Nitium Technology Sdn Bhd and Dr Rohana Ahmad from Faculty of Dentistry, UiTM Sungai Buloh for their great teamwork in developing porous NiTi dental screw. Authors would also like to thank Universiti Teknologi MARA (UiTM) for the awarded internal grants including; *Geran Inisiatif Penyeliaan (GIP)*: 600-IRMI/MYRA 5/3/GIP (059/2017) and *Research Entity Initiative (REI)*: 600-IRMI/DANA 5/3/REI (12/2017) for supporting the research of this project.

### REFERENCES

- [1] de Freitas Daudt, N., Bram, M., Barbosa, A. P. C., Laptev, A. M., & Alves Jr, C. (2017). Manufacturing of highly porous titanium by metal injection molding in combination with plasma treatment. *Journal of Materials Processing Technology*, 239, 202-209.
- [2] Li, Y. H., Rong, L. J., & Li, Y. Y. (2002). Compressive property of porous NiTi alloy synthesized by combustion synthesis. *Journal of Alloys and Compounds*, 345(1-2), 271-274.
- [3] Bansiddhi, A., Sargeant, T. D., Stupp, S. I., & Dunand, D. C. (2008). Porous NiTi for bone implants: a review. *Acta biomaterialia*, 4(4), 773-782.
- [4] German, R. M. (2005). *Powder metallurgy and particulate materials processing: the processes, materials, products, properties, and applications* (pp. 231-232). Princeton: Metal powder industries federation.
- [5] Ismail, M. H., Goodall, R., Davies, H. A., & Todd, I. (2012). Porous NiTi alloy by metal injection moulding/sintering of elemental powders: Effect of sintering temperature. *Materials Letters*, 70, 142-145.
- [6] Ismail, M. H., Goodall, R., Davies, H. A., & Todd, I. (2012). Formation of microporous NiTi by transient liquid phase sintering of elemental powders. *Materials Science and Engineering: C*, 32(6), 1480-1485.

# The optimization of welding parameter for AISI 1020 using robot welding

Mohd Hairizal Osman\*, Mohammad Khalid Wahid, Mohd Nazri Ahmad, Nurul Ain Maidin, Mohd Hidayat Ab Rahman

Fakulti Teknologi Kejuruteraan Mekanikal dan Pembuatan, Universiti Teknikal Malaysia Melaka,  
Hang Tuah Jaya, 76100 Durian Tunggal, Melaka, Malaysia

\*Corresponding e-mail: hairizal@utem.edu.my

**Keywords:** Robot welding; MIG welding; optimization

**ABSTRACT** –This paper presents the The optimization of welding parameter for AISI 1020 using robot welding with a thickness of 6mm was selected in this experiment. The specimens welded with MIG robot welding used 1.0mm electrode wire. Three welding parameters such as welding speed, Voltage, and welding pattern each at three levels were considered. An L9 Orthagonal Array and signal-to-noise (S/N) ratio were employed to analyse the significant and percentage of each parameter for maximum tensile strength. The results revealed that the welding pattern gave significant main effects on the highest percentage distribution 61%. Further, the results indicated that the combination of optimum parameter recorded as welding speed 5.5 mm/min, 22V for Voltage and straight pattern travel capable to offer high tensile strength.

## 1. INTRODUCTION

MIG Welding is also recognized by gas metal arc welding. In the 1920s, the basic concept of GMAW was introduced but it was not commercially available until 1948. Primarily it was considered to be fundamentally, a high current density, small diameter, bare metal electrode process using an inert gas for arc shielding. The application of this process was for welding aluminium and as a result, the term MIG (Metal Inert Gas) welding was used and till now a day. Subsequent process developments included operation at low-current densities and pulsed direct current, application to a broader range of materials and the use of reactive gases (particularly CO<sub>2</sub>) and gas mixtures [1-4].

## 2. METHODOLOGY

The most popular material in welding industries is AISI 1020 because it can be welded by performing the most common welding processes. In the cold drawn or turned and polished condition and it has better weldability. Table 1 shows the chemical composition of AISI 1020 low carbon steel used in these experiments. The experiments were carried out on ABB MIG Robot Welding as shown in figure 1. AISI 1020 low carbon steel was selected as workpiece which was prepared at 140 mm length X 130mm width X 6mm thickness size. The input of parametric values is generated using Minitab software and programming into a robotic welding machine. Figure 2 shows a specimen of AISI 1020 low carbon steel after the welding process.

Table 1 Chemical Composition of AISI 1020.

Carbon	Iron	Manganese	Phosphorous	Sulfur
0.23	99.3	0.06	0.04	0.05



Figure 1 ABB Robot MIG welding.

### 2.1 Design of Experiment

Welding parameter setup is based on L<sub>9</sub> Orthogonal Array Taguchi Method. This welding process has three different factors and three levels as shown in Table 2. The parameters selected according to the recommended range from the handbook.

Table 2 The parameter at three levels and three factors.

Parameters	Levels		
	1	2	3
Voltages (V)	21	22	23
Welding speed (mm/min)	4.5	5.5	6.5
Welding pattern	straight	triangle	spiral

### 2.2 Tensile Test

A tensile test is also called a tension test is the most common type of test used to test the material behavior or the strength of the welding part. In this experiment, the tensile test is used to get the value of strength for the welding part. By given a pulling force to a welding part until it breaks, you will find its strength along with how much it will elongate. The point of failure is usually called its Ultimate Strength. The machine used for this process is the Universal Tensile Testing Machine INSTRON 600DX. A specimen was placed at the Centre of the jig equally for top and bottom. Figure 2 (a) and 2 (b) shows the test specimens on which experiment was carried out, 2(a) before a tensile test and 2(b) after the tensile test.



Figure 2 Sample AISI 1020 before and after tensile test.

### 3. DATA ANALYSIS

The Experimental design was developed based on the Taguchi Method. Minitab software has been utilized to analyze the significant parameters that control the strength. Analysis of variance (ANOVA) was employed to establish the optimum conditions. Table 3 shows the S/N ratios and mean using the larger is better characteristics.

Table 3 Experimental design and the result of experiments.

Part	Volt (V)	Welding speed (mm/min)	Weld Pattern	Mean (Mpa)	S/N ratio
1	21	4.5	straight	232.37	47.30
2	22	5.5	triangle	218	46.76
3	23	6.5	spiral	164.41	43.86
4	21	4.5	spiral	206.23	46.28
5	22	5.5	straight	212.2	46.52
6	23	6.5	triangle	246.76	47.82
7	21	4.5	triangle	196.83	45.87
8	22	5.5	spiral	223.97	46.98
9	23	6.5	straight	222.67	46.95

### 4. RESULTS AND DISCUSSION

Table 3 shows the result of the tensile test and signal to noise ratio of nine holes that have been welded according to selected parameters. By referring to the Table 2, the graph plotted shows that the maximum tensile strength recorded at 246.767 MPa where the Voltage (V), welding speed (mm/min) and welding pattern were (23 V, 6.5 mm/min, triangle pattern). The level factor with the highest S/N ratio was the optimum level for responses measured. From Figure 3, it is clear that the optimum value levels for higher tensile are at a Welding speed (5.5mm/min), Voltage (22 Volts) and Welding pattern (straight). Welding pattern shows the number one ranks which means welding pattern is the critical parameter that contributed to the highest effect of strength. This is followed by welding speed and Voltage.

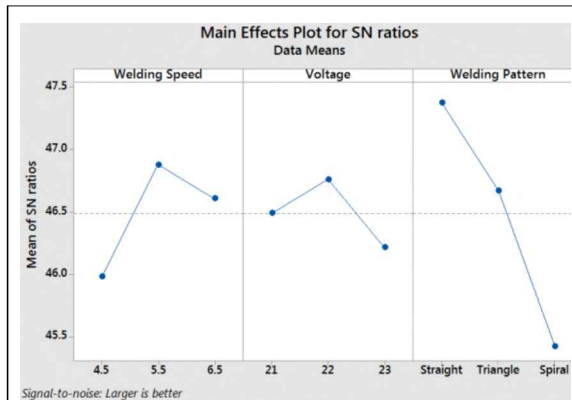


Figure 3 Main effect plot for S/N ratio.

### 5. CONCLUSIONS

The following conclusions to be concluded in this study:

- (a) The result shows that the welding pattern is the most significant factor compared to other factors with 61 % of the percentage of contribution.
- (b) The straight pattern has the highest value of tensile strength other than spiral and triangle.
- (c) The optimum parameter suggested from the Taguchi method that give the best tensile strength is the combination of 5.5 mm/min for welding speed, 22 V for voltage and straight pattern.

### REFERENCES

- [1] Utkarsh, S., Neel, P., Mahajan, M. T., Jignesh, P., & Prajapati, R. B. (2014). Experimental investigation of MIG welding for ST-37 using design of experiment. *International Journal of Scientific and Research Publications*, 4(5), 1-4.
- [2] Pires, J. N., Loureiro, A., & Bölsjö, G. (2006). *Welding robots: technology, system issues and application*. Springer Science & Business Media.
- [3] Patel, T., & Patel, S. C. (2015). The effect of process parameter on weld depth in GMA welding process. *International Journal for Innovative Research in Science & Technology*, 1(11).
- [4] Prajapati, R. B., Patel, D. B., & Patel, T. M. (2014). Experimental investigation of GMAW for AISI 1045 material using Taguchi Method. *International Journal of Scientific & Engineering Research*, 5(4), 15-19.

# Effect of Nb element on the oxide formation of Fe-40Ni-24Cr alloy

Noraziana Parimin<sup>1,\*</sup>, Esah Hamzah<sup>2</sup><sup>1)</sup> School of Materials Engineering, Universiti Malaysia Perlis, 02600 Arau, Perlis, Malaysia<sup>2)</sup> Faculty of Mechanical Engineering, Universiti Teknologi Malaysia, 81310 Skudai, Johor, Malaysia<sup>\*</sup>Corresponding e-mail: noraziana@unimap.edu.my**Keywords:** Fe-40Ni-24Cr alloy; isothermal oxidation; alloying element

**ABSTRACT** – Isothermal oxidation of heat-treated Fe-40Ni-24Cr alloy at 500 °C has been studied to further investigated the role of alloyed Nb during oxide formation. The oxidized heat-treated Fe-40Ni-24Cr alloy were analyzed in terms of oxidation kinetic, oxide formation and morphology by using FESEM and EDX techniques. All samples followed a parabolic rate law with fine-grained alloy recorded a lowest oxidation rate. The overgrown Nb oxide was formed at the longer exposure duration with coarse-grained heat-treated alloy developed massive overgrown Nb oxide. This phenomenon will initiate the crack propagated around the oxide and further induced the formation of oxide exfoliation.

## 1. INTRODUCTION

Fe-40Ni-24Cr alloy is a heat resistant alloy for petrochemical and high temperature application such as industrial-heating applications, industrial furnace and heat-treating operations. Fe-40Ni-24Cr alloy exhibits good resistance to oxidizing environment. It is the ability of alloys to form protective surface oxide scales at high temperatures that endows them with resistance to further high temperature oxidation [1]. Alloying element such as Nb, Mn and Ti are commonly added to form stable precipitates at the operating temperatures [2-4]. Fe-40Ni-24Cr alloy used in the petrochemical industries, typically contains a small amount of Nb and Ti as an alloying element, that provides stability of the structure under severe service condition. This alloy are strengthened by carbides precipitation such as MC carbides composed of NbC, TiC and (Nb,Ti)C [2]. This alloy experiences tremendously harsh conditions at various temperature and environment upon service. Under these conditions, the materials undergo compositional change of oxide layer formation due to oxidation at high temperature. Therefore, it is crucial to figure out the role of alloyed Nb in high temperature oxidation of Fe-24Ni-24Cr alloy by examined the oxide scale morphologies at high temperature oxidation.

## 2. METHODOLOGY

The Fe-40Ni-24Cr alloy was used in this study with chemical composition in weight percent (wt%): 40.45 Ni, 24.11 Cr, 0.05 C, 0.08 Al, 0.03 Ti, 0.44 Si, 0.7 Mn, 0.11 Cu, 0.25 Mo, 0.17 Co, 0.44 Nb, 0.05 W and balance Fe. The cut samples were undergoing a heat treatment process at two different temperatures for 3 hours soaking time, namely, 950 °C and 1100 °C, followed by water quench. The heat-treated sample at 950 °C and 1100 °C are denoted as HT950 and HT1100, respectively. The

heat-treated samples were exposed to isothermal oxidation at 500 °C for 500 hours. The oxidized samples were analysed using field emission scanning electron microscope (FESEM) equipped with energy dispersive x-ray (EDX).

## 3. RESULTS AND DISCUSSION

### 3.1 Heat Treatment

The heat treatment results recorded that increase in heat treatment temperature was increase the average grain size of Fe-40Ni-24Cr alloy from 27.27 $\mu$ m to 36.31 $\mu$ m for HT950 and HT1100, respectively.

### 3.2 Oxidation Kinetic

The weight change per surface area (w/A) as a function of time (t) of Fe-40Ni-24Cr alloy oxidized at 500°C is presented in Figure 1. The HT950 sample exhibited the low weight gain compared to HT1100 sample. At the beginning of the oxidation test, HT950 sample oxidized quite rapidly until 50 hours, that is 0.0208 mgcm<sup>-2</sup>. After 50 hours exposure time, HT950 sample gain more weight until 500 hours, which is 0.0753 mgcm<sup>-2</sup>. In contrast, the weight gains for HT1100 sample exhibited high weight gain due to the continuous oxide growth to develop a protective oxide layer on the alloy surface. This sample recorded an increasing weight change per surface area from 0.0367 to 0.1232 mgcm<sup>-2</sup> from 50 hours until 500 hours exposure time.

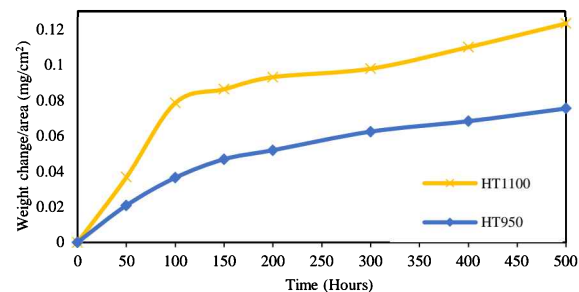


Figure 1 Oxidation kinetics.

The oxidation rate law was identified using a double log plot as shown in Figure 2 (a). The plot was based on equation (1), where  $x$  is weight change per surface area and  $m$  is constant. The  $m$  values of 1, 2 and 3 represent linear, parabolic and cubic rate, respectively. The  $m$  value for both samples are 1.86 and 2.21, denoted that both samples was followed parabolic oxidation rate law. The rate constant was determined from parabolic rate law equation (2) as shown in Figure 2 (b). The parabolic rate constant,  $K_p$  value for HT950 was smaller than HT1100 sample, which are  $3.12 \times 10^{-9} \text{ mg}^2\text{cm}^{-4}\text{s}^{-1}$  and  $7.11 \times 10^{-9}$

$\text{mg}^2\text{cm}^{-4}\text{s}^{-1}$ , respectively, indicating that HT950 sample has a low parabolic rate compared to HT1100, indicating good oxidation resistance.

$$\log x = (1/m) \log t + C \quad (1)$$

$$x^2 = K_p t + C \quad (2)$$

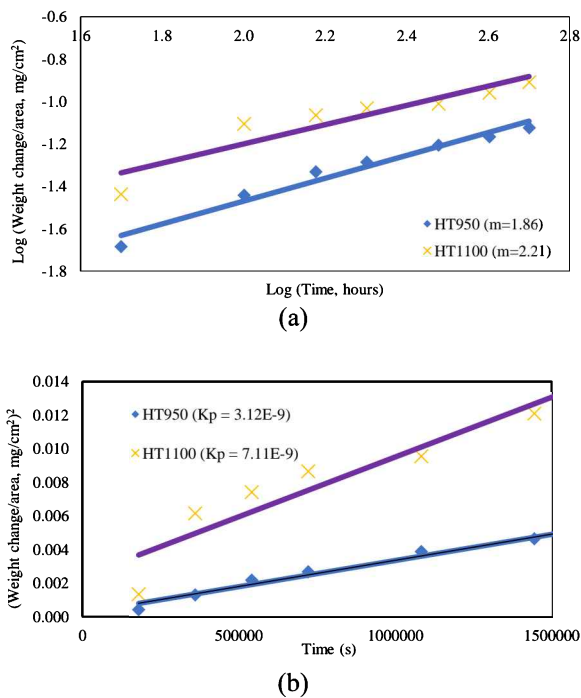


Figure 2 (a) Double log plot indicating parabolic rate law ( $m=2$ ); (b) square of weight change indicating  $K_p$ .

### 3.3 Oxide Morphology

Figure 3 shows FESEM images of HT950 sample of Fe-40Ni-24Cr alloy exposed at 500°C for 500 hours. The low magnification image in Figure 3 (a) indicate a formation uniform oxide scale with isolated oxide particles. The oxide layer formed at the alloy matrix was dense with no evidence of pore as shown in Figure 3 (b). An elemental EDX analysis at the matrix area A revealed the presence of major alloying element Fe, Ni and Cr, and also O, suggesting the formation of protective Cr-rich and spinel oxide phases. Whereas, the EDX analysis on the isolated oxide particle at area B revealed the enrichment of elements O and Nb, suggesting the presence of Nb-rich oxide. The  $\text{NbO}_2$  oxide phase was identified using XRD in this study.

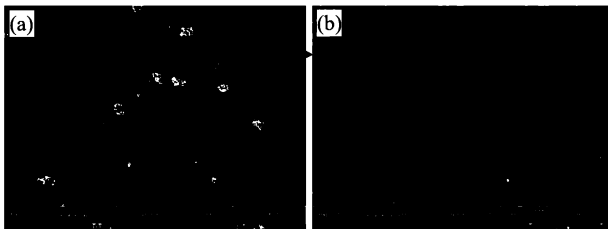


Figure 3 SEM images of HT950.

Figure 4 shows FESEM images for HT1100 sample. Figure 4 (a) shows the uniform oxide scale formed on the alloy surface with formation of overgrown oxide particle. The close-up image on the oxide particle in Figure 4 (b) shows an evidence of crack around the oxide particle.

This oxide particle seems to have loose structure, which have a tendency to spall. An elemental EDX analysis of the oxide particle at C indicated the presence of element O and Nb similarly identified for HT950 sample at area B in Figure 4 (b), indicating the formation of  $\text{NbO}_2$  oxide phase.

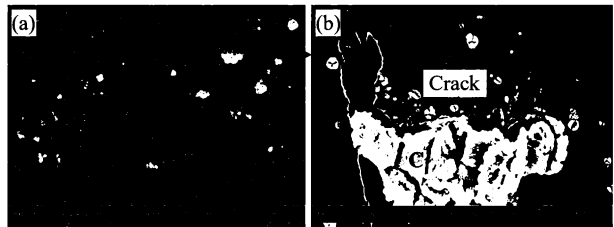


Figure 4 SEM images of HT1100.

Nb alloying element was added to the alloy system to enhance their properties, but significantly added to the development of Nb rich precipitates which are  $\text{NbC}$  and  $(\text{Nb}, \text{Ti})\text{C}$  that will strengthen the alloy [2]. However, the exposure of this material to high temperature and longer time will increase the tendency to formed Nb-rich oxide that will served as a preferred site for pit formation and further deteriorate the materials into the certain extend. The main feature of Fe-40Ni-24Cr alloy is the formation of Nb-rich oxide particle which tend to form overgrown large particle on the surface.

### 4. CONCLUSION

The isothermal oxidation of two heat-treated Fe-40Ni-24Cr alloys has been studied. Both samples tend to follow the parabolic rate law indicating the diffusion-control oxide growth rate. Oxidation exposure up to 500 hours developed a uniform oxide scale with overgrown  $\text{NbO}_2$  oxide phase.

### ACKNOWLEDGEMENT

The authors would like to thank the Ministry of Education Malaysia for the research fund under the Fundamental Research Grant Scheme (FRGS) (Project Code. FRGS/1/2016/TK05/UNIMAP/02/4).

### REFERENCES

- [1] Barnard, B. R., Liaw, P. K., Buchanan, R. A. & Klarstrom, D. L. (2010). Effects of applied stresses on the isothermal and cyclic high-temperature oxidation behavior of superalloys. *Materials Science and Engineering: A* 527 (16-17), 3813–3821.
- [2] Sustaita-Torres, I. A., Rodríguez, S. H., Guerrero-Mata, M. P., Garza, M., Valdés, E., Deschaux-Beaume, F. & Colás, R. (2012). Aging of a cast 35Cr-45Ni heat resistant alloy. *Materials Chemistry and Physics* 133, 1018–1023.
- [3] Xu, Y.X., Lu, J.T., Yang, X.W., Yan, J.B. & Li, W.Y. (2017). Effect and role of alloyed Nb on the air. *Corrosion Science* 127, 10-20.
- [4] Xu, Y.X., Lu, J.T., Li, W.Y. & Yang, X.W. (2018). Oxidation behavior of Nb-rich Ni-Cr-Fe alloys: Role and effect of carbides precipitates. *Corrosion Science* 140, 252-259.

# Tensile properties of graphene nanoplatelets/carbon black filled chloroprene rubber composites for engine mounting

Noraiham Mohamad<sup>1,\*</sup>, Cheng Lin Yi<sup>1</sup>, Khairu Ilwani Karim<sup>1</sup>, Mazliah Mazlan<sup>1</sup>, Hairul Effendy Ab Maulod<sup>2</sup>, Mohd Shahrizan Othman<sup>1</sup>, Nurzallia Mohd Saad<sup>3</sup>, Siow Ming Onn<sup>3</sup>, Jeefferie Abd Razak<sup>1</sup>

<sup>1)</sup> Fakulti Kejuruteraan Pembuatan, Universiti Teknikal Malaysia Melaka,  
Hang Tuah Jaya, 76100 Durian Tunggal, Melaka, Malaysia

<sup>2)</sup> Fakulti Teknologi Kejuruteraan Mekanikal & Pembuatan, Universiti Teknikal Malaysia Melaka,  
Hang Tuah Jaya, 76100 Durian Tunggal, Melaka, Malaysia

<sup>3)</sup> Saiko Rubber (M) Sdn Bhd, Senawang Industrial Estate, 70400 Seremban, Negeri Sembilan, Malaysia

\*Corresponding e-mail: noraiham@utem.edu.my

**Keywords:** Tensile; graphene nanoplatelets composite; engine mounting

**ABSTRACT** – This study focusing on the effect of hybrid fillers ratio of graphene nanoplatelets:carbon black loading to enhance the tensile properties of chloroprene (CR) rubber composite. The CR composites of with and without hybrid fillers at 3.0 phr and 6.0 phr were investigated. It was prepared via melt compounding using an industrial mixer and vulcanized using a hot press. The tensile properties were determined by using a universal testing machine (U-CAN) accordance to JIS K 6251. The CR hybrid composites have proven to exhibit enhanced tensile strength of about 24% than the commercial non-hybrid composites.

## 1. INTRODUCTION

Engine mounts provides vibration attenuation in isolating the vibration source [1] to the chassis. In current engine mounting application, the mounting rubber used is commonly utilizing a single polymer matrix composite namely natural rubber (NR). Although natural rubber has very good shock absorbing characteristics, it has limitations. NR has a poor resistance to heat and ozone [2]. This limitation is significant because rubber mount subjects to ozone deterioration during service. Synthetic rubber such as chloroprene rubber (CR) is also widely used in engine mounting. The conventional rubber composites alone do not possess excellent damping, heat and dynamic fatigue resistance well to the engine mount system. Hence, the incorporation of dispersed nanofillers into a polymer matrix will provide materials with tailored and controlled properties. Mechanical strength and stiffness, which are not inherent in conventional composites improved dramatically with a very low level of nanofiller loading. Hybridization of graphene nanoplatelets (GNP) and carbon black (CB) conventional filler provides a better compensation between price and properties. Therefore, this study focusing on the effect of filler ratio between GNP: CB to the tensile properties of CR composites. This is a preliminary study to see the potential of hybrid CB nanocomposites for the candidate of rubber part in engine mount application.

## 2. RAW MATERIALS & METHODOLOGY

General purpose Neoprene Type W of ML (1+4 at 100 °C) of 40-49 was supplied by Saiko Rubber (M) Sdn Bhd. Graphene nanoplatelets KNG-50 was purchased by Xiamen Graphene Technology Co. Ltd, China. Saiko

Rubber also supplies carbon black N660 and other ingredients (Table 1). The compounding process performed using an industrial mixer at the temperature of 95°C and the motor speed of 80 rpm. Then, compound vulcanized using a hot press at 160°C and cut into dog bone samples for tensile testing.

Tensile testing of CR nanocomposites was conducted using U-CAN UTM machine according to JIS K 6251. The tensile strength (TS), modulus at 100% elongation (M100), modulus at 300% elongation (M300), and elongation at break (EB) of the CR nanocomposites were determined at a load cell of 1 kN and crosshead speed of 500 mm/min.

Scanning electron microscopy analysis was conducted by using a Zeiss EVO-50 SEM to analyze the fracture surfaces of CR composites. Prior the analysis, the samples were coated with gold. All samples were examined with secondary electron imaging mode. The scanning electron micrograph was recorded at a magnification of 100x.

Table 1 Formulation.

Ingredient (phr)	*CS	3C	3G	1.5C: 1.5G	3C: 3G
Neoprene WRT	100	100	100	100	100
Stearic acid	0.5	0.5	0.5	0.5	0.5
Zinc oxide	5	5	5	5	5
High active magnesia	4	4	4	4	4
Octylated diphenylamine (Octamine)	2	2	2	2	2
Coumorone resin	8	8	8	8	8
ETU (75%)	0.75	0.75	0.75	0.75	0.75
CBS	0.75	0.75	0.75	0.75	0.75
Carbon black	3	3	0	1.5	3
GNPs	0	0	3	1.5	3
Precipitated silica	10	0	0	0	0

\*CS – commercial control sample

## 3. RESULTS AND DISCUSSION

The tensile strength of the hybrid systems 1.5C:1.5G and 3C:3G are the highest compared to the CS and single filler system owing to the incorporation of GNPs and good interaction between the GNPs and CB

hybrid fillers. This is in good agreement to the review article done by Bokobza [3] stating that carbon based nanofiller contributes to the enhancement in tensile properties. The higher surface area enables the GNPs to interact closely with the rubber phases. When there is higher specific surface area of nanofiller that is in contact with the rubber phase, it will lead to the higher stress transfer between the rubber phase and nanofiller. This phenomenon is explained as the strengthening mechanism [3] in which most of the applied load are distributed to the nanofiller in the filled elastomer matrix. Therefore, the sample is able to withstand higher stress and further increasing its tensile strength.

Table 2 Tensile properties of the CR composites.

Samples	Tensile Strength (MPa)	M100 (MPa)	M300 (MPa)	Elongation at break (%)
CS	17.2	0.81	1.71	800
3 C	18.7	0.94	2.06	839
3 G	18.4	0.88	2.21	923
1.5C:1.5G	19.3	1.12	2.60	830
3C:3G	21.1	0.91	2.08	860

Modulus is a measurement of stiffness of a material. The higher value of the tensile modulus indicates that higher stress is needed to produce a given strain. Table 2 shows the modulus at 100 and 300 % elongation of CR composites in different formulation. The incorporation of GNPs in both single filler system and hybrid system contributes to the noticeable increment in the tensile modulus of the CR composites. The GNPs with Young's modulus of 0.5 – 1 TPa and an ultimate strength of 130 GPa [2] are known as the stiffest and strongest elements. The presence of GNPs inside the rubber composites acted as rigid particles and their interaction with CR reduced the chain mobility and increased the stiffness of the rubber. This is in agreement with the findings by Mokhethu et al. (2014) in their work on EPDM/silica nanocomposites. Elongation at break (EB) is the ability of a material to withstand bending and shaping of it without cracking. Table 2 shows the EB of all CR composites increased drastically if compared to CS; especially for the composites with GNPs. This observation explained the interaction between GNPs with CR matrix to form tougher materials.

Figure 1 shows the tensile fractured surfaces of CS and 3C:3G composites obtained using SEM at 100x magnification. It is observed that the rubber composite exhibited a smooth and featureless fracture surface. This indicates that the absence of rigid nanofiller in the matrix had caused the rubber matrix easily deformed from shear yielding. On the other hand, the fractured surfaces of the CR nanocomposites filled with GNPs are observed to depict higher surface roughness than the CS composite. The study done by the Ismail et al., (2013) has also shown a similar phenomenon on the effect of halloysite nanotubes (HNTs) filled acrylonitrile–butadiene rubber nanocomposites. Improved dispersion of GNPs in the CR matrix provides a better interface condition to alter the crack path which then added to the crack-growth resistance, giving better mechanical strength to resist applied stress and lead to the enhancement of tensile

properties.

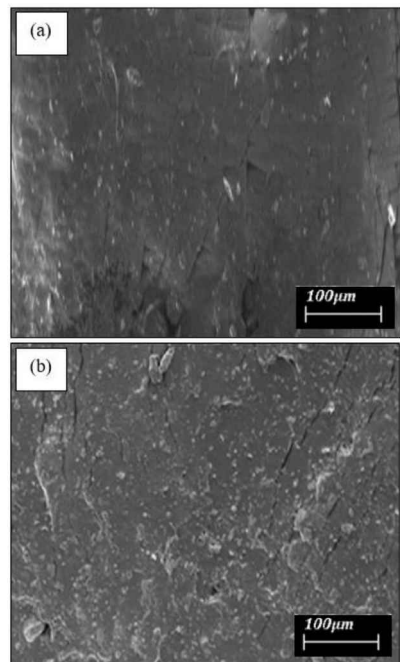


Figure 1 SEM micrographs of the tensile fracture surfaces of the (a) CS and (b) 3C:3G composites.

#### 4. CONCLUSION

As the results, the hybrid system coupling GNPs with CBs exhibited enhancement in the tensile strength as well as the elastic modulus of the CR composites compared to the control sample which is filled with CBs and precipitated silica. The tensile strength obtained of about 20 MPa showed the potential for the CR composites to replace natural rubber based components in an engine mounting.

#### REFERENCES

- [1] Ing, T. S. (2013). Vibration analysis of vehicle engine mounting. Thesis, Universiti Malaysia Pahang.
- [2] Mohamad, N., Yaakub, J., Ab Maulod, H. E., Jeefferie, A. R., Yuhazri, M. Y., et al. (2017) Vibrational damping behaviors of graphene nanoplatelets reinforced NR/EPDM nanocomposites. *J. Mech. Eng & Sci.*, 11(4), 3274–3287.
- [3] Bokobza, L. (2017) Mechanical and electrical properties of elastomer nanocomposites based on different carbon nanomaterials. *J. Carbon Res.*, 3(10), 1-22.
- [4] Mokhethu, T. H., Luyt, A. S. & Messori, M. (2014) Preparation and characterization of EPDM/silica nanocomposites prepared through non-hydrolytic sol-gel method in the absence and presence of a coupling agent. *eXPRESS Poly. Letters*, 8(11), 809–822.
- [5] Ismail, H. & Ahmad, H. S. (2014) Effect of halloysite nanotubes on curing behavior, mechanical and microstructural properties of acrylonitrile–butadiene rubber nanocomposites. *J. Elast. & Plast.*, 46(6), 483–498.

# Fabrication of Al-Zn based metal matrix composites with bamboo leaf ash

Maibam Bindya Devi, Anil Kumar Birru\*

Department of Mechanical Engineering, National Institute of Technology Manipur, Imphal, 795001, India

\*Corresponding e-mail: anilbirru@gmail.com

**Keywords:** Metal matrix composites; density; hardness

**ABSTRACT** – The research work discusses the fabrication of metal matrix composites (MMC) via stir casting route with aluminium A713 alloy as the base metal for matrix and bamboo leaf Ash (BLA) as the reinforcement. The composites have been fabricated successfully with the reinforcement addition of 2 to 8 wt. % in steps of 2 wt. %. The density, hardness and tensile strength of the composites are compared with the A713 alloy. The effect of the BLA on the mechanical properties of the composites are evaluated.

## 1. INTRODUCTION

An investigation on the properties of aluminium based metal matrix composite using BLA as reinforcement, fabricated via stir casting route, has been carried out.

Metal-matrix composites (MMCs) of light non-ferrous metals including aluminum, magnesium, copper and nickel alloys etc. reinforced with ceramic particulates or fibers are widely used in aerospace applications, marine applications and automotive [1, 2].

Aluminium being the most abundant metal in the earth's crust and a viable material for wide applications, it is a promising material for the present and also for the future. Many researchers around the globe have done a great deal of work on aluminium, its alloys and the composites based on aluminium alloys as matrix [1-5]. But still, there is very less research about the work on aluminium based composites with agro waste as the reinforcements. Hence this work is part of such an attempt to fill this gap of MMCs using agro-wastes as reinforcements. The aerospace and the automobile industries have a great demand of aluminium based MMCs for various applications.

## 2. METHODOLOGY

Metal matrix composite was prepared through stir casting route. The metal is heated upto about 750°C and then let it cool to about 660°C so that the metal alloy is at semi solid condition. At this temperature the reinforcement BLA which is preheated (at 350°C) is added progressively and stirred. It was observed that the matrix melted at 750°C, was not able to wet the reinforcement and hence semi-solid mixing at about 660°C of the matrix was carried out. At this temperature the reinforcement was able to be incorporated into the matrix. Wetting of the reinforcement was possible but stirring was difficult at this temperature and hence stirring was carried out after raising the temperature

again at 750°C for uniform distribution of the reinforcement particles. Stirring was performed for about 10 minutes at 600 rpm with the help of a stirrer. And then the composite is poured into a die. The size of the reinforcements added are less than 75 µm. Four composites (A, B, C and D) of different BLA content were fabricated. The BLA weight percent addition is about 2 wt.% to 8 wt.% in steps of 2 wt.%. The alloy A713 composition is as shown below in Table 1.

Table1 Base alloy A713 composition.

Alloy	Composition of the aluminium alloy (wt. %)				
	Zn	Cu	Mg	others	Al
A713	8.0	0.5	0.4	> 0.5	Balance

XRD and EDAX of BLA as shown in Figure 1 and Figure 2 were taken to know its composition and found that SiO<sub>2</sub> is the main component along with other trace elements.

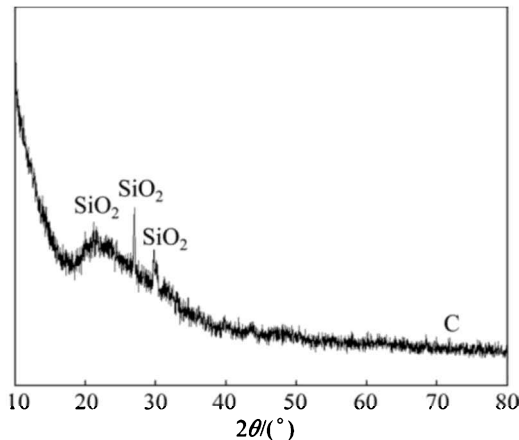


Figure 1 XRD of BLA [3].

## 3. RESULTS AND DISCUSSION

The mechanical properties viz. density, tensile strength and hardness are compared for the fabricated composites with the base alloy A713 as shown in the Table 2.

Comparing their properties, we observed that there is a decrease of density with the increase in addition of BLA and also there is an increase of both hardness and tensile strength with the increase in addition of BLA. The increase of both hardness and strength may be due to the influence of bamboo leaf ash which has SiO<sub>2</sub> as its major constituent.

Table 2 Mechanical properties of the fabricated composites and A713 alloy.

Alloy/MM Cs	Density (g/cc)	Tensile strength (MPa)	Brinell hardness (BH)
A713	2.87	170.854	82.17
A	2.82	177.549	87.99
B	2.68	187.767	88.64
C	2.61	199.125	108.53
D	2.48	220.020	110.55

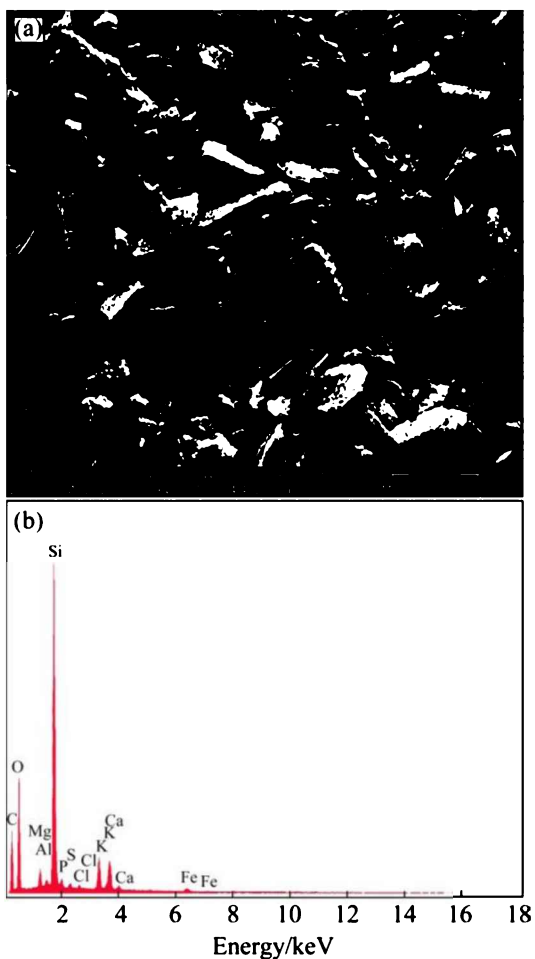


Figure 2 SEM image and EDAX of BLA [3].

#### 4. CONCLUSIONS

- (a) The metal matrix composites were successfully prepared. Liquid melt of A713 aluminium alloy and the reinforcements do not get mixed at 750 °C as the reinforcement are not wetted by the liquid melt due to the high surface tension of the liquid melt A713. And it was found to be wetted at about 660 °C.
- (b) The average density decreased with the increase in BLA addition.
- (c) Both the tensile strength and hardness of the composites increased with the increase in BLA addition.

#### REFERENCES

- [1] Prabu, S. B., Karunamoorthy, L., Kathiresan, S., & Mohan, B. (2006). Influence of stirring speed and stirring time on distribution of particles in cast metal matrix composite. *Journal of Materials Processing Technology*, 171(2), 268–273.
- [2] Yu, L. I., Li, Q. L., Dong, L. I., Wei, L. I. U., & Shu, G. G. (2016). Fabrication and characterization of stir casting AA6061—31% B4C composite. *Transactions of Nonferrous Metals Society of China*, 26(9), 2304-2312.
- [3] Kumar B. P., & Birru, A. K. (2017). Microstructure and mechanical properties of aluminium metal matrix composites with addition of bamboo leaf ash by stir casting method. *Transactions of Nonferrous Metals Society of China (English Edition)*, 27(12), 2555–2572.
- [4] Kumar, A., Lal, S., & Kumar, S. (2013). Fabrication and characterization of A359/Al<sub>2</sub>O<sub>3</sub> metal matrix composite using electromagnetic stir casting method. *Journal of Materials Research and Technology*, 2(3), 250–254.
- [5] Sajjadi, S. A., Ezatpour, H. R., & Torabi Parizi, M. (2012). Comparison of microstructure and mechanical properties of A356 aluminum alloy/Al<sub>2</sub>O<sub>3</sub> composites fabricated by stir and compo-casting processes. *Materials and Design*, 34, 106–111.

# Hygrothermal effect on kenaf fiber/epoxy reinforced aluminium laminates (KeRALL) fabricated via compression moulding

Edynoor Osman<sup>1,2,3,4</sup>, Mohd Warikh Abd. Rashid<sup>2,3,\*</sup>, Mohd Edeerozey Abd Mana<sup>2</sup>, Toshihiro Moriga<sup>3,4</sup>

<sup>1)</sup>Department of Polymer Composite Processing Technology, Kolej Kemahiran Tinggi MARA, Masjid Tanah, KM 1, Persiaran Paya Lebar, 78300 Masjid Tanah, Melaka, Malaysia

<sup>2)</sup> Fakulti Kejuruteraan Pembuatan, Universiti Teknikal Malaysia Melaka, Hang Tuah Jaya, 76100 Durian Tunggal, Melaka, Malaysia

<sup>3)</sup> Tokushima-UTeM Academic Center, Universiti Teknikal Malaysia Melaka, Hang Tuah Jaya, 76100 Durian Tunggal, Melaka, Malaysia

<sup>4)</sup> Department of Chemical Science and Technology, Graduate School Advanced Technology and Science, Tokushima University, 2-1 Minami-Josanjima, 770-8506 Tokushima, Japan

\*Corresponding e-mail: warikh@utm.edu.my

**Keywords:** Hygrothermal; KeRALL; mechanical properties

**ABSTRACT** – This study is focuses on the hygrothermal effect of kenaf fiber reinforced aluminium laminates (KeRALL). KeRALL immersed at 30, 60 and 80 °C in water bath. As a result, at 30 °C shows the lowest water absorption rate compared to those immersed at 60 and 80 °C. KeRALL immersion at temperature 80 °C show the fastest water absorption, followed by 60 and 30 °C. At 30 °C, 7 % decrement of interlaminar shear stress (ILSS) were recorded, followed by 66 % at 60 °C and 54 % at 80 °C. The decrease is associated with fibre pull out, matrix fracture and delamination as the result of the hygrothermal influence as manifested by the fractographic images.

## 1. INTRODUCTION

The properties and performance of the composite structure is a function of its moisture distribution, environmental history, and temperature exposure [1]. Thus, among the main concerns for the use of natural fibre reinforced composite materials are their susceptibility to moisture absorption and its effects on the physical and mechanical properties [2]. Moisture absorption can lead to the degradation of fibre-matrix interface region, which in turn creates poor stress transfer efficiencies and result in reduction of mechanical properties [3]. Also, exposure to elevated temperature can result in degradation of mechanical properties, cracking, chalking and flaking of polymers [4]. For instance, fibre metal laminates (FML) technologies is an effective way to solve the disadvantages of natural fibre composite. The use of kenaf fiber can provide mechanical properties as well as resulting in lightweight and eco-friendly polymer composites. Therefore, this study is emphasising on the hygrothermal effect on KeRALL's performance.

## 2. METHODOLOGY

Kenaf fibre (non-woven mat with surface density of 800 g/m<sup>2</sup>, Innovative Pultrusion S/B), epoxy resin (EPO DM A and B, Chemrex Corp. S/B) and aluminium sheet (Al 2024 T3 with 0.5 mm thickness, Kird Entreprise) were used as reinforcement, matrix and face

sheet respectively. Prior to compression, surface modification was carried out for both aluminium sheet and kenaf fibre. For this purpose, aluminium sheets underwent mechanical abrasion by using 60-grit sandpaper and kenaf fibre was alkalized by 5% sodium hydroxide. KeRALL was fabricated through warm compression using a hydraulic press (GOTECH) at 80 °C. The pressure of 65 kg/cm<sup>2</sup> was applied with a holding time of 15 minutes.

Mechanical cutting equipment was used for sample preparation. The sample was cut according to the ASTM standards. Prior to testing, all samples underwent immersion process in water bath (YAMATO BK 610) at 30, 60, and 80 °C. The readings of weight changes of sample were consistently taken every day. The duration for hygrothermal conditions was 5 days. The change due to water and heat affect was closely monitored in terms of their delamination, matrix and fibre swelling, cracking and others. The conditioned samples were tested by 3-point bending test. GOTECH A1-7000-LA 50 kN was used to perform the test at 23 °C ± 2 °C and 50% ± 5% relative humidity in accordance to ASTM D790. Lastly, scanning electron microscope (SEM) fractographic images was studied for morphological analysis.

## 3. RESULTS AND DISCUSSION

Figure 1 shows the percentage of water absorption as a function of exposed time at temperature of 30, 60, and 80 °C and immersed in water for KeRALL samples. It was observed that water diffusion behaviour of KeRALL can be classified into the Fickian behaviour, where water absorption increases linearly with the square root of time, and slowing gradually until an equilibrium state was reached [5]. This behaviour can be seen clearly at temperature 80 °C for KeRALL samples. Meanwhile, temperature of 30 °C and 60 °C show non Fickian and Anomalous behaviour, respectively. The behaviour of KeRALL at elevated temperature indicated that application of heat and humidity will give different findings especially on epoxy matrix of composite. Table 1 present the findings to summarize the hygrothermal effect on KeRALL .

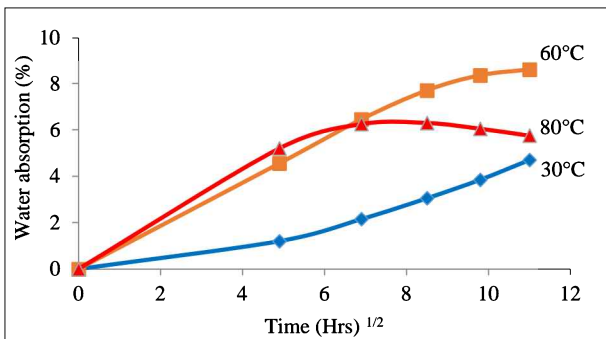


Figure 1 Water absorption behaviour of KeRALLs at temperature 30, 60 and 80 °C.

Table 1 Summary of hygrothermal effect on KeRALL samples in 5 days.

Temp. (°C)	Type of behaviour	Saturation (Hrs)	Water absorption	Degradation rate
30	Obey Fick's Law	> 120	Low	Slow
60	Non-Fick's Law	120	High	Medium
80	Anomalous (S shape)	24 to 48	Medium	Fast

The tested KeRALL was characterized by a decrease in ILSS defined in the 3-point bending test after hygrothermal condition. ILSS was calculated based on  $ILSS = (33P_{max})/(4Wt)$ ;  $P_{max}$  is a failure load on 3-point bending test,  $W$  = width of the specimens and  $t$  = thickness of the specimens. ILSS value shows a decremented proportional to the temperature increase (Figure 2). At 30 °C, 7% decremented of ILSS were recorded, followed by 66% at 60 °C and 54% at 80 °C. The highest value of decrement achieved at 60 °C probably because of saturation state before the  $T_g$  point. The hydrophilic nature of kenaf fibre also encourages the occurrence of earlier saturation stage of epoxy. Previous studied claimed that the decrease in ILSS due to environmental exposure is about 15% and it was strongly influenced by the temperature [6].

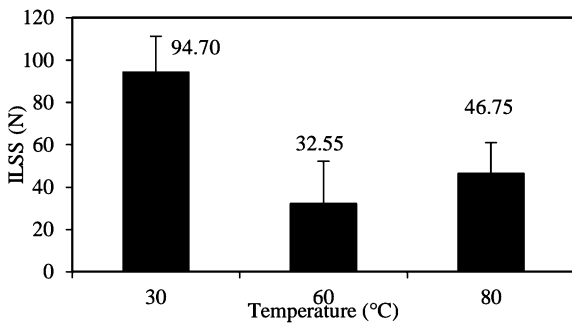


Figure 2 ILSS of KeRALL at temperature 30, 60 and 80 °C hygrothermal condition.

Hygrothermal effect on the microstructure was observed to clarify the fracture criterion of KeRALLs especially after flexural tested. Hence, the fracture observed will be divided based on the type of defect on the component of KeRALL i.e fibre pull out and fracture surface, fibre-matrix as well as Al sheet adhesion bonding as refer to Figure 3.

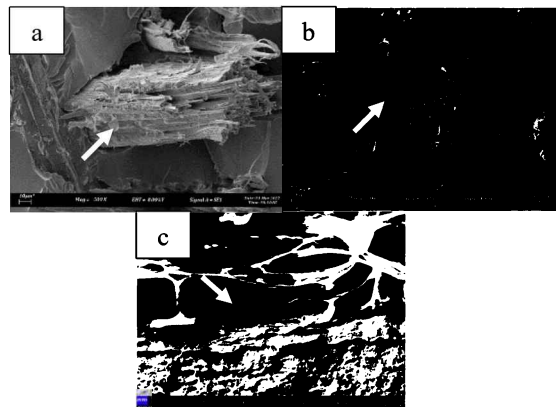


Figure 3 SEM image of KeRALL with hygrothermal at temperature 80 °C; a) fibre pull out and fracture surface, b) fibre-matrix adhesion and c) fibre/matrix-Al sheets adhesion.

#### 4. CONCLUSION

In conclusion, the behaviour of KeRALL at elevated temperature revealed and noted that application of heat and humidity will give different findings especially on epoxy matrix of composite. KeRALL at temperature 30 °C, showed the lowest water absorption rate compared to temperature 60 °C and 80 °C. KeRALL at temperature 80 °C showed the fastest water absorption and the earliest to reach saturation state, followed by temperature of 60 °C and 30 °C. An ILSS property shows the decremented trends. The microstructural analysis was observed through the defect on fractographic images.

#### REFERENCES

- [1] Daniel, I.M. & Ishai, O. (2006). Engineering mechanics of composite materials. New York: Oxford University Press.
- [2] Thwe, M.M. & Liao, K. (2002). Effects of environmental aging on the mechanical properties of bamboo-glass fibre reinforced polymer matrix hybrid composites. *Composites Part A: Applied Science and Manufacturing*, 33(1), 43-52.
- [3] Yang, H., Yan, R., Chen, H., Lee, D.H. & Zheng, C. (2007). Characteristics of hemicellulose, cellulose and lignin pyrolysis. *Fuel*, 86(12-13), 1781-1788.
- [4] Lin, Q., Zhou, X. & Dai, G. (2002). Effect of hydrothermal environment on moisture absorption and mechanical properties of wood flour-filled polypropylene composites. *Journal of Applied Polymer Science*, 85(14), 2824-2832.
- [5] Chandrasekar, M., Ishak, M.R., Jawaad, M., Leman, Z. & Sapuan, S.M. (2017). An experimental review on the mechanical properties and hygrothermal behaviour of fibre metal laminates. *Journal of Reinforced Plastics and Composites*, 36(1), 72-82.
- [6] Ypma, M. & Borgonje, B. (2001). Influence of Moisture and Temperature on GLARE Material Properties and GLARE Structures. *Proceeding of 13<sup>th</sup> International Conference on Composite Materials*, 2001.

# Synthesis and characterization of aluminium metal matrix composite with addition of bamboo leaf ash

B. Praveen Kumar<sup>1</sup>, Anil Kumar Birru<sup>1,\*</sup>, Chandan Mondal<sup>2</sup>

<sup>1)</sup>Department of Mechanical Engineering, National Institute of Technology Manipur, Imphal, Manipur, 795004, India

<sup>2)</sup>Defence Metallurgical Research Laboratory, Kanchanbagh, Hyderabad, 500058, India

\*Corresponding author: anilbirru@gmail.com

**Key words:** Aluminium metal matrix composites; stir casting; bamboo leaf ash

**ABSTRACT** – Aluminium Composites development in a vital class of design and light weight structural materials for encouragement of global engineering applications. Bamboo Leaf Ash (BLA) is an agro waste available in large quantities with low density used as prominent and inexpensive reinforcement among a variety of particles reinforcements. The present research work was carried out to the utilization of bamboo leaf ash in useful way by incorporating it into Al-4.5Cu matrix to produced composites by stir casting route. The bamboo leaf ash particles and fabricated composites were characterized. The density of the bamboo leaf ash particles and fabricated composites with addition of bamboo leaf ash at 0, 2, 4 and 6 wt. % were measured. The density of the fabricated composite was decreased with addition of bamboo leaf ash particles, conversely porosity was increased.

## 1. INTRODUCTION

Metal Matrix Composites (MMCs) are sophisticated engineering application materials which are combination of two or more materials (one of which is a metal) to achieve desired properties [1]. Aluminium alloys have fascinated in most attention as a matrix material in the composites due to their unique combination of light weight and good corrosion and wear resistance, and also excellent mechanical properties [2]. Aluminium Metal Matrix Composites (AMMCs) are broadly used in aircraft, aerospace, automobiles and various other fields [3]. The present research effort is directed at developing of AMMCs, to improve the fuel economy of automobiles, the research efforts aiming for high strength to weight ratio. For engine parts, cylinder block material is rapidly changing from cast iron to aluminium, and aluminium die-cast cylinder blocks with cast iron liners are now widely used [4]. Most conventional discontinuous AMMCs are expensive and, limiting their usages in the fabrication of several structural and non-structural materials. The research is being emphasized to produce cost effective AMMCs with similar, or possibly better for engineering applications. For inexpensive composites, researchers utilized silica-rich waste by-products as reinforcing material. Among the variety of agro and industrial waste by-products the Bamboo Leaf Ash (BLA) with low density and abundantly available in North-East region, India, is considered as a reinforcement materials and investigated as replacements for the comparatively more expensive reinforcements [5]. The addition of BLA in the aluminium matrix alloys has the potential to decrease the

density of aluminium matrix alloy and with improving the mechanical properties. The AMMCs with addition of BLA as reinforcement is probably may be overcome the cost barrier in automotive, aerospace and small engine applications. Yet, authors made an attempt on fabrication of BLA same to incorporate in the selected matrix for investigations.

## 2. EXPERIMENTAL DETAILS

### 2.1 Materials

Aluminium with 4.5 wt. % Cu as major alloying element was selected for the present investigation as the matrix material. Bamboo Leaf Ash processed as per the standard procedure. Magnesium in ingot form was incorporated to increase the wetting between the matrix alloy and the BLA particles during processing of the composite materials.

### 2.2 Preparation of Bamboo Leaf Ash

The Bamboo Leaf Ash was prepared as per a standard procedure. Dry bamboo leaves were collected from the farmlands, where having large quantities of bamboo trees within Manipur state, North East India as shown in Figure 1 shows the Dry Bamboo Leaf with Prepared BLA particles.



Figure 1 Dry Bamboo Leaf with prepared BLA particles.

### 2.3 Composite Production

The stir casting method was selected to fabrication of aluminium composite as it is relatively cost effective and offers ample selection of materials and processing conditions. The matrix alloy was in the form of ingot and cut into small pieces to accommodate in the crucible then melted in the induction electric resistance furnace, and heated up to 800 °C which maintained the melt in the argon atmosphere. The molten metal is allowed to cool to a semi-solid state in the furnace at a temperature of about 620-650 °C.

### 3. RESULTS AND DISCUSSION

#### 3.1 Characterization of Bamboo Leaf Ash

The chemical composition as per XRD investigation and EDAX analysis of BLA presented in Table 1. The SEM micrographs with EDAX and XRD profile of the BLA particles is observed that the BLA consists of different particles in various sizes.

The EDAX analysis revealed of the BLA shows peaks of silicon (Si), Aluminium (Al), Carbon (C), Oxygen (O), Calcium (Ca), Magnesium (Mg), Potassium (K) and Iron (Fe). From the synthesized BLA, further oxides combination may be present to the EDAX reveled elements i.e. Silicon dioxide ( $\text{SiO}_2$ ), Alumina ( $\text{Al}_2\text{O}_3$ ), Carbon (C), Calcium oxide ( $\text{CaO}$ ), Potassium oxide ( $\text{K}_2\text{O}$ ), Ferric oxide ( $\text{Fe}_2\text{O}_3$ ), and Magnesium oxide ( $\text{MgO}$ ) were detectable in the BLA particles. The XRD pattern peaks of the major element belong to  $\text{SiO}_2$  and values demonstrated as depicted in the Table 2.

Table 1 Chemical compositions of Bamboo Leaf Ash.

Element	$\text{SiO}_2$	$\text{CaO}$	$\text{K}_2\text{O}$	C	$\text{Al}_2\text{O}_3$	$\text{MgO}$	$\text{Fe}_2\text{O}_3$
Wt. %	76.2	6.68	5.62	4.2	4.13	1.85	1.32

Table: 2 -Peaks details of the XRD pattern of the BLA

Peak No.	2 theta (2θ)	d (Å)	FWHM	Intensity
1	26.959	3.30458	0.211	23.9
2	29.753	3.00031	0.387	18.4

#### 3.2 Microstructures Analysis

The properties of aluminium composite depend on the microstructure and interface characteristics between reinforcements and matrix. The optical microstructures SEM micrograph with EDAX profiles of Al-4.5Cu alloy and at 2, 4 and 6 wt. % of BLA composites as shown in Figure 2. The dendritic structure was observed as shown (a) due to may be rapid solidification induced. The super cooling forms the dendritic structure in the aluminium material which was processed by casting. The elongated primary  $\alpha$  (Al) dendritic arms which have high aspect ratios is characterized dendritic structure. SEM micrograph of matrix alloy with EDAX analysis, the white phase in SEM micrograph is  $\text{Al}_2\text{Cu}$  intermetallic phase. The copper is alloying element of the matrix alloy that is presented at a higher level than their solubility limit results imposed that the intermetallic phase Cu is in the region of the dendrites during stir casting process.

### 4. CONCLUSIONS

- The BLA particles were synthesized successfully with standard procedure and also observed silica ( $\text{SiO}_2$ ) is a major constituent in the BLA with EDAX and XRD analysis.
- The BLA particles incorporated in the Al-4.5Cu alloy with stir casting method successfully and observed with XRD and SEM with EDAX analysis.
- The density of the composites reduced with addition of BLA content. The density of Al-6BLA at weight percent composite was observed lowest, that indicating the pronounced

effect of BLA on the overall density of the composite.

### ACKNOWLEDGMENTS

Authors would like to acknowledge the Naval Research Board/DRDO, Government of India New Delhi-India for financial support to carry out the project in pursuing the experimentation work with Project Number: NRB/4003/PG/385.

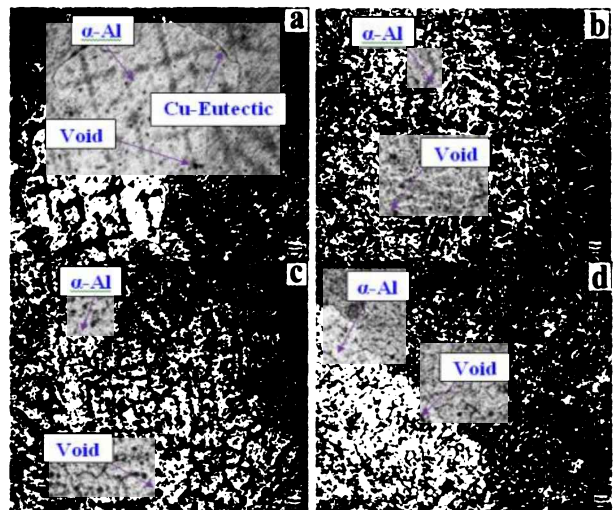


Figure 2 Optical micrograph of (a) Al-4.5Cu alloy, (b) Al-4.5Cu-2BLA, (c) Al-4.5Cu-4BLA and (d) Al-4.5Cu-6BLA at Wt.% of composites.

### REFERENCES

- Moses, J. J., & Sekhar, S. J. (2017). Investigation on the tensile strength and microhardness of AA6061/TiC composites by stir casting. *Transactions of the Indian Institute of Metals*, 70(4), 1035-1046.
- Miracle, D. B. (2005). Metal matrix composites—from science to technological significance. *Composites science and technology*, 65(15-16), 2526-2540.
- Ralph, B., Yuen, H. C., & Lee, W. B. (1997). The processing of metal matrix composites—an overview. *Journal of materials processing technology*, 63(1-3), 339-353.
- Fujine, M., Kato, S., Takami, T., & Hotta, S. (2000). *Development of Metal Matrix Composite for Cylinder Block* (No. 2000-05-0070). SAE Technical Paper.
- Bodunrin, M. O., Alaneme, K. K., & Chown, L. H. (2015). Aluminium matrix hybrid composites: a review of reinforcement philosophies; mechanical, corrosion and tribological characteristics. *Journal of Materials Research and Technology*, 4(4), 434-445.

# Microstructural properties of yttria stabilized zirconia (YSZ) prepared by ceramic injection moulding (CIM)

Mahfuzah Zainudin<sup>1,\*</sup>, Muhammad Hussain Ismail<sup>2,\*</sup>, Nor Shamimi Shaari<sup>1</sup>, Muhammad Faris Abd Manap<sup>1</sup>, Rosniza Rabilah<sup>1</sup>, Muhamad Faris Syafiq Khalid<sup>3</sup>

<sup>1)</sup> Faculty of Mechanical Engineering, Universiti Teknologi MARA, Cawangan Pulau Pinang, 13500, Permatang Pauh, Malaysia

<sup>2)</sup> Faculty of Mechanical Engineering, Universiti Teknologi MARA, 40450, Shah Alam, Selangor, Malaysia

<sup>3)</sup> Faculty of Mechanical Engineering, Universiti Teknologi MARA, Cawangan Johor, Kampus Pasir Gudang, 81750 Masai, Johor, Malaysia

\*Corresponding e-mail: mahfuzah065@uitm.edu.my; hussain305@salam.uitm.edu.my

**Keywords:** Advanced ceramic; injection moulding; powder metallurgy

**ABSTRACT –** Powder Injection Moulding (PIM) is a promising approach to produce an intricate near-net-shape product with cost-effective production. YSZ are renowned materials with their biocompatibility, superior dimensional stability and excellent mechanical properties resulting from mechanisms of transformation toughening. This study extensively investigates the microstructural properties of YSZ sintered part by CIM. The parts were injected moulded, debound and sintered. The microstructure properties at different powder loadings were discussed. A large porous region was clearly observed at 58 vol% compared to 60 vol%. Zirconia, yttria, carbon and oxygen elements were found through Energy-Dispersive X-Ray Spectrometer (EDX) without the presence of other interstitial elements.

## 1. INTRODUCTION

Preparation of feedstock in powder injection moulding (PIM) is a very crucial steps where the inadequacies of quality of the feedstock cannot be corrected by sub sequences processing adjustment [1]. Characterization of the powders and binders is the first step before proceeding to further processes. Moreover, characterization of the binder provides the parameters used in the mixing, injecting and debinding processes. The homogenous feedstocks were produced by mixing ceramic powder with the binders at the mixing stages monitored by the consistency of torque values. Binders supplied viscosity to the powder, thereby facilitating the process of filling feedstock into the molds during the injection molding stage. Concentration Powder Volume Percentage (CPVP) test is used to obtain the optimum powder loading ratio to ensure the success of PIM [2]. According to Iriany (2002), the common volume powder to binder ratio percentage ranges from 45% to 75% [3]. High powder loading had a low tendency to form high amount of porous due to its low binder content ratio. Furthermore, higher optimum powder loading percentage can minimize shrinkage, prevent cracking, and increase the densities as well as mechanical properties of materials [4].

## 2. METHODOLOGY

The YSZ powders used has 13 $\mu\text{m}$  of particle sizes and 5.60 g/cm<sup>3</sup> of pycnometer density. YSZ powder was mixed with binders of palm stearin (PS) and polyethelyne (PE) at 60:40 vol%. Powder loading of 57, 58, 59, and 60 vol% was chosen in this work. The mixing process was carried out at temperature, time and speed of rotation of 150 °C, 90 minutes and 30 rpm, respectively, to produce feedstock. The samples were injected at 170 °C in rectangular bar shape. Thermal pyrolysis (debinding) was performed where the parts were embedded in alumina powder that act as a wicking agent and heated in a furnace at 550 °C. The heating rate was 0.4 °C/min and the samples were soaked for 2 hours in order to remove the binders. The pre-sintering was carried out simultaneously after the debinding process at 1100 °C for 2 hours with a moderate heating rate to initiate the solidification process. The samples were subsequently sintered in the furnace for up to 1450 °C for 3 hours. The microstructures of as-sintered samples for all feedstocks were observed using tabletop microscope (SEM). The element existed in sintered samples were revealed by Energy-Dispersive X-Ray Spectrometer (EDX) using the same equipment.

## 3. RESULTS AND DISCUSSION

The characterization of the sintered parts is important to analyze the morphologies of the final samples. The goal of microstructure analysis was to ascertain that the particle was diffused with each other to form an as-sintered sample without the presence of other interstitial elements. In order to confirm the elements exist, further investigation was carried out using the back-scattered SEM, equipped with EDX as shown in Figure 1. The elemental contents of 3 mol% YSZ sintered sample at one point were found to be 50.646 wt% zirconia, 24.925 wt% carbon, 20.881 wt% oxygen and 3.458 wt% yttria. Higher carbon and oxygen content (wt%) were present because palm stearin and PE contained substantial amounts of carbon and oxygen. High carbon and oxygen values helped increase the hardness of the parts but weakened their ductility [5]. Figure 2 shows an example of the back-scattered SEM image for the surface, prepared at 57 and 60 vol% powder loadings. All samples, regardless of their powder loadings, showed an almost identical microstructure. All

sintered samples were not fully diffused in the morphology's studies; the grains overlapped with one another and some of the particles had only started to undergo necking as reported in previous studies using CIM methods with 3mol% YSZ powder [5]. Some of the grains grew where their grain boundaries were neatly attached onto each other with the size up to 30 $\mu\text{m}$ . The grain boundaries were able to withstand any external force that was applied on the particular part. By increasing the grain growth, the grain boundaries formed between each grain also increased. Thereby, strengthening the bond between grains builds up resistance to external force [5]. All the samples also showed different amounts of porosity. Lower powder loading had a high tendency to form the highest amount of porous due to lower powder content and higher binder content [6]. Hence, it will reduce the hardness value as reported by the previous study [7]. The porosity is known as the fraction of the component volume that is unoccupied by solid. The porosity occurs when the powder particles do not diffuse completely after the binder removing process completes. Thus, porosity is possible to be eliminated completely by controlling discontinuous grain growth and by sintering in hydrogen, oxygen or vacuum [8]

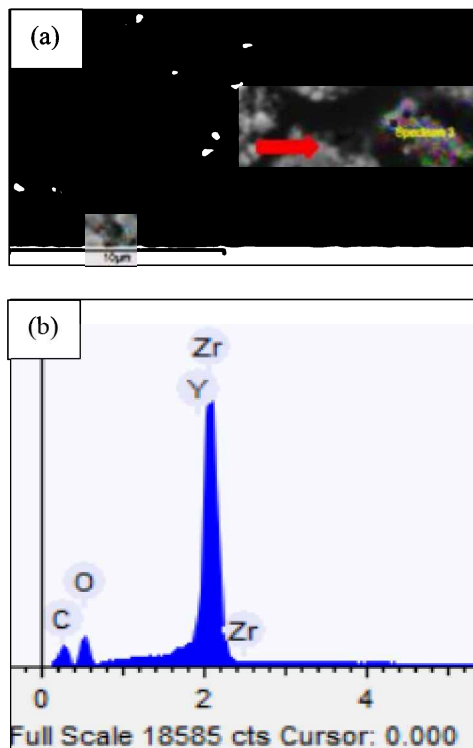


Figure 1. Microstructure of the sample prepared with 57vol% after sintering at 1450°C. (a) Back scattered SEM (b) Corresponding EDX peaks identified as carbon, oxygen, yttria and zirconia.

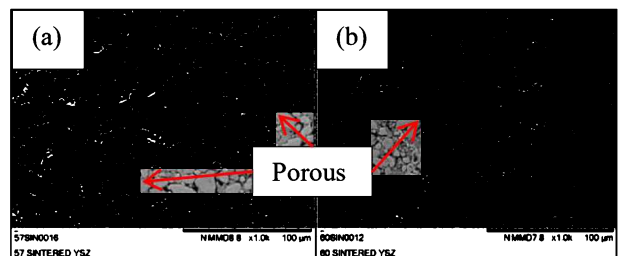


Figure 2 Back-scattered SEM image for the surface, prepared at (a) 57 and (b) 60 vol% powder loadings.

#### 4. CONCLUSION

Morphological studies showed that all samples incompletely diffused, and some of the particles retained the near spherical grain shape. Abundant void regions were clearly observed at the surface sintered samples at 57 vol% compared to other powder loadings. The elements exist shown by EDX were zirconia, carbon, oxygen and yttria with 50.646 wt%, 24.925 wt%, 20.881 wt% and 3.458 wt% respectively. Thus, no contaminated elements were present in the sintered samples.

#### REFERENCES

- [1] Gal, C. W., Han, S. S., Han, J. S., Lin, D., & Park, S. J. (2019). Investigation of stainless steel 316L/zirconia joint part fabricated by powder injection molding. *International Journal of Applied Ceramic Technology*, 16(1), 315-323.
- [2] Ismail, M. H. (2012). *Porous NiTi alloy by metal injection moulding (MIM) using partly water soluble binder system* (Doctoral dissertation, University of Sheffield).
- [3] Iriany. (2002). *Rheological study of metal injection molding feedstock containing palm stearin* (Doctoral dissertation, Universiti Kebangsaan Malaysia).
- [4] Roh, J. Y., Kwon, J., Lee, C. S., & Choi, J. S. (2011). Novel fabrication of pressure-less sintering of translucent powder injection molded (PIM) alumina blocks. *Ceramics International*, 37(1), 321-326.
- [5] Foudzi, F. M., Muhamad, N., Sulong, A. B., & Zakaria, H. (2013). Yttria stabilized zirconia formed by micro ceramic injection molding: Rheological properties and debinding effects on the sintered part. *Ceramics International*, 39(3), 2665-2674.
- [6] Zainudin, M. (2017). *Rheological and mechanical properties of Yttria Stabilized Zirconia (YSZ) produced by ceramic injection moulding* (Doctoral dissertation, Universiti Teknologi MARA).
- [7] Zainudin, M., & Ismail, M. H. (2017). Characteristic of the YTTRIA stabilized zirconia (YSZ) for ceramic injection moulding by using palm stearin as a primary binder. *Journal of Mechanical Engineering*, SI3(2), 133-143.
- [8] Denry, I., & Kelly, J. R. (2008). State of the art of zirconia for dental applications. *Dental materials*, 24(3), 299-307.

# Effect of sintering parameters on Cu/CNTs using quartz tube furnace under argon atmosphere

Nor Shamimi Shaari<sup>1,\*</sup>, Muhammad Hussain Ismail<sup>2</sup>, Mahfuzah Zainudin<sup>1</sup>, Ros Atikah Abd Kadir<sup>3</sup>, Mazyam Yahaya<sup>4</sup>, Rosniza Rabilah<sup>1</sup>

<sup>1)</sup> Faculty of Mechanical Engineering, Universiti Teknologi MARA Pulau Pinang,  
13500, Permatang Pauh, Pulau Pinang, Malaysia

<sup>2)</sup> Centre for Advanced Materials Research (CAMAR), Faculty of Mechanical Engineering,  
Universiti Teknologi MARA, 40450, Shah Alam, Malaysia

<sup>3)</sup> Faculty of Mechanical Engineering, Universiti Teknologi MARA Pasir Gudang,  
81750, Masai, Johor, Malaysia

<sup>4)</sup> Mechanical Engineering Department, Politeknik Nilai, 71760 Nilai, Negeri Sembilan, Malaysia

\*Corresponding e-mail: shamimi@uitm.edu.my

**Keywords:** Copper; carbon nanotubes; sintering

**ABSTRACT** – Carbon Nanotubes (CNTs) are considered to be an attractive reinforcement material for metallic matrix composites. The parameters of sintering in powder metallurgy (PM) are crucial in order to obtain good final parts of Cu/CNTs composites. This work attempts to investigate the effect of sintering parameters on physical properties using quartz tube furnace under argon atmosphere. The results showed that heating rate played an important aspect to produce a good sintered part. High heating rate induced large thermal stress and possibly increasing the pore volume and leading to swell. Thus, heating rate was useful in controlling microstructure evolution in sintering.

## 1. INTRODUCTION

In recent years, metal matrix composites (MMCs) have been widely investigated [1-3]. The production of MMCs based on copper (Cu) in electrical applications and bearing materials was being highly considered due to their excellent thermal and electrical conductivity properties [4]. One of the promising reinforcement in MMCs is by incorporating CNTs, owing to its superior mechanical strength as well as excellent electrical and thermal conductivities. The Cu/CNTs composites having higher potential for electrical sliding contact applications [5]. Incorporation of CNTs as reinforcement material in Cu could improve the properties of the current material due to its outstanding reputation. However, CNTs exhibited a major problem during fabrication with the metal matrix. The main issues in regulating Cu-matrix to maximizes overall performances are lack of complete understanding on how Cu-matrix attributes various composites properties and lack of method to control Cu-matrix attributes [6]. Metal-based CNTs composites prepared via powder metallurgy method usually possessed low mechanical properties than the expected due to problem of agglomeration of CNT powder which resulted porosity that existed in the composites [7]. Thus, these factors have a significant impact towards the success in formulating the Cu/CNTs composites. In this work, powder metallurgy (PM) route is a well-known technology considered to be the most common production technique for MMCs. This route involves

mixing, compacting and sintering. In order to get a good sintered part, different heating rate were used by deployed a quartz tube furnace. Quartz is highly purified glass favored for its inherent stability at high temperatures and its cleanliness. It usually used for temperature up to 1200° which suitable for this experiment. The final sintered part than was observed.

## 2. METHODOLOGY

In this study, the pristine CNTs (PCNTs) are and CNTs after acid treatment (ACNTs) were used. The powder was weighed and mixed using planetary ball mill at 250 rpm for 5 hours with 15 minutes interval. The mixtures of copper and CNTs powder were pressed into steel dies under a compression force of 8 tonne. After that, the sample was ejected gently from the die and the green part was produced. Then, the part was heated in a quartz tube furnace as shows in Figure 1 under argon atmosphere. Table 1 shows the parameter study and profile for the sintering process.

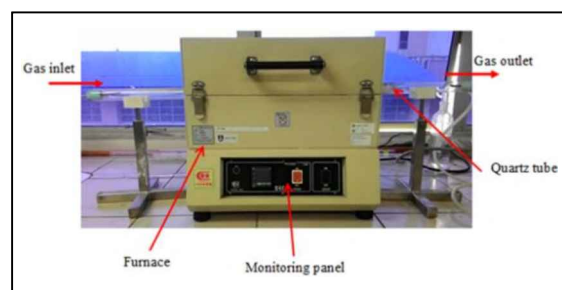


Figure 1 Quartz Tube Furnace.

Table 1 Parameter and profile for the sintering process.

Parameters	Trial 1	Trial 2	Trial 3	Trial 4
Heating rate 1 (°C/min)	5.0	3.0	2.0	1.0
Sintering temperature 1 (°C)	900	100	100	100
Soaking time 2 (min)	90	60	60	60
Heating rate 2 (°C/min)	-	2.0	1.0	0.5
Sintering temperature 2 (°C)	-	900	900	900
Soaking time 2 (min)	-	120	120	120

### 3. RESULTS AND DISCUSSION

Sintering process and parameters used during the sintering process are the most crucial aspects in ensuring good final parts of Cu/CNTs composites. For the first trial, the samples were sintered with the parameter as mentioned in Table 1. This trial had a similar condition with the study conducted by G. Goudah et al. [8] except for the gas flow rate which was set to 1.5 l/min. In their study, it was concluded that performing sintering at 900°C for 90 minutes was sufficient to produce a good product.

Figure 2(a) and 2(b) show the images of the sintered samples. Two out of four of the samples swelled instead of shrinking. In addition, the formation of pink layer was also observed covering the outer side of the samples, suggested that the samples were exposed more to the argon gas since they were located near to the inlet gas (refer to Figure 3). Meanwhile, the other two samples, crack and dark brown layer were observed. A study conducted by Yuan et al. [9], observed the effects of sample position and gas flow pattern on the sintering process. They suggested that the different gas flow patterns near the sintering surface resulted in variations of oxygen content from the incoming gas flow in the local sintering atmosphere, which affected the self-gettering process of the parts during sintering. Another cause of swelling in sintering was possibly due to gas trapped in closed pores thus, increasing in internal pressure that caused pore development [9].

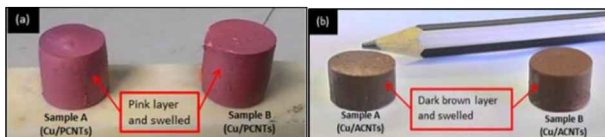


Figure 2 Samples of Cu/CNTs after sintering with sintering temperature of 900°C with heating rate of 5.0°C/min.



Figure 3 Samples position inside the quartz tube furnace under an argon gas flow.

For the second and third trials, the samples were sintered with the sintering profile as highlighted in Table 1. The samples were cracked and swelled. From the above results, the defective samples from trial 1 until trial 3 had occurred due to the rapid heating rate during sintering process. High heating rate induced large thermal stress and possibly increased the pore volume, thus leading to swelling [10]. The samples were finally sintered in an argon atmosphere at two stages (refer Table 1). Figure 4 compares the images of green and sintered parts. It was found that, after sintering process, the sample was successfully sintered and shrunk almost in every direction. The slow heating rate was used to prevent cracks and thermal stress in the samples.

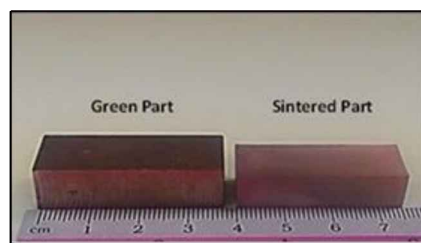


Figure 4 Images of green part and sintered part of Cu/CNTs composites.

### 4. CONCLUSIONS

It has been revealed that the Cu/CNTs composites has been successfully fabricated using conventional powder metallurgy route. The Cu/CNTs composites were successfully formulated by using heating rate of 0.5 °C/min. From observation, the unique aspects such as extremely high temperatures, fast heating rates, and short reaction times, may affect in controlling the behavior of the sample and microstructure.

### REFERENCES

- [1] Absawy E.-S. A. (2014). Manufacture And Mechanical Properties Study Of Copper- Matrix Nanocomposites Reinforced With Carbon Nanotubes, *Interciencia*, 246–248.
- [2] Pham V. T., Bui H. T., Tran B. T., Nguyen V. T., Le D. Q., Than X. T., Nguyen V. C., Doan D. P., and Phan N. M. (2011). The effect of sintering temperature on the mechanical properties of a Cu/CNT nanocomposite prepared via a powder metallurgy method,” *Adv. Nat. Sci. Nanosci. Nanotechnol.*, vol. 2, no. 1, 1–4.
- [3] Bakshi S. R., Lahiri D., and Agarwal A. (2010). Carbon nanotube reinforced metal matrix composites - a review, *Int. Mater. Rev.*, vol. 55, no. 1., 41–64.
- [4] Kainer K. (2006), Metal matrix composites: custom-made materials for automotive and aerospace engineering. Wiley-VCH.
- [5] Rajkumar K. and Aravindan S. (2011). Tribological studies on microwave sintered copper–carbon nanotube composites,” *Wear*, vol. 270, no. 9–10, 613–621.
- [6] Sundaram R. M., Sekiguchi A., Sekiya M., Yamada T., Hata K. (2018). Copper/carbon nanotube composites:research trends and outlook, *Royal Society Open Science* 5:180814,1-21.
- [7] Gubicza J. (2012). Defect structure in nanomaterials, 1st ed. WoodHead Publishing.
- [8] Goudah G., Ahmad F., and Mamat O. (2010). Microstructural Studies of Sintered Carbon Nanotubes ReinforcedCopper Matrix Composite, vol. 5, no. 3, 272–283.
- [9] Yuan X. N., Aminossadati S. M., Huo S. H., Schaffer G. B., and Qian M. (2012). The Effects of Sample Position and Gas Flow Pattern on the Sintering of a 7xxx Aluminum Alloy, *Metall. Mater. Trans. A*, vol. 43, no. November, 4345–4355.
- [10] German M. R. (1996). Sintering Theory and Practice. New York: John Wiley & Sons, Inc.

# Functional properties of hybrid MWCNT-Ag filled epoxy electrically conductive adhesive

Sow Jin Huat<sup>1</sup>, S.H.S.M. Fadzullah<sup>1,2,\*</sup>, M.M. Nasaruddin<sup>1</sup>, N.A.B. Masripan<sup>1,2</sup>, M.R. Mansor<sup>1,2</sup>, M.A. Salim<sup>1,2</sup>

<sup>1)</sup> Fakulti Kejuruteraan Mekanikal, Universiti Teknikal Malaysia Melaka,

Hang Tuah Jaya, 76100 Durian Tunggal, Melaka, Malaysia

<sup>2)</sup> Centre for Advanced Research on Energy, Universiti Teknikal Malaysia Melaka,

Hang Tuah Jaya, 76100 Durian Tunggal, Melaka, Malaysia

\*Corresponding e-mail: hajar@utem.edu.my

**Keywords:** Silver flakes; multiwalled carbon nanotube; electrically conductive adhesive; lap shear strength

**ABSTRACT** – This paper evaluates the effect of hybridizing silver flakes with varying filler loading of multiwalled carbon nanotube (MWCNT) to achieve good functional properties of the electrically conductive adhesive (ECA) with reduced amount of silver. Here, hybrid electrically conductive adhesive filled with 5 wt. % of silver flakes (Ag) and varying filler loading of the MWCNT were formulated using a centrifugal mixer and characterized in terms of the sheet resistance and lap shear test. The experimental results suggest that increasing MWCNT filler loading results in a decrease in the hybrid ECA sheet resistance, up to 7 wt. %, that is higher in electrical conductivity as compared with the normal ECA system. Nonetheless, the lap shear strength decreased with increasing MWCNT filler loading, since less amount of epoxy matrix is present in the hybrid ECA, hence result in inferior mechanical strength.

## 1. INTRODUCTION

Electrically conductive adhesive (ECA) is a composite in the form of dispersion of particle in an insulating adhesive matrix, in which the electrical conductivity is influenced by the filler, whilst the matrix determines the mechanical performance of the ECA composite system. The use of ECA have expanded widely in microelectronics industry, with the aim to replace solder by offering beneficial advantages in fastening and brazing, sealing, interconnection, and electrical shielding do come with friendliness advance as elimination of lead usage and reduce flux cleaner [1].

Silver is one of the most commonly employed metallic conductive fillers, because of its high electrical conductivity and chemical stability; whilst the multiwalled carbon Nanotube (MWCNT) exhibits numerous unique features in mechanical and electrical properties, as well as corrosion resistant, high strength, resistant to metal migration and lightweight [2]. Hence, mixing both materials as hybrid conductive materials for the ECA leads to promising potential for uses as interconnect materials

In this paper, functional properties of hybrid electrically conductive adhesive are studied with the aim to achieve good electrical conductivity and good lap shear strength for interconnect materials applications in electronic industries.

## 2. RESEARCH METHODOLOGY

Araldite 506 epoxy supplied by Sigma Aldrich was used as matrix. JEFFAMINE D-230 Polyether amine was supplied by Huntsman Singapore Pte LTD with a density of 79 lb/gal at 20°C. The fillers were MWCNT (average size: 5-10 µm) and silver flakes (average size :10 µm) with a relative density of 10.49 g/cm<sup>3</sup>. Specific amount of D-230 polyether amine was poured into the epoxy in a 10-ml container. The silver flakes and MWCNT conductive fillers were added into the resin container, which was then blended using a centrifugal mixture machine, Thinky Mixer Model ARE 310 for approximately 5 minutes at 2000 rpm. Table 1 shows the weight percentage to formulate 5 g of hybrid ECA. Following this, curing process took place, in which the formulated hybrid ECA was then placed in an oven at 100°C for 30 minutes.

Table 1 Formulation of hybrid ECA.

Silver flakes (wt. %)	MWCNT (wt. %)	Epoxy (wt. %)	Hardener (gram)
5 (0.15g)	90 (2.7g)	0.81	
5 (0.15g)	6 (0.18g)	89 (2.67g)	0.801
	7 (0.21g)	88 (2.64g)	0.792

JANDEL four-point probe was used to measure the specimen resistivity of printed ECA with reference to ASTM F390. The sheet resistivity was calculated by using Equation (1) below. As shown in Figure 1, a minimum of six strips of the hybrid ECA was printed onto a polymer substrate and minimum of 3 reading was taken for each specimen (strip) tested via four-point probe.

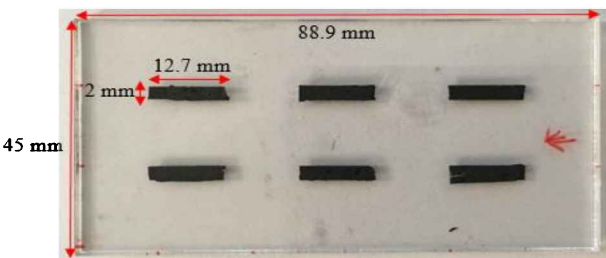


Figure 1 Printed hybrid ECA on substrate sheet.

$$P = \frac{V}{I} Gt, \Omega.cm \quad (1)$$

The universal testing machine was used to perform the lap shear test, in which the lap shear strength,  $\tau$  (MPa) is determined using an expression as given in Equation (2):

$$\tau = \frac{F}{A} \quad (2)$$

Whereby  $\tau$  is the lap shear strength in MPa,  $F$  is the load in Newton (N) and  $A$  is the cross-sectional area in  $\text{mm}^2$ . A schematic diagram of a lap shear test sample is given in Figure 2.

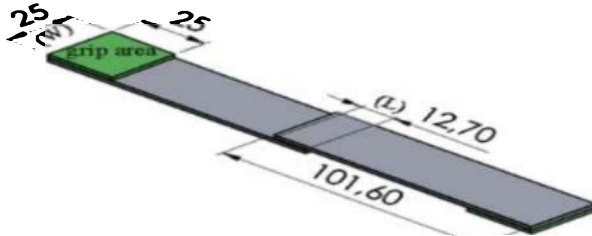


Figure 2 Schematic view of the tensile lap shear joint sample [3].

### 3. RESULTS AND DISCUSSION

From Figure 3, the average sheet resistance of the hybrid ECA decreases from  $3.23 \text{ k}\Omega/\square$  for 5 wt.% filler loading to  $2.31 \text{ k}\Omega/\square$  for 6 wt.% filler loading and lastly reached a plateau with a value of  $0.45 \text{ k}\Omega/\square$  at 7 wt.%, in which the percolation threshold is reached, associated with formation of conductive path with decreasing resistivity, thus indicate increasing conductivity of the hybrid ECA [3,4]. The trend suggests that an increase in filler loading results in a decrease in the volume resistivity. Clearly, the sheet resistance of hybrid ECA is lower than those of the normal ECA as reported in the literature [4], thus proven that enhanced electrical conductivity is achieved when hybridizing the conductive fillers by more than 90% relative to the normal ECA with single filler system.

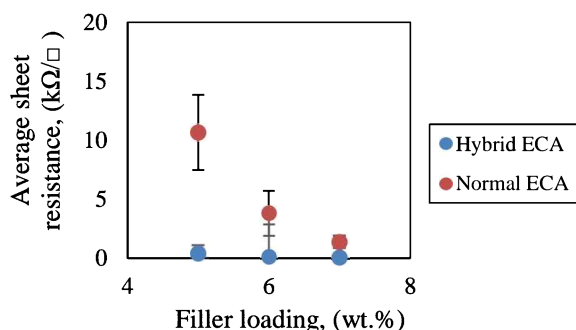


Figure 3 Average sheet resistance,  $\text{k}\Omega/\square$  vs. MWCNT filler loading wt.% of hybrid ECA in comparison with normal ECA [4].

Figure 4 presents the ECA average lap shear strength of the hybrid ECA, in which the value at 5 wt.% of MWCNT is highest (8.61 MPa). With increasing filler loading, at 6 wt.% MWCNT the shear strength reached a magnitude of 7.49 MPa, in which amount of epoxy is reduced by 1 wt.%, relative to the total amount of composite volume, thereby causing the hybrid ECA shear strength to drop. Such observation continued until the

MWCNT filler loading is up to 7 wt.%.

Visual inspection on the samples have shown that both hybrid ECA containing 5 and 6 wt.% MWCNT exhibit cohesive and adhesive failure, with some hybrid ECA retained on both sides of the aluminium substrate, and for the case of hybrid ECA at 7 wt.%, majority of the ECA is retained on either side, an indication of cohesive failure [5].

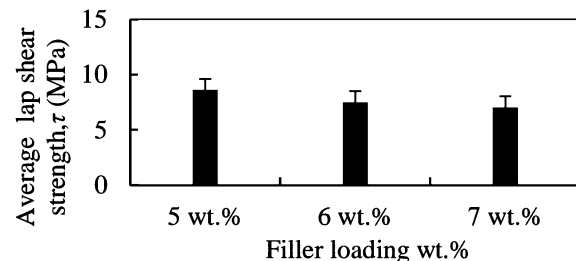


Figure 4 Average lap shear strength,  $\tau$  (MPa) against MWCNT filler loading wt.%.

### 4. SUMMARY

The experimental results from this study have shown that the percolation threshold of the hybrid ECA is achieved at 7 wt. % of the MWCNT (5 wt.% Ag + 7 wt. % MWCNT). Overall, hybridizing the fillers have proven to enhance the hybrid ECA conductivity as compared to those of the normal ECA. Nonetheless, increasing MWCNT filler loading results in a decrease in the hybrid ECA lap shear strength.

### ACKNOWLEDGEMENT

This work is funded by FRGS/2018/FKM-CARE/F00372 Ministry of Education Malaysia. Special thanks to Fakulti Kejuruteraan Mekanikal, Universiti Teknikal Malaysia Melaka (UTeM).

### REFERENCES

- [1] Zhang, R., Agar, J. C., & Wong, C. P. (2010, December). Recent advances on electrically conductive adhesives. In *2010 12th Electronics Packaging Technology Conference* (pp. 696-704).
- [2] Nasaruddin, M. M., Fadzullah, S. S. M., Omar, G., Mustafa, Z., Ramli, M., Akop, M. Z., Mohamad, I. S., & Coşut, B. (2019). The effect of aspect ratio on multi-walled carbon nanotubes filled epoxy composite as electrically conductive adhesive. *Journal of Advanced Manufacturing Technology (JAMT)*, 13(1).
- [3] Ekrem, M., Ataberk, N., Avci, A., & Akdemir, A. (2017). Improving electrical and mechanical properties of a conductive nano adhesive. *Journal of adhesion science and Technology*, 31(7), 699-712.
- [4] Raheem, A. M. A. (2018). *The Effect of Carbon Nanotube Aspect Ratio on the Functional Properties of Electrically Conductive Adhesive*. Universiti Teknikal Malaysia Melaka.
- [5] Ayatollahi, M. R., Shadlou, S., Shokrieh, M. M., & Chitsazzadeh, M. (2011). Effect of multi-walled carbon nanotube aspect ratio on mechanical and electrical properties of epoxy-based nanocomposites. *Polymer Testing*, 30(5), 548-556.

# Agglomerated TiO<sub>2</sub> powder synthesized by different methods for cold spray coating

A.R. Toibah<sup>1,\*</sup>, M. Yamada<sup>2</sup>, M. Fukumoto<sup>2</sup>

<sup>1)</sup> Fakulti Kejuruteraan Pembuatan, Universiti Teknikal Malaysia Melaka,  
Hang Tuah Jaya, 76100 Durian Tunggal, Melaka, Malaysia

<sup>2)</sup> Department of Mechanical Engineering, Toyohashi University of Technology,  
1-1, Tempaku-cho, Toyohashi, Aichi, 441-8580, Japan

\*Corresponding e-mail: toibah@utem.edu.my

**Keywords:** Titanium dioxide; synthesis; cold spray

**ABSTRACT** –In this study, agglomerated TiO<sub>2</sub> powders were synthesized via a simple hydrolysis (TiO<sub>2</sub>-H) and hydrothermal (TiO<sub>2</sub>-HT) process. The XRD patterns showed that single phase anatase TiO<sub>2</sub> was able to be produced by the hydrolysis and hydrothermal methods. SEM analysis confirmed that the TiO<sub>2</sub>-H powders were agglomerated into micrometer-size with homogeneous distribution, which is a preferable size for the cold spray process. On the other hand, TiO<sub>2</sub>-HT powders showed a formation of agglomerated particles with minimal particle agglomeration. Coating deposition showed that only TiO<sub>2</sub>-H powders can be deposited onto ceramic tile substrate. Meanwhile for TiO<sub>2</sub>-HT powders, only particle embedment can be observed on the surface of the substrate. The results reveal that morphology of the feedstock materials is important in order to build up the coating by cold spray process.

## 1. INTRODUCTION

The cold spray (CS) process is a thermal spray process that operates below the melting temperature of the feedstock materials [1]. Therefore, the properties of the powder material can be preserved even after the coating process. The success of the ceramic CS coating depends on several factors such as the nozzle geometry, characteristics of the feedstock powders (e.g. density, crystallinity, strength, and melting temperature), gas type, gas temperature, standoff distance, substrate and many more. Among these factors, feedstock materials play very important roles for ceramic deposition by CS method. Kim et al. [2] reported that the deposition mechanism of ceramic powders by CS depends on the particle size, shape, agglomeration, porosity, grain size, interphase, and etc. The agglomerated morphology is crucial as it coupled with pores, which promote easy material flow and a so-called fragmented bonding mechanism for cold spray deposition.

Suitable synthesis process with control parameters can produce feedstock powders for CS process in agglomerated structure with desired size, morphology, porosity, crystallinity and etc. Among the synthesis methods that can be used to produce TiO<sub>2</sub> powders, hydrolysis and hydrothermal method is among the simplest, cost-effective and scalable one. Moreover, these two process are possible to synthesis nanostructured powder which readily agglomerated into micrometer sized particles due to the tendency of the nanoparticles to agglomerate as a result of the van der

Walls attraction. Therefore, in this study, TiO<sub>2</sub> powders in agglomerated form were prepared as feedstock materials for CS process via the hydrolysis and hydrothermal methods using titanyl sulfate as the starting materials. The aim of the present study was to perform a comparative study on deposition of as-synthesized TiO<sub>2</sub> powders by CS process.

## 2. METHODOLOGY

### 2.1 Synthesis of TiO<sub>2</sub> Powders by Hydrolysis Method

10 wt.% of titanyl sulfate (TiOSO<sub>4</sub>. nH<sub>2</sub>O, Chameleon Reagent, Japan) was mixed with distilled water to perform the hydrolysis reaction and hereafter is known as TiO<sub>2</sub>-H. The prepared solution was stirred on a hot plate at 120 °C for 8 h. During the reaction, the white solution transformed into a clear solution. Upon completion of the synthesis, a white precipitate formed. The precipitate was washed with distilled water several times and then dried in an oven.

### 2.2 Synthesis of TiO<sub>2</sub> Powders by Hydrothermal Method

The TiO<sub>2</sub> powder synthesized by the hydrothermal method in this work was prepared using 10 wt.% of titanyl sulfate (TiOSO<sub>4</sub>. nH<sub>2</sub>O, Chameleon Reagent, Japan) and is hereafter known as TiO<sub>2</sub>-HT. The starting material was dissolved in distilled water by magnetic stirring for 30 minutes. The resultant transparent solution was then transferred to a Teflon-lined autoclave. The hydrothermal reaction was carried out at 150°C for 8h. Upon completion of the hydrothermal synthesis, the autoclave was allowed to cool naturally at room temperature. The obtained white precipitate was washed several times with distilled water and dried in an oven.

### 2.3 Preparation of Coatings by Cold Spray Process

The deposition of TiO<sub>2</sub> coatings was performed using a custom-made suction nozzle using a CGT KINETIKS 4000 (Cold Gas Technology, Germany). Ceramic tiles (INAX ADM-155M) were used as the substrate which had been grit blasted prior to their use. The gas temperature and pressure were 500°C and 3 MPa, respectively. Nitrogen gas was used as the process gas.

## 2.4 Characterization of TiO<sub>2</sub> Powder and Coating

The morphology of the as-synthesized powders and the obtained fractured cross-sections of the coating samples were characterized using a scanning electron microscope (SEM: JSM-6390, JEOL) and a field emission scanning electron microscope (FESEM: SU8000, Hitachi. The phase analysis of the synthesized powders were characterized by X-ray diffraction (XRD: RINT 2500, Rigaku) with Cu-K $\alpha$  radiation.

## 3. RESULTS AND DISCUSSION

Figure 1 shows the XRD patterns of TiO<sub>2</sub>-H and TiO<sub>2</sub>-HT powders which confirms the characteristics of the anatase phase of TiO<sub>2</sub> and are in good agreement with PDF card No. 21-1272. Figure 1 also revealed that the hydrothermal process produced TiO<sub>2</sub> powder with higher crystallinity compared to the hydrolysis method which indicates that TiO<sub>2</sub>-HT is of a bigger crystallite size. It is believed that this higher crystallinity characteristic will reduce the capability of the TiO<sub>2</sub> powder to be deposited by CS method due to difficulties to break the crystalline bridge upon the particle impact.

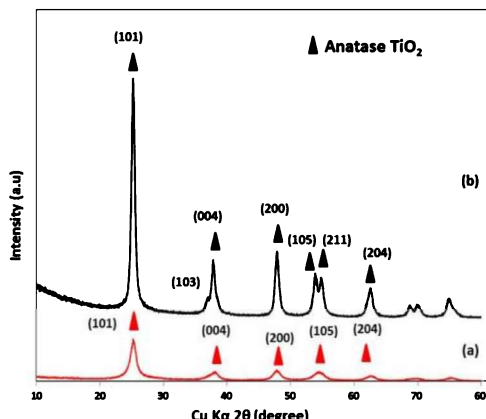


Figure 1 XRD pattern of TiO<sub>2</sub> powders that were synthesized by (a) hydrolysis (TiO<sub>2</sub>-H) and (b) hydrothermal (TiO<sub>2</sub>-HT).

SEM observation showed that the morphology and powder distribution for these two processes were not similar. From the SEM images, it can be seen that the TiO<sub>2</sub>-H powders have a relatively uniform distribution of powder and are agglomerated in the range from 5-20  $\mu$ m as revealed in Fig. 2(a). Meanwhile for the TiO<sub>2</sub> powders, which were synthesized by the hydrothermal method, agglomerated powder, with an aggregated particle size, is in the range of 0.5-25  $\mu$ m and random distribution was observed as shown in Fig. 2(b). Furthermore, Fig. 2(c) depicts that TiO<sub>2</sub>-H contains more pores as compared to TiO<sub>2</sub>-HT (Fig. 2(d)) which shows that TiO<sub>2</sub>-H has a more porous and loose structure between the fine particles.

Figure 2(e) and (f) show the cross-section of the TiO<sub>2</sub> coating that was obtained using the synthesized TiO<sub>2</sub> powders for both methods. It can be seen that the TiO<sub>2</sub>-H powders can be deposited on the ceramic tiles substrate and form a coating of about 50  $\mu$ m thickness as shown in Figure 2(e). Meanwhile, in the case of the TiO<sub>2</sub>-HT powders, only particle embedment, with very few particles attached to the surface of the substrate, was observed. The results obtained in this study revealed that

only TiO<sub>2</sub>-H powders were successful in building-up the coating due to the presence of higher amount of porosity and lower crystallinity which initiated the particles to break down during the collision [3]. The finding of this study suggested that coating of ceramic material by kinetic spraying is affected by the crystallinity, size and shape of the starting feedstock materials.

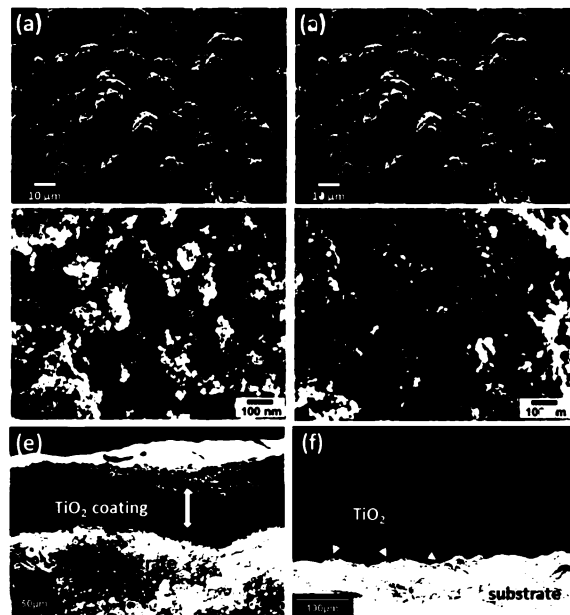


Figure 2 SEM images of TiO<sub>2</sub> powders that synthesized by different methods and their cross-sectional view of coating; TiO<sub>2</sub>-H (a, c & e) and TiO<sub>2</sub>-HT (b, d & f).

## 4. CONCLUSION

In conclusion, the feasibility of synthesizing anatase TiO<sub>2</sub> powders specifically for a cold spray process was studied by hydrolysis and hydrothermal methods at low synthesis temperatures. The results showed that only agglomerated TiO<sub>2</sub>-H powders could be used as feedstock material for the CS process due to the presence of a more porous structure. This study shows that selection of appropriate morphology together with the crystallinity of the feedstock powders is important to produce a ceramic coating on the substrate by cold spray.

## ACKNOWLEDGEMENT

The authors would like to thank to Toyohashi University of Technology and Universiti Teknikal Malaysia Melaka (PJP/2018/FKP(3A)/S01583) for laboratory facilities and financial assistance.

## REFERENCES

- [1] Viscusi, A., Astarita, A., Gatta, R. D., & Rubino, F. (2019). A perspective review on the bonding mechanisms in cold gas dynamic spray. *Surface Engineering*, 35(9), 743-771.
- [2] Kim, H., Yang, S., Pawar, R. C., Ahn, S. H., & Lee, C. S. (2015). Role of TiO<sub>2</sub> nanoparticles in the dry deposition of NiO micro-sized particles at room temperature. *Ceramics International*, 41(4), 5937-5944.
- [3] Jeandin, M., Rolland, G., Descurninges, L. L., & Berger, M. H. (2014). Which powders for cold spray?. *Surface Engineering*, 30(5), 291-298.

# Analysis on noise absorption coefficient for polyurethane filled by waste tire dust (PU-WTD) composite foam using response surface method

Jeefferie Abd Razak<sup>1,\*</sup>, Nor Amalina Rasmi<sup>1,2</sup>, Marina Mohamad<sup>1</sup>, Noraiham Mohamad<sup>1</sup>, Saw Chun Lin<sup>3</sup>, Lau Kok Tee<sup>4</sup>

<sup>1)</sup>Fakulti Kejuruteraan Pembuatan, Universiti Teknikal Malaysia Melaka,  
Hang Tuah Jaya, 76100 Durian Tunggal, Melaka, Malaysia

<sup>2)</sup>Hartalega Sdn. Bhd., No.7, Kawasan Perusahaan Suria, 45600, Bestari Jaya, Selangor, Malaysia

<sup>3)</sup>Politeknik Ungku Omar, Jabatan Kejuruteraan Mekanikal, Jalan Raja Musa Mahdi, 31400, Ipoh, Perak, Malaysia

<sup>4)</sup>Fakulti Teknologi Kejuruteraan Mekanikal & Pembuatan, Universiti Teknikal Malaysia Melaka,  
Hang Tuah Jaya, 76100 Durian Tunggal, Melaka, Malaysia

\*Corresponding e-mail: jeefferie@utem.edu.my

**Keywords:** Noise absorption; polyurethane; waste tire dust

**ABSTRACT** – Porous nature of rigid polyurethane has permits them to serve as noise absorber. This study has report the optimization of PU preparation in relation to the effects of waste tire dust loading and stirring period, toward the maximum coefficient of noise absorption ( $\alpha$ ). Two-level full factorial design was applied to evaluate  $\alpha$  response. It was found that, at 25.00wt.% of WTD and 5 mins of stirring period, able to produce optimum  $\alpha$  with 98.20 of  $R^2$  at lowest S.D of  $\pm 0.019$ . Morphological observation via SEM, suggests the PU/WTD composite foam with open pore cell structure, could enhanced the noise absorption coefficient.

## 1. INTRODUCTION

In general, the attenuation of noise and vibration can be enhanced by using the porous material structure. Polyurethane based composite foam is used as porous material for noise absorption and vibration damping. Addition of waste tire dust as rubber element in composite foam, could responsible as viscoelastic phase to enhance damping of PU material. However, up till now, there are still scarce study related to properties optimization of PU based composite foam. Especially, the exploratory study that correlates the relationship between the PU cell structure and its noise absorption.

In this study, the relationship between independent processing variables like WTD filler loading and stirring period with the resulted PU/WTD composite foam morphologies and noise absorption performance was established. Statistical design of experiment approach by using a two-level full factorial with response surface methodology was applied to simplify the experimental works and results analysis.

Noise is an important design consideration that must be carefully be considered, especially in vehicles and transportation field. Good material selection and consideration is required to complement with this. Research by Sung et al. [1] has successfully proved the potential of polymeric material to enhance the sound absorption performance. A good structural polymeric material with homogeneous pores dimension is commonly required for this purpose. Hence, the study of PU/WTD composite foam, which reported in this work, would provide the understanding towards the structure-

property relationships, between the studied processing variables and  $\alpha$  response.

## 2. METHODOLOGY

In this work, the PU/WTD composite foam preparation is performed through free-rise molding of 1:1.4 formulation ratio of between polyols and isocyanate. Polyols code R3114 was supplied by PolyGreen Chemicals Sdn. Bhd., while toluene di-isocyanate (TDI) with chemical formula of  $C_9H_{14}N_2O_2$  was supplied by Sigma-Aldrich (M) Sdn. Bhd., and WTD (< 250 $\mu$ m PSD size) was donated by GL Rubber Ind. Sdn. Bhd. Processing variables used are the WTD filler loading (5, 15 and 25 wt.%) as factor A and at different stirring period (5, 10 and 35 mins) as factor B. Open free rise mold with dimension of (200 x 200 x 100) mm. The optimization of PU/WTD preparation has been performed by the Design of Experiment (DOE) approach of Design Expert®. Two level full factorial ( $2^2$ ) with two factor of WTD loadings (5 – 25 wt.%) and stirring period (5 – 35 mins) with three repetition at a centre point and one block was executed to produce seven sets of experiment, in total. The polyols/WTD and TDI was further stirred at 1000 rpm within 2 mins prior of pouring and has allowed for further curing at 60°C for 24 hrs.

The dependent response that was evaluated in this work is noise or sound power absorption coefficient,  $\alpha$ . The test was performed in accordance to ASTM E1050-098 by using an impedance tube comprising of two units of microphones and digital frequency analysis system. Different frequencies of noise sound (500 – 4500 Hz) is introduced through the sound source. The wave ratio (SWR) indicates the ration between of maximum pressure into minimum pressure, and wave ratio value is used to determine the reflection coefficient amplitude ( $R_n$ ), as well as absorption coefficient,  $\alpha$ . This was simplified as in the following equation (1) into (3).

$$\text{Wave Ratio, SWR} = (A + B) / (A - B) \quad (1)$$

$$\begin{aligned} \text{Sound Power Reflection Coefficient, } R_n \\ R_n = [(SWR - 1) / (SWR + 1)]^2 \end{aligned} \quad (2)$$

$$\text{Sound Power Absorption Coefficient, } \alpha \\ \alpha = 1 - R^2 n = 1 - [(SWR - 1)^2 - (SWR + 1)^2] \quad (3)$$

For internal foam pore structure, the morphological observation using Zeiss Evo-50 SEM was performed under 150x of magnification power.

### 3. RESULTS AND DISCUSSION

In this work, the PU/WTD composite foams were carefully tested for their sound absorption coefficient,  $\alpha$  performance. The sound absorption coefficient shows an identical trend at higher frequency range starting at 4000 into 4500 Hz. This selected range is based on permanent human hearing loss that possibly occur at 4000 Hz and above as confirmed by OSHA (section III, Chap. 5 – Hearing Loss) and the value of  $\alpha$  was taken at 4250 Hz. The following Table 1, has summarized the experimental strategy and the extracted data response.

Table 1 Parametric results of PU/WTD composite foams.

WTD loadings (wt.%)	Stirring period (mins)	Sound abs. coeff. ( $\alpha$ )
5	5	0.2814
5	35	0.2103
15	20	0.2410
15	20	0.2772
15	20	0.2512
25	5	0.3935
25	35	0.1278

From the DOE analysis, the effect list shows that the factor B (stirring period) has significantly contributed about 73.17% toward the  $\alpha$  than only about 0.57% of contribution by factor A (WTD loadings). The 3-D response surface (Figure 1) showcase the interaction between factor A and B toward  $\alpha$  response. It was clearly depicts that the  $\alpha$  was only maximum at the combination interaction at maximum of WTD loading (25 wt.%) but at minimum of stirring period (5 mins). In preparing the PU/WTD composite foams, the stirring period need to be strictly controlled for not being too long as this will rupture the macromolecular structure of polymer, which obstruct the growth of cell structure, during the PU foaming. However, this factor also need to be ensure for not too short, as this will limits the dispersionability of added filler. Thus, the stirring period provides a major contribution towards the  $\alpha$  response.

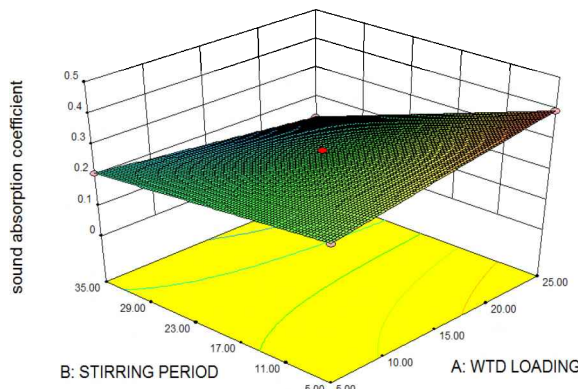


Figure 1 3-D response surface for  $\alpha$ .

For the response studied, the regression model equation has been generated (Equation 4). The linear equation contains of 1 offset, 2 linear and 1 interaction terms. Positive constant value indicate the parameter was at minimum level of the range while the negative constant value has indicated that the entire parameters are at higher level of their range. Big gap of percentage contribution between the factor A and B suggests less dependency between those variables. The negative value of factor B has justified higher contribution of this factor in effecting the  $\alpha$ . In addition, presence of high content of WTD, has responsible to absorb the noise through viscoelastic and damping mechanism.

$$\alpha = 0.25 + 7.4006e-0.003A - 0.084B - 0.049AB \quad (4)$$

The *p-value* of overall model was significant at 0.0269 which indicate the lowest probability about 2.69% of chance for the *Model of F-Value* this large could occur due to noise. The *p-value* for factor A is insignificant while both factor B and interaction term AB are significant. In overall, the coefficient of determination of  $R^2$ , was about 0.9829 which implies the higher desirability of the response studied which attributable by the tested independent variables.

The pore morphology of for optimum PU/WTD composite sample was depicted in Figure 2. Presence of WTD filler has modified the close pose structure of unfilled PU (Fig. 2a) into open pores (Fig. 2b). The acoustic performance is good for open cell. Open cell provides large surface area of cell wall, which acted as efficient barrier for sound energy dissipation, through the interconnected pores. The energy from the noise as dissipated as wave that creates friction in the pores before it changed into heat [2]. Observation on cell wall and pores morphologies provides hints on the variation of  $\alpha$  experimental values. Hence, clear property-morphology and performance inter-relationships has been successfully established in this research work.

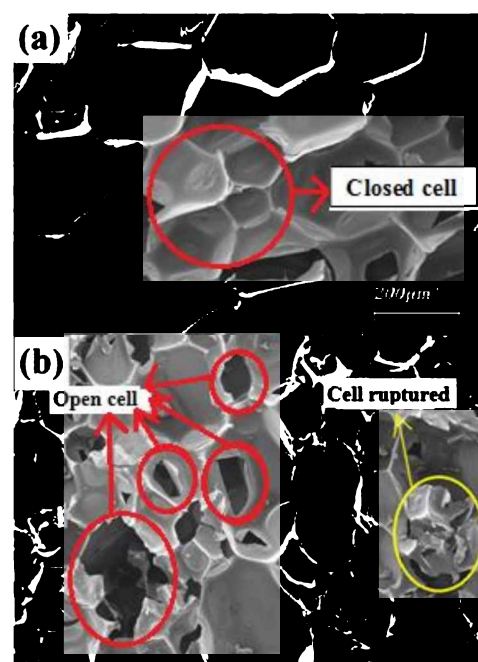


Figure 2 PU/WTD composite foam cell structure.

#### 4. CONCLUSION

In overall, it was found that the WTD filler loading and stirring period variables has significantly affecting the resulted  $\alpha$  response. The optimum PU/WTD composite foam could be manufactured at 25wt.% WTD at 5 mins of stirring period. Optimum variables also effecting the formation of internal pores cell morphology that gives benefits for improving the sound or noise absorption coefficient,  $\alpha$ .

#### ACKNOWLEDGEMENT

Authors would like to appreciate MOE and UTeM for funding the research: FRGS/2018/FKP-AMC/F00381.

#### REFERENCES

- [1] Sung, G., Kim, J. W., & Kim, J. H. (2016). Fabrication of polyurethane composite foams with magnesiumhydroxide filler for improved sound absorption. *Journal of Industrial and Engineering Chemistry*, 44, 99-104.
- [2] Gayathri, R., Vasanthakumari, R., & Padmanabhan, C. (2016). Sound absorption, thermal and mechanical behaviour of polyurethane foam modified with nanosilica, nano clayand crumb rubber fillers. *International Journal of Scientific & Engineering Research*, 4(5), 301-308.

# The effect of water content on biomechanical behavior of articular cartilage: An experimental study

Mohd Juzaila Abd Latif<sup>1,2,\*</sup>, Yew Sin Ru<sup>2</sup>, Mohamad Shukri Zakaria<sup>2</sup>

<sup>1)</sup> Advanced Manufacturing Center, Universiti Teknikal Malaysia Melaka,  
Hang Tuah Jaya, 76100 Durian Tunggal, Melaka, Malaysia

<sup>2)</sup> Fakulti Kejuruteraan Mekanikal, Universiti Teknikal Malaysia Melaka,  
Hang Tuah Jaya, 76100 Durian Tunggal, Melaka, Malaysia

\*Corresponding e-mail: juzaila@utem.edu.my

**Keywords:** Articular cartilage; water content; indentation

**ABSTRACT** – It is well recognized that degeneration of articular cartilage is the main cause of osteoarthritis. The cartilage mainly consists of water. Although extensive studies were carried out, the significant of water content has yet to be explored. Therefore, the aim of this study is to examine the effect of water content of the cartilage on biomechanical behavior of cartilage tissue using experimental method. Cartilage specimens were prepared and tested using indentation test rig. Significant effect of the water content towards the cartilage deformation was observed which denotes the importance of preserving the water content in experimental study.

## 1. INTRODUCTION

Osteoarthritis (OA) is the most common form of joint disease around the world. The OA syndrome includes joint pain and functional limitation of the affected joint that often impair the quality of life. It is frequently affects the hip, hand, feet and spinal joints but mostly prevalence at the knee joint [1, 2]. The main cause of OA is the degeneration of articular cartilage which could due to the age, genetic predisposition and obesity factors [3] [4].

Articular cartilage is a common type of hyaline cartilage to support the joint motion. Cartilage a smooth and glistening bluish-white tissue that encloses the articulating bone ends in synovial joint. There are two distinct phases of articular cartilage which are the fluid and solid phases. The fluid phase is mainly composed of 60-85% of water while the solid phase is composed of 15-22% collagens, and 4-7% proteoglycans by wet weight [5]. A healthy cartilage consists of different amount of water content from the surface to depth of cartilage [4].

Previous studies have found that the biomechanical parameters of the cartilage decreased between 20-80% during the early pre-OA stage [4-6]. However, most of the studies have been carried out using fresh cartilage to investigate the biomechanical behaviour [6,7]. The effects of water content of cartilage on its biomechanical behaviour are yet to be explored. Therefore, this study aims to examine the effects of water content on biomechanical behaviour of articular cartilage using experimental method.

## 2. METHODOLOGY

### 2.1 Specimen Preparation

The cartilage samples were harvested from femoral

head of bovine hip joints obtained from a local abattoir within 24 hours of slaughter as shown as Figure 1(a). Excessive tissues or any damaged surfaces was removed from the cartilage by using scalpel. Throughout the preparation process, the cartilage was washed with phosphate buffered saline (PBS) solution periodically to keep the cartilage hydrated.

The cartilage from the femoral head was then separated subchondral bone and cut into 4 mm diameter as shown in Figure 1(b). The cartilage specimens ( $n=7$ ) were then kept at PBS-moistened condition in room temperature of 25°C prior testing.

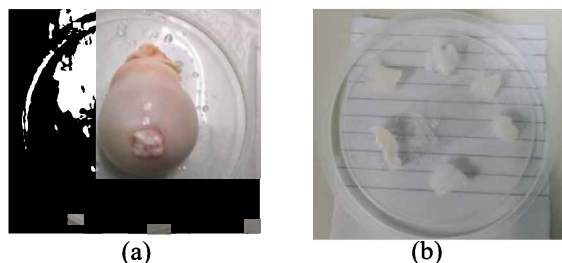


Figure 1 (a) Bovine hip joint and (b) cartilage specimens.

### 2.2 Water Content

The water content of cartilage specimens was examined for every 30 minutes. The specimens were weighed on analytical balance and recorded to calculate the percentage of water content based on the wet weight and dried weight. The percentage of water content was determined using Equation (1) [8].

Percentage of water content =

$$\left[ \frac{\text{wet weight} - \text{dried weight}}{\text{wet weight}} \right] \times 100\% \quad (1)$$

### 2.3 Indentation Test

The creep indentation test was performed on the cartilage specimens to study the time and deformation responses of the cartilage. The test was performed using the indentation test apparatus using spherical impermeable indenter shown in Figure 2. The overall indentation weight was 0.38 N which was the weight of the shaft assembly. The data collected from the linear variable differential transformer (LVDT) and force transducer were connected to data acquisition (DAQ) to store the displacement and force data into computer using LabVIEW 8.5.1 software.

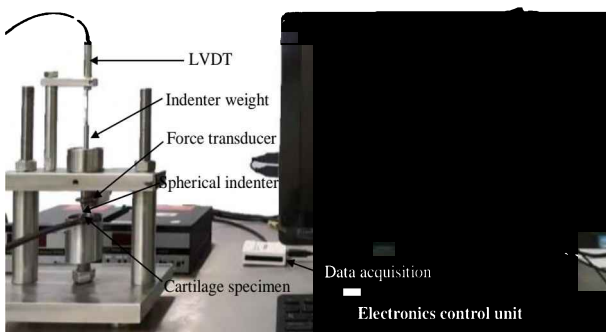


Figure 2 Indentation test setup.

### 3. RESULTS AND DISCUSSION

The average percentage of water content of cartilage specimens for initial state, 30 minutes, 60 minutes and 90 minutes were  $76.8 \pm 4.5\%$ ,  $72.9 \pm 6.1\%$ ,  $66.1 \pm 9.8\%$  and  $57.9 \pm 12.6\%$  respectively as shown in Figure 3. The initial percentage of water content was found to be in similar range of previous studies which is 70% to 80% [6,8]. Based on the results, the rate of dehydration increased to 5% at the first 30 minutes reaching to 25% after exposed in room temperature for 90 minutes.

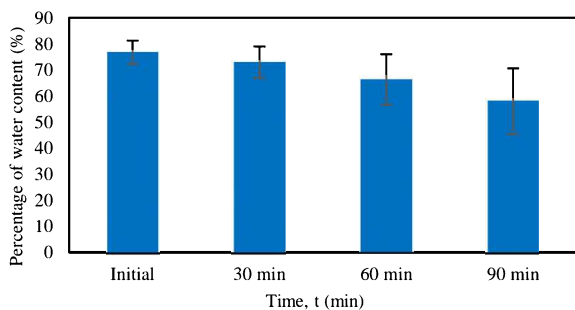


Figure 3 Water content of cartilage specimen.

This phenomenon was also found in the study from Boettcher et al. (2016) where the cartilage specimens were dehydrated overnight at room temperature of  $25^\circ\text{C}$  and a moisture environment of 49% [8]. The time needed for complete dehydration was 8-10 hours. The thickness of cartilage samples was decreased as the water content evaporated. Moreover, the general structure and the GAG content of the specimens of cartilage were altered after dehydration.

The equilibrium deformation of cartilage specimens for initial state, 30 minutes, 60 minutes and 90 minutes were  $0.592 \pm 0.050$  mm,  $0.397 \pm 0.097$  mm,  $0.257 \pm 0.045$  mm and  $0.247 \pm 0.031$  mm respectively as shown in Figure 4. It is expected that the highest deformation at the cartilage was found at initial state with the value of  $0.592 \pm 0.050$  mm. This was due to water content was the highest in the initial state and therefore lead to highest deformation of cartilage specimens. In 30 minutes, the deformation was decreased to 33% from the initial state. The deformation was then continuously decreased to 58% at 90 minutes.

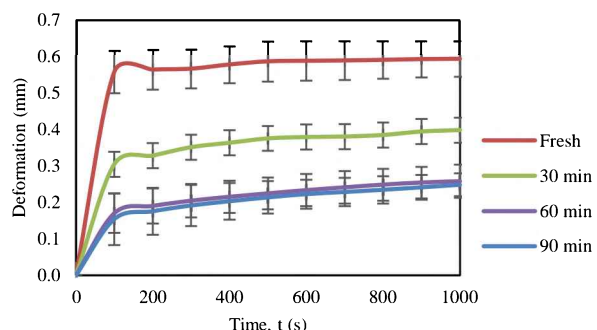


Figure 4 Deformation of articular cartilage.

### 4. CONCLUSIONS

The study presented the importance of preserving the water content in order to study the deformation of articular cartilage. Based on the results, there was significant effect of the water content towards the deformation of the cartilage. Therefore, consideration of the exposed period should be given during the preparation and testing of the cartilage specimen.

### ACKNOWLEDGEMENT

This study is fully supported by Universiti Teknikal Malaysia Melaka (UTeM).

### REFERENCES

- [1] Michael, J.W.P., Schlüter-Brust, K.U., & Eysel, P. (2010). The Epidemiology, Etiology, Diagnosis, and Treatment of Osteoarthritis of the Knee. *Deutsches Aerzteblatt Online*, 107(9).
- [2] Sadeghi, H., Lawless, B. M., Espino, D. M., & Shepherd, D. E. T. (2018). Effect of frequency on crack growth in articular cartilage. *Journal of the Mech. Behavior of Biomed. Materials*, 77, 40–46.
- [3] Lambova, S.N., & Muller-Ladner, U. (2018). Osteoarthritis-Current Insights in Pathogenesis, Diagnosis and Treatment, 14(2), 91–97.
- [4] Berberat, J.E., Nissi, M.J., Jurvelin, J.S., & Nieminen, M.T. (2009). Assessment of interstitial water content of articular cartilage with T1relaxation. *Magnetic Resonance Imaging*, 27(5), 727–732.
- [5] Hashim, N.H., Latif, M.J.A., & Jaafar, Y.L. (2015). The effects of contact area and surface curvature on biomechanical behavior of articular cartilage. *Proceedings - 2015 2nd Int. Conf. on Biomedical Eng., ICoBE 2015*, 30–31.
- [6] Knecht, S., Vanwanseele, B., & Stüssi, E. (2006). A review on the mechanical quality of articular cartilage - Implications for the diagnosis of osteoarthritis. *Clin. Biomech.*, 21(10), 999–1012.
- [7] Armstrong, C.G., & Mow, V.C. (1982). Variations in the intrinsic mechanical properties of human articular cartilage with age, degeneration, and water content. *Journal of Bone and Joint Surgery - Series A*, 64(1), 88–94.
- [8] Boettcher, K., Kienle, S., Nachtsheim, J., Burgkart, R., Hugel, T., & Lieleg, O. (2016). The structure and mechanical properties of articular cartilage are highly resilient towards transient dehydration. *Acta Biomaterialia*, 29, 180–187.

# The effect of water content of articular cartilage on low-field magnetic resonance imaging

Mohd Juzaila Abd Latif<sup>1,2,\*</sup>, Tan Kae Chin<sup>2</sup>, Nur Hazwani Mokhtar<sup>3</sup>

<sup>1)</sup> Advanced Manufacturing Center, Universiti Teknikal Malaysia Melaka,  
Hang Tuah Jaya, 76100 Durian Tunggal, Melaka, Malaysia

<sup>2)</sup> Fakulti Kejuruteraan Mekanikal, Universiti Teknikal Malaysia Melaka,  
Hang Tuah Jaya, 76100 Durian Tunggal, Melaka, Malaysia

<sup>3)</sup> Fakulti Teknologi Kejuruteraan Mekanikal dan Pembuatan, Universiti Teknikal Malaysia Melaka,  
Hang Tuah Jaya, 76100 Durian Tunggal, Melaka, Malaysia

\*Corresponding e-mail: juzaila@utem.edu.my

**Keywords:** Articular cartilage; water content; low-field MRI

**ABSTRACT** – Osteoarthritis (OA) is mainly caused by the degeneration of articular cartilage in human joint. At early stage of OA, the biomechanical properties are caused by morphological changes of the cartilage. The MRI techniques were used to examine OA. However, these MRI techniques are performed at the progressive stage of OA to describe the morphological alterations of cartilage. The ability to detect the disease at its earliest stages is crucial as the treatment of OA is often depending on early detection of symptomatic patient. Therefore, it is essential to develop an assessment to detect the early stage of degenerative articular cartilage using low-field MRI scan image based on the water content of cartilage.

## 1. INTRODUCTION

Osteoarthritis (OA) is the most common human joint disease worldwide. It is normally occurs in the joint that has weight-bearing such as hips, knees and spine [1]. The early symptom of OA includes pain during movement and after overuse. Approximately 10% of the persons over 65 years old or 2% of the adult population are suffer with the OA [2]. It is well known that the main cause of OA is degeneration of articular cartilage.

Articular cartilage is a thin tissue layer that covers the end of articular bone in human joint. It is a biphasic medium consists of fluid phase and solid phase. The main components in the fluid phase is water which contributes up to 80% of the wet weight of the articular cartilage [3]. The water forms from the combination of the frictional resistance and the pressurization of the water flow within the cartilage which is critical to withstand significant loads [4].

Magnetic resonance imaging (MRI) has become an important diagnosis severe OA patient. It is a non-invasive imaging method to visualize articular cartilage. In previous studies, similar diagnostic accuracy, specificity and sensitivity were observed between the high-field and low-field MRI systems while imaging the extremity human joints [5,6]. However, less attention was being made to study the cartilage using the low-field MRI. Furthermore, most of the studies were investigated using the fresh and healthy cartilage where the water content was in the range of 70% to 80% [5-7]. Therefore, this study aims to examine the effects of water content of articular cartilage on MRI image.

## 2. METHODOLOGY

### 2.1 Specimen Preparation

The cartilage specimens were obtained from bovine humeral head of hip joint as shown in Figure 1(a). The cartilage layer was separated from the subchondral bone by using scalpel. The layer was then cut into 4 mm diameter cartilage specimen ( $n=7$ ) as in Figure 1(b) and soaked in the phosphate buffered saline (PBS) to prevent dehydration.



Figure 1 (a) Humeral head and (b) cartilage specimens.

### 2.2 Water Content

The specimens were exposed at the room temperature of 25 °C and weighed at every 30 minutes using analytical balance. The percentage of the water content of the cartilage was calculated using Equation (1) [8].

$$\text{Percentage of water content} = \frac{\text{Wet weight} - \text{Dry weight}}{\text{Wet weight}} \times 100\% \quad (1)$$

### 2.3 Magnetic Resonance Imaging

The cartilage specimens were scanned using 0.18T low-field MRI Esaote C-scan system as shown in Figure 2(a). The specimens were scanned using gradient echo imaging sequence as used in previous study [9]. Each specimen was placed axially at the centre of the coil during scanning as in Figure 2(b).



Figure 2 (a) MRI system (b) specimen setup in MRI coil.

### 3. RESULTS AND DISCUSSION

Figure 3 shows the percentage of water content of the cartilage from the initial and 30 to 90 minutes exposed at room temperature. The average percentage of water content at the initial condition was  $76.8 \pm 4.5\%$  which was in similar range as in previous study [10]. It was expected that the percentage of water content decreased as the time increased [11]. In the first 30 minutes, the percentage of water content reduced to 5% from the initial condition and reached to 25% at 90 minutes.

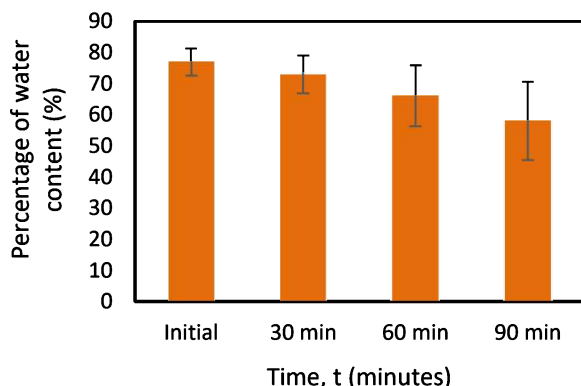


Figure 3 Percentage of water content at different times.

In terms of the MRI image, the greyscale was also decreased as the time increased as shown in Figure 4. This phenomenon was also observed in previous study [12]. The average value of the greyscale value at the initial condition was  $2201.3 \pm 241.3$ . At the first 30 minutes, the greyscale value reduced to 15% and 36% at 90 minutes.

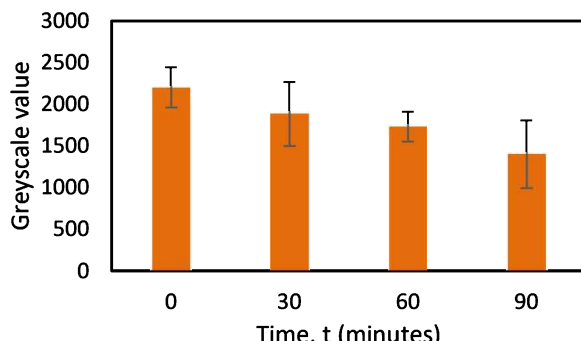


Figure 4 MRI image greyscale at different times.

### 4. CONCLUSION

The study presented the importance of preserving the water content in order to study the articular cartilage using MRI image. Based on the results, there was significant effect of the water content towards the greyscale of the MRI image. It indicates that the time of the MRI scan should be considered because the cartilage will be exposed in heat during the scan. These could also denote the potential application of low-field MRI to evaluate the water content of the articular cartilage. However, further studies are required to assess the low-field MRI on the water content of the articular cartilage.

### ACKNOWLEDGEMENT

This study is fully supported by Universiti Teknikal Malaysia Melaka (UTeM) and financially supported by the Ministry of Education Malaysia (FRGS/1/2015/TK05/FKM/02/F00272).

### REFERENCES

- [1] Taruc-Uy, R. L., & Scott A. L. (2013). Diagnosis and treatment of osteoarthritis. *Primary Care - Clinics in Office Practice*, 40(4), 821–36.
- [2] Kulkarni, K., Karssiens, T., Kumar, V., & Hemant, P. (2016). Obesity and osteoarthritis. *Maturitas*, 89, 22–28.
- [3] Armstrong, C. G., & Mow, V. C. (1982). Variations in the intrinsic mechanical properties of human articular cartilage with age, degeneration, and water content. *Journal of Bone and Joint Surgery - Series A*, 64(1), 88–94.
- [4] Buckwalter, J. A., Mankin, H. J., & Grodzinsky, A. J. (2005). Articular cartilage. *Articular Cartilage and Osteoarthritis*, 54, 466–80.
- [5] Eckstein, F., Cicuttini, F., Raynauld, J. P., Waterton, J.C. & Peterfy, C. (2006). Magnetic resonance imaging of articular cartilage in Knee Osteoarthritis: Morphological assessment. *Osteoarthritis and Cartilage*, 14(1), 46–75.
- [6] Roemer, F. W., Lynch, J. A., Niu, J., Zhang, Y., Crema, M. D., Tolstykh, I., El-Khoury, G. Y., Felson, D. T., Lewis, C. E., & Guermazi, A. (2010). A comparison of dedicated 1.0 T extremity MRI vs large-bore 1.5 T MRI for semiquantitative whole organ assessment of osteoarthritis: The MOST study. *Osteoarthritis and Cartilage*, 18(2), 168–74.
- [7] Berberat, J. E., Nissi, M. J., Jurvelin, J. S., & Nieminen, M.T. (2009). Assessment of interstitial water content of articular cartilage with  $T_1$  relaxation. *Magnetic Resonance Imaging*, 27(5): 727–732
- [8] Hannafin, J. A., & Arnoczky, S. P. (1994). Effect of cyclic and static tensile loading on water content and solute diffusion in canine flexor tendons: An in vitro study. *Journal of Orthopaedic Research*, 12(3), 350–56.
- [9] Yew, W. S., Latif, M. J. A., Saad, N. H. M., Alhabshi, S. M. I., Mahmud, J., & Kadir, M. R. A. (2018). Correlation of biomechanical properties and grayscale of articular cartilage using low-field magnetic resonance imaging. *International Journal of Eng. and Tech. (UAE)*, 7(4), 1–5.
- [10] Xu, J., Zhu, P., Morris, M. D., & Ramamoorthy, A. (2011). Solid-state NMR spectroscopy provides atomic-level insights into the dehydration of cartilage. *Journal of Physical Chemistry B*, 115(33), 9948–9954.
- [11] Maroudas, A., & Venn, M. (1977). Chemical composition and swelling of normal and osteoarthritic femoral head cartilage: Swelling. *Annals of the Rheumatic Diseases*, 36(5), 399–406.
- [12] Yew, W., Latif, M.J.A., & Saad, N.H.S. (2017). Characterization of articular cartilage using low-field magnetic resonance imaging image. *Journal of Medical Imaging and Health Informatics*, 7(6), 1149–52.

# Transesterification of waste cooking oil into green polyols based on FTIR spectral analysis

Jeefferie Abd Razak<sup>1,\*</sup>, Marina Mohamad<sup>1</sup>, Mazlin Aida Mahamood<sup>1</sup>, Noraiham Mohamad<sup>1</sup>, Rose Farahiyah Munawar<sup>1</sup>, Syahriza Ismail<sup>1</sup>, Lau Kok Tee<sup>2</sup>, Abdul Munir Hidayat Syah Lubis<sup>2</sup>

<sup>1)</sup> Fakulti Kejuruteraan Pembuatan, Universiti Teknikal Malaysia Melaka,  
Hang Tuah Jaya, 76100 Durian Tunggal, Melaka, Malaysia

<sup>2)</sup> Fakulti Teknologi Kejuruteraan Mekanikal & Pembuatan, Universiti Teknikal Malaysia Melaka,  
Hang Tuah Jaya, 76100 Durian Tunggal, Melaka, Malaysia

\*Corresponding e-mail: jeefferie@utem.edu.my

**Keywords:** Polyols; transesterification; waste cooking oil

**ABSTRACT** – Polyurethane (PU) foams are made up from petrochemical based polyols, that harmful to environment. Disposal of abundant waste cooking oil (WCO) from domestic usage has triggered serious pollution issue. Both situation has opened up an opportunity for green material development from WCO, to produce polyols for PU production. The outcome of reaction is evaluated by FTIR analysis, from the presence of OH<sup>-</sup> group in WCO triglyceride structure. This can be confirmed by 3341 cm<sup>-1</sup> IR peak and disappearance of C=C bond at polyol structure. The potential of recycling of WCO as green polyols, using simplified transesterification method has been successfully reported.

## 1. INTRODUCTION

In the future, reduction of petroleum-based feedstock will be of main issue for polymer industry, to maintain the production of polyurethane (PU). Bio-based polyols from renewable source like vegetable oils are expensive. Alternatively, waste cooking oil (WCO) could be used as a cheap option for green source of polyols. Massive disposal of WCO has led into major pollution issue. Malaysia had produced about 459,000 tons of WCO per year and this situation has caused serious disposal problem [1].

Polyols is an oligomeric backbone that contain of two or more hydroxyl group (OH<sup>-</sup>). Since WCO is from vegetable source, there are no presence of OH<sup>-</sup>. Hence, structural modification on WCO need to be performed, to introduce OH<sup>-</sup> functional group in their backbone. This could be done by performing the transesterification process, which consisted of methanolysis and epoxidation steps.

In this study, the potential of WCO to be converted as polyols, to be as future green feedstock material for PU production was evaluated further. FTIR analytical tool has been utilized to evaluate the presence of OH<sup>-</sup> group in produced WCO based polyol. In this study, WCO based polyol is categorized as polyester type polyol, due to initial presence of fatty acid or methyl ester in their triglyceride structure [2]. WCO that experienced repeated heating, during the frying process may also exposed with some reaction that changed their physiochemical behaviour and structure.

## 2. METHODOLOGY

WCO as raw feedstock for polyols production has been collected from banana fritters stall in Ayer Keroh Height, Melaka, Malaysia. At first, the collected WCO was filtered using the vacuum pump infiltration system, to eliminate contaminants. Then, the filtered WCO has undergone the important two main steps transesterification reaction consists of methanolysis and epoxidation, to introduce the OH<sup>-</sup> group in the molecular structure of WCO. For methanolysis, 500 g of WCO, 160.80 g of methanol and 9.00 g of sodium hydroxide (NaOH) are stirred by using hotplate magnetic stirrer at 1000 rpm, 70°C within 90 mins. The mixture was then transferred into separation funnel for overnight precipitation. The ester and glycerol layer are separated gravitationally due to density different. Later, the glycerol part is discarded and the ester at the upper layer is washed by using 100 ml of 0.015M of phosphoric acid at 60°C. During this saponification stage, excess solid that was soap is discarded and pH of the interest part is measured. Washing procedure is continue until neutral pH is yielded. Next, the collected liquid is evaporated for 3 hrs at 80°C to remove the excess methanol and producing the fatty acid methyl esters (FAME). Then, about 190 g of FAME and 7.71 g of formic acid is poured into 1000 ml of reaction flask, and heated into 40°C for 800 rpm. About 20.85 g of hydrogen peroxide was droopily added within 1 hr. The new solution is left for reaction for 11 hrs at constant temperature and stirring period. The colour change from orange to yellow was occurred and has been reashed into neutralized pH if the solution is still in acidic state. Lastly, the final product has been washed with 100 ml of sodium bicarbonate (5%) and sodium chloride (5%), prior of completely washing with DI water into the neutral pH. Finally, produced polyol was evaporated at 90°C for 4 hrs to remove the moisture.

The presence of hydroxyl group in molecular structure of WCO was characterized by using FTIR (FT/IR-6100, Jasco). OH<sup>-</sup> is important functional group for polyols production and FTIR is an analytical tool used to examine the type of chemical bond and functional group appear in WCO and WCO based polyols. IR spectra was recorded at between of 1000 to 4000 cm<sup>-1</sup> of wavenumber range, using the scanning speed of 2.00 mm/s with aperture size of 7.10 mm.

### 3. RESULTS AND DISCUSSION

In this study, the success of transesterification process of WCO conversion into polyols was evaluated from the presence of OH<sup>-</sup> functional group, which scanned through the Fourier transform infrared (FTIR) spectroscopy technique. To assist the comparison between produced polyols form WCO source, first the IR spectral comparison between the feedstock of fresh unused cooking oil, WCO and filtered-WCO, has been made (Figure 1). In WCO itself, it was confirmed that no presence of OH<sup>-</sup> bond. The entire spectral shows the similarities of having bond stretching, except the raw WCO which possessed C-C triple bond at 2400 cm<sup>-1</sup>. This might due to the presence of contaminants in unfiltered raw WCO.

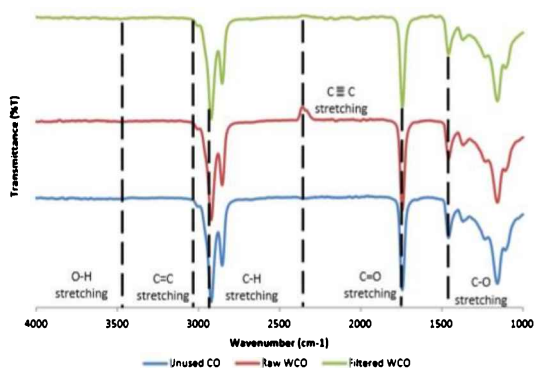


Figure 1 IR-spectral for UCO, R-WCO and F-WCO.

Figure 2 is referred for the IR spectral of WCO after the transesterification process. For the matter of comparison, the transesterified WCO spectral (red) has been compared with the resulted WCO-based polyol, after the methanolysis step (blue) and filtered WCO (green). Methanolysis step will produce fatty acid methyl ester (FAME) and generating polyols. There are two important peaks which are 3441 cm<sup>-1</sup> for OH<sup>-</sup> group formation and the disappearance of C=C peak at 3008 cm<sup>-1</sup>, which indicate the alkenes group.

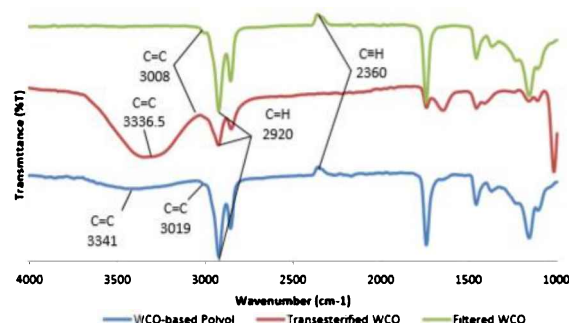


Figure 2 IR-spectral for WCO-polyols (blue), T-WCO (red) and F-WCO (green).

In WCO itself, there are C-H stretching at 2930 cm<sup>-1</sup> peak at medium intensity and narrow band, while C-C triple bond known as alkynes appeared at 2360 cm<sup>-1</sup> and C-O ester at 1158 cm<sup>-1</sup>. After the methanolysis step (addition of methanol and NaOH), broad intensities of OH<sup>-</sup> peak has appeared at 3441 cm<sup>-1</sup>, but C-H peak at 2920 cm<sup>-1</sup> are becoming weaker. Lastly, the formation of WCO-based polyols can be validated at the broad peak

of 3341 cm<sup>-1</sup> in the blue spectra, which indicated the presence of hydroxyl group, while C=C stretching was found disappeared.

During the transesterification, methanol (3CH<sub>3</sub>OH) and NaOH were reacted with WCO, and this step is called as methanolysis. WCO contains triglyceride structure which consists of glycerol and free fatty acid (FFA). Here, NaOH was acted as catalyst. The methanolysis has special purpose to separate the FFA from glycerol backbone to produce fatty acid ester. Hence, transesterification is to obtain monoglyceride (Figure 3).

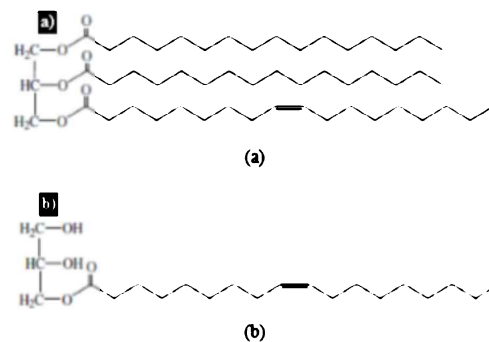


Figure 3 (a) triglyceride (b) monoglyceride.

The existence of broad peak at 3441 cm<sup>-1</sup> in transesterified WCO (T-WCO) has indicated the presence of OH<sup>-</sup> group in the structure of monoglyceride. The next epoxidation step was took place to introduce epoxy group exactly at the double bond position of monoglyceride. Ring opening has occurred during this stage. Performic acid (formic acid + hydrogen peroxide, H<sub>2</sub>O<sub>2</sub>) was added dropwise into transesterified WCO, to oxidize the unsaturated bond, donating O<sub>2</sub> atom to form epoxide group, which fairly reactive to undergo the ring opening reaction in oligomerization process [2]. This was validated at 3008 cm<sup>-1</sup> which indicates the disappearance of C=C bond, due to the epoxidation and formation of oxirane ring in T-WCO molecular structure. Based from the FTIR analysis, the conversion of WCO into polyols for PU production are absolutely possible.

### 4. CONCLUSION

In overall, it was proven that the WCO could be used as feedstock in polyurethane production by converting it first into polyols, through the transesterification process. Double steps of methanolysis and epoxidation involved in transesterification process was accurately validated from the FTIR spectral analysis as explained in the discussion part.

### ACKNOWLEDGEMENT

MOE and UTeM: FRGS/2018/FKP-AMC/F00381.

### REFERENCES

- [1] Arniza, M. Z., Hoong, S. S., Idris, Z., Yeong, S. K., Hassan, H. A., Din, A. K., & Choo, Y. M. (2016). Synthesis of transesterified palm olein-based polyol and rigid polyurethanes from this polyol. *Journal of the American Oil Chemists' Society*, 92(2), 243-255.
- [2] Omonov, T. S., Kharraz, E., & Curtis, J. M. (2016). The epoxidation of canola oil and its derivatives. *RSC Advances*, 6, 92874-92886.

# Effect of motorcycle brake operating parameters on braking performance on inertia roller brake dynamometer

R.J. Talib<sup>1,2</sup>, N.I. Ismail<sup>2,3,\*</sup>, M. Hisyam Basri<sup>2,3</sup>, M.A.H. Fahmi<sup>2,3</sup>, A.M. Zaharudin<sup>2</sup>, R.Z. Tajudin<sup>4</sup>

<sup>1)</sup>Zeta Scientific Sdn. Bhd, Blok 5, Kompleks Otomobil, 23-1B, Jalan Pahat H15/H, Seksyen 15, 40200 Shah Alam, Selangor, Malaysia

<sup>2)</sup> ARTeC, Universiti Teknologi MARA, 13500 Permatang Pauh, Pulau Pinang, Malaysia

<sup>3)</sup> Faculty of Mechanical Engineering, Universiti Teknologi MARA, 13500 Permatang Pauh, Pulau Pinang, Malaysia

<sup>4)</sup>Anchor Engineering & Trading Sdn Bhd, Lot 2 , Jalan Lada Hitam Satu 16/12A, Seksyen 16, 40200 Shah Alam, Selangor, Malaysia

\*Corresponding e-mail: iswadi558@ppinang.uitm.edu.my

**Keywords:** Optimization braking parameters; deceleration; motorcycle; Taguchi method

**ABSTRACT** – This investigation is to optimise the brake operating factors in getting an ideal deceleration of motorcycle during braking process. Taguchi orthogonal array L9 was used in designing the experimental set-up. The signal-to-noise (S/N) ratio was used to determine the optimum values of brake operating parameters in identifying the significant factors that producing the optimum braking deceleration. It could be concluded the active brake operating parameters that control deceleration is in the order of mode of brake actuation, followed by speed and rider mass. An ideal deceleration can be achieved when a 50 kg rider applying front and rear brakes simultaneously at the motorcycle speed of 40 km/h.

## 1. INTRODUCTION

The road accident and fatalities are increasing in Malaysia, with more than 6,000 kills and over 25,000 injuries yearly for the past 5 years [1]. Majority of road accident fatalities are involved with motorcyclists, constituting more than 50% of the total number of fatalities.. There are many factors contribute to motorcycle crashes, but improper braking was identified as a major factor in the motorcycle crash causation [2].

The braking system is one of the active safety systems in the motorcycle. The prevention of road accident for motorcycle is important where braking system plays a main role in succeeding it [3]. Braking is a phase to slow down and finally stop a movement of the motorcycle. During an act of braking, a force is applied to the brake friction materials against the rototating counterpart. It induces friction which converts the motorcycle kinetic energy to heat energy which lead to slow down the motorcycle and finally stop the vehicle movement. Current work objective is to optimise the brake operating factors on the brake drum brake such as speed, rider mass and mode of brake actuation. The optimum braking condition of brake drum was study by using Taguchi method DOE.

## 2. METHODOLOGY

The experimental design was executed according to Taguchi orthogonal array table L9 ( $3^3$ ). Three brake operating factors with three levels of speed, rider mass, and mode of braking actuation were chosen in this experimental study. The braking operating parameters

with different levels are listed in Table 1. The assignment of factors and levels selected of L9 orthogonal array are shown in Table 2.

Table 1 Factors and levels for performance tests.

Sample	Braking parameters	Level		
		1	2	3
A	Speed (km/h)	40	50	60
B	Rider mass (kg)	50	75	100
C	Mode of actuation	F	R	B

The brake performance tests were performed on an inertia roller brake dynamometer (shown in Figure 1). The brake inertia roller dynamometer simulates the kinetic energy of the motorcycle that moving at certain speed by utilizing a mechanical mass that fixed to a rotating shaft. The motorcycle was used to bring the rotating mass up to a speed set point. Once the set point speed has reached at the required magnitude, the throttle was then released, and the braking system was solely responsible for bringing the rotating mass to decelerate stop. The brake was applied in the emergency condition with a maximum force enforced on hand brake lever or foot pedal or hand brake lever combined with foot pedal.. The vehicle specifications used in the performance tests are shown in Table 3.

Table 2 Design of Taguchi orthogonal array L<sub>9</sub> ( $3^3$ ).

Experimental number	Parameters and levels		
	A	B	C
T1	1	1	1
T1	1	2	2
T2	1	3	3
T3	2	1	2
T4	2	2	3
T5	2	3	1
T6	3	1	3
T7	3	2	1
T8	3	3	2
T9	1	1	1



Figure 1 Test equipment set-up

Table 3 Motorcycle specifications.

Item	Specifications
Vehicle System Simulated	Modenas Kriss
Drum Diameter	130mm
Drum Effective Radius	130mm
Axle Load	250kg/48.8in
Test Inertia	0.5 kg m <sup>2</sup>
Static Loaded Radius	203 mm

### 3. RESULTS AND DISCUSSION

The results of the deceleration under different braking parameters are presented in Figure 2. Deceleration was chosen in this study to align with the quality objective which stated that higher deceleration shall stop the motorcycle at a shorter distance. The larger-the-better quality characteristic was taken for deceleration performances. The result of ANOVA for deceleration is shown in Table 4. The mode of brake actuation is considered as significant once the brake operating factor in influencing the deceleration marked (noted as p-value) less than 0.05.

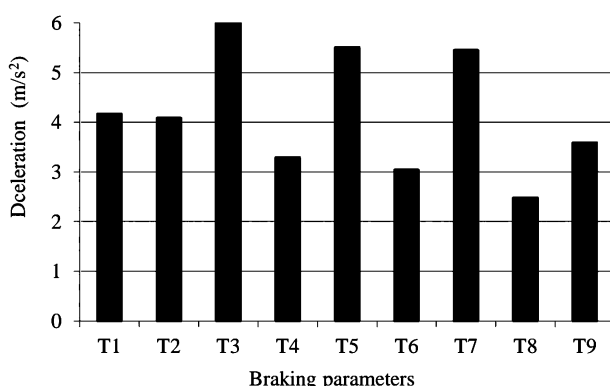


Figure 2 Effect of braking parameters on decelerations.

The S/N ratio responses are graphically shown in Figure 3. It can be seen that the mode of brake actuation had the strongest effect on the deceleration, followed by speed and rider mass. The deceleration is optimum when the brake hand lever and foot pedal are applied concurrently. The results also show that the best time to apply the brake was when speed of motorcycle at 40 km/hr. The rider mass has no significant influence on

the deceleration as differences in S/N ratio response for deceleration is small.

Analysis and evaluation of the influence of each brake operating parameters on braking dynamics shows that the brake performance characteristics was optimized at the motorcycle speed of 40 km/hr with rider mass of 50 kg and the rider applied both front and rear brake.

Table 4 ANOVA for deceleration.

Factor	Rank	SS	Contri. (%)	P-value
Speed (km/h)	2	0.7893	10.22	0.177
Rider mass (kg)	3	0.0635	0.00	0.727
Mode of actuation	1	5.1101	81.42	0.032

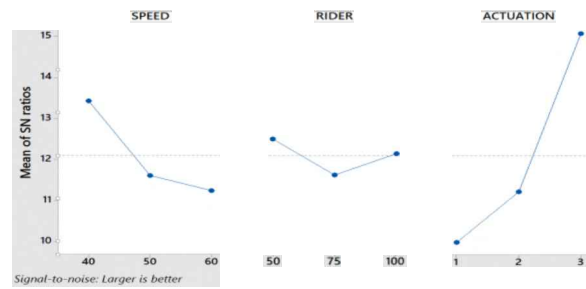


Figure 3 Main effect plots for S/N ratios for deceleration on braking parameters.

### 4. CONCLUSIONS

The ANOVA of the test results shows that mode of brake actuation has significant factor in influencing the deceleration. From S/N ratio of the test results, the active brake parameters that control the braking dynamics are in the order of mode of brake actuation, followed by speed and rider weight. To achieve an ideal deceleration, a 50 kg rider shall apply front and rear brakes simultaneously when approaching speed of the motorcycle is at 40 km/hr.

### ACKNOWLEDGEMENT

This research was supported by the Ministry of Science, Technology and Innovation, Malaysia through Sciencefund grant No. 06-01-01-SF0809. The author would like to acknowledge UiTM Palau Pinang for providing research facilities. The authors would like to acknowledge Focus Applied Technologies for successfully developing this inertia roller brake dynamometer.

### REFERENCES

- [1] Manan, M. M. A., & Várhelyi, A. (2012). Motorcycle fatalities in Malaysia. *IATSS Research*, 36(1), 30-39.
- [2] Talib, R. J., & Faber, G. (1999). Kes sebenar kemalangan jalan raya antara motosikal dengan kereta. *Jurnal Teknologi*, 32A, 63-80.
- [3] Jimenez, A., Bocarejo, J. P., Zarama, R., & Yerpez, J. (2015). A case study analysis to examine motorcycle crashes in Bogota, Colombia. *Journal of Safety Research*, 52, 29-38.

# Effect welding speed on thin plate lap joint using low energy arc welding technologies

Saiful Din Sabdin\*, Nur Izan Syahriah Hussein, Mohammad Kamil Sued

Fakulti Kejuruteraan Pembuatan, Universiti Teknikal Malaysia Melaka,  
Hang Tuah Jaya, 76100 Durian Tunggal, Melaka, Malaysia

\*Corresponding e-mail: saifulkdh@yahoo.com

**Keywords:** Thin plate; arc welding; steel; heat input

**ABSTRACT** – Welding process is a relatively common joint process in car manufacturing industry, one of which is the method gas metal arc welding (GMAW). The joint process is simple, strength and concise compared to the others method. This paper presents a welding parameters affect the joining process on welding speed. The lap joint will be used in this study with constant current and voltage to identify suitable welding speed. The experiment involves using a specimen of cold rolled material as base metal with dissimilar thickness and AWS ER 70S-6 as the filler metal in the lap joint process. The joint was tested to determine the effected welding speed on sample using welding gauge measurement. The results show that a decrease welding speed show higher result on distortion and increase welding speed shows the lowest distortion on sample.

## 1. INTRODUCTION

Most manufacturing industries now use robotic welding tools for joining processes, especially the automotive industry. This process has more advantages than manual conventional processes, such as higher process speeds, better weld quality than manuals, less waste and reduced costs.

GMAW welding method is one of the most important and versatile fabrication methods for the industry. This welding process uses the heating, smelting and solidification processes of the main metal and filler in the local mixed zone by the temporary heat source to form the connection between the main metals.

ColdArc is a new variation on low arc energy technology welding that introduces changes in order to improve the quality and the productivity of the welding performance [1]. The flexibility of the process of automatization using welding robots is vital. Therefore, the heat input can cause several issues in distortion and without a doubt residual stresses has become a priority in welding industry.

Welding speed is the most influential variable in the arc welding process which regulates burner wire speed, combined depth and geometry of weld elements. Welding speed is the most important variable that affects melting rate, sedimentation rate, penetration depth and amount of liquid base metals. The weld speed is determined as the rate of travel of the electrode along the seam or the rate of work travel under the electrode along the sewing [2]. Some general statements can be made regarding welding of speed.

## 2. METHODOLOGY

The cold rolled welded according to the information welding parameter in table 1. Welding has been done on robotic welding KUKA type KRC4 and the system is equipped by EWM ColdArc power source [3]. Specimens dimension dissimilar thickness of 250 mm × 50 mm x 1.0 mm and 250 mm x 50 mmx 0.8 mm were fabricated. The material plate is high strength steel on lap joint [4]. Process parameters chosen for bead-on-plate experiments performed and corresponding heat input values are detailed in Table 1.

Table 1 Welding parameter.

Rank	Ampere (A)	Voltage (v)	Welding speed (m/min)
Low	40	10.50	0.21
Median	40	10.50	0.55
high	40	10.50	0.89

Figure 1 showed that the high strength steel plate samples were arranged to be welded in a lap joint configuration and angle of welding torch. The experiments conducted on the room temperature.

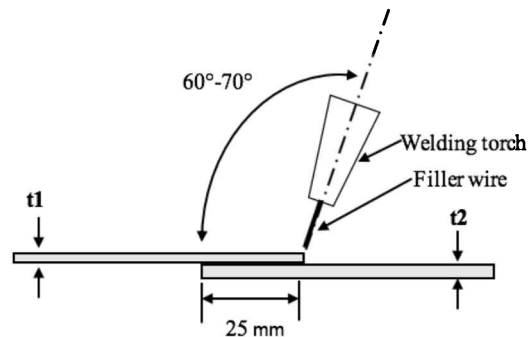


Figure 1 Lap joint preparation.

## 3. RESULTS AND DISCUSSION

An overview of Figure 2 showed the results on the welding distortion by parameter setting. Two type of graph red and blue representing on transverse and longitudinal distortion. These graphs showed higher value on low welding speed with constant current and voltage for transverse and longitudinal is 1 mm. Meanwhile the higher welding speed give lowest value of distortion is 0.250 mm for transverse and 0.8 mm for longitudinal. The results indicate the trend on bowing distortion more decrease when welding speed is increase [5-7].

Table 2 showed the visual effect of welding speed on sample. Visual examination showed that the different size measurement on sample of the lowest, median and the higher welding speed. It is essential to determine the right parameter to minimize defect in the product.

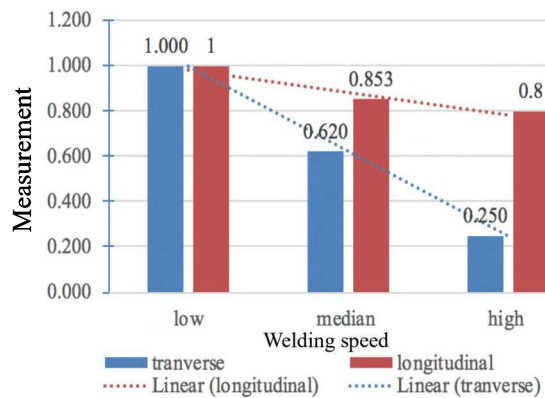


Figure 2 Results for distortion measurement.

Table 2 Effect of welding speed.

Parameter	Bowing Distortion	
	Transverse	Longitudinal
40A, 10.50V, 0.21m/min		
40A, 10.50 V, 0.55 m/min		
40A, 10.50V, 0.89 m/min		

#### 4. CONCLUSIONS

The present work studied the effect of welding speed on the thin plate lap joint using low energy arc welding technologies. The following conclusions can be drawn.

- (a) The welding speed increases, the bowing distortion on transverse and longitudinal reduced because of the low heat input in the weld pool.
- (b) The welding speed increases the heat affected zone decreased with decreasing heat input rate.
- (c) The lowest welding speed indicate the strength

of the weldment is weaker than the base metal.

More heat affected the zone of HAZ.

- (d) Welding speed 0.89 m/min (high speed) using low arc energy process giving good mechanical properties, the size of the weld bead and distortion in these weld joints are less.

#### ACKNOWLEDGEMENT

The authors would like to thank the Faculty of Manufacturing Engineering, Universiti Teknikal Malaysia Melaka (UTeM) for technical support throughout this research work. The first author gratefully acknowledges the scholarship support provided by the Public Service Department Malaysia, under the Hadiah Latihan Persekutuan (HLP) programmed.

#### REFERENCES

- [1] Sabdin, S. D., Izan, N., Hussein, S., Sued, M. K. M., Ayof, N. & Shah, M. A. (2018). The effect of voltage on weldment size cold rolled steel sheet joint using low arc joining technology. in *Proceedings of Innovative Research and Industrial Dialogue 2018*, 1–2.
- [2] Hussain, A. K., Lateef, A., Javed, M., & Pramesh, T. (2010). Influence of welding speed on tensile strength of welded joint in TIG welding process. *International Journal of Applied Engineering Research*, 1(3), 518.
- [3] Sabdin, S. D., Hussein, N. I. S., Sued, M. K., & Ayof, M. N. (2018). Joining of Thin Plates Using Various Arc Welding Heat Sources—A Review. *Journal of Advanced Manufacturing Technology (JAMT)*, 12(1 (1)), 357-370.
- [4] Sabdin, S. D., Hussein, N. I. S., Sued, M. K., Ayof, M. N., Ayob, M. S., & Rahim, M. A. S. A. (2018). Weld bead reinforcement on cold rolled carbon steel sheet joint using ColdArc technology. *Proceedings of Mechanical Engineering Research Day 2018*, 197–198.
- [5] Nuraini, A. A., Zainal, A. S., & Hanim, M. A. (2014). The effects of welding parameters on butt joints using robotic gas metal arc welding. *Journal of Mechanical Engineering and Sciences*, 6, 988-994.
- [6] Chuaiphan, W., & Srijaroenpramong, L. (2014). Effect of welding speed on microstructures, mechanical properties and corrosion behavior of GTA-welded AISI 201 stainless steel sheets. *Journal of Materials Processing Technology*, 214(2), 402-408.
- [7] Mondal, A., Kumar Saha, M., Hazra, R., & Das, S. (2016). Influence of heat input on weld bead geometry using duplex stainless steel wire electrode on low alloy steel specimens. *Cogent Engineering*, 3(1), 1143598.

# Motion sickness mitigation in autonomous vehicles by calming effect through vibration

Nidzamuddin Md. Yusof<sup>1,2,3,\*</sup>, Juffrizal Karjanto<sup>1,2,3</sup>, Nakul Shetty<sup>3</sup>, Jacques Terken<sup>3</sup>, Matthias Rauterberg<sup>3</sup>

<sup>1)</sup> Fakulti Kejuruteraan Mekanikal, Universiti Teknikal Malaysia Melaka,

Hang Tuah Jaya, 76100 Durian Tunggal, Melaka, Malaysia

<sup>2)</sup> Centre for Advanced Research on Energy, Universiti Teknikal Malaysia Melaka,

Hang Tuah Jaya, 76100 Durian Tunggal, Melaka, Malaysia

<sup>3)</sup> Department of Industrial Design, Eindhoven University of Technology,

PO Box 513, 5600 MB Eindhoven, the Netherlands

\*Corresponding e-mail: nidzamuddin@utem.edu.my

**Keywords:** Motion sickness; autonomous vehicle; calming effect

**ABSTRACT** – Non-driving related tasks inside an autonomous vehicle is expected to induce motion sickness symptoms. This study explored the vibration from a wearable forearm haptic device to mitigate the symptoms. A total of 20 participants took part in this within-subjects study. They were driven around a pre-determined route in an instrumented car while watching a video. Motion sickness level was evaluated by questionnaires including the participant's heart rate. Results suggested that there was indeed a calming effect through the vibration that helps reducing motion sickness symptoms.

## 1. INTRODUCTION

The advent of autonomous vehicles is proving to be an eventuality rather than a possibility in the current context [1]. Autonomous vehicles' occupants are expected to be more productive while travelling by doing non-driving tasks such as working on a laptop, watching a video, socializing with other occupants, or just doing nothing by observing the road scenery [2]. However, as mentioned by Diels [3], the occupants are likely to suffer from motion sickness symptoms.

Motion sickness is the uncomfortable feeling that anyone can experience which could lead to symptoms such as dizziness, sweating, headaches, drowsiness, and vomiting due to disturbance of their sense of balance by constant motion [4]. Motion sickness is known to be correlated with pulse rate variability (PRV) [5]. PRV represents the activity of two subsystems of our autonomic nervous system; the sympathetic and parasympathetic nervous systems. The sympathetic nervous system is linked with the fight-or-flight response that occurs in response to a stressful condition (i.e. motion sickness), while the parasympathetic nervous system is linked with the rest-and-digest response that occurs in response to help in calming the body down [6].

Patting is a commonly used form of touch used to convey feelings to loved ones or to calm a child down. This leads to the idea of using vibrations to simulate affective touch similar to someone patting the forearm. It can be used to achieve a calming effect on occupants by invoking the parasympathetic nervous system while riding in an autonomous vehicle. Hence, the purpose of this study is to investigate the calming effect on

occupants inside an autonomous vehicle while doing a non-driving related task (watching a video).

## 2. METHODOLOGY

Wizard of Oz autonomous car simulation method that was inspired by Baltodano et al. [7] was used. Based on Karjanto et al. [8] method, the defensive autonomous car driving style was simulated. The experiment was conducted using an instrumented car called Mobility Lab [9] as shown in Figure 1.



Figure 1 Mobility lab.

All participants were subjected to two experimental conditions, with (test-condition) and without (control-condition) the wearable forearm haptic device (see Figure 2). The only task for the participants inside the instrumented car was watching a video. A minimum gap of three days (between the two conditions) was adapted for each participant to reduce motion sickness effects that might have arose from the first condition of the experiment. A fully-counterbalanced order ( $2! = 2$  orders) was applied to balance potential order or learning effects. In order to ensure experimental consistency, all sessions were conducted on the exact same route on the Eindhoven University of Technology terrain. The independent variable was the presence or absence of the device, and the dependent variables were assessments on motion sickness level of the participants using the Motion Sickness Assessment Questionnaire (MSAQ) [10], a multidimensional method of assessing level of motion sickness across four constructs (gastrointestinal, central, peripheral, and sopite), and using PRV analysis.

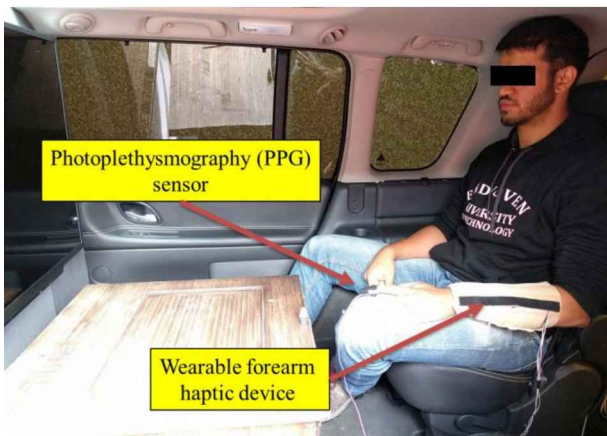


Figure 2 Experiment setup inside mobility lab.

### 3. RESULTS AND DISCUSSION

Figure 3 depicts the average of MSAQ results as a subjective measurement. It could be seen that most participants rated the implementation of the wearable forearm haptic device was indeed worsening the motion sickness level by 1% to 6%. This could be that the way they answered the questionnaire subjectively depended on the individual.

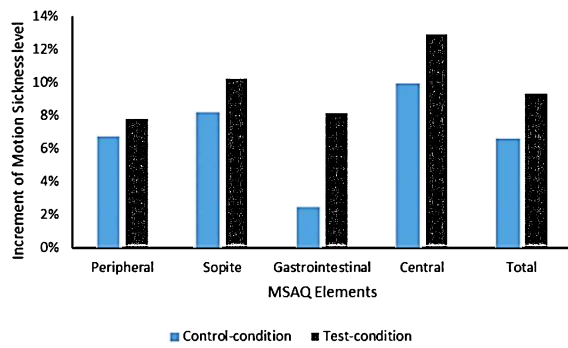


Figure 3 MSAQ results.

On the other hand, the continuous measurement using a PPG sensor shows a reduction in motion sickness level. This result was based on the root-mean-square of successive differences (RMSSD) in the PRV analysis (see Figure 4). An increment in the RMSSD was found to be correlated with the increment in the parasympathetic nervous system [11], indicating a decrease in motion sickness.

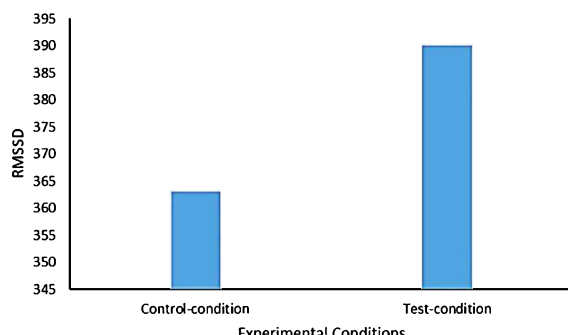


Figure 4 PRV results based on RMSSD.

### 4. CONCLUSION

Overall the results suggest that there was indeed an effect of vibrations on the autonomic nervous system during a simulated autonomous vehicle journey, although the subjective measurement reported otherwise. These results provide an interesting design direction that can be taken by car manufacturers as the autonomous future beckons.

### ACKNOWLEDGEMENT

This project is supported by Department of Industrial Design, Eindhoven University of Technology, the Netherlands.

### REFERENCES

- [1] Reed, R. (2012). IEEE Says That 75% Of Vehicles Will Be Autonomous by 2040. Retrieved from [http://www.thecarconnection.com/news/1079261\\_ieee-says-that-75-of-vehicles-will-be-autonomous-by-2040](http://www.thecarconnection.com/news/1079261_ieee-says-that-75-of-vehicles-will-be-autonomous-by-2040)
- [2] Kyriakidis, M., Happee, R., & de Winter, J. C. F. (2015). Public opinion on automated driving: Results of an international questionnaire among 5000 respondents. *Transportation Research Part F: Traffic Psychology and Behaviour*, 32, 127–140.
- [3] Diels, C. (2014). Will autonomous vehicles make us sick? In S. Sharples & S. Shorrock (Eds.), *Contemporary Ergonomics and Human Factors* 301–307.
- [4] Reason, J. T., & Brand, J. J. (1975). Motion Sickness. Oxford, England: Academic Press.
- [5] Gil, E., Orini, M., Bailón, R., Vergara, J. M., Mainardi, L., & Laguna, P. (2010). Photoplethysmography pulse rate variability as a surrogate measurement of heart rate variability during non-stationary conditions. *Physiological Measurement*, 31(9), 1271–1290.
- [6] McCorry, L. K. (2007). Physiology of the Autonomic Nervous System. *American Journal of Pharmaceutical Education*, 71(4), 78. Retrieved from <http://www.ncbi.nlm.nih.gov/pmc/articles/PMC1959222/>
- [7] Baltodano, S., Sibi, S., Martelaro, N., Gowda, N., & Ju, W. (2015). The RRADS platform: A Real Road Autonomous Driving Simulator. *Proceedings of the 7th International Conference on Automotive User Interfaces and Interactive Vehicular Applications - AutomotiveUI '15*, 281–288.
- [8] Karjanto, J., Md. Yusof, N., Wang, C., Terken, J., Delbressine, F., & Rauterberg, M. (2018). The effect of peripheral visual feedforward system in enhancing situation awareness and mitigating motion sickness in fully automated driving. *Transportation Research Part F: Traffic Psychology and Behaviour*, 58, 678–692.
- [9] Karjanto, J., Yusof, N. M., Terken, J., Delbressine, F., Rauterberg, M., & Hassan, M. Z. (2018). Development of On-Road Automated Vehicle Simulator for Motion Sickness Studies. *International Journal of Driving Science*, 1(1), 1–12.

- [10] Gianaros, P. J., Muth, E. R., Mordkoff, J. T., Levine, M. E., & Stern, R. M. (2001). A Questionnaire for the Assessment of the Multiple Dimensions of Motion Sickness. *Aviation Space and Environmental Medicine*, 72(2), 115–119.
- [11] Otzenberger, H., Gronfier, C., Simon, C., Charloux, a, Ehrhart, J., Piquard, F., & Brandenberger, G. (1998). Dynamic heart rate variability: a tool for exploring sympathovagal balance continuously during sleep in men. *The American Journal of Physiology*, 275(3 Pt 2), H946–H950.

# Fatigue life-based reliability assessment of a leaf spring under random strain loads

Lennie Abdullah, Salvinder Singh Karam Singh\*, Abdul Hadi Azman, Shahrum Abdullah, Ahmad Kamal Ariffin

Centre for Integrated Design for Advanced Mechanical Systems, Faculty of Engineering & Built Environment,  
Universiti Kebangsaan Malaysia, 43600 UKM Bangi, Malaysia

\*Corresponding e-mail: salvinder@ukm.edu.my.

**Keywords:** Gumbel distribution; durability; reliability; strain

**ABSTRACT** – This paper aims to assess a fatigue life-based reliability assessment under random strain loads for a leaf spring. Failure of this component is considered as a localised damage that is subject to a cyclic load. Random strain data was extracted through experimental analysis from three road conditions with a sampling rate of 500 Hz in 60 s. The goodness-of-fit test proposed a Gumbel distribution as the appropriate model for the three strain-life models in assessing the reliability of the leaf spring. Hence, the Gumbel distribution is proposed for assessing fatigue-based reliability as it provides better life cycle assessment.

## 1. INTRODUCTION

Leaf spring is an elastic component in a suspension system of a heavy vehicle, which absorbs shocks caused by different road conditions. The leaf springs have vertical loadings defined as a central force, which is applied onto the middle of the leaf length, hence causing the main failure due to bending during its operating condition [1].

Several distribution models were proposed by previous studies to model the reliability of various automobile components [2]. Anderson and Daniewicz [3] studied the effect of an initial crack size using Gumbel distribution to evaluate defects in metallic materials. In this study, Gumbel distribution for reliability assessment was applied to model the distribution of data. This is due to the sudden bumps from potholes and speed breakers. Also, the lack of research related to durability and reliability assessment of a leaf spring component. Hence, this paper proposes the Gumbel distribution to assess reliability based on the predicted fatigue life of a leaf spring component under operating condition.

## 2. METHODOLOGY

The process flow of the study is illustrated in Figure 1.

Random strain data of the leaf spring was captured for various road conditions (campus, rural, and highway) by placing the strain gauge on top of leaf spring. The random data was collected in microstrain ( $\mu\epsilon$ ) unit at a sampling rate of 500 Hz.

The random strain data were analysed using the global statistical parameters, followed by the normality and goodness-of-fit tests. The fatigue life prediction was then conducted together with the reliability based on life prediction.

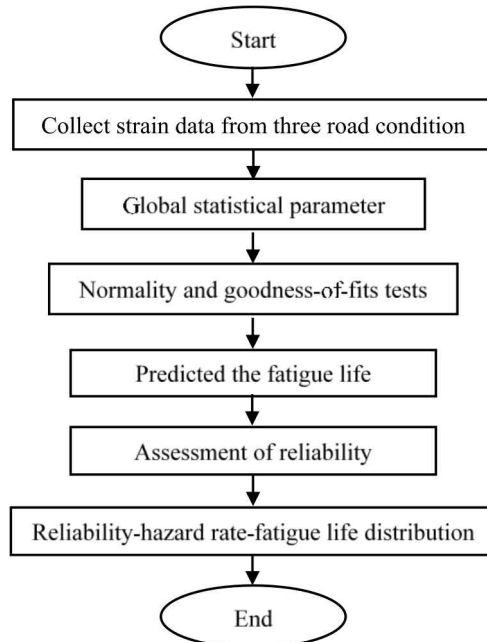


Figure 1 Process flow for random strain data analysis.

## 3. RESULTS AND DISCUSSION

The random strain data were extracted for the duration of 60 s, obtaining 30,000 discrete data points. Figure 2 shows the time history of the various road conditions. It is observed that campus and rural data contained several high amplitudes due to the bumpy and uneven road conditions.

Table 1 shows the normality and goodness-of-fit test results. It shows the normal distribution produce lowest Anderson-Darling (AD) value follows 3-parameter Weibull, smallest extreme value (Gumbel Type-I), largest extreme value (Gumbel Type-II) and 2-parameter exponential. Occasionally, the 3-parameter Weibull distribution is used in a failure-free time period. Therefore, the Gumbel type-I is considered suitable to apply in a random strain data according to goodness-of-fit result.

Table 2 shows the results for the global statistical parameters, namely, root-mean-square (RMS) and kurtosis. The characteristic of these road conditions was assessed based on the energy (RMS) and kurtosis (stationary or non-stationary). The RMS of a campus road has the highest value among other road conditions. The energy recorded in the campus data was higher due to several amplitude range events, where damage could have occurred earlier compared to a highway data. Meanwhile, the kurtosis value for the rural data was the

highest compared with the values for campus and highway data. This could be due to high amplitude events occurring on a rural road with uneven surfaces.

The durability analysis was conducted based on the Coffin-Manson, the Morrow, and the Smith-Watson-Topper (SWT) models as shown in Figure 2. Based on the SWT model, the campus data produced the lowest

fatigue life at  $3.21 \times 10^2$  cycles/block, with the rural data at  $4.02 \times 10^2$  cycles/block and the highway data at  $1.08 \times 10^5$  cycles/block. These results are consistent with the global statistical parameters, which showed that the campus and rural data contained most of the high amplitude events and higher energy that could lead to damages to the leaf spring.

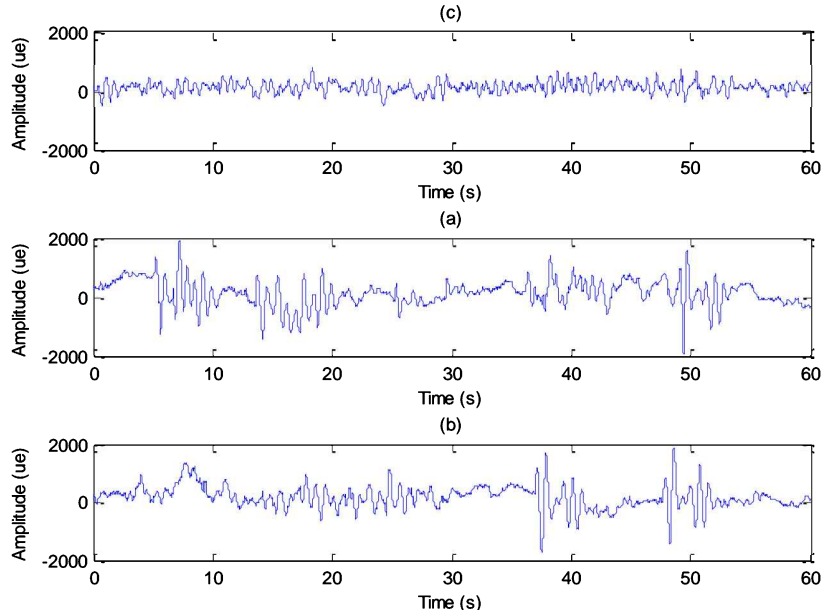


Figure 2 Random strain loads for various road condition (a) highway, (b) campus and (c) rural.

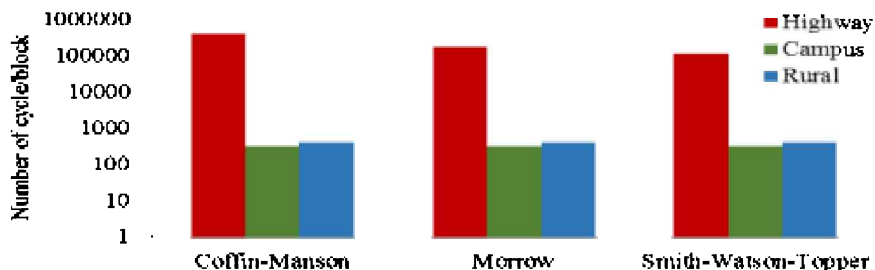


Figure 3 Fatigue life prediction strain-life based.

Table 1 Normality and goodness-of-fit test for campus road.

Distribution	AD	P
Normal	122.39	<0.005
3-Parameter Weibull	178.95	<0.005
Smallest Extreme Value	553.78	<0.010
Largest Extreme Value	1074.18	<0.010
2-Parameter Exponential	8534.46	<0.010

Table 2 Global statistical parameters for each road type.

Parameter	Highway	Campus	Rural
RMS	235	472	431
Kurtosis	3.31	4.50	5.85

The assessment of reliability and hazard rate is illustrated in Figure 4. The hazard rate reached  $2.5 \times 10^5$  cycles/block for the SWT model, while for the Coffin-Manson and the Morrow models, the hazard rates reached  $8.6 \times 10^5$  cycles/block and  $3.7 \times 10^5$  cycles/block, respectively. The hazard rate shows that when the number

of cycles is increased, the hazard rate will also increase until damage occurs. This could be due to the SWT model taking mean stress effect into consideration, and a leaf spring could experience compression and tension repeatedly.

The distribution of reliability-cycle to failure-hazard rate is illustrated in Figure 5, based on the SWT model. The hazard rate was lower when the reliability approached high fatigue life. Thus, the reliability-cycle to failure-hazard rate distribution can be used in assessing the durability and reliability of the random strain data.

Table 3 shows the Gumbel distribution parameter based on fatigue life prediction. The mean value of Gumbel distribution can be described as the mean cycle to failure ( $McTF$ ). The table shows the  $McTF$  value of  $1.20 \times 10^5$  cycles/block for the Coffin-Manson model, while it was at  $5.17 \times 10^4$  cycles/block for the Morrow model, and at  $3.36 \times 10^4$  cycles/block for the SWT model. Based on the  $McTF$  value, it can be said that the leaf spring was still reliable when it reached the 0.57  $McTF$  point [4].

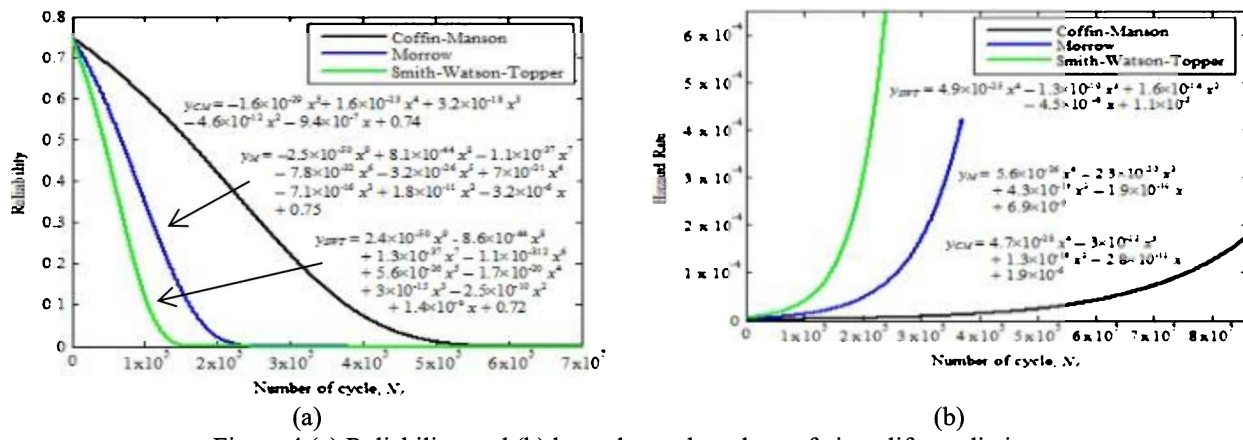


Figure 4 (a) Reliability, and (b) hazard rates based on a fatigue life prediction.

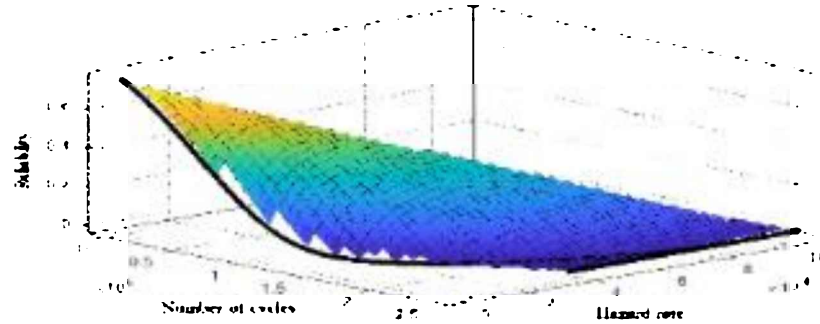


Figure 5 Reliability-cycle to failure-hazard rate distribution of the SWT model.

Table 3 Gumbel distribution parameter.

Strain-life model	Location (cycles /block)	Scale (cycles /block)	Mean cycle to failure (McTF) (cycles /block)
Coffin-manson	$2.26 \times 10^5$	$1.83 \times 10^5$	$1.20 \times 10^5$
Morrow	$9.68 \times 10^4$	$7.82 \times 10^4$	$5.17 \times 10^4$
SWT	$6.29 \times 10^4$	$5.07 \times 10^4$	$3.36 \times 10^4$

#### 4. CONCLUSION

This paper studied the fatigue life-based reliability assessment of a leaf spring under random strain loads. The RMS and kurtosis values of the campus and rural data were higher than the values for the highway data due to bumpy and uneven road conditions. This observation is consistent with the predicted fatigue life results, where the highway data showed the highest fatigue life because the leaf spring could have experienced less tension and compression conditions when moving on the highway. Based on the SWT model, the reliability assessment using Gumbel distribution showed rapidly decreasing values. The *McTF* point was at 0.57, and the hazard rate reached  $2.5 \times 10^5$  cycles/block that can be expected when

the failure occurs. Hence, the fatigue life-based reliability using Gumbel distribution is proposed in assessing the durability analysis of a leaf spring.

#### REFERENCES

- [1] Atig, A., Ben Sghaier, R., Seddik, R., & Fathallah, R. (2018). A simple analytical bending stress model of parabolic leaf spring. *Proceedings of the Institution of Mechanical Engineers, Part C: Journal of Mechanical Engineering Science*, 232(10), 1838-1850.
- [2] Zhao, Y. G., Zhang, X. Y., & Lu, Z. H. (2018). A flexible distribution and its application in reliability engineering. *Reliability Engineering & System Safety*, 176, 1-12.
- [3] Anderson, K. V., & Daniewicz, S. R. (2018). Statistical analysis of the influence of defects on fatigue life using a Gumbel distribution. *International Journal of Fatigue*, 112, 78-83.
- [4] Song, G., & Yang, S. (2018). Probability and reliability analysis of pillar stability in South Africa. *International Journal of Mining Science and Technology*, 28(4), 715-719.

## **Case study of the Lion Air JT-610 falling at Karawang, Indonesia: The critical time of the plane lost contact**

Tiara Nurhuda<sup>1,2,\*</sup>, Ahmad Rivai<sup>2</sup>, Ai Nurhayati<sup>2</sup>

<sup>1)</sup>Universitas Bandung Raya, Jl. Banten No.11, Kebonwaru, Kec. Batununggal, Kota Bandung, Jawa Barat 40272, Indonesia

<sup>2)</sup> Sekolah Tinggi Teknologi Bandung, , Soekarno-Hatta, 378 Bandung, Indonesia

\*Corresponding e-mail: tnurhuda@unbar.ac.id

**Keywords:** Mechanical engineering; dynamic of point

**ABSTRACT** - On October 28, 2018 a Lion Air JT 610 flew from Soekarno-Hatta International Airport in Cengkareng to Pangkalpinang, crashed in an accident after taking off from Cengkareng at 6.20 WIB. However, at 06.32 WIB, the plane lost contact in Karawang waters. This paper recalculates the time to explode after plane lost control. With the assumption that the plane is a point of mass, this case study will be solve using dynamics of point: Projectile motion. According to result of calculation by analyzing information obtained from flight history for Lionair flight JT610, the duration of projectile motion is 6.309 seconds that is similar with the fact of the accident.

## 1. INTRODUCTION

In the morning of October 29 2018, there was a shocking news. Lion Air PK-LQP aircraft crashed in the Java Sea north of Karawang, West Java [1]. Pilot Bhavye Sunjeja and Copilot Harvino flew the plane with the flight number JT 610 from Soekarno-Hatta Airport to Depati Amir Airport, Pangkalpinang. The aircraft took off at 6:20 a.m. carrying 189 people, including pilots, copilots, five flight attendants, and passengers.

This aircraft had requested to return to the original airport, aka return to base. The AirNav, flight navigation agency opens the road. However, at 06.32 WIB, the plane lost contact over Karawang waters. When the crash site was visited for the first time, what was found was fragments on the surface. So, it was concluded that the plane exploded in the air a few seconds after losing contact. Saturday, November 10, 2018, Basarnas stopped the search. Even so, the National Transportation Safety Committee (NTSC) is still continuing the search for CVR. Disaster and Victim Identification (DVI) Team from The National Police also continued to identify the bodies of victims, until November 23, it was confirmed that there could be 125 bodies of victims [2].

This paper recalculates the time to explode after plane lost control with projectile motion. Projectile motion is a form of motion experienced by an object or particle (a projectile) that is thrown near the Earth's surface and moves along a curved path under the action of gravity only (in particular, the effects of air resistance are assumed to be negligible). This curved path was shown by Galileo to be a parabola. The study of such motions is called ballistics. The only force of significance that acts on the object is gravity, which acts downward, thus imparting to the object a downward acceleration. Because of the object's inertia, no external horizontal

force is needed to maintain the horizontal velocity component of the object. Taking other forces into account, such as friction from aerodynamic drag or internal propulsion such as in a rocket, requires additional analysis. A ballistic missile is a missile only guided during the relatively brief initial powered phase of flight, and whose subsequent course is governed by the laws of classical mechanics.

## 2. METHODOLOGY

Having the facts and data of the accident, case studies are used in a systematic way by analyzing information obtained from flight history for Lionair flight JT610 and doing calculations. Assume that the plane is a point mass in the air, the principle of dynamics of point can be applied. The movement of airplane after loss of control will be calculated by projectile motion with using equation:

$$y = v_{0y}t + \frac{1}{2}gt^2$$

### 3. RESULTS AND DISCUSSION

Based on the information of flightradar24, data is obtained in the Figure 1 [3].

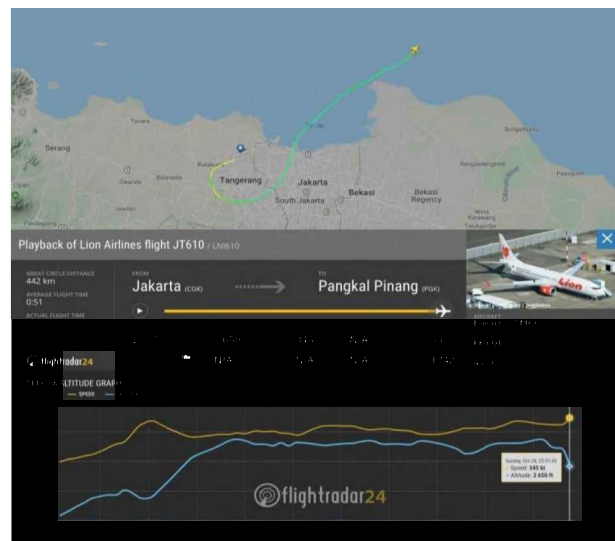
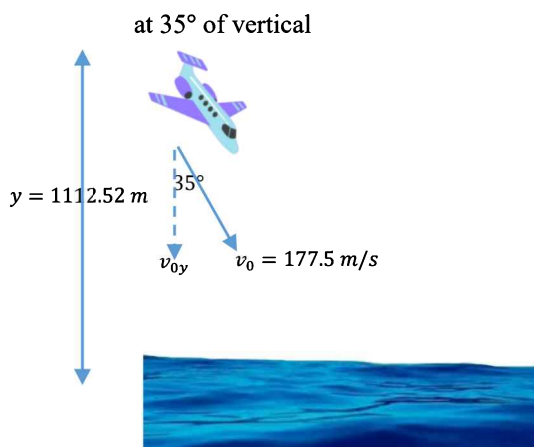


Figure 1 Playback of Lion Airlines JT 610

The Lion JT-610 crashed  $35^\circ$  to the vertical at an altitude of 3650 ft = 1112.52 meters, with ground speed increasing to 345 kts = 177.5 m/s. The time needed for the plane from the swoop until the contact is lost is solve

in the following way: before the swoop situation, the plane maneuvered and underwent rotational motion, but in this calculation is assumed that the rigid body reduce to a point of mass and the rotation of the airplane can be ignored. Because the plane has lost control means that there is no external force exerted, only the gravity applied to the plane, this situation is can be modelled by using projectile motion.



$v_{0y}$  = Vertical initial velocity (m/s)

$y$  = Vertical distance (m)

$t$  = time (s)

$$\begin{aligned} v_{0y} &= v_0 \cos 35^\circ \\ &= 177.5 \times 0.82 \\ &= 145.399 \text{ m/s} \end{aligned}$$

$$y = v_{0y}t + \frac{1}{2}gt^2$$

$$1112.52 = 145.399t + \frac{1}{2} \times 9.8t^2$$

Often, the simplest way to solve " $ax^2 + bx + c = 0$ " for the value of  $x$  is to factor the quadratic, set each factor equal to zero, and then solve each factor. But sometimes the quadratic is too messy, or it doesn't factor at all, or you just don't feel like factoring. While factoring may not always be successful, the Quadratic Formula can always find the solution. The Quadratic Formula uses the " $a$ ", " $b$ ", and " $c$ " from " $ax^2 + bx + c$ ", where " $a$ ", " $b$ ", and " $c$ " are just numbers; they are the "numerical coefficients" of the quadratic equation they have given you to solve

$$1112.52 = 145.399t + \frac{1}{2} \times 9.8t^2.$$

$$t = \frac{-b \pm \sqrt{b^2 - 4ac}}{2a}$$

$$t = \frac{-145.399 \pm \sqrt{145.39^2 - 4 \times 4.9(-1112.52)}}{2 \times 4.9}$$

$$t = 6,309 \text{ seconds}$$

So, the time it takes for the plane to land at Karawang Sea is 6,309 seconds.

#### 4. CONCLUSIONS

Based on the results of the case study, it was found that there was a similarity between the results of the flightradar24 application with the result of calculation. According to the flightradar24 application, the critical conditions, when the speed increases and the altitude decreases, it takes less than one minute, then it is proven by calculation of the critical condition that the plane exploded in 6.309 seconds after lost contact. With a note, assume that the plane is a point mass in the air, the principal of dynamics of point can be applied, then the effects of air resistance are assumed to be negligible.

#### REFERENCES

- [1] Tribunnews. (2018). Pesawat Lionair yang jatuh di perairan karawang tadi pagi adalah tipe boeing 737 max 8.<http://www.tribunnews.com/nasional/2018/10/29/pesawat-lion-air-yang-jatuh-di-perairan-karawang-pagi-tadi-adalah-tipe-boeing-737-max-8>
- [2] Liputan6. (2018). Berita terkini pesawat lionair jt 610 jatuh di karawang.<https://www.liputan6.com/news/read/3678866/update-berita-terkini-pesawat-lion-air-jt-610-jatuh-di-karawang>
- [3] Flightradar24. (2018). Flight history for lionair flight JT610.<https://www.flightradar24.com/data/flights/jt610>

# Experimental investigation of engine performance of algae fuel addition in diesel fuel engine

Hazim Sharudin<sup>1,\*</sup>, Nik Rosli Abdullah<sup>2</sup>, Nur Athirah Rahim<sup>1</sup>, M. Ridzuan Arifin<sup>1</sup>, M.N.A.M. Yusoff<sup>3</sup>, N.W.M. Zulkifli<sup>3</sup>

<sup>1)</sup> Fakulti Kejuruteraan Mekanikal, Universiti Teknologi MARA, Cawangan Pulau Pinang,  
13500 Permatang Pauh, Penang, Malaysia

<sup>2)</sup> Fakulti Kejuruteraan Mekanikal, Universiti Teknologi MARA, 40450 Shah Alam, Malaysia

<sup>3)</sup> Centre for Energy Sciences, Faculty of Engineering, University of Malaya,  
50603 Kuala Lumpur, Malaysia

\*Corresponding e-mail: hazim@uitm.edu.my

**Keywords:** Algae; diesel engine; engine performance

**ABSTRACT** – As the population growth, the demands of the diesel fuel increase and will cause the depletion of diesel fuel. The algae biodiesel become the interest to overcome these problems because it commonly produced from domestic resources that reduce the energy reliance. Thus, the objective of this study is basically to evaluate the engine performance of blended algae fuel with diesel fuel. Fuel blends of 1% (A1), 2% (A2), 3% (A3) and 4% (A4) of algae fuel to each 100ml of fuel blends volume are put to test on an unmodified single cylinder diesel engine with varying the engine load (0 Nm, 2 Nm, 4 Nm and 6Nm).

## 1. INTRODUCTION

The depletion of fossil fuel near future triggered the researchers to come out with the alternative fuel. It is crucial to develop renewable yet clean fuels to meet the world demands and need. This urges the researchers to find a solution to overcome the problem. The research of the new alternative fuels began due to the depletion of fossil fuel in the late 1970s and early 1980s [1]. Some of the important alternative fuels are alcohols (methanol, ethanol), vegetables oils and biodiesel, gaseous fuels, ethers, fuel cell, and future fuels [2]. Biofuels can be classified into primary and secondary biofuels and biofuel produced from algae were classified in the 3rd generation of secondary biofuel [3]. As the alternative liquid transportation fuels, algae fuel has been proposed as a both sustainable and economically feasible solution [4]. Compared to other crops, algae are the most promising source of oil due to the fastest growth, the ability to grow in wide range conditions, and the properties of biodiesel from algae fuel are comparable to the standard biodiesel [4]. According to Abishek et al. [5] algae has easy growth rate, renewable, very inexpensive to produce, emit fewer particulate emissions, and can minimize waste.

The increase in brake specific fuel consumption (BSFC) when using biodiesel has been found in most of the reviewed studies due to the reduction in heating value [6]. Biodiesel predicted to has the highest brake thermal efficiency (BTE) compared to diesel engine as the content of oxygen in algae increase the combustion and asses how efficient the energy in fuel was converted to mechanical output [7].

In this study, the engine performance (BTE and BSFC) of algae fuel addition in diesel fuel engine in different percentage were evaluated and the standard diesel fuel was used as a benchmark and to make the comparison.

## 2. METHODOLOGY

The experimental of engine performance and were conducted on a vertical single cylinder, four stroke, and air cooled, diesel engine by the Yanmar TF-M by Yanmar Co. Ltd. The engine is coupled with eddy current dynamometer with a maximum power input of 20kW at 2450 to 10000rpm. The full details of the engine were given in Table 1. In term of engine test condition, the engine speed was set at 1500 rpm constant while engine load was varied (2, 4, 6 Nm). Experimental set up was specified using the diesel fuel (D100), and then using algae fuel blended with diesel fuel (algae biodiesel) at 1% (A1), 2% (A2), 3% (A3) and 4% (A4). The blends of diesel-algae mixture were stirred continuously by using the magnetic stirrer for 15 minutes at room temperature with a speed of 500 rpm.

Table 1 The experimental engine specification

Parameters	Values
Type	Vertical cylinder, 4-cycle air cooled diesel engine
No of cylinders	1
Bore x Stroke	70mm x 57mm
Combustion	Direct injection
Maximum output	3.5kW
Engine rated speed	3600 rpm

Based on fuel consumption and calorific values obtained from the experiment, it allows obtaining the engine performance of the blends that required. BSFC and BTE were determined using Equation 1 and Equation 2.

$$\text{BSFC (g/kWHR)} = \frac{\text{Fuel consumption}}{\text{Engine power}} \quad (1)$$

Where engine power;  $\frac{2\pi NT}{60000}$  and  $N$  is rotational engine speed (rpm) and  $T$  is torque.

$$\text{BTE (\%)} = \frac{3600}{\text{calorific value}} \times \text{BSFC} \times 100 \quad (2)$$

### 3. RESULTS AND DISCUSSION

Figure 1 shows the BSFC with the engine load at constant speed of 1500 rpm. At 2 Nm engine load, pure diesel (D100) has the highest BSFC compared to the other fuel blends. This is due to the combination effects of the fuel density, viscosity and the lower calorific value of the blends. Higher biodiesel blends has higher BSFC compared to the mineral diesel due to the lower calorific value of the biodiesel [8]. Contrast from the result obtained, BSFC of the algae biodiesel decrease when increasing the engine load. The 16% decrease of A4 compared to D100 at engine load of 2 Nm is due to the increment the mass fuel consumption and the thermal efficiency [9].

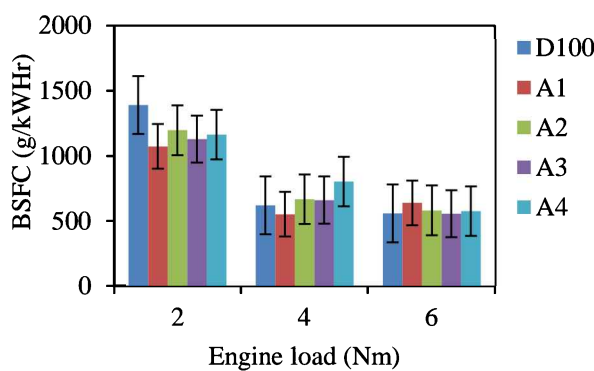


Figure 1 BSFC vs engine load.

The brake thermal efficiency of D100, A1, A2, A3 and A4 at different engine load at constant speed of 1500 rpm is shown in Figure 2. Based on the result, it can be seen that the BTE increase for all fuel blends when increasing the engine load. The higher concentration of the algae biodiesel improves the BTE of the engine. BTE for A2, A3 and A4 blends increase gradually along the engine load, but A1 shows 14% decrement compared to D100 at load 6 Nm. This is due to insufficient air during the experiment resulted in lower oxygen concentration that caused the incomplete combustion of the blends [10].

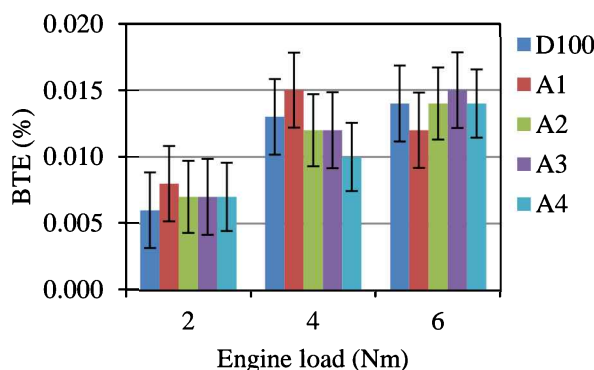


Figure 2 BTE vs engine load.

### 4. CONCLUSION

Based on the result of this experimental works, it can be concluded that blends that contain a high percentage of algae fuel addition with diesel fuel gives

higher BTE compared to diesel fuel at high engine load. It is due to higher viscosity and oxygen content in the blends. BSFC gives lower values (16% for A4) than diesel fuel when using algae biodiesel at low engine load. This is due to the lower density of algae biodiesel compared to diesel fuel. As a conclusion, algae are suitable for a diesel engine to reduce the usage of diesel fuel and as the replacement of diesel fuel.

### ACKNOWLEDGEMENT

The authors of this research would like to express their sincere gratitude to the Faculty of Chemical Engineering, Universiti Teknologi MARA, Cawangan Pulau Pinang, Department of Mechanical Engineering, Universiti Malaya and Faculty of Mechanical Engineering, Universiti Teknologi MARA Shah Alam for the generous assistance throughout this research.

### REFERENCES

- [1] Tüccar, G., Tosun, E., Özgür, T., & Aydin, K. (2014). Diesel engine emissions and performance from blends of citrus sinensis biodiesel and diesel fuel. *Fuel*, 132, 7-11.
- [2] Ramadhas, A. S. (Ed.). (2016). *Alternative fuels for transportation*. CRC Press.
- [3] Salvi, B. L., Subramanian, K. A., & Panwar, N. L. (2013). Alternative fuels for transportation vehicles: A technical review. *Renewable and Sustainable Energy Reviews*, 25, 404-419.
- [4] Lee, S., Speight, J. G., & Loyalka, S. K. (2014). *Handbook of alternative fuel technologies*. crc Press.
- [5] Paul Abishek, M., Patel, J., & Prem Rajan, A. (2014). Algae oil: a sustainable renewable fuel of future. *Biotechnology Research International*, 2014.
- [6] Lapuerta, M., Armas, O., & Rodriguez-Fernandez, J. (2008). Effect of biodiesel fuels on diesel engine emissions. *Progress in Energy and Combustion Science*, 34(2), 198-223.
- [7] Hulwan, D. B., & Joshi, S. V. (2011). Performance, emission and combustion characteristic of a multicylinder DI diesel engine running on diesel–ethanol–biodiesel blends of high ethanol content. *Applied Energy*, 88(12), 5042-5055.
- [8] Dhar, A., & Agarwal, A. K. (2014). Performance, emissions and combustion characteristics of Karanja biodiesel in a transportation engine. *Fuel*, 119, 70-80.
- [9] Bayındır, H., İşık, M. Z., Argunhan, Z., Yücel, H. L., & Aydin, H. (2017). Combustion, performance and emissions of a diesel power generator fueled with biodiesel-kerosene and biodiesel-kerosene-diesel blends. *Energy*, 123, 241-251.
- [10] Abdullah, N. R., Ismail, H., Michael, Z., Rahim, A. A., & Sharudin, H. (2015). Effects of air intake temperature on the fuel consumption and exhaust emissions of natural aspirated gasoline engine. *Jurnal Teknologi*, 76(9), 25-29.

# The performance of POME-algae-diesel as a fuel in diesel engines

Hazim Sharudin<sup>1,\*</sup>, F.N.A.R. Shah<sup>1</sup>, Nik Rosli Abdullah<sup>2</sup>, M. Hisyam Basri<sup>1</sup>, N.I. Ismail<sup>1</sup>, Arif Pahmi<sup>1</sup>, Y. Huzaifah<sup>1</sup>

<sup>1)</sup> Fakulti Kejuruteraan Mekanikal, Universiti Teknologi MARA, Cawangan Pulau Pinang,  
13500 Permatang Pauh, Penang, Malaysia

<sup>2)</sup> Fakulti Kejuruteraan Mekanikal, Universiti Teknologi MARA, 40450 Shah Alam, Malaysia

\*Corresponding e-mail: hazim@uitm.edu.my

**Keywords:** Biodiesel; diesel engine; POME

**ABSTRACT** – Biodiesel is an alternative fuel that is made from vegetable oils, animal fats and waste cooking oil. Researchers nowadays have grown a lot of interest in biodiesel fuels as it promotes much benefits to replace pure diesel fuel. One of the biodiesels, algae-diesel blends have high heating value which leads to unstable biodiesel. Palm Oil Mill Effluent (POME) will be added to algae-diesel fuel to overcome this problem. POME will be added in increment of 2.5 ml into algae-diesel fuel blends. The properties, brake specific fuel consumption (BSFC) and exhaust gas temperature (EGT) of all fuel blends will be analyzed.

## 1. INTRODUCTION

Fossil fuels are becoming one of the highest demands consumed energy sources in the entire world but in recent decades, there is a huge concern on the shortage amount of fossil fuels which caused by the heavy use of it. Thus, researchers grow their interest in finding alternative fuels to fulfil the energy demand. They found that biodiesel can solve those problems and it can provide the same engine efficiency as diesel fuel.

One of the researches shows that algae is fit for biodiesel production as it will undergoes some processes to lower its viscosity [1]. This will eventually improves the combustion rate in diesel engine [1]. However, the algae-diesel blend has high level of polyunsaturated fatty acids which then makes it to be an unstable biodiesel [2]. A further research is made upon Palm Oil Mill Effluent (POME) as one of the possible biodiesels. POME is a non-toxic waste water with high biochemical oxygen demand (BOD) and chemical oxygen demand (BOD) [3]. With treatment, POME can generates a new renewable sources and be the reason to the restoration of environment [3].

Based on the result from previous research regarding POME, a new approach of biodiesel is made to resolve the unstable algae-diesel blend condition by adding POME into it. The process will start with collecting the algae until the properties the engine performance such as Brake Specific Fuel Consumption (BSFC) and Exhaust Gas Temperature (EGT) of every fuel blend are obtained. POME-algae-diesel blends is expected to have better results than diesel fuel.

## 2. METHODOLOGY

### 2.1 POME-algae-diesel blend preparation

The 2 litres of algae collected from a pond were filtered using vacuum filtration to remove water contents. Then the algae were spread on several pieces of clothes

and dried in an oven for 24 hours to ensure that the remaining water in the algae were completely removed. The clothes then were sewn into small packs.

The algae oil was extracted using supercritical fluid extraction (SCFE) method as it can extract almost all of the oils. The SCFE Equipment used liquified carbon dioxide ( $\text{CO}_2$ ) as solvent and ethanol as co-solvent. After getting the algae oil, the rotary evaporator was used to remove the ethanol from algae oil. Then, the POME-algae-diesel blends were mixed using magnetic stirrer according to the specified fuel ratio as shown in Table 1.

Table 1 Specified fuel ratio for each blend.

Fuel	Diesel (ml)	Algae (ml)	POME (ml)
D100	100	0	0
D97.5	97.5	2.5	0
D95	95	2.5	2.5
D94	94	2.5	3.5
D93	93	2.5	4.5

### 2.2 Fuel properties identification

The fuel properties which are density and kinematic were identified under American Standard Test Material (ASTM) standards. The density and kinematic viscosity were measured using the Stabinger Viscometer SVM3000 according to ASTM D4052 at 15°C and ASTM D7042 at 40°C respectively. The calorific value was measured using C200 Bomb Calorimeter. The results of the properties identification were displayed in Table 2.

Table 2 Fuel blends properties.

Fuel	Density (g/cm <sup>3</sup> )	Kinematic Viscosity (mm <sup>2</sup> /s)	Calorific Value (kJ/kg)
D100	0.8500	2.6000	45500
D97.5	0.8453	3.0027	45243
D95	0.8452	3.0326	43693
D94	0.8462	3.0089	44136
D93	0.8466	2.9985	44240

### 2.3 Engine test procedure

The measurements of diesel engine performance were taken at constant engine speed of 1500 rpm with varies engine torque from 2 Nm to 6 Nm with increment of 2 Nm each. Table 3 shows the Yanmar diesel engine specification and Figure 1 below displayed the schematic diagram for the diesel engine setup. Three measurements were taken for each operating condition for an average data to ensure the accuracy of the data.

Table 3 Yanmar diesel engine specification.

Number of cylinders	1
Total displacement	0.320 L
Bore and Stroke	0.078 m × 0.068 m
Maximum output	4.9 kW at 3600 rpm

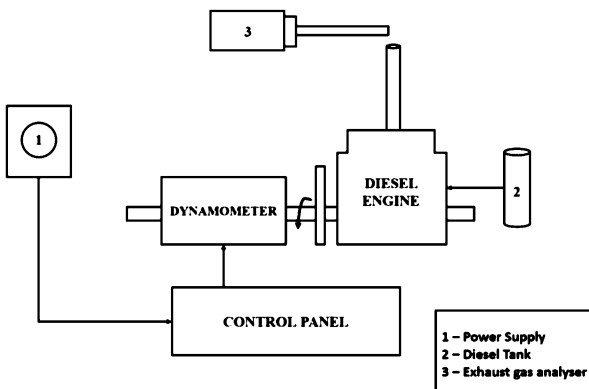


Figure 1 Schematic diagram of diesel engine setup.

### 3. RESULTS AND DISCUSSION

In this research, the performance of POME-algae-diesel blends were compared with D100. The density and kinematic viscosity for D93 are the most similar to D100 while for kinematic viscosity, D97.5 has the most similar value with D100.

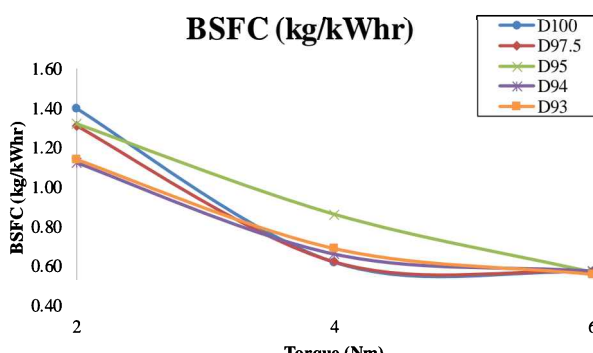


Figure 2 BSFC with increasing torque.

Figure 1 shows the result for BSFC with increasing torque. Generally, D93 is seen to give the similar traits as D100. When the torque is 2Nm, the percentage difference between D93 and D100 decreases with increasing torque from 20% to 0%. The whole graph shows that the POME-algae-diesel blends have higher BSFC compared to D100. This result may be affected from the lower calorific value of D97.5, D95, D94 and D93 [4]. When D93 is compared with other biodiesel fuel blends, the high density of D93 contributes to faster combustion, thereby increases the BSFC where more fuel will be discharged [5].

The result for EGT with respect to engine torque is shown in Figure 2. From the result, it can be clearly seen that initially, all fuel blends exhibit increasing EGT with increasing torque then decrease towards 6 Nm torque except for D95 where it keeps increasing with torque. For

D93, the EGT is very high when the torque is 4 Nm. It has the highest EGT for both 4 Nm and 6 Nm torque. The EGT of D97.5, D95, D94 and D93 is slightly higher than D100 as they have longer ignition delay because of low calorific value. This situation leads to slow rate of combustion of biodiesel fuel blends.

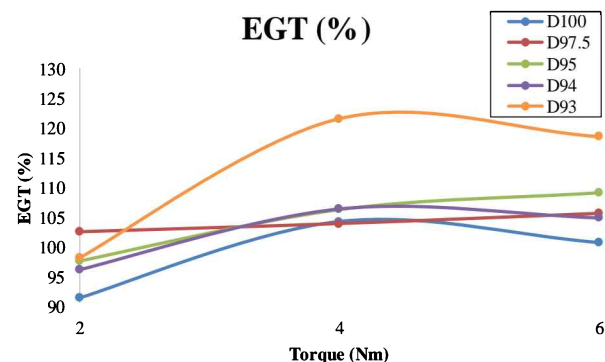


Figure 3 EGT with increasing torque.

### 4. CONCLUSION

The purpose of this research is to identify the compatibility of POME with algae-diesel blends whether it will give better result to the diesel engine performance. From the observation, the lower calorific value of D93 leads to higher BSFC and lower EGT when compared to D100. However, further result needs to be conducted to affirm the results. Few modifications to the diesel engine should interfere so that better results can be achieved.

### ACKNOWLEDGEMENT

The authors wish to thank for supports provided by Universiti Teknologi MARA, Cawangan Pulau Pinang for support throughout the research activities.

### REFERENCES

- [1] Basha, S. A., Gopal, K. R., & Jebaraj, S. (2009). A review on biodiesel production, combustion, emissions and performance. *Renewable and Sustainable Energy Reviews*, 13(6-7), 1628-1634.
- [2] Demirbas, A., & Demirbas, M. F. (2011). Importance of algae oil as a source of biodiesel. *Energy Conversion and Management*, 52(1), 163-170.
- [3] Lam, M. K., & Lee, K. T. (2011). Renewable and sustainable bioenergies production from palm oil mill effluent (POME): win-win strategies toward better environmental protection. *Biotechnology Advances*, 29(1), 124-141.
- [4] Zaharin, M. S. M., Abdullah, N. R., Najafi, G., Sharudin, H., & Yusaf, T. (2017). Effects of physicochemical properties of biodiesel fuel blends with alcohol on diesel engine performance and exhaust emissions: A review. *Renewable and Sustainable energy reviews*, 79, 475-493.
- [5] Chauhan, B. S., Kumar, N., Cho, H. M., & Lim, H. C. (2013). A study on the performance and emission of a diesel engine fueled with Karanja biodiesel and its blends. *Energy*, 56, 1-7.

# Study of EMI reduction techniques in the automotive DC-DC converter

Sivyanam Rajamanickam\*, Siva Kumar Subramaniam, Zamre Abd Ghani

Fakulti Kejuruteraan Elektronik dan Kejuruteraan Komputer, Universiti Teknikal Malaysia Melaka  
Hang Tuah Jaya, 76100 Durian Tunggal, Melaka, Malaysia

\*Corresponding e-mail: nyanam07@gmail.com

**Keywords:** EMI; EMC; automotive; DC-DC converter

**ABSTRACT** – The automotive sector started with combustion engines with almost 100% mechanical content. Nowadays, the automotive industry has transformed with the inclusion of higher content of electronic elements. Over the years this industry has grown as a complex technical system, employing subsystems with dedicated design functions. Some of these consist of thousands of parts that have evolved from breakthroughs in existing technology or newer technologies such as electronic computers, high-strength plastics, new alloys of steel and others. Some subsystems have come about as a result of factors such as air pollution, safety legislation, and market competition. Efficient semiconductor components in the vehicle contribute to emission reduction and also increase in the lifecycle of a vehicle. However, the increase of electronic components in a smaller area leads to electronic magnetic interference (EMI) in the system. The EMI problem exists in all electronic/electrical systems and it is a disturbance caused in a radio receiver or other electrical circuits by electromagnetic radiation emitted from an external source. The interference may interrupt, obstruct, or otherwise degrade or limit the performance of the electronic circuit. This paper describes the available techniques which can be utilized to optimize radiated (30 MHz–12 GHz) or conducted (several kHz–30 MHz) electromagnetic emission.

## 1. INTRODUCTION

In an automotive application, a DC-DC converter is widely used for high current application due to the high efficiency of DC voltage conversion. Besides, the needs for more components in a smaller PCB area generates severe electromagnetic interference issue. It can cause a malfunction in the system if not managed correctly. The switching DC-DC converter operates based on the charging and discharging activities of the external components such as inductor and capacitor [1-2]. The working principle and the mechanism of DC-DC buck converter consequently generate conducted emission and radiation noise. The EMI generated from the DC-DC converter will affect all adjacent devices. With a good understanding of the EMI on DC-DC converter, the system can be designed to this EMI problems.

Based on past literature review, there are several ways to reduce radiated emission and conducted emission. A detailed study has been carried out to comprehend the existing techniques pros and cons. The following are the measures used to reduce electromagnetic interference with methods identified as shielding, filtering, spread spectrum as well as some others.

## 1.1 Electromagnetic Interferences (EMI)

The EMI is a disturbance of operation in an electronic device when it is in the vicinity of an electromagnetic field (EM field) in the radio frequency (RF) spectrum that is caused by another electronic device. Generally, emission classified into two groups which are radiated and conducted. Radiated emission occurred when a considerable distance separates the source and victim that propagate through air. The source emits a signal which may be wanted or unwanted and the victim receives it in a way that disrupts its performance. Nevertheless, conducted emission occurs on the signal travel medium as an example along power cables, long traces or another interconnection cabling. The conduction can fall under two categories such as standard mode and differential mode.

## 1.2 Electromagnetic Compatibility (EMC) and Standard

Electromagnetic compatibility (EMC) is the ability of different electronic devices and components to work correctly even in the presence of other devices that emit electromagnetic waves. This means that each piece of equipment emitting EM waves or disturbances must have it limited to a certain range and that each device must have adequate immunity to EM disturbances in the environment it is meant to function in. EMC is also an entire branch of electrical engineering, a field of study concerned with the unintentional generation, propagation and reception of electromagnetic waves that cause unwanted effects on electronic equipment such as EMI or even physical damage. In the booming electronic market, EMC standard is a part of any electronic design project and there are several categories based on applications.

There are several standards defined for EMC to ensure no complication or malfunction in a system. CISPR 25 is a reference for vehicles, boats and internal combustion engines that governs radio disturbance characteristics. Moreover, CISPR 32 is required for the multimedia equipment to ensure during operation the emission within the sustainable rate.

## 2. TECHNIQUES OF EMI REDUCTION

There are several techniques in the market used to reduce emission. This technique can be varied according to application, PCB space, switching frequency and others.

### 2.1 Shielding Method

Electromagnetic shielding is one of the practices to minimise electromagnetic field in a space by blocking the

area with barriers made of conductive or magnetic materials. The most common purpose is to prevent radiated emission from affecting sensitive electronics [3]. Typically, sheet metal, metal screen, and metal foam materials used as electromagnetic shielding. The holes in the shield or mesh must be significantly smaller than the wavelength of the radiation that is being kept out. Otherwise, the efficiency will drop.

Figure 1. shows that Shielding Effectiveness (SE) is the ratio of the RF energy on one side of the shield to the RF energy on the other side of the shield expressed in decibels (dB) [4].

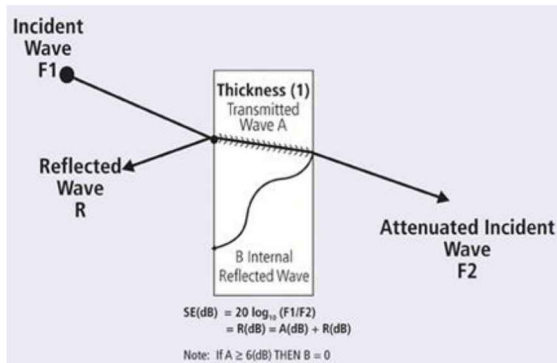


Figure 1 Graphical representation of a shielding.

For sources outside of the shield, the absorption and reflection of the shielding material, in dB, are added to obtain the overall SE of the shield. For sources within the shield, roughly only the absorption of the shield can be considered. The absorption of the shielding material at frequencies of concern is influenced by conductivity, permeability and thickness.

## 2.2 EMI Filters

An EMI filter is a passive electronic device used to suppress conducted interference present on any power or signal line. It may be used to suppress the interference generated by the device itself as well as to suppress the interference caused by other equipment to improve the immunity of a device to the EMI signals present within its electromagnetic environment. Generally, it covers common and differential mode interference.

The most popular differential mode EMI filter topologies are the  $\pi$  filter, the T filter and the L filter [5].

## 2.3 Spread Spectrum

Spread spectrum is one of the popular methods used to minimise the emission. This method used frequency modulation to spread the energy over a controlled band of frequencies to reduce peak EMI at the source. There are several modulation profiles used in the previous study as shown in Figure 2. Different driving signals resulted in different spectrum shape. The modulation profile can be varied according to the application or system [6].

## 3. ANALYSIS AND DISCUSSION

The studies show that typically shielding technique is having a problem at high frequency due to openings in the shield material [7]. While shielding is a primary option for most EMI related issues, the following material centres around the problems associated with

penetrations through the shielded enclosure, the Inputs and outputs of the electrical systems. This is the most vulnerable point in a shielded system. No different than the hull of a ship, a hole in the shielding system at any point can easily lead to catastrophic failure. As the inputs and outputs are the weakest points associated with the shielded enclosures, these are the most vulnerable locations, but also the locations where the implementation of EMI filtering is most effective.

Limited factors of shielding such as mechanical, cost, manufacturability, space and others.

The main drawback of this technique is the low precision at high frequencies. In fact, for low frequencies, the filter is very precise. While at high frequencies, the elements that constitute it have not more an ideal behaviour. This involves a low accuracy. The price to pay for good accuracy is an increase in the cost and the component. These compromises, often, are not accepted by consumers [8].

Spread spectrum is the technique can be applied to any circuit showing a non-negligible switching activity regardless of digital circuits or switching power converters [5]. This solution is quite efficient at high frequencies and cost-effective.

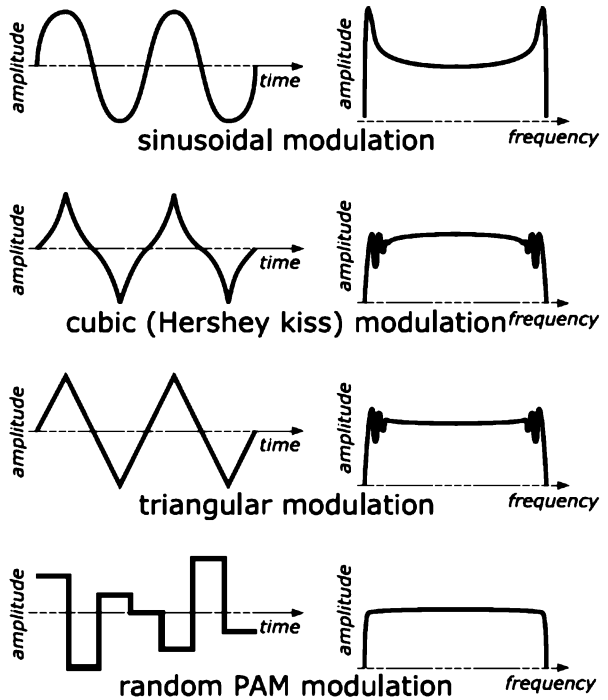


Figure 2 Sketch comparison between the output power spectra achieved with different  $\xi(t)$  modulating signal.

From top to bottom: sinusoidal modulation, cubic (Hershey kiss) modulation, triangular modulation and random PAM modulation.

## 4. CONCLUSION

In conclusion, an electromagnetic inference is very crucial in automotive application and there are several measures to overcome this issue. The approach can be varied according to the applications, cost, environment and others. As an example, shielding is not very suitable when we have space constraint. By the way, EMI filter components need to be automotive qualified to avoid any malfunction during operation. Generally, the material for

shield or components to be used in the automotive application must be capable to withstand a wide range of temperature (-43 deg Celsius up to 150 deg Celsius.) Spread spectrum is one of the most popular techniques applied to optimise emission. This approach can be further study by varying the key parameters to analyse the modulation profile. Besides that, hardware design study plays a vital role to minimise the EMI such routing, ground plane, component selection, component placement and others.

## REFERENCES

- [1] Mainali, K., & Oruganti, R. (2010). Conducted EMI mitigation techniques for switch-mode power converters: A survey. *IEEE Transactions on Power Electronics*, 25(9), 2344-2356.
- [2] Basso, C. (2008). *Switch-mode power supplies spice simulations and practical designs*. McGraw-Hill, Inc.
- [3] Li, M., Nuebel, J., Drewniak, J. L., DuBroff, R. E., Hubing, T. H., & Van Doren, T. P. (2000). EMI from cavity modes of shielding enclosures-FDTD modeling and measurements. *IEEE Transactions on Electromagnetic Compatibility*, 42(1), 29-38.
- [4] Jaskulski, S. M. (1997). *The basics of film processing in medical imaging*. Medical Physics Pub.
- [5] Katrai, C., & Arcus C. (1998). EMI Reduction Techniques (Application Note 11). Retrieved from PERICOM website: <https://www.diodes.com/assets/App-Note-Files/AN011-P.pdf>
- [6] Pareschi, F., Rovatti, R., & Setti, G. (2015). EMI reduction via spread spectrum in DC/DC converters: State of the art, optimization, and tradeoffs. *IEEE Access*, 3, 2857-2874.
- [7] Brett D. R., & Ydens., B. (2017). EMI Filtering, EMI Shielding.
- [8] Pasko, S., & Grzesik, B. (2012). High frequency model of EMI filter. *Electronics*, 16(1), 42-45.

# Analysis of efficiency on different types of fuel for perodua Myvi car

Muhamad Aimran Azhari<sup>1</sup>, Ezzatul Farhain Azmi<sup>1,\*</sup>, Adam Samsudin<sup>2</sup>

<sup>1)</sup> Fakulti Teknologi Kejuruteraan Mekanikal dan Pembuatan, Universiti Teknikal Malaysia Melaka,  
Hang Tuah Jaya, 76100 Durian Tunggal, Melaka, Malaysia

<sup>2)</sup> Fakulti Teknologi Kejuruteraan Elektrik dan Elektronik, Universiti Teknikal Malaysia Melaka,  
Hang Tuah Jaya, 76100 Durian Tunggal, Melaka, Malaysia

\*Corresponding e-mail: ez.farhain@utem.edu.my

**Keywords:** Fuels; road; Perodua Myvi

**ABSTRACT** – Types of gasoline provide different protection to the engine, these types of RON also give different impacts on performance in terms of the fuel consumptions. This project aims to study how much the difference between three types of RON to the engine in terms of fuel usage. In addition, this study will analyse the fuel usage of different types of fuel on Myvi by using ANOVA method by SPSS software. The result of this experiment will also satisfy and add knowledge on the effect of different types of RON to the public. In this study, it also emphasizes the use to a more specific vehicle, only the PERODUA type of vehicle, Myvi. Furthermore, this experiment will try to ensure that all aspects affecting fuel consumption are taken into consideration.

## 1. INTRODUCTION

In Malaysia, most of people use diesel and gasoline. There are three types of gasoline that are sold in Malaysia such as RON 95, RON 97 and RON100. The price of fuel is regulated by government. The price has been gradually increased since 2009. By 2014, RON 97 per litre price is 38% more than RON 95 [1]. This has resulted in dissatisfaction among many vehicle users in Malaysia. People argued because they were denied from using RON 97 that is a better fuel than RON 95. In order to evaluate the real effects of both types of fuel, there is a need to investigate engine responses to these two gasoline grades. The RON 100 is included in the same investigation. There were several of investigations and studies on the fuel consumption such as an investigation by using 1.3L Perodua Myvi 2012 with manual transmission to see the driving behaviour and vehicle engines condition effect on the fuel consumption [2]. Other than that, prediction of vehicle fuel consumption and emissions also have been done by the help of modelling of vehicle fuel consumption and emissions [3]. These past research were conducted by using not just different vehicles but also in a different method and parameter.

All experiments that have been implemented emphasize many aspects to get the right result. Among the important aspects to be aware of are engine types, speed levels, driving behaviours, road surfaces and types of gasoline. Besides that, weather , traffic and aerodynamic of a car also affect the fuel consumption of the vehicles. So all these aspects are very important to carry out experiments and studies on vehicle fuel

consumption. The experiment conducted in this study try to vary the types of fuel and the types of road and all other aspect we try to remain constant such as using the same car engine, driver behaviour, number of passenger and almost similar speed.

## 2. METHODOLOGY

In this research, data is obtained by how many litre of fuel is used for each fuel. Myvi 1.3 SE Automatic transmission car is being used and the type of fuel will be tested are RON 95, RON 97 and RON 100 from PETRON brand only.

The data for each type of RON have been taken nine times. For each RON used, it will be tested on three types of road condition. In terms of road conditions, three types of road condition have been chosen to handle this experiment which are normal road condition, highway condition and crowded conditions. Furthermore, for each types of road condition, three data have been taken to get the average value. Each data will be taken for every 5 kilometres in distance.

## 3. RESULTS AND DISCUSSION

Table 1 shows the result of experiment validation. Litre as a dependent variable since it is depending on types of RON and types of road conditions. "Sig" stands for significance which is all value in this column must be below than 0.05 to validate the experiment. The value 0.05 is the standard significance in engineering. The significance value need to be less than 0.05 in this experiment because it shows the intercept value between types of RON and types of road conditions, types of road conditions, types of RON and types of RON times types of road conditions. As stated in Figure 1 all the values for "sig" are below 0.05. Thus, all the data for each data group can be used and the result of this experiment is reliable.

Table 1 Analysis test between subject effects.

Source	Type III Sum of Squares	Degree of Freedom (df)	Mean Square	F-value	Significance Value
Corrected model	0.717	8	0.090	29.398	0.000
Intercept	6.152	1	6.152	2017.711	0.000
Type of fuel	0.089	2	0.045	14.595	0.000
type of road condition	0.538	2	0.269	88.2	0.000
type of fuel * type of road condition	0.090	4	0.023	7.399	0.001
Error	0.055	18	0.003		
Total	6.924	27			
Corrected Total	0.772	26			

Figure 1 shows the level of gasoline consumption (in litre) for each RON type. As stated in the methodology, the distance to be achieved for every RON type is 45 kilometres. RON 95 mean value in litre is 0.5514 which is the highest fuel consumption compared to the other types of gasoline. RON 97 mean value is in the second place with the value of 0.4691 litres. RON 100 was recorded as the least fuel consumption with 0.4115 litres. Overall, RON 100 is the most efficient fuel gasoline for Myvi.

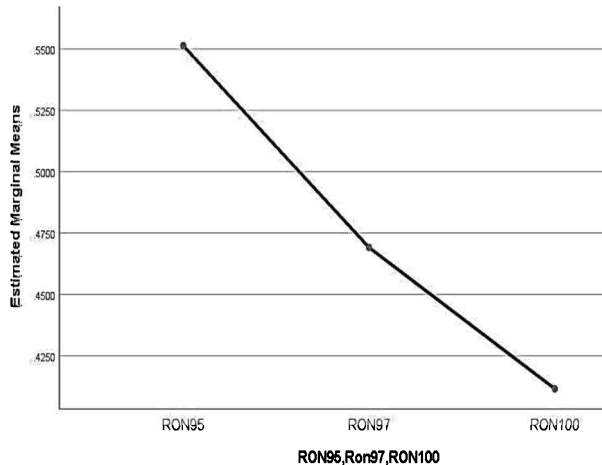


Figure 1 Estimated marginal means versus types of RON.

The price for each litres of gasoline is also important to know how far the savings in different types of RON used for this Myvi-type of vehicle. On November 2018, the price of Petron RON 95 is Ringgit Malaysia (RM) 2.20, Petron RON 97 RM 2.81 and Petron RON100 is RM 3.40. Table 2 shows the total cost of the RON usage at the different types of road.

Table 2 The price for a different type of fuel for distance of 5 kilometres.

Type of Road Condition	RON 95	Types of Fuel RON 97	RON 100
Normal condition	RM 1.03	RM 0.69	RM 0.67
Highway condition	RM 0.98	RM 1.45	RM 1.59
Crowded condition	RM 1.63	RM 1.80	RM 1.93

Based on the Table 2, on normal road condition, this type of Myvi consumed 0.1975 litres of RON 100 which costs RM0.67 cents for five kilometres. For RON 97, 0.2469 litres used by the Myvi which costs RM0.69 cents. However, RM1.03 cents is used for 0.4691 litres on RON 95. Therefore, RON 100 is the most saving fuel on normal road condition and Myvi users can save about RM0.36 cents for five kilometres. However, on highway road condition, RON 95 gives more savings

than RON 97 and RON 100 in which Myvi users can save about RM0.61 cents when comparing to RON 100 and RM0.47 when comparing to RON 97. In addition, on crowded road condition also RON 95 scores as the most savings fuel compared to RON 97 and RON 100. People can save up to RM0.30 cents by using RON 95 on crowded road condition.

#### 4. CONCLUSION

Multiple regression analysis revealed that RON 100 is a better fuel in term of minimum fuel usage for Myvi cars on normal road condition and crowded road condition. However, the price is quite expensive. Therefore, RON 95 is suggested on crowded road condition in terms of cost savings. In addition, RON 95 is also suggested if the user is using a highway road because it gives the best fuel-efficient performance and the most savings fuel on highway road conditions. The experimental results clearly state that RON 95 is better than RON 97 and RON 100 for the Perodua Myvi branded car on two types of road conditions; highway and crowded road conditions. Since Myvi 1.3 engine system is quite same with Myvi 1.5, we assume that RON 95 is also suitable fuel for all Myvi 1.5 usage in Malacca. Weather condition in all states in Malaysia is quite similar making RON 95 is suitable for Myvi cars throughout Malaysia.

#### ACKNOWLEDGEMENT

The authors would like to thank UTeM for sponsoring this work under short-term grant no. PJP/2018/FTK(16A)/S01642.

#### REFERENCES

- [1] Mohamad, T. I., & How, H. G. (2014). Part-load performance and emissions of a spark ignition engine fueled with RON95 and RON97 gasoline: Technical viewpoint on Malaysia's fuel price debate. *Energy conversion and management*, 88, 928-935.
- [2] Mustaqim, M. S., Hashim, M. S. M., Shahriman, A. B., Razlan, Z. M., Zunaidi, I., Wan, W. K., Harun, A., Kamarrudin, N. S., Ibrahim, I., Faizi, M. K., & Saad, M. A. M. (2018). Comparative Study on Fuel Consumption and Different Driving Cycles for a Passenger Car in Malaysia via 1-D Simulation. In *IOP Conference Series: Materials Science and Engineering* (Vol. 429, No. 1, p. 012057).
- [3] Faris, W. F., Rakha, H. A., Kafafy, R. I., Idres, M., & Elmoselhy, S. (2011). Vehicle fuel consumption and emission modelling: an in-depth literature review. *International Journal of Vehicle Systems Modelling and Testing*, 6(3-4), 318-395.

# Development of Brady-Tachy heart automotive monitoring (*BT-Heartomotive*) device to prevent motor-vehicle accident

Mohd Azrul Hisham Mohd Adib<sup>1,\*</sup>, Muhamad Hazim Khalili<sup>1</sup>, Nur Hazreen Mohd Hasni<sup>2</sup>

<sup>1)</sup> Medical Engineering & Health Intervention Team (MedEHiT), Human Engineering Group, Faculty of Mechanical Engineering, Universiti Malaysia Pahang, 26600 Pekan, Pahang, Malaysia

<sup>2)</sup> Family Health Unit, Pahang State Health Department, Jalan IM 4, 25582 Bandar Indera Mahkota, Kuantan, Pahang, Malaysia

\*Corresponding e-mail: azrul@ump.edu.my

**Keywords:** Brady-Tachy; heart rate; automotive; device; driving

**ABSTRACT** – The rate of car accidents is worrying nowadays. Other than problems in driving attitudes and skills, road accidents are also caused by uncontrollable factors such as medical conditions and drowsiness. These factors can be avoided by having early detection. The *BT-Heartomotive* device is a device that can detect early signs of drowsiness and health problems by measuring the heart rate of the drivers. Heart rate measurement can reveal a lot about the physical conditions of an individual. *BT-Heartomotive* device consists of three main components: the sensor, microcontroller, and heart rate monitor.

## 1. INTRODUCTION

The causes of road accidents vary between two groups of drivers: young and old drivers. Young drivers tend to be involved in road accidents due to the lack of experiences, risk-taking behaviors, over-speeding as well as alcohol and drug influence. Most of the accidents among older drivers are due to medical problems such as stroke, heart disease and psychoactive medications [1]. Another main factor contributing to road accidents is drowsiness. 21% of fatal road accidents were due to drowsiness according to the AAA Foundation for Traffic Safety between the year 2009 to 2013 [2] and 54% of adult driver's drive despite in the state of drowsiness [3].

The development of *BT-Heartomotive* device is to address the road safety issue among old drivers, people with medical problems and drowsiness. The mechanism of action of *BT-Heartomotive* is based on the measurement of the heart rate by a sensor. Many information can be extracted from the heart rate data. The most important data is the state of drowsiness. According to a study done by Abdul Rahim et al. [4], there is a big difference in the heartbeat between normal and drowsy states. In a normal, relaxed state, the heart beats in the range of 70 to 100 BPM but, only in the range of 45 to 65 BPM in an early drowsiness state.

Other than drowsiness, the measurement of heart rate can reveal information about the health state of an individual such as the risk of having the cardiovascular disease [5], undetected heart attack, blood pressure condition as well as the level of blood electrolyte [6].

*BT-Heartomotive* can also monitor blood pressure and blood oxygen saturation level ( $\text{SpO}_2$ ) level. The degree of hemoglobin binding to oxygen (lung factor), hemoglobin concentration (anemic factor) and cardiac output (cardiac factor) are the three factors that can affect

the quantity of oxygen transported throughout the body. Oxygen saturation is the ratio of the amount of oxygenated hemoglobin compared to the amount of hemoglobin in the blood to indicate the sufficiency or insufficiency of oxygen in our body. The level of healthy  $\text{SpO}_2$  ranges from 96% to 99%. The level decreases significantly for patients with pulmonary or cardiovascular chronic diseases [7].

In this paper, the *BT-Heartomotive* device was developed. We are working on the functional prototype to improve the consistency and reliability of the data so that it can be used for the intended purpose. Essentially, the data could be stored, and always reliable and usable. The proposed device would use the data to send an alert to the driver and passengers that they're in precaution. They should pull over and take action as early as possible to prevent a motor-vehicle accident. The device is also simple, easy to use, and automated.

## 2. METHODOLOGY

This *BT-Heartomotive* device consists of three main components; smartwatch, monitoring system, and mobile application as shown in Figure 1. The details of each component are described in this subsection.

### 2.1 Smartwatch

Consists of MAX30100, integrated pulse oximetry and solution of heart-rate monitor sensor that combines one photodetector, optimized optics, low-noise signal processing and two LED to detect heart-rate signal and pulse oximetry from which the heart rate, blood pressure, and  $\text{SpO}_2$  level can be obtained. The body of smartwatch was developed using Flexible TPU filament.

### 2.2 Monitor System

In this monitoring system, the device displays the heart rate, blood pressure and  $\text{SpO}_2$  level of the driver after receiving the value of heart rate in BPM from the microcontroller via a Bluetooth system. In order to develop this device, the microcontroller Arduino-Uno is used. Arduino Uno is an open-source electronics platform based on easy-to-use hardware and software. Arduino intended for making the interactive surface. The function is to obtain the value of heart rate in beats per minute (BPM) based on the photoplethysmograph (PPG) data from MAX30100. For the body of the monitor, the SUNLU PLA filament materials was used as shows in Table 1.

### 2.3 Mobile Application

The mobile apps. is developed to record and display the heart rate, blood pressure and SpO<sub>2</sub> data trend of the driver. The data keep in the storage system as a black box function. These data will use as the emergency tread record or research activity.



Figure 1 The final design of *BT-Heartomotive* device.

### 3. RESULTS AND DISCUSSION

Figure 2 shows the process flow of the *BT-Heartomotive* device operate. In this study we consider the driver's heart rate monitoring problem to decide the heart rate level for safety driving. To detect the heart rate of the driver, we adopt the oximeter sensors. This system consists of three parts as detecting, analysis, and feedback. The detecting part processes driver's physiological data and environment. The analysis part extracts the heart rate of the driver and determines whether the driver is an early stage of Brady-tachy or not. When the driver becomes or close to the Brady-tachy syndrome, the feedback part is triggered to stimulate/alert the driver. One of the direct information about the heart rate (heartbeat) is attained involved in the driver's body. Another drawback of the sensor based system is to mount some piece of the sensor to the driver body. The system seems to be attractive by its contact-free property but the effect of active detecting to driver's health is not clear.

Table 1 Material specification.

Material	Flexible TPU
Print Temperature	200-230°C
Length	335mm
Diameter	1.75mm +/- 0.03mm
Printing Speed	20/60mm/s
Material	SUNLU PLA
Print Temperature	190-220°C
Length	330mm
Diameter	1.75mm +/- 0.05mm
Printing Speed	20/60mm/s



Figure 2 Process flow of an implementation of the *BT-Heartomotive* device.

### 4. SUMMARY

As a summary, the proposed *BT-Heartomotive* device would use the data to send an alert to the driver and passengers that they're in a deterrent. They should pull over and take action as early as possible to prevent a motor-vehicle accident. The *BT-Heartomotive* device is still in the early development with positive progress. The device is also simple, easy to use, and automated.

### ACKNOWLEDGEMENT

A big thank you dedicated to University Malaysia Pahang (UMP) for providing us with a good environment, facilities and funding under research grant RDU 180330 in order to complete this research. By this opportunity, we would like to thank Dr. Zakri Ghazalli and Mr. Idris Mat Sahat from Human Engineering Group, Universiti Malaysia Pahang for sharing valuable information in accordance with our research interest. We would face many difficulties without their assistance.

### REFERENCES

- [1] Rolison, J.J., Regev, S., Moutari, S., Feeney, A. (2018) What are the factors that contribute to road accidents? An assessment of law enforcement views, ordinary drivers' opinions, and road accident records. *Accident Analysis & Prevention*, 115, 11-24.
- [2] Tefft, B.C. American Automobile Association (AAA) Foundation for Traffic Safety, 2014.
- [3] National Sleep Foundation, *National Sleep Foundation*, 2010.
- [4] Abdul Rahim,H., Dalimi, A., Jaafar, H. (2015) Detecting drowsy using pulse sensor. *Jurnal Teknologi*, 73(3), 5-8.
- [5] Hamill, V., Ford, I., Fox, K. (2015) Repeated heart rate measurement and cardiovascular outcomes in left ventricular systolic dysfunction. *The American Journal of Medicine*, 128(10), 1102-1.
- [6] The Ford Motor Company, *The Ford Motor Company*, 2011.
- [7] Konica Minolta, *Konica Minolta Sensing Inc*, 2006.

# Stability improvement of motor control unit for automatic steering system

Mohd Zakaria Mohammad Nasir<sup>1,\*</sup>, Mohd Hanif Harun<sup>2</sup>, Fauzi Ahmad<sup>2</sup>

Fakulti Teknologi Kejuruteraan Mekanikal dan Pembuatan, Universiti Teknikal Malaysia Melaka,  
zHang Tuah Jaya, 76100 Durian Tunggal, Melaka, Malaysia  
2) Jabatan Automotif, Fakulti Kejuruteraan Mekanikal,  
Universiti Teknikal Malaysia Melaka, Hang Tuah Jaya, 76100 Durian Tunggal, Melaka, Malaysia

\*Corresponding e-mail: mzakaria@utm.edu.my

**Keywords:** H-bridge; ECU; automatic steering system

**ABSTRACT** – A steer by wire concept is widely used for preparing future autonomous vehicle. Motor control unit is developed in this research attach with rack and pinion steering system to follow the desired direction. This paper present ECU consist microcontroller with motor driver using H-bridge system. Based on experiment for DLC and slalom input steering, the electric steering system that are developed using actual rack pinion type with the integration of the Electronic Control Unit (ECU) and sensors produce more accurate and smoothly with a little noise and 0.05 second delayed.

## 1. INTRODUCTION

Vehicle electrification or Drive by Wire has a trend in automotive industry and has been undergoing worldwide development. The SBW system is significant especially in the direction of autonomous vehicle development [1,2]. The rack and pinion type has been chosen in this research which offers advantage by using one motor to control the angle of both front tires. Therefore, DC motor must be precisely controlled to ensure steering capability and stability.

The steering system introduced in this research work consist of rack and pinion steering attached with DC motor, two position sensors, and ECU modules as shown in Figure 1.

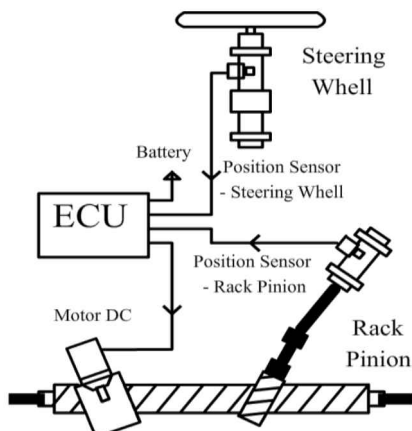


Figure 1 Schematic diagram of the SBW experiment.

## 2. METHODOLOGY

Rack and pinion system convert rotational motion of steering wheel or driver input into linear motion which turn the tire into desired direction, and provide gear reduction or steering ratio, making easier to turn the tire.

The DC motor generate required torque to push or pull the tie rod in rack pinion linkage system. Two precision potentiometer sensors are installed to measure pinion angle rotation and steering wheel angle rotation. The ECU controller compare shaft rotation angle between steering and rack pinion to generate feedback action through motor actuator.

Standard DC brush motor which provide 150W power rating and rotational speed 80 rpm used in this research. The torque calculated by dividing the motor power output (watt) against angular velocity (rad /sec) as follow:

$$T = (P_w * \eta) / \left( \frac{2 * \pi * n}{60} \right) \quad (1)$$

The ECU modules is designed consists of microcontroller unit minimum system and motor driver circuit. The MCU is installed within the microcontroller minimum system (minsys) circuit. The minsys refers to minimum configuration circuit for MCU to run properly.

### 1.1 Motor Driver Circuit

The electric steering system (SBW) designed require another circuit that can support the motor for turning the rack and pinion gear moving to left and right. The H-Bridge circuit designed provide and facilitate the motor to turn reverse and forward direction. This circuit can be composed with 4 MOSFET which function like a switch [4]. Thus, the motor driver circuit will act as the current buffer for the MCU designed to drive the DC motor accordingly.

### 1.2 Circuit Configuration

For circuit design configuration with I/O port, PORTA MCU is functioned as ADC input to read the position from potentiometer sensor data. PORTB work as output to signaling the H Bridge. There is protection circuit between H-bridge and MCU using opto-coupler to isolate MCU and H Bridge via light signaling to ensure no real electric connection occurs. To ensure the opto-coupler isolate the system, the supply voltage between MCU and motor driver are separated. This setup designed configuration resulting noise protection for MCU such as voltage spike generated from motor load. The circuit configuration is shown on the Figure 2.

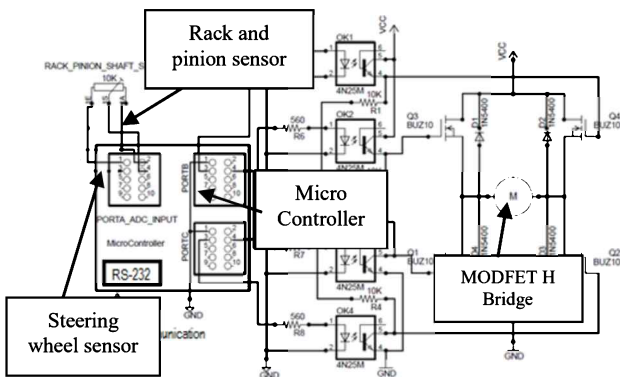


Figure 2 Schematic diagram of the experiment.

### 3. RESULTS AND DISCUSSION

Two types of signal data measured in the experiment simultaneously, namely the signal of the rotational and linear signal captured by the two potentiometer sensors for each of the circular motion and displacement which will be analyzed using self-tuning PID control method.

The experiment conducted on actual rack and pinion steering system in laboratory. Position tracking test is performed to ensure the motor could follow the desired steering input. Steering wheel is turned as input for Double lane change (DLC) and slalom test. USART communication is used to track and measure the position, which available inside the micro for logging the sensor data to PC.

Based on experiment, the DC motor attached with rack and pinion tend to closely follow the input signal for DLC test as shown on the Figure 3. It is demonstrating actual rack pinion shaft position measured from potentiometer sensor follow the steering wheel input accordingly. There is a bit delay around 0.05 second between the input and actuator. This error occurred due to mechanical delay in rack pinion system.

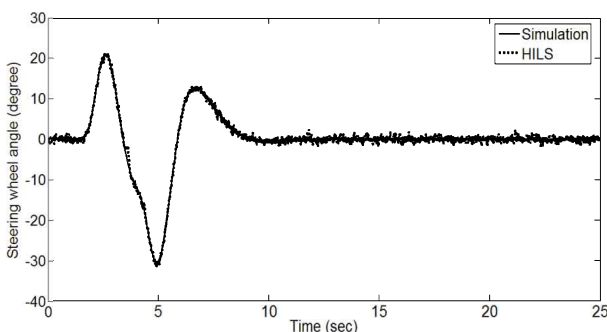


Figure 3 Double lane change signal.

Figure 4 shows the DC motor actuator run smoothly (HILS) for slalom input steering with fast responses. From experimental calibration, it's found only 1.6 second required for motor response to fully turning the tire angle from far-left position to far right through direct supply. This demonstrates that the motor has enough power and speed to drive this electric rack and pinion steering system designed. The steering torque need 0 to 2 Nm during normal driving ranges and emergency manoeuvre can demand up to 15Nm [3,4].

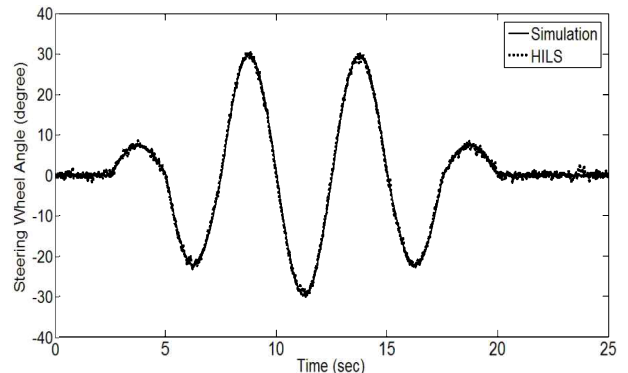


Figure 4 Slalom input signal.

### 4. CONCLUSION

In this study, a modification motor control unit for Steer by wire test rig has been developed. The hardware design using actual rack and pinion steering type and only one DC motor to control both of front wheel tire with slight modification prior installation. The MCU consist of ATMEGA32 provide many feature and computational power for this purpose. In advance, power MOSFET 1404 is used for switching element in H-bridge to drive high current motor designed working perfectly. Result from experimental proved that simple PID controller can effectively drive this SBW system. DLC and slalom test for input steering provide very good responses via DC motor and controller to follow the desired direction accurately.

### ACKNOWLEDGEMENT

This project is supported by Ministry of Higher Education Malaysia, CARE, FKM, Universiti Teknikal Malaysia Melaka

### REFERENCES

- [1] Sharp, R. S., & Granger, R. (2003). On car steering torques at parking speeds. *Proceedings of the Institution of Mechanical Engineers, Part D: Journal of Automobile Engineering*, 217(2), 87-96.
- [2] Park, T. J., Han, C. S., & Lee, S. H. (2005). Development of the electronic control unit for the rack-actuating steer-by-wire using the hardware-in-the-loop simulation system. *Mechatronics*, 15(8), 899-918.
- [3] Nasir, M. Z. M., Hudha, K., & Amir, M. Z. (2012). Modeling, simulation and validation of 9 DOF vehicle model for automatic steering system. *Journal of Applied Mechanics and Materials*, 16, 192-196.
- [4] Nasir, M. Z. M., Dwijotomo, A., Amir, M. Z., Abdullah, M. A., Hassan, M. Z., & Hudha, K. (2012, July). Position tracking of automatic rack and pinion steering linkage system through hardware in the loop testing. In *2012 IEEE Control and System Graduate Research Colloquium* (pp. 111-115). IEEE.

# Vehicle analysis design of vehicle occupant packaging analysis

A. Hazim N. Azman, Nur Hazwani Mokhtar\*

Fakulti Teknologi Kejuruteraan Mekanikal dan Pembuatan, Universiti Teknikal Malaysia Melaka,  
Hang Tuah Jaya, 76100 Durian Tunggal, Melaka, Malaysia

\*Corresponding e-mail: nurhazwani@utem.edu.my

**Keywords:** Vehicle; ergonomic; automotive

**ABSTRACT** - Vehicle ergonomics research deals with vehicle occupant's physical interaction with the interior of the vehicle under normal operating conditions. It includes understanding the effects of dimensions of the occupant body and factors of interior design of the vehicle such as the posture, position and comfort of the driver. The objectives of this project are to gather and analyse data of three types of car from different manufacturer region by comparing the dimension of these cars with initial dimension to develop driving simulator rig. The dimensions from three different car's manufacturer measurement helps to build initial dimension in driving simulator.

## 1. INTRODUCTION

Ergonomics are important in automotive, to develop the best fit between the driver and the vehicle to guarantee the safety, comfort, accommodation, improved execution and proficiency of the driver and diminished exhaustion. The keywords often describing ergonomics are both comfortable and safe environment [1].

One of the key areas considered by the design engineer when developed the vehicle was ergonomics. Ergonomic factor function is to ensure the vehicles are harmonized and fulfills customer expectation. The seating position is essential in automotive design. Car seat must be in the comfort position to ensure the driver's health and convenience while driving [2]. Besides car seats, others equipment such as steering wheel position, acceleration and braking pedals position are important to ensure driver comfortless. In comfort position, drivers are able to make an excellent judgement when facing critical condition such as pre accident situation.

The interior of the vehicle is designed to maximize accommodation for the target population within the limits of space or cab dimensions. Accommodation means the driver can perform the required task while sitting in a comfortable position. The driver is considered accommodated if the components of the workspace can be reached in the desired position without the limitations of the adjustment range [1].

The driving simulator is designed to conduct engineering studies on car interiors. In automotive industries, it can help to design and evaluate new vehicles or new advanced driver assistance systems to build in the actual vehicle. Many of scenarios can be run in the driving simulator which probably too costly, dangerous, time consuming and complicated to test in the real world.

Driving simulator in the market are expensive and mostly design for gaming purpose and incompatible for real driving situation in the car. One of the limitations is

fixed car seat, the height of headrest, angle of back cushion, high of seat, space between the seat and steering are fix. Structures of the cheaper driving simulator are fragile and not solid for the driver and monitor screen. The objective of this project is to gather and analyse data of three type of car from different manufacturer. The analyse dimension will be used to develop driving simulator rig. The references point and dimension in driver workspace are shown in Figure 1 (Parkinson & Reed, 2010).

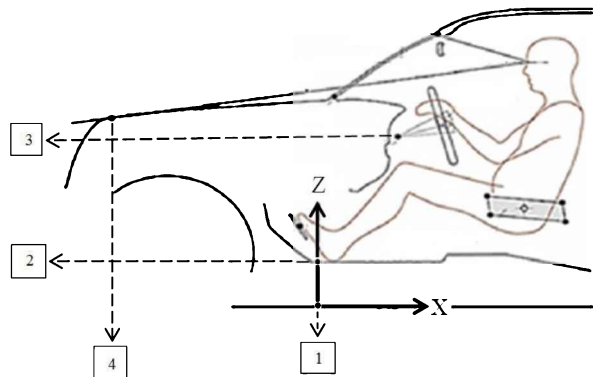


Figure 1 Dimension point in driver workspace [2].

## 2. METHODOLOGY

To achieve the objective, BMW i3, Toyota Prius and Proton Preve are selected to be measured and compared. BMW i3 is manufactured in German and represent the Europe region users. On the other hand, Toyota Prius is produced in Japan and represented Asia region users. The third car is Proton Preve, made in Malaysia and represented Malaysian users.

BMW i3 (Figure 2) has five door hatchback with power of electric motor 125 kiloWatt (168 brake horsepower). This is electric car with zero emissions. Toyota Prius (Figure 3) also has five door hatchback and semi hybrid car. This car produces 73 kiloWatt (98 horse power) of 1.8 litre engine power and 100 kiloWatt (134 horse power) from electric motor. Proton Preve (Figure 4) are compact car with 1.6 litre turbo engine produce 103 kiloWatt (138 horse power). The dimension parameters measured as refer to Figure 1 are accelerator heel point (AHP) at point 1, steering wheel pivot AHP at point 3, steering wheel diameter and hood point by using x and z axis. Reference point is ground at below of AHP as starting point for AHP and hood point, but for steering wheel pivot reference point at AHP.



Figure 2 BMW i3.



Figure 3 Toyota Prius.



Figure 4 Proton Preve.

### 3. RESULTS AND DISCUSSION

The dimension of the chosen cars is in Table 2. The AHP measurement for all cars were almost at same. It shows that three car manufacturers are preferred between 270mm to 280mm of high accelerator heel point from ground in z axis rather than 400mm as in initial dimension.

Steering wheel pivot for Toyota Prius are the closest to initial dimension value for both x and z axis. Have difference 5mm in x axis, and 10mm for z axis compared to initial dimension.

Steering wheel diameter of all three cars showed all three steering wheels are almost with the initial dimension value and the shape are not round. It's shows differences between x and z axis value in all three-car steering wheel diameter.

BMW i3 has smaller hood point distance because it does not have an engine. This car is running fully by electric power. The electric motor and the battery pack are located at rear luggage compartment. Whereas, Toyota Prius and Proton Preve have bigger hood point because it has engine in the front bonnet. However, this parameter was not considered in the initial dimension. For the driving rig simulator dimension, AHP value of 280mm was chosen because Proton Preve was design for Malaysian users and the difference is less than 10% <sub>initial</sub>

dimension, while initial dimension which is 400mm are too far from this three-car measurement are not relevant to be use. Two dimension parameters of Toyota Prius were selected for the simulator rig, which are steering wheel pivot and hood point. The reason are because the measurement meets the same agreement with the initial dimension. Hood point dimension is use for placing monitor display. Steering wheel diameter must be between 350mm to 370mm because all steering wheel diameter measured cars are in this range.

Table 2 Dimension measurement of the car.

No	Type of car	BMW i3		Toyota Prius		Proton Preve	
		x (mm)	z (mm)	x (mm)	z (mm)	x (mm)	z (mm)
1	Reference point	0	0	0	0	0	0
2	Accelerator Heel Point (AHP)	0	270	0	270	0	280
3	Steering Wheel Pivot re AHP	310	620	320	560	260	540
4	Hood Point	1040	820	1290	900	1460	940
-	Steering Wheel Diameter	360	350	370	340	360	350

### 4. CONCLUSION

Ergonomic is importance in automotive design to ensure the comfortable of driver while driving. To build driving simulator that ergonomic and user friendly, the dimension measurement in driver workspace had been gathered and analyzed. The result shows steering wheel pivot dimension for Toyota Prius are nearest to the initial value. Two dimension parameters of Toyota Prius were selected for the simulator rig, which are steering wheel pivot and hood point. The dimension for steering wheel diameter in all three cars are close to initial dimension with difference  $\pm 20$ mm. However for AHP, all measured car are not close to initial dimension. The measurement and comparison method used in this study to provide the best dimension to develop driving simulator rig ergonomically. Moreover, it helps researcher to run any simulation based on the situation needed with real driving space compartment in this simulator.

### ACKNOWLEDGEMENTS

The authors would like to thank ASEAN NCAP for the financial support provided through ASEAN NCAP Collaborative Holistic Research and short-term grant (PJP) 2018 Universiti Teknikal Malaysia Melaka (UTeM)(PJP/2018/FTK(8D)/S01601).

### REFERENCES

- [1] Rashid, Z. (2017). *Ergonomic Design Parameters For Malaysian Car Driverseating Position* (Doctor of Philosophy, Universiti Teknologi Malaysia)
- [2] Kyung, G., Nussbaum, M. A., & Babski-Reeves, K. (2008). Driver sitting comfort and discomfort (part I): Use of subjective ratings in discriminating car seats and correspondence among ratings. *International Journal of Industrial Ergonomics*, 38(5-6), 516-525.
- [3] Parkinson, M. B., & Reed, M. P. (2006). *Optimizing vehicle occupant packaging* (No. 2006-01-0961). SAE Technical Paper.

## Aerodynamic efficiency of paper planes

N.I. Ismail<sup>1,2,\*</sup>, R.J. Talib<sup>1</sup>, Hazim Sharudin<sup>1</sup>, M.M. Mahadzir<sup>1</sup>, M. Hisyam Basri<sup>1</sup>, R. Rabilah<sup>1</sup>

<sup>1)</sup> Faculty of Mechanical Engineering, Universiti Teknologi MARA, Cawangan Pulau Pinang,  
13500 Permatang Pauh, Pulau Pinang, Malaysia

<sup>2)</sup> ARTeC, Universiti Teknologi MARA, Cawangan Pulau Pinang, 13500 Permatang Pauh, Pulau Pinang, Malaysia

\*Corresponding e-mail: iswadi558@ppinang.uitm.edu.my

**Keywords:** Aerodynamics; paper plane; aerodynamic efficiency

**ABSTRACT** – Paper plane has been long recognized as a flying toy. It is seen as an economical toy that demands only a piece of paper with a standards skill of origami. Despite its easiness, the aerodynamic performance behind this flying object is still open to be explored. Thus, in this works, the study on the aerodynamic performance of certain paper plane designs was conducted. The paper plane design selection (known as The Glider, Stunt Plane and Wide Stunt Glider) was made based on its popularity and compatibility with remote control device. By using ANSYS-CFX simulation works, the aerodynamic efficiency of each paper plane was studied. The results shows that The Wide Stunt paper plane able to produce least 6.4% better maximum lift-to-drag ratio magnitude compared to the other paper plane design. Such condition is seen as advantages for the paper plane to perform excellently during hovering operation, take-off and landing maneuver.

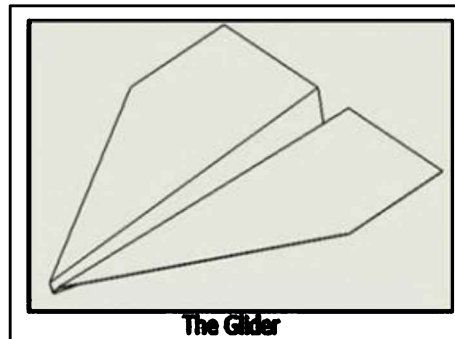
### 1. INTRODUCTION

Paper plane is a flying toy that easily develop based on a wide range of origami design[1]. It has been an economical toy since the building material demands only a piece of paper with a standards skill of origami. Despite its easiness and economical toy, the aerodynamic behind this flying object is still open to be explored. Thus, the main objective of current research is to explore the aerodynamic performance of popular paper plane designs. The paper plane design selection was made based on its compatibility with a remote-control device named as PowerUp 3.0. PowerUp 3.0 is special device develop for paper plane to enhance its flying capability. The device allows user to manoeuvre the paper plane by using smartphone. Based on its compatibility, there three selected paper plane designs known as the Glider, Stunt Plane and Wide Stunt Glider. CFD simulation commercial software known as ANSYS-CFX module was used in this study to analyse the aerodynamic performance of each paper plane. The aerodynamic efficiency magnitude is used in this study to compare and evaluate the overall performance of each paper plane design.

### 2. METHODOLOGY

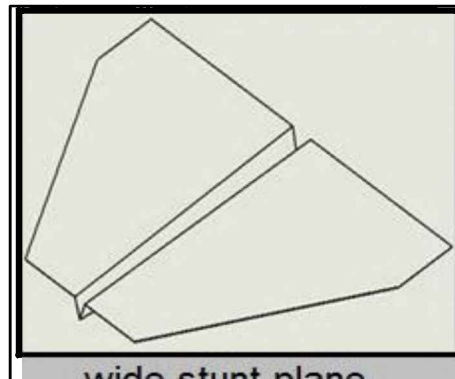
The Glider, Stunt Plane and Wide Stunt Glider paper plane designs are shown in Fig. 1 to 3. To ensure the paper plane comply with MAV standard, the input velocity for each paper plane is set to Reynolds Number  $Re = 100,000$  at the root chord. Based on the  $Re$  value, the calculated velocity, overall wing dimension and aspect

ratio for each paper plane is given in Table 1.



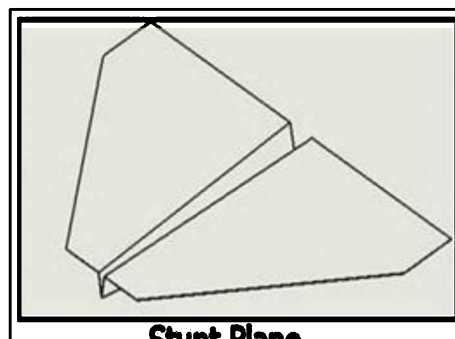
The Glider

Figure 1 The Glider paper plane.



wide stunt plane

Figure 2 The Wide Stunt paper plane.



Stunt Plane

Figure 3 Stunt paper plane.

In this works, CFD simulation was fully implemented for each paper plane analysis by using a commercial CFD software ANSYS-CFX[2]. To avoid computational burden and exploiting the symmetrical condition of paper plane design, thus only half of the computational domain was built. The simulation was

executed based on steady state and incompressible flow with Shear Stress Turbulence (SST) model was used to solve the turbulence viscosity problems surrounding the paper plane surface[3]. The turbulence intensity was set at 5% and the automatic wall function was fully implemented to capture the viscous effect. The angle of attack ( $\alpha$ ) for each paper planes were set to be varied between  $-5^\circ$  to  $40^\circ$  with  $2^\circ$  interval. In this study, the magnitude of lift-to-drag ratio ( $C_L/C_D$ ) or also known as aerodynamic efficiency[4] is used to determine the performance level for each paper plane design.

Table 1 The basic dimension of the paper plane designs.

Paper plane	The Glider	Wide Stunt Glider	Stunt Plane
Chord length (c)	120mm	165mm	122mm
Wing area (S)	3122.7mm	13166mm	7442.7mm
Aspect ratio (AR)	2.81	3.81	3.61
Velocity (U)	12.61 m/s	8.62 m/s	11.65 m/s

### 3. RESULTS AND DISCUSSION

Figure 4 presents the performance of aerodynamic efficiencies ( $C_L/C_D$ ) for each paper plane. In overall, all paper plane induced almost similar trend of  $C_L/C_D$  curve with the increment of  $C_L$  magnitude. The magnitude of  $C_L/C_D$  increase almost linearly at early  $C_L$  increment which is between  $C_L=-0.056$  to  $0.269$ . This  $C_L$  magnitude is induce at  $\alpha$  between  $-5^\circ$  to  $5^\circ$ . The  $C_L/C_D$  reach its maximum value (known as  $C_{L\max}/C_D$ ) at  $C_L=-0.056$  to  $0.222$  or at  $\alpha$  between  $2^\circ$  to  $5^\circ$ . However, as the  $C_L$  increase further (or  $\alpha > 5^\circ$ ), the  $C_L/C_D$  performance is gradually drop towards the stall condition at  $C_L$  between  $1.07$  to  $1.25$  (or  $\alpha$  between  $25^\circ$  to  $30^\circ$ ).

Comparative analysis was specifically conducted to study the difference in  $C_{L\max}/C_D$  magnitude among the paper plane. The result shows that Wide Stunt paper plane induced the best  $C_{L\max}/C_D$  magnitude among the paper plane at  $C_{L\max}/C_D=6.32$ . This condition happens at  $C_L=0.108$  and relatively  $\alpha=2^\circ$ . This is followed by Stunt paper plane at  $C_{L\max}/C_D=5.94$  which relatively occurred at  $C_L=0.138$  and  $\alpha=2^\circ$ . The Glider paper plane induced the lowest  $C_{L\max}/C_D$  magnitude among the paper plane at  $C_{L\max}/C_D=5.45$ . This is happening at  $C_L=0.269$  and  $\alpha=5^\circ$ . Based on these results, it clearly shows that Wide Stunt paper plane induced at least 6.4% better  $C_{L\max}/C_D$  magnitude compared to the other paper plane design. Furthermore, the  $C_{L\max}/C_D$  magnitude for Wide Stunt paper plane is also induced at almost two times lower  $\alpha$  angle compared to the Glider paper plane. Thus, one can conclude that Wide Stunt paper plane shows promising advantages in producing better aerodynamic efficiency at lower  $\alpha$  angle. Such advantages are very crucial for the paper plane especially during hovering operation, take-off and landing maneuver.

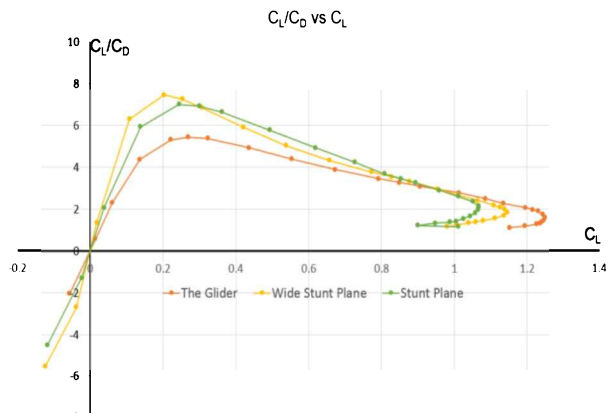


Figure 4  $C_L/C_D$  performance for Glider, Stunt Plane and Wide Stunt Glider paper plane.

### 4. CONCLUSION

In this work the analysis of aerodynamic efficiency for Glider, Stunt Plane and Wide Stunt Glider paper plane designs are presented. The simulation results show that Wide Stunt paper plane has a promising advantage in producing better aerodynamic efficiency at lower  $\alpha$  angle. The Wide Stunt paper plane able to produce least 6.4% better  $C_{L\max}/C_D$  magnitude compared to the other paper plane design at lower  $\alpha$  angle. Such condition is seen as advantages for the paper plane to perform excellently during hovering operation, take-off and landing maneuver. In future works, experimental validation based on wind tunnel testing will be conducted to confirm the aerodynamic efficiencies performances.

### ACKNOWLEDGEMENT

The authors acknowledge technical and financial support from Universiti Teknologi MARA, Cawangan Pulau Pinang.

### REFERENCES

- [1] Pounds, P. (2012). Paper plane: Towards disposable low-cost folded cellulose-substrate UAVs. In *Australasian Conference on Robotics and Automation*, 3–5.
- [2] N. I. Ismail, N. I., Yusoff, H., Sharudin, H., Pahmi, A., Suhaimi, S., & Hemdi, A. R. (2017). Lift and drag performances of O-ring paper plane. *International Journal of Engineering & Technology*, 5(3), 1–5.
- [3] Ismail, N. I., Sharudin, H., Talib, R. J., Hassan, A. A., & Yusoff, H. (2018). The influence of hoop diameter on aerodynamic performance of O-ring paper plane. *IOP Conference Series: Materials Science and Engineering*, 370(1), 012034.
- [4] Ismail, N. I., Zulkifli, A. H., Abdullah, M. Z., Basri, M. H., & Abdullah, N. S. (2014). Optimization of aerodynamic efficiency for twist morphing MAV wing. *Chinese Journal of Aeronautics*, 27(3), 475–487.

# Heterogeneous catalyst from white clams for biodiesel production

Mahanum Mohd Zamperi<sup>1,2,4,\*</sup>, Farid Nasir Ami<sup>2</sup>, Mohd Fadzli Bin Abdollah<sup>3,4</sup>, Nur Hazwani Mokhtar<sup>1,4</sup>

<sup>1)</sup> Fakulti Teknologi Kejuruteraan Mekanikal dan Pembuatan, Universiti Teknikal Malaysia Melaka,  
Hang Tuah Jaya, 76100 Durian Tunggal, Melaka, Malaysia

<sup>2)</sup> School of Mechanical Engineering, Faculty of Engineering, Universiti Teknologi Malaysia,  
81310 Skudai, Johor, Malaysia

<sup>3)</sup> Fakulti Kejuruteraan Mekanikal, Universiti Teknikal Malaysia Melaka,  
Hang Tuah Jaya, 76100 Durian Tunggal, Melaka, Malaysia

<sup>4)</sup> Centre for Advanced Research on Energy, Universiti Teknikal Malaysia Melaka,  
Hang Tuah Jaya, 76100 Durian Tunggal, Melaka, Malaysia

\*Corresponding e-mail: mahanum@utem.edu.my

**Keywords:** Rubber seed oil; heterogeneous; microwave

**ABSTRACT** – This work studied the potential of using high free fatty acids (FFA) of rubber seed oil (RSO) as a biodiesel fuels with the aid of heterogeneous catalyst from waste white clams using microwave irradiation method. The two step esterification-transesterification process reduces the FFA of RSO from 78.9% to below 1%. The optimum yield of biodiesel fatty acid methyl ester (FAME) was reached up to 92.91% under optimal conditions of 9:1 methanol molar ratio, catalyst loading of 7 wt% oil, 7 minutes of reaction time and 400-watt microwave power input.

## 1. INTRODUCTION

There are many efforts to develop a green and cost saving biodiesel production. Microwave and ultrasound assisted transesterification method are some of the advances method that enhanced the production compared to conventional techniques [1]. Even though non-edible oil has high free fatty acids which may leads to some serious drawbacks it is still often selected by researchers due to the issue of food versus fuel [2]. Solid heterogeneous are gaining more attention when dealing with high FFA oil because it can provide higher conversion rate compared to homogeneous which results in lowering the biodiesel production cost. In the present study the performance of very high free fatty acids (FFA) *Hevea brasiliensis* oil, commonly known as rubber seeds oil (RSO) as biodiesel feedstocks using calcium oxide derived from white clamps via batch processing microwave technique was investigated.

## 2. METHODOLOGY

### 2.1 Material Selection and Catalyst Preparation

A very high FFA (39.8) crude rubber seed oil was purchased from Kinetics Chemical, Vietnam. Waste white clams were collected at Pantai Puteri, Melaka, Malaysia. The preparation of heterogeneous calcium oxide catalysts and the properties of methyl ester of crude RSO were reported in our previous papers [3].

### 2.2 Catalyst Characteristic

The physio-chemical characteristics of the calcined white clams were determined using Bruker AXS D8 Advance XRD and Bruker AXS S8 Tiger XRF Spectrometry.

### 2.3 Biodiesel Production

Due to the high FFA content of the raw feedstock, a two-step process, acid esterification and followed by microwave transesterification process were needed to convert the crude RSO to methyl esters. Acid esterification process was carried out at 50°C using water bath. Sulfuric acid ( $H_2SO_4$ ) of 1 % w/w in reference to the mass of oil (80g) and methanol is the optimum value to reduce the FFA concentration of RSO below 4%.

The second step was performed using batch microwave using a modified 1000-Watt 2450Hz household Samsung brand microwave in the presence of calcined catalysts (5, 7, 9 and 12 wt%) and molar ratios of methanol to rubber seed oil (6:1, 9:1 and 12:1). The reaction times and microwave power was maintained at 7 minutes 400 watts. The end product was poured into a separation funnel and was left overnight for separation process. The lower layer which is glycerol is drawn out and the excessive amount of methanol was evaporated. The fatty acids methyl ester (FAME) obtained was analyzed with gas chromatography-mass spectrometry (GCMS-Agilent Technologies 6890 N) with inert mass selective detector 5975. The total yield obtained from the biodiesel was calculated according to Equation 1 and 2.

$$\text{Volume yield\%} = \frac{\text{Volume of product}/\text{Volume of oil fed}}{100} \times 100 \quad (1)$$

$$\begin{aligned} \text{Biodiesel yield\%} \\ = \text{FAMEs percentage from GC analysis} \times \frac{\text{Volume yield.}}{100} \end{aligned} \quad (2)$$

The physical and chemical properties of FAME including kinematic viscosity, density, flash point, acid value, and water content were analyzed according to ASTM methods

## 3. RESULTS AND DISCUSSION

Calcination temperature above 900°C was selected because at and above this temperature mostly an optimized CaO will be produced. This is supported by the results indicated in XRD shows in Figure 1. The intensified sharp peaks of CaO appeared at 2θ value of 29.97°, 37.58° and 54.07°. By increasing the calcination

temperature,  $\text{CaCO}_3$  was completely transforms to  $\text{CaO}$  by evolving the carbon dioxide ( $\text{CO}_2$ ) [4].

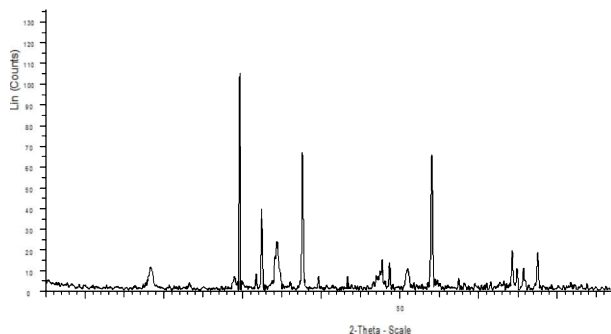


Figure 1 XRD patterns of white clams calcined at 900°C for 4h.

Table 1 Chemical composition of calcined white clam.

Formula	$\text{CaO}$	$\text{Na}_2\text{O}$	$\text{SrO}$	$\text{SO}_3$	$\text{MgO}$
Concentration (%)	94.33	1.56	0.45	0.38	0.11

Table 1 shows the XRF analysis on the catalyst. It is proven that the major compound produced by calcination of white clams mainly consists of calcium oxide,  $\text{CaO}$  (94.33%) with minor compounds such as sodium oxide ( $\text{Na}_2\text{O}$ ) and magnesium oxide ( $\text{MgO}$ ).

### 3.1 Methyl Ester Analysis

All fatty acid methyl esters (FAME) compounds of the optimum biodiesel production found in the Chromatography is listed in Table 2. The largest compound is 10,13-Octadecadienoic acid methyl ester followed by 9-Octadecenoic acid methyl ester. The influence of important variables such as catalyst concentration and molar ratio of methanol to oil on the FAME yield was summarized in Table 3.

Table 2 Composition of fatty acid methyl esters (FAME) for the optimum biodiesel production.

Peak #	Retention Time	FAME	GC-MS %yield	Common Name
1	8.8551	C16:0	9.1015	Myristic acid
2	12.2311	C18:1	14.794	Oleic acid
3	12.2654	C18:1	4.4922	Oleic acid
4	12.3284	C18:1	14.0609	Oleic acid
5	12.9979	C18:2	37.7475	Linoleic acid
6	13.982	C18:3	14.9292	Linolenic acid
Total			95.1253	

High biodiesel yield of 92.91% was obtained at 7 wt% catalyst, methanol/oil molar ratio of 9:1, 7 minutes of reaction time and at microwave exit power 400 watt. It is observed that most of heterogeneous catalyst produces is slightly having lower yields compared with homogeneous catalyst which could yield more than 99%, but this method offers more advantages especially when dealing with low grade feedstocks. The excessive amount of methanol will decrease the yield of biodiesel due to the reversible process in transesterification reaction. The RSO FAME fuel properties were comply with the ASTM D6751 and EN 14212 standards and qualifies for use in diesel engines.

Table 3 Effect of process variables on biodiesel yield.

Catalyst (wt%)	Reaction time (min)	Methanol : Oil	FAME Yield (%)
5	7	6	83.25
		9	86.06
		12	88.89
7	7	6	91.52
		9	92.91
		12	92.67
9	7	6	90.52
		9	91.63
		12	89.98
12	7	6	88.14
		9	84.32
		12	82.63

Table 4 Physico-chemical properties of RSO biodiesel.

Property	Unit	Prepared Biodiesel	ASTM D-6751	EN 14212
Kinematic Viscosity@40°C	$\text{mm}^2/\text{s}$	5.65	1.9 – 6.0	3.5-5
Acid Value	$\text{mgKOH/g}$	0.351	< 0.5	0.5 max
Flash Point	°C	198	> 93	120 min
Density	$\text{kg/m}^3$	898.2	N/A	860-900

## 4. CONCLUSION

Waste white clams was utilized to be used as heterogeneous catalyst. The transesterification reaction of very high FFA rubber seed oil into biodiesel via microwave irradiation was obtained at 92.91% under 12:1 methanol/oil, catalyst percentage of 7 wt.% and 7 minutes reaction time and 400 Watts microwave power. Catalyst concentration and effects of methanol to oil molar ratio contributes significant effects on the process.

## REFERENCES

- [1] Selvaraj, R., Praveenkumar, R., & Moorthy, I. G. (2019). A comprehensive review of biodiesel production methods from various feedstocks. *Biofuels*, 10(3), 325-333.
- [2] Demirbas, A., Bafail, A., Ahmad, W., & Sheikh, M. (2016). Biodiesel production from non-edible plant oils. *Energy Exploration & Exploitation*, 34(2), 290-318.
- [3] Zamberi, M. M., Ani, F. N., & Abdollah, M. F. (2018). The Application of Calcium Oxide from Waste Cockle for Biodiesel Production from Used Cooking Oil via Microwave Heating System. *Journal of Advanced Research in Fluid Mechanics and Thermal Sciences*, 49(2), 92-100.
- [4] Buasri, A., Rattanapan, T., Boonrin, C., Wechayan, C., & Loryuenyong, V. (2015). Oyster and Pyramidella shells as heterogeneous catalysts for the microwave-assisted biodiesel production from Jatropha curcas oil. *Journal of Chemistry*, 2015.

# Comparison of mathematical models for vertical tire load estimation

Amrik Singh Phuman Singh<sup>1,2,\*</sup>, Intan Zaurah Mat Darus<sup>3</sup>

<sup>1)</sup> Fakulti Kejuruteraan Mekanikal, Universiti Teknikal Malaysia Melaka,  
Hang Tuah Jaya, 76100 Durian Tunggal, Melaka, Malaysia

<sup>2)</sup> Centre for Advanced Research on Energy, Universiti Teknikal Malaysia Melaka,  
Hang Tuah Jaya, 76100 Durian Tunggal, Melaka, Malaysia

<sup>3)</sup> Department of Applied Mechanics and Design, School of Mechanical Engineering, Universiti Teknologi Malaysia,  
81310 UTM Skudai, Johor, Malaysia

\*Corresponding e-mail: amriksingh@utem.edu.my

**Keywords:** Acceleration; braking; cornering

**ABSTRACT** – The estimation of the vertical tire loads is important for the vehicle control system applications. This paper compares four estimation methods for vertical tire loads. The equations used to predict the tire vertical load includes the static load, longitudinal load transfer, and lateral load transfer. Simulations for combined cornering and acceleration/braking are performed to evaluate the estimation of the vertical tire loads. The simulation results demonstrate that the differences in the estimation of the vertical tire loads increase with the increase of the lateral acceleration.

## 1. INTRODUCTION

The estimation of the vertical tire loads is important for the application of the vehicle control systems. One example which requires the estimation of the vertical tire load is the optimal tire force allocation. The optimal tire force allocator distributes the desired vehicle longitudinal and lateral forces and the desired yaw moment to the desired longitudinal and lateral tire forces in such a way that the tire force saturation is avoided [1].

Previously, a comparison study was done in [2] but the previous study considered only two different approaches for the estimations of the vertical tire loads. In the present paper, four different types of approaches for the vertical tire load estimation are considered.

## 2. VERTICAL TIRE LOAD ESTIMATION

In this section, the approaches for the vertical tire load estimation are described and the relevant equations are provided.

In ref. [3], the vertical tire loads according to the longitudinal acceleration  $a_x$  and lateral acceleration  $a_y$  are written as

$$F_{z1} = \frac{mgl_r}{2l} - \frac{ma_x h}{2l} - \rho_f \frac{ma_y h}{l_w} \quad (1)$$

$$F_{z2} = \frac{mgl_r}{2l} - \frac{ma_x h}{2l} + \rho_f \frac{ma_y h}{l_w} \quad (2)$$

$$F_{z3} = \frac{mgl_f}{2l} + \frac{ma_x h}{2l} - \rho_r \frac{ma_y h}{l_w} \quad (3)$$

$$F_{z4} = \frac{mgl_f}{2l} + \frac{ma_x h}{2l} + \rho_r \frac{ma_y h}{l_w} \quad (4)$$

Where  $m$  is the total vehicle mass,  $g$  is the gravitational acceleration,  $l_f$  and  $l_r$  are the distances from the vehicle

center of gravity (CG) to the front and rear axles, respectively,  $h$  is the height of vehicle CG from the ground,  $l = l_f + l_r$  is the wheelbase, and  $l_w$  is the track width. The front roll stiffness ratio  $\rho_f$  and the rear roll stiffness ratio  $\rho_r$  are given as

$$\rho_f = \frac{k_{\phi f}}{k_{\phi f} + k_{\phi r}} \quad (5)$$

$$\rho_r = \frac{k_{\phi r}}{k_{\phi f} + k_{\phi r}} \quad (6)$$

Where  $k_{\phi f}$  and  $k_{\phi r}$  are the front and rear roll stiffnesses, respectively. In the right-hand side of Eqs. (1) to (4), the first term is the static load, the second term is the load transfer due to longitudinal acceleration, and the third term is the load transfer due to lateral acceleration. The subscripts 1, 2, 3, and 4 in the left-hand side of Eqs. (1) to (4) denote the front left, front right, rear left, and rear right tires, respectively.

The vertical load for front left tire given by Abe [4] is

$$F_{z1} = \frac{mgl_r}{2l} - \frac{m_s a_x h_s}{2l} - \rho_f \frac{m_s a_y h_s}{l_w} \quad (7)$$

Where  $m_s$  is the sprung mass and  $h_s$  is the height of the sprung mass CG from the ground. For simplicity, we assume the heights of the sprung mass CG and vehicle CG from the ground are the same. Compared to Eq. (1) which uses the total vehicle mass for the second and third terms, in Eq. (7), sprung mass is used.

Another form of vertical load of the front left tire is provided in [5] and [6], and represented as

$$F_{z1} = \frac{mgl_r}{2l} - \frac{ma_x h}{2l} - \frac{l_r}{l} \frac{ma_y h}{l_w} \quad (8)$$

Kiencke and Nielsen [7] gave the following equation for the vertical load of the front left tire:

$$F_{z1} = m \left( \frac{l_r g}{l} - \frac{a_x h}{l} \right) \left( \frac{1}{2} - \frac{a_y h}{l_w g} \right) \quad (9)$$

A gravitational acceleration of 9.8 m/s<sup>2</sup> is assumed for simulation purpose. The vehicle parameters based on [8] are used for simulation and these parameters are given in Table 1.

Table 1 Vehicle parameters.

Parameter	Value	Unit
Total vehicle mass	1707	kg
Sprung mass	1527	kg
Distance from front axle to CG	1.014	m
Distance from rear axle to CG	1.676	m
Height of CG from ground	0.512	m
Track width	1.540	m
Front roll stiffness ratio	0.5626	-
Rear roll stiffness ratio	0.4374	-

### 3. SIMULATIONS

#### 3.1 Cornering and Acceleration

Figure 1 shows the vertical load for front left tire as a function of lateral acceleration for different values of the longitudinal accelerations for combined cornering and acceleration. As indicated in Figure 1, three values for longitudinal acceleration are considered. The blue solid line, red dashed line, green dotted line, and magenta dashed dot line indicate Eqs. (1), (7), (8), and (9), respectively. Although there is a slight difference in Eqs. (1) and (7), the difference in the vertical tire loads given by these equations increases as the lateral acceleration increases. At given longitudinal and lateral accelerations, the vertical tire load given by Eq. (1) is lower than that given by Eq. (7). At zero longitudinal acceleration, the vertical loads given by Eqs. (8) and (9) are the same and the reason is that for zero longitudinal acceleration, Eqs. (8) and (9) are the same.

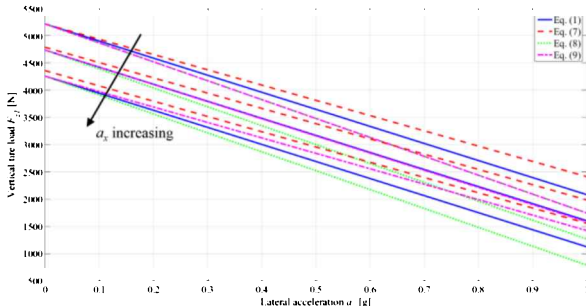


Figure 1 Front left tire vertical load as a function of lateral acceleration for  $a_x = 0, 0.3g$ , and  $0.6g$ .

#### 3.2 Cornering and Braking

The vertical load for front left tire as a function of lateral acceleration for different values of the longitudinal accelerations for a combined cornering and braking is shown in Figure 2. The negative value of the longitudinal acceleration indicates braking. The curves in Figure 2 can be described in a similar way as those for Figure 1.

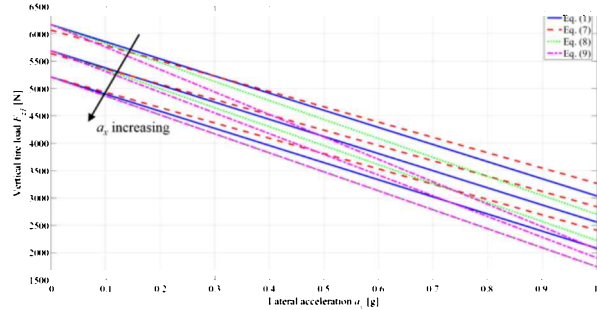


Figure 2 Front left tire vertical load as a function of lateral acceleration for  $a_x = 0, -0.3g$ , and  $-0.6g$ .

### 4. CONCLUSION

In the present paper, a comparison of the different approaches for the estimation of the vertical tire load is reported. The combined cornering and acceleration and combined cornering and braking cases were investigated. A future study could focus on the comparison of the vertical tire loads using the approaches considered in the present paper and those obtained by using high fidelity vehicle dynamics simulation software such as CarSim and IPG CarMaker.

### REFERENCES

- [1] Park, H. & Gerdes, J. C. (2017). Analysis of feasible tire force regions for optimal tire force allocation with limited actuation. *IEEE Intell. Transport. Syst. Mag.*, 9(3), 75-87.
- [2] Pauwelussen, J. P. (2015). Essentials of vehicle dynamics. Butterworth-Heinemann.
- [3] Alleyne, A. (1997). A comparison of alternative intervention strategies for unintended roadway departure (URD) control. *Veh. Syst. Dyn.*, 27(3), 157-186.
- [4] Abe, M. (2015). Vehicle handling dynamics. Butterworth-Heinemann.
- [5] Ren, H., Chen, S., Shim, T., & Wu, Z. (2014). Effective assessment of tyre-road friction coefficient using a hybrid estimator. *Veh. Syst. Dyn.*, 52(8), 1047-1065.
- [6] Nam, K., Fujimoto, H., & Hori, Y. (2014). Advanced motion control of electric vehicles based on robust lateral tire force control via active front steering. *IEEE/ASME Trans. Mechatronics*, 19(1), 289-299.
- [7] Kiencke, U. & Nielsen, L. (2005). Automotive control systems: For engine, driveline, and vehicle. Springer.
- [8] Shim, T., Chang, S., & Lee, S. (2008). Investigation of sliding-surface design on the performance of sliding mode controller in antilock braking systems. *IEEE Trans. Veh. Technol.*, 57(2), 747-759.

# Analysis of intake geometry on multi-cylinder of internal combustion engine performance

Arif Pahmi<sup>1,2,\*</sup>, M.E. Mustaffa<sup>4</sup>, Hazim Sharudin<sup>1,2</sup>, M. Hisyam Basri<sup>1,2</sup>, N.I. Ismail<sup>1,2</sup>, Mohd Fauzi Ismail<sup>1,2</sup>, R.J. Talib<sup>2,3</sup>

<sup>1)</sup> Faculty of Mechanical Engineering, Universiti Teknologi MARA, Cawangan Pulau Pinang,  
13500 Permatang Pauh, Pulau Pinang, Malaysia

<sup>2)</sup> Automotive Research and Testing Center (ARTeC), Universiti Teknologi MARA,  
Cawangan Pulau Pinang, 13500 Permatang Pauh, Pulau Pinang, Malaysia

<sup>3)</sup> Zeta Scientific Sdn. Bhd., Blok 5, Kompleks Otomobil, 23-1B, Jalan Pahat H15/H, Seksyen 15, 40200 Shah Alam,  
Selangor, Malaysia

<sup>4)</sup> Universiti Kuala Lumpur Malaysia France Institute,  
Section 14, Jalan Damai, Seksyen 14, 43650 Bandar Baru Bangi, Selangor, Malaysia

\*Corresponding e-mail: arif.hamid.pahmi@ppinang.uitm.edu.my

**Keywords:** Intake geometry; volumetric efficiency; brake power

**ABSTRACT** – Design of engine intake system will affect the performance of a multi-cylinder engine. This study focused on the effect of different intake geometry on the volumetric efficiency, brake torque, brake power and brake specific fuel consumption performance. Five types of intake geometry are simulated using a one-dimensional computational tool. It can be found the maximum volumetric efficiency predicted by taper design at 109.28%, the peak of brake torque of 162.73 N.m and brake power of 68.17 kW at 4000 rpm engine speed. In addition, no significance impacts the intake geometries on the brake specific fuel consumption.

## 1. INTRODUCTION

The intake manifold is a part of the engine to mix air with the fuel for the internal combustion engine. Many studies have been carried out with aims to improve the intake system. Intake tuning is a method to improve volumetric efficiency and engine brake power in a way exploit the airflow harmonics at a specific engine speed to force more air into engine cylinders [1]. The design of a tuned intake system was significantly useful in which various combinations of pipes and plenums were used to produce the desired torque curve [2].

During the intake stroke, a piston moved downward, reduced pressure at the inlet valve relative to the pressure at the open end of the pipe. At mid-stroke, the piston was near its maximum velocity and the maximum pressure drop occurs across the valve which resulted in the maximum negative pressure at the inlet valve. The rarefaction wave traveled down the pipe to open end and was reflected as a compression wave. A tuning effect occurred when the compression wave arrived at the time of inlet valve closure [1].

The intake design of the internal combustion engine has a significant effect in improving volumetric efficiency, brake torque and brake power of multi-cylinder engine. Five different intake configuration proposed by Mariucci [3] were modeled and simulated using Gt-Power software. The intake design is named as baseline, taper, bellmouth, single bend and s-bend.

## 2. METHODOLOGY

In this study, a four-cylinder spark ignition engine and five types of intake geometry are simulated in Gt-Power software. The intake geometries of baseline, taper, bellmouth, single bend and s-bend from Mariucci [3] are shown in Figure 1.

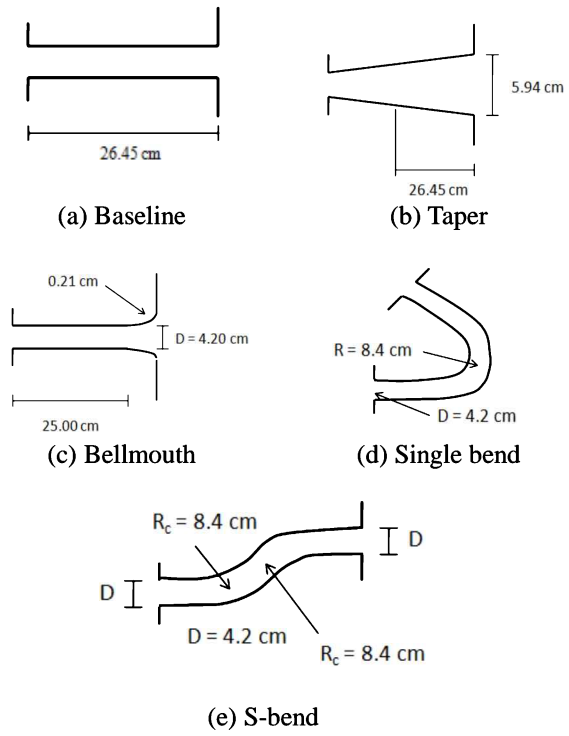


Figure 1 Intake geometry dimensions [3].

The engine has 76 mm bore, 88 mm stroke, 131 mm rod length and a compression ratio of 10. Intake valve open at 334 CAD and close at 64 CAD. Exhaust valve open at 123 CAD and close at 399 CAD. In addition, intake valve diameter is 29 mm and for the exhaust valve, the diameter is 22 mm. The engine model is validated to an experiment performed by Mohamad Edilan Mustaffa.

### 3. RESULTS AND DISCUSSION

Intake geometry influences pressures along with the intake system that significant factor to the improvement of engine performances. The engine performances such as volumetric efficiency, brake torque, brake power and brake specific fuel consumption will be discussed.

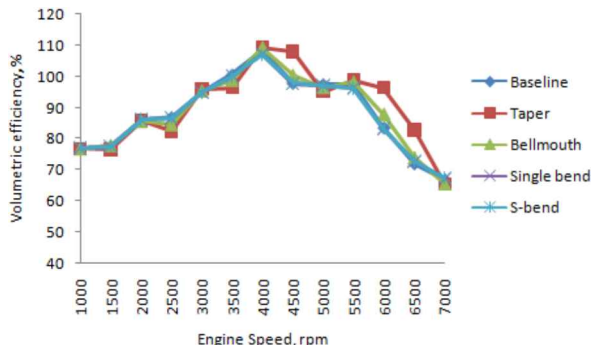


Figure 2 Volumetric efficiency performances.

Taper intake showed the highest maximum volumetric efficiency of 109.28% and brake torque of 162.73 N.m. at a speed of 4000 rpm, as shown in Figure 2 and Figure 3. The taper intake also predicted the highest brake power of 68.17 kW at 4000 rpm is shown in Figure 4. Similar prediction for the speed 4500 rpm, 6000 rpm and 6500 rpm where the highest volumetric efficiency, brake torque and brake power indicated by the taper intake. The increasing of volumetric efficiency is caused by the right timing of the compression wave at the inlet valve. More mixture is drawn to engine cylinder during the intake process that gave high brake torque and brake power of the multi-cylinder engine. The higher incoming pressure contributes the high volumetric during the intake valve opening and affects the overall brake torque and brake power predictions.

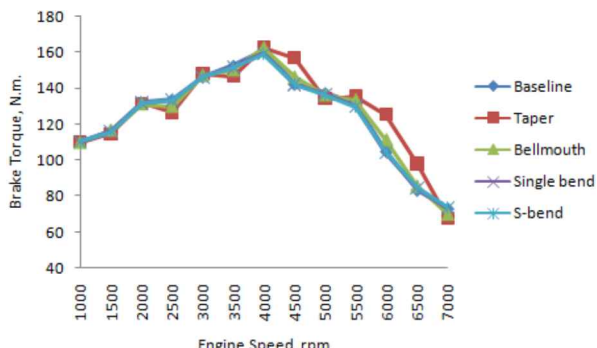


Figure 3 Brake torque performances.

Although the intake geometries affect the performances of volumetric efficiency, brake torque and brake power, there were small influences that less than 5% on the brake specific fuel consumption, as shown in Figure 5. The small effect of brake specific fuel consumption is due to a constant air-fuel ratio and ignition timing throughout the study.

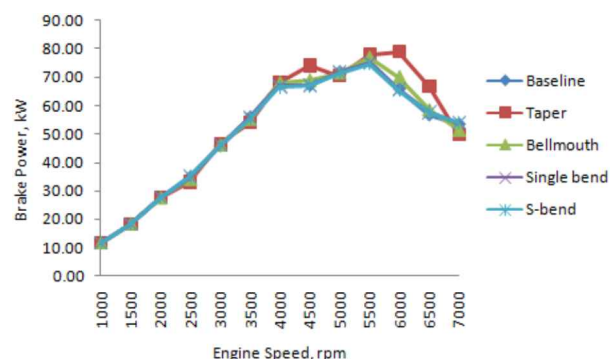


Figure 4 Brake power performances.

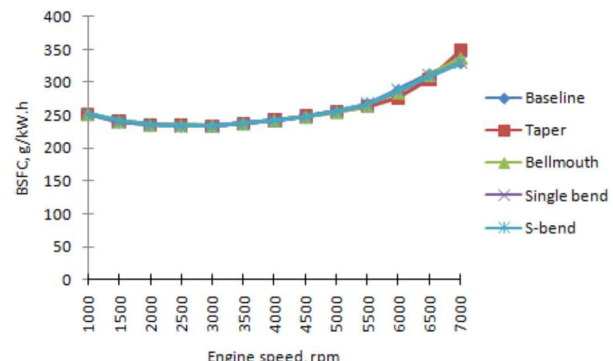


Figure 5 Brake specific fuel consumption performances.

### 4. CONCLUSION

Intake geometries affect the volumetric efficiency, brake torque and brake power predictions. Taper intake showed the highest volumetric efficiency of 109.28% and the lowest volumetric efficiency of 106.98% by s-bend intake at 4000 rpm. The same predictions of volumetric efficiency, brake torque and brake power were exhibited at the 4500 rpm, 6000 rpm and 6500 rpm for the taper design. In addition, brake specific fuel consumption has a small effect on the different intake geometries for all engine speed.

### ACKNOWLEDGEMENT

The authors would like to express gratitude to everyone involved in this project. This research is funded by Universiti Teknologi MARA, Cawangan Pulau Pinang and Fundamental Research Grant Scheme (600-IRMI/FRGS 5/3(084/2019) from the Ministry of Education. Technical support from Universiti Teknologi MARA, Cawangan Pulau Pinang is highly appreciated.

### REFERENCES

- [1] Hamilton, L. J., Cowart, J. S., & Rozich, J. J. (2009). *The Effects of Intake Geometry on SI Engine Performance* (No. 2009-01-0302). SAE Technical Paper.
- [2] Tabaczynski, R. J. (1982). *Effects of inlet and exhaust system design on engine performance* (No. 821577). SAE Technical Paper.
- [3] Mariucci, V. E. (2006). *An experimental and computational investigation of the effect of primary intake runner geometry on the performance of a single cylinder engine* (Doctoral dissertation, The Ohio State University).

# Kinetic modeling for palm oil epoxidation using genetics algorithm

Mohd Jumain Jalil<sup>1,\*</sup>, Alif Farhan Mohd Yamin<sup>2</sup>, Khairul Azhar Kamal<sup>1</sup>, Hamzah Hafizuddin<sup>1</sup>, Muhammad Salman Samin<sup>1</sup>

<sup>1)</sup> Faculty of Chemical Engineering, Universiti Teknologi MARA Cawangan Pulau Pinang,  
13500 Permatang Pauh, Pulau Pinang, Malaysia

<sup>2)</sup> Faculty of Mechanical Engineering, Universiti Teknologi MARA Cawangan Pulau Pinang,  
13500 Permatang Pauh, Pulau Pinang, Malaysia

\*Corresponding e-mail: mjumain0686@ppinang.uitm.edu.my

**Keywords:** Epoxidation; palm oil; kinetic study

**ABSTRACT –** In recent years, there are abundant of studies in epoxidation of vegetable oil, this is due to the rising demand for eco-friendly epoxide. As the epoxide is the important chemical precursor in the industry. So, kinetic model was being conducted in order to determine the optimum value of epoxidation process. Initial concentration of formic acid (FA), hydrogen peroxide ( $H_2O_2$ ) and oleic acid (OA) were 1.4714 mol/L, 1.4714 mol/L and 2.9483 mol/L respectively. Hence, the kinetic rate obtained are  $k_{11} = 0.1334$  mol.L/min,  $k_{21} = 0.0781$  mol.L/min,  $k_{31} = 0.0163$  mol.L/min,  $k_{51} = 0.0169$  mol.L/min. The minimum error is 0.2724.

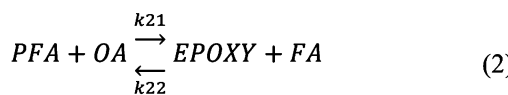
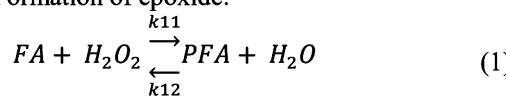
## 1. INTRODUCTION

Recently, epoxidized palm oil (EPO) is high in demand for its function as intermediate in production of paint and coating element [1]. It also happens because of rising in demand for eco-friendly product. According to Jumain [2], the palm oil is the type of vegetable oil which able to epoxidized because it contains unsaturated triglycerides. Epoxy ring-opening or epoxy ring degradation takes place in the epoxidation of vegetable oil as to control process in order to produce good yield and high peroxide values of EPO [3][4].

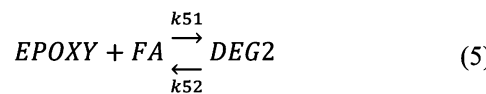
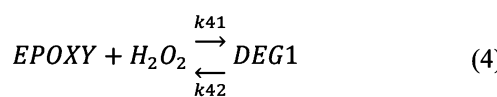
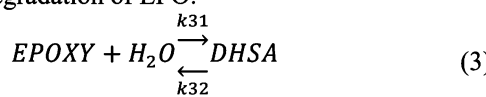
## 2. METHODOLOGY

Chemical reaction for formation of epoxide and degradation of epoxidation palm oil are shown below:

Formation of epoxide:



Degradation of EPO:



Where, FA is formic acid,  $H_2O_2$  is hydrogen

peroxide, PFA is performic acid,  $H_2O$  is water, OA is oleic acid, DHSA is dihydroxy stearic acid.

Computing ode45 function in MATLAB Simulation in order to determine the optimum kinetic reaction of epoxidation.

$$\begin{aligned} \frac{d[FA]}{dt} &= -k_{11}[FA][H_2O_2] + k_{12}[PFA][H_2O] \\ &\quad + k_{21}[PFA][OA] \\ &\quad - k_{22}[EPOXY][FA] \\ &\quad - k_{51}[EPOXY][FA] \\ &\quad + k_{52}[DEG2] \end{aligned} \quad (6)$$

$$\begin{aligned} \frac{d[H_2O_2]}{dt} &= -k_{11}[FA][H_2O_2] \\ &\quad + k_{12}[PFA][H_2O] \end{aligned} \quad (7)$$

$$\begin{aligned} \frac{d[PFA]}{dt} &= k_{11}[FA][H_2O_2] - k_{12}[PFA][H_2O] \\ &\quad - k_{21}[PFA][OA] \\ &\quad + k_{22}[EPOXY][FA] \end{aligned} \quad (8)$$

$$\begin{aligned} \frac{d[H_2O]}{dt} &= k_{11}[FA][H_2O_2] - k_{12}[PFA][H_2O] \\ &\quad - k_{31}[H_2O][EPOXY] \\ &\quad + k_{32}[DHSA] \end{aligned} \quad (9)$$

$$\begin{aligned} \frac{d[OA]}{dt} &= -k_{21}[PFA][OA] \\ &\quad + k_{22}[EPOXY][FA] \end{aligned} \quad (10)$$

$$\begin{aligned} \frac{d[EPOXY]}{dt} &= k_{21}[PFA][OA] \\ &\quad - k_{22}[EPOXY][H_2O] \\ &\quad - k_{31}[EPOXY][H_2O] \\ &\quad + k_{32}[EPOXY][H_2O] \end{aligned} \quad (11)$$

$$\begin{aligned} \frac{d[DHSA]}{dt} &= k_{31}[EPOXY][H_2O] \\ &\quad - k_{32}[DHSA] \end{aligned} \quad (12)$$

$$\begin{aligned} \frac{d[DEG1]}{dt} &= k_{41}[EPOXY][H_2O_2] \\ &\quad - k_{42}[DEG1] \end{aligned} \quad (13)$$

$$\frac{d[DEG2]}{dt} = k_{51}[EPOXY][FA] - k_{52}[DEG2] \quad (14)$$

## 3. RESULTS AND DISCUSSION

The reaction rate,  $k$  of experimental data is corresponding to the initial concentration which are 1.4714 mol/L: 1.4714 mol/L: 2.9483 mol/L (FA: $H_2O_2$ :OA). The result of  $k$  from the simulation are tabulated in Table 1.

**Table 1** Estimated reaction rate, k from simulation.

Kinetic reaction, k	Value (mol. L/min)
$k_{11}$	0.1334
$k_{21}$	0.0781
$k_{31}$	0.0163
$k_{51}$	0.0169
Minimum error = 0.2724	

From Table 1, the k will be input into the MATLAB Simulation in order to the plot the experiment data and simulation data. The plot graph is shows in Figure 1.

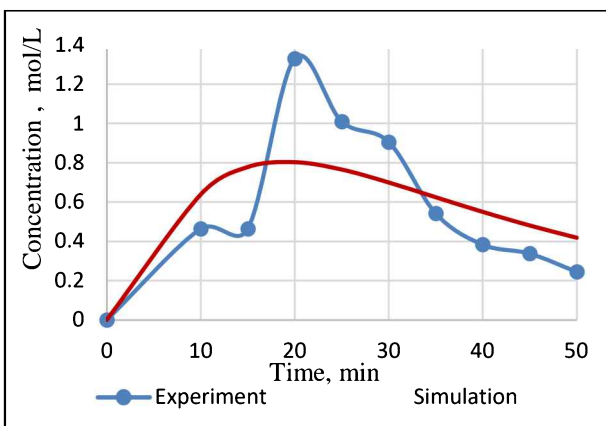


Figure 1 Comparison between experiment and simulation.

A comparison between experimental data and simulation based on kinetic reaction that obtained in Table 1 is plotted in Figure 1. From 0-20 min, it shows the formation of epoxide as the graph is increasing meanwhile from 20-50 min, the graph is decreasing, it shows the degradation of epoxidation is occurred. The simulation is deviated from experimental data as the simulation is solely depend on chemical equation and the reaction takes place at the same time. It is different from experimental as it takes a lot of other factor that influence the data. A mathematical model was developed by Levener et al., [5] to analyze an exothermic liquid-liquid reaction using epoxidation of oleic acid by performicacid *in situ* as example. The kinetics epoxidation of rubber seed oil (RSO) by peroxyacetic acid generated *in situ* were studied at various temperatures. This study was covered by Okiemen [6] and they found that epoxidation with almost complete conversion of unsaturated carbon and negligible oxirane cleavage can be attained by the *in situ* technique. The rate constant for epoxidation of RSO was found to be of the order of  $10^{-6}$  mol<sup>-1</sup> s<sup>-1</sup> and activation energy of epoxidation of 15.7 kcal mol<sup>-1</sup> was determined.

Figure 2 shows the reaction happen in epoxidation and degradation of epoxide process from MATLAB simulation. The simulation correctly predicted the reaction occur.

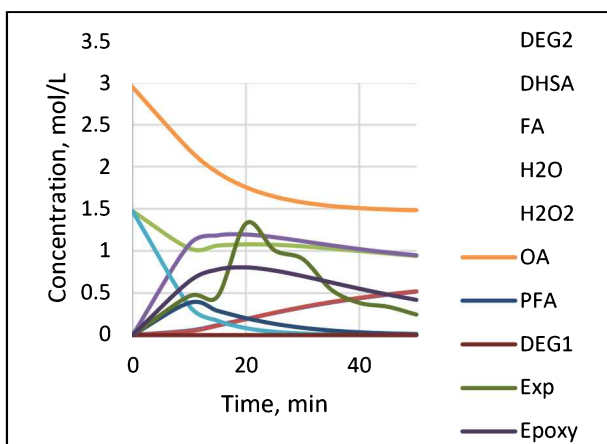


Figure 2 Concentration on each reaction.

#### 4. CONCLUSION

Thus, the simulated kinetic model successfully represents the experiment data. Therefore, the kinetic reaction obtained from the simulation are  $k_{11} = 0.1334$  mol.L/min,  $k_{21} = 0.0781$  mol.L/min,  $k_{31} = 0.0163$  mol.L/min,  $k_{51} = 0.0169$  mol.L/min. Besides, the minimum error that generated by genetic algorithm is 0.2724. From the minimum error value, it indicates that the simulation is acceptable.

#### REFERENCES

- [1] Jalil, A. Farhan, M. Yamin, S. H. Chang, I. S. Azmi, and N. Morad (2018). Selective epoxidation of crude oleic acid-palm oil with *in situ* generated performic acid. *International Journal Engineering and Technology*, 7(2), 152–155.
- [2] Jalil, S. K., Jamaludin, A., Rafizan (2018). Degradation Oxirane ring kinetics of epoxidized palm kernel oil-based crude oleic acid. *Chemistry and Chemical Technology*, 12(3) 296–299.
- [3] Campanella, A., & Baltanás, M. A. (2005). Degradation of the oxirane ring of epoxidized vegetable oils in liquid-liquid systems: I. Hydrolysis and attack by  $H_2O_2$ . *Latin American applied research*, 35(3), 205-210.
- [4] Vanags, M. Kirpluks, U. Cabulis, and Z. Walterova (2018). Highly Functional polyol synthesis from epoxidized tall oil fatty acids. *Journal of Renewable Materials*, 4(12), 1–8.
- [5] Levener, A. Ledoux, L. Estel, B. Taouk, and T. Salmi (2014). Epoxidation of vegetable oils under microwave irradiation. *Chemical Engineering Research and Design*, 2(11), 1495–1502.
- [6] Okiemen, O. I. Bakare, and C. O. Okiemen (2002). Studies on the epoxidation of rubber seed oil. *Industrial Crops and Products*, 15(1), 139–144.

# Comparative study of modeling method of synthetic-jet-assisted mixing

Hong Mun Hoh<sup>1</sup>, Cheng See Yuan<sup>2,\*</sup>, Lim Kim Chuan<sup>3</sup>

<sup>1)</sup>Fakulti Kejuruteraan Mekanikal, Universiti Teknikal Malaysia Melaka,

Hang Tuah Jaya, 76100 Durian Tunggal, Melaka, Malaysia

<sup>2)</sup>Centre for Advanced Research on Energy, Universiti Teknikal Malaysia Melaka,

Hang Tuah Jaya, 76100 Durian Tunggal, Melaka, Malaysia

<sup>3)</sup>Centre for Telecommunication Research & Innovation, Universiti Teknikal Malaysia Melaka,

Hang Tuah Jaya, 76100 Durian Tunggal, Melaka, Malaysia

\*Corresponding e-mail: cheng@utem.edu.my

**Keywords:** Numerical modelling; synthetic jet; mixing

**ABSTRACT** – The aim of the present study is to compare the mixing performance of 2D and 3D Computational Fluid Dynamics (CFD) models of synthetic-jet-assisted fluid mixer. Both geometric models which consist of a mixing channel with a pair of synthetic jet actuators were generated. The diaphragm motion of the synthetic jet actuators was realized by a moving mesh method. Mixing degree was numerically predicted as the result of the CFD models. The results were validated against experimental data. The study concludes that the 3D model shows a better agreement against the experimental result than the 2D model.

## 1. INTRODUCTION

A synthetic jet is a zero-net-mass-flux (ZNMF) jet, which can be generated by the synthetic jet actuator (SJA). The actuator has a closed volume cavity with an oscillating diaphragm attached at one side and an orifice on the other. Due to the oscillating motion of the diaphragm, the processes of expulsion and ingestion of fluid are created around the orifice exit. Thus, a train of vortical structures are produced interact with the ambient fluid before entraining them into the jet. Lately, some numerical studies have been carried out to investigate the mixing efficiency between different fluids in micromixers [1-3]. However, high computation cost might become a drawback for the numerical approaches as compared to the experimental approaches. Comparing to the 3D model, numerical approaches by a 2D model helps to reduce the computation cost due to lower mesh density. Yet, the difference between the mixing degree obtained from a 2D and 3D CFD model remains questionable due to limited reporting in the literature. Therefore, the aim of the present study is to compare the mixing performance of 2D and 3D CFD model of synthetic-jet-assisted fluid mixer in view that the outcome of the study could serve as a guideline of modeling of such fluid mixer.

## 2. METHODOLOGY

For the stated objectives, a commercial CFD software ANSYS, Inc is used to simulate all the cases. Viscous laminar model is applied to all the cases. The geometric model of the synthetic jet actuator (SJA) is created by using ANSYS DesignModuler (as shown in Figure 1 & 2). Both models have the similar parametric conditions. Next, grid is created on the geometric model.

ANSYS Fluent is utilized to solve the transient numerical simulation of the meshed model. Since the mixing performance of the fluid mixer is depending on the mixing degree between two fluids, hence, the mixing degree is numerically predicted as the result of the CFD models. By comparing the time-averaged mixing degree, the model is validated against the previous experimental study [4]. Notice that the experimental study [4] was conducted in 3D.

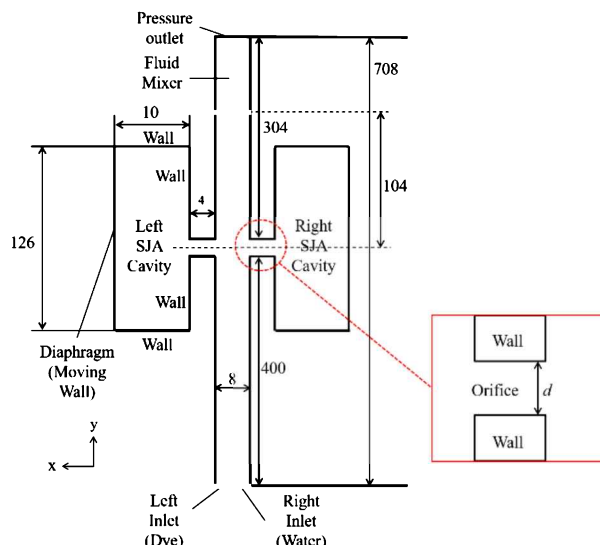


Figure 1 2D-Schematic diagram of the geometric model.

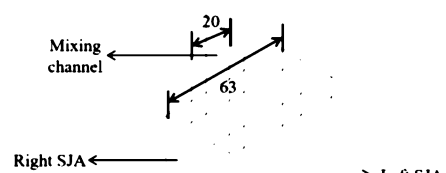


Figure 2 3D-Schematic diagram of the geometric model.

### 3. RESULTS AND DISCUSSION

As observed in Table 1, the 3D model slightly over predicted the mixing degree as compared to the experimental value. However, the agreement is deemed satisfactory. On the other hand, the mixing degree estimated from the 2D model is significantly lower than the experimental value.

Table 1 Comparison of mixing degree obtained from 2D and 3D model against the experimental data.

Model type	Present Mixing Degree	Exp Mixing Degree [5]	1/St
2D	0.07	0.677	0.3
3D	0.81	0.677	0.95

Figure 3 shows the instantaneous concentration contours from the experiment and the cases of 2D and 3D models. No mixing is attained in the case of 2D model as evidenced by concentrated red and blue contour on the left and right flow stream respectively. For the case with 3D model, similar flow patterns of the vortex structures are observed as compared to the one in the experimental study (as observed in Figure 3).

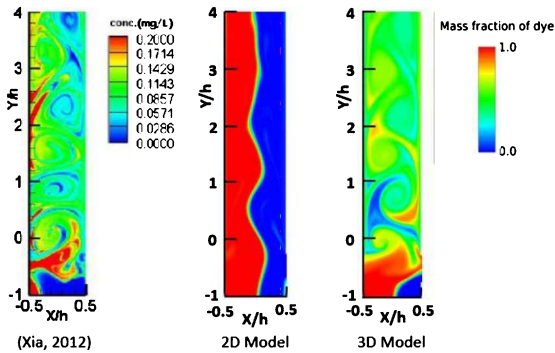


Figure 3 Comparison of instantaneous concentration contours around orifice exit region among experiment and two models (2D and 3D). Notice that the visualization results are captured at the end of the ejection cycle of left SJA.

Figure 4 compares the phase-averaged velocity vector fields and vorticity contours around the orifice exit region. As depicted, the jet does not form in the case of 2D model when the fluid is ejected from the orifices. For the 3D model, the vortices ejected from the orifices behave similarly to the one in the experimental flow visualization results. This phenomenon can be explained by the jet formation criterion proposed by the previous numerical and experimental studies [5] which reported that the jet formation criterion constant,  $K$  is approximately 1 and 0.16 for two-dimensional and axisymmetric synthetic jets, respectively. It is also shown that the jet formation criterion is governed by the equation,  $\frac{1}{St} = \frac{Re}{S^2} > K$  where,  $St$  = Strouhal number,  $Re$  = Reynolds number and  $S$  = Stoke number. By referring to Table 1, the values of  $1/St$  obtained from the 2D model is smaller than the jet formation criterion constant ( $K = 1$ ). Therefore, no jet can be observed from the case with 2D model and subsequently leads to lower mixing degree between two fluids in the fluid mixer.

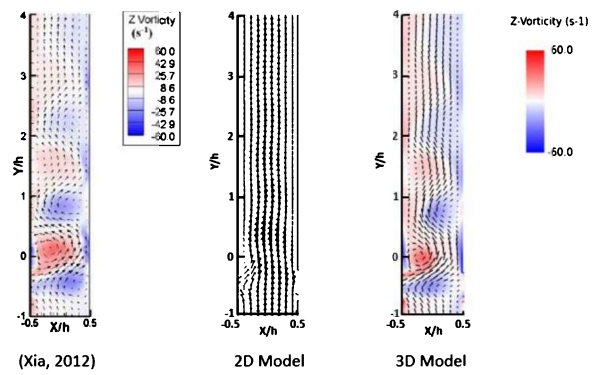


Figure 4 Comparison of phase-averaged velocity vector fields and vorticity contours around orifice exit region among experiment and two models (2D and 3D). Notice that the visualization results are captured at the end of the ejection cycle of left SJA.

### 4. CONCLUSION

A comparison between 2D and 3D numerical modeling of synthetic-jet-assisted mixing has been numerically investigated. The overall result showed that the approaches of using 2D and 3D model affected the mixing degree significantly. While the 3D model shows good agreement with the experimental result, the use of 2D model is proven ineffective for modeling of low Reynolds number synthetic-jet-assisted mixer due to relatively high jet formation criterion for 2D modeling.

### ACKNOWLEDGEMENT

This project is supported by Universiti Teknikal Malaysia Melaka (UTeM) and Ministry of Higher Education Malaysia under FRGS/2018/FKM-CARe/F00375.

### REFERENCES

- [1] Cao, Q., Han, X., & Li, L. (2015). An active microfluidic mixer utilizing a hybrid gradient magnetic field. *International Journal of Applied Electromagnetics and Mechanics*, 47(3), 583-592.
- [2] Liu, K., Yang, Q., Chen, F., Zhao, Y., Meng, X., Shan, C., & Li, Y. (2015). Design and analysis of the cross-linked dual helical micromixer for rapid mixing at low Reynolds numbers. *Microfluidics and nanofluidics*, 19(1), 169-180.
- [3] Chen, X., & Li, T. (2016). A novel design for passive misscromixers based on topology optimization method. *Biomedical microdevices*, 18(4), 57.
- [4] Xia, Q. (2012). *Enhancement of liquids mixing using active pulsation in the laminar flow regime* (Doctoral dissertation, The University of Manchester (United Kingdom)).
- [5] Holman, R., Utturkar, Y., Mittal, R., Smith, B. L., & Cattafesta, L. (2005). Formation criterion for synthetic jets. *AIAA Journal*, 43(10), 2110-2116.

# MyPhysio – A proposed telephysiotherapy system to reduce patient hospital waiting time and improve patient monitoring

Lee Pik Yun, Raja Rina Raja Ikram\*

Fakulti Teknologi Maklumat dan Komunikasi, Universiti Teknikal Malaysia Melaka,  
Hang Tuah Jaya, 76100 Durian Tunggal, Melaka, Malaysia

Corresponding e-mail: raja.rina@utem.edu.my

**Keywords:** Telemedicine; rehabilitation; physiotherapy

**ABSTRACT** - This paper presents MyPhysio, a proposed online physiotherapy rehabilitation system with telemedicine-based consultation service to allow patients eliminate the hassle of regular trips and long wait at hospital center. Requirements elicitation was conducted with 30 patients and 12 physiotherapists to collect critical features and survey previous experiences with telemedicine. MyPhysio, a telemedicine system, was developed based on the results of the requirements elicitation.

## 1. INTRODUCTION

In Malaysia, patients have to undergo long waiting times for physiotherapy in the hospitals with others patients. As survey carry out by Cheema, R.K. in 2017 showed that 40.02% of patients wait up to 4 hours to seek a doctor and 26.3% of patients stop look for medical treatment due to long queueing time [4]. In Malaysian government hospitals, patients can wait up to two months to open a new case due to long queues as the services are offered at a cheaper price than private hospitals [1].

This situation causes inconvenience and frustration for patients that have serious musculoskeletal based injury [3]. Besides, physiotherapist also face difficulty in keeping up to date on patients' case if patients skip appointment. Furthermore, patients are not aware about the importance of carry out physiotherapy treatment which help them recovery faster in the right way [1].

Thus, telemedicine is shall be able to provide access to physiotherapy services in the comfort of the patient's home. Telemedicine allow healthcare providers to evaluate patients' condition regardless of where they are located [5,6].

## 2. RELATED WORKS

Figure 1 showed the comparison between proposed system MyPhysio with existed system in Malaysia such as Door2Door, TELEME and Doctor2U application. MyPhysio mainly focused on telemedicine, hospital appointment, electronic medical record and rehabilitation function that mostly requested by the patients and physiotherapist. Doctor2u provides an e commerce platform together with their application. However, the e commerce platform is deemed not necessary to be included in telephysiotherapy application as there are many platforms out there such as Shopee and Lazada. Door2door and TELEME system both also have limited features such as appointment scheduling and limited telemedicine using a web-based

system. MyPhysio, our proposed application contains major functions that are required by patients and can be accessed via mobile devices. MyPhysio is one of the only applications that have access to web based and mobile devices, enabling more accessibility opportunities.

Features System	Platform	Home Care service	E-Commerce	Telemedicine	Hospital Appointment	Electronic Medical Record	Rehabilitation System
MYPhysio	Web Based + Android			✓	✓	✓	✓
Door2Door (2014)	Web Based	✓					
TELEME (2016)	Web-based			✓			
Doctor2U (2015)	Web Based+Android + IOS	✓	✓	✓		✓	

Figure 1 MYPhysio versus existed system.

## 3. METHODOLOGY

Requirement elicitation was done through two set of questionnaires involving thirty patients and twelve physiotherapists to obtain feedback on the issues below:

- (a) Experiences and opinions on current physiotherapy services
- (b) Features that are important to be implemented in telephysiotherapy

## 4. RESULTS

A total of twenty out of thirty patients (66.7%) agreed they would accept telemedicine as a means of communication for follow up physiotherapy sessions and eight participants were neutral about it. Only two participants of 6.7% did not agree using telemedicine during doctor patient consultations, particularly during follow up sessions. Based on physiotherapists feedback, eight out of twelve patients (66.67%) agreed that telemedicine can improve patient access, patient experience and reduce patients from not attending scheduled physiotherapy appointments. Thus, it is worth to note that the use of telehealth application during physiotherapy can continue to provide quality services for patients.

The main features highlighted by participants to be included in the telephysiotherapy application are hospital appointments, physiotherapy session video uploads, speech to text command feature and emergency call.

### 4.1 Current Framework

Figure 2 showed the flowchart of current system used in hospital when a patient meets a physiotherapist.

We can observe that patient took time to register and wait in different department in order to receive physiotherapy treatment. This not only inconvenient for

patients with serious musculoskeletal based injury, but also decrease hospitals' productivity.

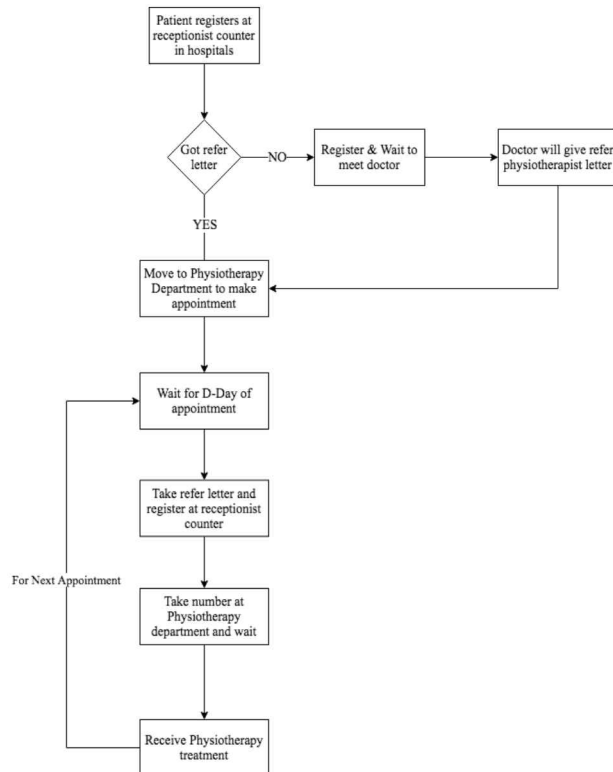


Figure 2 Flowchart of current system.

#### 4.2 Proposed System-MyPhysio

Figure 3 shows the process flow of MyPhysio, an online physiotherapy rehabilitation system. There are three main users of the system – patient, admin and physiotherapist. The patient is required to have a first meeting with the physiotherapist before registering to use MyPhysio. Registered patients can make appointments and carry out telemedicine consultations according to

schedule. They are also able to make online payments for consultations, rate the physiotherapist chosen, make appointments and access personalised health record. In addition, they are able to manage their own profile. After the first meeting with physiotherapist, the physiotherapist can design proper practice based on patient condition and provide feedback for every session.

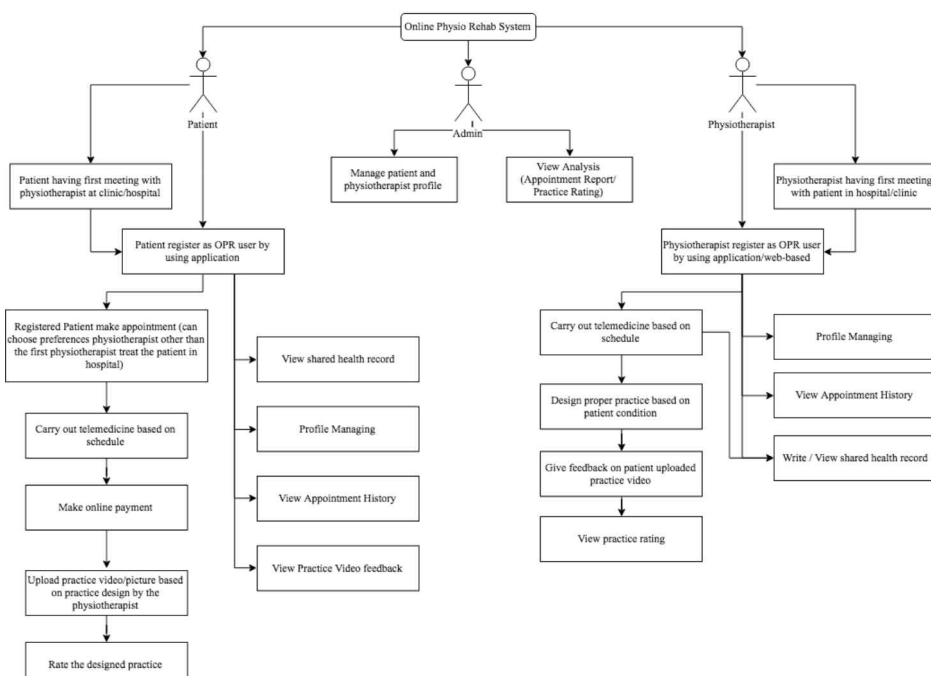


Figure 3 Proposed system MyPhysio.

## 5. CONCLUSION

In conclusion, MyPhysio proposed to allow patients eliminate the hassle of regular trips to hospital or physiotherapy center. In addition, it also enables monitoring of patients' health status to be done online by physiotherapists.

## REFERENCES

- [1] Ikram, R. R. R., Ghani, M. K. A., & Abdullah, N. (2015). An analysis of application of health informatics in Traditional Medicine: A review of four Traditional Medicine Systems. *International Journal of Medical Informatics*, 84(11), 988-996.
- [2] Ikram, R. R. R., Ghani, M. K. A., Ab Hamid, N. R., & Salahuddin, L. (2018). Enabling Ehealth in traditional medicine: a systematic review of information systems integration requirements. *Journal of Engineering Science and Technology*, 13(12), 4193-4205.
- [3] Afza, F., (2017). Major challenges the physiotherapy profession faces in expanding its role in health, prevention, and wellness services. *Journal Physiotherapy & Physical Rehabilitation*, 2(4), pp. 1-3.
- [4] Ahmad, B. A., Khairatul, K., & Farnaza, A. (2017). An assessment of patient waiting and consultation time in a primary healthcare clinic. *Malaysian family physician: the official journal of the Academy of Family Physicians of Malaysia*, 12(1), 14-21.
- [5] Chanen, J. S. Foley survey shows surging telemedicine services across the health care spectrum, into foreign markets. Available online: <https://www.foley.com/foley-survey-shows-surging-telemedicine-services-across-the-health-care-spectrum-into-foreign-markets-11-15-2017>. Accessed on 12 April 2019.
- [6] Cheema, R. K. Patients foregoing treatment due to long waiting time in Malaysia hospital service, survey reveals. Available online: <https://today.mims.com/patients-forgoing-treatment-due-to-long-waiting-time-in-malaysian-hospital-service-survey-reveals>. Accessed on 12 April 2019.

# Multifractal analysis for durability predictive criterion of suspension coil spring signal

C.H. Chin<sup>1,\*</sup>, S. Abdullah<sup>1</sup>, S.S.K. Singh<sup>1</sup>, A.K. Ariffin<sup>1</sup>, D. Schramm<sup>2</sup>

<sup>1)</sup> Centre for Integrated Design for Advanced Mechanical System (PRISMA), Faculty of Engineering & Built Environment, Universiti Kebangsaan Malaysia, 43600 UKM Bangi, Selangor, Malaysia

<sup>2)</sup> Departmental Chair of Mechatronics, University of Duisburg-Essen, 47057 Duisburg, Germany

\*Corresponding e-mail: chuinhao90@gmail.com

**Keywords:** Fatigue life; adaptive neuro-fuzzy inference system; multifractality

**ABSTRACT** – This work presents the fatigue life predictive model of suspension spring based on multifractal properties of road excitations. Random road excitations often possess obvious multifractal properties attributed to the surface irregularities. Hence, modelling of the coil spring fatigue life based on the road multifractality is feasible. Adaptive Neuro-Fuzzy Inference System (ANFIS) was used to model the relationship between the fatigue life and road multifractality, giving an acceptable accuracy in fatigue life prediction. The ANFIS model contributed to an accurate assessment of coil spring fatigue life based on road multifractality.

## 1. INTRODUCTION

Fatigue failure is a common type of failure found in many automotive mechanical components. This is mainly because ground vehicles are continuously exposed to complex road excitations under variable speeds, loads, and road excitations. Some studies have remarked that the combined effects of corrosion and wear as well as continuous exposure to vibrational loading have caused fatigue failure in suspension coil spring. Fatigue failure of the suspension coil spring will affect the ride comfort and the vehicle control. This may result in serious road accident and risk the passengers' life. Therefore, durability assessment is a key element in the production of coil spring to fulfil the requirements concerning safety, durability, reliability, and comfort [1]. In current industrial practice, the time domain approach is commonly utilised due to its high accuracy. This requires the knowledge of the service load (the time history of strain, acceleration, or displacement) for fatigue life prediction.

Strain-life approach is one of the widely applied time-domain approaches to evaluate the durability of automotive components owing to its simplicity and acceptable accuracy. Nonetheless, the complex geometry of coil spring and equipment limitations render the strain histories acquisition of coil spring a challenging task [2]. Additionally, the time-domain approach often requires high experimental cost because this method need large amount of data to sufficiently represent the real-life loading conditions [3]. This eventually causes lengthy and expensive field tests [1]. Besides that, long strain histories also significantly increase the computational duration. To reduce the manufacturing cost, automotive manufacturers demand for an alternative to alleviate the need for strain measurements of coil springs in

evaluations of their durability [2].

Multifractal properties of road excitations are closely related to the surface roughness and thus the road multifractality can be a durability predictive criterium of coil spring [4]. Therefore, the relationship between the road multifractality and coil spring durability need to be determined. This study presents the establishment of fatigue life predictive model based on road multifractality using Adaptive Neuro-Fuzzy Inference System (ANFIS). The trained ANFIS model will contribute to an accurate durability prediction of coil spring based on road multifractality.

## 2. METHODOLOGY

This study employed ANFIS modelling technique to develop the fatigue life predictive model for suspension coil spring. Figure 1 depicts the methodology flowchart.

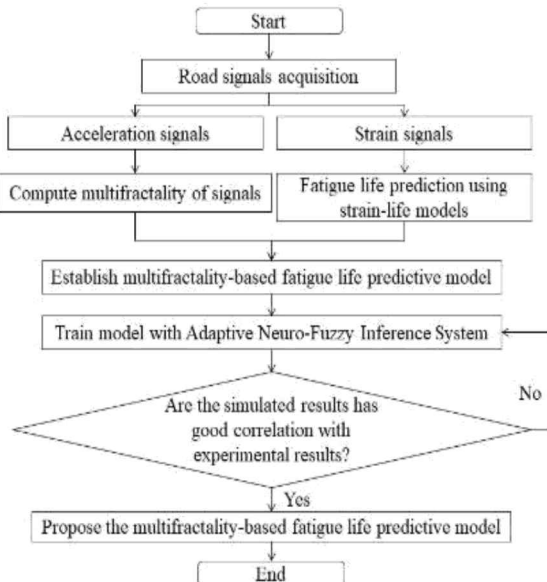


Figure 1 Formulation process of durability predictive model using ANFIS.

Acceleration and strain signals were acquired in road tests. Next, multifractal analysis was conducted on road acceleration signals to determine the singularity spectrum. The multifractality of signal was determined from the width of the spectrum. Morrow strain-life model was used to evaluate the fatigue life of coil springs. With the multifractality and fatigue life, a fatigue life predictive model was developed using ANFIS technique. During the training of the model, 90% input data was

used as the train data while another 10% was the checking data. Checking data was necessary to prevent the overfitting of the ANFIS model. Errors of the ANFIS model using checking data at each epoch of training were computed. Minimal checking error indicated least probability of overfitting. The root-mean-square-error (RMSE) is defined as:

$$RMSE = \sqrt{\frac{\sum_{n=1}^N (\hat{y}_n - y_n)^2}{N}} \quad (1)$$

Where  $\hat{y}$  is predicted value,  $y$  is observed value and  $N$  is number of samples.

Finally, validation of the ANFIS model was done by correlating the simulated fatigue life with the experimental fatigue life.

### 3. RESULTS AND DISCUSSION

A fatigue life predictive model based on road excitations multifractality was trained using ANFIS modelling. During the training, it is important to monitor the checking root-mean-square-errors (RMSE) to prevent overfitting. Figure 2 shows the training and checking errors of the model during the training process. It was found that the training RMSE gradually decreased after each epoch, showing that the model is getting better fitted to the training data. However, the checking RMSE started to increase at epoch 8 of the training process. This indicates that the model became overfitted to the training data after epoch 8. Hence, the training process was then stopped at epoch 8 with the minimum difference of 24% with the training RMSE and lowest checking RMSE of 0.6953 to ensure the general use of the model.

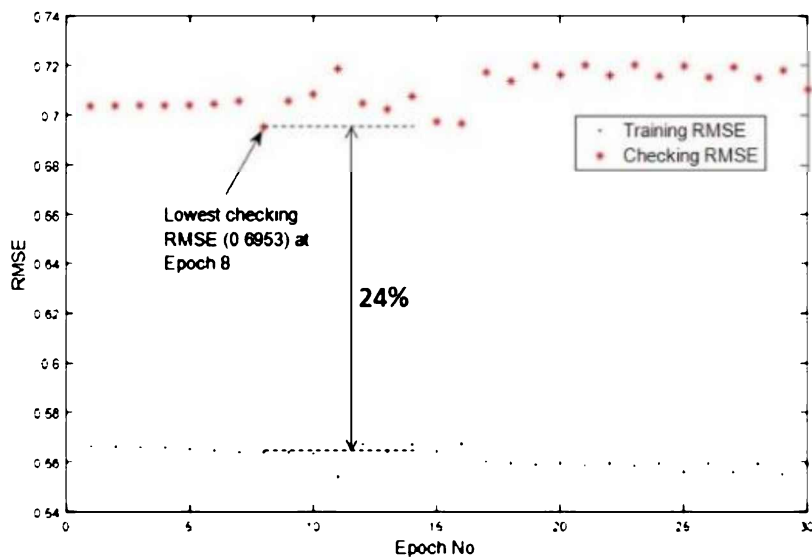


Figure 2 Training and checking RMSE of ANFIS model.

Figure 3 shows the outputs of the ANFIS model. The fatigue life of coil spring decreases as the road multifractality becomes higher. Road multifractality is closely related to the surface irregularities. A road with uneven surface contains irregularities like speed bumps, potholes or high surface roughness. The surface irregularities contributed to excessive vibration to the car body and caused fatigue damage to the coil spring. Quan et al. [4] proved that road surfaces possess obvious multifractal properties and the road multifractality increases with surface roughness. The surface roughness contributed to the fatigue damage of coil spring. It is noteworthy that the fatigue life of coil spring constantly maintained at  $10^4$  cycles when the multifractality reached 0.5 and above. This shows that road signals with higher multifractality above 0.5 will have no significant effect on the fatigue life of coil spring.

The fatigue lives of coil spring simulated by the ANFIS model were correlated with the experimental fatigue lives as shown in Figure 4. It was shown that the simulated fatigue lives had a good conservative relationship with the experimental fatigue lives. 96% of data distributed within the acceptance boundaries between 1:2 and 2:1 correlation.

### 4. CONCLUSION

In this study, a fatigue life predictive model based on road multifractality was established. It was found that higher road multifractality resulted in lower fatigue life of coil spring. The fatigue life of coil spring remained at  $10^4$  cycles at the road multifractality of 0.5 and above. The trained model gave a good accuracy in fatigue life prediction since 96% of the simulated data had a good conservative relationship with the experimental results.

### ACKNOWLEDGEMENTS

This work was financially funded by Universiti Kebangsaan Malaysia under the research grant GP-K007552. This work was also supported by the European Unions's Horizon 2020 research and innovation programme under the Marie Skłodowska-Curie grant agreement (No. 730888).

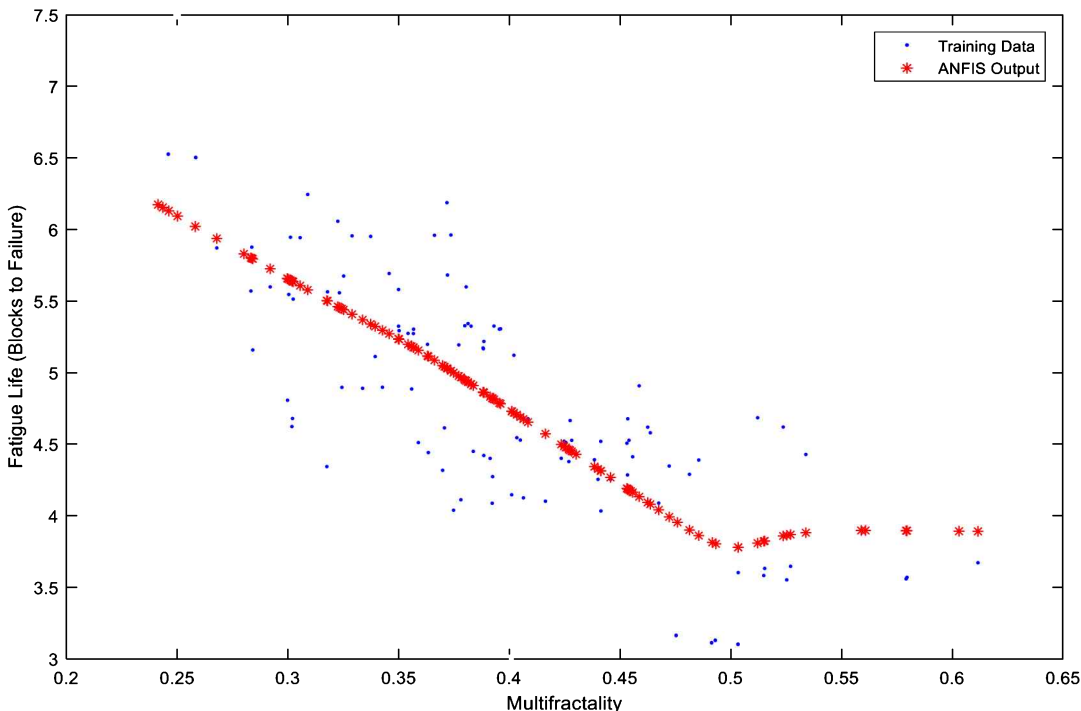


Figure 3 Output of ANFIS model.

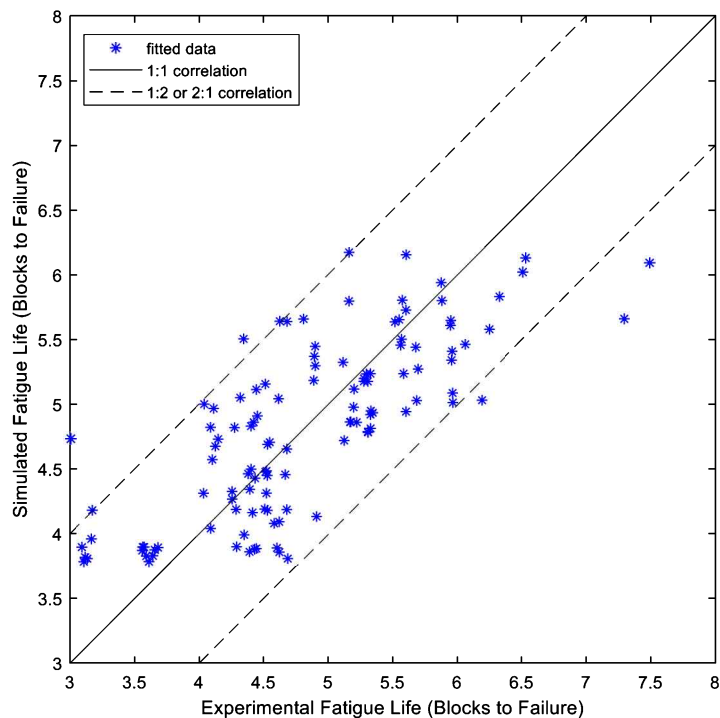


Figure 4 Relationship distribution between simulated and experimental fatigue lives.

## REFERENCES

- [1] Shafiullah, A. K. M. & Wu, C. Q. (2013). Generation and validation of loading profiles for highly accelerated durability tests of ground vehicle components. *Engineering Failure Analysis*, 33, 1–16.
- [2] Putra, T. E., Abdullah, S., Schramm, D., Nuawi, M. Z. & Bruckmann, T. (2017). The need to generate realistic strain signals at an automotive coil spring for durability simulation leading to fatigue life assessment. *Mechanical Systems and Signal Processing*, 94, 432–447.
- [3] Ugras, R. C., Alkan, O. K., Orhan, S., Kutlu, M. & Mugan, A. (2019). Real time high cycle fatigue estimation algorithm and load history monitoring for vehicles by the use of frequency domain methods. *Mechanical Systems and Signal Processing*, 118, 290–304.
- [4] Quan, W., Wang, H., Liu, X. & Zhang, S. (2013). Multi-fractal Analysis for Pavement Roughness Evaluation. *Procedia - Social and Behavioral Sciences*, 96, 2684–2691.

# Modified Anand model parameters for 95.5Sn-4.0Ag-0.5Cu lead-free solder material

A.F.M. Yamin\*, N.N. Azmi, N.A. Norrdin, H. Yusoff

Fakulti Kejuruteraan Mekanikal, Universiti Teknologi MARA, Cawangan Pulau Pinang,  
Kampus Permatang Pauh, 13500 Permatang Pauh, Pulau Pinang, Malaysia

\*Corresponding e-mail: aliff.farhan6205@uitm.edu.my

**Keywords:** Solder joint; creep; Anand model

**ABSTRACT** – Anand model is often used to represent the deformation behavior of solder in an electronic package. To increase the capability of the model, two model parameters in the Anand model namely the initial value of state variable,  $s_0$  and hardening constant,  $h_0$  are modified. The 15 material parameters of the model for 95.5Sn-4.0Ag-0.5Cu (SAC405) were determined by a series of experimental data with 3 different test temperatures (25 °C, 75 °C and 150 °C) inelastic strain rates ( $10^{-5}$  s<sup>-1</sup>,  $10^{-4}$  s<sup>-1</sup>, and  $10^{-3}$  s<sup>-1</sup>). The comparison of the experimental and simulated results showed that the modified Anand model captured the simulation capability.

## 1. INTRODUCTION

Solder joints are extensively used in electronic industries to mount the electronic components into printed circuit boards (PCBs). It provides not only for electrical connections, but it includes the mechanical integrity and thermal dissipation. During system operation, the heat produced in the electronic components expands and shrinks the package assembly in different rates due to the variation of the material in the package. This mismatch of thermal expansion induces shear stress in the solder joints and subsequently fatigue failure when prolonged used. Since most of the electronics failure comes directly from the solder joint itself, thus, the study of the creep in the solder material is important. A unified constitutive model called Anand model [1 - 2] is widely used to predict the viscoplastic behaviors of the solder joints. But, the existing model had minor flaw since it cannot accurately predict in the strain-hardening for low-temperature applications. Thus, a modified Anand model was proposed to reduce this error [3]. This paper reports on the modified Anand model parameters extraction and its reliability to predict the inelastic behavior of the lead-free solder material namely 95.5Sn-4.0Ag-0.5Cu (SAC405) solder alloys. The material parameters for the constitutive model were taken out from available experimental data [4] and later as a validation purpose to capture the reliable response in terms of stress and inelastic strain.

## 2. UNIFIED CONSTITUTIVE EQUATION MODEL

Anand model is a phenomenological constitutive equation developed by Anand and Brown [1 - 2]. The model uses an internal state variable,  $s$ , to resist the

inelastic flow at the local material point. The model is summarized as Equation (1), Equation (2) and Equation (3):

Flow Equation:

$$\dot{\varepsilon}_{in} = Ae^{-\frac{Q}{RT}} \left[ \sinh \left( \zeta \frac{\sigma}{s} \right) \right]^{\frac{1}{m}} \quad (1)$$

Evolution of internal state variable,  $s$ :

$$\dot{s} = \left[ h_0 \left( 1 - \frac{s}{s^*} \right)^a \operatorname{sign} \left( 1 - \frac{s}{s^*} \right) \right] \dot{\varepsilon}_{in} \quad (2)$$

with:

$$s^* = \hat{s} \left( \frac{\dot{\varepsilon}_{in}}{A} e^{\frac{Q}{RT}} \right)^n \quad (3)$$

Where  $\dot{\varepsilon}_{in}$  is inelastic strain rate,  $\sigma$  is equivalent stress and  $T$  is the temperature in absolute scale. Another definition of the model parameters is concluded in Table 1. In order to improve the existing model, the material parameters can be modified as a function of temperature and inelastic strain rate [3 - 4]. Two Anand model parameters were selected ( $s_0$  and  $h_0$ ) and modified accordingly as depicted in Equation (4) and Equation (5):

$$s_0 = c_0 + c_1 T + c_2 T^2 \quad (4)$$

$$h_0 = k_0 + k_1 T + k_2 T^2 + k_3 \dot{\varepsilon}_{in} + k_4 \dot{\varepsilon}_{in}^2 \quad (5)$$

## 3. DETERMINATION OF MODEL PARAMETERS

There are 15 material parameters of the modified Anand model and can be obtained through non-linear optimization methods from a series of stress-inelastic strain experiment data over a wide range of temperatures and inelastic strain rates. For determination of the parameters, the equivalent stress must be computed, and it's defined as:

$$\sigma = cs; \quad c < 1 \quad (6)$$

Whereby  $c$  is defined in Equation (7) as follow:

$$c = \frac{1}{\zeta} \sinh^{-1} \left[ \left( \frac{\dot{\varepsilon}_{in}}{A} e^{\frac{Q}{RT}} \right)^{\frac{1}{m}} \right] \quad (7)$$

From Equation (2), the increment of the state variable,  $ds$  is calculated:

$$ds = h_0 \left( 1 - \frac{s}{s^*} \right)^a d\varepsilon_{in}; \quad s < s^* \quad (8)$$

Integrate  $s \rightarrow s_0$  to  $s$  and  $\varepsilon_{in} \rightarrow 0$  to  $\varepsilon_{in}$ , respectively, yields:

$$s = s^* - \left\{ [s^* - s_0]^{(1-a)} + (a-1)h_0[s^*]^{-a}\varepsilon_{in} \right\}^{\frac{1}{1-a}} \quad (9)$$

Substituting Equation (9) with Equation (6), the evolution of stress is summarized as Equation (10):

$$\sigma = c \left\{ s^* - \left\{ [s^* - s_0]^{(1-a)} + (a-1)h_0[s^*]^{-a}\varepsilon_{in} \right\}^{\frac{1}{1-a}} \right\} \quad (10)$$

The parameters extraction is started from the initial guess values within acceptable ranges found from published literature [3 - 4]. This is followed by the substitution of the predicted material parameters into Equations (3), (4), (5), (7) and (10). The accuracy of the model parameters is determined by minimizing the mean squared error (MSE) computed between the predicted stress in Equation (10) and actual stress from experimental data [4]. Since the model is highly nonlinear, two stages optimization method was used. The first stage is a particle swarm optimization (PSO) technique with the aim of to search-space the region of global minimum of MSE. This is followed by a direct search method using the Nelder-Mead simplex algorithm to find optimal parameters based on the PSO results.

#### 4. RESULTS AND DISCUSSION

Table 1 shows the results of the modified Anand model for SAC405 using optimization techniques discussed in Section 3. Based on the results from Table 1, the MSE computed is 0.589.

Table 1 Modified Anand parameters for SAC405.

Parameter	Description	Values
$s_0$ (MPa)	Initial value of state variable, $s$	As below
$Q/R$ (K)	Activation energy term	10750
$A$ ( $s^{-1}$ )	Pre-exponential factor	11089
$\zeta$	Stress multiplier	20.986
$m$	Strain rate sensitivity of stress	0.8793
$h_0$ (MPa)	Hardening coefficient	As below
$\hat{s}$ (MPa)	Coefficient for deformation resistance saturation value	60.173
$n$	Strain rate sensitivity of the saturation value	$-7.0368 \times 10^{-7}$
$a$	Strain rate sensitivity of the hardening coefficient	2.0110

$$s_0 = 26.76 + 0.04586T - 5.4317 \times 10^{-5}T^2$$

$$h_0 = 62.84 - 506.35T + 4.172T^2 - 1.4788 \times 10^8 \dot{\epsilon}_{in} - 1.1169 \times 10^5 \dot{\epsilon}_{in}^2$$

Once the Anand parameters were determined, the model can be used to predict the stress-inelastic strain curve at a particular temperature and inelastic strain rate. The reliability of the model is evaluated by comparing the stress-inelastic strain curves of the experimental test in terms of the goodness of fit between the model and test data. Figure 1 and Figure 2 shows a comparison between the predicted model and experiments at various inelastic strain rate and temperature, respectively. In most cases, good correlation is obtained indicating that the extracted parameters provide a good fit to the experimental data. However, at  $10^{-3} s^{-1}$  and  $150^\circ C$  curve, the goodness of fit ( $R^2$ ) is around 70%. This is due to the calculated saturation stress being slightly lower compared to the experimental data which is 25.0 MPa instead of 26.7 MPa. The problems may arise from the process in determining the temperature and inelastic strain rate

dependent parameters, such as  $s^*$ . This problem may be solved by building a correlation between the parameters representing the influence of strain rate and temperature with these conditions appropriately.

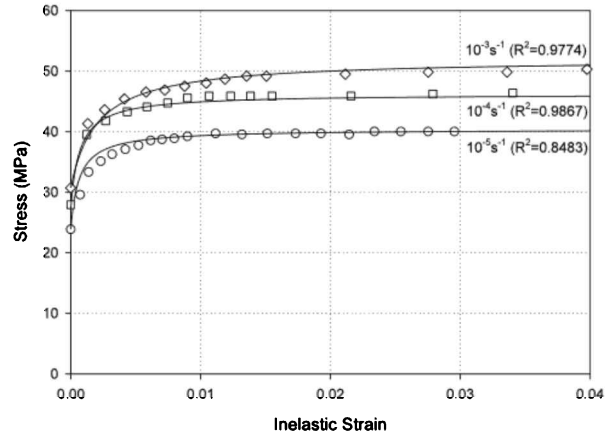


Figure 1 Numerical and experimental stress-inelastic strain curves for SAC405 at  $25^\circ C$  with 3 different inelastic strain rates.

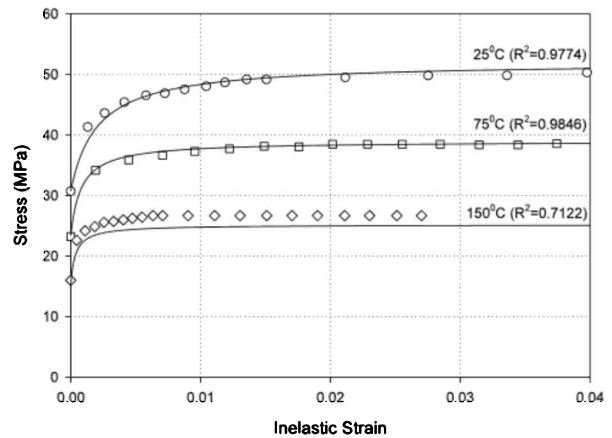


Figure 2 Numerical and experimental stress-inelastic strain curves for SAC405 at  $10^{-3} s^{-1}$  with 3 different temperatures.

#### 5. CONCLUSION

A unified constitutive model Anand is largely used to predict the inelastic behavior of SAC405 solder material. By using optimization techniques and a series of tensile tests with various temperature and strain rate, the model parameters are determined. Results show that a modified Anand model can capture the flow stress and especially at the low inelastic strain. A good comparison was found between test data and a numerical model. It illustrates that the model can predict the flow stress and inelastic strain over a wide range of temperatures and inelastic strain rates.

#### REFERENCES

- [1] Anand, L. (1985). Constitutive equations for hot-working of metals. *International Journal of Plasticity*, 1(3), 213-231.
- [2] Brown, S. B., Kim, K. H., & Anand, L. (1989). An internal variable constitutive model for hot working of metals. *International Journal of Plasticity*, 5(2), 95-130.

- [3] Chen, X., Chen, G., & Sakane, M. (2005). Prediction of stress-strain relationship with an improved Anand constitutive model for lead-free solder Sn-3.5 Ag. *IEEE Transactions on Components and Packaging Technologies*, 28(1), 111-116.
- [4] Qiang, W., Lihua, L., Xuefan, C., Xiaohong, W., Liu, Y., Irving, S., & Luk, T. (2007, April). Experimental determination and modification of Anand model constants for Pb-free material 95.5 Sn4. 0Ag0. 5Cu. In *2007 International Conference on Thermal, Mechanical and Multi-Physics Simulation Experiments in Microelectronics and Micro-Systems. EuroSime 2007* (pp. 1-9).

# Feature identification from product reviews for product evaluation modeling

Syaza Athirah Ramli, Soon Chong Johnson Lim\*, Ming Foong Lee

Faculty of Technical and Vocational Education, Universiti Tun Hussein Onn Malaysia,  
86400, Parit Raja, Batu Pahat, Johor, Malaysia.

\*Corresponding e-mail: scjohnson.lim@gmail.com

**Keywords:** Product review; feature identification; product evaluation modeling

**ABSTRACT** – Product evaluation concerns the consumer satisfaction on a product being used, which is essential for quality improvement purpose. Nowadays, users are willing to share their product experience online through product reviews. This study aims to discover important features from product reviews for evaluation modeling. With the focus on phone camera, review documents for two distinctive phones were downloaded from two websites. Salient product features and their corresponding textual descriptions were manually identified and tagged. Product models were also constructed using ontology for analysis at later stage. We report our outcomes in this paper with some indications for further work.

## 1. INTRODUCTION

Product evaluation is an important study in product design, especially when it involves consumer satisfaction of a product being used that affects perceived product quality. Therefore, in order to produce a product that can meet the needs of consumers, salient features that users emphasized in a product should be identified. Operations of designing a product indirectly involve constantly changing market needs and requirements from time to time. Therefore, product designers should be aware of the latest design trends in accordance with the current technological development to meet with the needs of users [1]. User requirements in this context refer to users' needs to be resolved and also the characteristics and specifications envisioned by the user themselves.

Production of quality products is important to ensure product marketability. Thus, there is a pressing need to manufacture products that meet the contemporary needs of consumers. Product design that is timely is crucial for market success. Therefore, product evaluation needs to be conducted to manufacture products that suite mass user requirements. From previous literature, method such as Analytical Hierarchy Process (AHP) is commonly used for product evaluation. However, problem definition using AHP can be unclear due to the ambiguous oral expression during the decision making process [2].

Nowadays, users shared their experience on the product that they have used through online product reviews. These product reviews are used to help researchers gain product features that are emphasized by consumers. From this aspect, there are also research that focused on analyzing various digital sources of

customer voices, which includes user social media data using topic modeling and sentiment analysis [3], and Kansei-based customer evaluation based on linguistic representation [4]. In this study, we wish to explore product evaluation from the perspective of semantic-based product evaluation. In order to perform this, important product features from product reviews should be identified beforehand for product modeling. We report our outcomes of such an activity, from dataset preparation towards the preliminary product evaluation modeling using ontology in this paper.

## 2. METHODOLOGY

The overall methodology of our work is as described in Figure 1. From Figure 1, The first phase involves the data collection and pre-processing, where relevant product information is extracted from review websites (e.g., review text) and pre-processed, i.e. cleaned and saved in appropriate format. Second phase involves the model building, which includes mainly two tasks: product feature identification & tagging, and model building based on identified features. The first task aimed to determine the salient product features that customers are interested with and followed by building a computational product representation or modeling using these identified features. Upon the model completion, different product models can be better evaluated.

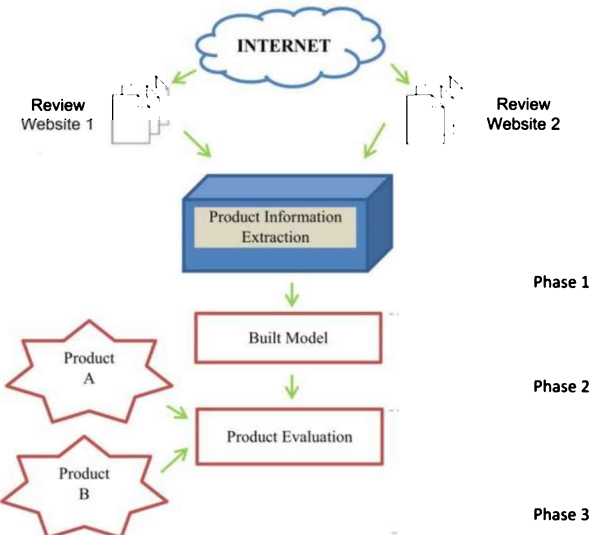


Figure 1 Proposed methodology.

### 3. RESULTS AND DISCUSSION

Firstly, text-based product reviews information was downloaded from two websites. The product in focus is the camera feature of mobile phones. Two websites are chosen for this purpose, *Amazon* and *DPRewiew*. Product reviews from *Amazon* represents the views from normal users or amateurs, while *DPRewiew* represent those users who has higher demands, i.e., professionals. In the context of this study, phone models of year 2015-2017 were preferred because most of these models have larger user base and thus many reviews were available. Two mobile phone models were selected: Apple iPhone 7 Plus and Google Pixel XL. The two popular phone models were selected as there are a lot of reviews available compared to other phone models, thus better details of the two models can be explored. Technically, product reviews are downloaded using specially designed web-scraping script written in the R language. Downloaded data were saved in comma-separated value (CSV) for easier analysis.

Table 1 Summary of product review dataset.

Source	Product	No. of Sentences	No. of Words	No of Tags
Amazon (amazon.com)	Apple iPhone 7 Plus	323	7165	460
	Google Pixel XL	144	4567	426
DPRewiew (dpreview.com)	Apple iPhone 7 Plus	240	5175	504
	Google Pixel XL	211	4382	336

There are four sets of documents that have been collected: two sets of documents each from *Amazon* and *DPRewiew*. At this stage, product features were manually extracted and tagged from every review downloaded. The identification for every product feature is in accordance with the features listed in the product specification of a mobile phone. Upon feature identification, tagging of product features is performed where it is aimed to remark important product features in a product review. For instance, HTML-like tags can be used to indicate features identified in the document text. For instance, <f> optical </f> can be used to tag a possible important camera feature in a review document. Table 1 presents a summary of the review statistics of downloaded review data and identified tags, with some examples of identified features presented in Table 2.

Table 2 Salient features of amateur user for Pixel XL and iPhone 7 Plus.

Battery	RAM	Processor
Time lapse	HDR	Sound
Snapdragon 821	Mode	Megapixel

Based on the discovered features, computational product representation is built using ontology modeling. Ontology model is an able to model the inherent relationship of product features, enabling rich product information modeling for in-depth semantic-based comparison. For instance, based on product structure, comparison can be performed based on multiple facets of product features. Figure 2 shows an example of a preliminarily completed product ontology model for iPhone 7 Plus.

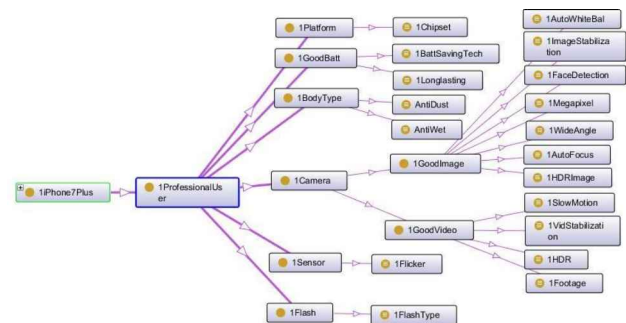


Figure 2 Ontology model for Apple iPhone 7 Plus.

### 4. CONCLUSION

In this study, a tagged product review dataset that consists of two mobile phones that are collected from two websites is produced. Based on such a tagged data, ontology models for the two mobile phones is constructed to enable analysis at the later stage. In overall, the outcome of the study can be used as a basis for in-depth comparison of products, which is crucial for various purpose of product improvement and competitive analysis.

### ACKNOWLEDGEMENT

The work described in this paper was partially supported by a research grant by University Tun Hussein Onn Malaysia under the Ministry of Education, Malaysia (Grant Ref: PPG V023).

### REFERENCES

- [1] Ceschin, F., & Gaziulusoy, I. (2016). Evolution of design for sustainability: From product design to design for system innovations and transitions. *Design studies*, 47, 118-163.
- [2] Lee, S. H. (2010). Using fuzzy AHP to develop intellectual capital evaluation model for assessing their performance contribution in a university. *Expert systems with applications*, 37(7), 4941-4947.
- [3] Jeong, B., Yoon, J., & Lee, J. M. (2017). Social media mining for product planning: A product opportunity mining approach based on topic modeling and sentiment analysis. *International Journal of Information Management*.
- [4] Chanyachatchawan, S., Yan, H. B., Sriboonchitta, S., & Huynh, V. N. (2017). A linguistic representation based approach to modelling Kansei data and its application to consumer-oriented evaluation of traditional products. *Knowledge-Based Systems*, 138, 124-133.

# Mathematical modeling of a simple quarter road vehicle suspension systems on sinusoidal road profile

Adam Samsudin<sup>1,\*</sup>, Ezzatul Farhain Azmi<sup>2</sup>, Amar Faiz Zainal Abidin<sup>1</sup>, Mohd Fariduddin Mukhtar<sup>2</sup>, Abdul Munir Hidayat Syah Lubis<sup>2</sup>, Muhammad Ilman Hakimi Chua Abdullah<sup>2</sup>

<sup>1)</sup> Fakulti Teknologi Kejuruteraan Elektrik dan Elektronik, Universiti Teknikal Malaysia Melaka,  
Hang Tuah Jaya, 76100 Durian Tunggal, Melaka, Malaysia

<sup>2)</sup> Fakulti Teknologi Kejuruteraan Mekanikal dan Pembuatan, Universiti Teknikal Malaysia Melaka,  
Hang Tuah Jaya, 76100 Durian Tunggal, Melaka, Malaysia

\*Corresponding e-mail: adam.samsudin@utem.edu.my

**Keywords:** Mathematical modeling; suspension systems; road profile

**ABSTRACT** – Suspension systems have been extensively applied to vehicles. It gives a better ride comfort and road handling to the driver across many type of road profile. A simple mathematical model of a passive quarter car suspension system has been formulated analytical to determine whether the suspension of car model will give a comfortable ride. This study is expected to see the suspension system of heavy road vehicle which is bus and truck model data that are being applied to sinusoidal road profile with considering the basic quarter car model.

## 1. INTRODUCTION

A suspension system has been applied to vehicles and plays a vital role in order to smooth out the ride while maintaining excellent control. A good suspension system should provide a comfortable ride and good handling within a reasonable range of deflection as previous study [1]. Basically, the function of car suspension system is to keep the car's wheels in firm contact with the road as previous study [2]. This may sound simple, but with acceleration comes force, and forces it to translates into raw energy, when a vehicle accelerates down a road bumps cause forward energy to be converted into vertical energy, which travels through the frame of the vehicle. Without coil and springs to absorb this, vertical energy would cause vehicles to jump up off the road, reduce tire friction and control. Consequently, the car suspension system needs to be investigated and suspension for car also has their potential to improve vehicle performance.

By combining the masses values, the stiffness constant and damping of the quarter car model, it is possible to model any type of road vehicle like car, bus, truck or bicycle.

## 2. METHODOLOGY

In this study, we formulate a basic quarter car suspension model by a ‘sinusoidal road profile’. Numerical solution of 4<sup>th</sup> order Runge-Kutta methods are used in Maple 13 to solve the suspension system. Where, the result of car suspension system applied to bus and truck for simple model and can be shown graphically.

### 2.1 Model Analysis

Figure 1 and Figure 2 shows the quarter car model and the force diagram car model where we are able to formulate a mathematical suspension system with

satisfying Newton’s second law of motion.

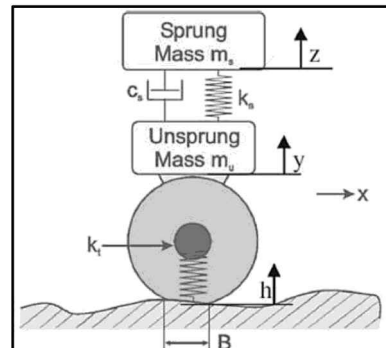


Figure 1 Quarter car model [3].

By applying the Newton’s second law of motion, the equations of the simple car motion can be found as in Equation (1).

$$m\ddot{z} + c\dot{z} + kz = kh + c\dot{h} \quad (1)$$

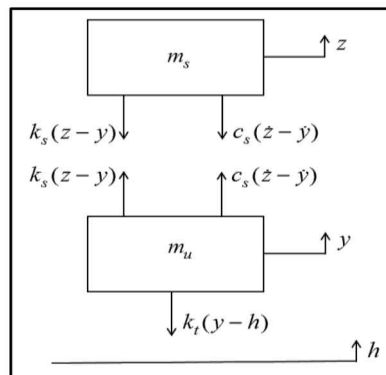


Figure 2 Force diagram of quarter car model.

The equations of the simple car motion can be converted into Equation (2) and Equation (3).

$$m_s\ddot{z} - k_s(z - y) - c_s(\dot{z} - \dot{y}) = 0 \quad (2)$$

$$m_u\ddot{y} + k_s(z - y) + c_s(\dot{z} - \dot{y}) - k_t(y - h) = 0 \quad (3)$$

One method of modeling the suspension system is using the general form of the state space model,  $\dot{x} = Ax + b$ . Where  $z$  is the vector  $[z \ y \ u \ v]^T$  and  $b = [0 \ 0 \ 0 \ kh]^T$ . The state space model is derived as follow:

Taking  $x = u$ ,  $y = v$ ,  $z = y$ ,  $v = \dot{y}$  as the state space variable, the state vector will be:

$$A = \begin{bmatrix} 0 & 0 & 1 & 0 \\ 0 & 0 & 0 & 1 \\ -\frac{k_s}{m_s} & \frac{k_s}{m_s} & -\frac{c_s}{m_s} & \frac{c_s}{m_s} \\ \frac{k_s}{m_u} & -\frac{(k_s + k_t)}{m_u} & \frac{c_s}{m_u} & -\frac{c_s}{m_u} \end{bmatrix}$$

The parameters [3] used are as Table 1.

Table 1 Parameters used for bus and truck.

Parameters	Bus	Truck
$m_s$	4000	4500
$m_u$	550	650
$k_s$	320000	570000
$c_s$	10000	21000
$k_t$	1700000	3000000

## 2.2 Sinusoidal Road Profile

Assume that the road vehicle is travelling with an average horizontal speed  $V$  and hence that  $z = Vt$ .

Then, form for  $y$  can be expressed as Equation (4) by referring to Figure 3.

$$y = h \sin\left(\frac{\pi V t}{d}\right), \quad \ddot{y} = h \left(\frac{\pi V}{d}\right)^2 \cos\left(\frac{\pi V t}{d}\right), \quad (4)$$

Where:  $V=14\text{ms}^{-1}$ ,  $d=2\text{m}$ ,  $h=0.1\text{m}$

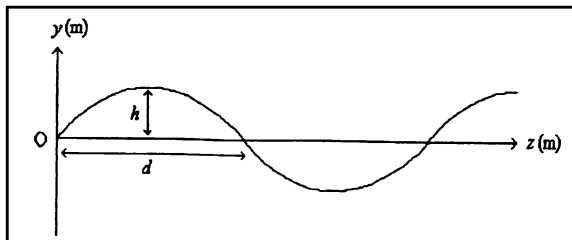


Figure 3 Sinusoidal road profile.

## 3. RESULTS AND DISCUSSION

The good suspension system should satisfy the prediction by graph [4],

- (a)  $|z| \leq 0.1$  for all value of time,  $t$ .
- (b)  $|\ddot{z}| \leq 0.6g$  for all value of time,  $t$ .

The graph of Figure 4, 5, 6 and 7 indicate that both vertical displacement and acceleration for both bus and truck model shows that it bound implied the prediction I and prediction II.

## 4. CONCLUSION

In conclusion, the study of heavy road vehicle suspension system on sinusoidal road profile found that this simple car model applied to bus and truck shows both bus and truck fulfilled the prediction to have a good suspension system on sinusoidal road profile.

## ACKNOWLEDGEMENT

The authors would like to thank UTeM for funding this work under short Grant Scheme no. PJP/2019/FTKEE3(A)/S01655.

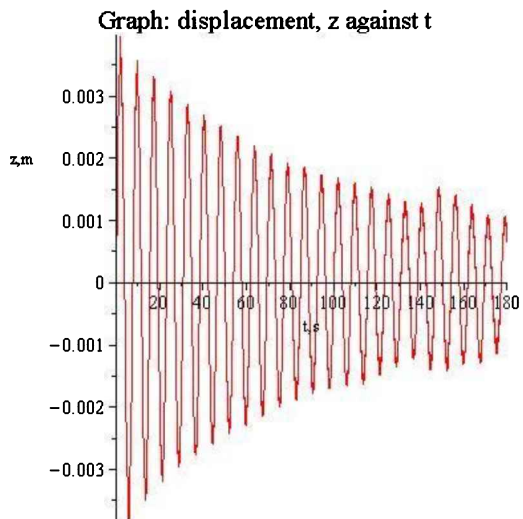


Figure 4 Graph of displacement of Bus  $z$  against  $t$ .

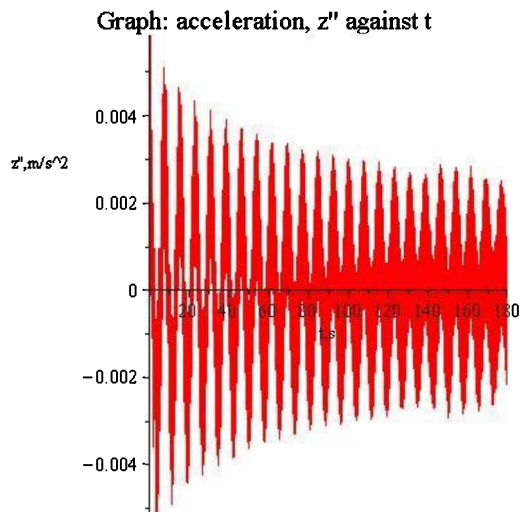


Figure 5 Graph of acceleration of Bus  $z''$  against  $t$ .

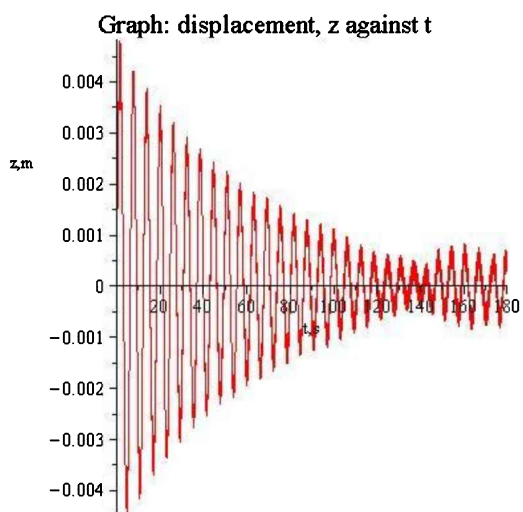


Figure 6 Graph of displacement of truck  $z$  against  $t$ .

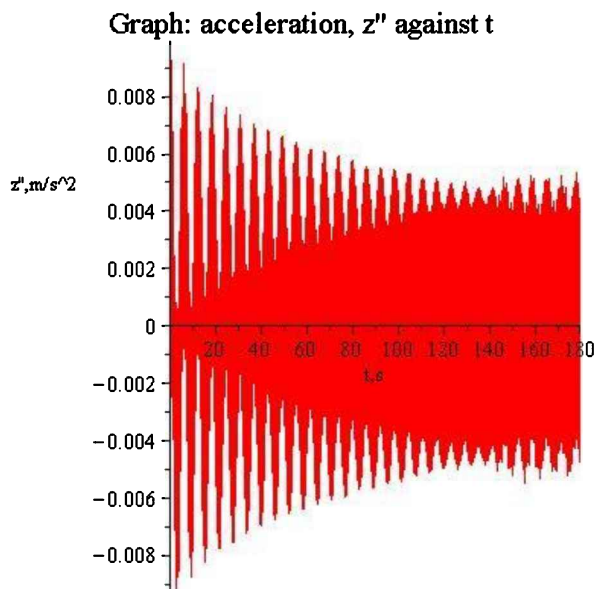


Figure 7 Graph of acceleration of truck  $z''$  against  $t$ .

## REFERENCES

- [1] Jayachandran, R., & Krishnapillai, S. (2012). Modeling and optimization of passive and semi active suspension systems for passenger cars to improve ride comfort and isolate engine vibration. *Journal of Vibration and control*, 19(10), 1077-5463.
- [2] Jha, S. N., Banarjee, S., & Jain, N. (2013). A Textbook of Automobile Technology for Class IX (Level 1). Goyal Brothers Prakashan.
- [3] Tejas, P. T. & Modi, M. J. (2016). Mathematical modeling and simulation of a simple quarter car vibration model. *International Journal for Scientific Research & Development*, Vol. 3(11), 2321-0613.
- [4] Ahmad, Z. M. A, Shamsuddin, A. & Yeak, S. H. (2017). Mathematical modelling of an electromagnetics automobile suspension. *AIP Conference Proceedings*, 1830, 020051(2017).

# Impact of optimization on high-k material gate spacer in DG-FinFET device

Ameer F. Roslan\*, F. Salehuddin, A.S.M. Zain, K.E. Kaharudin

Micro and Nano Electronics (MiNE), CeTRI, Fakulti Kejuruteraan Elektronik dan Kejuruteraan Komputer, Universiti Teknikal Malaysia Melaka, Hang Tuah Jaya, 76100 Durian Tunggal, Melaka, Malaysia

\*Corresponding e-mail: ameerfarhan@aol.com

**Keywords:** FinFET; Taguchi; optimization

**ABSTRACT** – This paper investigates the impact of the high-*K* material gate spacer on short channel effects (SCEs) for the 16 nm double-gate finFET, with output responses optimized using L9 orthogonal array (OA) Taguchi method. Virtual fabrication process and electrical characterization is implemented, and significant improvement is shown towards TiO<sub>2</sub> and HfO<sub>2</sub> material in terms of the I<sub>ON</sub>/I<sub>OFF</sub> ratio obtained at 4.0337×10<sup>6</sup> and 3.6089×10<sup>6</sup> for 0.179±12.7% V of threshold voltage (V<sub>TH</sub>). The I<sub>ON</sub> from high-*K* materials has proved to meet the minimum requirement by International Technology Roadmap Semiconductor (ITRS) 2013 for high performance Multi-Gate technology for the year 2015.

## 1. INTRODUCTION

The size of integrated devices reduces day by day with higher demand in multiple operations and therefore, causing size of MOSFETs which is the main component in memory and processors to be scaled down [1]. On top of that, Moore's Law scaling prediction suppression can be done through the proposed new semiconductor devices and applications [2]. The reduction to nanometer regime has triggered the short channel effects to arise which degrades the system performance and reliability. Therefore, a FinFET of 16nm technology is designed along with the performance of the transistor that is improved in relation to the Moore's Law [3]. The devices performance may have been degraded via scaling process for the transistor miniaturization. The short channel effects (SCEs) has affected the device and the performance of the circuit in electron drift characteristics limitation within the channel, besides the reconstruction of the threshold voltage.

Therefore, the gate oxide thickness and the gate-controlled junction or depletion depth in the silicon have to be reduce in proportion to L (Gate Length). Accordingly, alternative structure such as Double Gate FinFET (DG-FinFET) is believed to have solved the scaling problems especially on the device short channel performance and scalability of nanoscale. Appropriate statistical analysis techniques have been implemented to apply the input process parameter optimization from data collected. In fabricating a proper DG-FinFET device, each steps of fabrication and its order have been prioritized. Other than that, in obtaining the desired threshold voltage level (V<sub>TH</sub>), drive current (I<sub>ON</sub>), leakage current (I<sub>OFF</sub>), and sub-threshold swing (SS), several device characteristics is studied and optimized

by implementing L<sub>9</sub> orthogonal array (OA) Taguchi statistical method due since the variations of the process parameters may result in variations to the output responses [4].

## 2. METHODOLOGY

### 2.1 Virtual Fabrication Process

In this study, ATHENA and ATLAS modules from Silvaco International is used to simulate the fabrication process of DG-FinFET device. Each ATHENA and ATLAS differs in its functionality in which is for process simulation of MOSFET device as shown in Figure 1. By using Device simulation, electrical characteristics of parameters, namely V<sub>TH</sub>, I<sub>OFF</sub>, I<sub>ON</sub> and SS can be extracted. HfO<sub>2</sub>, Si<sub>3</sub>N<sub>4</sub> and TiO<sub>2</sub> both have been used as dielectric materials in the construction of 16 nm DG-FinFET. The device performance has been analyzed in term of V<sub>TH</sub>, I<sub>OFF</sub>, I<sub>ON</sub> and SS and subsequently the ratio of I<sub>ON</sub>/I<sub>OFF</sub> by performing variation on gate length, channel doping and S/D doping concentration.

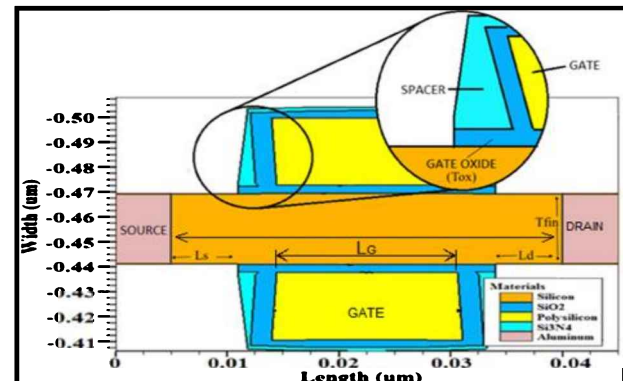


Figure 1 Simulated Structure of the PolySi/SiO<sub>2</sub>-based DGFinFET.

### 2.2 Design of Experiment using L<sub>9</sub> OA Taguchi Method

Based on the parameters identified, the optimization process has been done through variations of process parameter that is identified as in Table 1, along with two levels of noise factor, which is consisting of gate oxidation temperature, Y and polysilicon oxidation temperature, Z of 870°C and 875°C to observe the changes towards the output responses in V<sub>TH</sub>, I<sub>ON</sub>, I<sub>OFF</sub> and SS.

Table 1 Process parameter levels for  $\text{Si}_3\text{Ni}_4$ ,  $\text{HfO}_2$  &  $\text{TiO}_2$ .

Process Parameters	Unit	Level 1	Level 2	Level 3
$V_{TH}$	$\text{Si}_3\text{Ni}_4$	3.85	3.8	3.89
Doping	$\text{HfO}_2$	$\times 10^{13}$ atom/cm <sup>3</sup>	$\times 10^{13}$	$\times 10^{13}$
Dose	$\text{TiO}_2$	3.75	3.77	3.79
$V_{TH}$ Doping Tilt	deg.	5	6	7
Polysilicon	atom/cm <sup>3</sup>	2.10	2.12	2.14
Doping Dose	$\times 10^{14}$	$\times 10^{14}$	$\times 10^{14}$	
Polysilicon Doping Tilt	deg.	-22	-21	-20

### 3. RESULTS AND DISCUSSION

#### 3.1 Characteristics of Double Gate FinFET Device

The I-V characteristics is known as the relationship between the electric current through a device and the corresponding voltage across it. The  $V_{TH}$ ,  $I_{ON}$ ,  $I_{OFF}$  and SS can be extracted from the curve of Drain Current (A) against Gate Voltage (V) from the

ATLAS module. Since transistors should have a high  $I_{ON}$  and a low  $I_{OFF}$  to increase the switching speed of this transistor, the respective output responses are set to have larger-the-best and smaller-the-best for each  $I_{ON}$  and  $I_{OFF}$ .

#### 3.2 Electrical Characteristic of High-K Dielectric Material

This paper uses the High-K dielectric material from Silicon Nitride ( $\text{Si}_3\text{Ni}_4$ ), Hafnium Oxide ( $\text{HfO}_2$ ) and Titanium Oxide ( $\text{TiO}_2$ ) as the gate oxide in 16nm Double Gate FinFET structure. All the devices are set to  $0.179 \pm 12.7\%$  V based on prediction from ITRS 2013 for high performance (HP) multi-gate technology in the year 2015. This is to precisely evaluate the performance in terms of the corresponding  $I_{ON}$ ,  $I_{OFF}$ ,  $I_{ON}/I_{OFF}$  ratio, and SS of the aforementioned device. Table 2 shows the comparison between the L9 OA Taguchi method of three different high-K dielectric materials with its best combination settings.

Table 2 Comparison between three different high-K dielectric materials with its best combination settings.

Spacer material	$V_{TH}$ (V)	$I_{ON}$ (mA/ $\mu\text{m}$ )	$I_{OFF}$ (nA/ $\mu\text{m}$ )	$I_{ON}/I_{OFF}$ ratio	SS (mV/dec)
$\text{Si}_3\text{Ni}_4$	Initial	0.1871	1916.8725	0.8121	93.1799
	Optimized	0.1801	1740.9700	0.6496	94.4728
$\text{HfO}_2$	Initial	0.1838	1913.075	0.5818	93.8911
	Optimized	0.1811	1840.5975	0.5104	93.7842
$\text{TiO}_2$	Initial	0.1851	1961.19	0.5974	93.5863
	Optimized	0.1868	1882.35	0.4666	4.0337
ITRS Prediction	$0.179 \pm 12.7\%$	$\geq 1.7$	$\leq 100$	$\geq 1.48E6$	N/A

The FinFET structures spacers is studied by implementing different materials such as Silicon Nitride ( $\text{Si}_3\text{N}_4$ ), Hafnium Oxide ( $\text{HfO}_2$ ) and Titanium Oxide ( $\text{TiO}_2$ ) having dielectric constants 7keV, 25keV and 85keV respectively due to its high- $K$  dielectric properties. The analysis of the results revealed that the  $\text{TiO}_2$  device has superior electrical characteristics compared to others as listed in Table 2.

### 4. CONCLUSION

In conclusion, the DG- FinFET from simulations have established good electrical properties such as high drive current and low leakage current based on the electrical characteristic analysed. With sufficing  $V_{TH}$  that is within the predicted  $\pm 12.7\%$  of 0.179V, the  $\text{TiO}_2$  and  $\text{HfO}_2$  meanwhile have resulting in improvement of the device due to increment towards the  $I_{ON}/I_{OFF}$  ratio at respective  $4.0337 \times 10^6$  and  $3.6089 \times 10^6$  due to the permittivity of the material alongside the optimization that allows the values of  $I_{OFF}$  to be minimized despite lower  $I_{ON}$  acquired. That said,  $\text{TiO}_2$ -materialized spacer shows the best  $I_{ON}/I_{OFF}$  ratio in conjunction to the device's power consumption efficiency. Besides that, the device characteristics have met the requirement of high performance (HP) multi-gate (MG) technology predicted by ITRS 2013 for the year 2015 requirements.

### ACKNOWLEDGEMENT

The authors would like to thank the Ministry of Higher Education (MOHE) for sponsoring this work under project (FRGS/1/2017/TK04/ FKEKK-CeTRI /F00335) and MiNE, CeTRI, Faculty of Electronics and Computer Engineering, Universiti Teknikal Malaysia Melaka (UTeM) for the moral support throughout the project.

### REFERENCES

- [1] Kaharudin, K. E., Salehuddin, F., Zain, A. S. M., & Abd Aziz, M. N. I. (2015). Optimization of process parameter variations on leakage current in silicon-on-insulator vertical double gate MOSFET device. *Journal of Mechanical Engineering and Sciences*, 9, 1614-27.
- [2] Panda, S. (2015). *Performance Analysis of Single Gate and Double Gate MOSFET with and without Effect of Noise* (Doctoral dissertation).
- [3] Ilatikhameneh, H., Ameen, T., Novakovic, B., Tan, Y., Klimeck, G., & Rahman, R. (2016). Saving Moore's law down to 1 nm channels with anisotropic effective mass. *Scientific reports*, 6, 31501.
- [4] AH, A. M., Menon, P. S., Ahmad, I., ZA, N. F., Zain, A. M., Salehuddin, F., & Sayed, N. M. (2018). Threshold voltage and leakage current variability on process parameter in a 22nm PMOS device. *Journal of Telecommunication, Electronic and Computer Engineering*, 10(2-8), 9-13.

# The vortex shedding for an inclined flat plate of thrombosis using CFD simulation

Nursyaira Mohd Salleh<sup>1</sup>, Mohamad Shukri Zakaria<sup>1,2,\*</sup>, Mohd Juzaila Abd Latif<sup>1,3</sup>

<sup>1)</sup>Fakulti Kejuruteraan Mekanikal, Universiti Teknikal Malaysia Melaka,

Hang Tuah Jaya, 76100 Durian Tunggal, Melaka, Malaysia

<sup>2)</sup>Centre for Advanced Research on Energy, Universiti Teknikal Malaysia Melaka,

Hang Tuah Jaya, 76100 Durian Tunggal, Melaka, Malaysia

<sup>3)</sup>Advanced Manufacturing Centre, Universiti Teknikal Malaysia Melaka,

Hang Tuah Jaya, 76100 Durian Tunggal, Melaka, Malaysia

\*Corresponding e-mail: mohamad.shukri@utem.edu.my

Keywords: Flat plate; vortex shedding; CFD; thrombosis

**ABSTRACT** – The formation of blood clotting due to the combination of vortex shedding that effect by recirculation at the sinus and leaflet. Blood clotting also known as a thrombosis that cause by the non-physiological flow through leaflet of mechanical heart valve (MHV) which lead to high stress and high residence time. This research presents the computational fluid dynamics (CFD) simulation using ANSYS FLUENT 16.1 software to investigate the fundamental knowledge of vortex shedding for inclined flat plate that reacts as a leaflet on MHV which responsible of thrombosis. The simulation flow at different phase of vortex shedding cycle show different development and shedding mechanism for the two train of vortices in the vortex stress which has different vortex strength. This, paper also determine the mechanism of the fluctuating lift and drag on the plate thus relationship with the vortex shedding.

## 1. INTRODUCTION

The potential complication in mechanical heart valve MHV system is thrombosis which necessitates chronic systemic anticoagulation after heart valve replacement [1]. Thrombosis is the presence of a blood clot when activated platelets aggregates with damaged blood element. Then, formation of larger platelet aggregates causes by vortex pairing within the wake that could yield both high shear stress and high residence time compared by single vortex which responsible for blood clotting [2]. The recirculation at the sinus and from leaflet produce combination vortex shedding when there are sharp edges in mechanical heart valve design [1]. Figure 1 shows the flow past through leaflet of heart valve during deceleration phase that characterize by periodic vortex shedding (von Karman vortex street) in the wake of the valve leaflets [3]. The angle of attack,  $\alpha$  for inclined plate will affect the wake region which dominated by vortices at the trailing edge of the plate. The smaller angle of attack will lead to the smaller of wake width and smaller vortices length scales [4]. Thus, the vortex shedding frequency,  $f$  scales with the projected width of the plate normal to the free-stream which strouhal number are approximately constant at  $St = fB/U_\infty \approx 0.15$  for  $\alpha = 30^\circ$ ,  $U_\infty$  being the free-stream velocity. Then, a high numerical solution is required to capture the details of shed vortex.

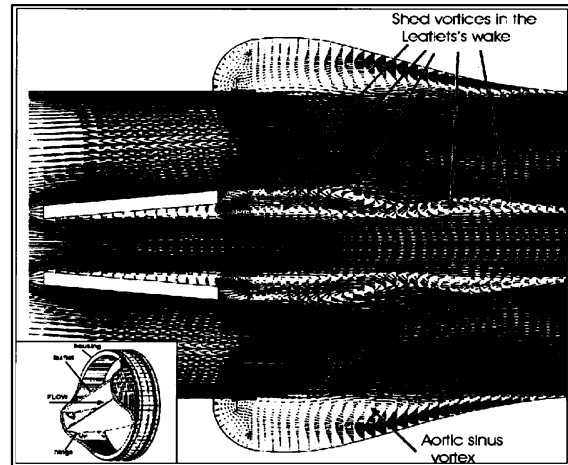


Figure 1 The flow past through leaflet of heart valve during deceleration phase that characterize by periodic vortex shedding (von Karman vortex street) in the wake of the valve leaflets [3].

## 2. METHODOLOGY

In this study, ANSYS-FLUENT 16.1 software was used to simulate the vortex shedding of 2D flat plate and the geometry was inspired by Lam et al. [4]. The boundary condition at inlet using Reynold number,  $Re=U_\infty B/v$  was  $Re=2\times 10^4$  with the velocity at 2 m/s and width  $B=15\text{cm}$ . The surface of the plate was then set as solid wall with no-slip condition and the standard wall function. Figure 2 shows mesh of inclined flat plate.

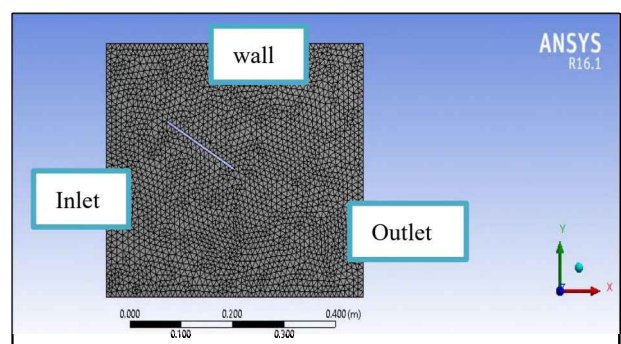


Figure 2 The mesh for inclined plate at  $\alpha=30^\circ$ .

The turbulent flow cases with  $k-\epsilon$  model was used in physics setup with standard values for model constant;

$C_D=0.0845$ ,  $C_1=1.42$  and  $C_2=1.68$  [4]. The grid independence test is done by element and node

### 3. RESULTS AND DISCUSSION

#### 3.1 Vortex Pattern

Figure 3 shows the velocity vector and contour for the inclined flat plate at  $\alpha=30^\circ$ . For the solutions of flow velocity, vorticity and pressure at successive phases of a vortex shedding cycle was analyzed to investigate the vortex shedding for inclined flat plate that reacts as a leaflet on MHV that caused the thrombosis. The vortex within the wake indicate to the formation of larger platelet aggregates [5]. Based on Figure 3, the vortex shedding occurs from the two edges of an inclined plate which leading to velocity field in the very near wake which comprises the recirculation region. The wake was found by a train of counterclockwise vortices shed from the trailing edge of the flat plate at the angle of attack,  $\alpha=30^\circ$  in the simulation.

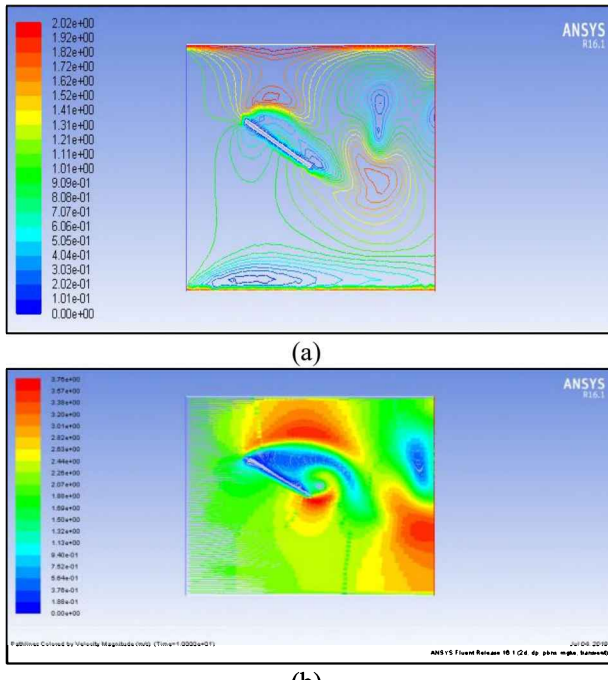


Figure 3 The velocity vector of inclined flat plate (a) velocity vector and (b) velocity contour.

#### 3.2 Lift and Drag Coefficients with Strouhal Number

The inclined flat plate was projected to the size of wake width which affected by the angle of attack. The projected plate width  $B_1 = B \sin \alpha$  was shown as a better characteristic length for the wake. The width plate  $B_1$  was used to calculate the Strouhal number for vortex shedding,  $St = fB_1/U_\infty = 0.125$ . The time history from lift fluctuation was determined as the vortex shedding frequency,  $f$ . Figure 4 shows the graph of lift and drag coefficients on inclined flat plate at angle of attack,  $\alpha=30^\circ$ .

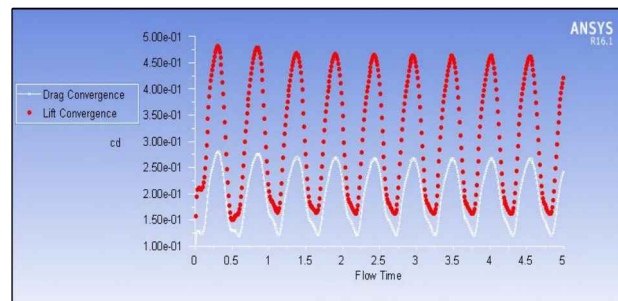


Figure 4 The graph for fluctuating lift and drag coefficients on inclined flat plate at  $\alpha=30^\circ$ .

The finding of the graph was according to the previous study by Lam et al. [4] in which lift coefficient is based on projected flat plate width that show less variations with the angle of attack than the lift force. Then, the lift coefficient increased with decreased in angle of attack. Meanwhile the drag on the plate,  $C_D$  increased when the angle of attack increased which the projected plate width was used to define the coefficient. The shear layer from the plate leading edge entrains fluid and then produce the suction pressure on upper plate surface which its outward movement leads to lower suction pressure and lower lift and drag force on the plate [7]. The lower shear layer at the plate leading edge indicate to vortex shedding. The bluff body and sharp edge can produce vortex due to inertia [8].

### 4. CONCLUSION

The vortex shedding phenomenon of inclined flat plate develop blood clotting through lift and drag for angle of attack which indicate the shear layer formation. The recirculation region could increase the shear stress and residence time of the blood thereby contributing to blood clotting. The investigation of vortex shedding on the flat plate at angle of attack,  $\alpha=30^\circ$  revealed that the vortex rolling up at leading edge remained attached to the rear of flat plat than trailing edge vortex. However, the present study only acknowledges a single vortex case for flat plate to understand the formation that could increase the shear stress which responsible for blood clotting.

### ACKNOWLEDGEMENT

The author would like to thank the facilities provided by Universiti Teknikal Malaysia Melaka and research grant funded from Ministry of Higher Education of Malaysia (FRGS/2018/FKM-CARE/F00367)

### REFERENCES

- [1] Zakaria, M. S., Ismail, F., Tamagawa, M., Aziz, A. F. A., Wiriadidjaja, S., Basri, A. A., & Ahmad, K. A. (2017). Review of numerical methods for simulation of mechanical heart valves and the potential for blood clotting. *Medical & Biological Engineering & Computing*, 55(9), 1519-1548.
- [2] Bluestein, D., Rambod, E., & Gharib, M. (2000). Vortex shedding as a mechanism for free emboli formation in mechanical heart valves. *Journal of Biomechanical Engineering*, 122(2), 125-134.
- [3] Lam, K. M., & Wei, C. T. (2010). Numerical simulation of vortex shedding from an inclined flat

- plate. *Engineering Applications of Computational Fluid Mechanics*, 4(4), 569-579.
- [4] Bluestein, D., Rambod, E., & Gharib, M. (2000). Vortex shedding as a mechanism for free emboli formation in mechanical heart valves. *Journal of Biomechanical Engineering*, 122(2), 125-134.
- [5] Fage, A., & Johansen, F. C. (1927). On the flow of air behind an inclined flat plate of infinite span. *Proceedings of the Royal Society of London. Series A, Containing Papers of a Mathematical and Physical Character*, 116(773), 170-197.
- [6] Luo, S. C., Yazdani, M. G., Chew, Y. T., & Lee, T. S. (1994). Effects of incidence and afterbody shape on flow past bluff cylinders. *Journal of Wind Engineering and Industrial Aerodynamics*, 53(3), 375-399.
- [7] Zhen, T. K., Zubair, M., & Ahmad, K. A. (2011). Experimental and numerical investigation of the effects of passive vortex generators on Aludra UAV performance. *Chinese Journal of Aeronautics*, 24(5), 577-583.

# Development of an integrated vaccine system (IVS) for vaccination healthcare database

Mohd Azrul Hisham Mohd Adib<sup>1,\*</sup>, Muhammad Shahminan Lukman<sup>1</sup>, Nur Hazreen Mohd Hasni<sup>2</sup>

<sup>1)</sup> Medical Engineering & Health Intervention Team (MedEHiT), Human Engineering Group, Faculty of Mechanical Engineering, Universiti Malaysia Pahang, 26600 Pekan, Pahang, Malaysia

<sup>2)</sup> Family Health Unit, Pahang State Health Department, Jalan IM 4, 25582 Bandar Indera Mahkota, Kuantan, Pahang, Malaysia

\*Corresponding e-mail: azrul@ump.edu.my, drhazreen@gmail.com

**Keywords:** Vaccine; integrated system; database; data storage; computer system

**ABSTRACT** – Hospital Information System or also recognized as a Healthcare Information System (HIS) is an integrated computer system installed throughout the hospital to expand the hospital clinical and administrative function. Nevertheless, the conservative guide method of recording vaccination information is less organized and problematic to be recovered back. IVS is an integrated information technology system that efforts to address the weaknesses in the conventional method by organizing storage for vaccination information and also mobile application to remind the parents of the next vaccination date. IVS is immobile in the initial development thru positive progress.

## 1. INTRODUCTION

Albania, Vietnam, Guatemala, Senegal and South Sudan are between the countries that have employed this integrated information technology system on vaccination [1,2]. Immunization Information system (IIS) was established by Albania to support birth and vaccination registration, vaccine stock management, cold chain management, and hostile events management following vaccination [2]. More on IIS, it is an intimate electronic database that is population-based, recording all immunization doses residing in convinced geopolitical areas. The compensations of IIS contain providing the immunization histories that are combined to determine suitable vaccination and also amassed vaccination data for surveillance and program operations to improve vaccination rates and decrease diseases that can be prohibited by a vaccine. By having a consolidated record, it can offer official immunization records for school, camping, and other activities entry necessities. IIS also able to prompt immunization due date, guaranteeing the children to only take the desirable vaccination

The Integrated Vaccine System (IVS) is about storing vaccine intake information in a database by the healthcare organization and recovering the data as a reviewed schedule regarding vaccination dates and information by the parents on an application [3]. The parents would also be informed for the next vaccination date through the application. The objective is to have proper and organized information storage regarding vaccine intake information and also to alert the parents of the vaccination date which is not able to be fulfilled by the conventional manual method.

In Malaysia, this kind of vaccination integrated system has not been established yet [4,5]. For this time

being, our Malaysia's authorities under the programme of Immunise4life [6] have developed an application called *MYVaksinBaby*. The application can offer information about vaccines and vaccine-preventable diseases. It provides a list of endorsed vaccines under Malaysia's National Immunization Programme and also additional optional vaccines that can be acquired in private hospitals and clinics [7]. Issues or questions such as the safety of vaccines and vaccination status in Islam are also addressed by the *MYVaksinBaby* application. Other than that, this app is also able to send auto-reminder for the next vaccination date [5].

In this paper, the integrated vaccine system for vaccination healthcare database is well developed for address the weaknesses in the conventional method by preparing storage for vaccination information and also mobile application to prompt the parents of the next vaccination date.

## 2. METHODOLOGY

### 2.1 Development of IVS

In the IVS development, the registration form was first created using Bracket software. The script from the registration system was sent into the *phpMyAdmin* database (Figure 1) using php and SQLi coding. The *phpMyAdmin* is the database used to store information such as background information of the parents, date of birth, place of birth, gender, permanent address and babies' details including the vaccination schedule (appointment date, type of vaccine and baby weight) and others.



Figure 1 phpMyAdmin database to create the registration form and vaccine database.

## 2.2 Appearance of IVS

A second database known as IVS interface vaccine database (Figure 2) was created using *phpMyAdmin* as well to connect php in the registration form with the database. The vaccine database consists of two separate tables: a patient information table and the vaccine schedule table (Figure 3). A patient information table is to store all data in the registration form while vaccine schedule table is to record vaccination information of the babies.



Figure 2 IVS interface for "registration purpose".



Figure 3 Vaccine database for patient vaccination schedule.

## 3. RESULT AND DISCUSSION

### 3.1 Implementation of IVS

The first step, the parents need to sign up the registration form. All of the compulsory information of the registration form needs to be filled up first before the vaccine schedule table can be generated. By registration, the patients will obtain their own unique ID. After registration, a new appointment date for the next immunization will be set up. The parents will be guided to install a reminder application to remind them of the next vaccination date. The remainder will be triggered one week and one day before the appointment date using the application. In the next vaccination appointments, the patients will go through the same procedure excluding the registration and application installation parts as shown in Figure 4.

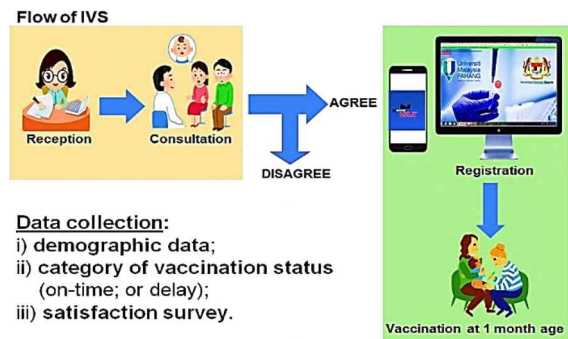


Figure 4 Process flow of implementation the IVS.

## 4. SUMMARY

As we knew that the IVS development is still in the early stage and so far is presenting the great progress based on the registration form and vaccine database created. For the next progress, the vaccine database will be updated more and the reminder application will be developed.

## ACKNOWLEDGEMENT

A big thank you dedicated to University Malaysia Pahang (UMP) for providing us with a good environment and facilities in order to complete this research. By this opportunity, we would like to thank Dr. Siti Suhaila Binti Suradi, MD. from Klinik Kesihatan Kurnia and Dr. Fatimah Binti A. Majid from Pejabat Kesihatan Daerah Kuantan, for sharing valuable information in accordance to our research interest. We would face many difficulties without their assistance.

## REFERENCES

- [1] World Health Organization (WHO) and Path, Optimize, (2013).
- [2] Centers for Disease Control and Prevention (CDC), U.S. Department of Health & Human Services, (2016).
- [3] Adib, M.A.H.M., Hasni, N. H. M., Zabudin, N. F., Zabudin, Lukman, M.S. (2018) Enhancing the Integrated Vaccine System (IVS) using *MyKidVAX* Mobile Application. *Proceedings of the 10<sup>th</sup> National Technical Seminar on Underwater System Technology 2018, Lecture Notes in Electrical Engineering*, 2018, 531-539.
- [4] Kim, C., Lee, J., Kim, Y. (2002) Early stage evaluation of a hospital information system in a middle-income country: a case study of Korea. *International Journal of Healthcare Technology and Management*, 4, 514-524.
- [5] Zakaria, N., Mohd Yusof, S.A. (2016) Understanding technology and people issues in the hospital information system (HIS) adoption: a case study of a tertiary hospital in Malaysia. *Journal of Infection and Public Health*, 9(6), 774-780.
- [6] Immunise4life, Ministry of Health Malaysia, (2016).
- [7] Multimedia Super Corridor, Ministry of Health Malaysia, (1997).

# Enhanced electron mobility in strained Si/SiGe 19nm n-channel MOSFET device

Ahmad F.N.C. Razak, F. Salehuddin\*, Ameer F. Roslan, A.S.M. Zain, K.E. Kaharudin

Micro and Nano Electronics (MiNE), CeTRI, Fakulti Kejuruteraan Elektronik dan Kejuruteraan Komputer, Universiti Teknikal Malaysia Melaka, Hang Tuah Jaya, 76100 Durian Tunggal, Melaka, Malaysia

\*Corresponding e-mail: fauziyah@utem.edu.my

**Keywords:** Strained MOSFET; high-k material

**ABSTRACT** – In this study, the effects of strain on the 19nm n-channel MOSFET device performance have been investigated. The comparison of performances between unstrained and strained 19nm n-channel MOSFET device was also explored. The virtual fabrication of the device was performed using ANTHENA module while the device's electrical characteristics were simulated using ATLAS module. In this work, higher electron mobility or drive current ( $I_{ON}$ ) for a device has been achieved by using a high-k material for the gate spacer with Strain Si/SiGe. The result shows that the value of  $I_{ON}$  (600  $\mu$ A/ $\mu$ m) meet the ITRS 2013 prediction for low power performance technology.

## 1. INTRODUCTION

MOSFET has experienced various changes in improvement. The device continuously scaled down, obeying Moore's Law. Moore's Law states that the feature size transistors are scaled down at a rate of about 0.7 every 18 months [2]. It is estimated that the physical gate length is scaled around 30% for every generation [2]. The reason for scaling down of the MOSFET is to decrease the IC size without downgrading it or to increase the functionality with the same size. The power efficiency also improves as the transistor is scaled smaller and smaller. However, approaching near to 20nm, it becomes more complicated such as SCE to intensify. Shivam et al. [1] informed that by approaching dimension to the nanometer, it had affected the gate leakage current, drain induced barrier lowering and other characteristic parameters arise and the device performance becomes worse. To address this problem, some improvement and changes in device structure and material are needed to provide higher drive current, faster speed, and lower power consumption [1].

Therefore, in this research the performance analysis of single gate n-channel strained with 19nm channel length is studied and investigated. Strained silicon engineering provides higher mobility and helps to reduce power consumption by allowing the use of lower drain voltage ( $V_{DS}$ ) and higher threshold voltage while maintaining desirable device speed [2/10]. Singh et al. [3/5] mentioned that strained silicon has the potential to achieve high mobility, enhancement in drive current and fit when combining with conventional silicon processing. The researchers also stated that the strain could improve MOSFET drive current by modifying the channel of band structure to enhance the performance even channel length in nanoscale [2,3].

## 2. METHOD AND MATERIALS

The Strained Si/SiGe 19nm n-channel MOSFET device was fabricated virtually by using ATHENA simulator module. The substrate used for the device was p-type silicon (Si), with a <100> orientation. Then, the device was analysed using ATLAS simulator module. Several electrical characteristics were retrieved from this structure such as threshold voltage ( $V_{TH}$ ), drive current ( $I_{ON}$ ), leakage current ( $I_{OFF}$ ),  $I_{ON}/I_{OFF}$  ratio and subthreshold swing (SS). All the values must be compared and met the requirement predicted by International Technology Roadmap Semiconductor (ITRS) for low power (LP) performance single-gate technology [4/ITRS ref]. Figure 1 shows the complete structure of the device where material silicon germanium (SiGe) was acted as a strain and using titanium oxide ( $TiO_2$ ) as gate spacer. Titanium Oxide ( $TiO_2$ ) was known as the good material which had the highest permittivity of dielectric constant [5].

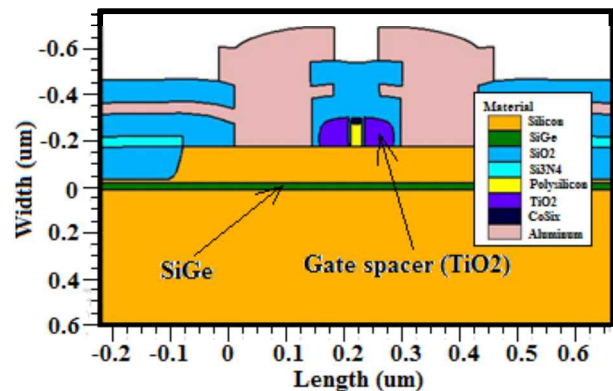


Figure 1 Complete structure of Strained Si/SiGe 19nm n-channel MOSFET device.

Figure 2 shows the characteristic of the Strained Si/SiGe 19nm n-channel MOSFET with  $TiO_2$  material as gate spacer. The two curves in the graph were obtained from the ATLAS simulator module. At the right y axis show a linear scale while on the left y axis shows a logarithmic scale. The number of electrons in the channel increases when the gate voltage ( $V_G$ ) is increased. The  $I_{OFF}$  is at the minimum gate voltage (0V) and the  $I_{ON}$  is at the maximum gate voltage (> 1V). The slope of this exponential increase on a logarithmic scale is called the subthreshold slope (SS) and is expressed in millivolts per decade of current [6].

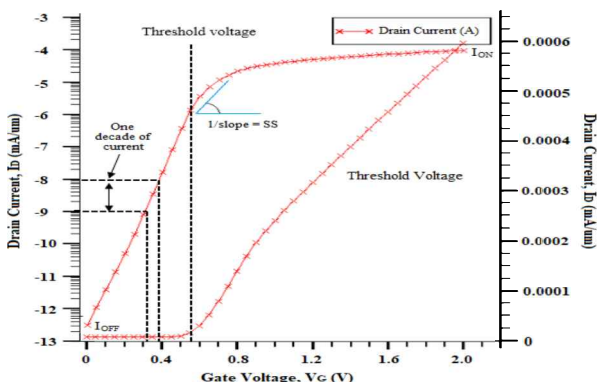


Figure 2 The characteristic of Strained Si/SiGe 19nm n-channel MOSFET with  $\text{TiO}_2$  as gate spacer.

### 3. RESULT AND DISCUSSION

Analysis was performed after the process and device simulation for bulk, silicon on insulator (SOI) and strain 19nm n-channel MOSFET device have been completed. The usage of material doping and the design structure also were considered in this analysis. At the end of the analysis, all results were considered to compare with ITRS and other types of materials. Table 1 shows the comparison between bulk planar and Strain/SOI 19nm single gate MOSFET device with Silicon nitride ( $\text{Si}_3\text{N}_4$ ) and  $\text{TiO}_2$  as gate spacer.

Table 1 Comparison between bulk planar and Strain/SOI 19nm n-channel MOSFET device.

Electrical Characteristics	ITRS 2013 (For year 2015)	19nm Bulk	19nm SOI with $\text{Si}_3\text{N}_4$ as gate spacer	19nm strain with $\text{Si}_3\text{N}_4$ as gate spacer	19nm SOI with $\text{TiO}_2$ as gate spacer	19nm strain with $\text{TiO}_2$ as gate spacer
$V_{\text{TH}}$ (V)	0.533	0.533	0.532	0.533	0.534	0.533
$I_{\text{ON}}$ ( $\mu\text{A}/\mu\text{m}$ )	$\geq 456$	444.7	322.2	363.2	548.8	600.0
$I_{\text{OFF}}$ ( $\text{pA}/\mu\text{m}$ )	$\leq 20$	450.5	135.5	304.4	113.5	75.4
SS (mV/dec)	70 - 90	99.81	85.77	85.51	91.06	80.49
$I_{\text{ON}}/I_{\text{OFF}}$ ratio	22.8E6	9.9E5	2.4E6	1.19E6	4.84E6	7.95E6

In designing the MOSFET device, technically the transistors should have a high drive current and a low sub-threshold voltage swing in order to increase the switching speed of the device and low power consumption. The optimum value of  $V_{\text{TH}}$  and minimum leakage current ( $I_{\text{OFF}}$ ) value were the aims to be achieved. The  $V_{\text{TH}}$  value must in range of  $\pm 12.7\%$  as stated in ITRS 2013 [4]. Another parameter that can be considered is subthreshold swing (SS), where with small values of SS will become high value in  $I_{\text{ON}}$ . Thus, 19nm strain Si/SiGe with  $\text{TiO}_2$  as gate spacer give the best value in SS equal to 80.49 mV/decade. It means that an 80.49mV increase in the gate voltage brings about a tenfold increase in the drive current [6].

Meanwhile, the  $I_{\text{ON}}/I_{\text{OFF}}$  ratio shows in term of power consumption. By comparing both tables, Strained Si/SiGe 19nm n-channel MOSFET device with  $\text{TiO}_2$  as a gate spacer has the highest  $I_{\text{ON}}/I_{\text{OFF}}$  ratio which indicates in less of power consumption. Despite the

lower  $I_{\text{ON}}/I_{\text{OFF}}$  ratio of the high-k materials, they have better performance compared to the conventional  $\text{Si}_3\text{N}_4$ . The subthreshold swing is improved as the gate spacer dielectric constant is increased. These results imply that the gate-to-channel control ability is enhanced due to the assistance of the High-k gate spacer dielectric. As a result, a lower leakage current and high driving current for 19nm n-channel MOSFET device can be achieved by using a high-k material for the gate spacer with Strain Si/SiGe. Thereby effectively reducing the power dissipation and increasing the performance of the transistor.

### 4. CONCLUSION

In conclusion, the Strained Si/SiGe 19nm n-channel MOSFET device has established good electrical characteristics such as high drive current and high  $I_{\text{ON}}/I_{\text{OFF}}$  ratio compare to the bulk planar and SOI MOSFET device. It means strained silicon engineering provides higher mobility and helps to reduce power consumption by allowing the use of lower  $V_{\text{DS}}$  and higher  $V_{\text{TH}}$  while maintaining desirable device speed. Besides that, the value of  $I_{\text{ON}}$  ( $600 \mu\text{A}/\mu\text{m}$ ) has met the requirement of low power performance single-gate technology predicted by ITRS 2013 for the year 2015.

### ACKNOWLEDGEMENT

The authors would like to thank the Ministry of Higher Education (MOHE) for sponsoring this work under project (FRGS/1/2017/TK04/FKEKK-CeTRI/F00335) and MiNE, CeTRI, Faculty of Electronics and Computer Engineering (FKEKK), Universiti Teknikal Malaysia Melaka (UTeM) for the moral support throughout the project.

### REFERENCES

- [1] Sharma, S., Pundir, A., Pandey, R., Patel, V. K., & Agrawal, N. K. An Analysis of Device Characteristics of Strained N-Channel MOSFET. *International Journal of Electronics and Communication Engineering*, 3(8), 14-17.
- [2] Chaudhry, A., & Sangwan, S. (2013). Modeling of the effect of uniaxial mechanical strain on drain current and threshold voltage of an n-type MOSFET. *Solid-State Electronics*, 79, 133-137.
- [3] Singh, A., Kapoor, D., & Sharma, R. (2017). Performance analysis of SiGe double-gate N-MOSFET. *Journal of Semiconductors*, 38(4), 044003.
- [4] ITRS (2013). [www.ITRS2013.net](http://www.ITRS2013.net)
- [5] Ruan, D. B., Chang-Liao, K. S., Li, C. C., Lu, C. C., Liao, Y. L., Chen, L. T., ... & Hsieh, T. L. (2015). Improved electrical characteristics of high-k gated MOSFETs with post-growth treatment on interfacial layer. *Microelectronic Engineering*, 138, 81-85.
- [6] Ferain, I., Colinge, C. A., & Colinge, J. P. (2011). Multigate transistors as the future of classical metal–oxide–semiconductor field-effect transistors. *Nature*, 479(7373), 310.

# The omni-directional of autonomous underwater vehicle (AUV)

Mohd Shahriel Mohd Aras\*, Keek Joe Siang, Grace Wong Mee Sing, Mohd Bazli Bahar, Mohamad Haniff Harun, Ho Gui Yan

Center for Robotics and Industrial Automation (CeRIA), Fakulti Kejuruteraan Elektrik,  
Universiti Teknikal Malaysia Melaka, Hang Tuah Jaya, 76100 Durian Tunggal, Melaka, Malaysia

\*Corresponding email: shahriel@utem.edu.my

**Keywords:** Omni-directional autonomous underwater vehicle; system identification; depth control; pose controller

**ABSTRACT** – This paper describes development of an Omni-directional movement of an Autonomous Underwater Vehicle (AUV). AUVs needed high maneuverable and responsive to fulfill different underwater tasks in hard-to-reach areas. AUV with an Omni-directional with the configuration of four thrusters which is able to control all six degrees of freedom. Developing an Omni-directional driven using the manual configuration of eight thrusters but only four thrusters will be used. The AUV should be fully holonomic such as it has the ability to control all six degrees of freedom and can perform arbitrary movements in the 3D space while holding any position. The AUV will be developed based on the design parameters then system identification took place once the platform was ready to be tested to get input-output signals. MATLAB System Identification Toolbox is employed to infer the model. Then the model obtained from a toolbox was verified using a fuzzy logic controller. This AUV can perform inspection tasks in restricted areas like underwater installations or shipwrecks.

## 1. INTRODUCTION

Autonomous underwater vehicle (AUV) is commonly known as unmanned underwater vehicle and is a robot that travels underwater without requiring input from an operator. It is an onboard intelligence which a task can be carried out without human operator interference or ship support [1]. AUV is also capable in navigation by following the pre-programmed course. It is suitable in geoscience application which requires constant altitude as the AUV can maintain a linear trajectory through water [2-3]. High maneuverable and agile AUV is needed to fulfill different underwater tasks in hard-to-reach areas. AUV with an Omni-directional with the configuration of four thrusters which are able to control all six degrees of freedom. This project describes its full holonomic control realizing a smooth omni-directional underwater movement. The next steps will be the implementation of different high-level autonomous behaviors, like circle movements around ship hulls in the case of optical investigation missions such as looking for partial damages. The central idea in developing an omni-directional driven AUV using the configuration of four thrusters as shown in Figure 1. Further, the AUV should be fully holonomic such as it has the ability to control all six degrees of freedom (DOF) and can perform arbitrary movements in the 3D space while holding any pose. To perform inspection tasks in restricted areas like underwater installations or shipwrecks, the scale factor

has to be small compared to popular underwater robots [4].

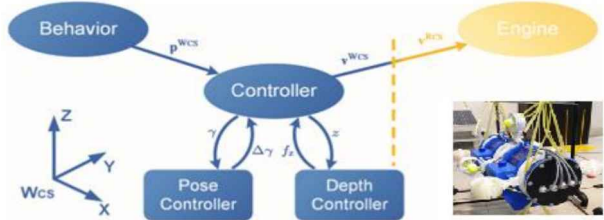


Figure 1 The full holonomic control of AUV.

Beside the construction of the AUV, the full holonomic control of AUV is the second main challenging task. Therefore, a mathematical force model based on the work in [4] is extended to the scenario of the 3D holonomic movement. The control of all six degrees of freedom enables the robot to hold any pose while moving into any direction and is realized with two controllers that is one controller for the depth and one for the pose regulation. The force model as well as the system identification approach. The both models (mathematical and system identification) will be verified.

The full holonomic control of the AUV is subdivided into three parts that is the depth control, the pose control and the movement inside the x-y-plain of the world coordinate system (WCS). Depending on the task, the WCS is given as the inertial measurement unit coordinate system (ICS) without any rotations, such as the yaw, pitch and roll angles between WCS and ICS are assumed to be zero, or it is described by the initial ICS, such as the first pose estimated by the ICS as shown in Figure 1. In such cases, the control of AUV is started when it floats on the water surface and the top of the AUV faces the sky. In the following, this pose is named neutral pose. Further, the ICS is situated in the AUV in a way that its coordinate system directly overlays the AUV coordinate system.

## 2. METHODOLOGY

For system identification approach, the development of the AUV is considered first and referred as platform development as shown in Figure 1. Generally, the system identification approach consisted of five steps such as (1) design parameter, (2) platform development, (3) system identification technique, (4) model generated based on testing data, and (5) model verification. At step 4, if the model is not good enough, steps 3, 2, or 1 may need to be repeated. The first stage is the design parameter followed by a decision on the design

parameters. The dynamic motion equation must be familiarized. Some of the parameters were obtained from measurement and experiments. After identifying the design parameter, the next stage is the platform development. In this stage, the AUV will be developed based on the design parameters. System identification took place once the platform was ready to be tested to get input-output signals. MATLAB® System Identification Toolbox was employed to infer the model. Then the model obtained from a toolbox was verified using a fuzzy logic controller and also conventional PID controller. MATLAB® command was used to generate transfer function's model from state space method for the designed AUV's model. This model was based on an open-loop model. In, the next step, a controller was designed to follow the set point.

$$\text{Transfer function (TF): } G(s) = \frac{Y(s)}{X(s)} \quad (1)$$

$$G(s) = \frac{35.62s + 84.32}{s^2 + 1.027s + 0.5668} \quad (2)$$

The evaluation is subdivided into two tests such as the depth control and the pose control. For the first real test scenarios a test pool is used to reduce influences like external drifts. The robot has to adjust the current depth to a desired one while holding the neutral pose over a time period. The target and reached depths are logged in cm and plotted over the time. A depth value of 0cm represents the depth while the robot floats on the surface of the water. Both scenarios emphasize that the approach based on controlling the angle of the pose difference, given in the axis angle representation, and the determined parameter of the proposed controller work very well. For this project, two approaches controller will be implemented that is conventional PID controller and Fuzzy Logic Controller (FLC) as shown in Figure 2.

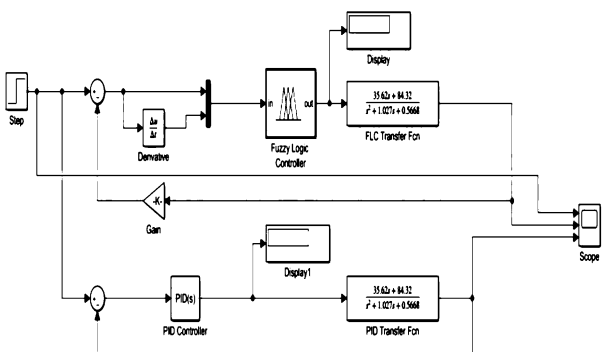
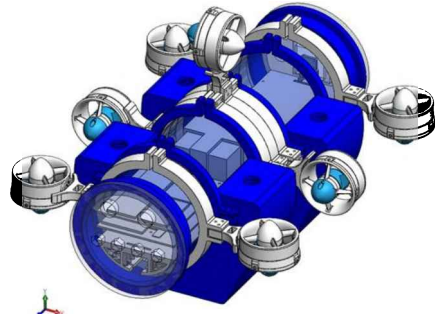


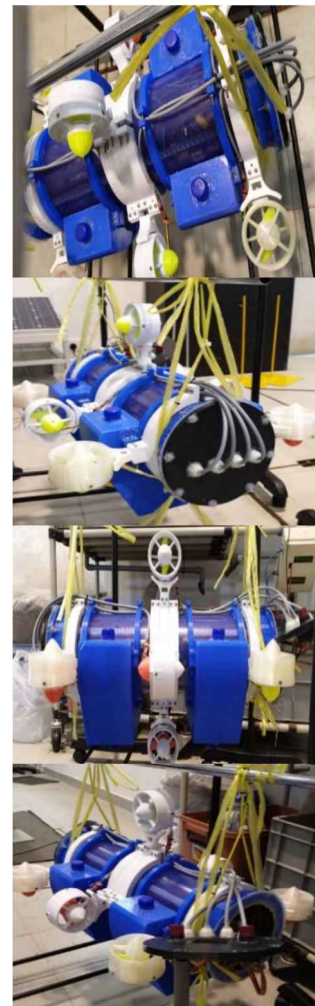
Figure 2: Simulation of depth control of AUV based on system identification model.

### 3. RESULTS AND DISCUSSION

Figure 3 shows the design of AUV using SolidWorks® software and final hardware of AUV. This AUV consists of eight thrusters that each thruster can be manipulate the configuration of thrusters. In this project only use four thrusters to control of six DOF. The rest thruster as standby mode. All the thrusters can adjust manually to set up configuration as needed.



(a) AUV design using SolidWorks software.



(b) Different view of AUV hardware.



(c) AUV testing on swimming pool.

Figure 3 Autonomous underwater vehicle (AUV).

## ACKNOWLEDGEMENT

We wish to express our gratitude and appreciation the support granted by Universiti Teknikal Malaysia Melaka in pursuing this research specially to Underwater Technology Research Group, Faculty of Electrical Engineering, Centre of Research and Innovation Management for supporting this research under PJP (PJP/2019/FKE(3C)/ S01667).

## REFERENCES

- [1] Aras, M. S. M. (2015). Adaptive simplified fuzzy logic controller for depth control of underwater remotely operated vehicle. *Doctoral dissertation*, Universiti Teknikal Malaysia Melaka.
- [2] Rojas, R. (2015). Omnidirectional control. *Robotik*, Freie Universität Berlin, Germany.
- [3] Liu, X., Zhang, M., & Yao, F. (2018). Adaptive fault tolerant control and thruster fault reconstruction for autonomous underwater vehicle. *Ocean Engineering*, 155, 10-23.
- [4] Ehlers, K., Meyer, B., & Maehle, E. (2014). Full holonomic control of the omni-directional AUV SMART-E. In *ISR/Robotik 2014; 41st International Symposium on Robotics* (pp. 1-6). VDE.

# Quality of Service (QoS) in campus network: Significant survey

Khaled J K Hommouda<sup>1</sup>, Zulkiflee Muslim<sup>1,2,\*</sup>

<sup>1)</sup> Fakulti Teknologi Maklumat dan Komunikasi, Universiti Teknikal Malaysia Melaka,  
Hang Tuah Jaya, 76100 Durian Tunggal, Melaka, Malaysia

<sup>2)</sup> Centre for Advanced Computing Technology, Universiti Teknikal Malaysia Melaka,  
Hang Tuah Jaya, 76100 Durian Tunggal, Melaka, Malaysia

\*Corresponding email: zulkiflee@utem.edu.my

**Keywords:** Quality of Service (QoS); Software-Defined Networking (SDN); OpenFlow controller

**ABSTRACT** – The Internet has provided end-to-end connectivity for users, allowing Quality of Service (QoS) management of network resources for new applications, such as data center, cloud computing, and network virtualization. Although many solutions have proposed to solve the QoS drawbacks of the recent networking, numbers of them are failed or were not implemented. This paper is to address the comparison between available solutions of QoS in campus network which is related targeted goals of QoS future development in the campus network. The analysis will help future research to decide the best technique to be used in any QoS solution domain.

## 1. INTRODUCTION

Nowadays, the explosive growth of real-time applications that require stringent Quality of Service (QoS) guarantees, brings the network programmers to design network protocols that deliver certain performance guarantees. The objective of the present paper is to get a clear understanding for the Quality of Service (QoS) in campus network obstacles which necessary to address the multiple challenges and realizing the QoS future development for campus networks uses. The effect is represented by attention to the architecture of these networks in which control and the Service (QoS) in the campus network.

## 2. RELATED STUDY

A role-based SDN campus network slicing approach has been proposed by [1]. The approach involves with authentication controller and the virtualization technology of Flow-Visor which led to reduce the flow setup latency 14% to 60% compared to that of MAC-based slicing. While the proposed approach is required to be applicable in real campus networks to efficiently manage them. A technique for stitching inter-domain paths under the control of centralized routing brokers which known as IXPs has been introduced by [2], it allows for providing paths with end-to-end guarantees for mission-critical applications. A new technique which known as an open northbound API has been proposed by [3]. The method is enables streaming video applications to easily enforce Quality of Service (QoS) requirements in a high-level fashion, without incurring any controller's code coupling or network operator intervention. However, the approach needs to be integrated with other OpenFlow controllers beyond to better support its communication between a single streaming video

application and disparate SDN controllers. Another technique of Bandwidth-allocation controller which called (NN-SPID) is developed by [4]. The proposed technique is based on PID control strategy to control QoS requirements relying on an auto-adaptive neural network to ensures the minimum guaranteed bandwidth levels to users according to their contracted SLA, and it also shows more stability and robustness than GA-SPID. However, the proposed technique does not consider on controlling other QoS parameters such as jitter, packet delay of sensitive traffic, or packet loss ratio. In [5] new Scheduling algorithms for evaluating the performance of QoS over MPLS/VPN/WiMAX networks has been presented. Based on the proposed scheduling algorithms, it clearly observed that MWRR has the lowest delay in both VPN and WiMAX. However, the long-term Evolution advanced (LTE-adv) networks have not been achieved yet.

## 3. METHODOLOGY

The purpose of this systematic review is to classify the literature that is related to our target objectives and create a significant review to identify the most efficient method that is more effective in our research area. In addition to that, challenges and obstacles that were reported in the provided tables which are discussed to identify the problems of the current of campus network framework and related application with Quality of Service (QoS) guaranty approaches (Figure 1).

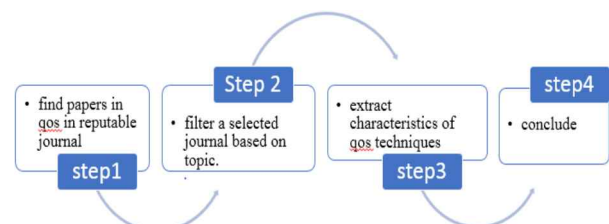


Figure 1 QoS guaranty approaches.

## 4. ANALYSIS AND RESULTS

After analyzing several papers from several project related to QoS, a comparison was made for a better understanding. Table 1 shows the list of previous projects which had been analyzed and their contribution and drawbacks of their project.

**Table 1 Contribution and drawbacks of the previous project.**

Technique	Contribution and drawbacks	Ref.
An OpenFlow controller design	A novel approach to stream video over OpenFlow networks with QoS, it fulfilled end-to-end QoS support which is possible with OpenFlow's centralized control capabilities over the network.	[6]
Scheduling mechanism for IMM applications	A new scheduling and channel allocation mechanisms that ensure QoS for IMM applications over WCNs. It delivers QoS with the least handoff delay and minimizes the call dropping probabilities.	[7]
QoS-based Network Virtualization	A constraint placement language used when mapping virtual network (node and links) over the substrate infrastructure to ensure QoS requirements of application flows.	[8]
Optimized Routing in OpenFlow Networks	Streaming setup that utilizes the flexible routing possibilities provided by an SDN implemented with OpenFlow. It improves the QoS by changing the metric model of the Dijkstra algorithm.	[9]
QoS control and SRTP for real-time multimedia streaming	Quality of Service (QoS) control and Secure Real-time Transport Protocol (SRTP) approach to provide a smooth streaming under various network bandwidths, while maintaining effective security.	[10]
A novel SHRP strategy	A novel QoS routing strategy called Swarm-based Hybrid Routing Protocol (SHRP) which able to select the minimum delay path with the maximum available bandwidth at nodes	[11]

Meanwhile, Table 2 is about a summarization about the QoS in respect to Hard and Soft QoS. Each project is defined the metric that being used to evaluate the technique performance.

## 5. DISCUSSION

The effect of software-defined networks on quality of service of applications is inevitable. Wthe considering the routing methods and metrics used in each of them, one may infer that some novel software techniques and other methods based on Flow Broker architectures are suitable for Quality of Service (QoS) guarantees in networks. In addition, tables above offer a comparison between the most significant methods suggested in the present paper for use of campus networks and other related applications that could be adopted.

## 6. CONCLUSION

We can conclude that SDN and OpenFlow will most likely become pervasive technologies in the future networks since they have an enormous potential contribution in a large number of different applications and fields. In addition, for QoS in networks, the lack of sufficient bandwidth, as well as high packet loss or delay, can impact very negatively on the quality of service. Finally, more work and focus is needed toward an

efficient Quality of Service (QoS) in campus network and related applications is control and guaranty.

## REFERENCES

- [1] Chen, C. H., Chen, C., Lu, S. H., & Tseng, C. C. (2016, November). Role-based campus network slicing. In *2016 IEEE 24th International Conference on Network Protocols (ICNP)*(pp. 1-6). IEEE.
- [2] Kotronis, V., Klöti, R., Rost, M., Georgopoulos, P., Ager, B., Schmid, S., & Dimitropoulos, X. (2016, March). Stitching inter-domain paths over IXPs. In *Proceedings of the Symposium on SDN Research* (p. 17). ACM.
- [3] Vasconcelos, C. R., Gomes, R. C. M., Costa, A. F., & da Silva, D. D. C. (2017, January). Enabling high-level network programming: A northbound api for software-defined networks. In *2017 International Conference on Information Networking (ICOIN)* (pp. 662-667). IEEE.
- [4] Merayo, N., Juárez, D., Aguado, J. C., De Miguel, I., Durán, R. J., Fernández, P., ... & Abril, E. J. (2017). PID controller based on a self-adaptive neural network to ensure QoS bandwidth requirements in passive optical networks. *Journal of Optical Communications and Networking*, 9(5), 433-445.
- [5] Elkarash, H. H., Elshennawy, N. M., & Saliam, E. A. (2017, December). Evaluating QoS using scheduling algorithms in MPLS/VPN/WiMAX networks. In *2017 13th International Computer Engineering Conference (ICENCO)* (pp. 14-19). IEEE.
- [6] Egilmez, H. E., Dane, S. T., Bagci, K. T., & Tekalp, A. M. (2012, December). OpenQoS: An OpenFlow controller design for multimedia delivery with end-to-end Quality of Service over Software-Defined Networks. In *Proceedings of The 2012 Asia Pacific Signal and Information Processing Association Annual Summit and Conference* (pp. 1-8). IEEE.
- [7] Alam, M. K., Latif, S. A., Masud, M. H., Akter, M., Anwar, F., & Yalli, J. S. (2013, December). An analysis of scheduling scheme for qos guaranteed interactive multimedia over high speed wireless campus networks. In *2013 1st International Conference on Artificial Intelligence, Modelling and Simulation*(pp. 421-427). IEEE.
- [8] Ayadi, I., Diaz, G., & Simoni, N. (2013, October). QoS-based network virtualization to future networks: An approach based on network constraints. In *2013 Fourth International Conference on the Network of the Future (NoF)* (pp. 1-5). IEEE.
- [9] Karl, M., Gruen, J., & Herfet, T. (2013, December). Multimedia optimized routing in OpenFlow networks. In *2013 19th IEEE International Conference on Networks (ICON)* (pp. 1-6). IEEE.
- [10] Kim, J., Choi, H. J., Lee, S. H., Park, S. H., Song, M. S., & Chang, H. (2013, November). Implementation of quality of service control and security based on real-time transport protocol. In *2013 5th IEEE International Conference on*

- Broadband Network & Multimedia Technology* (pp. 10-13). IEEE.
- [11] Nivetha, S. K., Asokan, R., & Senthilkumaran, N. (2013, July). A swarm-based hybrid routing protocol to support multiple Quality of Service (QoS) metrics in mobile ad hoc networks. In *2013 Fourth International Conference on Computing, Communications and Networking Technologies (ICCCNT)* (pp. 1-8). IEEE.

Table 2 Summary of the QoS in respect to Hard and Soft QoS.

<b>QoS models Technique</b>	<b>Hard Quality of Service (QoS)</b>				<b>Soft Quality of Service (QoS)</b>			
	<b>Bandwidth</b>	<b>Delay</b>	<b>Jitter</b>	<b>Loss</b>	<b>Bandwidth</b>	<b>Delay</b>	<b>Jitter</b>	<b>Loss</b>
New (WIFI AP) mechanism						✓		✓
Bandwidth controller (NN-SPID)	✓					✓		
Q-Ctrl system for video flow handling	✓					✓		
O en northbound API	✓	✓						
Flow Broker architecture	✓	✓		✓	✓	✓		✓
Role-based SDN campus network slicing							✓	
IXPs					✓	✓		
A (QoE) evaluation model					✓	✓		
Trust CoS model and Trust DSCP for QoS evaluation					✓		✓	✓
A new QoS mechanisms							✓	
Distributed QoS-oriented Model					✓	✓		
A fine granular API for QoS configuration						✓		
A novel software defined automatic QoS management model	✓	✓			✓	✓		
Scheduling mechanism for IMM applications					✓	✓		
New scheduling algorithms						✓	✓	
A new campus SWAN architecture					✓			
QoS-based Network Virtualization					✓	✓		
Real-time QoS-Aware video streaming					✓		✓	✓
A framework for automatic QoS control	✓				✓			
O en Cache API					✓	✓		
Optimized Routing in O enFlow Networks					✓	✓		
QoS control and SRTP for multimedia streaming					✓	✓		
Allocation algorithm with Xen and Linux QoS					✓			
Flexible 5G architecture for network slicing					✓	✓		
A novel SHRP strategy					✓	✓		

# Taguchi GRA for multi-response optimization of 16 nm WSi<sub>2</sub>/TiO<sub>2</sub> NMOS device

Nor F. Shamsudin<sup>1</sup>, F. Salehuddin<sup>1,\*</sup>, Ameer F. Roslan<sup>1</sup>, A.S.M. Zain<sup>1</sup>, K.E. Kaharudin<sup>1</sup>, A.H. Afifah Maheran<sup>1</sup>, I. Ahmad<sup>2</sup>

<sup>1)</sup> Micro and Nano Electronics (MiNE), CeTRI, Fakulti Kejuruteraan Elektronik dan Kejuruteraan Komputer, Universiti Teknikal Malaysia Melaka, Hang Tuah Jaya, 76100 Durian Tunggal, Melaka, Malaysia

<sup>2)</sup> Department of Electronics & Communication Engineering, College of Engineering, Universiti Tenaga Nasional, Jalan IKRAM-UNITEN, 43000 Kajang, Selangor, Malaysia

\*Corresponding e-mail: fauziyah@utem.edu.my

**Keywords:** Multi-Response; Taguchi; grey rational analysis

**ABSTRACT** – In this research, multi response characteristics of 16 nm NMOS device were analyzed using Taguchi GRA. The L<sub>9</sub> Taguchi method, Signal Noise Ratio and ANOVA were used to optimize the effect of process parameters such as Source/Drain and Halo implantation processes. All the simulated values for characteristic are converted to grey relational grade (GRG) and the level of process parameter with the highest GRG are selected as the most optimal level. Most of the results obtained were within the range and met the requirement of low power technology as predicted by ITRS 2013. As a conclusion, the optimization of multi response from the device has been achieved using Taguchi GRA.

## 1. INTRODUCTION

Scaling down was used to ensure the robust performance of transistor due to the high demand for smaller, faster, and cheaper technology. However, there is some problem to further technology scaling due to the increasing of wafer fabrication process parameter variation. The problem such as short-channel effect (SCE) and drain induced barrier (DIBL) lead to the introducing of high-K material such as Titanium Oxide (TiO<sub>2</sub>) [1]. Silicon oxide (SiO<sub>2</sub>) has been used as the gate dielectric material over a decade. Nowadays, replacing SiO<sub>2</sub> with high-k material as one of the new research initiatives to overcome those problems. Metal gate such as Tungsten Silicide (WSi<sub>2</sub>) is used to eliminate Poly-Si depletion which make the leakage current are too high. This helps in producing better physical and electrical properties of a transistor [2].

In order to obtain the best value of electrical properties of a transistor which is closed to predicted value, several input process parameters are needed. Process parameter plays very important roles in determining the variation. These variations cause significant unpredictability in the power and performance characteristic of integrated circuit [3]. In order to identify the parameter that contribute the most of this variation and get the optimal value of electrical properties, statistically modelling is required. One of the statistical methods for identifying semiconductor process parameters, whose variability would impact most on the device characteristics, is realized using Taguchi method. Taguchi method has become a powerful tool for improving productivity during

research and development. However, the application of Taguchi method is only limited to a single response. For multiple response problems, it relies on the decision makers to make judgment and usually leads to a solution that is not globally optimized. Hence, Taguchi method is combined with grey relational analysis (GRA) to solve the multi-response optimization with multiple performance characteristics. A lot of previous reports have employed the Taguchi-based GRA approach to solve multiple objective problems in many engineering fields [4,5].

In this paper, the process parameters of the 16 nm WSi<sub>2</sub>/TiO<sub>2</sub> NMOS device were optimized by using Taguchi method with GRA in acquiring a nominal threshold voltage (V<sub>TH</sub>), a high drive current (I<sub>ON</sub>) and a low leakage current (I<sub>OFF</sub>) that meet the requirement of low power technology as predicted by ITRS 2013 [6].

## 2. METHOD OF THE RESEARCH

The process module starts with wafer preparation followed by well formation, isolation formation, transistor making and interconnection. The wafer preparation includes epitaxial silicon growth, wafer clean and alignment mark etch. Transistor making involves gate oxide growth, high-k deposition, photolithography, metal gate etch, ion implantation and thermal annealing. These are the most crucial process steps in the Integrated Circuit (IC) processing sequences. Several process parameters are needed to obtain the best value of electrical characteristics of the device. In this work, the process parameter that were used are halo implant dose (A), halo implant energy (B), source/drain (S/D) implant dose (C) and S/D implant energy (D). These process parameters will be optimized using Taguchi GRA. Figure 1 shows the 16nm NMOS structure device with TiO<sub>2</sub> as high -k dielectric and WSi<sub>2</sub> as metal gate.

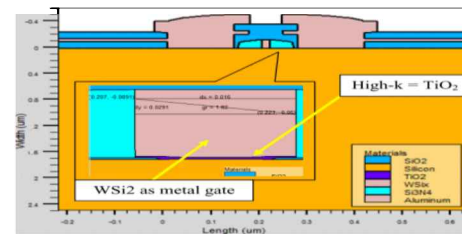


Figure 1 16nm NMOS Structure with TiO<sub>2</sub> as high -k dielectric and WSi<sub>2</sub> as metal gate.

### 3. RESULTS AND DISCUSSION

Table 1 shows the result of the electrical characteristics based on L<sub>9</sub> OA of Taguchi GRA. The computation for data normalization according to the type of performance characteristics for the device were performed. Then, the deviation sequence was figured before the calculation of the grey relational coefficient (GRC) and grey relational grade (GRG) were computed.

Table 1 Results of the electrical characteristics.

Exp.No.	Process Parameter				V <sub>TH</sub> (V)	I <sub>ON</sub> ( $\mu$ A/ $\mu$ m)	I <sub>OFF</sub> (pA/ $\mu$ m)	I <sub>ON</sub> / I <sub>OFF</sub> ratio (x 10 <sup>6</sup> )
	A	B	C	D				
1	1	1	1	1	0.5326	507.24	10.20	50.28
2	1	2	2	2	0.5290	513.56	16.67	31.16
3	1	3	3	3	0.5283	513.50	18.66	27.82
4	2	1	2	3	0.5412	484.55	5.604	87.37
5	2	2	3	1	0.5319	509.03	10.56	48.76
6	2	3	1	2	0.5310	508.34	13.15	39.09
7	3	1	3	2	0.5412	485.55	5.038	97.52
8	3	2	1	3	0.5434	479.73	4.498	107.72
9	3	3	2	1	0.5338	504.03	8.441	60.37

The GRC is to represent the deviation of the actual sequence from the desired sequences. The GRG is defined as the average value of all GRCs corresponding to each performance characteristics [7]. Table 2 shows the GRG of process parameters at different levels. Basically, the higher GRG indicated the better overall quality of the design [5]. Table 3 shows the comparison optimum values of V<sub>TH</sub>, I<sub>ON</sub>, I<sub>OFF</sub> and I<sub>ON</sub>/I<sub>OFF</sub> ratio characteristics between Taguchi Method and Taguchi GRA.

Table 2 Results for GRG of process parameters.

Param/S	Process Parameters	Grey relational grade (GRG)			Overall mean of GRG
		Level 1	Level 2	Level 3	
A	Halo Implant Dose	0.5219	0.5779	0.7238	
B	Halo Implant Energy	0.6598	0.6358	0.5281	
C	S/D Implant Dose	0.6279	0.5925	0.6033	0.6079
D	S/D Implant Energy	0.5637	0.5904	0.6695	
GRG of optimal levels = 0.8573					

Table 3 Comparison between Taguchi Method and Taguchi GRA.

Condition Description	V <sub>TH</sub> (V)	I <sub>ON</sub> ( $\mu$ A/ $\mu$ m)	I <sub>OFF</sub> (pA/ $\mu$ m)	I <sub>ON</sub> /I <sub>OFF</sub> ratio (x 10 <sup>6</sup> )
Taguchi Method	0.542	485.66	4.04	120.21
Taguchi GRA	0.547	476.16	3.25	146.51
ITRS 2013 predict for year 2017 [6]	0.530 $\pm 12.7\%$	$\geq 422$	$\leq 50$	8.440

Based on Table 3, V<sub>TH</sub> was 3.1% higher than ITRS 2013 after the optimization using the Taguchi GRA method but it still in the range of prediction which was between 0.463 V and 0.597 V [6]. Meanwhile, the value of I<sub>OFF</sub> was decreased by 24.3% after the optimization with Taguchi GRA. In fact, the I<sub>OFF</sub> was significantly decreased if compared to ITRS 2013 prediction. The I<sub>ON</sub> value was observed to be decreased by 19.9% after the

optimization with Taguchi GRA. However, the I<sub>ON</sub> value was still above 422  $\mu$ A/ $\mu$ m as predicted by ITRS 2013 [6]. The I<sub>ON</sub>/I<sub>OFF</sub> ratio value after the optimization via L<sub>9</sub> OA of Taguchi-based GRA was increased by 17.9% and higher than ITRS 2013 prediction. Hence, it is concluded that the V<sub>TH</sub>, I<sub>ON</sub>, I<sub>OFF</sub> and I<sub>ON</sub>/I<sub>OFF</sub> ratio of the device can be simultaneously optimized using a L<sub>9</sub> OA of Taguchi- based GRA.

### 4. CONCLUSION

The GRA based on Taguchi method was proposed as a method to optimize multi-response of 16 nm WSi<sub>2</sub>/TiO<sub>2</sub> NMOS device. The multiple electrical properties such as V<sub>TH</sub>, I<sub>ON</sub>, I<sub>OFF</sub> and I<sub>ON</sub>/I<sub>OFF</sub> ratio were converted into a single multi- performance characteristic, known as GRG. The most optimal values for V<sub>TH</sub>, I<sub>ON</sub>, I<sub>OFF</sub> and I<sub>ON</sub>/I<sub>OFF</sub> ratio after the optimization were 0.547 V, 476.16  $\mu$ A/ $\mu$ m, 3.25 pA/ $\mu$ m and 146.51x10<sup>6</sup> respectively with 0.8573 of predicted GRG. It can be concluded that the multi response of the device can be simultaneously optimized using a L9 OA of Taguchi- based GRA.

### ACKNOWLEDGEMENT

Ministry of Education Malaysia under grant FRGS/1/2017/TK04/FKEKK-CeTRI/F00335. The members of Universiti Teknikal Malaysia Melaka.

### REFERENCES

- Ruan, D. B., Chang-Liao, K. S., Li, C. C., Lu, C. C., Liao, Y. L., Chen, L. T., ... & Hsieh, T. L. (2015). Improved electrical characteristics of high-k gated MOSFETs with post-growth treatment on interfacial layer. *Microelectronic Engineering*, 138, 81-85.
- Kaharudin, K. E., Salehuddin, F., & Zain, A. S. M. (2018). Optimization of Electrical Properties in TiO<sub>2</sub>/WSix-based Vertical DG-MOSFET using Taguchi-based GRA with ANN. *Journal of Telecommunication, Electronic and Computer Engineering*, 10(1), 69-76.
- Li, Y., Yu, S. M., & Chen, H. M. (2007). Process-variation-and random-dopants-induced threshold voltage fluctuations in nanoscale CMOS and SOI devices. *Microelectronic Engineering*, 84(9-10), 2117-2120.
- Lin, H. L. (2012). The use of the Taguchi method with grey relational analysis and a neural network to optimize a novel GMA welding process. *Journal of Intelligent Manufacturing*, 23(5), 1671-1680.
- Achuthamnen Sylajakumari, P., Ramakrishnasamy, R., & Palaniappan, G. (2018). Taguchi Grey Relational Analysis for Multi-Response Optimization of Wear in Co-Continuous Composite. *Materials*, 11(9), 1743.
- ITRS (2013). [www.ITRS2013.net](http://www.ITRS2013.net)
- Kaharudin, K. E., Salehuddin, F., Zain, A. S. M., Aziz, M. N. I. A., Manap, Z., Salam, N. A. A., & Saad, W. H. M. (2016, August). Multi-response optimization in vertical double gate PMOS device using Taguchi method and grey relational analysis. In *2016 IEEE International Conference on Semiconductor Electronics (ICSE)* (pp. 64-68).

# Intruder system with raspberry pi in rural areas of Malaysia

Kasthuri Subaramaniam<sup>1,\*</sup>, Abdul Samad Shibghatullah<sup>1</sup>, Harry Lean Fu Liang<sup>1</sup>, Zaheera Zainal Abidin<sup>2</sup>

<sup>1)</sup> School of Information Technology, Faculty of Business & Information Science,  
UCSI University, 56000 Kuala Lumpur, Malaysia

<sup>2)</sup> Information Security Forensics and Computer Networking (INFORSNET),  
Centre for Advanced Computing, Universiti Teknikal Malaysia Melaka,  
Hang Tuah Jaya, 76100 Durian Tunggal, Melaka, Malaysia

\*Corresponding e-mail: kasthurisuba@ucsiuniversity.edu.my

**Keywords:** Intruder system; Raspberry Pi; rural areas

**ABSTRACT** – Urban households have better security options compared to rural households. Closed-Circuited Television (CCTV) is a surveillance tool designed to assist in monitoring events. However, the passive monitoring feature of CCTV does not provide any feedback nor respond to the user when a crime incident arises. Thus, a low-cost intruder system with Raspberry Pi which adopts a similar feature and functionality for a home security system is proposed. This is by integrating the feature of the OpenCV library to the Pi Camera to enhance the overall functionality. The use of sensors like a magnetic switch for door and PIR sensors allow the home security system to take in feedback regarding the environment. This will serve as a security layer or enhancement for the home security measurements. The proposed system will help to remedy the passive monitoring feature of CCTV as a smarter and intelligent home security system. The system will be developed in an iteration process and prototyping test will be conducted.

## 1. INTRODUCTION

Founded by the Raspberry Pi Foundation (UK) the Raspberry Pi computer is a low-cost and high-performance credit card-sized single-board computer that cost around 25 pounds. The Raspberry Pi is designed to teach the younger generation how to program with computers. A single-board computer is referred as a single personal computer board incorporates components such as processor, memory and several types of input and output device that sufficiently to allow it to function as a computer [1]. The credit-card sized Raspberry Pi computer provides alternatives to users to conduct inexpensive and flexible hardware experimentation with programming and electronics.

The rural area is defined as an area which is apart from a city or a non-metropolitan area. Rural is the opposite of urban. In comparison to rural areas, urban areas are usually occupied by a lot of inhabitants, whereas rural area has a smaller number of residents. For instance, rural areas in Malaysia has defined as an area with a population less than 10,000 population, acquire agriculture and natural resources either it is clustered, linear or scattered [3]. The crime rate for property crimes in Malaysia comprises house break-in and theft, vehicles theft, snatch and others. The total property crime cases according to the Department of Statistics of Malaysia (DoSM) is 77,802 cases. With the statistics provided,

21% of the property crime cases come from house break-in and theft [3]. This indicates that an intruder system can be useful in preventing cases like property break-ins and theft.

The Closed-Circuited Television (CCTV) monitoring feature does not provide any feedback nor respond to the user when crime or suspicious incident arise [4]. Using a CCTV as a security system without incorporating the use of sensors can be far less efficient. A modern home security system can provide high efficiency and effectiveness for preventing property theft and break-ins, however subscription to such services is expensive and can cause a burden to household owners in rural areas or urban areas. Thus, a low-cost intruder system with Raspberry Pi which adopts the similar feature and functionality of a modern home security system is proposed.

## 2. METHODOLOGY

In this proposed system of intruder system with raspberry pi in rural areas will be adopting the prototyping model as the main approach [2]. The prototyping model consists of four (4) stages of development. First, analysis of requirements will be conducted. Approaches or techniques for analyzing the user's requirements and needs can be done via observation or questionnaire. Next, the developer will develop the prototype based on the requirements and needs analyzed from the first stage of prototyping SDLC. Developers then conduct testing on the prototype to ensure it meets the user requirements and needs by involving users in feedback and testing. These two stages are often called the prototype revision or refinement which will repeat until the best version of the prototype is produced. The final product release is achieved when the final version of the prototype produced has met all the user's requirements and needs and it consists of the best efficiency among the prototype version [2].

## 3. RESULTS AND DISCUSSION

The tables 1 and 2 below shows a brief comparison of the reviewed system and the proposed system [4-8].

The expected contribution of this proposed research is to provide a low-cost security measurement for community household and to reduce the crime rate index of house break-ins in Malaysia. Besides, installing such security measurement for the convenience and protection of the household, owners can also increase the value of

the property. Furthermore, the real-time security updates provide a sense of security for the household owners when they are travelling or not available at home especially in rural areas.

Table 1 Comparison of reviewed and proposed system.

Description	Raspberry Pi	3rd Party Software	Portable	Motion Detection
Smart Home Security with Object Recognition and PIR Sensor	✓	✓	✓	✓
Low-Cost Building Monitoring System (BMS) using Raspberry Pi	✓	✓	✓	
Raspberry Pi Security Camera with Night Vision Capability and PIR Sensor	✓	✓	✓	✓
Smart Home System using Raspberry Pi	✓	✓	✓	✓
Smart Surveillance System using Think Speak and Raspberry Pi	✓	✓	✓	✓
Intruder System with Raspberry Pi in Rural Areas	✓	✓	✓	✓

#### 4. CONCLUSION

In this academic paper, a home intruder system for rural areas has been proposed by adopting the Raspberry Pi technology. The proposed system consists of Raspberry Pi Model 3B+, door sensors, microwave radar sensor and Pi camera with night vision functionality. The overall system includes human detection features and notification system which will alert the household owner once it is triggered by the intruder trespassing the secured parameter. For future research, the plan is to expand the capability of the proposed system such as the accuracy of detection, clarity of image quality and to collaborate with the law-enforcement party to assist in improving the efficiency and effectiveness of crime investigations.

#### ACKNOWLEDGEMENT

Authors would like to extend their gratitude to CERVIE, UCSI University for funding of the research.

Table 2 Comparison of reviewed and proposed system.

Description	Night Vision Feature	Surveillance Feature	Feedback Feature	Alarm Feature
Smart Home Security with Object Recognition and PIR Sensor			✓	✓
Low-Cost Building Monitoring System (BMS) using Raspberry Pi		✓		✓
Raspberry Pi Security Camera with Night Vision Capability and PIR Sensor	✓	✓		✓
Smart Home System using Raspberry Pi		✓	✓	
Smart Surveillance System using Think Speak and Raspberry Pi	✓	✓	✓	
Intruder System with Raspberry Pi in Rural Areas	✓	✓	✓	✓

#### REFERENCES

- [1] Raspberry Pi — Teach, Learn, and Make with Raspberry Pi. <https://www.raspberrypi.org/>. Accessed on 11-Feb-2019.
- [2] Isaias, P., & Issa, T. (2015). *High level models and methodologies for information systems* (pp. 1-145). New York, NW: Springer.
- [3] Department of statistics malaysia press release. *Dep. Stat. Malaysia, 2016*, 5-9.
- [4] Abaya, W. F., Basa, J., Sy, M., Abad, A. C., & Dadios, E. P. (2014, November). Low cost smart security camera with night vision capability using Raspberry Pi and OpenCV. In *HNICEM2014* (pp. 1-6).
- [5] Surantha, N., & Wicaksono, W. R. (2018). Design of Smart Home Security System using Object Recognition and PIR Sensor. *Procedia Computer Science, 135*, 465-472.
- [6] Perumal, V. S. A., Baskaran, K., & Rai, S. K. (2017). Implementation of effective and low-cost building monitoring system (BMS) using Raspberry PI. *Energy Procedia, 143*, 179-185.
- [7] Kumar S., & Mehta, N. (2017). Smart home system using BECAMEDA, 8(2), 1108–1112.
- [8] Chandana, R., Jilani, S., & Hussain, S. J. (2015). Smart surveillance system using thing speak and Raspberry Pi. *International Journal of Advanced Research in Computer and Communication Engineering, 4(7)*, 214-218.

# Enhancing performance of wireless local area network using channel assignment

Noor Atiqah Fatahurahman<sup>1</sup>, Zaheera Zainal Abidin<sup>2,\*</sup>, Abdul Samad Shibghatullah<sup>3,\*</sup>, Effendi Mohamad<sup>4</sup>

<sup>1)</sup> Kolej Poly-Tech MARA Batu Pahat, Jalan Gading Emas, Sri Gading, 83000 Batu Pahat, Johor, Malaysia

<sup>2)</sup> Information Security Forensics and Computer Networking (INFORSNET), Centre for Advanced Computing, Universiti Teknikal Malaysia Melaka, Hang Tuah Jaya, 76100 Durian Tunggal, Melaka, Malaysia

<sup>3)</sup> School of IT, Faculty of Business & Information Science (FoBIS), UCSI University, Kuala Lumpur, Malaysia

<sup>4)</sup> Fakulti Kejuruteraan Pembuatan, Universiti Teknikal Malaysia Melaka, Hang Tuah Jaya, 76100 Durian Tunggal, Melaka, Malaysia

\*Corresponding e-mail: zaheera@utem.edu.my; AbdulSamad@ucsiuniversity.edu.my

**Keywords:** Wireless LAN; channel assignment; 802.11

**ABSTRACT** – Wireless Local Area Network (WLAN) has become popular for organisation because of its flexibility and easy to install. The performance of WLAN can be greatly affected due to interference from neighbouring WLAN. In normal 2.4 GHz (802.11b/g/n/ax) WLAN access point has 14 frequency channel and assigning a particular frequency channel to each access point is termed as channel assignment. Efficient channel assignment techniques can improve the performance of WLAN by minimizing the interference from neighbouring access point. This research investigates the performance of WLAN in one private university in Malaysia by assigning 3 types of channel assignment that are Current Channel Assignment (CCA), Non-overlapped Channel Assignment (NCA) and Random Channel Assignment. The research uses OPNET Simulation to evaluate the performance of every type of channel assignment. The result shows RCA is better in terms of throughput and delay compare to CCA and NCA.

## 1. INTRODUCTION

Nowadays, Wireless Local Area Network (WLAN) has been growing rapidly in the world, especially in business and education institutions. There is much type of wireless technology on the market today such as Institute of Electrical and Electronics Engineer (IEEE) 802.11a, b, g, and n series. This wireless networking technology designed for simple data transfer in the area of 100-300 square feet. This wireless networking technology has replaced the wired network and has now been widely used in education centers such as universities and colleges. This wireless network provides the same capability and speeds compare able to wire 10BASE-T, without the problems associated with set up the wire, drill into walls to install wires or install Ethernet cables throughout an office building at a university and college.

WLAN generally consist of a central point connection called an Access Point (AP). It is the same function as hubs or switches in a star topology-based, traditional wired networks in the local area network. The Access Point (AP) can transmit data between different node of the wireless local area network and it serves as the only connection between wireless LAN and wired LAN. Typically, the Access Point (AP) can handle some number of users within 100 - 300 feet. The current

researchers show that coverage optimization become big challenge in deployment of WLAN [1-4]. The researcher proposed a solution to self-optimization coverage performance with adjust the power of each beam AP and Received Signal Strength (RSS) and Signal to Interference ratio (SIR) of the sensor. With this solution, the researchers able to improve the performance of coverage and saving cost.

Overlapping eventually make more users within the same coverage area with some AP. AP placement require different frequency channels between neighboring AP to operate in order to avoid co-channel interference within APs. In addition, to increase capacity, the Access Point (AP) must be assigned the appropriate channels and consumers need to make intelligent decisions about which AP to associate with. Furthermore, the decision on the channel assignment, and unity must be based on a global view of the entire campus WLAN, from the point of view of the individual local clients or AP.

Study of Abbasi et al. [5] show that the importance of the issues channel assignment to minimum availability of orthogonal channel of WLAN. The authors find an efficient method to utilize channel overlap of 2.4 GHz band, was achieve high throughput to minimum interferences within backhaul and directional antennas. The researchers propose channel assignments that have the limited number of channels, the concept to assign the sets of channels to connect in the interference area of each node, where the nodes are works with directional antenna. The study has found that it can decrease the channel interference and increase the throughput.

In a study conduct by Tewari and Ghosh [6], it was shown that the frequency assignment and the association control entertainment be an important role and its should be considered simultaneously to improve the network performance. The researcher uses greedy algorithm that deal with the frequency assignment and the association control to increase the throughput.

## 2. METHODOLOGY

In order to evaluate the performances of different channel assignment this research proposes 3 types of channel assignment that are Current Channel Assignment (CCA), Random Channel Assignment (RCA), and Non-overlapped Channel Assignment (NCA). The CCA is the current channel assignment that is being used in this case

the university uses Channel 1. The RCA is a random channel assignment where any channel is chosen as long as there is no interference from neighbouring access point. The NCA is the non-overlapping channels designated in WLAN that are channels 1,6 and 11. OPNET simulation will be used to implement the proposed channel assignment. Access Point and wireless network are distributed in service area of 60 feet x 100 feet.

### 3. RESULTS AND DISCUSSION

Figure 1 shows the delay time for CCA, NCA and RCA for FTP application. The graph shows the delay versus time for three channel assignment scheme technique. Horizontal axis refers to time in second while the vertical axis refers to delay in bit/sec. From the figure it shows CCA have the higher delay compare to NCA and RCA.

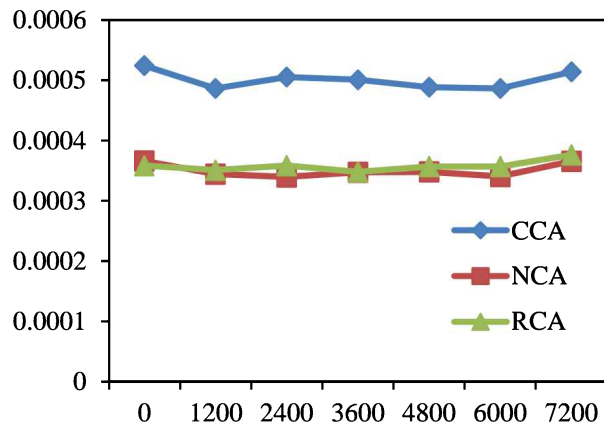


Figure 1 The delay for CCA, NCA and RCA for FTP application.

Figure 2 shows the throughput of CCA, NCA and RCA for FTP application. RCA is the highest in term of throughput compare to NCA and CCA.

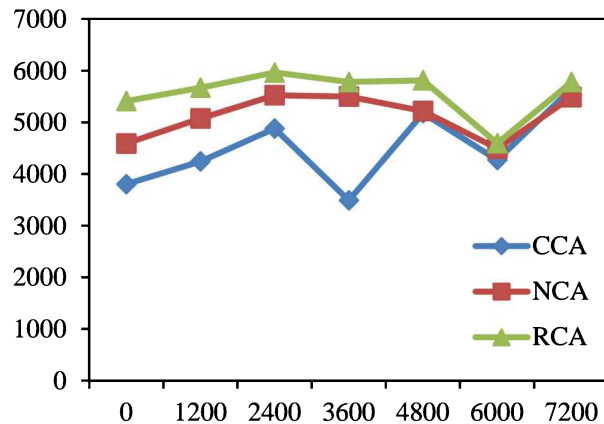


Figure 2 The throughput for CCA, NCA and RCA for FTP application.

Figure 3 shows the average delay in running email application for CCA, NCA and RCA. The results show CCA has the higher delay compare to NCA and RCA.

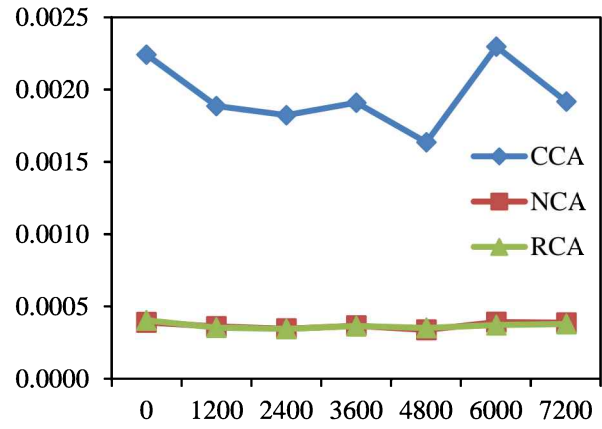


Figure 3 The average delay for CCA, NCA and RCA for email application.

Figure 4 shows the throughput in bit/sec for CCA, NCA and RCA for email application. The results show the RCA and NCA are better throughputs compare to CCA.

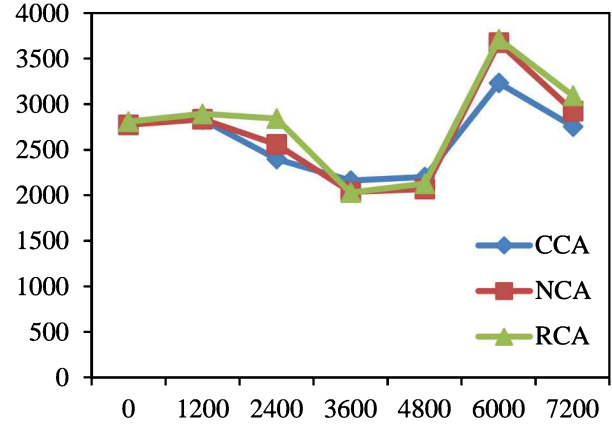


Figure 4 The WLAN throughput for CCA, NCA and RCA for Email application.

### 4. CONCLUSION

In this paper, two scheme of channel assignment has been proposed on maximizing the performance of WLAN by proposing the non-overlapping channels (NCA) designated in WLAN that are channels 1,6 and 11, and the random channel assignment (RCA). The current or existing channel assignment is CCA. The research used OPNET simulation to evaluate the performance of every scheme of channel assignment for two application that are email and FTP. The results show the RCA is better compare to NCA and CCA.

### REFERENCES

- [1] Zhou, K., Jia, X., Xie, L., Chang, Y., & Tang, X. (2012). Channel assignment for WLAN by considering overlapping channels in SINR interference model. In *2012 International Conference on Computing, Networking and Communications (ICNC)* (pp. 1005-1009). IEEE.
- [2] Arya, L., Sharma, S. C., & Pant, M. (2010). Performance analysis of indoor positioning

- system. *International Journal of Advanced Computer Science and Applications*, 1(4), 37–41.
- [3] Chatterjee, S., Sarddar, D., Saha, J., Banerjee, S., Mondal, A., & Naskar, M. K. (2012). An improved mobility management technique for IEEE 802.11 based WLAN by predicting the direction of the mobile node. In *2012 National Conference on Computing and Communication Systems* (pp. 1-5). IEEE.
- [4] Choi, J., Lee, K., Lee, S. R., & Ihm, J. J. (2011). Channel selection for IEEE 802.11 based wireless LANs using 2.4 GHz band. *IEICE Electronics Express*, 8(16), 1275-1280.
- [5] Abbasi, S., Kalhoro, Q., & Kalhoro, M. A. (2011). Efficient use of partially overlapped channels in 2.4 GHz WLAN backhaul links. In *2011 International Conference on Innovations in Information Technology* (pp. 7-11). IEEE.
- [6] Tewari, B. P., & Ghosh, S. C. (2014). Interference avoidance through frequency assignment and association control in IEEE 802.11 WLAN. In *2014 IEEE 13th International Symposium on Network Computing and Applications* (pp. 91-95). IEEE.

# Finite Element Analysis on critical relative slippage of bolted joint under transverse loading

Hairul Bakri<sup>1,2,\*</sup>, Mohd Adnin Hamidi<sup>3</sup>, Mohd Shukri Yob<sup>1,2</sup>

<sup>1)</sup>Fakulti Kejuruteraan Mekanikal, Universiti Teknikal Malaysia Melaka,

Hang Tuah Jaya, 76100 Durian Tunggal, Melaka, Malaysia

<sup>2)</sup>Centre for Advanced Research on Energy, Universiti Teknikal Malaysia Melaka,

Hang Tuah Jaya, 76100 Durian Tunggal, Melaka, Malaysia

<sup>3)</sup>Fakulti Kejuruteraan Mekanikal dan Pembuatan, Universiti Malaysia Pahang,

26600 Pekan, Pahang Darul Makmur, Malaysia

\*Corresponding e-mail: hairul.bakri@utem.edu.my

**Keywords:** Critical relative slippage; transverse loading; Finite Element Analysis

**ABSTRACT** – Critical relative slippage ( $S_{cr}$ ) is known as a limit before loosening mechanism to occur. This limit is very crucial to predict the performance of bolted joint. Therefore, in this study, investigation of  $S_{cr}$  for M10 bolted joint under transverse loading was conducted using finite element (FE) analysis. FE model was validated by comparing the relationship between preload and twisting torque for FE model and theoretical values.  $S_{cr}$  values from FE analysis and experimental results were compared and good qualitative agreement was obtained.

## 1. INTRODUCTION

Nowadays, bolted joint is still relevant as a discussion and research topic since bolted joint is widely used for its low cost in production and producing a high fastening power with low tightening force. In addition, troubles related to loosening and failure of bolt is still occurring. This is an indicator that focus is needed at this joint structure to improve the reliability and its performance.

In this paper, attention is given to study the self-loosening behaviour under transverse loading. This type of loading is said to be the main contributor of failure in bolted joint [1]. According to Junker [2], Pai and Hess [3], the fastening preload immediately decrease by the rotation of nuts if the relative slippage on interface between nut and fastened body goes beyond certain critical limit. This critical limit is called critical relative slippage ( $S_{cr}$ ) which can be determined by relationship between transverse load and displacement of fastened body.

Therefore, aim of the current study is to provide database related to  $S_{cr}$  for bolted joint under transverse loading. FE analysis is used to complete this task due to cost and time limitation and its repeatability. Results of FE analysis is compared to experimental results done by Nishimura et al. [4] for verification purpose.

## 2. METHODOLOGY

ANSYS 16.0 is used as general purpose FE analysis software to carry out elastic analysis and determine the relationship between transverse loading and displacement of fastened body. Bolt size M10 is used and the specification of M10 is shown in Table 1. Plates are used as fastened body with length, width and thickness are 45 mm, 40 mm and 9 mm respectively. FE model is

shown in Figure 1. Lower plate is a fixed plate while upper plate is a movable plate which subjected to 0.5 mm displacement in  $x$  direction.

Table 1 Specification of M10.

Nominal diameter	Property class	Pitch	U.T.S (MPa)	Standard axial tension (N)
M10	4.8	1.5	392	12732

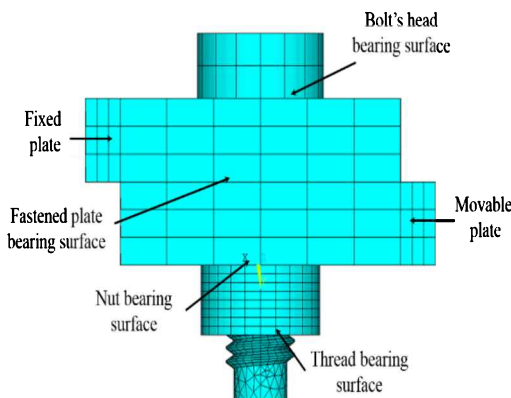


Figure 1 FE model.

Element pair TARGET170 and CONTA174 are used as contact element on bolt head bearing surface, nut bearing surface, fastened plates bearing surface and thread surface. These element pair are suitable for surface to surface contact between three dimensional objects and can deal with Coulomb Friction. Coefficient of friction at all contact surfaces is 0.2 while total number of nodes and elements are 19770 and 7058 respectively.

Fastening preload is generated by slightly shorten the length of body of bolt and permitting its interference movable plate under the constrained of the side of nut surface. 3 different fastening preloads are used 8 kN, 10 kN and 12 kN, respectively. Young's Modulus and Poisson ratio are 205 GPa and 0.3 respectively.

To conform the applicability of presented FE model, verification is done by comparing FE model and theoretical values [5] in term of relationship between fastening preload and twisting torque of nut. In addition, cyclic transverse loading experiment done by Yamamoto and Kasei [6] is also used for verification. Both

comparisons showed good qualitative agreement. Therefore, presented FE model can be used to investigate the  $S_{cr}$  for M10 bolted joint.

Finally, FE analysis results are compared to experimental results that conducted by Nishimura et al. [4] same settings are set between experiment and FE analysis in order to obtain reliable results.

### 3. RESULTS AND DISCUSSION

Due to difficulty to obtain values of  $S_{cr}$  from quasi-static experimental results, different approach is used to determine  $S_{cr}$  by experiment. Cyclic loading experiments were carried out to determine the relationship between preloads ( $F$ ) and number of cycles ( $N$ ) for various relative displacement of fastened plates. Then, loosening speeds ( $dF/dN$ ) were obtained and plotted with various relative displacement of fastened plates to determine  $S_{cr}$  as shown in Figure 2 [7]. Besides, Figure 3 shows the relationship between transverse load and relative slippage for FE analysis.  $S_{cr}$  for FE analysis results can be used directly from the relationship in contrast to experimental approach. Since  $S_{cr}$  is calculated for 1 complete displacement cycle, therefore the real  $S_{cr}$  value need to be multiplied by 2 in FE analysis result.

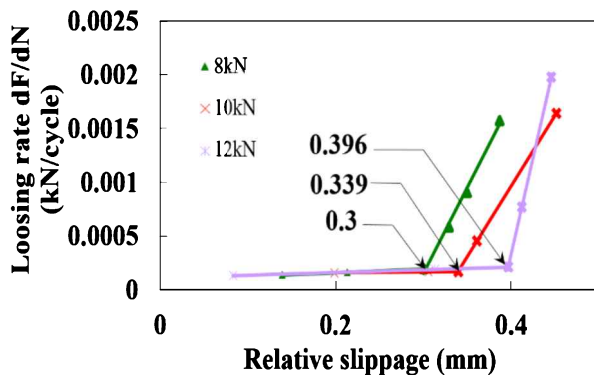


Figure 2 Relationship between fastening preload and relative displacement of fastened plate.

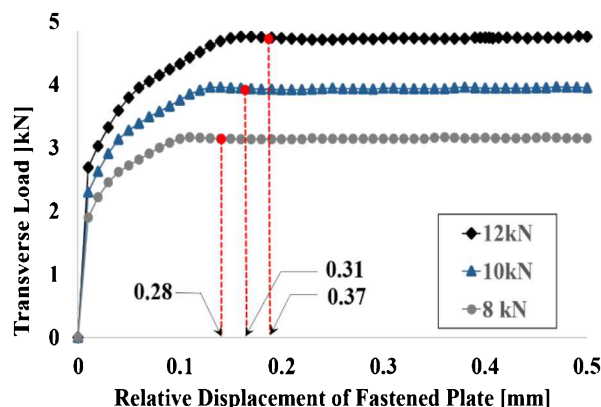


Figure 3 Relationship between transverse load and relative slippage for FE analysis.

Meanwhile, Table 2 shows comparison of  $S_{cr}$  values for both FE analysis and cyclic loading

experiment. Good qualitative agreements were determined with low percentage of errors between FE analysis and experimental results.

Table 2 Comparison of  $S_{cr}$  value.

Fastening Preload (kN)	$S_{cr}$ FE analysis (mm)	$S_{cr}$ Exp. (mm)	Error (%)
8	0.28	0.3	6.6
10	0.31	0.339	8.6
12	0.37	0.396	6.5

### 4. CONCLUSION

In this presented study, FE analysis was used to investigate the  $S_{cr}$  and comparison with experimental method was established for results verification. Therefore, conclusion can be made as following:

- (a) Presented FE model is applicable to run FE analysis for bolted joint under transverse loading.
- (b) Good qualitative agreements were observed between FE analysis and experimental results.  $S_{cr}$  value of FE analysis for preload 8 kN, 10 kN and 12 kN are 0.28, 0.31 mm and 0.37 mm, respectively.

### REFERENCES

- [1] Bickford, J. H. (2007). Introduction to the design and behavior of bolted joints: non-gasketed joints. CRC press.
- [2] Junker, G. H. (1969). New criteria for self-loosening of fasteners under vibration. Sae Transactions, 314-335.
- [3] Pai, N. G., & Hess, D. P. (2002). Experimental study of loosening of threaded fasteners due to dynamic shear loads. Journal of sound and vibration, 253(3), 585-602.
- [4] Nishimura, N., Hattori, T., Yamashita, M., & Hayakawa, N. (2007). Self loosening behavior of metal thread joints under transverse cyclic loading. In Key engineering materials (Vol. 340, pp. 1467-1472).
- [5] Izumi, S., Yokoyama, T., Iwasaki, A., & Sakai, S. (2005). Three-dimensional finite element analysis of tightening and loosening mechanism of threaded fastener. Engineering Failure Analysis, 12(4), 604-615.
- [6] Yamamoto, A., & Kasei, S. (1977). Investigations on the Self-Loosening of Threaded Fasteners under Transverse Vibration—A Solution for Self-loosening Mechanism. Journal of the Japan Society of Precision Engineering, 43(4), 470-475.
- [7] Yamagishi, T., Asahina, T., Araki, D., Sano, H., Masuda, K., & Hattori, T. (2018). Loosening and sliding behaviour of bolt-nut fastener under transverse loading. Mechanical Engineering Journal, 5(3), 16-00622.

# Analysis of SOI PD-MOSFET device using different gate spacer materials

S. Husna S. Hameed, F. Salehuddin\*, Ameer F. Roslan, Aida Maziah Manin, Noreazira Mohd Daud, A.H. Afifah Maheran, A.S.M. Zain, K.E. Kaharudin

Micro and Nano Electronics (MiNE), Centre for Telecommunication Research and Innovation, Fakulti Kejuruteraan Elektronik dan Kejuruteraan Komputer, Universiti Teknikal Malaysia Melaka, Hang Tuah Jaya, 76100 Durian Tunggal, Melaka, Malaysia

\*Corresponding e-mail: fauziyah@utem.edu.my

**Keywords:** Silicon on Insulator (SOI); high-k material; PD-MOSFET

**ABSTRACT** – This project is executed by using Silvaco TCAD software to simulate process and electrical characteristics for the structure of Silicon on Insulator Partially Depleted (PD-SOI) MOSFET that has been designed by following the ITRS 2013. Furthermore, this project facilitates the performance improvement of 19nm SOI PD-MOSFET using high-k material as the gate spacer. Through this project, the device with a SOI layer thickness of 30nm and titanium oxide as the gate spacer yields the highest drive current of  $548.78\mu\text{A}/\mu\text{m}$  and the lowest leakage current of  $113.475\text{pA}/\mu\text{m}$  at the threshold voltage of  $0.533\text{V}$  compared to other high-k materials as gate spacer and Bulk-Si MOSFET device.

## 1. INTRODUCTION

Miniaturizing the dimension of Metal Oxide Semiconductor Field Effect Transistor (MOSFET) allows numbers of a transistor to be integrated on a chip. As proofs, in the year 2014, the best Intel processor available contains 1.7 billion transistors while in year 2016, Intel's has well-E CPUs contained 2.6 billion transistors and the high-end Xeon server chips are reported to have more than two billion transistors [1]. Besides, transistor scaling technology gives benefits in reducing the cost per production per single IC, increase the speed and performance, better stability of the operation and less power dissipation of the device. Unfortunately, there are several challenges arise as the device becomes smaller such as performance degradation and short channel effects (SCEs) which make it difficult to continue reducing the device's size follows the conventional law [2]. When downscaling MOSFET, it is hard to maintain a nominal threshold voltage ( $V_{TH}$ ) as well as reduce the leakage current ( $I_{OFF}$ ) and subthreshold swing (SS) to improve the device's performance. Therefore, the researchers put their extreme efforts in finding solutions to solve the arising problems. The use of high-k materials and new structure of MOSFET which is known as Silicon-On-Insulator (SOI) technology are then introduced to the semiconductor industry [3]. As what its name imposed, high-k materials have a high dielectric constant ( $k$ ) which provide improvement of oxide capacitance, less leakage current and better stability to the device operation. Meanwhile, SOI technology refers to a method of depositing a Buried Oxide (BOX) layer on the silicon substrate. It works as an insulating layer to

the structure so that when the device is operated, the charge carrier will not be scattered far away from the channel, thus provides a higher speed and a better response of the device. On that account, a new structure of SOI PD-MOSFET device is designed in this project with four different high-k gate spacer materials to increase the drive current hence meet the requirement of high performance.

## 2. METHODOLOGY

Figure 1 shows one of the structures of 19nm SOI PD-MOSFET with the conventional gate spacer and BOX layer thickness of 30nm. From this figure, the gate length created in the structure is 19nm, the insulating layer thickness shown is 30nm with the  $\text{Si}_3\text{N}_4$  as gate spacer.

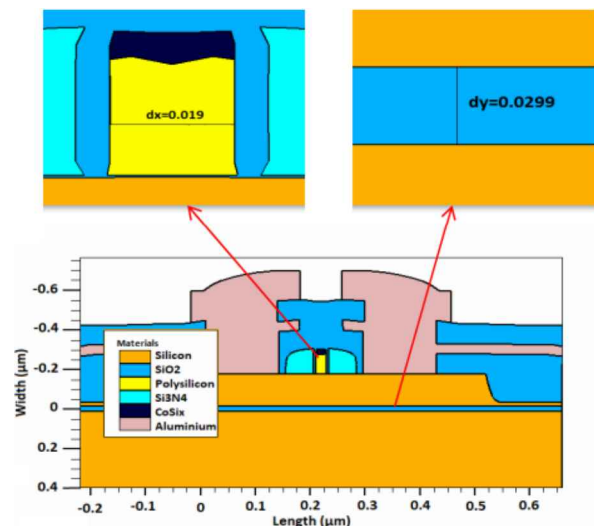


Figure 1 Structure of 19nm SOI PD-MOSFET and  $\text{Si}_3\text{N}_4$  as the gate spacer.

Throughout this project, Silvaco TCAD software that is commercially available in the industry is used to simulate both fabrication process and electrical characteristics. Silvaco TCAD software consists of two simulators which are ATHENA and ATLAS modules. ATHENA module will be used to simulate the virtual fabrication of SOI PD-MOSFET device while the simulation of electrical characteristics will be implemented using ATLAS module. ATLAS module can produce several graphs such as  $I_D$  versus  $V_G$ ,  $I_D$  versus

$V_D$  and log  $I_D$  versus  $V_{DS}$  to show their electrical behaviour. Four electrical responses that were analysed include drive current ( $I_{ON}$ ), leakage current ( $I_{OFF}$ ), threshold voltage ( $V_{TH}$ ) and the current ratio ( $I_{ON}/I_{OFF}$ ). After the electrical behaviour is obtained from the simulation, those data are used to be compared with the conventional Bulk-Si MOSFET to prove the performance efficiency.

### 3. RESULTS AND DISCUSSION

After all the virtual fabrication and device simulation for both Bulk-Si MOSFET and SOI PD-MOSFET designs are completed, those data from ATLAS simulator window are tabulated in Table 1 to ease the comparison.

Table 1 Comparison table for 19nm SOI PD-MOSFET with BOX layer thickness of 30nm.

Condition Description for 19nm MOSFET	$V_{TH}$ (V)	$I_{ON}$ ( $\mu A/\mu m$ )	$I_{OFF}$ ( $pA/\mu m$ )	$I_{ON}/I_{OFF}$ ratio ( $\times 10^6$ )
Bulk-Si MOSFET	0.533	444.72	450.50	0.99
SOI with $Si_3N_4$ as gate spacer	0.533	322.23	135.48	2.38
SOI with $Al_2O_3$ as gate spacer	0.533	342.78	169.18	2.03
SOI with $ZrO_2$ as gate spacer	0.533	423.40	154.40	2.74
SOI with $HfO_2$ as gate spacer	0.533	434.77	150.70	2.88
SOI with $TiO_2$ as gate spacer	0.533	548.78	113.47	4.84
ITRS 2013 predict for year 2015 [4]	$\pm 12.7\%$	$\geq 456$	$\leq 50$	9.21

The result obtained from the designed structure of 19nm Bulk-Si MOSFET shown in Table 1 portrays the highest leakage current ( $I_{OFF}$ ) value of  $450.50 pA/\mu m$  alongside with a value of the drive current ( $I_{ON}$ ) which is  $444.72 \mu A/\mu m$ . This result proves the problem of larger leakage current occurs through scaling down planar MOSFET in the semiconductor industry. This is due to the fact that scaling the gate length to 19nm caused the effective channel length to decrease as well and might attach together and cause movement of electrons (leakage current) in the device even though there is no gate voltage being applied [5]. As the gate length is only 19nm, the depletion regions of drain and source merged together as both regions extended, thus causes the punch through inside the device as well. The  $I_{ON}/I_{OFF}$  ratio obtained from the result is only  $0.99 \times 10^6$  compared to other ratios.

Table 1 shows the expected result is achieved when the  $TiO_2$  is used as the gate spacer for the design of 19nm SOI PD-MOSFET with 30nm BOX layer thickness. This is because  $TiO_2$  with the highest dielectric constant ( $k=85$ ) helps in enhancing the performance in terms of increase the drive current ( $I_{ON}$ ) in SOI PD-MOSFET device. As  $TiO_2$  has the highest dielectric constant, it provides higher fringing field that will reduce the barrier height between source and drain in on-state [2]. This design attained a maximum  $I_{ON}$  of  $548.78 \mu A/\mu m$  which is the highest  $I_{ON}$  among the other

designs (included the 19nm Bulk-Si MOSFET) and the smallest leakage current which is  $113.48 pA/\mu m$  compared to the other MOSFET designs in this project (included the Bulk-Si MOSFET). This result proves that the leakage current and SCE could be reduced by using SOI technology and at the same time the drive current increases when high-k material is used as the gate spacer in the structure. This is in line with the aims stated at the beginning of the project which is to prove that 19nm SOI MOSFET with high-k gate spacer material yields better electrical characteristics compared to the Bulk-Si MOSFET with the same gate length.

### 4. CONCLUSION

Throughout this project, the 19nm Silicon-on-Insulator (SOI) PD-MOSFETs with four different high-k gate spacer materials are successfully designed with two different BOX layer thicknesses by using ATHENA module while the electrical characteristics for each are analyzed through ATLAS module. Based on the results obtained, it is verified that SOI technology is able to reduce the Short Channel Effect (SCE) and leakage current in the device compared to the Bulk-Si MOSFET, meanwhile the used of high-k gate as the gate spacer is proven useful to improve the performance of SOI PD-MOSFET in terms of both drive current and leakage current.

### ACKNOWLEDGEMENT

The authors would like to thank the Ministry of Higher Education (MOHE) for sponsoring this work under project (FRGS/1/2017/TK04/ FKEKK-CeTRI/F00335) and Faculty of Electronics and Computer Engineering, Universiti Teknikal Malaysia Melaka (UTeM) for the moral support throughout the project.

### REFERENCES

- [1] Rahman, L. F., Arith, F. B., Idris, M. I. B., Reaz, M. B. I., & Marufuzzaman, M. (2014). Low power in nano-scale CMOS memory. *Journal of Theoretical and Applied Information Technology*, 61(2), 297–303.
- [2] Rajneesh S., Rituraj S. R., & Ashwani K. R. (2018). Impact of High-k spacer on device performance of nanoscale underlap fully depleted SOI MOSFET. *Journal of Circuits, Systems and Computers*, 27(4), 1850063.
- [3] Kale, S., Banchhor, S., & Kondekar, P. (2015). Performance study of high-k gate & spacer dielectric Dopant Segregated Schottky Barrier SOI MOSFET. *Proceeding of International Conference on Electronics and Communication Systems 2015*, 2015, 1142-1145.
- [4] ITRS (2013). [www.ITRS2013.net](http://www.ITRS2013.net).
- [5] Chinnappan, U., & Sanudin, R. (2017). Investigation of short channel effects on device performance for 60nm NMOS transistor. *IOP Conf. Series: Material Science and Engineering*, 226(2017), 012143.

# Characteristic of metal magnetic memory signals under uniaxial fatigue loading for SAE1045 steel

Siti Norbaya Sahadan<sup>1,2,\*</sup>, Shahrum Abdullah<sup>1</sup>, Azli Ariffin<sup>1</sup>, Salvinder Singh Karam Singh<sup>1</sup>

<sup>1)</sup> Centre for Integrated Design for Advanced Mechanical System, Faculty of Engineering and Built Environment, Universiti Kebangsaan Malaysia, 43600 UKM, Bangi Selangor, Malaysia

<sup>2)</sup> Fakulti Kejuruteraan Mekanikal, Universiti Teknikal Malaysia Melaka, Hang Tuah Jaya, 76100 Durian Tunggal, Melaka, Malaysia

\*Corresponding e-mail: norbaya@utem.edu.my

**Keywords:** Metal magnetic memory; stress concentration zone; tension-tension fatigue

**ABSTRACT** – The objective of this study is to evaluate changes in the metal magnetic memory method, MMM parameter during cyclic loading test from the beginning until fracture. Flat specimen with a notch made of SAE 1045 steel was used. MMM signals were collected during an experiment at one-hour interval using tester of stress concentration (TSC) device. From the experiment, it was found that the maximum value of magnetic flux leakage gradient  $dH/dx_{(max)}$  is increasing as cycles number increase, and slightly decrease towards fracture. From this study, it shows that this method can detect a high-stress concentration zone on the material with high sensitivity.

## 1. INTRODUCTION

Detecting a high-stress concentration zone on a ferromagnetic component is crucial. It is due to the high-stress concentration zone is the potential position of damage. The conventional method only detects damage, that already developed. However, this method detects at an early stage of damage. In this study, the magnetic metal memory method (MMM) has been proposed to detect the high-stress concentration zone. At service loads condition where high strains on the elements will induce high metal magnetisation on the elements [1].

Fatigue failure occurred when components exposed to fluctuating service load leads to unforeseen failure. Parts with notch or holes have risen fatigue failure as this cause high concentration on components. Study by Yang et. al [2] found that decreasing of fatigue life and increasing of fatigue mean stress sensitivity due to notch. In this study, it is aimed to evaluate changes in MMM parameter during cyclic loading from the beginning until fracture.

## 2. METHODOLOGY

The tensile test experiment has been conducted to gather mechanical properties of the specimen. In this study, the specimen made of ferromagnetic material, SAE1045 which have much application in industry. The monotonic properties were tabulated in Table 1. Figure 1 shows the schematic drawing of the specimen with the scanning line. The distance between each line is 5 mm and the length is 100 mm. MMM signals collected at each of scanning line. For the cyclic test, the load used in this study is 65% UTS and stress ratio,  $R$  is equal to zero.

The 100kN servo-hydraulic universal testing machine used to conduct the cyclic test. A TSC device

used to collect magnetic signals. Signals collected before loading, at one cycle loading and every one-hour loading cycles interval until specimen fracture. Figure 2 shows the arrangement of the UTM machine, the TSC device, and the specimen during testing. The collected signals stored in the TSC device and transferred to a computer and later analysed using a MMM 3.0 system software.

Table 1 Monotonic properties of SAE 1045.

Properties	Data
Ultimate Tensile Strength, $\sigma_{UTS}$	772.0 MPa
Yield Strength, $\sigma_y$	473.4 MPa
Young Modulus, E	169.7 GPa

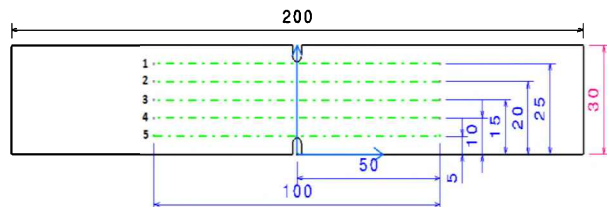


Figure 1 Fatigue specimen and scanning lines.

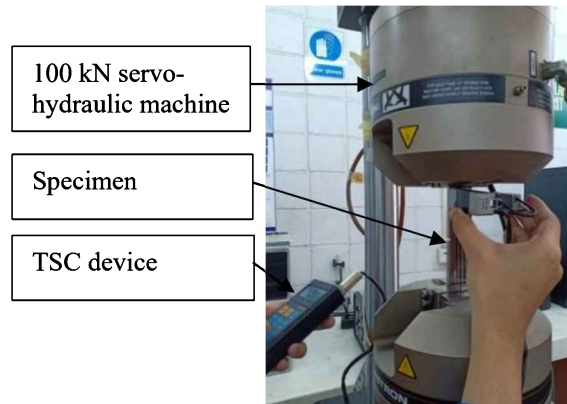


Figure 2 Scanning process using MMM instruments – the TSC device.

## 3. RESULTS AND DISCUSSION

In this experiment, the specimen failure at 15969 cycles. MMM signals has been collected at 10, 100, 1000, 3600, 7200, 10800 cycles and 14400 cycles. Tabulation of magnetic flux leakage gradient  $dH/dx$  shows in Figure 3, the surface contour between  $dH/dx$  with the length of the scanning lines. In Figure 3, the  $dH/dx$  represents by the axis -y named as  $|grad H|$ . From

Figure 3, at the center of the scanning lines, at the length of 50 mm, it can be seen high-intensity color tabulation. From this color intensity, it demonstrates that there is high-stress concentration zone in that area. With comparison to the specimen, it is matched with the notch position on the specimen as shown in Figure 2. From these results it can confirm the ability of MMM method in detecting high-stress concentration zones in the specimen.

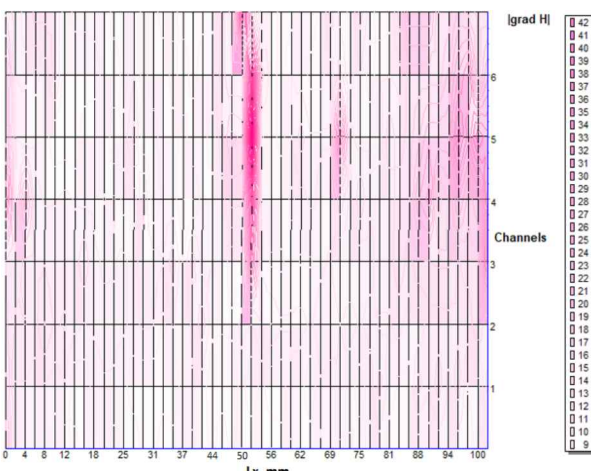


Figure 3 Surface contour mapping of  $dH/dx$  distribution along scanning lines.

Further analysis conducted to evaluates changes in the maximum value of magnetic flux leakage gradient  $dH/dx_{(max)}$ . Figure 4 shows the plot of  $dH/dx_{(max)}$  with numbers of cycles. From Figure 4, the value of  $dH/dx_{(max)}$  increased as the number of cycles increased during the experiment, until the number of cycles reaches 10000 cycles. However, as the experiment continues, the value of  $dH/dx_{(max)}$  starts to decrease until the number of cycles reach 14400 cycles, given by the last MMM signal collected before the specimen fracture at 15969 cycles. The trend of this data tabulations is consistent with the previous study by Huang et al. [3] and Wang et al. [4]. Microstructure changes in ferromagnetic material given high impact to magnetic properties. Dislocation movement in ferromagnetic leads to the accrual of magnetic charge around the crack. As the cycles increased near to fracture, tabulation of magnetic charge distributed evenly at the length of the crack, that causes a decrease in  $dH/dx_{(max)}$ .

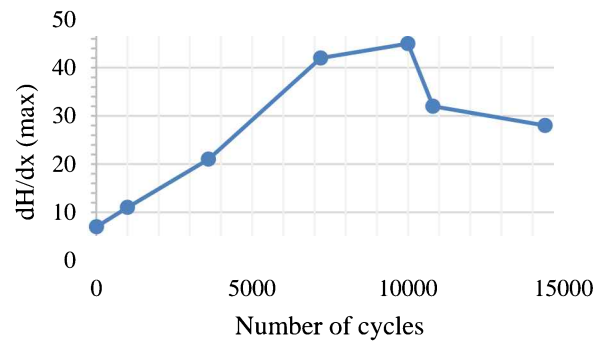


Figure 4 Changes in  $dH/dx_{(max)}$  concerning the numbers of cycles.

#### 4. CONCLUSION

The metal magnetic memory used in this study has high sensitivity in detecting high-stress concentration zone during the cycling loading. High-color intensity given by surface contour mapping of  $dH/dx$  distribution at the length of 50 mm scanning. This position identified as the position of the notch on the specimen. By evaluating maximum changes in  $dH/dx_{(max)}$  concerning the number of cycles, it is found that  $dH/dx_{(max)}$  value increased as the number of cycle increased. Decreasing of the  $dH/dx_{(max)}$  value indicated that, the specimen was near to failure as magnetic-charge distribution began to distribute evenly along the crack.

#### 5.

#### ACKNOWLEDGEMENT

The authors would like to express their gratitude to Universiti Teknikal Malaysia Melaka, Universiti Kebangsaan Malaysia and Ministry of Higher Education Malaysia for this research opportunity.

#### REFERENCES

- [1] Vlasov, V. T., & Dubov, A. A. (2004). Physical bases of the metal magnetic memory method. *Moscow: ZAO "Tisso*, 424.
- [2] Yang, K., Zhong, B., Huang, Q., He, C., Huang, Z.-Y., Wang, Q., & Liu, Y.-J. (2018). Stress ratio and notch effects on the very high cycle fatigue properties of a near-alpha titanium alloy. *Materials*, 11(9), 1778.
- [3] Huang, H., Jiang, S., Yang, C., & Liu, Z. (2014). Stress concentration impact on the magnetic memory signal of ferromagnetic structural steel. *Nondestructive Testing and Evaluation*, 29(4), 377.
- [4] Wang, H., Dong, L., Dong, S., & Xu, B. (2014). Fatigue damage evaluation by metal magnetic memory testing. *Journal of Central South University*, 21(1), 65.

# Counterproductive work behavior, organizational support, personality traits and emotional intelligence among industrial workplace

Norida Abdullah\*, Ali Hafizar Mohd Rawi, Mohd Firdaus Abdullah

Pusat Bahasa dan Pembangunan Insan, Universiti Teknikal Malaysia Melaka,  
Hang Tuah Jaya, 76100 Durian Tunggal, Melaka, Malaysia

\*Corresponding e-mail: noridaha@utem.edu.my

**Keywords:** Counterproductive work behavior; organizational support; personality traits; emotional intelligence

**ABSTRACT** – Employees who display Counterproductive Work Behavior (CWB) are more likely to develop stress related problems, intention to resign, experience low self-esteem, and increased lack of confidence at work. Various factors that may predict CWB. These include individual differences such as employees' personal traits, work stress, and emotional intelligence (EI). Therefore, the objective of this study is to identify the relationship among perceived organizational support, personality traits, emotional intelligence and counterproductive work behavior among technical staffs. Finding from this study will help the human resource management to propose the alternatives employee assistant program for the benefit of staffs at the industry.

## 1. INTRODUCTION

Research done previously found that various factors that may predict CWB. These include individual differences such as employees' personal traits and abilities, work stress such as difficult work conditions, harsh supervision, and emotional intelligence (EI). Other research suggested that organizational diversity could influence turnover intention [1]. Employee turnover refers to a group of employee movements that create a vacancy within the organization unit. Turnover intention is defined as an employee's intent to find a new job with another employer within the near future. Employees' turnover always implies a high cost to companies, seriously hindering efficient, effective customer service and undermining competitiveness. Ponniah et al. [2] found that organizational diversity and diversity programs could decrease turnover intention and the actual turnover rate.

Based on the study done on productivity and profitability, concluded / indicated that factors contributing to the deficit in organizations' profitability due to physical and /or emotional health problems, stress, burnout of employees, poor management strategies, and lack of effective training programs [3]. Study done by Zain et al. [4] showed that when organization is concerned about the employees then employees would try to change their inner feelings to achieve organizational objectives. It means that if employees are emotionally intelligent, they can manage their emotions in a better way while interacting with others. In their study also found that emotional intelligent also moderates counterproductive work behaviors.

Employees with a high level of emotional intelligence can modify their inner feeling and emotions according to the situation due to which they can tackle counterproductive work behaviors in a better way.

Therefore, this study aims to identify the relationship among perceived organizational support (POS), personality traits (PT), emotional intelligence (EI) and counterproductive work behavior (CWB) among technical staffs.

## 2. METHODOLOGY

### 2.1 Objective of the study

To identify whether a relationship exists among perceived organizational support, personality traits, emotional intelligence and counterproductive work behavior among technical staffs.

### 2.2 Hypotheses of the study

The hypotheses postulated in this study are:

- Perceived Organizational Support (POS) influences Counterproductive Work Behavior (CWB) among technical staffs.
- Personality Traits (PT) influences Counterproductive Work Behavior (CWB) among technical staffs.
- Emotional Intelligence (EI) influences Counterproductive Work Behavior (CWB) among technical staffs.

### 2.3 Sample and Population / Participants

The population of this study consists of approximately 2,000 technical staff employed at CTRM of Melaka branch. The questionnaire distributed to 350 staff randomly and enough in order to generalize the results [5].

### 2.4 Instruments and Data Analysis

There are four instruments used to measures construct variables involve in this research such as, Counterproductive work behavior (CWB), Perceived Organizational Support (POS), Personality Traits (PT), and Emotional Intelligence (EI). Frequency analysis used to determine the demographic characteristics of the sample. Explanatory factor analysis used to test the construct validity of the measurement model while structural equation modelling (SEM) used to test the hypotheses.

## 2.5 Research framework

Figure 1 illustrated the framework for this study.

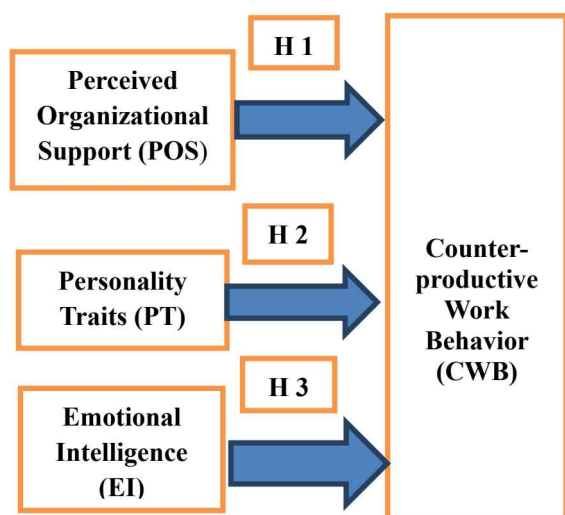


Figure 1 Research framework.

## 3. RESULTS AND DISCUSSION

Based on previous literature review done by other researchers, found that Perceived Organizational Support (POS) influences Counterproductive Work Behavior (CWB), such as related with management strategies [3], strengthen employee' meaning of work [6], organization behavior and interest of organization [7]. For Personality Traits (PT) and CWB, previous study [6, 8, 4, and 9] found that personality has the potential to influence CWB process. Another study done by [4, 10, and 11] found that emotional intelligence moderates the CWB. Findings from this study will confirm the results as mentioned by other researchers in order to sustain the productivity for the industry to overcoming the psychological and emotional issues of the human capital development in the industry.

## 4. CONCLUSION

The present study intends to explore and examine the relationship among perceived organizational support, personality traits, emotional intelligence and counterproductive work behavior among technical staffs employed at CTRM of Melaka branch. Hopefully, the HRM at the industrial level will continue take the necessary action towards staff well-being at the workplace in order to sustain the productivity for the industry and for the nation. Focusing from the HRM based on the variables mention in the Employee Assistant Program (EAP) will not only help in overcoming the psychological and emotional issues but it has the potential to result in positive functioning of an individual of the human capital development in the industry.

## ACKNOWLEDGEMENT

The authors would like to thank for the cooperation given from the industry CTRM, C-TED Coe group, and SICOM group research. We also would like to express our gratitude to Universiti Teknikal Malaysia Melaka for supporting these research activities through grant PJP/2019/PBPI/ (5D)/S01694.

## REFERENCES

- [1] Spector, P. E. (2010). The relationship of personality to counterproductive work behavior (CWB): An integration of perspectives. *Human Resources Management Review*, 21(4), 342-352.
- [2] Raman, P., Sambasivan, M., & Kumar, N. (2016). Counterproductive work behavior among frontline government employees: Role of personality, emotional intelligence, affectivity, emotional labor, and emotional exhaustion. *Revista de Psicología del Trabajo y de las Organizaciones*, 32(1), 25-37.
- [3] Zerbes, M. V., Cioca, L. I., & Neamu, V. S. (2019). Occupational health programs and workplace absenteeism. *Quality-Access to Success*, 20, 129-134.
- [4] Riaz, Z., Arif, A., Nisar, Q. A., Ali, S., & Sajjad, M. (2018). Does perceived organizational support influence the employees emotional labor? Moderating & mediating role of emotional intelligence. *Pakistan Journal of Humanities and Social Sciences*, 6(4), 526-543.
- [5] Var, I. (1998). Multivariate data analysis. *vectors*, 8(2), 125-136.
- [6] Akgunduz, Y., Alkan, C., & Gök, Ö. A. (2018). Perceived organizational support, employee creativity and proactive personality: The mediating effect of meaning of work. *Journal of Hospitality and Tourism Management*, 34, 105-114.
- [7] Ponte, D., & Rizzi, C. (2010). Understanding socialization practice: factors fostering and hindering its evolution. *Society and Business Review*, 5(2), 144-154.
- [8] Chang, K., & Smithikrai, C. (2010). Counterproductive behaviour at work: an investigation into reduction strategies. *The International Journal of Human Resource Management*, 21(8), 1272-1288.
- [9] Ferreira, M. F., & Nascimento, E. D. (2016). Relationship between Personality Traits and Counterproductive Work Behaviors. *Psico-USF*, 21(3), 677-685.
- [10] Deshpande, S. P., Joseph, J., & Shu, X. (2005). The impact of emotional intelligence on counterproductive behaviour in China. *Management Research News*, 28(5), 75-85.
- [11] Petrides, K. V., Frederickson, N., & Furnham, A. (2004). The role of trait emotional intelligence in academic performance and deviant behavior at school. *Personality and individual differences*, 36(2), 277-293.

# Improvement of work system through designing pedal control facilities for nenggala tactical vehicles in the workshop of the national Indonesian army equipment center

Rimba Krisnha Sukma Dewi\*, Angling Sugiatna, Bedy Ubaedillah

Sekolah Tinggi Teknologi Bandung, Soekarno-Hatta St No.378, Kebon Lega, Bojongloa Kidul, Bandung City, West Java 40235, Indonesia

\*Corresponding e-mail: rimbakrisnha80@gmail.com; rimbakrisnha@sttbandung.ac.id

**Keywords:** Driver cabin working system; pedal control; tactical vehicles

**ABSTRACT** – The workshop of the army equipment center (Bengpuspalad) is an agency engaged in the improvement and design of combat vehicles and tactical vehicle and the manufacture of parts of combat vehicles in limited numbers. One of them is the prototype of tactical vehicle (rantis) Nenggala. Previously on Nenggala rantis there are problems related to the actual condition of the cabin that is less support the work activities carried out that is on the pedal pedals and technical pedals are used. The results of improvements to the work system is done to improve the size, angle and distance between the pedals and the addition of pedestal pedestal rest for left foot sole. On the technical aspect, there is improvement with brake type selection with the addition of brake booster and replacement of clutch drive system into fluid feeding coupling.

## 1. INTRODUCTION

The Equipment Center Workshop (Bengpuspalad) is an agency under the auspices of the Indonesian Armed Forces Army (TNI AD). At its inception, Bengpuspalad was still in the form of a master workshop owned by the Dutch which at that time colonized Indonesia which was founded in 1920. Where bengpuspal was a storage industry from small industries that moved to Bandung and became one became a large workshop owned by the Indonesian government whose operations were carried out by the Army for military purposes in particular and the country generally.

Basically, Bengpuspalad's activities cover the actions or complete repairs of various types of combat vehicles, the complete manufacture or repair of combat vehicles of various types of tactical vehicles (rantis), weapons holders, combat vehicle parts and so on. Bengpuspalad, which has 546 members, occupies an area of 12 hectares, has a vision to support the movement and firepower of TNI-AD units, as well as the mission to assist the Directorate of equipment in maintaining and maintaining equipment maintenance up to level VI (the highest level of damage) and producing equipment or spare parts in a limited way to support their first duties.

As mentioned earlier, one of the products is a tactical vehicle (rantis). At this time for the first time the TNI army made a cargo type Rantis under the name Nenggala. Based on a preliminary study of the rantis as a whole, it was decided the study was carried out in the driver's cabinet with consideration of the main priority in driving lies in the driver, hence driver safety is very influential in the success of a mission. Where the vehicle

and its contents must arrive at the destination safely and the driver feels comfortable to drive for a long period of time.

Based on the Nordic Body Map questionnaire, drivers experience complaints of discomfort with existing facilities. Complaints experienced by the driver during and after driving in a sitting position is aching pain, especially on the soles of the feet, ankles, calves, knees and thighs. This complaint is based on observations, caused by the pedal control system facilities used by the driver made with no regard to the dimensions of the driving body that does not match the pedal makes the driver have to lift his legs while braking and stepping on the clutch, besides the pedals do not take into account the angles formed by the legs feet so that the back of the foot is too bent inward and the calf feels tension because the angle formed is too pointed. The displacement distance that is too far away causes fatigue to appear too early because repetitive work will make the displacement distance more and more.

In addition to work facilities technical facilities also influence the performance of the driver even though the driver can adapt to the technical aspects of the pedal control system such as the brake system and clutch drive system. However, this condition has the potential to make the driver feel uncomfortable in driving. The brake system that uses drum allows for still movement during braking, this can lead to conditions that allow accidents to occur, as well as the clutch drive system, clutch locking is not perfect so the gear shift is repeated, this causes the clutch to often slip and the left leg is very tired because it has to step on the clutch many times. The braking process that occurs and is carried out by the driver is very strong causing the driver to get tired because the pressure given is very large, thus a tool is needed to reduce the burden of emphasis on the brakes.

The driver's performance in performance is greatly influenced by the conditions of the work system where the work is carried out. For that we need a pedal control system design that includes ergonomic and technical aspects in order to support the work activities carried out so that it is expected to provide comfort to the driver. Therefore the improvements made on the pedal control system in the Nenggala Rantis steering wheel are expected to be able to answer the needs of workers for a more effective, comfortable, safe, healthy, efficient (ENASE) working system condition, so as to improve worker performance. As for the conditions of the Nenggala Rantis pedal system can be seen in Figure 1.



Figure 1

For this reason, the formulation of the problem of this research is how to improve the work system in the steering cabin by providing design suggestions for pedal control facilities along with technical aspects to improve the driver's comfort in carrying out his activities. Thus in accordance with the formulation of the problem, the purpose of this study is to: (1) conduct an analysis to find out the weaknesses of the steering cabin that have the potential to cause problems that can disrupt driving nets; (2) Provide a proposal for the design of the steering cabin which includes work facilities and technical aspects in accordance with the driver's needs and the activities carried out; and (3) Evaluating the design of the steering cabin system improvements proposed through ergonomic and technical criteria to determine the extent to which the repairs were carried out.

## 2. METHODOLOGY

This research method (Figure 1) uses a mixed method that is done by combining or combining quantitative and qualitative methods used together in a study to obtain more comprehensive, valid, reliable and objective data. In addition, this study uses ergonomic evaluation and technical evaluation in order to assess the results of the design.

## 3. RESULTS AND DISCUSSION

Data collection in this study was carried out through questionnaires accompanied by interviews with the aim of finding out the complaints experienced by the players at the time and after driving a tactical nenggala vehicle. The documentation study was carried out in order to obtain data such as the data cabin of the Bengali rantis steering wheel, work facilities, technical facilities and user anthropometry. The processing of data is done through the development of conceptualization of the proposed work system, namely the design of pedal facilities and the design of technical facilities. The design of the pedal facility is divided into testing for normal distribution, averaging the data, calculating the standard deviation, calculating percentiles, determining percentiles and dimensions of the pedals. While the design of technical facilities is divided into replacing the brake system, adding brake booster and replacing the clutch drive system.

Based on calculations from the results of improvements to the working system of the Naggala rantis vehicle pedal, improvements have been made to the size, angle and distance between the pedals and the addition of a pedestal pedal rest to the left foot with dimensions as shown in Table 1.

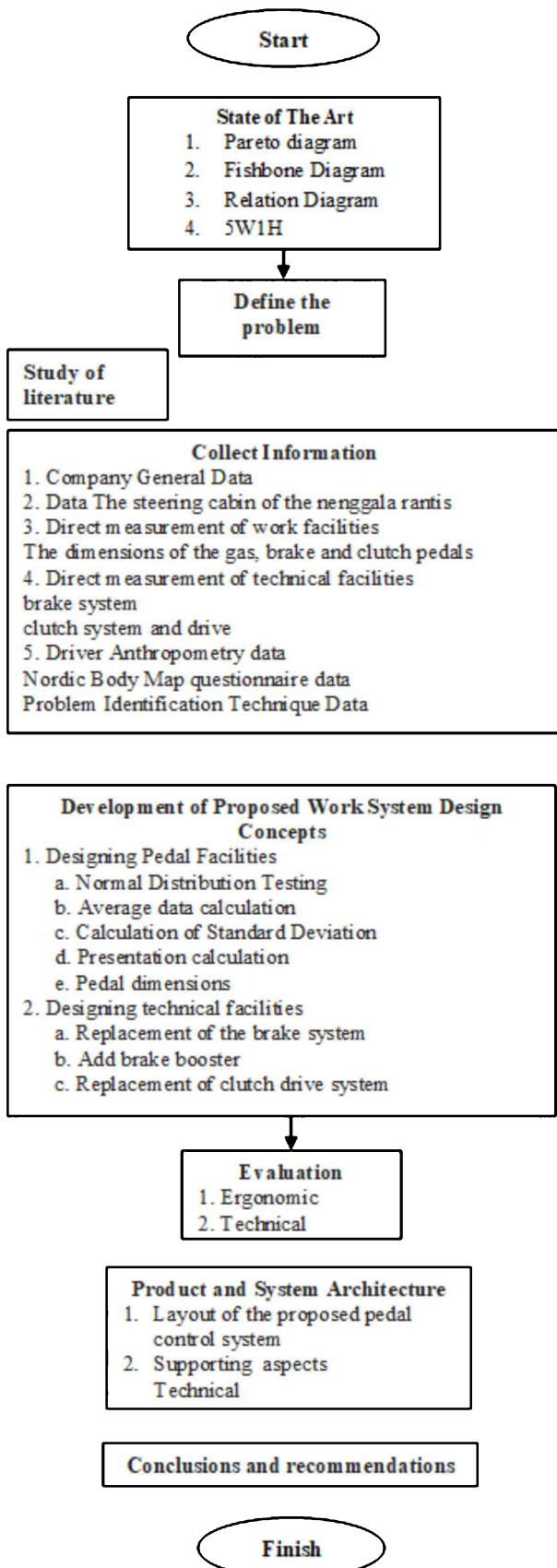


Figure 1 Flowchart of the methodology.

Table 1 Calculation results from work system improvement.

Pedal/Dim.	Gas	Brake	Clutch	Hanging pedal
Length (cm)	13	9	9	13
Width (cm)	8	5,75	5,75	5,75
Height (cm)	9,1	10	10	7,5
Corner of the leg (°)	25-45	25-45	25-45	35

From Figure 2, the results of the design evaluation show that the design can be useful in the operationalization of the Nenggala Rantis vehicle. This is based on an ergonomic evaluation where the dimensions of the pedal must follow the length of the sole of the foot so that the load can be evenly distributed on the thighs, calves and soles of the feet. This can also increase user comfort. In addition, the distance between the pedals is adjusted using the permitted rules to reduce the displacement carried out not to the extent that is carried out in actual conditions and reduce pain and aches in the thighs and calves.

Ergonomics evaluation on the control system also explains the principle of using leg-forming angles where the palms and legs form angles that are in good position with the legs and feet so that it can increase comfort and is good for health and can reduce pain or soreness in the ankles and palms feet. This is produced by making a resting place for the left foot allowing the left foot to be stretched out on the spot in an idle position without having to hang in front of the clutch pedal, when the clutch is intended / not used. As a result, the driver feels comfortable in a hanging position waiting for the clutch pedal to be used. Communication devices are used properly so that they do not disturb the main function of the pedal control system, where the activities carried out are in the portion that should be done by the driver and do not violate its main function.

The results related to technical evaluation are carried out by comparing the technical aspects of the actual conditions with the conditions after the repairs are carried out, which are expected to be better than the actual conditions or before repairs are carried out. In this result emphasize on the use of disc brakes because pengermanan occurs so that the condition of all wheels will be locked at the same time, causing the termination of road conditions or any terrain safer because of the stops that have better accuracy compared to the use of drum brakes as in actual conditions. The results also explain the use of a booster device on the proposed repair brake system can ease the work of the driver in operating the brakes on this vehicle. The money booster work reduces the burden during hatching, making the driver's feet do not get tired and reduce the risk of injury leading to the driver.

The results of this evaluation also revealed that the use of feeder fluid couplings in the proposed conditions has advantages over the mechanism of use where there are bumps on the side of the clutch making the locking process occur strongly. The use of a hydraulic system in the clutch drive also takes faster time compared to mechanical means.

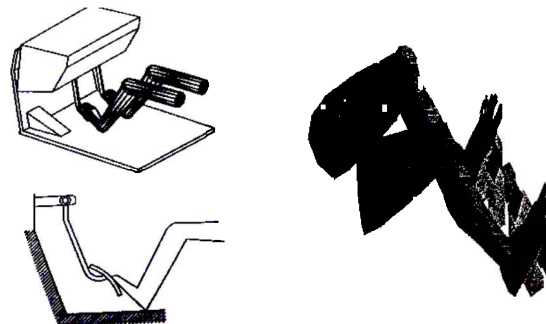


Figure 2 Results of the Nenggala Rantis pedal design.

#### 4. CONCLUSION

Based on research carried out in the cabin pedal system of a nenggala tactical vehicle, conclusions can be taken as follows:

- (a) Based on the system analysis carried out, the weaknesses of the most dominant actual work system are from the Nenggala Rantis work facility namely pedal control facilities and from the technical aspects of the vehicle which is the implementation or successor of the pedal control facility, namely the brake system, use of booster and drive system clutch.
- (b) Improving the technical aspects is done by selecting the type of brakes namely disc brakes with the addition of brake booster in the technical part of the brakes so that the process can run better.
- (c) Improvements are also made to the mechanical clutch system, namely the replacement of the use of a mechanical clutch system by using a hydraulic feeder fluid coupling so that the clutch gear locking process can help improve safety for the driving process with a tactical nenggala vehicle.
- (d) Evaluation of the proposed design is an ergonomic evaluation and technical evaluation of the pedal system driver.
- (e) Ergonomic evaluation is carried out by comparing the actual conditions with the proposed conditions, while the technical evaluation on the machining of the vehicle is the actual and proposed conditions.
- (f) The evaluation results show the condition of the proposal is better than the actual conditions that exist.

Suggestions that can be given for future research are:

- (a) This research can be further developed by improving the work system as a whole in the steering cabin of a tactical vehicle built by an army equipment center workshop. This research can also be developed by improving the layout of the entire section of the nenggala tactical vehicle to support a better work system.
- (b) This research can be further developed by conducting an economic evaluation on the improvement of the work system so that the costs incurred can be known.

**REFERENCES**

- [1] Ari Samadhi, T. M. A. (2011). *Diktat mata kuliah seminar tugas akhir*. Jurusan Teknik Industri. Bandung.
- [2] Chaffin, D. B., Anderson, G. B. J. (2006). *Occupational Biomechanics*, 2<sup>nd</sup> edition, John Wiley and son Inc., New York.
- [3] Daryanto. (2008). *Sistem Rem Mobil*, Bandung.
- [4] Lesmana, N. *Usulan Rancangan Perbaikan Stasiun Kerja Penjahitan Melalui Perbaikan Fasilitas Kerja dan Lingkungan fisik di PD. Italia*, Bandung.
- [5] McCormick, E., & Sanders, M. S. (1993). *Human Factor Engineering and Design*, McGraw-Hill, USA, 1993.
- [6] MQPro, *Human Modeling System User Guide*, Mannequin, 2007.
- [7] Nurmianto, E. (2007). *ERGONOMI Konsep Dasar dan Aplikasinya*, Surabaya.
- [8] Pullat, B. Mustafa. (2002). *Fundamental of Industrial Ergonomics*, Wafeland Press Inc., USA.
- [9] Sugiyono. (2007). *Statistika untuk Penelitian*, Bandung.
- [10] Sutalaksana, I. Z., Ambhawisastra, R., Tjakraatmadja J. H. (2006). *Teknik Perancangan Sistem Kerja*, Bandung.
- [11] Wignjosoebroto, S. (2003). *ERGONOMI Studi Gerak dan Waktu, Guna Widya*, Surabaya.

# Determination of correlation between age and working period: a study of NIHL between case and control group

Rosniza Rabilah\*, N.I. Ismail, Mahfuzah Zainudin, Nor Shamimi Shaari, Nor Azirah Mohd Fohimi

Faculty of Mechanical Engineering, Universiti Teknologi MARA Pulau Pinang,  
13500 Permatang Pauh, Pulau Pinang, Malaysia

\*Corresponding e-mail: rosniza.rabilah@ppinang.uitm.edu.my

**Keywords:** Noise-induced hearing loss; occupational disease; working period

**ABSTRACT** – Noise-induced hearing loss (NIHL) becomes a major occupational disease for many years in Malaysia. This study investigates the relationship between age and working period among the two groups. The case group was workers who had exposed to noisy workplace and administration department workers as control group. The results showed that age and working period has no significant difference for both groups. The 73.3% workers of control group had normal hearing compared to case group. About 33.33% workers faced NIHL with working over 10 years. It was found that the incidence of NIHL increased when the working period increased.

## 1. INTRODUCTION

Noise exposure has been observed to be able to affect the quality of life on humans. High noise levels in the workplace are considered to cause hearing loss, affect workers safety and health and decrease labour productivity and job performance. However, occupational noise is being accepted as an integral part of the job. Occupational noise can lead to auditory and non-auditory effects. Examples of auditory effects are noise-induced hearing loss (NIHL), tinnitus and acoustic trauma. According to NIOSH [1], NIHL is caused by exposure to sound levels or durations that damage the hair cells of the cochlea. It can be divided into permanent and temporary hearing loss. Leensen et al. [2] found that duration exposure is more important compared to noise level. If the noise exposure is longer, then the hearing will take longer to return back to normal. Furthermore, a repeated or continuous noise exposure for a long duration leads to a permanent hearing loss. Mostaghaci et al. [3] stated that a high incidence of NIHL among workers in tile and ceramic industry. That study reported that the important of using hearing protectors and the hearing conservation program should be installed in order to reduce the hearing impairment. One study among quarry workers in Malaysia found that 57% workers experienced NIHL and they had poor knowledge about NIHL [4]. This study investigates the relation between age and working period of NIHL among case and control group.

## 2. METHODOLOGY

The noise levels at several locations in production floor and administration department were measured using sound level meter. Samples were randomly selected from population and they were divided into two groups. The case group was workers who had exposed

to noisy workplace and samples workers in the administration department as control group. There were 15 workers in the production area as the case group and 15 workers of administration department as control group. The inclusion criteria were workers who had been working at the factory for minimal two years continuously and age between 20 to 45 years. The exclusion criteria were workers who had hearing loss, previously worked in noisy work area, workers with middle ear infection, brain injury, alcohol drinker, heavy smoker, ototoxic medication and systemic disease. The Chi-square test was used to determine the level of significant level in relation between working period and noise-induced hearing loss in the case group.

## 3. RESULTS AND DISCUSSION

The average noise level in the production floor was 102.4 dBA, above the permissible limit which is 90 dBA. While, in the administration room, the average of noise was 66.6 dBA. The area with noise level above 102 dBA and continuous exposure should be no longer than 1.5 hours per day [5]. The production workers and administration workers work 9 hours per day excluding break time. The production workers had to wear hearing protector, but most of them were unwilling to wear it. These factors contributed to NIHL especially to the production workers.

Average age of the case group was 31.13 year and average working period was 8.53 year. For control group, the average age was 31.07 year and average working period was 5.00 year. There was no significant difference between age and working period of the both groups. Case and control group showed the coefficient of correlation,  $r$ , were close to zero, so there was evidence of no linear relation between these two variables. To complement this statement, Harmadji and Kabullah [6] stated that average age and working period of a case group are 37.80 year and 16.76 year, respectively. It was reported that the average age was 36.12 year and average working period was 13.68 year of control group. From that study, it showed that age and working period has no significant difference.

Table 1 indicates the baseline audiogram resulted in the case and control group. About 66.7% workers had NIHL in the case group and only 6.7% worker of control group had NIHL. From this study, 73.3% workers of control group had normal hearing compared to case group which is 13.3% workers had normal hearing. This is because they always used ear protection during work at the noisy work area.

Table 1 Baseline audiogram.

Baseline audiogram	Case group	Control group
Normal hearing	13.3%	73.3%
NIHL	66.7%	6.7%
Non NIHL	20.0%	20.0%

Table 2 shows relation between working period and NIHL of the case group. Incidence of NIHL on workers was only 6.67% with 2 to 4 years of working period. For 5 to 7 years and 8 to 10 years of working period, 13.33% of NIHL occurred. About 33.33% workers faced NIHL with working over 10 years at the factory. From the study, it was found that the incidence of NIHL increased when the working period increased as well.

There was a significant difference in relation between NIHL and duration of work on the case group. This is in agreement with a study conducted by Hidayat et al. [7] that reported about 17% of NIHL on workers at textile factory with 10 years working period and 46% with 15 years working period. It is also supported in another study carried out by Suheryanto [8] that found 44% of workers experienced NIHL with 5 to 9 years, 67% with 10 to 14 years and almost 86% with 15 to 19 years of working period.

Table 2 Relation between working period and audiogram of case group.

Working period (years)	NIHL	Non NIHL
2 - 4	6.7%	20.0%
5 - 7	13.3%	0%
8 - 10	13.3%	13.3%
>10	33.3%	0%

The results of Chi-square test were shown in Table 3. From Chi-square for the level of significant,  $\alpha = 0.05$  and the degree of freedom (dof) = 4, the critical value of the Chi-square obtained was 9.45. From Table 3, it showed that the test result was 20.25 and exceeded the critical value. With Chi-square test, there was a significant difference in relation between working period and noise-induced hearing loss in the case group.

Table 3 Results of Chi-square test between NIHL and working period of case group.

Working period (years)	O	E	$(O-E)^2/E$
2 - 4	1	4	2.25
5 - 7	2	1	1.00
8 - 10	2	4	1.00
>10	5	1	16.00
<b>Total</b>			<b>20.25</b>

#### 4. CONCLUSION

The noise level in production plant was 102 dBA and the noise level in administration department was 67 dBA. Many workers are exposed to continuous noise for long working period. Almost 70% of workers of case group have NIHL compared to only 7% of workers in control group. This study was found that there was no significant difference between age and working period of case and control group. However, Chi-square test found that there was a significant difference in relation between working period and noise-induced hearing loss in the case group. In conclusion, the incidence of NIHL increased as the working period increased. For recommendations, the management should provide effective and comfortable hearing protectors to workers in order to protect them and at the same time to reduce noise-induced hearing loss (NIHL) among the workers. The use of ear protection should be compulsory to all workers who are exposed to above permissible noise level. Furthermore, warning letter should be given to any worker who is not wearing hearing protectors so that they will alert with hearing protection.

#### REFERENCES

- [1] National Institute of Occupational Safety and Health (NIOSH) Malaysia (1998). Ministry of Human Resource. Occupational Safety and Health.
- [2] Leensen, M. C. J., Duivenbooden, J. C. V., & Dreschler, W. A. (2011). A retrospective analysis of noise-induced hearing in the Dutch construction industry. *International Archives of Occupational and Environmental Health*, 84(5), 577-590.
- [3] Mostaghaci, M., Mirmohammadi, S. J., Mehrparvar, A. H., Bahaloo, M., Mollasadeghi, A., & Davari, M. H. (2013). Effect of workplace noise on hearing ability in tile and ceramic industry workers in Iran: A 2-year follow-up study. *The Scientific World Journal*, 2013, 1-7.
- [4] Nyarubeli, I. P., Tungu, A. M., Bråteit, M., & Moen, B. E. (2019). Occupational noise exposure and hearing loss: A study of knowledge, attitude and practice among Tanzanian iron and steel workers. *Archives of Environmental & Occupational Health*, 1-10.
- [5] Department of Occupational Safety and Health (DOSH) Malaysia (2010). Annual Report 2009: Occupational Diseases, Kuala Lumpur.
- [6] Harmadji, S., & Kabullah, H. (2004). Noise induced hearing loss in steel factory workers. *Folia Medica Indonesiana*, 40(4), 171-174.
- [7] Hidayat, W., Suhardono, Rasyid, R., Haryuti, & Choiyiyah, (1991). Penyakit akibat kerja melalui pendekatan epidemiologi. Penelitian gangguan kesihatan akibat kebisingan pada unit pintal dan tenun di fabric tekstil. *Badan Penelitian Dan Pengembangan Surabaya*, 1-5.
- [8] Suheryanto, R. (1994). Pengaruh kebisingan mesin fabrik tekstil terhadap pendengaran karyawan.

# Development of smart infant-wrap (*InfaWrap*) device for neonates

Mohd Azrul Hisham Mohd Adib<sup>1,\*</sup>, Mohammad Asyral Abd Rashid<sup>1</sup>, Nur Hazreen Mohd Hasni<sup>2</sup>

<sup>1)</sup> Medical Engineering & Health Intervention Team (MedEHiT), Human Engineering Group, Faculty of Mechanical Engineering, Universiti Malaysia Pahang, 26600 Pekan, Pahang, Malaysia

<sup>2)</sup> Family Health Unit, Pahang State Health Department, Jalan IM 4, 25582 Bandar Indera Mahkota, Kuantan, Pahang, Malaysia

\*Corresponding e-mail: azrul@ump.edu.my

**Keywords:** Infant; ankle wrap; device; neonate; oximeter

**ABSTRACT** – Nowadays, with advanced technology, most of the parents choose to monitor their baby's health using a pulse oximeter device. However, the existing pulse oximetry device was a hassle for infant and this makes the monitoring process difficult. In this study, we focus on the development of smart infant wrap or so-called *InfaWrap* device for neonates in order to accommodate clinician and parents in monitoring the heart rate and oxygen level of the baby with advanced wireless network sensor. This device easier to use, fast and accurate readings of the baby's oxygen and heart rate.

## 1. INTRODUCTION

A study was conducted [1] where they found that 90% infant with congenital cyanotic heart disease were detected with the use of pulse oximeter for screening within several hours of birth. This data show there is a very serious issue related to cyanotic heart disease. Pulse oximetry was considered abnormal if oxygen saturation at room air or on oxygen therapy measured  $<90\%$  [2]. This is due to issue with the heart valves, which are the flaps in the heart that make sure the blood flows through in the right direction, an interruption in the aorta, and abnormalities in the large blood vessels can occur congenital cyanotic heart disease.

The Sudden Infant Death Syndrome ("SIDS") also can be related to congenital cyanotic heart disease. The main causes of SIDS may be difficult to determine [3], many parents do an extraordinary effort and are worried about checking their baby's health. For this reason, a simple but efficient system is required to monitor the conditions of the patient continuously. To help parents in this effort, nowadays various products to monitor the health of infants, especially when the baby is sleeping.

Currently in monitoring system hospitals used cable connections and the size and power consumption are often too large and not easy to carry [4]. The system becomes unsuitable in the development of today's technology. By applying the wireless health care technology there are many advantages one of them, people who carry the sensing devices can move around freely without the obstacle from complex connecting cables; and finally, doctors in the remote server center can watch the patient's health condition closely and hence provide real-time advice for the patients' recovery and long-term care [4,5].

In this paper, the smart infant wrap (*InfaWrap*) device is developed. One of the features of this device

implements healthcare monitoring using wireless network sensor. This device need is equipped with several sensors such as oximeter MAX30100 and LM35 which can measure several parameters. Bluetooth HC05 is used to display the parameter result at smartphone. In addition, the buzzer and display are applying in this system to ensure physician and parent more alert if the parameter value at the system indicates a negative value.

## 2. METHODOLOGY

The *InfaWrap* device consists of three main components; ankle wrap, monitoring system, and mobile application as shown in Figure 1.

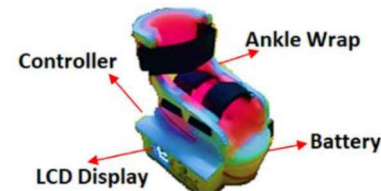


Figure 1 The smart infant wrap (*InfaWrap*) device.

For the *InfaWrap* device circuit of the project to connect all the component as shown in Figure 2. The details of each component are described in this subsection.

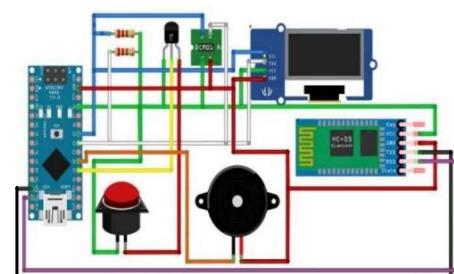


Figure 2 The *InfaWrap* device circuit.

### 2.1 Ankle Wrap

Consists of MAX30100 and LM35 sensor. MAX30100 is the combination of two LEDs, a photodetector, optimized optics, and low noise analog signal processing to detect the parameter of heart rate and SpO<sub>2</sub> level. LM35 is used to monitoring the body temperature of the infant. This sensor is safe for an infant because it does not emit any harmful electromagnetic wave to the infant. The main body of the device was developed using Flexible TPU filament and the inside of the ankle has been insulated using a sponge to protect the

skin of the infant.

## 2.2 Monitor System

In this monitoring system, the device displays the heart rate, SpO<sub>2</sub> and temperature level of the infant after receiving output feedback from the microcontroller. The buzzer was used to alert the clinician or parent if the parameter showing unhealthy reading. In order to develop this device, the microcontroller Arduino pro mini is used. This Arduino is chosen because of the size is easy to attach with the device.

## 2.3 Mobile Application

The mobile apps. is developed to record and display the heart rate, blood pressure and temperature data trend of the infant as shown in Figure 3. The data keep in the storage system as a black box function. These data will use as the emergency tread record or research activity.

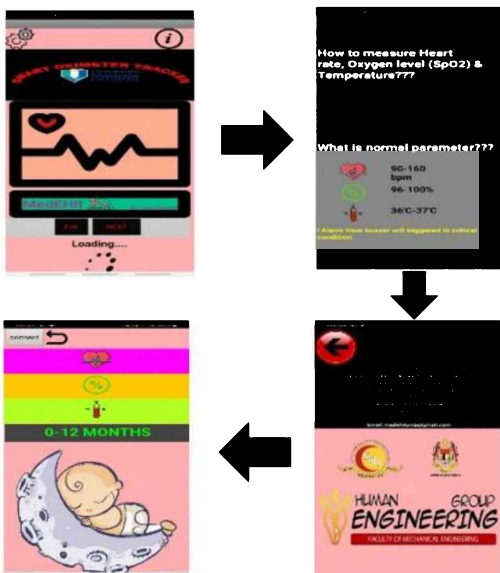


Figure 3 Illustrated the design of *InfaWrap* device mobile application.

## 3. RESULTS AND DISCUSSION

In this study, the *InfaWrap* device is well developed. Figure 4 clearly shows the stress analysis of the *InfaWrap* device developed using two differences material, between PLA and TPU. This analysis has been done to ensure the safety of the infant. According to the result for PLA material, the parts will not crack or bend when it is pressed. This is because the maximum stress for PLA material is only  $1.084e+006 \text{ N/mm}^2$ . For TPU material shows a similar result with the PLA material but the mechanical properties for TPU is different which is the natural characteristic for this material is soft. To ensure the accuracy of this device, one ability test has been done for two hours without non-stop. Data from parameter device is taken for every 10 minutes. This test is very important to make sure after the occurrence of voltage drop, the battery output still remain the same and exactly as in starting reading. In Figure 5 clearly shows the accepted output parameters. The output value start changes in 100 minutes but the value still under the maximum limit.

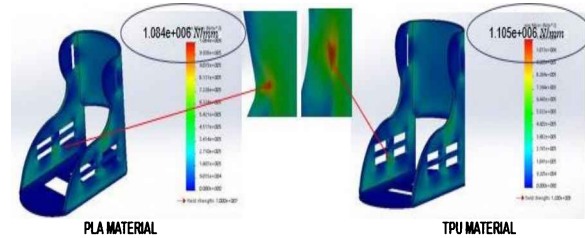


Figure 4 Stress analysis: the comparison between PLA and TPU materials.

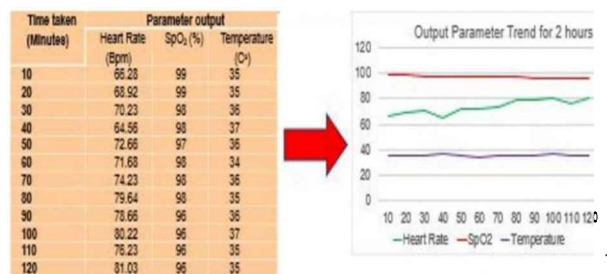


Figure 4 Demonstrated the output parameter value within two hours' test.

## 4. SUMMARY

As a summary, the proposed smart infant wrap (*InfaWrap*) device is well developed and really integrated with a mobile application. We forecast that the *InfaWrap* device has the potential to be used widely in Malaysia with affordable price.

## ACKNOWLEDGEMENT

A big thank you dedicated to University Malaysia Pahang (UMP) for providing us with a good environment and facilities in order to complete these research activities. We would like to thank Mr. Idris Mat Sahat from Human Engineering Group, Universiti Malaysia Pahang for sharing valuable information in accordance with our research interest.

## REFERENCES

- [1] Mathur, N. B., Gupta, A., & Kurien, S. (2015). Pulse oximetry screening to detect cyanotic congenital heart disease in sick neonates in a neonatal intensive care unit. *Indian pediatrics*, 52(9), 769-772.
- [2] Jortveit, J., Eskedal, L., Hirth, A., Fomina, T., Døhlen, G., Hagemo, P., ... & Holmstrøm, H. (2015). Sudden unexpected death in children with congenital heart defects. *European Heart Journal*, 37(7), 621-626.
- [3] Pradnya Kamble, P. G. (2017). Patient's vital sign monitoring system using a wireless personal area network. *Imperial Journal of Interdisciplinary Research*, 458-460.
- [4] Gubbi, S. V., & Amrutar, B. (2014). Adaptive pulse width control and sampling for low power pulse oximetry. *IEEE Transactions on Biomedical Circuits and Systems*, 9(2), 272-283.
- Thomas, S. S., Saraswat, A., Shashwat, A., & Bharti, V. (2016, October). Sensing heart beat and body temperature digitally using Arduino. In *2016 International Conference on Signal Processing, Communication, Power and Embedded System (SCOPES)* (pp. 1721-1724).

# Development of bilirubin jaundice (*BiliDice*) device for neonates

Mohd Azrul Hisham Mohd Adib<sup>1,\*</sup>, Mohd Hanafi Abdul Rahim<sup>1</sup>, Nur Hazreen Mohd Hasni<sup>2</sup>

<sup>1)</sup> Medical Engineering & Health Intervention Team (MedEHiT), Human Engineering Group, Faculty of Mechanical Engineering, Universiti Malaysia Pahang, 26600 Pekan, Pahang, Malaysia

<sup>2)</sup> Family Health Unit, Pahang State Health Department, Jalan IM 4, 25582 Bandar Indera Mahkota, Kuantan, Pahang, Malaysia

\*Corresponding e-mail: azrul@ump.edu.my

**Keywords:** Neonatal jaundice; bilirubin; color sensor; Arduino uno; phototherapy

**ABSTRACT** – In Malaysia, generally the blood samples are taken and various laboratory experiments are performed to determine the exact jaundice level for newborn. As the process is repetitive, it causes trauma to infants and also requires experts to perform the test. In this paper, the bilirubin jaundice so-called *BiliDice* device is proposed. The device consists of three main components: RGB colour sensor, microcontroller, and LCD display. The advantage of this prototype is affordable and portable. This device is simple, easy to handle, fast and accurate readings for the bilirubin level of the newborn.

## 1. INTRODUCTION

Jaundice in neonates is mutual. When the red blood cells are wrecked down, a constituent called bilirubin is made. Primarily new baby liver is undeveloped and hence it cannot do the task efficiently [1]. Thus bilirubin level increasing which is the cause of jaundice. Bilirubin level will increase gradually if the severity is not detected within a proper time interval and if jaundice is left untreated. Once it exceeds a certain level there is the possibility of deafness or certain forms of brain damage may occur. Therefore, blood samples are taken, and various laboratory experiments are performed to access the exact bilirubin level [2].

In this paper, a portable hardware device which can detect the bilirubin level and jaundice state by non-invasive technique has been proposed. The successful bilirubin jaundice called *BiliDice* device using RGB color sensor is well developed. Using colour sensor (TCS230), an Arduino-Uino board based on microcontroller and an OLED display 0.96-inch unit have been used in manufacture this device. TCS230 is a colour sensor which programmable light to a frequency converter. There are sixteen photodiodes each for Blue, Green and Red filters. In [3], image analysis of stool colour is compared to colour grading by a colour card, and the stool bilirubin level test is done to detect cholesteric jaundice in infants. In [4], digital images are acquired in colour, in palm, soles, and forehead. RGB attributes are analyzed with diffuse reflectance spectra as the parameter to characterize patients with either jaundice or not, and those parameters are correlated with the level of bilirubin.

## 2. METHODOLOGY

### 2.1 Device Setup

At the beginning of the device setup, the TCS230 colour sensor has been organized to obtain suitable RGB values. Regarding this purpose, the three main colour of Red, Blue, and Green level printed on paper has been used. For the calibration of Red component, the value of Red set with “255” and the value of Black set with “0” have been plotted. The similar technique is followed for the calibration of the Green and Blue component. After that, the percentage of blue colour is assigned as the bilirubin level. Figure 1 shows the block diagram of the operation in *BiliDice* device.

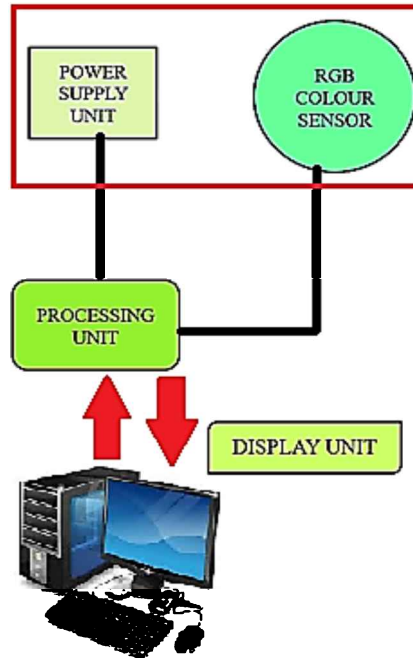


Figure 1 Block diagram of the operation in *BiliDice* device.

The power supply unit provides 9V DC supply to the processing unit. RGB colour sensor (TCS230) senses the RGB component of skin level processing based on Arduino Uno. The processing unit plots RGB value to precise values in order to arrange the colour sensor tracked by the percentage of blue taken from the colour sensor. Therefore the state of jaundice is determined and the result is transferred to the LCD display.

Figure 2 Final product of *BiliDice* device.

Table 1 Material specification.

Material	SUNLU PLA
Print Temperature	190-220°C
Length	330mm

### 3. RESULTS AND DISCUSSION

In this study, the *BiliDice* device is successfully developed by using the non-invasive method as shown in Figure 2. The infected area is irradiated with light of specific wavelength and change in properties of light after reflection from the skin is noted. In order to detect neonatal jaundice, Light Emitting Diodes (LED) of a specific wavelength is employed as a source of light, which is an occurrence on baby skin. The light is reflected back and absorbed by photo-detector. In Table 1 show details the material specification of the *BiliDice* device.

Table 2 Implementation of colour level and bilirubin level [5].

Colour series (CS)	Label of colour	Bilirubin level (mg/dl)
CS-1		8
CS-2		11
CS-3		18
CS-4		22

The preliminary study on jaundice and non-jaundice was observed base on correlating the label of skin colour as shown in Table 2 and the decision making on jaundice and non-jaundice as shown in Table 3. The bilirubin level is intended conforming to a specific level. The physical process flow of an implementation of the *BiliDice* device as shown in Figure 3.

### 4. SUMMARY

As a summary, the proposed *BiliDice* device would use technique detection of jaundice by using a non-invasive method which can regularly monitor the bilirubin levels. The use of color sensor is a good alternative in detection of jaundice. However, this *BiliDice* device is still in the early development with

positive progress. The device is also simple, and easy to use.

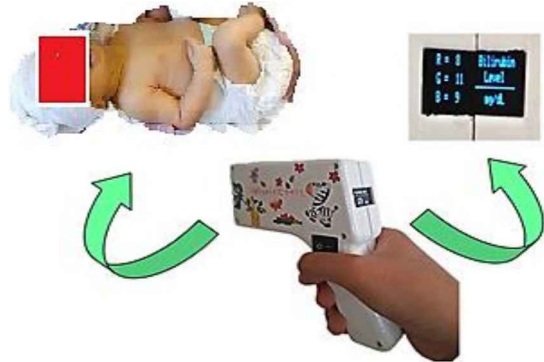
Figure 3 Process flow of an implementation of the *BiliDice* device.

Table 3 Reference for decision making on jaundice and non-jaundice.

Bilirubin level (mg/dl)	Jaundice level
BL < 5	Normal
5 < BL < 11	Mild
11 < BL < 19	Severe
19 < BL	Critical

### ACKNOWLEDGEMENT

A big thank you dedicated to University Malaysia Pahang (UMP) for providing us with a good environment and facilities in order to complete these research activities. By this opportunity, we would like to thank Mr. Idris Mat Sahat from Human Engineering Group, Universiti Malaysia Pahang for sharing valuable information in accordance with our research interest. We would face many difficulties without his assistance.

### REFERENCES

- [1] Ku, L.C., & Lazim, N. S. M. (2017) Direct photometry non invasive bilirubin device. *International Research Journal of Engineering and Technology*, 4(5), 2372-2395.
- [2] Ali, N., Muji, S., Joret, A., Amirulah, R., Podari, N., & Risep, N. D. (2006). Optical technique for jaundice detection. *ARPJN Journal of Engineering and Applied Sciences*, 10, 9929-9933.
- [3] Reflective Color Sensing with Avago Technologies. (2015). *RGB Color Sensor*.
- [4] Mohammadi, S. H., & Indikar, S. I. L. (2013). Embedded based preemies monitoring system with jaundice detection and therapy. *International Journal of Scientific & Technology Research*, 2(6), 153-162.
- [5] Chowdhary, A. K., Dutta S., & Ghosh R. (2017). Neonatal jaundice detection using color detection method. *International Advance Research Journal in Science, Engineering and Technology*, 4, 197-203.

# Acoustic emission technology for monitoring die condition in sheet metal forming process

Ng Chuan Huat<sup>1,\*</sup>, Wong Hui Ing<sup>1</sup>, Lai Chee Fung<sup>1</sup>, Shamy Nazrein Md Yahaya<sup>1</sup>, Rahizar Ramli<sup>2</sup>, Sim Hoi Yin<sup>2</sup>

<sup>1)</sup> Faculty of Mechanical and Manufacturing Engineering, Universiti Tun Hussein Onn Malaysia,  
86400 Parit Raja, Johor, Malaysia

<sup>2)</sup> Department of Mechanical Engineering, Faculty of Engineering, University of Malaya,  
50603 Kuala Lumpur, Malaysia

\*Corresponding e-mail: ahuat@uthm.edu.my

**Keywords:** Acoustic emission; condition monitoring system; sheet metal forming

**ABSTRACT** – Condition monitoring system (CMS) on sheet metal forming had always been important. With an appropriate CMS, the quality of stamping dies and products can be maintained. This paper presents the application of acoustic emission monitoring system on sheet metal stamping process, obtaining a relationship between the signal amplitude and die condition. It was founded that die cavity with high surface roughness causes increasing of average amplitude. Apart from that, the clearance value within dies set would affect the varying of peak amplitude and the additional machining on the die edges was shown to reduce the peak amplitude acquired from sensor.

## 1. INTRODUCTION

Since Industry Revolution 4.0 (IR4.0) originated, acoustic emission (AE) testing has become much wider in scope. It is a well-matched with for IR4.0 as it can be used as condition monitoring system through analysing production data and identify patterns to predict issues before they happen [1]. By implementing industrial internet of things (IoT) technology and cyber-physical system, acoustic emission monitoring system can be optimized the maintenance schedules, and gaining immediate alerts to operational risks, allowing manufacturers to reduce service costs, maximizing uptime, and improving production output effectively [2]. In sheet metal forming process, a metal blank is transferred and plastically deformed between dies and acquired desired geometry without producing any scrap in short time. To gain the desired shape and properties in the product, the metal flow should be well controlled. Thus, the geometry of blank should be predicted before the stamping process is conducted.

The cost of dies signifies a major proportion of total costs associated with automotive parts production. Henceforth, dies replacement due to wear mechanism is very costly. When considered about the poor component quality, operation downtime and unscheduled maintenance of die wear issue; it is clear that economic impact of tool wear of dies is important [3]. Monitoring sheet metal forming process, it was not much be concerned and emphasized, compared to machining process and pipe leakage monitoring. Assessing tool wear and part quality by visual inspection can result in late detection of deterioration of tool wear. Therefore, an appropriate condition monitoring system for maintaining quality of die and products is necessary for

every manufacturer. This paper applied the use of acoustic emission technology to monitor and identify the die condition in real time cold stamping process.

## 2. METHODOLOGY

For the material of metal blank, aluminium sheet has selected, with thickness of 0.25mm and diameter of 64mm. The dies and punch were made out of aluminium alloy 6061 (AA6061), with design diameter of 64.85mm, enough clearance for sheet deformation without disturbance of frictional effect. Two types of die geometry was prepared to study the effect of die design on signal condition, shown in Figure 1. From the figure below, the left die have just undergo CNC milling; whereas the die on right side have undergone additional machining to increase the die clearance and minimize the punch force from press machine.

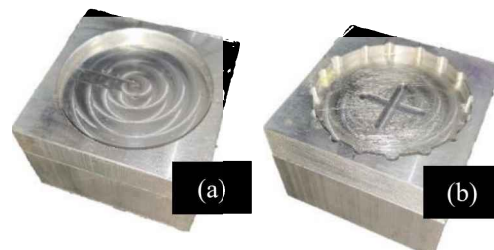


Figure 1 Two types of die geometry with (a) and without (b) additional machining.

The apparatus for this experiment consisted of hydraulic press machine, acoustic emission sensor and DAQ system. The punch and die installed on press machine to perform stamping process. KISTLER 8152C acoustic emission sensor was equipped to receive signal waves generated from blank deformation. KISTLER Piezotron Coupler Type 5125C was used to receive the high frequency outputs. DAQ system consisted of computer with LabVIEW software to collect and display the raw signal data from sensor and National Instruments PXI-1031 chassis as the medium between coupler and computer to synchronize the sensor signals. The entire apparatus setup for the experiment was shown in Figure 2.

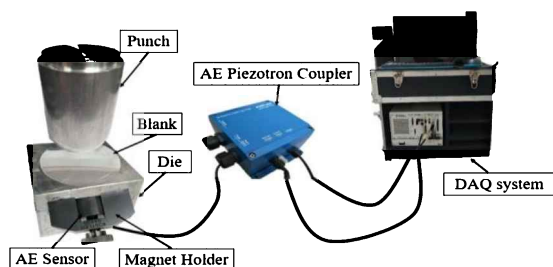


Figure 2 Overview of experimental work.

### 3. RESULTS AND DISCUSSION

The raw signal data that displayed from LabVIEW would further be processed through MATLAB. Eventually the graph of acoustic emission signals plotted again from MATLAB as the result for analysing and discussion. Both of dies with different geometry design have brought different range of amplitude. Four. The raw signal data of stamping operation was as shown in Figure 3.

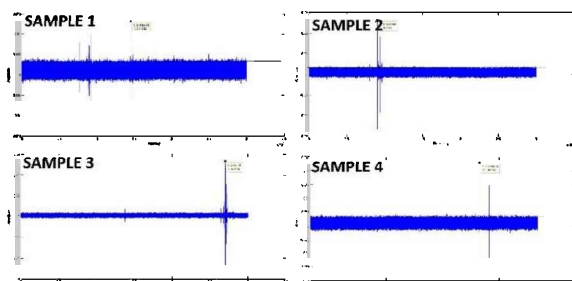


Figure 3 Raw Signal data of stamping operation.

For the ease of results analysing and discussion, the average amplitude and peak amplitude (the maximum amplitude in signal graph) were tabulated in Table 1, with respective workpiece condition as well.

Table 1 Summary of data.

	Die 1			Die 2		
	Avg	Peak	Cond.	Avg	Peak	Cond.
1	0.0034	0.0131	Tear	0.0052	0.0160	Good
2	0.0034	0.0264	Good	0.0053	0.0078	Tear
3	0.0034	0.0528	Tear	0.0050	0.0120	Good
4	0.0032	0.0230	Good	0.0055	0.0160	Good

Based on Table 1, the range of average amplitude emitted by die 1 was within 0.0032 to 0.0034 while for die 2, the range was within 0.0050 to 0.0055. Die 2 has higher average amplitude than die 1, which might be due to die surface roughness. Before conducting the stamping operation, scratches were added on die surface with the aid of sharp tool, hence the die surface of die 2 was rougher than die 1. Therefore, there is a possibility that with greater surface roughness, higher amplitude will be emitted [4].

However, the peak value emitted by die 1 during press forming was higher than die 2. This was due to the existence of additional clearance that in die 2. During the stamping process, the clearance between the die and punch were considered to reduce the effect of friction. The optimum punch-and-die clearance will maintain the

lifespan of tool. According to the research of Subramonian et al. [5], the severe wear was observed at the area with sharp edges and radii. The larger clearance allows the workpieces to be formed without large friction that leads to tear and wear occurrence. During experiment, die 2 has better geometry clearance while die 1 had smaller clearance and sharp edges that create greater friction when pressing process operate. As a result, workpieces formed by die 2 were in better condition than that of die 1. In die 1, the small clearance between die and punch leads to the tear occurrence for the aluminium sheet because great friction and shear had occurred at the moment of deformation. Due to the effect of tear, the signal of amplitude emitted was high which indicates the damage. The burst signal emitted during pressing of workpieces by die 1 was high due to occurrence of tear [6].

### 4. CONCLUSION

This research presented a technique to monitor the cold stamping process by means of acoustic emission signals that able to track the condition for both die and workpiece in order to avoid poor quality production. Several findings were concluded as follows:

- (a) The existence of scratches on surface of die 2 has cause the greater average amplitude than die 1.
- (b) Larger clearance due to the additional machining on the edges of die cavity in die 2 was observed to relieve the frictional effect hence reducing tore occurrence
- (c) The relationship between die surface condition and amplitude from acoustic emission system were shown and observed.
- (d) The reliability of acoustic emission system on monitoring sheet metal forming process was proven.

### ACKNOWLEDGEMENTS

The authors would like to acknowledge Universiti Tun Hussein Onn Malaysia for the support and help throughout the study. Special acknowledge goes to the Research Management Center (RMC) and Ministry of Education Malaysia for funding this study under Tier 1 Grant (H137) and Fundamental Research Grant Scheme (FRGS). Author would also like to thank Universiti Malaya (UM) for supporting this study and providing consultancy.

### REFERENCES

- [1] Shen, G., Zhang, Y., Dong, Y., & Liu, S. (2015). Development of High-Speed Wi-Fi Wireless Acoustic Emission System. In *Advances in Acoustic Emission Technology* (pp. 3-13). Springer, New York, NY.
- [2] Nazarchuk, Z., Skalskyi, V., & Serhiyenko, O. (2017). *Acoustic emission: methodology and application*. Springer.
- [3] Altan, T., & Tekkaya, A. E. (Eds.). (2012). *Sheet metal forming: processes and applications*. ASM international.
- [4] Viera, M. A., Alexandre, F. A., Aguiar, P. R., Silva, R. B., & Bianchi, E. C. (2018). Correlation

- between surface roughness and AE signals in ceramic grinding based on spectral analysis. In *MATEC Web of Conferences* (Vol. 249, p. 03003).
- [5] Subramonian, S., Altan, T., Campbell, C., & Ciocirlan, B. (2013). Determination of forces in high speed blanking using FEM and experiments. *Journal of Materials Processing Technology*, 213(12), 2184-2190.
- [6] Shanbhag, V. V., Rolfe, B. F., Arunachalam, N., & Pereira, M. P. (2018). Investigating galling wear behaviour in sheet metal stamping using acoustic emissions. *Wear*, 414, 31-42.

# Finite element analysis of the thermal response test for road thermoelectric energy harvesting system (RTEHs)

K.N. Khamil<sup>1,2</sup>, M.F.M. Sabri<sup>1,\*</sup>, A.M. Yusop<sup>2</sup>, M.S. Sharuddin<sup>2</sup>

<sup>1)</sup> Department of Mechanical Engineering, University of Malaya, 50603 Kuala Lumpur, Malaysia.

<sup>2)</sup> Advance Sensor and Embedded Control Research Group, Centre for Telecommunication Research & Innovation, Fakulti Kejuruteraan Elektronik dan Kejuruteraan Komputer, Universiti Teknikal Malaysia Melaka, Hang Tuah Jaya, 76100 Durian Tunggal, Melaka, Malaysia

\*Corresponding e-mail: faizul@um.edu.my

**Keywords:** Thermoelectric, FEA, RTEHs

**ABSTRACT** – This paper investigates the thermal response for the road thermoelectric energy harvesting system (RTEHs) application where the finite element analysis (FEA) is used to predict the real condition for the RTEHs. The findings for both FEA and in-lab experiment able to gives less than 1.5 % for the structure of rod and 6.6% for the flat bar of the percentage of difference. Both findings able to gives a similar maximum temperature at the top plate used as the heat collector at 43°C for the flat bar and 48°C for the rod. This proved the greater the thermal diffusivity, the more reliable the materials able to conducts heat more rapidly than the flat bar.

## 1. INTRODUCTION

A proliferation of studies in energy harvesting has risen tremendously for the past decades in solar, wind, piezoelectric and thermoelectric. The Technology Readiness Level (TRL) which originally conceived from NASA since the 1980s based on a nine-level scale was used to categorize the readiness level of one's technology [1]. The solar and wind can be label as matured technology with TRL level approaching 9 where the system has been tested, launched and operated for a considerable amount of time.

In Thermoelectric Technology used to harvests the energy from road pavement, TRL level only reached up to 6. There are numerous designs for the road thermoelectric energy harvesting system (RTEHs) that aims to achieve the most optimum temperature difference from the cooling method of the RTEHs use [2]. Therefore, this study seeks to obtain findings which will help to address these research gaps on the most efficient cooling method that able to provide the maximum voltage-generated of the RTEHs through finite element analysis (FEA) simulation.

## 2. METHODOLOGY

FEA simulation was conducted using COMSOL Multiphysics where it able to predicts the thermal response in certain conditions and different geometry for our RTEHs before commencing into an actual experiment. Our RTEHs uses a subterranean cooling method where the cooling element will be installed under the asphalt and submerge into the soil as depicted in Figure 1 and the dimensions are given in Table 1.

In this FEA simulation, the aluminium plates are placed in between two cascaded thermoelectric modules

(TEM), APH-127-10-25-S as discussed in [3]. The top plate will perform as the heat collector for the system. The bottom plate of the aluminium is bond to the cooling element which is either rod or flat bar. This FEA simulation will determine which of this cooling element structure able to provide the best thermal response since the temperature difference,  $\Delta T$  between the hot and cold side of the TEM are highly influencing the output voltage.

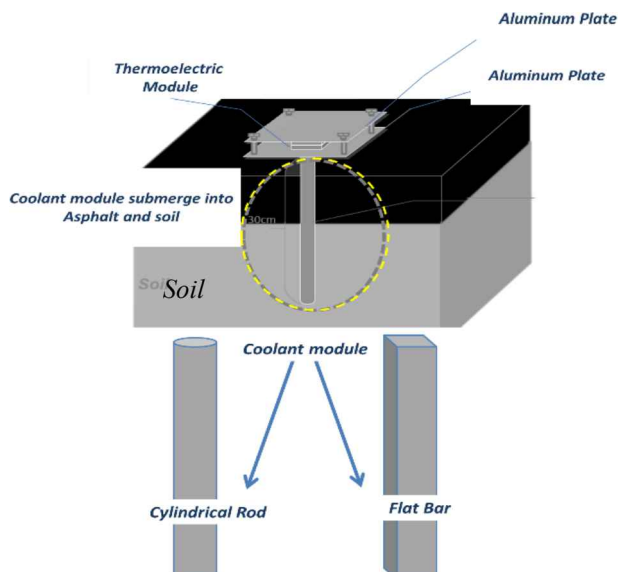


Figure 1 Illustration of the experimental setup.

Table 1 Size and Properties on experimental setup.

Type	Dimension (mm)	Material	Thermal Cond. (W/mK)	Density (kg/m <sup>3</sup> )
Flat Bar	25.4 X 50.8 X 300	Aluminum 6061	187	2712.51
Rod	Diameter (25.4), Length (300)	Aluminum 6061	187	2631.37
Plate	Aluminium SIC 0.128	60 X 100 X 3	222	2.71
Asphalt box	Plywood	Base (320 X 320)	-	-

In every material, the properties parameters such the thermal conductivity,  $k$ , density,  $\rho$ , and specific heat,  $C_p$  are following the standard parameters given by the manufacturer or it can easily refer to the handbook [4]. As the heat runs through the material, thermal diffusivity,  $\alpha$  control the time speed of the temperature's fluctuation where when  $\alpha$  is high, the quicker the temperature disperses out.

$$\alpha = \frac{k}{C_p \rho} \quad (2)$$

### 3. RESULTS AND DISCUSSION

The solar irradiance's value used in this FEA simulation is based from the halogen lamp used in the lab which is 75 W with the square area of 0.11-meter square. Both FEA and in-lab experiment are tested for the durations of 2 hours.

Depicted in Figure 2 and Figure 3, the thermal response in structure using rod is much higher than the structure using a flat bar which proven the  $\alpha$  of the rod was higher than the flat bar since the heat flows quickly through the material where it able to conducts heat more rapidly compared to its volumetric heat capacity.

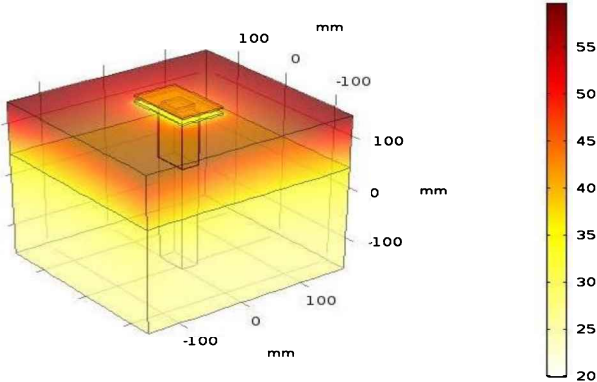


Figure 2 Temperature distributions for the cooling elements of flat bar.

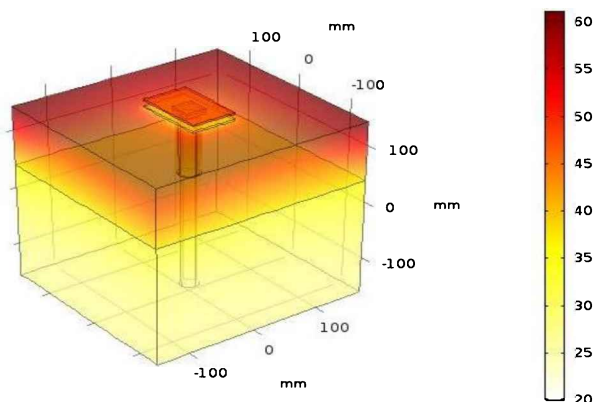


Figure 3 Temperature distributions for the cooling elements of rod.

From Figure 4, the simulation and the experiment's temperatures for the top plate are similar to each other with the percentage difference of 1%. While the bottom plate's temperature between simulation and experiments are varied by 6.6% of differences. The unknown properties for the material used in the FEA simulation may have contributed in the

larger discrepancy in the percentage difference.

However, in Figure 5, the percentage of differences between simulation and experiment was less than 1.5%. This proved when  $\alpha$  is high, the more reliable the material able to conducts heat more rapidly than the flat bar.

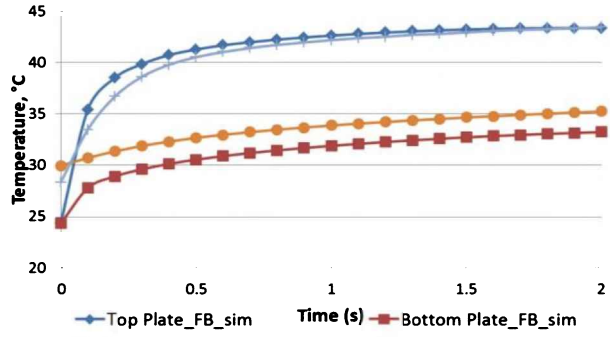


Figure 4 Temperature behaviors of flat bar for simulation vs experiment.

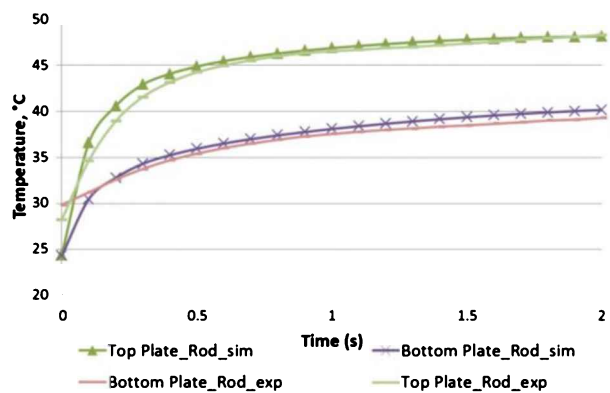


Figure 5 Temperature behaviors of rod for simulation vs experiment.

### 4. CONCLUSION

As the conclusion, the finite element analysis showed the cooling element of the rod has a higher thermal response than a flat bar where the percentage of differences between simulation and in-lab experiment is less than 1.5%. Both findings able to gives a similar maximum temperature at the top plate used as the heat collector at 43°C for the flat bar and 48°C for the rod.

### ACKNOWLEDGEMENT

This project is supported by Ministry of Education Malaysia (grant number: FRGS/1/2017/TK07/FKEKK-CETRI/F00337).

### REFERENCES

- [1] NASA. (2012). Technology Readiness Level Definitions. Nasa, 1. Retrieved from [https://www.nasa.gov/pdf/458490main\\_TRL\\_Definitions.pdf](https://www.nasa.gov/pdf/458490main_TRL_Definitions.pdf)
- [2] Tahami, S. A., Gholikhani, M., Nasouri, R., Dessouky, S., & Papagiannakis, A. T. (2019). Developing a new thermoelectric approach for energy harvesting from asphalt pavements. *Applied Energy*, 238, 786-795.

- [3] Khamil, K. N., Sabri, M. F. M., Yusop, A. M., & Sharuddin, M. S. (2018, November). An Evaluation of TEC and TEG Characterization for a Road Thermal Energy Harvesting. In *2018 International Conference on Sustainable Energy Engineering and Application (ICSEEA)* (pp. 86-91). IEEE.
- [4] Mehrkam, Q. D., Easterday, J. R., Payne, B. R., Vukovich, D., Godding, A. D., & Foreman, R. W. (1991). Liquid Nitriding. *ASM International, ASM Handbook*, 4, 410-419.

# Determination of solar panel maximum output power using predictor variables method

Aziah Khamis\*, Nurdiana Nordin, Lim Li Yao

Fakulti Kejuruteraan Elektrik, Universiti Teknikal Malaysia Melaka,  
Hang Tuah Jaya, 76100 Durian Tunggal, Melaka, Malaysia

\*Corresponding e-mail: aziah@utem.edu.my

**Keywords:** Solar Power forecasting; statistical analysis; correlation

**ABSTRACT** – The optimization of the output of solar photovoltaic (PV) system is highly important to harness its maximum potential as the alternative energy source. This paper identifies the importance of the PV system variables on solar power output and enables the predictor variables identification using statistical analysis. This technique analyses the significant correlation between the variables and solar output power. The correlation attributes are used as a guideline in identifying the most influential variables towards the prediction of solar power output. The simulation results showed the variables can be evaluated based on the correlation between the predictor variables and the solar output power.

## 1. INTRODUCTION

The demand for electrical energy nowadays has substantially increased as the electronics and high-powered machines are immensely introduced and used worldwide. Malaysia that is located near the equator typically receives solar power between 4,000 to 5,000 Wh per square meter per day.

Under the encouragement of Malaysia Tenth Plan, the government of Malaysia aimed to contribute 5.5% of total electrical generation in Malaysia from renewable energy [1]. Aligned with this aim, the installation of photovoltaic (PV) system around the Malaysia area has to show an increasing trend, where it used as a heating purpose and also electrical generation [2].

Solar forecasting based on the prediction model have been implemented either with the statistical or physical method or the combination of both with the help of artificial intelligence and neural network [3,4]. The computation and training of weather data are carried out to predict the future solar output generation. However, the time sensitivity must be considered in actual practice and it is necessary to update the data in real time [5]. The inconsistent of outcome due to the weather change in four season countries also an important consideration for the forecasting of solar output [6]. These research gaps show that forecasting should be simpler and considers external factors such as temperature and humidity.

According to the statistical survey in 2012, the solar radiation received by northern area of Malaysia such as Kedah, Penang, and Sabah are the highest while the

southern area of Malaysia like Johor received the least of solar radiation among the other states of Malaysia as shown in Figure 1.

Thus, the main objective of this study is to propose an investigation of solar maximum output panel using the correlation and coefficient analysis using PV variables and weather data. Initially, PV variables were acquired from Mono solar panel in the Faculty of Electrical Engineering (FKE), Universiti Teknikal Malaysia Melaka (UTeM). The five variables are global tilted irradiance (GTI), global horizontal irradiance (GHI), temperature, humidity, and panel temperature. They were used as an input predictor variable, while the power output from the panel is the output. Using the correlation and coefficient analysis in the SPSS software (SPSS Inc. 2007), the most influential variable towards the solar output power can be identified. Thus, the general equation of the solar panel system can be formulated.

## 2. Impact of PV Parameter to Solar Power Output

The main objective of this study is to find out the predictor variables and parameters that affect the solar output generation the most. In order to achieve this objective, multi-regression method is utilized to show the influence of the variables to the solar output. The implementation steps are described in the flow chart in Figure 2.

Samples were taken from the Mono solar panel in the Faculty of Electrical Engineering (FKE), Universiti Teknikal Malaysia Melaka (UTeM) in the year 2015. A total of 52,347 instances of PV system variables were taken every 5 minutes' interval from 7.25 am to 7.25 pm every day. There were 24 units of solar panel that contributed to this data.

### 3.1 Performance of Each Predictor Using Linear Regression Analysis

In order to determine the importance of each parameter toward the solar output, the correlation between the dependent variable and the independent variable is the key. The coefficient of determination,  $R^2$ , is the measure of the correlation between the dependent and independent variable. If the value is closer to 1, it means that there is a strong correlation between the variables.

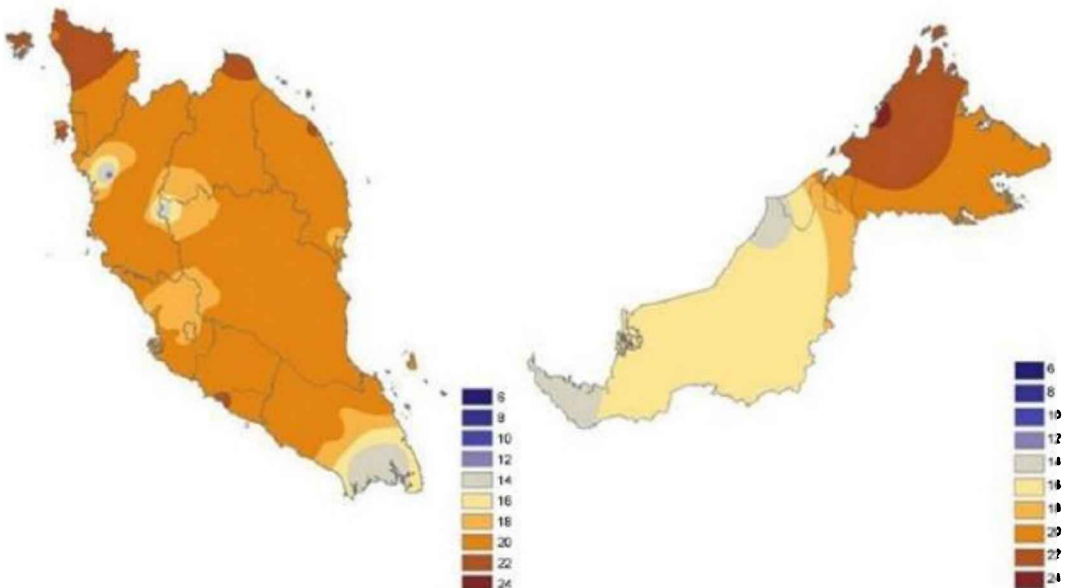


Figure 1 Average daily solar radiation (MJ per sq. m) across Malaysia [7].

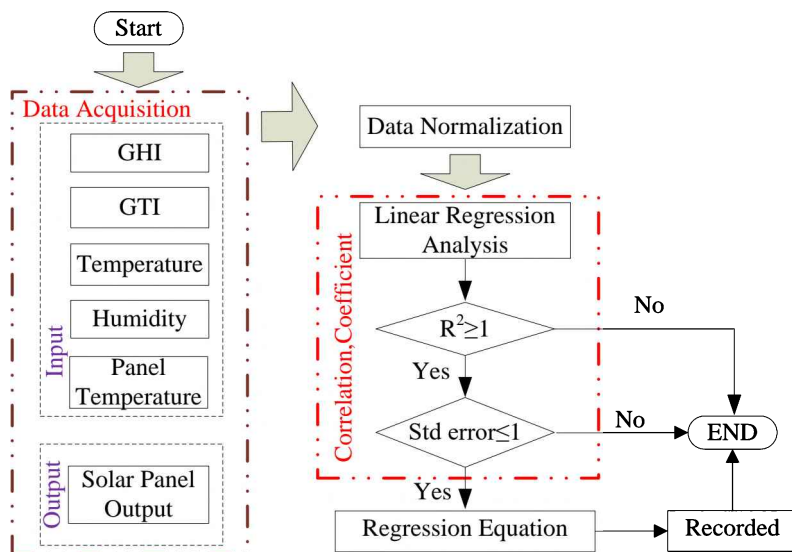


Figure 2 Summary of the proposed technique.

The result obtained in Table 1 showed that the global tilted irradiance (GTI) has the highest  $R^2$  value. This result indicates that it has the strongest correlation which has the highest impact on the solar output. Meanwhile, the temperature variable has the lowest value of  $R^2$  which is only 0.201.

The standard error of the estimate measures the accuracy of the prediction. The lower the value the higher the prediction accuracy. GTI has the highest value of  $R^2$ , and the lowest standard error of the estimation among all the predictors as tabulated in Table 1. On the other hand, temperature has the lowest correlation and has highest value of the standard error of the estimation. Thus, it is evident that the GTI has a good correlation in predicting the solar power output rather than the temperature.

Table 1 Model summary for each predictor.

Model	R	$R^2$	Standard error estimation
GHI	.900 <sup>a</sup>	.811	.10959
GTI	.920 <sup>a</sup>	.847	.09864
Temperature	.448 <sup>a</sup>	.201	.22522
Humidity	.477 <sup>a</sup>	.227	.22147
Panel temperature	.813 <sup>a</sup>	.660	.14686

<sup>a</sup>Predictors: (Constant), Panel Temperature, Humidity, GTI, Temperature, GHI.

### 3.2 Performance of Five Predictors with the Output

The performance of the five predictors with the output is then simulated in order to evaluate the coefficients of the predictor variables. These coefficients (shown in Table 2) were evaluated and analysed in order to find the regression equation in estimating the solar power output. It is evident in Table 2 that the evaluation of all parameters is at  $P < 0.05$ , which concludes that all the parameters are statistically significant. Hence the findings found in this study is likely to generalize to the broader population of PV system across Malaysia. Therefore, an estimated solar output power using regression equation can be formulated by Equation (1).

$$\begin{aligned} P_{out} = & 0.95(GTI) + 4.752(\text{PanelTemperature}) + 0.021(\text{Humidity}) \\ & - 0.061(\text{Temperature}) - 0.057(\text{GHI}) - 0.012 \end{aligned} \quad (1)$$

Table 2 Coefficients of all predictor variables.

Model	Unstandardized coefficients		Standardized coefficients		Sig.
	B	Std error	Beta	t	
Constant	-.012	.005		-2.677	.007
GHI	-.057	.011	-.055	-5.384	.000
GTI	.950	.011	.879	86.817	.000
Temperature	-.061	.007	-.043	-9.239	.000
Humidity	.021	.003	.020	5.881	.000
Panel temperature	4.752	.191	.145	24.879	.000

<sup>a</sup>Dependent variable:  $P_{out}$ .

This regression equation summarizes that GTI has the highest influence on the output with a positive coefficient of 0.95 and the GHI has the least influence on the solar output when all the variables are used together to predict the output.

### 3. SUMMARY

This paper proposed the solar output forecasting by using predictive model based on the predictive variables. The advantage proposed method is that it does not require a complicated calculation and mathematical model with only historical weather data. The forecasting of solar output based on the predictive model can be made by determining the correlation of the attributes. Based on these findings, the future work of the authors will include the development of modelling the predictor variables using a machine learning technique.

### REFERENCES

- [1] Malaysia. Department of Prime Minister, the economic planning unit, tenth Malaysia plan 2011-2015, Putrajaya 2010.
- [2] Islam, M. R., Saidur, R., Rahim, N. A., & Solangi, K. H. (2010). Usage of solar energy and its status in Malaysia. *Engineering e-Transaction*, 5(1), 6-10.
- [3] Zhu, H., Li, X., Sun, Q., Nie, L., Yao, J., & Zhao, G. (2016). A power prediction method for photovoltaic power plant based on wavelet decomposition and artificial neural networks. *Energies*, 9(1), 1–15.
- [4] Ding, M., Wang, L., & Bi, R. (2011). An ANN-based approach for forecasting the power output of photovoltaic system. *Procedia Environmental Sciences*, 11, 1308-1315.
- [5] Kipp & Zonen, “The difference between horizontal and tilted irradiance”, 2 July 2013.
- [6] Zhu, H., Li, X., Sun, Q., Nie, L., Yao, J., & Zhao, G. (2016). A power prediction method for photovoltaic power plant based on wavelet decomposition and artificial neural networks. *Energies*, 9(1), 1–15.
- [7] Annual solar radiations in different cities in Malaysia, 31 August 2013. [Online]. Available: <http://www.thegreenmechanics.com/>

# An experimental study of the cooking stove waste heat energy conversion using thermoelectric generator for night market application

Mohd Arizam Abdul Wahap<sup>1\*</sup>, A. Shamsul Rahimi Subki<sup>2</sup>, Shahrizal Saat<sup>2</sup>, Mohammad Hadir Maslan<sup>1</sup>, Mohd Shariminizam Harun<sup>1</sup>

<sup>1)</sup> Fakulti Teknologi Kejuruteraan Mekanikal dan Pembuatan, Universiti Teknikal Malaysia Melaka, Hang Tuah Jaya, 76100 Durian Tunggal, Melaka, Malaysia

<sup>2)</sup> Fakulti Teknologi Kejuruteraan Elektrik dan Elektronik, Universiti Teknikal Malaysia Melaka, Hang Tuah Jaya, 76100 Durian Tunggal, Melaka, Malaysia

\*Corresponding e-mail: arizam@utem.edu.my

**Keywords:** Night market; energy conversion; thermoelectric generator

**ABSTRACT** – Electrical power requirement used to power up electrical appliances at night market usually provided by a petrol-electric generator which also contribute to air and noise pollution. Quite a few stalls at night market are involved with cooking activities and therefore produced waste heat which can be converted to electrical energy using a thermoelectric generator (TEG). The experimental work conducted managed to convert a maximum of 46.8 mW electrical power with the usage of five units TEG. However, the remaining heat energy is still high and therefore the power generated can further enhanced by increasing the total number of TEG used.

## 1. INTRODUCTION

Night markets usually operate from late in the evening and continue could be up to midnight, hence requires light source which normally using either fluorescent or LED type. Power consumed ranging between 50-100 W/hr per night for each stall, the light normally powered by gasoline electrical generator which consumed an average of RM2 to RM4 [1]. Additional cost for generator set maintenance will further increase the overhead cost. On top of that, the usage of the generator set also contributes to noise and air pollution which can affect the quality of food as well as disturbing the customers.

Cooking activity is one of the major activities at the night market which can cover up to 25% of the total available stalls [2]. This activity produces a huge amount of waste heat energy which normally can be seen by the coverage set up by the stall operator used to reduce the heat effect towards the customers. This excess heat has the potential to be converted into electrical power using a thermoelectric generator (TEG) and further used to power up the night market stall.

Worked based on the principle of Seebeck effect where the temperature difference ( $\Delta T$ ) and therefore the heat or thermal energy acts as a replacement of input or supply electrical voltage as the driving force of the electron's movement or the electrical current in the circuit [3]. The electrical energy produced is proportionate to the temperature difference between the two sides of TEG [4] as follows:

$$V_0 = \alpha_{TEG}(T_H - T_C) = \alpha_{TEG}\Delta T \quad (1)$$

Where  $V_0$  is voltage output,  $\alpha_{TEG}$  is Seebeck coefficient,

while  $T_H$  and  $T_C$  are the temperature at hot the and cold side of the TEG respectively. Seebeck coefficient is very much depends on the individual element used in constructing the TEG which is based on the concept of the semiconductor.

This project interest is to generate electricity using excess heat from the cooking activity at night marking with the intention to power up lights at their stall.

## 2. METHODOLOGY

A set of five TEG units modeled SP1848-27145 and connected in series were used during the experimental process. The modules were arranged next to each other to minimize the length of wiring and hence the potential current loss due to wiring. The terminals of the modules are then connected to load, rated 2 Volts. The hot side of the TEGs was attached to a 0.5 mm thick copper plate which will be heated at one end using butane gas stove. Figure 1 shows the schematic diagram of the TEG arrangement.

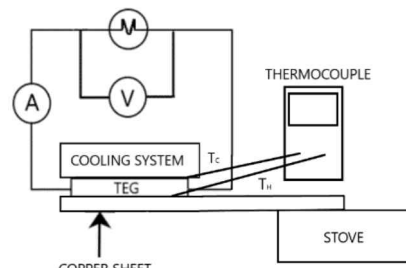


Figure 1 TEG's schematic diagram.

Four sets of parameter were measured for 200 seconds namely voltage and current; measured using multi-meter, while the temperature at both the hot and cold side; measured using dual channel thermocouple. The power output was then calculated as follows:

$$P_{TEG} = V_0 I_0 \quad (2)$$

## 3. RESULTS AND DISCUSSION

The output value of voltage  $V_0$ , current  $I_0$ , and power  $P_0$  had increased uniformly over time as shown in Figure 2 during the pre-heating period before became stable at 72 seconds. Time taken for the pre-heating process is very much depends on the amount of heat produced. The output values further slowly drop over

time during a constant temperature range, after achieved the maximum values at 90 sec heating time, similar to the one reported in [5]. Since TEG is a semiconductor type which made of two materials which highly govern the Seebeck coefficient and thus therefore the voltage output.

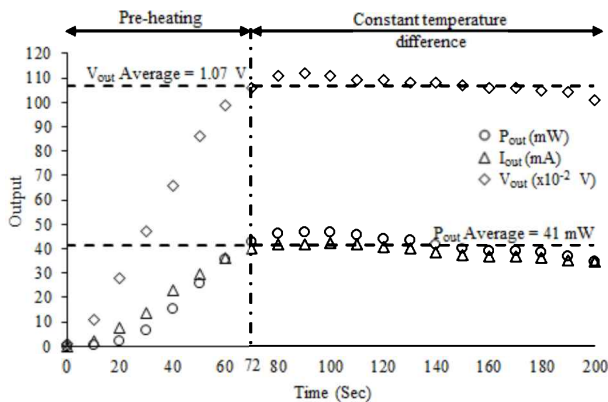


Figure 2 Voltage output against heating time.

The amount of current produce relatively very low and so for the power produced. Apartet et al. [6] have solved the numerical solution for TEG power output also found a similar pattern of power dropped. Table 1 shows the average and maximum value for every output.

Table 1 Output's average and maximum values.

Output values	Average values	Maximum values
Voltage (V)	1.07	1.12
Current (mA)	38.6	42.1
Power (mW)	41.3	46.8

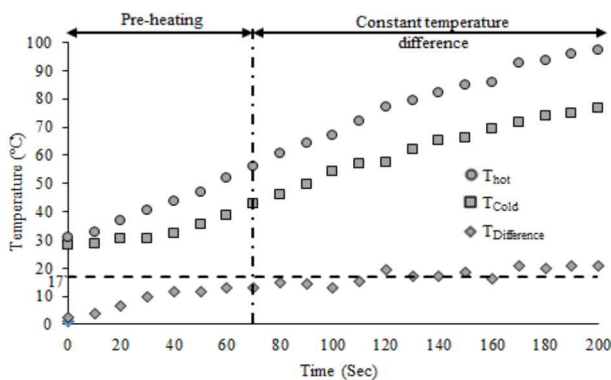


Figure 3 Temperature comparison over heating time.

Figure 3 shows the temperature at the hot and cold side, as well as the difference. Temperatures at both sides of the TEG modules increases exponentially from the moment copper plate been heated and keep increasing after 200 seconds. This showed that the amount of heat been transferred to the copper plate still not yet achieve the maximum level. However, the calculated temperature difference showed almost constant at an average value of 17°C after the pre-heating range which is similar to the one recorded in [5]. This constant in temperature difference had resulted in the constant output values, but rather lower relative to the heat input. Further,

the continuous temperature increment at the hot side shows that the TEG capable of producing higher output values, considering the cold side temperature can further be reduced with cooling mechanisms [4].

After the excess heat been converted using only five sets of TEG, it is assured there is still abundant of heat been released by the stove. A series of TEG modules fitted along the heat flux mechanism will receive the same amount of average heat energy in terms of the temperature difference and thus will produce the same amount of power output [7]. Therefore, additional TEG modules with the proper arrangement on heat transfer mechanism will further increase the power output.

#### 4. CONCLUSION

This study showed the application of thermoelectric generator used to harvest waste heat from cooking activities at night market and further converts into electrical energy used to power up their electrical appliances. Even though the output power produced relatively low (maximum of 46.8 mW) as compared to the waste heat input, but it is evident that it can be further improved by increasing the number of TEG used and incorporating a cooling mechanism.

#### ACKNOWLEDGEMENT

The authors would like to gratitude and acknowledge Universiti Teknikal Malaysia Melaka for the funding under short term grant, UTeM/PJP/2018/FTK (11A)/S01612.

#### REFERENCES

- [1] Harun, M.S. (2018). Development of waste-heat recovery using the thermoelectric generator at night market. (Unpublished Bachelor Degree dissertation). Universiti Teknikal Malaysia Melaka.
- [2] Chin, O., and Harun, M.Z.M., (2015). Night market: A platform for creating new entrepreneurs. *Humanities and Social Science*, 3(1), 32-36.
- [3] Singh, M., Nirapure, S., and Mishra, A. (2015). Thermoelectric generator: A Review. *IOSR Journal of Mechanical and Civil Engineering*, 12(3), 40-45.
- [4] Wang, L., and Romagnoli, A., (2016). Cooling system investigation of thermoelectric generator used for marine waste heat recovery. *2016 IEEE 2nd Annual Southern Power Electronics Conference*, 1-6.
- [5] Ma, Z., Wang, X., and Yang, A (2014). Influence of temperature on characters of thermoelectric generators based on test bed. *Journal of Nanomaterials*, 2014, 1-6.
- [6] Apertet, Y., Ouerdane, H., Goupil, C., and Lecoer, P. (2014). Influence of thermal environment on optimal working conditions of thermoelectric generators. *Journal of Applied Physics*, 116, 1-5.
- [7] Sempels, E., and Lesage, F. (2017). Optimal thermal conditions for maximum power generation when operating thermoelectric liquid-to-liquid generators. *IEEE Transactions on Components, Packaging and Manufacturing Technology*, 8(9), 1573-1580.

# Current Consumption and welding force measurement of bobbin friction stir welding on 6 mm thick AA1100

Siti Noor Najihah Mohd Nasir<sup>1</sup>, Mohammad Kamil Sued<sup>1,2,\*</sup>, Muhammad Zaimi Zainal Abidin<sup>1,2</sup>

<sup>1)</sup>Fakulti Kejuruteraan Pembuatan, Universiti Teknikal Malaysia Melaka,

Hang Tuah Jaya, 76100 Durian Tunggal, Melaka, Malaysia

<sup>2)</sup>Advance Manufacturing Centre, Universiti Teknikal Malaysia Melaka,

Hang Tuah Jaya, 76100 Durian Tunggal, Melaka, Malaysia

\*Corresponding e-mail: kamil@utem.edu.my

**Keywords:** Bobbin friction stir welding; current consumption; force measurement

**ABSTRACT** – The weld formation of bobbin friction stir welding (BFSW) process is hardly to observe. The interaction of the bobbin tool that used to generate frictional heat and enhance the material flow to form a weld joint require a comprehensive understanding. One of the ways is by measuring the signal processing to explain how much energy demand needed by the BFSW process to form the weld joint. This study investigates the phenomenon of weld formation of bobbin friction stir welded AA1100 through measurement of the current consumption and welding forces.

## 1. INTRODUCTION

The weld formation produced by bobbin friction stir welding (BFSW) is one of the crucial thing to be observed. Although various researchers attempt to discover the material flow in BFSW [1-2], however less documentation on signal processing measurement of the bobbin tool interacts with material to form a weld joint. This is important as to give an information that may help to point out the reason of the uncertainty phenomenon like tool breakage and incomplete weld joint. Also, it helps to sustain the BFSW by improving the tool features development and combination of parameters used. Therefore, in this study, the current consumption and welding forces measurement of BFSW was recorded and analyzed in order to investigate the interaction of bobbin tool to form the weld joint on AA1100 plates.

## 2. METHODOLOGY

The base material used for this investigation was 6 mm thick of aluminium alloy (AA) 1100 which were cut into plates with dimension of 140 mm long by 140 mm wide. These plates were butt joined parallel to the rolling direction via CNC milling machine and a fixed gap bobbin tool. The fixed gap bobbin tool was made from H13 tool steel consists of three main components which are the upper shoulder, tool pin and lower shoulder. The upper and lower shoulders having the same diameter of 25 mm and only lower shoulder having the taper of 5° feature. The tool pin has the diameter of 10 mm with three flats feature on the smooth cylindrical feature.

Before welding, the UNI-T232 clamp current meter with USB connection was placed at the spindle motor of the CNC milling machine and Kristler dynamometer were clamped underneath the jig for measuring the current and welding force, respectively. For welding trials, the spindle speed was varied from 750 to 950 rpm

at fixed welding speed of 150 mm/min. Figure 1 displays the experimental setup for this investigation.

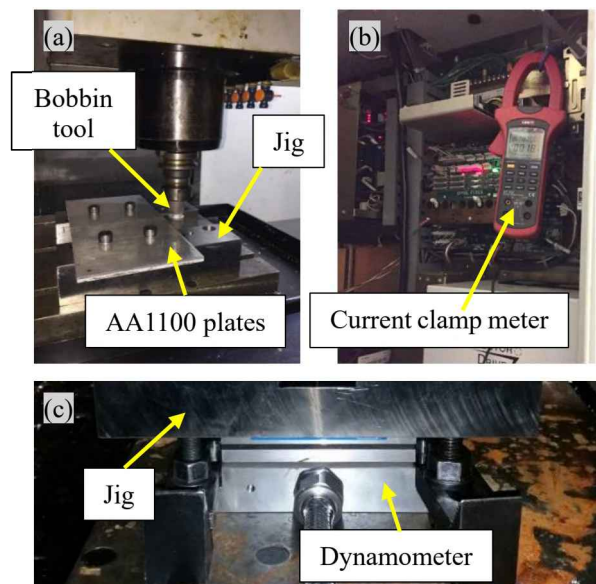


Figure 1 Experimental setup of the (a) welding work, (b) placement of current clamp meter and (c) dynamometer.

## 3. RESULTS AND DISCUSSION

Figure 2 vividly reveals the result of the current-time and force-time plots. Noted that the variation of the plot curves in Figure 2(a) for all of the welding trials were similar to the defined phases namely milling current, tool entry, weld phase and tool exit. On the other hand, the force-time plot in Figure 2(b) was recorded at spindle speed of 950 rpm and welding speed of 150 mm/min indicated three welding forces which were the travel force (force in y direction, Fy), transverse force (force in x direction, Fx) and axial force (force in z direction, Fz).

Referring to Figure 2(a), the milling current phase is the current that consumed by the CNC milling machine to operate the bobbin tool without any welding work taken into action. For this investigation, the average current was consumed about 1.6 A. On the contrary, the forces of all directions found to be zero value as no welding was conducted.

When the bobbin tool started to touch the edge of the AA1100 plates, the current increase remarkably with the average value of 11.9 A. Similar pattern was found in force-time plot whereby the force in Fx and Fy showing

sudden increase with average value of 5 kN and 3 kN, respectively, while the force in Fz was nearly to zero. The increase of both current and force reading were due to the bobbin tool begun to stir the material from the retreating side (RS) of the weld and around the back of the bobbin tool and then transferred the material on the advancing side (AS) of the weld. As the bobbin tool rotated and traversed slightly, the peak current and all the forces values were slightly drop which believed that the AA1100 plates started to soften resulting from the frictional heat generated by bobbin tool to form the weld [3].

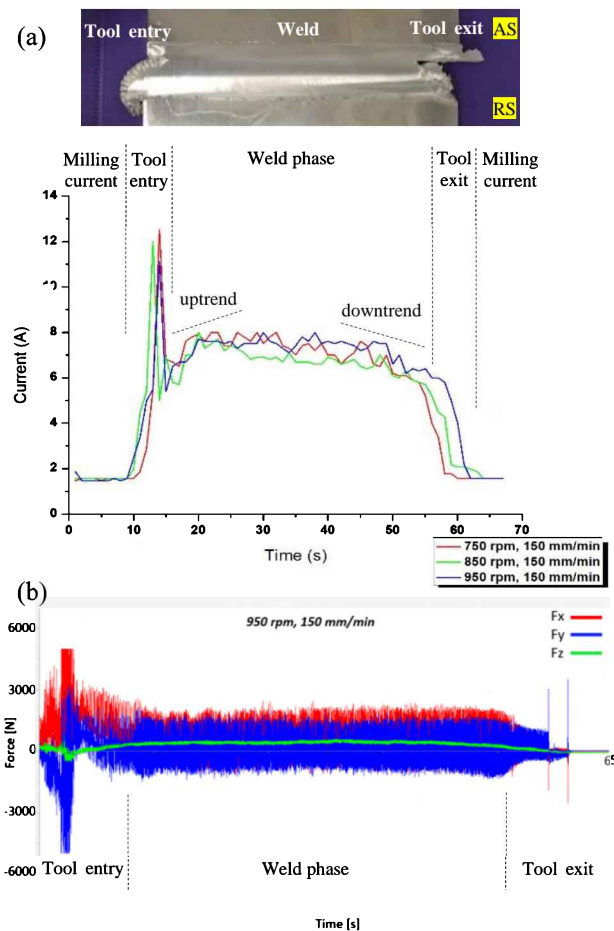


Figure 2 (a) Current-time plot and (b) force-time plot.

Entering the weld phase, there were two noticeable graph trend as depicted in Figure 2(a) which are the uptrend and downtrend. The uptrend was due to the load of the bobbin tool produced by the opposing shoulders as well as the material flow behind the bobbin tool to form the weld joint [4]. As the bobbin travels forward, the current became stable with the average value of 7.1 A. The downtrend indicated that the temperature of the material near the tool was increased causing the bobbin tool to have less effort to generate the frictional heat as the material was already softened.

On the other hand, as highlighted in Figure 2 (b) the forces in Fx and Fy display a stable trend with average peak value of 2 and 1.5 kN, respectively. The axial force in Fz direction was minimal compared to the force in Fx and Fy direction. Unlike the conventional friction stir welding process, the axial force of BFSW is minimal and

absence due to the BFSW process started to penetrate the tool from the edge of the material which consequently influence the force in Fx and Fy more than the Fz. This result matches with the finding found in [5-6].

Entering to the tool exit phase, the current reading of all the weld had sudden decrease before reaching the average value of 1.6 A at the milling phase current. In the same way, the force measurement in all direction shows that the peak force value started to drop reaching to the value of zero. The reason is that there was a disruption that stopped the softened material to circulate from AS to RS of the weld which consequently due to insufficient material to stir [7] that resulted the bobbin tool released out from the material.

#### 4. CONCLUSION

As conclusion, throughout experimental work, the current consumption and force measurement of the BFSW on AA1100 was discovered and presented. Both signal processing measurements increased remarkably at tool entry as the bobbin starts to build a weld. When the tool enters the weld phase, both measurements depicted stable data. Sudden decrease in both measurements found at the tool exit.

#### ACKNOWLEDGEMENT

Author would like to be obliged to the Ministry of Education Malaysia and Universiti Teknikal Malaysia Melaka for financial support under Short Term Research Grant (Grant no. PJP/2017/FKP/H18/S01525).

#### REFERENCES

- [1] Sued, M. K., Tamadon, A. & Pons, D., (2017), Material flow visualization in bobbin friction stir welding by analogue model. *Proceedings of Mechanical Engineering Research Day 2017*. 368-369
- [2] Chen, S., Lu, A., Yang, D., Lu, S., Dong, J. & Dong, C. (2013), Analysis on flow pattern of bobbin tool Friction stir welding for 6082 aluminum. *Proceedings of the 1st International Joint Symposium on Joining and Welding*. Woodhead Publishing.
- [3] Kumbhar, N.T. & Bhanumurthy, K., (2008) Friction Stir Welding of Al 6061 alloy. *Asian Journal of Experimental Sciences*, 22(2), 63-74.
- [4] Sued, M. K., Samsuri, S. S. M., Kassim, M. K. A. M. & Nasir, S. N. N. M., (2018) Sustainability of welding process through bobbin friction stir welding. *IOP Conference Series: Materials Science and Engineering*, 318, 012068.
- [5] Martin, J. & Wei, S., (2015) Friction stir welding technology for marine applications *Friction Stir Welding and Processing VIII*, 219-226.
- [6] Threadgill, P. L., Ahmed, M. M. Z., Martin, J. P., Perrett, J. G. & Wynne, B. P., (2010) The use of bobbin tools for friction stir welding of aluminium alloys. *Materials Science Forum*, 638-642, 1179-1184.
- [7] Tamadon, A., Pons, D. J., Sued, K. & Clucas, D., (2018) Formation mechanisms for entry and exit defects in bobbin friction stir welding. *Metals*, 8(33), 1-22.

# Barriers and motivation of the solid waste management among manufacturing companies in Malaysia

Nor Ratna Masrom<sup>1,2,\*</sup>, Najiah Atira Abd Rahman<sup>1</sup>, Mohammed Hariri Bakri<sup>1,2</sup>, Raja Zuraidah Raja Mohd Rasi<sup>3</sup>, Badru At Tamam Daut<sup>3</sup>, Irwan Ibrahim<sup>4</sup>

<sup>1)</sup> Fakulti Pengurusan Teknologi dan Teknousahawan, Universiti Teknikal Malaysia Melaka,  
Hang Tuah Jaya, 76100 Durian Tunggal, Melaka, Malaysia

<sup>2)</sup> Centre for Technopreneurship Development, Universiti Teknikal Malaysia Melaka,  
Hang Tuah Jaya, 76100 Durian Tunggal, Melaka, Malaysia

<sup>3)</sup> Fakulti Pengurusan Teknologi dan Perniagaan, Universiti Tun Hussein Onn Malaysia,  
86400 Parit Raja, Johor, Malaysia

<sup>4)</sup> Fakulti Perniagaan dan Pengurusan, Universiti Teknologi MARA, 42300 Shah Alam, Selangor, Malaysia

\*Corresponding e-mail: norratna@utem.edu.my

**Keywords:** Waste management; manufacturing

**ABSTRACT** – Solid waste management refers to the process of production, storage, source separation, collection, transportation, processing, recycling and disposal of solid waste. The objective of this study are to analyze the practice of solid waste management by manufacturing company, to investigate the barriers in manufacturing company and to identify a factor that can be the catalyst to execution solid waste management in manufacturing company. This paper is using qualitative method through semi-structured interview with five respondents in Malaysia. It was found there were six factor of barriers of the solid waste management, size is an important factor on solid waste management and maintenance the barriers to manufacturing company to implement solid waste management. This paper recommends to explore the solution of the awareness problem in the society about environmental issue.

## 1. INTRODUCTION

The increase of solid waste is a big problem faced by global. This was due because of the increase in the population of Malaysia at the rate of 2.4% or 600, 000 people on yearly basis. This has also led to an increase in Malaysia industry to fulfil need and waste of the Malaysia population. According to Jalil [1], solid waste produced from both industrial and household sector in the capital of Malaysia was 3500 metric tons each day [2]. Solid waste can be split into eight categories which are imported solid waste, commercial waste, garden waste, construction and demolition waste, household waste, industrial waste, institutional solid waste and public solid waste [3]. This proves that the industry is also one of the major contributor to increasing of solid waste in Malaysia. The quantities and type of industrial waste usually depend on the characteristic of industrial activity.

This problem will be worsened if solid waste management is not well-managed because it can cause pollution, resource degradation and health problem for humans and animals [3]. Example of environmental impacts is the loss of recreational facilities, damage or loss of biodiversity, air, water, land and noise pollution, loss of aesthetic landscapes and scenery and burst hazards [3]. To solve this problem, the government implement a landfill and recycling method of solid waste

generated. However, the landfill method also has problems and weakness such as difficult to implement and cause environmental pollution. Meanwhile, recycling method is difficult to implement because not all waste can be recycled. This problem has led into the implementation of solid waste management in manufacturing companies to help the government effort to reduce industrial solid waste. This is because effective waste management within the company can contribute to minimize and control the solid waste generated by manufacturing companies

## 2. METHODOLOGY

The qualitative research is often associated with an interpretive philosophy. It is interpretive because researchers need to make sense of the subjective and socially constructed meanings expressed about phenomena being studied. The needs to understand deeply about this study and the gaining accurate and strong data. Moreover, the researcher will give respondent some opportunity to discuss this topic in depth. Therefore qualitative method has been chosen, besides the researcher also can increase understanding of this topic.

In the study, interviewed with top-level managers and middle level managers. This is because top-level managers have a vast of the experience for managing solid waste in their company. In addition, the respondent is also in charge of decision making in managing the company solid waste. Meanwhile, the middle-level managers are responsible for implementing solid waste management and have extensive knowledge of the company solid waste. The respondent will create the objective of department to achieve a vision that has been set by top-level managers.

Thematic Analysis is a type of the qualitative research method. It is used to analyse categorizations and present themes (patterns) that relate to the data. According to Ibrahim [4], it illustrates the data in great detail and deals with various subjects via interpretations. Thematic analysis is considered the most suitable for any study that seeks to discover using interpretations [4]. Other than that, thematic analysis gives a systematic element to data analysis [4]. The researcher develops case

studies and need to use the interview method to gain a clear view and also get more detail data to improve the understanding of the research

### 3. RESULTS AND DISCUSSION

In conclusion, this research is about barriers and motivation of the solid waste management among manufacturing company in Malaysia. Overall, all the research objectives were achieved which is barriers of the implementation solid waste management, motivation of the implementation solid waste management solid waste management and the most influenced barriers of the manufacturing company to implement solid waste management. From Figure 1, it was found that six barriers to the implementation of the solid waste management among manufacturing company and six motivation implementation of solid waste management of solid waste management among manufacturing company. This research using the various method in finding answer objective of the research such as interview method and observation method. Other than that, the researcher found that maintenance factor is the factor that prevents the manufacturing company to implement solid waste management. This factor was never mentioned in any past study about barriers of the solid waste management. The researcher also found that the size of the company is playing the main role in this implementing the solid waste management. This is because the implementation of solid waste involves cost and procedures which the small size company mostly does not have the capability in terms of money and skills.

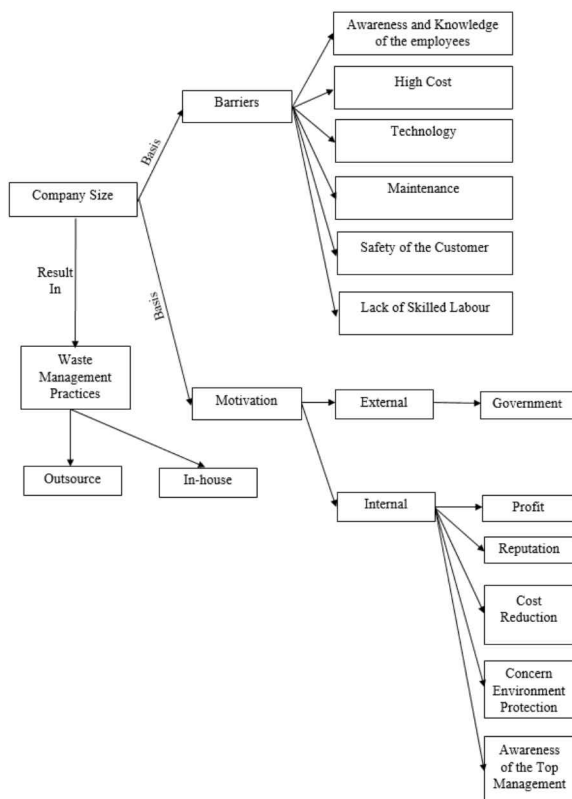


Figure 1 Result of the interview.

### REFERENCES

- [1] Jalil, M. A. (2010). Sustainable development in Malaysia: A case study on household waste management. *Journal of Sustainable Development*, 3(3), 91-102.
- [2] Mallak, S. K., Ishak, M. B., & Mohamed, A. F. (2014). Waste Minimization Benefit and Obstacles for Solid Industrial Waste in Malaysia. *IOSR Journal of Environmental Science, Toxicology and Food Technology*, 8(2), 43-52.
- [3] Hamid, A., Bariyah, K., Ishak, M. Y., & Abu Samah, M. A. (2015). Analysis of Municipal Solid Waste Generation and Composition at Administrative Building Café in Universiti Putra Malaysia: A Case Study. *Polish Journal of Environmental Studies*, 24(5), 1969–1982.
- [4] Ibrahim, A. M. (2012). Thematic analysis: A critical review of its process and evaluation. *West East Journal of Social Sciences*, 1(1), 39-47.

# Methodological hardware design and development of health monitoring

Muhammad Faiz Aqil Ahmad Fairuz<sup>1,2</sup>, Ranjit Singh Sarban Singh<sup>1,2,\*</sup>, Muhamad Izzat Nurdin<sup>1,2</sup>

<sup>1)</sup> Fakulti Kejuruteraan Elektronik dan Kejuruteraan Komputer, Universiti Teknikal Malaysia Melaka,  
Hang Tuah Jaya, 76100 Durian Tunggal, Melaka, Malaysia

<sup>2)</sup> Centre for Telecommunication, Research & Innovation, Universiti Teknikal Malaysia Melaka,  
Hang Tuah Jaya, 76100 Durian Tunggal, Melaka, Malaysia

\*Corresponding e-mail: ranjit.singh@utem.edu.my

**Keywords:** Health monitoring system; data acquisition system; internet of things

**ABSTRACT** – This paper presents the hardware methodological design and development of health monitoring system for an individual solar module. The proposed system comprises of four units of Thermocouple Sensors – MAX31855 Amplifiers, one INA 219 DC Voltage/Current Sensor, Raspberry Pi Zero Wireless, 16GB Micro SD CARD. The design and development of the proposed system is explained chronologically till preliminary system operation is achieved. Preliminary system operation findings for Thermocouple – MAX31855 Amplifier Sensors for Temperature and INA 219 DC Current/Voltage Sensor for current and voltage results are observed, recorded and analyzed. And, overall system integration is also validated based on the preliminary obtained results.

## 1. INTRODUCTION

Several solar module forecasting methods can be found in the specific literature [1-7]. All these systems are developed to sense and measure the solar module output based on the real-time condition. Therefore, real-time temperature, current and voltage parameters monitoring allows to predict the health of solar module. Moreover, real-time temperature, current and voltage parameters [8] monitoring provides real local information of an individual solar module and ensure the output reliability of an individual solar module [9].

This paper methodologically explains about the hardware design and development of health monitoring system for an individual solar module. The proposed system comprises of four (4) thermocouple sensors each integrated with a MAX31855 amplifier, an INA 219 DC Current/Voltage Sensor and Raspberry Pi Zero Wireless system board to integrate all the thermocouple sensors and INA 219 DC Current/Voltage Sensor. The thermocouple sensors integrated with MAX31855 amplifier is embedded at the back of the solar module to detect the solar module temperature which can be used to analyses the solar module performances when the temperature fluctuate. Meantime, INA 219 DC Current/Voltage Sensor is connected to the positive solar module wire to sense and measure the output voltage and current of the solar module.

## 2. METHODOLOGY

The proposed health monitoring system section shows the conceptual block design of the proposed health monitoring system in Figure 1 before the actual hardware shown in Figure 2 is developed after reviewing the previously developed system. General architecture

shown in Figure 2 explain about the proposed hardware development of health monitoring system for individual solar module.

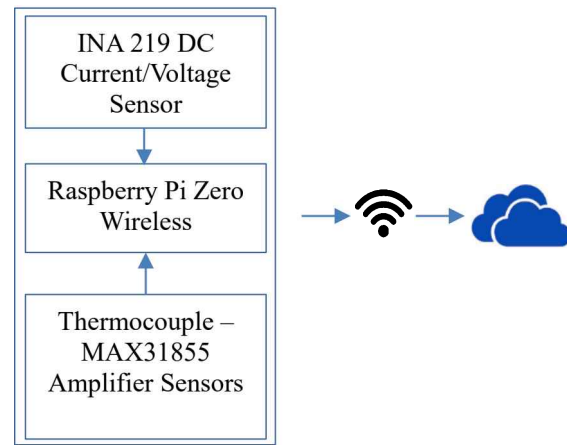


Figure 1 Block Diagram of solar health monitoring system.

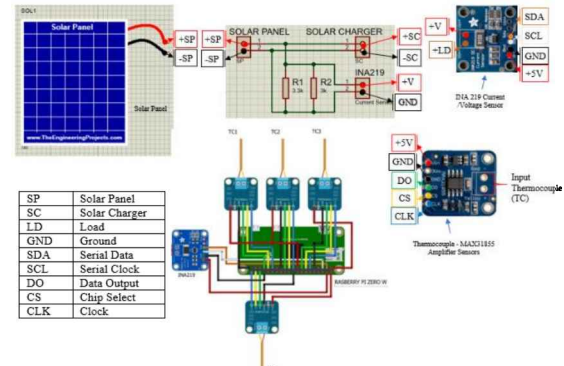


Figure 2 Proposed hardware system design – solar health monitoring system.

Figure 2 shows the proposed hardware system design for the solar module health monitoring system. Referring to the conceptual design in Figure 1, the components mentioned in Figure 1 is used to design the layout shown in Figure 2. Some other additional components such as the solar module and current divider is also used in the layout. The solar module is connected to the current divider to limit the output current before entering the INA 219 DC Current/Voltage Sensor. The high output current from solar module is stepped down to support the characteristic of INA 219 DC Current/Voltage Sensor. This also to allow the INA 219 DC

Current/Voltage Sensor to perform the real-time voltage and current sensing and measurement.

### 3. HARDWARE SYSTEM DEVELOPMENT

The +SP and -SP is connectivity of solar module to the current divider. The +SC and -SC is the connectivity to the charge controller and +V at current divider connects +V at the INA 219 DC Current/Voltage Sensor, whereas the GND at the current divider connects to the GND at the INA 219 DC Current/Voltage Sensor. The INA 219 DC Current/Voltage Sensor is powered using +5V. The SDA and SCL connected to the SDA and SCL of the Raspberry Pi Zero Wireless. The MAX31855 Amplifier Sensor is powered using +5V, and the DO, CS and CLK is connected to the Raspberry Pi Zero Wireless.

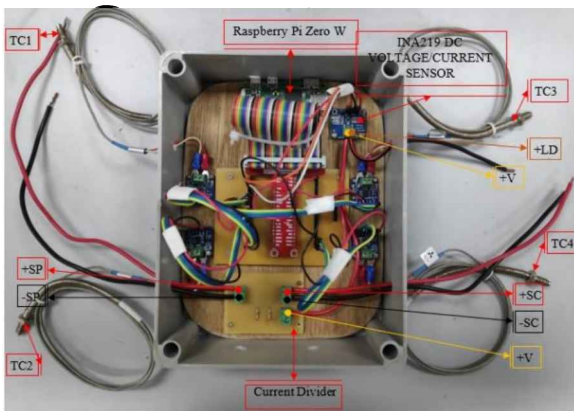


Figure 3 Developed health monitoring system – integrated with thermocouple MAX31855, INA219 DC voltage/current sensor, raspberry pi zero wireless.

### 4. RESULTS AND DISCUSSION

Figures 4 and 5 presents the preliminary results of current, voltage, power and temperature obtained from the installed INA 219 DC Current/Voltage Sensor and Thermocouple – MAX31855 Amplifier Sensors.

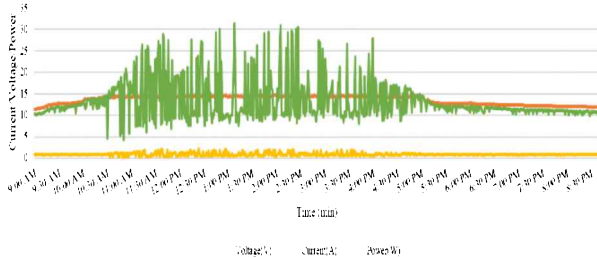


Figure 4 Measured current, voltage and calculated power.

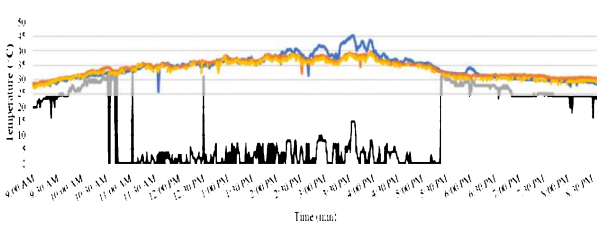


Figure 5 Sensed and measured solar module temperature.

### 5. CONCLUSION

The proposed methodology shown in Figure 2 is used to develop the system shown in Figure 3. Thus, the proposed methodology is validated by obtaining the results presented in Figures 4 and 5. The obtained results in Figures 4 and 5 explained the successfulness of the proposed hardware system operation and functionality to achieve the objective to monitor the health of an individual solar module.

### REFERENCES

- [1] Nieto, J., Carpintero, Ó., & Miguel, L. J. (2018). Less than 2 °C? An economic-environmental evaluation of the Paris agreement. *Ecological Economics*, 146, 69-84.
- [2] Feldman, D., Barbose, G., Margolis, R., James, T., Weaver, S., Darghouth, N., Fu, R., Davidson, C., Booth, S., & Wiser, R. (2014). Photovoltaic system pricing trends. *US Department of Energy*.
- [3] Khan, M. R. B., Jidin, R., Shaaya, S. A., & Daryll, D. (2012). Wireless PV Module performance monitoring system. In *Proceedings National Graduate Conference 2012* (pp. 1-4).
- [4] Badave, P. M., Karthikeyan, B., Badave, S. M., Mahajan, S. B., Sanjeevikumar, P., & Gill, G. S. (2018). Health monitoring system of solar photovoltaic panel: an internet of things application. In *Advances in Smart Grid and Renewable Energy* (pp. 347-355).
- [5] Gusa, R. F., Sunanda, W., Dinata, I., & Handayani, T. P. (2018). Monitoring system for solar panel using smartphone based on microcontroller. In *2018 2nd International Conference on Green Energy and Applications (ICGEA)* (pp. 79-82).
- [6] Paredes-Parra, J., Mateo-Aroca, A., Silvente-Niñirola, G., Bueso, M., & Molina-García, Á. (2018). PV module monitoring system based on low-cost solutions: Wireless Raspberry application and assessment. *Energies*, 11(11), 3051.
- [7] Sabry, A. H., Hasan, W. Z. W., Ab. Kadir, M. Z. A., Radzi, M. A. M., & Shafie, S. (2018). Wireless monitoring prototype for photovoltaic parameters,” *Indonesian Journal of Electrical Engineering and Computer Science*, 11(1), 9-17.
- [8] Prasad, M. J. C., & Rani, M. U. (2014). Design and Development of a Remote Monitoring and Maintenance of Solar Plant Supervisory System. *International Journal of Research Studies in Science, Engineering and Technology*, 1, 57-61.
- [9] Petrone, G., Spagnuolo, G., Teodorescu, R., Veerachary, M., & Vitelli, M. (2008). Reliability issues in photovoltaic power processing systems. *IEEE Transactions on Industrial Electronics*, 55(7), 2569-2580.

# Measurement and analysis of energy consumption in a university building

Abdalraouf Alhammali<sup>1</sup>, Shamsul Shamsudin<sup>1,2,\*</sup>

<sup>1)</sup> Fakulti Kejuruteraan Mekanikal, Universiti Teknikal Malaysia Melaka, Technology Campus, 75450 Ayer Keroh, Melaka, Malaysia

<sup>2)</sup> Centre for Advanced Research on Energy (CARe), Universiti Teknikal Malaysia Melaka, Technology Campus, 75450 Ayer Keroh, Melaka, Malaysia

\*Corresponding e-mail: shamanuar@utem.edu.my

**Keywords:** Energy consumption; educational building; energy audit

**ABSTRACT** – In this paper, proposed a measure and evaluate existing internal parameters, which focused on the Language and Human Development Centre (PBPI) building at the Universiti Teknikal Malaysia Melaka (UTeM) main campus. Physical parameter requirements compared to current Malaysian Standards (MS 1525:2014). The paper also analyses the effects of indoor parameters at the comfort level of the occupants and investigates the impact of lighting changes as well as to evaluate energy consumption. The air-conditioning recorded the highest rate consumption that was 72% of electricity usage in the building, followed by the consumption of lighting at 18% and other equipment 10%. Finally, economic analysis is accompanied by potential alternative measures to achieve optimum building energy utilization.

## 1. INTRODUCTION

Nowadays, sustainability and environmental issues has great attention in relevant policies and strategies for developing countries [1]. The growing number of commercial premises and development projects for a residential and non-residential buildings impact the demand of energy in the country. Therefore, relevant policies and strategies are adopted to preserve and sustain the environment [2,3]. It is evident that electrical energy utilized in buildings continues to increase and will continue to grow in demand [4], utilized by the advanced technology used in electrical equipment [5]. An energy audit is crucial to obtain an optimal energy performance by reducing the energy waste and improve the efficiency of air-conditioning and lighting systems [6,7].

In this present work, a Detailed Energy Audit has been conducted at the selected building and all related data about that building was collected in order to get overall picture of the building energy consumption. Energy saving measures that can be implemented in the building are discussed.

## 2. EVALUATION STRATEGIES

The methods applied in this study, included gathering field data by doing measurements and field study on the energy consumption at the PBPI building. Inspection of the air-conditioning and mechanical ventilation (ACMV) and lighting systems were conducted for the building.

The PBPI building provides many of facilities such as language laboratories, lecturer rooms, classrooms and

administration offices as shown in Table 1. The area of the building is 5992.58 m<sup>2</sup> and a picture of this building that consists of three levels. The normal operating hours of this building is from 8:00 AM to 5:00 PM.

Table 1 PBPI building description.

Floor	Content
Ground	Lobby, SALL, 7 Lecturer's room 3 Language lab Main office
First	Language teacher rooms Lecturer rooms 4 Language lab Dean office BAKUTE unit
Second	9 Lecture room ISO room Seminar room

## 3. RESULTS AND DISCUSSION

This section discusses about the data collected and the result obtained from the calculation and sites walk through. All the data will be interpreted and discussed related to the case study building in this study. The results of physical parameter measurement will be compared with the Malaysian Standards for future recommendation to evaluate their performance

The collected data for electricity consumption for the duration of two years (July 2016 to Jun 2018) is presented in Figure 1. As the figure indicates, most of the energy consumption was decreased in March until April. The PBPI timetable will decrease in January until February and July until August.

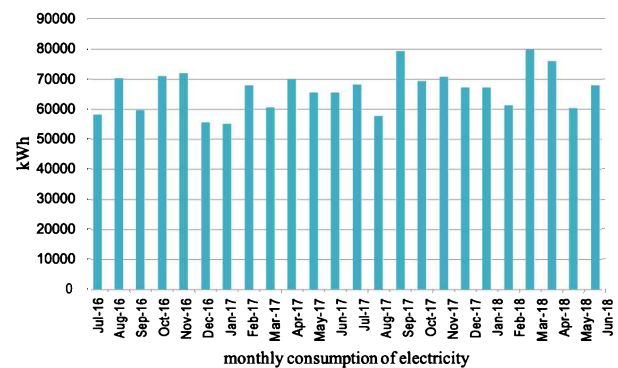


Figure 1 Monthly energy consumption between July 2016 into June 2018.

The case study building was divided into levels and each level is divided into ten measuring points and the

process of observation was conducted. The process observes the ACMV and Lighting specifications of every zone. Figures 2 below shows the total energy consumption for the building.

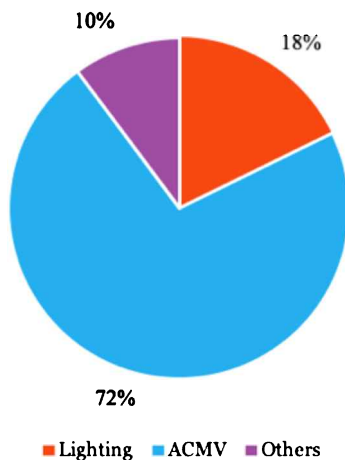


Figure 2 Energy Consumption (%) for PBPI building.

The following steps are recommended for reducing energy consumption.

- Reduce cooling loads: A simple method for reducing cooling load can be implemented through isolating the building from the environment using high scale types of insulation, enhancing the glazing area, and minimizing the infiltration of outside air.
- Reduce lighting loads: Energy usage for lighting can be reduced in two ways: reducing the amount of artificial light required and using more efficient technology.
- Increase efficiency of appliances and cooling equipment, and ventilation.
- Implement commissioning and improve operations and maintenance:
- The actual performance of a building depending on the type of construction as on the quality of the design itself.

#### 4. CONCLUSION

Based on the results, existing ACMV system was found contributing about 72% of the total energy usage. It was followed by lighting, contributing about 18%. All other appliances, however, were found contributing only 10%. This result reveals the importance of taking actions to reduce energy consumption, especially the use of air-conditioning in the building.

#### REFERENCES

- Zhang, K. M., & Wen, Z. G. (2008). Review and challenges of policies of environmental protection and sustainable development in China. *Journal of environmental management*, 88(4), 1249-1261.
- Allouhi, A., El Fouih, Y., Kousksou, T., Jamil, A., Zeraouli, Y., & Mourad, Y. (2015). Energy consumption and efficiency in buildings: current status and future trends. *Journal of Cleaner production*, 109, 118-130.
- Chua, S. C., & Oh, T. H. (2011). Green progress and prospect in Malaysia. *Renewable and Sustainable Energy Reviews*, 15(6), 2850-2861.
- Singh, H., Seera, M. and Idin, M.A.M., 2012, December. Electrical energy audit in a Malaysian university-a case study. In *Power and Energy (PECon), 2012 IEEE International Conference* (pp. 616-619).
- Dincer, I. (2000). Renewable energy and sustainable development: A crucial review. *Renewable and Sustainable Energy Reviews*, 4(2), 157-175.
- Poel, B., van Cruchten, G., & Balaras, C. A. (2007). Energy performance assessment of existing dwellings. *Energy and Buildings*, 39(4), 393-403.
- Menezes, A. C., Cripps, A., Bouchlaghem, D., & Buswell, R. (2012). Predicted vs. actual energy performance of non-domestic buildings: Using post-occupancy evaluation data to reduce the performance gap. *Applied energy*, 97, 355-364.

# An integrated approach of monitoring indoor environment inside building

Afiqah Ngah Nasaruddin<sup>1,\*</sup>, Tee Boon Tuan<sup>1,2</sup>, Musthafah Mohd Tahir<sup>1,2</sup>

<sup>1)</sup>Fakulti Kejuruteraan Mekanikal, Universiti Teknikal Malaysia Melaka,

Hang Tuah Jaya, 76100 Durian Tunggal, Melaka, Malaysia

<sup>2)</sup>Centre for Advanced Research on Energy, Universiti Teknikal Malaysia Melaka,

Hang Tuah Jaya, 76100 Durian Tunggal, Melaka, Malaysia

\*Corresponding e-mail: afiqah\_ngahn@yahoo.com

**Keywords:** Arduino; python; live-feed

**ABSTRACT** – Comprehensive utilization of open-source platform for indoor environment monitoring and visualization is getting prominently accepted due to their admissible tolerance of observational error. The Arduino-based platform is one of a flexible open source microprocessor developmental boards that allowed monitoring activities while permitting multiple platforms for streaming and storing of input from the sensor. This article provides the building blocks for streaming live-feed data from Arduino-based platform using python. Arduino Uno and DHT11 sensor combinations were used to test for a live streaming of temperature and humidity. The live-feed projection of both data was showed in the result section.

## 1. INTRODUCTION

Human spends almost an eternity perfecting an indoor environment for the sake of providing a comfort daily activity and working environment. One of the significant efforts is by conducting a monitoring activity to obtaining a full figure on the real environment condition. Since then, the monitoring activity keep improving and evolving succeeding the technology of microcontroller. For a compact microcontroller development board, it surely offered significant features revolving around collectively assessing program for a network of heterogeneous embedded devices. Moreover, Louis [1] described Arduino-based microcontroller development board as a very convenient, affordable yet open source option for utilizing sensors and actuators functionalities. Furthermore, Ali et. al. [2] introduced the term Open Source Building Science Sensors (OSBSS) to further described variety of Arduino platform integration. OSBSS was characterizes as a low-cost open source platform to serve the purpose of capturing an indoor environment and building operational quantifiable parameter for further analysis.

Even though Arduino Integrated Development Environment (IDE) provides a serial monitor which represent as a location where all the input from sensor being dumped however, it is more interactive to project the reading in a form of live-feed graph. Any irregularities can be easily spotted with proper sensor reading projection. For instance, El Hammoumi et. al. [3] utilizing LabVIEW Interface for Arduino (LIFA) as a medium for a real time sensor reading plotting and visualization. Constructing a block diagram for virtual instrumentation thus enables LabVIEW to have serial

connection with Arduino and visualizing the sensor reading. This article provides the building blocks for streaming a live-feed data from Arduino-based platform using python.

## 2. METHODOLOGY

The key element in determining a whole framework is by dictating the whole system architecture which includes software, hardware and algorithm arrangement.

### 2.1 System Architecture

For the purpose of this case study the sensing unit consists of a DHT11 sensor module (temperature and humidity sensor) and Arduino Uno board (ATmega328P) as shown in Figure 1. On the other hand, temperature humidity module provides humidity ratio reading in the range of 20 to 90% and for the temperature reading in the range of zero to 50° C. Moreover, the communication between the DHT11 sensor module and Arduino was assigned on the digital pin.

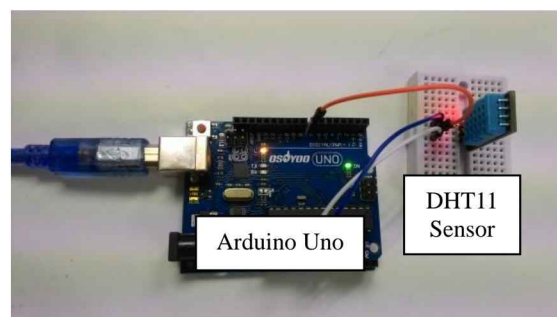


Figure 1 Circuit assembly.

The flow chart in Figure 2 described the algorithm of the passage of Arduino sketch and python code for sensing unit and live-feed streaming respectively. First and foremost, the programs line begins with the inclusion of all necessary python library modules to assist in communication, plotting and updating live graph and provide data array. Next in the line is defining the communication path by which declaring the input pin for sensor and stating the baud rate where python receiving sensor input from the Arduino. Further step is introducing a program loop which enable live feed log and plotting of sensor data. The program stops once the Arduino was disconnected.

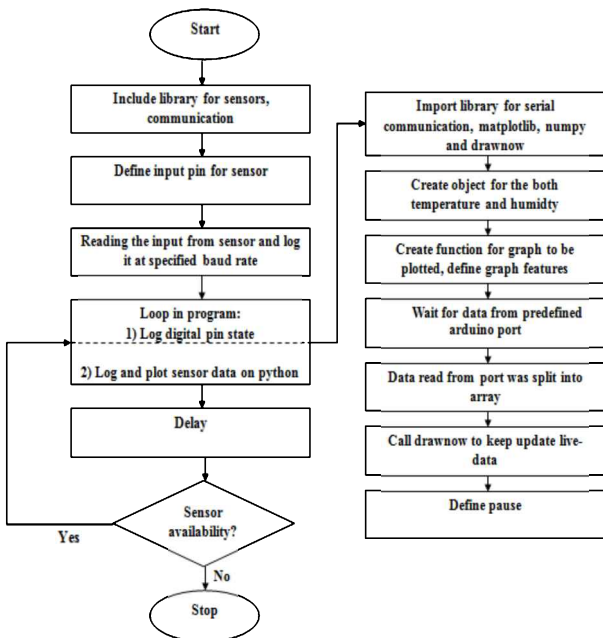


Figure 2 Algorithm on the flow of the Arduino sketch and python code.

### 3. RESULTS AND DISCUSSION

Figure 3 shows a sample projection of live-feed DHT11 sensor module reading. The features observed on the graph are pre-defined in between the line of code as described in the algorithm section of methodology. To avoid any unnecessary interruption of sensor data projection, ensure only pythons were allowed to listen to the Arduino port in the pre-determined serial connection. To enable the live-feed graph using python, highlighted libraries (numpy, matplotlib, drawnow) in the algorithm must first be retrieved. This all the libraries that are crucial to keep the data feed from the serial connection being updating and plot instantaneously.

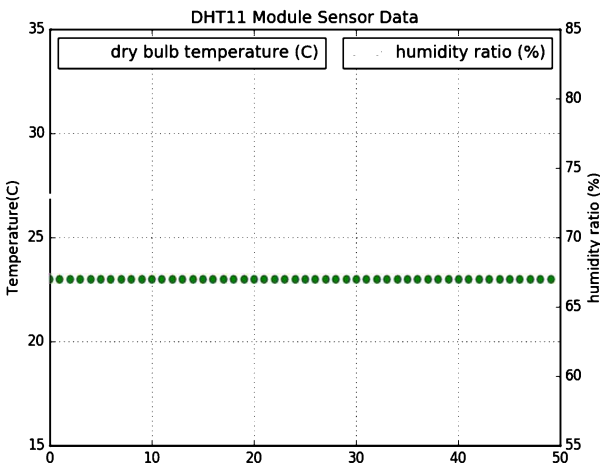


Figure 3 Live-feed sensor module reading projection by using Python.

The features appear on the live-feed graph for instance, the plot lines, set limit and range, colour choices and labelling style is totally flexible and comes in handy with varieties. As for example, the lines `plt.plot(temperature, 'r-', label='dry bulb temperature (C)')` and `plt2.plot(humidity, 'go', label='humidity ratio (%)')` in the program was written to specify and differentiate between temperature and humidity reading respectively. On the other hand, Figure 4 shows a building block that describes the element to be integrated between Arduino and Python itself. Arduino platform was described sensing unit which obligated to receive sensor input and provides a serial connection thus the listening port for Python. While Python actively streams the real-time sensor data it also permitting data dumping into the Comma-separated Values (CSV) file format. Thus, it can be securely stored for further analysis.

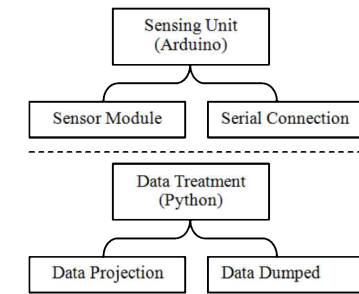


Figure 4 Building block of integration between Arduino and Python.

### 4. CONCLUSION

DHT11 sensor module data projection using python is quite straightforward thus, very convenient. With little effort and basic programming knowledge whole system that utilized an open source platform for monitoring and data visualization can be accomplished successfully. Though Live-feed sensor data streaming is considered as interactive and convenient, other aspects such as data dumping must carefully plan for effortless access.

### ACKNOWLEDGEMENT

The authors gratefully acknowledge the financial support from Universiti Teknikal Malaysia Melaka (UTeM), Malaysia

### REFERENCES

- [1] Louis, L. (2016). Working principle of arduino and using it as a tool for study and research. *International Journal of Control, Automation, Communication and System*, 1(2), 21-29.
- [2] Ali, A. S., Zanzinger, Z., Debose, D., & Stephens, B. (2016). Open source building science sensors (OSBSS): a low-cost arduino-based platform for long term indoor environmental data collection. *Building and Environment*, 100, 114-126.
- [3] El Hammoumi, A., Motahhir, S., Chalh, A., El Ghzizal, A., & Derouich, A. (2018). Real-time virtual instrumentation of Arduino and LabVIEW based PV panel characteristics. *IOP Conf. Series: Earth and Environmental Science*, 161, 1-11.
- [4] Ngah Nasaruddin, A., Tee, B.T. Musthafah, M.T. and Ito, T. (2018). Theoretical framework of Building Lighting Intensity Control by Using IoT. In *Proceeding of 2nd Malaysia University-Industry Green Building Collaboration Symposium*, pp. 1-5.

# Investigation on air conditioning oversizing impact using computational approach

Abdul Qayyum Abdul Halim<sup>1,3,\*</sup>, Tee Boon Tuan<sup>1,2</sup>, Wan Shah WaliAllah Wan Mat Zain<sup>3</sup>, Afiq Mohamad Johari<sup>3</sup>

<sup>1)</sup>Fakulti Kejuruteraan Mekanikal, Universiti Teknikal Malaysia Melaka,

Hang Tuah Jaya, 76100 Durian Tunggal, Melaka, Malaysia

<sup>2)</sup>Centre for Advanced Research on Energy, Universiti Teknikal Malaysia Melaka,

Hang Tuah Jaya, 76100 Durian Tunggal, Melaka, Malaysia

<sup>3)</sup>Jabatan Kerja Raya Malaysia, Jalan Sultan Salahuddin, 50480, Wilayah Persekutuan Kuala Lumpur, Malaysia

\*Corresponding e-mail: aqayyum13@gmail.com

**Keywords:** Oversizing; air conditioning, computational

**ABSTRACT** - This paper aims to investigate air conditioning system's oversizing impact through direct observation and computational approach. In this study, oversizing is determined when a system is sized higher than industry's practice, formation of mold and rapid fluctuation of temperature and relative humidity in a room. The simulation shows that oversized air conditioning system does lead to higher energy consumption and promotes favorable condition for mold growth.

## 1. INTRODUCTION

According to Suruhanjaya Tenaga Malaysia, Residential and commercial sector accounted for 14.6% of Malaysia's total energy consumption in 2015 [1]. With the construction industry projected to grow 7-8% annually, it is safe to assume that energy consumption will steadily increase in the future. With air conditioning system typically contributed around 58% of energy use, it is an important area to analyze in order to avoid any energy wastage in commercial buildings. Despite that, there is tendency to over-design and over-specified by the engineers during design process to mitigate risk, which impact the ability of these systems to operate at their optimum efficiency point.

Study on the impact of oversized air conditioning system has been conducted many times in the past. Simulation tools has been widely used to study oversizing impact due to its dynamic ability to simulate various building condition. The study by Djunaedy et al for example has shown that oversizing of rooftop unit (RTU) amounted to 37% to 48% of energy increases compared to as-designed condition [2]. Woradechjumroen et al analysis of 268 RTUs finds that oversized capacities is prevalent with energy penalty between 34.66 kW to 226.41 kW [3]. James et al collected data on 368 homes and found 3.7% to 9.3% increases of energy with oversized capacity between 20% to 50% [4]. Booten et al provides further explanation in explaining that oversized air conditioning unit leads to additional energy use due to increase on-off cycling relative to correctly sized unit [5].

Another undesirable consequence of poorly designed air conditioning system is that it can promote mold growth in buildings. Mold growth is undesirable since it creates odor problems, cause damage to building material and hazardous to human health. Source of mold

in air conditioning system can come from outdoor air or inside the air conditioning system components itself. Malaysia's tropical climate means that outside air flowing inside the air conditioning system is naturally high in moisture content favorable by mold. Furthermore, the air conditioning system components itself provides conducive breeding ground as it is easily found in filters, insulation and drain pan as reported by Prezant et al [6]. According to Yau and Ng, mold growth in a room is exacerbated when the air conditioning system's cooling coil fails to remove air moisture content below 70% relative humidity [7].

However, majority of the studies as discussed earlier are conducted in seasonal countries and cannot be compared to Malaysia's tropical weather. Furthermore, the seasonal countries weather is not conducive for mold growth. Thus, this study aim to understand the impact of air conditioning oversizing to both energy and mold based on real building facing these issues.

## 2. BACKGROUND AND METHODOLOGY

A University Bio-Molecule Laboratory in Perak has been severely infected by mold which raises health concern among its occupants. The air into the room is delivered by water cooled, ducted fan coil unit (FCU) and returned back through ceiling plenum. Room temperature and relative humidity is recorded using data logger. To ensure that mold problem originates from air conditioning system, all other potential causes of mold such as leak water pipe or unnecessary infiltration openings were checked and confirmed to be non-existent. Existing air conditioning system's parameters are then compared to recommended figures as provided in ASHRAE Handbook – Fundamental [8].

To achieve the objective of this work, the existing FCU cooling capacity and air flow is remodeled using IES-VE 2017 software as shown in Figure 1.

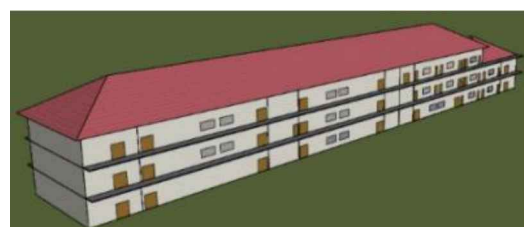


Figure 1 Building model using IES-VE.

The simulation setting is modelled to resemble the actual building as closely as possible including its building envelope properties, internal and external heat sources and air conditioning system's components as shown in Table 1. The simulation setting was then resized using the simulation tool in order to establish the room's optimal air conditioning needs. The simulation result's capacity, temperature and relative humidity were then compared and analyzed to draw conclusion.

Table 1 Simulation setting using IES-VE 2017/

Component	Setting
Building Envelope	Area
	0.4 Btu/hr/ft <sup>2</sup> /°F
	Window
	0.25 Btu/hr/ft <sup>2</sup> /°F
Internal Heat Source	People
	Lighting
	Equipment
Air Conditioning System Components	1. Fan 2. Cooling Coil 3. Ducting 4. Chilled Water From Chiller

### 3. RESULTS AND DISCUSSION

From the gathered data, temperature and relative humidity recorded is at favorable range for mold growth as manifested by its formation at wall and office furniture. The temperature and relative humidity recorded is shown in Figure 2 and Table 2.

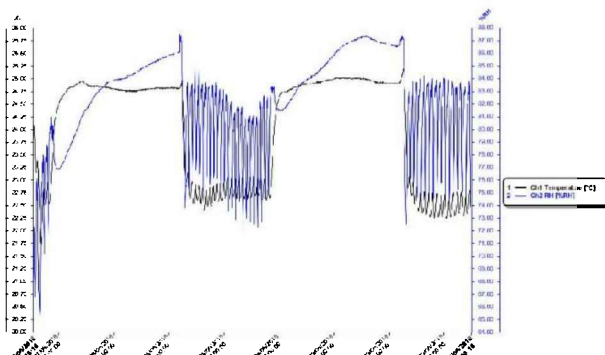


Figure 2 Temperature and relative humidity profile.

Table 2 Average recorded temperature and relative humidity.

Time	Temperature (°C)	RH (%)
Overall	23.99	82.3
0700 - 1800	22.5	77.1
1800 - 0700	24.8	84.9

Using ASHRAE Pocket Guide for Air Conditioning, Heating, Ventilation, Refrigeration's recommendation, the FCU unit capacity can be categorized as oversized considering that the cooling load per area is 70.2 Btuh/ft<sup>2</sup> and flow rate per area is 2.4 cfm/ft<sup>2</sup> which is higher than the recommended value of 60 Btuh/ft<sup>2</sup> and 1.4 cfm/ft<sup>2</sup> [9]. Room temperature profile supports this observation where it shows that temperature rise and fall within short period of time. This indicate that the FCU only need short time to cool

the room before cooling process stops by shutting off the control valve. Relative humidity also show rapid rise whenever control valves shuts off. Its consistently high room relative humidity during operating hours shows that the cooling coil is improperly sized and fail to dehumidify incoming air.

The simulated optimal air conditioning capacity of the room is compared with existing FCU as shown in table 3 while the simulated temperature and relative humidity between existing and re-calculated FCU is shown in table 4. Result shows that the simulated FCU cooling capacity per area and flowrate per area falls within ASHRAE recommended average which implies that the existing FCU cooling capacity is oversized by 42.3% while its air flowrate is oversized by 95.6%.

Table 3 Comparison of FCU capacity.

Comparison	Existing	Simulated
Capacity (Btu/hr)	143,000	100,518
Airflow (CFM)	4,500	2,300
Cooling per area (Btuh/ft <sup>2</sup> )	75.9	50.6
Air Change (nos.)	14.6	7.2
Airflow per area (CFM/ft <sup>2</sup> )	2.3	1.2
Energy (MWh)	3.8	1.3

Table 4 Comparison of room temperature and relative humidity.

Average	Simulated existing		Simulated re-calculated	
	Temp. (°C)	RH (%)	Temp. (°C)	RH (%)
Overall	25.6	74.5	25.7	65.6
0700 - 1800	23.3	75.2	23.1	59.1
1800 - 0700	27.3	73.9	27.5	70.2

Similar to field data, relative humidity for simulated FCU at original cooling capacity remain consistently high. Result of simulated re-calculated FCU on the other hand shows that relative humidity has been reduced to within acceptable range as shown in Figure 3. In term of energy, the impact of reducing FCU capacity is significant as it only consumes 34.2% power compared to existing FCU.

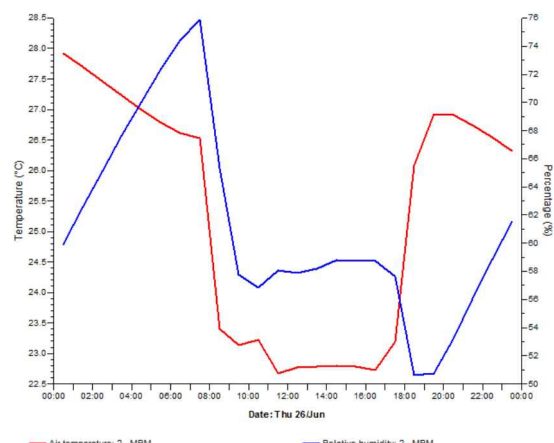


Figure 3 Simulated temperature and relative humidity profile.

#### 4. CONCLUSION

The simulation results has shown that (i) oversized air condition system lead to higher relative humidity which is favorable for mold growth and (ii) leads to unnecessary energy wastage due to high power consumption. As the simulation above only represents FCU blower, the energy saving for the whole air conditioning system should be higher once saving from other energy-intensive equipment such as chillers, pumps and cooling towers are considered.

#### REFERENCES

- [1] Suruhanjaya Tenaga. (2016). Guidelines on No-Cost and Low-Cost Measures for Efficient Use of Electricity in Buildings. Suruhanjaya Tenaga Malaysia.
- [2] Djunaedy , E ., Van Den Wymelenberg , K ., Acker , B ., Thimmanna, H . (2011). Rightsizing: using simulation tools to solve the problem of oversizing. *Building Simulation*, 14–16.
- [3] Woradechjumroen, D., Yu, Y., Li, H., Yu, D., & Yang, H. (2014). Analysis of HVAC system oversizing in commercial buildings through field measurements. *Energy and Buildings*, 69, 131–143.
- [4] James, P., Cummings, J., Sonne, J., Vieira, R., Klongerbo, J. (1997). The Effect of Residential Equipment Capacity on Energy Use, Demand, and Run-Time. *ASHRAE Transactions*, 29(4), 522–529.
- [5] Booten, C., Christensen, C., & Winkler, J. Energy Impacts of Oversized Residential Air Conditioners - Simulation Study of Retrofit Sequence Impacts. (2014). National Renewable Technology Laboratory.
- [6] Prezant, B., Weekes, D., Miller, J. (2008). Recognition, Evaluation, and Control of Indoor Mold. American Industrial Hygiene Association.
- [7] Yau, Y. H., & Ng, W. K. (2011). A comparison study on energy savings and fungus growth control using heat recovery devices in a modern tropical operating theatre. *Energy Conversion and Management*, 52(4), 1850–1860.
- [8] American Society of Heating, Refrigerating and Air-Conditioning Engineers. (2009). ASHRAE handbook: Fundamentals. Atlanta, GA. American Society of Heating, Refrigerating and Air-Conditioning Engineers.
- [9] American Society of Heating, Refrigerating and Air-Conditioning Engineers. (2018). ASHRAE Pocket Guide for Air Conditioning, Heating, Ventilation, Refrigeration, 9<sup>th</sup> Edition. Atlanta, GA. American Society of Heating, Refrigerating and Air-Conditioning Engineers.

# Performance analysis of DC-DC converters for road pavement thermoelectric system

Muhammad Syadza Sharuddin\*, Azdiana Md. Yusop, Ahmad Sadhiqin Mohd Isir, Khairun Nisa Khamil

Fakulti Kejuruteraan Elektronik dan Kejuruteraan Komputer, Universiti Teknikal Malaysia Melaka,  
Hang Tuah Jaya, 76100 Durian Tunggal, Melaka, Malaysia

\*Corresponding e-mail: muhd\_syadza@yahoo.com

**Keywords:** Road pavement; thermoelectric; DC-DC converter

**ABSTRACT** – This paper aims to investigate the performance and behavior of road pavement thermoelectric system which can generate electrical power based on thermal energy harvesting. Two types of DC-DC converters were studied to find which can store generated power from TEG (Thermoelectric generator) efficiently into a supercapacitor. Both the indoor and outdoor experiments showed that DC1577A can charge supercapacitor faster than ECT310.

## 1. INTRODUCTION

Sun produces sunlight or light energy that also offer thermal energy. This thermal energy will be absorbed to earth surface causing them to be hot. Road surface which is paved by human absorbs and stores more thermal energy due to its black color causing them to be hotter than soil. This provides an idea for researchers to harvest thermal energy from road pavement.

Datta has developed TE energy harvesting prototypes for road pavement by studying the metal conducting plate dimension. The prototypes able to produce average power of 10mW in 8 hours for weather condition in South Texas [1].

DC-DC converter is a device that can convert an input voltage to another desired voltage. DC-DC converter can be divided into two; buck converter to produce a lower voltage than the input voltage, while a boost converter generates a higher voltage. MPPT or Maximum Power Point Tracking is a DC-DC converter that can optimize or maximize the power extraction from solar panel or TEG to a storage device by changing the current or voltage, so it matches the storage device.

Several researchers have proved that DC-DC converter can help produce higher power efficiency. Experiment done by Mamur and Ashika [2] showed that their portable TEG device can produce 92% of power efficiency when using DC-DC boost converter with MPPT compared to direct connection to the battery with only 55% efficiency. According to Montecucco et al., a system which computes MPPT algorithm using a buck converter embedded with a microcontroller can quickly and precisely track more than 90% maximum power from TEG [3].

Aim of the paper is to examine the performance of road pavement TEG system based on the output voltage from DC-DC converters. The experiments are conducted inside and outside laboratory experiments to show the real world performance of the system.

## 2. METHODOLOGY

A pavement sample was constructed using a plywood box with a dimension of 300mm x 300mm x 100mm (length x width x height) which is then filled with cold premix asphalt. 5 copper plates with dimension of 300mm x 40mm x 1mm (length x width x thickness) were used as heat collectors. One ends of the copper plates were planted into the pavement sample while the other ends were glued to the hot side of TEGs. A water tank with a dimension of 350mm x 150mm x 160mm (length x width x height) is then attached to the cold side of TEG using thermal paste. The water tank is used to cool down the TEG and generate high temperature gradient between both side of TEG (hot and cold sides) because the higher the temperature difference, the greater the voltage output.

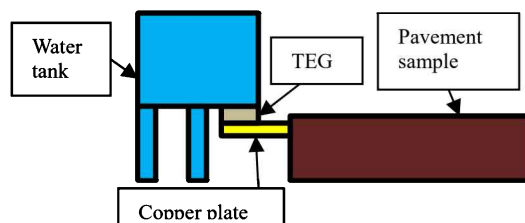


Figure 1 Experimental setup diagram.



Figure 2 Outdoor experimental setup.

Two types of DC-DC converters were used in the experiment; DC 1577A and ECT 310. Both converters were chosen because they can produce output voltage about 5 V while the storage device to be charged were 2 pieces of 2.5V 5F supercapacitors in series which produced 5V total of electrical power. The experiments were conducted up to four hours.

These tests are divided into two parts; Part I: Indoor Test and Part II: Outdoor Test. For indoor test, the experiments were conducted inside a laboratory. The pavement sample was covered with a box which contain of two 100W incandescent light bulbs. The box and bulbs will provide constant environment to ensure the data is reliable. The outdoor tests were done by harvesting thermal energy from sun to the asphalt sample and

transfer it to metal plates. The outdoor test is important because it will show the performance of the prototype in the real world. The outdoor test is conducted at 11.00 AM until 3.00 PM because highest amount of sunlight is produced during that time.

### 3. RESULTS AND DISCUSSION

All the graph has the same setting, where “Input 0” is the input voltage from TEGs to the DC-DC converter while “Input 2” is the supercapacitor voltage.

#### 3.1 Part I: Indoor Test

As shown in Figure 3, the input voltage increases and maintain at nearly 60mV. At this time, the ECT310 already produces 5V output because ECT310 just need a minimal of 20mV input to boost to 5V. The supercapacitor charging slowly from 0V until a maximum value of 750.10mV.

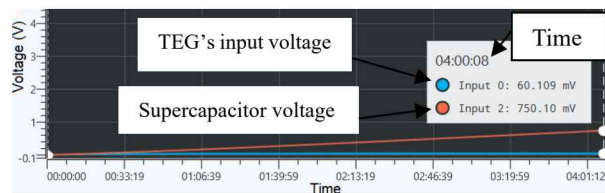


Figure 3 Graph for ECT310 indoor.

Figure 4 shows the TEG input voltage increases from 0 to 405.43mV in 15 minutes and 19 seconds. During this time, the input voltage is less than the MPPT voltage (400mV), thus the MPPT circuit adjusts its inductor current so the voltage input ascends to 400mV. When it reaches 400mV, the MPPT voltage is maintained but the MPPT’s current increases. Thus, the charging of supercapacitor becomes faster. The maximum voltage stored in the supercapacitor is 4.3766V.

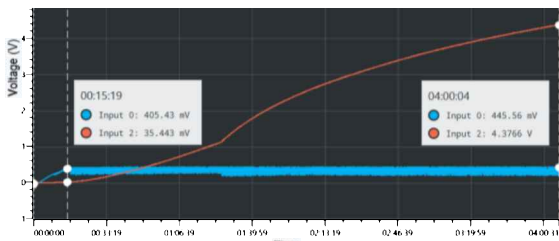


Figure 4 Graph for MPPT DC1577A indoor.

#### 3.2 Part II: Outdoor Test

Based on Figure 5, input voltage increased from 0V and maintain at about 50mV. Supercapacitor final value is 732.34mV.

Figure 6 shows the TEG’s input voltage increases from 0V to 0.4V in about 15 minutes and 5 seconds. The voltage of supercapacitor increases until 4.1524V.

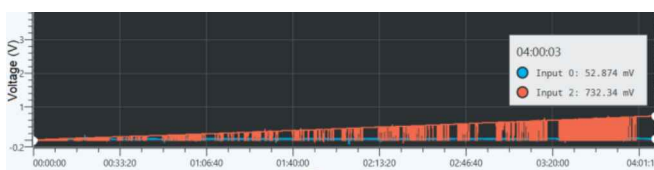


Figure 5 Graph for ECT310 outdoor.

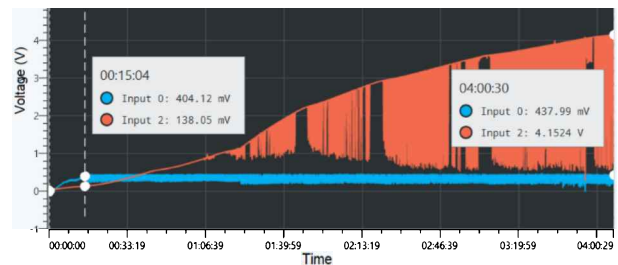


Figure 6 Graph for MPPT DC1577A outdoor.

In comparing for both DC-DC converters, the DC1577A showed more promising ability to charge supercapacitor more efficiently. This is due to the fact of DC1577A is an MPPT which enable it to extract the maximum available power from TEG, while ECT310 is a normal DC-DC converter which only able to produce higher voltage output. Moreover, the experiments showed that the indoor test can charge supercapacitor faster compared to outdoor test because pavement sample does not have to experience external noises such as wind and cloud. Wind can blow cool air to pavement surface which makes the thermal energy is carried away consequently make it cooler than it should be. Cloud movement can also affect the heat absorption from sun because cloud can prevent solar to reach the pavement surface for a short period of time frequently, which makes it less hot.

### 4. CONCLUSION

In conclusion, DC-DC converter for thermal energy harvesting from road pavement can increase voltage input from TEGs to charge supercapacitor. DC-DC converter with MPPT ability (DC1577A) can charge supercapacitor faster 4.1524V compare to normal DC-DC converter 0.732mV within the same period of time. Wind and cloud can affect road pavement heat absorption thus decreasing power output from TEG.

### ACKNOWLEDGEMENT

The authors would like to thank the Universiti Teknikal Malaysia Melaka (UTeM), with Grant No. FRGS/1/2017/TK07/FKEKK-CeTRI/F00337, and the Ministry of Higher Education for the operational and financial support for this project.

### REFERENCES

- [1] Datta, U., Dessouky, S., & Papagiannakis, A. T. (2017). Harvesting thermoelectric energy from asphalt pavements. *Transportation Research Record*, 2628(1), 12-22.
- [2] Mamur, H., & Ahiska, R. (2015). Application of a DC-DC boost converter with maximum power point tracking for low power thermoelectric generators. *Energy Conversion and Management*, 97, 265-272.
- [3] Montecucco, A., Siviter, J., & Knox, A. R. (2012). Simple, fast and accurate maximum power point tracking converter for thermoelectric generators. In *2012 IEEE Energy Conversion Congress and Exposition (ECCE)* (pp. 2777-2783).

# Classroom design attributes: An investigation of staffs' and students' preferences

Hii Ching Lik<sup>1,\*</sup>, Ong Sze Pheng<sup>1</sup>, Chiang Choon Lai<sup>1</sup>, Laura De Pretto<sup>2</sup>, Cheng Heng Pang<sup>3</sup>, Darlene Elizabeth Tan<sup>4</sup>

<sup>1)</sup> Faculty of Science and Engineering, University of Nottingham Malaysia,  
Jalan Broga, 43500 Semenyih, Selangor Darul Ehsan, Malaysia

<sup>2)</sup> School of Social and Health Sciences, Leeds Trinity University,  
Horsforth, Leeds, LS18 5HD, United Kingdom

<sup>3)</sup> Faculty of Science and Engineering, University of Nottingham Ningbo China,  
199 Taikang East Road, Ningbo, 315100 China

<sup>4)</sup> Faculty of Arts and Social Sciences, University of Nottingham Malaysia,  
Jalan Broga, 43500 Semenyih, Selangor Darul Ehsan, Malaysia

\*Corresponding e-mail: Ching-Lik.Hii@nottingham.edu.my

**Keywords:** Classroom; environment; pedagogy

**ABSTRACT** – This exploratory research utilizes interviews and online survey collected from staffs and students and examines on how lecturers and students perceive effective classroom design attributes at the University of Nottingham Malaysia Campus. The studies were carried out among students and staffs from all the faculties namely Engineering, Science, Arts and Social Science. The findings demonstrate how several classroom design attributes relate naturalness, individualization and simulation to students' learning experience. In addition, this research highlights the importance of conducting assessment on classroom redesign initiatives to justify and improve classroom spaces conducive to future generation of students.

## 1. INTRODUCTION

The design, facilities and conditions inside a classroom play significant role in ensuring both lecturers and students experience the best teaching and learning environment, respectively [1]. Literature studies have indicated several design attributes that affect these aspects namely naturalness, individualization and stimulation as described in Table 1 [2].

Table 1 Classroom design attributes.

Design principles	Attributes
Naturalness	Light, sound, temperature, air quality
Individualization	Choice, flexibility, connection
Stimulation	Complexity, colour, texture

Barret et al. [2] investigated the above attributes for primary school students (UK). Current investigation was conducted to collect information among undergraduate students and lecturers at the University of Nottingham Malaysia Campus to determine the key attributes affecting undergraduate classroom design.

## 2. METHODOLOGY

The studies were carried out at the University of Nottingham Malaysia Campus involving students and lecturers from the Faculty of Engineering, Science and Art and Social Science. It consisted of two parts namely

a survey interview to identify the key attributes and an online survey. In Part 1, the interview consisted of 20 students and 11 lecturers (voluntary participants) from various academic backgrounds such as Science, Engineering and Arts & Social Science. During interview, the interviewees were asked about their opinions/comments on their teaching/learning experience in classroom, possible improvement, special requirement in classroom and concept of an ideal classroom etc. All interviews were transcribed and coded using NVivo software (ver. 10 released 2012, QSR International).

In Part 2, an online survey was created based on the feedbacks from part 1. Several key design attributes were identified, and an online survey form was created using Qualtrics software (Qualtrics Int., USA). A total of 374 students participated in the online survey. The survey consisted of 50 questions where the participant needs to rate based on categories such as 'Strongly Disagree', 'Somewhat Disagree', 'Neither agree nor disagree', 'Somewhat Agree' and 'Strongly Agree'.

## 3. RESULTS AND DISCUSSION

Analyses of interviewees' answers in Part 1 confirmed the design attributes as proposed by Barrett et al. [2]. Outcomes from the survey show the following design parameters frequently raised from the interviewees such as (i) Quality and user-friendliness of equipment, (ii) Flexibility of furniture, classroom layout and equipment, (iii) Level of naturalness of the learning environment and (iv) Classroom decoration, especially in terms of walls colours.

However, among the three design principles, individualisation and naturalness seemed to be more important than stimulation as described by both lecturers and students. For example, although wall's colour was mentioned several times during interview, but it was not emphasized as an important attribute. Lecturers preferred plain, light, bright and white colours with minimal décor while students preferred more colourful walls and do not need to be white colour all the times. These very different preferences (lecturers vs students) could be due to generational gap as the current generation of students are more exposed to technology

and requires more stimulating environment [3,4].

Based on the above findings, an online survey questionnaire was developed, and 374 students responded. Key findings are as summarized in Table 2 for questions with more than 80% rating.

**Table 2 Key findings from online survey.**

Question	Agreed & strongly agreed
a) Blinds and/ or curtains should be present, of good quality, in good condition and easily accessible, so that the natural lighting level can be controlled manually.	91%
b) There would be a good sound isolation system, so that noise from the corridors and the outdoor areas would be eliminated.	94%
c) The shape/size of the classroom is such that I can hear the lecturer clearly wherever I am seated.	94%
d) The air conditioning should not be centralized; students and lecturers can decide the ideal temperature is in each lecture.	83%
e) Classroom should be adapted to various learning activities.	84%
f) Classroom should have ergonomic and comfortable furniture.	87%
g) The facilities available in the classroom should be well maintained.	95%
h) The desks/chairs should be comfortable, ergonomic and suitable for both left- and right-hand users.	89%
i) There should be more sockets or ports for electrical device/ laptop.	81%

Based on the above findings, it can be seen that students demanded several attributes such as follows:

- a) Access to natural lighting/air conditioning which is controllable.
- b) Good soundproof system.
- c) Good classroom layout that enable students to hear/see clearly during lecture.
- d) Flexible classroom equipped with ergonomic/comfortable furniture.
- e) Well maintained facilities.
- f) Classroom equipped with more sockets/ports for electrical devices.

#### 4. CONCLUSION

The studies clearly indicate the needs to improve and take into consideration of key classroom design attributes in future. This is to fulfil the needs of both lecturers and students and also to improve the teaching and learning experience.

#### ACKNOWLEDGEMENT

This research was funded by Teaching & Learning Strategic Project Fund, Vice-Provost Office (Teaching & Learning), University of Nottingham Malaysia.

#### REFERENCES

- [1] Tanner, C. K. (2009). Effects of school design on student outcomes. *Journal of Educational Administration*. 47(3), 381–399.
- [2] Barret, P., Zhang, Y., Moffat, J., & Kobbacy K. (2013). A holistic, multi-level analysis identifying the impact of classroom design on pupils' learning. *Building and Environment*. 59, 678-689.
- [3] Rowan, C. (2010). Unplug-don't drug: a critical look at the influence of technology on child behaviour with an alternative way of responding other than evaluation and drugging. *Ethical Human Psychology and Psychiatry*. 12(1), 60-68.
- [4] Rowan, C. (2010). *Virtual Child: The terrifying truth about what technology is doing to children*. CreateSpace, USA.

# Enhancing classroom engagement through web-based interactive tools

Chiang Choon Lai\*, Hii Ching Lik, Ong Sze Pheng, Lim Siew Shee, Tiong Timm Joyce  
Nurzulaikha Rosli

Faculty of Science and Engineering, University of Nottingham Malaysia Campus,  
43500 Semenyih, Selangor Darul Ehsan, Malaysia

\*Corresponding e-mail: cl.chiang@nottingham.edu.my

**Keywords:** Kahoot; Padlet; Socrative

**ABSTRACT** – Technology has seen a recent widespread integration into teaching environments in view of generation Z of students whom has grown up with technology all around them. The study was carried out by conducting online surveys among students from foundation in engineering and undergraduate from Department of Chemical and Environmental Engineering. It examined how students perceive the effectiveness of Web-Based Interactive Tools (WIT) at the University of Nottingham Malaysia (UNM). Key findings demonstrated that the WIT tools were helpful in retaining student interests and encouraged engagement in learning. In addition, this research highlighted the importance of using WIT tools to foster students' engagement and enriched the quality of student learning in the classroom.

## 1. INTRODUCTION

Under the University of Nottingham's Global Strategy 2020, with mission to provide high quality education to students, UNM needs to consolidate and strengthen the teaching quality in order to address the changing expectations from students. It is time to change the ways of teaching to align to the values and learning styles of these new learners, especially Generation Z, which grown up with ubiquitous access to information technology and internet. Generally, the prevalent weakness of typical teaching style at UNM is the overwhelm emphasis on lectures where there is a paucity of two-way interaction between learners and teachers. Laurillard [1] considers the learning process as a kind of conversation and asserts that this process 'must be constituted as a dialogue between teacher and student (or student and student) and operating at the level of description of actions in the world' (see Figure 1). In alignment with the concept proposed by Laurillard, the web-based interactive tool could address the above weak point in a generic way that principally can help in every subject.

Personal response system that was offered by web-based interactive tools could allow students in a class to contribute an anonymous response to the questions queried by the lecturer, providing immediate feedback on the aggregated class responses via Open Ended Questions or Multiple-Choice Questions (MCQ), all of which increase interactivity in lectures for all audience sizes, can use this in any way expressible.

Literatures [2-6] reported the pedagogical benefits of using web-based interactive tools (WIT) in classroom, such as:

- (a) It encourages collaborative learning, which allow students to share information easily and provide opportunity to partake in lesson
- (b) It makes responses/feedbacks anonymous and this encourages more participations from students
- (c) It helps to address a variety of learning styles among students where the learning process fits individual requirements
- (d) It helps knowledge retention instead of just listening to lectures in conventional classroom
- (e) The tools are user friendly. All they (students) need is a device that can be connected to the internet (e.g. smartphone/tablet).
- (f) It makes learning process fun and enjoyable. It can boost engagement and motivation in the classroom.

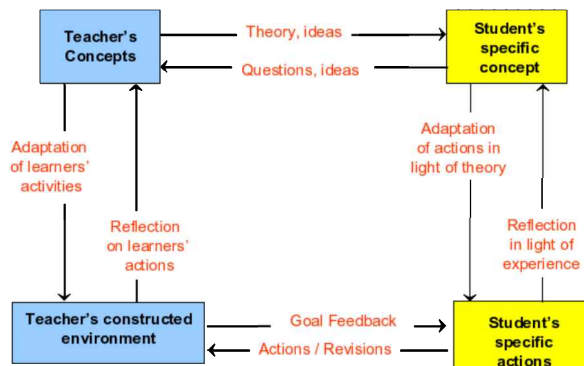


Figure 1 The Laurillard's conversational model [1].

Therefore, seeing the benefits of WIT, the present study aimed to assess the effectiveness of various WIT in enhancing student engagement in class. The main objectives are as follow:

- (a) To explore and assess the features and reliability of selected WIT.
- (b) To evaluate and analyse the student engagement activities when using WIT in class.
- (c) To compare and measure the effectiveness of WIT versus conventional teaching.

## 2. METHODOLOGY

The studies were carried out at the University of Nottingham Malaysia involving students from Foundation in Engineering and undergraduate from Department of Chemical and Environmental Engineering. Three types of WIT, namely Padlet, Kahoot

and Socrative, were explored and evaluated using an online survey. These tools are easy to access and can be downloaded free of charge from the internet. Features of these tools could range from canvas (where users can write their opinions/answers anonymously), clicker (provides instant feedback from students), quizzes/survey and flowchart/diagram/graph. These interactive tools were applied in selected teaching modules from the foundation/undergraduate studies as well as intermediate and advanced level according to Bloom's taxonomy. Observations will be made in class to measure the response of students qualitatively, when these tools are used in the classroom. Students were also invited to fill up survey questionnaires at the end of class to obtain students' feedbacks on the use of WIT versus conventional classroom teaching. The online survey, consisting of 11 questions, was designed using Likert type questions using scale from 1 (strongly disagree) to 5 (strongly agree), and was created using Qualtrics software (Qualtrics Int., USA). Statistical analyses will be carried out using SPSS software upon data collection. Cronbach's alpha test was performed to check the reliability of survey questions, with an alpha value of > 0.70 signifying a good reliability in the results.

### 3. RESULTS AND DISCUSSION

A total of 396 students have participated in this survey. From the total study population, 44% of respondents were from Foundation in Engineering and 56% from Department of Chemical and Environmental Engineering students. The breakdown of the students were shown in Figure 2.

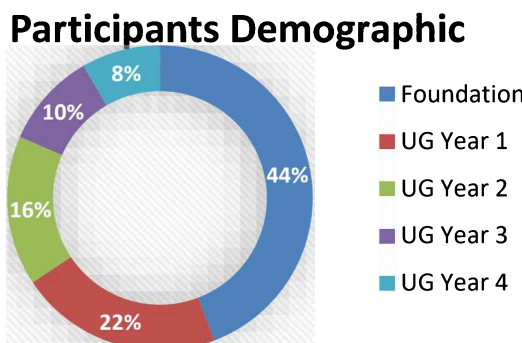


Figure 2 Participants Demographic, where UG: Undergraduate.

Key findings from the survey are summarized in Table 1.

The points below showed some additional feedback obtained from the students regarding the use of WIT (comments are posted as received).

- (a) Padlet is a great way to communicate with the lecturer during class time without having to interrupt his/her teaching flow as they can check padlet when they are ready to address the questions or comments. The fact that it is anonymous as well encourages more people to use it and not be shy. I hope more classes incorporate this sort of communication tool.
- (b) This WIT should be used in all module, to have more interaction with student, create a lively

- class & make students more enthusiast be present
- (c) It's fun and a really interactive way of learning as well as being innovative.
- (d) I think WIT made the learning process more fun and it made my understanding of the subject better. It engaged me to do better every time so i would study the content after class so i could get a better score every time.
- (e) WIT is really an interactive tool and i feel that lectures are made fun through WIT as everyone can actively engage in the learning process. Personally I feel that Kahoot is a really nice tool and it has seen that a lot of lecturers start to appreciate WIT.

Table 1 Key findings from online survey.

Questions	(% Agree & strongly agree)
1. I think the WIT tool is easy to use.	84.1
2. I could focus in every item/question in the WIT activities.	68.7
3. WIT has made the lecture/class more fun and engaging.	85.1
4. WIT has motivated me to learn in the classroom.	64.5
5. WIT has made me keen to participate more in the classroom.	76.8
6. WIT activities has improved my understanding in the covered topic.	65.8
7. WIT activities has enhanced my thinking and problem solving skills.	63.5
8. WIT activities has encouraged me to continue study even after the lecture class.	50.9
9. I think I will attend the class more often if WIT activities is implemented in this course.	61.9
10. I think the lecturer has conveyed his/her enthusiasm for the course through the WIT activities.	79.9
11. I wish these WIT activities are used in other courses as well.	74.4

Additionally, the usage of WIT was mentioned in a Learning Community Forum (LCF) of the Department of Chemical and Environmental Engineering in October 2018, with comment stated: "*Wall for offline communication (padlet.com) is very useful for students not comfortable with speaking aloud; students suggest implementing a similar concept in other lectures to increase interactivity and student engagement.*" Based on the findings above, results showed that:

- (a) > 70% students agreed WIT help them in

- classroom response system (Q1, Q3, Q5, Q10, Q11).  
 (b) 50% - 70 % students agreed WIT bring a lot of interaction to the classroom (Q2, Q4, Q6, Q7, Q8, Q9).

The collated results had also showed a good reliability, with a Cronbach alpha value of 0.919 among the questions. Majority of students enjoyed the competitive/interactive nature of the WIT and comment that it helps them retain knowledge and actively engage in learning. Classroom should be a fun place and lecture should be engaging.

#### 4. CONCLUSION

This work concludes that WIT tools helped to engage students and improve students learning experience at UNM. With the implementation of WIT, we could provide a more conducive learning environment for students. Students will be more proactive and engaged with the lecturers in their learning. This will ensure their knowledge retention in a more effective way and could improve the students' academic performance significantly.

#### ACKNOWLEDGEMENT

This research was funded by Teaching & Learning Funding Scheme 2018, University of Nottingham Malaysia.

#### REFERENCES

- [1] Laurillard, D. (2002). *Rethinking university teaching: A conversational framework for the effective use of learning technologies*. Routledge.
- [2] Licorish, S. A., Owen, H. E., Daniel, B., & George, J. L. (2018). Students' perception of Kahoot!'s influence on teaching and learning. *Research and Practice in Technology Enhanced Learning*, 13(1), 9.
- [3] Plump, C. M., & LaRosa, J. (2017). Using Kahoot! in the classroom to create engagement and active learning: A game-based technology solution for eLearning novices. *Management Teaching Review*, 2(2), 151-158.
- [4] Poon, J. (2013). Blended learning: An institutional approach for enhancing students' learning experiences. *Journal of Online Learning and Teaching*, 9(2), 271-288.
- [5] Coca, D. M., & Sliško, J. (2017). Software Socrative and smartphones as tools for implementation of basic processes of active physics learning in classroom: An initial feasibility study with prospective teachers. *European Journal of Physics Education*, 4(2), 17-24.
- [6] DeWitt, D., Alias, N., & Siraj, S. (2015). Collaborative learning: Interactive debates using Padlet in a higher education institution. *Journal of Educational Technology & Society*, 17(1), 89-101.

# MyMUET – An interactive crowdsourced Malaysia University English Test online learning application

Yarshini Thamilarasan<sup>1,\*</sup>, Raja Rina Raja Ikram<sup>1</sup>, Muliati Sidek<sup>2</sup>

<sup>1)</sup> Center of Advanced Computing Technology (C-ACT), Fakulti Teknologi Maklumat dan Telekomunikasi, Universiti Teknikal Malaysia Melaka, Hang Tuah Jaya, 76100 Durian Tunggal, Melaka, Malaysia

<sup>2)</sup> Pusat Bahasa dan Pembangunan Insan, Universiti Teknikal Malaysia Melaka, Hang Tuah Jaya, 76100 Durian Tunggal, Melaka, Malaysia

Corresponding e-mail: yarshinithamilarasan@gmail.com

**Keywords:** MUET; crowdsource; education

**ABSTRACT** - This paper presents MyMUET, a proposed interactive Online Learning for MUET Examination with crowdsourcing assessment. The design of MyMUET was the result of data collection from ninety one participants and a subject matter expert, an English lecturer. The advantages of MyMUET includes crowdsourced peer-to-peer assessment which are found to be highly correlated with instructor assessment and demonstrate strong inter-rater reliability.

## 1. INTRODUCTION

Recent technologies in education support the use of crowdsourcing for the purpose of creating education contents, provide practical experience for learners, exchanging complementary knowledge and provide evaluation for learner [1]. Crowdsourcing for education is defined as a type of online activity in which an educator, or an educational organization proposes to a group of individuals via a flexible open call to directly help learning or teaching [2]. Actors involved in crowdsourcing includes both human and non-human actors and may be divided into four roles: organizers, learners, contributors, and information technology platforms [3]. This paper shall propose a design of crowdsourcing tutor assessment for MUET to enable flexible participation for educators in the learners education

MUET Malaysia is an English proficiency test administered by the Malaysian Examination Council (MEC). It is also known as the Malaysian University English Test, it is usually taken by students who aim to further their degree studies in Malaysian public universities [4]. The main purpose of E-MUET mobile application is to provide an effective online learning and practice for the students that takes MUET examination [5]. Examination due to insufficient practices and exposure to MyMUET will provide practices for all the four main modules which are reading, writing, speaking and listening.

## 2. METHODOLOGY

A survey was conducted to ninety one participants who have experience sitting for the MUET exam. The

sampling method used was convenience sampling. A MUET subject matter, a UTeM English lecturer was also involved to provide opinion on the current and proposed model or solution for an E-MUET application. Other information that was elicited from the data collection was

- (a) What is the process flow or current framework of the current manual system?
- (b) What are the limitations and technical constraints of the current manual system or process?
- (c) What are the major problems encountered that require the proposed system to solve?

The data obtained from the study was used to design MyMUET, a crowdsourced tutor assessment application.

## 3. RESULTS

A significant number of 90% of students who participated had achieved a band of 3 and above in MUET examination, implying a good command of English in the participants as most university require a band of 2 or 3 and above.

Speaking module has been rated as the toughest examination for the participants. A total of 55.6% or 50 out of 91 students believed that the in-class training provided for MUET is not sufficient to provide practices to score for MUET examination. This is quite alarming as it is a very significant figure.

The current system or framework of registering and sitting for MUET examination is shown in Figure 1. The students are required to attend several coaching classes in their institution before sitting for the exam. The coaching provided by their respective institutions however is deemed not sufficient by the respondents. There is also no approach for those who want to register themselves as tutors to participate in the interaction because the lecturers have been selected by the university and the places are limited. Students also require to sit in groups for their speaking lesson to have more practise according to the MUET format. This is may be time consuming and may only allow practise to take place when there are accessibility to a group of students. Individual speaking practices are not available, decreasing opportunities of self-improvements in the speaking section.

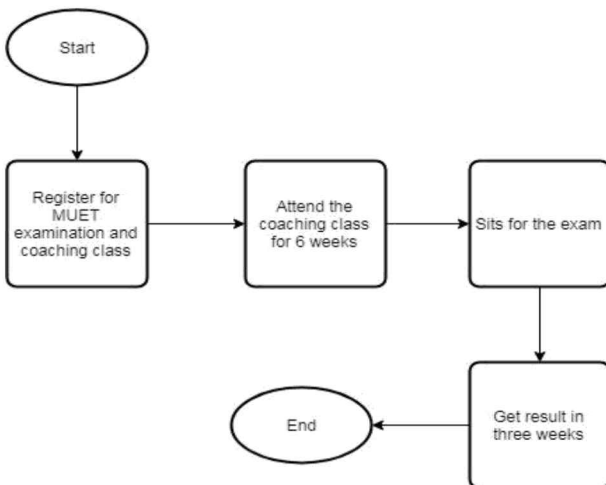


Figure 1 Flowchart of current system.

An overwhelming 76.7% of students also responded that they prefer a combination of classroom and online learning. An astounding figure of 91% of students also supported the idea of using a mobile application. A feature to include feedback for tutor service also was positively received by 88% of participants.

#### 4. PROPOSED SOLUTION

The proposed MyMUET solution process flow is found in Figure 2. Reading is one of the sections that will be tested for the students during examination. A student needs to answer the multiple-choice questions by reading a paragraph given. In the reading module, students will be given practices for their verbs, nouns, vocabulary and grammar. Multiple choice of questions will be given, and it may improve the reading skills of the students. Second section is listening, students need to listen to the audio being played in the examination hall and answer the questions. Meanwhile, listening module in E-MUET application will provide the audio and together with the questions for the students to practice themselves.

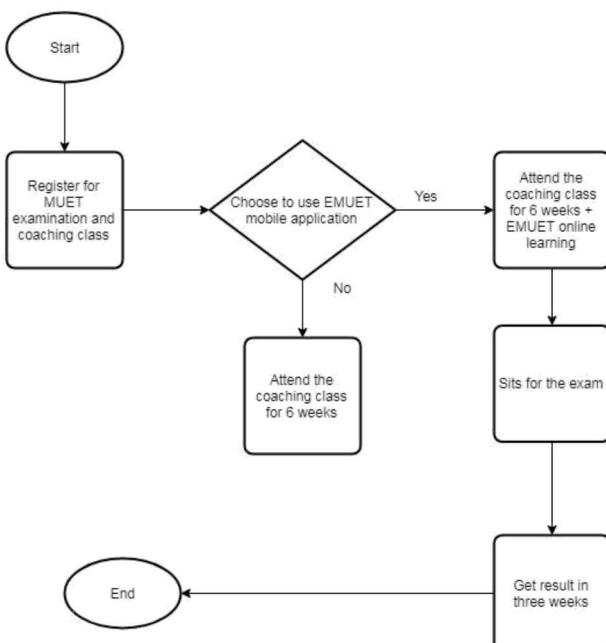


Figure 2 Proposed MyMUET.

The third section is the writing section. The students may submit their writing answer in the application. The final module is speaking. There will be a group of four students who will need to participate according to the given topic for them. Students may improve their speaking skills through this E-MUET mobile application. In E-MUET mobile application, each student may choose their own tutor. The tutor would be providing their feedback for the writing and speaking.

#### 5. CONCLUSION

Challenges still exist to elevate the application of crowdsourcing in education. Invalid, inaccurate, or biased contribution is to be concerned [1,6]. Quality control methods for crowdsourcing in education is significant and need further research [5].

#### REFERENCES

- [1] Jiang, Y., Schlagwein, D., & Benatallah, B. (2018, June). A Review on Crowdsourcing for Education: State of the Art of Literature and Practice. In *PACIS* (p. 180).
- [2] Al-Jumeily, D., Hussain, A., Alghamdi, M., Dobbins, C., & Lunn, J. (2015). Educational crowdsourcing to support the learning of computer programming. *Research and Practice in Technology Enhanced Learning*, 10(1), 13.
- [3] Zahirović Suhonjić, A., Despotović-Zrakić, M., Labus, A., Bogdanović, Z., & Barać, D. (2019). Fostering students' participation in creating educational content through crowdsourcing. *Interactive Learning Environments*, 27(1), 72-85.
- [4] Daniel, F., Kucherbaev, P., Cappiello, C., Benatallah, B., & Allahbakhsh, M. (2018). Quality control in crowdsourcing: A survey of quality attributes, assessment techniques, and assurance actions. *ACM Computing Surveys (CSUR)*, 51(1), 7.
- [5] Rethinasamy, S., & Chuah, K. M. (2011). The Malaysian University English Test (MUET) and its use for placement purposes: A predictive validity study. *Electronic Journal of Foreign Language Teaching*, 8(2), 234-245.
- [6] Ikram, R. R. R., & Ghani, M. K. A. (2015). An overview of traditional Malay medicine in the Malaysian healthcare system. *Journal of Applied Sciences*, 15(5), 723.

# The suitability of the case teaching method and problem-solving strategies to improve problem solving skills of undergraduate: A literature review on mechanical engineering

Tiara Nurhuda<sup>1,2,\*</sup>, Agus Rahmat Hermawanto<sup>2</sup>, Abdul Fatah<sup>2</sup>

<sup>1)</sup> Universitas Bandung Raya, Jawa Barat, 40272, Indonesia

<sup>2)</sup> Sekolah Tinggi Teknologi Bandung, Jawa Barat, 40272, Indonesia

\*Corresponding e-mail: tnurhuda@unbar.ac.id

**Keywords:** Distributed force, mechanical engineering

**ABSTRACT** – Distributed force in mechanical engineering's unit can be package in case studies, then students make models of mechanics and mathematical equations. However, students find it difficult to identify a problem to solve it. Problem solving skills is need by an engineer. In this paper the method of improvement is introduced. The ability to solve problems through a combination of The Case Teaching Method and problem solving strategies are made to be more effective in increasing them.

## 1. INTRODUCTION

Mechanical engineering is the application of the principles and problem-solving techniques of engineering from design to manufacturing to the marketplace for any object. This course is conducive to students' capacity of mechanics analysis required by upper-division courses and engineering practice activities [1]. Mechanics can be defined as that science which describes and predicts the conditions of rest or motion of bodies under the action of forces. It is divided into three parts: mechanics of *rigid bodies*, mechanics of *deformable bodies*, and mechanics of *fluids* [2]. Mathematical and physics-related concepts are extensively covered in the learning process which requires students to have strong abstract thinking and reasoning ability. Equations in physics are only consequences of statement simplification from a process that happens in nature. This kind of presentation causes the loss of some vital concepts in physics that are supposed to invite students to think more deeply [3]. Mechanical engineers need to take active and leading roles in solving these challenges associated with the transformation to a sustainable society. Stakeholders and students are expecting engineering programs to prepare the students for the challenges described above and the education must continuously be developed to meet these needs, see, eg. [4,5].

Case studies have been found to increase students' critical thinking and problem-solving skills, higher-order thinking skills, conceptual change, and their motivation to learn. Despite the popularity of the case study approach within engineering, the empirical research on the effectiveness of case studies is limited and the research that does exist has primarily focused on student

perceptions of their learning rather than actual learning outcomes. The case study approach was rated higher than the traditional lecture approach. Students reported that case studies were better at helping them to improve their communication skills, ability to think critically, and apply the concepts and skills learned in the course [6].

Solving problems effectively requires students to identify, define and solve problems using logic, as well as lateral and creative thinking. In the process, students arrive at a deep understanding of the topic area and construct new knowledge an understanding on which they are able to make decisions [7]. Students need to be able to transfer the ability to solve problems in one context into new and different contexts and situations. Certain aspects of problem solving are transferable, even if the particular problem to be solved is discipline- or context-specific.

## 2. METHODOLOGY

The research method used in this study is a qualitative method. We completed this study in two parts. Part 1 involved a literature search and structured summary. Part 2 consisted of synthesizing the results of the literature review and developing recommendations by an expert panel about teaching practice-based learning and improvement for effective learning in mechanical engineering course.

## 3. RESULTS AND DISCUSSION

This paper examined about distributed force and centroid used the case teaching method and problem-solving strategies. We have assumed so far that the attraction exerted by the earth on rigid body could be represented by a single force. This force, called the force of gravity or the weight of the body, was to be applied at the center of gravity of the body. Actually, the earth exerts a force on each of the particles forming the body. The action of the earth on a rigid body should thus be represented by a large number of small forces distributed over the entire body.

Problem solving is a iterative, or cyclical process. The various steps in the process outlined below need to be carry out and revisited from time to time. Figure 1 shows the combination of the case teaching method and problem-solving strategies.

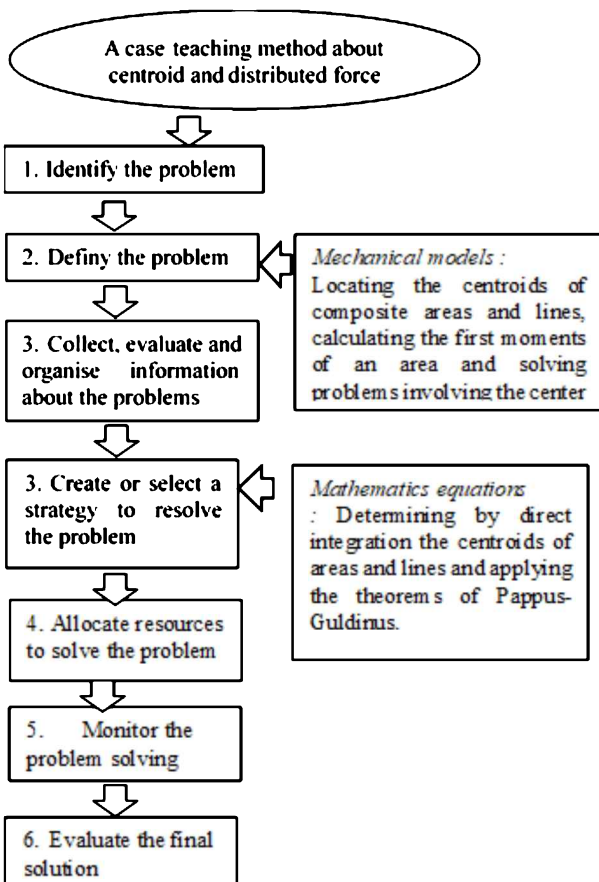


Figure 1 Case teaching method and problem-solving strategies.

#### 4. CONCLUSIONS

The main question raised in this article concerned the suitability of the Case Teaching Method and problem-solving strategies as an overall strategy for engineering education.

We conclude from the literature review and the practical examples that Case Teaching Method and problem-solving strategies can be successfully applied in engineering programs. Problem solving skills reasons to use Case Teaching Method and problem-solving strategies are equally important in engineering. The accent, however, will be more on application and integration of knowledge than on acquisition. In engineering some topics are characterised by a hierachic knowledge structure and complex problem solving.

These topics cannot be approached without risk in Case Teaching Method and problem-solving strategies setting. Therefore, separate direct instruction and supervised practice are needed: direct instruction of outlines, demonstration of expert problem solving, teacher-guided discussions, problem solving tutorials with specially structured group work.

#### REFERENCES

- [1] Ha, O., & Fang, N. (2015). Spatial ability in learning engineering mechanics: Critical review. *Journal of Professional Issues in Engineering Education and Practice*, 142(2), 04015014.
- [2]
- [3] Johnston, E. R., Beer, F., & Eisenberg, E. (2009). *Vector Mechanics for Engineers: Statics and Dynamics*. McGraw-Hill.
- [4] Nurhuda, T., Rusdiana, D., & Setiawan, W. (2017, February). Analyzing students' level of understanding on kinetic theory of gases. In *Journal of Physics: Conference Series* (Vol. 812, No. 1, p. 012105).
- [5] Enelund, M., Knutson Wedel, M., Lundqvist, U., & Malmqvist, J. (2013). Integration of education for sustainable development in the mechanical engineering curriculum. *Australasian Journal of Engineering Education*, 19(1), 51-62.
- [6] Hanning, A., Priem Abelsson, A., Lundqvist, U., & Svanström, M. (2012). Are we educating engineers for sustainability? Comparison between obtained competences and Swedish industry's needs. *International Journal of Sustainability in Higher Education*, 13(3), 305-320.
- [7] Yadav, A., Shaver, G. M., & Meckl, P. (2010). Lessons learned: Implementing the case teaching method in a mechanical engineering course. *Journal of Engineering Education*, 99(1), 55-69.
- [8] Crebert, G., Patrick, C. J., Cragnolini, V., Smith, C., Worsfold, K., & Webb, F. (2011). Problem-solving Skill Toolkit (2nd Edition) (Retrieved from the World Wide Web 4th April, 2011) <http://www.griffith.edu.au/gihe/resources-support/graduate-attributes>

# The impact of EQ, SQ and IQ towards AQ using path analysis and Rasch logit for modelling purpose among mechanical engineering students

Mohd Effendi @ Ewan Bin Mohd Matore\*

Faculty of Education, Universiti Kebangsaan Malaysia, 43600 UKM Bangi, Selangor, Malaysia

\*Corresponding e-mail: effendi@ukm.edu.my

**Keywords:** Emotional Quotient; Spiritual Quotient; Adversity Quotient; Path analysis; Rasch logit; mechanical

**ABSTRACT** – This paper investigated the impact of EQ, SQ and IQ towards AQ among Mechanical Engineering students for modelling purpose using path analysis and Rasch logit. The quantitative approach with survey design involved 383 students using proportionate stratified multistage cluster sampling. The path analysis and multiple regressions revealed 29.2 percent's of AQ may explained by the predictors. The EQ ( $\beta = .337$ ,  $p < .001$ ) was the highest significant impact, followed by SQ ( $\beta = .301$ ,  $p < .001$ ) and IQ ( $\beta = -.02$ ,  $p > .05$ ). The final predictive model was  $AQ = .893 + .288*EQ + .285*SQ - .011*IQ$  with good model fitness.

## 1. INTRODUCTION

Most students are struggle for many pressures from various aspects such as inner and external factors of adversities. Adversity is a difficult situation or event that brings challenges in the lives of people [1]. For technical students, they need to prepare themselves to be a part of Fourth Industrial Revolution (4IR). Oosthuizen [2] stated that ten types of intelligence framework (Fourth Industrial Revolution Intelligence Framework). In Malaysia, we are relying on three dominant types of intelligences such as EQ, SQ and IQ based on National Education Philosophy (NEP) for student self-development. To strengthen this framework of NEP, we see that Adversity Quotient (AQ) was needed as a factor to help students to cope with a variety of challenges of future life, thus actively take up possible challenges in the future [3]. Stoltz [4] defined AQ as the ability of someone to withstand the difficulties and to overcome it. Furthermore, continuous demands of the mechanical industry were encouraged to investigate the impact of Emotional Quotient (EQ), Spiritual Quotient (SQ), and Intellectual Quotient (IQ), towards AQ and how to evaluate purposed models by examining the relationships between all variables.

## 2. METHODOLOGY

The research approach was a fully quantitative with survey research design. The variables involved exogenous (EQ, SQ, and IQ) and endogenous (AQ). The AQ generated based on four constructs of CORE model from IKBAR instrument [5]. EQ was measured by USMEQ-i with seven constructs of (i) emotional control; (ii) emotional maturity; (iii) emotional conscientiousness; (iv) emotional awareness; (v) emotional commitment; (vi) emotional fortitude and (ix) emotional expression [6], SQ was measured by Integrated Spiritual Intelligence Scale (ISIS) with five constructs of (i) consciousness; (ii) grace; (iii) meaning;

(iv) transcendence and (v) truth [7], and the IQ was measured by Ravens Advanced Progressive Matrices (RAPM) which just contained general intelligence [8]. All the instruments have been tested their validity and reliability aspects. The study involved 383 respondents of Mechanical Engineering students using clustered multistage stratified proportional sampling in five polytechnics according to zone (West, North, East, South, and Borneo).

### 2.1 Rasch Measurement Model

Rasch model will transform the ordinal data into interval data through the logits to be applied for regression and path analysis. Rasch Model combines the algorithm that specifies the expected probability of an item as  $i$  and individual capacity as  $n$  in the mathematical form equations. The mathematical formula for the Rasch model is as followed by Bond & Fox [9]. The rating-scale model is an extension of the dichotomous model which items have more than two response categories (e.g., Likert-type scales). In this research, each item has four response choices (1 = strongly disagree, 2 = disagree, 3 = agree, 4 = strongly agree) it is modelled as having three thresholds. The model is represented in the Equation (1).

$$P_i = \frac{\exp[\beta_n - (\delta_i + \tau_k)]}{1 - \exp[\beta_n - (\delta_i + \tau_k)]} \quad (1)$$

Where,

$P_i$  = probability of getting a correct answer for item  $i$

$\beta_n$  = ability parameter for respondent  $n$

$\delta_i$  = difficulty parameter of an item  $i$

$\tau_k$  =  $k$ th threshold

### 2.2 Regression and Path Analysis

Multiple regressions are useful to see the impact based on Beta ( $\beta$ ) coefficients or beta weights that is able to estimates the results that have been standardized so that the variances are one. The extension of the path analysis is multiple regressions. Model from the correlation matrix, two or more causal models are compared. Path analysis is useful to evaluate causal models by examining the relationships between a dependent variable and two or more independent variables. Regression weight is predicated by the model. Then the goodness of fit statistic is calculated in order to see the model fitness through three categories such as absolute fit (Chisq, RMSEA, GFI), incremental fit (AGFI, CFI, TLI, NFI) and parsimonious fit (Chisq/df).

### 3. RESULTS

Multiple regression analysis revealed 29.2 percent's of AQ variance may explained by the predictors. The EQ ( $\beta = .337$ ,  $p < .001$ ) was the highest impact, followed by SQ ( $\beta = .301$ ,  $p < .001$ ) and IQ ( $\beta = -.02$ ,  $p > .05$ ). The final predictive model was  $AQ = .893 + .288*EQ + .285*SQ - .011*IQ$ . It can be used to predict AQ among respondents. The data also relatively normal based on Durbin Watson test (1.802) within the range of 1.5 to 2.5 [10]. However, Hair [11] stated that at least three fit indexes by including at least one index from each category of model fit mentioned in Table 1.

Table 1 The summary of model fitness.

Name of index	Indices value	Comments for level of acceptance
Root Mean Square Error Approximation (RMSEA)	.097	RMSEA with 0.05 to 0.10 Acceptable
Goodness of Fit Index (GFI)	.994	GFI > 0.9 Acceptable
Adjusted Goodness of Fit Index (AGFI)	.941	AGFI > 0.9 Acceptable
Tucker Lewis Index (TLI)	.899	TLI > 0.9 Acceptable
Normed Fit Index (NFI)	.979	NFI > 0.9 Acceptable
Comparative Fit Index (CFI)	.983	CFI > 0.9 Acceptable
Chi-square/ degree of freedom ( $\chi^2/df$ )	4.582	$\chi^2/df \leq 5.0$ is acceptable

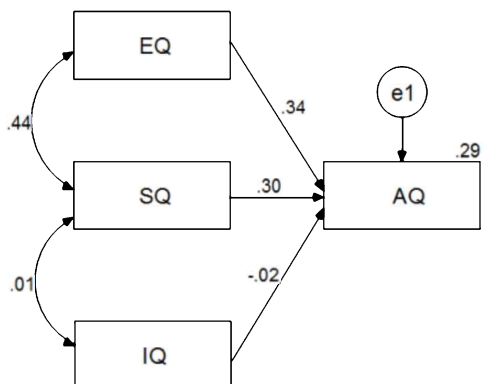


Figure 1 The path analysis.

Figure 1 through the estimates of standardized regression weights shows the moderate and significant impact of EQ and SQ towards AQ. In the other side, the impact of IQ towards AQ is very small and non-significant results. The moderate correlation between EQ and SQ shows the mixture of emotional and spiritual elements are beneficial to AQ compared to IQ.

### 4. SUMMARY

In conclusion, the moderate impact of the EQ and SQ towards AQ statistically shows the potential of these intelligences to be applied in self-resilience programme

development for mechanical students. It proved statistically the relationships between the variables. The newly found results would encourage further studies on exploring new types of intelligences as tested variables.

### ACKNOWLEDGEMENT

This research was supported by the Universiti Kebangsaan Malaysia under the Geran Galakan Penyelidik Muda (GGPM) No. GGPM – 2017 – 088.

### REFERENCES

- [1] Singh, S., & Sharma, T. (2017). Affect of Adversity Quotient on the Occupational Stress of IT Managers in India. *Procedia Computer Science*, 122, 86–93.
- [2] Oosthuizen, J. H. (2017). The determinants of fourth industrial revolution leadership dexterity: A proposed framework for 4IR-intelligence and subsequent 4IR leadership development. *Proceedings of the 4th International Conference on Responsible Leadership*. South Africa: University of Pretoria.
- [3] Bingquan, L., Weisheng, C., Xudong, Z., & Wenxiu, Z. (2019). The Compilation of the Adversity Quotient Scale for College Students. *Psychology and Behavioral Sciences*, 8(1), 9–14.
- [4] Stoltz, P. G. (1997). *Adversity quotient: turning obstacles into opportunities*. Canada: John Wiley & Sons.
- [5] Mohd Effendi, M. M , & Ahmad Zamri, K. (2015). Psychometric assessment on Adversity Quotient instrument (IKBAR) among polytechnic students using Rasch model. *Proceedings of the International Conference on Education and Educational Technologies (EET 2015)* (pp. 52–57). Barcelona, Spain: Institute for Natural Sciences and Engineering.
- [6] Muhamad Saiful Bahri, Y, Ahmad Fuad, A. R., & Ab Rahman, E. (2010). *The USM Emotional Quotient Inventory (USMEQ-i) manual*. Kota Bharu.
- [7] Amram, Y., & Dryer, D. C. (2008). The Integrated Spiritual Intelligence Scale (ISIS): development and preliminary validation. In *116th Annual Conference of the American Psychological Association* (pp. 1–46). Boston.
- [8] Raven, J. C., Court, J. H., & Raven, J. (1977). *Manual for Ravens Progressive Matrices and Vocabulary Scales: Section 4 (Advanced Progressive Matrices Set 1 & 2)*. London: H.K. Lewis & Co. Ltd.
- [9] Bond, T. G., & Fox, C. M. (2015). *Applying the Rasch model: fundamental measurement in the human sciences*. New Jersey: Routledge.
- [10] Field, A. (2009). *Discovering statistics using SPSS*. London: SAGE Publications.
- [11] Hair J. F., Black, W. C., Rabin, B. J. and Anderson, R.E. (2010). *Multivariate Data Analysis* (7<sup>th</sup> ed). Englewood Cliffs, NJ: Prentice Hall.

# Line balancing of two-sided assembly cell in lean manufacturing

Kamarudin Abu Bakar\*, Anis Masyitah Musa

Fakulti Pengurusan Teknologi & Teknousahawan, Universiti Teknikal Malaysia Melaka,  
Hang Tuah Jaya, 76100 Durian Tunggal, Melaka, Malaysia

\*Corresponding e-mail: kamarudin@utem.edu.my

**Keywords:** Lean manufacturing; line balancing; two-sided assembly

**ABSTRACT** – The concept of line balancing is an important part in lean manufacturing. It ensures that effective work will keep improving productivity. In this study, the load balancing down the two-sided assembly work cell of glove making facility have been enhanced by stopper jigs installation and repositioning of operators. Result of the value stream levelling (mura) maximized operation capacity, avoided bottleneck, and achieved new output at maintainable fixed costs. The findings are evidence that this technique is useful in reducing operational wastes (muda). Hence, lean practices successfully enable flexible cells production to be carried out at a constant and predictable rate.

## 1. INTRODUCTION

One of the most important process in gloves making facility is cuffing. Cuff is a part of glove encircling the wrist. It is essential to determine effective cycle time or the repeated gloves entries by practical integration such as u-shaped lines, parallel stations or processing alternatives [1-4]. In defining the underlying concept, an assembly line here involved similar work done manually at individual workstations in the work cells. The cuffed gloves are streamed down from one operator (cuffer) to another until they reach the end of the cell line and pack into boxes. Lean manufacturing can enhance manufacturing capacity by controlling relevant work levelling and waste [4-6]. Thus, the purpose of this research is to investigate efficiency of operators and improve the cuffing speed.

## 2. METHODOLOGY

The objective of this study is to achieve 27 pieces/minute target for each operator (cuffer) and load balancing of higher than 68 packs/min between both sides of workstations at a consistent glove cuffing length of about 210mm (Figure 1). Baseline data for current position cuffing speed is average at 23 pieces/minute per operator (cuffer). So, two solutions were proposed which are by adding-on stopper jig and position rotation (and repositioning) of the cuffers.

### 2.1 Stopper Jigs Installation

Stopper jig (Figure 2) is a component that will help the cuffing process to standardize the length of gloves. Modification of the two-sided assembly line is done by adding stopper jigs at each workstation on the left (L) and right (R) sides that carry similar cuffing process.



Figure 1 Cuff length of gloves.

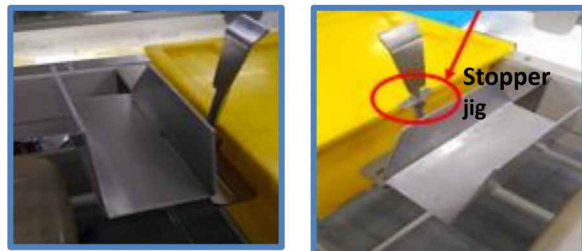


Figure 2 Stopper jig installation on cuffing tool.

### 2.2 Operator's Position Rotation and Repositioning

Figure 3 shows the three cuffers (P) arrangement on left (L) side and right (R) side, who shall each rotate position at P1L, P2L, P3L, P1R, P2R, and P3R. P1 needs to work faster than the other two. While P2 has to cuff the gloves to back up P1, P3 must perform cuffing even faster to back up P1 and P2. The purpose of position rotation is to verify that they are able to produce the best output given different situations. Next, the cuffers repositioning is implemented in which changes only affected the left side, in particular P1L and P2L positions. As operators are right-handed, the change helps P1L and P2L to work comfortably. This is exhibited by Figure 4. The original and new cuff outputs for both sides are recorded. Data collection were carried out for two weeks.

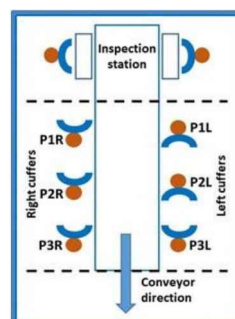


Figure 3 Position rotation.

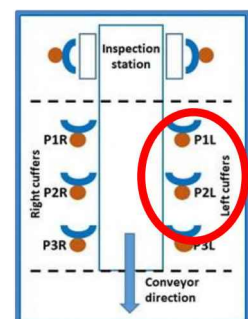


Figure 4 repositioning.

### 3. RESULTS AND DISCUSSION

After two weeks of monitoring, comparison between before and after stopper jigs installation was analysed. Results in Figure 5 clearly demonstrated that the stopper jigs have improved the cuffing speed. The left side cuffers were able to cuff more gloves than the right side. Productivity exceeded the expected target by 30 pieces/min for the left workstations. Stopper jigs have successfully facilitated standardization of the glove's length in the process. The load balancing was improved from 68 packs/minutes to 72 packs/minutes with six cuffers. However, load balancing remains the same for left and right sides of P3 workstations, while P1 and P2 could achieve 70 and 72 packs/minutes respectively. Although the target was positive, cuffers P3 must maintain its critical role to built-up buffers for P1 and P2 because the needs for gloves checking and screening. The cuffers repositioning as in Figure 4 complimented the stopper jigs installation and helped to off-set the cuffing process setback due to rejection and quality issues [7].

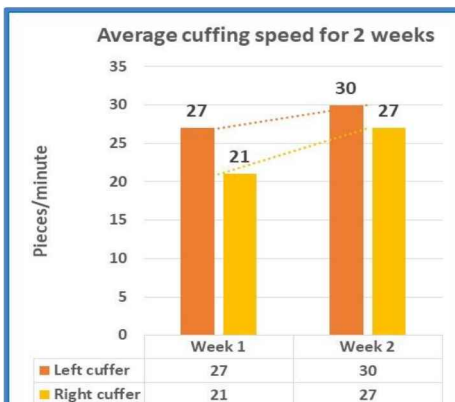


Figure 5 Improved output with stopper jigs.

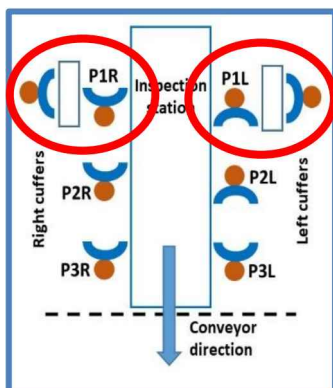


Figure 6 Attachment of P1 with inspection station.

Further analysis as in Figure 6 has indicated another possible solution played by P1L and P1R cuffers. For this case, position 1 attached to the respective inspection stations could save time when loading gloves. The output of position 1 was also improvised on both sides of the workstations. Therefore, it should help position 2 to increase buffers for downstream packing process. The load balancing between all left and right sides workstations was indeed equally effective.

### 4. CONCLUSION

The study presented an effective model to improve two-sided assembly line balancing. In this sense, it was essential to introduce two add-ons modification in the forms of stopper jigs and positions rotation (and reposition) as alternative solutions in lean manufacturing [8]. Left sides workstations showed dominant results compared to the right-hand sides. At no additional cost, the lean value stream or mura as a process-based practice enable production to eliminate muda factors mainly transportation, inventory, motion and waiting wastes that are bottleneck to gloves cuffing process [4,9]. These are achieved by the increase in cuff speed of 27 pieces/min and 72 pieces/min. Hence, it is possible to adopt and maintain flexibility of cells production using two-sided assembly line with right methodology [10]. While this model can be useful for other cell workstations of such nature, various products samples and operators' profiles (and numbers) can be considered for better understanding in the future research of two-sided assembly line.

### ACKNOWLEDGEMENT

The authors like to thank the Centre for Technopreneurship Development (C-TED) and the Sustainable IT-economics, Information Systems, Technology Management & Technopreneurship (SuITE) of the Universiti Teknikal Malaysia Melaka (UTeM) for their support and success conduct of the research.

### REFERENCES

- [1] Grzechca, W. (2009). Assembly line balancing problem single and two-sided structures. In *Automation and Control-Theory and Practice*. IntechOpen.
- [2] Bareduan, S. A., & Elteriki, S. A. (2016). Methodology for solving two-sided assembly line balancing in spreadsheet. *ARPN J. Eng. Appl. Sci.*, 11(10), 6568-6573.
- [3] Gansterer, M., & Hartl, R. F. (2018). One-and two-sided assembly line balancing problems with real-world constraints. *International Journal of Production Research*, 56(8), 3025-3042.
- [4] Qattawi, A., & Chalil Madathil, S. (2019). Assembly line design using a hybrid approach of lean manufacturing and balancing models. *Production & Manufacturing Research*, 7(1), 125-142.
- [5] Naderi, B., Azab, A., & Borooshan, K. (2019). A realistic multi-manned five-sided mixed-model assembly line balancing and scheduling problem with moving workers and limited workspace. *International Journal of Production Research*, 57(3), 643-661.
- [6] Kucukkoc, I., & Zhang, D. Z. (2014). Simultaneous balancing and sequencing of mixed-model parallel two-sided assembly lines. *International Journal of Production Research*, 52(12), 3665-3687.
- [7] Rachmawaty, D., Karningsih, P. D., & Santosa, B. (2018). Two-Sided assembly line balancing to minimize number of workstation with considering the relationships between tasks. In *MATEC Web of Conferences* (Vol. 204, p. 02015). EDP Sciences.

- [8] Lopes, T. C., Michels, A. S., Sikora, C. G. S., & Magatão, L. (2019). Balancing and cyclical scheduling of asynchronous mixed-model assembly lines with parallel stations. *Journal of Manufacturing Systems*, 50, 193-200.
- [9] Make, M. R. A., Rashid, M. F. F., & Razali, M. M. (2016, November). Modelling of Two-sided Assembly Line Balancing Problem with Resource Constraints. In *IOP Conf. Ser. Mater. Sci. Eng.* (Vol. 160, No. 1).
- [10] Özbakır, L., & Tapkan, P. (2011). Bee colony intelligence in zone constrained two-sided assembly line balancing problem. *Expert Systems with Applications*, 38(9), 11947-11957.

# Structural Equation Model (SEM) in assimilating EQ, SQ and AQ for mechanical students' context

Mohd Effendi @ Ewan Bin Mohd Matore\*

Faculty of Education, Universiti Kebangsaan Malaysia, 43600 UKM Bangi, Selangor, Malaysia

\*Corresponding e-mail: effendi@ukm.edu.my

**Keywords:** Emotional Quotient; Spiritual Quotient; Adversity Quotient; Structural equation model; SEM; mechanical students

**ABSTRACT** –This paper investigated the fitness of a measurement model of intelligences for mechanical students using Structural Equation Modelling (SEM). The research was performed on 383 mechanical engineering students chosen randomly in polytechnic. The results using AMOS 21 software from SEM indicated that the measurement model of intelligences with  $\chi^2=198.928$ ,  $p<0.05$ ,  $\chi^2/df = 1.970$ , GFI=0.941, AGFI=0.920, RMR=0.01, CFI=0.977, RMSEA=0.05, provided a better model fit. All factor loadings are ranging from 0.73 to 0.87, with standardized coefficient,  $\beta$  ranging from 0.54 to 0.76. In conclusion, the model proposed represents an adequate description of EQ, SQ and AQ for mechanical students.

## 1. INTRODUCTION

Fourth Industrial Revolution (4IR) Intelligence Framework suggested by Oosthuizen [1] concentrating on ten types of intelligences. In Malaysia, we are count on three dominant types of intelligences such as EQ, SQ and IQ based on National Education Philosophy (NEP) for student self-development. This research will be testing new measurement model provided for technical students especially for mechanical students with the added value of AQ to the framework. The basic idea is to see how well the combinations of existing intelligences such as IQ and SQ can be strengthen with the third element of intelligence i.e AQ. The combination of EQ, SQ and AQ is important because previous research by Effendi [2] proved empirically that EQ and SQ had a moderate correlation with AQ among polytechnic students. However, IQ shown very weak correlation with AQ and this study clearly boost a motivation on how the EQ and SQ has a potential to be assimilated with AQ from technical student context worldwide. Technical field are closely related to the 4IR in terms of the intelligences need to be acquired by the students. The framework is not emphasized directly to AQ even though this factor is vital to face the challenges. Stoltz [3] defined AQ as the ability of someone to withstand the difficulties and to overcome it. This paper will be investigating the measurement model fitness of intelligences for mechanical students using Structural Equation Modelling (SEM).

## 2. METHODOLOGY

The research approach was a fully quantitative with survey research design. The variables involved exogenous (EQ, SQ, and IQ) and endogenous (AQ). The AQ generated based on four constructs of CORE model

from IKBAR instrument [4]. EQ was measured by USMEQ-i with seven constructs of (i) emotional control; (ii) emotional maturity; (iii) emotional conscientiousness; (iv) emotional awareness; (v) emotional commitment; (vi) emotional fortitude and (ix) emotional expression [5], SQ was measured by Integrated Spiritual Intelligence Scale (ISIS) with five constructs of (i) consciousness; (ii) grace; (iii) meaning; (iv) transcendence and (v) truth [6]. The suitability of the instruments have been tested from Effendi [2] for their validity and reliability. However, the previous research was not providing evidence on factor loading for each item. This research will fill the gaps by investigate the quality by interlinking the items in one model for the application for local context. The study involved 383 Mechanical Engineering students using clustered multistage stratified proportional sampling in five polytechnics according to zone (West, North, East, South, and Borneo). The results analysed using AMOS 21 software and useful in Structural Equation Modelling, path analysis, and confirmatory factor analysis. SEM can be defined as CFA and multiple regressions because SEM is more of a confirmatory technique, but it also can be used for exploratory purposes. SEM, in comparison with CFA, extends the possibility of relationships among the latent variables and encompasses two components: (a) a measurement model (essentially the CFA) and (b) a structural model.

## 3. RESULTS

Figure 1 shows both the standardized beta estimate of intelligences are moderate ( $\beta = .31$  and  $.34$ ) with measure correlation of EQ and SQ is  $.40$ . The value of R<sup>2</sup> indicated EQ and SQ contributed 29% in estimating AQ. The 71% may affected by other factors that can be investigate such as another types of intelligences or any other internal or external factors. Durbin Watson test (1.802) also revealed that the data relatively normal and within the range of 1.5 to 2.5 [7]. In Structural Equation Modelling, there is a series of goodness of fit statistic in order to see the model fitness through three main categories such as Absolute Fit (Chisq, RMSEA, and GFI), Incremental Fit (AGFI, CFI, TLI, NFI) and Parsimonious Fit (Chisq/df) [8]. Md Fauzi Ahmad [9] stated that the general model of goodness of fit is assessed using six criteria such as Chi-square/ degree of freedom ( $\chi^2/df$ ), Goodness of Fit Index (GFI), Adjusted Goodness of Fit Index (AGFI), Comparative Fit Index (CFI), Tucker Lewis Index (TLI) and Root Mean Square Error Approximation (RMSEA). However, Hair [10]

stated that at least three fit indexes by including at least one index from each category of model fit mentioned in Table 1. The researcher could choose at least one fitness index from which category to report in depending on literature is being referred.

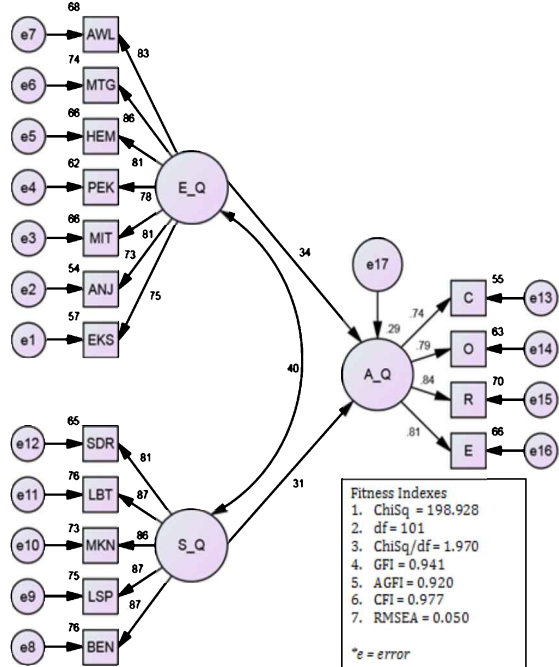


Figure 1 The measurement model.

Table 1 show the validity of the construct is defined as how well the proposed model is compared to the observed data. Initially, the measurement model provided a good fit. The  $\chi^2/df$  was 1.97 ( $\chi^2=198.928$ ,  $p<0.05$ ,  $df = 101$ ). Furthermore, the GFI was 0.941, AGFI=0.920, RMR=0.01, CFI=0.977, RMSEA=0.05 (see Table 1). All factor loadings are ranging from 0.73 to 0.87, with standardized coefficient,  $\beta$  ranging from 0.54 to 0.76. All fitness indexes are accepted.

Table 1 The summary of fitness index.

Name of index	Indices value	Level of acceptance
$\chi^2/df$	1.970	$1.0 \leq \chi^2/df \leq 3.0$
RMSEA	.050	$RMSEA \leq 0.08$
GFI	.941	$GFI \geq 0.9$
AGFI	.920	$AGFI \geq 0.9$
TLI	.973	$TLI \geq 0.9$
NFI	.954	$NFI \geq 0.9$
CFI	.977	$CFI \geq 0.9$

Modification indices (MI) shows only one pair (e7 <-> e12; 15.112) is considered high and deemed to be redundant which is above 15 as stated by Zainuddin [11]. No modification needed because the items are not in the same construct. In the other side, this measurement model with combination of three intelligences is fit with the mechanical students. This result will open more discussions on how we can strengthen the resilience element using EQ and SQ.

#### 4. SUMMARY

The suggested model proven statistically that other intelligence purely had high potential to be applied for technical students in facing the 4IR adversities. The research impact is to open the door on how to improve the NEP that only emphasized on EQ and SQ from original framework. The newly found results would encourage further studies on exploring new types of testing for item development and assessing the fitness for new items created.

#### ACKNOWLEDGEMENT

This research was supported by the Universiti Kebangsaan Malaysia under the Geran Galakan Penyelidik Muda (GGPM) No. GGPM – 2017 – 088.

#### REFERENCES

- [1] Oosthuizen, J. H. (2017). The determinants of fourth industrial revolution leadership dexterity: A proposed framework for 4IR-intelligence and subsequent 4IR leadership development. *Proceedings of the 4th International Conference on Responsible Leadership*. South Africa: University of Pretoria.
- [2] Mohd Effendi, M. M., Matore, E. M., & Khairani, A. Z. (2016). Correlation between Adversity Quotient (AQ) with IQ, EQ and SQ Among Polytechnic Students Using Rasch Model. *Indian Journal of Science and Technology*, 9(47), 1-8.
- [3] Stoltz, P. G. (1997). *Adversity quotient: turning obstacles into opportunities*. Canada: John Wiley & Sons.
- [4] Mohd Effendi, M. M , & Ahmad Zamri, K. (2015). Psychometric assessment on Adversity Quotient instrument (IKBAR) among polytechnic students using Rasch model. *Proceedings of the International Conference on Education and Educational Technologies (EET 2015)* (pp. 52–57). Barcelona, Spain: Institute for Natural Sciences and Engineering.
- [5] Muhamad Saiful Bahri, Y, Ahmad Fuad, A. R., & Ab Rahman, E. (2010). *The USM Emotional Quotient Inventory (USMEQ-i) Manual*. Kota Bharu.
- [6] Amram, Y., & Dryer, D. C. (2008). The Integrated Spiritual Intelligence Scale (ISIS): development and preliminary validation. In *116th Annual Conference of the American Psychological Association* (pp. 1–46). Boston.
- [7] Field, A. (2009). *Discovering statistics using SPSS*. London: SAGE Publications, 2009.
- [8] Zainuddin, A. (2013) *Structural Equation Modeling Using AMOS Graphic*, 2nd ed. Shah Alam: UiTM Press.
- [9] Md. Fauzi, A.M. (2017) *Application of Structural Equation Modelling (SEM) in Quantitative Research*, 1st ed. Batu Pahat: Penerbit UTHM.
- [10] Hair J. F., Black, W. C., Rabin, B. J. and Anderson, R.E. (2010). *Multivariate Data Analysis* (7<sup>th</sup> ed). Englewood Cliffs, NJ: Prentice Hall.
- [11] Zainuddin, A. (2012) *A Handbook on SEM (5<sup>th</sup> ed)*. Kota Bharu: UiTM.

# Variability in the group's academic background is weakly associated to the outcome of a Problem-Based Learning project attainment for engineering undergraduates

Nurdiana Nordin\*, Fariz Ali @ Ibrahim, Muhammad Herman Jamaluddin

Fakulti Kejuruteraan Elektrik, Universiti Teknikal Malaysia Melaka,  
Hang Tuah Jaya, 76100 Durian Tunggal, Melaka, Malaysia

\*Corresponding e-mail: nurdiana@utem.edu.my

**Keywords:** Problem-based Learning; engineering undergraduates

**ABSTRACT** – In the Problem-based learning curriculum, problem drives learning. Studies have shown that the successful learning process in the PBL assignment may rely on group composition. Thus, this study focuses on one of the group's attributes: the member's prior academic achievement variability. A Spearman rank-order correlation analysis was performed to determine the association between dispersion of individual Cumulative Grade Point Average (CGPA) from the Mean Group CGPA and the final marks of the Problem-Based Learning project. A significant but weak correlation was found. Thus, it can be concluded that prior academic achievement is weakly associated with the outcome of PBL project.

## 1. INTRODUCTION

Problem-based learning is pedagogical methodology by which learning is initiated by a posed problem. Problem-based learning course is introduced to engineering undergraduates to stimulate a process of determining engineering solution, which is by nature, is their calling when they are in the job market.

Students are typically placed in a group and assume roles that needed them to reconvene to integrate the information, generate and evaluate possible solutions, make needed decisions and communicate results as appropriate for the problem resolutions [1].

With various roles and responsibilities, it is indeed a challenge for every group to harness the members' strengths and downplay their weaknesses to emerge successfully as a team. Hence this study is conducted to find the relationship between the individual dispersion from the group's average CGPA with the outcome of the Problem-Based Learning project through the final project marks.

## 2. PREVIOUS WORK

In a study focusing on the ingredients contributing to a successful problem-based learning, Schmidt et al. concluded that the extent of learning in PBL results from neither group collaboration only nor individual knowledge acquisition only; both activities contribute equally to learning in PBL [2]. This finding shows that the basis of group formation is important to ensure that outcomes of problem-based learning can be maximized. Yeo in his studies involving human dynamics in PBL assignments [3], had pointed out that it is essential that students' learning ability and social adaptability be carefully considered in any PBL group formation. Hence,

this study is directed towards highlighting one of the bases of the group formation: the prior academic performance of the group.

## 3. METHODOLOGY

A sample of 81 students (22 females) enrolled to BEKM 4753: Programmable Logic Controller (PLC) and Automation subject was used for this study. All students were in their third year of Bachelor of Mechatronics Engineering program. Their Cumulative Grade Point Average (CGPA) in the prior semester is used obtain the Mean Group CGPA and subsequently the dispersion of individual from their group's mean. The total marks of PBL is 20% which consist of 4% from Technical Report, 4% from Oral presentation, 6% from Prototype Quality, 4% from Project Progress and 2% from Peer Assessment. The total marks of the Problem-Based Learning project and the dispersion of the individual from their group's mean CGPA are used as the dependent and independent variable respectively.

The mean group's CGPA is calculated by taking the average of all the group member's prior semester's CGPA. Then the dispersion of each individual is calculated by computing sample's standard deviation of each individual CGPA to his respective mean group's CGPA. Table 1 explains the demographic of the data which also includes the mean and standard deviation of each variable.

Table 1 The demographic of the samples.

Demographic	Data
Student's Mean CGPA	3.07±0.5
Mean Group's CGPA	3.07±0.25
Mean PBL marks	16.55±1.18

The title of the PBL project is 'The design, development and control of a miniature chocolate wrapping work cell'. Students were divided into a 4 to 5-members per group. Students were informed of the title and project members as early as Week 3 in the semester and the presentation is at Week 13. A total of 6 weeks of brainstorming was set for the group to discuss ideas and proposed a solution. Then, students were allowed to work in the PLC lab for 4 weeks prior to the presentation week to come out with a prototype of the solution. Students were assessed in terms of the quality of the prototype, design progress and report writing. A total of 20 marks is the maximum possible marks to attain.

A Spearman's rank-order correlation analysis [4] was performed in SPSS (SPSS Inc.) to this sample to determine whether the outcome of the Problem Based Learning project can be explained by the student's CGPA dispersion from the average group's CGPA. The hypothesis of this research is that the outcome of the PBL project has a strong relationship to the variability of the prior academic performance in the group.

#### 4. RESULTS

Figure 1 summarizes the attainment for the PBL project. The maximum marks that they can attain is 20. The mean is at 16.55 which is at the highest quarter of the maximum marks attainable. It is evident in Figure 2 that the data was not normally distributed, thus a Spearman's rank-order correlation analysis is performed to evaluate the results.

The Spearman rank-order correlation calculates a coefficient,  $r_s$  or  $\rho$  which is a measure of the strength and direction of the association. The coefficient,  $r_s$  or  $\rho$  is obtained from the following equation.

$$\rho = 1 - \frac{6 \sum d_i^2}{n(n^2 - 1)}$$

Where  $n$  is the number of samples and  $d$  is the difference between ranks.

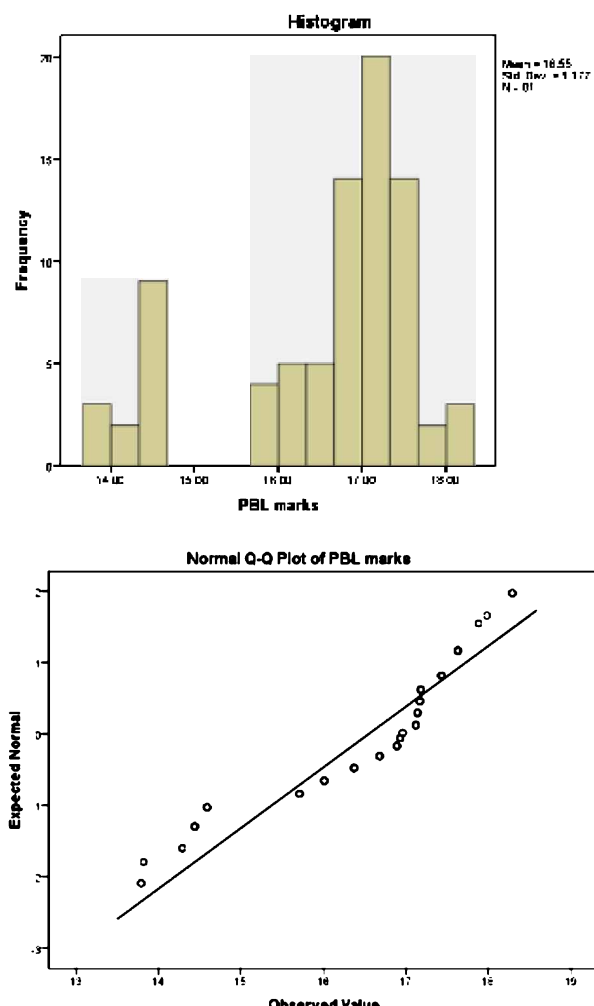


Figure 1 Distribution of the PBL project marks.

#### 4.1 Analyzing Monotonic Relationship

A pre-requisite to run a Spearman's rank coefficient analysis is the evidence of monotonic relationship. Figure 2 shows a scatterplot between the two variables in the study.

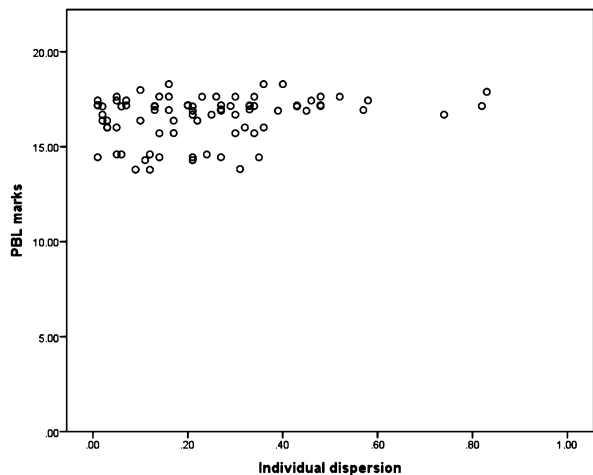


Figure 2 Plot of PBL marks attained against the individual dispersion from the group's mean CGPA.

It can be concluded from the visual inspection that there is a monotonic relationship between the individual dispersion of CGPA from their group's mean CGPA and the PBL marks, thus the Spearman's rank coefficient analysis is a viable option to investigate the relationship.

#### 4.2 Spearman's Rank-Order Correlation

There was a statistically significant, weak positive correlation between the individual dispersion of CGPA from their group's mean CGPA and the PBL marks in BEKM 4753: PLC and Automation course,  $r_s(81) = .222$ ,  $p < .046$ . Therefore, it can be concluded that based on the result obtained from this course, the previous academic scores are weakly associated with the attainment of the PBL marks. It is also supported from the data plotted in Figure 2. Even an individual dispersion from group's CGPA is up to 0.8, the PBL mark is similar to the one's that had a CGPA at the group average.

#### 5. SUMMARY

Problem-based learning is crafted to mirror real-world demands. Previous research claimed that the learning process is contributed equally from individuals and group ideas. This study attempted to support the idea by looking at one of the aspects of PBL group's attributes: academic variation. It can be seen from the results of this course that prior academic achievements are weakly correlated with the attainment of the PBL project marks.

This result may induce two contrasting perspectives. The weaker students may either receive over-performed assessment marks because their respective group members are able to downplay their weaknesses, or the assessments were unable to capture the variability of the group's performance and roles at the individual level. These perspectives warrant a further study on the achievement at subject level to investigate whether the learning process in PBL project translates to

the individual attainment.

**REFERENCES**

- [1] Azer, S.A. (2004). Becoming a student in a PBL course: twelve tips for successful group discussion. *Medical Teacher*, 26(1),12-15
- [2] Schmidt, H. G., Rotgans, J. I. and Yew, E. H. (2011). The process of problem - based learning: what works and why. *Medical Education*, 45, 792-806.
- [3] Yeo, R. (2005). Problem - based learning: lessons for administrators, educators and learners. *International Journal of Educational Management*, 19(1), 541-551.
- [4] Laerd Statistics (2018). Spearman's correlation using SPSS Statistics. Statistical tutorials and software guides. Retrieved from <https://statistics.laerd.com/>

# Parameter effects on thrust force for one-shot drilling of carbon fibre reinforced plastics (CFRP)

Mohd Fairuz Jaafar<sup>1</sup>, Mohd Shukor Salleh<sup>1,\*</sup>, Raja Izamshah Raja Abdullah<sup>1,2</sup>, Muhamad Hafiz Hassan<sup>3</sup>, Mohammad Shah All-Hafiz Mohd Shahrim<sup>1</sup>, Syahrul Azwan Sundi @ Suandi<sup>1</sup>, Mohd Shahir Kasim<sup>1,2</sup>

<sup>1)</sup> Fakulti Kejuruteraan Pembuatan, Universiti Teknikal Malaysia Melaka,  
Hang Tuah Jaya, 76100 Durian Tunggal, Melaka, Malaysia

<sup>2)</sup> Precision Machining Group, Universiti Teknikal Malaysia Melaka,  
Hang Tuah Jaya, 76100 Durian Tunggal, Melaka, Malaysia

<sup>3)</sup> School of Mechanical Engineering, Universiti Sains Malaysia, 14300 Nibong Tebal, Pulau Pinang, Malaysia.

\*Corresponding e-mail: shukor@utem.edu.my

**Keywords:** One-shot drilling; thrust force; CFRP

**ABSTRACT** – In this work, parameter effects on thrust force for one-shot drilling of CFRP was conducted. A total of eight parameters has been selected in order to study against thrust force generated — an experiment using L<sub>18</sub> Taguchi design to evaluate the contribution percentage of thrust force. Analysis of variance (ANOVA) and signal-to-noise (S/N) ratio statistical tools were used to obtain the most significant parameters contributes to high thrust force measurement. Dominating parameters contribution to thrust force are drilling feed rate (71.72%) for machining parameter and drill point angle (14.48%) for drill geometrical feature parameter.

## 1. INTRODUCTION

Aircraft manufacturing had been expanding throughout the last decades. The need for lightweight, high strength to weight ratios and stiffness to weight ratios structural parts are critical to manufacturing the aircraft. Carbon fibre reinforced plastic (CFRP) is the most adopted materials due to its mechanical properties excel and near net shape production. The drilling process is mandatory in the assembly of CFRP to make holes for bolts and rivets.

Due to its strong anisotropy and bond strength, thrust force produced during drilling leads to delamination damage. Urgent needs to optimise drill geometry to lowered the thrust force generated is mandatory for exhibits drilling induced delamination. Drill types are differentiated with drill bit fluting and geometry. Numerous investigations among researchers to study the effects of thrust force using standard twist drill and unique drill bit geometry to enhance drilled holes quality[1] but still lack study regards to special drill optimisation. This study concentrates on contributions of parameters to thrust force for one-shot drilling of CFRP.

## 2. DETAILS OF EXPERIMENT

### 2.1 Experimental Setup, Material and Drill

The drilling process was conducted using 15kW DMU40 monoBLOCK® Deckel Maho CNC machining centre. The workpiece was clamped using a backing plate specially made for this experiment to constrain any vibration during drilling process that may clout thrust

force measurement data[2]. The Kistler dynamometer was placed beneath the vice and measurement data processed using DynoWare software. Figure 1 shows the experimental setup conducted. There was no pilot hole made for all drilled hole. No coolant has also been used in the experiment to prevent any contamination.

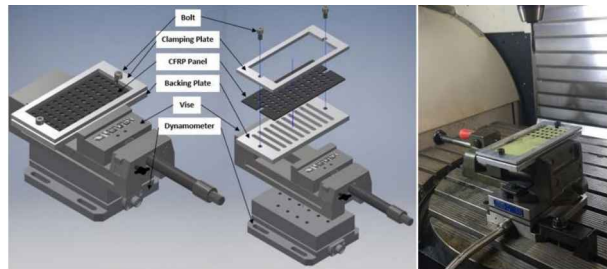


Figure 1 Experimental setup.

The workpiece of CFRP composite laminates used in this experiment thickness was 3.587 mm in total after base paint application and consisted of 26 unidirectional plies manufactured by local aircraft composite manufacturer. Areal density for CFRP and woven fabrics is 203 g/m<sup>3</sup> and 107 g/m<sup>3</sup>, respectively. After the curing process, the laminates compacted to achieve a nominal volume fraction of 60%.

The drilling trials were executed using 6.35 mm special one-shot drill. All drills were fabricated into 18 different geometrical features by Walter Helitronic Mini Power CNC grinding centre and made from tungsten carbide (WC 93% & Co 7%). Geometrical features of drill design are shown in the next section.

### 2.2 Taguchi's Design of Experiments

The multiple runs were conducted and treated using S/N ratio is the approach used in this experiment[3]. Taguchi's experimental design of L<sub>18</sub> was used to establish the optimum parameters for the thrust force factor. There were five drill geometry parameters in the experimental design, including three machining parameters in a total of 8 parameters selected. Table 1 shows the L<sub>18</sub> Taguchi orthogonal array design factors assigned for the present study. Figure 2 shows the variation of drill geometry in the experiments.

Table 1 L<sub>18</sub> Taguchi orthogonal array design.

Factor	Level 1	Level 2	Level 3
1: Drilling angle (°)	0°	5°	
2: Spindle speed (rpm)	1000	2000	3000
3: Feed rate (mm/rev)	0.05	0.10	0.15
4: Point angle (°)	90	100	110
5: Web thickness (%)	15	17.5	20
6: Helix angle (°)	0	5.5	11
7: First primary clearance (°)	6	7.5	9
8: Second primary clearance (°)	10	12.5	15

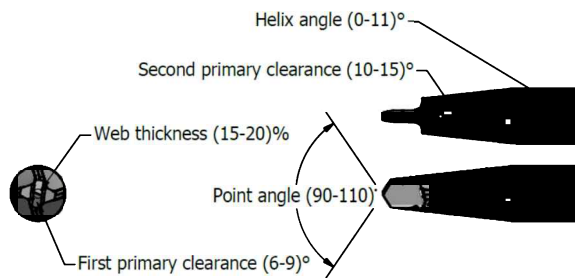


Figure 2 Variation of drill geometrical features.

### 3. RESULTS AND DISCUSSION

Table 2 shows the results and analysis of the S/N ratio and Table 3 show the contribution percentage for maximum thrust force based on ANOVA. Feed rate parameters contribute to the most significant contribution percentage as much as 71.72%, followed by point angle parameter and spindle speed parameters for 14.48% and 6.93%, respectively.

Table 2 Experimental results

Maximum thrust force, F <sub>tmax</sub> (N)			
Trial	F <sub>tmax</sub> 1	F <sub>tmax</sub> 2	S/N ratio
1	78.55	79.07	-37.93
2	117.00	109.60	-41.09
3	179.60	175.70	-44.99
4	63.52	69.92	-36.50
5	127.00	121.40	-41.88
6	155.20	150.70	-43.69
7	68.36	67.72	-36.66
8	112.30	114.40	-41.09
9	130.50	127.10	-42.20
10	91.25	95.71	-39.42
11	91.52	90.94	-39.20
12	173.30	175.50	-44.83
13	76.26	77.51	-37.72
14	133.30	130.20	-42.40
15	116.20	116.50	-41.32
16	83.01	85.69	-38.52
17	91.56	92.22	-39.27
18	116.30	119.90	-41.45

Feed rate is the dominating machining parameter that profoundly influenced thrust force measurement. This finding coincides with numerous previous study conducted on drilling thrust force[4]. Increasing feed will

increase thrust force measurement. For the cutting tool geometry, point angle most influenced the thrust force measurement. Smaller point angle will decrease the thrust force due to a small sharp tip indenting composite laminates until last plies.

Table 3 Contribution of S/N ratio for F<sub>tmax</sub>.

Parameter	Standardized Effects	Sum of Squares	% Contribution	Rank
Drilling penetration angle	-40.46	0.21	0.62	7
Spindle speed	-39.86	1.38	6.93	3
Feed rate	-37.79	5.29	71.72	1
Point angle	-39.4	2.28	14.48	2
Web thickness	-40.22	0.69	1.21	6
Helix angle	-40.43	0.33	0.31	8
First primary clearance	-40.16	1.14	2.75	4
Second primary clearance	-40.4	0.37	1.96	5

### 4. SUMMARY

The conducted experiments results are summarized as follows:

- (a) The significant factors of drilling process determined by ANOVA. The dominating factor is the machining feed rate and drill point angle for 71.72% and 14.48%, respectively.
- (b) The thrust force is increased when increasing the machining feed rate.
- (c) Smaller drill point angle contributes to low thrust force measurement.

### REFERENCES

- [1] Rajakumar, I. P. T., Hariharan, P., & Vijayaraghavan, L. (2012). Drilling of carbon fibre reinforced plastic (CFRP) composites - A review. *International Journal of Materials and Product Technology*, 43(1–4), 43–67.
- [2] Dogrusadik, A., & Kentli, A. (2017). Comparative assessment of support plates' influences on delamination damage in micro-drilling of CFRP laminates. *Composite Structures*, 173, 156–167. <https://doi.org/10.1016/j.compstruct.2017.04.031>
- [3] Izamshah, R., Akmal, M., Kasim, M. S., Sued, M. K., Sundi, S. A., & Amran, M. (2018). Parametric Study on Parameter Effects in Hybrid Micro Wire Electrical Discharge Turning. *Journal of Advanced Manufacturing Technology (JAMT)*, 12(1), 1–12.
- [4] Su, F., Wang, Z., Yuan, J., & Cheng, Y. (2015). Study of thrust forces and delamination in drilling carbon-reinforced plastics (CFRPs) using a tapered drill-reamer. *International Journal of Advanced Manufacturing Technology*, 80(5–8), 1457–1469.

# Conceptualizing new product development by inserting value via blue ocean strategy

M.F.M. Sam<sup>1,3</sup>, H. Hafizuddin<sup>1</sup>, B.C. Chew<sup>1</sup>, Sivaraos<sup>2</sup>, Y.F. Yusof<sup>1</sup>

<sup>1)</sup> Fakulti Pengurusan Teknologi dan Teknousahawan, Universiti Teknikal Malaysia Melaka,  
Hang Tuah Jaya, 76100 Durian Tunggal, Melaka, Malaysia

<sup>2)</sup> Fakulti Kejuruteraan Pembuatan, Universiti Teknikal Malaysia Melaka,  
Hang Tuah Jaya, 76100 Durian Tunggal, Melaka, Malaysia

<sup>3)</sup> Centre for Robotics and Industrial Automation, Fakulti Kejuruteraan Elektrik, Universiti Teknikal Malaysia Melaka,  
Hang Tuah Jaya, 76100 Durian Tunggal, Melaka, Malaysia

**Keywords:** New product development; value; blue ocean strategy; tire technology

**ABSTRACT** – In today's world that is full of uncertainty, the number of new products to achieve a breakthrough innovation in the industry are relatively low. Based on previous research, the researcher has discovered that all this successful product has shares a similar trait that help them to seize the market which is the element of value. This value has been receiving a lot of attention and has been deemed as one of the most significant factors to help new product to achieve a sustainable business and market success. When the first air-filled rubber tires were invented by Dunlop on 1888, the number of acceptances was low, and it took a total of three years to be accepted by the consumer. This indicates that consumers are not aware of its value and it is difficult to integrate value into a new product. We believed that if the element of Value can be embedded into the New Product using the Blue Ocean strategy, it can represent the next step in a long innovation path for tire industry. Therefore, the main objective of this research is to focus on a strategy that could help the Airless tires Modula Wheel to develop their own value which that can reconstruct the current market. The research design that was used is the exploratory research and the data that was analyzed will be using the qualitative method. Thus, at the end of this research there will be a model that integrates the element of value into New Product Development Process.

## 1. INTRODUCTION

Marketing research conceptualizes that the innovation process is composed of a few phases that start from idea generation to commercialization. While the New Product Development is entrenched in the innovation process and is the prelaunch part of the innovation process. Because of this, the New Product Development was defined as all the new offering that a company can develop no matter, they are tangible goods, new technologies or even new services Cambridge [1] and Morgan [2].

However, Kim and Mauborgne (2015) disagree with this definition. They knew that the Conventional New Product Development process could give a positive impact on sales and company profitability, but question why the failure rate for a new product to penetrate the market is high. In the late 1900, Takeuchi and Nonaka [3] had predicted that one day the conventional and sequential in developing a new product will be not suitable and there will be a gap in the New Product

## Development Process.

According to Schneider and Hall [4], this gap was invoked because most companies are not fully ready in term of market preparation and cooped up in designing a product or service that could please the customer. Schneider and Hall [4] notice that brand's novel product shares similar element that was missing in the New Product which is the element of Value. This finding has reached the same conclusion as Kim and Mauborgne [5], where both agree that the element of value is not being embedded in the new product and the company should have emphasized the importance of creating value in their product and service.

## 1.2 Research Question

The overarching research question is: What is the strategy that can be used to embed value for the Airless Tires as along the process of new product development?

## 1.3 Research Objective

The purpose of this research is to focus on a strategy that could help the Airless tires Modula Wheel to develop their own value which that can reconstruct the current market: To investigate the strategy that can be used to embed value for the Airless Tires as along the process of new product development

## 2. METHODOLOGY

On May 2018, the researcher took five months conducted an interview session on two different parties which are from the Tire Manufacturer (Silverstone Berhad Malaysia and Toyo Tires Malaysia), and the Automotive Industries (MBSA Mercedes Benz Melaka and UMW Toyota Motors Sdn Bhd) make it a total of 4 company. The result as in Figure 1. Since the focus of the case study is to investigate the strategy that can be used to create value for the Airless Tires as along the process of new product development. Therefore, it was decided that the result will be presented based in the objective of the research.

## 3. RESULTS AND DISCUSSION

Based on the analysis that was conducted beforehand, the researcher has found out that there are four values that can be integrated for the Airless Tires in developing a new market and differentiate themselves from the current one in the market via the Blue Ocean Strategy. Therefore, by apprehending the Blue Ocean

Strategy by Kim and Mauborgne [5], each phase will be discussed carefully below before going to the next stage to propose a new model to integrate value into the new product development.

### 3.1 Opportunity and Selection

The term “Opportunity” used by Cobb [6] refer to a favourable situation that makes it possible to do something at a given point in time and places where once it was found, it need to be analyse thoroughly to determine whether it has potential or not. This process is call as Opportunity Identification. However, there are two common problem occurrences in this phase which is the Scope Creeps (a constant change of the project’s definition) and Unstable Product Specification (product requirements or desired performance level changing as the product).

According to Toyo Technical Assistant Manager, to underestimate the complexity of a project and not clearly defined it at the early stage will give birth to a lot of problems at the upcoming stages. Which is why, he suggested using the Visual Awakening as along the process rather than relying solely on the PIC. Kim and Mauborgne [5] states that the Visual Awakening process have the capabilities to resolve difference of opinion between the managers by forcefully giving them a wake-up call using the value curve that they draw. The differences in opinion will be debated to reveal the defect in the company strategy and be presented in a form of canvas before reaching a common understanding.

### 4.2 Concept Generation

Based on the previous phase, Crawford and Benedetto [7] agree that it is hard to identify an opportunity and the most logical way of solving this is to approach the source of problem which is the customer. However, the main problem with this approach is that, the customer themselves are clueless about it. Cobb [6] mentioned that by integrating the existing concepts or replacing it with other concepts, it can be used to tackle this issue on hand.

Toyo Technical Assistant Manager agree with Cobb [6] opinions and suggested of rearranging the sequence of the process by integrating the Visual Exploration Strategy and Problem-Based Ideation that can help them to identify the opportunity and distinct advantage of a product. Starting with the Visual Exploration Strategy to have a better understanding on how to develop a new product based on the customer perception. This required them to carefully observe on the customer behaviour and identified the value that can be integrated into the new product via the Four Action Framework.

### 4.3 Concept/Project Evaluation

In phase three, there are two types of initial evaluation that will be carried out to evaluate, screened and sorted out the new idea which are the End User Screening and the Technical Screening (Crawford and Benedetto [7]). However, UMW Toyota Executive disapprove the use of End User Screening in the initial evaluation. This because when the manager was asked to approach the customer directly in phase 2, they have evaluated a product feature, hurdles and criteria with a

real user by using the Four Action Framework to eliminate all the unnecessary value for the new product. Plus, the discover values will later be counter checked by the Problem Based Ideation to further improve the evaluation process.

The scoring model will narrow down the number of new product concepts to those that fit the company. From his experience as a developer, Toyo Technical Assistant Manager believe that this decision-making process can be improved by using the Visual Strategy Fair before the Scoring Model Process. He explains that by taking into consideration of the manager’s opinions and the element that of Value that was discovered, the judges can give marks accordingly without overlooking any great idea. As such, by using both of this concept, the decision maker can avoid any bias during the evaluation process and choose the concept that fits the most with company strategy before going to the next phase.

### 4.4 Development

In this phase, the product that have been selected to be developed will be required to undergo 3 major part which are Resources Preparation, the Major Body of Effort (Prototype) and Comprehensive Business Analysis before they can acquire a finite form. However, among this 3 major part, the part that catches the attention of Mercedes Benz Production Manager is the Business Analysis. Business Analysis consists of several important components (such as sales forecast, cost estimation, profit projections, and risk assessment) to estimate the new product concept commercial performance. That eventually led of using the Visual Communication to strengthen the Business Analysis as suggested by Mercedes Benz Production Manager.

Silverstone Technical Assistant Manager highlight that the use of Visual Communication will make the evaluation process much stricter. If we look the other side of the coin, it shows that this concept has the potential to be commercialize and penetrate the market which be essential in the launching phase.

### 4.5 Launch

In this phase, the term “Launch” is usually associated with when a company decided to utilize their resources to commercialize a new product. During this period, the marketer will conduct a multimillion-dollar advertising campaign via Public Relation Agency to increase its output before the day of the launch Genc [8]. The Public Relation Agency will craft a press release and leak information about the new product to arouse the reporter’s curiosity. Silverstone Technical Assistant Manager foresee that this conventional way of introducing a new product will be consumed by the rapid speed of social media. This is because the news can be forgotten within minute as the unceasing flow of even “newer news” can pushes your announcement out of the collective mindshare. Thus, making it unreliable.

Mercedes Benz Branch Manager proposed of aligning with a market influencer by sharing the discovered value with them to elevate the customer level of awareness of the new product. By utilizing the discovered value to align the audience interest with the company objective, they can increase 30% of likeliness

of a customer to purchase Forbes [9] and Haran [10]. Mercedes Benz Production Manager remind that an influencer can only persuade the consumer. What determine whether a consumer buy it or not will be

depend on the product's value that they gain. Therefore, it is important for a company to make sure the influencer to abide by the term and condition that been construct beforehand to avoid unfavourable situation.

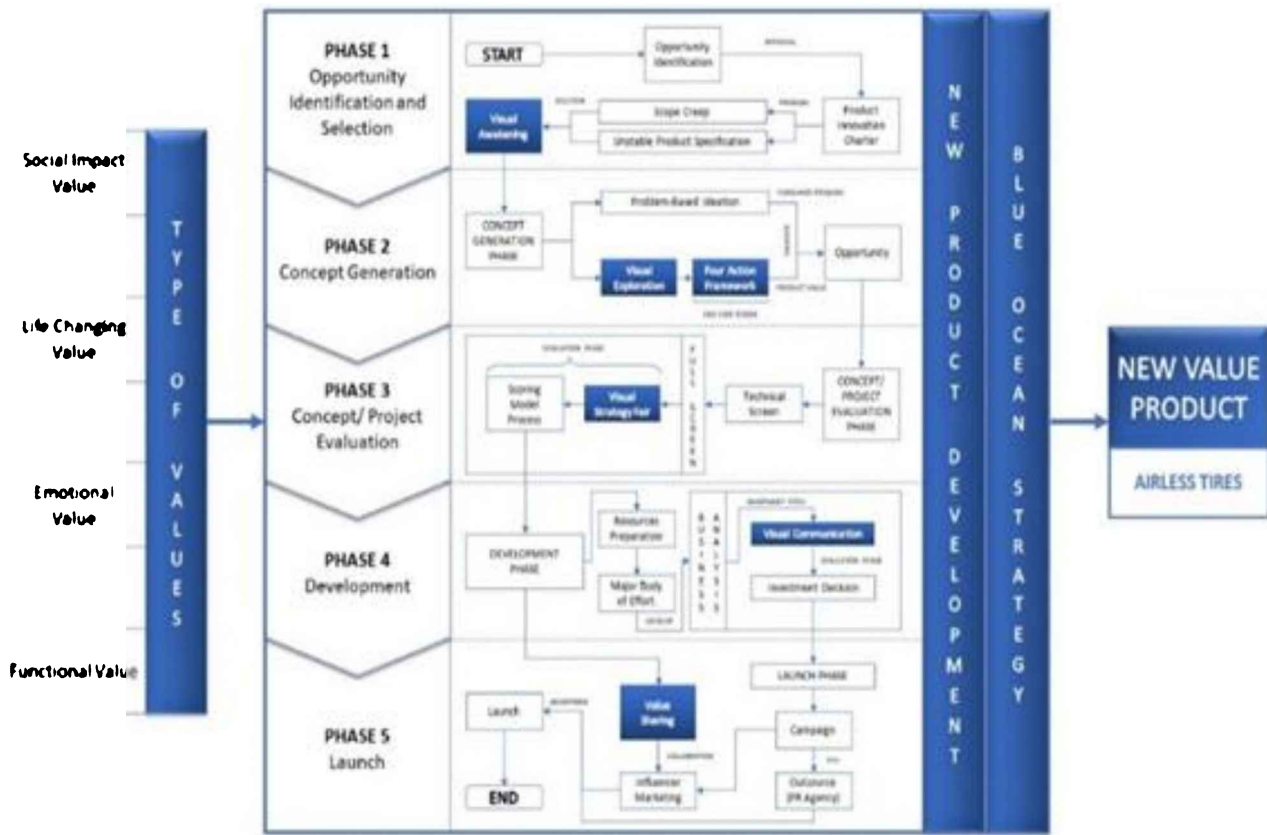


Figure 1 Proposed model summarized by researcher. Sources: [5,7,8,11,12,13,14,15,16].

#### 4. CONCLUSION

The main idea of this model is to embed the element of Value in the New Product Development Process via Blue Ocean Strategy in order to increase the success rate of penetrating the market. By going through each phase, the model was constructed based on the discussion with the respondents that are well versed in the Blue Ocean Strategy in embedding the value of a new product into the NPD process as shown in the figure above.

Theoretically, this model has the capabilities to open a new market space and create new demand for a new product. It will serve as a guideline for the manufacturer to embed the element of value into the new product to increase the company's growth in both revenue and profit. Especially for a new product that have low acceptance rate. Kim and Mauborgne said that, when a consumer have acknowledged a product's value, the product's demand will be stimulated to the point that it can create a profitable growth for the company. Therefore, for a company that wish to differentiate themselves from their competitors, this model might suit them.

#### ACKNOWLEDGEMENT

The researchers feel thankful to Universiti Teknikal Malaysia High Impact Short Term Research Grant (Project No. PJP/2017/FKP/HI15/ (S01549) which funds this publication

#### REFERENCES

- [1] Cambridge. (2017). Cambridge Dictionary : New Product Development. Retrieved December 12, 2017, from <https://dictionary.cambridge.org/dictionary/english/new-product-development>
- [2] Morgan, T. (2015). Antecedents, Consequences, and Boundary Conditions of Customer Participation in the New Product Development Process. Ph.D. Kent State University
- [3] Takeuchi, H. & Nonaka, I., 1986. The New New Product Development Game. [Online] Available at: <https://hbr.org/1986/01/the-new-new-product-development-game>
- [4] Schneider, J. & Hall, J., 2011. Why Most Product Launches Fail. [Online] Available at: <https://hbr.org/2011/04/why-most-product-launches-fail>
- [5] Kim, W. C. & Mauborgne, R., 2015. Blue Ocean Strategy: How to Create Uncontested Market Space and Make the Competition Irrelevant. EBook ed. Boston: Harvard Business School.
- [6] Cobb, M. (2017). Traditional Strategic Planning Models Don't Work ... There's A Better Way. Retrieved July 11, 2018, from <http://innovanet.com/2017/12/06/a-better-way-strategic-planning-models/>

- [7] Crawford, M., & Benedetto, A. D. (2014). New Product Management (11 ed.). California: McGraw Hill Higher Education.
- [8] Genc, E., Lancioni, R. A., Eisenstein, E. M., & Wattal, S. (2013). Sustainable New Product Development: The Role of The Environmental Specialist and Environmental Marketing Strategy Development.
- [9] Forbes. (2018). 15 Reasons To Add Influencer Marketing To Your Business Strategy. Retrieved July 22, 2018, from <https://www.forbes.com/sites/forbesagencycouncil/2018/01/09/15-reasons-to-add-influencer-marketing-to-your-business-strategy/#1aae1a212c3b>
- [10] Haran, R. (2018). How to Grow Your Business with Influencer Marketing. Retrieved July 22, 2018, from <https://www.singlegrain.com/content-marketing-strategy-2/what-is-influencer-marketing-chris/>
- [11] Gordon, J. M. (2016). The Business Professor : Blue Ocean Strategy. Retrieved September 25, 2017, from <http://thebusinessprofessor.com/knowledge-base/blue-ocean-strategy/>
- [12] Cooper, R. G., & Edgett, S. J. (2010). Lean, rapid, and profitable new product development. Ancaster, Ont.: Product development Institute.
- [13] Almquist, E., Senior, J., & Bloch, N. (2016). The Elements of Value. Retrieved from Harvard Business Review: <https://hbr.org/2016/09/the-elements-of-value>
- [14] Jayabal, J. (2016). Problem-Based Ideation on New Products. Retrieved December 21, 2017, from <http://fhyzics.com/problem-based-ideation-on-new-products.html>
- [15] Bain. (2016). Explore the Elements of Value. Retrieved from <http://www.bain.com/bainweb/media/interactive/elements-of-value/#>
- [16] Toro, J. M. d., 2016. Forbes : Five Steps to Develop a New Product. [Online] Available at: <https://www.forbes.com/sites/iese/2016/06/01/five-steps-to-develop-a-new-product/#316efb702eef> [Accessed 18 12 2017].

# Essential values for the airless tyres to be developed as a new product

M.F.M. Sam<sup>1,3</sup>, H. Hafizuddin<sup>1,\*</sup>, B.C. Chew<sup>1</sup>, Sivaraos<sup>2</sup>, Y.F. Yusof<sup>3</sup>

<sup>1)</sup> Fakulti Pengurusan Teknologi dan Teknousahawan, Universiti Teknikal Malaysia Melaka,  
Hang Tuah Jaya, 76100 Durian Tunggal, Melaka, Malaysia

<sup>2)</sup> Fakulti Kejuruteraan Pembuatan, Universiti Teknikal Malaysia Melaka,  
Hang Tuah Jaya, 76100 Durian Tunggal, Melaka, Malaysia

<sup>3)</sup> Centre for Robotics and Industrial Automation, Fakulti Kejuruteraan Elektrik, Universiti Teknikal Malaysia Melaka,  
Hang Tuah Jaya, 76100 Durian Tunggal, Melaka, Malaysia

\*Corresponding e-mail: hafizuddin.hissamuddin@gmail.com

**Keywords:** Value; tire technology; air filled tires; airless tires

**ABSTRACT** – Based on previous research, the researcher has discovered that all this successful product has shares a similar trait that help them seize the market which is the element of value. This value has been receiving a lot of attention and has been deemed one of the most significant factors to help new product to achieve a sustainable business and market success. When the first air-filled rubber tires were invented by Dunlop on 1888, the number of acceptances was low, and it took a total of three years to be accepted by the consumer. It indicates that consumers were not aware of its value and it is difficult to integrate value into a new product. We believed that if the element of Value can be embedded into the airless tires, it can represent the next step in a long innovation path for tire industry. Therefore, the main objective of this research is to focus on identifying values that could help the Airless tires Modula Wheel to penetrate the market as a new product. The research design is the exploratory and the analyzed data will be using the qualitative method. Thus, at the end of this research we may identify the type of value that is necessary for the airless tires as a new product.

## 1. INTRODUCTION

The world has started to consider the importance of embedded value in a product or service [1]. Which cause the demand for manager that can access this value to increase especially if this value can help them to achieve a sustainable business and market success [2-5]. Value is the thing that drives people to make a buying decision and its uniqueness depends on what the customer perceived toward a product that makes it is important to them. Which makes it regarded as a decisive weapon to attract and retain the customer to their prospective company.

However, due to its dynamic feature, it can be hard to truly capture or define it as it depends on the type of demand that the customer needs. Only a few numbers of people have the abilities to tap in on the product value for a segment of people [2-5]. The firm need to manage this value while simultaneously anticipate thing other people consider valuable. By any chance they failed in doing so, there is a high chance that company may be forever stuck in the red ocean traps [2].

Under those circumstances, most companies will have the tendency to only focus on one value rather than two. Thus, verifying Kim and Mauborgne [2]

declaration in the Blue Ocean Strategy books where they state that most companies will only embed one type of value in the new product is true. For those who integrate two or more of these elements will not only stimulate the demand but will also open new market possibilities for the company who successfully execute it. Therefore, by apprehending the Blue Ocean Strategy by Kim and Mauborgne [2], those who understand the importance of creating value for the customer will surely be able utilize this theory with hope to integrate the value.

### 1.1 Research Question

The overarching research question is: What are the values that could be developed for the Airless Tyres as a new product?

### 1.2 Research Objective

The purpose of this research is to focus on identifying values that could help the Airless tires Modula Wheel to penetrate the market as a new product. To identify the value that could be developed for the Airless Tyres as a new product

## 2. METHODOLOGY

On May 2018, the researcher took five months conducted an interview session on three different parties which are from the tire manufacturers (Silverstone Berhad Malaysia and Toyo Tires Malaysia), the automotive industries (UMW Toyota Motors Sdn Bhd) and the academic research (Universiti Teknikal Malaysia Melaka) that formed a total of 4 company. The result will be presented in this chapter. Since the focus of the case study is to identify the value that could be developed for the Airless Tyres as a new product. Therefore, it was decided that the result will be presented based in the objective of the research.

## 3. RESULTS AND DISCUSSION

Based on the analysis that was conducted beforehand, the researchers have found that there are four values that can be integrated for the Airless Tires to develop a new market and differentiate themselves from the current market. Each one of these values will help the company to capture or caters the exact need and want of the customer accordingly. As such, the finding will be further discussed about what Value is essential

for the Airless Tyres from three different angles which is Tyre Manufacturer, Automotive Company and UTeM Researcher as shown in the figure below.

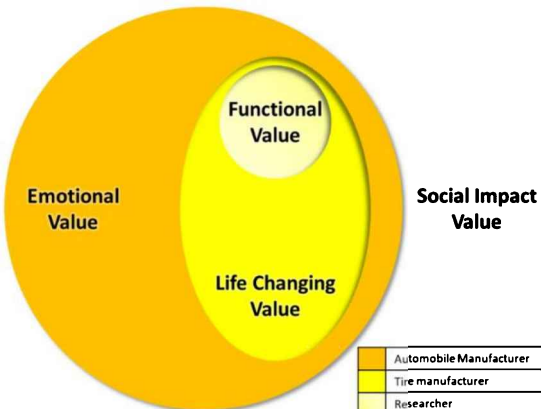


Figure 1 The value of airless tires from three different perspective.

#### 4. CONCLUSION

From the discussion above, the researcher concluded that there are three value that are essential for the airless tires which are functional value, emotional value and life changing value as shown in the figure below.

It has been shown that the common value that was shared by all perspective is the functional value (the basis of the need for every consumer). The majority of the respondent agree that the airless tires will contribute to a greater safety and peace of mind in driving. The hassle of checking the tire pressure or puncture will be completely remove from their mind as the airless tires do not contain any air within it. Plus, the possibilities of a catastrophic failure occur due to inflation, puncture, and tire blowouts are next to zero.

The second value is the emotional value. Only one disapprove the integration of emotional value in the airless tires which is the academic research. The researcher believe that the Academic Researcher has a strong sense of duty to solve the problem that is happening in their surroundings and prioritize the life and safety of the passenger before their own interest.

The third value is the life changing value. According to UMW Toyota Executive, the world is currently moving forward where the technology development is rapidly changing and believe that this

value is related with social infrastructure that Toyota wanted to achieve. Which is to reduce the Carbon Dioxide Emission from its vehicle and to create a world that is free from accidents. While Toyo Tyre on the other hand, wish to make a product that is much safer and greener.

Lastly, the social impact value. Even if the social impact value has the potential of helping the communities in changing the way others view their surroundings and provide a positive change of a pressing social challenge. The researchers cannot deny that the acceptance level for the airless tyres is still low. The consumers do not have a good perception toward the airless tyres, as it is still under development and still a new technology. Because of this, consumer was not able to fully grasp the Value that were an exhibited by the airless tyres. The researcher believes that the value that was seen by the customer, in some sense equal to the level of perception that they have. Which is why the researcher believes that the social impact value is not necessary for the time being and could be considered in the future when the tires are able to gain more customer acceptance and prove that the airless tyres is ready to be commercialized.

#### ACKNOWLEDGEMENT

The researchers feel thankful to Universiti Teknikal Malaysia High Impact Short Term Research Grant (Project No. PJP/2017/FKP/HI15/ (S01549) which funds this publication.

#### REFERENCE

- [1] Almquist, E., Senior, J., & Bloch, N. (2016). The elements of value. *Harvard Business Review*, 94(9), 47-53.
- [2] Kim, W. C., & Mauborgne, R. A. (2017). *Red Ocean Traps (Harvard Business Review Classics)*. Harvard Business Review Press.
- [3] Lu, I. Y., & Shiu, J. Y. (2011). Decision-making framework of customer perception of value in Taiwanese spa hotels. *Social Behavior and Personality: An International Journal*, 39(9), 1183-1192.
- [4] Lapierre, J. (2000). Customer-perceived value in industrial contexts. *Journal of Business & Industrial Marketing*, 15(2/3), 122-145.

# Process redesign to increase throughput and improved product flow for bake-wares-producing company

Dzullijah Ibrahim\*, Hamid Yusoff, Yusli Yaakob, Norasikin Hussin

Fakulti Kejuruteraan Mekanikal, Universiti Teknologi MARA, Cawangan Pulau Pinang,  
13500 Permatang Pauh, Pulau Pinang, Malaysia

\*Corresponding e-mail: dzullijah@uitm.edu.my

**Keywords:** Decorative nozzle; jig; process improvement

**ABSTRACT** – One of the factors influencing the production rate of Small and Medium Enterprise (SME) is the implementation of process improvement. For this reason, this project intends to improve the process of making decorative nozzle which is one of the highly demanded products produced by a bake-wares-producing SME company. Waste and process time can be reduced without compromising its quality. An improved design is proposed for stamping die such that a saving of almost 20% material can be obtained from the decorative nozzle design improvement. The production rate is increased by 18.5% after implementing the improvement of jig and process design.

## 1. INTRODUCTION

Malaysian SMEs are a vital component of the country's economic development. There are many challenges to sustain the influence of SME's in the economic growth of Malaysia. One of the challenges is the importance of technology diffusion and adoption in manufacturing sector in Malaysia. Process technology employed can be the determinants of SME success [1]. Often by applying current technology into process designs in the industry, the potential that the industry can achieve manufacturing production goal is increasing. However, small companies are often limited in terms of investment and research facilities [2]. Therefore, this project intends to help SMEs to improve their process and be competitive in market. A case study was done at a company which produced various type of bake ware located at Entrepreneurial Park, Kepala Batas, Pulau Pinang. Decorative nozzle is one of the highest demand products for the current year. The production flow is observed, and the current process design is studied. Suitable method is used to improve the current process. This in turn will able to improve the production flow as well as increasing the production rate. The increased production rate helps greatly in achieving the company's manufacturing production goal [3].

## 2. JIG AND PROCESS IMPROVEMENT

One of the main concerns of the company is the processes used in the workshop. Most of the processes are done manually using specialized jigs and tools; some require skill workers with years of experience. If this worker is absence for some reasons, then the affected production line must be put on hold for the day. Rolling process is identified as the process that requires improvement so that it will not depend on one operator to run. However, to improve the rolling process, some

features on the nozzle must be removed to reduce working step for nozzle shaping process.

### 2.1 Punching jig

The current punching jig design included the shaded area shown in Figure 1. This feature acts as a joining surface to solder to join the nozzle together. Besides, the gap between each punching part from the metal strip feed into the punching machine is not consistent. This inconsistency sometimes produced defective parts and waste raw materials. The modified part design removed the shaded area and reduced 4575mm<sup>2</sup> of the raw material for each part. It is a saving of 19.9% of raw material for each part.

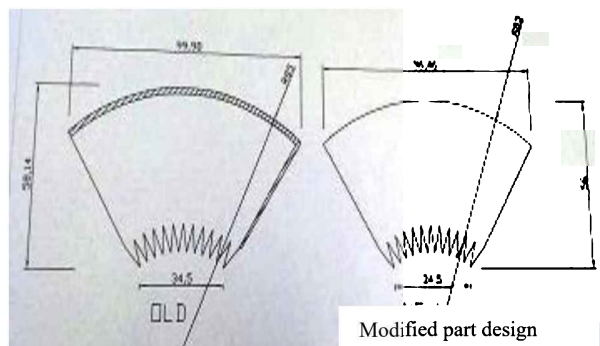


Figure 1 Shaded area is removed to save material and reduce process (eliminate bending the edge process).

### 2.2 Rolling machine

The current rolling clamp used in the workshop is shown in Figure 2. The worker will shape the nozzle using his hand and wood stick to whack on the nozzle following the cone shape jig distending from the clamp. This will cause defect on the surface of the nozzle. The improved rolling jig is designed such that no whacking process is required.



Figure 2 Manual process for shaping cone decorative nozzle by one expert worker.

### 2.3 Simulation of current layout and proposed layout

To visualize the layout clearly, both layouts are then drawn and simulated using DELMIA Quest software as shown in Figure 3. The changes in the production flow and cycle time for each process for both layout of the workshop is summarized in Table 1. The cycle time for the current layout is obtained from the observation of the actual production line. The cycle time for proposed layout is changed especially for rolling process and one process is eliminated. Bending the edge process is eliminated due to the improvement of the punching jig. From the simulation, the data collected is used to determine the production rate of both layouts. The data is then analyzed by comparing the production rate for both layouts.

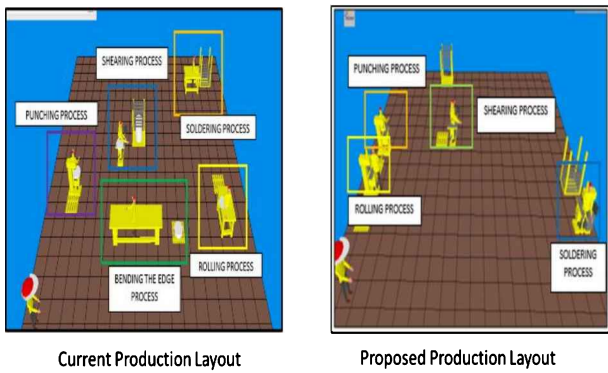


Figure 3 The layout sketched using DELMIA Quest for both production layouts.

Table 1 Parameters and the flow of processes used in DELMIA Quest for both layouts.

Process	Current layout	Proposed layout
Shearing process	12 secs	12 secs
Punching process	12 secs	12 secs
Rolling process	72 secs	36 secs
Bending the edge process	12 secs	Eliminated
Soldering process	12 secs	12 secs
<b>Total cycle time</b>	<b>120 secs</b>	<b>72 secs</b>

The calculation steps are tabulated in Table 2. The data used in these calculations are based on the actual data collected from the workshop which is tabulated in Table 1. For the new proposed layout, the cycle time used is estimated according to the capability of the production line in the workshop. From the analysis of the data calculated, the proposed production line can produce more from the current production line. The average production rate calculated for current production layout is only 27.65 % while for the proposed production layout is 46.15%. This shows an increase of 18.5% when the new proposed production line based on the process redesign is applied.

Table 2 The comparison for current and proposed layout

Items	Current	Proposed
Batch Processing Time ( $T_b$ )	$T_c = 2.07 \text{ mins}$ $T_b = 390 \text{ mins}$ $Q = 300 \text{ pieces} = 651 \text{ mins}$ $\text{Set up Time} = 1.5 \text{ days}$ $(T_{su}) = 30 \text{ min}$	$T_c = 1.2 \text{ mins}$ $T_b = \text{less than 1 day}$
Average Production Time ( $T_p$ )	$T_b = 651$ $T_p = 2.17$	$T_b = 390$ $T_p = 1.3$
Average Production Rate ( $R_p$ )	$T_p = 2.17$ $R_p = 27.65 \%$	$T_p = 1.3$ $R_p = 46.15 \%$ (increase 18.5%)

### 3. CONCLUSION

The modified part design reduced 4575mm<sup>2</sup> of the raw material for each part. It is a saving of 19.9% of raw material for each part. The modified part design also enables the company to eliminate the “bending the edge” process. Another reason for the significance changed in the production rate was by the changes made in rolling process. The simulation data from these improvements were then supported by the production rate calculated using the production rate formulas. The production rate was increased by 18.5% after implementing the improvement of jig and process design. Therefore, the process improvement implemented has significant effect to the production rate of the product thus will enable the company to be more competitive in the market.

### ACKNOWLEDGEMENTS

The authors wish to acknowledge the Ministry of Higher Education (MOHE) for the PPRN Grant given to enable this project to be carried out in the company. The authors also wish to thank for the financial assistance from UiTM CPP to present this paper and the technical support from the Faculty of Mech. Eng. UiTM CPP.

### REFERENCES

- [1] Yoon, J. S., Kim, J., & Kang, B. S. (2016). Deformation analysis and shape prediction for sheet forming using flexibly reconfigurable roll forming. *Journal of Materials Processing Technology*, 233, 192-205.
- [2] Murad, M. A., & Thomson, J. D. (2011). The importance of technologies diffusion in Malaysian Manufacturing SME. In *3rd International Conference on Information and Financial Engineering*, Singapore.
- [3] Aziz, N. N. A., & Samad, S. (2016). Innovation and competitive advantage: Moderating effects of firm age in foods manufacturing SMEs in Malaysia. *Procedia Economics and Finance*, 35, 256-266.

# Effects of driving signal waveforms on the force characteristics of a tubular linear switched reluctance actuator (T-LSRA)

Fawwaz Nadzmy, Mariam Md Ghazaly\*, Chin Kiat Yeo, Siau Ping Tee, Shin Horng Chong

Center for Robotics and Industrial Automation (CeRIA), Faculty of Electrical Engineering,  
Universiti Teknikal Malaysia Melaka, Hang Tuah Jaya, 76100 Durian Tunggal, Melaka, Malaysia

\*Corresponding e-mail: mariam@utem.edu.my

**Keywords:** Driving signal waveform; force characterization; tubular linear switched reluctance actuator (T-LSRA)

**ABSTRACT** – This paper discusses the effects of driving signal waveforms on the force characteristics of the tubular linear switched reluctance actuator (T-SLRA). This paper includes the investigation of the characteristics with three driving signal waveforms candidates, i.e.: (i) fundamental step signal (ii) 2.4mm extended period of positive step signal (iii) 2.4mm extended period of negative step signal. The numerical analysis was evaluated by using 2-D finite element analysis. The results revealed that the customized driving signal waveforms with the 2.4mm extended period with the positive and negative signals both improved the average thrust force up to 7% and 19%, respectively.

## 1. INTRODUCTION

Linear switched reluctance actuators (LSRA) have become an attraction among researchers due to its simple structure, low production cost, absence of both permanent magnet and mechanical part; i.e.: gears. The topologies of typical LSRA are single-sided planar, double-side planar and tubular type. According to previous research [1], the single-sided type of LSRA produced unexpected normal force. The increase in the normal force would cause large friction between the mover tooth and the stator. The double-sided type LSRA can ease this problem with the symmetrical stator structure; however if the air gaps on both sides of the mover are not uniform due to the manufacturing and installation technology, the normal force would not be eliminated [2]. To ensure perfect mover installation, the tubular type LSRA (T-LSRA) is capable of eliminating the radial electromagnetic force. By comparing to the planar type of LSRA, T-LSRA inherently has two advantages which are higher thrust-to-volume and the magnetic field is uniformly distributed along circumferential direction.

T-LSRAs can be classified as longitudinal flux and transverse flux depending on the surrounding magnetic flux path. A new structure of longitudinal has been investigated in previous studies [3,4]. In longitudinal T-LSRA, bread type winding is implemented which has no end. Therefore, the usage of the winding ratio can be improved. The electromagnetic characteristics of transverse T-LSRA has been discussed in previous research [5]. By comparing both types of T-LSRA, the construction of the longitudinal type is simpler with lower numbers of coil windings per unit stator. However, according to Chen et. al [6], by comparing them with the same volume and mass, transverse T-LSRA provides higher average trust per unit volume and per unit mass.

However, literature reviews have found that there is a gap in knowledge where optimization of customize driving waveform signals may help to improve the force characteristics and the synchronization control for precision motion of longitudinal T-LSRA.

## 2. METHODOLOGY

The proposed T-LSRA was analyzed using commercial 2-D finite element analysis program (Maxwell 2-D ver. 15.0 from ANSYS Inc.). 2-D FEA analysis was used since it requires lower computation power and time compared to 3-D FEA analysis. **Error! Reference source not found.**(a) illustrates the 2-D FE model. The 2-D FE model is an axial symmetric (RZ) model which represents a cross-section that is revolved 360° around an axis of symmetry (the Z-axis).

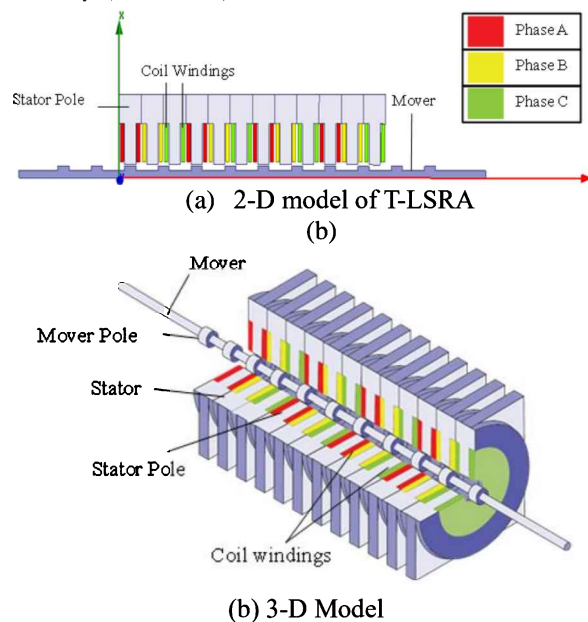


Figure 1 Finite element analysis modeling.

In **Error! Reference source not found.**(b), the designed longitudinal T-LSRA consists of twelve stators and a mover is made from carbon steel. The stator slots are split into multiple parts thus the stator winding can be easily embedded between the stators. To produce a continuous motion, three phases of current excitation are implemented. The driving current of T-LSRA was applied to the phase coils sequentially for performing a linear motion of the mover. The thrust force was generated by the mover tooth near to the active stator pole. When the mover tooth moves near to the centre of

the pole, the active coils are switched to generate a continuous motion. Table 1 shows the current excitation sequence for forward motion. Three driving signal waveforms are examined for improving the actuator performances.

**Table 1 Current excitation sequence for forward motion.**

Position	Phase
0mm -5.0mm	A
5.0mm - 10.0mm	C
10.0mm -15.0 mm	B

Figure 2 shows three candidate driving signal waveforms for the T-LSRA which are DS1, DS2 and DS3, respectively. DS1 driving signal shown in Figure 2(a) is a fundamental step signal where only a single phase is driven at specific times and the active phase is switched in series for mover movement in linear motion. The DS2 driving signal applies positive current for 2.4mm extended period, during which two phases are driven to increase a thrust force. The DS3 driving signal drives negative current on the 2.4mm extended period.

### 3. RESULTS AND DISCUSSION

Figure 3 shows the results of thrust force curve for the three proposed driving signal waveform. Table 2 shows the comparison of the generated thrust force by DS1, DS2 and DS3. DS2 and DS3 generate large thrust force on average with 1.64N and 1.82N respectively; an improvement of up to 7% and 19% respectively in compared to DS1.

### 4. CONCLUSION

In conclusion, the average thrust force of the proposed T-LSRA can be improved by suitable exciting driving signal waveforms and configurations. The signal with extended negative step is able to improve the average force by up to 19% with a lower standard deviation compared to the fundamental step signal. The further enhancement of the driving characteristics is essential to increase the positioning precision of the T-LSRA. This is planned for future research works.

### ACKNOWLEDGEMENT

The authors wish to express their gratitude to Motion Control Research Laboratory (MCon Lab), Center for Robotics and Industrial Automation (CeRIA) and Universiti Teknikal Malaysia Melaka (UTeM) for supporting the research and publication. This research is supported by Universiti Teknikal Malaysia Melaka grant no. JURNAL/2018/FKE/Q00006, Center for Robotics and Industrial Automation (CeRIA) and Center for Research and Innovation Management (CRIM).

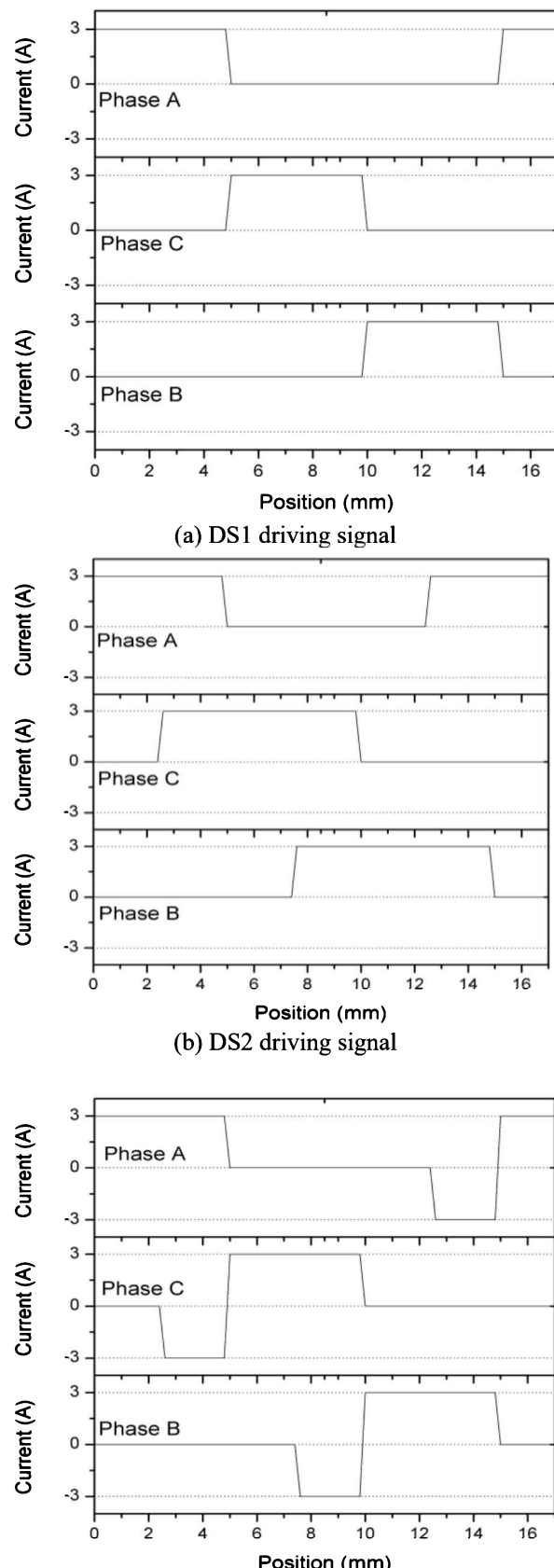


**Figure 2 Candidate driving signal waveforms for the proposed T-LSRA with maximum amplitude of 3A.**

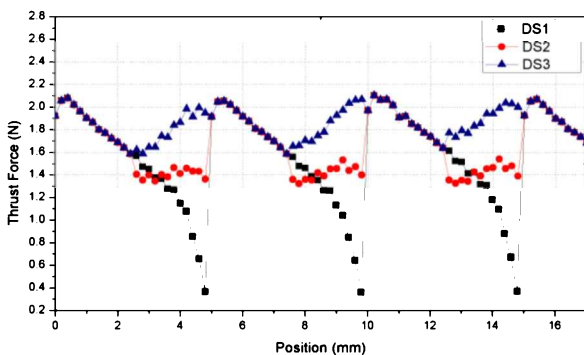


Figure 3 Comparison of thrust force generated by three driving signal waveforms.

Table 2 Performances comparison of excitation signal.

Driving signal	Measurement			
	Avg.	Max	Min	Std. Dev.
DS1	1.53N	2.10N	0.36N	0.443
DS2	1.64N	2.10N	1.35N	0.254
DS3	1.82N	2.10N	1.59N	0.154

## REFERENCES

- [1] Sato, K. (2013). Novel compact linear switched reluctance motor with a thin shape and a simple and easily replaceable mover. *Journal of Advanced Mechanical Design, Systems, and Manufacturing*, 7(3), 295–304.
- [2] Chen, H., Nie, R., & Wang, Q. (2016). Unbalanced normal force reduction in the eccentric double-sided linear switched reluctance machine. *IET Electric Power Applications*, 10(5), 384–393.
- [3] Yeo, C. K., Ghazaly, M. M., Chong, S. H. & Jamaludin, I. W. (2018). Design optimization of a three phase tubular linear switched reluctance actuator. *ARPN Journal of Engineering and Applied Sciences*, 13(5), 1600–1607.
- [4] Wang, D., Shao, C., & Wang, X. (2016). Design and performance evaluation of a tubular linear switched reluctance generator with low cost and high thrust density. *IEEE Transactions on Applied Superconductivity*, 26(7).
- [5] Pan, J. F., Cheung, N. C., & Zou, Y. (2012). Design and analysis of a novel transverse-flux tubular linear machine with gear-shaped teeth structure. *IEEE Transactions on Magnetics*, 48(11), 3339–3343.
- [6] Chen, H., Nie, R., & Yan, W. (2017). A novel structure single-phase tubular switched reluctance linear motor. *IEEE Transactions on Magnetics*, 53(11), 10–13.

# Assessment on manual handling lifting precast concrete panel process via NIOSH equation

Sinatu Sadiyah Shapie<sup>1,2,\*</sup>, Hussein Md Zan<sup>3</sup>, Seri Rahayu Kamat<sup>4</sup>

<sup>1)</sup> Department of Civil Engineering, Politeknik Melaka, Plaza Pandan Malim, 75250 Melaka, Malaysia

<sup>2)</sup> Polytechnic Centre of Technology IBS, Politeknik Melaka, Plaza Pandan Malim, 75250 Melaka, Malaysia

<sup>3)</sup> Department of Mechanical Engineering, Politeknik Melaka, Plaza Pandan Malim, 75250 Melaka, Malaysia

<sup>4)</sup> Fakulti Kejuruteraan Pembuatan, Universiti Teknikal Malaysia Melaka,

Hang Tuah Jaya, 76100 Durian Tunggal, Melaka, Malaysia

\*Corresponding e-mail: s\_sadiyah@polimelaka.edu.my

**Keywords:** Precast concrete panel; recommended weight limit; lifting index

**ABSTRACT** – The objective of this study to analysis the construction workers during the manual handling process on lifting Precast Concrete Panel (PCP). The issue of Musculoskeletal Disorders (MSDs) occurred in this industry when IBS workers lifting PCP repeatedly manually. NIOSH equation define as Recommended Work Limit (RWL) includes Lifting Index (LI) calculation were used as tools. The outcomes yielded the MSDs problem based on recommended weight limit value which is more than the “Load constant” itself besides lifting index more than 1. They benefit workers and increase their awareness on the MSDs issues.

## 1. INTRODUCTION

The construction sector shows a significant indicator in any country's economic growth. It comes with establishes infrastructure essential for socioeconomic growth to becomes major contributor to extensive economic impact [1]. In Malaysia, the construction sector play as spine in contribution in Gross Domestic Product (GDP) as 50.1 billion or close to 5% of the national GDP in 2016 with number of wages employment of 1.25 million or 9% of national manpower [2]. This will have created huge number of job opportunities within the industry and indirectly industries as company in supply chain [3]. Meanwhile, another latest technology comes along in construction sector is Industrial Building system (IBS) with offer the advantages of high quality of good acceptance, faster accomplishment of projects, organised components storing and judicious material conveyance; reducing cost of on-site worker and cost of transferring waste material [4-5].

The construction job done by employee comprises scrubbing and arranging the sites, excavating, functional with power tool, unloading and loading of material, placing and maxing concrete and also work at different times [6] . All these items will lead the worker to ergonomic risk and becomes seriously injures as sprains and strains at upper limb especially at hip, spine and shoulder blades. These factors caused by contact stress of vibration, awkward postures, high repetitive movement and carrying heavily loads which related to MSDs [7-8].

## 2. METHODOLOGY

This project starts by collecting data by observation on construction site at *Projek Perumahan Awam 1 Malaysia (PPA1M) Jasin, Melaka* that apply the nearly 70% IBS on their project. PCP is one of categories IBS have been used on this project by contractor due its low cost. The size of PCP depends on specification and model produced by the manufacturer. The specifications of PCP been used in this project are 135 kg/m<sup>2</sup> of weight distribution, range mass between 240 kg to 260 kg with compressive strength 40 MPa. While, the dimensions of PCP are 100 mm thick, 600 mm width, 3300 mm length. Generally, this PCP comes in bulk in form of 5 units of PCP for each pallet in the position of the horizontally. Once at the construction site, the workers lay the PCP on the floor to lifting vertically.

The NIOSH equation has been used for analysis of PCP weightlifting tasks done by the workers rather it signification to ergonomic risk that can contribute to MSDs. This mathematical model developed by NIOSH useful to predict the risk of lifting – related injuries. The equation defines as RWL which describe the maximum acceptable load that most workers could perform of an 8 hour without develop risk of MSDs to upper limb. While, Lifting Index (LI) is calculated to perform a relative approximation the rate of physical stress and MSDs risk [9]. The equation (1) of RWL and equation (2) of LI shows as figure below;

$$RWL = LC(23) \times HM \times VM \times DM \times AM \times FM \times CM \quad (1)$$

$$Lifting\ Index = RWL / weight \quad (2)$$

The parameters of RWL for weight of PCP which ware; load constant (LC) is estimate about 23 kg of maximum recommended load to be lifted with ideal condition, (HM) is parallel position of the item comparative to the body, (VM) is perpendicular position of the item comparative to the floor, (DM) is distance the item is moved vertically, (AM) is asymmetry angle, (FM) is lifting duration and (CM) is quality of the workers grip on the object were measured for every worker. There are 8 workers involved in this study and can categories in 3 different types of Body Mass Index (BMI) which are underweight, normal and overweight. Then, the RWL results were analysed for LI base on signification to (below than 1.0) nominal or (more than 1.0) high risk.

### 3. RESULTS AND DISCUSSION

The result of the RWL to determine NIOSH equation of the task conditions manipulated in the psychophysical and biomechanical experiments, the six multipliers must be calculated first. The measurements and data needed are shown in Figure 1. In general, all the respondents were categorized to three groups based on the BMI namely Normal, Underweight and Overweight.



Figure 1 Psychophysical and biomechanical determination of respondents.

While, the mean of RWL by the BMI group is illustrated in Table 1. As the mass load in this study was about 250kg which was divided to 3 workers responsible for lifting activities. It was more than the LC itself which was 23 kg ware; 26.81 kg for underweight, 27.91 kg for normal and 28.96 kg respectively.

Table 1 The mean of RWL of the BMI groups.

BMI			
Less than 18.5 (Underweight)	18.5 – 24.99 (Normal)	25- 29.99 (Over weight)	
Average			
Concrete panel per person (kg) (MAWL)	83	83	83
RWL (kg)	26.81 kg	27.91 kg	28.96 kg

Note: MAWL – Maximum Acceptable Weight of Limit

Speciously, Figure 2 indications that the LI analysis verified that all groups of respondents scored more than 1 which between 2.80 and 3.10; an overall mean of 3.10 for underweight group, 2.98 for the normal group and 2.88 for the overweight group. All the LI values were greater than 2, indicative of a possible high risk for the respondents performing such tasks of suffering Low Back Pain (LBP). A further analysis was carried out with LI values of more than the baseline 1, verifying that RWL values that exceeded the baseline of LC supports imposed a higher risk of LBP for each respondent.

### 4. CONCLUSION

The results of the RWL, LI and physiological experience among workers while lifting the precast concrete panel with sizes 3300 mm x 600 mm yield that IBS workers have been bearing with a higher risk of LBP and drive ultimately suffer MSDs specifically in the spine

and waist. This scenario should be taken multiple party comprises government and NGO such NIOSH in practicing safety and health in construction especially in term of ergonomic risk. This is aligning with new legislation of the ISO 45001 which to purposes and managing systematically ergonomics' workplace base on hierarchy control solution [10].

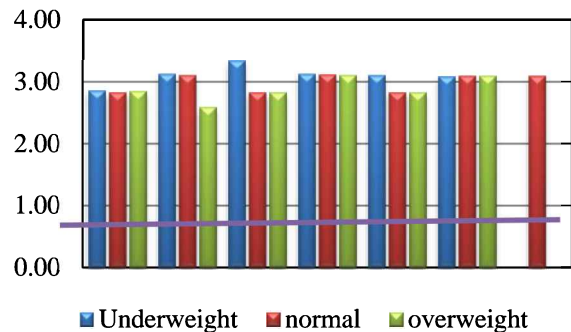


Figure 2 LI for each BMI group.

### REFERENCES

- [1] IBS-Roadmap 2011-2015. (2010). Construction Industry Development Board Malaysia, 72, 79.
- [2] Fadhlil, A., Voon Chiet, C., Anuar, K., & Tien Shen, T. (2004). An overview on the growth and development of the Malaysian construction industry. *Work. Constr. Contract Manag.*, 1-12.
- [3] Ipsos Business Consulting. (2017). Market review of building materials in the construction industry. 203.
- [4] Nawi, M., Nasrun, M., Mydin, M. A. O., Nifa, A., Akmar, F., Osman, W. N., & Anuar, H. S. (2015). Malaysian Industrialised building system (IBS): A review of studies. *Australian Journal of Basic and Applied Sciences*, 9(7), 99-101.
- [5] Badir, Y. F., Kadir, M. A., & Hashim, A. H. (2002). Industrialized building systems construction in Malaysia. *Journal of Architectural Engineering*, 8(1), 19-23.
- [6] Adnan, N. H., & Ressang, A. (2016). Ergonomics awareness on construction site. *Construction Management, Geotechnics and Transportation*, 12, 190-203.
- [7] Al swaity A., & Enshassi, A. 2012). Construction Ergonomics related to safety. In *4th International Engineering Conference*, 1-12.
- [8] Md. Zan, H., Md Yusop, M. S., M. Y., Shapie, S. S., Ishak, R., & Mat, S. (2018). Preliminary study toward musculoskeletal disorders among industrialized building system workers. *Proceedings on Mechanical Engineering Research Day*, 2018, 150-151.
- [9] Middlesworth, M. (2011). NIOSH lifting equation.
- [10] Rostykus, W. G., Ip, W., & Dustin, J. A. (2016). Managing Ergonomics: Applying ISO 45001 as a Model. *Professional Safety*, 61(12), 34-42.

# Fuzzy-analytical hierarchy process (Fuzzy-AHP) approach for choosing the best design concept of material transport system

Khairun Najmi Kamaludin, Lokman Abdullah\*, Nur Adila Shaffini Suhaimi

Fakulti Kejuruteraan Pembuatan, Universiti Teknikal Malaysia Melaka,  
Hang Tuah Jaya, 76100 Durian Tunggal, Melaka, Malaysia

\*Corresponding e-mail: lokman@utem.edu.my

**Keywords:** Fuzzy-AHP; conceptual design selection; product development process

**ABSTRACT** – Precise concept selection during product development is a crucial process. Imprecise selection can lead to an unwanted scenario in manufacturing. Fuzzy Logic with Analytical Hierarchy Process (Fuzzy-AHP) is an optional tool to explore and cater decision-making process. Fuzzy-AHP has an advantage of being able to process ambiguous criteria. This paper presents the methodology and results of a case study which adopts Fuzzy-AHP concepts and guidelines to effectively analyze various design criteria, alternatives at the conceptual design stage, and finally a precise decision-making. This paper presents an alternative to traditional decision making methods.

## 1. INTRODUCTION

This paper presents the Fuzzy Logic with Analytic Hierarchy Process (Fuzzy-AHP) application for selecting the best design concept of material handling system that integrates the qualitative and quantitative of each criterion in the decision structure. The traditional method of AHP has a limitation in addressing the ambiguity of subjective judgment. Variant of Fuzzy-AHP was developed and applied to model the ambiguity of judgment by representing the verbal scale in terms of fuzzy number [1].

## 2. METHODOLOGY

A few methods of Fuzzy-AHP can be applied. In this study, Triangular Fuzzy is implemented. Based on the characteristics defined as below, we will be implementing Triangular Fuzzy-AHP. Firstly, characteristic of requirement must be defined:

Table 1 Characteristic of each design concept.

	Cost (€/h)	Speed (m/min)	Item width (cm)	Item weight (kg)	Flexibility (%)	Safety (%)	Ergonomic s (%)
DC1	1.50-2.00	8-12	2-15	0-10	13-17	80-90	80-90
DC2	1.85-2.30	9-13	2-20	0-10	15-19	75-92	78-90
DC3	1.75-2.25	7-11	3-30	0-20	16-20	80-90	80-92
DC4	1.90-2.40	6-10	3-25	0-15	14-18	70-85	86-90

The characteristics of each of the design concept is as shown in the Table 1. Selection of the best concept design (Figure 1) must meet the manufacturing requirement as follows:

- (a) The cost must be in range of 1.50 to 2.00 (€/h)
- (b) Speed of conveyor must be in range of 8 to 10 (m/min)
- (c) Item width is in range of 10 to 20 cm
- (d) Item weight is in range of 0 to 10 Kg

- (e) Flexibility must be in range of 16 to 20 %
- (f) Safety must be in range of 85 to 95 %
- (g) Ergonomics must be in range of 85-95 %

The next step is to apply the Triangular Fuzzy-AHP steps as follow:

- (a) Comparison of criteria via linguistic term:

$$\tilde{A} = \begin{bmatrix} \tilde{d}_{11} & \tilde{d}_{12} & \tilde{d}_{1n} \\ \tilde{d}_{21} & \dots & \tilde{d}_{2n} \\ \tilde{d}_{n1} & \tilde{d}_{n2} & \tilde{d}_{nn} \end{bmatrix} \quad (1)$$

Where  $\tilde{A} = k^{th}$  decision maker's preference of  $i^{th}$  over  $j^{th}$  criterion,  $\sim$  = triangular number demonstration

$\tilde{d}_{12}$  = first decision maker's preferences of first criterion over second criterion

- (b) Averaging the preferences of decision maker:

$$\tilde{d}_{ij} = \frac{\sum_{k=1}^k \tilde{d}_{ij}}{k} \quad (2)$$

- (c) Updating the pair-wise contribution matrices. The pair-wise contribution matrices are updates according to the average preferences:

$$A = \begin{bmatrix} d_{11} & d_{1n} \\ M & O \\ d_{n1} & d_{nn} \end{bmatrix} \quad (3)$$

Calculate the geometric mean of fuzzy comparison value:

$$\tilde{r}_i = (\prod_{j=1}^n \tilde{d}_{ij})^{1/n}, i = 1, 2, \dots, n \quad (4)$$

- (d) Calculate the fuzzy weight of each criterion:

$$\tilde{w} = (\tilde{r}_1 \oplus \tilde{r}_2 \oplus \dots \oplus \tilde{r}_n)^{-1} \quad (5)$$

$$= (l_{wi}, m_{wi}, u_{wi})$$

- (e) Defuzzification of fuzzy triangular numbers:

$$Mi = \frac{l_{wi} + m_{wi} + u_{wi}}{3} \quad (6)$$

- (f) Normalize of  $Mi$ .  $Mi$  must be normalized by using the equation as it is non-fuzzy number.

$$Ni = \frac{Mi}{\sum_{i=1}^n Mi} \quad (7)$$

- (g) Calculate the score of alternative.

- (h) Ranking of priority value.

### 3. RESULTS AND DISCUSSION

The steps in methodology is used to determine the best design concept of conveyor system for the applied manufacturing [4-6].

Comparison of criteria via linguistic term . This step must be completed on all of the  $n \times n$  criteria (Table 3).

Then sum the pair-wise comparison criteria as shown in Table 4. Averaging the preferences:

$$\sum ML = \frac{1}{116.2500}, \sum MM = \frac{1}{87.4841},$$

$$\sum MU = \frac{1}{63.8250}$$

Calculate the geometric mean of fuzzy comparison value. Three rules to calculate the weightage:

- (a)  $M2 \geq M1 = 1$
- (b)  $L1 \geq U2 = 0$
- (c)  $(L1 - L2) / (L1-M1)-(U2-M2)$

Final weight of criteria = {1,0,0,0,0,0,0}. Then, ranking of priority value as shown in Table 5.

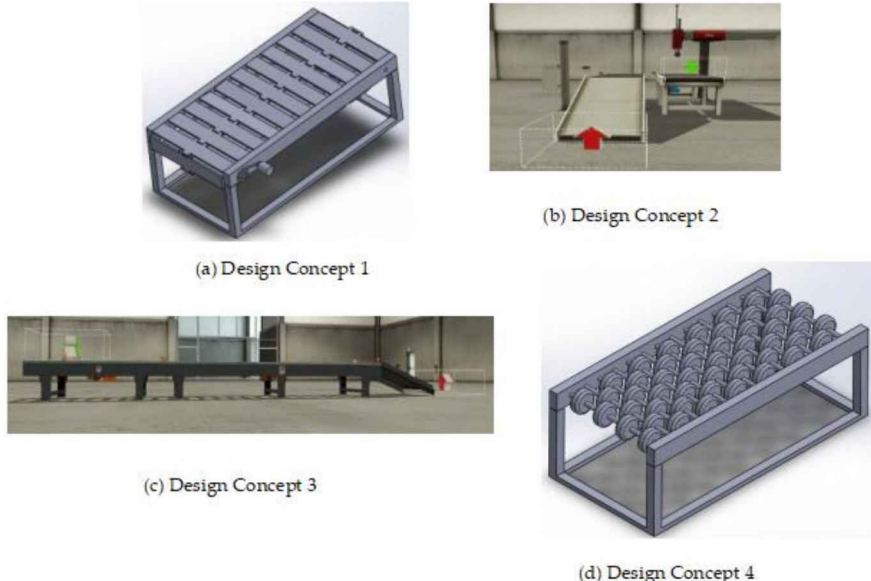


Figure 1 Conveyor design concepts.

Table 3 Pairwise comparison of criteria of two rows.

	Cost			Flexibility			Speed			Item Width		
Cost	1	2	1	1	2	3	6	7	8	8	9	10
Flexibility	1/3	1/2	1	1	1	1	1	2	3	1	2	3

Table 4 Adjusted pairwise comparison of criteria.

	L	M	U
Cost	$36.0000 \times 1/116.2500 = 0.3097$	$42.0000 \times 1/87.4841 = 0.4801$	$48.0000 \times 1/63.8250 = 0.7521$
Flexibility	$7.3333 \times 1/116.2500 = 0.0631$	$12.5000 \times 1/87.4841 = 0.1429$	$18.0000 \times 1/63.8250 = 0.2820$

Table 5 Ranking of priority value.

Design concept	Weightage
DC 1	4.4723
DC 2	2.0800
DC 3	0.4477
DC 4	0

### 4. SUMMARY

This research extracts the methodology of calculating the most appropriate design concepts at a conceptual design stage, by implementing Fuzzy-AHP. This method is slightly more complex than a traditional AHP, in addition with a certain basic criterion (and with more sub-criteria) and an ambiguity of a decision. Design concept 1 has been determined as the best design in this analysis, as it resulted the highest value of 4.4723. Application of Fuzzy-AHP can cater factors during

product development process to cater decision on ambiguity and also precise criteria. A more complex simulation software (MATLAB) will be subject of interest to gain a deeper knowledge of the subject.

### REFERENCES

- [1] Bellman, R.E., & Zadeh, L.A. (1960). Decision making in a fuzzy environment. *Management Science*, 17(4), 141-164.

- [2] Abdullah, L., & Najib, L. (2014). A new type-2 fuzzy set of linguistic variables for the fuzzy analytic hierarchy process. *Expert Systems with Applications*, 41(7), 3297–3305.
- [3] Saaty, T. L. (1980). The Analytic Hierarchy Process, New York: McGraw Hill. *International, Translated to Russian, Portugueses and Chinese, Revised edition, Paperback (1996, 2000)*, Pittsburgh: RWS Publications, 9, 19-22.
- [4] Bhushan, N., & Rai, K. (2007). *Strategic decision making: applying the analytic hierarchy process*. Springer Science & Business Media.
- [5] Chang, D. Y. (1996). Applications of the extent analysis method on fuzzy AHP. *European Journal of Operation Research*, 95, 649–655.
- [6] Kulak, O. (1994). A decision support system for fuzzy multi-attribute selection of material handling equipment. *Expert Systems with Applications*, 29(2), 310.

# The innovative tungku for new mother recovers during postnatal period

Mohammad Kamil Sued<sup>1,2,\*</sup>, T. Joseph Sahaya Anand<sup>1,2</sup>, Laavanya Sothi<sup>1,2</sup>, Sim Yiew Yiew<sup>1,2</sup>, Abdul Aziz Ajid<sup>1,2</sup>, Gogulan Manickavelu<sup>1,2</sup>

<sup>1)</sup>Fakulti Kejuruteraan Pembuatan, Universiti Teknikal Malaysia Melaka,  
Hang Tuah Jaya, 76100 Durian Tunggal, Melaka, Malaysia

<sup>2)</sup>Advanced Manufacturing Centre, Universiti Teknikal Malaysia Melaka,  
Hang Tuah Jaya, 76100 Durian Tunggal, Melaka, Malaysia

\*Corresponding e-mail: kamil@utem.edu.my

**Keywords:** Tungku; postnatal; massage

**ABSTRACT** – Traditional Tungku is commonly a typical river stone that has a certain weight and geometry. The high temperature stone be wrapped with herbs before being covered with cloth. The heat produced by the stone is difficult to maintain and less reliable. There is a need to innovate and modernize the traditional tungku. The new innovative tungku is not only to provide the main function of its traditional counterpart but also able to do massage, generate heat which can be adjustable, portable and with less weight. The system is also ergonomically well designed for any new mother during the postnatal period.

## 1. INTRODUCTION

Traditionally, there's a lot of materials used as tungku device such as river stone, hill stone, steel block and also sand and rock salt. The basic procedure to use this tungku device is by heating that manually using stove or charcoal before placing it on stomach. The essential features in the Malay postpartum care include the use of herbs, heat, and Malay postnatal massage. Heat is used in the form of direct exposure such as hot compression (bertungku), warm bath or indirect exposure such as consuming 'hot food' during confinement. The former is also an essential practice in the Malay postnatal massage apart from whole body massage and body wrapping (barut). Massage is performed for at least three consecutive days, six to seven times during the confinement period. Hot compression is believed to be able to dissolve residual blood clots in the uterus, to help it to contract, break down fat tissue and help woman's body return to its pre-pregnancy state. During the heating process, the temperature of the material needs to take in to concern because max temperature that can be handled by skin of a postnatal woman is 43°C [1].

After giving birth, it is normal for a woman to experience bleeding and to pass some blood clots as the uterus contracts and becomes smaller which is shown in Figure 1. During this recovery time, the woman's body begins the process of restoring itself to a pre-pregnancy state and prepares for breastfeeding. There are two types of blood clots that women may experience after childbirth which is clot that are passed through the vagina in the days after birth, which are from the shedding of the womb's lining and the detachment of the placenta and clots that happen inside the body's veins [2]. As the body sheds the placenta after childbirth, blood may pool inside the uterus and form clots. The normal discharge of the

uterine lining after childbirth is called lochia. It is made up of blood, mucus, other tissue, and some bacteria.

Our product can produce heat and vibration to treat postnatal women. Heat therapy increases blood flow when applied, helping to dilate blood vessels and improving circulation. Meanwhile, childbirth is the most frequent causes of weak and loose pelvic floor muscles [3]. This therapy helps to tone and strengthen the muscles of the pelvic floor while improving core stability and posture [4].

## 2. METHODOLOGY

To develop this product a product design and manufacture has been followed. In general, the steps are shown in Figure 1.

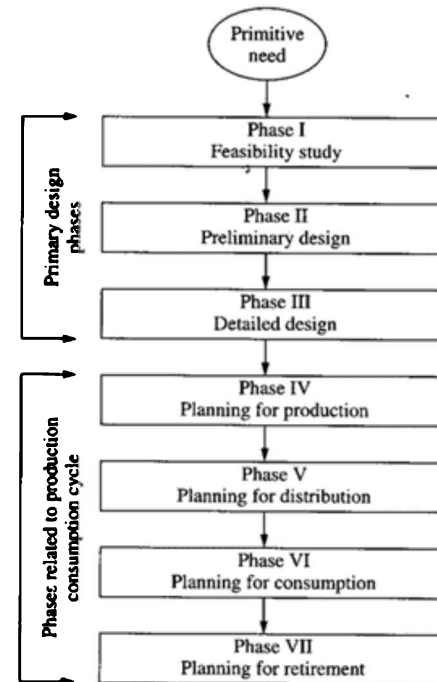


Figure 1 Design process.

At start feasibility study has been conducted. Responses were collected from the mothers in terms of their thinking about the way they expects the modern and innovative tungku. A survey has been conducted among different gender (new parents and future parents) and races. The results are shown in Figure 2. Both the needs and limitations are highlighted, and the responses are recorded in Figure 3.

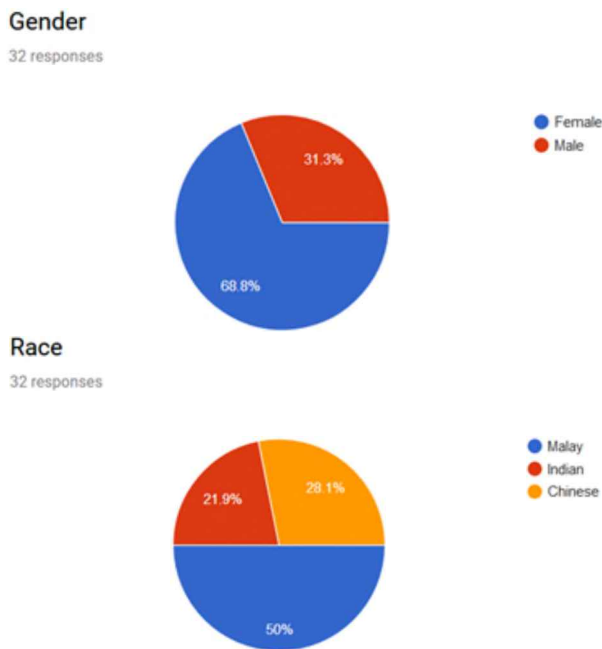
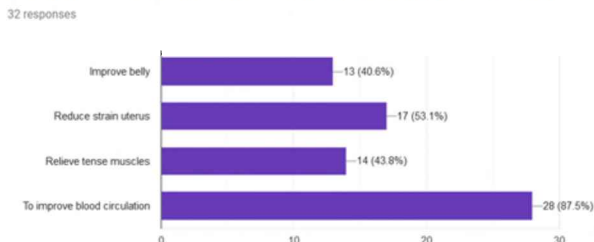


Figure 2 Background of the respondent.

From the survey results it is well understood that the expectation of such a device at different race is highly appreciated. By considering the above factors this new innovative tungku can serve the community in a better manner.

#### 1. Why Traditional Tungku is needed? (you can answer more than one)



#### 2. What do you think about Traditional Tungku weakness? (you can answer more than one)

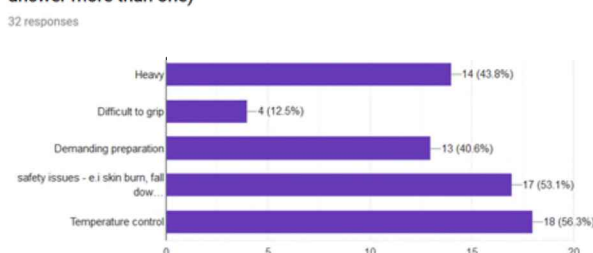


Figure 3 Needs and limitations of the traditional tungku.

By understanding the situation product are being designed and detail planning are being constructed. Design selection and process were conducted. Figure 4 illustrated the innovative tungku that being fabricated. This product is claimed the needs of the traditional tungku and solve all the weakness of the traditional tungku. Having the heating elements powered by electrical and power pack, the demanding heating

preparation is simplified. The weight is now manageable with a heating control that suitable for the skin. Additional advantage of this innovative tungku is it has a motor that is used for rotating the front ball to create a smoothing massage.



Figure 4 The innovative modern tungku.

Figure 5 shows the agreement of the respondents regarding the innovative of the product. About 90% of the potential customer agreed that the product will solve the difficulties and challenges of the Traditional tungku.

#### 3. Do you agree that this innovative Tungku solve the weakness of the Traditional Tungku?

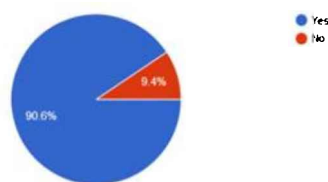


Figure 5. Response on accepting the innovative tungku.

### 3. CONCLUSION

The new innovative tungku is not only to provide the main function of its traditional counterpart but also able to do massage, generate heat which can be adjustable, portable and with less weight. The system is also ergonomically well designed for any new mother during the postnatal period.

### REFERENCES

- [1] Saman, N. (2014). Tungku herba elektronik berbara, MYPI 2012005359.
- [2] Avery, M. D., & Burkett, B. A. (1986). Effect of perineal massage on the incidence of episiotomy and perineal laceration in a nurse-midwifery service. *Journal of Nurse-Midwifery*, 31(3), 128-134.
- [3] Ghodsi, Z., Asltohgiri, M., & Hajiloomohajerani, M. (2012). Exercise and pregnancy: duration of labor stages and Perinea tear rates. *Procedia-Social and Behavioral Sciences*, 31, 441-445.
- [4] Kondo, Y., Sawa, R., Ebina, A., Takada, M., Fujii, H., Okuyama, Y., ... & Ono, R. (2017). Influence of habitual physical activity during late pregnancy on the duration of labor. *Journal of Physical Activity and Health*, 14(3), 203-207.

# Design and development of origami corner chair for children with Cerebral Palsy

Mohd Azlan Mohamed<sup>1,2,\*</sup>, Umi Hayati Ahmad<sup>1,2</sup>, Nur Hanis Harun<sup>1</sup>, Mohd Kamal Musa<sup>1,2</sup>, Mohd Qadafie Ibrahim<sup>1,2</sup>, Nurul Amira Jallil<sup>1</sup>, Muhammad Noor Ikmal Abdul Jalil<sup>1</sup>

<sup>1)</sup> Fakulti Teknologi Kejuruteraan Mekanikal dan Pembuatan, Universiti Teknikal Malaysia Melaka,  
Hang Tuah Jaya, 76100 Durian Tunggal, Melaka, Malaysia

<sup>2)</sup> Advance Manufacturing Center, Universiti Teknikal Malaysia Melaka,  
Hang Tuah Jaya, 76100 Durian Tunggal, Melaka, Malaysia

\*Corresponding e-mail: mohd.azlan@utem.edu.my

**Keywords:** Product design; corner chair; Cerebral Palsy

**ABSTRACT** – This paper presents the design and development of new corner chair for Cerebral Palsy (CP) children with regards to therapists and parent requirement. Concepts were generated with regards to product's portability, user-friendliness, and affordable to parent. Using concept scoring matrix, concepts were rated to its effectiveness in encouraging involvement of non-therapy professionals in performing therapy routines. Origami concept was chosen and advanced to prototype. The prototype was undergone field test at Hospital Besar Melaka. Therapists and parents agree that origami corner chair design is portable, compact, and affordable, thus encourage involvement of parent to practice therapy routines at home.

## 1. INTRODUCTION

Cerebral Palsy (CP) is a disorder of movement and postures caused by abnormal development or damage to the brain that control the movement, balance and body posture. The prevalence reported is 1.5 to 2.5 per 1000 live birth [1]. According to [2], in Malaysia, there are about 800,000 children with some form of disability and 8.1% are from CP children which are 64 800 cases. CP child posture development can be improved with proper seating aids like corner chair.

The occupational therapist believed that more time reinforcing therapy at home would improve the children's progress [3]. Many corner chair designs in the market to help the patients in this regard but not very successful to encourage home therapy due to their heaviness, pricy, and non-user-friendly design. Their weight ranges from 7kg to 12 kg and the price is at least RM1200. Available corner chairs in the market does not provide the ease to fold and collapse the chair thus making them bulky and is restricted to a particular place only. The development of new and improved corner chair design aims to generate concepts with less complexity thus reduce the overall weight, cost and is mobile.

## 2. METHODOLOGY

The key information was collected through survey and interview at Occupational Therapy (OT) Unit at Hospital Besar Melaka and Pusat Pemulihan Dalam Komuniti (PDK) with respondent of 50 person being the occupational therapists and parents. Survey carried out suggests that multiple unsatisfactory characteristic founds in existing corner chairs. 62% agree that those

corner chairs are heavy, 54% finds it difficult to store and 86% suggested that those corner chairs are not mobile. 68% of the parent have household income of less than RM3000 per month and unable to afford one at home.

Occupational therapists and parents favour lightweight, cheap, and portable corner chair. With regards on these requirements, 4 conceptual designs were generated. Conceptual design 1 as shown in Figure 1(a) inspired by the Lego® concept. This concept uses customize fasteners to attach separate parts into a usable corner chair and disassemble for storage and commute purpose. Conceptual design 2 proposed a briefcase inspired concept, where the corner chair can be collapsed into a considerably thin briefcase, as shown in Figure 1(b). Conceptual design 3 as shown in Figure 1(c) intended to change the corner chair backrest into flexible and light material and uses retractable ribbon system that commonly used in queuing barrier. Conceptual design 4 as shown in Figure 1(d) applies origami concept, with linear and simultaneous opening and folding movement.

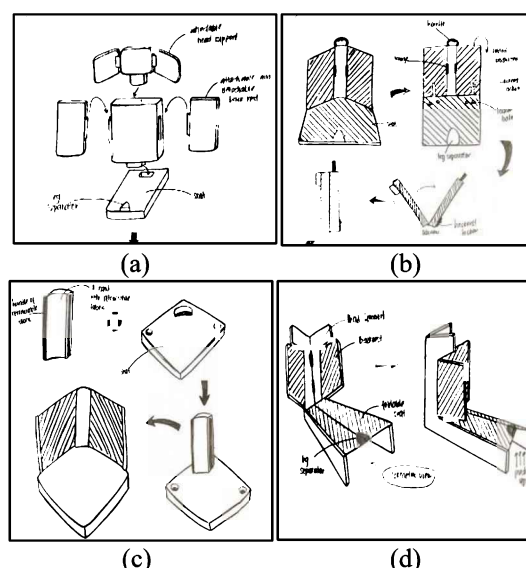


Figure 1 The conceptual designs of corner chair.

These concepts were evaluated and rated to its effectiveness in encouraging involvement of non-therapy professionals in performing therapy routines, as shown in Table 1. Concept 4, inspired by origami movement, ranked first and proceeded to the prototyping stage, of which it received several iterations and refinements

during proof-of-concept prototyping stage. Final prototype was developed using plywood as material for body, and cushion upholstered with soft fabric.

**Table 1 Concept scoring matrix.**

Criteria	CONCEPTS								
	Concept 1		Concept 2		Concept 3		Concept 4		
	Importance Weight (%)	Rating	Weighted Rating						
<b>Lightweight</b>	20	2	0.4	3	0.6	5	1	3	0.6
<b>Ease of storage</b>	15	2	0.3	3	0.45	4	0.6	4	0.6
<b>Functionality</b>	15	1	0.15	2	0.3	3	0.45	5	0.75
<b>Low Cost</b>	20	2	0.4	2	0.4	1	0.2	4	0.8
<b>Ease of use</b>	10	1	0.1	4	0.4	2	0.2	5	0.5
<b>Life time</b>	5	1	0.05	4	0.2	3	0.15	3	0.15
<b>Ease to manufacture</b>	5	3	0.15	3	0.15	2	0.1	4	0.2
<b>Safety</b>	10	2	0.2	4	0.4	1	0.1	3	0.3
<b>Total Score</b>	1.75		2.9		2.8		<b>3.9</b>		
<b>Rank</b>	4		2		3		<b>1</b>		
<b>Develop?</b>	No		No		No		<b>YES</b>		

The prototype was undergone field test at OT unit, Hospital Besar Melaka. 5 childrens with CP, aged from 2 to 15 years old, with mild and severe CP level, was randomly seated. The occupational therapist performed their routines with or without presence of the parents, as shown in Figure 2. The experience of the therapist and parents handling the corner chair and patient were recorded, and their feedback was taken into consideration.



Figure 2 Field test at OT unit, hospital Melaka.

### 3. RESULTS AND DISCUSSION

Origami concept corner chair enables the user to use the chair without hassle to attach and detach nor to assemble and dissemble the component because of its linear and simultaneous opening and folding movement.

When in operable position as shown in Figure 3(a), the overall dimension in W x H x D is 600mm x 600mm x 500mm, and in folded position as shown in Figure 3(b), the dimension is 100mm x 600mm x 500mm. The prototype weighted only at 4kg, and the cost to produce one unit is RM200 and is expected to reduce further in production phase. The corner chair is equipped with standard accessories like chest strap, belt, and pommel.



Figure 3 Origami corner chair prototype.

Positive feedback was received from the field test. The prototype exceeds the expectation on the portability and weight. Respondent agree that origami corner chair is easier to be used than the corner chair available in the market. It is handy, can be transported whenever the user is in commute. It is also proved that this corner chair requires small space for storage. Respondents shows interest to own a unit when the selling price estimated is at most RM600.

### 4. CONCLUSION

Origami concept corner chair had successfully developed and had shown significant improvements in reducing the complexity, weight, and cost when compared to available products in the market. With more than 50% less in weight and selling price, more parents with CP children will able to afford one-unit corner chair and thus contribute to the effectiveness of therapy by extending the therapy routines at home.

### ACKNOWLEDGEMENT

The authors gladly acknowledge the support of Universiti Teknikal Malaysia Melaka through Short Term Grant PJP/2018/FTK(14D)/S01640.

### REFERENCES

- [1] Paneth, N., Hong, T., Korzeniewski, S. (2006). The Descriptive Epidemiology of Cerebral Palsy. *Clin Perinatol*, 33(2), 251– 267.
- [2] Hamzah, F., Hashim, N., Hassan, N., Hamzah, M. H., Yazit, T. S. B. R., Razak, R. F. H., Mawardi, H. Cerebral Palsy Child Seat: Ergonomic Consideration. (2017). *Advanced Journal of Technical and Vocational Education* 1 (1), 46-55.
- [3] Hinojosa, J., Sproat, C. T., Mankhetwit, S., Anderson, J. (2002). Shifts in Parent-Therapist Partnerships: Twelve Years of Change. *American Journal of Occupational Therapy*, 56(5), 556–563.

# Indoor cabinet fertigation: A new concept design for urban agriculture

Mohd Arizam Abdul Wahap\*, Umi Hayati Ahmad, Mohd Kamal Musa, Mohd Qadafie Ibrahim, Ng Shek Yi

Fakulti Teknologi Kejuruteraan Mekanikal dan Pembuatan, Universiti Teknikal Malaysia Melaka,  
Hang Tuah Jaya, 76100 Durian Tunggal, Melaka, Malaysia

\*Corresponding e-mail: arizam@utem.edu.my

**Keywords:** Urban farming; design concept; cabinet fertigation

**ABSTRACT** – Urbanization has transformed vast agricultural land into the concrete forest due to the increase in world population. With this increasing amount of population, traditional agriculture techniques are unable to sustain sufficient crops for consumers. Without choice, urban farming by self is by far become one of the option to overcome the current situation. Indoor farming or garden is the newly developed phenomenon which in line with the urban farming concept able to offer few advantages including water-saving watering system and power-saving lighting features. This new concept of indoor cabinet fertigation system will be introduced with a systematic design process and analysis which therefore explain the practicality of this idea.

## 1. INTRODUCTION

The world population is estimated to be increased at least up to nine billion by 2050, while the food demand will speed up at a far faster rate than population growth Dorling [1]. The limited spaces due to development has become the main factor of the increased in urban farming [2]. Smart garden is an indoor garden that focus to provide a low cost and easy to farm concept. There are already many smart gardens available in the market, where the design concept is either based on hydroponic, aquaponics or aeroponic [3,4].

The main objectives for this project is to design a practical and compact feature beside developing a cabinet indoor fertigation system with water-saving watering system and power-saving lighting system features. A full-scale prototype of this design will be constructed and tested to analyze the practicality of this concept.

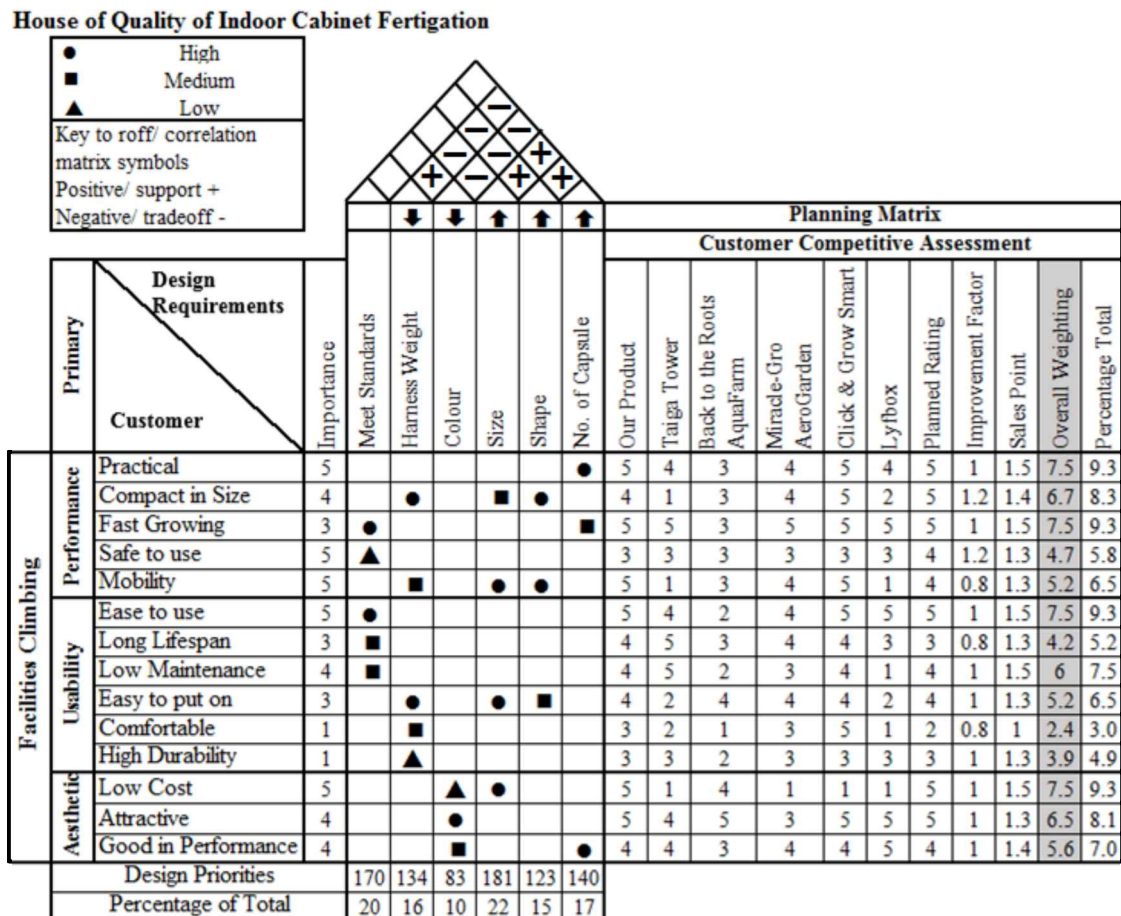


Figure 1 House of quality (HOQ) for the new concept design.

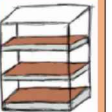
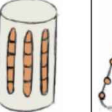
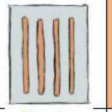
Topic \ Option	I	II	III	IV
Planting System	Hydroponics	Aquaponics	Fertigation	Aeroponics
Structure				
Replacement	Book Shelf	Console Table	Shoe Rack	Sink Cabinet
Place to locate	Kitchen	Living Room	Entrance	Bathroom
Dimension (Size)	60cm x 120cm x 35cm	80cm x 100cm x 25cm	30cm x 50cm x 15cm	50cm x 65cm x 30cm
Characteristics	<ul style="list-style-type: none"> <li>• Rotatable</li> <li>• Complex Shape</li> <li>• Automated Watering</li> <li>• Attractive Design</li> </ul>	<ul style="list-style-type: none"> <li>• Size in compact</li> <li>• Automated Watering</li> <li>• Supply Light</li> <li>• Self-fertilize</li> <li>• Attractive Design</li> </ul>	<ul style="list-style-type: none"> <li>• Convenience</li> <li>• Easy to carry</li> <li>• Within Handle Design</li> <li>• Supply Light</li> <li>• Attractive Design</li> </ul>	<ul style="list-style-type: none"> <li>• Size in compact</li> <li>• Portable</li> <li>• Supply Light</li> <li>• Manual Fertilize</li> <li>• Attractive Design</li> </ul>
Growing Days	10 – 30 days	40 – 60 days	60 – 90 days	90 – 110 days
Layout				
Fertilizer Used	Liquid Fertilizer	Powder Fertilizer	Tablet Fertilizer	Inorganic Fertilizer

Figure 2 Morphological chart of the design specifications.

## 2. METHODOLOGY

A survey consists of 30 urban respondents had been conducted to determine the customer expectation. The concern criteria were then being analyzed and transformed into design requirement before further compared with the existing agricultural product or system. The overall process can be summarized using house of quality (HOQ) as shown in Figure 1.

The conceptual design stage was then being established using morphological chart (Figure 2). This diagrammatic technique is used to catalogue and help evaluate combinations of alternative system elements. Figure 2 shows the morphological chart which based on the existing method in agriculture (arranged in column) versus the design criteria which finalize from the customers need (arranged in row).

Based on the analysis, the practical combination of design parameters for the cabinet is a fertigation system due to its characteristics in a table console arrangement. Monitoring, maintenance and plant growth monitoring are few important factors when designing this cabinet. Therefore, accessibility of the plant and the system become main priority.

Kitchen room been selected as the place to locate for ease of reachable, thus the size should be compact. Liquid fertilizer is the one that commonly used in fertigation will eases the irrigation process as this design allows the separation of the top layer plants and the bottom layer plants.

Five types of vegetables had been chosen to cultivate in the prototype and plant growth rate in this cabinet were recorded and compared to conventional farming. Selected plants were water spinach (*kangkong*), Chinese flowering cabbage (Choy Sum), spinach, onion, and sweet potato leaves. The selection was based on their popularity to Malaysian, easy harvest and easy to grow.

## 3. RESULTS AND DISCUSSION

### 3.1 Design of the Cabinet Fertigation

The design utilized kitchen cabinet concept, where it equipped with two flipped transparent glass doors to increase the accessibility of the inner section as well as plant growth monitoring (Figure 3). This cabinet provide three console of planting section whereas one layer at the upper level and two layers (frontal and back) at the lower level. The top console is for small size of vegetables, while the back-lower console for medium size. Both are side pull-over drawer type. The frontal-lower console is for the largest size vegetable were allowed to grow up to the upper level. Mesh net was placed below the glass on the frontal console door for air ventilation.

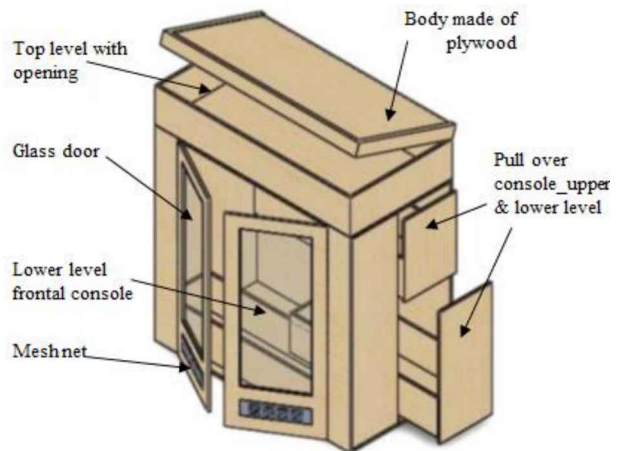


Figure 3 The final conceptual design of the cabinet fertigation system.

The irrigation system is using gravity based type where the tank of fertilizer-solution is placed on the top level of the cabinet to ensure enough static pressure for the supply. This concept enable energy saving since no pump required for irrigation system. Microtube with diameter of 4 mm and fitted with adjustable dripper was used for the irrigation. System is controlled by a water timer which also made the system become self-watering and thus therefore allowed for minimum monitoring.

Besides the drip irrigation system, the lighting system is part of the whole design system as it helps the plants to go through photosynthesis. The lighting system built out of light bars with Ultraviolet rays that become the light source for the plants. The system allowed 24 of light availability to maximize the growth of the plants. Since the vegetables been cultivated inside the cabinet, therefore it is fresh.

### 3.2 Plant Growth Rate

The plant growth rate of each type of the vegetables are shown in Table 1. From the analysis, each of the vegetables grow faster to their optimum harvesting period. Therefore, it is proved that the plant grows faster by using fertigation system as compared to the conventional planting system.

Table 1 Comparison of plant growth rate for cabinet fertigation and conventional farming system.

Vegetables	Planting System	Cabinet fertigation (cm/day)	Conventional farming (cm/day)
Water spinach		1.52	0.5
Chinese flowering cabbage		0.65	0.6
Spinach		0.54	0.5
Onion		0.39	0.17
Sweet potato leaves		0.75	0.42

#### 4. CONCLUSION

The indoor cabinet fertigation able to demonstrate indoor small-scale farming using compact space mainly for urban residence. By utilizing the fertigation agriculture concept, this design is able to provide fresh vegetables for daily consumption.

#### ACKNOWLEDGEMENT

The authors gratefully acknowledge the support of Universiti Teknikal Malaysia Melaka through Short Term Grant PJP/2018/FTK (14D)/S01640.

#### REFERENCES

- [1] Dorling, D. (2013). *Population 10 billion*. Hachette UK.
- [2] Banerjee, C., & Adenaeuer, L. (2014). Up, up and away! The economics of vertical farming. *Journal of Agricultural Studies*, 2(1), 40-60.
- [3] Frail, T.A. (2010). The rise of urban farming. [Online]. Available at: <https://www.smithsonianmag.com/science-nature/the-rise-of-urban-farming-762564/>.
- [4] Leatherbury, M. U. (2014, July). VEGILAB and aquaponics indoor growing system. In *2014 IEEE Conference on Technologies for Sustainability (SusTech)* (pp. 135-139).

# The mechanical transmission system glutinous rice shredder

Rosad Ma'ali El Hadi<sup>1</sup>, Rina Indrayani<sup>2,\*</sup>, Agus Rahmat Hermawanto<sup>2</sup>

<sup>1)</sup> Telkom University Bandung, Jl. Telekomunikasi Jl. Terusan Buah Batu No.01, Sukapura, Kec. Dayeuhkolot, Kota Bandung, Jawa Barat 40257, Indonesia

<sup>2)</sup> Sekolah Tinggi Teknologi Bandung, Soekarno-Hatta St No.378, Kebon Lega, Bojongloa Kidul, Bandung City, West Java 40235, Indonesia

\*Corresponding e-mail: rina@sttbandung.ac.id

**Keywords:** Transmission system; applied technology; production; glutinous rice

**ABSTRACT** – The process of destruction of the glutinous rice as raw material for the manufacture of opaque sticky rice until the moment is still using manual processes, where sticky rice is made in the media made of stone and mortar in mash using the tool pounder, move up and down by utilizing the power of man. The process of destruction is very easy to use when it is sticky rice so that optimal results are obtained, besides sticky party crafts found it is difficult to look for sticky rice crushing labor, the utilization of the glutinous rice with shredder motor movers and gearbox methods, to drive the tools of destruction up and down, rotates the dimples come with glutinous rice to move the stopper from the edge to the middle. The design of this technology, the focus of the manual process for dissolution, besides the limitations of manpower, the hygienic and the quantity of industry, this small, the speed and smoothness of the process of destruction can become very varied So, craftsmanship could not meet the high demand. The Glutinous rice with shredder motor 1.5 HP Activator method and 70 rpm gearbox, the transmission system. Transmission system can change the rotary motion into alternating motion of the gearbox for ascending lower pounder and with the transmission system into the rotary motion using the chain and gears tire, forwarded to change the rotary motion vertically, finally can play the dimples. The performance analysis and feasibility of glutinous rice with shredder motor method is that the continuity of products can be fulfilled and when the process of destruction is not a dependency to the manual process. Manufacture, test and analysis of the performance of glutinous rice with a shredder transmission system fulfilled.

## 1. INTRODUCTION

Buahdua village is a village located in Sumedang Indonesia, land of the village of Buahdua is mostly used as farmland, rice crops such as manioc, soybeans, and chili. Agricultural activity is the main sector of the community of the village of Buahdua and is the people's livelihoods, one crop is glutinous rice plant that would produce a sticky rice glutinous as a raw material. Buahdua village is famous for the production of sticky rice crackers and its producers have fulfilled orders from various cities in Java, such as Bandung, Garut and Tasikmalaya Indonesia. Craftsmen in villages Buahdua sticky rice crackers in corporate into the combined group of farmer's organizations. Craftsman opaque sticky rice is one of the perpetrators of the creative industries in the

field of culinary, opaque is a typical snack of West Java and has the potential to develop up to outside West Java. Creative industries in the field of culinary already has a broad market and be able to compete with the modern retail market, because it has more economic value but still get the profit. Based on the initial survey to the village of Buahdua, opaque sticky rice production process can be seen in Figure 1.



Figure 1 Flow in glutinous opaque creation process.

Figure 1 shows the process of making opaque sticky rice and glutinous rice destruction problems as raw sticky rice is traditionally opaque, see Figure 2, so that productivity is very low, while demand for glutinous opaque (market) is very high. It needs to be created and implemented (applied) glutinous rice shredder with transmission system, in order to address the problems experienced by the craftsmen of the sticky rice crackers.



Figure 2 The process of the destruction of the opaque sticky rice is traditionally.

The most crucial process in the manufacture of the sticky rice crackers process of destruction of glutinous rice, glutinous rice because if already pounded rough or less gently, then it will affect quality of glutinous opaque impact on poor quality opaque sticky rice is cooked.

Problems of glutinous rice ball-crushing labor of a problem, because of the difficulty of finding a workforce ready for the pounding glutinous rice. Because in the sticky rice pounding power required a large and quite a long time starting from the hours of 1.00 up to 6.00 hours, so that the workforce should have the physical condition of a healthy and strong. Glutinous rice destruction work also has the highest workload in comparison with other place work, it would have an impact to the increasingly difficult sticky opaque craftsmen to find labor is willing to pound rice sticky rice. Based on observation and issues that do, need to be designed, created and implemented (applied) glutinous rice shredder with transmission system by utilizing only 1 (one) 1.5 HP driving motorcycles and 1 (one) the fruit of 70 rpm gearbox, can move up and down mortar and pestle spin that comes with a stopper. Glutinous rice Shredder based appropriate technology, the cost is relatively cheap, all components of local content, easily made in the workshop of welding workshop and machining tooling as well as her treatment very easily that's fundamental idea and original as contribution to Science and technology (science and technology).

## 2. LITERATURE

### 2.1 Opaque Sticky Rice

Opaque sticky rice is a type of snack food and are business activities that still exist and become the livelihood for most of the Buah dua village community. Production process opaque sticky rice until ready for distribution or consumption, it takes time for one day. The production was

Done in traditional and hereditary, with the simple equipment such as the "mortar" large-sized (for mashing sticky rice).

The process of destruction of the glutinous rice glutinous rice into a smooth, as raw material for the manufacture of opaque sticky rice by using sticky rice with shredder transmission system, is a technology product innovations have invest and novelty, the sustainability of the production and market of glutinous rice with shredder transmission system is extensive, because the sticky opaque widely produced in several parts of Indonesia and se Shredder glutinous rice can be used for pounding rice, coffee, corn and others.

Shredder product with transmission system will compete in a market that is competitive enough, then the differentiation of the product has to do make different Shredder product with similar products that exist in the market, his strategy is pretty give you 1 unique value alone and there has never been, then the shredder products will stand out in the market, it is there in glutinous rice shredder with the transmission system.

### 2.2 Product Design

The economic success of a company depends on the manufacturing capabilities in identifying customer needs and quickly create products that can meet the

needs of the customer and can be produced with a low cost. This becomes a problem product development which includes a marketing function, function design, function and manufacturing to other functions within the company [1-6].

Product development is a series of events that began with the perception of the market opportunity and ends with the production, sale, and delivery of the product. Product development is also an activity that requires contributions from almost all functions in an enterprise, but three functions that became the center of product development, namely marketing, design and manufacturing.

The specific dimensions that are commonly used to estimate the success of product development, among other things:

- (a) product quality that affect market share and price willing to be paid by the customer;
- (b) the cost of products that illustrate the advantages to be gained in volume and sales price;
- (c) development time describing how the company became responsive to technological developments;
- (d) development costs describe costs that must be incurred to develop products company;
- (e) ability Development i.e. the ability of the team and the company in developing the product.

Understanding new products are generally accepted among others:

- (a) new-to-the-world products, is the product of the invention of the first;
- (b) new category entries, products not including new-to-the-world products, but can bring the company into the new categories for the product;
- (c) additions to product lines, new products that provide additional/product lines long (the size of the packaging, flavors, and others);
- (d) product Improvement (improvement of product), product that showed improved performance/value and replace old products;
- (e) repositioning, old products directed at market or new market segments.

### 2.3 Transmission System

Manual transmission is a combination of tooth wheels that move round and moment crankshaft to the driving wheels, with the intention of:

- (a) produce a greater power for the start time and running in place;
- (b) move the wheels at high speeds (light speed driving);
- (c) move the wheels turning.

To do 3 things above, then needed the addition or reduction of the moment (speed) and change the direction of rotation of one of the gears. Transmission of important terms are:

- (a) should be easy, precise and fast it works;
- (b) power can move gently and precisely;

- (c) light, practically in the form, trouble free and easy to operate;
- (d) must be economical and have a high efficiency;
- (e) should be easy to care for.

Transmission system has a purpose to continue a power. From the power source to the source of power, the power user so the machine can work according to the desired needs. Design tools or machines should have the basic concept of planning. The basic concept of this planning will discuss the theoretical foundations that will be used as guidelines in designing a tool/machine. Design of transmission system of this part of the tools that will be planned or taken into account are:

- (a) An electric motor is the main component of machine construction serves as a driving force. The movement generated by the motor is a rotation of the shaft. Other components of the motor shaft are Other components that will be connected to a motor shaft are pulleys or gears which will then be connected to a belt or chain.
- (b) Power mover is defined as the skills needed to do work, expressed in units of Nm/s, Watts, or HP/PK. Determination of large power needed need to pay attention to several things, among them is the price of yangempengaruhnya force, torque, speed dial and heavy working on such mechanisms;
- (c) the Gearbox, transmission gearbox system essentially is a tool or mechanism transmits power by wearing gear transmission system, the transfer of power which can provide a fixed round or rounds changed so much used either large or small scale.
- (d) Pulley is as modifiers of a motor speed, the engine uses a pair of Pulley that works to reduce the speed of the generated by a motor. Pulley is a Mechanism of the tool used to run something that functions flow power to conduct such a power. The workings of pulleys are often used to change the direction of a given force, send motion and change the direction of rotation
- (e) Belts / chains, most transmission belts use V-belts, because they are easy to handle and cheap. Besides this transmission system can also produce large power transmissions at relatively low voltages. The distance that is far enough to separate the two shafts does not allow it to use direct transmission with the gears. Belt-V is a solution that can be used. The V-Belt is one of the connecting transmissions made of rubber and has a trapezoidal cross section. In its use the V-belt is wrapped around the V-shaped groove of the pulley as well. The part of the belt that wraps around the pulleys will experience curvature so that the width of the inside will increase.
- (f) Shaft is one part of a rotating machine elements which function to forward the power from one place to another. In its application combined with a pulley, shaft bearings, gears and other elements.

### 3. RESULTS AND DISCUSSION

#### 3.1 Glutinous Rice Shredder Design

Design of glutinous rice with shredder transmission system based on structural and functional which is divided into various sections, among others: the framework and the activator is equipped with a transmission system for moving the pestle and mortar spinning up and down redirect glutinous rice stopper and is being pounded into the middle section. Construction of glutinous rice with shredder transmission system, can be seen in Figure 3.

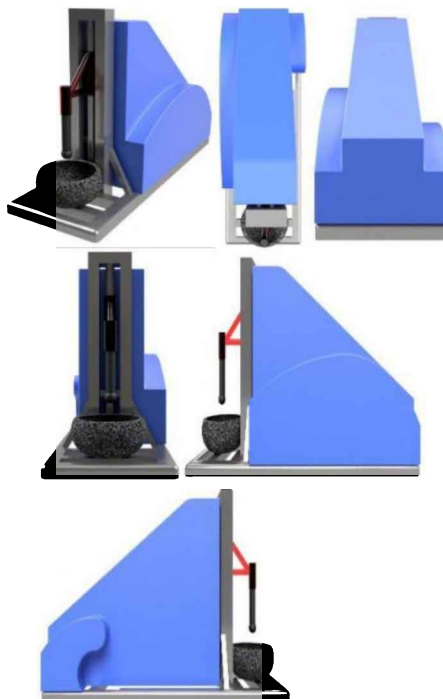


Figure 3 Perspective drawing, looking up, Rear, front, right and left.

#### 3.2 The Transmission System of the Glutinous Rice Shredder

- (a) Transfer the round motor to gearbox.

Processing machines in the production process, are generally driven by using electromotor (electric motor). Electric motors are generally used to drive or rotate industrial machinery, either directly or indirectly, through the process of reducing the rotation quantity or commonly called a speed reducer or gearbox.

For some machines that operate with a large rotation equal to the rotation of an electric motor, the installation of the motor does not need to use a gearbox. Considering some processing machines, one of which is glutinous rice pounder machine which requires a large amount of rotation or speed, the electric motor as a driver will be equipped with a gearbox, to change the rotation of the electric motor, according to the needs of the engine, see Figure 4.



Figure 4 The system electric motor with gearbox.

- (b) The transfer gearbox rounds into the movement back and forth.

In order to change the rotating motion of the gearbox, using the chain converted into movement playing us equipped with gears and wheels without teeth, see Figure 5.

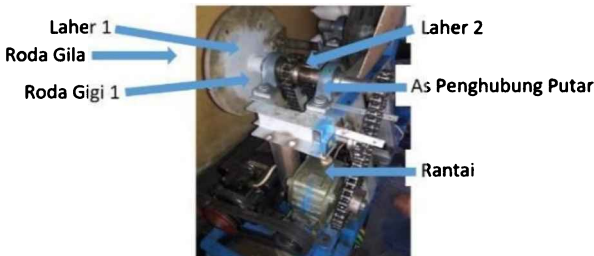


Figure 5 System modifier.

Play Movement Rotation of As. liaison will rotate the flywheel, using a lever connected to the flywheel part edge wheels, then will change the rotary motion into a translational motion back and forth, see Figure 6.

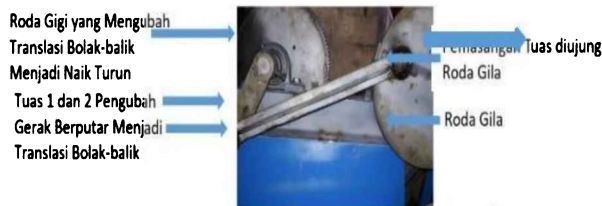


Figure 6 Rotating motion converter.

- (d) System be translated back and forth transfer of alternating movement to movement up and down the masher.

The alternating motion of the gears will be changed to an up and down motion of the pestle, meaning that the pestle will move up and down according to its function, see Figure 7. It will move up and down in accordance with its functions, see Figure 7.

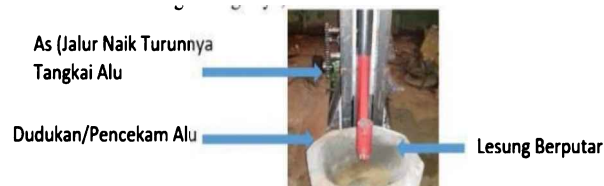


Figure 7 movement of up and down the pounder.

- (c) Horizontal round displacement becomes a vertical rotating movement to rotate dimples.

The rotation of the result using a chain is transformed into a lower axle rotating motion which is equipped with a tapered shape plus a cross-screw

mechanism as a reverse screw power movement occurs due to a change in the screw angle from positive to negative in the screw end part gradually. By changing the parabolic screw angle (quadratic function) at the maximum screw angle rotation interval, the dynamic effect due to the change in speed can be minimized, see Figure 8.

Horizontal axle rotation is transformed into a vertical rotating motion which is equipped with a tapered shape plus, a cross thread mechanism as a reverse screw power movement occurs due to changes in the screw angle from positive to negative at the end of the screw, the rotating motion will rotate the dimples, see Figure 9.



Figure 8 Transmission of as rotating movement to as horizontal rotating movement.



Figure 9 The process of transmitting the rotating horizontally into a spinning vertical.

#### 4. CONCLUSION

Glutinous rice pounder machine can move the pestle up and down and the spinning of the mortar which is equipped with a stopper, made with a mechanical transmission system. The use of a mechanical transmission system on sticky rice pounding machines is enough to use 1 (one) electric motor 1.5 and 1 (one) gearbox 70 rpm.

#### REFERENCES

- [1] Sularso & Suga K. (2004). mesin da rangkaian listrik. Erlangga
- [2] Sularso (1983). Dasar perencanaan dan pemilihan elemen mesin. Pradya Paramita, Jakarta.
- [3] Mott, R. L. (2009). Elemen-elemen mesin dalam perancangan mekanis; perancangan elemen mesin terpadu. Andi Offset, Yogyakarta.
- [4] Srigley, J. F. (1986). Perencanaan teknik mesin, Edisi Keempat, Jilid 2, Erlangga, Jakarta.
- [5] Vincent, G. (1992). Analisis sistem terapan berdasarkan pendekatan teknik industry. Tarsito, Bandung.
- [6] Widodo, I. D. (2003). Perencanaan dan pengembangan produk. UII Press Yogyakarta.

# Energy absorption of circular honeycomb out-of-plane dynamic impact under oblique loading

Sze Pei Tan, Siti Nadiah Mohd Saffe\*, Siti Aishah Rusdan

Faculty of Engineering Technology, University Malaysia Pahang, Lebuhraya Tun Razak, 26300, Pahang, Malaysia

\*Corresponding e-mail: sitinadiah@ump.edu.my

**Keywords:** Circular honeycomb; dynamic impact; oblique loading

**ABSTRACT** – This paper presents the circular honeycomb filler subjected to oblique loading ( $\theta = 0^\circ$  to  $30^\circ$ ). The models are tested by dynamic impact test. In this research, aluminium alloy AA 6060 T4 circular honeycomb which bottom is fixed, and top is subjected to  $\theta$ . The finite element analysis using ABAQUS code was validated according to the relevant experimental data. The performance of energy absorption (EA) and specific energy absorption (SEA) on different angles of loading were presented. The result showed, increased of  $\theta$ , the decreased of both EA and SEA.

## 1. INTRODUCTION

In a crashworthiness, the thin-walled components of the space frame absorb energy through a combination of bending and axial collapse [1,2]. Among previous works done, the dynamic behavior of out-of-plane for both filled and non-filled aluminium honeycombs with fillers are all the more regularly utilized as a part of energy absorption design.

The circular honeycombs are not much found on the out-of-plane crushing behaviors. However, honeycombs are typically utilized as the core of sandwich panels in terms of out-of-plane [3]. In this study, the main objective is to study performance of out-of-plane circular honeycomb under dynamic impact. The thicknesses of every cell are investigated which  $t = 0.06\text{mm}$  is investigated. All models are carried out by both axial and oblique loading which  $\theta = 0^\circ, 10^\circ, 20^\circ$  and  $30^\circ$ .

## 2. METHODOLOGY

To evaluate the energy-absorbance of structures, it is necessary to define the crashworthiness indicators. The parameters, such as energy absorption (EA), specific energy absorption (SEA), and peak crush force (PCF), can efficiently evaluate the crashworthiness of structures. EA is calculated as:

$$EA(\delta) = \int_0^{\delta} F(x)d\delta \quad (1)$$

Where  $F(x)$  is the instantaneous crushing force with a function of the displacement  $\delta$ .

SEA indicates the absorbed energy ( $EA(\delta)$ ) per unit mass ( $M$ ) of a structure as:

$$SEA(\delta) = \frac{EA(\delta)}{M_{total}} \quad (2)$$

Where  $M_{total}$  is the structure's total mass. In this case, a higher value indicates the higher energy absorption efficiency of a material.

The ABAQUS-Explicit was used to develop the circular-celled honeycombs that were impacted by a

dynamic loading. The walls of the honeycombs were modelled using four node shell continuum elements with five integration points along the element's thickness direction. The honeycombs were impacted by prescribed velocity of 15 m/s with mass block of 400kg. A 0.4mm element size was chosen [4]. The contact interactions between all components were the general contact algorithm and hard contact used to avoid interpenetration of walls. Meanwhile, the friction coefficient value for all contact surfaces was set at 0.2 for the dynamic case [5].

Figure 1(a) shows the schematics of circular-celled honeycombs under different impact loadings. The length of the honeycomb block,  $h$  is 50mm subjected to load angles,  $\theta$  with  $0^\circ, 10^\circ, 20^\circ$  and  $30^\circ$ . The honeycomb cross-section is shown in Fig. 1(b), thicknesses are specific as 0.06mm and the radius of every single cell of the honeycombs 5.2mm. The honeycomb fillers are 25 cells each block ( $5 \times 5$ ) is numerically worked to verify the validity [6].

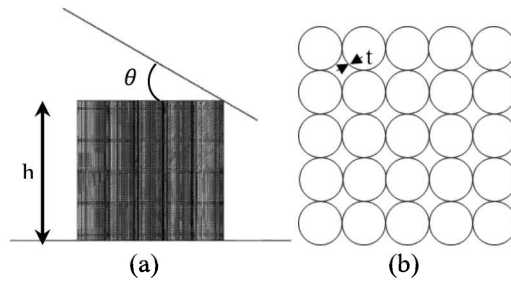


Figure 1 Finite Element Model (a) Circular-celled honeycomb and (b) cross section view of circular-celled honeycomb.

The circular-celled honeycomb was modelled using shell element. The material used is aluminium alloy AA 6060 T4 with mechanical properties of density,  $\rho = 2700\text{kg/m}^3$ , Young's modulus,  $E = 68.2\text{GPa}$ , Poisson's ratio,  $\nu = 0.3$ , initial yielding stress,  $\sigma_y = 80\text{ MPa}$ . The explicit finite element code ABAQUS was applied in the simulation. The boundary condition of bottom was fixed, and the top of the circular honeycomb was subjected to  $\theta$ .

## 3. VALIDATION

Finite element model has been validated by experimental and simulation model in the literatures to determine whether it was sufficient accurate [7].

The validation results of circular hollow tube under dynamic impact loading are presented by Zarei and Kröger's. Three circular thin-walled tubes under force of the empty circular tubes that compare between the FE result and experiment result [8]. It is achieved a good

agreement and FE model has capability of simulating the numerical response of each tubes under dynamic impact loading were validated. Table 3 displays the energy absorption and the average crushing dynamic impact. All the results are showing all differences are under acceptance variance which is not more than 5%.

Table 2 Details of experimental models for validation.

<b>Impactor</b>		<b>Geometry parameter</b>		
Velocity, <i>v</i> (m/s)	Mass, <i>M</i> (kg)	Length, <i>L</i> (mm)	Dia- meter, <i>d</i> (mm)	Thick- ness, <i>t</i> (mm)
Z1	6.6	104.5	180	40
Z2	6.6	104.5	180	40
Z3	10.7	91	180	50

Table 3 Result of validation between experiment and FE models [16]

	<b>Experiment</b>		<b>FE</b>		<b>Error</b>	
	EA (J)	F <sub>m</sub> (kN)	EA (J)	F <sub>m</sub> (kN)	EA (%)	F <sub>m</sub> (%)
Z1	2326	45.6	2238	43.46	3.783	4.693
Z2	2260	42.3	2259	42.57	0.044	0.634
Z3	5081	86.0	5127	86.49	0.897	0.567

#### 4. RESULTS AND DISCUSSION

Figure 2 shows the force-displacement of circular honeycomb versus angle of loading. The performance of energy absorption (EA) and specific energy absorption (SEA) result of circular honeycomb subjected to angle loading ( $0^\circ$  to  $30^\circ$ ) is showed in Table 4.

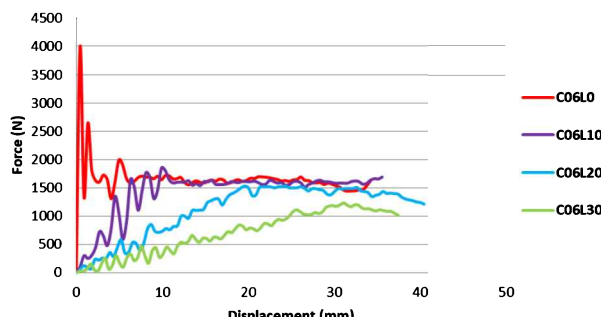


Figure 2 Force-displacement of circular honeycomb versus angle of loading.

Table 4 Result of circular honeycomb versus angle of loading.

	<b>C06L0</b>	<b>C06L10</b>	<b>C06L20</b>	<b>C06L30</b>
EA (J)	118.1	80.4	45.5	30.5
SEA (kJ/kg)	17.8334	12.1456	6.8715	6.5661

Figure 2 and Table 4 show the influence of angle loading on the EA and SEA. The increased of angle of  $\theta$ , the decreased of performance of crashworthiness.

#### 5. CONCLUSION

This paper presented the circular honeycomb subjected to dynamic impact under oblique loading. The angle of loading,  $\theta$  does affect the performance of FE model. Where by, every  $10^\circ$  increase in  $\theta$ , resulting a 40% decrease in its EA, SEA compare to its previous stage. Meanwhile, the SEA of model seems stable between  $20^\circ$  and  $30^\circ$ . There are only 4.5% variances to each other.

#### ACKNOWLEDGEMENT

Authors acknowledge the financial support provided by Research & Innovation Department under, Universiti Malaysia Pahang under Grant No. 180303.

#### REFERENCES

- [1] Langseth, M., & Hopperstad, O. S. (1996). Static and dynamic axial crushing of square thin-walled aluminium extrusions. *International Journal of Impact Engineering*, 18(7-8), 949-968.
- [2] Tan, S. P., Mohd Saffe, S. N., Rusdan, S. A., & Hamran, N. (2017). Oblique impact on crashworthiness: Review. *International Journal of Engineering Technology and Sciences (IJETS)*, 8(1), 1-17.
- [3] Qin, Q. H., Wang, T. J., & Zhao, S. Z. (2009). Large deflections of metallic sandwich and monolithic beams under locally impulsive loading. *International Journal of Mechanical Sciences*, 51(11-12), 752-773.
- [4] Sun, G., Jiang, H., Fang, J., Li, G., & Li, Q. (2016). Crashworthiness of vertex based hierarchical honeycombs in out-of-plane impact. *Materials & Design*, 110, 705-719.
- [5] Li, G., Zhang, Z., Sun, G., Xu, F., & Huang, X. (2014). Crushing analysis and multiobjective optimization for functionally graded foam-filled tubes under multiple load cases. *International Journal of Mechanical Sciences*, 89, 439-452.
- [6] Mellquist, E., & Waas, A. (2004). Size effects in the crushing of honeycomb structures. In *45th AIAA/ASME/ASCE/AHS/ASC Structures, Structural Dynamics & Materials Conference* (p. 1640).
- [7] Robinson, S. (1997, December). Simulation model verification and validation: increasing the users' confidence. In *Winter Simulation Conference* (pp. 53-59).
- [8] Zarei, H. R., & Kröger, M. (2006). Multiobjective crashworthiness optimization of circular aluminum tubes. *Thin-Walled Structures*, 44(3), 301-308.

# Optimization of process parameters for synthesis of graphene on copper by oil palm fiber source

Noor Ayuma Mat Tahir<sup>1</sup>, Mohd Rody Bin Mohamad Zin<sup>1,2</sup>, Mohd Fadzli Bin Abdollah<sup>1,2,\*</sup>, Noreffendy Tamaldin<sup>1,2</sup>, Hilmi Amiruddin<sup>1,2</sup>

<sup>1)</sup> Fakulti Kejuruteraan Mekanikal, Universiti Teknikal Malaysia Melaka,  
Hang Tuah Jaya, 76100 Durian Tunggal, Melaka, Malaysia

<sup>2)</sup> Centre for Advanced Research on Energy, Universiti Teknikal Malaysia Melaka,  
Hang Tuah Jaya, 76100 Durian Tunggal, Melaka, Malaysia

\*Corresponding e-mail: mohdfadzli@utem.edu.my

**Keywords:** Graphene; solid source; Taguchi; Raman spectroscopy

**ABSTRACT** – This paper presents the optimization of process parameters used to synthesize graphene by using Taguchi method. The synthesis method used in this study was Chemical Deposition Method (CVD) whereas the source used is Oil Palm Fiber (OPF) and substrate used is copper. Nine arrays ( $L_9$ ) created based on three parameters to be analyzed. The response used are the intensity ratio of peak 2D against G ( $I_{2D}/I_G$ ). The finding in this study concluded that the optimum parameters to grow graphene from OPF source are by using hydrogen gas at 1000°C for 30 minutes. The error between the experimental and predicted value lies between 13 to 17%.

## 1. INTRODUCTION

A new class of material known as graphene has the potential to reduce friction and wear due to its high level of hardness and stiffness [1–3]. Several solutions have been created to reduce unwanted friction and wear in many applications, including the use of bearings, lubricants, additives, and modifier technology [3–10].

Allotropes of carbon, especially activated carbon, graphite, graphene and carbon nanotubes, have been recorded as excellent anti-friction and wear materials [10–12].

There are several emerging methods to produce graphene, such as organic synthesis, chemically derived, unzipping carbon nano-tubes, mechanical exfoliation, and also deposition [4,9]. Thus far, deposition is the most practical method to produce graphene on a large scale as it is more easily controlled. Deposition methods, called chemical vapour deposition (CVD), can be divided into several categories: atmospheric pressure CVD (APCVD), low-pressure CVD (LPCVD), microwave plasma-assisted CVD (MPCVD), plasma-enhanced CVD (PECVD), and many more [4].

CVD is a method whereby a chemical reaction is used to induce the deposition of a thin film. Transition metals such as nickel (Ni) and copper (Cu) act as a catalyst and substrate for the growth of graphene.

Limited study has been carried out to investigate the potential graphene synthesis by using solid source, especially on the waste products. Hence, this paper reports the findings on the optimum parameters for synthesizing graphene from solid waste products by using the CVD method.

## 2. METHODOLOGY

### 2.1 Design of Experiment (DOE)

The experiment was designed by using Taguchi method. Three parameters to be tested (type of gas, growth temperature, growth time) at three levels. Nine arrays created based on the (3 parameters x 3 levels). The parameters and levels tested are shown in Table 1. The graphene was then synthesised based on the arrays created on Oil Palm Fiber (OPF) source. The response selected were the intensity of 2D against G peak ( $I_{2D}/I_G$ ).

Table 1 Parameters and levels of the study.

Parameters			
Level	Type of Gas	Growth Temperature (°C)	Growth Time (min)
1	Ar	950	30
2	Ar + H	1000	60
3	H	1020	90

### 2.2 Synthesis process

The schematic diagram of the CVD method was shown in Figure 1. The process involves pre-heat, annealing, growth, and cooling. The substrate used were copper with 96% purity. The source used was OPF.

### 2.3 Analysis

The CVD method may produce variety of type of carbon such as single layered graphene, multi layered graphene, graphite, single walled nanotube, multiwalled nanotube, etc. Raman spectroscopy analysis were used to determine the allotrope and type of the carbon of the coating. The  $I_{2D}/I_G$  from Raman spectroscopy analysis for all arrays were then tabulated into the arrays created by the Taguchi method and analysed. The coated surface was then analysed by using the Scanning Electron Microscope embedded with Electron Dispersed X-ray (SEM/EDX) to check the element contents on the surface.

## 3. RESULTS AND DISCUSSION

Table 2 shows the  $I_{2D}/I_G$  on Taguchi arrays with the analyzed S/N ratios.

Figure 3 shows the optimum parameters obtained from the S/N ratio analysis. The optimum parameters to synthesize graphene OPF source are by using hydrogen gas at 1000°C growth temperature for 30 minutes.

Confirmation test were conducted by comparing the theoretical value that obtained from the Analysis of Variance (ANOVA) with the experiment data. Table 3

shows the comparison value where the error for the finding is 13.6%.

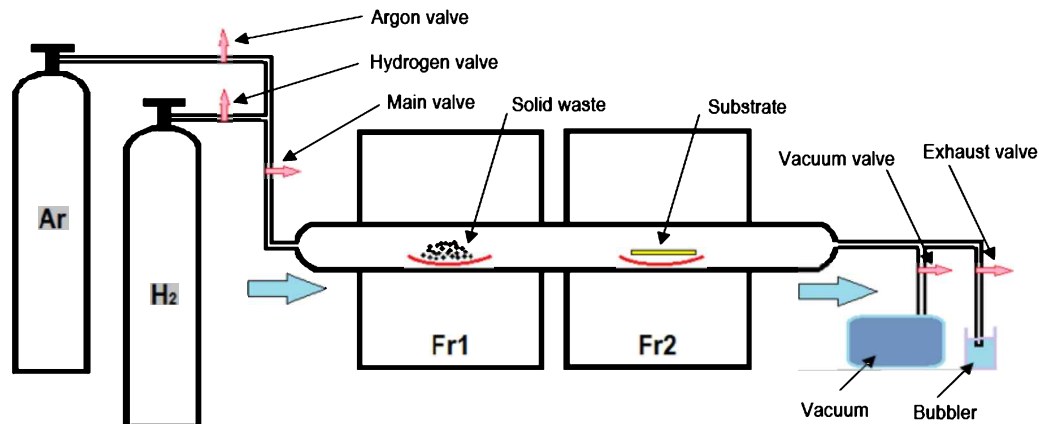


Figure 1 Schematic diagram of CVD method.

Table 2 Response ( $I_{2D}/I_G$ ) and S/N ratios for OPF coating.

Test	Type of Gas	Parameters		$(I_{2D}/I_G)$	S/N ratio
		Growth Temperature (°C)	Growth Time (min)		
1	Ar	950	30	0.20774	-13.6496
2	Ar	1000	60	0.49345	-6.13514
3	Ar	1020	90	0.36744	-8.69627
4	Ar + H	950	60	0.34321	-9.2888
5	Ar + H	1000	90	0.46949	-6.56747
6	Ar + H	1020	30	0.33977	-9.3763
7	H	950	90	0.24863	-12.0889
8	H	1000	30	0.88618	-1.04956
9	H	1020	60	0.3469	-9.19591

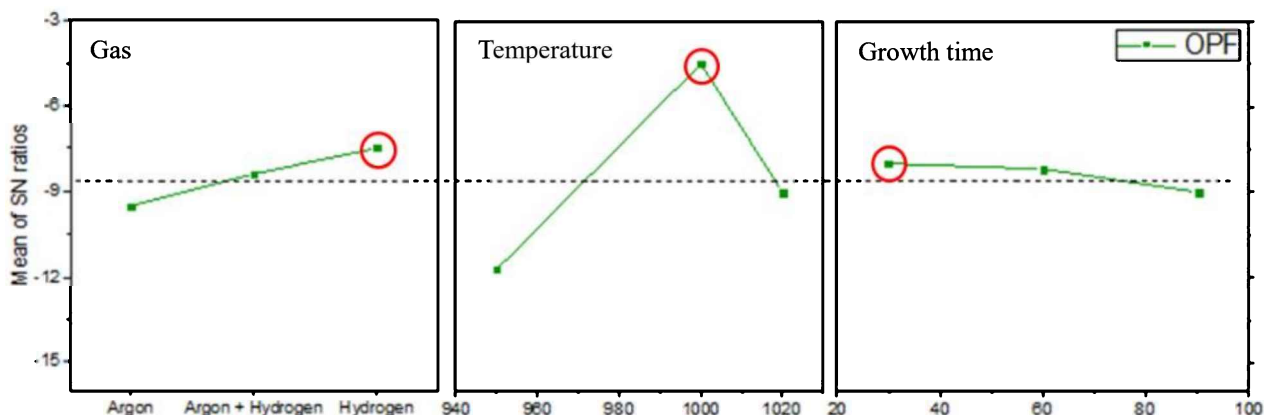


Figure 3 The optimum parameters to synthesize graphene from OPF source.

Table 3 Comparison between theoretical and experimental finding.

Variable	n	Experimental value	Predicted value	Error %
$I_{2D}/I_G$	9	0.88618	0.76533	13.6

The SEM/EDX image shows there were distinct difference between the coated and uncoated surface. The uncoated surface contains machining line whereas the coated surface shows no machining line instead showing ripples for the coated surface. The EDX analysis shows that the content of carbon increased drastically. The SEM image and EDX analysis were shown in Figure 4 and Table 4, respectively.

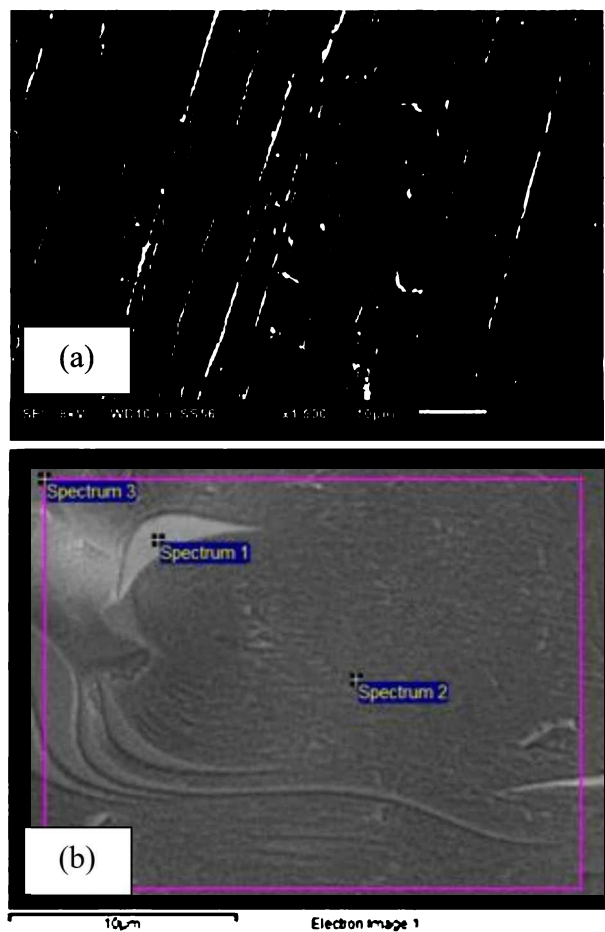


Figure 4 SEM image of (a) uncoated copper and (b) OPF coated.

Table 4 EDX analysis for the uncoated copper and OPF coated surface.

Sample	Weight %		
	Carbon	Oxygen	Copper
Uncoated copper	2.49	0.79	96.72
OPF coated	61.03	0.87	38.1

#### 4. CONCLUSION

In this study, temperature played a crucial role in the growing of graphene by means of the CVD method. It can be concluded that the optimum parameters to grow graphene from OPF source are by using hydrogen gas at 1000°C for 30 minutes.

#### ACKNOWLEDGEMENT

This study is supported by the grant from the Universiti Teknikal Malaysia Melaka (Grant no.: PJP/2019/FKM(11A)/S01684).

#### REFERENCES

- [1] Berman, D., Erdemir, A., & Sumant, A. V. (2014). Graphene: A new emerging lubricant. *Materials Today*, 17(1), 31–42.
- [2] Zhai, W., Shi, X., Wang, M., Xu, Z., Yao, J., Song, S. and Wang, Y., (2014). Grain refinement: A mechanism for graphene nanoplatelets to reduce friction and wear of Ni3Al matrix self-lubricating composites. *Wear*, 310(1–2), 33–40.
- [3] Bressan, J, and Daros,D. (2008). Influence of hardness on the wear resistance of 17-4 PH stainless steel evaluated by the pin-on-disc testing. *Journal of Materials Processing Technology*, 205, 353–359.
- [4] Singh, V., Joung, D., Zhai, L., Das, S., Khondaker, S. I. and Seal, S. (2011). Graphene based materials: Past, present and future. *Progress in Materials Science*, 56(8). 1178–1271.
- [5] Abdollah, M. F. B., Yamaguchi, Y., Akao, T., Inayoshi, N., Miyamoto, N., Tokoroyama, T. and Umebara, N., (2012). Deformation-wear transition map of DLC coating under cyclic impact loading. *Wear*, 274–275, 435–441.
- [6] M. Batzill, (2012). The surface science of graphene: Metal interfaces, CVD synthesis, nanoribbons, chemical modifications, and defects. *Surface Science Reports*, 67(3–4), 83–115.
- [7] Findik, F. (2014). Latest progress on tribological properties of industrial materials. *Materials & Design*, 57, 218–244.
- [8] Mohmad, M., Abdollah, M. F. B., Tamaldin, N., and Amiruddin, H., (2018). Frictional characteristics of laser surface textured activated carbon composite derived from palm kernel. *International Journal of Advance Manufacturing Technology*, 95(5–8), 2943–2949.
- [9] Saiful Badri, M. A., Mat Salleh, M., Md Noor, N. F., Abd Rahman, M. Y. and Umar, A. A. (2017). Green synthesis of few-layered graphene from aqueous processed graphite exfoliation for graphene thin film preparation. *Materials, Chemicals, and Physics*, 193, 212–219.
- [10] Brostow, W., Kovačevic, V., Vrsaljko, D., and Whitworth, J. (2010). Tribology of polymers and polymer-based composites. *Journal of Materials Educations*, 32, 273–290.
- [11] Zamri Y., and Shamsul, J. B., (2011). Physical properties and wear behaviour of aluminium matrix composite reinforced with palm shell activated carbon (PSAC). *Kov. Mater.*, 49, 287–295.
- [12] Mat Tahir, N. A., Abdollah, M. F. B., Hasan, R. and Amiruddin, H. (2016). The effect of sliding distance at different temperatures on the tribological properties of a palm kernel activated carbon-epoxy composite. *Tribology International*, 94, 352–359.

# Reverse engineering process of car side mirror using convectional and 3D scanning methods

Shafizal Mat<sup>1,2,\*</sup>, Ng Shu Tyng<sup>1</sup>, Faiz Redza Ramli<sup>1,2</sup>, Mohd Rizal Alkahari<sup>1,2</sup>, Mohamad Ridzuan Jamli<sup>3</sup>, Syahibudil Ikhwan Abdul Kudus<sup>1,4</sup>

<sup>1)</sup> Fakulti Kejuruteraan Mekanikal, Universiti Teknikal Malaysia Melaka,  
Hang Tuah Jaya, 76100 Durian Tunggal, Melaka, Malaysia

<sup>2)</sup> Centre for Advanced Research on Energy, Universiti Teknikal Malaysia Melaka,  
Hang Tuah Jaya, 76100 Durian Tunggal, Melaka, Malaysia

<sup>3)</sup> Fakulti Kejuruteraan Pembuatan, Universiti Teknikal Malaysia Melaka,  
Hang Tuah Jaya, 76100 Durian Tunggal, Melaka, Malaysia

<sup>4)</sup> Fakulti Teknologi Kejuruteraan Mekanikal & Pembuatan, Universiti Teknikal Malaysia Melaka,  
Hang Tuah Jaya, 76100 Durian Tunggal, Melaka, Malaysia

\*Corresponding e-mail: shafizal@utem.edu.my

**Keywords:** Reverse engineering; conventional method; scanning method

**ABSTRACT** – The study of development of computational model through reverse engineering is an effort to understand the reverse engineering process. The aim of this study is to differentiate the 3D model using conventional and scanning method. Two prototypes were created using existing car side mirror through conventional and 3D scanning drawing. The difference dimension and processes between the 3D model of CAD drawing and 3D scanner are observed. It can provide differences between two prototypes of side mirror through reverse engineering and existing product. From this study, it can be concluded that 3D scanning method is more appropriate as a method for reverse engineering.

## 1. INTRODUCTION

Reverse Engineering (RE) is the process of discovering the technological principles of a device, object or system through analysis of its structure, function and operation. It often involves taking something apart and analyzing its workings in detail to be used in maintenance or to try to make a new device or program that does the same thing without copying anything from the original [1]. As computer-aided design has become more popular, reverse engineering becomes a viable method to create a 3D virtual model of an existing physical part for use in 3D CAD, CAM, CAE and other software. The reverse engineering process involves measuring an object and then reconstructing it as a 3D model [2].

Cheng and Jin [3] said that 3D laser scanning technology can measure 3D coordinates point on object surface. Therefore, it belongs to three-dimensional measurement technology. Compared with the traditional surveying method, laser scanning technology has superiority such as rapidity of data acquisition, great quantity of data and high accuracy as well as extensive application. Fisher [4] claimed that the goal of RE is to generate a CAD model from measured data of a physical model as a replica of the original one and pass the CAD model to CAE and CAM. In RE, significant differences can exist in the requirement of the design and expression of forms, due to the distinct

characteristics of products and different source of input data.

## 2. METHODOLOGY

Project methodology involves the usage of reverse engineering, comparison of 3D scanning and conventional method. It is required to fabricate 2 rapid prototypes; these are from the same model of drawing at which practitioner should acquire the drawing through both methods. Starting with acquisition of drawing data, it should be done for both conventional drawing and 3D scanning method. For conventional method, it starts with the use of bending ruler for conventional measurement; it is then followed by the drawing sketch by using CATIA software and transfer into file format of STL for future prototype fabrication purpose.

As for reverse engineering that requires the use of 3D scanner, existing product was scanned with 3D scanner. During this process, it requires to use several software in order to completely acquire drawing data. After stages of conversion, final drawing was saved as STL file format, it is for the purpose of fabricating rapid prototype [5]. Next, it will be the comparison of drawing data and dimension of product for both processes [6].

## 3. RESULTS AND DISCUSSION

Case study conducted was to perform comparison between data of CAD using conventional method and 3D scanner. Figure 1 shows the result of drawing using conventional method. Dimension of side mirror is measured by using conventional method. Drawing shows dissimilarity compared to existing product, this is due to parts like screw hole is not being included in the sketches. However, it does not affect the study for it is concentrated on the external surface of the side mirror.

During the construction of rapid prototyping for conventional methods, the build time takes 13 hours and 46 minutes. Fabrication of prototype A can allow the chooses of several slice height, specification of slice height for conventional prototype A is 0.3302 mm, volume of model material used is 231.43 cm<sup>3</sup> and support material is 109.41 cm<sup>3</sup>. As slice height is set to

be quite big, it turns out that surface of prototype produce is rougher, and prototype is shown in the Figure 2.

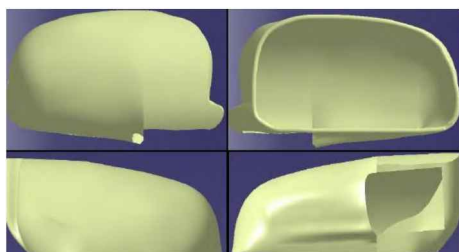


Figure 1 Drawing data from CATIA.



Figure 2 Prototype A.

Figure 3 shows the result model using 3D scanning method that was transferred into Insight software after being repaired by TransMagic software. As for prototype B, the build time is 34 hours and 21 minutes.

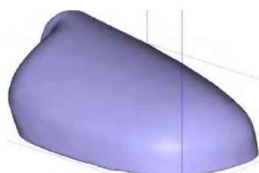


Figure 3 Drawing in Insight program.

During the fabrication of prototype B, specification of 2D scanner prototype slide height is measured 0.1778 mm, volume of model material consumes 141.47 cm<sup>3</sup> and support material consumes 142.57 cm<sup>3</sup>. Slide height setting is rather small on Prototype B, surface of prototype is smoother compares prototype A which shown in the Figure 4. White color indicates the model of prototype and brown color material provides support for prototype. Support used in the prototype has to be removed in order to obtain the real model for measurement. Removal process of support is done by immersing rapid prototype into chemical solution, support will then decay into the solution and process consumes a day for complete removal.

#### 4. CONCLUSION

Results and discussion show that average percentage of difference of conventional method with product is 3.99% and difference of 3D scanning method is 1.33%. Therefore, study indicates a conclusive understanding that dimension of 3D scanning's

prototype is nearer to dimension of existing product. Presence of methodology used in 3D scanning method is more systematic compare to conventional method. Non-symmetry and curvature surface when drawing by applying with drawing skills is more complicated. Therefore, conventional method of drawing is hugely depending on personal drawing skills. Comparing with 3D scanning methods, proper application of this method will provide higher success rate of fabrication on prototype. It can be conclusively said that 3D scanning method is more appropriate as a method for reverse engineering [5].

It can be concluded that 3D scanning is appropriate method for reverse engineering technique. This technique should be recommended to industry application and especially for work that requires design field. 3D scanning method requires the use of much software before fabrication of prototype can begin.



Figure 4 Prototype B with support.

#### ACKNOWLEDGEMENT

Authors would like to thank Universiti Teknikal Malaysia Melaka (UTeM) for funding this research (PJP/2019/FKM(6A)/S01677).

#### REFERENCES

- [1] Shabani, B., & Vrtnoski, G., & Dukovski, V. (2019). Integrated reverse engineering and additive technology systems. *Mechanical Engineering – Scientific Journal*, 36, 47-54.
- [2] Ahmed, N. (2019). Direct metal fabrication in rapid prototyping: A review. *Journal of Manufacturing Processes*, 42, 167-191.
- [3] Cheng, X. J., & Jin, W. (2006). Study on reverse engineering of historical architecture based on 3D laser scanner. *Journal of Physics: Conference Series*, 48, 843-849.
- [4] Fisher, R. B. (2003), Applying knowledge to reverse engineering problems. *Computer-Aided Design*, 39, 501-510.
- [5] Brajlih, T., Tasic, T., Drstvensek, I., Valentan, B., Hadzistevic, M., Pogacar, V., Balic, J., & Acko, B. (2011). Possibilities of using three-dimensional optical scanning in complex geometrical inspection. *Strojniški vestnik - Journal of Mechanical Engineering*, 57(11), 826-833.
- [6] Mat, S., Saedon, J., Mahmud, J., & Salim, M. A. (2009). The development of computational model through reverse engineering: side mirror case study. *Journal of Mechanical Engineering and Technology (JMECT)*, 1(1), 25-41.

# Effect of damage on vibration characteristic of FDM printed lattice structure material

Muhamad Syafwan Azmi<sup>1</sup>, Rainah Ismail<sup>1,2,\*</sup>, Rafidah Hasan<sup>1,2</sup>, Azma Putra<sup>1,2</sup>, Muhammad Nasruddin Nurdin<sup>1</sup>

<sup>1)</sup> Fakulti Kejuruteraan Mekanikal, Universiti Teknikal Malaysia Melaka,

Hang Tuah Jaya, 76100 Durian Tunggal, Melaka, Malaysia

<sup>2)</sup> Centre for Advanced Research on Energy, Universiti Teknikal Malaysia Melaka,

Hang Tuah Jaya, 76100 Durian Tunggal, Melaka, Malaysia

\*Corresponding e-mail: rainah@utem.edu.my

**Keywords:** Lattice structure; vibration analysis; damage

**ABSTRACT** – The aims of this study are to investigate the effect of damage extent and damage location on natural frequencies of the BCC lattice bar. The bar samples were fabricated by using fused deposition modeling (FDM) additive manufacturing (AM) technique. The damage is represented by missing lattice unit cells within the structure. Findings show that natural frequency values decrease with the increase of damage extents. Meanwhile, the natural frequency values increase as the damage location became farther from the clamped edge. This research provides good information on the influence of damage existence to the natural frequency values of the lattice structure.

## 1. INTRODUCTION

Damage is defined as alteration introduced into a system in which will affect the way of that system behaves in term of its performance. Structural damage detection has been one of the main popular concerns in scientific community as many incidents that have caused human loses such as airplane crashes or collapsed bridges or buildings [1]. The types of damage that can happen in structures are cracks, delamination and deformations due to fatigue from constant exposure to the uncontrol vibration. Presence of damage can lead to unwanted instances of high vibration that can cause long-term and short-term damaging effects on the structure's integrity. This phenomenon is extremely dangerous as structures cannot function as designed which can then ultimately fail. Failure of a structure can result in dreadful consequences such as loss of life as evidently happened from collapsed buildings during earthquake. Hence, damage detection to the structure at the initial stage of research and development can provide insight into the real behavior of the system, evaluate its performance, suitability, limitations and this in due course can provide better safety of the structure in real dynamic applications. For this reason, various effect of damages on vibration characteristics of the lattice core material sandwich structures numerically using experimentally validated FEM models are explored [2,3]. Therefore, this study attempted to investigate the effects of damage extent and damage location on the natural frequency values of the lattice structures experimentally in order to correlate the findings. The hypothesis that will be tested are that larger the damage area and the closest damage region to the boundary condition will have higher effect on the natural frequency values of the lattice bars.

## 2. METHODOLOGY

### 2.1 Sample Preparation

Lattice bar samples with dimension of 160mm x 30mm x 15mm size were made by using the FDM AM. The strut diameter of the BCC lattice bars was kept at 1.8 mm with standard print quality mode combination [4]. The damage extent is represented by using a damage parameter  $\eta$ .

$$\eta = \frac{n}{N} \quad (1)$$

Where  $n$  is the number of missing unit cells and  $N$  is total unit cells of the intact lattice bar sample. For damage extent study, different damage parameters ranging from  $\eta = 0.00$  (intact) to  $\eta = 0.50$  were used with all damage location starting near the clamped edge boundary condition as illustrated in Figure 1. Meanwhile for damage location study, damage extent was kept at damage parameter  $\eta = 0.02$  and the damaged region was set to be at the clamped edge, at the opposite free end or in between them as illustrated in Figure 2.

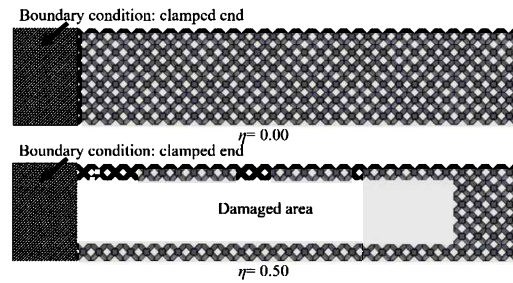


Figure 1 Illustration of lattice bar with different damage extent (top view).

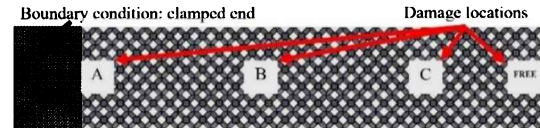


Figure 2 Illustration of the lattice structure's damage location (top view).

### 2.2 Vibration Testing

The experimental setup for vibration testing consists of Dataphysics Quattro as signal generator and analyzer, accelerometer sensor, force sensor, shaker, signal amplifier and fabricated test rig to clamp the bar samples was used. Details of the vibration testing procedure and schematic experimental set-up is available in previous study [4]. The measurement points and excitation point are as illustrated in Figure 3.

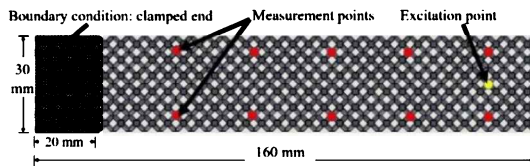


Figure 3 Excitation and measurement point locations (top view).

### 3. RESULTS AND DISCUSSION

#### 3.1 Effect of Damage Extent

The effects of damage extents on the first two natural frequencies are displayed in Figure 4. Based on Figure 4, it can be seen from the trendline, generally that the influence of damage to the natural frequency values increase with the increase in the damage parameter. The natural frequency values decrease due to loss of stiffness caused by damage present in the lattice bars [2]. The percentage different of the natural frequency for the first and second modes of vibration are 17.56 % and 9.56% respectively. This shows that the influence of damage extent was greater for the first mode natural frequency.

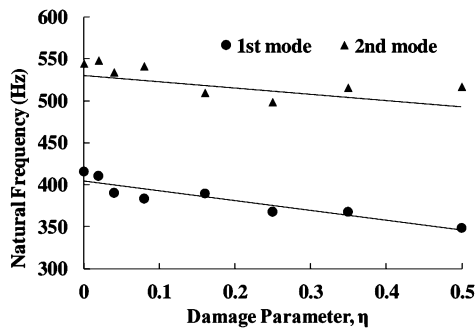


Figure 4 Effect of damage extents on the natural frequency values.

#### 3.2 Effect of Damage Locations

Figure 5 shows the effects of damage locations on the first two natural frequencies. It can be seen from Figure 5 that both natural frequency values increase as the damage location became farther from the clamped edge. This indicates that the effect of damage on the natural frequencies become smaller as the damage zone moves from clamped edge boundary condition to the free end. This behavior is due to more flexibility at the free end of the lattice bar samples. A similar finding was obtained by Lou et al., (2014) and Li et al., (2015) numerically [2-3]. From Figure 5, only first mode natural frequency at the location A shows lesser natural frequency value as compared to that of the intact lattice bar. This shows that loss of stiffness was more significant when the damage is closest to the boundary condition. On the other hand, at the location B, C and 'Free', higher natural frequency values can be observed. This phenomenon is believed to be due to lower mass value with less effect to the stiffness of the lattice bar samples. This is proven especially by result at the location 'Free' where stiffness was not affected by the existence of damage as the lattice bar sample was excited before the damage location 'Free'. However, the mass of the lattice bar sample at the location 'Free' was lower as compared to that of the intact lattice bar. Based on equation (2), the

natural frequency is inversely proportional to mass. Therefore, lower mass would increase the natural frequency values.

$$\omega_n = \sqrt{\frac{k}{m}} \quad (2)$$

Where  $\omega_n$  is the natural frequency [Hz],  $k$  is the stiffness [N/m]  $m$  is the mass [kg]  $l$  is the length of the lattice bar [m]

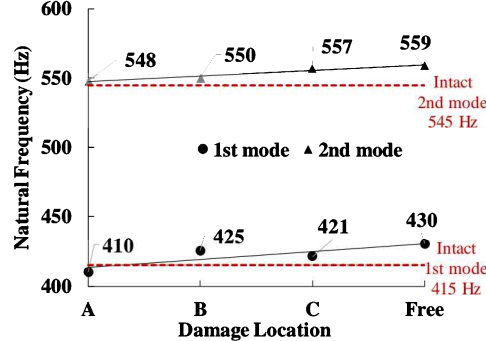


Figure 5 Graph of natural frequency values against damage location.

### 4. CONCLUSIONS

The effect of artificial damage on the lattice bar samples were studied experimentally. In the damage extent study, it was found that the natural frequency values decrease with the increase of damage parameter. On the other hand, for damage locations study, it was found that the natural frequency values increase as the distance of damage to the boundary condition became far. The findings indicated that the damage zone should be placed far away from the clamped edge and small when embedding additional component such as screw or motor in the real applications of lattice structures bar so that natural frequency can be decreased by smaller extents.

### ACKNOWLEDGMENT

This research was fully funded by research grant FRGS/1/2016/TK03/FKM-CARE/F00316 provided by Ministry of Education Malaysia. All equipment's used for specimens' fabrication and testing are provided by Universiti Teknikal Malaysia Melaka.

### REFERENCES

- [1] Sampaio, R. P. C., Maia, N. M. M., & Silva, J. M. M. (1999). Damage detection using the frequency-response-function curvature method. *Journal of sound and vibration*, 226(5), 1029-1042.
- [2] Lou, J., Wu, L., Ma, L., Xiong, J., & Wang, B. (2014). Effects of local damage on vibration characteristics of composite pyramidal truss core sandwich structure. *Composites part b: Engineering*, 62, 73-87.
- [3] Li, B., Li, Z., Zhou, J., Ye, L., & Li, E. (2015). Damage localization in composite lattice truss core sandwich structures based on vibration characteristics. *Composite Structures*, 126, 34-51.
- [4] Azmi, M. S., Ismail, R., Hasan, R., Alkahari, M. R., & Tokoroyama, T. (2017). Vibration analysis of FDM printed lattice structure bar. *Proceedings of SAKURA Symposium on Mechanical Science and Engineering*, 33-35.

# Wireless control of two wheels self-balancing robot using arduino microcontroller

Nurul Muthmainnah Mohd Noor\*, Ahmad Nurussalam Yusof

Fakulti Kejuruteraan Mekanikal, Universiti Teknologi MARA, Cawangan Pulau Pinang, Kampus Permatang Pauh,  
13500 Permatang Pauh, Pulau Pinang, Malaysia

\*Corresponding email: muthmainnah@uitm.edu.my

**Keywords:** Inverted pendulum, two wheels self-balancing robot, gyroscope

**ABSTRACT** – This paper presents the design and implementation of two wheels self-balancing robot based on the concept of inverted pendulum. A small two-wheel balancing robot using a mobile robot kit is designed with ability to balance the upright position on the level landscape. The route of movements of the robot are controlled by wireless condition through Bluetooth. To balance the platform, the sensor which called MPU is used to detect the tilt angle of the robot by using Kalman Filter algorithm. Lastly, the results show that the wireless control system of the robot using Arduino microcontroller meets its objective.

## 1. INTRODUCTION

The working principle of the two wheels balancing robot is really straightforward. The robot will try to drive its wheels in the direction where the upper part of the robot body is falling to maintain the position of wheels under the centre of gravity and then achieve the balancing effect [1]. Regularly, the two wheels self-balancing robot is planned based on the inverted pendulum idea which has been considered or investigated seriously by many research education institutes and business organizations. As the outcome, balancing robots that fill different needs have been developed. The most conspicuous case is the Segway Human Transporter by the Segway Company which has been marketed as transportation for humans [2].

The fundamental of the controller is to use the wheel encoder, gyroscope and accelerometer sensors to estimate the state of mind of the platform and after that to utilize this data to drive their activity wheel in the direction to keep up an upright and balanced position platform [3]. It implies to continue falling off away from the vertical axis, and then a gyro chip is expected to give the point position of the inverted pendulum or robot base and input into the controller. The Arduino controller will give a sort of feedback signal through MPU sensor to turn the stepper motor clockwise or anticlockwise, along these lines balancing the platform. These two estimations are summed and fed-back to the stepper motor which delivers the counter torque required to balance the platform robot.

In contrast with the two wheels balancing robot, the traditional three or four wheels' robots have a few limitations. These robots are steady when static yet effectively to be precarious in dynamic condition because of too high centre point of gravity or too quick changing movement of the robots. In this circumstance, the robots have high probability to topple during movement.

This paper is organized as follows: Section 2 describes the methodology of robot; Section 3 presents the implementation and results followed by some conclusion in last section.

## 2. METHODOLOGY

The methodology is a list of actions need to do in order to accomplish the self-balancing robot. There are three main parts involved; design prototype, circuit for sensor and implementation prototype with circuit. The sensor circuit was required to control the stepper motor. The prototype of the self-balancing two wheels also was constructed based on the designing using CATIA. This was followed by software algorithm implementation and hardware integration. Finally, the model was tested and fine-tuned for performance improvement. Figure 1 shows the balancing robot.



Figure 1 Balancing robot.

### 2.1 Circuit Design Construction

The fundamental segments in the circuit of the self-balancing robot are the multi-purpose unit (MPU), Arduino Leonardo, the stepper motor driver and the Bluetooth module. Arduino Leonardo R3 is acted as a module for control unit to handle the peripherals of the robot. The MPU6050 as a gyro sensor is utilized to quantify both accelerometer and gyroscope. Kalman Filter in programming is to obtain the tilt angle of the robot. After that, the obtained tilt angle is sustained into PID controller that compensates error between the actual tilt angle and the desired tilt angle and afterward controls the robot correspondingly for balancing purpose. The Bluetooth Module, HC-06 goes about as the wireless communication platform between the Arduino Mainboard and the Android Smartphone. Through this module, the development of the robot is controlled physically in wireless condition through an Android Smartphone. The stepper motor driver, A4988 is utilized to drive the robot stepper motors which control the development of the robot.

## 2.2 Hardware Design Construction

In this project, the hardware and mechanism of the balancing robot is crucial as it requires accurate measurement and symmetrical design in order for the robot to balance nicely. Much thought must be considered, for example, the torque of the stepper motor; the height of the robot is 13cm and the centre of gravity of the robot. Figure 2 shows the robot structure that designed using CATIA software.

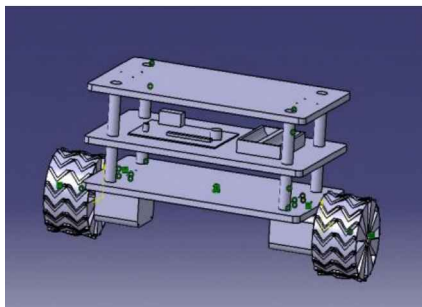


Figure 2 CATIA drawing of the robot structure.

## 2.3 Software Algorithm

The software algorithm and coding is certainly the most difficult and time consuming part. It involves the programming of the microcontroller to perform the desired task, to receive and process inputs from sensors and to produce correct and accurate output to control the stepper motor.

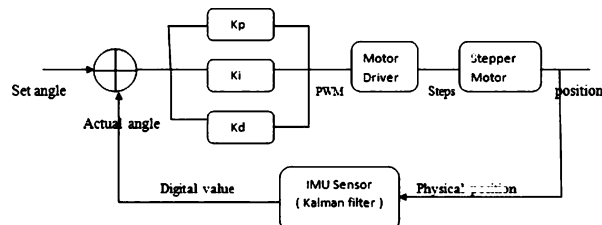


Figure 3 Block diagram for self-balancing robot.

Figure 3 shows a basic block diagram for the balancing robot. The desired set point is the angle that allows the robot to balance in upright position, while the actual tilt angle is the instantaneous angle of the robot as the robot try to balance. The actual tilt angle is measured by the IMU and the Kalman Filter is used to produce a more stable angle measurement and this angle is deducted from the desired set point. From there, an error, which is the difference between the desired and actual tilt angle is obtained and is fed into PID controller. The PID controller will then generate the appropriate speed output to control the stepper motors in order to balance the robot.

## 3. RESULTS AND IMPLEMENTATION

In this section, the working of self-balancing robot will be discussed. Figure 4 shows the control circuit of the robot. The Bluetooth module establishes a wireless connection between Arduino and android application to control robot movement manually for navigation in wireless condition. The implementation of the Kalman Filter and the PID controller making it balances nicely on the flat surfaces. Therefore, Figure 5 shows the robot balancing on flat surfaces.

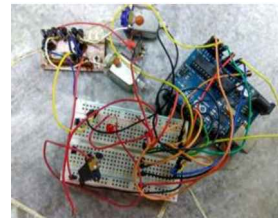


Figure 4 Controller circuit for robot.



Figure 5 Robot balancing on flat surfaces.

## 4. CONCLUSION

The project has successfully met the objectives to design using CATIA and ready to balance at its upright position on the level surfaces by using the wireless condition for navigation. The next future, the fuzzy logic controller also can be implemented to provide better performance in balancing.

## ACKNOWLEDGEMENT

This paper is contributed with Universiti Teknologi MARA cawangan Pulau Pinang.

## REFERENCES

- [1] Juang, H. S., & Lurrr, K. Y. (2013). Design and control of a two-wheel self-balancing robot using the arduino microcontroller board. In *2013 10th IEEE International Conference on Control and Automation (ICCA)* (pp. 634-639).
- [2] Anderson, D. P. (2016) nBot balancing robot. Available online: <http://www.geology.smu.edu/dpa-www/robo/nbot>.
- [3] An, W., & Li, Y. (2013). Simulation and control of a two-wheeled self-balancing robot. In *2013 IEEE International Conference on Robotics and Biomimetics (ROBIO)* (pp. 456-461).

# The assessment of vibration level among female passengers in Malaysia KTM commuter

Fatimah Abdullah<sup>1,\*</sup>, Wan Hasrulnizzam Wan Mahmood<sup>2</sup>, Seri Rahayu Kamat<sup>1</sup>

<sup>1)</sup> Fakulti Kejuruteraan Pembuatan, Universiti Teknikal Malaysia Melaka,  
Hang Tuah Jaya, 76100 Durian Tunggal, Melaka, Malaysia

<sup>2)</sup> Fakulti Kejuruteraan Teknologi Mekanikal dan Pembuatan, Universiti Teknikal Malaysia Melaka,  
Teknologi Kampus, 75450, Hang Tuah Jaya, Melaka, Malaysia

\*Corresponding e-mail: fatimah.abd@mara.gov.my

**Keywords:** Ergonomic; vibration, KTM Komuter Berhad

**ABSTRACT** – The purpose of this study is to assess the exposure of the whole body vibration (WBV) to the passenger. In this experiment, three factors, namely the route, the location of the tri-axial pad, and the WBV value as the response were studied. Results showed that WBV value at gangway area in Experiment 5 gives the higher values than others. Result of this study can provide awareness to the passengers in order to have less effect of WBV when travelling using KTM Komuter Berhad.

## 1. INTRODUCTION

Vibration, as defined in Oxford Dictionaries, is “an instance of vibrating or a person’s emotional state, the atmosphere of a place, the associations of an object, as communicated to and felt by others”. In physic, vibration is defined as an “oscillation of the parts of a fluid or an elastic solid whose equilibrium has been disturbed or of an electromagnetic wave”. In ergonomic environment meaning, vibration is defined as any regular movement a body makes about a fixed point [1]. In the industry environment, ergonomics seeks to prevent injuries and to improve comfort while on the job, whereas ergonomic risk factors will impose a biomechanical stress on worker. There are also examples about vibration studies in scope of transportation for an ergonomic attempt such as two-wheeler riders, coach bus, car, truck, and also for railway. Fast development of technology over the last decade has contributed to the negative effect such as vibration that can affect human health (both physical and mental). Exposure to vibrations is associated with a risk of body injury in the form of vascular disorder, nerve malfunction, and effects on the musculoskeletal system [2]. From the vibration produced in the train coach, it will greatly cause a significant amount of discomfort among the passengers. However, vibrations are commonly felt in the train coaches but rarely noticed by the passengers and thus they neglected its implications to them. This research focuses only on the WBV when travelling using train. WBV can be defined as vibration that occur when a greater part of the body weight is supported on a vibrating surface. WBV principally occurs in vehicles and wheeled working machines. Public transport also belongs to the category vehicles that contribute to the ergonomic value; so, it should be taken into account if users want a comfortable ride. One of the daily challenges face by public

transportation sector is WBV activities while riding train along passengers’ journey. Therefore, it is important to the users to have ergonomics knowledge in making decision which place to stand or to sit during their journey.

## 2. METHODOLOGY

This study focuses on the WBV inside KTM Komuter women cabin, which placed on three locations of the floor train; near the exit door, under the passenger seat and gangway (as showed in Figure 1) when travelling along 18 stations from Tampin to KL Sentral and return from KL Sentral to Tampin using different track routes. From authors’ observation, these three places became are the focus when passengers boarded the train. For every six station, the data recorded were stopped and recontinued until it reached the destination. The aim of this study is to investigate and analyze the WBV value in order to ascertain that it meets the standard of International Standard ISO 2631-1:1997 (as showed in Table 1) and to suggest improvements of good vibration environment to enhance passengers’ experience.

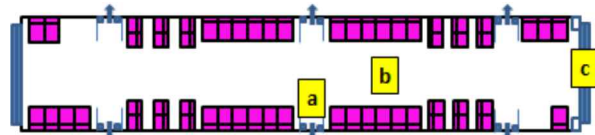


Figure 1 Dytran Model 5313A Tri-Axial IEPE location of seat pad accelerometer at train floor used in this study. (a=at seat, b=at door and c=at gangway).

Table 1 International Standard ISO 2631-1:1997.

RMS acceleration (m/s <sup>2</sup> )	Mental reaction of a person
Less than 0.315	Not uncomfortable
0.315 to 0.63	A little uncomfortable
0.5 to 1.0	Fairly uncomfortable
0.8 to 1.6	Uncomfortable
1.25 to 2.5	Very uncomfortable
Greater than 2.0	Extremely uncomfortable

The Dytran Model 5313A was used as a tri-axial Integrated Electronics Piezo Electric (IEPE) seat pad accelerometer for this study. This seat pad accelerometer, which is made of an integral ten (10) foot

cable and terminating to BNC (Bayonet Neil-Concelman) plug, was connected directly to a 4-Channel VI-400PRO human vibration meter (HVM) to record the vibration measurement value. This system was furnished with anti-liasing filters and has International Standard ISO 2631-1:1997 weighting filters. Vibrations were measured in three translational directions: x-axis (longitudinal), y-axis (transverse), and z-axis (vertical). As for the post processing and further analysis, these data were downloaded to a personnel computer and dedicated MATLAB-based software was used to enable reading of large waveform audio (WAV) files. There are four values of measures that can be determined using this instrument: acceleration, peak acceleration, crest factor (ratio of peak to average acceleration), and vibration dose value (VDV). This study focuses on root mean square (RMS). WBV measurement explored by the passenger was done 6 times at different train trips areas with a different track as shown in Table 2.

Table 2 Locations of measurement.

Experiment	Location
1	From Tampin to Tiroi
2	From Tiroi to Kajang
3	From Kajang to KL Sentral
4	From KL Sentral to Kajang
5	From Kajang to Tiroi
6	From Tiroi to Tampin

### 3. RESULTS AND DISCUSSION

Figure 2 results of exposures of vibration between three pad acceleration locations and the experiment area. The highest vibration magnitude computed from the weighted acceleration history of the train floor was obtained as  $2.2182 \text{ m/s}^2$  and in the z-direction at the gangway area in the Experiment 5, which travel from Kajang to Tiroi. This value shows that it is extremely uncomfortable for the passenger according to ISO 2631 (in Table 1) when they have to stand around the gangway area. Tracks for the train need to be made maintenance such as grinding the track to get a smooth track surface, so that it can reduce high vibration value along journey at Experiment 5 that affect to the passenger inside the train cabin. Meanwhile, the low value of RMS is at floor near the exit door in x-axis for the journey of KL Sentral to Kajang in the Experiment 4 with the value of  $0.5352 \text{ m/s}^2$ . By referring Table 1, this low value still gives fairly uncomfortable feeling to the passenger because as mentioned in the introduction, WBV principally occurs in vehicles and wheeled working machines. So, it relates with the fairly uncomfortable result of WBV value for this experiment.

Low level of vibration is an important element for commercialization of public transport because it affects passengers' comfort and satisfaction. Vibration control is an important consideration in train as the constant motion of parts while the train is moving because there

will be possible damage to the structural frame or components. The suggestion to using foam tapes can prevent parts such as aircond units, fans, interior panels, floor from touching or rattling during train movement can reduce the vibration value from inside train. The reduction of train track at ground can be done by adding some elastic element such rail pads and sleeper pads. Another suggestion is to put rail vibration absorber to reduce the measurement of vibration along the track.

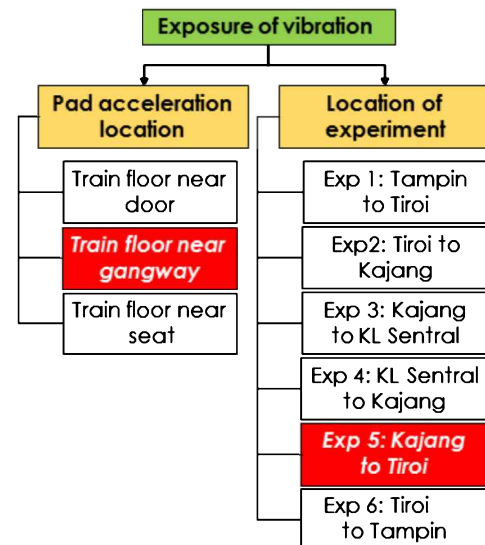


Figure 2 Case study results on exposure of vibration.

### 4. CONCLUSION

Passengers are advised not to stand within the gangway area because the measurement vibration is high in that floor area. Passengers are recommended to sit and stand near the seat place where the average results of vibration in that area are lower than another place. In conclusion, different values were recorded based on the sitting or standing position of the passengers when riding train. Further studies are required on specific part that influences vibration that leads to high value of WBV and how to overcome it.

### ACKNOWLEDGEMENT

This research was co-funded by University Teknikal Malaysia Melaka, Ministry of Higher Education for MyBrain 15 Programme, KTM Komuter Berhad and Majlis Amanah Rakyat (MARA).

### REFERENCES

- [1] Kolgiri, S., Hiremath, R., & Bansode, S. (2016). Literature Review on Ergonomics Risk Aspects Association to the Power Loom Industry. *IOSR J. Mech. Civ. Eng. Ver. III, 13*(1), 2278-1684.
- [2] Vihlborg, P., Bryngelsson, L., Lindgren, B., Gunnarsson, L. G., & Graff, P. (2017). Association between vibration exposure and hand-arm vibration symptoms in a Swedish mechanical industry. *International Journal of Industrial Ergonomics, 62*, 77-81.

# Parametric study on absorption coefficient of inhomogeneous double-layer MPP

Ali I. Mosa<sup>1,3</sup>, A. Putra<sup>1,2,\*</sup>, R. Ramalan<sup>1,2</sup>, Al-Ameri Esraa<sup>1</sup>

<sup>1)</sup>Fakulti Kejuruteraan Mekanikal, Universiti Teknikal Malaysia Melaka,  
Hang Tuah Jaya, 76100 Durian Tunggal, Melaka, Malaysia

<sup>2)</sup>Centre for Advanced Research on Energy, Universiti Teknikal Malaysia Melaka,  
Hang Tuah Jaya, 76100 Durian Tunggal, Melaka, Malaysia

<sup>3)</sup>Mechanical Engineering Department, Collage of Engineering, University of Baghdad, Jadriyah - Baghdad, Iraq

\*Corresponding e-mail: azma.putra@utem.edu.my

**Keywords:** Sound absorption, inhomogeneous MPP, multi-cavity depth

**ABSTRACT** – A micro-perforated panel (MPP) has been presented as an alternative absorber to the conventional fibrous and porous absorber. However, it's bandwidth still narrow comparing to porous materials. In this paper a parametric study of applying an inhomogeneous panel pattern on double layer MPP is presented. Using the equivalent circuit method, the mathematical model has been developed. Results shows that applying the inhomogeneous panel pattern to double layer MPP system can produce a wider absorption bandwidth comparing to the homogeneous one. Predicted results are validated through the experiment.

## 1. INTRODUCTION

As a fibre-free materials, lightweight and have an attractive and aesthetic appearances traditional micro-perforated panel (MPP) sound absorbers are used for building acoustics and interior surfaces because noise control is a major concern that should be considered [1], also they are more robust and suitable for various application [2-4]. MPPs are slim sheets having a set of very small holes, diameters ( $d < 1 \text{ mm}$ ) and set in front of rigid wall separated by an air-gap. Through the recent years, the researchers presented several studies to improve the absorption bandwidth of single layer MPP by preform L shape cavity structure [5], used of mechanical impedance plate [6], MPP with membrane cell [7], inhomogeneous perforation [8]. This paper will present a parametric study of applying an inhomogeneous pattern on double layer MPP absorber system and compare with homogeneous one.

## 2. METHODOLOGY

Figure 1 shows the Schematic diagram of double-layer-inhomogeneous-MPP model, where  $d_1$ ,  $d_2$ ,  $d_3$  and  $d_4$  are the hole diameter for each sub-MPP,  $t_1$  and  $t_2$ , are the panel thickness,  $D_1$  and  $D_2$  are the cavity depths of the air gaps. Based on equivalent electrical circuit method the total system impedance can be calculated as [8]

$$Z_1 = Z_{iMPP_1} + Z_{D_1} \quad (1)$$

$$Z_2 = Z_{iMPP_2} + Z_{D_2} \quad (2)$$

$$Z_{total} = Z_1 + Z_2 \quad (3)$$

Where  $Z_{iMPP_1}$  and  $Z_{iMPP_2}$  are the impedance of the first panel and the second panel,

$Z_{D_1}$  and  $Z_{D_2}$  are the impedance of the first and second cavity which can be calculate by

$$Z_{D_{1,2}} = -j \cot\left(\frac{\omega D_{1,2}}{c}\right) \quad (4)$$

And  $Z_{total}$  is the total impedance of the system. Thus, the normal sound absorption coefficient is calculated by

$$\alpha = \frac{4\text{Re}\{Z_{total}\}}{[1+\text{Re}\{Z_{total}\}]^2 + \text{Im}\{Z_{total}\}^2} \quad (5)$$

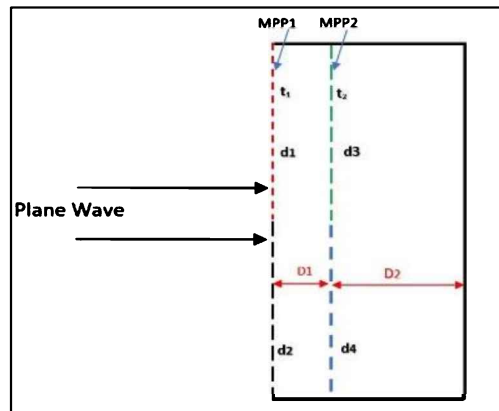


Figure 1 Schematic diagrams of double-layer-inhomogeneous-MPP.

## 3. RESULTS AND DISCUSSION

Figure 2 shows the comparison of the normal coefficients between conventional single layer (SL-MPP), double layer (DL-MPP) and the presented model (DL-iMPP) connecting in a series arrangement. It clear that wider absorbing bandwidth can be obtained by performing an inhomogeneous pattern for double layer MPP, however the first peak slightly shifts toward high frequency. The structure parameters of the simulated models are listed in Table 1, all thicknesses are set at 1 mm.

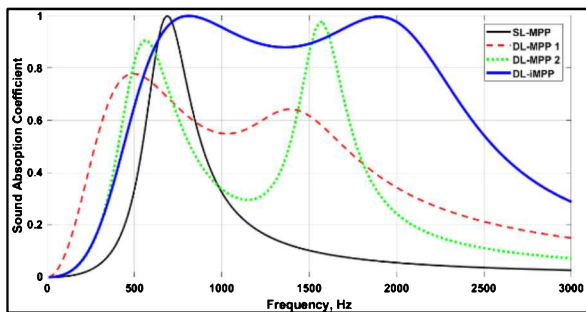


Figure 2. Comparison of absorption coefficients between SL-MPP, DL-MPP and DL-iMPP, cavity depth:  $D_1 = 20$  mm,  $D_2 = 32$  mm.

Table 1 list of Parameters of SL-MPP, DL-MPP and DL-iMPP.

Model	MPP layer 1				MPP layer 2			
	$d_1$ mm	$d_2$ mm	$p_1$ %	$p_2$ %	$d_1$ mm	$d_2$ mm	$p_1$ %	$p_2$ %
SL MPP	0.8		0.6					
DL MPP <sub>1</sub>	0.3		1		0.3		1	
DL MPP <sub>2</sub>	0.8		1.5		0.8		1.5	
DL iMPP	0.8	0.2	0.6	1.5	0.3	0.7	2.5	1

#### 4. EXPERIMENTAL WORK

Figure 3 shows the verifying of the presented (DL-iMPP) model by a comparing the predicted normal coefficient data with experimentally measured data in frequency range from 10 Hz up to 3 kHz. Samples were test in impedance tube in lab. The MPPs are constructed with a two size of hole diameter and ratio with large difference to produce a wide bandwidth of absorption as found in [8-9]. Figure 3a parameters are: 1<sup>st</sup> layer MPP:  $t_1 = 1$  mm,  $d_1 = 0.3$  mm,  $d_2 = 0.6$  mm,  $p_1 = 4.0\%$ ,  $p_2 = 0.6\%$  and 2<sup>nd</sup> layer MPP:  $t_2 = 1$  mm,  $d_3 = 0.3$  mm,  $d_4 = 0.5$  mm,  $p_3 = 3.5\%$ ,  $p_4 = 1.5\%$ . Figure 3b parameters are: 1<sup>st</sup> layer MPP:  $t_1 = 1$  mm,  $d_1 = 0.3$  mm,  $d_2 = 0.5$  mm,  $p_1 = 0.2\%$ ,  $p_2 = 3.0\%$  and 2<sup>nd</sup> layer MPP:  $t_2 = 2$  mm,  $d_3 = 0.5$  mm,  $d_4 = 0.3$  mm,  $p_3 = 1.5\%$ ,  $p_4 = 3.5\%$ .

Measured results show a good agreement with the predict results, however the 3<sup>rd</sup> peak of the predicted curve shows slightly shift in Figure 3(a) and lower value in Figure 3(b).

#### 5. CONCLUSION

In this paper a parametric study of applying an inhomogeneous panel pattern on double layer MPP absorber system model is presented. Mathematical equations are developed based on the equivalent circuit method. Results shows that double layer inhomogeneous MPP model can produce wider absorption bandwidth with than the conventional double layer MPP for the same setting parameters without enlarging the cavity depth. Predicted results are validated through the experiment, which are show a good agreement.

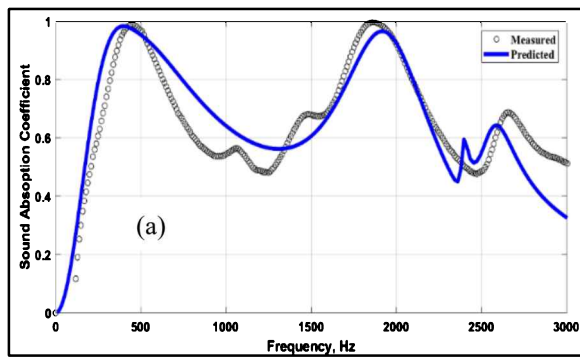


Figure 3 Comparison of normal absorption coefficients between predicted and measured data of DL-iMPP model, cavity depths are  $D_1 = 20$  mm,  $D_2 = 75$  mm.

#### ACKNOWLEDGEMENT

Part of this project is supported by the Fundamental Research Grant Scheme from Ministry of Higher Education Malaysia. (Grant no.: FRGS/1/2016/TK03/FTK-CARE/F00323).

#### REFERENCES

- [1] Dah-You, M. A. A. (1975). Theory and design of microperforated panel sound-absorbing constructions. *Scientia Sinica*, 18(1), 55-71.
- [2] Ismail, A. Y., Putra, A., & Ayob, M. R. (2011). Application of micro-perforated panel (MPP) in a Vehicle cabin: Overcoming the ‘mass-air-mass’ resonance. *Hari Penyelidikan FKM 2011*, 46–51, 2011.
- [3] Shi, X., & Mak, C. M. (2017). Sound attenuation of a periodic array of micro-perforated tube mufflers. *Applied Acoustics*, 115, 15-22.
- [4] Yu, X., Lau, S. K., Cheng, L., & Cui, F. (2017). A numerical investigation on the sound insulation of ventilation windows. *Applied Acoustics*, 117, 113-121.
- [5] Gai, X. L., Xing, T., Li, X. H., Zhang, B., Wang, F., Cai, Z. N., & Han, Y. (2017). Sound absorption of microperforated panel with L shape division cavity structure. *Applied Acoustics*, 122, 41-50.
- [6] Zhao, X. D., Yu, Y. J., & Wu, Y. J. (2016). Improving low-frequency sound absorption of micro-perforated panel absorbers by using mechanical impedance plate combined with Helmholtz resonators. *Applied Acoustics*, 114, 92-98.

- [7] Gai, X. L., Li, X. H., Zhang, B., Xing, T., Zhao, J. J., & Ma, Z. H. (2016). Experimental study on sound absorption performance of microperforated panel with membrane cell. *Applied Acoustics*, 110, 241-247.
- [8] Mosa, A. I., Putra, A., Ramlan, R., Prasetyo, I., & Esraa, A. A. (2019). Theoretical model of absorption coefficient of an inhomogeneous MPP absorber with multi-cavity depths. *Applied Acoustics*, 146, 409-419.
- [9] Mosa, A. I., Putra, A., Ramlan, R., Esraa, A., & Halim, Z. (2018). Parametric study on performance of an inhomogeneous MPP absorber. *Proceedings of Mechanical Engineering Research Day 2018*, 303–304.

# Study of sound absorption of micro perforated panel with visco-thermal effects

Al-Ameri Esraa<sup>1</sup>, A. Putra<sup>1,2,\*</sup>, Ali I. Mosa<sup>1,3</sup>, R.M. Dan<sup>1,2</sup>

<sup>1)</sup> Fakulti Kejuruteraan Mekanikal, Universiti Teknikal Malaysia Melaka,  
Hang Tuah Jaya, 76100 Durian Tunggal, Melaka, Malaysia

<sup>2)</sup> Centre for Advanced Research on Energy, Universiti Teknikal Malaysia Melaka,  
Hang Tuah Jaya, 76100 Durian Tunggal, Melaka, Malaysia

<sup>3)</sup> Mechanical Engineering Department, Collage of Engineering, University of Baghdad, Jadriyah - Baghdad, Iraq

\*Corresponding e-mail: azma.putra@utem.edu.my

**Keywords:** Sound absorption, inhomogeneous MPP, finite element method (FEM)

**ABSTRACT** – Micro-perforated panel (MPP) absorbers, are recognized as the next group of sound absorbing materials. Most recent presented research used the analytical method to calculate the acoustic performance of the MPP considering the impedance of single hole and then use the porosity to determine the whole impedance. However, this method not effective for panels with inhomogeneous hole perforation. This study presents 3D model to study the sound absorption of inhomogeneous MPP using FEM considering the visco-thermal effects. Results shows that the simulated data does not match with analytical one. Experiment data showed a good agreement with the simulations data.

## 1. INTRODUCTION

MPPs absorbers without additional fibrous or porous material has been widely used as the next group of sound absorbing materials. MPPs are tiny panels with a mesh of sub-millimetre size holes circulated over its surface and can made from metal, plastic or etc. [1]. MPP has been taken more interest the researchers because simple construction and obvious sound absorption effect and easy for use. The applications of MPP are extensively used in noise control engineering such as Acoustic silencers [2-3], ducted ventilation [4], building acoustic systems [5-6]. However, the total sound absorption bandwidth is still limited [7]. Most of studies used the analytical method to compute the acoustic performance of the MPP by considering the impedance of a single hole and then use the porosity to determine the whole impedance of the panel. However, this method is not effective for panels with inhomogeneous hole size [8]. Thus, whole or half structure of the model should be implemented to study the impedance of non-homogenous panels. This study presents 3D model to study the acoustic performance of single layer inhomogeneous MPP using FEM considering the visco-thermal effects.

## 2. SIMULATION ANALYSIS

The theoretical normalized acoustic impedance of inhomogeneous MPP model is calculated by implement a 3D visco-thermal model using a finite element method (FEM) based on the linearized Naiver Stokes equations in the frequency domain [8-9]. Figure 1 shows the MPP sample and its symmetry boundaries, it performed inside a cylindrical impedance tube has a length of 30 cm and inner diameter of 3.3 cm.

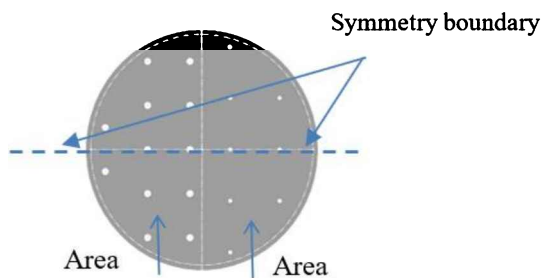


Figure 1 Schematic graph of inhomogeneous MPP with the assumed symmetry boundaries.

The calculated transfer acoustic impedance ( $Z_{trans}$ ) of the panel by FEM including the visco-thermal effect, which can give by [10].

$$Z_{MPP} = Z_{trans} = \frac{\int P_{in} - \int P_{out}}{\rho c \int v} \quad (1)$$

Where  $\Delta p$  is the pressure drop across the panel,  $v$  is the velocity in the perforation hole,  $\rho$  density of air. Thus, the normal absorption coefficient  $\alpha$  of the model including the visco-thermal effect by FEM can be represented as [10].

$$\alpha = 1 - |R|^2 \quad (2)$$

Where  $R$  is the pressure reflection coefficient that gives as

$$R = \frac{\int P_{scat}}{\int P_{inc}} \quad (3)$$

Where  $P_{scat}$  is the scattered sound pressure and  $P_{inc}$  is incident sound pressure. The calculation was made under ideal air physical properties. While the total impedance calculated by electric circuit method (ECM) is

$$Z_{total} = r + j\omega m + Z_D \quad (4)$$

Where  $r$  is  $Z_{resistive}$ ,  $m$  is  $Z_{reactive}$ ,  $Z_D$  is impedance of cavity depth.

## 3. RESULTS AND DISCUSSION

Figure 2. shows the comparison between the imaginary part of the normalized impedance  $imag(Z_{trans})$  calculated by FEM and (ECM) described of the MPP model. Model structure parameters are for area 1 are hole diameter  $d_1 = 0.9\text{mm}$ , perforation ratio  $p_{1=} = 1.76\%$ , for

area 2 are hole diameter  $d_2 = 0.5$  mm, perforation ratio  $p_2 = 0.4\%$ . Thickness is set to be  $t=1$  mm for the whole panel and cavity depth  $D=30$ mm.

Figure 3 shows comparison of absorption coefficient between analytical ECM with the simulated FEM. it can be observed that the results showed un-agreement. These un-agreement are mainly due to the finite geometry effect and to the spatial distribution of the perforations for the numerical case [8].

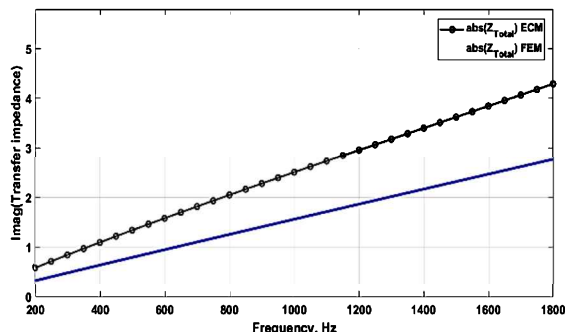


Figure 2. Total impedance comparison between FEM and ECM of a single layer inhomogeneous MPP, cavity depth  $D= 30$  mm.

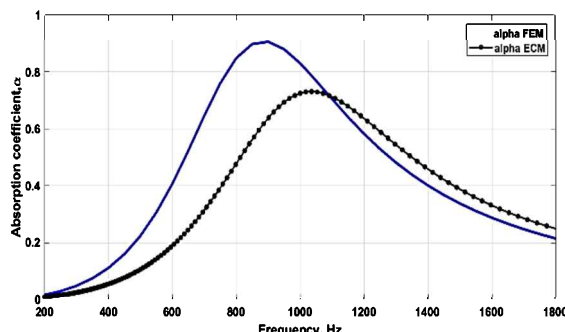


Figure 3. Absorption coefficient comparison between FEM and ECM of single layer inhomogeneous MPP, cavity depth  $D= 30$ mm.

#### 4. MODEL VALIDATION

Figure 4 shows the validation of the FEM model with experimentally measured data of normal absorption coefficients. Experiment data were obtained in lab by using of impedance tube according to the standard ISO 10534-2[11] .A good agreement can be observed This lead that the FE model with considering the visco-thermal effect can accurately describe the acoustic performance for the analysed configurations. [8].

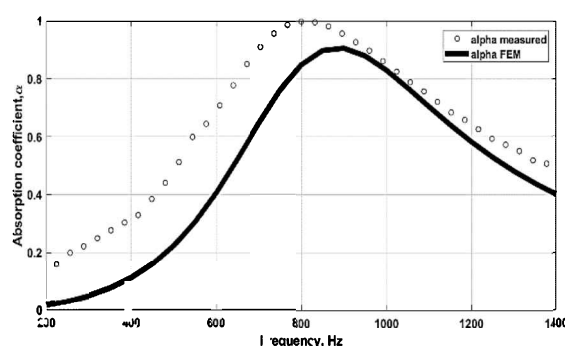


Figure 4. Absorption coefficient comparison between measured data and FEM data, cavity depth  $D= 30$ mm.

#### 5. CONCLUSION

In this paper, a 3D FEM model is present in order to study the acoustic properties of inhomogeneous MPPs including the visco-thermal effects. Results show that the absorption performance of MPPs with viscous and thermal is mostly affected and dos not much with the one that obtained by analytical method. The model is experimentally verified and showed a good agreement. This lead that the FE model can accurately describe the acoustic performance for the analysed configurations of inhomogeneous MPPs.

#### ACKNOWLEDGEMENT

Part of this project is supported by the Fundamental Research Grant Scheme from Ministry of Higher Education Malaysia. (Grant no.: FRGS/1/2016/TK03/FTK-CARE/F00323).

#### REFERENCES

- [1] Dah-You, M. A. A. (1975). Theory and design of microperforated panel sound-absorbing constructions. *Scientia Sinica*, 18(1), 55-71.
- [2] Shi, X., & Mak, C. M. (2017). Sound attenuation of a periodic array of micro-perforated tube mufflers. *Applied Acoustics*, 115, 15-22.
- [3] Yu, X., Cheng, L., & You, X. (2015). Hybrid silencers with micro-perforated panels and internal partitions. *The Journal of the Acoustical Society of America*, 137(2), 951-962.
- [4] Yu, X., Cui, F. S., & Cheng, L. (2016). On the acoustic analysis and optimization of ducted ventilation systems using a sub-structuring approach. *The Journal of the Acoustical Society of America*, 139(1), 279-289.
- [5] Yu, X., Lau, S. K., Cheng, L., & Cui, F. (2017). A numerical investigation on the sound insulation of ventilation windows. *Applied Acoustics*, 117, 113-121.
- [6] Mosa, A. I., Putra, A., Ramlan, R., Prasetyo, I., & Esraa, A. A. (2019). Theoretical model of absorption coefficient of an inhomogeneous MPP absorber with multi-cavity depths. *Applied Acoustics*, 146, 409-419.
- [7] Li, D., Chang, D., Liu, B., & Tian, J. (2014, October). Improving sound absorption bandwidth of micro-perforated panel by adding porous materials. In *INTER-NOISE and NOISE-CON Congress and Conference Proceedings* (Vol. 249, No. 6, pp. 1877-1882). Institute of Noise Control Engineering.
- [8] Carbajo, J., Ramis, J., Godinho, L., Amado-Mendes, P., & Alba, J. (2015). A finite element model of perforated panel absorbers including viscothermal effects. *Applied Acoustics*, 90, 1-8.
- [9] Kampinga, W. R., Wijnant, Y. H., & de Boer, A. (2010). Performance of several viscothermal acoustic finite elements. *Acta acustica united with Acustica*, 96(1), 115-124.
- [10] Li, L., Gang, X., Liu, Y., Zhang, X., & Zhang, F. (2018). Numerical simulations and experiments on thermal viscous power dissipation of perforated plates. *AIP Advances*, 8(10), 105221.

# Development of 3D-printed vibration dynamic absorber

Mohamad Syafiq Hamdan<sup>1</sup>, Azma Putra<sup>1,2,\*</sup>, Mohd Rizal Alkahari<sup>1,2</sup>

<sup>1)</sup> Fakulti Kejuruteraan Mekanikal, Universiti Teknikal Malaysia Melaka,  
Hang Tuah Jaya, 76100 Durian Tunggal, Melaka, Malaysia

<sup>2)</sup> Centre for Advanced Research on Energy, Universiti Teknikal Malaysia Melaka,  
Hang Tuah Jaya, 76100 Durian Tunggal, Melaka, Malaysia

\*Corresponding e-mail: azma.putra@utem.edu.my

Keywords: 3D printer; vibration absorber; ABS plastic

**ABSTRACT** – Vibration of a system can be reduced by using a dynamic vibration absorber. In this study, a vibration absorber is fabricated using using 3D printer machine technology from Acrylonitrile Butadiene Styrene (ABS). The effectiveness of the vibration absorber is tested on a cantilever beam and it is found to successfully reduce the amplitude of the first mode of the beam.

## 1. INTRODUCTION

A dynamic vibration absorber is a combination of spring-mass system, where its natural frequency is tuned to the vibration frequency of the host structure [1]. The absorber can therefore be of any form, such as lumped system of mass-spring-damper like those installed at the Taipei 101 building in Taiwan and at Millennium bridge in London, or a continuous system such as the Stockbridge damper.

The most recent research is a study to create vibration absorber using the metamaterial. Metamaterial is a material engineered to have a property with combinations of multiple elements fashioned from composite materials such as plastics or metals.

Lee et al. [2] proposed a vibro-acoustic metamaterial for suppressing longitudinal vibration waves transmitted between two mechanical parts. The absorber is found to effectively reduce vibration in extremely low frequency range of longitudinal vibration.

He et al. [3] designed structural vibration suppression in laminate acoustic metamaterials which is composed of carbon-fiber-reinforced polymer (CFRP) and periodic array of mass-spring-damper subsystems. By integrating these two parallel orthotropic laminates, the stopband becomes wider compared to that of a conventional vibration absorber. Similar study was also conducted by Yang et al. [4], where meta-structure beam is attached with multiple absorbers.

Nowadays, 3D printer machine technology becomes increasingly popular because its flexibility in printing any shape of structure into three dimensions [5]. In this study, the 3D print is used to fabricate a single structure of vibration absorber that able to reduce the vibration amplitude of a targeted system.

## 2. METHODOLOGY

### 2.1 Design and Fabrication of Vibration Absorber

The vibration absorber for this project was designed by using Solidwork software. It was designed where part of the vibration absorber will have spring like properties

and another part will act as the inertial mass. The model of vibration absorber in this study is as shown in Figure 1.

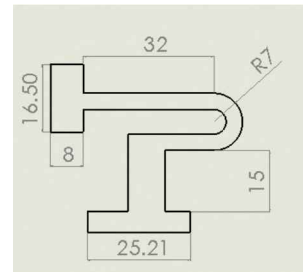


Figure 1 Proposed model of vibration absorber (the dimensions are in mm unit).

The model was then transferred to ANSYS software to calculate the natural frequency of the absorber. The natural frequency of the vibration absorber must in the range of 100 Hz to 200Hz in order to satisfy the requirement for the testing in the lab. The natural frequency of the vibration absorber in Figure 1 is 144 Hz.

The model was then fabricated using 3D printer machine, i.e. Flash Print method. The product is shown in Figure 2.

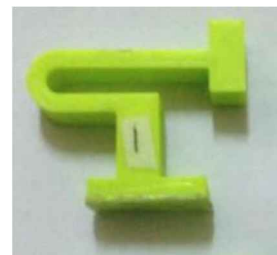


Figure 2 The 3D print product of the designed vibration absorber.

### 2.2 Experiment

The fabricated vibration absorber was then tested on a cantilever beam model to observe its efficiency in reducing the vibration amplitude of the beam. The experimental setup can be referred in Figure 2. However, prior to this test, the absorber was first installed on the vibration shaker to measure its real natural frequency. The length of the beam was then adjusted, so that its first mode of vibration matches with the natural frequency of the absorber.

The vibration was measured using ‘tear drop’ accelerometer located off the midspan of the beam. The absorber was attached at distance 7 cm from the free-end

of the beam. One and two absorbers were used and the effect is discussed.

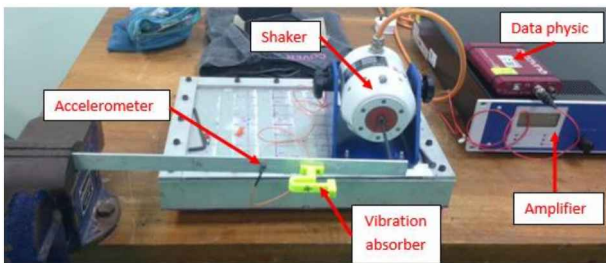


Figure 2 Experimental set up for vibration absorber testing.

### 3. RESULTS AND DISCUSSION

#### 3.1 Stress Analysis

The stress analysis has been done using ANSYS software to determine the strength and the weakest point of the vibration absorber. The result is shown in Figure 3.

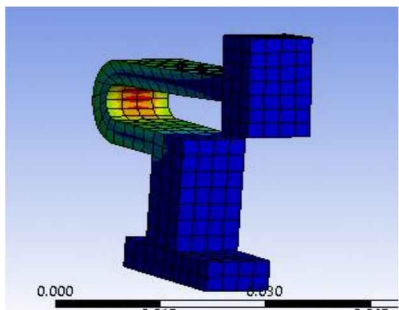


Figure 3 Stress analysis on the vibration absorber.

From Figure 3, the red colour section showed the weakest point on the vibration absorber where stress amplitude is the greatest. During vibration, this curved section in the absorber has the greatest deflection due to its lowest dynamic stiffness.

#### 3.2 Dynamic Test Results

Figure 4 and Figure 5 show the measured vibration amplitude without and with the vibration absorber, for single and two absorbers, respectively. The beam can be seen to have the natural frequency of 144 Hz, which has been set to be the same as the natural frequency of the absorber. From Figure 4, it can be seen that the vibration amplitude of the beam can be reduced significantly at 144 Hz.

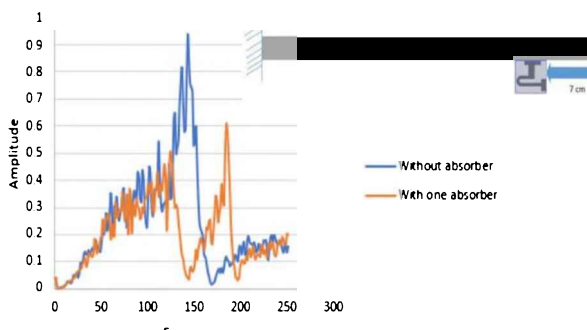


Figure 4 The measured vibration amplitude of the beam with one absorber.

Two resonant frequencies at 130 Hz and 180 Hz can be observed as the consequences of the dynamics of two-degree-of freedom system due to the presence of the absorber on the beam.

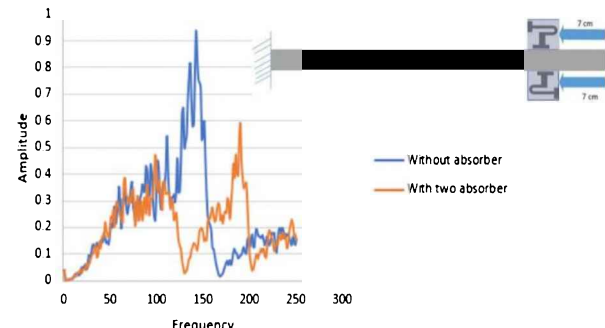


Figure 4 The measured vibration amplitude of the beam with two absorbers.

From Figure 5, adding parallel absorber (on the other side of the beam) can be seen to improve the bandwidth of reduction where the first resonant peak is now reduced at around 120 Hz and the second peak has a lower amplitude.

### 4. CONCLUSION

Vibration absorber produced from 3D print has been successfully fabricated. The dynamic test on a cantilever beam reveals that the product can act as the dynamic absorber to reduce the vibration of the host structure.

It is interesting for the future study to observe the effect of multiple absorbers with different type of arrangement in the structure. The life span of this kind of 3D print product is also of interest to know the reliability of the absorber in practice.

### ACKNOWLEDGMENT

Part of this project is supported by Universiti Teknikal Malaysia Melaka with research grant no. JURNAL/2018/FKM/Q00010.

### REFERENCES

- [1] Rao, S. S., & Yap, F. F. (2011). *Mechanical vibrations* (Vol. 4). Upper Saddle River: Prentice hall.
- [2] Lee, S., Ahn, C. H., & Lee, J. W. (2018). Vibro-acoustic metamaterial for longitudinal vibration suppression in a low frequency range. *International Journal of Mechanical Sciences*, 144, 223-234.
- [3] He, Z. C., Xiao, X., & Li, E. (2017). Design for structural vibration suppression in laminate acoustic metamaterials. *Composites Part B: Engineering*, 131, 237-252.
- [4] Yang, W., Seong, Y., Jeong, S., & Park, J. (2018). Vibration reduction using meta-structures composed of tuned dynamic absorbers employing mass impacts. *Composite Structures*, 183, 216-220.
- [5] Habeeb, H. A., Alkahari, M. R., Ramli, F. R., Hasan, R., & Maidin, S. (2016). Strength and porosity of additively manufactured PLA using a low cost 3D printing. *Proceedings of Mechanical Engineering Research Day*, 2016, 69-70.

# Vibration analysis for angular misalignment on spur and helical gear

K. Amri Tofrowaih<sup>1,2,\*</sup>, Abdul Munir Hidayat Syah Lubis<sup>1,2</sup>, Mohd Anas Amir<sup>1</sup>

<sup>1)</sup> Fakulti Teknologi Kejuruteraan Mekanikal dan Pembuatan, Universiti Teknikal Malaysia Melaka,  
Hang Tuah Jaya, 76100 Durian Tunggal, Melaka, Malaysia

<sup>2)</sup> Centre for Advanced Research on Energy, Universiti Teknikal Malaysia Melaka,  
Hang Tuah Jaya, 76100 Durian Tunggal, Melaka, Malaysia

\*Corresponding e-mail: khairul.amri@utem.edu.my

**Keywords:** Condition-based maintenance (CBM); misalignment gear; spectral analysis

**ABSTRACT** – Vibration of angular misaligned spur and helical gear was analyzed by using spectral analysis in this work to determine the effect of load on misaligned spur and helical gear. Vibration signal for angular misalignment 0°, 30°, and -30° with different load of 0 Nm, 1.7 Nm, and 3.4 Nm is recorded. Angular misalignment could be observed clearly at 2X RPM at acceleration sensor 1 position. Vibration reading also increases as the load from Brake & Load unit is connected to the output shaft of the gear train system.

## 1. INTRODUCTION

Common rotating machinery issues such as unbalance, looseness, misalignment, bent shaft and bearing defects can cause undesirable vibration to the overall mechanical system. Gear misalignment could affect its nearby bearing to high wear rate earlier than it should by giving more fatigue stress due to higher concentrated load than design specification [1]. Condition-based maintenance (CBM) is a common technique to assess and monitor condition of pump, gearbox or other machinery components without physically assess it. This method allows maintenance work to be scheduled and provide time for the action to be taken before a failure occurs [2]. Aherwar & Khalid [3] listed four main vibration analysis technique for diagnostic of gearbox namely Time Domain Analysis, Frequency Domain Analysis which includes Spectral Analysis, Order Analysis, and Time Synchronous Averaging. On the other hand, Sait & Eldeen [4] categorized vibration-based analysis into two main different processing groups namely Time-Statistical Analysis and Time-Frequency Analysis. Dalpiaz [5] in his work observed that spectral (or frequency) analysis is the most frequently used vibration analysis method for condition-based monitoring in gear train systems. It is also recommended for detection and basic diagnosis of errors in simple rotating equipment.

## 2. METHODOLOGY

Vibration signal of a normal condition gear without misalignment, and angular misaligned gear 30°, and -30° which obtained through asymmetrical adjustment of the bearing covers are measured for two types of gear namely spur gear and helical gear. Technical specification of the gears is as shown in Table 1. Vibration is measured by using two acceleration sensors located horizontally at two ends of gear casing to observe vibration tendency. Position of accelerometer 1 is at the right back of the gear

casing which near to an induction motor. The 0.37 kW motor provides rotation to the simple gear train via coupling at the shaft at 1800 RPM speed. Brake and Load unit located on the right box as shown in Figure 1 comprises of control unit, electric display and magnetic particle brake. The unit purpose is to simulate the addition of load into the gear system which are 1.7 Nm and 3.4 Nm. There is no adjacent machine operate next to this experiment that would affect vibration level through foundation or structure [1]. Spectral analysis method is used to analyse the vibration signal. Data from spectral analysis is extracted and summarized to a line graph as shown in Figure 2.

Table 1 Technical specification for gear.

Dimension (L x W x H)	260 x 210 x 180 mm
Weight	20kg
Basic profile	DIN 867
Modulus	2
Pressure angle	20°
Helix angle	10°
Transmission ratio	i = 3
Centre distance	101.543 mm
Pitch diameter of large gear	151 mm
Pitch diameter of small gear	51 mm

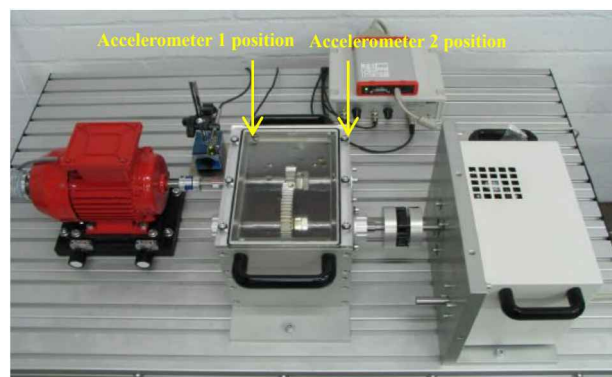


Figure 1 Experimental setup for vibration on gearbox.

The benefit of frequency spectrum analyser in a machine monitoring environment is its capability to display vibration data in the frequency domain as a spectrum. The frequency spectrum shows root mean square (rms) velocity and frequency reading in vertical and horizontal axis respectively. Brue and Kjaer suggested that a vibration severity is best indicated by velocity-rms for velocity in the range of 10 to 1000 Hz [6]. Moreover, velocity-rms is the standard unit of

vibration measurement as recommended by International Standards Organization (ISO) because it best represents the energy content in a vibration signal, [7]. The ratio of the gear is 1:3 small gear to large gear number of teeth difference. The frequency of 10Hz and 30Hz was derived from the gear ratio considering the induction motor speed equals to 30 Hz. Meanwhile, 60Hz from the graph is 2X RPM of the gear. Engagement frequency or Gear Mesh Frequency (GMF) is equal to 750 Hz.

### 3. RESULTS AND DISCUSSION

In overall, vibration signal obtained from accelerometer 2 is larger than the vibration signal obtained from accelerometer 1 for most range of loads, gear types and misalignment setting. This shows that the

vibration tendency is towards the side of brake & load unit where the accelerometer 2 is located. The graph at 0° angle, accelerometer 1 without load indicates control sample reading where only inertia is acting on the gear for 10 Hz is 0.38 mm/s at spur gear and 0.09 mm/s at helical gear. On the other hand, acceleration sensor position 2 with similar parameter recorded 0.69 and 0.30 mm/s. Addition of 1.7 Nm load to the system increase the vibration reading for instance at frequency of 10 Hz for spur gear at 0° misalignment angle at sensor 1 position is 0.75 mm/s of spur gear and for helical gear is 0.10 mm/s. At the 2X RPM, the result from spur gear is 0.15 mm/s and from helical gear is 0.04 mm/s, at the 750 Hz the spur gear is 0.07 mm/s and helical gear is 0.01 mm/s.

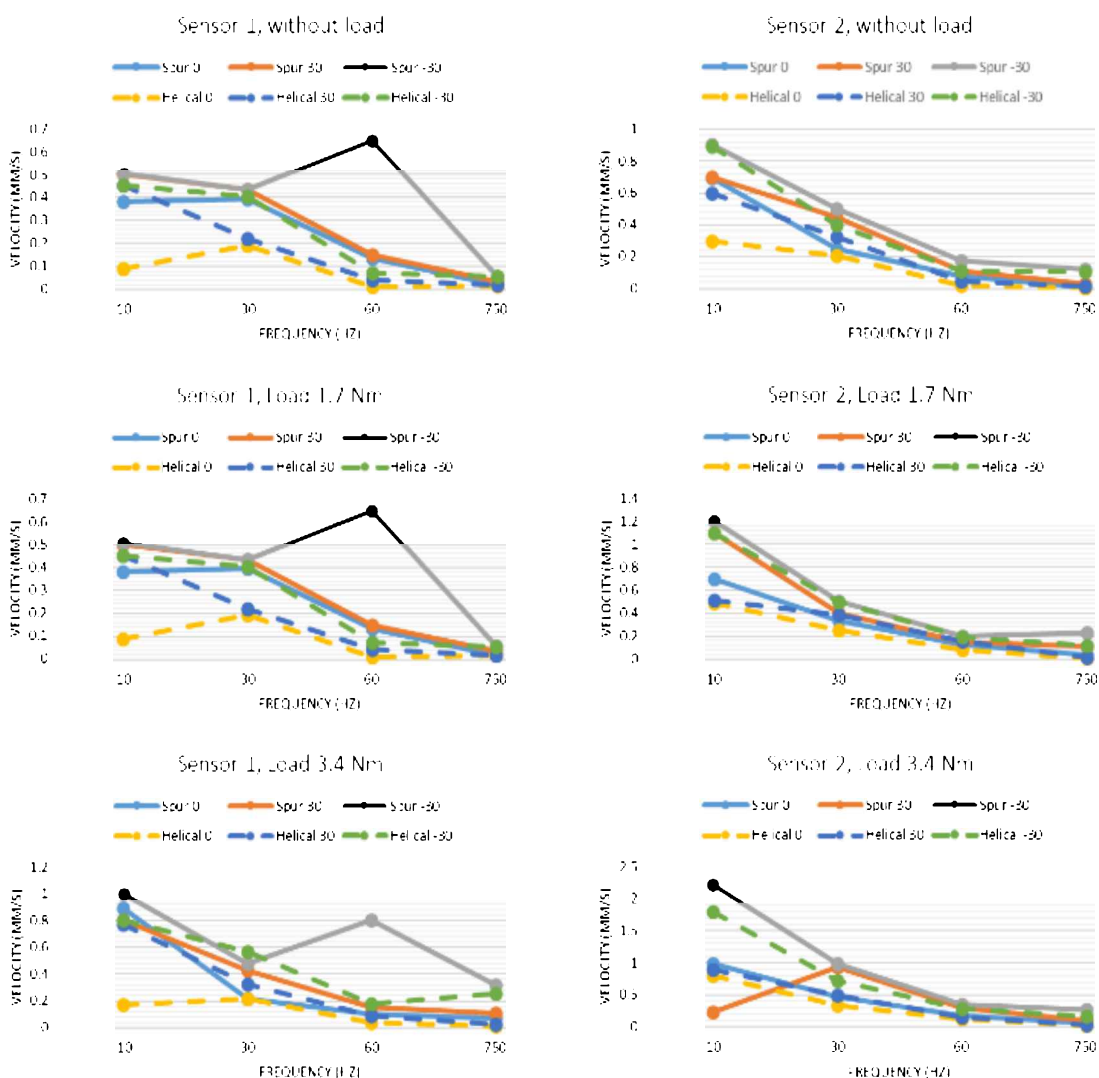


Figure 2 Vibration signals of misaligned spur and helical gear with various load across frequency range.

As the bearing cover is adjusted at 30°, at acceleration sensor position 1 with frequency of 10 Hz on 3.4 Nm load, the rms velocity reading is 0.89 mm/s for spur gear and 0.17 mm/s for helical gear, whereas at frequency 30 Hz the result is 0.22 mm/s for spur gear and 0.21 mm/s for helical gear was recorded for spur gear and helical gear at frequency 30 Hz with similar load. The value from frequency spectrum of spur gear at 2X RPM is 0.10 mm/s and helical gear is 0.04 mm/s, while the

mesh frequency for 30° is 0.11 mm/s for spur and 0.03 mm/s for helical gear. However, when the cover is adjusted to -30°, the spur gear is observed to experience angular misalignment at accelerometer 1 position by the spike of the velocity value at 2X RPM (60Hz). This occurred because load distribution of the gear pair vibration has shifted as suggested in previous study [8]; whereas helical gear is still operating under normal curve pattern. From this single graph, the tolerance of helical

gear towards misalignment is higher. The overall rms velocity decrease with increasing frequency as shown in Figure 2 indicates the vibration energy declines.

#### 4. CONCLUSION

The more load imposed on the gear, higher the vibration level that will affect the gear. Helical gear vibration level is lower than that of spur gear due to helical gear helix angle that smoothen the gear mesh which in turn shows the its higher tolerance towards misalignment than spur gear type.

#### REFERENCES

- [1] J. Mais (2012) Spectrum Analysis: The key features of analyzing spectra, SKF reliability system, SKF USA Inc.
- [2] Nuawi, M. Z., Khamis, N. K., Zali, Z., Wan Mahmood, W. M. F., Abdullah, S., & Mohd Nopiah, Z. (2013). A study of engine monitoring system using statistical method. *Applied Mechanics and Materials*, 471, 193–196.
- [3] Aherwar, A., & Khalid, S. (2012). Vibration analysis techniques for gearbox diagnostic: A review. *International Journal of Advanced Engineering Technology*, 3(2), 4–12.
- [4] Sait, A. S., & Sharaf-Eldeen, Y. I. (2011). A review of gearbox condition monitoring based on vibration analysis techniques diagnostics and prognostics. In *Rotating Machinery, Structural Health Monitoring, Shock and Vibration, Volume 5* (pp. 307-324). Springer, New York, NY.
- [5] Dalpiaz, G., Rivola, A., & Rubini, R. (1998, October). Gear fault monitoring: comparison of vibration analysis techniques. In *3rd International Conference Acoustical and Vibratory Surveillance Methods and Diagnostics Techniques* (pp. 623-632).
- [6] Brüel, & Kjaer. (1982). Measuring vibration. Denmark-K Larson and Son.
- [7] Scheffer, C., & Girdhar, P. (2004). *Practical machinery vibration analysis and predictive maintenance*. Elsevier.
- [8] Houser, D., Harianto, J., & Talbot, D. (2006). Gear mesh misalignment. *Gear Solutions*, 34-43.

## 3D-printed lattice structure as sound absorber

Muhammad Fakrul Syahid Che Hamid<sup>1</sup>, A. Putra<sup>1,2,\*</sup>, D.H. Kassim<sup>1,2</sup>, M.R. Alkahari<sup>1,2</sup>

<sup>1)</sup>Fakulti Kejuruteraan Mekanikal, Universiti Teknikal Malaysia Melaka,  
Hang Tuah Jaya, 76100 Durian Tunggal, Melaka, Malaysia

<sup>2)</sup>Centre for Advanced Research on Energy, Universiti Teknikal Malaysia Melaka,  
Hang Tuah Jaya, 76100 Durian Tunggal, Melaka, Malaysia

\*Corresponding e-mail: azma.putra@utem.edu.my

**Keywords:** Lattice structures; sound absorber; absorption coefficient

**ABSTRACT** – Existing sound absorbers, typically consist of fibres and foams. However, it has low life span and poor resistant to damage. This study investigates on the sound absorption characteristics of lattice structure produce by additive manufacturing to improve acoustical characteristics that cannot be fulfilled by typical sound absorber. Sound absorption coefficient ( $\alpha$ ) measurement were conducted by using impedance tube apparatus according to ISO 10534-2 standard. The effect of thickness, strut diameter of lattice arms and air gap were determined by comparing  $\alpha$  for each sample. It is shown that the lattice structures are able to absorb sound mostly above 1 kHz.

### 1. INTRODUCTION

Noise pollution become more apparent in the process of modernization that cause various harmful effect to people around the world. These situation can be controlled by using sound absorption materials such as fibres and foams [1-5]. However, producing the sound absorber itself brought harmful effect to environment especially foams materials. Most sound absorbers are poor in strength, tend to deteriorate and bulky which are not favourable in lightweight application such as transportation industries and aerospace [6]. Ensuring repeatability in quality is difficult and sometimes increase production time and cost [7-8]. Additive manufacturing enable manufacturers to skip complex process on the new product development and also produce closer characteristics to stochastic foams standard. It became reliable to industrial application due to the simple processing to produce a complex and reliable product [9]. The objective of this paper is to study body centre cubic (BCC) lattice design structure sound absorption coefficient characteristics. Apart from these, the lattice structure and its porosity also considered for making a good absorber.

### 2. METHODOLOGY

#### 2.1 Lattice Sample

The design of lattice structures was drawn by referring to the BCC type lattice. A single lattice was arranged and stacked to form cylindrical shape to fit in the impedance tube. Sample thickness were varied to 15 mm, 20 mm and 40 mm as shown in Figure 1. The strut diameter of the lattice arms was varied to 1.4 mm, 1.6 mm and 1.8 mm as shown in Figure 2.

Samples were printed by CubePro3D printer using fused deposition method. The material use for the printing is Acrylonitrile Butadiene Styrene (ABS) plastic

as it is known with flexibility, smoothness and more reliable when subjected to external impacts compared to other raw materials.



Figure 1 Example of the lattice structure with height of 15 mm and 20 mm.

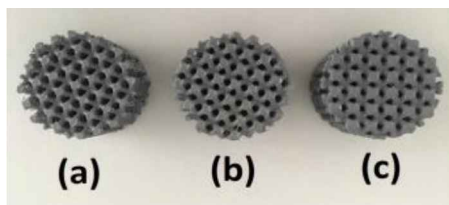


Figure 2 Different strut diameter for lattice (a) 1.4 mm, (b) 1.6 mm and (c) 1.8 mm.

#### 2.2 Experimental Setup

Sound absorption coefficient characteristics were measured using impedance tube with diameter of 33.33 mm with a rigid backing. All measurements were performed using two microphone method following the ISO 10534-2 standard.

### 3. RESULTS AND DISCUSSION

The data for the sound absorption characteristics of the lattice structures from the experiment were analysed based on the effect of the thickness, strut diameter of lattice structure and application of air gap behind the samples.

#### 3.1 Effect of Thickness

The effect of lattice thickness is shown in Figure 3. However, the peak of  $\alpha$  barely reach 0.5 thus a more consideration need to be taken for this parameter. Thicker sample increase peak of  $\alpha$  and shift it to the lower frequency. Thicker sample increase flow resistance in the sample and the sound energy dissipation.

#### 3.2 Effect of Strut Diameter

For the effect of strut diameter, the peak of  $\alpha$  increase as the strut diameter increase as shown in Figure 4. The samples that have a greater diameter have the higher amplitude of absorption coefficient compared to other sample. The peak value of  $\alpha$  is about 0.7 between

tested frequency which is around 1.5 kHz to 2 kHz.

A bigger strut diameter reduce the opening on top of the sample (as seen on Figure 2). A smaller holes produce higher viscous effect thus assist the acoustic dissipation.

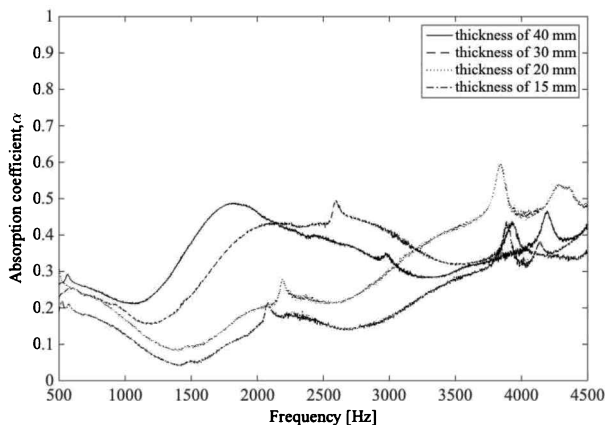


Figure 3 Comparison of lattice structures with different thickness.

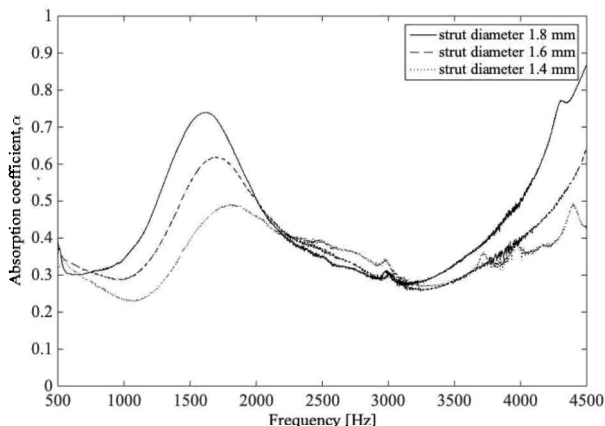


Figure 4 Comparison of lattice structures with different strut diameter.

### 3.3 Effect of Air Gap

Figure 5 shows with the increasing depth of air gap shift  $\alpha$  to lower frequency without much change in its peak. Mass spring resonance created by the presence of air gap and thus peak of  $\alpha$  occur when the stiffness of the air gap cancels the mass of the holes in the sample. The presence of air gap layer can be a good alternative technique in order to improve the sound absorption coefficients. However, in dusty environment, unprotected and lowly maintain sound absorber promote the accumulation of dust inside the air gap.

## 4. CONCLUSION

The performance of lattice structure has been studied and presented in this paper. Based on the result on this experiment, the lattice structures can be suggested to be the next possible sound absorber.

## ACKNOWLEDGMENT

Part of this project is supported by Universiti Teknikal Malaysia Melaka with research grant no. JURNAL/2018/FKM/Q00010.

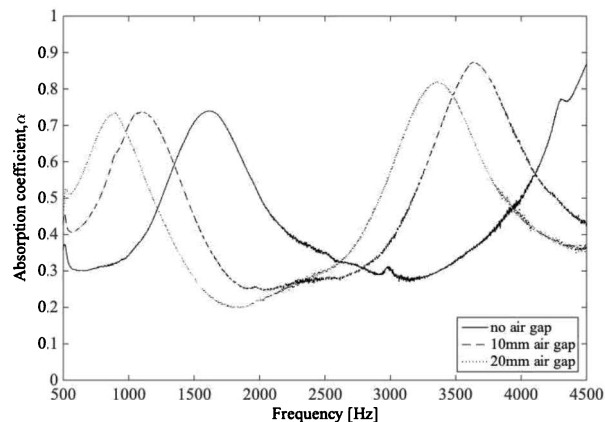


Figure 5 Comparison of lattice structure with the presence of air gap.

## REFERENCES

- [1] Wang, Y., Zhang, L., Daynes, S., Zhang, H., Feih, S., & Wang, M. Y. (2018). Design of graded lattice structure with optimized mesostructures for additive manufacturing. *Materials & Design*, 142, 114-123.
- [2] Lim, Z. Y., Putra, A., Nor, M. J. M., & Yaakob, M. Y. (2018). Sound absorption performance of natural kenaf fibres. *Applied Acoustics*, 130, 107-114.
- [3] Ismail, L., Ghazali, M. I., Mahzan, S., & Zaidi, A. M. A. (2010). Sound absorption of Arenga Pinnata natural fiber. *World Academy of Science, Engineering and Technology*, 67, 804-806.
- [4] Paşayev, N., Kocatepe, S., & Maraş, N. (2019). Investigation of sound absorption properties of nonwoven webs produced from chicken feather fibers. *Journal of Industrial Textiles*, 48(10), 1616-1635.
- [5] Lu, T. J., Hess, A., & Ashby, M. F. (1999). Sound absorption in metallic foams. *Journal of Applied Physics*, 85(11), 7528-7539.
- [6] Fotsing, E. R., Dubourg, A., Ross, A., & Mardjono, J. (2019). Acoustic properties of a periodic micro-structures obtained by additive manufacturing. *Applied Acoustics*, 148, 322-331.
- [7] Sauceau, M., Fages, J., Common, A., Nikitine, C., & Rodier, E. (2011). New challenges in polymer foaming: A review of extrusion processes assisted by supercritical carbon dioxide. *Progress in Polymer Science*, 36(6), 749-766.
- [8] Jacobs, L. J., Kemmere, M. F., & Keurentjes, J. T. (2008). Sustainable polymer foaming using high pressure carbon dioxide: a review on fundamentals, processes and applications. *Green Chemistry*, 10(7), 731-738.
- [9] Petrovic, V., Vicente Haro Gonzalez, J., Jordá Ferrando, O., Delgado Gordillo, J., Ramón Blasco Puchades, J., & Portolés Griñan, L. (2011). Additive layered manufacturing: sectors of industrial application shown through case studies. *International Journal of Production Research*, 49(4), 1061-1079.

# Experimental determination of sound absorption coefficient of green materials polymer from different compositions

Farah Liana, Mohamad Ali Ahmad\*

Fakulti Kejuruteraan Mekanikal, Universiti Teknologi MARA Shah Alam, 40450 Shah Alam, Selangor, Malaysia

\*Corresponding e-mail: mohama9383@uitm.edu.my

**Keywords:** Green materials; sound absorption coefficient; two-microphone method

**ABSTRACT** – The usage of synthetic materials has been replaced to natural materials such as banana stem, grass, lemongrass and palm oil leaves to study their sound absorption coefficients. The usage of synthetic materials may lead to numerous problems on human's health and environment. The usage of natural materials may reduce cost and having less health and safety risk while handling and processing. The samples made with diameter 28mm and 100mm and the thickness are 10mm. The sound absorption coefficients of samples were measured according to ASTM E1050-98/ISO 105342-2 two-microphone method. It is evident palm oil leaves material shows high absorption coefficient.

## 1. INTRODUCTION

Sound can be defined as a physical disturbance in media which has the force and as a transfer medium of sound waves through air, gasses and solids. According to the Minister of Environment Indonesia, noise can be defined as unwanted sound from the business or human activities in the rate and time that can cause human health problems and harm environment [1].

In this study, the most important role to reduce noise is the material of sound absorption [2]. Sound absorptive materials that normally used are fibrous and porous to soften the acoustic environment of a closed volume by reducing the amplitude of the reflected waves. Sound absorber made of synthetic fibre produce significant CO<sub>2</sub> into the atmosphere compared to natural materials [3].

Synthetics porous and fibrous acoustic materials is frequently used in building acoustics also in noise control applications are harmful to human health as well as to the environment [4]. The acoustic panels made from natural fibres are less harmful to human health and eco-friendlier than those made of conventional synthetic fibres [5]. Thus, manufacturers and engineers are inspired to seek alternative materials from natural fibres to replace synthetic fibres due to concern for human health and safety issues. This study is proposed to replace the used of synthetic materials to natural materials by using banana stem, grass, lemongrass and palm oil leaves.

## 2. METHODOLOGY

The construction flow process of sound absorber was given in Figure 1.

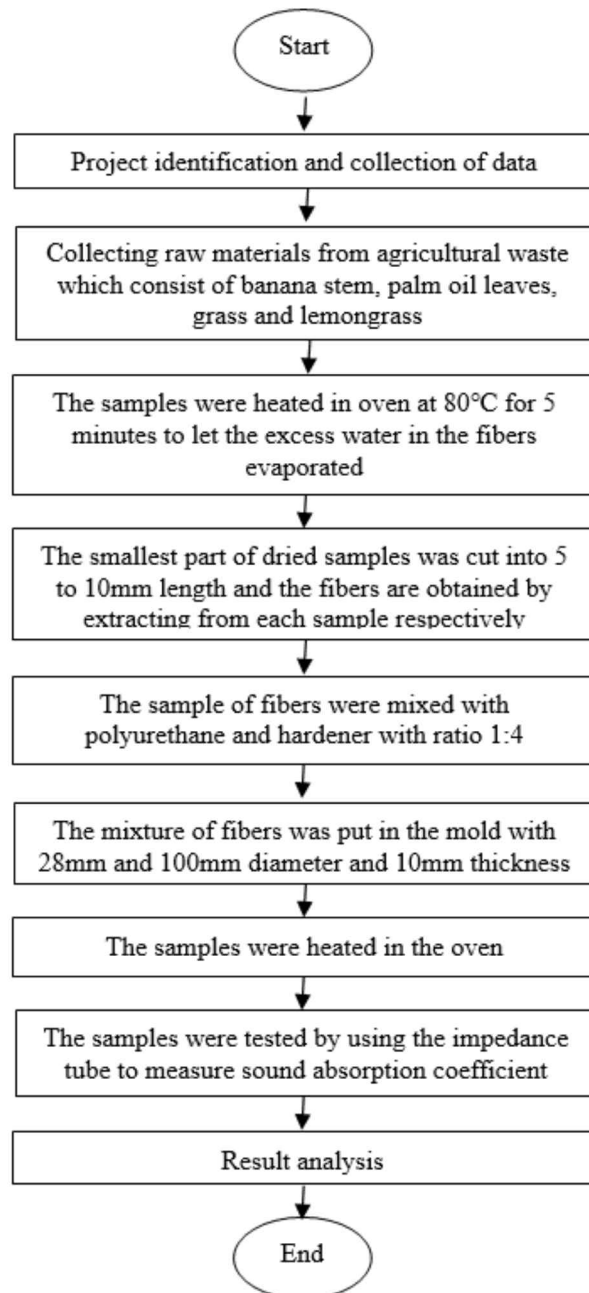


Figure 1 Flow chart of construction process of sound absorber.

### 3. RESULTS AND DISCUSSION

The measurements were based on a two-microphone (Figure 2) method according to ASTM E1050-98. Figure 3 shows the equipment used in the test and the test set-up. The sample was placed at the middle of the impedance tube. Figure 4 shows the variation of sound absorption coefficient against frequency for 4 different samples. It is evident that type of green materials influences the sound absorption coefficients.

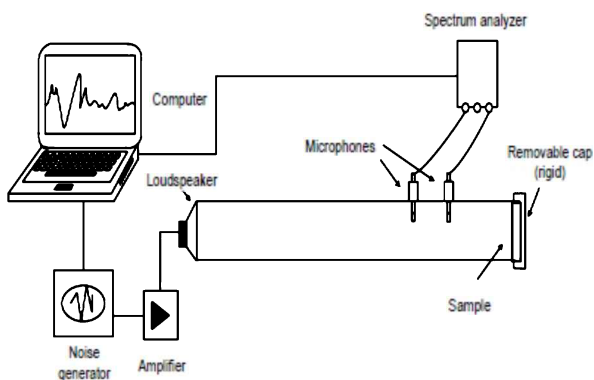


Figure 2 Diagram of the measurement set-ups [5].



Figure 3 Experimental setup and sample specimens.

Table 1 Sound absorption coefficient.

Freq.	Banana stem	Grass	Palm oil leaves	Lemon grass
125	0	0	0	0
250	0.03316	0.03429	0.03075	0.03123
500	0.05282	0.05966	0.04569	0.06323
1000	0.10339	0.14697	0.07852	0.14822
2000	0.42014	0.43586	0.18864	0.45460
4000	0.54971	0.89008	0.95232	0.79980

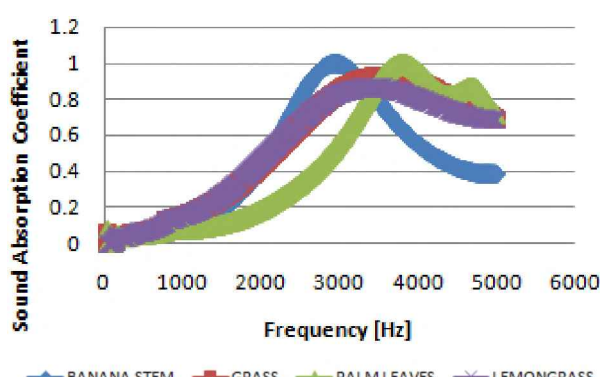


Figure 4 Comparison of sound absorption coefficient of banana stem, grass, palm oil leaves and lemongrass.

All the samples exhibit similar pattern of sound absorption at all frequencies. For all the samples, when the frequency increased, sound absorption coefficient also increased. However, they decreased somewhat at a frequency of 3300 Hz and then increased again. The measured values of the samples show less significant differences on sound absorption coefficient. The sample made of palm leaves shows higher sound absorption coefficients compared to the other materials.

### 4. CONCLUSIONS

Utilizing green materials as an alternative sound absorbing material has been investigated. The result show that the samples made palm oil leaves have high sound absorption coefficients compared with the other samples. By introducing the sound absorber from green material, the resulting materials show a good potential to be an environmentally products. The new green materials have a good future because they are cheaper and environmentally superior compare to synthetic materials.

### REFERENCES

- [1] Panggabean, H., Triono, S., & Sukardi. (2017). Acoustic sound absorption material characteristics of fiber using the king banana stem polyurethane and gypsum as matrix. *International Journal of Engineering Research & Technology*, 6(3), 315-322.
- [2] Asdrubali, F. (2006). Survey on the acoustical properties of new sustainable materials for noise control. *Proceedings of Euronoise, Tampere*, 1-10.
- [3] Jayamani, E., Hamdan, S., & Suid, N. B. (2013). Experimental determination of sound absorption coefficients of four types of Malaysian wood. In *Applied Mechanics and Materials*, 315, 577-581.
- [4] Putra, A., Abdullah, Y., Efendy, H., Farid, W. M., Ayob, M. R., & Py, M. S. (2013). Utilizing sugarcane wasted fibers as a sustainable acoustic absorber. *Procedia Engineering*, 53, 632-638.
- [5] Fouladi, M. H., Nassir, M. H., Ghassem, M., Shamel, M., Peng, S. Y., Wen, S. Y., ... & Nor, M. J. M. (2013). Utilizing Malaysian natural fibers as sound absorber. In *Modeling and Measurement Methods for Acoustic Waves and for Acoustic Microdevices*, 161-170.

## Mobile robotic arm with embedded PID system

Khairuddin Osman<sup>1,2,\*</sup>, Muhammad Irshad Shaffar Saman<sup>1</sup>, Nur Syahirah Eshah Budin Shah<sup>1</sup>, Norzahirah Zainuddin<sup>3</sup>

<sup>1)</sup> Fakulti Kejuruteraan Elektronik dan Komputer, Universiti Teknikal Malaysia Melaka,  
Hang Tuah Jaya, 76100 Durian Tunggal, Melaka, Malaysia

<sup>2)</sup> Centre for Telecommunication Research & Innovation, Universiti Teknikal Malaysia Melaka,  
Hang Tuah Jaya, 76100 Durian Tunggal, Melaka, Malaysia

<sup>3)</sup> Kolej Komuniti Selandar, Jalan Batang Melaka, 77500 Selandar, Melaka, Malaysia

\*Corresponding e-mail: khairuddin.osman@utem.edu.my

**Keywords:** 5-DOF; arduino UNO; PID

**ABSTRACT** – This paper, the mobile robot has a 5-DOF robotic arm to perform the pick and place task. Besides that, the mobile robot has 4 wheels for mobility. The mobile robot is powered up by 2200mAH Li-PO Battery which can last for an hour. Furthermore, it is built with an Arduino UNO and controlled by Android Smartphone with an app called “JoyStick Controller”. Bluetooth is used as a connection between the Arduino and Android Smartphone. The User Interface of the application is designed in a way to allow the user to handle the mobile robot easier. PID controller is used in this project to make the arm movements smooth without barrier and lagging.

### 1. INTRODUCTION

Nowadays, Robots are significantly increase as robots being immersed into our daily tasks, machines are replacing human especially in industrial sector whereas the automation of process has increase the efficiency while decreasing time consume and human energy. As the technologies getting move advance, the improvement of technologies has inspired whole generation of engineer to push the barriers of technology. The main challenge such as to develop a robotic arm to work the way human arm does.

Human are restricted by physical and mentally limitation whereas robot is invisible. They can work repetitively and way more effectively and efficiency compare to human. They replace human to outperform a duty which human unable to do. Robot do not have soul, they are lifeless. They perform what they are programmed to be and they can work 24/7. They can lift heavy weight and can accurately perform the job with less errors. Robots are widely used in many fields of application including office, industrial automation, military task, hospital operations, security system, dangerous environment, and agriculture [1].

Generally, industrial robotic arm widely used for pick and place task where it is programmed to execute the task to be fast and accurate. From SMT machine to automation, it can work independently or cooperate with human force especially in large scale or heavy weight which human unable to handle. This can greatly reduce the risk factor as well as increase the efficiency of work done [2].

Furthermore, robots are deployed especially in hazardous situation as terrorist bomb threat, land mine patrol and nuclear disaster. They often used to deal with hazardous materials to enhance the human safety

especially in hazardous environment such as extremely hot or cold temperature, polluted air, and radioactivity. Human is unable to endure these hazardous environments for a long period [3].

### 2. METHODOLOGY

Flow chart shows the progression of the research from initial till the end. It is act as a guidance to keep in track on the progress. Whenever there is problem arises, Flow Chart is one of the fastest method to troubleshoot problem. Figure 1 shows the general flowchart of the project.

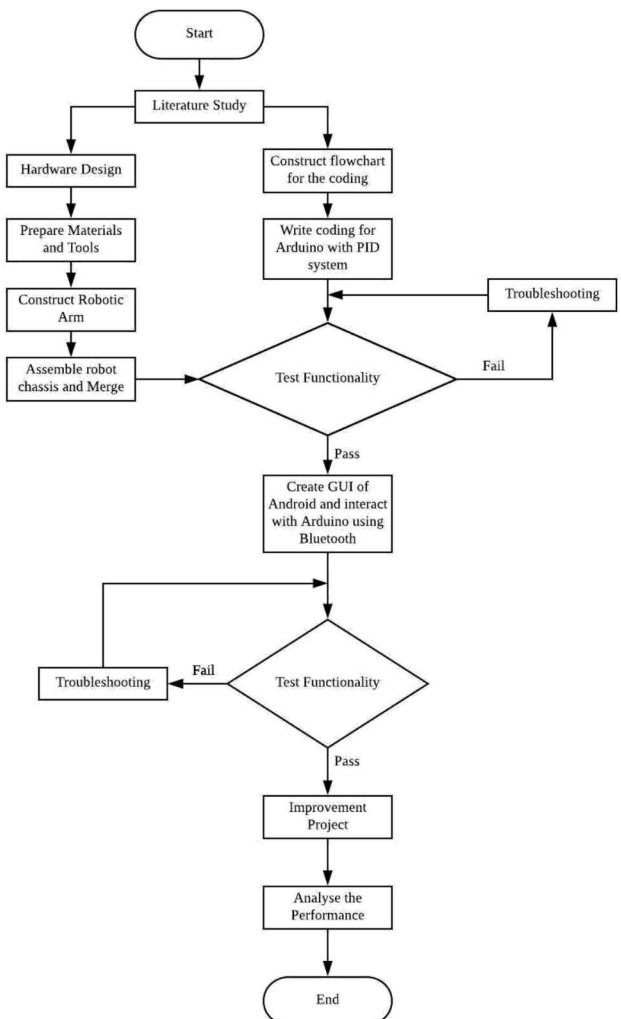


Figure 1 General Flowchart of the project.

Block diagram illustrate the component used in this project. This allows the reader to understand the concept of the project by visualize. In this project, the robot is controlled by android smartphone via Android application, Joystick Controller through Bluetooth Communication. Figure 2 shows the block diagram of the project while the real mobile robot arm with angle for each servo motor is determined based on the Figure 3.

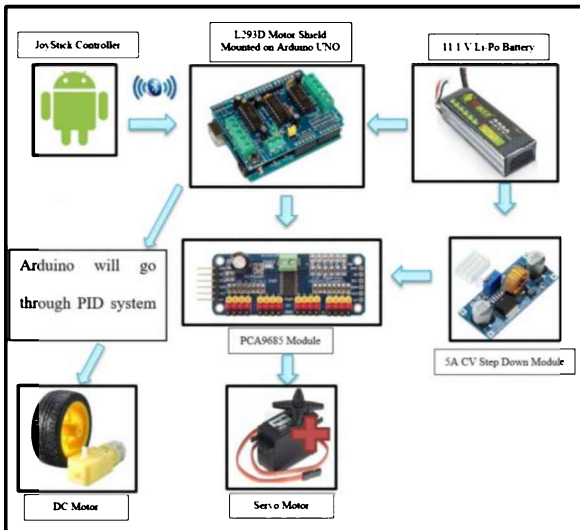


Figure 2 Block diagram of the mobile robot.

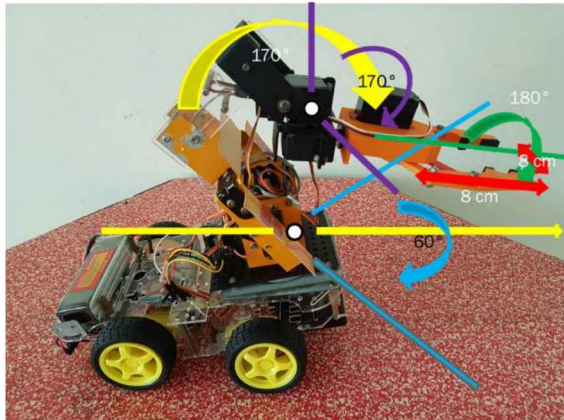


Figure 3 Mobile robot with angle analysis parts.

### 3. RESULTS AND DISCUSSION

Figure 4 show the graph of distance over time for each speed. It clearly shows that speed 5 took the fastest time to reach the 200m whereas speed 0 took the longest time to reach.

Figure 5 show the comparison between step response with and without the PID controller. The graph without PID controller is in blue colors. There are overshoot occurs in this step response. The steady state error and the settling time are also shown in this graph. Without PID controller the steady state error is 0.33 and the rise time are 1.21 second. The graph in red color is indicate to system with PID controller. In this system there are no overshoot occurs because I can eliminate the overshoot by tune the 3 parameters. The steady state errors are equal to 1 and the rise time is 0.107. The system with PID controller are more appropriate to use because the rise time are 0.107 and make the system steady state

error equal to 1. If the rise time decreasing means the input transfer to output are fast. The system with low rise time and steady state error equal to 1 are the stable system. In this project it makes the arm movement with no barrier and lagging.

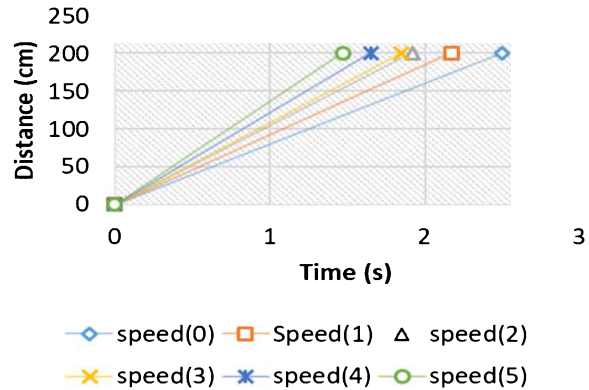


Figure 4 Graph of Distance over Time for each speed.

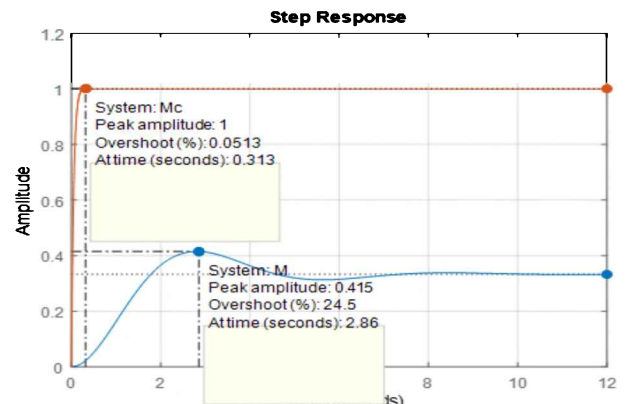


Figure 5 PID controller performance for servo motors.

### 4. CONCLUSION

The mobile robot with robotic arm can pick and place an object from a destination to another. This has fulfilled the objectives. Besides, the mobile robot is controlled using an Android smartphone. It uses the application called JoyStick Controller to control it, with a polished version of User Interface, it will allow the user to be easier to control the mobile robot as well as the robotic arm. The movement of the robotic arm are smooth and stable with help of PID controller.

### ACKNOWLEDGEMENT

The authors would like to thanks Universiti Teknikal Malaysia Melaka (UTeM) under Short Term Research Grant No. PJP/2018/FKEKK(10B)/S01623, Faculty of Electronic and Computer Engineering (FKEKK) and Centre for Telecommunication Research and Innovation (CeTRI) for their support.

### REFERENCES

- [1] Faravar, A. (2014). *Design, implementation and control of a robotic arm using PIC 16F877A microcontroller* (Doctoral dissertation, Eastern Mediterranean University (EMU)-Doğu Akdeniz Üniversitesi (DAÜ)).
- [2] Shah, M. S., & Borole, P. B. (2016, April). Surveillance and rescue robot using Android

- smartphone and the Internet. In *2016 International Conference on Communication and Signal Processing (ICCSP)* (pp. 1526-1530).
- [3] Kit, W. S., & Venkatratnam, C. (2016, September). Pick and place mobile robot for the disabled through voice commands. In *2016 2nd IEEE International Symposium on Robotics and Manufacturing Automation (ROMA)* (pp. 1-4).

# Motion characteristics of a tubular linear switched reluctance actuator (T-LSRA) using phase-to-phase switching algorithm

Chin Kiat Yeo<sup>1</sup>, Mariam Md Ghazaly<sup>1,\*</sup>, Siau Ping Tee<sup>1</sup>, Fawwaz Nadzmy<sup>1</sup>, Shin Horng Chong<sup>1</sup>, Zulkeflee Abdullah<sup>2</sup>

<sup>1)</sup> Center for Robotics and Industrial Automation (CeRIA), Fakulti Kejuruteraan Elektrik,  
Universiti Teknikal Malaysia Melaka, Hang Tuah Jaya, 76100 Durian Tunggal, Melaka, Malaysia.

<sup>2)</sup> Fakulti Kejuruteraan Pembuatan, Universiti Teknikal Malaysia Melaka,  
Hang Tuah Jaya, 76100 Durian Tunggal, Melaka, Malaysia

\*Corresponding e-mail: mariam@utem.edu.my

**Keywords:** Tubular linear switched reluctance actuator; motion characterization; phase-to-phase switching algorithm

**ABSTRACT** – This paper discussed the motion characteristics of a Tubular Linear Switched Reluctance Actuator (T-LSRA) using phase-to-phase switching algorithm. This paper validates the motion characteristics for both forward and reverse motion. In order to achieve a smooth and fast reciprocating motion, the suitable phase-to-phase switching algorithm corresponding to the mover position was investigated. The mover response time was obtained by reciprocating the mover between 0 mm and 25 mm at maximum rated phase current of 2 A. The tubular LSRA has an overshoot of 33.3 % and requires approximately 0.18 s for the mover to reach the equilibrium position at 5.071 mm.

## 1. INTRODUCTION

Linear switched reluctance actuator (LSRA) is a fresh type of actuator that has great advantages due to its low cost and simple design construction. However, the key concerns of a SRA are the unwarranted force ripples, vibration and acoustic noise compared to the conventional actuator [1,2]. Hence, the control strategy of the actuator is crucial in order to overcome the drawbacks. Based on studies, several types of controllers have been proposed and applied to switched reluctance actuator (SRA) mechanism; i.e: modified PID control, intelligent control, linearization control and two degrees of freedom control. The PID controller is commonly used in speed and position control applications due to its simplicity, easy tuning and robustness. However, the applied of the conventional PID controller will reduce the positioning performances due to the highly nonlinear characteristics of the SRA. Thus, in order to implement the knowledge of linear controller to a nonlinear system, this system requires to undergo linearization control [3–5]. Hence, Maslan et al. and Ghazaly et al. proposed a new controller to overcome these drawbacks with respect to the precision control by introducing the linearizer unit without any added mechanism [4,5]. Based on the controllers developed by Maslan et al. [4], the proposed PID controller with linearizer unit eliminates the residual vibration caused by applying a linear controller on the LSRA whereby the actuator's characteristic is nonlinear in nature. Subsequently, the maximum steady-state error is approximately four times lower compared to the conventional PID controller. In this research, the phase-to-phase switching algorithm based on Maslan et al. on

linear type planar single-sided SRA was implemented in order to evaluate the motion characteristics of the Tubular Linear Switched Reluctance Actuator (T-LSRA) prototype.

## 2. METHODOLOGY

In this research, the T-LSRA prototype was developed in order to validate the motion characteristics of a T-LSRA by using the phase-to-phase switching algorithm. The linear motion is measured using a linear incremental encoder (RGH24W30D33A, Renishaw) via Micro-box with the interface of MATLAB Simulink Software. Figure 1 shows the full experimental setup in which the assembled T-LSRA prototype. Two polytetrafluoroethylene (PTFE) coated linear bushings are accurately aligned and fitted on both the mover's ends in the direction of motion. This is to ensure the air gap is uniform throughout the actuator and allow low friction sliding surface. Three high current amplifiers (one PBZ60-6.7, Kikusui Electronic Corporation and two TS250-0, Accel Instruments) were used throughout the experimental validation.

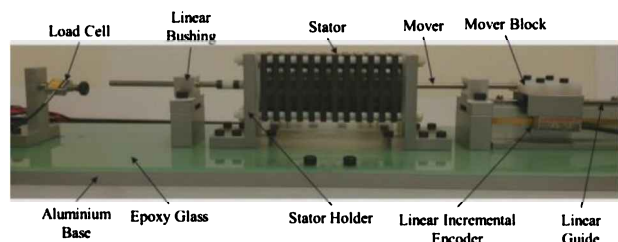


Figure 1 T-LSRA prototype.

In order to achieve smooth and fast reciprocating motion, the suitable phase-to-phase switching algorithm which corresponded to the mover position was investigated. In this paper, forward motion is referred as the mover moves to the left direction and reverse motion is referred as the mover moves to the right direction. The magnetic circuit (magnetic flux) for Phase A at the initial mover position is depicted in Figure 2. When the coils on Phase A are applied with excitation current, magnetic flux is generated and flows from the stator poles with active phase coils to the mover poles and flows back to the stator poles to form a complete cycle of the magnetic circuit. The forward motion and reverse motion sequences in the first pitch for the T-LSRA are shown in Table 1 which was

determined from the open-loop characterization based on the fully aligned mover-to-stator position.

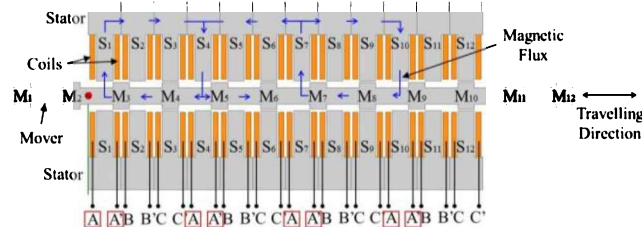


Figure 2 Magnetic circuit for Phase A at initial position.

Table 1 Forward motion sequence in the first pitch.

Position (mm)	Phase	Stator	Mover
0 – 5	AA'	S <sub>1</sub> -S <sub>4</sub> -S <sub>7</sub> -S <sub>10</sub>	M <sub>3</sub> -M <sub>5</sub> -M <sub>7</sub> -M <sub>9</sub>
5 – 10	BB'	S <sub>2</sub> -S <sub>5</sub> -S <sub>8</sub> -S <sub>11</sub>	M <sub>4</sub> -M <sub>6</sub> -M <sub>8</sub> -M <sub>10</sub>
10 – 15	CC'	S <sub>3</sub> -S <sub>6</sub> -S <sub>9</sub> -S <sub>12</sub>	M <sub>5</sub> -M <sub>7</sub> -M <sub>9</sub> -M <sub>11</sub>

### 3. RESULTS AND DISCUSSION

The motion characteristics of the T-LSRA was examined through driving characteristics via open-loop experiments. Figure 3 illustrates the block diagram of the open-loop control for the T-LSRA. The open-loop motion characteristic of the mover is evaluated by applying a constant current from 0.9 A to 2 A with 0.1 A increments for 4 s. The excitation phase is depending on the mover position as validated in Table 1.

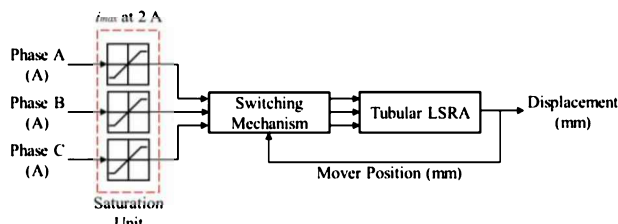


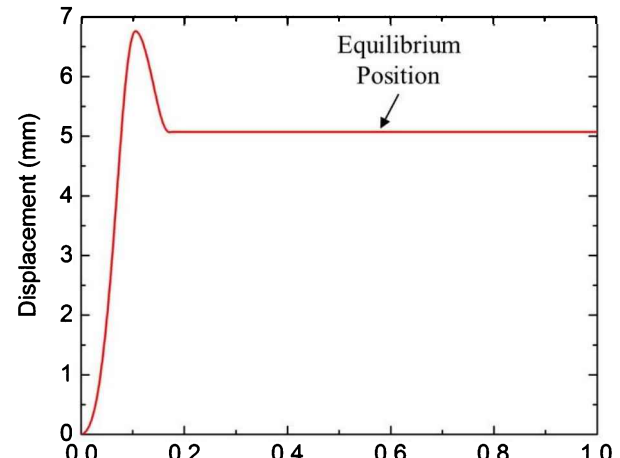
Figure 3 Block diagram of open-loop control for reciprocating motion.

Figure 4(a) depicts the open-loop control of the T-LSRA for one step forward motion at maximum rated phase current of 2 A. Based on the result, the T-LSRA has an overshoot of 33.3 % and requires approximately 0.18 s for the mover to reach the equilibrium position at 5.071 mm instead of 5 mm due to insufficient of energy when the stator and mover poles reach the equilibrium position. To further validate the effectiveness of the phase-to-phase switching algorithm, the open loop control performances for continuous six steps forward and reverse motion at maximum rated phase current of 2 A was evaluated as shown in Figure 4(b).

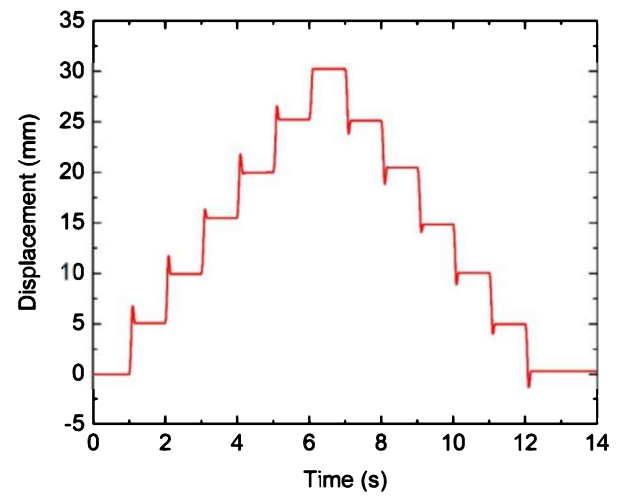
### 4. CONCLUSION

In conclusion, the motion characteristics of a T-LSRA using phase-to-phase switching algorithm was successfully verified. The functionality of the developed T-LSRA has been experimentally validated. The T-LSRA motion performances show an overshoot of 33.3 % and require approximately 0.18s for the mover to reach the equilibrium position at 5.071 mm. Through

the open-loop reciprocating motion, dynamic responses of the T-LSRA were obtained. The maximum velocity and maximum acceleration that the T-LSRA capable to achieve is approximately 210 mm/s and 8 m/s<sup>2</sup> respectively. Future works include improving T-LSRA control performances toward precision motion.



(a)



(b)

Figure 4 T-LSRA motion characterization. (a) Open-loop control for one step response and (b) open-loop control for continuous six steps forward motion and reverse motion.

### ACKNOWLEDGEMENT

The authors wish to express their gratitude to Motion Control Research Laboratory (MCon Lab), Center for Robotics and Industrial Automation (CeRIA) and Universiti Teknikal Malaysia Melaka (UTeM) for supporting the research and publication. This research is supported by Universiti Teknikal Malaysia Melaka grant no. JURNAL/2018/FKE/Q00006, Center for Robotics and Industrial Automation (CeRIA) and Center for Research and Innovation Management (CRIM).

**REFERENCES**

- [1] Pestana, L. M., Calado, M. R., & Mariano, S. (2016). Experimental force characterization of linear switched reluctance machine. *IEEE 16th International Conference on Environment and Electrical Engineering (EEEIC 2016)*. 2016, 1-4.
- [2] Yeo, C. K., Ghazaly, M. M., Chong, S. H. & Jamaludin, I. W. (2018). Design optimization of a three phase tubular linear switched reluctance actuator. *ARPN Journal of Engineering and Applied Sciences*, 13(5), 1600–1607.
- [3] Gao, X., Wang, X., Li, Z., & Zhou, Y. (2015). A review of torque ripple control strategies of switched reluctance motor. *International Journal of Control Automation*, 8(4), 103-116.
- [4] Maslan, M. N., Kokumai, H., & Sato, K. (2017). Development and precise positioning control of a thin and compact linear switched reluctance motor. *Precision Engineering*, 48, 1-14.
- [5] Ghazaly, M. M., & Sato K. (2012). Basic characteristics of a multilayer thin electrostatic actuator supported by lubricating oil for a fine-motion stage. *Precision Engineering*, 36(1), 77-83.

# Positioning control performance of a rotary switched reluctance actuator (SRA) using modified PID control scheme

Siau Ping Tee<sup>1</sup>, Mariam Md Ghazaly<sup>1,\*</sup>, Chin Kiat Yeo<sup>1</sup>, Fawwaz Nadzmy<sup>1</sup>, Shin Horng Chong<sup>1</sup>, Zulkeflee Abdullah<sup>2</sup>

<sup>1)</sup> Center for Robotics and Industrial Automation (CeRIA), Fakulti Kejuruteraan Elektrik,  
Universiti Teknikal Malaysia Melaka, Hang Tuah Jaya, 76100 Durian Tunggal, Melaka, Malaysia.

<sup>2)</sup> Fakulti Kejuruteraan Pembuatan, Universiti Teknikal Malaysia Melaka,  
Hang Tuah Jaya, 76100 Durian Tunggal, Melaka, Malaysia

\*Corresponding e-mail: mariam@utem.edu.my

Keywords: Rotary switched reluctance actuator; positioning control; modified PID controller

**ABSTRACT** – This research discusses on the positioning control performance of a rotary switched reluctance actuator (SRA). In this research, the positioning control of the rotary SRA is achieved by implementing the modified PID control scheme. The procedures to construct the linearizer unit is the key elements in the modified PID control scheme. This paper emphasizes on the positioning control performances between the modified PID with the conventional PID. The findings showed that modified PID controller with linearizer unit demonstrated an improved performance, i.e.: at position 74.5°, error is completely eliminated, overshoot and settling time is improved by 81.4% and 76.2%, respectively.

## 1. INTRODUCTION

A switched reluctance actuator (SRA) is a type of electromagnetic stepper actuator that is gaining approval for its simple and robust design and its ability of exceeding high-speed operation [1-3]. SRA has gained control over permanent magnet actuators due to the fact that its material construction is relatively low cost compared to the expensive and rare permanent magnets. It is well known that the SRA is a highly non-linear characteristic actuator, thus it is particularly difficult to control its position. At present, there are several control methods proposed and established for motion control of linear SRA [2]. However, for rotary SRA they are fairly limited and are mostly involved in model-based control which are highly dependent on the system's modelling [3]. As an option for a much simpler controller, conventional PID controller is a decent option [4]. However, the PID controller is not designed to control a non-linear system. Therefore, this paper discussed the implementation of a modified PID controller for evaluating the positioning performance of an SRA, where the modified PID controller is an improved version of the conventional PID controller.

## 2. METHODOLOGY

To evaluate the positioning control performance of a rotary switched reluctance actuator (SRA) using modified PID control scheme, several experimental works are evaluated using the prototype shown in Figure 1. Figure 2 shows the block diagram of modified PID controller. The system consists of PID controller, Linearizer unit, and an anti-windup unit. The switching mechanism plays an important role which decides the

correct activation of the SRA excitation phase current (Phase A, B and C). Different phases are activated when specified conditions are fulfilled based on the rotor current position. The anti-windup was implemented to avoid the saturation of PID signal due to the integral term.

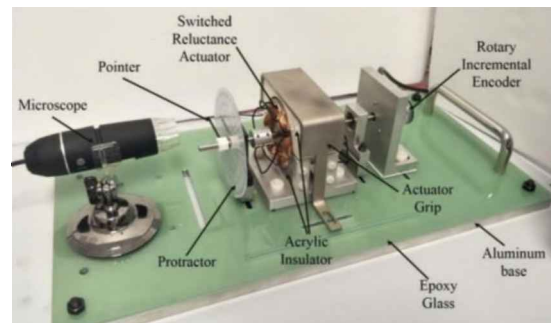


Figure 1 Rotary SRA prototype.

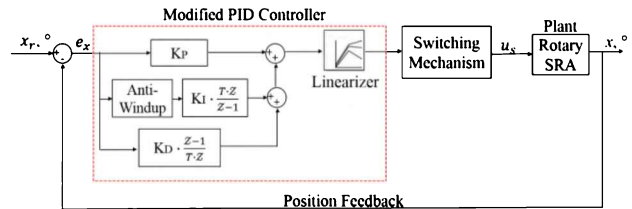


Figure 2 Block diagram of modified PID controller.

Since SRA has a highly non-linear characteristic, thus the presence of the linearizer unit is to compensates for the non-linear current-displacement relationship of SRA system. Figure 3 shows the current-displacement relationship used to construct the linearizer unit for Phase A. Each phase has its own Linearizer unit. Using a customized waveform which consist of combination of positive and negative step signal shown in Figure 4, the residue magnetic flux in rotary SRA can be discharged.

## 3. RESULTS AND DISCUSSION

To evaluate the effectiveness of the modified PID controller, the SRA is evaluated at reference position 74.5°. The specific positions are tested which includes decimal specific positions to assess the robust performance of the controllers. The controller parameters for both conventional PID controller and modified PID controller is shown in Table 1. Figure 5 shows the point-to-point positioning performances of

the SRA using modified PID controller and the conventional PID controller. The conventional PID controller is validated as a comparative comparison. It can be depicted that the PID controller showed difficulties in achieving positions that are close to the fully aligned position at  $74.5^\circ$ . From Table 2, the modified PID controller displayed an excellent performance in compared to PID controller where the positioning error is 100% eliminated, overshoot and settling time is improved by 81.4% and 76.2%, respectively.

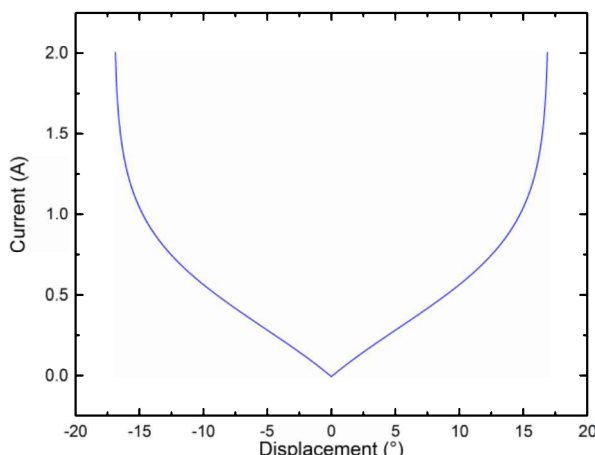


Figure 3 Current-displacement relationship to construct linearizer block for Phase A.

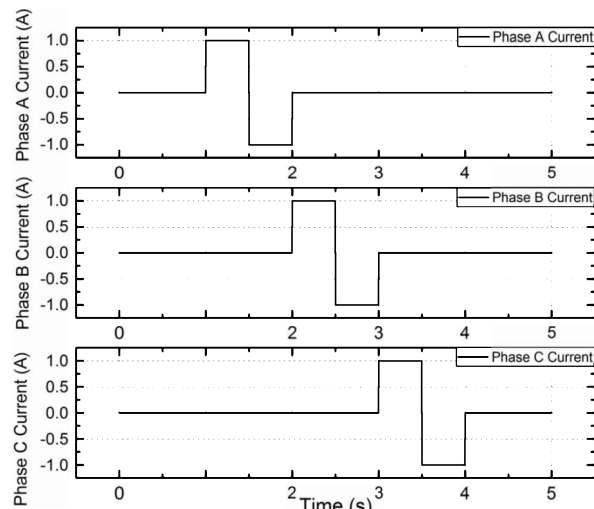


Figure 4 Customized waveforms for discharge of magnetic flux in SRA.

Table 1 Controller parameters for conventional PID and modified PID controllers.

Modified PID	Conventional PID
$K_P$ ( $^\circ$ )	2.02
$K_I$ ( $^\circ s^{-1}$ )	22
$K_D$ ( $s^{-1}$ )	0.07
	0.3
	3.28
	0.01

#### 4. CONCLUSION

In conclusion, the positioning control performance of a rotary switched reluctance actuator (SRA) using modified PID control scheme is validated. It shows that the linearizer unit and anti-windup elements are able to greatly improve the positioning performance of the rotary SRA. Future works includes the improvement of the linearizer unit using high resolution encoder and the inclusion of system's frictional force for micro-positioning and trajectory tracking.

Table 1 Transient parameters for modified PID and PID controller at reference position  $74.5^\circ$ .

Parameters	Modified PID	PID	Improvement (%)
Steady-state Error ( $^\circ$ )	0.00	$7.90 \times 10^{-1}$	100.0
Overshoot (%)	3.56	$1.91 \times 10^1$	81.4
Settling Time (s)	$1.73 \times 10^{-1}$	$7.24 \times 10^{-1}$	76.2

#### ACKNOWLEDGEMENT

The authors wish to express their gratitude to Motion Control Research Laboratory (MCon Lab), Center for Robotics and Industrial Automation (CeRIA) and Universiti Teknikal Malaysia Melaka (UTeM) for supporting the research and publication. This research is supported by Universiti Teknikal Malaysia Melaka grant no. JURNAL/2018/FKE/Q00006, Center for Robotics and Industrial Automation (CeRIA) and Center for Research and Innovation Management (CRIM).

#### REFERENCES

- [1] Yusri, I., Ghazaly, M. M., Alandoli, E. A. A., Rahmat, M. F., Abdullah, Z., Ali, M. A. M. & Ranom, R. (2016). Force optimization of the permanent magnet switching flux (PMSF) and switching reluctance (SR) actuators using finite element analysis. *Proceedings of Mechanical Engineering Research Day 2016*, 2016, 1-2.
- [2] Wang, S. Y., Liu, F. Y. & Chou, J. H. (2016). Design on sliding mode controller with adaptive fuzzy compensation for switched reluctance motor drive systems. *2016 International Symposium on Computer, Consumer and Control, Xi'an, China*, 2016, 239-242.
- [3] Kojima, T. & De Doncker, R. W. (2015). Optimal torque sharing in direct instantaneous torque control of switched reluctance motors. *IEEE Energy Conversion Congress and Exposition, Montreal, Canada*, 2015, 327-333.
- [4] Veena, N. D. & Raghuram, N. L. (2017). Minimization of torque ripple using ditc with optimum bandwidth and switching frequency for srm employed in electric vehicle. *International Conference on Smart Grids, Power and Advanced Control Engineering, Bangalore, India*, 2017, 143-148.

# Dynamic compression properties of E-glass/basalt and E-glass/flax using SHPB

Muhamad Shahirul Mat Jusoh<sup>1,\*</sup>, Mohd Yazid Yahya<sup>2</sup>, Haris Ahmad Israr Ahmad<sup>2</sup>

<sup>1)</sup> Department of Polymer Composite Processing Engineering Technology, Kolej Kemahiran Tinggi MARA Masjid Tanah, Persiaran Paya Lebar, Ramuan China Besar, 78300 Masjid Tanah, Melaka, Malaysia

<sup>2)</sup> School of Mechanical Engineering, Universiti Teknologi Malaysia, 81310, Skudai, Johor, Malaysia

\*Corresponding e-mail: shahirul.jusoh@mara.gov.my

**Keywords:** SHPB; hybrid; composite

**ABSTRACT** – Investigation on the dynamic compression properties of natural fibres hybrid composites is less reported especially using split Hopkinson pressure bar (SHPB) due to the availability of dynamic testing apparatus. The split Hopkinson pressure bar (SHPB) was utilized in this present study to characterize the dynamic mechanical properties of hybrid composite between E-glass with basalt and flax fibres at the strain rates of 850 to 2350 s<sup>-1</sup>. Result shows that the tested specimens significantly influenced by the value of strain rates applied. The hybrid composites of E-glass/basalt (E/B<sub>asalt</sub>) and E-glass/flax (E/F<sub>lax</sub>) exhibited the strain-rate dependent, whereby the higher of dynamic compression properties were recorded when the higher strain rates were imposed. Both hybrid specimens exhibited the similar trend.

## 1. INTRODUCTION

The strain-rate effect is widely recognised as a crucial factor influencing the mechanical properties of material [1]. The hybrid composite of hemp/glass was characterized using SHPB with its dynamic compression properties was recorded between the glass and hemp laminates [4]. Natural fibres of pultruded jute and kenaf reinforced composites were investigated experimentally using SHPB at different strain rates of 1021, 1150, and 1340 s<sup>-1</sup>. The higher of dynamic compression properties were recorded when the tested specimen was imposed at 1340 s<sup>-1</sup> rather than 1021 s<sup>-1</sup> [2]. Previous study revealed that the strain rate effects of the composite materials are highly correlated with materials hardening factors as tested on the hybrid composite of carbon/glass. Three different strain rates of 200, 600, and 1000 s<sup>-1</sup> were imposed and found significantly influenced on the properties of the material being investigated. In addition, there are few contributed factors involved such as types of materials used, manufacturing process, surficial adhesion between fibre and matrix, fibre architecture and loading direction [3]. The SHPB test was applied on the rice husk/linear low-density PE with the strain rates of 650, 900, and 1100 s<sup>-1</sup>. The higher of dynamic compression strength and modulus were recorded with the increasing strain rates [5]. The objectives of the present work are to investigate the influence of the different high strain rates on the stress-strain curves of E/B<sub>asalt</sub> and E/F<sub>lax</sub> using SHPB.

## 2. METHODOLOGY

The hybrid composites of E/B<sub>asalt</sub> and E/F<sub>lax</sub> were fabricated using vacuum infusion process. Dynamic compression test was conducted using SHPB at the strain rates between 850 to 2350 s<sup>-1</sup>. Figure 1 shows the schematic diagram of SHPB equipment which consists of gun barrel, striker bar, incident bar and transmitter bar. All the bars should maintain their elasticity throughout the test.

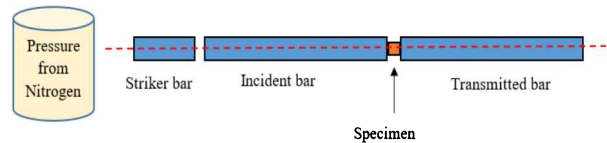


Figure 1 SHPB setup.

During the test, generated pressure from nitrogen tank will accelerate the striker bar, then collide with the incident bar. As a result of collision, the compression wave was generated and travelled down along the incident bar and known as incident wave ( $\varepsilon_i$ ). Meanwhile, at the specimen interface, the wave was partially transmitted into the specimen and referred as transmitted wave ( $\varepsilon_t$ ). The remaining wave was reflected and known as reflected wave ( $\varepsilon_r$ ) due to the impedance mismatch between the incident bar and the specimen.

## 3. RESULTS AND DISCUSSION

As shown in Figure 2 and 3, the stress-strain curves of E/B<sub>asalt</sub> and E/F<sub>lax</sub> composites had been dominated by the strain rates effect. The higher the strain rates imposed, the higher the maximum stress exhibited by the tested specimens. The E/B<sub>asalt</sub> and E/F<sub>lax</sub> composites recorded the maximum compressive stress of 387, 328, 300 and 283, 247, 214 MPa at the strain rates of 2350, 1300, and 850 s<sup>-1</sup>, respectively. Similar findings were also reported by the previous literatures [2], [5]–[8] and the increment is attributed by the strengthening effect of the material towards the strain rate applied as suggested by Omar et al. [7]. Conversely, the dynamic failure strain decreases with the increasing strain rates for both tested hybrid composites due the rapid crack propagation and fibre's failure occurred within a very short time which caused the total failure of the specimens, as stipulated in previous literatures [1].

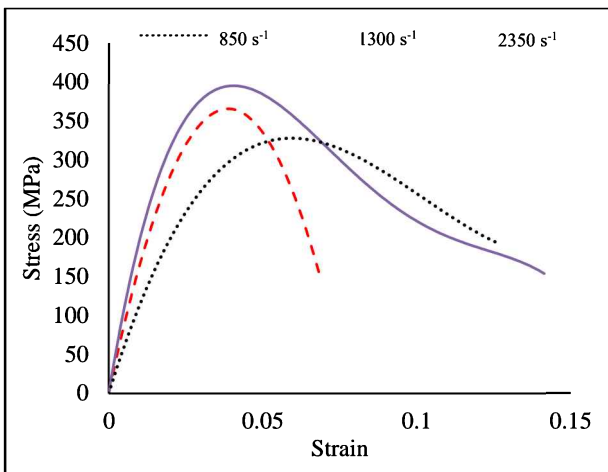
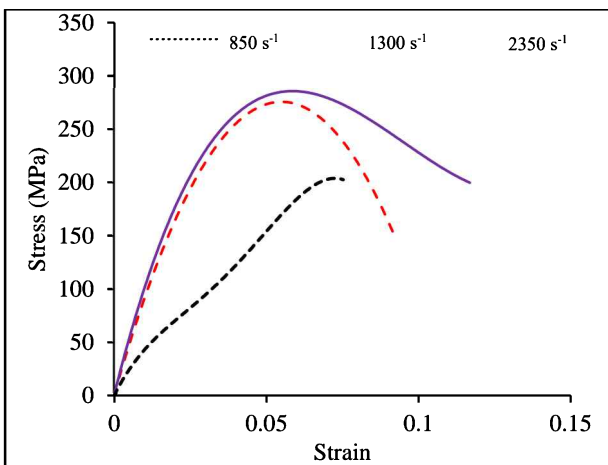
Figure 2 Stress-strain curves of E/B<sub>asalt</sub>.

Figure 3 Stress-strain curves of E/Flax.

#### 4. CONCLUSION

This study explored the high strain rates effect on the dynamic compression properties of E/B<sub>asalt</sub> and E/Flax at the strain rates of 850, 1300, and 2350 s<sup>-1</sup>. It was found that the dynamic properties were dependent on the applied strain rates with the E/B<sub>asalt</sub> dominated on the maximum compressive stress compared to E/Flax. However, the dynamic strain recorded the contrary pattern with increasing strain-rates with E/Flax recorded the lower strain than E/B<sub>asalt</sub>. It can be concluded that the effect of hybridisation significantly affected on the dynamic compression properties as revealed between E/B<sub>asalt</sub> and E/Flax.

#### ACKNOWLEDGEMENT

Authors would like to thank to Kolej Kemahiran Tinggi MARA (KKTm) Masjid Tanah, Melaka for providing research fund to support this study and has made this work possible.

#### REFERENCES

- [1] Song, Z., Wang, Z., Ma, H., & Xuan, H. (2014). Mechanical behavior and failure mode of woven carbon/epoxy laminate composites under dynamic compressive loading. *Composites Part B: Engineering*, 60, 531-536.
- [2] Omar, M. F., Akil, H. M., Ahmad, Z. A., Mazuki, A. A. M., & Yokoyama, T. (2010). Dynamic properties of pultruded natural fibre reinforced composites using split Hopkinson pressure bar technique. *Materials & Design*, 31(9), 4209-4218.
- [3] Zhu, P., Lu, J., Ji, Q., & Cheng, Z. (2016). Experimental study of in-plane mechanical performance of carbon/glass hybrid woven composite at different strain rates. *International Journal of Crashworthiness*, 21(6), 542-554.
- [4] Kim, W., Argento, A., Lee, E., Flanigan, C., Houston, D., Harris, A., & Mielewski, D. F. (2012). High strain-rate behavior of natural fiber-reinforced polymer composites. *Journal of Composite Materials*, 46(9), 1051-1065.
- [5] Wahab, A., Suhaili, N., Omar, M. F., Md Akil, H., Ahmad, Z. A., & Noimam, N. Z. (2016). Effect of surface modification on rice husk (Rh)/linear low density polyethylene (LLDPE) composites under various loading rates. *Materials Science Forum*, 840, 3-7.
- [6] Akil, H. M., Ahmad, Z. A., Omar, M. F., Lin, O. H., & Hui, D. (2010). Measurement on the dynamic properties of nanosilica/polypropylene composite using split Hopkinson pressure bar technique, *University of New Orleans*. 1-3.
- [7] Omar, M. F., Akil, H. M., & Ahmad, Z. A. (2011). Measurement and prediction of compressive properties of polymers at high strain rate loading. *Materials & Design*, 32(8-9), 4207-4215.
- [8] Suharty, N. S., Ismail, H., Diharjo, K., Handayani, D. S., & Firdaus, M. (2016). Effect of kenaf fiber as a reinforcement on the tensile, flexural strength and impact toughness properties of recycled polypropylene/halloysite composites. *Procedia Chemistry*, 19, 253-258.

# Multiple linear regression application for generating entropy characteristics of magnesium alloy

M.A. Fauthan<sup>1,\*</sup>, S. Abdullah<sup>1</sup>, M.F. Abdullah<sup>2</sup>, I.F. Mohamed<sup>1</sup>

<sup>1)</sup> Centre for Integrated Design for Advanced Mechanical Systems (PRISMA), Faculty of Engineering & Built Environment, Universiti Kebangsaan Malaysia, 43600 UKM Bangi, Selangor, Malaysia

<sup>2)</sup> Department of Mechanical Engineering, Faculty of Engineering,

Universiti Pertahanan Nasional Malaysia, Kem Sg. Besi 57000 Kuala Lumpur, Malaysia

\*Corresponding e-mail: p85968@siswa.ukm.edu.my

**Keywords:** Magnesium alloy; entropy; multiple linear regression

**ABSTRACT** – This paper focused on the development of a multiple linear regression approach based on the stress ratio and applied load. This relationship was developed for the purpose of predicting a complete entropy generation by means of a statistical approach, whereby a constant amplitude loading was applied to evaluate the fatigue life. By conducting compact tension tests, different stress ratios of 0.1, 0.4 and 0.7 were applied to the specimen. During the tests, the change in temperature was also observed. The assumptions of the models were considered through a graphical residual analysis. As a result, the predicted regression model based on the applied load and stress ratio was found to be in agreement with the results of the experiment.

## 1. INTRODUCTION

The selection of magnesium alloy for applications in, for example, the aerospace, automotive and electronic industries, is becoming more important as this material offers admirable features such as high stiffness, light weight, high specific strength, and good heat conductivity. Since magnesium alloy is a relatively new material compared to mild structural steel and aluminium, further investigations are needed to ensure its safe application. A major problem with structural systems is fatigue failure since there is no significant indication that failure is about to occur. This is because failure can occur even with a low load if it is applied repeatedly. Therefore, crack propagation plays a key role in determining the life span of a component.

Fatigue is probabilistic in nature and involves, at the same time, a multimode process. In a conventional test, many unknown input parameters are required. Therefore, the dissipation of energy is introduced to predict the life span of a material [1]. Furthermore, this relationship can also be described through the introduction of multiple linear regression (MLR). MLR is used to predict the value of a variable based on the values of two or more other variables [2]. Mayan et al. suggested multiple linear regression in order to evaluate the number of cycles, stress amplitude and crack length of aluminium alloy [3]. If the total generation of entropy can be approached through regression, then fatigue life can be predicted. Hence, this paper was aimed at describing the MLR relationship in order to predict the total entropy generation of magnesium alloy, AZ31B.

## 2. MATERIAL AND EXPERIMENTAL PROCEDURE

This study utilised the commercial AZ31B magnesium alloy. The mechanical properties of the AZ31B is listed in Table 1.

Table 1 Mechanical properties of AZ31B [1].

Properties	Yield strength, $\sigma_s$ (MPa)	Ultimate strength, $\sigma_{UTS}$ (MPa)	Young's modulus, E (GPa)
AZ31B	144	238	40.66

To study the fatigue crack growth (FCG), compact tension (CT) test specimens were prepared according to the recommendations of E647-95. Before the fatigue tests, the surface of the specimens facing the thermal sensor was coated with a layer of black paint to improve the thermal emissivity and to reduce the error rate.

All the specimens were tested using a constant amplitude sinusoidal loading of 2600 N and 2800 N, and stress ratios (ratio of minimum to maximum load) of  $R = 0.1, 0.4$  and  $0.7$ , respectively at a constant frequency of 10 Hz. During the test, the temperature trend of the specimens was detected with an infrared sensor that had been set up.

The total entropy generation was obtained from the beginning of the FCG test until the occurrence of fracture, and it was calculated as shown below:

$$\dot{\gamma} = \frac{W_p}{T} \quad (1)$$

Where  $\dot{\gamma}$  is the entropy generation rate,  $W_p$  is cyclic plastic energy per unit volume and  $T$  is surface temperature.

Multiple regression analysis is statistical method used for predicting the unknown value of a variable from the known value of two or more variable [2]. The general multiple regression model with  $n$  observations is defined as:

$$y_1 = \alpha + \beta_1 x_{i,1} + \beta_2 x_{i,2} + \dots + \beta_n x_{i,n} + \varepsilon_i \quad (2)$$

Where  $y$  is a variable,  $x$  is the independent variable, and  $\beta$  is the unknown regression coefficient.

### 3. RESULTS AND DISCUSSION

For the load of 2600 N, just after the cycles reached  $4.34 \times 10^3$  for a stress ratio of 0.1, the crack began to grow, followed by  $3.73 \times 10^3$  and  $2.28 \times 10^3$  cycles for stress ratios of 0.4 and 0.7, respectively. As shown in Figure 1, the final crack cycle was lower when a higher stress ratio was applied. This also affected the fatigue crack growth rate, causing it to increase as the mean stress value changed. This trend was followed by the load of 2800 N, when stress ratios of 0.1, 0.4 and 0.7 were applied to the specimen.

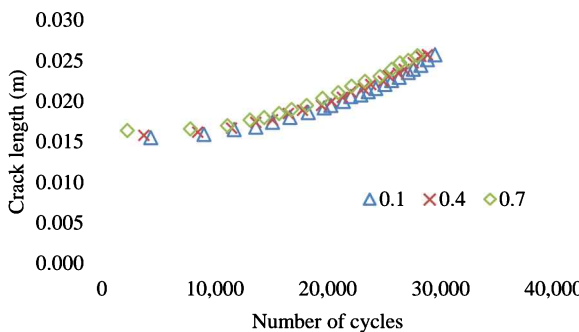


Figure 1 Crack length reading for 2600N at stress ratio of 0.1, 0.4 and 0.7.

At the start of the test, no entropy was generated. As the crack growth increased, the total entropy was calculated until the specimen fractured completely. The total entropy generation when a load of 2600 N was applied was 3.424, 3.101 and 2.922  $\text{MJm}^{-3} \text{K}^{-1}$  for stress ratios of 0.1, 0.4 and 0.7, respectively. According to Figure 2, the total entropy generation increased as a higher stress ratio was applied. This was due to the distribution of a higher energy per unit volume, which led to failure. It showed that with a higher entropy generation, the specimen should have a lower fatigue life.

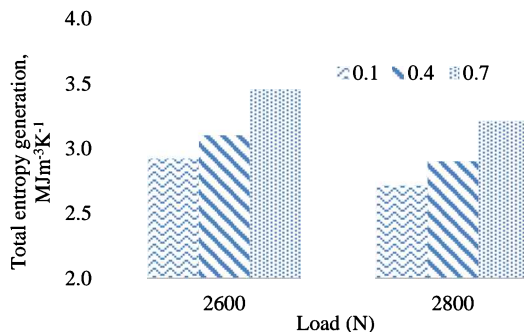


Figure 2 Total entropy generation with different loads and stress ratios.

Next, the assumptions of the MLR model were assessed. The four different conditions that need to be evaluated for multiple regression to give a valid result are the linear function, independent function, normal distribution and equal variance. The results are shown in Figure 3. The versus fits plot shows that the average of the residuals remained approximately 0, the variation of the residuals appeared to be roughly constant, and there were no excessively outlying points. There was little in the histogram of the residuals to suggest a violation of the normality assumption.

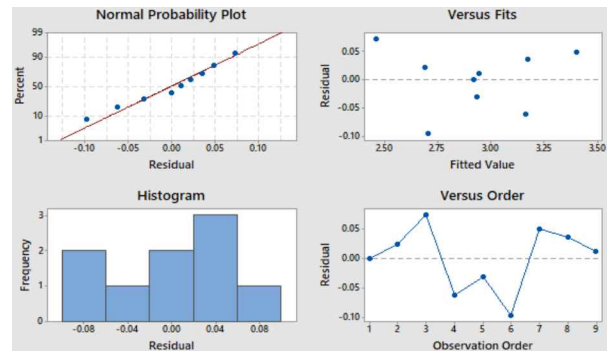


Figure 3 Observation of multiple regression to evaluate data from experiment for MLR model.

The datasets comprising the entropy generation values of the CT specimens, stress ratio ( $R$ ), and load applied ( $N$ ), as shown in Eqn. 3, were used to establish the MLR-based entropy models. The MLR-based entropy generation model was obtained as:

$$\gamma = 5.827 - 0.001148 N + 0.8044R \quad (3)$$

Table 2 The percentage of difference entropy generation with respect to the experimental data.

Stress ratio	Experimental entropy	Predicted entropy	% of differences
0.1	2.536	2.608	2.83%
0.4	2.607	2.849	9.29%
0.7	2.956	3.090	4.55%

Once the assumption on MLR-based entropy model had been clarified to be acceptable, the models were compared to the experimental values done with another new load, 3000 N. Table 2 shows the percent of difference between the experimental and predicted data for new load conditions. The difference is less than 10%, and this indicates that the calculated entropy generation well predicts the experimental data under new load conditions. This explains most of the experimental entropy generation were near to similar predicted values.

### 4. CONCLUSION

Entropy generation was deployed as an effective way of measuring the crack growth behaviour of a material with changes in the temperature during the fatigue process. An approach to develop an MLR relationship between the entropy generation, applied load, and stress ratio was shown in this paper. The results were indeed encouraging, where the percentage difference between the MLR-based entropy models was less than 10%, indicating that the entropy values obtained from the experiment and regression model were in good agreement.

### ACKNOWLEDGEMENT

The authors graciously acknowledge the financial support provided by Universiti Kebangsaan Malaysia.

### REFERENCES

- [1] Xu, Z., Zhang, H., Yan, Z., Liu, F., Liaw, P. K., & Wang, W. (2017). Three-point-bending fatigue behavior of AZ31B magnesium alloy based on

- infrared thermography technology. *International Journal of Fatigue*, 95, 156-167.
- [2] Kong, Y. S., Abdullah, S., Schramm, D., Omar, M. Z., & Haris, S. M. (2019). Development of multiple linear regression-based models for fatigue life evaluation of automotive coil springs. *Mechanical Systems and Signal Processing*, 118, 675-695.
- [3] Mayén, J., Abúndez, A., Pereyra, I., Colín, J., Blanco, A., & Serna, S. (2017). Comparative analysis of the fatigue short crack growth on Al 6061-T6 alloy by the exponential crack growth equation and a proposed empirical model. *Engineering Fracture Mechanics*, 177, 203-217.

# Microhardness and sound velocity characterization of heat treated AISI 1050 carbon steel

Zakiah Abd Halim<sup>1,2,\*</sup>, Nur Farah Hani Nor Alzahari<sup>1,2</sup>

<sup>1)</sup> Fakulti Kejuruteraan Mekanikal, Universiti Teknikal Malaysia Melaka,

Hang Tuah Jaya, 76100 Durian Tunggal, Melaka, Malaysia

<sup>2)</sup> Centre for Advanced Research on Energy, Universiti Teknikal Malaysia Melaka,

Hang Tuah Jaya, 76100 Durian Tunggal, Melaka, Malaysia

\*Corresponding e-mail: zakiah@utem.edu.my

**Keywords:** Microhardness; sound velocity; heat treatment

**ABSTRACT** – This paper investigates the microhardness and sound velocity of heat treated AISI 1050 carbon steel. Three samples were subjected to different austenization temperatures of 800°C, 900°C and 1000°C for 30 minutes and then water-quenched, followed by tempering at 300°C for 50 minutes. Microhardness testing and ultrasonic testing were performed on the specimen before and after each heat treatment processes. It was observed that the hardness of the AISI 1050 carbon steel has inverse relationship with the sound velocity. The results show the sound velocity are affected by the type of heat treatment process.

## 1. INTRODUCTION

Heat treatment process is a process of heating and cooling a metal that is widely used to modify the mechanical properties of materials such as hardness, machinability and formability [1]. Medium carbon steel such as AISI 1050 is widely used for high quality cutting components, surgery equipment and small ball bearing due to its renowned properties of high hardness and subsequently high wear resistance. The high hardness is achieved through heat treatment processes such as quenching and tempering to suit the specific applications. Up to date, the research on mechanical properties on heat treated metal mainly focus on the influence of microstructure properties [2]. These methods are destructive and impair the usability of the future usefulness of the material. Literatures on non-destructive characterization of the mechanical properties is very scant. Previous studies successfully used ultrasonic testing to characterize the hardness and microstructures of heat treated and welded joints [3,4]. The request for fast and reliable non-destructive characterization of material properties after heat treatment is increasing due to its advantages over destructive testing. This paper studies the effect of quenching and tempering on the sound velocity and microhardness of AISI 1050 medium carbon steel. Characterization of material properties non-destructively enable cutting down testing time and ensure that the material can be reused after the test.

## 2. METHODOLOGY

The material in this study was carbon steel AISI 1050. The material composition consists of carbon (0.47–0.55%), sulphur ( $\leq 0.05\%$ ), manganese (0.60–0.90%), phosphorus ( $\leq 0.47\%$ ) and iron (98.4–98.92%). The material has dimension of 20 mm  $\times$  20 mm  $\times$  10 mm.

There were four specimens involved in this study. The sample designation and its heat treatment conditions are tabulated in Table 1. One specimen was used as a control specimen and three specimens were subjected to different austenization temperatures, which are 800°C, 900°C and 1000°C.

Table 1 Details of heat treatment conditions.

Sample	Austenization temperature	Quenching medium	Tempering temperature
R	-	-	-
A	800	Water	300
B	900	Water	300
C	1000	Water	300

The time taken for heating the specimen in the furnace from room temperature was set to 15 minutes and then was held at the austenization temperature for 30 minutes. The specimens were then quenched into water. The specimens were then reheated and held at tempering temperature for 50 minutes. The specimen were air cooled to room temperature. The heat treatment processes for the specimen were summarized in Figure 1.

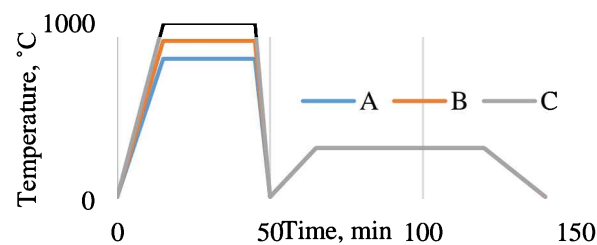


Figure 1 Temperature profile of heat treatment process on AISI 1050.

Ultrasonic tester USM35 and 5MHz ultrasonic sensor as illustrated in Figure 2 were used to measure the sound velocity of the specimen at all stages of the heat treatment process. The sensor was calibrated using International Institute of Welding reference block. Oil couplant was used to facilitate the longitudinal ultrasonic transmission from the sensor and reflection from the material. The sound velocity of heat treated,  $V_h$  was determined by thickness scaling factor between calibrated specimen thickness,  $t_c$  and measured thickness,  $t_h$  with the sound velocity of calibrated specimen,  $V_c$  using Equation (1).

$$V_h \text{ (m/s)} = \frac{\text{Calibrated thickness, } t_c \text{ (mm)}}{\text{Measured thickness, } t_h \text{ (mm)}} \times V_c \text{ (m/s)} \quad (1)$$

The hardness of the specimen was verified by Vickers microhardness testing. The average of ten indentations were taken for each specimen to represent the hardness of the materials before and after subjected to quenching as well as tempering.

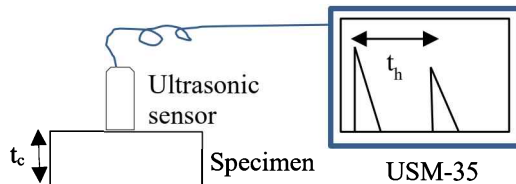


Figure 2 Sound velocity measurement.

### 3. RESULTS AND DISCUSSION

Figure 3 depicts the effect of quenching temperature on AISI 1050 medium carbon steel. It was observed that the hardness of AISI 1050 increased to slightly more than 400 HV when subjected to quenching compared to its initial hardness of 200 HV. However, the sound velocity of AISI 1050 did not show significant differences from its initial of 5960 m/s when subjected to different quenching temperature.

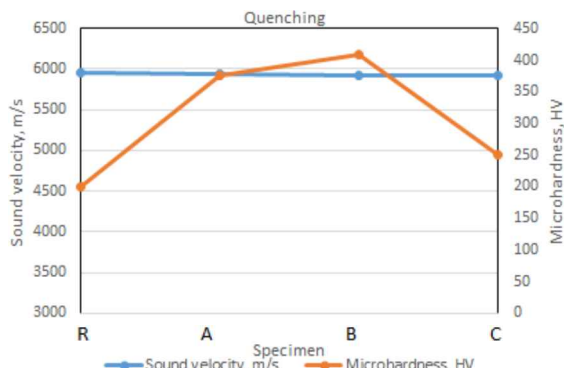


Figure 3 Sound velocity and microhardness of AISI 1050 after quenched.

Figure 4 portrays that the tempering process reduced the high hardness of AISI 1050 to 250 HV. There was a significant difference shown by the tempered specimens. The high hardness shown by quenched materials were reduced by tempering the materials. It was observed that the sound velocity in the AISI 1050 also decreased significantly to 4000 m/s from the initial sound velocity. The result obtained indicates that the sound emission in the heat treated specimen are affected by the type of heat treatment process. Quenching produced martensite microstructure that contains high stress [5]. Hence it is difficult for sound to propagate in the specimen. Tempering relives the stress inside the specimen and form a more stable microstructure of pearlite [6]. At similar specimen thickness, the time taken for the sound to be reflected in quenched specimen was longer compared after it was tempered. The hardness of sample C reduced to 250 HV as transformation above 950°C retained austenite, which reflected low hardness for both heat treatment [2].

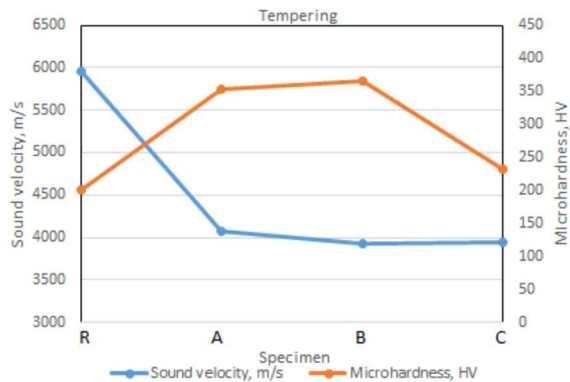


Figure 4 Sound velocity and microhardness of AISI 1050 after quenched and tempered.

### 4. CONCLUSION

A non-destructive material characterization of heat treated AISI 1050 using sound velocity has been proposed in this paper. Both quenching and tempering processes increased the hardness of material. It was found that quenching temperature does not affect the sound velocity of the material, but the tempering process shown a significant change in sound velocity. The sound velocity is dependent on the type of heat treatment. Verification of microstructural is needed to form a strong relationship for non-destructive evaluation of material properties.

### ACKNOWLEDGEMENT

The authors gratefully acknowledged the financial support from Universiti Teknikal Malaysia Melaka (UTeM) under Short Term Grant Scheme with reference no. PJP/2019/FKM(8B)/S01680.

### REFERENCES

- [1] Bryson, W. E. (2005). *Heat treatment, selection, and application of tool steels*. Hanser Gardner Publications.
- [2] Essoussi, H., Elmouhri, S., Ettaqi, S., & Essadiqi, E. (2019). Heat treatment effect on mechanical properties of AISI 304 austenitic stainless steel. *Procedia Manufacturing*, 32, 883-888.
- [3] Uzun, F., & Bilge, A. N. (2015). Application of ultrasonic waves in measurement of hardness of welded carbon steels. *Defence Technology*, 11(3), 255-261.
- [4] Ruiz, A., Fuentes-Corona, K. J., López, V. H., & León, C. A. (2017). Microstructural and ultrasonic characterization of 2101 lean duplex stainless steel welded joint. *Applied Acoustics*, 117, 12-19.
- [5] de Araújo Freitas, V. L., de Albuquerque, V. H. C., de Macedo Silva, E., Silva, A. A., & Tavares, J. M. R. (2010). Nondestructive characterization of microstructures and determination of elastic properties in plain carbon steel using ultrasonic measurements. *Materials Science and Engineering: A*, 527(16-17), 4431-4437.
- [6] El Rayes, M. M., El-Danaf, E. A., & Almajid, A. A. (2015). Ultrasonic characterization of heat-treatment effects on SAE-1040 and 4340 steels. *Journal of Materials Processing Technology*, 216, 188-198.

# Investigation on the effects of electrospinning distance and applied voltage on morphology of poly(vinyl alcohol) electrospun nanofibres

Abdul Hamid Nurfaizey<sup>1,2,\*</sup>, Fatin Hanani Abdullah<sup>1</sup>, Siti Hajar Sheikh Md Fadzullah<sup>1,2</sup>, Zaleha Mustafa<sup>3</sup>, Mohd Azli Salim<sup>1,2</sup>, Mohd Zaid Akop<sup>1,2</sup>

<sup>1)</sup> Fakulti Kejuruteraan Mekanikal, Universiti Teknikal Malaysia Melaka,  
Hang Tuah Jaya, 76100 Durian Tunggal, Melaka, Malaysia

<sup>2)</sup> Centre for Advanced Research on Energy, Universiti Teknikal Malaysia Melaka,  
Hang Tuah Jaya, 76100 Durian Tunggal, Melaka, Malaysia

<sup>3)</sup> Fakulti Kejuruteraan Pembuatan, Universiti Teknikal Malaysia Melaka,  
Hang Tuah Jaya, 76100 DurianTunggal, Melaka, Malaysia

\*Corresponding e-mail: nurfaizey@utem.edu.my

**Keywords:** Electrospinning; electrospun nanofibre; electrospinning distance; fibre diameter

**ABSTRACT-** In electrospinning process, the applied voltage and electrospinning distance are the two most important parameters that affect the quality of the fibres. In this study, these two parameters were studied. Polyvinyl alcohol (PVOH) electrospun fibres were produced using electrospinning technique. The morphology and fibre diameter of the fibres were examined using scanning electron microscopy and ImageJ. From the results, fibre diameter decreased when electrospinning distance decreased. However, there was no direct relationship between applied voltage and fibre diameter. The best electrospinning parameters were 10 kV of applied voltage and 10 cm of electrospinning distance.

## 1. INTRODUCTION

Electrospinning process is a version of electrospraying process which involves high electric potentials to charge a liquid, forcing the liquid to disperse onto an oppositely charged or grounded collector electrode [1]. The main difference is that in electrospinning, the liquid does not break up into fine droplets but instead forming strands of ultra-fine fibres when collected at the collector electrode.

There are several crucial parameters that influence the morphology of electrospun fibres such as flow rate, solution concentration, distance between the nozzle and the collector and the applied voltage. This study investigates the effect of the different applied voltage and the distance from the nozzle to the collector on the morphology of electrospun polyvinyl alcohol nanofibres. The best parameters for producing thin and defect free nanofibres were also determined.

## 2. METHODOLOGY

Poly(vinyl alcohol) or PVOH pellets with an average molecular weight of 124,000-130,000 g/mol and distilled water were mixed to get 8 wt.% of final concentration. The solution was stirred using IKA RW20 digital stirrer machine for 6 hours until a clear solution was obtained. A laboratory scale electrospinning machine, Electrospinz Model ES1a (Electrospinz Ltd., NZ) was used throughout the study. The flow rate was set at 1.100 ml/h. Samples were collected at various combinations of applied voltages

and electrospinning distances. The samples were sputtered with platinum in JEOL JEC-300FC auto fine coated machine for 180 seconds. The samples were scanned under scanning electron machine Model JSM-6010PLUS/LV (JEOL Ltd., Japan) to observe the morphology of electrospun nanofibres. The average fibre diameter of nanofibres was measured based on SEM micrographs using IMAGEJ software.

## 3. RESULTS AND DISCUSSION

Figure 1 and 2 show the SEM micrographs of the samples. For the first experiment, fibres started to produce at 10 kV of applied voltage. From the Figure 1 (a) and (b), solid and smooth fibres were produced when the applied voltage was at 10 kV to 15 kV. However, increasing the applied voltage further to 35 kV, abnormal fibres started to form that randomly interconnected to each other (Figure 1(f)). This was because at 35 kV, the fibres were being withdrawn at a very high speed due to excessive applied electric forces. In the second experiment, a wet film of polymer was formed at short distance of 2.5 cm (Figure 2 (a)). This happened because the solvent did not have enough time to evaporate before reaching the collector. The production rate of the fibres was also decreased as the electrospinning distance increased as evidenced in Figure 2 (b) to Figure 2 (g).

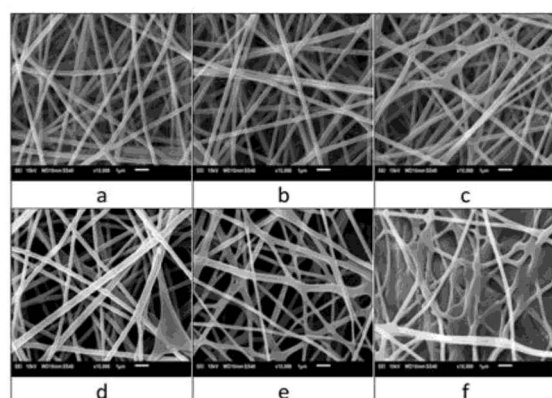


Figure 1 SEM micrographs of samples ( $\times 10,000$  magnification) produced at different applied voltages of (a) 10kV (b) 15kV (c) 20kV (d) 25kV (e) 30kV (f) 35kV.

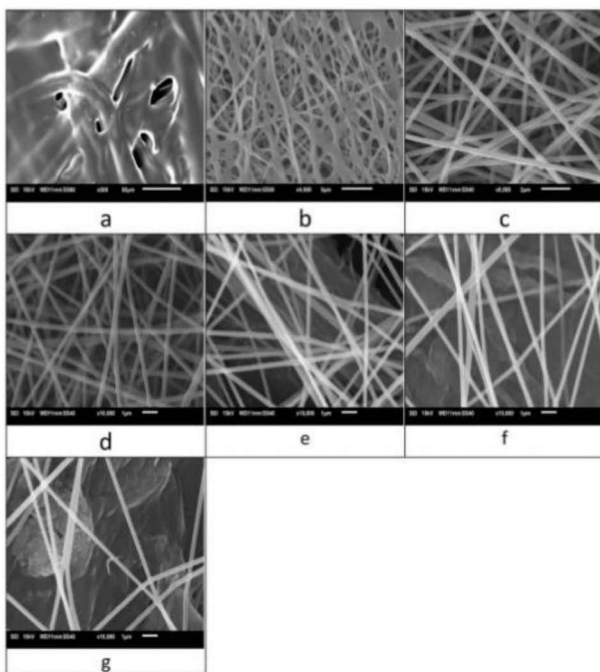


Figure 2 SEM micrographs of samples ( $\times 10,000$  magnification) produced at different electrospinning distances of (a) 2.5cm (b) 5cm (c) 7.5cm (d) 10cm (e) 12.5cm (f) 15cm (g) 17.5 cm.

The average fibre diameters of all samples are presented in Figure 3 and Figure 4. From Figure 3, the diameter of the fibres decreased as the distance increased. A similar finding was reported by Jayesh Doshi et al. [2]. This happened because extending the distance also prolonged the fibre's stretching time, thus producing finer fibres [3-4].

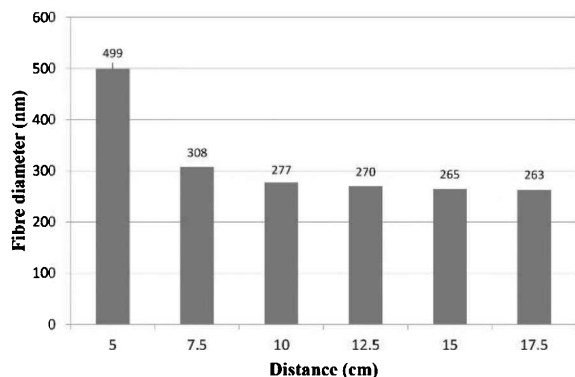


Figure 3 Fibre diameter as a function of electrospinning distance.

From Figure 4, there was no significant relationship between fibre diameter and applied voltage. Although a high applied voltage is required to form smooth fibres, however excessive applied electric forces could also cause the fibres to be prematurely deposited onto the collector as shown previously in Figure 1(f).

From the experiment, the best electrospinning parameters were 10 kV of applied voltage and 10 cm of electrospinning distance. At these parameters, the diameter of the fibres was consistent at  $277 \pm 25$  nm.

Furthermore, there were no sign of abnormal fibres such as beaded fibres or flat fibres.

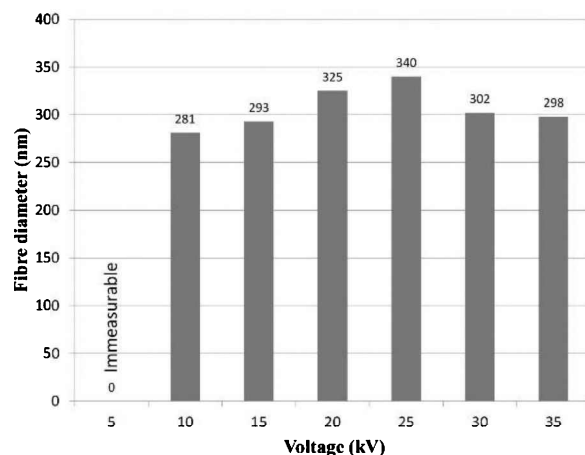


Figure 4 Fibre diameter as a function of applied voltage.

#### 4. CONCLUSION

In this study, the effects of applied voltage and electrospinning distance on the morphology of PVOH electrospun fibres were studied. Extending the electrospinning distance would decrease the fibre diameter, however increasing the applied voltage would not directly relate to fibre diameter. The best electrospinning parameters were 10 kV of applied voltage and 10 cm of electrospinning distance.

#### ACKNOWLEDGEMENT

This work is funded by FRGS/2018/FKM-CARE/F00372 Ministry of Education Malaysia. Special thanks to Fakulti Kejuruteraan Mekanikal, Universiti Teknikal Malaysia Melaka (UTeM).

#### REFERENCES

- [1] Pillay, V., Dott, C., Choonara, Y. E., Tyagi, C., Tomar, L., Kumar, P., ... & Ndesendo, V. M. (2013). A review of the effect of processing variables on the fabrication of electrospun nanofibers for drug delivery applications. *Journal of Nanomaterials*, 2013.
- [2] Doshi, J., & Reneker, D. H. (1995). Electrospinning process and applications of electrospun fibers. *Journal of electrostatics*, 35(2-3), 151-160.
- [3] Doustgani, A. (2015). Effect of electrospinning process parameters of polycaprolactone and nanohydroxyapatite nanocomposite nanofibers. *Textile Research Journal*, 85(14), 1445-1454.
- [4] Long, F., Kamsom, R., Nurfaizey, A., Isa, M., & Masripan, N. (2017). The influence of electrospinning distances on fibre diameter of poly (vinyl alcohol) electrospun nanofibres. *Proceedings of Mechanical Engineering Research Day 2017*, 377-378.

# A study on tensile properties of poly(vinyl alcohol) electrospun nanofibers

Abdul Hamid Nurfaizey<sup>1,2,\*</sup>, Nor Amalina Azmi<sup>1</sup>, Nor Azmmi Masripan<sup>1,2</sup>, Zaleha Mustafa<sup>3</sup>, Adzni Md. Saad<sup>1,2</sup>, Faizil Wasbari<sup>1,2</sup>

<sup>1)</sup> Fakulti Kejuruteraan Mekanikal, Universiti Teknikal Malaysia Melaka,  
Hang Tuah Jaya, 76100 Durian Tunggal, Melaka, Malaysia

<sup>2)</sup> Centre for Advanced Research on Energy, Universiti Teknikal Malaysia Melaka,  
Hang Tuah Jaya, 76100 Durian Tunggal, Melaka, Malaysia

<sup>3)</sup> Fakulti Kejuruteraan Pembuatan, Universiti Teknikal Malaysia Melaka,  
Hang Tuah Jaya, 76100 Durian Tunggal, Melaka, Malaysia

\* Corresponding email: nurfaizey@utem.edu.my

**Keywords:** Electrospinning; nanofibres; tensile test

**ABSTRACT -** Electrospinning is an easy and flexible method for the production of nanofibers. It has generated a great amount of interest for use in many areas, mainly due to its high surface area. For these applications, it is important to understand the mechanical properties of this material. In this study, tensile strength of polyvinyl alcohol (PVOH) electrospun fibres was investigated. PVOH nanofibres were produced using electrospinning method. The morphology of the fibres was observed under scanning electron microscopy (SEM). The tensile properties of PVOH were examined according to ASTM D882: *Standard Test Method for Tensile Properties of Thin Plastic Sheeting* using a universal tensile machine. The average tensile strength was found to be 2.5838 MPa which was comparable to previous studies.

## 1. INTRODUCTION

Nanofibers are defined as fibres with diameters below 100 nm [1]. To date, nanofibres have been produced from a wide range of materials, including natural polymers, synthetic polymers, carbon based nanomaterials, semi-conducting nanomaterials and composite nano-materials [2]. Currently, there are three techniques available for the synthesis of nanofibers: electrospinning, self-assembly, and phase separation. Of these techniques, electrospinning is the most widely studied technique due to its simple configuration, the ability to mass produce continuous nanofibres from different polymers and the ability to mass produce continuous nanofibres from different polymers [3]. Because of their high volume surface area, high porosity and interconnected permeable network [2], electrospun nanofibers have been proposed for a wide variety of applications such as filtration, tissue engineering scaffolds, drug delivery system and sensor [4]. In electrospinning, focus is normally given on the production of uniform fibres and how the diameter values and their distribution can vary with the materials and the processing conditions [5]. However, there is little information about the structure of nanofibers, the

mechanical properties that accompany them and how they vary with the processing conditions. Therefore, it is important to understand the nature of the process and the tensile properties of the fibres. In this study, tensile strength of poly(vinyl alcohol) (PVOH) electrospun fibres was investigated.

## 2. MATERIALS AND METHODS

PVOH with an average molecular weight of 124,000-130,000 g/mol and degree of hydrolysis (DH) of 86-89% was obtained from Polyscientific, Malaysia. The polymer solution was prepared by weighing the PVOH pellets and distilled water using a digital weighing balance machine to a final concentration of 8 wt.%. It was then placed on an IKA RW20 digital stirrer for 6 hours using a stirring speed of 380 rpm. The solutions were electrospun immediately after preparation. The setup used for electrospinning Electropinz Model ES1a (Electropinz Ltd., NZ) with 1.100 ml/h of flow rate. The electrospinning process was carried out for a period of 60 minutes. The distance from the tip of the needle to the collector was 10 cm and the applied voltage was 20 kV. The collected samples were sputtered with platinum using JEOL JEC-300FC auto fine coating machine for 180 seconds. The average fibre diameter was measured using ImageJ software based on SEM micrograph obtained earlier. Tensile test was conducted according to ASTM D882 using a universal testing machine (200 Series Single Column Test Machines, Shimadzhu) with a load cell of 1 kN. Five dumbbells shaped specimens were cut using Super Dumbbell Cutter (SD lever controlled, Model SDL-100). The average thickness of the film for the electrospun samples was 0.01mm, which was measured using a digital micrometre (Mitutoyo, 293-340). The size of the specimens were approximately 4 mm in width, and 20 mm in gauge length. The samples were mounted onto the machine grip and stretched with a strain rate of  $0.011\text{s}^{-1}$  until breakage as shown in Figure 1.



Figure 1 Tensile test was conducted using a universal testing machine.

### 3. RESULTS AND DISCUSSION

The calculated average fibre diameter was  $325 \pm 51$  nm. The produced PVOH nanofibers were smooth and uniform as evidenced by SEM micrograph in Figure 2.

The average tensile strength of PVOH electrospun fibres was 2.5838 MPa as shown in Table 1. The result is compared with previous study; Ismail and Zaaba [6] reported that the tensile strength of PVOH film was about 10.0 MPa. The difference in tensile value as compared to present study was mainly due to different sample structure and test conditions. The most notable difference was the thickness of the nanofibers which in this study was 0.01 mm while in the mentioned study was 0.10 mm.

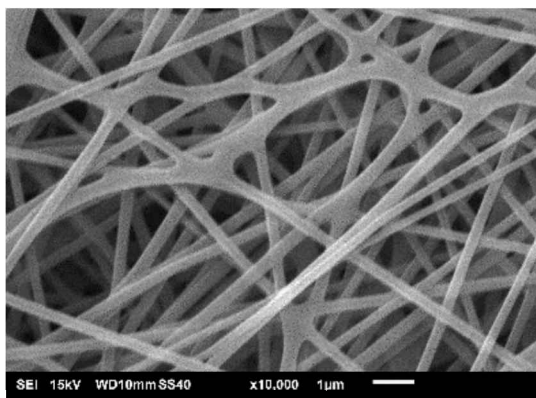


Figure 2 SEM micrograph of electrospun PVOH nanofibers at  $\times 10,000$  magnification.

Table 1 Tensile strength of poly (vinyl alcohol) electrospun fibers.

Sample	Tensile strength (TS) (MPa)
1	2.6227
2	2.5654
3	2.539
4	2.3561
5	2.8361
Average	2.5838

### 4. CONCLUSION

Nanofibres of poly(vinyl alcohol) were successfully produced using electrospinning. From SEM micrograph, smooth and uniform fibres were produced. The average tensile strength of the PVOH electrospun fibers was 2.58 MPa.

### ACKNOWLEDGEMENT

This work is funded by FRGS/1/2015/TK10/FKM/02/F00275 Ministry of Education Malaysia. Special thanks to Fakulti Kejuruteraan Mekanikal, Universiti Teknikal Malaysia Melaka (UTeM).

### REFERENCES

- [1] Zhou, F. L., & Gong, R. H. (2008). Manufacturing technologies of polymeric nanofibres and nanofibre yarns. *Polymer International*, 57(6), 837-845.
- [2] Lim, C. T. (2017). Nanofiber technology: current status and emerging developments. *Progress in Polymer Science*, 70, 1-17.
- [3] Mirjalili, M., & Zohoori, S. (2016). Review for application of electrospinning and electrospun nanofibers technology in textile industry. *Journal of Nanostructure in Chemistry*, 6(3), 207-213.
- [4] Long, F. C., Nurfaizey, A. H., & Daud, M. A. M. (2016). A preliminary study of greyscale intensity and deposited electrospun fibres using image analysis technique. *Proceedings of Mechanical Engineering Research Day 2016*, 2016, 165-166.
- [5] Lasprilla-Botero, J., Alvarez-Lainez, M., & Lagaron, J. M. (2018). The influence of electrospinning parameters and solvent selection on the morphology and diameter of polyimide nanofibers. *Materials Today Communications*, 14, 1-9.
- [6] Ismail, H., & Zaaba, N. F. (2011, September). Effect of polyvinyl alcohol on tensile properties and morphology of sago starch plastic films. In *2011 National Postgraduate Conference* (pp. 1-3). IEEE.

# An investigation on degree of crystallinity of poly(vinyl alcohol) electrospun nanofibers

Abdul Hamid Nurfaizey<sup>1,2,\*</sup>, Nur Hidayah Hashim<sup>1</sup>, Zaleha Mustafa<sup>3</sup>, Mohd Afzanizam Rosli<sup>1,2</sup>, Muhd Ridzuan Mansor<sup>1,2</sup>, Nadlene Razali<sup>1,2</sup>

<sup>1)</sup> Fakulti Kejuruteraan Mekanikal, Universiti Teknikal Malaysia Melaka,  
Hang Tuah Jaya, 76100 Durian Tunggal, Melaka, Malaysia  
<sup>2)</sup> Centre for Advanced Research on Energy, Universiti Teknikal Malaysia Melaka,  
Hang Tuah Jaya, 76100 Durian Tunggal, Melaka, Malaysia  
<sup>3)</sup> Fakulti Kejuruteraan Pembuatan, Universiti Teknikal Malaysia Melaka,  
Hang Tuah Jaya, 76100 Durian Tunggal, Melaka, Malaysia

\*Corresponding e-mail: nurfaizey@utem.edu.my

**Keywords:** Electrospinning, electrospun nanofibres, crystallinity, poly(vinyl alcohol)

**ABSTRACT** – This study investigates the degree of crystallinity of poly(vinyl alcohol) (PVOH) electrospun nanofibres. PVOH fibres were produced using electrospinning process. Differential scanning calorimetry (DSC) was used to examine the degree of crystallinity. The characterization of PVOH electrospun nanofibres was analyzed using scanning electron microscope and Image J software. From the results, electrospun PVOH nanofibres was found to have higher degree of crystallinity compared to raw PVOH. The increase of degree of crystallinity of the polymer was mainly due to mechanical stretching of polymer chains during electrospinning process.

## 1. INTRODUCTION

Poly(vinyl alcohol) or PVOH has earned a great amount of attention for various applications due to its unique characteristics. PVOH is known to have good mechanical properties, biodegradable and could provide excellent gas barrier. Recently, PVOH has been successfully transformed into nanoscale fibres using a process known as electrospinning. One of the important parameters in the electrospinning is the distance between the tip of the spinneret and the grounded collector [2]. This parameter plays important role in order to produce perfect nanofibres with no defects during electrospinning process occurred.

A typical electrospinning machine has three main components i.e. high voltage power supply, a capillary tube with a small diameter orifice and at grounded collector [1]. According to Huang et. al. [1], due to repulsive electrostatic forces, the applied high voltage will stretch the polymer before being collected at the collector electrode. This mechanical stretching could change the alignment of the polymer molecules, thus affecting the degree of crystallinity of the polymer. However, little is known about the effect of electrospinning process on degree of crystallinity. This study aimed at investigating the effect of electrospinning process on the degree of crystallinity of electrospun fibres.

## 2. METHODOLOGY

PVOH with molecular weight of 124,000-130,000 g/mol was purchased from Polyscientific, Malaysia.

Samples of PVOH fibres were produced using electrospinning process with time, distance and voltage at 40 minutes, 10cm and 15kV, respectively. The aqueous PVOH solution was prepared at 8 wt.% using mechanical stirrer (IKA RW20, IKA Works, Malaysia) for 6 hours.

The samples were cut to a dimension of approximately 1cm × 1cm. The sample was coated with platinum using an auto fine coater (JEOL JEC-300FL) for 180 seconds and scanned using a scanning electron microscope Model JSM-6010PLUS/ LV (JEOL Ltd., Japan). ImageJ software was used to determine the average diameter of the fibres. Differential scanning calorimetry samples were prepared by peeling the nanofibre mat to a mass of approximately 5 mg. The temperature range was set between 30° to 250°C with the heating/cooling rate set at 10°C/min. The nitrogen flow rate was set at 20 ml/min.

From the enthalpy under the curves, the degree of crystallinity can be calculated by using the following equation:

$$\% \chi_c = \frac{\Delta H_m - \Delta H_c}{\Delta H_m(100\%)} \times 100\% \quad (1)$$

Where  $\Delta H_m$  is the melting enthalpy,  $\Delta H_c$  is the crystallization and  $\Delta H_m(100\%)$  is the melting enthalpy in J/g of totally crystallized PVOH. In this case for PVOH, the value 138.6 J/g is the melting enthalpy of totally crystallized PVOH.

## 3. RESULTS AND DISCUSSION

From SEM micrograph, the average fibre diameter of the fibres was  $287 \pm 25$  nm. The thermal properties of nanofibres PVOH and raw PVOH are shown in Table 1. The glass transition temperatures of electrospun fibres taken at 71.8°C and raw PVOH at 71.91°C were observed similar. The enthalpy of melting raw and electrospun fibres,  $\Delta H_m$  increases from 22.9931 J/g to 28.6842 J/g. The results obtained were comparable to Ricciardi et al. [5] who claimed that the increase of  $\Delta H_m$  was due to increase of degree of crystallinity. Figure 1 and 2 show the DSC cycles of both electrospun fibres and raw PVOH. There were two cycles shown in each of the graph representing heating and cooling rate. The first heating cycle was carried out to eliminate thermal history and moisture content [3]. When the test was carried out on electrospun fibres, it produced larger and broader

endothermic curve since the PVOH nanofibres are highly interacted with water. Meanwhile, raw PVOH sample only show slight endothermic curve at melting temperature ( $T_m$ ). Overall, the degree of crystallinity

electrospun nanofibres PVOH at 22.14% was higher than raw PVOH at 19.41%. According to Reneker and Yarin [4], the degree of crystallinity increases due to molecular chains stretching during electrospinning.

Table 1 Thermal properties DSC.

Samples	No of cycle (Heating/Cooling rate)	Glass transition	Heat capacity	Melting		Crystallization		% $\chi_c$ fibre
		$T_g$ (°C)	$\Delta C_p$ (J/g)	$T_m$ (°C)	$\Delta H_m$ (J/g)	$T_c$ (°C)	$\Delta H_c$ (J/g)	
Raw PVOH	1	-	-	189.44	22.9931	107.64	-3.9126	19.41
Fibre PVOH	2	71.91	0.504	-	-	102.78	-1.1527	-
Fibre PVOH	1	55.3	64.7383	190.3	28.6842	93.62	-2.0024	22.14
Fibre PVOH	2	71.81	0.539	-	-	90.78	-0.8612	-

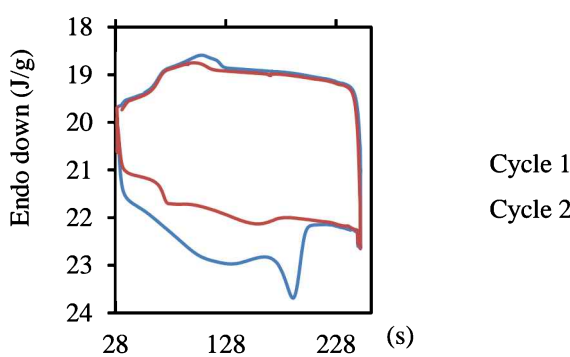


Figure 1 Thermograph of raw PVOH.

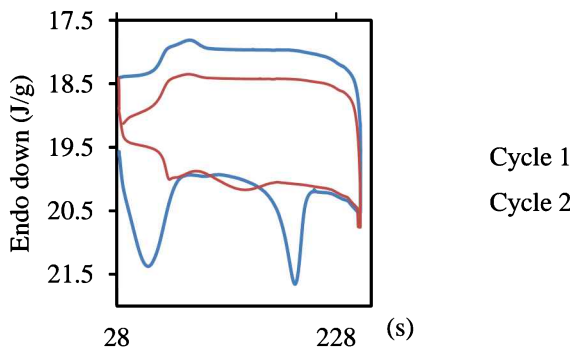


Figure 2 Thermograph of nanofibres PVOH.

#### 4. CONCLUSION

Electrospun PVOH nanofibres from electrospinning process was found to have higher degree of crystallinity compared to raw PVOH. The degree of crystallinity PVOH electrospun fibres was 22.14% which was slightly higher than that of raw PVOH at 19.41%. The increase of degree of crystallinity was due to mechanical stretching of the fibres during electrospinning process.

#### ACKNOWLEDGEMENT

This work is funded by ANCHOR/2019/FKM-CARE/A00020. Special thanks to Fakulti Kejuruteraan Mekanikal, UTeM.

#### REFERENCES

- [1] Huang, Z. M., Zhang, Y. Z., Kotaki, M., & Ramakrishna, S. (2003). A review on polymer nanofibers by electrospinning and their applications in nanocomposites. *Composites science and technology*, 63(15), 2223-2253.
- [2] Long, F., Kamsom, R., Nurfaizey, A., Isa, M., & Masripan, N. (2017). The influence of electrospinning distances on fibre diameter of poly (vinyl alcohol) electrospun nanofibres. *Proceedings of Mechanical Engineering Research Day*, 377-378.
- [3] Othman, N., Azahari, N. A., & Ismail, H. (2011). Thermal properties of polyvinyl alcohol (PVOH)/corn starch blend film. *Malaysian Polymer Journal*, 6(6), 147-154.
- [4] Reneker, D. H., & Yarin, A. L. (2008). Electrospinning jets and polymer nanofibers. *Polymer*, 49(10), 2387-2425.
- [5] Ricciardi, R., Auriemma, F., Gallet, C., De Rosa, C., & Lauprêtre, F. (2004). Investigation of the crystallinity of freeze/thaw poly (vinyl alcohol) hydrogels by different techniques. *Macromolecules*, 37(25), 9510-9516.

# Study on modulus of ABS single strut and reclaimed carbon fibre

Rafidah Hasan<sup>1,2,\*</sup>, Zurina Shamsudin<sup>3</sup>, Muhammad Fakhrur Iqbal Muslim<sup>1</sup>, Azira Mat Yusof<sup>1</sup>

<sup>1)</sup> Fakulti Kejuruteraan Mekanikal, Universiti Teknikal Malaysia Melaka,  
Hang Tuah Jaya, 76100 Durian Tunggal, Melaka, Malaysia

<sup>2)</sup> Centre for Advanced Research on Energy, Universiti Teknikal Malaysia Melaka,  
Hang Tuah Jaya, 76100 Durian Tunggal, Melaka, Malaysia

<sup>3)</sup> Fakulti Kejuruteraan Pembuatan, Universiti Teknikal Malaysia Melaka,  
Hang Tuah Jaya, 76100 Durian Tunggal, Melaka, Malaysia

\*Corresponding e-mail: rafidahhasan@utem.edu.my

**Keywords:** Lattice structure strut; reclaimed carbon fibre; tensile test

**ABSTRACT** – This study focusses in the determination of elastic property for 3D printed ABS single strut specimen and comparison with that of reclaimed carbon fibre (rCF). The study was applied for straight struts using compliance correction method with different gauge lengths of between 8 mm to 30 mm and single fibre testing of the reclaimed carbon fibre at fix gauge length. The tensile test was performed with reference to ASTM D638 standard procedure by using Shimadzu EZ Test (EZ-LX) machine. It was found that a reliable modulus was determined for ABS single strut using compliance correction method, meanwhile, the rCF modulus was strongly correlated with the condition of the tested fibres.

## 1. INTRODUCTION

The applications of lattice structures are widely used in additive manufacturing (AM) in recent years. Now, studies proved that open-pored cellular lattice structures with more complex geometrical structures are able to be created where the structures are mostly in regular rectangular forms and mostly used in heat exchangers or filter elements [1]. Lattice structure is a lightweight material with the properties of high stiffness and strength-to-weight scaling where the assembly methods of the strut-based lattice structure require a flexible configuration for complex geometrical designs as well as its mechanical properties [2,3]. Lattice structure comprises of many struts connected to each other by nodes, in many architectural arrangements such as body-centred-cubic (BCC), face-centred-cubic (FCC) and hexagonal close-packed (HCP) where possible architectural arrangements can be proposed [4]. The value for mechanical properties, the performance and the quality of lattice structure can be concluded through an examination of struts thus making struts as a fundamental element for lattice structure [5]. Meanwhile, reclaimed carbon fibre (rCF) has been explored and its potential as reinforcement in composite is still under study, especially to enhance the properties of modulus. Therefore, this research is examining the single strut under tensile loading, which lead to the determination of elastic modulus for 3D printed ABS strut and comparison with that of values of the rCF, in order to provide useful information for selection of excellent structure to benefit industrial applications.

## 2. METHODOLOGY

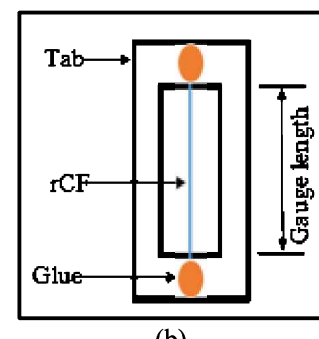
ABS single strut was designed by using CATIA with 1.6 mm diameter, at 35.26° build angle, in order to represent the strut position in BCC lattice structure material. The designed single strut was then fabricated by using CubePro 3D printer machine, using 200 µm layer resolution, ‘Solid’ print strength, and ‘Cross’ print pattern. Strut specimens with five different lengths were produced as shown in Table 1. Tensile test was done on the specimens as shown in Figure 1(a), using 1 kN load cell at rate 0.1 mm per minute. Compliance correction method [5] was applied in the analysis of elastic modulus value. Meanwhile, the rCF was received in pyrolysed form with diameter between 7 µm to 8 µm and 10 fibres were mounted on rectangular frame at fix gauge length of 25 mm as illustrated in Figure 1(b). The load cell was also rated to 1 kN with similar constant rate displacement.

Table 1 Specimens with different lengths for ABS strut.

Specimen Length, mm	Gauge Length, mm	Appearance
24	8	
45	15	
50	20	
75	25	
90	30	



(a)



(b)

Figure 1 Tensile test arrangement for (a) ABS single strut and (b) rCF specimen (schematic).

### 3. RESULTS AND DISCUSSION

The modulus of elasticity for ABS single strut was determined by calculating the gradient of the best-fit line on each stress-strain graph for each gauge length. Each gauge length produced different value of elastic modulus, hence, further analysis using compliance correction method [5] was carried out to determine a reliable and robust value of elastic modulus for the single strut.

Apparent compliance,  $C_a$  was obtained from force against elongation of specimen. Plot of apparent compliance,  $C_a$  against length  $L$  over square of diameter  $D^2$ , has produced the value of machine compliance,  $C_m$ . This is shown in Figure 2.

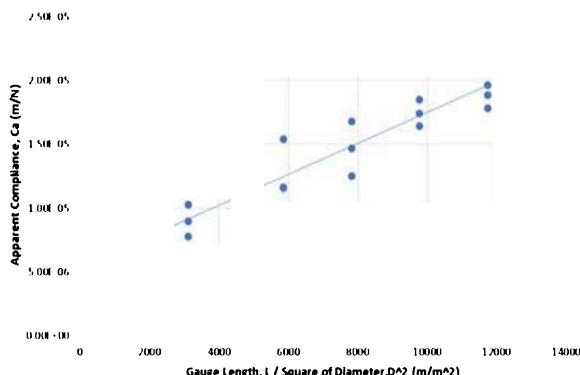


Figure 2 Plot of  $C_a$  against  $L/D^2$ .

Equation (1) was used to determine elastic modulus values,  $E$  for all gauge lengths.  $E_u$  is uncorrected elastic modulus, determined directly from stress-strain graph for each gauge length. Table 2 shows the results of corrected elastic modulus values for ABS 3D printed single struts.

$$E = \frac{E_u C_a}{C_a - C_m} \quad (1)$$

Table 2 Corrected elastic modulus value for ABS strut.

Gauge Length, mm	Apparent Compliance, $C_a$	Un-corrected Elastic Modulus, $E_u$ (MPa)	Corrected Elastic Modulus, $E$ (MPa)
8	$9.03 \times 10^{-6}$	$315.6 \pm 56$	$1095.1 \pm 139$
15	$12.9 \times 10^{-6}$	$545.5 \pm 57$	$1036.6 \pm 227$
20	$14.7 \times 10^{-6}$	$625.3 \pm 44$	$1067.8 \pm 179$
25	$17.3 \times 10^{-6}$	$684.2 \pm 36$	$1040.6 \pm 87$
30	$18.8 \times 10^{-6}$	$749.3 \pm 48$	$1199.3 \pm 95$
<b>Average corrected value</b>			$1087.9 \pm 146$

It can be observed that the corrected values are all similar, with average value of  $1087.89 \pm 145$  MPa. Thus, this has eliminated the uncertain various values of elastic modulus from different gauge lengths. The determined elastic modulus value is found as comparable to that of standard value of ABS elastic modulus (between 1100 to 2900 MPa). However, for rCFs modulus were calculated directly and average modulus was between 120 to 170 MPa. A low value indicates there is a wide range of flaw size in the fibres as shown in Figure 3.

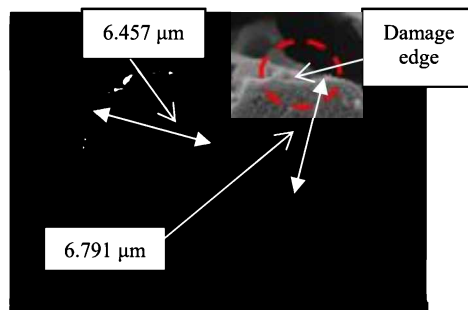


Figure 3 Flaw at edge of the rCF.

### 4. SUMMARY

Strut is a basic unit of lattice structure material, and it is an important part to be characterized. The result from this study shows that a reliable and robust elastic modulus value of single strut can be determined by using compliance correction method, thus eliminate the uncertain values that are affected by different gauge lengths. The corrected elastic modulus value is found as comparable to that of standard property, thus can be used in future analysis of lattice structure material. The rCF modulus shows variation in values and the low values are likely to be caused by the introduction of further surface flaws during processing and handling.

### ACKNOWLEDGEMENT

Authors gratefully acknowledge Universiti Teknikal Malaysia Melaka (UTeM) for facilities and financial supports. This research was partially supported by short-term grant PJP/2018/FKP(9A)/S01590.

### REFERENCES

- [1] Afshar, M., Anaraki, A. P., Montazerian, H., & Kadkhodapour, J. (2016). Additive manufacturing and mechanical characterization of graded porosity scaffolds designed based on triply periodic minimal surface architectures. *Journal of the mechanical behavior of biomedical materials*, 62, 481-494.
- [2] Al-Ketan, O., Rowshan, R., & Al-Rub, R. K. A. (2018). Topology-mechanical property relationship of 3D printed strut, skeletal, and sheet based periodic metallic cellular materials. *Additive Manufacturing*, 19, 167-183.
- [3] Hasan, R., Mines, R. A., Shen, E., Tsopanos, S., & Cantwell, W. (2011). Comparison on compressive behaviour of aluminium honeycomb and titanium alloy micro lattice blocks. In *Key Engineering Materials*, 462, 213-218.
- [4] Azman, A. H. (2017). *Method for integration of lattice structures in design for additive manufacturing* (Doctoral dissertation, Université Grenoble Alpes).
- [5] Hasan, R., Mines, R. A. W., & Tsopanos, S. (2010). Determination of Elastic Modulus Value for Selectively Laser Melted Titanium Alloy Micro-Strut. *Journal of Mechanical Engineering and Technology*, 2(2), 17-25.

# Design of bamboo bending tools on bird cage making based on anthropometric analysis

Teguh Aprianto\*, Herman Ruswan Suwarman, Mochamad Saidiman

Sekolah Tinggi Teknologi Bandung, Soekarno-Hatta St No.378, Kebon Lega, Bojongloa Kidul, Bandung City, West Java 40235, Indonesia

\*Corresponding e-mail: teguh@sttbandung.ac.id

Keywords: Bamboo bending tools; bird cage making; anthropometric analysis

**ABSTRACT** – The high number of bird enthusiasts has increased the need for bird cages. The frame material for making bird cages is usually made of bamboo, wood, rattan, metal and plastic. The Government of Garut Regency, West Java, developed the North Garut area in Selaawi District as a bamboo handicraft tourism to grow the economy of the people who mostly work as bamboo craftsmen. Bird cage business is able to bring profits that can be said big. Cage making still uses simple equipment and takes a long time in making it. One of the processes in the manufacture of cages is the bending of bamboo bird cages in Selaawi sub-district still using human power by heating bamboo then bending using the legs. For this reason, it is necessary to make improvements in the bending process, namely by designing a bamboo bent in the manufacture of bird cages in Garut regency. So that the results of bird cages increase and can meet consumer needs. The design is based on anthropometric analysis, thus, in this study samples were taken from workers to obtain the desired dimensions.

## 1. INTRODUCTION

The use of bamboo plants in Indonesia has been going on for a very long time. Our rural communities have used bamboo since ancient times for various life support purposes, such as making houses or household furniture. As a herbaceous plant, bamboo also has strong and flexible stems. Bamboo plants are also used as material for making bird cage frames.

The birds singing with their sweet voice makes birds chirp with many fans. The high number of bird enthusiasts has increased the need for bird cages. The frame material for making bird cages is usually made of bamboo, wood, rattan, metal and plastic. The Government of Garut Regency, West Java, developed the North Garut area in Selaawi District as a bamboo handicraft tourism to grow the economy of the people who mostly work as bamboo craftsmen.

Residents in Selaawi Subdistrict have 39 thousand inhabitants, around 1,900 of them work as bamboo artisans making bird cages, home appliances and various other interesting accessories. The opportunity for a bird cage business is one of the most profitable businesses. Bird cage business is able to bring profits that can be said big. The bird cage business is indeed not a new business, but the opportunity is very large. The prospect of a bird cage business can indeed be said to be very promising. Day after day the demand for bird cages continues to increase. In running a bird cage

business requires raw materials for its manufacture. To make bird cages requires raw materials, namely bamboo.

In the process of making cages, craftsmen still use simple and manual equipment. Cage making still uses simple equipment and takes a long time in making it. One of the processes in the manufacture of cages is the bending of bamboo bird cages in Selaawi sub-district still using human power by heating bamboo then bending using the legs.



Figure 1 The process of making bird cages.

For this reason, it is necessary to make improvements in the bending process, namely by designing a bamboo bent in the manufacture of bird cages in Garut regency. So that the results of bird cages increase and can meet consumer needs.

## 2. METHODOLOGY

The research method uses anthropometric analysis to design the bending tools. Bird cage craftsmen were taken as research sample to meet the desired ergonomic dimension. The research was done by steps illustrated in Figure 2.

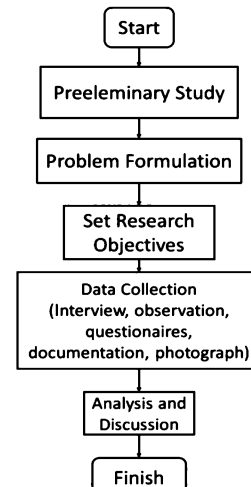


Figure 2 Research flow chart.

### 3. RESULTS AND DISCUSSION

Anthropometric data used are body dimensions needed in the design of bamboo bending in the manufacture of bird cages in Selaawi district, Garut Regency. The collection process was carried out to obtain the dimension needed in the design of bamboo bending in the manufacture of bird cages in Selaawi sub-district, Garut Regency. In designing bamboo bending (Figure 3) in the manufacture of bird cages in Selaawi District, Garut Regency, anthropometric data is needed. The steps of data processing are explained below:

Step 1 The data is processed before the design is carried out, namely the distribution of questionnaires, drafting of draft concepts, processing of anthropometric data and design of bamboo bending in the manufacture of bird cages in Selaawi sub-district, Garut Regency.

Step 2 Body dimension data was tested using data normality test, uniformity test and data adequacy test.

#### Step 3 Percentile calculation

Percentile values can be determined from the table of normal distribution probabilities. Percentile is a range that can be used. 5th percentile, the calculation is:  $X - 1.645 \cdot SD$ ; 50th percentile, calculation is :  $X$  ; 95th percentile , the calculation is :  $X + 1.645 \cdot SD$

Step 4 Design of bamboo bending in the manufacture of bird cages

In this process what will be made is a bamboo bending tool for making bird cages in Selaawi sub-district, Garut Regency

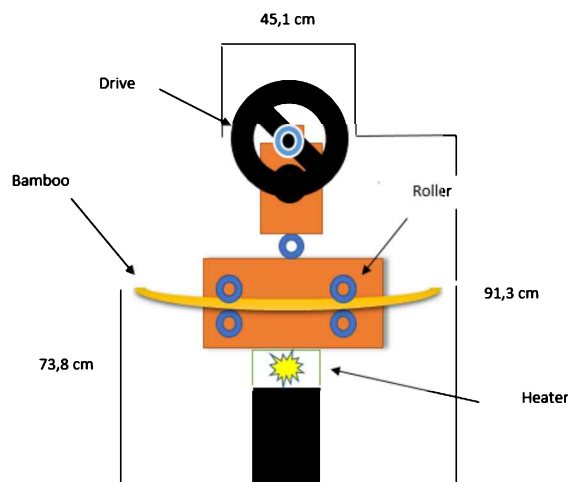


Figure 3 Bamboo bending design on bird cage making.

### 4. CONCLUSIONS

- (a) Design of bamboo bending in the manufacture of bird cages has height 91,3 cm, drive 45,1 cm, height of bamboo on the roller is 73,8 cm
- (b) Using anthropometric data is shoulder width, elbow height of standing position, knuckle height of standing position
- (c) Design of bamboo bending in the manufacture of bird cages has dimension ergonomic

### REFERENCES

- [1] Anonim. (2019). Bambu sebagai tanaman konservasi. Received online: <http://www.medcofoundation.org/bambu-sebagai-tanaman-konservasi/>
- [2] Feri. (2017). Garut utara dikembangkan sebagai wisata kerajinan bambu. Received online: <https://jabar.antaranews.com/berita/62378/garut-utara-dikembangkan-sebagai-wisata-kerajinan-bambu>.
- [3] Kurniawan, A. (2012). Asal usul tanaman bambu. Received online: <http://www.neraca.co.id/article/8948/asal-usul-tanaman-bambu>
- [4] Nurmianto, E. (2008). Ergonomi konsep dasar dan aplikasinya, Guna Widya.
- [5] Suwandi, D. (2015). Mengenal tanaman bambu. Received online: <https://dapuraw31.wixsite.com/bambu-indonesia/single-post/2015/02/22/Mengenal-Tanaman-Bambu>
- [6] Tarwaka, S., & Lilik. (2004). Ergonomi untuk keselamatan, kesehatan kerja dan produktivitas, Uniba Press, Surakarta.
- [7] Tarwaka. (2014). Ergonomi industri: Dasar-dasar pengetahuan ergonomi dan aplikasi di tempat kerja. Harapan Press Surakarta.
- [8] Wigjnosoebroto, S. (1995). Ergonomi studi gerak dan waktu, Guna Widya.

# Prediction of crack propagation direction in fretting fatigue

M.H. Maslan\*, O. Ifayefunmi, M.A.A. Wahap

Fakulti Kejuruteraan Mekanikal, Universiti Teknikal Malaysia Melaka,  
Hang Tuah Jaya, 76100 Durian Tunggal, Melaka, Malaysia

\*Corresponding e-mail: haidir@utem.edu.my

**Keywords:** Fretting fatigue; finite element; crack propagation

**ABSTRACT** – Nucleation and propagation of cracks under fretting conditions has been a subject of study for many years. The aim of this research is to predict crack propagation direction in complete contact fretting fatigue. This study uses the earlier experimental results with Royal Aerospace Establishment (RAE Farnborough) as the reference for comparison. Two crack propagation criterions, Maximum Tangential Stress (MTS) and Maximum Tangential Stress Range ( $\Delta$ MTS) are compared using a commercial finite element code, ABAQUS. Results clearly show that Maximum Tangential Stress Range ( $\Delta$ MTS) can become good estimation tool for predicting crack propagation direction in complete contact fretting fatigue.

## 1. INTRODUCTION

Correct crack path is important on modelling in analysing crack propagation especially for small crack. Difference crack angle influenced value of stress intensity [1] and affecting crack propagation analysis as crack length is now has been differ as the crack is kinked out. Hence, the determination of accurate crack path become significant in order to make better prediction of specimen life under cyclic loading.

In this study, two criterions that have been proved to work well for complete contact crack direction is compared. Those criterions are Maximum Tangential Stress (MTS) based on study by Faanes [2] and Maximum Tangential Stress Range ( $\Delta$ MTS) based on study by Giner [3]. Faanes do the analysis using mathematical equation to determine stress intensity factor in mode I and mode II. These values is then determine using stress in front of crack tip. Meanwhile, Giner analysed with the aid of ABAQUS on a single pad complete contact.

## 2. MODEL DESCRIPTION

The basis for this study is the Royal Aerospace Establishment (RAE Farnborough) experimental works of Sheikh et al [1]. In his work, a general fretting fatigue test apparatus was used which consisted of flat fretting bridge pads over a specimen of rectangular cross section.

The material investigated was BS-L65, a fully artificially aged 4 percent copper aluminium alloy (also known as Al 2014). The fretting pads were made of BS S98 steel (2.5% Nickel-Chrome-Moly steel. Table 1 gives the elastic properties of these materials.

Table 1 Materials properties.

Materials	Young Modulus, $E$	Poisson Ratio, $\nu$	Yield Stress, $\sigma_y$
BS L65	74.0 GPa	0.33	420 MPa
BS S98	210 Gpa	0.29	1002 MPa

Due to symmetry, a quarter 2D finite element model has been used to represent the fretting fatigue tests, as shown in Figure 1. Since the specimen is 8 mm thick, plane strain elements are used in the analysis. Mesh is refined towards the edges of contact region with a coarse mesh away from the contact region to reduce processing time. Matched meshes are used on the master and slave contact surfaces.

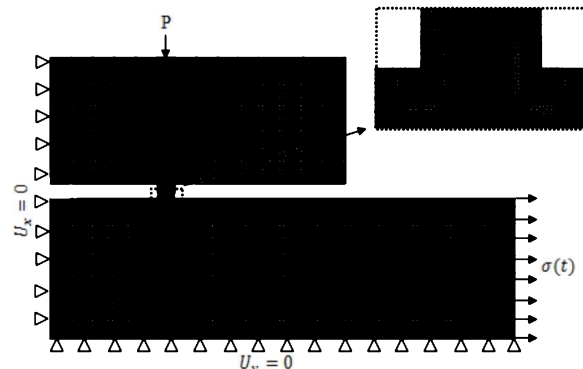


Figure 1 Finite element model of a quarter of the fretting specimen-pad arrangement.

A Lagrange multiplier contact algorithm is used to strictly enforce the sticking condition when shear stress is less than the critical value according to the Coulomb friction law [4].

The loading history is represented in Figure 2. In the first analysis step, a normal load,  $P$  is applied to the fretting pads. In the next step, the specimen is loaded by a cyclic fatigue load  $\sigma(t)$  with a maximum value  $\sigma_{max}$  and a stress ratio of  $R = -1$ .

In ABAQUS, crack is modelled using embedded line, which known as “seam” in ABAQUS. In order to get better results, mesh refining toward the crack tip is required. Partitioning strategy is used to create the desired crack and to facilitate the generation of uniform focused mesh.

In order to obtain the maximum value of MTS or  $\Delta$ MTS,  $K_I$  and  $K_{II}$  values obtained from each simulation are used to calculate the tangential stress ( $\sigma_{\theta\theta}$ ).  $\theta$  is varied for each degree and plotted to get the maximum tangential stress angle and maximum tangential stress range.

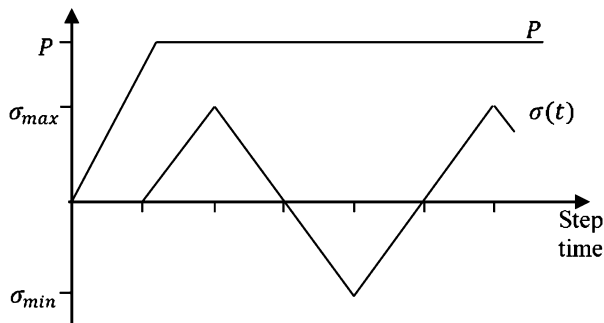


Figure 2 Normal load and cyclic axial load history applied to the finite element model.

### 3. RESULTS AND DISCUSSION

Figure 3 shows the results from the analysis. In overall,  $\Delta$ MTS give better prediction compared to MTS criterion.

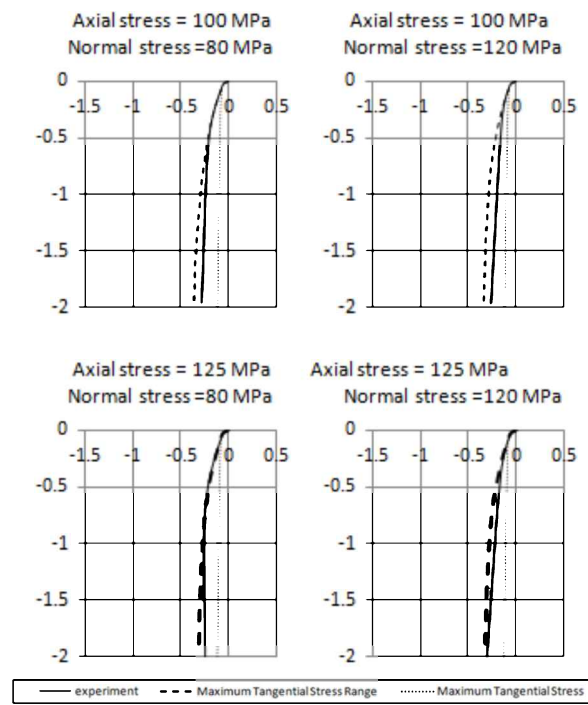


Figure 3 One-column illustration.

Although Both criterions assumed that crack will propagate to the direction where tangential stress is maximum, MTS only consider stress field in front of crack tip at particular time when the tangential stress is maximum only which will occur when the axial stress applied is in tension. While  $\Delta$ MTS consider stress field in a range of time for one complete cycle.

Contact Stress during maximum tension and compression axial stress can be observed in Figure 4. It can be seen that there is no contact stress occur at the

surface near leading edge in tension loading. But the contact stress is very high in maximum compressive cycle due to slightly small rotation movement by the fretting pad. In other word, in maximum tensile loading, the stress in front leading edge is almost like specimen with only uniaxial stress without the contact effect. This may be the reason why MTS crack is almost a straight. Meanwhile,  $\Delta$ MTS that consider stress field for a cycle able to use the multi axial effect in the prediction.

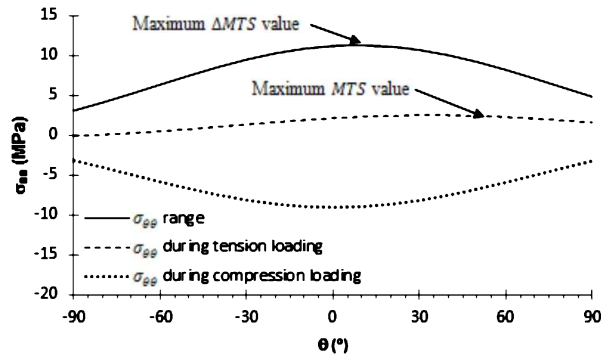


Figure 4 Example of  $\sigma_{\theta\theta}$  value over  $180^\circ$  range.

### 4. CONCLUSION

From the results, it can be concluded that  $\Delta$ MTS criterion can provide a good estimation tool for estimating crack propagation direction in complete contact fretting fatigue.

### ACKNOWLEDGEMENTS

The authors would like to acknowledge the financial support received from University Teknikal Malaysia Melaka (UTeM) and the Ministry of Education Malaysia under Fundamental Research Grant Scheme FRGS/2018/FTKMP-CARE/F00386

### REFERENCES

- [1] Sheikh, M. A. (1994). Elastic stress intensity factors for fretting cracks using the finite element method. *Fretting Fatigue*, 83.
- [2] Faanes, S. (1995). Inclined cracks in fretting fatigue. *Engineering Fracture Mechanics*, 52(1), 71-82.
- [3] Giner, E., Sabsabi, M., Ródenas, J. J., & Fuenmayor, F. J. (2014). Direction of crack propagation in a complete contact fretting-fatigue problem. *International Journal of Fatigue*, 58, 172-180.
- [4] ABAQUS, *ABAQUS 6.11 Analysis User's Manual*. Dassault Systèmes, Providence, RI, USA, 2011.

# Effect of edge trimming parameters on surface quality of carbon fiber reinforced polymer composites (CFRP): Taguchi Method

S.A. Sundi<sup>1,2,\*</sup>, R. Izamshah<sup>2</sup>, M.S. Kasim<sup>2</sup>, M.F. Jaafar<sup>2</sup>, N. Syuhada Nasir<sup>1</sup>, M.H. Hassan<sup>3</sup>

<sup>1)</sup> Fakulti Teknologi Kejuruteraan Mekanikal dan Pembuatan, Universiti Teknikal Malaysia Melaka,  
Hang Tuah Jaya, 76100 Durian Tunggal, Melaka, Malaysia

<sup>2)</sup> Fakulti Kejuruteraan Pembuatan, Universiti Teknikal Malaysia Melaka,  
Hang Tuah Jaya, 76100 Durian Tunggal, Melaka, Malaysia

<sup>3)</sup> School of Mechanical Engineering, Universiti Sains Malaysia,  
14300 Nibong Tebal, Pulau Pinang, Malaysia

\*Corresponding e-mail: syahrul.azwan@utem.edu.my

**Keywords:** Edge trimming; CFRP; surface roughness; Taguchi method

**ABSTRACT** – The main objective of this research was to investigate the effect of machining parameters towards surface quality during edge trimming process on a specific Carbon Fiber Reinforced Polymer (CFRP). The machining parameters focused in this work were namely cutting speed ( $V_c$ ) and feed per tooth ( $f_z$ ). The CFRP panel used is measured 3.25 mm in thickness with 28 number of plies in total. Burr tool geometry made of uncoated tungsten carbide diameter of 6.35 mm was used to perform the edge trimming process. Taguchi method is adopted to plan the overall experimental. Mitutoyo Surftest SJ-410 has been utilized to measure the surface roughness value. From ANOVA analysis, both studied factors proven to be the significant factors towards the surface quality of the trimmed surface. Details results elaborated and discussed further in this paper.

## 1. INTRODUCTION

Machining composite materials is hard to be performed due to the mechanical, thermal properties and the high abrasiveness of the reinforcement constituents. In manufacturing of aero-structural composite material, milling and drilling are critical for finishing trimmed edges of panels or making accurate holes to rivet pieces together. The behavior of composite such as its inhomogeneity and interaction with the cutting tool whilst machining is a complex phenomenon to be understood [1]. Gara and Tsoumarev [2] discovered that the transverse roughness does not depend on cutting conditions, it depends only on tool geometry. Contrary to the longitudinal roughness which was not only depending on the tool geometry but also the cutting conditions. Feed per tooth was found to be the highest statistical and physical influence on the surface roughness for knurled or burr tool. Meanwhile, Sundi et al. [3] summarized that spindle speed was found to be the main influential factor towards surface finish in edge trimming a specific CFRP material. In different research experimented by Duboust et al. [4] proved that surface roughness increased with machining distance. They also concluded that diamond coated tool with multiple cutting teeth (burr tool) was able to produce a good quality surface although at high feed rate in comparison with polycrystalline diamond (PCD) tool. Statistical methods obtained indicate that the feed rate and tool type had the most significant effect on the surface quality.

## 2. METHODOLOGY

The CFRP panel measured 3.25 mm in thickness and the type of fabric was unidirectional (UD). It has 28 number of plies in total which consist of 2 thin layer of glass/epoxy woven fabrics 0.08 mm at the top and bottom of the CFRP laminate play the role of protecting the outer surfaces of the panel. The stacking sequence was [45/135/90/0/90/0/90/0/135/45/135]. The nominal fiber volume fraction was 60%.

The type cutting tool used was router or burr tool made of tungsten carbide (uncoated) and diameter 6.35mm (refer Figure 1). The machine utilized in this work was a Hass CNC Gantry Router – 3 Axis GR-510. Down milling has been selected as the mode of machining configuration. Total travel distance of each run was 260 mm. In this study, the edge trimming process performed with 100% of tool diameter or step width ( $a_e$ ) and the depth of cut ( $a_p$ ) was taken in full thickness of the selected composite panel. This is to replicate the actual industrial practice done by composite manufacturers.



Figure 1 Geometrical feature of router or burrs tool.

There were two machining parameters focused namely cutting speed ( $V_c$ ) and feed per tooth ( $f_z$ ). The range of cutting speeds applied were of 50 m/min (low), 100 m/min (moderate), and 150 m/min (high) speed whilst for feed per tooth; 0.05, 0.1, and 0.15 mm/rev. Table 1 represents the machining parameters applied in this work. Taguchi method (Orthogonal Array L9) one of the statistical techniques was adopted to plan the overall experiment.

Surface roughness tester; Surftest SJ-410 manufactured by Mitutoyo (Figure 2) is used to measure the surface finish of the workpiece. In this study, Ra (Arithmetical mean deviation) is referred to measure the surface roughness. Longitudinal surface roughness is evaluated with the stylus travel distance set at 4 mm on each measurement. There were 5 points of measurement taken on every machined surface and final average Ra is obtained to represent the result of surface finish on every specimen (Table 2).

Table 1 Machining parameters.

Run (R)	Cutting Speed, $V_c$	RPM	Feed per Tooth, $F_z$ (mm/rev)	$V_f$ mm/min
1	50	2506	0.05	125
2	100	5012	0.15	752
3	50	2506	0.1	251
4	100	5012	0.05	251
5	100	5012	0.1	501
6	150	7518	0.1	752
7	150	7518	0.05	376
8	50	2506	0.15	376
9	150	7518	0.15	1128



Figure 2 Surface roughness measurement by SJ-410.

### 3. RESULTS AND DISCUSSION

Analysis of Variance (ANOVA) was carried out to determine which factor or machining parameter namely cutting speed,  $V_c$  and feed per tooth,  $F_z$  significantly affect the performance characteristics or selected response namely surface roughness.

Table 2 Overall result of surface roughness, Ra

Run	1	2	3	4	5	Avg.
1	1.95	1.28	0.94	2.80	1.11	1.62
2	7.57	7.79	6.50	9.35	2.44	6.73
3	4.59	4.14	2.43	2.43	2.63	3.25
4	2.50	2.46	2.42	2.95	3.06	2.68
5	2.80	3.92	8.09	6.98	4.59	5.28
6	7.43	7.55	9.23	7.45	8.89	8.11
7	2.30	3.66	3.93	3.97	4.34	3.64
8	6.07	5.33	5.98	6.41	6.77	6.11
9	15.72	13.33	10.68	13.33	10.03	12.62

Tables 3 illustrates the result of ANOVA analysis for the average Ra values during edge trimming of a specific CFRP chosen in this study. This analysis was computed for a level of confidence of 95 %. The Model F-value (in bold) from Table 3 shows 10.800 which implies the model is significant. There is only a 2.03% chance that a "Model F-Value" this large could occur due to noise. Thus, both factors; A = cutting speed and B = feed per tooth have significant effect to the chosen response; surface finish. Meanwhile, Figure 3 exhibits a 3D bar graph which summarized the effect of both factors; cutting speed and feed per tooth towards the surface quality of the trimmed surface. Lower cutting speed and feed per tooth are preferred to obtain the minimized surface roughness.

Table 3 ANOVA Result for surface roughness.

Source	SOS	df	Square	Mean value	Prob > F
Model	83.492	4	20.873	10.800	0.0203
A-Cutting Speed	31.120	2	15.560	8.0511	0.0396
B-Feed per Tooth	52.372	2	26.186	13.550	0.0165
Residual	7.7304	4	1.9326		
Cor Total	91.222	8			

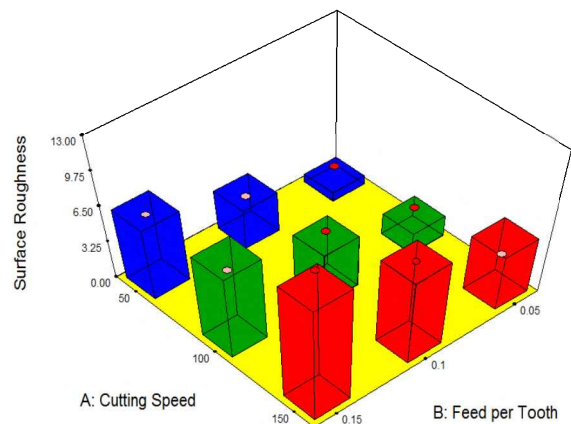


Figure 3 3D bar graph illustrates the effect of cutting speed and feed per tooth towards surface roughness.

### 4. CONCLUSION

This paper presented an evidence on the effect of machining parameters namely cutting speed and feed rate towards the edge trimmed surface quality of a specific CFRP material according to the result obtained by ANOVA analysis.

### ACKNOWLEDGEMENT

Authors would like to thank Ministry of Education Malaysia for their financial support. (FRGS/2018/FKP-AMC/F00378).

### REFERENCES

- [1] Sheikh-Ahmad, J. Y. (2009). *Machining of polymer composites* (Vol. 387355391). New York: Springer.
- [2] Gara, S., & Tsoumarev, O. (2016). Effect of tool geometry on surface roughness in slotting of CFRP. *The International Journal of Advanced Manufacturing Technology*, 86(1-4), 451-461.
- [3] Sundi, S. A., Izamshah, R., Kasim, M. S., & Abdullah, M. K. A. (2019, January). Effect of machining parameters on surface quality during edge trimming of multi-directional CFRP material: Taguchi method. In *IOP Conference Series: Materials Science and Engineering* (Vol. 469, No. 1, p. 012095). IOP Publishing.
- [4] Duboust, N., Melis, D., Pinna, C., Ghadbeigi, H., Collis, A., Ayvar-Soberanis, S., & Kerrigan, K. (2016). Machining of carbon fibre: optical surface damage characterisation and tool wear study. *Procedia CIRP*, 45, 71-74.

# Optimization of treated SN 0W20 grade engine oil enhance with hBN nanoparticles

Muhammad Ilman Hakimi Chua Abdullah<sup>1,2,\*</sup>, Mohd Redzuan Jamil<sup>1</sup>, Mohd Fadzli Bin Abdollah<sup>2,3</sup>

<sup>1)</sup> Fakulti Teknologi Kejuruteraan Mekanikal dan Pembuatan, Universiti Teknikal Malaysia Melaka,  
Hang Tuah Jaya, 76100 Durian Tunggal, Melaka, Malaysia

<sup>2)</sup> Centre for Advanced Research on Energy, Universiti Teknikal Malaysia Melaka,  
Hang Tuah Jaya, 76100 Durian Tunggal, Melaka, Malaysia

<sup>3)</sup> Fakulti Kejuruteraan Mekanikal, Universiti Teknikal Malaysia Melaka,  
Hang Tuah Jaya, 76100 Durian Tunggal, Melaka, Malaysia

\*Corresponding e-mail: ilmanhakimi@utem.edu.my

**Keywords:** SN 0W20; hBN; friction

**ABSTRACT** – The purpose of this study is to determine the optimal design parameters in obtaining the lowest coefficient of friction (COF) and wear by hexagonal boron nitride (hBN) nanoparticles, dispersed in fully synthetic engine oil (SN 0W20). L9 orthogonal arrays was constructed using the Taguchi method to determine the parameter contribution. Four-ball tester is used for conducting tribological testing according to ASTM standard D4172. By referring to the analysis of S/N ratio, COF and wear scar was reduced significantly with addition hBN nanoparticles into the treated engine oil SN 0W20. As conclusion hBN nanoparticles able to be the next future additive for oil manufacturer.

## 1. INTRODUCTION

Nowadays, the demand of new lubricant is highly undoubtedly due to the diverse application that keeps on increasing. It is a must for producing new lubricant to meet future demand. Most of current lubricants are derived from the crude oil which is not adaptable to the environment because of its toxicity and non-biodegradability. The waste oil can be threatening to the world if it is not handled correctly. The recycling and regeneration of waste oil can be an alternative way to prevent pollution by treated the waste oil.

Recently, numerous studies have been conducted on how to improve engine oil by enhancing with nanoparticles. Nanoparticles are particles that have a size normally around 100 nanometers or less. It possesses better characteristics through its size, shape, hardness and the weight percentage of usage. Unlike any lubricant additives, nanoparticles are readily good at entering contact asperities, thermal stability, a variety of particle chemistries, and reaction rate with the surface without an induction period, which is important for conventional [1,2]. Over the past decades, researcher has stated the addition of nanoparticles such as copper (Cu), titanium oxide (TiO<sub>2</sub>), and aluminium oxide (Al<sub>2</sub>O<sub>3</sub>) to lubricant is effective on decreasing wear and friction [3,4].

Capable of hBN nanoparticle as an additive in conventional engine oil already been widely study but several successful studies not yet been discovered for treated engine oil. Therefore, this study mainly focuses on the capability of hBN as a new additive with suitable homogenized parameter on the tribological properties for treated SN 0W20 engine oil.

## 2. EXPERIMENTAL SETUP

The samples composition was prepared according to Table 1 and Table 2 shows the L9 orthogonal arrays for testing condition.

Table1 Sample preparation.

Types of nanoparticles	Concentration of nanoparticles	Vol.% SN-0W20	Concentration of surfactant agent (oleic acid)
Hexagonal boron nitride (hBn)	0.5 vol% (1.15 g)	9.2	0.3 vol%
	0.05vol% (0.115 g)	99.65	
	0.1vol % (0.23 g)	99.6	

Table 2. L9 Orthogonal arrays Taguchi Method

Level	Parameter	hBN (vol.%)	Time (min)	Temperature (°C)
1	0.05	10	40	
2	0.05	20	60	
3	0.05	30	80	
4	0.1	10	60	
5	0.1	20	80	
6	0.1	30	40	
7	0.5	10	80	
8	0.5	20	60	
9	0.5	30	40	

Tribological testing was performed to identify the coefficient of friction (COF) and wear rate accordance to ASTM D 4172 followed by scanning electron microscope (SEM). The parameters setup was 1200 rpm, 392.4 N, 3600 sec, and 75°C, respectively. Within the four-ball tester, three 12.7 mm diameter carbon-chrome steel balls were clamped together and covered with lubricant for evaluation. Fourth steel ball (of the same diameter), referred to as the top ball, was held in a special collet inside a spindle and rotated by an AC motor. The top ball was rotated in contact with the three fixed balls, which were immersed in the sample oil.

### 3. RESULTS AND DISCUSSION

According to the S/N ratios analysis shows by Figure 1, the optimal parameter obtained was 0.1 vol.% of hBN nanoparticles composition that heated at 40°C for 30 minutes. Based on the result, homogenized time and temperature show a significant contribution in obtaining the lowest friction and wear.

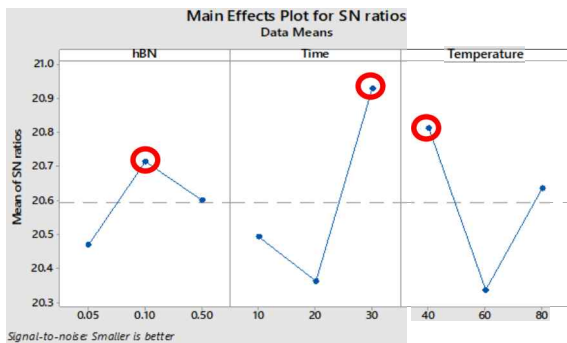


Figure 1 Main effects plot for S/N ratios.

The optimal parameters enhance the tribological property of the sample with a characteristic of low coefficient of friction and wear rate. Based on the result, the longest time exposure during the homogenization process improves the stability of the nanoparticles between the oil molecules [5], beside the control temperature help to reduce the lubricity changes while samples were prepared. This was the advantages of sonification process for dispersed the nanoparticles. Figure 2 shows the CoF result obtained for all the tested sample which show the optimal result give the lowest CoF value indicated by sample 6. Figure 3 shows the wear scar diameter for all tested samples. Sample of optimized parameter obtained the smallest WSD which is 404 μm compared to sample 5 which are the smaller WSD obtained by L9 Orthogonal arrays samples with 631.5 μm and the worse is retained by sample 8 with 643.2 μm.

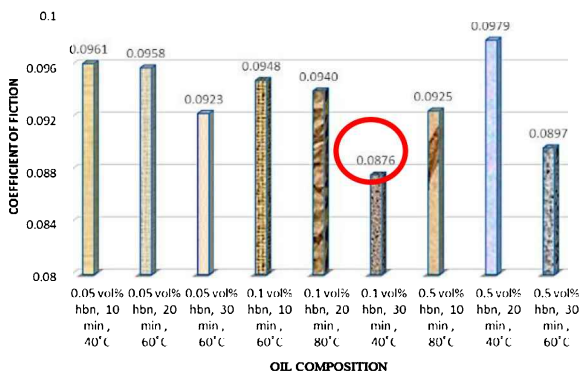


Figure 2 Average CoF value obtained for tested samples.

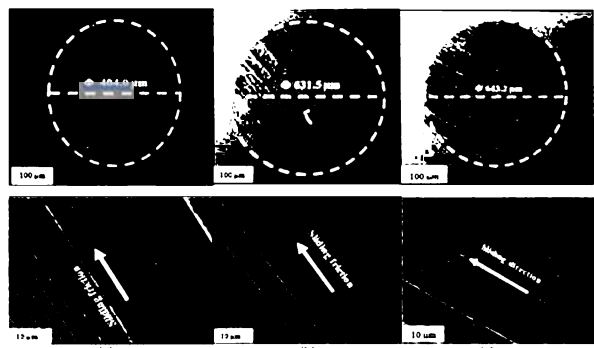


Figure 3 Wear Scar Diameter for sample (a) optimized parameter, (b) sample 5 and (c) sample 8.

### 4. CONCLUSION

The optimal parameter for obtaining the lowest CoF and WSD is given by 0.1 vol.% of hBN nanoparticles composition that heated at 40°C for 30 minutes. Homogenized time and temperature play a significant effect in obtaining the lowest CoF and WSD. Further investigation may help in term of developing solid proved for future nanoparticles as and promising additives in treated SN 0W20 engine oil.

### ACKNOWLEDGEMENT

The author would like to thank Universiti Teknikal Malaysia Melaka and Ministry of Education Malaysia for funding this research under Fundamentals Grant Scheme (FRGS/2018/FTKMP-CARE/F00385).

### REFERENCES

- [1] Abdullah, M. I. H. C., Abdollah, M. F. B., Amiruddin, H., Tamaldin, N., Nuri, N. R. M., Masjuki, H., & Rafeq, S. A. (2014). Improving engine oil properties by dispersion of hBN/Al<sub>2</sub>O<sub>3</sub> nanoparticles. *Applied Mechanics and Materials*, 607, 70-73.
- [2] Shahnazar, S., Bagheri, S., & Hamid, S. B. (2016). Enhancing lubricant properties by nanoparticle additives. *International Journal of Hydrogen Energy*, 41(4), 3153-3170.
- [3] Guzman, B. F. L., Ribeiro, O. S. J., Seabra, M. L., & Kalab, L. A. J. (2018). Experimental investigation of the tribological behavior of lubricants with additive containing copper nanoparticles. *Tribology International*, 117, 52-58.
- [4] Nanthagopal, K., Ashok, B., Tamilarasu, A., Johny, A., & Mohan, A. (2017). Influence on the effect of zinc oxide and titanium dioxide nanoparticles as an additive with Calophyllum inophyllum methyl ester in a CI engine. *Energy Conversion and Management*, 146, 8-19.
- [5] Mohd Nawi, A. E., Abdullah, M. I. H. C., & Abdollah , M. F. B. (2018). Dispersion stability of hBN nanoparticle in liquid phase with different dispersion agents. *Journal of Mechanical Engineering*, 15(2), 143-153.

# Characterization of aluminium oxide composites

Sunil Pathak<sup>1,\*</sup>, Balmukund Dhakar<sup>2</sup>

<sup>1)</sup> Faculty of Engineering Technology, Universiti Malaysia Pahang, Lebuhraya Tun Razak  
26300 Gambang, Kuantan, Pahang, Malaysia

<sup>2)</sup> Department of Mechanical Engineering, Shri G. S. Institute of Technology and Science Indore, 452003, India

\*Corresponding e-mail: sunilpathak@ump.edu.my; sunilpathak87@gmail.com

Keywords: Alumina; hardness; roughness

**ABSTRACT** - Three alumina-based composites were fabricated by die compaction followed by sintering. The porous microstructure was analyzed by SEM (Scanning Electron Microscopy) and EDS (Energy Dispersive X-Ray). In order to know the variation in surface roughness parameters ( $R_a$ ,  $R_z$ ,  $R_{max}$ ) of alumina composites the surface roughness of the samples was measured using a three-dimensional laser surface roughness analyzer. The microhardness values of the composites were evaluated using Vickers microhardness tester.

## 1. INTRODUCTION

In general, the average mechanical properties of alumina composite increase with the increase in alumina composition [1,2]. The bonding of the particles of alumina composite prepared by compaction improves by sintering process. The sintering process starts with the powdered form. The powder of particles is poured into the feed ram. The feed ram moves across the die opening and deposits the alumina powder into the die. The compression ram compresses part is ejected out of the die. The feed ram then moves the compressed part away. The compressed part is placed in oven and heated to a very high temperature which further fuses and sinter, the metal into totally solid form. The part is allowed to cool slowly. The work focuses to study and investigate the morphology of the  $\text{Al}_2\text{O}_3$  composites through Scanning Electron Microscope (SEM) SEM (Scanning Electron Microscopy) and EDS (Energy Dispersive X-Ray). In order to know the variation in surface roughness parameters ( $R_a$ ,  $R_z$ ,  $R_{max}$ ) of alumina composites the surface roughness, this research also aims to study the microhardness of the composites.

## 2. METHODOLOGY

$\alpha$ -alumina powder was used as a raw material. The nomenclature of the samples is shown in Table 1. The alumina powders were consolidated into compacts by pressing un-axially at 30 MPa. The pellets were sintered at 1350°C, 1500°C and 1600°C for 2h soaking time. The surface roughness of the samples has been measured using a laser three dimensional Surface roughness analyzer (COMS, EMS2002 AD-3D 100XY, Japan). The surface roughness profile was obtained using EMS2002AD-3D program. The  $R_a$ ,  $R_z$  and  $R_{max}$  values of each surface were obtained by taking the average of five profiles. The microstructures of the sintered samples have been observed by using a scanning electron microscope (SEM: JEOL, JSM 5600 LV, Japan). It equipped with energy dispersive spectroscopy (EDC,

Oxford Link ISIS 300). The surface and cross-sections were polished by using silicon carbide papers. The related SEM pictures were then processed by image analysis (ImageJ) software to observe the porosity level and pores distribution. Microhardness measurement was carried out by using a Vickers micro indenter (VMHT MOT, Leica Microsystems, Wetzlar, Germany). The indentations were performed at a load of 9.84 N for a dwell time of 15 s.

Table 1 Nomenclature of the samples.

Alumina % composition	Name
86.54	A
93.37	B
84.94	C

## 3. RESULTS AND DISCUSSION

### 3.1 Microstructure

As shown in Figures 1, 2 and 3 the cross-section of the sintering alumina exhibits a typical porous microstructure, characterized by pores with different sizes. The formation of an amorphous phase at lesser extent as displayed in Figure 1, the alumina powder is composed of fused and crushed particles with blocky and angular morphology. Figure 2 shows some pores, microcracks (denoted by black arrows) embedded in microstructure. By analyzing the cross-sectional SEM microstructure in Figure 3 it can be seen that the alumina coating exhibits a lamellar and relatively dense microstructure and pores with different sizes.

### 3.2 Surface Roughness

The variation in surface roughness has been studied by analyzing the variation in surface roughness parameters  $R_a$ ,  $R_z$  and  $R_{max}$  of various surfaces at different composition of alumina. Table 2 presents the detailed results of the surface roughness values in all the three selected samples. The variation in  $R_a$  value for the coating samples were obtained by consolidation using different percentage of alumina.  $R_a$  value for sample A is 3.82  $\mu\text{m}$ , sample B is 10.58  $\mu\text{m}$  and sample C is 1.22  $\mu\text{m}$ . Sample B possesses the highest surface roughness due to the high composition of alumina. There is least difference in  $R_a$  for sample A and sample C as the composition of alumina differences is not really significant. This may be due to effective migration of surface grains during the sintering process. Lesser difference in  $R_z$  is observed for the sample A and sample C. For the sample A,  $R_z$  values show that the roughness is 2.94  $\mu\text{m}$  and for the sample C is 0.933  $\mu\text{m}$  compared to sample B it reached 4.43  $\mu\text{m}$ . It

can also be observed that there was a dramatic change in  $R_z$  value for sample B when the huge amount of alumina was used for the compaction. For the samples,  $R_{max}$  value of 3.827, 10.588 and 1.226 is observed while consolidated using different percentage of alumina, respectively.

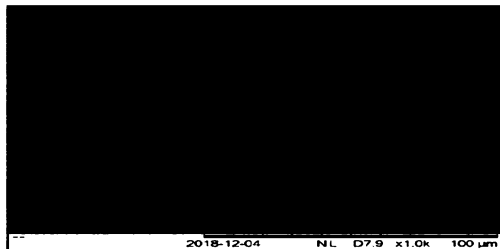


Figure 1 Micrographs of sample A i.e. 86.54% alumina.

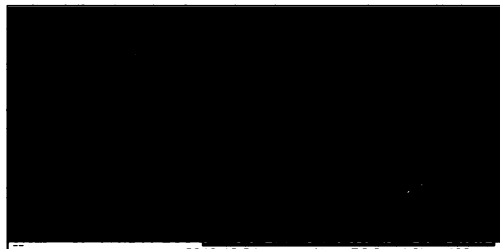


Figure 2 Micrographs of sample B i.e. 93.37% of alumina.



Figure 3 Micrographs of sample C i.e. 84.94% of alumina.

Table 2 Roughness values of the different samples.

<b>Roughness values from 9 different locations</b>	<b><math>R_a</math> (<math>\mu\text{m}</math>)</b>	<b><math>R_z</math> (<math>\mu\text{m}</math>)</b>	<b><math>R_{max}</math> (<math>\mu\text{m}</math>)</b>
Sample A	Average	0.374	2.945
	SD	0.0239	0.245
Sample B	Average	0.457	4.435
	SD	0.321	2.162
Sample C	Average	0.0962	0.926
	SD	0.0151	0.258
			0.442

### 3.3 Microhardness

Table 3 presents the microhardness of the samples. The hardness of the surface of components is an important property affecting their tribological performance. Variations in hardness of alumina composite containing 86.54%, 93.37% and 84.94% weight fractions of  $\text{Al}_2\text{O}_3$  are shown in Table 3. Vickers microhardness of the composite is 1878.82, 1981.94 and 1905.8 HV for the composite containing 86.54%, 93.37% and 84.94% of  $\text{Al}_2\text{O}_3$  respectively. The average hardness increased due to the increase in 37.763% and 37.819% of

$\text{Al}_2\text{O}_3$  weight fraction respectively. It is believed that due to high hardness of  $\text{Al}_2\text{O}_3$  and stronger interfacial bonding between particulates at higher sintering temperature, the improvement in the hardness of the ceramic coatings occurred. However, the value of the hardness for all the compositions is although different in number but all the materials are considered possessing same hardness. This is because the value of hardness is measured in the range and if there is small difference in value, the material is not considered as difference in hardness.

Table 3 Microhardness of the different samples.

SAMPLE	A	B	C	
1748.9	1977.2	2204.9		
1748.9	1921.9	1658.5		
1689.9	2158.2	1621.9		
2253.2	1961.1	2121.8		
1953.2	1891.3	1921.9		
Average (HV)	1878.82	1981.94	1905.8	
SD	231.917	104.097	263.691	

### 4. CONCLUSION

The microstructure of the alumina composite C is the best from the other sample because the amount/quantity of the porous is less as compared to other samples. If the process happened at the optimum level the structure will be more systematic and the bonding between the particles is stronger because there will be no space for the porous between the atomic or elements structure.

Attempts have been made to study the variation in the roughness parameters when the alumina percentage is different. It is important to make compacts with the least alumina compositions to the roughness of the surface to analyze a homogeneous uniform microstructure. The roughness values found high in the sample where alumina percentage is more [3].

Hardness of the alumina-based composite depend on alumina percentage as can be seen from sample B which has the highest hardness value and contain maximum amount of alumina ceramics [4,5]. However, the least differences in percentage of alumina in case of sample A and C, the result still showing there is insignificant difference in the hardness value. It can be said that the alumina powder that possessing in the composite affected the surface hardness of the materials significantly.

### ACKNOWLEDGEMENT

Authors thank Universiti Malaysia Pahang for the funding provided to conduct this research through Research Grant (RDU1703113).

### REFERENCES

- [1] Pathak, S., & Saha, G. (2017). Development of sustainable cold spray coatings and 3D additive manufacturing components for repair/manufacturing applications: a critical review. *Coatings*, 7(8), 122.
- [2] Dhakar, B., Chatterjee, S., & Sabiruddin, K. (2017). Phase stabilization of plasma-sprayed alumina coatings by spraying mechanically blended

- alumina–chromia powders. *Materials and Manufacturing Processes*, 32(4), 355-364.
- [3] Dhakar, B., Chatterjee, S., & Sabiruddin, K. (2017). Measuring mechanical properties of plasma-sprayed alumina coatings by nanoindentation technique. *Materials Science and Technology*, 33(3), 285-293.
- [4] Dhakar, B., Chatterjee, S., & Sabiruddin, K. (2017). Influence of process parameters on the formation of phases and mechanical properties of plasma sprayed Al<sub>2</sub>O<sub>3</sub>–Cr<sub>2</sub>O<sub>3</sub> coatings. *Materials research innovations*, 21(6), 367-376.
- [5] Dhakar, B. M., Dwivedi, D. K., & Sharma, S. P. (2012). Studies on remelting of tungsten carbide and rare earth modified nickel base alloy composite coating. *Surface engineering*, 28(1), 73-80.

# Friction and wear mechanisms of palm kernel activated carbon polymer composite by Raman spectroscopy study

Dayang Nor Fatin Mahmud<sup>1</sup>, Hilmi Amiruddin<sup>1,2</sup>, Mohd Fadzli Bin Abdollah<sup>1,2,\*</sup>, Nor Azmmi Bin Masripan<sup>1,2</sup>, Mohd Rody Bin Mohamad Zin<sup>1,2</sup>, Noreffendy Tamaldin<sup>1,2</sup>

<sup>1)</sup> Fakulti Kejuruteraan Mekanikal, Universiti Teknikal Malaysia Melaka,  
Hang Tuah Jaya, 76100 Durian Tunggal, Melaka, Malaysia

<sup>2)</sup> Centre for Advanced Research on Energy, Universiti Teknikal Malaysia Melaka,  
Hang Tuah Jaya, 76100 Durian Tunggal, Melaka, Malaysia

\*Corresponding e-mail: mohdfadzli@utem.edu.my

**Keywords:** Palm kernel activated carbon; polymer; friction; wear; Raman spectroscopy

**ABSTRACT** – The objective of this paper is to investigate the friction and wear mechanisms of palm kernel activated carbon (PKAC) polymer composite by Raman spectroscopy study. A ball-on-disc tribometer was used to conduct the dry sliding test at different degree of contact pressures with constant sliding speed, sliding distance and operating temperature. The results found that the coefficient of friction (COF) of the composite decreases with the contact pressure, though the wear rate remains at an almost constant value. Then, COF and wear rate increased drastically when exceeding a critical limit of 90MPa. Raman spectroscopy study reveals that phase transformation of PKAC polymer composite changed from a carbon-like-structure to a graphite-like-structure ( $sp^2$ ) on the top layer of the composite.

## 1. INTRODUCTION

At the present times, there is an encouraging emergence of alternative technologies such as thin bio/eco-materials, film coatings and green lubricants that were being used to offer a sustainable supply for the global need by reducing friction and wear of components or parts as a mean to save energy [1]. Malaysia is one of the biggest user and exporters of palm oil in the global arena. The palm oil industry produces a vast amount of waste comprising of around 90% of biomass waste and just around 10% of the palm oil. The utilization of agricultural waste as another composite material has additionally been observed to be inexhaustible and generally more affordable and at last could use the waste viably into riches. In this way, this propelled us to explore the capability of enacted carbon got from one of the biggest waste palm oils called activated carbon-epoxy composite derived from palm kernel be used as a new tribological material [2].

The activated carbon-epoxy composite derived from palm kernel also known as palm oil extraction waste materials, is composed of carbonaceous, highly porous adsorptive medium that has a similar atomic structure to that of graphite, but in a disorganised form. Furthermore, this activated carbon in the form of composite has high potential to be a self-lubricating material with a little friction coefficient and more durable wear resistance caused by the presence of the remaining natural oils in palm kernel [3].

There were few researches that describe the operating state effects on the features of activated carbon-epoxy composite tribology from the palm kernel, such as effect of composition, operating parameter and surface texture. Nevertheless, studies on effect of contact pressure and its mechanisms is still limited to explore the features of palm kernel activated carbon (PKAC) polymer composite. Therefore, the purpose of this study is to investigate the friction and wear mechanisms of palm kernel activated carbon (PKAC) polymer composite by Raman spectroscopy study at various contact pressures dry sliding conditions.

## 2. EXPERIMENTAL PROCEDURE

A disc with 74mm in diameter, 5mm thickness was produced by mixing 60 wt.% PKAC (250  $\mu$ m particle size) with 40 wt.% epoxy, where the hardener to resin ratio is 1:4. The mixture was then put into a mould and pressed using a hot-press machine.

The dry sliding experiment was carried out utilising a ball-on-disc tribometer, in accordance with ASTM G99-05 (2016). All tests were performed at different applied contact pressure between 59.84 and 119.99MPa, with a 500rpm sliding speed at 3000 m of perpetual sliding distance. The operating temperature is 27°C. ASTM52100 (EN31) chrome steel ball, as a counter surface, with two different diameter sizes of 10mm and 12.7mm, was used in this study. Each of the test was then repeated for three times to lessen the errors in the experimental. The phase transformation of composite was analysed by adopting the UniRAM 3500 Raman spectroscopy. The physical-mechanical properties of both disc and ball are shown in Table 1.

Table 1 Physical-mechanical properties of the ball and disc materials before testing.

Properties	<sup>a</sup> Disc	<sup>b</sup> Steel ball
Hardness, $H$ [GPa]	8.36	7.45
Young Modulus, $E$ [GPa]	7.61	210
Poisson's ratio, $\nu$	0.23	0.3
Density, $\rho$ [g/cm <sup>3</sup> ]	1.4	7.81
Surface roughness, $R_a$ [ $\mu$ m]	0.4	0.022

<sup>a</sup> Properties acquired from laboratory measurements.

<sup>b</sup> Properties acquired from manufacturer.

### 3. RESULTS AND DISCUSSION

Figure 1 presents the data on coefficient of friction (COF) and the wear rate of PKAC polymer composite. It can be seen that at the beginning, COF decreases with contact pressure, though the wear rate remains at an almost constant value. This could imply that the transfer layer formation on the counter surfaces, could have accounted for the decreasing COF and wear rate due to the surface contact changes from carbonised-steel to carbonised-carbonised materials [4]. This phenomenon could also be deduced by the friction-induced phase

transformation; which will be discussed later. However, when the contact pressure increases to the critical limit of 90MPa, the COF and wear rate rose dramatically due to the deterioration of this transfer layer, thus forcing the counter surface of the protective layer to disappear. This also signifies that the contact surface has experienced high abrasion due to the ploughing between the contact surfaces, which might have influenced the increment of the friction force and wear rate, which led to removal of the material [5].

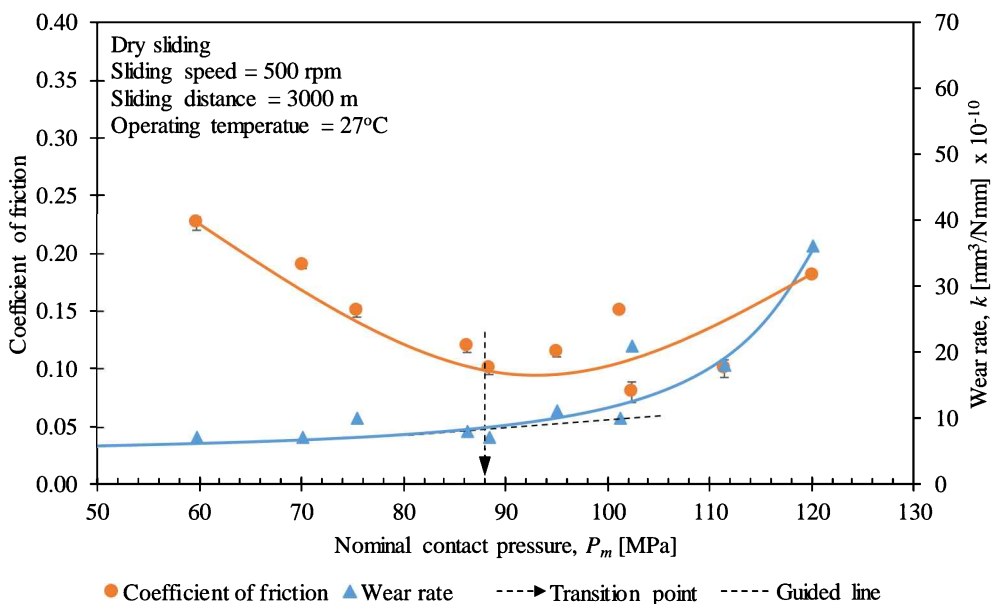


Figure 1 Effect of contact pressure on the coefficient of friction and wear rate of PKAC polymer composite.

Figure 2 presents typical Raman spectra obtained from the activated carbon derived of palm kernel epoxy disc composite before testing and from the wear track region after dry sliding test (500 rpm sliding speed). Based on this study, the composite bond structure, at atomic scale, was described with the ratio of intensity ( $I_D/I_G$ ), G-shift and full-width at half maximum (FWHM) of G peak. From Figure 2, it shows that the G peak shifted to a higher frequency at  $1583.87\text{ cm}^{-1}$  (G peak), compared to the composite before testing at  $1577.76\text{ cm}^{-1}$  (G peak). While, the  $I_D/I_G$  ratio increased with contact pressure, accompanied by a narrowing of FWHM for the G peak, which correlated well to a higher  $\text{sp}^2$  content [6]. Thus, the Raman spectra clearly show a change in the wear track surface structure from carbon-like to graphite-like structure.

### 4. CONCLUSION

In a dry sliding test, at the beginning when the value of contact pressure increase it can be seen that COF decreases, though the wear rate remains at an almost constant value. However, when the contact pressure exceeds a critical limit of 90MPa, the friction coefficient and the wear rate of PKAC polymer composite rapidly increased. Furthermore, from phase transformation study, the stability of friction and wear of disc composite is due to the changes of surface layer phase transformation.

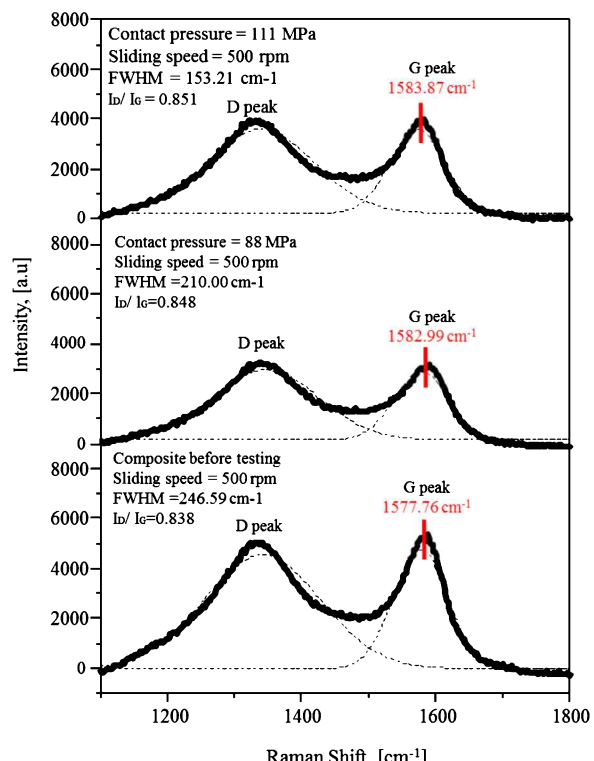


Figure 2 Raman spectra of the disc composite.

**ACKNOWLEDGMENT**

The project is supported by a grant from Universiti Teknikal Malaysia Melaka (Grant no.: PJP/2019/FKM(10A)/S01683).

**REFERENCES**

- [1] Abdollah, M. F. B., Yamaguchi, Y., Akao, T., Inayoshi, N., Tokoroyama, T., and Umehara, N., 2011. The effect of maximum normal impact load, absorbed energy, and contact impulse, on the impact crater volume/depth of DLC coating. *Tribology Online*, 6(6), pp. 257-264.
- [2] Lagel, M. C., Hai, L., Pizzi, A., Basso, M. C., Delmotte, L., Abdalla, S., Zahed, A., and Al-Marzouki, F.M., (2016). Automotive brake pads made with a bioresin matrix. *Industrial Crops and Products*, 85, pp. 372-381.
- [3] Yahya, M. A., Al-Qodah, Z., Ngah, C. Z., (2015). Agricultural bio-waste materials as potential sustainable precursors used for activated carbon production: A review. *Renewable and Sustainable Energy Reviews*, 46, 218-235.
- [4] Mahmud, D. N. F., Abdollah, M. F. B., Masripan, N. A. B., Tamaldin, N., & Amiruddin, H. (2019). Influence of contact pressure and sliding speed dependence on the tribological characteristics of an activated carbon-epoxy composite derived from palm kernel under dry sliding conditions. *Friction*, 7(3), pp. 227–236.
- [5] Chowdhury, M. A., and Helali, M. M., 2008. The effect of amplitude of vibration on the coefficient of friction for different materials. *Tribology International*, 41(4), pp. 307–14.
- [6] Jiu, J. T., Wang, H., Cao, C. B., Zhu, J. T., Jiu, H., Wang, C. B., and Cao Zhu, H. S., 1999. Effect of annealing temperature on the structure of diamond-like carbon films by electrodeposition technique. *Journal of Materials Science*, 34(21), pp. 5205-5209.

# An Investigation of chip formation on different penetration angle for orthopaedic surgical bone drilling

M.S. Noorazizi<sup>1,2,\*</sup>, K.R. Jamaludin<sup>1</sup>, S. Sarip<sup>1</sup>, R. Izamshah<sup>2</sup>, R. Zamri, L. Abdullah, M.N. Maslan<sup>2</sup>

<sup>1)</sup> Fakulti Teknologi dan Informatik Razak, Universiti Teknologi Malaysia,  
Jalan Sultan Yahya Petra, 54100, Kuala Lumpur, Malaysia

<sup>2)</sup> Fakulti Kejuruteraan Pembuatan, Universiti Teknikal Malaysia Melaka,  
Hang Tuah Jaya, 76100 Durian Tunggal, Melaka, Malaysia

\*Corresponding e-mail: noorazizi@utm.my

**Keywords:** Chips formation; bone drilling; hole quality

**ABSTRACT** – This work is to investigate the effects of chips formation type on the quality of bone drilling procedure. Totals of 17 drills were design and tested with different geometry namely point angle, helix angle and web thickness on different penetration angle ( $0^\circ$ ,  $15^\circ$ , and  $30^\circ$ ) to mimic the manually control penetration by the surgeon. The results depict that variation in chip formation morphology depends on drills design geometry, drilling parameters and different penetration angle. The chip morphology physical shape in bone drilling in this experiment can be categorized as powder, needle, conical fan, short spiral fan and long conical fan with different size. It can be observed that penetration angle  $0^\circ$  and  $15^\circ$  give the small sizes chips morphology compared to  $30^\circ$  for all the drills design.

## 1. INTRODUCTION

One of the principal methods for repairing and reconstruction of a bone fracture are achieved by drilling the bone and fixing the separate parts together using screws, wires and plates. Many problems are encountered with the bone drilling process such as holes accuracy, drill wander and excessive heat generation which were directly related with the drilling parameter [1,4]. Many different drill-bit designs and geometries have been suggested over the years each with its own promising results [2-4]. However, most of the studies neglected the effects of penetration angle on the drilling performances. Generally, in normal orthopedic surgery, bone drilling is performed using hand drills and the penetration angles is greatly dependent on the surgeon's manual skill and are normally deviated from the normal axis. Hole quality in bone drilling is evaluated in terms of hole error diameter and cylindricity, surface roughness, and burr [1]. Equally important, drilling quality includes aperture deviation, migration and gradient of the aperture axis and the changes of surface geometry. In this paper knowledge between both drill geometrical parameter and drilling penetration angle on the chip formation will be identified.

## 2. EXPERIMENTAL WORK

In this experiment, AISI 420B stainless steel medical grade rod with diameter 4.3 mm were ground to form the drill bits with varying angles namely point angle, helix angle and web thickness as depicted in Table 1. Stainless steel drill bit exhibits good corrosion resistance and can minimize the tool wear effect. Totals

of 51 holes were drilled with 3 holes replication for each run. To eliminate the apparatus wear impact on the result, the apparatus was cleaned with a brush and wet tissue before each drilling process.

Table 1 Drill geometrical angles design level.

Name	Unit	Low	High
A Web Thickness	%	14	32
B Point Angle	°	90	140
C Helix Angle	°	16	38
D Penetration Angle	°	0	30

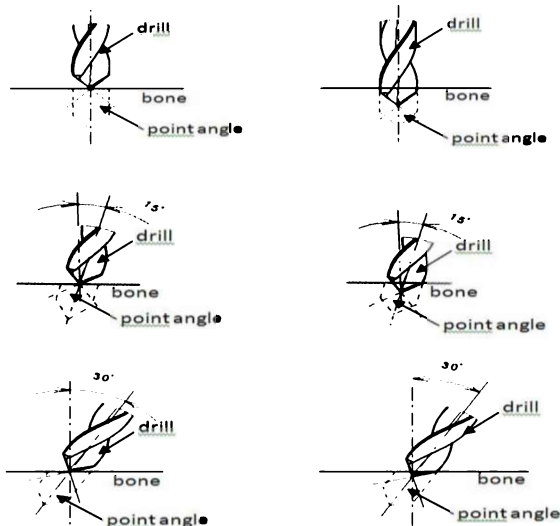


Figure 1 Drill bit position before entry and after  $0^\circ$ ,  $15^\circ$ , and  $30^\circ$  penetration angles.

Bovine cortical femur bone was chosen as the work material due to its closeness properties and characteristics with human bone [3-5]. Fresh cortical (compact bone) samples are cuts and mills from bovine femur with a uniform thickness of 4 mm. The drilling tests were performed using a DMU60 monoBLOCK DECKEL MAHO CNC 5-Axis Machine. The drilling speed of 1000 rpm and 100 mm/min feed rate were employed to represent the actual manual surgical hand drills speed and surgeon penetration feed ( $0^\circ$ ,  $15^\circ$ , and  $30^\circ$ ) as shown in Figure 1. Optical microscope (EMZ-Meiji) equipped with a digital camera was used for the analysis and observation of hole accuracy, burr and chip

formation. This optical microscope has a 93mm working distance with rotatable through 360° as shown in Figure 2.



Figure 2 Optical microscope (EMZ-Meiji) equipped with digital camera.

### 3. RESULTS AND DISCUSSION

In this experiment, the chip formation was observed from the moment the drill lips touched the bone surface until the end of the hole. More importantly, it has two flutes to carry the chips up from the cutting edges to the top of the hole where they are cast off. From the observation, the bone chips were seen rotating along the drill bit rubbing against the hole's surface and blocking the flutes. The bone chips also impacted the hole wall surface which produced a bending moment in the chip leading to its fracture once the strain in the chip exceeded the critical value. In general, the chip morphology physical shape in bone drilling in this experiment can be categorized such as powder, needle, conical fan, short spiral fan and long conical fan as shown in Figure 3.



Figure 3 Chip shapes generated by drilling bone powder with needle and conical fan.

Some bone chip samples were taken to determine the chip morphology during bone drilling. The comparison bone chip shapes produce by different penetration mode were shown in Table 2.

Table 2 Comparison chip shapes produce by different penetration mode.

Penetration	0	15	30
Morphology	Long spiral fan shape	Short spiral fan shape	Short conical fan shape
Shape	Long spiral fan shape	Short spiral fan shape	Short conical fan shape
Size	1.55mm	1.82mm	2.02mm

From the results shape chip formation of sample 15 design drill bit (Web Thickness: 23%, Point Angle: 115°, Helix Angle: 27°) at 0° penetration angle. Macroscopic observations show that long spirals fan shape were built with the conical top size = 1.55mm and the down size = 478μm. It is different as short spiral fan shape chip formation of at 15° penetration angle. The conical size of the chip is higher at the top = 1.82mm and down conical shape size = 670μm. Meanwhile at 30° penetration angle from macroscopic observation shows that short conical fan shape was built with the conical top size = 2.02mm and the conical down size = 707μm.

### 4. CONCLUSION

Hence, understanding the effects of drilling geometry parameter on the hole performances is important to provide the reference values for the development of high-performance surgical drill designs in orthopedic bone surgery application. It can be seen that drilling in the higher penetration angle slightly increased the size of chip shape compared to the 0° and 15° penetration angles.

### ACKNOWLEDGEMENT

The authors wish to thank Universiti Teknologi Malaysia, Universiti Teknikal Malaysia Melaka, Hospital Angkatan Tentera Kem Terendak Melaka and the UTM RMC through Research University Grant Tier 2 for the technical and financial support for the experiment.

### REFERENCES

- [1] Samsuddin, N. M., Izamshah, R., Kasim, M. S., & Haron, C. H. C. (2017). Evaluation of Hole Performance and Force Magnitude on Drilling Parameter for Orthopaedic Surgical Bone Drilling. *Journal of Mechanical Engineering*, (2), 37-47.
- [2] Pandey, R. K., & Panda, S. S. (2013). Drilling of bone: A comprehensive review. *Journal of clinical orthopaedics and trauma*, 4(1), 15-30.
- [3] Izamshah, R., Noorazizi, M. S., Kasim, M. S., & Haron, C. C. (2016, February). Influence of Orthopaedic Drilling Parameters on Surface Roughness and Cutting Force of Bone Drilling Process. In *International Conference on Electronics, Mechanics, Culture and Medicine*. Atlantis Press.
- [4] Hillery, M. T., & Shuaib, I. (1996). The Drilling of Bone Using Guide Wires and Twist Drills, MT Hillery, ed. In *Proceedings of the 13th Irish Manufacturing Conference (IMC-13)*, Limerick, Ireland, September (pp. 4-6).
- [5] Vashishth, D., Tanner, K. E., & Bonfield, W. (2000). Contribution, development and morphology of microcracking in cortical bone during crack propagation. *Journal of Biomechanics*, 33(9), 1169-1174.

# Effect of single zincating duration on the properties of copper activated aluminium Alloy 7075 substrate

Intan Sharhida Othman<sup>1,\*</sup>, Marco Starink<sup>2</sup>, Shun Chai Wang<sup>2</sup>

<sup>1)</sup>Fakulti Kejuruteraan Pembuatan, Universiti Teknikal Malaysia Melaka,

Hang Tuah Jaya, 76100 Durian Tunggal, Melaka, Malaysia

<sup>2)</sup>School of Engineering, University of Southampton, SO17 1BJ Southampton, United Kingdom

\*Corresponding e-mail: intan\_sharhida@utm.edu.my

**Keywords:** aluminium alloy 7075, nickel coating, copper activation, adhesion, zincating, electrodeposition

**ABSTRACT** – A combination of copper activation processing with various single zincating durations was applied on aluminium alloy 7075 (AA7075) substrate, in order to overcome the drawbacks of conventional single zincating. The evolution of surface morphology and surface composition during the zincating process at various durations were characterized by scanning electron microscopy (SEM) and energy dispersive x-rays analysis (EDX). The adhesion of the coating was investigated using a scratch tester. SEM result shows the uniformity of the zinc particles on the substrates was improved by increasing the single zincating duration. The adhesion of the composite coating was improved at longer zincating duration as compared to the conventional single zincating process. The morphology has contributed to the improvement of coating adhesion.

## 1. INTRODUCTION

Extensive research has been carried out in academia and in industry to find the most suitable and effective method of surface pre-treatment on aluminium alloys. The research included direct plating on aluminium alloys [1], a pre-electrodeposition process [2], zincating processes [3], zincating process with copper pre-treatment [4], and nickel striking [5]. Among these, the most satisfactory and practical method of surface pre-treatment process for plating on aluminium alloys is the zincate immersion treatment, which is known as zincating. Zincating treatment produces a zinc layer on the surface of the aluminium alloys, thus preventing the formation of aluminium oxide and providing adequate contact with any metal electroplated onto these alloys [6,7].

However, Azumi et al. [8] found a continuous dissolution of the aluminium alloys during the first and second zincating. The high dissolution reaction of the aluminium substrate in a concentrated alkaline zincating solution may lead to a serious damage of the substrate [9]. The dissolution of substrates and uniform distribution of zinc deposits can be improved by applying a copper pre-treatment before the zincating process [4, 8]. These copper deposit act as nucleation sites for zinc deposition during the zincating process and produce a uniform and dense layer of zinc deposits which almost completely cover the substrate [4].

To the best of our knowledge, the effects of combination of copper activation process with various single zincating duration on electrodeposited nickel coating on AA7075 substrate has not been reported.

Therefore, the objective of this paper is to improve the conventional single zincating process by extending the immersion duration of the copper activated substrate in zincating solution.

## 2. METHODOLOGY

The AA 7075 substrate was first immersed in an etching solution containing  $0.5\text{ M H}_2\text{SO}_4 + 3.13 \times 10^{-4}\text{ M CuSO}_4$  at room temperature for 10 minutes to achieve the copper activation process. The conventional single zincating process involves immersion of the substrate in the zincating solution for 1 minute and in this work, this was extended to 5, 15, 10 and 20 minutes. The current density used for the electrodeposition process was  $4\text{ A/dm}^2$  under direct current mode with the total time of electrodeposition set at one hour. The composition of the electrolyte is as follows:NiSO<sub>4</sub>.6H<sub>2</sub>O (200 g/l), NaCl (20 g/l), C<sub>12</sub>H<sub>25</sub>SO<sub>4</sub>Na (0.2 g/l), C<sub>7</sub>H<sub>5</sub>NO<sub>3</sub>S (3 g/l), H<sub>3</sub>BO<sub>3</sub> (30 g/l) and 2-butyne-1,4-diol,C<sub>4</sub>H<sub>6</sub>O<sub>2</sub> (0.5 g/l). The zincating solution consists of ZnO (100 g/l), NaOH (525 g/l), FeCl (1 g/l) and KNaC<sub>4</sub>H<sub>4</sub>O<sub>6</sub>.4H<sub>2</sub>O (9.8 g/l). The coating adhesions were evaluated by scratch tester (Teer Coating, ST-3001) and the failures were then analyzed using optical microscopy (OM).

## 3. RESULTS AND DISCUSSION

### 3.1 Surface Morphology and Elemental Composition of Copper Activated Substrate

From EDX analysis in the SEM, it was confirmed that bright particles which were deposited on the substrate after the copper activation process are copper (Figure 1).

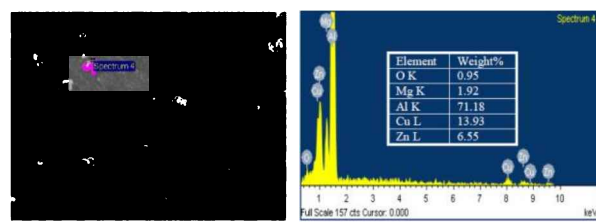


Figure 1 SEM micrograph and EDX analysis of copper activated AA7075 substrates at 10 minutes.

### 3.2 Effect of Single Zincating Duration on the Surface Morphology of Copper Activated Substrate

After 5 minutes of immersion in the zincating solution, growth of zinc nuclei was observed on the

surface (Figure 2(b)). As the duration increased to 10 minutes, the zinc particles became bigger and some agglomerations occurred (Figure 2(c)). After 15 minutes, the zinc particles were continuously growing and by 20 minutes, the zinc particles completely covered the surface (Figure 2(d,e)). It is apparent in the figure that a high density of zinc particles occurs for the longer zincating duration studied.

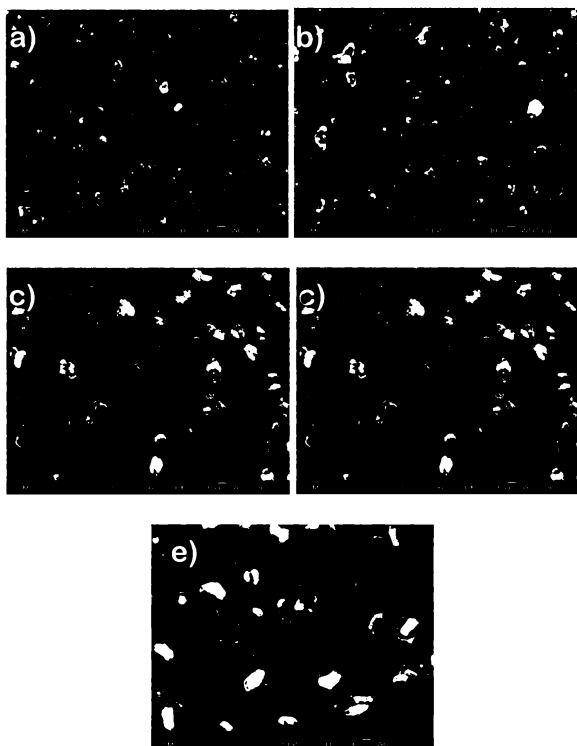


Figure 2 SEM micrographs of AA7075 substrates after various single zincating durations with copper activation, (a) 1, (b) 5, (c) 10, (d) 15 and (e) 20 minutes.

### 3.3 Effect of Single Zincating Durations on the Adhesion of Composite Coatings

As the progressive applied loads increased during the scratch test, more cracks were generated by the diamond stylus (Figure 3). The most striking result to emerge from the scratch testing is that only the sample which was produced from 1 minute of single zincating showed adhesive failure. The coating was ruptured by wedge spallation at the end of the scratch track, which indicates this coating had poor bonding to the substrate. On the other hand, samples which were produced using the 5, 10, 15 and 20 minutes of modified single zincating process only exhibited cohesive failure as the progressive applied load increased, with no adhesive failure observed along the track. This means these coatings adhered well to the substrate. It is thought that a good coverage of zinc particles on the substrate enhances the uniform growth of the subsequent coating and increases the adhesion of the coating to the substrate (see also [10]).

## 4. CONCLUSION

SEM morphologies show that the size and density of zinc particles for single zincating with copper activation increased with increasing zincating duration. Coatings which were produced at a longer duration did

not show any delamination even at high progressive load. These coatings only experienced a cohesive failure mode, which means the coatings adhered well to the substrate. The sufficient coverage of zinc particles on the substrate has increased the adhesion between coating and the substrate.

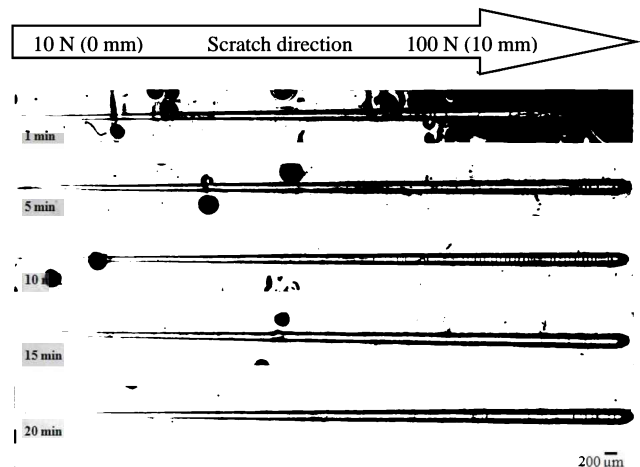


Figure 3 OM of the scratch tracks of nickel electrodeposited on AA7075 produced at various single zincating durations with copper activation.

## ACKNOWLEDGEMENT

The authors would like to thank Ministry of Education Malaysia (KPT(BS)810526086238) for sponsoring this research. Also, thanks to Faculty of Engineering and the Environment, University of Southampton for the laboratory facilities and the chemical supplies.

## REFERENCES

- [1] Rajendran, R., Sha, W., & Elansezhan, R. (2010). Abrasive wear resistance of electroless Ni-P coated aluminium after post treatment. *Surface and Coatings Technology*, 205(3), 766-772.
- [2] Azumi, K., Yugiri, T., Kurihara, T., Seo, M., Habazaki, H., & Fujimoto, S. (2003). Direct plating of electroless Ni-P layers on sputter-deposited Al-Ni alloy films. *Journal of The Electrochemical Society*, 150(7), C461-C464.
- [3] Schwankl, M., Wedler, J., & Körner, C. (2016). Wrought Al-Cast Al compound casting based on zincate treatment for aluminum wrought alloy inserts. *Journal of Materials Processing Technology*, 238, 160-168.
- [4] Tang, J., & Azumi, K. (2011). Effect of copper pretreatment on the zincate process and subsequent electroplating of a protective copper/nickel deposit on the AZ91D magnesium alloy. *Electrochimica Acta*, 56(24), 8776-8782.
- [5] Sudagar, J., Venkateswarlu, K., & Lian, J. (2010). Dry sliding wear properties of a 7075-T6 aluminum alloy coated with Ni-P (h) in different pretreatment conditions. *Journal of Materials Engineering and Performance*, 19(6), 810-818.
- [6] Lee, J. H., Lee, I. G., Kang, T., Kim, N. S., & Oh, S. Y. (2005). The effects of bath composition on the morphologies of electroless nickel under-bump

- metallurgy on Al input/output pad. *Journal of Electronic Materials*, 34(1), 12-18.
- [7] Robertson, S. G., Ritchie, I. M., & Druskovich, D. M. (1995). A kinetic and electrochemical study of the zincate immersion process for aluminium. *Journal of applied electrochemistry*, 25(7), 659-666.
- [8] Azumi, K., Egoshi, S., Kawashima, S., & Koyama, Y. (2007). Effect of copper pretreatment on the double zincate process of aluminum alloy films. *Journal of The Electrochemical Society*, 154(4), D220-D226.
- [9] Egoshi, S., Azumi, K., Konno, H., Ebihara, K., & Taguchi, Y. (2012). Effects of minor elements in Al alloy on zincate pretreatment. *Applied Surface Science*, 261, 567-573.
- Jin, J. G., Lee, S. K., & Kim, Y. H. (2004). Adhesion improvement of electroless plated Ni layer by ultrasonic agitation during zincating process. *Thin Solid Films*, 466(1-2), 272-278.

# Surface characterization of oxide films formed on aluminium alloy with the incorporation of graphite

Syazwani Mohamad, Shahira Liza Kamis\*, Jun Ishimatsu

TriPreM i-Kohza, Mechanical Precision Engineering Department, Malaysia - Japan International Institute of Technology (MJIIT), Universiti Teknologi Malaysia, Jalan Sultan Yahya Petra, 54100 Kuala Lumpur, Malaysia

\*Corresponding e-mail: shahiraliza@utm.my

**Keywords:** Aluminum alloy; anodic composite film; surface porosity

**ABSTRACT** – Hard anodizing represents useful surface treatment on aluminium alloy which provide good microhardness and wear resistance. Graphite is a good reinforcement in the oxide film due to its good mechanical, low friction and self - lubricating behavior. Thus, the aim of this research is to investigate the growth mechanism of oxide film surface containing graphite. The surface morphology and 3D images were observed on scanning electron microscopy and 3D profiler respectively. The film structure was examined by Raman spectroscopy. The result showed the surface porosity was reduced when comparing to the oxide film without graphite. Raman spectra of D and G peak proved the existence of graphite on the oxide film surface can be observed in early 5 min of anodizing process.

## 1. INTRODUCTION

Aluminium (Al) alloy is one of the light weight and high strength materials which widely being used in aircraft, aviation industries and automotive parts such as power transmission gears, sprockets, drill pipes and engineering tools [1]. However, low hardness and poor wear resistance are the main obstacles to prolong the service life of Al alloys and further industrial applications as mentioned by Yang et al. [2]. Although surface modification like anodizing had been introduced to improve their surface properties, it is complicated to serve complex heat treatable Al alloy like 2XXX series that has high constituents of copper as alloying element which disturb the oxide layer formation during anodization process [3]. Some intermetallic precipitates (e.g. Al<sub>2</sub>Cu, Al<sub>2</sub>CuMg) in Al alloy 2XXX may cause difficulty in order to get a hard and compact oxide layer [4]. In addition, oxygen evolution induced porous structure of the oxide layer and lead to highly flaws on the surface. These issues have received considerable critical attentions from many researchers by improving the parameters of the anodizing process.

The incorporation of particles such as TiO<sub>2</sub>, ZrO<sub>2</sub>, Al<sub>2</sub>O<sub>3</sub>, SiC and PTFE in the matrix of the oxide films had improved its hardness and tribological properties as stated by Kamis and Sofi [5]. Indeed, graphite may be a good candidate as reinforcement particle due to its good mechanical properties and low friction. However, the surface characterization of oxide film containing graphite is still less study. The aim of this research is to study the surface properties based on the incorporation of graphite particles in the oxide film produced by anodizing process.

## 2. METHODOLOGY

Anodization was performed on Al alloy A2017-T4 disk with diameter Ø25 mm and thickness 4 mm by using the laboratory anodizing system as shown in Figure 1 that consist of a direct current (DC) power supply and an electrolytic solution contains 20 wt. % diluted sulfuric acid with graphite. The graphite was added into the electrolyte. The anodizing process was experimented by using a constant current (2.0 A) and operating fluctuant voltage ( $\pm 15$  V) of DC power supply. The cell consisted of a copper plate 30 mm x 60 mm at the cathode and the specimen as the anode. The temperature of electrolyte was kept at the room temperature. Firstly, the samples were anodized with 1.0 g/L of graphite contains at different times, being 5, 30 and 60 min respectively. After that, anodization process was continued by using different content of graphite; 0 g/L, and 1.0 g/L in order to clarify the improvement of mechanical and tribological characteristic of oxide films compared to the neat Al alloy.

The surface morphology will be characterized by using spectroscopy electron microscopy (SEM) JEOL JSM-6010PLUS/ LV. The 3D optical surface profiler ZeGage™ Ultra Precision Technology AMETEK (Zygo) was used to determine the 3D image profiling and to verify the size of micropores. Raman spectroscopy mainly be used to determine the structure of films and the existence of graphite in the oxide films.

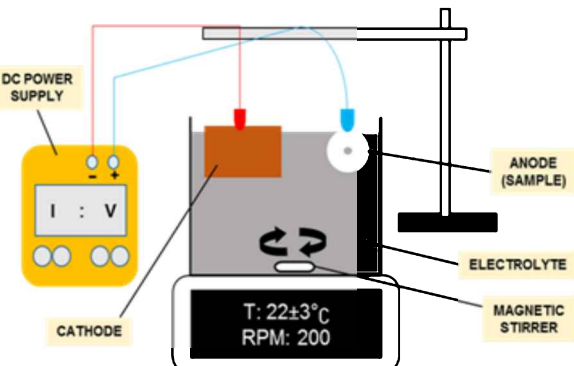


Figure 1 The schematic diagram of anodizing setup.

## 3. RESULTS AND DISCUSSION

Figure 2 shows the surface morphology of oxide films containing graphite at 5, 30, and 60 min. Anodize oxide film with graphite at 5 min, the surface morphology is seemed quite similar to the neat Al alloy which consist of a circle and granulate shapes of intermetallic precipitates where they can be clarified as the initial stage

of the growing oxide film. At 30 min, the obvious porosity started to form on the film and at 60 min, the films seem compact as longer time, but it still cannot determine the bumps or pores of films. In order to prove the assumption, the 3D image of oxide films at 5 min, 30 min and 60 min were studied as shown in Figure 2. It can be seen that the porosity started to develop at 30 min. The depth and width of porosity were found to increase as the longer anodizing duration as shown in Table 1. Thus, the time can affect surface defect of oxide film.

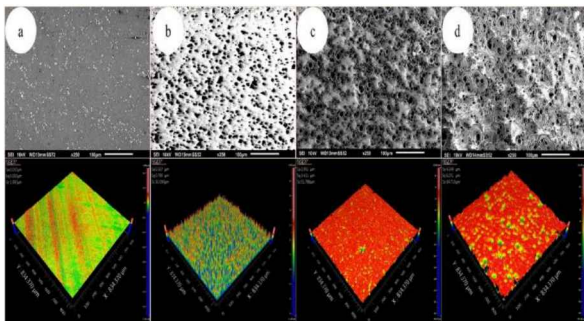


Figure 2 Surface morphology and 3D surface profile of neat Al alloy and oxide films with graphite at different anodizing time: (a) neat Al alloy (b) 5 min (c) 30 min (d) 60 min.

Table 1 The depth and width porosity measurement of oxide films containing graphite.

	5 min	30 min	60 min
Depth ( $\mu\text{m}$ )	-	28.7217 $\pm$ 6.02	38.227 $\pm$ 5.99
Width ( $\mu\text{m}$ )	-	33.6054 $\pm$ 3.75	63.5547 $\pm$ 14.13

However, when comparing the surface morphology and 3D surface profile of oxide films with and without graphite as shown in Figure 3, it proved that the addition of graphite had reduced the surface porosity. This could be due to the graphite embedded in the pores and reduce the porosity [5]. Peak of carbon around  $1350 \text{ cm}^{-1}$  (D-peak) and  $1580 \text{ cm}^{-1}$  (G-peak) can be clearly seen in Figure 4 which indicate that the graphite had incorporated into oxide films at the early 5 min.

#### 4. CONCLUSION

Graphite can significantly improve the surface properties of oxide film. The growth of oxide film containing graphite seemed to enhance the surface porosity when increasing the anodizing duration. However, the surface porosity of oxide film containing graphite was reduced compared to the oxide film without graphite. This porosity reduction can significantly contribute as a good technology material for wide range mechanical applications.

#### ACKNOWLEDGEMENT

The author acknowledges the financial help provided by Universiti Teknologi Malaysia through Tier2 research grant No. Q. K130000.2643.15J17.

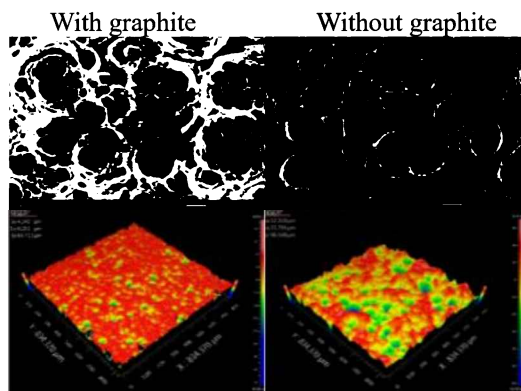


Figure 3 Surface morphology and 3D surface profile of oxide films with and without graphite at 60 min of anodizing time.

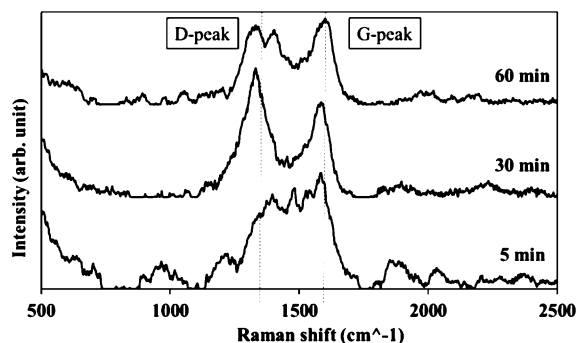


Figure 4 Raman spectra of oxide films with graphite at different anodizing time: (a) 5 min (b) 30 min (c) 60 min.

#### REFERENCES

- [1] Jung, J., Oak, J. J., Kim, Y. H., Cho, Y. J., & Park, Y. H. (2017). Wear behaviors of pure aluminum and extruded aluminum alloy (AA2024-T4) under variable vertical loads and linear speeds. *Metals and Materials International*, 23(6), 1097-1105.
- [2] Yang, F., Qin, Q., Shi, T., Chen, C., & Guo, Z. (2019). Surface strengthening aluminum alloy by in-situ TiC-TiB<sub>2</sub> composite coating. *Ceramics International*, 45(4), 4243-4252.
- [3] Zalnezhad, E., Sarhan, A. A., & Hamdi, M. (2013). Investigating the effects of hard anodizing parameters on surface hardness of hard anodized aerospace AL7075-T6 alloy using fuzzy logic approach for fretting fatigue application. *The International Journal of Advanced Manufacturing Technology*, 68(1-4), 453-464.
- [4] Zhao, X., Liu, W., Zuo, Y., & Yang, L. (2009). The cracking behaviors of anodic films on 1050 and 2024 aluminum alloys after heating up to 300° C. *Journal of Alloys and Compounds*, 479(1-2), 473-479.
- [5] Kamis, S. L., & Sofi, M. L. N. M. (2018). Fabrication of hard composite anodic films on aluminium alloy. *Proceedings of Mechanical Engineering Research Day 2018*, 2018, 228-229.

# Optimization of waste cooking oil enhanced with hBN nanoparticles

Muhammad Ilman Hakimi Chua Abdullah<sup>1,2,\*</sup>, Aliatul Syafiqah Nabilah Mohamad<sup>1</sup>, Abdul Munir Hidayat Syah Lubis<sup>1,2</sup>, Adam Samsudin<sup>3</sup>, Mohd Afdhal Shamsudin<sup>1,2</sup>, Mohd Fadzli Bin Abdollah<sup>2,4</sup>

<sup>1)</sup> Fakulti Teknologi Kejuruteraan Mekanikal dan Pembuatan, Universiti Teknikal Malaysia Melaka, Hang Tuah Jaya, 76100 Durian Tunggal, Melaka, Malaysia

<sup>2)</sup> Centre for Advanced Research on Energy, Universiti Teknikal Malaysia Melaka, Hang Tuah Jaya, 76100 Durian Tunggal, Melaka, Malaysia

<sup>3)</sup> Advance Manufacturing Center, Universiti Teknikal Malaysia Melaka, Hang Tuah Jaya, 76100 Durian Tunggal, Melaka, Malaysia

<sup>4)</sup> Fakulti Kejuruteraan Mekanikal, Universiti Teknikal Malaysia Melaka, Hang Tuah Jaya, 76100 Durian Tunggal, Melaka, Malaysia

\*Corresponding e-mail: ilmanhakimi@utem.edu.my

**Keywords:** WCO; hBN; nanoparticles; friction, wear

**ABSTRACT** – The aims of this study is to determine the optimal design parameters in obtaining the lowest coefficient of friction (COF) and wear by hexagonal boron nitride (hBN) nanoparticles, dispersed in waste cooking oil. L9 orthogonal arrays was constructed using the Taguchi method to determine significant parameter contribution. Four-ball tester is used for conducting tribological testing according to ASTM standard D4172. By referring to analysis of S/N ratio, COF and wear scar was reduced significantly with addition hBN nanoparticles into the treated waste cooking oil. As conclusion, hBN nanoparticles promising to be next future additive for plant oil.

## 1. INTRODUCTION

Utilization of the plants and animals' oils had been practiced in industrial application for many years especially in lubricant fields due to economic impact and environmental concern. Plants oils-based lubricants shown an excellent in lubricity and may lead to major used in industries. This is because oil from plants has superior viscosity index and great anticorrosion properties which suitable towards metallic surface [1]. Besides, it also included with a property of non-flammability, non-polluting, non-toxic, and biodegradable to nature [2].

According to Panadre et al. [3] the use of the waste cooking oil is one of the afford to reduce the pollution occur. Vegetable-based oil is highly recommended utilized in industries due the potential of the oil in the lubricant is high. The significant advantages of vegetable oil to an environment such as ecological and possessed acceptable performance in a variety of utilization help researcher to study the potential of vegetable oil as a new lubricant. However, the vegetable/plant oil has its weakness which is they volatile for a long period of using for high temperature. Therefore, it needs an additive to overcome this problem. Most recommended additives nowadays are toward nanoparticles.

This study focuses on the capability of hBN as a new additive with suitable homogenized parameter on the tribological properties for optimized parameter on waste cooking oil.

## 2. EXPERIMENTAL SETUP

The samples composition was prepared according to Table. 1 and the Table. 2 for L9 orthogonal arrays for testing condition. The sample was homogenized shown in Figure 1.

Table 1 Sample parameters.

Parameters			
Level	hBN (vol. %)	Oleic acid (vol. %)	Time (min)
1	0	0	20
2	0.25	0.1	30
3	0.5	0.3	40

Table 2 L9 Orthogonal arrays Taguchi method.

Parameters			
Test	hBN (vol. %)	Oleic acid (vol. %)	Time (min)
1	0	0	20
2	0.25	0.1	30
3	0.5	0.3	40
4	0.25	0.1	30
5	0.5	0.3	40
6	0	0	20
7	0.5	0.3	40
8	0	0	20
9	0.25	0.1	30

Tribological testing was performed to identify the coefficient of friction (COF) and wear rate accordance to ASTM D 4172 followed by scanning electron microscope (SEM).

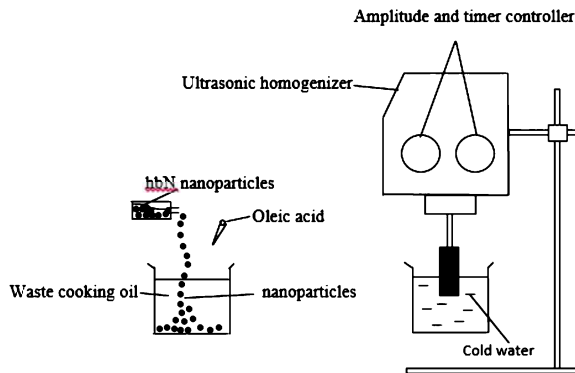


Figure 1 Homogenized process for sample preparation.

### 3. RESULTS AND DISCUSSION

According to the S/N ratios analysis shows by Figure 2, the optimal parameter obtained was 0.5 vol.% of hBN nanoparticles composition with 0.3 vol.% Oleic acid and 40 minutes of homogenized time. This optimized value reflex on sample 5 based on the L9 orthogonal arrays. Based on the result, all parameter shows the same significant contribution in obtaining the lowest friction and wear.

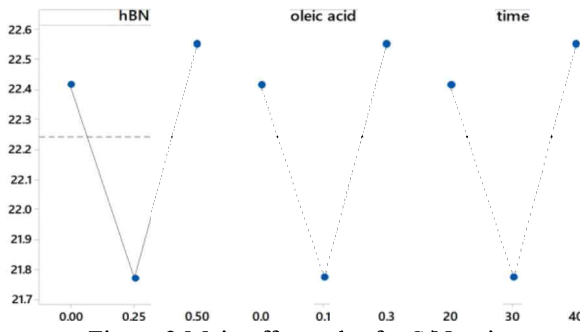


Figure 2 Main effects plot for S/N ratios.

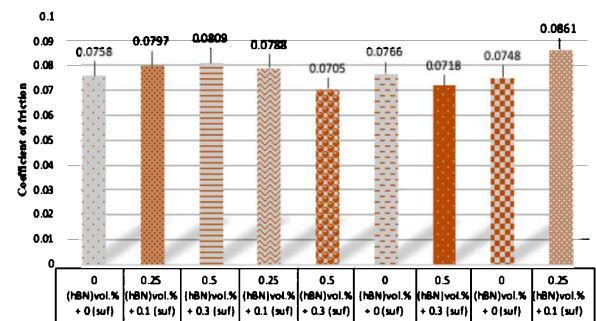
Figure 3(a) shows the CoF result obtained for all the tested sample which show the optimal result give the lowest CoF value, while Figure 3(b). shows the wear scar diameter for contributed sample as references. Higher composition of hBN resulting on lowest CoF and WSD which coherence with other work [4], which stated that hBN nanoparticles able to reduce the wear and friction of the contacting surface. The morphological contact surfaces show in Figure 4.

### 4. CONCLUSION

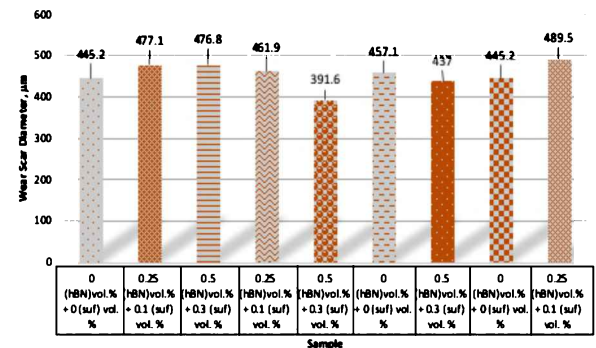
The optimal parameter for obtaining the lowest CoF and WSD is given by 0.5 vol.% of hBN nanoparticles composition with 0.3 vol.% Oleic acid and 40 minutes of homogenized time. Further investigation may help in term of developing stable WCO as new lubricant with help of hBN nanoparticles.

### ACKNOWLEDGEMENT

The author would like to thank Universiti Teknikal Malaysia Melaka for funding this research under short Grant Scheme (PJP/2019/FTKEE(3A)/S01655).



(a)



(b)

Figure 3 (a) Average CoF value and (b) average WSD obtained for tested samples.

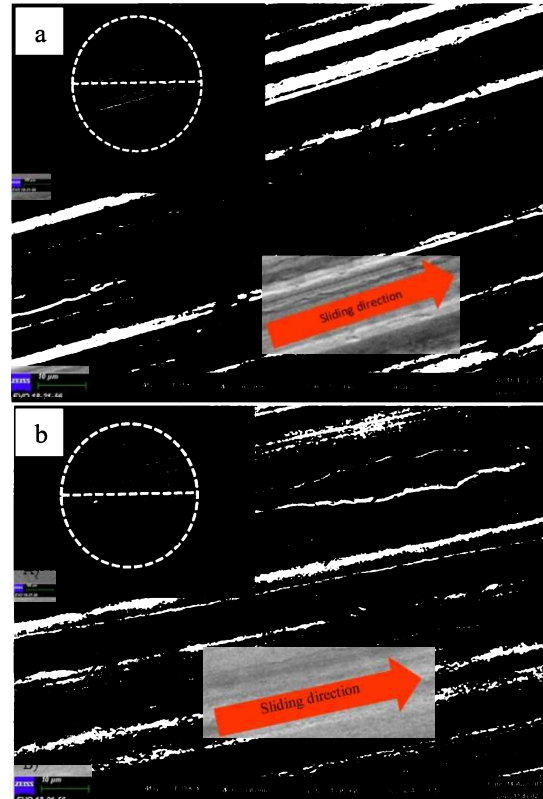


Figure 4 (a) Contact surface for sample optimized parameter (sample 5) and (b) worse condition (sample 9).

**REFERENCES**

- [1] Abdullah, M. I. H. C., Talip, J., Abdollah, M. F. B., & Jumaidin, R. (2018). Optimization of tribological performance for filtration waste cooking oil enhance by ZrO<sub>2</sub> and graphite nanoparticle. *Proceedings of Mechanical Engineering Research Day, 2018*, 111-112.
- [2] Kulkarni, M. G., & Dalai, A. K. (2006). Waste cooking oil an economical source for biodiesel: a review. *Industrial & Engineering Chemistry Research, 45*(9), 2901-2913.
- [3] Panadare, D. C. (2015). Applications of waste cooking oil other than biodiesel: a review. *Iranian Journal of Chemical Engineering, 12*(3), 55-76.
- [4] Abdullah, M. I. H., Abdollah, M. F. B., Amiruddin, H., Tamaldin, N., Nuri, N. R. M., Masjuki, H., & Rafeq, S. A. (2014). Improving engine oil properties by dispersion of hBN/Al<sub>2</sub>O<sub>3</sub> Nnanoparticles. *Applied Mechanics and Materials, 607*, 70-73.

# Tribological influence of hBN and MoS<sub>2</sub> nanoparticles as additive in modified jatropha based oil nanofluids

Norfazillah Talib<sup>1,\*</sup>, Shahirah Azua A Khalid<sup>1</sup>, Lee Woon Kiow<sup>1</sup>, Haslina Abdullah<sup>1</sup>, Nor Athirah Jamaluddin<sup>1</sup>, Aslinda Saleh<sup>2</sup>

<sup>1)</sup> Faculty of Mechanical and Manufacturing Engineering, Universiti Tun Hussein Onn Malaysia,  
86400 Batu Pahat, Johor, Malaysia

<sup>2)</sup> Faculty of Engineering Technology, Universiti Tun Hussein Onn Malaysia,  
Pagoh Higher Education Hub, 84600 Pagoh, Muar, Johor, Malaysia

\*Corresponding e-mail: fazillah@uthm.edu.my

**Keywords:** Tribology; nanoparticle; nanofluid

**ABSTRACT** – Nanofluid has attracted great interest to be studied in recent years due to its potential as machining lubricant. The aim of this study is to investigate the influence of nanofluids from modified jatropha based oil (MJO) in term of tribological characteristic. MJO was mixed with hBN and MoS<sub>2</sub> nanoparticles at 0.05wt.% concentration. The nanofluid samples were compared with synthetic ester through four ball test. The results found that the usage of nanofluids (MJO+hBN and MJO+MoS<sub>2</sub>) showed excellent tribological characteristic compared to SE and have the potential to substitute SE as the sustainable lubricant.

## 1. INTRODUCTION

Tribological characteristic is the most important consideration in selecting a suitable lubricant. It relates to the lubricant performance in terms of lubricity, friction and wear which associated with the formation of lubrication film or tribofilm on the sliding surfaces. The addition of nanoparticles additives in the based oil known as nanofluid promised a significant effect on the tribological characteristic. Padmini et al. [1] identified that the usage of nanofluid was found to form consistent lubrication film separating the contact surfaces thus imparts a better surface quality of the workpiece.

This finding similar to the study by Kong et al. [2] which indicates that the usage of nanoparticles ultimately lowers the friction coefficient. They stated that nanoparticles provided a rolling mechanism theory and form a sliding system thus reducing the friction and wear. Moreover, Kim et al. [3] found that the usage of nanoparticles in the vegetable based fluid was advantageous to reduce friction and increase the thermal conductivity of the nanofluid. The results found that the usage of nanofluids during the micro-end-milling process significantly reduced the forces.

In this study, the modified jatropha oils with the addition of 0.05wt.% of hBN and 0.05wt.% of MoS<sub>2</sub> were compared with synthetic ester through four-ball test. The testing results were discussed in terms of coefficient of friction, wear scar diameter and the worn surface analysis.

## 2. METHODOLOGY

### 2.1 Lubricant Preparation

Modified jatropha based oil (MJO) was formulated through the transesterification process of jatropha methyl

ester and trimethylolpropane at the molar ratio of 3.5:1 in the presence of 1% (wt./wt.) sodium methoxide. Previously, MJO has been proved to offer better lubrication properties [4]. Hexagonal boron nitride (hBN) and molybdenum disulfide (MoS<sub>2</sub>) with a diameter of 100nm were used as the nanoparticles. Both particles were used as the additives and blended with MJO at the weight concentration of 0.05wt.% to obtain nanofluid. The nanofluids were compared with the synthetic ester (Unicut Jinen MQL) as the reference oil as shown in Table 1.

Table 1 Oil samples.

Samples	Description
MJO+hBN	MJO with 0.05wt.% hBN
MJO+MoS <sub>2</sub>	MJO with 0.05wt.% MoS <sub>2</sub>
SE	Synthetic ester

### 2.2 Tribology Test

Tribological characteristic was evaluated through four ball test using tribotester according to ASTM D4712. This testing used a new set of four steel balls (AISI52100) with a diameter of 12.7 mm. Prior to this, three stationary balls were clamped together as shown in Figure 1. 10 ml nanofluid sample was poured into the ball pot. The rotating ball was locked inside the container and stripped into the spindle. The ball pot assembly was mounted in the tribotester machine. The normal load of  $392 \pm 2\text{N}$  was pressed slowly at the stationary balls. The operating temperature was regulated at  $75 \pm 2^\circ\text{C}$ . The rotating ball was rotated at the constant speed of 1200 rpm for 60 minutes of operation time. The coefficient of friction (COF) was determined by the Winducom 2010 software. The wear scar diameter of the stationary balls was measured through an optical microscope. The morphology of the worn surfaces was analyzed via a scanning electron microscope (SEM).

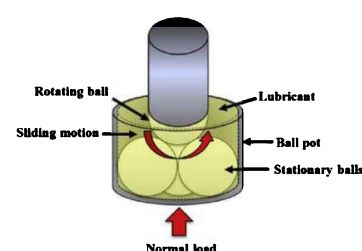


Figure 1 Four ball test set up [5].

### 3. RESULTS AND DISCUSSION

Figure 2 shows that SE recorded the highest COF of 0.098 and WSD of 0.94  $\mu\text{m}$  compared to nanofluid samples. MJO+hBN nanofluids exhibited the smallest COF of 0.048 and WSD of 0.523  $\mu\text{m}$ . Meanwhile, the COF and WSD values of MJO+MoS<sub>2</sub> nanofluid was recorded at 0.05 and 0.544  $\mu\text{m}$ , respectively. The COF and WSD values of MJO+hBN and MJO+MoS<sub>2</sub> were improved by 49 to 51 % and 42 to 44 % compared to SE. The usage of both nanofluids sample demonstrated the lowest value of COF and WSD. This phenomenon occurs due to the presence of long and branched carbon chains in MJO that provided excellent lubrication layer [5]. In addition, the presence of a minimum concentration of hBN and MoS<sub>2</sub> nanoparticles (0.05wt.%) in MJO tended to form better protective films and cause a rolling effect at the contact surfaces [6]. The addition of nanoparticles in based oil can withstand compressive stress concentration subsequently reduced the friction and wear. Further, the addition of hBN nanoparticles in MJO provided better tribological property compared to the addition of MoS<sub>2</sub> in MJO. It was due to the crystalline structure of hBN nanoparticles that contributed to the excellent lubricating properties.

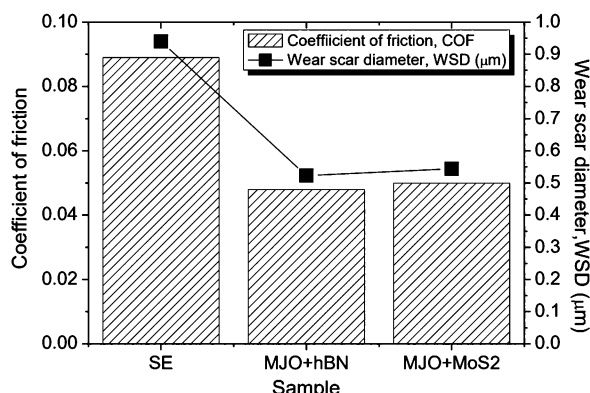


Figure 2 Results of four ball test

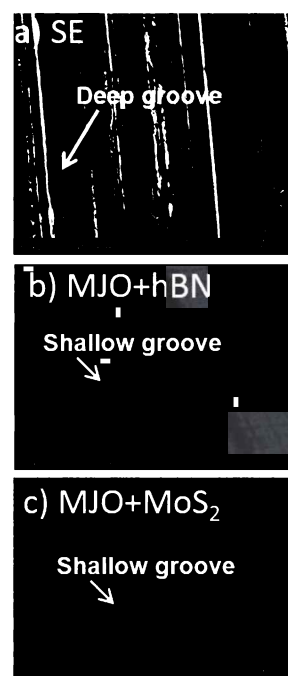


Figure 3 Morphology of the worn surfaces.

Figure 3 illustrated the surface morphology of the worn surfaces of all samples. It can be observed that the high COF of SE was proven by the formation of parallel deep groove on the worn surface as shown in Figure 3(a). This evidence proved that the lubrication film form by SE was not able to support the applied load during the operation time. Furthermore, a few parallel shallow grooves found on the worn surface of MJO+hBN and MJO+MoS<sub>2</sub> as shown in Figures 3(b) and 3(c). The results revealed that both nanofluids form an adequate lubrication thin layer that able to withstand the friction at the contact surfaces resulting low COF.

### 4. CONCLUSION

The results of the four-ball test showed that the presence of minimum concentration (0.05wt.%) of nanoparticles additive in modified jatropha oils nanofluid successfully enhanced the tribological properties by reducing the COF and WSD. Moreover, the addition of hBN nanoparticles as the additive provided better lubrication film compared to MoS<sub>2</sub> nanoparticles. It can be concluded that, both nanofluids have a potential to substitute SE as the sustainable lubricant.

### ACKNOWLEDGEMENT

This work was supported by Universiti Tun Hussein Onn Malaysia and Ministry of Education Malaysia under the TIER 1 research grant (H176) and FRGS (K077).

### REFERENCES

- [1] Alves, S. M., Schroeter, R. B., Bossardi, J. C. D. S., & Andrade, C. L. F. De. (2011). Influence of EP additive on tool wear in drilling of compacted graphite iron. *Journal of the Brazilian Society of Mechanical Sciences and Engineering*, 33(2), 197–202.
- [2] Dai, W., Kheireddin, B., Gao, H., & Liang, H. (2016). Roles of nanoparticles in oil lubrication. *Tribology International*, 102, 88–98.
- [3] Kim, J. S., Kim, J. W., & Lee, S. W. (2017). Experimental characterization on micro-end milling of titanium alloy using nanofluid minimum quantity lubrication with chilly gas. *International Journal of Advanced Manufacturing Technology*, 91(5–8), 2741–2749.
- [4] Kong, L., Sun, J., & Bao, Y. (2017). Preparation, characterization and tribological mechanism of nanofluids. *Royal Society of Chemistry*, 7(21), 12599–12609.
- [5] Talib, N., Nasir, R. M., & Rahim, E. A. (2017). Tribological behaviour of modified jatropha oil by mixing hexagonal boron nitride nanoparticles as a bio-based lubricant for machining processes. *Journal of Cleaner Production*, 147, 360–378.
- [6] Talib, N., & Rahim, E. A. (2018). Experimental evaluation of physicochemical properties and tapping torque of hexagonal boron nitride in modified jatropha oils-based as sustainable metalworking fluids. *Journal of Cleaner Production*, 171, 743–755.

# Tribological properties characterization of green polyol

Abdul Munir Hidayat Syah Lubis<sup>1,2,\*</sup>, Adam Samsudin<sup>3</sup>, Jeefferie Abd Razak<sup>3</sup>, Muhammad Ilman Hakimi Chua Abdullah<sup>1,2</sup>, Amir Abdullah Muhamad Damanhuri<sup>1,2</sup>, Khairul Amri Tofrowaih<sup>1,2</sup>, Mohd Fariduddin Mukhtar<sup>1</sup>

<sup>1)</sup> Fakulti Teknologi Kejuruteraan Mekanikal dan Pembuatan, Universiti Teknikal Malaysia Melaka, Hang Tuah Jaya, 76100 Durian Tunggal, Melaka, Malaysia

<sup>2)</sup> Centre for Advanced Research on Energy, Universiti Teknikal Malaysia Melaka, Hang Tuah Jaya, 76100 Durian Tunggal, Melaka, Malaysia

<sup>3)</sup> Advance Manufacturing Center, Universiti Teknikal Malaysia Melaka, Hang Tuah Jaya, 76100 Durian Tunggal, Melaka, Malaysia

\*Corresponding e-mail: munir@utem.edu.my

**Keywords:** Polyol; friction; wear

**ABSTRACT** – Awareness of mineral oil resources depletion has been increasing in the past decade which drive the utilization of bio-based lubricant. In this research, tribological properties of palm oil-based polyol was investigated. The viscosity, viscosity index, flash point, friction coefficient and wear preventive properties were observed by following corresponding ASTM standard testing. Palm oil-based polyol was found to possesses good friction and wear preventive properties. It also possessed higher viscosity, but lower viscosity index compared to palm oil. The polyol sample show higher coefficient of friction compared to palm oil and better wear preventive properties compared to palm oil.

## 1. INTRODUCTION

Bio-based lubricant has been acknowledged as alternative to petroleum-based lubricant. The use of vegetable oils as lubricant become popular again due to their good lubricating properties, from renewable sources, and more environmentally friendly. This kind of oil already used as lubricant long before the exploration of petroleum product in the 18th century. However, their application is still limited because of their oxidation properties, low and high temperature resistant, and storability. However, several researchers found that this disadvantages can be overcome by performing structural modification of the fatty acid contained in the vegetable oil [1].

Polyol is a type of organic compound containing two or more hydroxyl groups (OH groups) per molecule. Polyols from renewable are typically of trifunctional glycerol and hexafunctional sorbitol [2]. Polyol ester has been used as lubricant due to its excellent thermal and oxidation stability, lubricating properties and excellent viscosity characteristics at low temperatures [3]. Polyols can be synthesized through transesterification of vegetable oils with other polyols or alcohols, producing fatty acid polyol mono- and di-esters [4], [5]. The objective of this work is to investigate tribological properties of palm oil-based polyol as lubricant source.

## 2. METHODOLOGY

Palm oil-based polyols obtained from local polyol manufacturer was used as lubricant sample without any further treatment and palm oil was used as properties

comparison. Fourier Transformed Infra-Red (FTIR) analysis was conducted to analyse functional group of the polyol by using a JASCO-6100 FTIR analyser at scanning range of 500 cm<sup>-1</sup> – 4000 cm<sup>-1</sup>. Kinematic viscosity of the sample was measured by using Kittiwake viscometer at temperature of 40°C and 100°C. Viscosity Index (VI) of the polyols sample was calculated based on ASTM D-2270 method. Flash point of the sample determined by closed cup method following ASTM D-93 standard. Friction and wear prevention properties of the sample was observed by Four ball methods according to ASTM D-4172. Scanning electron microscope (SEM) was employed to observed wear morphology of the solid sample lubricated with the polyol.

## 3. RESULTS AND DISCUSSION

FTIR spectra of the polyol sample is shown in Figure 1. Peaks at 3458 cm<sup>-1</sup> is shows absorption bands of the OH group and peak at 1740 cm<sup>-1</sup> is related to C-O stretching bond. Peaks in 1094 – 1240 cm<sup>-1</sup> region are belonging to C-O group stretching related to ester, ether and hydroxyl groups. Peaks at 2848 and 2920 cm<sup>-1</sup> are attributed to stretching of CH<sub>3</sub> groups and peaks at are attributed to bending of CH<sub>2</sub> groups [6]. Peak at 722 cm<sup>-1</sup> is correspond to the (CH<sub>2</sub>)<sub>n</sub> sequence of the aliphatic chains of the fatty acids [7].

Table 1. Viscosity and flash point of polyol sample.

Properties	Viscosity @40°C	Viscosity @100°C	VI	Flash point
Polyol	975.1 cS	47.23 cS	91.2	180°C
Palm Oil	36.95 cS	9.12 cS	166.3	224°C

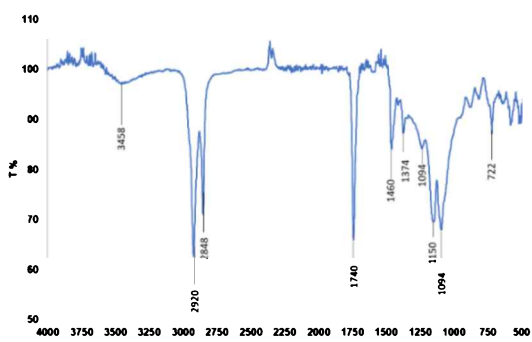


Figure 1 FTIR spectra of polyol sample.

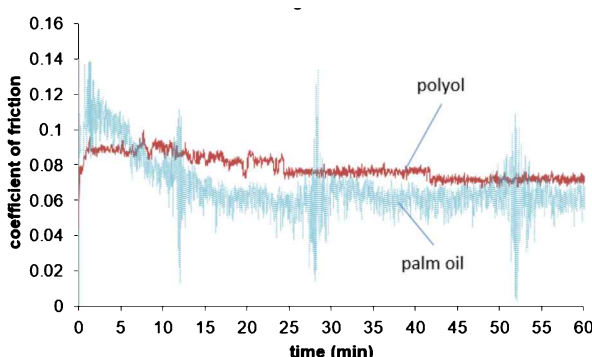


Figure 2 Friction graph of steel lubricated with polyol and palm oil.

Table 1 show the viscosity, viscosity index, and flash point of the polyol and palm oil. The polyol is thicker fluid with viscosity of 975.1 cS at 40°C and 47, 23 cS at 100°. However, the viscosity index of the polyol sample is 91.2, lower to the palm oil. The thicker viscosity is considered related to the molecular structure of the polyol sample. Flash point of the polyol sample also found lower than the palm oil sample.

Friction of the samples is shown in Figure 2. It is observed that the steel lubricated with the polyol sample exhibit initial friction coefficient of 0.085 then reduced to 0.071 with extension of sliding time. The lubricated friction of polyol was found higher than the palm oil (steady coefficient of friction = 0.064). Higher coefficient of friction of polyol compared to palm oil obtained is considered related to polyol's high viscosity causing more resistance during the sliding.

Figure 3 shows the SEM micrograph of wear scar observed on the steel ball sample. Wear scar diameter (WSD) of average 624  $\mu\text{m}$  was obtained from sample lubricated with polyol and WSD of 660  $\mu\text{m}$  was obtained from sample lubricated with palm oil. This result indicates that the palm oil-based polyol sample still possesses good friction and wear preventive properties like most vegetable oil. The morphology of the wear surface shows significant wear track at the center of wear circle (Figure 3a). Further magnification on the wear track indicating mild adhesive wear mechanism has been operated during the sliding (Figure 3b).

#### 4. CONCLUSION

The palm oil-based polyol found to possesses good friction and wear preventive properties. It is also possessed higher viscosity, but lower viscosity index compared to palm oil. The polyol sample show higher coefficient of friction compared to palm oil which related to its high viscosity that cause resistance during sliding. Wear preventive properties of the polyol show a better result compared to palm oil.

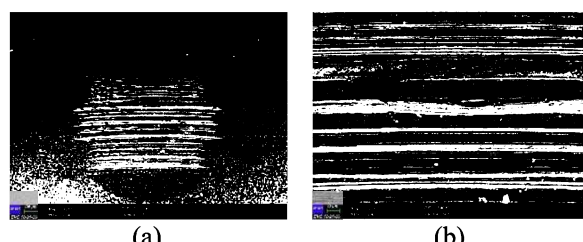


Figure 3 SEM Micrograph of steel ball worn surface, (a) 100X magnification, (b) 500X magnification.

#### ACKNOWLEDGEMENT

The authors would like to thank University Teknikal Malaysia Melaka for supporting this research under PJP grant no PJP/2019/FTKEE(3A)/S01655.

#### REFERENCES

- [1] Sharma, B. K., & Erhan, S. Z. (2013). 23 Modified Vegetable Oils for Environmentally Friendly Lubricant Applications. *Synthetics, Mineral Oils, and Bio-based Lubricants: Chemistry and Technology*, 385-411.
- [2] Rudnick, L. R. (2005). *Synthetics, mineral oils, and bio-based lubricants: chemistry and technology*. CRC press.
- [3] Mang, T., Dresel, W., & Wiley, J. (Eds.). (2007). *Lubricants and lubrication* (Vol. 2, pp. 185-190). Weinheim, Germany: Wiley-Vch.
- [4] Yunus, R., Fakhru'l-Razi, A., Ooi, T. L., Omar, R., & Idris, A. (2005). Synthesis of palm oil based trimethylolpropane esters with improved pour points. *Industrial & Engineering Chemistry Research*, 44(22), 8178-8183.
- [5] Hayes, D. G., & Dumont, M. J. (2016). Polymeric products derived from industrial oils for paints, coatings, and other applications. In *Industrial Oil Crops* (pp. 43-73). AOCS Press.
- [6] Radojčić, D., Ionescu, M., & Petrović, Z. S. (2013). Novel potentially biodegradable polyurethanes from bio-based polyols. *Contemporary Materials*, 1(4), 9-21.
- [7] Mizera, K., & Ryszkowska, J. (2016). Polyurethane elastomers from polyols based on soybean oil with a different molar ratio. *Polymer Degradation and Stability*, 132, 21-31.

# Superhydrophilicity of laser surface textured TiO<sub>2</sub> coating for self-cleaning surfaces

Yusliza Yusuf<sup>1,2,\*</sup>, Mariyam Jameelah Ghazali<sup>1</sup>, Mohd Fadzli Bin Abdollah<sup>3</sup>, Yuichi Otsuka<sup>4</sup>, Susumu Nakamura<sup>5</sup>

<sup>1)</sup> Centre for Materials Engineering and Smart Manufacturing, Faculty of Engineering and Built Environment, Universiti Kebangsaan Malaysia, 43600 UKM Bangi, Selangor, Malaysia.

<sup>2)</sup> Fakulti Teknologi Kejuruteraan Mekanikal dan Pembuatan, Universiti Teknikal Malaysia Melaka, Hang Tuah Jaya, 76100 Durian Tunggal, Melaka, Malaysia.

<sup>3)</sup> Fakulti Kejuruteraan Mekanikal, Universiti Teknikal Malaysia Melaka, Hang Tuah Jaya, 76100 Durian Tunggal, Melaka, Malaysia

<sup>4)</sup> Department of System Safety, Nagaoka University of Technology, 1603-1 Kamitomioka Nagaoka, Niigata 940-2188, Japan

<sup>5)</sup> Department of Electrical and Electronic Systems Engineering, National Institute of Technology, Nagaoka College, 888 Nishikatakai, Nagaoka, Niigata 940-8523, Japan

\*Corresponding e-mail: yusliza@utem.edu.my

**Keywords:** Laser surface texturing; TiO<sub>2</sub>; self cleaning

**ABSTRACT** – In this study, the effect of laser surface texturing on TiO<sub>2</sub> coating surface to create a self-cleaning surface was studied. The TiO<sub>2</sub> coating deposition was carried out on API steel substrate by using plasma spraying prior to laser texturing. Picosecond laser system was used to create a micro-dimpled texture on the TiO<sub>2</sub> surface. Laser texturing process changed the TiO<sub>2</sub> coating wettability properties from hydrophilic to superhydrophilic. The superhydrophilic properties showed that laser texturing is a facile method for developing self-cleaning TiO<sub>2</sub> surfaces, which are applicable for various industrial applications.

## 1. INTRODUCTION

Superhydrophobic surface (contact angle >150°) and superhydrophilic surfaces (contact angle~ 0°) have been broadly explored by researchers because of their significance for applications in modern times. The self-cleaning superhydrophilic surface spreads water droplets to form a film throughout itself, thereby, allowing light waves to pass through. Following this discovery, a rigorous study is in progress worldwide to analyse the mechanism and to develop superhydrophilic coatings.

Examples of TiO<sub>2</sub>-derived materials have been discovered to understand the fundamental principles of self-cleaning with hydrophilic and hydrophobic surfaces. The hydrophilic character of TiO<sub>2</sub> was first reported by Wang et al. [1] in 1997. Wang et al. reported that TiO<sub>2</sub> film is irradiated with light, and the contact angle being reduced to 0° results in spreading of water droplets on the surface. The hydrophilic TiO<sub>2</sub> surface has been exploited commercially to develop anti-fogging and self-cleaning surface for various applications, such as fabrics, paints, glass and tiles (Table 1). Therefore, this study evaluated the effect of laser surface texturing on the properties of TiO<sub>2</sub>-coated surfaces. Laser surface texturing involves creating different patterns on substrates and has been proven effective in improving surface features [6]. Immediately after laser texturing, the surface becomes either

hydrophilic or hydrophobic [6]. In this work, dimple structures were fabricated on TiO<sub>2</sub> coating through the use of a picosecond laser. The effect of dimples on the TiO<sub>2</sub> coating on the wettability properties was investigated.

Table 1 Uses of self cleaning materials.

Substrate	Application	Ref
Tiles	Kitchen, building roof and walls	[2]
Glass	Mirrors for vehicles and indoor uses, windows, tunnel, road light	[3]
Textiles	Hospitals garments, medical devices,protective clothing	[4]
Plastic/ polycarbonate	Automotive industry and buildings	[5]

## 2. METHODOLOGY

### 2.1 Preparation of TiO<sub>2</sub> Coating

Commercial titanium dioxide, TiO<sub>2</sub> (Metco 102 Oerlikon Metco ≥ 99.0 wt. %), with a nominal particle size distribution of 11-45 μm was used as raw materials. The coatings were deposited onto carbon steel API 5L grade B 30 cm (length) × 5 cm (width) × 7 mm (thickness) by using an atmospheric plasma spray system with SG-100 torch (Praxair, USA) mounted on ABB IRB Industrial robot. Prior the deposition, the substrate were grit-blasted and ultrasonically cleaned in ethanol and deionized water.

### 2.2 Laser Surface Texture Preparation

Areas with dimensions of 8 mm × 8 mm on the plasma sprayed TiO<sub>2</sub> coating were subjected to laser surface texturing. A laser manufacturing system (Q-switched Nd:YAG picosecond laser) was used to create a micro-dimpled texture on the TiO<sub>2</sub> surface. The dimple diameter, dimple depth and area density at 20μm, 7μm and 0.2% respectively. The morphologies of the textured surface were observed by using scanning electron microscope (SEM). The area density, AD is calculated from Eq.1 [7].

$$AD = \frac{\pi r^2}{16l^2} \quad (1)$$

### 2.3 Wettability Test

Surface wettability of the samples was evaluated by measuring the static contact angle (CA) with a CA analyser (DMe-201 Kyowa) using the 1  $\mu\text{l}$  sessile drop technique. All measurements were performed when the water droplets reached stability on the surface.

## 3. RESULTS AND DISCUSSION

### 3.1 Surface Morphology Using SEM

SEM images (Figure 1) revealed that the plasma-sprayed  $\text{TiO}_2$  coating contained partially melted and unmelted particles that adhered to fully melted splats. The laser impact sites surrounding the dimples underwent material transformation. Ejected matter associated with the coating material can be observed around the dimples.

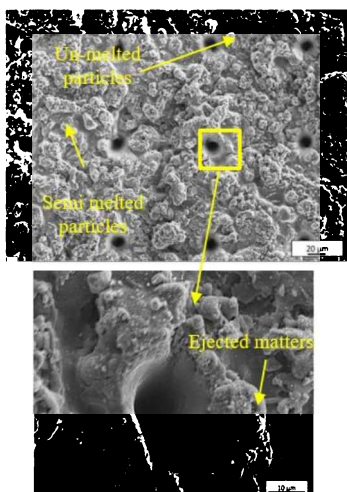


Figure 1 Surface SEM images of laser textured  $\text{TiO}_2$  coating.

### 3.2 Surface Wettability

Surface wettability of the prepared laser-textured  $\text{TiO}_2$  coating was evaluated by measuring the static CA. An increase of CA indicated decreased wettability. Comparison of the CA of the laser-textured  $\text{TiO}_2$  coating with non-textured surface is shown in Figure 2. Each data point presents an average of over three dimensions.

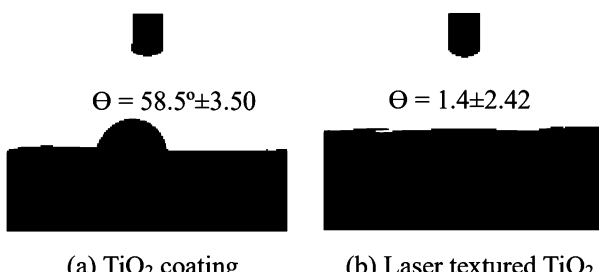


Figure 2 Contact angle of  $\text{TiO}_2$  coating.

The initial  $\text{TiO}_2$  coating (non texture) was hydrophilic with a CA of  $58.5^\circ$ . After the laser ablation, all the samples exhibited superhydrophilic behaviour with low CA of less than  $4^\circ$ . This may be attributed to the modifications of chemical composition (hydroxyl

group) and surface morphology during laser texturing [6]. The superhydrophilic properties obtained in this study showed a facile method to develop a self-cleaning  $\text{TiO}_2$  surface. The surface water drops spread over the surface of laser-textured  $\text{TiO}_2$  and form a water film. During spreading, the contamination on the surface was washed away [8].

## 4. CONCLUSION

Experimental results indicated that the wettability properties of  $\text{TiO}_2$  coating changed from hydrophilic to superhydrophilic after laser texturing. This study may provide a potential facile method to construct textured surfaces that undergo changes with wetting behaviour, thereby extending the industrial applications especially for pipeline usage.

## ACKNOWLEDGEMENT

The authors thank Universiti Kebangsaan Malaysia and Nagaoka University of Technology Japan for their support and cooperation during the conduction of the experiments. The authors acknowledge Universiti Teknikal Malaysia Melaka for financially supporting the authors' Ph.D.

## REFERENCES

- [1] Wang, R., Hashimoto, K., Fujishima, A., Chikuni, M., Kojima, E., Kitamura, A., ... & Watanabe, T. (1997). Light-induced amphiphilic surfaces. *Nature*, 388(6641), 431.
- [2] Xie, T. H., & Lin, J. (2007). Origin of photocatalytic deactivation of  $\text{TiO}_2$  film coated on ceramic substrate. *The Journal of Physical Chemistry C*, 111(27), 9968-9974.
- [3] Takata, Y., Hidaka, S., Cao, J. M., Nakamura, T., Yamamoto, H., Masuda, M., & Ito, T. (2005). Effect of surface wettability on boiling and evaporation. *Energy*, 30(2-4), 209-220.
- [4] Liu, K., Cao, M., Fujishima, A., & Jiang, L. (2014). Bio-inspired titanium dioxide materials with special wettability and their applications. *Chemical reviews*, 114(19), 10044-10094.
- [5] Yaghoubi, H., Taghavinia, N., & Alamdari, E. K. (2010). Self cleaning  $\text{TiO}_2$  coating on polycarbonate: surface treatment, photocatalytic and nanomechanical properties. *Surface and coatings technology*, 204(9-10), 1562-1568.
- [6] Yan, H., Rashid, M. R. B. A., Khew, S. Y., Li, F., & Hong, M. (2018). Wettability transition of laser textured brass surfaces inside different mediums. *Applied Surface Science*, 427, 369-375.
- [7] Mohmad, M., Abdollah, M. F. B., Tamaldin, N., & Amiruddin, H. (2018). Frictional characteristics of laser surface textured activated carbon composite derived from palm kernel. *The International Journal of Advanced Manufacturing Technology*, 95(5-8), 2943-2949.
- [8] Banerjee, S., Dionysiou, D. D., & Pillai, S. C. (2015). Self-cleaning applications of  $\text{TiO}_2$  by photo-induced hydrophilicity and photocatalysis. *Applied Catalysis B: Environmental*, 176, 396-428.

# Various quarry dust content influences the tribological properties of Ni-P composite coating

Muhamad Ammar Farhan Maula Mohd Azam<sup>1</sup>, Intan Sharhida Othman<sup>1,\*</sup>, Mohd Shahir Kasim<sup>1</sup>, Jariah Muhamad Juoi<sup>1</sup>, Mohd Rody Bin Mohamad Zin<sup>2</sup>

<sup>1)</sup>Fakulti Kejuruteraan Pembuatan, Universiti Teknikal Malaysia Melaka,  
Hang Tuah Jaya, 76100 Durian Tunggal, Melaka, Malaysia

<sup>2)</sup>Fakulti Kejuruteraan Mekanikal, Universiti Teknikal Malaysia Melaka,  
Hang Tuah Jaya, 76100 Durian Tunggal, Melaka, Malaysia

\*Corresponding e-mail: intan\_sharhida@utem.edu.my

**Keywords:** Electrodeposition; quarry dust; wear

**ABSTRACT** – The advance and overview of new coated cutting tool carry out several studies with the purpose to optimize the coatings content. Nickel-phosphorus-quarry dust (Ni-P-QD) composite coatings using various quarry dust (QD) content were deposited on tungsten carbide substrate by using an electrodeposition technique. The electrodeposition process was carried out for 1 hour at 40°C under the current density of 3 A/dm<sup>2</sup> in a modified nickel Watt's bath containing 20, 60, and 100 g/l of quarry dust particles. The effects of quarry dust content on the hardness and wear properties of electrodeposited Ni-P-QD composite coatings on WC substrate were investigated before and after heat treatment. As the quarry dust content increases, the hardness and wear resistance also improved, due to the presence of high silica and alumina content in the quarry dust particles.

## 1. INTRODUCTION

Numerous cutting tools have been developed continuously since the first cutting tool material suitable for use in carbon steel, metal cutting, was industrialized a century ago [1]. As in the case of the machining, Ayed et al. [2] conducted machining of Ti17 with uncoated tungsten carbide tools under different cutting environments. Notch wear, plastic deformation, adhesion and abrasion wear were found to be the main wear mechanisms during machining. Coatings are applied to improve surface properties of the substrate, such as mechanical properties, adhesion, corrosion, wettability, wear resistance, lubrication, and scratch resistance [3-5]. The properties of Ni-P can be improved by co-deposition with hard particles (e.g. SiC, WC, Al<sub>2</sub>O<sub>3</sub>) and dry lubricant (e.g. MoS<sub>2</sub>) [6]. In this study, quarry dust particles were added to the Ni-P solution. Quarry dust is one of the by- product from quarrying activities which lead to waste management proposal. The quarry dust can be employed as inexpensive strengthening particles which can increase wear resistance and enhanced microhardness due to presence of high SiO<sub>2</sub> and Al<sub>2</sub>O<sub>3</sub> in the particles [7]. Thus, Ni-P-QD composite coatings were introduced by using electrodeposition technique. The present work is aimed to investigate the effect of various quarry dust content and heat treatment process on the properties of Ni-P-QD composite coatings electrodeposited on tungsten carbide substrate.

## 2. METHODOLOGY

The tungsten carbide substrate with dimension of 40 mm x 30 mm x 3 mm were grind using silicon carbide paper from 240 to 1200 grit paper and polished with diamond paste 0.3μm. Then, substrate was cleaned with ethanol and acetone for 20s to remove the oily surface of the substrate. The substrate was then attached to a glass cell fitted with a water jacket, through which water from a thermostat bath was circulated. A power supply was employed for nickel electrodeposition using a typical two-electrode system consisting of anode electrode nickel plate (99.99%) and cathode electrode of tungsten carbide plate. The chemical composition and operating condition for electrodeposition of Ni-P-QD composite coating were summarized in Table 1.

Table 1: Composition of modified nickel Watt's bath and electrodeposition operating condition.

Modified Watt's bath solution	
Chemical compound	Content (g/l)
NiSO <sub>4</sub> .6H <sub>2</sub> O	200
NiCl <sub>2</sub> .6H <sub>2</sub> O	20
C <sub>6</sub> H <sub>5</sub> Na <sub>3</sub> O <sub>7</sub> .2H <sub>2</sub> O	30
NaH <sub>2</sub> PO <sub>2</sub>	10
Quarry Dust	20,60,100

Condition Parameter	Electrodeposition
Time	1 hour
Temperature	40°C
Current	3 A/dm <sup>2</sup>
Speed	300 rpm

## 3. RESULTS AND DISCUSSION

### 3.1 Characterization of Quarry Dust

The elemental composition for quarry dust particles is found by XRF technique and shown in Table 2.

Table 2 Composition of quarry dust particles.

Element	SiO <sub>2</sub>	Al <sub>2</sub> O <sub>3</sub>	CaO	Fe <sub>2</sub> O <sub>3</sub>	MgO	Na <sub>2</sub> O	K <sub>2</sub> O	SO <sub>3</sub>	TiO <sub>2</sub>	P <sub>2</sub> O <sub>5</sub>
Concentration (Wt%)	72.6	15.1	1.1	1.9	0.8	3.0	4.9	0.2	0.3	0.1

### 3.2 Effect of Various Quarry Dust Content on The Wear Scar of Composite Coatings

From SEM image of wear scar of Ni-P-QD 20,60 and 100 g/l with (Figure 2 (b,d,f)) and without heat treatment (Figure 2 (a,c,e)) shows that's worn area of

the samples. The scar presents a ploughing wear. The wear scar improves after the heat treatment at 200°C within increasing of the QD content due to the existing of Si and Al<sub>2</sub>O<sub>3</sub> in the composite coatings.

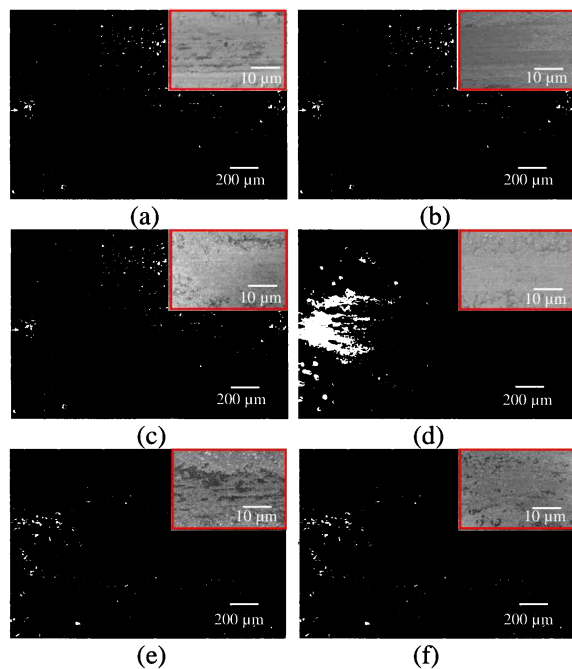


Figure 2 (a) 20 g/l QD (b) 20 g/l QD heat treatment (c) 60 g/l QD (d) 60 g/l QD heat treatment (e) 100 g/l QD (f) 100 g/l QD heat treatment.

Overall, the microhardness value of the Ni-P-QD coating shows an improvement by increasing the quarry dust content and applying a heat treatment process to the coated substrate (Figure 3). Due to the heat treatment process its can be shown that at Ni-P-QD 60 g/l the microhardness increases from 876.6 HV to 972.3 HV. This finding is consistent with the XRD analysis in Figure 4 which reported that the present peak of the Ni<sub>3</sub>P phase at 31.5° and 48.8° is present and produce intermediate layer between coating and substrate will enhance the microhardness properties of the coatings. There are several reports concerning the phase transformation within the Ni-P plating in which various temperature and heating rates were applied. Keong et al. [8] revealed that lower temperatures of heat treatment resulted in the presence not only of amorphous phase (Am), Ni and Ni<sub>3</sub>P but also the metastable phases. Therefore, Ni-P-QD 60 g/l composite coating was optimum due to the distribution of the SiO<sub>2</sub> particles towards the substrate uniformly and excessive particles were distributed on Ni-P-QD 100 g/l effects the microhardness value.

#### 4. CONCLUSION

In summary, the Ni-P QD 60 g/l with heat treatment at 200°C shows that successfully improved the wear resistance compared to other composite coatings. This is due to the presence of high silica and alumina content in the quarry dust particles co-deposited in the nickel matrix. Furthermore, it is also due to the phase transformation from Ni to Ni<sub>3</sub>P after the heat treatment process.

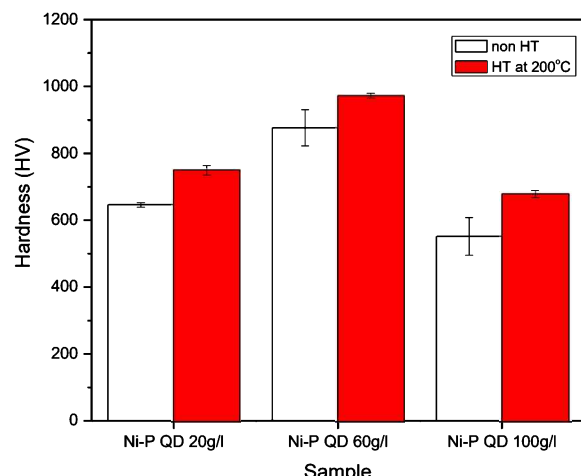


Figure 3 Microhardness of Ni-P-QD composite coatings.

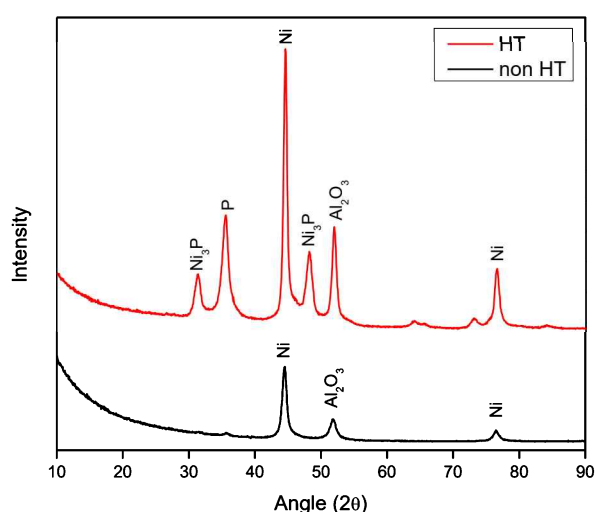


Figure 4 XRD pattern of Ni-P-QD composite coating 60g/l.

#### ACKNOWLEDGEMENT

We greatly acknowledge the research funding from Fundamental Research Grant Scheme (FRGS/1/2017/TK10/UTEM/03/4) and Universiti Teknikal Malaysia Melaka (UTeM) for sponsoring this work.

#### REFERENCES

- [1] Boothroyd, G. (1988). *Fundamentals of metal machining and machine tools* (Vol. 28). Crc Press.
- [2] Ayed, Y., Germain, G., Ammar, A., & Furet, B. (2013). Degradation modes and tool wear mechanisms in finish and rough machining of Ti17 Titanium alloy under high-pressure water jet assistance. *Wear*, 305(1-2), 228-237.
- [3] Smith, G. T. (1989). *Advanced machining: the handbook of cutting technology*. IFS.
- [4] Torabinejad, V., Rouhaghdam, A. S., Aliofkhazraei, M., & Allahyari, M. H. (2016). Electrodeposition of Ni-Fe and Ni-Fe-(nano Al<sub>2</sub>O<sub>3</sub>) multilayer coatings. *Journal of Alloys and Compounds*, 657, 526-536.
- [5] Jiang, S. W., Yang, L., Pang, J. N., Lin, H., & Wang, Z. Q. (2016). Electrodeposition of Ni-

- Al<sub>2</sub>O<sub>3</sub> composite coatings with combined addition of SDS and HPB surfactants. *Surface and Coatings Technology*, 286, 197-205.
- [6] Liu, W. Q., Lei, W. N., Wang, C. Y., Qian, H. F., & Ding, L. H. (2015). Ni-SiC nanocomposites electroplating process under ultrasonic and agitation. *Integrated Ferroelectrics*, 167(1), 192-198.
- [7] Othman, I. S., Azhar, E. N., Azam, M. A. F. M. M., Kasim, M. S., Abidin, M. Z. Z., Sundi, S. A., & Jun, L. P. (2018). Tribological properties of malaysian quarry dust reinforced nickel matrix composite coatings. *Proceedings of Asia International Conference on Tribology 2018*, 87-89.
- [8] Keong, K. G., Sha, W., & Malinov, S. (2002). Crystallisation kinetics and phase transformation behaviour of electroless nickel-phosphorus deposits with high phosphorus content. *Journal of Alloys and Compounds*, 334(1-2), 192-199.

# Surface topography study of CNC milled zirconia dental restoration

Rahimah Abdul Hamid\*, Wan Nur Amirah Wan Muhamad, Raja Izamshah Raja Abdullah, Mohd. Shahir Kasim

<sup>1)</sup>Fakulti Kejuruteraan Pembuatan, Universiti Teknikal Malaysia Melaka,  
Hang Tuah Jaya, 76100 Durian Tunggal, Melaka, Malaysia

\*Corresponding e-mail: rahimah.hamid@utem.edu.my

**Keywords:** Zirconia ceramic; surface structure; SEM

**ABSTRACT** – The aim of the study was to analyze the surface topography of computer-aided-design-computer-aided-manufacturing (CAD-CAM) milled zirconia dental restoration. The surface analysis was studied by using Scanning Electron Microscopy (SEM) machine. SEM results showed periodic surface profile of the surface structure due to the scallop-height effect. In addition, the micro-pitting was also observed. This has caused average surface roughness of 0.04-0.5 $\mu\text{m}$  of some random measurement points as a result of different stylus locations during the measurement. The improvement of the untreated surface profile could be achieved with some finishing and polishing techniques which are not considered in the present study.

## 1. INTRODUCTION

A complex curved surface is widely used in dental restoration with a rapidly varied geometric feature. The milling of this complex geometric feature with uniform processing parameters for the whole machining region has created the scallop-height effect on the milled restorations. The scallop-surface depends on the toolpath and the size of the cutter [1]. As a result of scallop-height formation, the milled dental restorations exhibit a variation in surface roughness which requires additional finishing and polishing of the restorations. In dentistry, the surface roughness is responsible for the microbial attractiveness of denture surfaces [2] and has to be strictly monitored. Microbial adhesion is enhanced with increasing surface roughness between 0.1 and 0.4  $\mu\text{m}$  [3], and Bollen et al. [4] stated that the  $R_a$  value of 0.2  $\mu\text{m}$  will not influence bacterial adhesion or colonization. Therefore, the aim of the present study was to study the surface topology of the untreated milled dental restoration and discuss the effect of this scallop-height towards its surface roughness. The testing hypothesis was that the surface roughness would be below 0.5  $\mu\text{m}$ .

## 2. MATERIAL AND METHOD

### 2.1 Experimental Set-up

Machining experiment was performed on Ardent DT 100 milling machine under dry machining with a carbide tool. The work material used for the experiment was NEXXZr T, which is dental zirconium oxide (Y-TZP ZrO<sub>2</sub>) from Sagemax Bioceramics, Inc. The disc had undergone a sintering temperature between 1500-1530 °C.

### 2.2 Surface Roughness Measuring Procedure

The roughness characteristic measured was arithmetic average ( $R_a$ ), which is determined as the

arithmetic mean of absolute values of the roughness profile ordinates that was measured using a contact-type stylus profilometer: Mitutoyo surface roughness tester. The stylus traversing length,  $L_t$ , was set to 0.24mm with the cut-off,  $\lambda_c$ , at 0.08 mm as to set the number of sampling,  $\lambda$  of three. The specified points were selected at the buccal and lingual area of the restoration, as shown in Fig. 1. The occlusal surface was not examined in this surface roughness measurement due to the complicated geometry profile of this region. Average surface roughness was recorded based on 3 traces of each point.

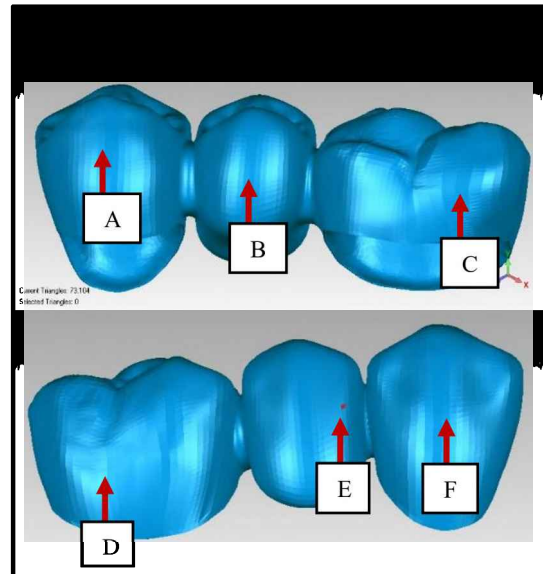


Figure 1 The measurement points.

### 2.3 Surface Topography Analysis

The surface structure of the milled dental restoration was analyzed using SEM machine. The purpose of this investigation was to study the surface topography of the untreated Zirconia restoration. The sample was initially sputter coated to avoid electrostatic discharge of the non-metallic sample. The surface images were captured by using Carl Zeiss Evo 50 at 15.00kV accelerating voltage for 100x and 500x of magnification power at secondary electron.

## 3. RESULTS AND DISCUSSION

### 3.1 Surface Roughness Data

The average surface roughness of each measurement point is summarized in Table 1. All specimens yielded the  $R_a$  values lower than 0.5  $\mu\text{m}$ , except for point F. In this study, three times of measurement were taken for each point and the average data was calculated in order to reduce the random error.

The  $R_a$  value could be improved if a greater number of traces for each point is taken, as the outlier of the reading will be eliminated so that the standard deviation,  $\sigma$  of each sample is less than to 0.05.

Table 1 Surface roughness data ( $R_a$ ) for all points.

Point	Reading 1 ( $\mu\text{m}$ )	Reading 2 ( $\mu\text{m}$ )	Reading 3 ( $\mu\text{m}$ )	Mean ( $\mu\text{m}$ )
A	0.04	0.03	0.04	0.037
B	0.04	0.04	0.16	0.08
C	0.29	0.38	0.32	0.33
D	0.27	0.28	0.45	0.33
E	0.42	0.55	0.36	0.44
F	0.56	0.34	0.65	0.52

According to Shahir et al. [5], the  $R_a$  values depend on the stylus location of the profilometer, as shown in Fig. 2. This could explain the variation of  $R_a$  values for each point during the multiple tracing.

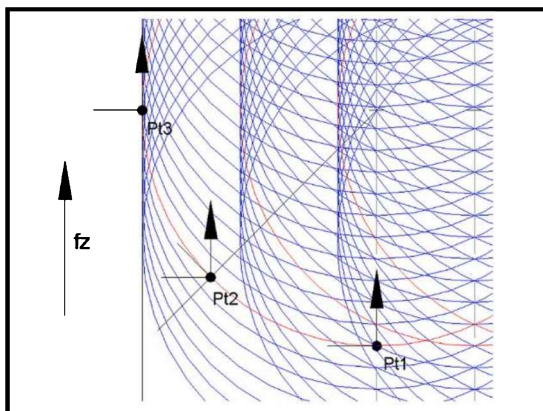


Figure 2 Schematic diagram that shows the  $R_a$  value varies depending on the stylus location [5].

### 3.2 Surface Topography Data

SEM images showed the scallop-height effect of the untreated surface of the milled zirconia restoration due to the cutter. The profile of the machined surface is dominated by the reflective deflection between the tool and the workpiece during machining [6]. In addition, the micro-pitting of the surface was also observed, as a result of the compaction process of zirconia-powder during the manufacturing of the ceramic disc.

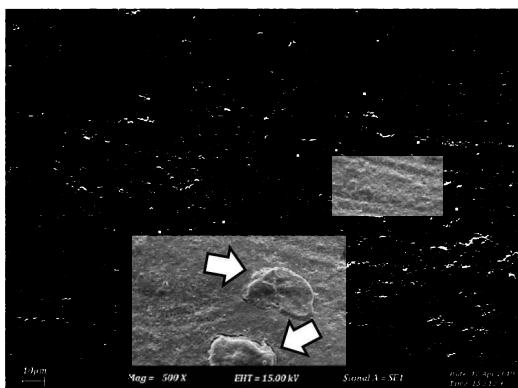


Figure 3 SEM image of the specimen (x500) with scratch grooves. The arrow indicates micro-pitting.

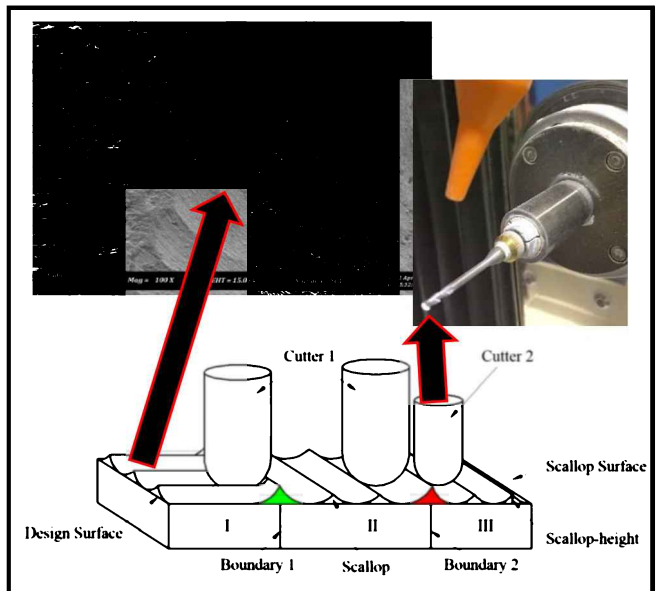


Figure 4 Illustration of scallop-height effect [1], and SEM image of the restoration (x100).

### CONCLUSION

The scallop-height effect, the scratch grooves, and the micro-pitting of the surfaces contributed to the high surface roughness of the fabricated dental restoration.

### ACKNOWLEDGEMENT

The authors are grateful to UTeM and the Ministry of Higher Education Malaysia for funding this research project through a grant FRGS/2018/FKP-AMC/F00378.

### REFERENCES

- [1] Jia, Z. Y., Zhao, X. X., Ma, J. W., Chen, S. Y., Qin, F. Z., & Liu, Z. (2019). Toolpath generation in sub-regional processing with constraint of constant scallop-height at boundary for complex curved surface. *Precision Eng.*, 55(2019), 217–230.
- [2] Steinmassl, O., Dumfahrt, H., Grunert, I., & Steinmassl, P. A. (2018). Influence of CAD/CAM fabrication on denture surface properties. *Journal of Oral Rehabilitation*, 45(5), 406–413.
- [3] Tamada, M., Katakai, A., Yuasa, A., Terada, A., Kushimoto, T., & Tsuneda, S. (2006). Bacterial adhesion to and viability on positively charged polymer surfaces. *Microbiology*, 152(12), 3575–3583.
- [4] Bollen, C. M. L., Papaioanno, W., Van Eldere, J., Schepers, E., Quirynen, M., & Van Steenberghe, D. (1996). The influence of abutment surface roughness on plaque accumulation and peri-implant mucositis. *Clinical Oral Implants Research*, 7(3), 201–211.
- [5] Chung, Y. J., & Jun H. O. (1991). Improvement of surface waviness by cutting force control in milling. *Int. Journal of Machine Tools and Manufacturing*, 31(1), 9–21.
- [6] Kasim, M. S., Hafiz, M. S. A., Ghani, J. A., Haron, C. H. C., Izamshah, R., Sundi, S. A., & Othman, I. S. (2018). Investigation of surface topology in ball nose end milling process of Inconel 718. *Wear*, 426–427(Dec. 2018), 1318–1326.

# The effect of coconut fibre as friction modifier on mechanical and tribological characteristics of friction materials

Hazim Sharudin<sup>1,\*</sup>, R.J. Talib<sup>2</sup>, M. Hisyam Basri<sup>1</sup>, N.I. Ismail<sup>1</sup>, Arif Pahmi<sup>1</sup>, M.F.S. Khalid<sup>3</sup>

<sup>1)</sup> Faculty of Mechanical Engineering, UniversitiTeknologi MARA,  
Kampus Pulau Pinang, Permatang Pauh, Pulau Pinang, Malaysia

<sup>2)</sup> Zeta Scientific Sdn. Bhd, Blok 5, Kompleks Otomobil, 23-1B, Jalan Pahat H15/H, Seksyen 15,  
40200 Shah Alam, Selangor, Malaysia

<sup>3)</sup> Faculty of Mechanical Engineering, UniversitiTeknologi MARA Cawangan Johor,  
Kampus Pasir Gudang, 81750 Masai, Johor, Malaysia

\*Corresponding e-mail: hazim@uitm.edu.my

**Keywords:** Coconut fibres friction materials; hardness; friction and wear

**ABSTRACT** – The main purpose of this project is to investigate the effect of different volume percentage (vol.%) of coconut fibres on mechanical and tribological characteristics of friction materials. Four brake friction material formulations of different compositions were prepared through powder metallurgy process. All the test samples were examined for their density, porosity, hardness, thickness loss and coefficient of friction (COF) which follow the international standard test procedure. Test results obtained show that sample J2 which composed of 15% coconut fibres is the best formulation as it produced stable COF and lower thickness loss results.

## 1. INTRODUCTION

Brake pad friction materials is an element of the brake system used in the automotive and other applications and the friction material does its job by converting the energy of motion to heat energy through brake pads and disc. Friction materials behaviour depend on the speed, deceleration, and mode of braking; whether it is continuous or intermittent. In addition, a good friction material should compose of four components; classified as binders, reinforcements, fillers and frictional additives [1]. Friction modifier such as graphite, kenaf, iron oxide is used to improve the coefficient of friction (COF) and wear properties of the brake friction materials. It is important to note that certain material content in the friction material composition perform multiple functions includes stable friction, adequate wear resistance and improved fade.

In order to obtain reliable brake performance, some modifications need to be made on the formulations and several methodologies on the formulation of frictional material have been reported [2,3]. All the proper formulations for optimum brake performance were obtained by undergoing different design of experiments. Besides the friction modifier that has been stated before, coconut fibres are one of the natural fibres that provide excellent insulation against temperature, unaffected by moisture and dampness, most ductile and energy absorbent material. Thus, coconut fibres appeared to be suitable to use as a base material in friction material [4]. This work investigates the compatibility of coconut fibres as friction modifier in the fabrication of brake friction materials.

## 2. METHODOLOGY

### 2.1 Test Samples Preparation

Four types of brake friction material formulations have been prepared after undergoing powder metallurgy process. Firstly, the composition were mixed together in the tubular mixer with the speed and timer were adjusted to 50 rpm and 10 minutes of mixing time. All the test samples then were warm compacted by using SANTEC Hydraulic Hot Press Machine under a pressure of 15 tonne at a temperature of 170°C for 4 minutes. In order to improve the dimensional stability and improve compressive creep resistance, the compacted test samples were post-baked at a temperature of 200°C for 4 hours, in an oven. Table 1 shows all the test samples consists of coconut fibre and other composition at the volume percentages (vol %).

Table 1 Samples composition.

Composition	J1	J2	J3	J4
Coconut Fibre	10.0	15.0	5.0	7.9
Resin	15.0	14.1	15.9	11.8
Graphite	15.0	14.1	15.9	11.8
Steel Fibre	30.0	28.4	31.6	45.0
Iron Powder	20.0	18.9	21.1	15.8
Copper	10.0	9.5	10.5	7.9
Total (vol %)	100	100	100	100

### 2.2 Testing and Analysis

All the four test samples were tested for the Rockwell hardness and porosity tests in accordance to currents available test standard which are MS 474: Part 2 and JIS D 4418. In terms of friction and wear tests, it was performed using CHASE dynamometer and the test procedure was accordance to the SAE J616 standard. The test was carried out by pressing the sample against rotating brake drum under a constant load of 647 N and constant rotating speed of 417 rpm. Further explanation of the test program can be referred in the previous publication [3].

## 3. RESULTS AND DISCUSSION

Table 2 shows the effects of coconut fibers on the material properties (density, hardness and porosity) of the developed brake friction materials. It indicates that the coconut fibers significantly increase hardness, while in the case of porosity, the effect is opposite. Based on these

results, it was noted that there is no direct correlation between vol.% of coconut fibers with the mechanical properties as well as the correlation between porosity with the hardness behavior. This is because, the hardness increase with coconut fibers is attributed to good bonding as well as due to the high hardness of the thermosetting binder resin after cure [3]. On the other hand, coconut fibers decrease porosity for sample J2 and J3 because it flows through gaps inside the friction material during hot pressing process and fills voids before it is combined during curing. As the vol.% of coconut fibers decreases from J2 until J4, the density is increasing due to the difference in formulations and also the factor of post-baking the brake pad as it changes the structure of material in the friction materials.

Table 2 Samples test results.

Sample	Density (g/cm <sup>3</sup> )	Hardness (Shore D)	Porosity (%)
J1	2.734	89.50	27.63
J2	2.421	19.70	23.56
J3	2.708	41.77	21.31
J4	2.717	77.03	29.13

Figure 1 shows the Coefficient of Friction (COF) increased with increasing temperature for all the four samples. Beginning of braking, the harder asperities on the brake disc being ploughed into the wear surface and widening the contact area of the brake pad which making the COF increased. Thereafter, the degradation of the coconut fibers causes the mechanical integrity of formulation to become gradually weaker that makes the COF decreased. The shearing of the peak asperities and formation of friction film could also reduce the COF as observed by other researchers [4]. Sample J4 which composed of 7.9 vol.% coconut fibers has the lowest COF. This is could be due to the decomposition of coconut fibers at elevated temperature resulting the lower bonding of the composition. It can be seen from Figure 1 that sample J2 showed an excellent fade resistance and more stable COF compared to sample J3 and J4.

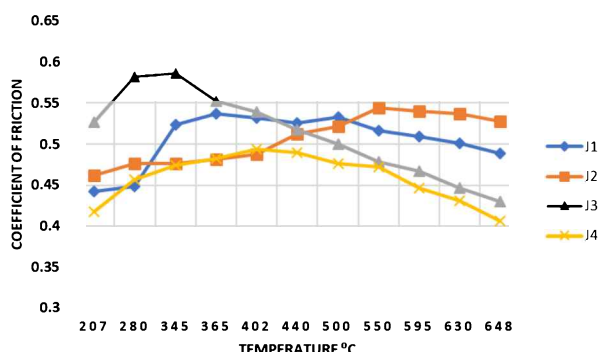


Figure 1 COF characteristics of different vol% of coconut fibers in the formulations.

Figure 2 shows that sample J1 which composed of 10 vol.% of coconut fibers has the lowest thickness loss while sample J3 which composed of 5 vol.% of coconut fibers has the highest thickness loss. Decrement in vol. % of coconut fibers would result a higher thickness loss, thus increase weight loss of the sample. This

phenomenon could be due to increase in hardness and reduction in porosity with respect of vol.% coconut fibers in the formulation. In addition, it is observed that there is no direct correlation between vol.% coconut fibers with the thickness loss during braking because other parameter such as wear mechanism and mode of braking might influence the thickness loss [4].

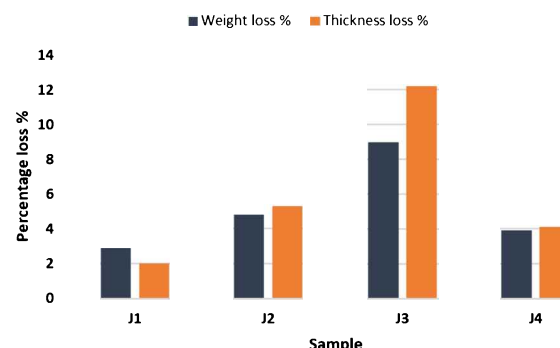


Figure 2 Thickness loss characteristics of different vol. % of coconut fibers in the formulation.

#### 4. CONCLUSION

It can be concluded that coconut fibres improves the mechanical and tribological properties of friction materials in which the porosity decrease and the thickness loss increase with decreasing of vol. % of coconut fibres in the formulation. Sample J2 which composed of 15 vol. % of coconut fibres is the best formulation which produced on stable COF and lower thickness loss results.

#### ACKNOWLEDGMENT

The authors would like to thank Universiti Teknologi MARA Cawangan Pulau Pinang and AMREC, SIRIM Berhad for the support and providing characterisation equipments and the research facilities.

#### REFERENCES

- [1] N. A. Norrdin, R. J. Talib, R. Rabilah, Hazim Sharudin, N. N. Azmi, S. N. A. M. Halidi, & N. S. Abdullah. (2018). Influence of resin on mechanical and tribological properties of friction materials. *Proceedings of Asia International Conference on Tribology 2018*, 489-490.
- [2] Zaharudin, A. M., Berhan, M. N., & Talib, R. J. (2011). The effect of phenolic resin, rubber, calcium carbonate and graphite on tribological characteristic of semi - metallic brake. *AIP Conference Proceedings*, 1400(1), 274-279.
- [3] Almaslow, A., Ratnam, C. T., Ghazali, M. J., Talib, R. J., & Azhari, C. H. (2013). Effects of electron-beam and sulfur crosslinking of epoxidized natural rubber on the friction performance of semimetallic friction materials. *Composites Part B: Engineering*, 54, 377-382.
- [4] Jaafar, T. R., Othman, E. A., Selamat, M. A., & Kasiran, R. (2016). On-road braking performances of semi-metallics brake friction materials developed through powder metallurgy process. *Journal of Engineering Science*, 12, 27-41.

# Adhesion modelling for load-dependence, double-Hertz based elliptical contacts

Nurul Hilwa Mohd Zini<sup>1,2,\*</sup>, Matthijn de Rooij<sup>3</sup>, Mohammad Bazrafshan<sup>3</sup>, Aydar Akchurin<sup>3</sup>, Dik Schipper<sup>3</sup>, Nurhidayah Ismail<sup>1,2</sup>

<sup>1)</sup> Fakulti Kejuruteraan Mekanikal, Universiti Teknikal Malaysia Melaka,  
Hang Tuah Jaya, 76100 Durian Tunggal, Melaka, Malaysia

<sup>2)</sup> Centre for Advanced Research on Energy, Universiti Teknikal Malaysia Melaka,  
Hang Tuah Jaya, 76100 Durian Tunggal, Melaka, Malaysia

<sup>3)</sup> Department of Surface Technology and Tribology, Faculty of Engineering Technology,  
University of Twente, the Netherlands

\*Corresponding e-mail: nurulhilwa@utem.edu.my

**Keywords:** Double-Hertz model; elliptical contact; pull-off force

**ABSTRACT** – The recently developed Double-Hertz (DH) model for adhesive elliptical contacts is shown to be suitable only for nearly circular contacts; this is due to the geometry of the adhesive region is unknown a priori. To solve this problem, the geometry of the adhesive region at the pull-off moment is predicted numerically using the Boundary Element Method and the data is then used to curve-fit equations of the ellipticity ratio and the semi-major axis of the elliptical area. The resulting equations can then be incorporated into the extended DH model for accurate pull-off force predictions.

## 1. INTRODUCTION

The Double-Hertz model for adhesive contacts has been extended recently in [1] to describe adhesion between two cylindrical bodies that cross each other at a skew angle,  $\theta_{skew}$  ranging between 0 to 90 degrees. The resulting adhesive region is shown in Figure 1.

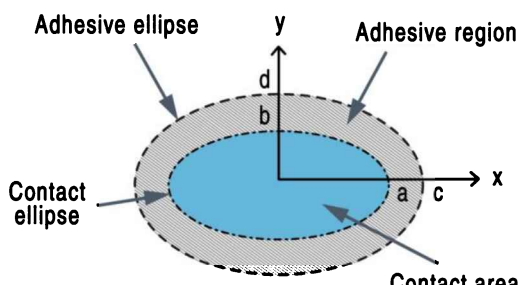


Figure 1 Adhesive region of a DH-based elliptical contact [2].

Although the load effect on boundary of the adhesive regions during contact is recognized in [1] as the correct geometrical behaviour for the DH based adhesive region, analytical solutions that can be used to calculate the ellipticity ratios for contact and adhesive ellipses,  $\beta_{ab}$  and  $\beta_{cd}$  at the pull-off force moment are unavailable. This limits the application of the DH elliptical model to nearly circular contacts ( $\theta_{skew} \approx 90^\circ$ ). Thus, to ensure that the DH elliptical model can predict accurately other contacts with lower  $\theta_{skew}$ , a numerical solution becomes necessary to accurately predict both  $\beta_{ab}$  and  $\beta_{cd}$  values, for a wide range of adhesive elliptical contacts.

## 2. ADHESIVE CONTACT MODELLING

The development of the extended DH model in [1] is continued for adhesive elliptical contacts with lower  $\theta_{skew}$ , with a new assumption which the adhesive region is allowed to change without the constraint of a Hertzian contact. Both  $\beta_{ab}$  and  $\beta_{cd}$  that act as the inner and the outer boundaries of the adhesive region have ellipticity ratios that vary with load, with both having similar values of ellipticity ratio at the beginning of the contact. As the contact progresses to the pull-off force moment, both boundaries begin to change in size, with the inner boundary having a different ellipticity ratio compared to the outer boundary, though both boundaries are assumed to maintain their elliptical shapes.

In this work, the adhesive region is assumed to be load-dependent hence at the pull-off moment both,  $\beta_{ab}$  and  $\beta_{cd}$  can be expressed as:

$$\beta_{ab} = \beta_{ab,pull-off} \quad (1a)$$

$$\beta_{cd} = \beta_{cd,pull-off} \quad (1b)$$

$\beta_{Hertz}$  is the constant ellipticity ratio obtained from a normal elliptical Hertzian contact while  $\beta_0$  is the initial ellipticity ratio at the beginning of the adhesive contact. Before the ellipticity ratio changes due to the applied load, the assumption for the adhesive contact at the initial load can be summarized as:

$$\beta_0 = \beta_{0,ab} = \beta_{0,cd} \quad (2a)$$

$$\beta_0 = \beta_{Hertz} \quad (2b)$$

where  $\beta_{0,ab}$  and  $\beta_{0,cd}$  are the initial ellipticity ratios for the contact and adhesive ellipses, respectively. Assumptions in Equation (2) are made to approximate the behaviour for both contact and adhesive ellipses; though these assumptions are more suitable for ‘rigid’ materials with low value of Tabor parameter,  $\mu$ .

The geometry of DH based adhesive regions due to elliptical contacts can be simulated by a Boundary Element Model (BEM) with a Dugdale approximation for the adhesive stress, developed by [3]. The developed numerical model utilizes the Conjugate Gradient Method (CGM). The numerical model is suitable to solve non-linear contact problems such as adhesive elliptical contacts where the contact geometry is unknown a priori. In the method, the contribution of each element in the pressure and the deformation profiles is considered separately. The CGM algorithm is shown in Figure 2.

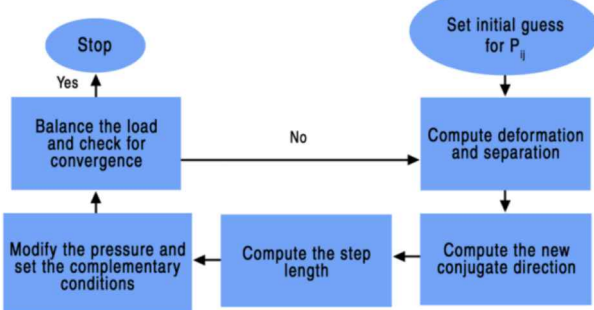


Figure 2 CGM based algorithm for adhesive contacts [3].

Numerical simulations are conducted for various  $\beta_0$  values of 0.3 ( $\theta_{skew} = 43.63^\circ$ ), 0.4 ( $\theta_{skew} = 53.14^\circ$ ), 0.6 ( $\theta_{skew} = 68.51^\circ$ ) and 0.8 ( $\theta_{skew} = 80.45^\circ$ ), within the range of  $0.5 \leq \mu \leq 4$ . Results from the numerical simulations are obtained using a minimum element number of  $N = 2048$  for  $0.5 \leq \mu < 2$  (the domain size is  $2048 \times 2048$  elements) and a maximum element number of  $N = 4096$  for  $2 \leq \mu \leq 4$  (the domain size is  $4096 \times 4096$  elements). In all cases, the calculation domain is set six times greater than the contact domain. An increased resolution is required for larger  $\mu$  values due to the small adhesive zone outside the contact. The accurate prediction of  $\beta_{ab}$  and  $\beta_{cd}$  values at the pull-off moment uses a negative load input in the numerical algorithm; this negative load represents the pull-off force required to separate the contacting surfaces. The pull-off force is determined by the greatest negative load that first converges within 200 iterations.

### 3. RESULTS AND DISCUSSION

An example of the numerical model's results on predicting adhesive elliptical contacts at the pull-off moment are shown in Figure 3. The results are obtained using the contact parameters in Table 1 as the input. Figure 3a shows the image of a three-dimensional pressure profile within the computation domain with 2048 elements along the semi-major and semi-minor axes while Figure 3b and Figure 3c show the resulting pressure distribution along the semi-major axis and semi-minor axis. The selected points of  $a$  and  $b$  are obtained from the semi-major and semi-minor axes of the contact ellipse while the points of  $c$  and  $d$  are obtained from the semi-major and semi-minor axes of the adhesive ellipse.

Table 1 Parameter of the adhesive elliptical contact at the pull-off moment.

Parameters	Values	Unit
Predicted pull-off force	75	nN
Fiber diameter	3.5	μm
Skew angle, $\theta_{skew}$	43.63	°
Hertzian ellipticity ratio, $\beta_0$	0.3	-
Tabor parameter, $\mu$	0.5	-
Number of elements, $N$	2048	-

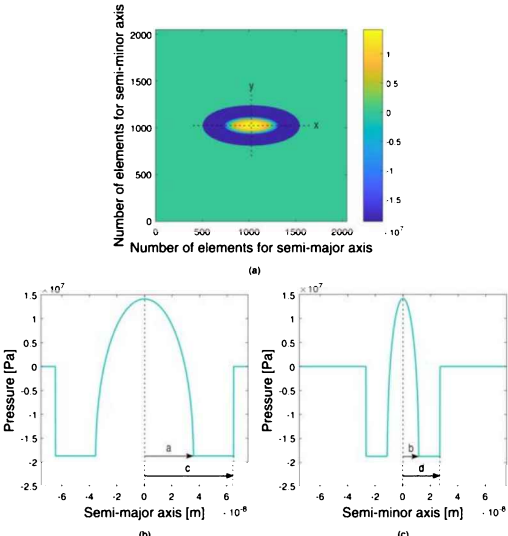


Figure 3 Numerical solutions for the elliptical contact (a) pressure profile for the elliptical contact (b) stress distribution along the semi-major axis and (c) stress distribution along the semi-minor axis.

Using the data from the numerical model, we have obtained the equations that can predict the values of  $\beta_{ab}$  and  $\beta_{cd}$  at the pull-off moment, as a function of  $\mu$  and  $\theta_{skew}$ . These ellipticity ratio equations at the pull-off moment are given as:

$$\beta_{ab} = 0.389\theta_{skew}^{1.767} + 0.083\mu^{0.332} + 0.023 \quad (3a)$$

$$\beta_{cd} = 0.414\theta_{skew}^{1.584} + 0.72\mu^{-0.007} - 0.578 \quad (3b)$$

The equation to predict the semi-major axis of the contact ellipse at the pull-off moment,  $a$  is given as:

$$a = \left( \frac{R^2 \Delta Y}{E^*} \right)^{1/3} (\sinh(1.05\beta_{ab}^{-0.16} - 0.065\mu^{-1.2}))^2 \quad (4)$$

Equation (3) and (4) can then be incorporated into the extended DH model to predict the elliptical contacts.

### 4. SUMMARY

The work on the extended DH model has been continued to include the assumption of an adhesive region with boundaries that vary with load. The resulting curve-fitted equations for the geometry of the adhesive regions obtained numerically can be incorporated into the extended DH model for an accurate pull-off prediction of elliptical contacts.

### REFERENCES

- [1] Zini, N.H.M., de Rooij, M.B., Bazrafshan, M., Ismail, N., Schipper, D.J. (2018). Extending the double-Hertz model to allow modeling of an adhesive elliptical contact. *Tribology Letters*, 66(1), 30-43.
- [2] Zini, N.H.M., de Rooij, M.B., Bazrafshan, M., Ismail, N., Schipper, D.J. (2018). Response to Dr. Greenwoods's comments on "Extending the double-Hertz model to allow modeling of an adhesive elliptical contact". *Tribology Letters*, 66(9), 99.
- [3] Bazrafshan, M., de Rooij, M.B., Valefi, M., Schipper, D.J. (2017). Numerical method for the adhesive normal contact analysis based on a Dugdale approximation. *Tribology International*, 112(8), 117-128.

# A simulation study of tubercles effect of aerodynamics performance on delta wing

Hamid Yusoff<sup>1,\*</sup>, Dzullijah Ibrahim<sup>1</sup>, Aliff Farhan Mohd Yamin<sup>1</sup>, Mohamad Rafiuddin Abdul Razak<sup>1</sup>, Salina Budin<sup>1</sup>, Shafiq Suhaimi<sup>2</sup>

<sup>1)</sup> Faculty of Mechanical Engineering, Universiti Teknologi MARA, Cawangan Pulau Pinang,  
Kampung Tok Ebot, 14000, Bukit Mertajam, Pulau Pinang, Malaysia

<sup>2)</sup> Faculty of Mechanical Engineering, Universiti Teknologi MARA, 40450, Shah Alam, Selangor, Malaysia

\*Corresponding e-mail: hamidyusoff@ppinang.uitm.edu.my

**Keywords:** Bio-inspiration; tubercles; delta wing

**ABSTRACT** – The tubercle effect is a recently discovered phenomenon where the sinusoidal pattern ‘bumps’ on the leading edge of an airfoil can improve the aerodynamic performance. This effect was inspired by looking at the humpback whale pectoral flippers that give an exceptional acrobatic maneuverability in the water such as somersaults, also allowing for easier capture of prey. The objective of this research is to study the effect of implementing the tubercles concept on the delta wing in order to see whether it bring advantage or disadvantage in the aerodynamic performance of a delta wing apply on the military aircraft. A delta wing with NACA 64-204, a 5m chord length, 2m tip length and 5m wingspan was designed. A sinusoidal pattern was added to on the edge to resemble the tubercle of a humpback whale. Where model one has 3 bumps, model two has 5 bumps and model three has 7 bumps. The investigation shown that the delta wing with tubercles can increase the lift coefficient by 13.38 %.

## 1. INTRODUCTION

Tubercles referred to the rounded protuberances at the leading edge of airfoils with a sinusoidal pattern shape that can provide improvement in performance under certain condition. It is inspired by humpback whale pectoral flippers that give exceptional acrobatic manoeuvrability such as somersaults; an accomplishment that is novel among Baleen whales [1].

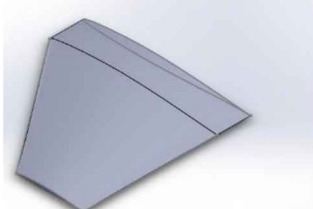
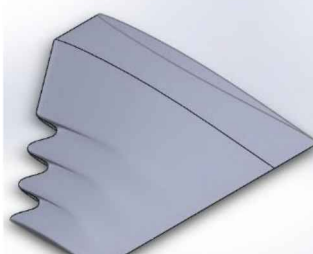
Several of numerical and experimental analysis have been performed to achieve more quality information and better understanding on tubercle concept [2-4]. According to the past studies, the researchers have exposed that the principle impact of leading-edge tubercles on wing performance is softening and delaying of stall [5-6], resulting in the reduction of drag as well increase lift at high angles of attack.

However, the investigation on implementing leading edge tubercles by existing researchers are limited to the airfoil wings rather than delta wing. The objective of this study is to study the effect of tubercles on the aerodynamic performance of a delta wing.

## 2. METHODOLOGY

Table 1 shows the four tested delta model with M0 is the Baseline delta wing, M1 is the 3 bumps delta wing, M2 is the 5 bumps delta wing, M3 is the 7 bumps delta wing. Each wing was is tested for lift and drag at 80m/s using computational fluid dynamics (CFD) simulation.

Table 1 Model design.

Configuration	Solidworks Models
M0 Baseline	
M1 $h = 400 \text{ mm}$ $\lambda = 1000 \text{ mm}$	
M2 $h = 240 \text{ mm}$ $\lambda = 600 \text{ mm}$	
M3 $h = 171.43 \text{ mm}$ $\lambda = 428.67 \text{ mm}$	

## 3. RESULTS AND DISCUSSION

From Figure 1, for lift coefficient, the value of the M0 indicate better increment compare to M1, M2, M3, before 20° angle of attack. The reduction lift coefficient can be seen after 20° of the angles of attack was shown a M1, M2, M3 was delayed the decreasing of the lift coefficient compare to the M0. This also shown after the stall angle at 20° the M1, M2, and M3 shown a better performance. This answered the hypothesis that tubercles are delaying stall at high angle of attack.

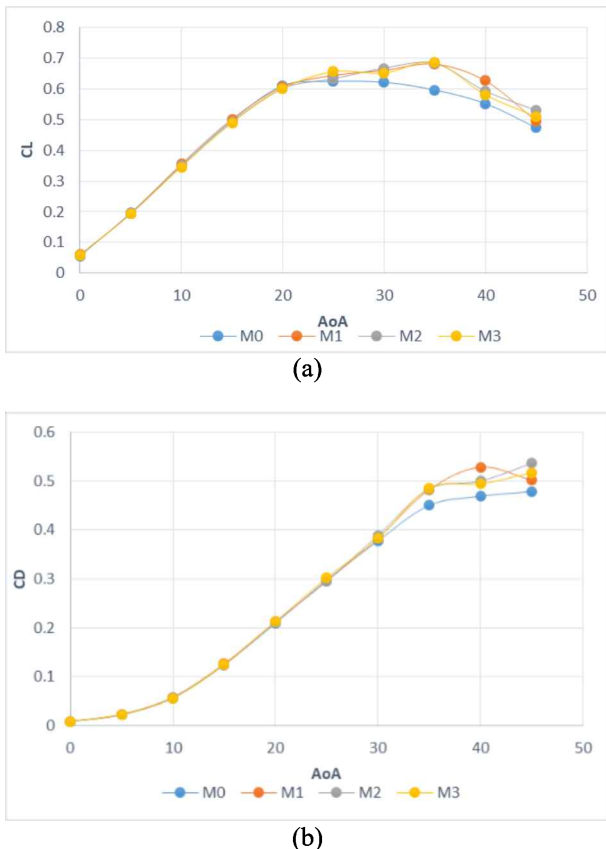


Figure 1 Aerodynamics performance where (a) is the lift coefficient vs angle of attack and (b) is the drag coefficient vs angle of attack at  $V=80\text{m/s}$ .

#### 4. CONCLUSION

The configuration of tubercles on delta wing was proved in term of aerodynamics performances such as increasing lift and delayed stall. The configuration of tubercles also improved in flow pattern behind the delta wing which is the flow separation is better compare to

base delta wing because it delayed flow separation. Overall, the implementation of tubercles on the delta wing can delayed stall and the lift coefficient up to 13.38%. However, as the number of tubercles configuration on leading edge of the delta wing increase, the effectiveness toward the aerodynamics performance of the wing decrease.

#### ACKNOWLEDGEMENT

The financial support from Universiti Teknologi MARA, Cawangan Pulau Pinang is highly appreciated.

#### REFERENCES

- [1] Jurasz, C. M., & Jurasz, V. P. (1979). Feeding modes of the humpback whale, *Megaptera novaeangliae*, in Southeast Alaska. *Scientific Reports of the Whales Research Institute*, 31, 69–83.
- [2] Fish, F. E., Weber, P. W., Murray, M. M., & Howle, L. E. (2011). The tubercles on humpback whales' flippers: application of bio-inspired technology. *Integrative and comparative biology*, 51(1), 203-213.
- [3] Stanway, M. J. (2008). *Hydrodynamic effects of leading-edge tubercles on control surfaces and in flapping foil propulsion* (Doctoral dissertation, Massachusetts Institute of Technology).
- [4] Van Nierop, E. A., Alben, S., & Brenner, M. P. (2008). How bumps on whale flippers delay stall: an aerodynamic model. *Physical review letters*, 100(5), 054502.
- [5] Hansen, K. L. (2012). *Effect of leading edge tubercles on airfoil performance* (Doctoral dissertation).
- [6] Miklosovic, D. S., Murray, M. M., Howle, L. E., & Fish, F. E. (2004). Leading-edge tubercles delay stall on humpback whale (*Megaptera novaeangliae*) flippers. *Physics of fluids*, 16(5), L39-L42.

# Experimental test of a standing-wave thermocoustic rig

Fatimah Al Zahrah Mohd Saat<sup>1,2,\*</sup>, Dahlia Johari<sup>1</sup>, Ernie Mat Tokit<sup>1,2</sup>

<sup>1)</sup> Fakulti Kejuruteraan Mekanikal, Universiti Teknikal Malaysia Melaka,  
Hang Tuah Jaya, 76100 Durian Tunggal, Melaka, Malaysia

<sup>2)</sup> Centre for Advanced Research on Energy, Universiti Teknikal Malaysia Melaka,  
Hang Tuah Jaya, 76100 Durian Tunggal, Melaka, Malaysia

\*Corresponding e-mail: fatimah@utem.edu.my

**Keywords:** Standing-wave; thermoacoustics; experiment

**ABSTRACT** – In this paper, an experimental tests of flow inside a standing-wave thermoacoustic rig of two different flow frequencies are reported. The rig consists of a quarter wavelength resonator attached to a loudspeaker that acts as an acoustic driver. A ‘stack’ is located at a location of  $0.18\lambda$  from the pressure antinode. Results showed that the resonance frequency of the two setups are 14.2 Hz and 23.6 Hz, respectively. Measured velocity at several locations indicated that the thermoacoustic flow conditions are achieved. The rig could be used for investigations of fluid dynamics of the less understood oscillatory flow of thermoacoustics.

## 1. INTRODUCTION

Fluid dynamics conditions of an oscillatory flow inside thermoacoustic system is not well known. This leads to difficulties in predicting losses for thermoacoustic based cooler or generator [1]. Earlier investigations reported many special characteristics such as early stage turbulence [2], entrance region [3] and non-linear flow and heat transfer characteristics [4]. These investigations are, however, limited to only several flow conditions. Fluid dynamics changes with operating conditions. Hence more investigations are needed to cover the wide range of thermoacoustic flow conditions. For complex flow conditions, such as those found in thermoacoustics, theoretical solutions are only available for linear model [5]. In most real and complex cases, experimental investigations are needed to help understand the complex nature of the fluid dynamics inside thermoacoustic environment. In order to conduct the fluid dynamic study, an experimental rig that is able of producing the correct oscillatory flow of thermoacoustics environment must be build. In this paper, a test of an experimental rig of a quarter wavelength size with standing wave environment is reported. The rig can be used for detail fundamental investigations of fluid dynamics of an oscillatory flow inside thermoacoustic systems.

## 2. METHODOLOGY

The experimental rig was first designed using DelteEC in order to make sure that thermoacoustic flow conditions could be achieved through the design [6]. Once a correct design is achieved, the experimental rig is build. The experimental rig is as shown in Figure 1. The rig is designed with several segments to allow for investigations of two flow frequencies. The first rig (as is shown in Figure 1) is 6.6 m long while the second rig is

3.8 m long. One side of the resonator is connected to a 700W subwoofer (Model PD180). The input of the loudspeaker is controlled by a DDS function generator and a power amplifier (FLP-MT1201). The loudspeaker is 18 inch in diameter while the resonator is an aluminium duct with a square cross-section of 152.4 mm x 152.4 mm. A loudspeaker box with converging channel is used to connect the subwoofer to the resonator so that standing-wave could be created inside the resonator. A parallel-plate structure (shown as ‘stack’ in Figure 1) is placed at a location of  $0.18\lambda$  from the hard-end of the resonator (the pressure antinode). A piezoresistive sensor (Meggit model 8510B) is used for measuring pressure amplitude of the flow and a hot wire (Sentry model ST732) is used to measure velocity. Sensors are connected to a data logger (Dataq DI-718B) that is fitted with signal conditioner (Model DI-8B41-01). Measured data are processed using Windaq software. The resonator is filled with air at atmospheric pressure.

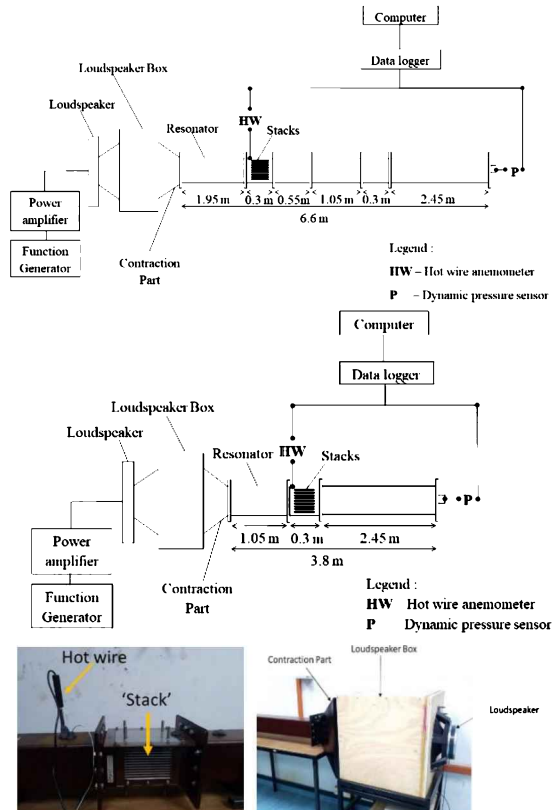


Figure 1 The schematic diagram of the 6.6 m rig (top), the 3.8 m rig (middle) and pictures of the real rig (bottom).

### 3. RESULTS AND DISCUSSION

For ease of fabrication and instrumentation purposes, the experimental rig was designed according to a quarter wavelength criterion with low frequency range. According to calculation, the 6.6 m long resonator is corresponding to a resonance frequency of 13.1 Hz while the 3.8 m long resonator is corresponding to a resonance frequency of 23.1 Hz. However, experiments are needed to confirm the real value of the resonance frequency for the rig as the presence of additional fixtures, like the loudspeaker box and segmentations of resonator, may lead to changes to the resonance frequency.

#### 3.1 Resonance frequency

The resonance frequency is tested by keeping the voltage input of the loudspeaker at a constant minimum value. The frequency is then varied with an increment of 1 Hz until maximum value of pressure is recorded by the pressure sensor. Figure 2 shows the measured resonance frequency for the 6.6 m long and 3.8 m long resonator, respectively. The drive ratio represents the ratio between the measured value of pressure at antinode and the mean pressure. Results show that the resonance frequency of the 6.6 m long rig is 14.2 Hz and the resonance frequency of the 3.8 m long rig is 23.6 Hz.

#### 3.2 Velocity distribution along resonator

Measurements are done for velocity values in several locations along the resonator. The locations are as defined in Figure 3. Locations A to D represent data from

a 6.6 m long resonator while locations E and F represent data from a 3.8 m long resonator.

The measured values are also compared to the values predicted by the non-linear one-dimensional theory of thermoacoustics. The theoretical results of first order harmonic velocity amplitude,  $u_1$ , are calculated using Equation (1).

$$u_1 = \frac{k \cdot p_a \sin(kx)}{\omega \rho_m} \quad (1)$$

The terms  $k$ ,  $p_a$ ,  $x$ ,  $\omega$  and  $\rho_m$  represent the wave number, pressure amplitude at antinode (hard end), location from the antinode, angular velocity and mean density, respectively. The results are as shown in Figure 4.

In general, both theoretical and experimental values show the same pattern of flow increment as drive ratio increases. Location wise, the velocity amplitude reduces as the flow is approaching the hard end (in the direction from A to D for the 6.6 m long resonator and from E to F for the 3.8 m long resonator). In the experiment, the velocity decreases by 0.41 m/s while the theory predicts a reduction of 1.85 m/s. This corresponds to a difference of around 70% which may be related to ‘streaming’ or ‘non-linear’ effects that are not counted in the theoretical equations. Nevertheless, the similar pattern of velocity changes between experiment and theory indicates that a correct thermoacoustic environment have been achieved.

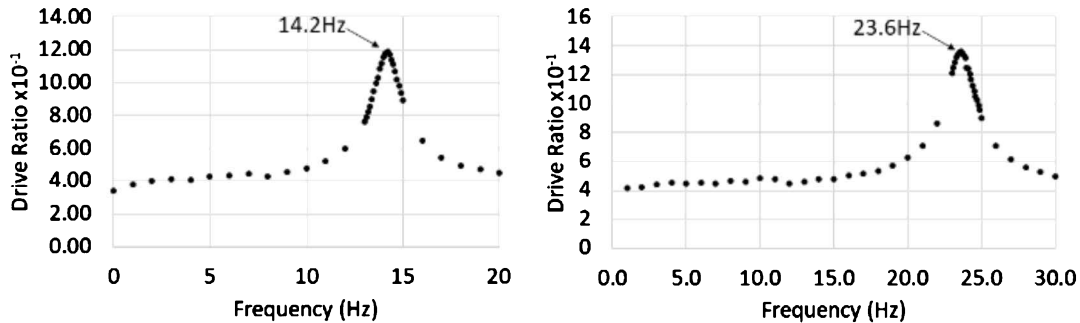


Figure 2 Resonance frequency for the 6.6 m long resonator (left) and the 3.8 m long resonator (right).

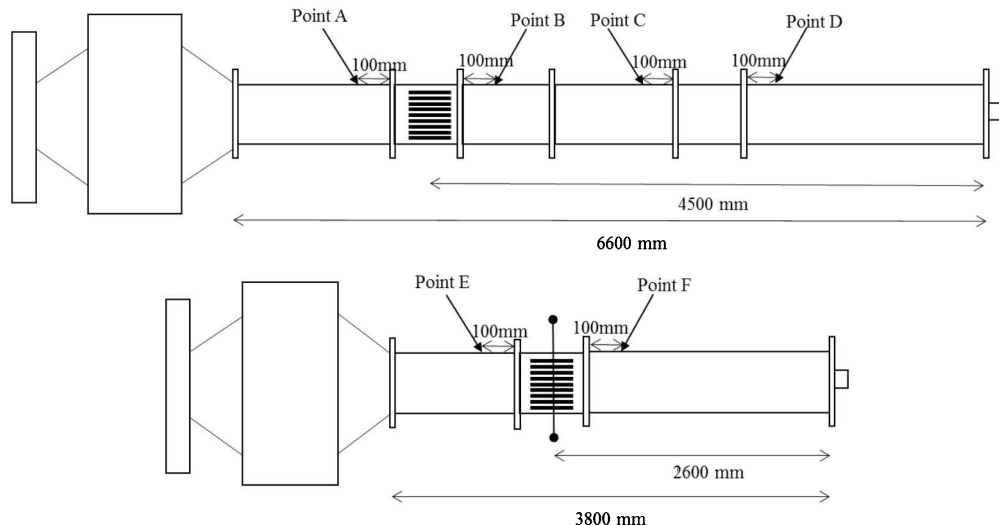


Figure 3 Locations for measurement points along the resonator of 6.6 m long (top) and 3.8 m long (bottom).

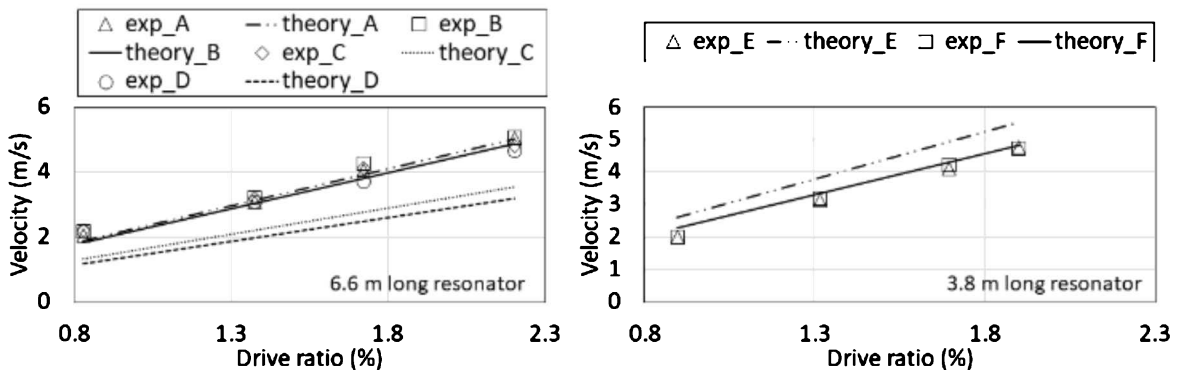


Figure 4 Comparison of velocity amplitude along the resonator between measurement and theoretical values.

#### 4. SUMMARY

Two experimental setups for a standing wave thermoacoustic rig with a quarter wavelength resonator were successfully build with resonance frequency of 14.2 Hz and 23.6 Hz, respectively. The rigs can be used for future investigations of the fluid dynamics phenomena of the less understood thermoacoustic flow conditions.

#### ACKNOWLEDGEMENT

The authors would like to thank Prof. Artur J. Jaworski for his valuable input regarding the experimental measurement practices.

#### REFERENCES

- [1] Abdoulla-Latiwish K. O. A., Mao X., Jaworski A. J. (2017). Thermoacoustic micro-electricity generator for rural dwellings in developing countries by waste heat from cooking activities. *Energy*, 134, 1107-1120.
- [2] Mohd Saat, F.A.Z. and Jaworski, A.J. (2017). Numerical predictions of early stage turbulence in oscillatory flow across parallel plate heat exchangers of a thermoacoustic system. *Applied Sciences*, 7, 673.
- [3] Jaworski, Artur J., Xiaoan Mao, Xuerui Mao, and Zhibin Yu. (2009). Entrance effects in the channels of the parallel plate stack in oscillatory flow conditions. *Experimental Thermal and Fluid Science*, 33(3), 495-502.
- [4] Kuzuu K. and Hasegawa S. (2017). Numerical investigation of heated gas flow in a thermoacoustic device. *Applied Thermal Engineering*, 110, 1283-1293
- [5] Swift G. W., 2002. Thermoacoustics: a unifying perspective for some engines and refrigerators. Sewickley (PA): Acoustical Society of America Publications.

# Simulation study of drying chamber for marine product

Nur Izzati Mohd Azhar<sup>1</sup>, Mohd Afzanizam Mohd Rosli<sup>1,2,\*</sup>, Ahmad Syakir Ghazali<sup>1</sup>, Hiew Sit Jing

<sup>1)</sup>Fakulti Kejuruteraan Mekanikal, Universiti Teknikal Malaysia Melaka,

Hang Tuah Jaya, 76100 Durian Tunggal, Melaka, Malaysia

<sup>2)</sup>Centre for Advanced Research on Energy, Universiti Teknikal Malaysia Melaka,

Hang Tuah Jaya, 76100 Durian Tunggal, Melaka, Malaysia

\*Corresponding e-mail: afzanizam@utem.edu.my

**Keywords:** Drying; CFD simulation; velocity; temperature distribution

**ABSTRACT** – Drying chamber is one of the applications in the drying process. This application is widely used in marine product. In this study, a drying chamber for drying process on salted fishes was selected. It able to produce high quality of products in term of drying uniformity and hygienic. The purpose design of drying chamber consists of three trays that are arranged in different levels as a place to dry the products and chimney for the exhaust air. The prediction of the distribution of velocity and temperature in the chamber along the trays has been simulated by CFD which Ansys Fluent 16. The simulation results show that design (b) is most uniform velocity and temperature distribution than design (a).

## 1. INTRODUCTION

Drying is a mass transfer process resulting in the removal of water moisture or moisture from another solvent, by evaporation from a solid, semi-solid or liquid (hereafter product) to end in a solid state [1-3]. The purpose of drying process is to prolong the shelf-life of products and decrease the expenses of transportation and storage capacity. The most famous application in drying is developed drying chamber [4]. The main problem in applied this application is non-uniformity of end product [5-7]. This non-uniformity contributed to the low quality of products. Basically, the parameters that most affected drying air are temperature and velocity [8,9]. Therefore, Computational Fluid Dynamics is used to predict the flow distribution of velocity and temperature in the chamber. CFD simulation is used in order to cut the budget as the experiment needed a lot of budgets, difficult and took a long period of time consuming. CFD simulation also abled to calculated and solved the equations such as conservation of mass, momentum and energy in order to predict the distribution of temperature and velocity. The most significance parameters inside dryers is the uniformity of air distribution because it is determined both the performance and homogeneity of end dried products [7].

In this study, the main objectives of this work are: (i) to predict the distribution of velocity and temperature in the chamber (ii) to analyze best performance between two difference designs.

## 2. METHODOLOGY

### 2.1 CFD Modeling

The drying chamber is designed by consist of three trays that arranged in different level makes a symmetrical

2D flow domain. The model of chamber has been model by Ansys Fluent 16.1. The dimensions of chamber is 1.15m x 0.625m and the thickness of the tray is 0.025 m.

### 2.2 Basic Governing Equations for CFD Simulation

The conservation of mass, momentum and energy for drying air result in the continuity, Navier-Stokes and energy equation respectively [10]. In this study, the simulation was used turbulent model. Following equations are used in this simulation which are:

$$\text{Continuity equation: } \frac{\partial \rho}{\partial t} + \nabla \cdot (\rho \vec{v}) = 0 \quad \dots (1)$$

$$\text{Momentum conservation equations: } \frac{\partial}{\partial t} (\rho \vec{v}) + \nabla \cdot (\rho \vec{v} \vec{v}) = -\nabla p + \nabla \cdot (\vec{\tau}) + \rho \vec{g} + \vec{F} \quad \dots (2)$$

Energy conservation equation:

$$\frac{\partial}{\partial t} (\rho E) + \nabla \cdot (\vec{v} (\rho E + p)) = \nabla \cdot (k_{eff} \nabla T) + S_h \dots (3)$$

### 2.3 Simulation

The simulation was done by using Ansys Fluent 16.1 to solve the governing equations (1), (2) and (3) on to the structured tetrahedral grid. The standard k-e turbulence model was applied in steady state conditions. The boundary conditions were set as follows: (i) inlet: The velocity inlet is 1, 2, 3 m/s, and the air temperature was 0, 20, 30 and 40 °C. (ii) exhaust: The gauge pressure was assumed to be equal to 0 at the outlet.

## 3. RESULTS AND DISCUSSION

### 3.1 Velocity and Temperature Profile

In order to analyze the best performance of drying chamber, there are two data analysis of proposed designs were carried out by using CFD. The most practicable design can be evaluated by comparing the uniformity of air flow distribution in the drying chamber as shown in Figure 1. The distribution of temperature profiles for both designs are shown in Figure 2.

In the design (a), the velocity distribution is poor than design (b). This is because air inlet and exit are small compared to the tray width. For the design (b), it shows sensible in term of uniformity of distribution of temperature in the chamber and tray's zone that close to inlet is preserved maximum temperature. The average velocity and temperature of both designs are calculated. From both designs, it shows that changing the geometrical of drying chamber in term of position of outlet and the size of inlet has some affected on air velocity distribution than temperature distribution.

The increasing angle of divergence can improve the distribution of velocity and relocate exit at the center contributed to the more uniform velocity distribution at the tray zone. Therefore, design (b) can be concluded as the best design compared to the design (a).

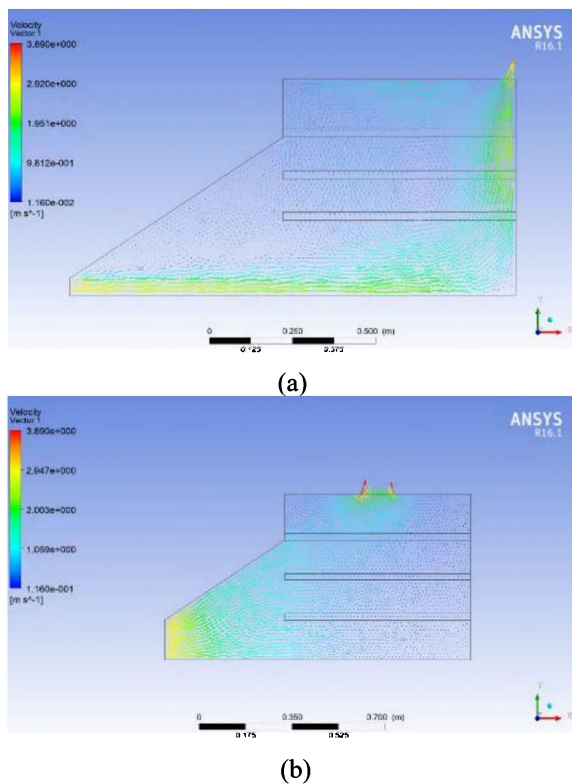


Figure 1 Air velocity distribution profiles for two designs by CFD at inlet air velocity = 3 m/s.

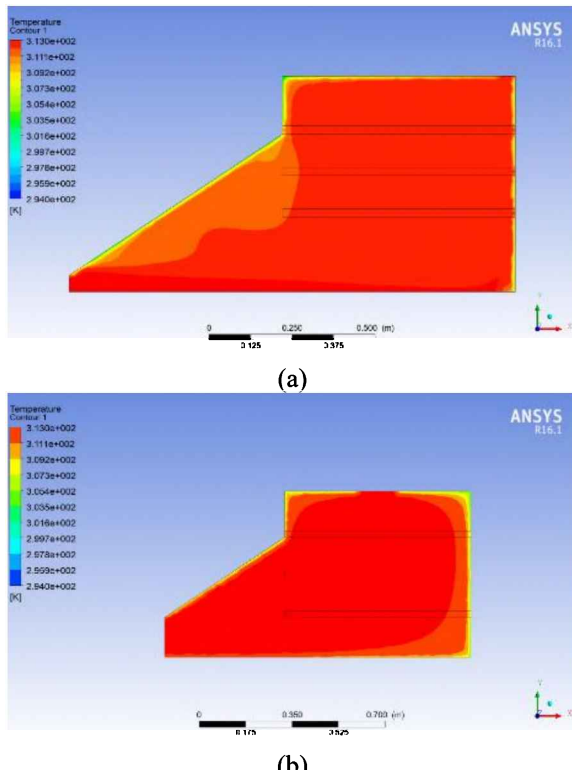


Figure 2 Temperature distribution profiles for two designs by CFD at temperature = 40°C.

#### 4. SUMMARY

Two designs of drying chamber with different position of outlet has been simulated by using ANSYS Fluent 16.1 to investigate the affected of outlet to the uniformity velocity and temperature distribution. From the results of simulation, it showed that the best performance of drying chamber is design (b) as the most uniform of distribution. However, the changing of geometry more affected to the velocity distribution rather than temperature distribution.

#### ACKNOWLEDGEMENT

The authors would like to thank the Fakulti Kejuruteraan Mekanikal and Centre for Advanced Research on Energy of Universiti Teknikal Malaysia Melaka.

#### REFERENCES

- [1] Mujumdar, A. S., & Menon, A. S. (1995). Drying of solids: principles, classification, and selection of dryers. *Handbook of Industrial Drying, 1*, 1-39.
- [2] Noh, A. M., Mat, S., & Ruslan, M. H. (2018). CFD simulation of temperature and air flow distribution inside industrial scale solar dryer. *Journal of Advanced Research in Fluid Mechanics and Thermal Sciences*, 45(1), 156-64.
- [3] Gupta, P. M., Das, A. S., Barai, R. C., Pusadkar, S. C., & Pawar, V. G. (2017). Design and construction of solar dryer for drying agricultural products. *International Research Journal of Engineering and Technology*, 4(3), 1946.
- [4] Amanlou, Y., & Zomorodian, A. (2010). Applying CFD for designing a new fruit cabinet dryer. *Journal of food engineering*, 101(1), 8-15.
- [5] Adams, R. L., & Thompson, J. F. (1985). Improving drying uniformity in concurrent flow tunnel dehydrators. *Transactions of the ASAE*, 28(3), 890-0892.
- [6] Mathioulakis, E., Karathanos, V. T., & Belessiotis, V. G. (1998). Simulation of air movement in a dryer by computational fluid dynamics: application for the drying of fruits. *Journal of Food Engineering*, 36(2), 183-200.
- [7] Mirade, P. S. (2003). Prediction of the air velocity field in modern meat dryers using unsteady computational fluid dynamics (CFD) models. *Journal of Food Engineering*, 60(1), 41-48.
- [8] Mulet, A., Berna, A., Borr, M., & Pinaga, F. (1987). Effect of air flow rate on carrot drying. *Drying technology*, 5(2), 245-258.
- [9] Karathanos, V. T., & Belessiotis, V. G. (1997). Sun and artificial air drying kinetics of some agricultural products. *Journal of Food Engineering*, 31(1), 35-46.
- [10] Yongson, O., Badruddin, I. A., Zainal, Z. A., & Narayana, P. A. (2007). Airflow analysis in an air conditioning room. *Building and Environment*, 42(3), 1531-1537.

# Investigation of heat effects on electronic sensors in a lightning detection system

Tuan Nurul Husna Tuan Zakaria<sup>1,\*</sup>, Maslan Zainon<sup>2</sup>, Maaspaliza Azri<sup>1</sup>, Zikri Abadi Baharudin<sup>2</sup>, Ahmad Aizan Zulkefle<sup>2</sup>, Ahmad Idil Abdul Rahman<sup>2</sup>, Mohd Ariff Mat Hanafiah<sup>2</sup>, Shahrudin Zakaria<sup>2</sup>

<sup>1)</sup> Fakulti Kejuruteraan Elektrik, Universiti Teknikal Malaysia Melaka,  
Hang Tuah Jaya, 76100 Durian Tunggal, Melaka, Malaysia

<sup>2)</sup> Fakulti Teknologi Kejuruteraan Elektrik dan Elektronik, Universiti Teknikal Malaysia Melaka,  
Hang Tuah Jaya, 76100 Durian Tunggal, Melaka, Malaysia

\*Corresponding e-mail: husnazakaria94@gmail.com

**Keywords:** Heat effects; electronic sensors; lightning detection system

**ABSTRACT** – This paper describes the investigation of a lightning detection system that focuses on heat effects on electronic sensors. The study involves designing and performing simulations of a lightning detection circuit with several types of Integrated Circuits (ICs). BUF602, LMH6559, and THS4631 ICs were used to determine how heat from solar radiation can affect their performances. OrCAD software was used to simulate and analyse a series of data via electric field measurements.

## 1. INTRODUCTION

Integrated circuits are circuits composed of transistors, diodes, resistors, and capacitors fabricated on a single chip of semiconductor material. Each of these integrated circuits is designed and built to withstand particular amounts or level of heat. When overheating occurs, the ability and performance of integrated circuits are affected. Thus, this research paper explores and discusses the effects of heat on electronic components in a lightning detection system.

The primary goal of this research is to design and simulate a lightning detection circuit with several types of integrated circuits (ICs) or sensors, which are BUF602, LMH6559 and THS4631, mainly due to their economic values and accessibility. The schematic diagrams of these three different types of ICs were designed in OrCAD software.

Overheating can potentially affect or even damage electric components, which the causes of overheating and how to protect electronic components from the damaging effects of excessive heat were explained with some recommendations by Almubarak [1].

Integrated circuits are semiconductor devices that mostly made of Silicon materials, however, many researchers had also been conducted to study the performance of integration between Silicon and Germanium semiconductors [2][3][4]. ICs in electronic

devices that operated at elevated temperature is a major cause of failures and a critical problem in developing more advanced electronic packages. Thermal management issues such as heat dissipation from the electronic control unit need to be resolved [5].

Temperature is the main factor or source attributed to the efficient performance of electronic components since there is a relationship between the performances, including the lifecycle of electronic components and its particular range of operating temperature [6,7].

Among other factors, lightning is a major contributor to electrical power disruptions. For many years Eskom has had to improvise to make sure the most effective mitigation methods and applications to address the impact of lightning on the delivery of power within its operational border [8].

## 2. METHODOLOGY

The circuit development for electronic sensors in a lightning detection system is divided into two sections, which are the software and hardware. The design of the modelling circuits must be determined and simulated accordingly prior to designing and constructing the related hardware. This paper focuses on the software section.

Initially, for example in THS4631 circuit, the circuit modelling was designed in OrCAD software and the compatibility of the circuit output must be determined whether it was feasible to be used in this research or vice versa. After the circuit was successfully simulated in OrCAD software, the next stage was to design the PCB layout, and then proceeded to its hardware development. This part consists of all the selected ICs; BUF602, LMH6559, and THS4631. Figure 1 shows the schematic diagram of one of the ICs that was designed and successfully simulated.

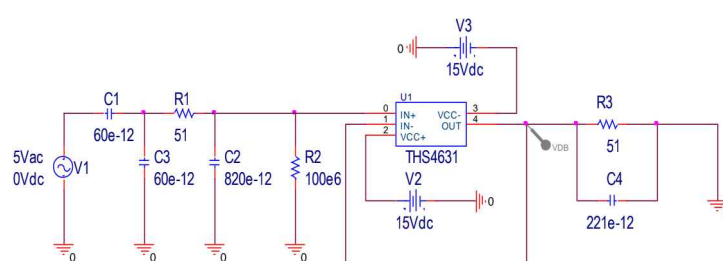


Figure 1 Schematic diagram for THS4631.

Figure 2 depicts the system measuring scheme by which at the sensor stage, the plate of antenna was set at a specific location and connected to the input using a Bayonet Neill-Concelman (BNC) cable. The output was connected to the compensator and Yokogawa oscilloscope to record the data waveform that occurred when a lightning strike is detected. The combination of the circuit and antenna was set up as one detection system at the investigation station.

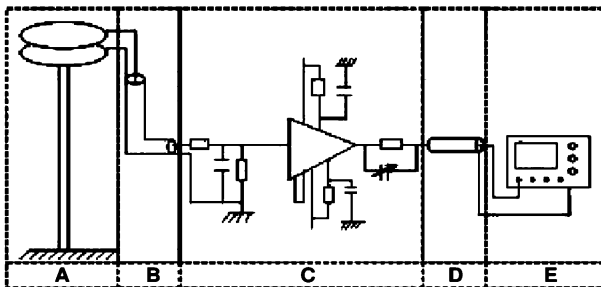


Figure 2 Scheme of the measuring system. (A) antenna, (B) short coaxial cable, (C) electronic circuit, (D) long coaxial cable, (E) recording equipment.

In this research, the data of heat effects on BUF602, LMH6559, and THS4631 were determined from the measured waveforms by using an OrCAD software. These data were compared to investigate and analyse to determine which of the integrated circuits is the most suitable to be used in a lightning detection system.

### 3. RESULTS AND DISCUSSION

Figure 3 represents the preliminary result of a waveform from the simulated circuit for THS4631.

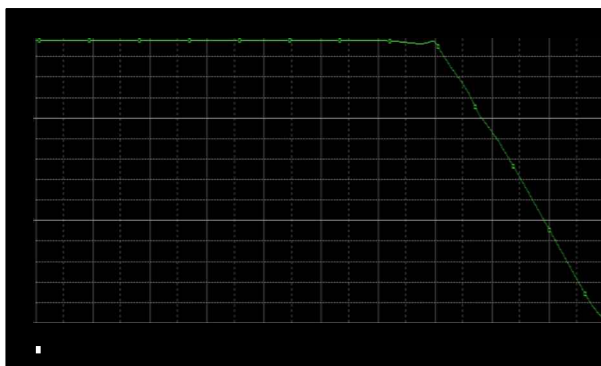


Figure 3 Waveform result of THS4631.

The emergence of this waveform simulation result can be attributed to a certain level of heat effect for the electronic sensor. In order to investigate the actual heat effects on electronic sensors in a lightning detection system, all of the electric field waveform results will be compared according to the changes of temperatures that occur inside the electronic control box. The results can further determine the sensors' performances, particularly for their time rising and zero crossing parameters.

### 4. CONCLUSION

Lightning is a universe's natural phenomenal activity that always manage to attract interests of many researchers in their studies. Lightning is a universe natural phenomenon activity that always attracts the

interest of many researchers in their studies. In Malaysia, the effects of heat on electronic sensors in a lightning detection system are yet to be further investigated in obtaining reliable data. This research is one of the initial steps towards the stated investigation, which involved designing and performing simulations of a lightning detection circuit with several types of integrated circuits by using an OrCAD software. BUF602, LMH6559, and THS4631 ICs were selected and used as the electronic sensors, which the data results were compared to determine which of the integrated circuits has the best performance and suitable to be implemented in a lightning detection system.

### REFERENCES

- [1] Almubarak, A. A. (2017). The effects of heat on electronic components. *Int. J. Eng. Res. Appl.*, 7(5), 52–57.
- [2] Zulkefle, A. A., Zainon, M., Zakaria, Z., Hanafiah, M., Ariff, M., Razak, N. H. A., ... & Amin, N. (2015). A comparative study between silicon germanium and germanium solar cells by numerical simulation. *Applied Mechanics and Materials*, 761, 341-346.
- [3] Mohamad, R. T., Zulkefle, A. A., Baharudin, Z. A., Rahman, A. A., Zainon, M., Hanafiah, M. A. M., Salim, S. N. S., Abu Shah, I., Ibrahim, M., Adnan, H., Amran, A. C., Ibrahim, I. M., Abdullah, L., Aman, O., Raja Abd Rahman, R. R., & Adnan, W. A. W. (2015). Effect of temperature on 1 micron thick silicon solar cell. *International Journal of Applied Engineering Research*, 10(11), 29127-29133.
- [4] Zulkefle, A. A., Zainon, M., Zakaria, Z., Shahahmadi, S. A., Bhuiyan, M. A. M., Alam, M. M., Sopian, K., & Amin, N. (2013). Effects of germanium layer on silicon/germanium superlattice solar cells. In *2013 IEEE 39th Photovoltaic Specialists Conference (PVSC)* (pp. 3484-3486).
- [5] Ekpu, M., Bhatti, R., Ekere, N., Mallik, S., Amalu, E., & Otiaba, K. (2011). Investigation of effects of heat sinks on thermal performance of microelectronic package. In *3rd IEEE International Conference on Adaptive Science and Technology (ICAST 2011)* (pp. 127-132).
- [6] Lakshminarayanan, V., & Sriraam, N. (2014, January). The effect of temperature on the reliability of electronic components. In *2014 IEEE International Conference on Electronics, Computing and Communication Technologies (CONECCT)* (pp. 1-6).
- [7] Watson, J., & Castro, G. (2012). High-temperature electronics pose design and reliability challenges. *Analog Dialogue*, 46(2), 3-9.
- [8] Evert, R., & Schulze, G. (2005). Impact of a new lightning detection and location system in South Africa. In *2005 IEEE Power Engineering Society Inaugural Conference and Exposition in Africa* (pp. 356-363).

# Mathematical modeling of two-phase flow under Dusty Williamson fluid model

N.S. Arifin, S.M. Zokri, A.R.M. Kasim\*, M.Z. Salleh

Applied & Industrial Mathematics Research Group, Faculty of Industrial Sciences & Technology,  
Universiti Malaysia Pahang, 26300 UMP Kuantan, Pahang, Malaysia

\*Corresponding e-mail: rahmanmohd@ump.edu.my

**Keywords:** Aligned magnetic field; two-phase flow; dusty Williamson fluid

**ABSTRACT** – A physical phenomenon involving two-phase system (fluid and solid) is encountered in many applications like air or water pollution, blood flow in arteries, flows in rocket tubes, sedimentation and fluidized bed. In all of these implementations, the suitable knowledge concerning such system is very essential for predicting the behavior of the flow processes to obtain the expected outcome. Therefore, this paper provides some theoretical assumptions of the possible scenarios occurring in the particular flow system by presenting the mathematical model of two-phase flow. Specifically, the Williamson fluid flow in the presence of dust particles is analyzed with the amalgamate influences of buoyancy force, modified magnetic field and thermal condition of Newtonian heating. The rheology of the respective two-phase flow model is characterized by a set of partial differential equations, which describes its physical properties.

## 1. INTRODUCTION

In many practical circumstances such as impurities in common fluid, combustion chambers, environmental pollutants, fluidized beds, treatment of waste-water and petroleum industry draw heavily on two-phase flow system [1]. Moreover, the contamination of solid particles (ash and shoot) exerts a profound influence on the performance of combustion MHD generators and plasma MHD accelerators which then instigates a number of studies relating to two-phase flow system associated with uniform magnetic field [2-3]. Besides, the recent mathematically studied has been done by [4-5]. In connection to these studies, the present investigation aims to give a special focus on the application of modified magnetic field to non-Newtonian Williamson fluid flow embedded with dust particles from the perspectives of mathematical analysis.

Among non-Newtonian fluids, Williamson fluid with the capability to portray the characteristics of both elastic and viscous effects has also engaged attention of many researchers. Furthermore, the flow of Williamson fluid containing solid particles is an important preamble to the understanding of behaviour of blood in stenosed arteries, polymer solution and chyme in small intestine by assuming the whole system as fluid-solid suspension. This paper endeavours to account for the two-phase flow properties of Williamson fluid over a vertical stretching sheet.

## 2. METHODOLOGY

### 2.1 Mathematical Formulation

A steady two-dimensional incompressible dusty Williamson fluid over a vertical stretching sheet has been considered. The sheet is stretched with uniform velocity,  $u_w(x) = ax$  and magnetic field is inclined at angle  $\alpha_1$  to the flow direction, as shown in Figure 1. Note that, the following assumptions for dust particles are adapted, in which the dust particles are in spherical shape, uniform size and number density of these are taken as constant throughout the flow.

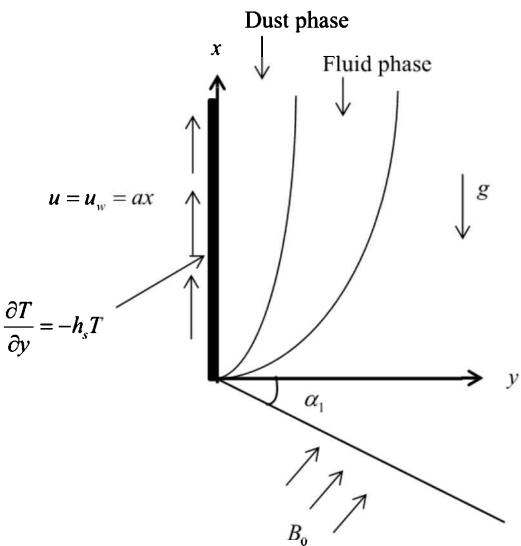


Figure 1 Flow configuration.

The governing boundary layer equations for this two-phase model can be written as

Fluid phase:

$$\frac{\partial u}{\partial x} + \frac{\partial v}{\partial y} = 0, \quad (1)$$

$$u \frac{\partial u}{\partial x} + v \frac{\partial u}{\partial y} = \frac{\mu_0}{\rho} \left( \frac{\partial^2 u}{\partial y^2} + \sqrt{2\Gamma} \frac{\partial u}{\partial y} \frac{\partial^2 u}{\partial y^2} \right) \quad (2)$$

$$+ \frac{\rho_p}{\rho \tau_v} (u_p - u) - \frac{\sigma}{\rho} B_0^2 \sin^2 \alpha_1 u + \beta^* g (T - T_\infty), \quad (3)$$

Dust phase:

$$\frac{\partial u_p}{\partial x} + \frac{\partial u_p}{\partial y} = 0, \quad (4)$$

$$\rho_p \left( u_p \frac{\partial u_p}{\partial x} + v_p \frac{\partial u_p}{\partial y} \right) = \frac{\rho_p}{\tau} (u - u_p), \quad (5)$$

$$\rho_p c_s \left( u_p \frac{\partial T_p}{\partial x} + v_p \frac{\partial T_p}{\partial y} \right) = -\frac{\rho_p c_s}{\gamma_T} (T_p - T). \quad (6)$$

The boundary conditions associated with the model are  
 $u = u_w(x), v = 0, -k(\partial T / \partial y) = h_f(T_f - T)$  at  $y = 0$   
 $u \rightarrow 0, u_p \rightarrow 0, v_p \rightarrow v, T \rightarrow T_\infty, T_p \rightarrow T_\infty$  at  $y \rightarrow \infty$       (7)

The similarity transformations for both phases are

$$u = axf'(\eta), v = -\sqrt{av}f(\eta), \eta = \sqrt{\frac{a}{v}}y, u_p = axF'(\eta), \\ v_p = -\sqrt{av}F(\eta), \theta(\eta) = \frac{T - T_\infty}{T_\infty}, \theta_p(\eta) = \frac{T_p - T_\infty}{T_\infty}, \quad (8)$$

By using Equation (8), Equations (1)-(7) become

$$f'''(\eta) + f(\eta)f''(\eta) - (f'(\eta))^2 + \lambda_1 f''(\eta)f'''(\eta) \\ + \beta N(F'(\eta) - f'(\eta)) - M \sin^2 \alpha_1 f'(\eta) + \lambda \theta(\eta) = 0, \quad (9)$$

$$\theta''(\eta) + Pr f(\eta)\theta'(\eta) + \frac{2}{3}\beta N(\theta_p(\eta) - \theta(\eta)) = 0, \quad (10)$$

$$(F'(\eta))^2 - F(\eta)F''(\eta) + \beta(F'(\eta) - f'(\eta)) = 0, \quad (11)$$

$$\theta_p'(\eta)F(\eta) + \frac{2}{3}\frac{\beta}{\lambda Pr}(\theta_p(\eta) - \theta(\eta)) = 0, \quad (12)$$

and the transformed boundary conditions become

$$f(0) = 0, f'(0) = 1, \theta'(0) = -b(1 - \theta(0)) \text{ at } \eta = 0 \\ f'(\eta) \rightarrow 0, F'(\eta) \rightarrow 0, \quad (13) \\ \theta(\eta) \rightarrow 0, \theta_p(\eta) \rightarrow 0 \quad \text{as } \eta \rightarrow \infty$$

Note that,  $\beta, N, M, \alpha_1, \lambda, Pr, \gamma$  and  $b$  are the physical parameters of fluid-particle interaction, mass concentration of particle phase, magnetic field, aligned angle, mixed convection, Prandtl number, specific heat ratio of mixture and Biot number.

## 2.2 Numerical Computation

Equations (9)-(13) have been solved by using the Keller-box method in Matlab software. The finite boundary layer thickness of  $\eta_\infty = 8$  is selected for boundary conditions to fully satisfied.

## 3. RESULTS AND DISCUSSION

To ascertain the present results, the validation has been made by a direct comparison with existing outcome in literature. The comparative values displayed in Table 1 are in a good agreement, which shows reliability in the numerical solutions obtained.

Figures 2 and 3 illustrated the influences of fluid particle interaction parameter  $\beta$  on velocity and temperature profiles. The velocity and temperature profiles of fluid phase are reported to decrease with the increase value of  $\beta$ . In contrast, the opposite behavior occurs for dust phase when  $\beta$  increased. Physically, the growing effect of  $\beta$  reduces the relaxation time of dust particles which then motivates the dust particles motion so that the equilibrium stage between their velocities and fluid velocity is achieved. Additionally, the fluid temperature decreases as the thermal relaxation time is also reduced.

Table 1 Comparative values of  $-f''(0)$  when  $Pr = 10$ ,  $N = \beta = \lambda = 0, \alpha_1 = \pi/2, \gamma \rightarrow \infty$ .

<b>M</b>	<b>Fathizadeh et al. [6]</b>	<b>Present</b>
0	1.00000	1.00000
1	1.41421	1.41421
5	2.44948	2.44949
10	3.31662	3.31662

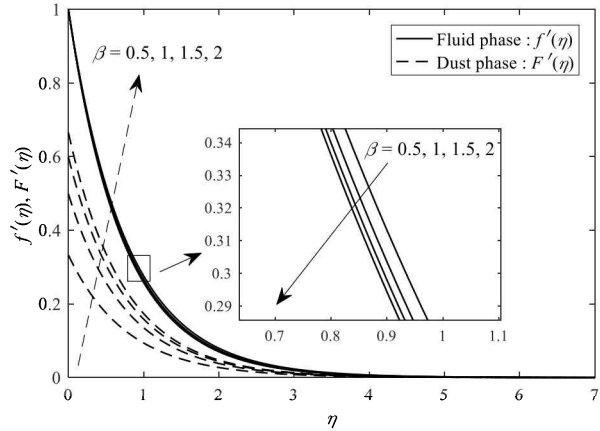


Figure 2 Velocity profile for various values of  $\beta$ .

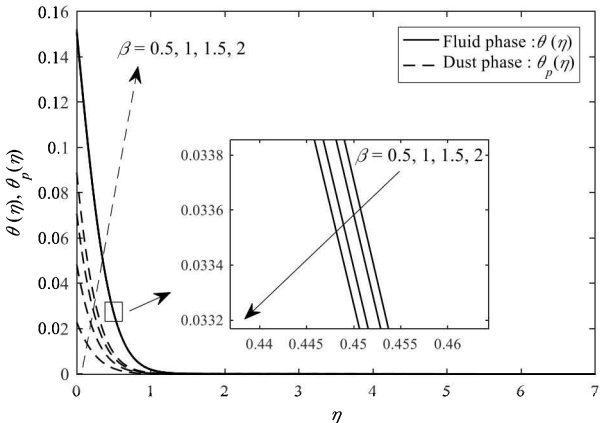


Figure 3 Temperature profile for various values of  $\beta$ .

## 4. CONCLUSION

Exploration into the analysis of fluid-solid system has shown that the accumulation of dust particles near the wall could reduce the performance of certain engineering devices. Thus, it is envisaged that the present solutions will contribute to the understanding of behavior in this system by providing anticipating outcomes. Note that,  $\beta$  has influenced the flow and temperature of fluid as well as dust phases, respectively.

## ACKNOWLEDGMENT

The authors gratefully acknowledge the financial support received Universiti Malaysia Pahang (UMP) under RDU 170328 and RDU 190303.

## REFERENCES

- [1] Siddiq, S., Begum, N., Hossain, M. A., & Gorla, R. S. R. (2017). Natural convection flow of a two-phase dusty non-Newtonian fluid along a vertical surface. *International Journal of Heat and Mass Transfer*, 113, 482-489.

- [2] Venkateshappa, V., Rudraswamy, B., Gireesha, B. J., & Gopinath, K. (2008). Viscous dusty fluid flow with constant velocity magnitude. *Electronic Journal of Theoretical Physics*, 5(17), 237-252.
- [3] Nandkeolyar, R., & Sibanda, P. (2013). On convective dusty flow past a vertical stretching sheet with internal heat absorption. *Journal of Applied Mathematics*, 2013.
- [4] Arifin, N. S., Zokri, S. M., Kasim, A. R. M., Salleh, M. Z., & Mohammad, N. F. (2018). Aligned magnetic field flow of Williamson fluid over a stretching sheet with convective boundary condition. *MATEC Web of Conferences*, 189, 11005.
- [5] Arifin, N. S., Zokri, S. M., Kasim, A. R. M., Salleh, M. Z., & Mohammad, N. F. (2019). Two-Phase Mixed Convection Flow of Dusty Williamson Fluid with Aligned Magnetic Field over a Vertical Stretching Sheet. In *Proceedings of the Third International Conference on Computing, Mathematics and Statistics (iCMS2017)* (pp. 209-216). Springer, Singapore.
- [6] Fathizadeh, M., Madani, M., Khan, Y., Faraz, N., Yıldırım, A., & Tutkun, S. (2013). An effective modification of the homotopy perturbation method for mhd viscous flow over a stretching sheet. *Journal of King Saud University-Science*, 25(2), 107-113.

# Turbulence measurements in the centerline region of a turbulent round jet using a software-driven laser doppler system

Mohd Rusdy Yaacob<sup>1,\*</sup>, Preben Buchhave<sup>2</sup>, Clara Marika Velte<sup>3</sup>

<sup>1)</sup> Fakulti Kejuruteraan Elektrik, Universiti Teknikal Malaysia Melaka,

Hang Tuah Jaya, 76100 Durian Tunggal, Melaka, Malaysia

<sup>2)</sup> Intarsia Optics, Sønderskovvej 3, 3460 Birkerød, Denmark

<sup>3)</sup> Department of Mechanical Engineering, Technical University of Denmark, 2800 Kgs. Lyngby, Denmark

\*Corresponding e-mail: rusdy@utem.edu.my

**Keywords:** Turbulent round jet; laser Doppler anemometer; turbulence measurements

**ABSTRACT** – This paper demonstrates turbulence measurements of a turbulent round jet. It is aimed to map the energy cascade and turbulent scales along the jet centerline, spanning from the developing region to the fully developed counterpart. Measurements were performed using a software-driven LDA system, which was tested and proven to deliver high accuracy measurements. The velocity static moments show a similar trend with previous jet studies, as expected. The spatial kinetic energy spectra and second-order structure functions have been compared to the Kolmogorov -5/3 and 2/3 power laws. Good agreement is only obtained in the fully developed region.

## 1. INTRODUCTION

An axisymmetric turbulent round jet has been considered as a classical flow problem since this in principle simple flow still exhibits many of the elementary physical behavior patterns of turbulent flow [1]. Experimental investigation on it will therefore be significant in solving different kinds of problems identified in various types of flow processes [2]. Measurement wise, the centerline region is considered less challenging compared to the shear region, where the velocity fluctuation and turbulence intensity are much higher [3]. Investigation on this region may therefore be not as central as across the shear layer but a higher resolution and rigorous measurement along the jet centerline can be of the great interest in mapping the energy cascade and turbulent scales in the centerline region. This even becomes more essential when the measurements are performed using a novel and sophisticated laser Doppler system [4], which has been proven to function robustly even in the more difficult regions of the jet [5]. In fact, a significantly higher data rate is also expected from the measurements in the centerline region, which allows us to compute more accurately and obtain meaningful plots of the higher order turbulence statistics.

## 2. METHODOLOGY

Measurements were performed along the jet centerline (exit diameter,  $D=10$  mm) to investigate the centerline profiles of the mean streamwise velocity and its higher order statistics. The measurement points range from  $x/D=10$  up to  $x/D=37$ , with 10 mm increments between each point (see Figure 1), which should cover both the non-equilibrium (developing) and equilibrium

(fully developed) regions of the jet. The exit velocity was set to nearly 40 m/s that corresponds to a jet exit Reynolds number,  $Re \approx 25000$ . The data was then transferred to a computer for signal processing and data interpretation using our in-house LDA processing software, which has been thoroughly described in [4,5].

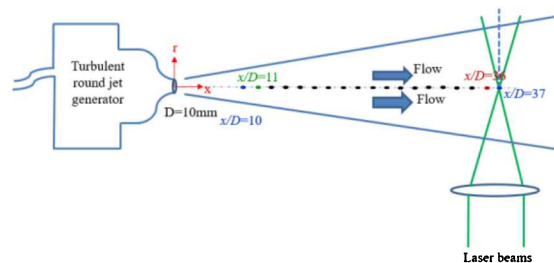


Figure 1 Distribution of measurement points along the jet centerline.

## 3. RESULTS AND DISCUSSION

The mean streamwise velocity, velocity variance and turbulence intensity profiles with downstream distance along the centerline are displayed in Figure 2. The first two of these decay approximately inversely proportionally with the downstream distance, as expected, with a faster decay in the developing region [6][7]. The turbulence intensity builds up more gradually in the developing region and asymptotes to a nominal value of around 24% in fully developed counterpart.

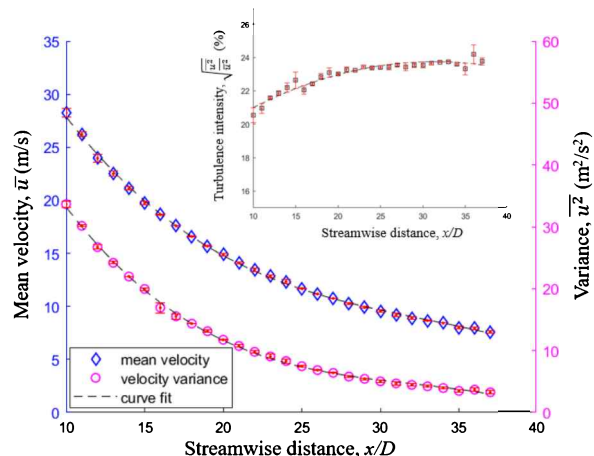


Figure 2 The downstream profiles of mean streamwise velocity, velocity variance and turbulence intensity, with 3<sup>rd</sup>-order polynomial fit.

Further, the energy spectra were also computed, which describe the distribution of turbulent kinetic energy,  $E$  across different wavenumbers,  $k$  of the flow (see Figure 3). Each spectrum is deliberately normalized in the low wave number asymptote for a better comparison in shapes. The shape of the spectrum corresponding the fully developed region ( $x/D \geq 25$ ) appears to nearly follow the  $-5/3$  slope as postulated by the Kolmogorov  $-5/3$  law [8][9]. The spectra obtained in the non-equilibrium counterpart revealed a symptom of invalidity of the law.

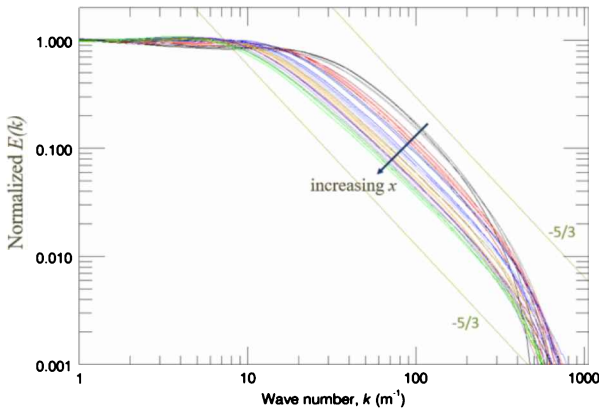


Figure 3 Downstream development of spatial turbulent kinetic energy spectra. Following arrow direction:  $x/D = 10, 11, 12, 13, 14, 15, 16, 17, 18, 19, 20, 21, 22, 23, 24, 25, 26, 27, 28, 29, 30, 31, 32, 33, 34, 35, 36, 37$ .

The second order structure functions,  $S_2(\ell)$  are plotted in Figure 4 to show the development of turbulent scales,  $\ell$  across the jet centerline. The large scales are seen to grow, and more large-scale activity is relatively noticed in the downstream direction. The tendency to follow the  $2/3$  slope is again higher in the equilibrium region compared to the non-equilibrium counterpart [10,11].

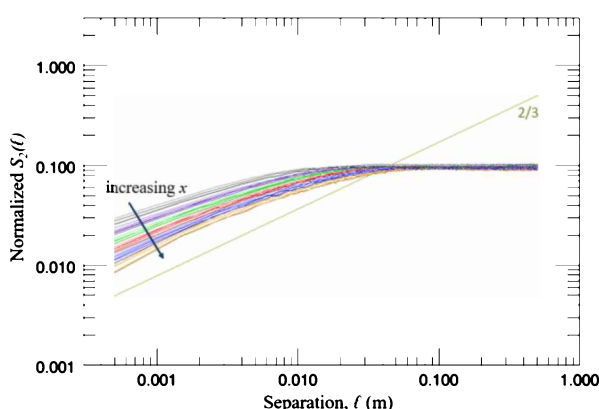


Figure 4 Downstream development of spatial second order structure functions. Following arrow direction:  $x/D = 10, 11, 12, 13, 14, 15, 16, 17, 18, 19, 20, 21, 22, 23, 24, 25, 26, 27, 28, 29, 30, 31, 32, 33, 34, 35, 36, 37$ .

#### 4. CONCLUSION

Measurements have been successfully performed to map the energy cascade and turbulent scales along the jet centerline, while revealing different degree of validity of the Kolmogorov  $-5/3$  and  $2/3$  laws. The disagreement to

the laws found in the developing region open doors to work on deeper statistical analysis, which can be useful for numerical turbulence modelers.

#### ACKNOWLEDGEMENT

The authors wish to acknowledge the support of Ministry of Education Malaysia, DTU Mechanical Engineering, Reinholdt W. Jørk og Hustrus Fond (grant journal no. 13-J9-0026), Fabriksejer, Civilingenør Louis Dreyer Myhrwold og hustru Janne Myhrwolds Fond (grant journal no. 13-M7-0039, 15-M7-0031 and 17-M7-0035) and Siemens A/S Fond grant no. 41.

#### REFERENCES

- [1] Capp, S. P. (1984). Experimental investigation of the turbulent axisymmetric jet. State University of New York, Buffalo.
- [2] Islam, M. T., & Ali, M. A. T. Flow characteristics of a turbulent axisymmetric jet. *J. Inst. Eng. (India). Mech. Eng. Div.*, 76, 65–71.
- [3] Yaacob, M. R., Schlander, R. K., Buchhave, P., & Velte, C. M. (2018). Mapping of the turbulent round jet developing region using a constant temperature anemometer (CTA). *Malaysian Journal of Fundamental and Applied Sciences*, (Special Issue on Natural Sciences and Mathematics (ESCon 2018)), 443-446.
- [4] Yaacob, M. R., Schlander, R. K., Buchhave, P., & Velte, C. M. (2018). Validation of improved laser Doppler anemometer (LDA) based on the fully developed turbulent round jet. In *Symposium on Electrical, Mechatronics and Applied Science 2018*.
- [5] Yaacob, M. R., Schlander, R., Buchhave, P., & Velte, C. M. (2018). Experimental evaluation of Kolmogorov's  $-5/3$  and  $2/3$  power laws in the developing turbulent round jet," *Journal of Advanced Research in Fluid Mechanics and Thermal Sciences*, 45(2), 14–21.
- [6] Grandchamp, X., Van Hirtum, A., & Pelorson, X. (2013). Centreline velocity decay characterisation in low-velocity jets downstream from an extended conical diffuser. *Meccanica*, 48(3), 567-583.
- [7] Ball, C. G., Fellouah, H., & Pollard, A. (2012). The flow field in turbulent round free jets. *Progress in Aerospace Sciences*, 50, 1-26.
- [8] Batchelor, G. K. (1953). *The theory of homogeneous turbulence*. Cambridge university press.
- [9] George, W. K., & Gibson, M. M. (1992). The self-preservation of homogeneous shear flow turbulence. *Experiments in fluids*, 13(4), 229-238.
- [10] Danaila, L., Anselmet, F., & Antonia, R. A. (2002). An overview of the effect of large-scale inhomogeneities on small-scale turbulence. *Physics of Fluids*, 14(7), 2475-2484.
- [11] Romano, G. P., & Antonia, R. A. (2001). Longitudinal and transverse structure functions in a turbulent round jet: effect of initial conditions and Reynolds number. *Journal of Fluid Mechanics*, 436, 231-248.

# The application of spectral methods in two-dimension fluid flow

Farida Nurmala Sihotang\*, Diyah Wijayati, Robi Dany Riupassa

Program Studi Teknik Informatika, Sekolah Tinggi Teknologi Bandung,  
Bandung, 40235 Bandung, Jawa Barat, Indonesia

\*Corresponding e-mail: farida@sttbandung.ac.id

**Keywords:** Vorticity; spectral methods; fluid

**ABSTRACT** – Spectral method is a numerical method for solving partial differential equation using Fourier transform. The application of Fourier transform is changes differential equation into ordinary equation. The differential equation is used in 2D fluid flow turbulence problem governed by incompressible constant density Navier Stokes equation.

## 1. INTRODUCTION

In this paper we will consider the 2D turbulence problem whre flow is governed by incompressible constant density Navier Stokes equation. Navier Stokes equation is differential equation for 2D case who's interesting to discuss. The solution of the equation needs numerical approach. The numerical methods will use spectral method with Fourier series expansion. The spectral methods transform partial differential equation with time, this make easily to find numerical solution. The solution of numerical equation is obtained from inverse transform Fourier with periodic boundary.

## 2. METHODOLOGY

### 2.1 Vorticity Equation

We consider the problem of two-dimensional turbulence where the flow is governed by Navier Stokes equation which consists of consevation of mass and momentum.

Conservation of mass

$$\nabla \cdot \mathbf{u} = 0 \quad (1)$$

momentum

$$\frac{\partial \mathbf{u}}{\partial t} + \mathbf{u} \cdot \nabla \mathbf{u} = -\frac{1}{\rho} \nabla P + \nu \nabla^2 \mathbf{u} - \frac{\mathbf{u}}{\tau} + \mathbf{F} \quad (2)$$

Where  $\mathbf{u} = [u, v]$  is a velocity vector of fluid particle,  $\rho$  is the fluid mass density,  $P$  is the pressure,  $\nu$  is the kinematic viscosity,  $\tau$  is the constants for linear friction damping and  $\mathbf{F}$  is the forcing term which can be a function of space and time [2]. The equation has 3 unknown variables, the two of velocity and the pressure  $P$ .

The vorticity equation is obtained by taking curl from Navier Stokes equation, so

$$\frac{\partial \omega}{\partial t} + \mathbf{u} \cdot \nabla \omega = \nu \nabla^2 \omega - \frac{\omega}{\tau} + f \quad (3)$$

Where  $\omega = \nabla \times \mathbf{u}$  is vorticity in the z direction and  $f = \nabla \times \mathbf{F}$ . Given that  $\nabla \cdot \mathbf{u} = 0$ , then there is a scalar function  $\Psi(x, y) : \mathbb{R}^2 \rightarrow \mathbb{R}$  so that relation between velocity vector and stream function is obtained:

$$\mathbf{u} = \nabla \times \omega \quad or \quad \mathbf{u} = [u, v] = [\Psi_y - \Psi_x] \quad (4)$$

By substitution (2.4) to  $\omega = \nabla \times \mathbf{u}$ , we obtained relation between vorticity with streamfunction

$$\omega = -\nabla^2 \Psi \quad (5)$$

To reduce free parameter vorticity equation (3) we make dimensionless parameter with length scale  $L_0 = L/2\pi$ , velocity scale and time scale  $t_0 = L_0/U_0$  and dimensionless variable  $\tilde{x} = x/L_0$ ,  $\tilde{u} = u/L_0$ ,  $\tilde{\omega} = \omega t_0$ . Defining dimensionless variabels to vorticity equation, we obtain normal term vorticity equation are defined on domain  $0 < x < 2\pi$  and  $0 < y < 2\pi$ .

Reynold number  $Re = L_0 U_0 / \nu$  as famous parameter dimensionless number in fluid dynamic whose represent the ratio of inertia to viscosity and the large value is indicated of turbulent flow. Next, we obtain forcing term

$$f = F_0 \sin(ny) \text{ with } n \text{ is integer, } \beta = L_0^2 / \tau \nu .$$

Dimensionless vorticity equation without tilda term is obtained

$$\begin{aligned} & \frac{\partial \omega}{\partial t} + u \frac{\partial \omega}{\partial x} + v \frac{\partial \omega}{\partial y} \\ &= \frac{1}{Re} \left( \nabla^2 \omega - \beta \omega + n(n^2 + \beta) \sin(ny) \right) \end{aligned} \quad (6)$$

The equation (6) has 2 dimensionless parameters, they are  $\beta$  and Reynolds number. This is consistent with the main objective of reducing unknown variabels.

### 2.2 Equilibrium Solution

Equilibrium solution with forcing term  $f = F_0 \sin(ny)$  is obtained

$$\omega = n \sin(ny)$$

$$u = \cos(ny)$$

$$v = 0 \quad (7)$$

$$\psi = \frac{1}{n} \sin(ny)$$

### 2.3 Spectral Methods of Vorticity Equation

In the domain  $0 \leq x \leq 2\pi$  dan  $0 \leq y \leq 2\pi$ , every variable is defined as  $N \times N$  matrices. Numerically, the application of Fourier Series in vorticity equation is obtained

$$\omega(x, y, t) = \sum_{k=1}^{\frac{N}{2}} \sum_{l=1}^{\frac{N}{2}} \hat{\omega}_{k,l}(t) e^{ikx} e^{ily} \quad (8)$$

Where  $k, l$  are integer and  $\hat{\omega}_{k,l}$  are Fourier equation, and assumed that  $N$  is even. The coefficients Fourier can be found numerically with the used of the Fast Fourier Transform (FFT) dan the invers are Invers Fast Fourier Transform (IFFT). In Matlab we can use syntax `fft2` for FFT 2D and `ifft2` for IFFT 2D.

If vorticity is known than using the relation of vorticity and stream function, we obtained stream function 2D:

$$\psi_{k,l} = \frac{\hat{\omega}_{k,l}}{k^2 + l^2} \quad (9)$$

When  $k = l = 0$ , we defined that  $\psi_{0,0} = 0$ . By the same way, we find relation vorticity coefficient and velocity vector

$$\begin{aligned} \hat{u}_{k,l} &= il\hat{\psi}_{k,l} \\ \hat{v}_{k,l} &= -ik\hat{\psi}_{k,l} \end{aligned} \quad (10)$$

### 3. RESULTS AND DISCUSSION

#### 3.1 Linear Part

Linear part of the vorticity equation (8) is defined:

$$\frac{\partial \omega}{\partial t} = \frac{1}{Re} (\nabla^2 - \beta) \omega \quad (11)$$

The application Fourier Transform for (11) is obtained:

$$\frac{d\hat{\omega}_{k,l}}{dt} = -\frac{1}{Re} (k^2 + l^2 + \beta) \hat{\omega}_{k,l} \quad (12)$$

Using numerically Crank Nicholson method in (12) is defined:

$$\hat{\omega}_{k,l}^{n+1} = \frac{1 - \frac{\Delta t}{2Re} (k^2 + l^2 + \beta)}{1 + \frac{\Delta t}{2Re} (k^2 + l^2 + \beta)} \hat{\omega}_{k,l}^n \quad (13)$$

For our purposes, the Crank-Nicholson method will work well [1].

#### 3.2 The Simulation Without Forcing Term

This simulation will show how the initial conditions  $\omega(x, y, 0)$  of evolve with time regardless of the forcing term. Set Reynold number  $Re=10$ ,  $\beta=1$ , and initial condition  $\omega = \sin(y) \cdot \sin(x)$ .

Figure 1 shows that there is a damping effect. This is as expected that the solved linear part is diffusion equation. The diffusion equation has a numerical error, damping.

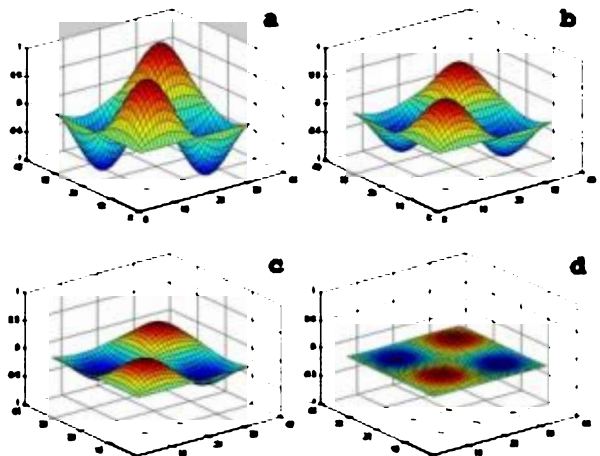


Figure 1 Simulation linear part without forcing term time by time.

#### 3.2 Linear and Nonlinear Part

The solving vorticity equation consist of linear and nonlinear parts with the application of transform Fourier:

$$\frac{d\hat{\omega}_{k,l}}{dt} = -(\mathbf{u} \cdot \nabla \omega)_{k,l} - \frac{1}{Re} ((k^2 + l^2 + \beta) \hat{\omega}_{k,l}) + \hat{f}_{k,l} \quad (14)$$

as  $\hat{f}$  is Fourier transform of  $f = 1/Re n(\beta + n^2) \sin(ny)$ . By using Crank Nicholson method, we solved the vorticity equation (14)

$$\hat{\omega}_{k,l}^{n+1} = \frac{\Delta t / 2 (3(u \cdot \nabla \omega))_{k,l}^n - ((u \cdot \nabla \omega))_{k,l}^n + (1 - \Delta t / 2Re (k^2 + l^2 + \beta)) \hat{\omega}_{k,l}^n + \Delta t \hat{f}_{k,l}}{1 + \Delta t / 2Re (k^2 + l^2 + \beta)} \quad (15)$$

The (15) equation will be used in Matlab [1].

#### 3.3 Simulation with Forcing Term

$$1/Re n(\beta + n^2) \sin(ny)$$

Set forcing term  $f = 1/Re n(\beta + n^2) \sin(ny)$ , initial condition  $\omega = n \sin(ny)$ ,  $Re = 60$  dan  $\beta = 32$ .

From Figure 2, the solution of vorticity shows that no changes time by time. This happen became bacause the initial condition is equilibrium solution.

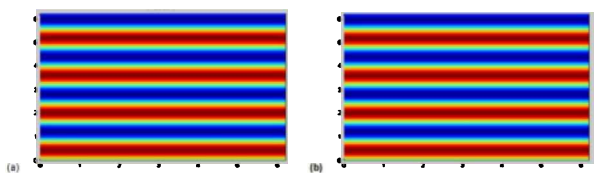


Figure 2 Simulation vorticity without forcing term.

#### 3.3 Simulation with Enlarged Forcing Term

Now, we show how stability solution work if forcing term enlarge, with Matlab use  $f = 1/Re * n * (\beta + n^2) \sin(ny) + 0.1 * randm(size(y))$ .

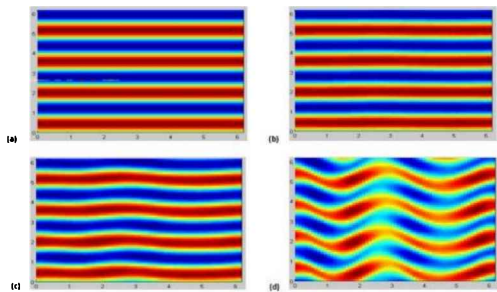


Figure 3 Simulation results with enlarged forcing term.

The above solution shows us that an enlarged forcing term will cause an unstable low. In a long time, it will cause turbulent flow. The turbulent nature of fluid flow depends on the size of Reynolds number parameter. The larger Reynolds number make the flow became faster turbulent.

#### 4. CONCLUSION

The application of the spectral method with Fourier series expansion can be carried out on 2D fluid flow. The application of this spectral method can be producing simulation that show a steady of fluid and can also show turbulence of fluid flow.

#### REFERENCES

- [1] Storey, B. D. (2012). Modelling 2D Turbulence. *Modelling Franklin W.Olin College of Engineering*, 1-10.
- [2] Zhou, Y., Luo, Z., & Teng, F. (2018). A Crank–Nicolson finite spectral element method for the 2D non-stationary Stokes equations about vorticity–stream functions. *Journal of Inequalities and Applications*, 2018(1), 320.

# DeltaEC prediction of pressure along a quarterwave thermoacoustic test rig

Dahlia Johari<sup>1</sup>, Ernie Mattokit<sup>1,2,\*</sup>, Fatimah Al Zahrah Mohd Saat<sup>1,2</sup>, Normah Mohd Ghazali<sup>3</sup>

<sup>1)</sup> Fakulti Kejuruteraan Mekanikal, Universiti Teknikal Malaysia Melaka,

Hang Tuah Jaya, 76100 Durian Tunggal, Melaka, Malaysia

<sup>2)</sup> Centre for Advanced Research on Energy, Universiti Teknikal Malaysia Melaka,

Hang Tuah Jaya, 76100 Durian Tunggal, Melaka, Malaysia

<sup>3)</sup> Faculty of Engineering, Universiti Teknologi Malaysia, 81310 Skudai, Johor, Malaysia

\*Corresponding e-mail: ernie@utem.edu.my

**Keywords:** Thermoacoustics; DELTAEC; standing wave

**ABSTRACT** – This paper reports thermoacoustic models for a standing wave type resonator with quarter wavelength design and frequencies of 14.2 Hz and 23.6 Hz. The models were solved using a thermoacoustic design software known as DELTAEC. The result of pressures distribution across the resonator was discussed based on the converged models. It was observed that by using 200 mm-long stack, pressure drops as much as 806.6 Pa and 834.3 Pa at stack's location of  $0.19\lambda$  and  $0.11\lambda$  for 14.2 Hz and 1.0 drive ratio. At the same frequency and drive ratio, longer stack causes higher pressure drop of 806.6 Pa as compared to shorter stack with 777.5 drops in pressure. Using 200 mm-long stack, pressure drops as much as 1204.9 Pa (23.6 Hz, drive ratio of 1.35) as compared to 806.6 Pa (14.2 Hz, drive ratio of 1.0).

## 1. INTRODUCTION

Thermoacoustics is a principle of science that can be used to produce a generator or a cooler if specific conditions are met [1,2]. At this moment, the fluid dynamics of flow inside the system is not well known, therefore investigation is needed in this direction [3]. However, investigating the fluid dynamics phenomena requires development of experimental rig that can produce the thermoacoustic field. Therefore, the system needs to be designed carefully at early stage of investigation to avoid too much expensive expenditure. In thermoacoustic community, this is usually done through a design software known as DeltaEC [4]. The design software helps designer to assemble parts into the model and then solve the model so that flow distribution inside the system is in accordance to the thermoacoustic principle. Although, the system has been designed by many in another parts of the world [1,2,5], but investigation here in Malaysia is very scarce. This paper reports an initial effort of modelling thermoacoustic resonator using DELTAEC for the purpose of the investigation of fluid dynamics of flow inside a standing

wave rig with quarter wavelength resonator.

## 2. METHODOLOGY

The standing wave thermoacoustic model was designed using a software known as DELTAEC. Figure 1 shows the segments that were defined in DELTAEC. It consists of a 'Begin' segment that allows the setting up of the initial values and operating conditions for the numerical modelling. The 'begin' segment is then connected to a 'duct' labelled 1 which represented loudspeaker.

The loudspeaker was connected to segment 2 named as a 'short duct'. This segment was to be considered the box for the loudspeaker to enclose the sound that came out of the loudspeaker and this sound was then channeled into the resonator through segment 3 (a conical duct). Segment 4 which was known as 'minor' is introduced into the model to represent losses of the flow when it was being forced into the resonator through the converging channel. The resonator started at segment 5 and ended at segment 15. The total length of the resonator was 6.6 m. The stack was located in segment 7 and it was sandwiched between segments 6 and 8. The presence of big number of segments in the resonator was due to the design requirement so that the rig could be used for two different flow frequencies. The schematic diagram shown in Figure 1 represents the 14.2 Hz resonator. Investigation was also done for another frequency of 23.6 Hz. The DELTAEC model for 23.6 Hz is as shown in Figure 2.

For high frequency of 23.6 Hz, the total length of the resonator was 3.8 m. Therefore, the total number of segments were now reduced to 10. In this 23.6 Hz model, the stack was located in segment 6 of Figure 2.

The models were solved for several cases as summarized in Table 1. The stack was located at two locations of  $0.19\lambda$  and  $0.11\lambda$  relative to the hard end of the resonator (pressure antinode location).

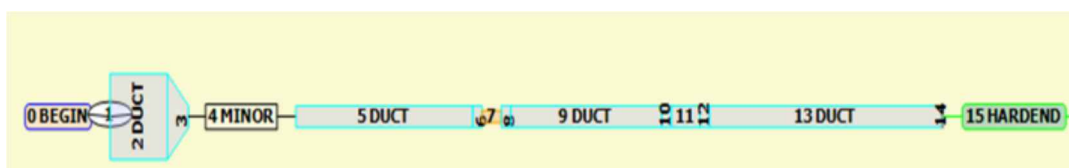


Figure 1 The 14.2 Hz thermoacoustic model.

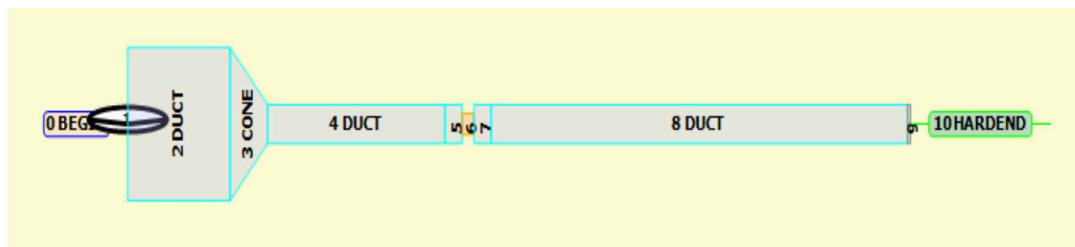


Figure 2 The 23.6 Hz thermoacoustic model.

Table 1 Summary of cases for thermoacoustics models.

Case	Frequency (Hz)	Stack's length (mm)	Stack's location
1	14.2	200	0.19λ
2	14.2	200	0.11λ
3	14.2	70	0.19λ
4	23.6	200	0.19λ
5	23.6	70	0.19λ

### 3. RESULTS

Figure 3 shows the pressure distribution plotted data for cases 1, 2 and 3, which is explained accordingly to Equation 1 and calculated from the pressure antinode at the right end of the resonator (segment 15).

$$p_1 = p_a e^{i\omega t} \cos(kx) \quad (1)$$

An empty resonator (without stack) leads to decrement in pressure with locations according to standing wave characteristics. The presence of 200 mm stack in the resonator leads to pressure drops depending on the location of the stack. When the stack is located at  $0.19\lambda$ , the pressure drop is appeared at segment 6. For location of  $0.11\lambda$ , the pressure starts dropping in segment 10. It is also observed that the pressure drops steeper than the pressure drop without stack. Pressure drops within the stack at  $0.19\lambda$  is found to be higher as much as 806.6 Pa than when the stack is placed at  $0.11\lambda$  with 834.3 Pa drops.

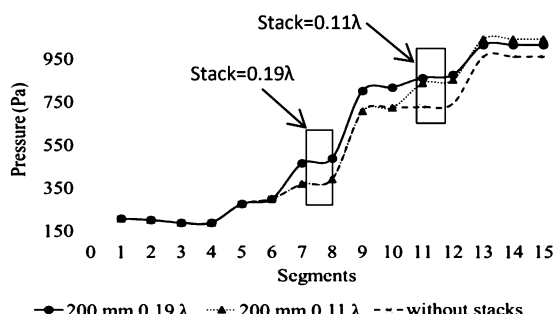


Figure 3 Pressure distribution for cases 1, 2 and 3 (14.2 Hz, drive ratio of 1.0).

Figure 4 depicted the effect of stack's length located at  $0.19\lambda$ , on the pressure distribution. As expected, the pressure drop is smaller with 777.5 Pa for case with shorter stack. The presence of the 70 mm long stack has very little impact on pressure distribution inside the resonator and seemed to be unnoticeable as compared to 200 mm length stack. Higher pressure drop of 806.6 Pa is attained throughout longer stack which might due to longer obstruction faced by the air flow. The boundary layer development might also be the reason that reducing

the air velocity, and yet dropping the pressure flow.

Figure 5 shows the pressure distribution data for two different flow frequencies and drive ratio. Pressure drop is not the function of the wavelength, but the wavelength is a function of frequency. For 23.6 Hz-designed system, pressure drops as much as 1204.9 Pa for 200 mm long stack, and 1112.5 Pa for 70 mm long stack respectively. However, for 14.2 Hz-designed system, less pressure drops are predicted as much as 806.6 Pa for 200 mm long stack, and 777.5 Pa for 70 mm long stack respectively. The predicted data from DELTAE is then used for designing thermoacoustic system for further study in this work.

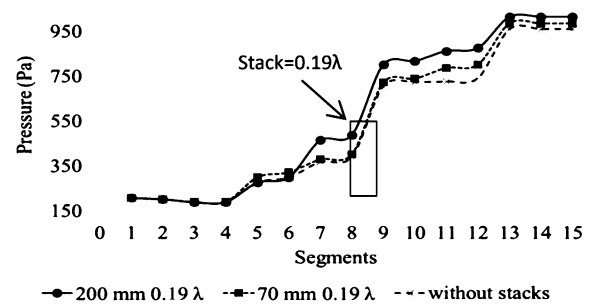


Figure 4 Pressure distribution for cases 1 and 3 (14.2 Hz, drive ratio of 1.0).

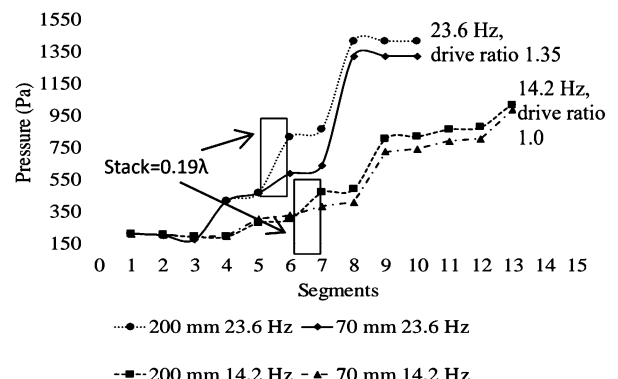


Figure 5 Pressure distribution for cases with different stack's length, frequency and drive ratio.

### 4. SUMMARY

The predicted work can be summarized as listed here:

- (a) By using 200 mm-long stacks, pressure drops as much as 806.6 Pa and 834.3 Pa at stack's location of  $0.19\lambda$  and  $0.11\lambda$  for 14.2 Hz and 1.0 drive ratio.
- (b) At the same frequency and drive ratio, longer stack causes higher pressure to drop of 806.6 Pa as compared to shorter stack with 777.5 drops in

pressure.

- (c) By using 200 mm-long stacks, pressure drops as much as 1204.9 Pa (23.6 Hz, drive ratio of 1.35) as compared to 806.6 Pa (14.2 Hz, drive ratio of 1.0).

## REFERENCES

- [1] Abdoulla-Latiwish, K. O., Mao, X., & Jaworski, A. J. (2017). Thermoacoustic micro-electricity generator for rural dwellings in developing countries driven by waste heat from cooking activities. *Energy*, 134, 1107-1120.
- [2] Sharify, E. M., & Hasegawa, S. (2017). Traveling-wave thermoacoustic refrigerator driven by a multistage traveling-wave thermoacoustic engine. *Applied Thermal Engineering*, 113, 791-795.
- [3] Mohd Saat, F., & Jaworski, A. (2017). Numerical predictions of early stage turbulence in oscillatory flow across parallel-plate heat exchangers of a thermoacoustic system. *Applied Sciences*, 7(7), 673.
- [4] Swift, G. W. (2017). *Thermoacoustics: A unifying perspective for some engines and refrigerators*. Springer.
- [5] Saechan, P., & Jaworski, A. J. (2019). Numerical studies of co-axial travelling-wave thermoacoustic cooler powered by standing-wave thermoacoustic engine. *Renewable Energy*, 139, 600-610.

# Continuous water quality monitoring for water hydraulics applications in food processor

Ahmad Anas Yusof<sup>1,2,\*</sup>, Suhaimi Misha<sup>1,2</sup>, Syarizal Bakri<sup>1,2</sup>

<sup>1)</sup> Fakulti Kejuruteraan Mekanikal, Universiti Teknikal Malaysia Melaka,

Hang Tuah Jaya, 76100 Durian Tunggal, Melaka, Malaysia

<sup>2)</sup> Centre for Advanced Research on Energy, Universiti Teknikal Malaysia Melaka,

Hang Tuah Jaya, 76100 Durian Tunggal, Melaka, Malaysia

\*Corresponding e-mail: [anas@utem.edu.my](mailto:anas@utem.edu.my)

**Keywords:** Water hydraulics; water quality; sustainability

**ABSTRACT** – This study proposes an application of water hydraulics technology in a food processor for a traditional cookies production. The objective of the study is to provide a hygienic and safe condition for water hydraulics that is used in a food processor test bed. The test bed is tested by using distilled water, and operated for duration of six months. The quality of the water used in the system is monitored and tested for total dissolved solids and pH value. The result shows that the pH value can be stabilized by using a filtration system, while total dissolved solids continues to accumulate throughout the test duration.

## 1. INTRODUCTION

Water hydraulics encourages a sustainable approach in power transmission. [1-3]. The objective of this project is to monitor the quality of a water-based pressure medium that is used to power up a food processor system. The hygienic, safe and low maintenance cost characteristics of water should provide interesting viewpoints due to concern over issues in hydraulic fluid contamination, flammability, disposal, and costly maintenance. Thus, the project focuses on the development of a traditional food processor apparatus powered by water hydraulics. The quality of the water used in the power transmission medium is tested for pH and TDS readings [4-7]. A test rig consists of two water hydraulics cylinders have been developed for the system and assembled into a robotic manipulator driven by a low-cost water hydraulic system. The cylinders have double acting configuration, with bore size and stroke of 40 mm and 125 mm respectively. The system resembles an automated cookies extrusion system, whereby the cookie dough is pressed to form a unique shape for the cookies [8].

## 2. METHODOLOGY

The test rig (Figure 1) has been setup to work in an automatic mode in producing batches of cookies continuously. The water qualities data obtained are on weekly period for nine months, from June 2017 to March 2018. A stainless steel in-line water filter has been assembled during the second run of the test, between January to March 2018. The samples are taken from the water tank after every usage. They are tested three times per week and taken before and after the experiment. A TDS-3 digital PH and TDS meter are used in the measurement of the water quality.

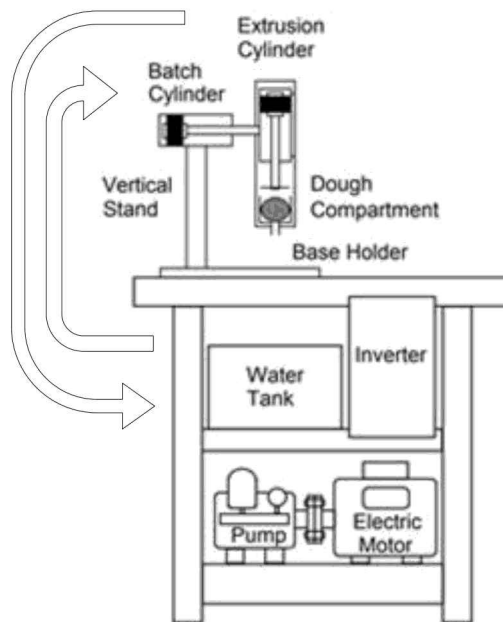


Figure 1 Water quality monitoring of water hydraulics flow.

## 3. RESULTS AND DISCUSSION

Figure 2 shows the result obtained for pH measurement. A control sample in the form of distilled water is used as a reference, where the pH reading of 7.66 is recorded. It is recorded that in between September and November 2017, the test rig shows an increase in pH values. This is noted when the experiment is conducted without the installation of a high-pressure water filter. The filter was later installed in November 2017. In between November and December 2017, the pH value is noted to be increased. It is possible that the pH measurement is high due to the prolong unused operation for the food processor. In general, however, the overall pH readings are acceptable to reduce corrosion effect. It is noted that corrosion will aggressively occur below pH 4. In between pH 4 to pH 10, corrosion is independent of pH value. [9-10]. In 2018, the test continues from January till March. It is noted that within that period, the pH values of the water is at a constant pH 7.8. The values coincide with the installation of the water filter and the constant usage of the system starting from January 2018.

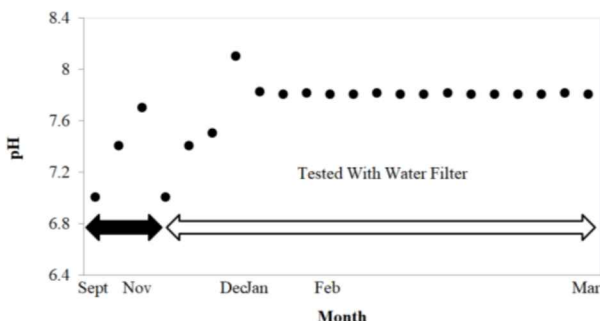


Figure 2 Water pH values for 6 months test duration.

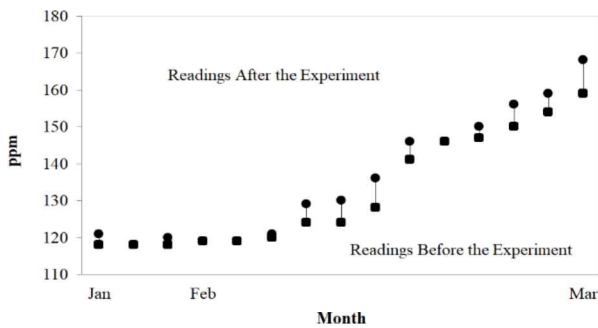


Figure 3 TDS readings for 3 months test duration.

Figure 3 shows the result for TDS readings. Within a span of 3 months, the samples are taken three times a week. For reference purposes the distilled water has been recorded having a TDS reading of 57 ppm. The lowest reading for the used water is of 118 ppm, which rises to 121 ppm after the operation of the food processor rig. Although a filter has been used in the system, it is noted that this filter is unable to reduce the TDS readings. The highest TDS reading is of 168 ppm (before) and 159 ppm (after). The increasing trend of TDS is noticeable in the graph, from February to March 2018.

#### 4. CONCLUSION

The quality of the water hydraulic system for a food processor system has been studied. It is suggested that the quality of the water filters should be monitored and replaced when necessary. In addition, dissolved solids may be introduced by the outside air that flows in when the volume of water is being reduced during the operation. Water is also capable of picking up copper, lead and other metals as it passes through pipes used to move the cylinder, during the extrusion process. High dissolve solids levels may also indicate the presence of harmful chemicals. It may also indicate that the origin of the scale build-up may originate from the valves and pipes, which is situated after the position of the filter. The increasing trend of dissolve solids is noticeable in

the food processor, which suggest for a more detailed study for the quality of the water in the system.

#### ACKNOWLEDGMENT

This work was funded by Ministry of Higher Education (MOHE) of Malaysia, under the Fundamental Research Grant Scheme (FRGS). FRGS/1/2016/TK03/FKM-CARE-F00317. The authors wish to thank Mr. Ariff Shazal bin Mohd Salim for his contribution in the simulation and experimentation of the project.

#### REFERENCES

- [1] Trostmann, E. (2000). *Tap water as a hydraulic pressure medium*. CRC Press.
- [2] Higgins, M. (1996). Water hydraulics—the real world. *Industrial Robot: An International Journal*, 23(4), 13-18.
- [3] Lim, G. H., Chua, P. S. K., & He, Y. B. (2003). Modern water hydraulics—the new energy-transmission technology in fluid power. *Applied Energy*, 76(1-3), 239-246.
- [4] Backe, W. (1999). Water-or oil-hydraulics in the future. In *The 6th Scandinavian Int. Conf. On Fluid Power-SICFP'99* (Vol. 51).
- [5] Yusof, A. A., Mat, S., & Din, A. T. (2013). Promoting sustainability through water hydraulic technology—The effect of water hydraulic in industrial scissor lift. *Applied Mechanics and Materials*, 315, 488-492.
- [6] Pham, P. N., Ito, K., & Ikeo, S. (2017). Energy saving for water hydraulic pushing cylinder in meat slicer. *JFPS International Journal of Fluid Power System*, 10(2), 24-29.
- [7] Yusof, A. A., Wasbari, F., Zakaria, M. S., & Ibrahim, M. Q. (2013). Slip flow coefficient analysis in water hydraulics gear pump for environmental friendly application. In *IOP Conference Series: Materials Science and Engineering* (Vol. 50, No. 1, p. 012016).
- [8] Yusoff, A. A., Misha, S., Md Isa, M. H., Wasbari, F., Ibrahim, M. Q., & Kasim, M. S. (2017). Low cost water hydraulics technology for Malaysian traditional cookies production. In *Proceedings of the 10<sup>th</sup> JFPS International Symposium on Fluid Power*, 1-8.
- [9] Salvato, J. A., Nemerow, N. L., & Agardy, F. J. (2003). *Environmental engineering*. John Wiley & Sons.
- [10] Vigil, K. M. (2003). *Clean water. As Introduction to Water Quality and Water Pollution Control*.



CENTRE FOR ADVANCED RESEARCH ON ENERGY  
Universiti Teknikal Malaysia Melaka

